MOTOR SYSTEM AND MOTOR DISEASES: FROM MOLECULES TO CIRCUITS

EDITED BY: Jing-Ning Zhu, Ying Shen and Paul G. Mermelstein

PUBLISHED IN: Frontiers in Cellular Neuroscience and Frontiers in Neural Circuits

frontiers Research Topics

ISSN 1664-8714
ISBN 978-2-88963-734-8
DOI 10.3389/978-2-88963-734-8

About Frontiers

Frontiers is more than just an open-access publisher of scholarly articles: it is a pioneering approach to the world of academia, radically improving the way scholarly research is managed. The grand vision of Frontiers is a world where all people have an equal opportunity to seek, share and generate knowledge. Frontiers provides immediate and permanent online open access to all its publications, but this alone is not enough to realize our grand goals.

Frontiers Journal Series

The Frontiers Journal Series is a multi-tier and interdisciplinary set of open-access, online journals, promising a paradigm shift from the current review, selection and dissemination processes in academic publishing. All Frontiers journals are driven by researchers for researchers; therefore, they constitute a service to the scholarly community. At the same time, the Frontiers Journal Series operates on a revolutionary invention, the tiered publishing system, initially addressing specific communities of scholars, and gradually climbing up to broader public understanding, thus serving the interests of the lay society, too.

Dedication to Quality

Each Frontiers article is a landmark of the highest quality, thanks to genuinely collaborative interactions between authors and review editors, who include some of the world's best academicians. Research must be certified by peers before entering a stream of knowledge that may eventually reach the public - and shape society; therefore, Frontiers only applies the most rigorous and unbiased reviews.
Frontiers revolutionizes research publishing by freely delivering the most outstanding research, evaluated with no bias from both the academic and social point of view. By applying the most advanced information technologies, Frontiers is catapulting scholarly publishing into a new generation.

What are Frontiers Research Topics?

Frontiers Research Topics are very popular trademarks of the Frontiers Journals Series: they are collections of at least ten articles, all centered on a particular subject. With their unique mix of varied contributions from Original Research to Review Articles, Frontiers Research Topics unify the most influential researchers, the latest key findings and historical advances in a hot research area! Find out more on how to host your own Frontiers Research Topic or contribute to one as an author by contacting the Frontiers Editorial Office: researchtopics@frontiersin.org

MOTOR SYSTEM AND MOTOR DISEASES: FROM MOLECULES TO CIRCUITS

Topic Editors:
Jing-Ning Zhu, Nanjing University, China
Ying Shen, Zhejiang University, China
Paul G. Mermelstein, University of Minnesota Twin Cities, United States

Movement is the basis for many forms of behaviors, and is tightly controlled by a hierarchical system containing cerebral cortex, basal ganglia, cerebellum, brainstem, and spinal cord. Each level of this hierarchy contributes to motor planning, motor initiation, motor execution, and motor coordination, respectively. However, they all receive continuous sensory inputs and generate accurate sensorimotor integrations that are necessary for both predictive and reflexive/servo controls of movements. The motor system contains various types of neurons with different morphological, neurochemical and electrophysiological properties, which are significantly dependent on many intracellular signaling molecules. Interestingly, these neurons are interconnected by intricate neuronal circuits for motor control, and even interacted with other non-motor systems to orchestrate somatic-nonsomatic integration. Furthermore, synaptic and neural plasticity endows motor system with amazing abilities for not only motor learning but also compensation and recovery from motor diseases, such as Parkinson's disease, ataxias, motion sickness and amyotrophic lateral sclerosis, etc. Therefore, the motor system is of great importance for understanding information processing, integrative function, and neural plasticity of the central nervous system.

The aim of this Research Topic is to discuss the latest advances in our understanding of motor system, motor control, motor learning and motor diseases from molecular, cellular, synaptic, circuit, and behavioral levels, especially in an integrative perspective.

Citation: Zhu, J.-N., Shen, Y., Mermelstein, P. G., eds. (2020). Motor System and Motor Diseases: From Molecules to Circuits. Lausanne: Frontiers Media SA.
doi: 10.3389/978-2-88963-734-8

Table of Contents

frontiers in Cellular Neuroscience

ORIGINAL RESEARCH
published: 08 August 2018
doi: 10.3389/fncel.2018.00241

Investigation of Behavioral Dysfunctions Induced by Monoamine Depletions in a Mouse Model of Parkinson's Disease

*Yong Li, Qian Jiao, Xixun Du, Mingxia Bi, Shuaishuai Han, Lingling Jiao and Hong Jiang**

Department of Physiology, Shandong Provincial Key Laboratory of Pathogenesis and Prevention of Neurological Disorders and State Key Disciplines, Physiology, Qingdao University Medical College, Qingdao University, Qingdao, China

Parkinson's disease (PD) is characterized not only by typical motor symptoms, but also by nonmotor symptoms in the early stages. In addition to the loss of dopaminergic (DAergic) neurons, progressive degenerations of noradrenergic (NA) and serotonergic (5-HT) neurons were also observed. However, the respective effects and interactions of these monoamine depletions on certain nonmotor symptoms are still largely unknown. In the present study, we performed selective depletions of NA, 5-HT and DA in mice by intraperitioneal injection of N-(2-chloroethyl)-N-ethyl-2-bromobenzylamine hydrochloride (DSP-4), 4-chloro-L-phenylalanine (pCPA) and 1-methyl-4-phenyl-1,2,3,6-tetrahydropyridine (MPTP), respectively. DSP-4 led to a 34% decrease in the number of NAergic neurons in the locus coeruleus, and MPTP led to a 30% decrease in the number of DAergic neurons in the substantia nigra. Although there was no obvious change in the number of 5-HTergic neurons in the dorsal raphe nucleus after pCPA treatment, the levels of 5-HT and its metabolite in the frontal cortex and hippocampus were reduced, respectively. Locomotor activity deficit was induced by DA depletion and a decrease in traveled distance was potentiated by additional NA depletion. Despair-associated depressive-like behavior could be observed in every group. Anxiety states emerged only from the combined depletion of two or three monoamines. However, combined depletion of the three monoamines dramatically induced anhedonia, and it could also aggravate the depressive-like and anxiety behavior. Furthermore, NA depletion significantly reduced spatial learning and memory ability, which was not enhanced by additional 5-HT or DA depletion. Our data highlighted the interactive role of NA, 5-HT and DA in the motor, emotional and cognitive deficits, providing new insight into the complex orchestration of impaired monoaminergic systems that related to the pathology of PD.

Keywords: Parkinson's disease, dopamine, noradrenaline, serotonin, motor symptoms, nonmotor symptoms

OPEN ACCESS

Edited by:
Jing-Ning Zhu,
Nanjing University, China

Reviewed by:
Yong Shen,
University of Science and Technology of China, China
Qiaoling Cui,
Northwestern University, United States

****Correspondence:***
Hong Jiang
hongjiang@qdu.edu.cn

Received: *24 March 2018*
Accepted: *17 July 2018*
Published: *08 August 2018*

Citation:
Li Y, Jiao Q, Du X, Bi M, Han S, Jiao L and Jiang H (2018) Investigation of Behavioral Dysfunctions Induced by Monoamine Depletions in a Mouse Model of Parkinson's Disease. Front. Cell. Neurosci. 12:241. doi: 10.3389/fncel.2018.00241

INTRODUCTION

Parkinson's disease (PD) is a common neurodegenerative disorder characterized by the loss of dopaminergic neurons in the substantia nigra (SN) and depletion of dopamine (DA) in the striatum. However, the depletion of DA *per se* is unable to cause the manifestation of both motor and nonmotor features of PD observed in different animal models

(Wolters, 2009; Palmeri et al., 2017). Recently, increasing evidence implicated that other monoaminergic systems such as noradrenergic (NA) and serotonergic (5-HT) are also affected in the process of PD (Fornai et al., 2007; Kish et al., 2008). The degeneration of these neurons has been shown to play essential roles in the emergence of various clinical symptoms (Delaville et al., 2012). However, a specific role for each monoamine and their interaction in PD are still largely undetermined.

The widely accepted Braak's staging of PD has proposed a six-stage scheme that a characteristic Lewy pathology initially occurs in the lower brainstem and spreads an ascending course to the higher cortical structures (Braak et al., 2003). The following studies have reported that the pathology in regions adjacent to the medulla oblongata including the locus ceruleus (LC), a principal site of NA neurons, and the dorsal raphe nuclei (DRN), a main site of 5-HT neurons, occur at stage 1 or 2, whereas the SN neuronal loss occurs at stage 3 or 4 and induces a striking motor symptom (Braak et al., 2004; Burke et al., 2008). Nevertheless, the neuronal loss of NA has shown to be a greater extent than DA loss in PD patients (Buchman et al., 2012). A previous study showed that there were 83% loss of NA neurons and 78% loss of DA neurons in the PD brains (Zarow et al., 2003). Although the loss extent of 5-HT neurons in the DRN is under debate, 5-HT concentrations in the putamen and caudate nucleus of dorsal striatum are highly reduced by 51–66% in PD patients (Kish, 2003; Kish et al., 2008).

Several studies have reported a correlation between the severity of NA, 5-HT, and DA depletions and worsening of PD neurological symptoms (Delaville et al., 2012; Faggiani et al., 2015). Because of the widespread projections, LC NAergic system dominates a variety of neural circuits through releasing NA into the distinct brain regions, such as olfactory bulb, hippocampus, subthalamic nucleus, striatum and cerebral cortex (Benarroch, 2009). The loss of NA may account for many nonmotor symptoms experienced by PD patients and animal models, including cognitive impairment (Del Tredici and Braak, 2013), sleep disorder (Kalaitzakis et al., 2013), depression and anxiety (Remy et al., 2005), and sympathetic autonomic failure (Palma and Kaufmann, 2014). Moreover, NA lesions in the LC also affects firing activity of the SN, which decreases DA release into the striatum, thus leading to the typical motor deficits associated with PD symptoms (Srinivasan and Schmidt, 2003; Masilamoni et al., 2017). In addition, a range of studies have reported that 5-HT plays a vital role in the development of depression and anxiety, which are recognized as other landmarks of the disease. For example, depression appears in about 45% of PD patients and considerably reduces the patient's quality of life (Reijnders et al., 2008). 5-HTergic innervations originate from the medial and dorsal RN, and that mainly projects to the basal ganglia, such as striatum. The neurodegeneration of 5-HT neurons leads to a defect of limbic function, a detrimental process which is not only involved in the motor control but also in the regulation of emotion and cognition (Teissier et al., 2017).

Since NA, 5-HT and DA have a prominent role in both pathophysiology process and phenotypical aspect of PD, we, therefore, investigated the respective effects and interactions of these monoamine depletions on motor and nonmotor symptoms including depressive-like, anxiety and cognitive dysfunctions in mice with serial neurotoxic monoamine lesions.

Abbreviations: DSP-4, N-(2-chloroethyl)-N-ethyl-2-bromobenzylamine; pCPA, 4-Chloro-D-phenylalanine; MPTP, 1-Methyl-4-phenyl-1,2,3,6-tetrahydropyridine; NA, noradrenaline; MHPG, 3-Methoxy-4-hydroxyphenylglycol; 5-HT, serotonin; 5-HIAA, 5-Hydroxyindoleacetic acid; DA, dopamine; DOPAC, 3,4-Dihydroxyphenylacetic acid; HVA, homovanillic acid; LC, locus ceruleus; DRN, dorsal raphe nuclei; SN, substantia nigra; HPLC, high performance liquid chromatography; DβH, dopamine β-hydroxylase; SERT, serotonin transporter; TH, tyrosine hydroxylase; 6-OHDA, 6-hydroxydopamine; PD, Parkinson's disease.

MATERIALS AND METHODS

Animals

Male C57BL/6 mice (8 weeks of age) were purchased from the Cavens Laboratory Animal Center (No. 201608441, Changzhou, China). All animals were maintained on a 12:12 h light/dark cycle under constant temperature (22°C) with food and water available *ad libitum*. The mice were allowed for acclimation in a colony room for 2 weeks and handled daily before starting experiments. This study was carried out in accordance with the recommendations of the National Institutes of Health Guide for the Care and Use of Laboratory Animals, and the protocol was approved by the Animal Ethical Committee of Qingdao University. Total 192 mice were randomly divided into eight groups, comprising a saline-treated group, and NA, 5-HT, DA, NA/5-HT, NA/DA, 5-HT/DA as well as NA/5-HT/DA depleted group ($n = 24$ in each group). To avoid interference between multiple test performances, each group was divided into three subgroups, which contained 8 mice. Animals in the first subgroup were used for open field test, sucrose preference test and forced swim test; mice in the second subgroup were underwent bar test, elevated plus maze and tail suspension tests; mice in the third subgroup were used for the Morris water maze assay. Afterwards, 12 mice from each group were randomly selected for tissue content determination, and another 12 mice for immunohistochemical analysis.

Drug Administration for Monoamine Depletions

NA depletion was obtained using N-(2-chloroethyl)-N-ethyl-2-bromobenzylamine (DSP-4, C8417, Sigma), a selective neurotoxin for NAergic projections originating from the LC. DSP-4 was dissolved in saline and intraperitoneally (i.p.) injected at a dose of 50 mg/kg according to the work (Grzanna et al., 1989). 5-HT depletion was achieved using 4-Chloro-D-phenylalanine (pCPA, C9419, Sigma), a selective inhibitor of 5-HT synthesis. pCPA was dissolved in saline and i.p. injected at a dose of 300 mg/kg during three consecutive days. This procedure was performed 3 days after DSP-4 treatment based on the occurrence of pathological deficits of NAergic system (Heal et al., 1993). 1-Methyl-4-phenyl-1,2,3,6-tetrahydropyridine (MPTP, M0896, Sigma), a neurotoxin to dopaminergic neurons in the SN, was dissolved in saline and injected in a subacute regimen (i.p., 25 mg/kg/day for 5 days) following the last pCPA injection. The vehicle-treated mice were administrated

using saline in a comparable volume with the same protocol. The depletion of NA and/or 5-HT was executed prior to DA depletion according to the sequential Lewy pathology presented in PD patients (Braak et al., 2003). Behavioral tests were initiated one week after the last injection of MPTP or saline (**Figure 1**).

Behavioral Measurements

Open Field Test (OFT)

OFT was achieved between 9:00 a.m. and 1:00 p.m. in an isolated room, which was used to assess the spontaneous locomotor activity of animals. All mice were habituated for 30 min before the test. Individual mouse was placed in a square arena (27.3 × 27.3 × 20.3 cm) equipped with a camera. The test was lasted for 10 min. Total traveled distance and rearing were analyzed using an EthoVision XT video-tracking software (Noldus, Netherlands).

Sucrose Preference Test (SPT)

Sucrose consumption was conducted to evaluate anhedonia in rodents. Each mouse was individually housed in a separate cage and allowed free access to two bottles of water in the first day morning. In the second day morning, one bottle of water was changed to 1% sugar for another day. In the third day morning, the mice were deprived food and water until the lights turned off at 7:00 p.m., followed by supplying 1% sucrose and water in two bottles for 2 h. The position of the two bottles was always switched in the intermediate time. The weight of the bottles was measured before and after the test. Sucrose preference (%) = 100 × sucrose intake/(sucrose intake + water intake).

Bar Test

The degree of catalepsy resulting from monoamine depletions was measured using the bar test by placing mice with both forepaws on a horizontal bar (diameter: 6 mm), which was set up 4.5 cm above the floor. The latency was recorded as the mouse grabbed the bar until their forepaws touched the floor or climbed over the bar. The cut-off of the test was set at 60 s.

Forced Swim Test (FST)

FST is the most commonly used method for monitoring despair-associated depression in rodents. Mice were individually forced to swim in a plastic cylindrical container (25 × 10 cm) irrigated with fresh water (25 ± 1°C) to a height of 15 cm. The duration of immobility was recorded over a period of 5 min. A mouse was judged as immobility when without struggling or only the rear feet slightly slide to keep its head above the water.

Tail Suspension Test (TST)

TST is another typical assay for evaluation of the despair-associated depressive behavior. Using adhesive tape to bind the tip of mice tail, each mouse was suspended 25 cm above the floor. The duration of immobility was measured manually during a total 5 min of test. A mouse was defined as immobility when minimal movements of the front legs instead of the hind legs. Furthermore, small oscillations and pendulum like swings which gained momentum from the earlier mobility were also consider as immobility (Zhang et al., 2017).

Elevated Plus Maze (EPM)

EPM was used to assay anxiety-related behavior. An applied apparatus is composed of two open arms and two closed arms (29 × 8 cm, with walls of 16 cm height), which was set up 30 cm above the floor. Each mouse was placed in the central square of the maze and allowed to explore the elevated plus maze for 5 min. The animals' movement track was recorded with EthoVision XT video-tracking software (Noldus, Netherlands). The percentage of time spent in open arms and numbers of arm entries were analyzed. Each arm was cleaned with alcohol before the next test.

Water Maze Training and Spatial Memory

Morris water maze test was performed to assess the spatial learning and memory skill of mice as described previously (Cui et al., 2016). The circular water maze pool (120 cm in diameter, 50 cm in depth) contained a movable platform (15 cm diameter), which was submerged 1 cm below the water surface. During training, each mouse will learn how to escape from the water by climbing the platform; if the mouse failed to find the platform within 60 s, it will be guided onto the platform by experimenter and allowed to stay for 30 s. Each mouse was subjected to four training trials each day. On day 5 and day 7 of training trials, the platform was removed and a probe test was performed to assay the spatial memory ability of mice. Animals' movement tracks in the training trials and the probe tests were recorded using an automated tracking system (Actimetrics, USA). The escape latency and the times crossing the platform were analyzed.

Biochemical Determination of Monoamine Depletion

In order to validate the experimental model, tissular concentrations of the three monoamines as well as the metabolite 3,4-Dihydroxyphenylacetic acid (DOPAC) and homovanillic acid (HVA) of DA, the metabolite 3-Methoxy-4-hydroxyphenylglycol (MHPG) of NA, the metabolite 5-Hydroxyindoleacetic acid (5-HIAA) of 5-HT were determined by high performance liquid chromatography (HPLC) with electrochemical detection, as previously described (Shen et al., 2017). At the end of behavioral tests, 12 randomly selected mice per group were decapitated, and their brains were rapidly dissected. Both sides of the frontal cortex, hippocampus and striatum were weighed and homogenized in 300 μl liquid A (0.4 M $HClO_4$) and centrifuged at 12,000 rpm for 30 min at 4°C. Eighty microliter of supernatant was mixed with 40 μl liquid B (20 mM potassium citrate, 300 mM K_2HPO_4, 2 mM disodium EDTA, and 2 octane sulfonic acid plus 7% methanol) and filtered through a 0.22 μm filter (Millipore, Germany). An electrochemical detector (Waters, USA) was operated in a screen mode. The flow rate was kept constant at 1 mL/min. The results were expressed as ng/g wet weight of the brain tissue.

Immunofluorescence Labeling and Stereological Quantification

Another 12 mice per group were deeply anesthetized by 8% chloral hydrate, followed by ventricular perfusion with normal saline and 4% paraformaldehyde solution in 0.1 M PBS. Frozen brain blocks were coronally sectioned to 20 μm using a freezing microtome (Leica CM1900, Germany). After

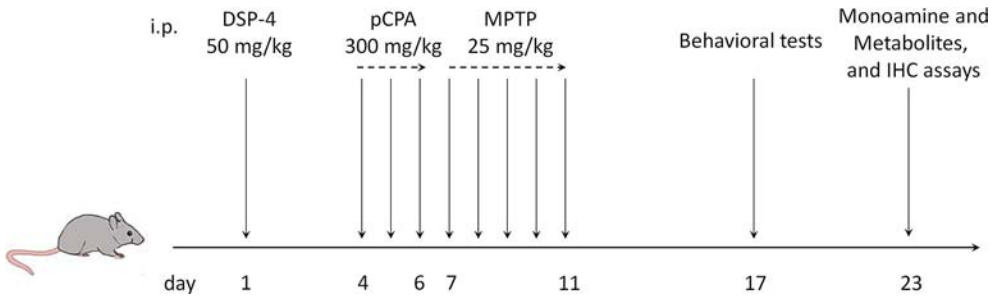

FIGURE 1 | Time course of drug injection, behavior tests and neurochemical analyses. i.p., intraperitoneal injection; DSP-4, N-(2-chloroethyl)-N-ethyl-2-bromobenzylamine hydrochloride; MPTP, 1-Methyl-4-phenyl-1,2,3,6-tetrahydropyridine; pCPA, 4-chloro-L-phenylalanine.

rinse with PBST (0.3% Triton-100 in 0.01 M PBS), sections were blocked by 10% goat serum for 30 min and then incubated with primary antibodies, dopamine beta-hydroxylase (DβH, ab209487, Abcam, 1:1,000), serotonin transporter (SERT, AB9726, Millipore, 1:1000) and tyrosine hydroxylase (TH, AB152, Millipore, 1:2000) for overnight at 4°C. Subsequently, the second antibody fluorophore-conjugated donkey anti-rabbit IgG H&L (Alexa flour 555, Invitrogen, 1:500) was added to incubate for 2 h at room temperature. After three times rinse, the sections were mounted with 70% glycerol. Stereological quantification was performed as previously described in our laboratory (Zhang et al., 2015). The number of DβH-, SERT- and TH-immunoreactive (ir) neurons was counted by optical fractionator unbiased stereological method using a fluorescent microscope (Zeiss, Germany) with Stereo Investigator (Micro Bright Field, USA).

Statistical Analyses

All statistical analyses were performed using GraphPad Prism Software (version 5). Escape latencies in Morris water maze for the individual trial and biochemical data were analyzed by two-way analysis of variance (ANOVA) with repeated measures. Statistical analyses for the rest of the data were performed by one-way ANOVA with Bonferroni's multiple comparison tests. All data were shown as mean ± SEM. $p < 0.05$ is considered statistically significant.

RESULTS

Monoamine Contents and Turnover Are Altered by Selective Drug Administrations

The tissue contents of NA, 5-HT and their metabolites in the frontal cortex and hippocampus, as well as DA and its metabolites in the frontal cortex and striatum in eight groups were quantified by post-mortem HPLC.

DSP-4 is a selective neurotoxin that is widely used to lower brain NA to investigate the functions of the central noradrenergic system (Grzanna et al., 1989). In this study, DSP-4 injection dramatically decreased by 60% tissue level of NA [one-way ANOVA, $F_{(7, 72)} = 28.61$, $p < 0.001$, **Table 1**) and by 36% tissue level of MHPG [$F_{(7, 72)} = 8.54$, $p < 0.05$] in the frontal cortex, and decreased by 58% of NA [$F_{(7, 69)} = 25.82$, $p < 0.001$] and by 33% of MHPG [$F_{(7, 69)} = 6.68$, $p < 0.05$] in the hippocampus compared to saline-treated animals. Notably, significantly decreased NA and MHPG levels in the frontal cortex and hippocampus were also observed in DSP-4/pCPA, DSP-4/MPTP and DSP-4/pCPA/MPTP groups [two-way ANOVA, $F_{(3, 76)} = 40.50$ and $F_{(3, 72)} = 35.49$, $p < 0.001$, respectively]; however, these decreased values were similar to that in DSP-4 group, suggesting that pCPA and/or MPTP injections did not modify by themselves tissue content of NA and its metabolite in DSP-4-injected mice. A ratio of MHPG/NA represents the metabolic rate of NA. Furthermore, we found that DSP-4 treatment significantly increased MHPG/NA ratios in the frontal cortex and hippocampus [$F_{(7, 66)} = 9.13$ and $F_{(7, 70)} = 7.43$, $p < 0.05$, respectively], suggesting that DSP-4 has an effect on NA metabolism.

PCPA has been used extensively to target serotonergic afferents and reduce overall 5-HT in the rodent brain (Kornum et al., 2006). PCPA injection significantly decreased by 53% tissue level of 5-HT [one-way ANOVA, $F_{(7, 72)} = 35.74$, $p < 0.001$, **Table 2**] and by 73% tissue level of 5-HIAA [$F_{(7, 72)} = 27.31$, $p < 0.001$] in the frontal cortex, and decreased by 57% of 5-HT [$F_{(7, 69)} = 38.32$, $p < 0.001$] and by 76% of 5-HIAA [$F_{(7, 69)} = 45.64$, $p < 0.001$] in the hippocampus compared to saline-treated animals. Similarly, significantly decreased 5-HT and 5-HIAA levels in the frontal cortex and hippocampus were also observed in DSP-4/pCPA, pCPA/MPTP and DSP-4/pCPA/MPTP groups when compared to saline-treated group [two-way ANOVA, $F_{(3, 80)} = 23.46$ and $F_{(3, 78)} = 36.14$, $p < 0.001$, respectively]; however, these decreased values were similar to that in pCPA group, suggesting that DSP-4 and/or MPTP injections did not modify by themselves tissue content of 5-HT and its metabolite compared to pCPA-injected mice. A ratio of 5-HIAA/5-HT represents the metabolic rate of 5-HT. We found that the ratio of 5-HIAA/5-HT was significantly decreased in the frontal cortex and hippocampus after pCPA treatment [$F_{(7, 72)} = 10.75$, $p < 0.05$ and $F_{(7, 69)} = 18.48$, $p < 0.01$], suggesting that pCPA could decrease the metabolism of 5-HT.

The neurotoxin MPTP is the most commonly used to damage dopaminergic system in mice for PD model (Blume et al., 2009). The treatment of MPTP induced a significant decreased tissue levels of DA [78%, $p < 0.001$, one-way ANOVA, $F_{(7, 65)} = 43.81$, **Table 3**], DOPAC [44%, $F_{(7, 65)} = 33.96$,

TABLE 1 | Tissue contents of NA and MHPG (represents in ng/g of tissue) in the frontal cortex and hippocampus of mice brain were measured by HPLC, and the ratios of MHPG/NA were analyzed after DSP-4, pCPA, and MPTP administration respectively.

Treatments	Frontal cortex			Hippocampus		
	NA	MHPG	MHPG/NA	NA	MHPG	MHPG/NA
Saline ($n = 12$)	224.3 ± 16.1	57.3 ± 3.5	0.25 ± 0.03	303.7 ± 22.1	104.6 ± 12.6	0.34 ± 0.07
DSP-4 ($n = 10$)	88.5 ± 7.6***	36.8 ± 4.9*	0.43 ± 0.09*	125.4 ± 19.4***	69.5 ± 10.6*	0.55 ± 0.09*
pCPA ($n = 12$)	212.7 ± 18.4	46.9 ± 2.7	0.21 ± 0.04	284.9 ± 26.6	106.7 ± 14.2	0.37 ± 0.04
MPTP ($n = 9$)	228.5 ± 20.6	45.1 ± 4.5	0.19 ± 0.05	315.8 ± 20.9	89.2 ± 9.5	0.28 ± 0.04
DSP-4/pCPA ($n = 11$)	79.5 ± 9.4***	39.6 ± 3.8*	0.51 ± 0.11*	127.2 ± 15.5***	63.2 ± 5.3*	0.49 ± 0.07*
DSP-4/MPTP ($n = 9$)	91.7 ± 8.4***	45.4 ± 3.1	0.48 ± 0.05*	131.5 ± 16.9***	75.6 ± 8.5*	0.57 ± 0.08*
pCPA/MPTP ($n = 10$)	201.5 ± 23.4	53.6 ± 6.7	0.26 ± 0.07	296.4 ± 36.7	92.7 ± 7.3	0.31 ± 0.03
DSP-4/pCPA/MPTP ($n = 11$)	66.7 ± 10.4***	32.7 ± 5.1**	0.49 ± 0.06*	116.3 ± 20.1***	78.2 ± 7.9*	0.67 ± 0.12**

*All values are expressed as mean ± S.E.M. *p < 0.05, **p < 0.01, ***p < 0.001 in comparison with the saline group.*

TABLE 2 | Tissue contents of 5-HT and 5-HIAA (represents in ng/g of tissue) in the frontal cortex and hippocampus of mice brain were measured by HPLC, and the ratios of 5-HIAA/5-HT were analyzed after DSP-4, pCPA, and MPTP administration respectively.

Treatments	Frontal cortex			Hippocampus		
	5-HT	5-HIAA	5-HIAA/5-HT	5-HT	5-HIAA	5-HIAA/5-HT
Saline (n=12)	443.1 ± 19.7	275.6 ± 22.4	0.62 ± 0.11	379.2 ± 24.5	375.2 ± 25.9	0.99 ± 0.14
DSP-4 ($n = 10$)	447.3 ± 19.9	349.5 ± 21.3	0.78 ± 0.15	353.4 ± 22.7	427.1 ± 33.6	1.21 ± 0.21
pCPA ($n = 12$)	205.9 ± 33.7***	74.8 ± 9.2***	0.36 ± 0.05*	164.5 ± 24.9***	87.9 ± 5.9***	0.53 ± 0.08**
MPTP ($n = 9$)	435.1 ± 19.6	253.3 ± 17.3	0.58 ± 0.09	366.9 ± 28.8	325.7 ± 23.8	0.89 ± 0.11
DSP-4/pCPA ($n = 11$)	182.6 ± 37.5***	123.8 ± 10.5***	0.67 ± 0.09	166.6 ± 20.7***	153.1 ± 11.2***	0.91 ± 0.18
DSP-4/MPTP ($n = 9$)	419.3 ± 19.1	255.6 ± 14.2	0.61 ± 0.13	339.7 ± 28.4	285.7 ± 18.4	0.84 ± 0.07
pCPA/MPTP ($n = 10$)	191.8 ± 34.7***	79.3 ± 4.8***	0.41 ± 0.06*	171.8 ± 24.0***	81.3 ± 9.2***	0.47 ± 0.05**
DSP-4/pCPA/MPTP ($n = 11$)	178.5 ± 37.7***	69.4 ± 5.6***	0.39 ± 0.03*	163.2 ± 27.4***	74.3 ± 5.5***	0.45 ± 0.07**

*All values are expressed as mean ± S.E.M. *p < 0.05, **p < 0.01, ***p < 0.001 in comparison with the saline group.*

$p < 0.001$] and HVA [46%, $F_{(7, 65)} = 39.42$, $p < 0.001$] in the striatum but not in the frontal cortex. The additional treatment of DSP-4 and/or pCPA to MPTP further aggravated the depletion of DA and its metabolite contents in the striatum. It showed that the contents were decreased by 43% for DA, 46% for DOPAC and 57% for HVA in DSP-4/MPTP group, by 34% for DA, 38% for DOPAC and 57% for HVA in pCPA/MPTP group, and by 58% for DA, 52% for DOPAC as well as 64% for HVA in DSP-4/pCPA/MPTP group compared to MPTP group [$F_{(7, 67)} = 31.64$, $p < 0.001$], respectively. Consistently, a ratio of (DOPAC+HVA)/DA reflecting the metabolic rate of DA did not differ in the frontal cortex between MPTP group and saline group, while it was increased in DSP-4/pCPA/MPTP group [$F_{(7, 63)} = 19.94$, $p < 0.01$]. In striatum, (DOPAC+HVA)/DA ratio was significantly increased after MPTP treatment [$F_{(7, 68)} = 17.62$, $p < 0.01$], suggesting that MPTP could increase striatal DA metabolism.

Effects of Monoamine Depletions on Locomotor Activity

Consistent with previousstudies (Blume et al., 2009; Li et al., 2016), MPTP-induced DA depletion significantly decreased a total distance of spontaneous movement by 22% in the OFT compared to saline-treated mice [one-way ANOVA, $F_{(7, 51)} = 8.81$, $p < 0.05$, **Figure 2A**]. Depletion of NA and/or 5-HT did not affect locomotor activity. However, additional depletion of NA but not 5-HT potentiated the decreased total distance induced by DA depletion (with 29% reduction compared to DA-depleted mice, $p < 0.05$). Additionally, MPTP-induced DA depletion also decreased the number of rearing by 49% [one-way ANOVA, $F_{(7, 51)} = 19.23$, $p < 0.01$, **Figure 2B**), and similar decreases in rearing number could be seen in DSP-4/MPTP, pCPA/MPTP and DSP-4/pCPA/MPTP groups.

In addition to the locomotor activity, we determined whether monoaminergic depletions could promote catalepsy using the bar test. DA depletion significantly increased catalepsy time compared to saline-treated animals [one-way ANOVA, $F_{(7, 56)} = 14.33$, $p < 0.01$, **Figure 2C**]. Depletion of NA and/or 5-HT did not either trigger catalepsy or potentiate the increased catalepsy induced by DA depletion.

Effects of Monoamine Depletions on Depressive-Like Disorder and Anxiety Behavior

To evaluate mood behavioral disabilities we used different common tests. In SPT, mice with single depletion of NA or 5-HT or DA did not alter the sucrose consumption compared to saline-treated animals. However, only combined depletions of

TABLE 3 | Tissue contents of DA, DOPAC, and HVA (represents in ng/g of tissue) in the frontal cortex and striatum of mice brain were measured by HPLC, and the ratios of (DOPAC + HVA)/DA were analyzed after DSP-4, pCPA, and MPTP administration respectively.

Treatments	Frontal cortex				Striatum			
	DA	DOPAC	HVA	(DOPAC+HVA) /DA	DA	DOPAC	HVA	(DOPAC+HVA) /DA
Saline ($n = 12$)	521.7 ± 45.8	32.8 ± 2.6	48.9 ± 3.1	0.15 ± 0.06	7,020 ± 551.4	617.7 ± 56.8	997.8 ± 78.2	0.23 ± 0.04
DSP-4 ($n = 10$)	506.4 ± 27.9	30.3 ± 4.3	43.1 ± 5.3	0.14 ± 0.05	6,742 ± 600.7	553.8 ± 58.4	889.9 ± 96.3	0.21 ± 0.08
pCPA ($n = 12$)	531.5 ± 28.4	34.4 ± 2.9	56.5 ± 6.1	0.17 ± 0.05	6,574 ± 391.6	698.2 ± 67.3	941.4 ± 88.5	0.25 ± 0.08
MPTP ($n = 9$)	496.9 ± 44.1	36.8 ± 5.1	69.5 ± 5.6	0.21 ± 0.07	1,494 ± 155.8***	347.9 ± 25.7***	543.5 ± 63.1***	0.59 ± 0.12**
DSP-4/pCPA ($n = 11$)	507.5 ± 44.6	28.9 ± 3.5	43.6 ± 4.4	0.14 ± 0.06	7,175 ± 532.4	603.7 ± 67.6	897.8 ± 74.4	0.21 ± 0.04
DSP-4/MPTP ($n = 9$)	473.9 ± 20.5	34.1 ± 3.6	52.1 ± 3.7	0.18 ± 0.06	847.7 ± 71.0***##	189.1 ± 23.1***	235.6 ± 21.3***	0.51 ± 0.11**
pCPA/MPTP ($n = 10$)	474.8 ± 28.9	31.7 ± 2.9	42.6 ± 3.2	0.15 ± 0.04	977.2 ± 105.6***#	213.3 ± 24.4***	231.2 ± 18.4***	0.45 ± 0.12*
DSP-4/pCPA/MPTP ($n = 11$)	127.1 ± 15.9***	10.7 ± 1.2***	24.6 ± 2.1**	0.28 ± 0.08**	620.4 ± 81.3***###	165.4 ± 19.9***	193.2 ± 15.7***	0.57 ± 0.14**

*All values are expressed as mean ± S.E.M. *$p < 0.05$, **$p < 0.01$, ***$p < 0.001$ in comparison with saline group; #$p < 0.05$, ##$p < 0.01$, ###$p < 0.001$ in comparison with MPTP group.*

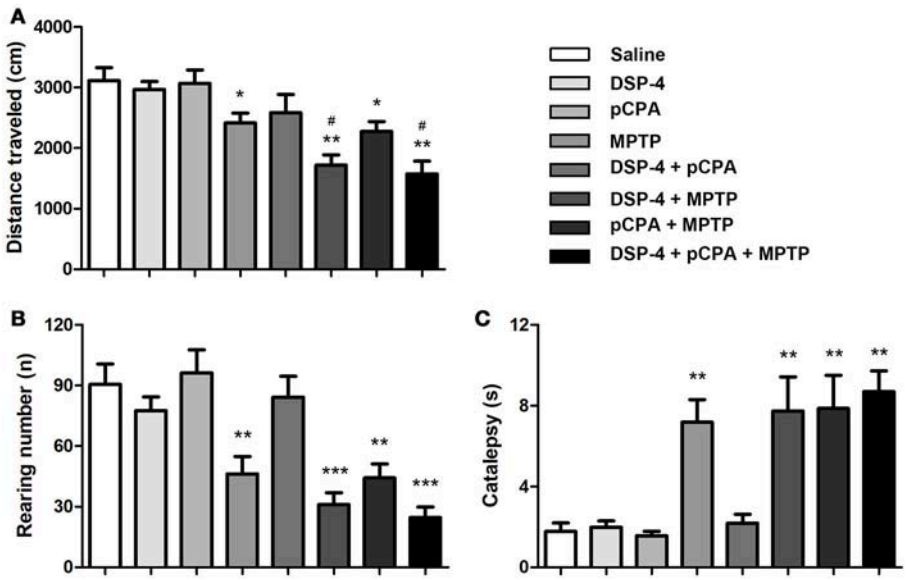

FIGURE 2 | Monoaminergic depletion induced changes in locomotor activity and catalepsy. The total distance traveled **(A)** and number of rearing **(B)** during 10 min was reduced by MPTP treatment in the OFT. **(C)** MPTP-induced DA depletion promoted catalepsy in the Bar test. Each value represents mean ± SEM. *$p < 0.05$, **$p < 0.01$, ***$p < 0.001$ in comparison with the saline group, and #$p < 0.05$ in comparison with the MPTP group was assessed using one-way ANOVA followed Bonferroni's tests. $N = 8$ in saline group, $n = 6$ in MPTP group, $n = 7$ in DSP-4 group, $n = 8$ in pCPA group, $n = 7$ in DSP-4/pCPA group, $n = 6$ in DSP-4/MPTP group, $n = 8$ in pCPA/MPTP group, $n = 7$ in DSP-4/pCPA/MPTP group.

NA, 5-HT and DA induced an anhedonia behavior as the sucrose consumption was significantly decreased [one-way ANOVA, $F_{(7, 51)} = 3.81$, $p < 0.01$, **Figure 3A**].

In FST for despair-associated depression assay, our results showed that single depletion of NA, 5-HT, or DA significantly increased the immobility time compared to saline-treated animals. In addition, mice with depletion of NA or 5-HT combined with DA depletion also showed a significant increase in immobility time compared to saline-treated animals [one-way ANOVA followed by Bonferroni's multiple comparison test, $F_{(7, 53)} = 5.5$, $p < 0.001$, **Figure 3B**], although not significantly different from that in mice with depletion of monoamine alone. Interestingly, there is a trend toward an increased depressive-like behavior when combined depletions of the three monoamines. To further verify the effects of NA, 5-HT and DA on depression, we performed TST. A similar statistical result was obtained as for FST (**Figure 3C**).

Anxiety behavior was evaluated by EPM under NA, 5-HT or DA depletion. As shown, the time spent in open-arms and the number of entries were not affected by depletion of NA, 5-HT, or DA alone (**Figures 3D,E**), suggesting that NA, 5-HT and DA are insufficient by themselves to control anxiety behavior. However, depletions of any two of the monoamines induced a significant anxiety behavior ($p < 0.05$). Furthermore, combined depletions of the three monoamines seem to increase the anxiety behavior as the time spent in open-arms [one-way ANOVA, $F_{(7, 53)} = 5.80$,

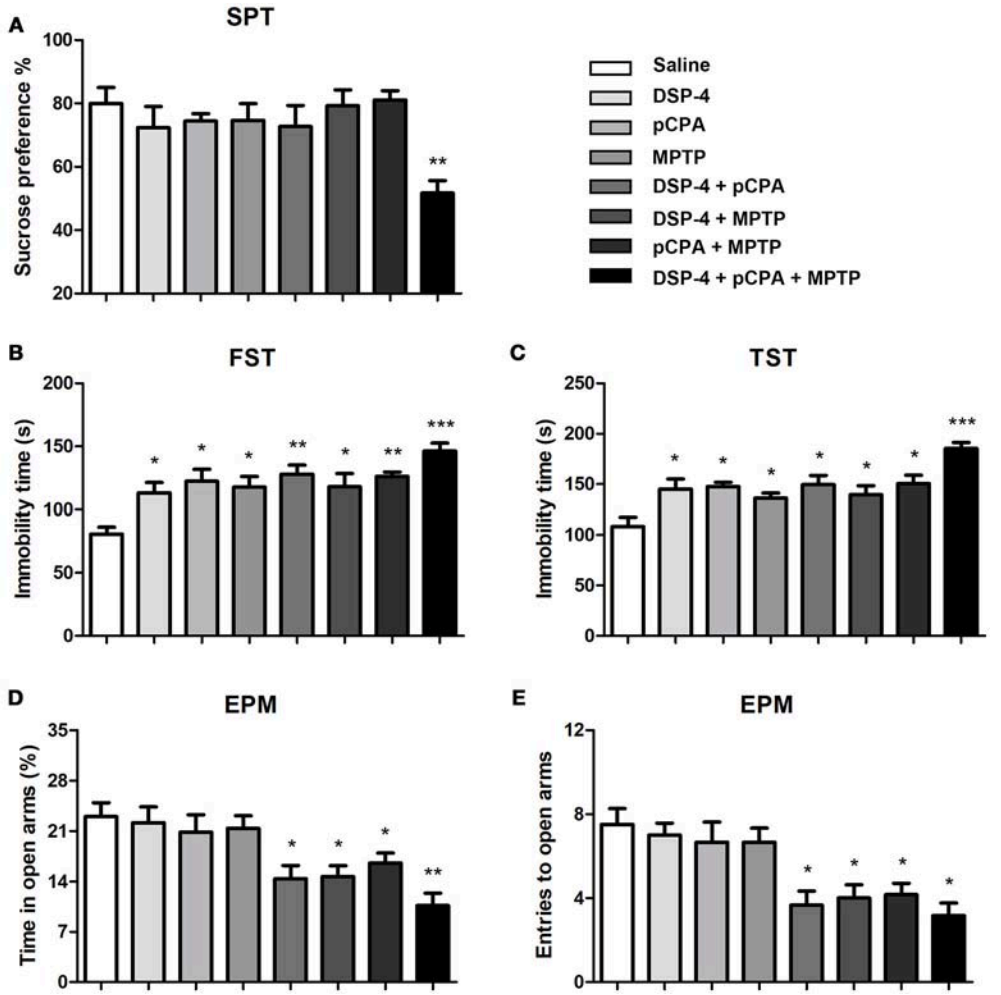

FIGURE 3 | Monoaminergic depletions diversely affect anhedonia, depressive-like and anxiety behaviors. **(A)** Only combined depletions of all the three monoamines reduced the percentage of sucrose consumption measured by the SPT. **(B,C)** Despair-associated depression was measured by the FST and TST. All treated groups showed an increased duration of immobility during a 5 min measurement. **(D,E)** Anxiety was determined by the EPM. The time spent in open arms and number of open arms entries were decreased in group with combined any two or three neurotoxins treatment. Each value represents mean ± SEM. All data were analyzed using one-way ANOVA followed, when significant, by Bonferroni's tests. $^{*}p < 0.05$, $^{**}p < 0.01$, $^{***}p < 0.001$ in comparison with the saline group. The number of mice used in SPT and FST were same with that in OFT. For TST and EPM, $n = 8$ in saline group, $n = 7$ in DSP-4 group, $n = 8$ in pCPA group, $n = 6$ in MPTP group, $n = 6$ in DSP-4/pCPA group, $n = 6$ in DSP-4/MPTP group, $n = 7$ in pCPA/MPTP group, $n = 7$ in DSA-4/pCPA/MPTP group.

$p < 0.001$, **Figure 3D**] and the number of entries into open-arms [one-way ANOVA, $F_{(7, 53)} = 6.55$, $p < 0.001$, **Figure 3E**) were even lower.

NA Depletion-Induced Spatial Learning and Memory Deficits

To examine the changes of spatial learning and memory deficits, the monoamine-lesioned mice were trained and tested in Morris water maze. Our results showed that depletion of NA but not 5-HT or DA affects spatial learning during training as a tendency of the overall escape latency to hidden platform was significantly delayed in contrast to that of saline-treated group [two-way ANOVA, $F_{(1, 14)} = 8.93$, $p < 0.001$, **Figure 4A**]. Additional depletions of 5-HT and/or DA failed to induce any potentiation of the learning impairment caused by NA depletion. In probe test, the number of platform crossing was significantly decreased in NA-depleted group compared to the controls [one-way ANOVA, $F_{(3, 25)} = 4.93$, $p < 0.05$, **Figure 4B**], indicating NA-depleted mice had a spatial memory deficit. Similarly, combining 5-HT and/or DA depletions with NA depletion did not aggravate the decrease in the number of platform crossing.

Toxic Effect of DSP-4, pCPA, and MPTP on Monoaminergic Neurons in the Mice Brain

Using immunofluoresent staining, we evaluate whether the toxic effects of the three neurotoxins are associated with the survival of monoaminergic neurons. DβH catalyzes the conversion of DA to NA, and it is expressed and identified as a marker in

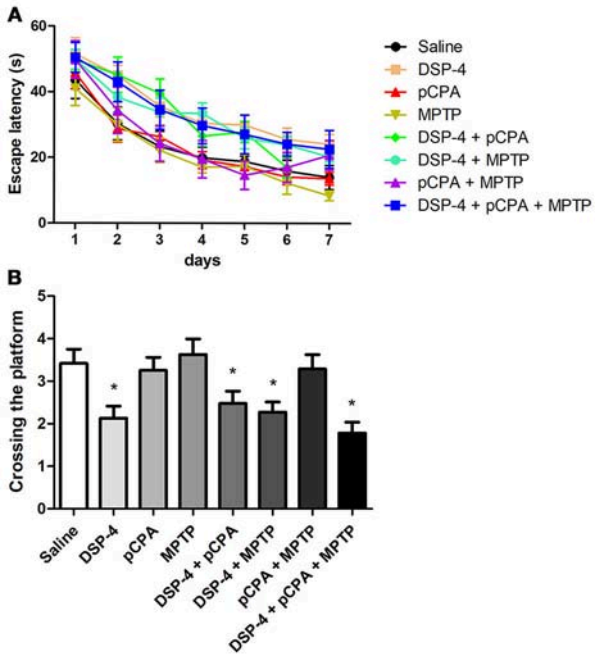

FIGURE 4 | NA depletion reduced mice spatial learning and memory ability measured by the Morris water maze test. **(A)** Escape latency defined as time to find the hidden platform was increased in all DSP-4-treated groups compared to saline group on training day. **(B)** Platform crossing times during the probe test conducted 24 h after training were decreased not only in DSP-4 treatment group but also in groups of DSP-4 combined with pCPA and/or MPTP treatment. Each value represents mean ± SEM. $^*p < 0.05$ in comparison with the saline group was analyzed using one-way ANOVA followed by Bonferroni's tests. $N = 8$ in saline group, $n = 7$ in DSP-4 group, $n = 8$ in pCPA group, $n = 7$ in MPTP group, $n = 8$ in DSP-4/pCPA group, $n = 5$ in DSP-4/MPTP group, $n = 7$ in DSP-4/pCPA group, $n = 6$ in DSP-4/pCPA/MPTP group.

NAergic neurons. As shown, the number of DβH-ir cells in the LC was reduced by 34% in DSP-4 group compared with saline group [one-way ANOVA, $F_{(7, 37)} = 6.25$, $p < 0.001$, **Figure 5**]. However, the percentage decrease in DβH-ir cells was no longer less in the groups of DSP-4 combined with other toxins. PCPA and MPTP injection alone or combined together had no effect on the survival of NAergic neurons in the LC ($p > 0.05$). SERT is a type of monoamine transporter protein that transports 5-HT from the synaptic cleft to the presynaptic neuron. The number of SERT-ir cells in the DRN was not changed in any treated groups compared with the saline-treated group [one-way ANOVA, $F_{(7, 37)} = 0.36$, $p > 0.05$, **Figure 6**]. TH catalyzes the rate limiting step in the synthesis of DA, and it is used as an important indicator of DAergic neurons in the SN. MPTP injection significantly reduced 30% TH-ir cells in the SN [one-way ANOVA, $F_{(7, 37)} = 5.15$, $p < 0.001$, **Figure 7**]. Similarly, the loss of TH-ir cells in MPTP group was parallel in the groups of MPTP accompanied DSP-4 and/or 5-HT injection.

DISCUSSION

There are a number of researches to focus on the PD models produced by DA depletion, because the classic pathology of PD is the progressive loss of DAergic neurons in the SNpc. However, new evidence has recently shown that NAergic and 5-HTergic transmitter systems are also extensively compromised in PD patients (Espay et al., 2014; Deusser et al., 2015). In contrast, these systems have received relatively few attentions in PD field, although their impairment could contribute to the early nonmotor symptoms including emotional and cognitive disorders (Wolters, 2009). In this study, we used three selective toxins to generate a novel mice model that mimic several behavioral and neurochemical depletions which present in the progression of a majority of PD patients (Braak et al., 2003).

For the motor performance, our results showed that DA depletion has been expected to induce a motor deficit, which is in line with many previous studies describing movement disorder after subacute MPTP injection (Blume et al., 2009; Li et al., 2016). In addition, 6-hydroxydopamine (6-OHDA)-lesioned rats were also demonstrated severe motor deficits. Nevertheless, our results showed 22% reduction in movement distance that was lower than 6-OHDA-induced 56% reduction of movements in rats (Delaville et al., 2012). The difference may be due to the depletion of DA in the striatum, which MPTP reduced by 78% DA in our study but 6-OHDA reduced by almost 95% tissue level of DA in the striatum (Delaville et al., 2012; Faggiani et al., 2015). Besides, it has been reported that NA depletion induced motor deficits that resemble to those observed after DA depletion (Rommelfanger et al., 2007). We demonstrated that mice with DSP-4 treatment alone failed to alter spontaneous movement, whereas NA depletion significantly aggravated the motor deficits induced by DA depletion in support of previous results obtained in mice model (Archer and Fredriksson, 2006) as well as rat model of PD (Srinivasan and Schmidt, 2003). In fact, DSP-4 treatment potentiated DA loss induced by MPTP, whereas this enhancement is only achieved when DSP-4-induced neurotoxic insult before MPTP treatment (Fornai et al., 1997; Thomas et al., 2007). The explanation might be that some neurotrophic factors, such as brain-derived neurotrophic factor and fibroblast growth factor, are down-regulated and thus result in a reduced protective effect of NA on DA neurons in the SN (Rommelfanger and Weinshenker, 2007). One previous study showed that stimulation of the NA neurons facilitates firing activity of DA neurons and striatal DA release (Belujon et al., 2007). Therefore, NA depletion decreased the activity of DA neurons and the transmission of nigro-striatal DA, which enhanced the consequences of DA depletion that observed in our study and others (Archer and Fredriksson, 2006; Belujon et al., 2007).

Depression is one of the most common psychiatric symptoms, and it has been demonstrated to occur prior to the onset of motor symptoms of PD (Ou et al., 2017). According to the natural phenomenon that mice prefer a sweetened solution rather than water, whereas depressed mice will no longer exhibit that preference, we performed SPT to assess an anhedonic state of animals (Branchi et al., 2008). We found that NA, 5-HT or DA depletion alone did not induce anhedonia but significant increased the despair-associated depression detected in the FST. Mice of distinct neurotoxin treated groups and controls showed an obvious preference for sucrose as they drank about 80% sucrose solution and 20% water, and such preference might

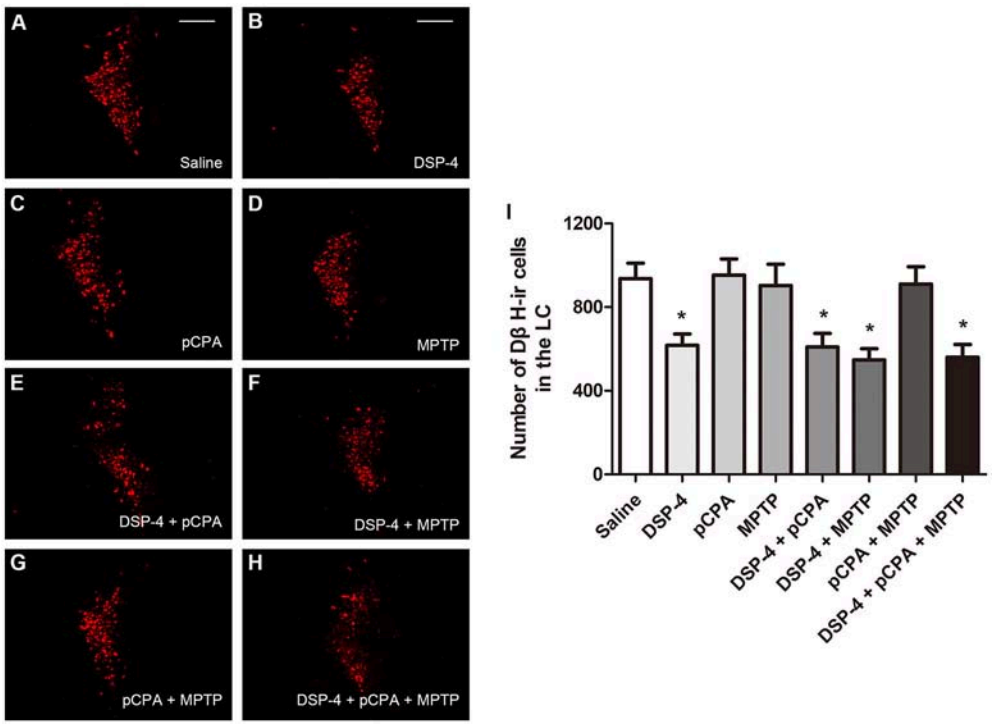

FIGURE 5 | The number of DβH-immunostaining cells in the LC was reduced by neurotoxin treatments. **(A–H)** Micrographs of DβH-ir cells in different groups were shown. **(I)** Stereological counting of DβH-ir cells in all groups. Decreased number of DβH-ir cells was observed in DSP-4 group and DSP-4 along with pCPA and/or MPTP treated groups. Each value represents mean ± SEM. All data were analyzed using one-way ANOVA, $n = 9$. *$p < 0.05$ in comparison with the saline group. Scale bars = 100 μm.

cover the possible differences in anhedonia among the groups which may explain the discrepancy between the results measured in the SPT and FST. However, combined depletion of the three monoamines induced anhedonia and further lengthened the immobility time in the FST. In order to exclude the possibility that the depressive disposition of mice is owing to familiarity with the environment or an adaptive response to an inescapable situation (Nishimura et al., 1988), we reevaluated despair-associated depression of mice using TST and obtained consistent results with the FST. These data support the notion that depressive-like behavior reported in our study could result from the deficits of NA, 5-HT or DA as well as the interaction of the three monoaminergic systems.

Increasing evidence suggests dopaminergic deficits in the SNpc and ventral tegmental area contribute to the depressive behavior independently. DA depletion in nigrostriatal pathway influences limbic function through inducing a high-frequency stimulation of subthalamic nucleus (Gubellini et al., 2009). The similar abnormalities could be resulted from inhibiting the activity of 5-HTergic neuron (Temel et al., 2007). Moreover, 5-HT and its metabolites levels are decreased in several brain regions of PD patients with depression (Kish, 2003), suggesting the depletion of 5-HT contributes to the depressive behavior. Our results also showed that a decline of NA content is related with depressive behavior, which fit with the studies that a reduction in either LC pigmentation or NA transporter binding in the limbic regions leads to depression (Remy et al., 2005). In addition, the utilization of NA and/or 5-HT reuptake inhibitors as antidepressants further indicates the essential role of these monoamines in depressive behavior (Lee et al., 2010).

In contrast to the depressive-like behavior, depletion of NA, 5-HT, or DA alone did not lead to an anxiety behavior. However, the anxiety state of mice was induced by combined depletions of the two or three monoamines. Our data, to a certain extent, support the assumption that DA depletion alone was necessary but not sufficient to induce anxiety disorder (Gareri et al., 2002). However, these findings challenge the results that DA depletion alone decreased the number of entries into the open-arms (Tadaiesky et al., 2008). The discrepancy might be ascribed to the neurotoxin utilized in both studies. Tadaiesky et al. created rodent models using 6-OHDA injection, while we performed MPTP injection for DA depletion. It should be noticed that 6-OHDA as catecholaminergic neurotoxin lesioned not only DAergic neurons but also NAergic neurons (Glinka et al., 1997). There is one study reported that mice deficient in vesicular monoamine transporter 2 (VMAT2), a protein that transports neurotransmitters including NA, 5-HT and DA, exhibited obvious anxiety behavior (Taylor et al., 2009). Although the VMAT2-deficient mice have elucidated the association between the three monoamines and the anxiety behavior, it did not clarify which monoamine plays predominant role in the observed disorder.

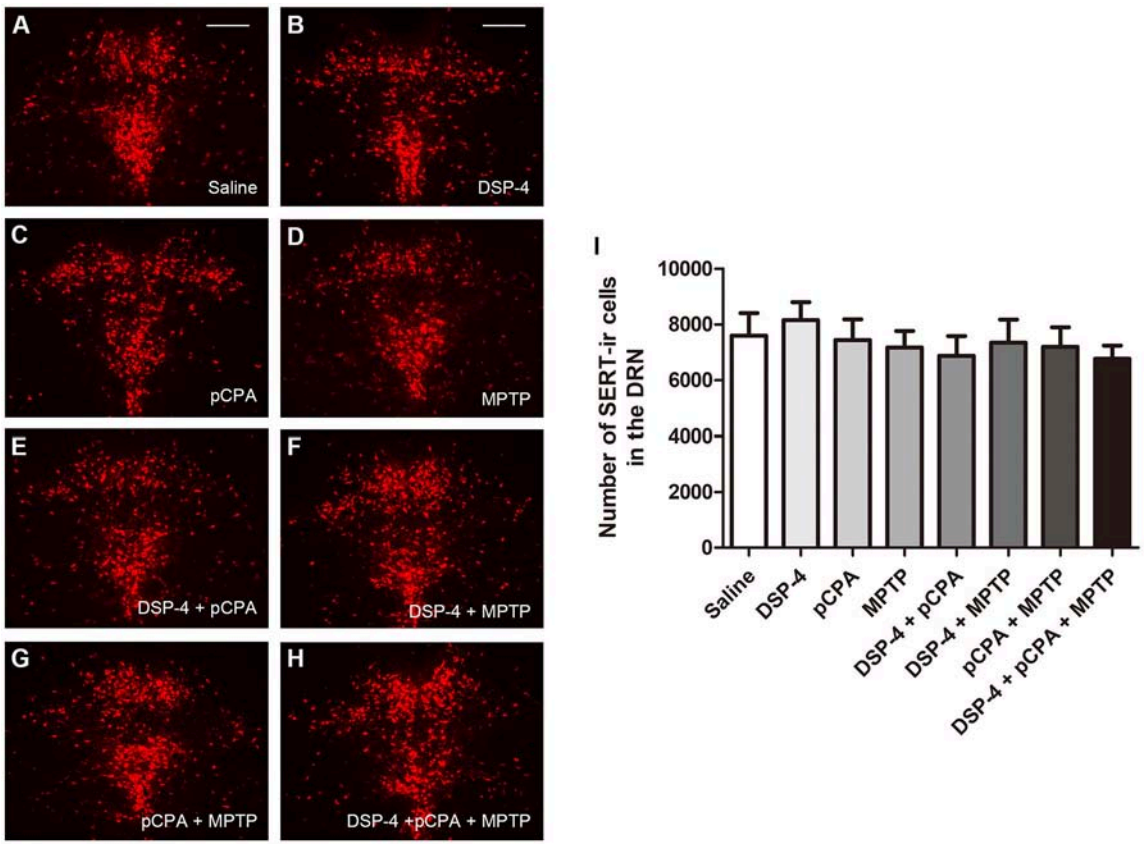

FIGURE 6 | The number of SERT-immunostaining cells in the DRN was unchanged by neurotoxin treatments. **(A–H)** Micrographs of SERT-ir cells in different groups were shown. **(I)** Stereological counting of SERT-ir cells in all groups. There is no changed number of SERT-ir cells observed in all treatment groups. Each value represents mean ± SEM. All data were analyzed using one-way ANOVA, $n = 9$. Scale bars = 100 μm.

Besides emotional deficits, we also observed a cognitive deficit in the form of impaired spatial learning and memory. This deficit is a result of NA depletion, since we did not find an impairment of spatial learning and memory in pure MPTP- or pCPA-treated groups. Our study and others showed the learning and memory impairment induced by NA depletion is similar to that achieved after bilateral inactivation of LC in both novel object recognition and Morris water maze (Khakpour-Taleghani et al., 2009). Loss of 5-HT innervations in the brain could lead to memory deficits. Tryptophan depletion has been shown to reduce 5-HT contents in the hippocampus and frontal cortex that impairs memory in novel object recognition test (Jenkins et al., 2010). However, it is noted that tryptophan depletion induced a chronic and more extensive lowering of 5-HT levels than our neurotoxin paradigm. These data suggest that NA and 5-HT play an important role in cognitive functions and their impairments have been noticing in PD. One of the major challenges for studying motor and nonmotor behaviors in PD models is that the nonmotor symptoms to some extent is affected by motor abilities. We present here that, for example, DSP-4-lesioned mice displayed obvious depression but without motor deficits; MPTP-lesioned mice induced dyskinesia, but they did not appear anxiety. Thus, our data at least partially indicate that some of the nonmotor behaviors delineated in monoamine-depleted mice are not affected by motor deficits.

DSP-4 treatment reduced the number of NAergic neurons in the LC and MPTP treatment reduced the number of DAergic neurons in the SN. Nevertheless, pCPA as a 5-HT synthesis inhbitor did not affect 5-HTergic neurons in the DRN, which may suggest that endogenous 5-HT synthesis is not a prerequisite for proliferation, differentiation and survival of 5-HTergic neurons (Gutknecht et al., 2012). It has long been known that MPTP can cause the degeneration of DAergic neurons in SN through inhibiting mitochondrial complex I of the electron transport chain. However, the toxic mechanism of DSP-4 to LC NAergic neurons is not fully clear. Previous studies reported that DSP-4 crosses the blood-brain barrier and is metabolized into a reactive aziridinium derivative, which is accumulated into the NAergic nerve terminals via NA transporter. The toxic aziridinium derivative reacts with unknown cellular components and thus destroys the terminals and finally leads to cell death (Ross and Stenfors, 2015). Nevertheless, we cannot overlook the possibility that DSP-4 may influence DβH expression in a few days after treatment (Fritschy and Grzanna, 1991). Regarding to DSP-4

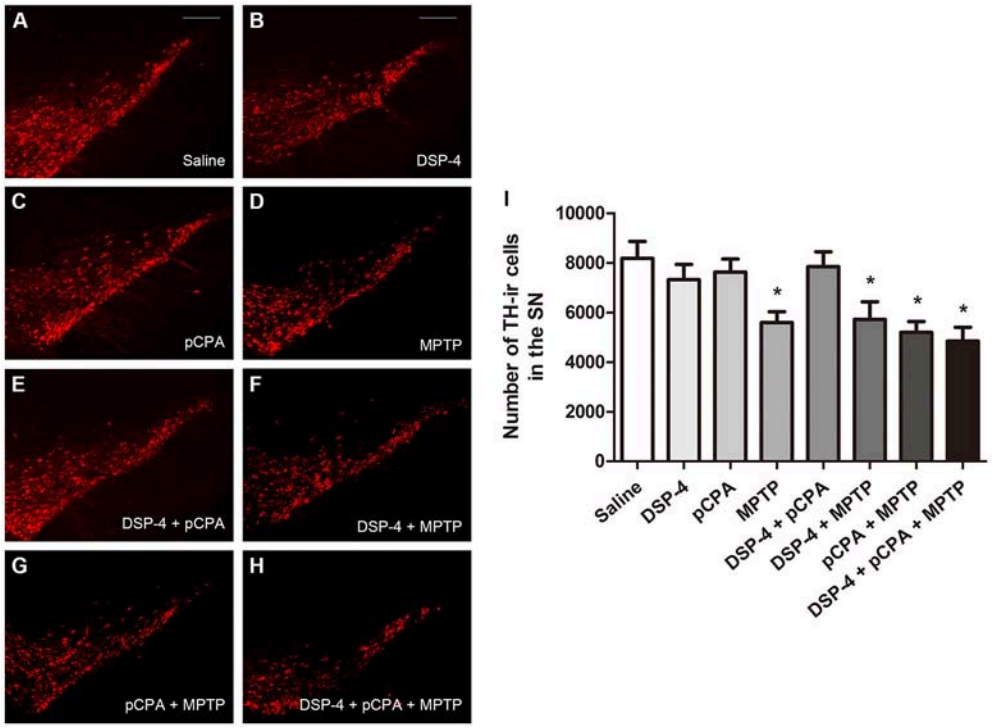

FIGURE 7 | The number of TH-immunostaining cells in the SNpc was reduced by neurotoxin treatments. **(A–H)** Micrographs of TH-ir cells in different groups were shown. **(I)** Stereological counting of TH-ir cells in all groups. Decreased number of TH-ir cells was observed in MPTP group and MPTP together with DSP-4 and/or pCPA groups. Each value represents mean ± SEM. All data were analyzed using one-way ANOVA, $n = 9$. $^*p < 0.05$ in comparison with the saline group. Scale bars = 100 μm.

potentiates the loss of DA levels in the striatum, we did not observe a further decrease in DAergic neurons in DSP-4/MPTP group compared to MPTP group, implicating that DSP-4 may affect the excitability of DAergic neurons and thus reduce the release of DA (Rommelfanger and Weinshenker, 2007).

CONCLUSION

Our results provide new insights into the roles of NA, 5-HT, and DA in the performance of nonmotor and motor symptoms of PD. DA depletion in mice induced hypokinesia and additional depletion of NA enhanced the motor deficits. NA, 5-HT, or DA by themselves had an impact on depressive-like behavior. Anxiety behavior is induced by combined depletions of the two or three monoamines. Furthermore, a synergetic effect could be seen among the three monoamines on anhedonia, depression and anxiety. Depletion of NA rather than 5-HT or DA dramatically affected animals' spatial learning and memory ability. We, therefore, propose that in the context of experimental Parkinsonism the motor and nonmotor symptoms caused by monoamine lesions are more complicated than previously anticipant.

AUTHOR CONTRIBUTIONS

YL and HJ conceived the project and designed the study. YL, SH, and LJ performed the experiments, analyzed data and interpreted results. YL wrote the manuscript. HJ, QJ, and XD reviewed and edited the manuscript. All authors have read and approved the final version of the manuscript.

ACKNOWLEDGMENTS

This work was supported by the National Foundation of Natural Science of China (31471114, 31771110, and 81430024), Taishan Scholarship, the Key Research and Development Program of Shandong Province (2016GSF201053), Qingdao Municipal Science and Technology Project (16-6-2-2-nsh), and the Shandong Provincial Natural Science Foundation of China (ZR2017BH048).

REFERENCES

Archer, T., and Fredriksson, A. (2006). Influence of noradrenaline denervation on MPTP-induced deficits in mice. *J. Neural Transm. (Vienna)* 113, 1119–1129. doi: 10.1007/s00702-005-0402-5

Belujon, P., Bezard, E., Taupignon, A., Bioulac, B., and Benazzouz, A. (2007). Noradrenergic modulation of subthalamic nucleus activity: behavioral and electrophysiological evidence in intact and 6-hydroxydopamine-lesioned rats. *J. Neurosci.* 27, 9595–9606. doi: 10.1523/JNEUROSCI.2583-07.2007

Benarroch, E. E. (2009). The locus ceruleus norepinephrine system: functional organization and potential clinical significance. *Neurology* 73, 1699–1704. doi: 10.1212/WNL.0b013e3181c2937c

Blume, S. R., Cass, D. K., and Tseng, K. Y. (2009). Stepping test in mice: a reliable approach in determining forelimb akinesia in MPTP-induced Parkinsonism. *Exp. Neurol.* 219, 208–211. doi: 10.1016/j.expneurol.2009.05.017

Braak, H., Del Tredici, K., Rüb, U., de Vos, R. A., Jansen Steur, E. N., and Braak, E. (2003). Staging of brain pathology related to sporadic Parkinson's disease. *Neurobiol. Aging* 24, 197–211. doi: 10.1016/S0197-4580(02)00065-9

Braak, H., Ghebremedhin, E., Rüb, U., Bratzke, H., and Del Tredici, K. (2004). Stages in the development of Parkinson's disease-related pathology. *Cell Tissue Res.* 318, 121–134. doi: 10.1007/s00441-004-0956-9

Branchi, I., D'Andrea, I., Armida, M., Cassano, T., Pèzzola, A., Potenza, R. L., et al. (2008). Nonmotor symptoms in Parkinson's disease: investigating early-phase onset of behavioral dysfunction in the 6-hydroxydopamine-lesioned rat model. *J. Neurosci. Res.* 86, 2050–2061. doi: 10.1002/jnr.21642

Buchman, A. S., Nag, S., Shulman, J. M., Lim, A. S., VanderHorst, V. G., Leurgans, S. E., et al. (2012). Locus coeruleus neuron density and parkinsonism in older adults without Parkinson's disease. *Mov. Disord.* 27, 1625–1631. doi: 10.1002/mds.25142

Burke, R. E., Dauer, W. T., and Vonsattel, J. P. (2008). A critical evaluation of the Braak staging scheme for Parkinson's disease. *Ann. Neurol.* 64, 485–491. doi: 10.1002/ana.21541

Cui, L., Sun, W., Yu, M., Li, N., Guo, L., Gu, H., et al. (2016). Disrupted-in-schizophrenia1 (DISC1) L100P mutation alters synaptic transmission and plasticity in the hippocampus and causes recognition memory deficits. *Mol. Brain* 9:89. doi: 10.1186/s13041-016-0270-y

Delaville, C., Chetrit, J., Abdallah, K., Morin, S., Cardoit, L., De Deurwaerdère, P., et al. (2012). Emerging dysfunctions consequent to combined monoaminergic depletions in Parkinsonism. *Neurobiol. Dis.* 45, 763–773. doi: 10.1016/j.nbd.2011.10.023

Del Tredici, K., and Braak, H. (2013). Dysfunction of the locus coeruleus-norepinephrine system and related circuitry in Parkinson's disease-related dementia. *J. Neurol. Neurosurg. Psychiatr.* 84, 774–783. doi: 10.1136/jnnp-2011-301817

Deusser, J., Schmidt, S., Ettle, B., Plöttz, S., Huber, S., Müller, C. P., et al. (2015). Serotonergic dysfunction in the A53T alpha-synuclein mouse model of Parkinson's disease. *J. Neurochem.* 135, 589–597. doi: 10.1111/jnc.13253

Espay, A. J., LeWitt, P. A., and Kaufmann, H. (2014). Norepinephrine deficiency in Parkinson's disease: the case for noradrenergic enhancement. *Mov. Disord.* 29, 1710–1719. doi: 10.1002/mds.26048

Faggiani, E., Delaville, C., and Benazzouz, A. (2015). The combined depletion of monoamines alters the effectiveness of subthalamic deep brain stimulation. *Neurobiol. Dis.* 82, 342–348. doi: 10.1016/j.nbd.2015.07.010

Fornai, F., Alessandrì, M. G., Torracca, M. T., Bassi, L., and Corsini, G. U. (1997). Effects of noradrenergic lesions on MPTP/MPP+ kinetics and MPTP-induced nigrostriatal dopamine depletions. *J. Pharmacol. Exp. Ther.* 283, 100–107.

Fornai, F., di Poggio, A. B., Pellegrini, A., Ruggieri, S., and Paparelli, A. (2007). Noradrenaline in Parkinson's disease: from disease progression to current therapeutics. *Curr. Med. Chem.* 14, 2330–2334. doi: 10.2174/092986707781745550

Fritschy, J. M., and Grzanna, R. (1991). Experimentally-induced neuron loss in the locus coeruleus of adult rats. *Exp. Neurol.* 111, 123–127. doi: 10.1016/0014-4886(91)90058-K

Gareri, P., De Fazio, P., and De Sarro, G. (2002). Neuropharmacology of depression in aging and age-related diseases. *Ageing Res. Rev.* 1, 113–134. doi: 10.1016/S0047-6374(01)00370-0

Glinka, Y., Gassen, M., and Youdim, M. B. (1997). Mechanism of 6-hydroxydopamine neurotoxicity. *J. Neural Transm.* 50(suppl.), 55–66. doi: 10.1007/978-3-7091-6842-4_7

Grzanna, R., Berger, U., Fritschy, J. M., and Geffard, M. (1989). Acute action of DSP-4 on central norepinephrine axons: biochemical and immunohistochemical evidence for differential effects. *J. Histochem. Cytochem.* 37, 1435–1442. doi: 10.1177/37.9.2768812

Gubellini, P., Salin, P., Kerkerian-Le Goff, L., and Baunez, C. (2009). Deep brain stimulation in neurological diseases and experimental models: from molecule to complex behavior. *Prog. Neurobiol.* 89, 79–123. doi: 10.1016/j.pneurobio.2009.06.003

Gutknecht, L., Araragi, N., Merker, S., Waider, J., Sommerlandt, F. M., Mlinar, B., et al. (2012). Impacts of brain serotonin deficiency following Tph2 inactivation on development and raphe neuron serotonergic specification. *PLoS* ONE 7:e43157. doi: 10.1371/journal.pone.0043157

Heal, D. J., Butler, S. A., Prow, M. R., and Buckett, W. R. (1993). Quantification of presynaptic alpha 2-adrenoceptors in rat brain after short-term DSP-4 lesioning. *Eur. J. Pharmacol.* 249, 37–41. doi: 10.1016/0014-2999(93)90659-6

Jenkins, T. A., Elliott, J. J., Ardis, T. C., Cahir, M., Reynolds, G. P., Bell, R., et al. (2010). Tryptophan depletion impairs object-recognition memory in the rat: reversal by risperidone. *Behav. Brain Res.* 208, 479–483. doi: 10.1016/j.bbr.2009.12.030

Kalaitzakis, M. E., Gentleman, S. M., and Pearce, R. K. (2013). Disturbed sleep in Parkinson's disease: anatomical and pathological correlates. *Neuropathol. Appl. Neurobiol.* 39, 644–653. doi: 10.1111/nan.12024

Khakpour-Taleghani, B., Lashgari, R., Motamedi, F., and Naghdi, N. (2009). Effect of reversible inactivation of locus ceruleus on spatial reference and working memory. *Neuroscience* 158, 1284–1291. doi: 10.1016/j.neuroscience.2008.11.001

Kish, S. J. (2003). Biochemistry of Parkinson's disease: is a brain serotonergic deficiency a characteristic of idiopathic Parkinson's disease? *Adv. Neurol.* 91, 39–49.

Kish, S. J., Tong, J., Hornykiewicz, O., Rajput, A., Chang, L. J., Guttman, M., et al. (2008). Preferential loss of serotonin markers in caudate versus putamen in Parkinson's disease. *Brain* 131(Pt 1), 120–131. doi:10.1093/brain/awm239

Kornum, B. R., Licht, C. L., Weikop, P., Knudsen, G. M., and Aznar, S. (2006). Central serotonin depletion affects rat brain areas differently: a qualitative and quantitative comparison between different treatment schemes. *Neurosci. Lett.* 392, 129–134. doi: 10.1016/j.neulet.2005.09.013

Lee, S., Jeong, J., Kwak, Y., and Park, S. K. (2010). Depression research: where are we now? *Mol. Brain* 3:8. doi: 10.1186/1756-6606-3-8

Li, X. H., Dai, C. F., Chen, L., Zhou, W. T., Han, H. L., and Dong, Z. F. (2016). 7,8-dihydroxyflavone ameliorates motor deficits via suppressing alpha-synuclein expression and oxidative stress in the mptp-induced mouse model of Parkinson's disease. *CNS Neurosci. Ther.* 22, 617–624. doi: 10.1111/cns.12555

Masilamoni, G. J., Groover, O., and Smith, Y. (2017). Reduced noradrenergic innervation of ventral midbrain dopaminergic cell groups and the subthalamic nucleus in MPTP-treated parkinsonian monkeys. *Neurobiol. Dis.* 100, 9–18. doi: 10.1016/j.nbd.2016.12.025

Nishimura, H., Tsuda, A., Oguchi, M., Ida, Y., and Tanaka, M. (1988). Is immobility of rats in the forced swim test "behavioral despair"? *Physiol. Behav.* 42, 93–95.

Ou, R., Wei, Q., Hou, Y., Yuan, X., Song, W., Cao, B., et al. (2017). Vascular risk factors and depression in Parkinson's disease. *Eur. J. Neurol.* 25, 637–643. doi: 10.1111/ene.13551

Palma, J. A., and Kaufmann, H. (2014). Autonomic disorders predicting Parkinson's disease. *Parkinsonism Relat. Disord.* (20 Suppl. 1), S94–S98. doi: 10.1016/S1353-8020(13)70024-5

Palmeri, R., Lo Buono, V., Corallo, F., Foti, M., Di Lorenzo, G., Bramanti, P., et al. (2017). Nonmotor symptoms in Parkinson disease: a descriptive review on social cognition ability. *J. Geriatr. Psychiatry Neurol.* 30, 109–121. doi: 10.1177/0891988716687872

Reijnders, J. S., Ehrt, U., Weber, W. E., Aarsland, D., and Leentjens, A. F. (2008). A systematic review of prevalence studies of depression in Parkinson's disease. *Mov. Disord.* 23, 183–189. quiz:13. doi: 10.1002/mds.21803

Remy, P., Doder, M., Lees, A., Turjanski, N., and Brooks, D. (2005). Depression in Parkinson's disease: loss of dopamine and noradrenaline innervation in the limbic system. *Brain* 128(Pt 6), 1314–1322. doi: 10.1093/brain/awh445

Rommelfanger, K. S., Edwards, G. L., Freeman, K. G., Liles, L. C., Miller, G. W., and Weinshenker, D. (2007). Norepinephrine loss produces more profound motor deficits than MPTP treatment in mice. *Proc. Natl. Acad. Sci. U.S.A.* 104, 13804–13809. doi: 10.1073/pnas.0702753104

Rommelfanger, K. S., and Weinshenker, D. (2007). Norepinephrine: the redheaded stepchild of Parkinson's disease. *Biochem. Pharmacol.* 74, 177–190. doi: 10.1016/j.bcp.2007.01.036

Ross, S. B., and Stenfors, C. (2015). DSP4, a selective neurotoxin for the locus coeruleus noradrenergic system. a review of its mode of action. *Neurotox. Res.* 27, 15–30. doi: 10.1007/s12640-014-9482-z

Shen, X. L., Song, N., Du, X. X., Li, Y., Xie, J. X., and Jiang, H. (2017). Nesfatin-1 protects dopaminergic neurons against MPP+/MPTP-induced

neurotoxicity through the C-Raf-ERK1/2-dependent anti-apoptotic pathway. *Sci. Rep.* 7:40961. doi: 10.1038/srep40961

Srinivasan, J., and Schmidt, W. J. (2003). Potentiation of parkinsonian symptoms by depletion of locus coeruleus noradrenaline in 6-hydroxydopamine-induced partial degeneration of substantia nigra in rats. *Eur. J. Neurosci.* 17, 2586–2592. doi: 10.1046/j.1460-9568.2003.02684.x

Tadaiesky, M. T., Dombrowski, P. A., Figueiredo, C. P., Cargnin-Ferreira, E., Da Cunha, C., and Takahashi, R. N. (2008). Emotional, cognitive and neurochemical alterations in a premotor stage model of Parkinson's disease. *Neuroscience* 156, 830–840. doi: 10.1016/j.neuroscience.2008.08.035

Taylor, T. N., Caudle, W. M., Shepherd, K. R., Noorian, A., Jackson, C. R., Iuvone, P. M., et al. (2009). Nonmotor symptoms of Parkinson's disease revealed in an animal model with reduced monoamine storage capacity. *J. Neurosci.* 29, 8103–8113. doi: 10.1523/JNEUROSCI.1495-09.2009

Teissier, A., Soiza-Reilly, M., and Gaspar, P. (2017). Refining the role of 5-HT in postnatal development of brain circuits. *Front. Cell. Neurosci.* 11:139. doi: 10.3389/fncel.2017.00139

Temel, Y., Boothman, L. J., Blokland, A., Magill, P. J., Steinbusch, H. W., Visser-Vandewalle, V., et al. (2007). Inhibition of 5-HT neuron activity and induction of depressive-like behavior by high-frequency stimulation of the subthalamic nucleus. *Proc. Natl. Acad. Sci. U.S.A.* 104, 17087–17092. doi: 10.1073/pnas.0704144104

Thomas, B., von Coelln, R., Mandir, A. S., Trinkaus, D. B., Farah, M. H., Leong Lim, K., et al. (2007). MPTP and DSP-4 susceptibility of substantia nigra and locus coeruleus catecholaminergic neurons in mice is independent of parkin activity. *Neurobiol. Dis.* 26, 312–322. doi: 10.1016/j.nbd.2006.12.021

Wolters, E. (2009). Non-motor extranigral signs and symptoms in Parkinson's disease. *Parkinsonism Relat. Disord.* 15(Suppl. 3), S6–S12. doi: 10.1016/S1353-8020(09)70770-9

Zarow, C., Lyness, S. A., Mortimer, J. A., and Chui, H. C. (2003). Neuronal loss is greater in the locus coeruleus than nucleus basalis and substantia nigra in Alzheimer and Parkinson diseases. *Arch. Neurol.* 60, 337–341. doi: 10.1001/archneur.60.3.337

Zhang, J. P., Zhang, K. Y., Guo, L., Chen, Q. L., Gao, P., Wang, T., et al. (2017). Effects of 1.8 GHz radiofrequency fields on the emotional behavior and spatial memory of adolescent mice. *Int. J. Environ. Res. Public Health* 14:E1344. doi: 10.3390/ijerph14111344

Zhang, Z., Du, X., Xu, H., Xie, J., and Jiang, H. (2015). Lesion of medullary catecholaminergic neurons is associated with cardiovascular dysfunction in rotenone-induced Parkinson's disease rats. *Eur. J. Neurosci.* 42, 2346–2355. doi: 10.1111/ejn.13012

Conflict of Interest Statement: The authors declare that the research was conducted in the absence of any commercial or financial relationships that could be construed as a potential conflict of interest.

frontiers in Cellular Neuroscience

BRIEF RESEARCH REPORT
published: 28 September 2018
doi: 10.3389/fncel.2018.00328

Reduced Excitability and Increased Neurite Complexity of Cortical Interneurons in a Familial Mouse Model of Amyotrophic Lateral Sclerosis

Rosemary M. Clark[1†], Mariana Brizuela[2†], Catherine A. Blizzard[1] and Tracey C. Dickson[1]*

[1]*Menzies Institute for Medical Research, University of Tasmania, Hobart, TAS, Australia,* [2]*Flinders Medical Centre, Flinders University, Adelaide, SA, Australia*

Cortical interneurons play a crucial role in regulating inhibitory-excitatory balance in brain circuits, filtering synaptic information and dictating the activity of pyramidal cells through the release of GABA. In the fatal motor neuron (MN) disease, amyotrophic lateral sclerosis (ALS), an imbalance between excitation and inhibition is an early event in the motor cortex, preceding the development of overt clinical symptoms. Patients with both sporadic and familial forms of the disease exhibit reduced cortical inhibition, including patients with mutations in the copper/zinc superoxide-dismutase-1 (SOD1) gene. In this study, we investigated the influence of the familial disease-causing hSOD1-G93A ALS mutation on cortical interneurons in neuronal networks. We performed whole-cell patch-clamp recordings and neurobiotin tracing from GFP positive interneurons in primary cortical cultures derived from Gad67-GFP::hSOD1^{G93A} mouse embryos. Targeted recordings revealed no overt differences in the passive properties of Gad67-GFP::hSOD1^{G93A} interneurons, however the peak outward current was significantly diminished and cells were less excitable compared to Gad67-GFP::WT controls. *Post hoc* neurite reconstruction identified a significantly increased morphological complexity of the Gad67-GFP::hSOD1^{G93A} interneuron neurite arbor compared to Gad67-GFP::WT controls. Our results from the SOD1 model suggest that cortical interneurons have electrophysiological and morphological alterations that could contribute to attenuated inhibitory function in the disease. Determining if these phenomena are driven by the network or represent intrinsic alteration of the interneuron may help explain the emergence of inhibitory susceptibility and ultimately disrupted excitability, in ALS.

Keywords: excitability, structure, interneuron, cortex, SOD1 G93A mutant

OPEN ACCESS

Edited by:
Paul G. Mermelstein, University of Minnesota Twin Cities, United States

Reviewed by:
Steven M. Graves, University of Minnesota Twin Cities, United States
Rashid Giniatullin, University of Eastern Finland, Finland

***Correspondence:**
Tracey C. Dickson
tracey.dickson@utas.edu.au

[†]These authors have contributed equally to this work

Received: *25 July 2018*
Accepted: *10 September 2018*
Published: *28 September 2018*

Citation:
Clark RM, Brizuela M, Blizzard CA and Dickson TC (2018) Reduced Excitability and Increased Neurite Complexity of Cortical Interneurons in a Familial Mouse Model of Amyotrophic Lateral Sclerosis. Front. Cell. Neurosci. 12:328. doi: 10.3389/fncel.2018.00328

INTRODUCTION

Amyotrophic lateral sclerosis (ALS) is the most common and severe form of motor neuron (MN) disease. It is clinically characterized by selective loss of the upper and lower MNs in the primary motor cortex and spinal cord, resulting in progressive motor system failure and death within 3–5 years of diagnosis (Talbot, 2014; Brown and Al-Chalabi, 2017). This currently incurable

disease is clinically heterogeneous and its etiology remains unknown. However, accumulating evidence from several clinical and experimental studies suggests the disease pathogenesis may center on altered regulation of MN excitability (Turner and Kiernan, 2012; Clark et al., 2015; Geevasinga et al., 2016).

In both sporadic and familial forms of ALS, patients have been found to present with neurophysiological alterations described as hyperexcitability (Vucic and Kiernan, 2006; Vucic et al., 2008; Geevasinga et al., 2015). Originating in the motor cortex and preceding detectable lower MN dysfunction and symptom onset (Menon et al., 2015), it is proposed that hyperexcitability enhances the susceptibility of MNs to cell death through glutamatergic excitotoxicity (Blizzard et al., 2015; Eisen et al., 2017). In ALS, hyperexcitability likely results from dysfunctional inhibition exerted by GABAergic interneurons, as well as intrinsic changes to sodium (Na^+) and potassium (K^+) channel function on MNs (Geevasinga et al., 2016; Do-Ha et al., 2018).

Evidence for ion channel dysfunction is highlighted by a convergent hyperexcitability phenotype in patient-derived MNs, including *TARDBP*, *C9ORF72* and superoxide-dismutase-1 (*SOD1*) mutation carriers (Wainger et al., 2014; Devlin et al., 2015). TDP-43 and SOD1 ALS rodent models identify changes in the excitability of MNs prior to symptoms (Fogarty et al., 2015; Handley et al., 2017). However, more recent studies recognize progressive alterations in the number and excitability of interneurons throughout the disease course in TDP-43 and SOD1 models (Zhang et al., 2016; Clark et al., 2017; Kim et al., 2017). Clinical imaging studies indicate loss of inhibitory activity is a common and early feature of cortical hyperexcitability (Menon et al., 2015), and a key determinant of clinical disease progression (Shibuya et al., 2016). As such, there is a growing body of evidence to suggest dysregulated inhibition, presumably mediated by cortical interneurons, may drive an excitatory/inhibitory imbalance in ALS.

Here, we focused on the potential for the familial $hSOD1^{G93A}$ mutation to influence firing properties and morphology of cortical interneurons in Gad67-GFP::$hSOD1^{G93A}$ cultures. Structural alteration of pyramidal neurons is demonstrated in $hSOD1^{G93A}$ studies (Jara et al., 2012; Fogarty et al., 2016; Saba et al., 2016), but few studies report changes to the morphological fine structure of interneurons (Clark et al., 2017). Additionally, mutant SOD1 is theorized to mediate non-cell autonomous pathogenicity through perturbed function of multiple cell types early in development (Kuo et al., 2004; van Zundert et al., 2008; Martin et al., 2013; Wainger et al., 2014; Devlin et al., 2015). As such, we hypothesize that the $hSOD1^{G93A}$ mutation can perturb the excitability and neurite structure of cortical interneurons in culture.

METHODS

Animals

All procedures were approved by the Animal Ethics Committee of the University of Tasmania (#A0013586) and conducted in accordance with the Australian Code of Practice for the Care and Use of Animals for Scientific Purposes. Gad67-GFP knock-in transgenic mice (Tamamaki et al., 2003) express green fluorescent protein (GFP) under the interneuron-specific *Gad67* promoter. High copy number $hSOD1^{G93A}$ mice were maintained and fully backcrossed to the C57BL/6 background (Gurney et al., 1994; B6.Cg-Tg($SOD1^{G93A}$)1Gur.J[1], Jackson Laboratories, Bar Harbor, ME, USA).

Cortical Culture Electrophysiology

Primary cortical cultures were prepared by carefully dissecting individual mouse embryo neocortices to enrich for neurons as previously described (Brizuela et al., 2015, 2017), with some modifications. Cells were plated at 3.5×10^4 cells/mm^2 for up to 12 days and genotyped for GFP (Brizuela et al., 2015) and the $hSOD1^{G93A}$ mutation (Leitner et al., 2009). Whole-cell voltage and current clamp recordings were performed as previously described (Brizuela et al., 2015), with minor modifications. Glass capillaries (impedance 7–9 Ω) were filled with intracellular solution containing neurobiotin for *post hoc* cell identification. Voltage responses to current injection were recorded from the cell's resting potential (applying 25 pA steps for 200 ms from −100 pA to 500 pA). Recordings were filtered at 5 kHz and sampled at 10 kHz and terminated when access resistance was ≥15 MΩ. Voltage-gated sodium and potassium currents were investigated as previously described (Brizuela et al., 2015). Data was analyzed using the programs Igor (WaveMetrics, USA) and Axograph (Axograph Scientific, Australia).

Immunocytochemistry

Cultures were processed for immunocytochemistry as previously described (Brizuela et al., 2015). Primary antibodies (rat anti-GFP, 1:3,000, Nacalai tesque, RRID: AB_10013361). Secondary antibodies (Alexa Fluor anti-rat 488, 1:1,000, Molecular Probes, RRID: AB_2534074). Neurobiotin-filled interneurons were labeled with streptavidin-546 and imaged using a UltraView Spinning disc confocal microscope (Perkin Elmer) with Velocity Software (Velocity v6 3.0, 2013, Perkin Elmer).

Morphological Analyses

Cell processes were traced through Z-stack series (5 μm, 0.5 μm intervals) with Neurolucida™ (MBF Bioscience, VT, USA) and assessed using branched structure and sholl analyses with Neurolucida Explorer 11 (MBF Bioscience). Interneurons that met electrophysiology inclusion criteria were morphometrically assessed.

Statistical Analysis

All statistical analysis was performed in GraphPad Prism (Version 6.0c, GraphPad Software La Jolla, CA, USA). Unless otherwise stated, comparisons utilized Mann-Whitney tests, after applying d'Agostino and Pearson's normality test, results

[1]http://www.jax.org/strain/004435

expressed as median with interquartile range. Sholl analysis and current-frequency relationships used two-way ANOVA. Data was considered significant at $^*p < 0.05$.

RESULTS

Membrane Properties and Reduced Excitability in Cultured Gad67-GFP::hSOD1^{G93A} Interneurons

Previous studies have demonstrated that mutant hSOD1^{G93A} can perturb neuronal excitability during development, which may contribute to cellular vulnerability in disease (Kuo et al., 2004; van Zundert et al., 2008; Martin et al., 2013; Wainger et al., 2014; Devlin et al., 2015). Here, we focus on investigating cortical interneuron excitability in neuronal culture by examining firing patterns and membrane properties of interneurons in Gad67-GFP::hSOD1^{G93A} cultures.

We used whole-cell recordings from multipolar cortical interneurons to characterize the effect of the hSOD1^{G93A} mutation on cortical interneuron excitability in the presence of synaptic currents. Selection of GFP-positive neurons ensured studied cells were interneurons, with neurobiotin labeling used for *post hoc* identification (**Figure 1A**). We found the hSOD1^{G93A} mutation significantly affected firing properties of cortical interneurons, decreasing the number of action potentials (APs; **Figure 1B**) in response to 200 ms depolarizing current step injections at 350pA (**Figure 1C**; 8.675 ± 2.752pA for hSOD1^{G93A}, 27.42 ± 3.888pA for WT; $p < 0.05$, two-way ANOVA, Bonferroni *post hoc*; $F_{(8,47)} = 2.305$, $p = 0.0357$, interaction between genotype and frequency in two-way ANOVA). There was no significant difference in passive electrophysiological properties, including the resting membrane potential (RMP; **Figure 1D**; −66.5 mv, −67.30 to −63.82 for WT ($n = 16$) v −63.73, −68.75 to −58.71 for hSOD1^{G93A} ($n = 11$), $p > 0.05$), capacitance (**Figure 1E**; 32.50 pF, 27.17–38.20 for WT ($n = 16$) v 32.00, 25.39–35.89 for hSOD1^{G93A} ($n = 11$), $p > 0.05$) and input resistance (**Figure 1F**; 463 MΩ, 394.1–652.1 for WT ($n = 16$) v 378.0, 255.9–513.4 for hSOD1^{G93A} ($n = 11$), $p > 0.05$). Further alterations in excitability were not detected through investigation of AP characteristics, including the spike threshold (**Figure 1G**; −35.24 mv, −41.59 to −31.07 for WT ($n = 16$) v −33.43, −36.52 to −29.64 for hSOD1^{G93A} ($n = 11$), $p > 0.05$), the minimal stimulus required to initiate an AP (**Figure 1H**; rheobase, 150.0 pA, 156.2–186.1 for WT ($n = 16$) v 187.5, 158.6–206.4 for hSOD1^{G93A} ($n = 11$), $p > 0.05$) and the AP duration (**Figure 1I**; 5.504 ms, 4.649–7.086 for WT ($n = 16$) v 6.066, 4.849–7.563 for hSOD1^{G93A} ($n = 11$), $p > 0.05$). However, investigation of voltage-dependent currents identified a significant decrease in the peak outward current (**Figure 1J**; 1.644 nA, 1.524–2.442 for WT ($n = 16$) v 1.151, 0.6636–1.624 for hSOD1^{G93A} ($n = 11$), $p < 0.05$), while there was no significant difference in the peak inward current (**Figure 1K**; −1.575 nA, −2.691 to −1.207 for WT ($n = 16$) v −1.598, −2.214 to −1.273 for hSOD1^{G93A} ($n = 11$), $p > 0.05$). Taken together, this data suggests that cortical interneurons are less excitable and have decreased peak outward currents in the presence of the hSOD1^{G93A} mutation.

The Morphology of Cortical Interneurons Is Changed in Gad67-GFP::hSOD1^{G93A} Cultures

GABAergic interneurons have dynamic axonal structures that can alter in response to changes in activity, to modify post-synaptic targets (Flores and Méndez, 2014). Given the role of interneuron morphology in shaping inhibition during development (Huang, 2009; Le Magueresse and Monyer, 2013), we determined whether there was evidence of changes to the interneuron neurite arbor in Gad67-GFP::hSOD1^{G93A} cultures.

Interneuron morphology was characterized by tracing the three-dimensional structure of neurobiotin-filled GFP-positive interneuron processes in WT and hSOD1^{G93A} cultures. Initial examination revealed a distinct increase in the complexity of hSOD1^{G93A} interneurons (**Figure 2A**). Assessing the characteristics of the interneuron neurite field with sholl analysis (intersections per concentric shell placed at 10 μm radiating outward from the soma), we identified a significant increase in the number of processes on hSOD1^{G93A} interneurons at 110–150 μm from the cell soma compared to WT ($p < 0.05$, two-way ANOVA, Bonferroni *post hoc*; $F_{(1,849)} = 24.77$, $p = 0.0001$, main effect of genotype in two-way ANOVA; see **Figure 2B**). The distance from the soma also independently influenced the neurite arbor complexity ($F_{(40,849)} = 10.58$, $p = 0.0001$, main effect of distance in two-way ANOVA). To investigate the increased complexity of hSOD1^{G93A} interneurons we next used branched structural analyses. As shown in **Figure 2C**, the path length was significantly increased in hSOD1^{G93A} interneurons (2363 μm, 1914–3020 for WT ($n = 20$) v 3380, 2673–4929 for hSOD1^{G93A} ($n = 11$), $p < 0.05$). However, there was also a significant increase in total branch numbers (**Figure 2D**; 91.00, 76.65–121.0 for WT ($n = 20$) v 117.0, 105.1–166.7 for hSOD1^{G93A} ($n = 11$), $p < 0.05$) and the highest order of branches on hSOD1^{G93A} interneurons (**Figure 2E**; 10.00, 9.77–12.83 for WT ($n = 20$) v 14.0, 12.16–19.30 for hSOD1^{G93A} ($n = 11$), $p < 0.05$). These results suggest that the presence of the hSOD1^{G93A} mutation can result in early inhibitory arbor structural remodeling in cortical networks.

DISCUSSION

This study is the first investigation of changes in the excitability and neurite arborization of cortical interneurons in neocortical embryonic cultures from a SOD1 rodent model. The principal finding is that excitability of cultured cortical interneurons may be altered by the hSOD1^{G93A} mutation, and that changes to the complexity of the neurite structure accompany this effect *in vitro*. Specifically, attenuation of excitability is supported by differences in the current-voltage relationship between WT and hSOD1^{G93A} mouse interneurons, and by the observation of reduced peak outward currents in hSOD1^{G93A} interneurons. Interestingly, outward potassium currents are affected in MNs derived from SOD1 ALS patients (Wainger et al., 2014), and by mutant SOD1 oligomers (Zhang et al., 2017), which could account for the changes in the hSOD1^{G93A} cortical interneurons.

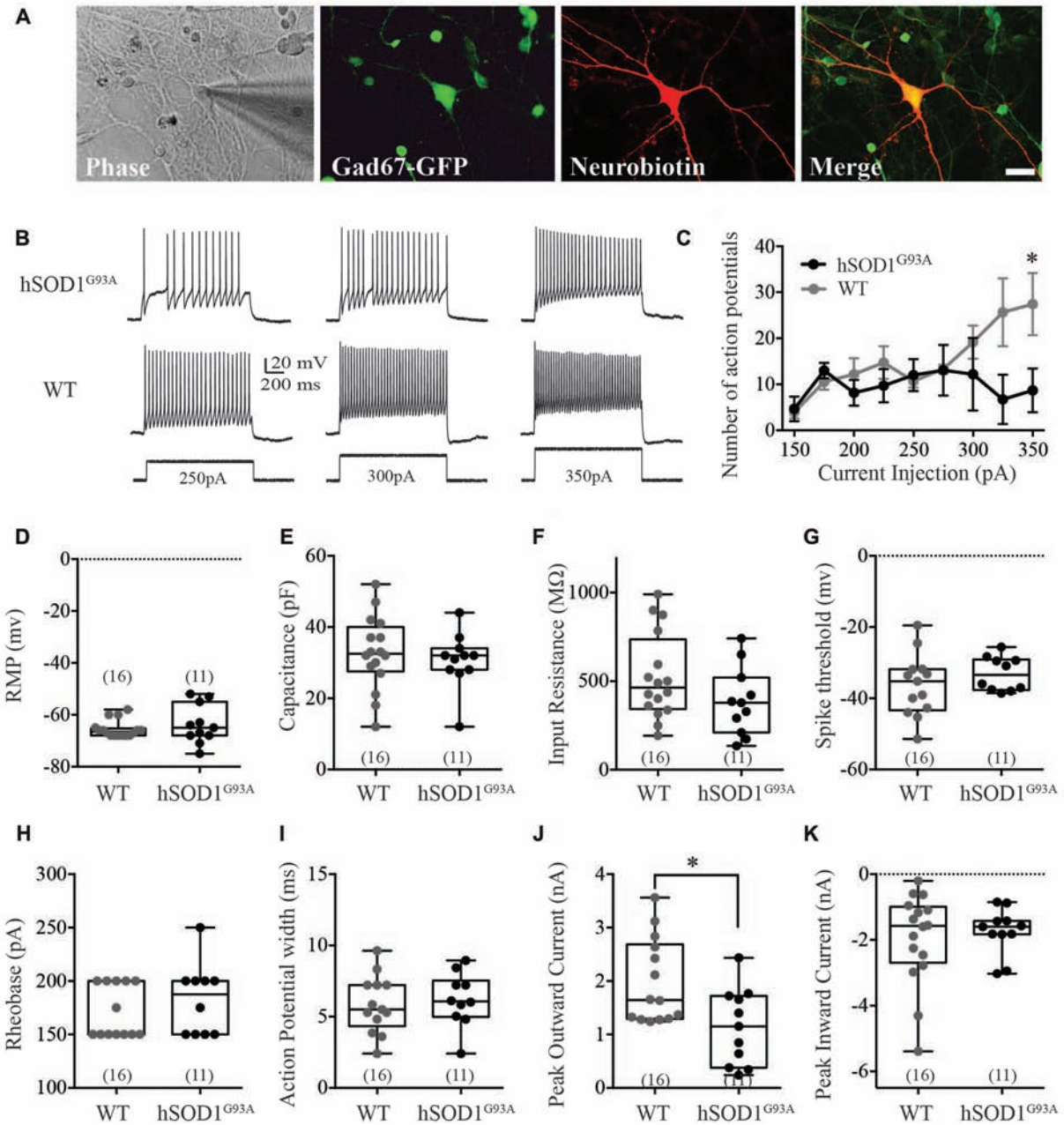

FIGURE 1 | Electrophysiological characterization of Gad67-GFP positive hSOD1^{G93A} cortical interneurons *in vitro*. Primary neuronal cultures were prepared from E15.5 Gad67-GFP::hSOD1^{G93A} embryos as described in "*Methods*" section. **(A)** Whole cell patch-clamped interneurons were positive for Gad67-GFP and *post hoc* labeled for neurobiotin-streptavidin-546. **(B,C)** Representative voltage traces **(B)** and current-spike frequency relationship **(C)** measured from GFP-positive interneurons in 12 DIV cortical culture (Gad67-GFP::hSOD1^{G93A}, $n = 11$ cells from five cultures; Gad67-GFP::WT, $n = 16$ cells from five cultures; $^*p < 0.05$, two-way ANOVA), error bars show mean ± SEM. **(D–K)** The active and passive electrophysiological properties of GFP-positive interneurons, including: the resting membrane potential (RMP; **D**), capacitance **(E)**, input resistance **(F)**, threshold to fire **(G)**, rheobase **(H)**, action potential (AP) width **(I)**, peak inward current **(J)** and significantly decreased peak outward current (**K**; Gad67-GFP::hSOD1^{G93A}, $n = 11$ cells from five cultures; Gad67-GFP::WT, $n = 16$ cells from five cultures; $^*p < 0.05$, Mann-Whitney test). Box-and-whisker plots show the interquartile range.

However, a number of studies highlight increased excitability of cortical pyramidal neuron populations both *in vivo* and *in vitro* (Pieri et al., 2009; Fogarty et al., 2015), which could drive changes in the morphological development of cortical interneurons. The inhibitory neurite arbor can undergo activity-dependent structural remodeling (Bartolini et al., 2013; Babij and De Marco Garcia, 2016) and the level of network activity can produce subtle but significant

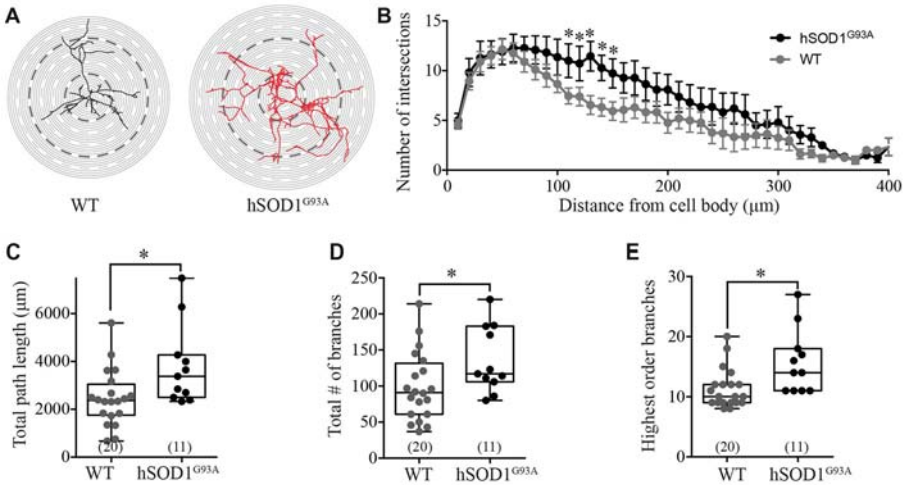

FIGURE 2 | Morphological characterization of Gad67-GFP positive hSOD1^{G93A} cortical interneurons *in vitro*. **(A)** Representative images of patched interneurons reconstructed from *post hoc* neurobiotin-streptavidin labeling in Gad67-GFP::hSOD1^{G93A} and Gad67-GFP::WT cultures. Each concentric circle represents 10 μm, and each dashed line represents 50 μm from the cell soma. **(B)** Sholl analysis denoting the morphological complexity of GFP-positive interneurons as measured by the average number of neurites intersecting with concentric circles placed at 10 μm intervals from the cell soma (Gad67-GFP::hSOD1^{G93A}, $n = 11$ cells from five cultures; Gad67-GFP::WT, $n = 20$ cells from five cultures; $^*p < 0.05$, two-way ANOVA), error bars show mean ± SEM. **(C–E)** Histograms quantifying significantly increased total neurite path length (μm; **C**), total branch number **(D)** and average number of branches **(E)** of Gad67-GFP::hSOD1^{G93A} interneurons compared to Gad67-GFP::WT controls (Gad67-GFP::hSOD1^{G93A}, $n = 11$ cells from 5 cultures; Gad67-GFP::WT, $n = 20$ cells from five cultures; $^*p < 0.05$, Mann-Whitney test). Box-and-whisker plots show the interquartile range.

changes to interneuron morphology (Schuemann et al., 2013). Importantly, in networks deprived of activity, cortical interneurons have been shown to extend collaterals beyond their normal projection range (Marik et al., 2010). While the data presented here are correlational not causal, altered structural and electrophysiological properties of cortical interneurons provide evidence that hSOD1^{G93A} could disturb the inhibitory/excitatory balance in developing neuronal networks, early in the disease pathogenesis.

Previous studies highlight progressive and differential interneuron involvement in the hSOD1^{G93A} mouse model (Clark et al., 2017; Kim et al., 2017). In particular, Kim et al support altered interneuron excitability in hSOD1^{G93A} models, finding progressive hyperexcitability with disease progression *in vivo* (Kim et al., 2017). In the current study we find evidence for intrinsically hypoexcitability. These data support a role for the hSOD1^{G93A} mutation in the early perturbation of inhibitory neuron populations in the disease. However, to determine the effect on functional inhibition, future studies should establish if synaptic excitability is changed to compensate for abnormal firing properties which could normalize firing rates (Turrigiano, 2008). In addition, further experimentation will be required to delineate if this is the cause or consequence of perturbed excitatory neuron excitability in the disease.

DATA AVAILABILITY

All data generated or analyzed in this study are available from the corresponding author upon request.

AUTHOR CONTRIBUTIONS

RC performed cortical culturing, genotyping, immunocytochemistry, data analysis and was a major contributor in writing the manuscript. MB performed electrophysiology and data analysis. CB, MB and TD contributed to experimental design, drafting and editing of manuscript. All authors read and approved the final manuscript.

FUNDING

This work was supported by the Stanford Family Motor Neuron Disease Collaboration Grant (#D0023678) and the Betty Laidlaw Motor Neuron Disease Research Grant (#BLP17), Motor Neuron Disease Research Institute of Australia; the Tasmanian Masonic Centenary Medical Research Foundation (#D0019780); Motor Neuron Disease Research Institute of Australia PhD Scholarship (C0021191); the Select Foundation Fellowship (#D0020742); Australian Research Council Discovery Early Career Research Award (#DE170101514) and the Broadreach Holdings Post-doctoral Medical Research Fellowship.

ACKNOWLEDGMENTS

We authors would like to thank Profs. John Bekkers (Australian National University) and Nobuaki Tamamaki (Kyoto University) for access to *Gad67*-GFP mice. We thank our colleagues Dr. Kaylene Young and Dr. Kimberley Pitman, and in particular Dr. Katherine Lewis for manuscript feedback.

REFERENCES

Babij, R., and De Marco Garcia, N. (2016). Neuronal activity controls the development of interneurons in the somatosensory cortex. *Front. Biol.* 11, 459–470. doi: 10.1007/s11515-016-1427-x

Bartolini, G., Ciceri, G., and Marin, O. (2013). Integration of GABAergic interneurons into cortical cell assemblies: lessons from embryos and adults. *Neuron* 79, 849–864. doi: 10.1016/j.neuron.2013.08.014

Blizzard, C. A., Southam, K. A., Dawkins, E., Lewis, K. E., King, A. E., Clark, J. A., et al. (2015). Identifying the primary site of pathogenesis in amyotrophic lateral sclerosis—vulnerability of lower motor neurons to proximal excitotoxicity. *Dis. Model. Mech.* 8, 215–224. doi: 10.1242/dmm.018606

Brizuela, M., Blizzard, C. A., Chuckowree, J. A., Dawkins, E., Gasperini, R. J., Young, K. M., et al. (2015). The microtubule-stabilizing drug Epothilone D increases axonal sprouting following transection injury *in vitro*. *Mol. Cell. Neurosci.* 66, 129–140. doi: 10.1016/j.mcn.2015.02.006

Brizuela, M., Blizzard, C. A., Chuckowree, J. A., Pitman, K. A., Young, K. M., and Dickson, T. (2017). Mild traumatic brain injury leads to decreased inhibition and a differential response of calretinin positive interneurons in the injured cortex. *J. Neurotrauma* 34, 2504–2517. doi: 10.1089/neu.2017.4977

Brown, R. H., and Al-Chalabi, A. (2017). Amyotrophic lateral sclerosis. *N. Engl. J. Med.* 377, 162–172. doi: 10.1056/NEJMra1603471

Clark, R. M., Blizzard, C., and Dickson, T. (2015). Inhibitory dysfunction in amyotrophic lateral sclerosis: future therapeutic opportunities. *Neurodegener. Dis. Manag.* 5, 511–525. doi: 10.2217/nmt.15.49

Clark, R. M., Blizzard, C. A., Young, K. M., King, A. E., and Dickson, T. C. (2017). Calretinin and Neuropeptide Y interneurons are differentially altered in the motor cortex of the SOD1G93A mouse model of ALS. *Sci. Rep.* 7:44461. doi: 10.1038/srep44461

Devlin, A. C., Burr, K., Borooah, S., Foster, J. D., Cleary, E. M., Geti, I., et al. (2015). Human iPSC-derived motoneurons harbouring TARDBP or C9ORF72 ALS mutations are dysfunctional despite maintaining viability. *Nat. Commun.* 6:5999. doi: 10.1038/ncomms6999

Do-Ha, D., Buskila, Y., and Ooi, L. (2018). Impairments in motor neurons, interneurons and astrocytes contribute to hyperexcitability in ALS: underlying mechanisms and paths to therapy. *Mol. Neurobiol.* 55, 1410–1418. doi: 10.1007/s12035-017-0392-y

Eisen, A., Braak, H., Del Tredici, K., Lemon, R., Ludolph, A. C., and Kiernan, M. C. (2017). Cortical influences drive amyotrophic lateral sclerosis. *J. Neurol. Neurosurg. Psychiatry* 88, 917–924. doi: 10.1136/jnnp-2017-315573

Flores, C. E., and Méndez, P. (2014). Shaping inhibition: activity dependent structural plasticity of GABAergic synapses. *Front. Cell. Neurosci.* 8:327. doi: 10.3389/fncel.2014.00327

Fogarty, M. J., Mu, E. W., Noakes, P. G., Lavidis, N. A., and Bellingham, M. C. (2016). Marked changes in dendritic structure and spine density precede significant neuronal death in vulnerable cortical pyramidal neuron populations in the $SOD1^{G93A}$ mouse model of amyotrophic lateral sclerosis. *Acta Neuropathol. Commun.* 4:77. doi: 10.1186/s40478-016-0347-y

Fogarty, M. J., Noakes, P. G., and Bellingham, M. C. (2015). Motor cortex layer V pyramidal neurons exhibit dendritic regression, spine loss, and increased synaptic excitation in the presymptomatic $hSOD1^{G93A}$ mouse model of amyotrophic lateral sclerosis. *J. Neurosci.* 35, 643–647. doi: 10.1523/JNEUROSCI.3483-14.2015

Geevasinga, N., Menon, P., Nicholson, G. A., Ng, K., Howells, J., Kril, J. J., et al. (2015). Cortical function in asymptomatic carriers and patients with C9orf72 amyotrophic lateral sclerosis. *JAMA Neurol* 72, 1268–1274. doi: 10.1001/jamaneurol.2015.1872

Geevasinga, N., Menon, P., Özdinler, P. H., Kiernan, M. C., and Vucic, S. (2016). Pathophysiological and diagnostic implications of cortical dysfunction in ALS. *Nat. Rev. Neurol.* 12, 651–661. doi: 10.1038/nrneurol.2016.140

Gurney, M., Pu, H., Chiu, A., Dal Canto, M., Polchow, C., Alexander, D. D., et al. (1994). Motor neuron degeneration in mice that express a human Cu, Zn superoxide dismutase mutation. *Science* 264, 1772–1775. doi: 10.1126/science.8209258

Handley, E. E., Pitman, K. A., Dawkins, E., Young, K. M., Clark, R. M., Jiang, T. C., et al. (2017). Synapse dysfunction of layer V pyramidal neurons precedes neurodegeneration in a mouse model of TDP-43 proteinopathies. *Cereb. Cortex* 27, 3630–3647. doi: 10.1093/cercor/bhw185

Huang, Z. J. (2009). Activity-dependent development of inhibitory synapses and innervation pattern: role of GABA signalling and beyond. *J. Physiol.* 587, 1881–1888. doi: 10.1113/jphysiol.2008.168211

Jara, J. H., Villa, S. R., Khan, N. A., Bohn, M. C., and Ozdinler, P. H. (2012). AAV2 mediated retrograde transduction of corticospinal motor neurons reveals initial and selective apical dendrite degeneration in ALS. *Neurobiol. Dis.* 47, 174–183. doi: 10.1016/j.nbd.2012.03.036

Kim, J., Hughes, E. G., Shetty, A. S., Arlotta, P., Goff, L. A., Bergles, D. E., et al. (2017). Changes in the excitability of neocortical neurons in a mouse model of amyotrophic lateral sclerosis are not specific to corticospinal neurons and are modulated by advancing disease. *J. Neurosci.* 37, 9037–9053. doi: 10.1523/JNEUROSCI.0811-17.2017

Kuo, J. J., Schonewille, M., Siddique, T., Schults, A. N., Fu, R., Bär, P. R., et al. (2004). Hyperexcitability of cultured spinal motoneurons from presymptomatic ALS mice. *J. Neurophysiol.* 91, 571–575. doi: 10.1152/jn.00665.2003

Le Magueresse, C., and Monyer, H. (2013). GABAergic interneurons shape the functional maturation of the cortex. *Neuron* 77, 388–405. doi: 10.1016/j.neuron.2013.01.011

Leitner, M., Menzies, S., and Lutz, C. (2009). *Working with ALS mice: Guidelines for Preclinical Testing and Colony Management*. Bar Harbor, ME: Prize4Life and The Jackson Laboratory.

Marik, S. A., Yamahachi, H., McManus, J. N., Szabo, G., and Gilbert, C. D. (2010). Axonal dynamics of excitatory and inhibitory neurons in somatosensory cortex. *PLoS Biol.* 8:e1000395. doi: 10.1371/journal.pbio.1000395

Martin, E., Cazenave, W., Cattaert, D., and Branchereau, P. (2013). Embryonic alteration of motoneuronal morphology induces hyperexcitability in the mouse model of amyotrophic lateral sclerosis. *Neurobiol. Dis.* 54, 116–126. doi: 10.1016/j.nbd.2013.02.011

Menon, P., Kiernan, M. C., and Vucic, S. (2015). Cortical hyperexcitability precedes lower motor neuron dysfunction in ALS. *Clin. Neurophysiol.* 126, 803–809. doi: 10.1016/j.clinph.2014.04.023

Pieri, M., Carunchio, I., Curcio, L., Mercuri, N. B., and Zona, C. (2009). Increased persistent sodium current determines cortical hyperexcitability in a genetic model of amyotrophic lateral sclerosis. *Exp. Neurol.* 215, 368–379. doi: 10.1016/j.expneurol.2008.11.002

Saba, L., Viscomi, M. T., Caioli, S., Pignataro, A., Bisicchia, E., Pieri, M., et al. (2016). Altered functionality, morphology and vesicular glutamate transporter expression of cortical motor neurons from a presymptomatic mouse model of amyotrophic lateral sclerosis. *Cereb. Cortex* 26, 1512–1528. doi: 10.1093/cercor/bhu317

Schuemann, A., Klawiter, A., Bonhoeffer, T., and Wierenga, C. J. (2013). Structural plasticity of GABAergic axons is regulated by network activity and GABAA receptor activation. *Front. Neural Circuits* 7:113. doi: 10.3389/fncir.2013.00113

Shibuya, K., Park, S. B., Geevasinga, N., Menon, P., Howells, J., Simon, N. G., et al. (2016). Motor cortical function determines prognosis in sporadic ALS. *Neurology* 87, 513–520. doi: 10.1212/wnl.0000000000002912

Talbot, K. (2014). Amyotrophic lateral sclerosis: cell vulnerability or system vulnerability? *Epidemiology* 224, 45–51. doi: 10.1111/joa.12107

Tamamaki, N., Yanagawa, Y., Tomioka, R., Miyazaki, J., Obata, K., and Kaneko, T. (2003). Green fluorescent protein expression and colocalization with calretinin, parvalbumin, and somatostatin in the GAD67-GFP knock-in mouse. *J. Comp. Neurol.* 467, 60–79. doi: 10.1002/cne.10905

Turner, M. R., and Kiernan, M. C. (2012). Does interneuronal dysfunction contribute to neurodegeneration in amyotrophic lateral sclerosis? *Amyotroph. Lateral Scler.* 13, 245–250. doi: 10.3109/17482968.2011.636050

Turrigiano, G. G. (2008). The self-tuning neuron: synaptic scaling of excitatory synapses. *Cell* 135, 422–435. doi: 10.1016/j.cell.2008.10.008

van Zundert, B., Peuscher, M. H., Hynynen, M., Chen, A., Neve, R. L., Brown, R. H. Jr., et al. (2008). Neonatal neuronal circuitry shows hyperexcitable disturbance

in a mouse model of the adult-onset neurodegenerative disease amyotrophic lateral sclerosis. *J. Neurosci.* 28, 10864–10874. doi: 10.1523/JNEUROSCI.1340-08.2008

Vucic, S., and Kiernan, M. C. (2006). Novel threshold tracking techniques suggest that cortical hyperexcitability is an early feature of motor neuron disease. *Brain* 129, 2436–2446. doi: 10.1093/brain/awl172

Vucic, S., Nicholson, G. A., and Kiernan, M. C. (2008). Cortical hyperexcitability may precede the onset of familial amyotrophic lateral sclerosis. *Brain* 131, 1540–1550. doi: 10.1093/brain/awn071

Wainger, B. J., Kiskinis, E., Mellin, C., Wiskow, O., Han, S. S., Sandoe, J., et al. (2014). Intrinsic membrane hyperexcitability of amyotrophic lateral sclerosis patient-derived motor neurons. *Cell Rep.* 7, 1–11. doi: 10.1016/j.celrep.2014.03.019

Zhang, Y., Ni, W., Horwich, A. L., and Kaczmarek, L. K. (2017). An ALS-associated mutant SOD1 rapidly suppresses KCNT1 (Slack) Na^+-activated K^+ channels in *aplysia* neurons. *J. Neurosci.* 37, 2258–2265. doi: 10.1523/JNEUROSCI.3102-16.2017

Zhang, W., Zhang, L., Liang, B., Schroeder, D., Zhang, Z. W., Cox, G. A., et al. (2016). Hyperactive somatostatin interneurons contribute to excitotoxicity in neurodegenerative disorders. *Nat. Neurosci.* 19, 557–559. doi: 10.1038/nn.4257

Conflict of Interest Statement: The authors declare that the research was conducted in the absence of any commercial or financial relationships that could be construed as a potential conflict of interest.

The reviewer SG and the handling Editor declared their shared affiliation.

frontiers in Neural Circuits

REVIEW
published: 10 October 2018
doi: 10.3389/fncir.2018.00083

Shaping Diversity Into the Brain's Form and Function

*Lauren N. Miterko[1,2,3], Elizabeth P. Lackey[1,3,4], Detlef H. Heck[5] and Roy V. Sillitoe[1,2,3,4]**

[1] Department of Pathology and Immunology, Baylor College of Medicine, Houston, TX, United States, [2] Program in Developmental Biology, Baylor College of Medicine, Houston, TX, United States, [3] Jan and Dan Duncan Neurological Research Institute of Texas Children's Hospital, Houston, TX, United States, [4] Department of Neuroscience, Baylor College of Medicine, Houston, TX, United States, [5] Department of Anatomy and Neurobiology, University of Tennessee Health Science Center, Memphis, TN, United States

The brain contains a large diversity of unique cell types that use specific genetic programs to control development and instruct the intricate wiring of sensory, motor, and cognitive brain regions. In addition to their cellular diversity and specialized connectivity maps, each region's dedicated function is also expressed in their characteristic gross external morphologies. The folds on the surface of the cerebral cortex and cerebellum are classic examples. But, to what extent does structure relate to function and at what spatial scale? We discuss the mechanisms that sculpt functional brain maps and external morphologies. We also contrast the cryptic structural defects in conditions such as autism spectrum disorders to the overt microcephaly after Zika infections, taking into consideration that both diseases disrupt proper cognitive development. The data indicate that dynamic processes shape all brain areas to fit into jigsaw-like patterns. The patterns in each region reflect circuit connectivity, which ultimately supports local signal processing and accomplishes multi-areal integration of information processing to optimize brain functions.

Keywords: neuron, glia, folding, layering, connectivity, topography, patterning

OPEN ACCESS

Edited by:
Jing-Ning Zhu,
Nanjing University, China

Reviewed by:
Jiayi Zhang,
Fudan University, China
Annalisa Buffo,
Università degli Studi di Torino, Italy

***Correspondence:**
Roy V. Sillitoe
sillitoe@bcm.edu

Received: *22 May 2018*
Accepted: *18 September 2018*
Published: *10 October 2018*

Citation:
Miterko LN, Lackey EP, Heck DH and Sillitoe RV (2018) Shaping Diversity Into the Brain's Form and Function. Front. Neural Circuits 12:83. doi: 10.3389/fncir.2018.00083

INTRODUCTION

The brain is responsible for a seemingly endless number of behaviors that require cognition, sensation, and action. How the brain processes information from its environment, develops thoughts, weighs emotions, and drives the repertoire of responsive behaviors depends on a precisely coordinated interaction of different structures, each with its own specialized functions. The cerebral cortex, subcortical structures, and the cerebellum broadly plan behaviors by controlling emotions, organizing and interpreting external and internal sensory information, forming memories, maintaining homeostasis, coordinating appropriate muscle activity, and instructing language. Brain functions are clearly diverse; therefore, it makes sense that none of the brain regions have morphologies that look alike from the outside and that their networks are comprised of distinct layers and cell types. However, there are many genetic, cellular, molecular, and developmental processes that are shared between brain regions. Given that these similarities are superimposed upon a multitude of differences, can structure tell us anything about function?

While the answers to these questions might, at first glance, seem to be an overwhelming "yes," there is not always clear linkage between structure and function for many brain areas. To address this problem, one must consider the developmental mechanisms that generate the brain.

The central nervous system arises from a simple neuroepitehlium that is initially unremarkable in its specificity along its rostral-caudal axis. Gene function during embryogenesis transforms the neuroepithelium into distinct domains that will form particular brain regions. It is at this stage of development that one may ask how structures are uniquely shaped to acquire their final function. Cells in each region begin to proliferate according to a specific spatial and temporal timetable. At least two classes are produced: neurons and glia. The glia serve as a lineage source for neurons, but they also form the cellular substrate for neuronal migration to occur. Therefore, depending on the classes of neurons and glia and their organization, it has been argued that the suggested ratio of 90% glia to 10% neurons in the mammalian brain could provide clues as to how the brain acquires its intricate morphologies. But, this ratio has been challenged recently, suggesting a ratio closer to 50:50 (Herculano-Houzel, 2014). Moreover, although relatively simple in form, the *drosophila melanogaster* brain only has 10% glia (Kremer et al., 2017), yet there is still considerable complexity in the fly brain that includes intricate folds and specialized functions. But, why fold in the first place? It may be argued that massive regions such as the cerebral cortex must fold in order to accommodate the sheer quantity of critical circuits. However, the cerebellum contains fewer types of circuits (certainly at the basic anatomical level, although this could be challenged based on molecular complexity, as discussed later), yet it has more neurons than any other part of the brain. Based on these problems, we then face the question, what drives the folding, and are there equivalent mechanisms in different parts of the brain? In this review, we address these issues and take into account that each brain region contains an array of distinct cell types with unique morphologies, densities, and functions, and we also consider how neurons migrate and how their axons are guided into precise locations to form brain networks. We ask, what physical forces assemble these network components into a brain region (Garcia et al., 2018)? We discuss how functionality is assembled across brain regions and how neural circuits link up into previously unappreciated wiring diagrams that are critical for behavior. Our attempt is not to solve every question and conundrum in the field of cerebellar and cerebral cortical folding. Instead, our efforts are to take a wholistic view of how the brain is packaged from the outside to its inside, and to stimulate a discussion about how one level of complexity, be it cellular or molecular, feeds into the next, in developing and adult circuits. This view might also teach us about brain function.

MAIN TEXT

Multiple Levels of Heterogeneity in the Brain

Regional Variation and Specificity

Historically, the cerebral cortex and cerebellum have been extensively studied for their structures and functions. For example, Brodmann (1909) identified 43 areas in the human brain based on the general cytoarchitecture of the cerebral cortex. After taking into account regional cellular composition and density, Penfield (1968) considered the functional contributions of the cerebral cortex, elucidating the areas responsible for processing somatosensory, visual, auditory, and motor information through producing an exhaustive functional map based on responses to stimulation techniques that he pioneered for therapy in epilepsy. Thereafter, impairments to these cortical subdivisions have been linked to a large number of diverse developmental and pathological features of brain disease.

Cerebellar studies also have a rich and fascinating history (Manto, 2008), with suggestions of functional topography dating back to the early 1900s (Bolk, 1906). The cerebellar cortex, which is often described as having a uniform cellular composition, is in fact heterogeneous in its molecular properties. As we will discuss later, the cerebellar cortex is divided into an array of parasagittal patterns that segment all of its cell classes. Importantly, however, the molecular patterning is accompanied by anatomical divisions, both in the cerebellar cortex (Ozol and Hawkes, 1997) and the white matter (Voogd and Ruigrok, 1997). Indeed, much like the cerebral cortex, the different domains within the cerebellum reflect developmental (Sillitoe and Joyner, 2007; Apps and Hawkes, 2009; Apps et al., 2018), functional (Cerminara et al., 2015), and pathological features (Sarna and Hawkes, 2003). Strikingly, each of these medial-lateral patterning properties is superimposed upon a broader anatomical plan that is also segmented upon the same axis. From medial to lateral the vermis, paravermis, and hemispheres occupy distinct locations, have specific folding architectures, contain specific circuits, and contribute to largely different behaviors.

Findings in the cerebral cortex and cerebellum have been complemented by studies into understanding the unique structures and functions characteristic to other areas such as the hippocampus. We will not review the thousands of studies devoted to hippocampal functional specificity, but suffice it to say that a large body of work has revealed an intricate and remarkable segmentation of its functions (Hitti and Siegelbaum, 2014; Kohara et al., 2014; Okuyama et al., 2016). Support for these modern animal model studies, like many sectors of neuroscience, came from older studies from human patients and the field of psychiatry. The concept that the cerebral cortex segments and shuttles information into distinct brain regions and that this process can be compromised in disease was found to be shared with the hippocampus. For example, the resulting amnesia after lesioning the hippocampus revealed its critical roles in memory formation (Scoville and Milner, 1957). The main issue to consider, as a starting point, is that each unique brain structure appears to come equipped with a unique set of capabilities. The question we ask is how do these capabilities arise, and are there common mechanistic themes for how they arise?

Cell Layering and Connectivity

One common feature between the cerebral cortex, cerebellum, and hippocampus is that they all have an exquisite layering of cells. Importantly, the layering in all three structures is disrupted in mice that lack REELIN and related proteins (Howell et al., 1997). These data indicate a common requirement for specific genetic programs and at least some shared dependence on developmental processes such as neuronal migration

(Wasser and Herz, 2017). Still, each structure must use these "common" cues to assemble unique circuits. The layering and interactions of cells between the layers of the cerebellar cortex are a prime example. To appreciate these ideas, it is useful to recall that connectivity within the cerebellum is understood at a considerable level of detail, with each cell type forming stereotypical connections with its neighbors. The cerebellum has three distinct layers, and for comparison, the much more complicated cerebral cortex has six main layers. The most superficial cerebellar layer contains inhibitory interneurons and excitatory parallel and climbing fibers. Both project onto Purkinje cells, which make up the middle layer called the Purkinje cell layer. The Purkinje cells perform the main computations in the cerebellum. The deepest layer is called the granular layer and it contains millions of excitatory neurons called granule cells as well as mossy fibers that deliver sensory signals to the Purkinje cells. Below the three layers is a dense network of fiber tracks. Embedded in this network are the cerebellar nuclei. The cerebellar nuclei are specialized neurons that transmit the final output of the cerebellum. They link the cerebellum to the rest of the brain and spinal cord. Early studies of the cerebellum revealed an incredible level of structural and functional variation in the circuitry as was found in the cortex (Fox and Snider, 1967). Work from Marr (1969) and Albus (1971) used this structural map of the cerebellum, and at that time the quickly emerging details of its functional connectivity (Eccles, 1965), to postulate theories on its computational power over motor control. Given that the cerebellum has one neuronal population responsible for the output of its cortex, the Purkinje cell, and that this cell type is innervated by inputs in a predictable, reproducible pattern, the cerebellum is thought to execute a multitude of motor behaviors by modulating Purkinje cell spiking and the downstream consequences on cerebellar nuclear neuron firing (Marr, 1969; Gilbert, 1974; Ruigrok, 2011). It is also important to note that Purkinje cells project to distinct cerebellar output nuclei as revealed by the pattern of axonal projections, compartmental expression of molecules, and functional designation. These combined features further subdivide the cerebellum and potentially add complexity to its computational capabilities (Ruigrok, 2011; Apps et al., 2018; Miterko et al., 2018). In a similar manner, but for different behavioral consequences, the hippocampus is separated into distinct areas [cornu ammonis (CA) fields, dentate gyrus, and subiculum] and layers that are conceptually reminiscent of those in the cerebellum, where cells are organized in a predictable, spatial pattern (Arbib et al., 1998). This particular organization is thought to promote information processing and neuronal coupling (Arbib et al., 1998) to support different non-motor and motor behaviors.

Functional Specializations

The heterogeneity of the brain, as exemplified by these three examples—the cerebral cortex, cerebellum, and hippocampus—spans a great number of structures and their associated functions. Among the anatomical differences, there are also physiological and chemical differences that affect circuit formation and function. Nonetheless, what each of these three brain regions have are subdivisions, which is theorized to support their functions. Comparative analyses upheld this belief, adding to it that as mammals evolved, so did brain structure to accommodate higher order functions. This manifested in a trend in toward a greater subdivision of the cerebral cortex into functionally distinct areas, where early mammals likely had on the order of 20 distinct cortical areas while humans may have more than 200 distinct cortical areas (Kaas, 2013). Neuroimaging of the human cerebellar cortex also reveals functional topography spanning not only motor control but also specific higher order limbic and cognitive tasks, including lateralization of language-related activity (Stoodley and Schmahmann, 2009).

Modules and Maps

How should we determine whether structural features of the brain constitute functionally separate areas or nuclei, without under-dividing or over-dividing? Kaas (1982) proposed five criteria to test for this problem: that distinct cortical areas and nuclei should have differences in cytoarchitecture, a relatively complete single representation of the sensory surface, unique inputs and outputs, different response properties, and dissociable behavioral impairments after lesions. In the cerebellum, the repeating Purkinje cell circuit is subdivided into olivocorticonuclear modules, which also contain micromodules that could either represent distinct or combinations of functional entities (Apps et al., 2018). For instance, lesions made into distinct olivary sub-nuclei, key components of the cerebellar modules, result in specific behavioral deficits during movement (Horn et al., 2010). Moreover, *in vivo* recordings in mice and rats demonstrate different Purkinje cell firing properties that are dependent on location within the cerebellar cortical patterns (Xiao et al., 2014; Zhou et al., 2014). However, a more fundamental feature that has been a useful and reliable landmark for locating distinct areas is the overlying brain morphology. Most notably, the folds overlying the cerebral cortex and cerebellum. The relationship between external morphology and functional organization has also been essential for studying the brain functions of extinct species, as we are only able to examine skull endocasts. The cerebral cortex contains a series of gyri that are separated by sulci, whereas the cerebellum has lobules separated by fissures (**Figure 1**). Cortical folds are consistent across individuals (and between some mammalian species), whereas cerebellar folds are highly conserved as the major pattern across species, from birds through mammals (Larsell, 1970). In primates, larger brains preserve neuronal packing density and generally have more and deeper folds (Herculano-Houzel et al., 2007), which are especially evident in the massive and proportional expansion of the human neocortex and cerebellar cortex. There has been a long-standing debate as to how folding is accomplished, and how it might relate to brain function (Mota and Herculano-Houzel, 2015). We next discuss and debate some of the theories and experimental evidence.

Mechanics of Folding a Neural Sheet

In recent years, much focus has been placed on testing the tension theory proposed by Van Essen (1997). The general tenet of his theory is that cortico-cortical axons physically pull on regions of the cortex and result in gyri formation, and almost by default, the

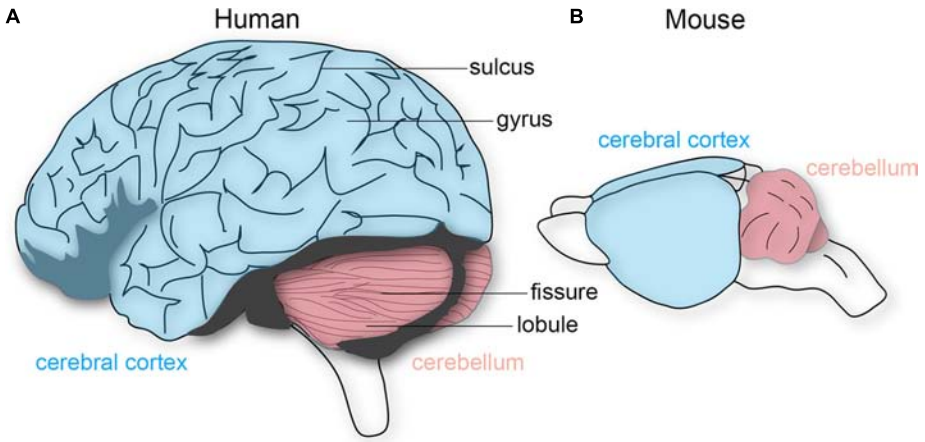

FIGURE 1 | Schematic depiction of the human and mouse brain. **(A)** The human cerebral cortex (blue) and cerebellum (pink) both have characteristic folding patterns. The cerebral cortex contains gyri (peaks) that are interrupted by sulci (valleys). An equivalent architecture is observed in the cerebellum, which is comprised of lobules and fissures. **(B)** The mouse cerebellum is folded whereas the cerebral cortex is not. The brains are not drawn to scale.

sulci form as well. Other prominent theories, such as the radial gradient hypothesis, propose that an increase in the expansion of supragranular cortical layers relative to the infra-granular layers causes buckling of adjacent regions (Richman et al., 1975). In the differential tangential expansion hypothesis, it is proposed that tangential expansion of the cortex causes an increase in tangential pressure, and as a consequence buckling acts to reduce the pressure (Le Gros Clark, 1945; Ronan et al., 2013). In this case, the theory leans on Brodmann's findings on cytoarchitectural differences, which allow for pattern-specific folding. Following this theory, the stability of folding patterns reflects the stability of expansion forces in a given region. It is worth mentioning that these theories share the idea that cortical folding upon itself is necessary for packing the large brain into the small skull, an idea that could be challenged by experimental evidence almost 70 years ago (Barron, 1950).

Moreover, empirical studies of the cerebral cortex argue against features of these theories, and an emerging counter argument is that the timing of developmental events simply could not facilitate tension or buckling (Ronan and Fletcher, 2015). We could make similar arguments for the cerebellum. Van Essen (1997) posits that tension along parallel fibers, the axons of granule cells, could explain why the cerebellar cortex is highly elongated but also folded like an accordion into lobules. Arguing against Van Essen's tension-based mechanism is the fact that cerebellar cortical folding starts embryonically whereas most parallel fibers form postnatally, and, despite the number of fiber tracts entering, no one class could drive the folding because afferents enter the cerebellum starting from mid-embryogenesis and continue to sequentially invade the structure throughout postnatal development (White and Sillitoe, 2013). Moreover, the several theories above do not take into account the highly dynamic nature of circuit formation as fibers are also pruned away, and the target cells—not the axons—are key regulators of wiring processes that should also impact tension and buckling based on these theories (Uesaka et al., 2014). One attractive idea, based on the original hypothesis of Altman and Bayer (1997), is that the shape of folds is driven by the precise timing of the appearance of specialized "anchoring centers" at the future base of each cerebellar fissure and the subsequent coordinated proliferation and migration of granule cells down Bergmann glia astrocytes (Sudarov and Joyner, 2007). But, the fact that cerebellar folds are well conserved and reliably patterned in every animal points to genetic mechanisms that support what might be a functional necessity. Indeed, sonic hedgehog (SHH) morphogen signaling and engrailed transcription factor function, among other pathways (Ryan et al., 2017), could play integrated roles in shaping the cerebellum (Sudarov and Joyner, 2007; Blaess et al., 2008).

The idea of neuronal proliferation driving folding extends to the cerebral cortex as well (Hevner, 2006; Ronan and Fletcher, 2015; Sun and Hevner, 2016). However, it is not just the progenitors that exhibit spatial organization. It was postulated that perhaps folds encompass units with functional restriction (Welker, 1990). Genetic clonal analysis uncovered a modular mode of development for cerebellar granule cells, with lineages restricted within folds (Legue et al., 2015). In the cerebral cortex, neurons born from a common lineage form local clusters that migrate into distinct cortical, hippocampal, and striatal regions (Sultan et al., 2016); although this idea is challenged by Mayer et al. (2016). These early patterns are reminiscent of protomaps (Rakic et al., 2009). More importantly, developmental clusters produce the maps required for adult function and behavior. In the cerebellum, clusters might not directly determine function, but we know they are part of a framework for establishing topography, which is important for function. There is also a possibility that clusters, and the genes that are differentially expressed within each subset, instruct the cellular and molecular properties that eventually produce the diversity of cerebellar-related behaviors.

Still, there are many features of the theories put forth by Van Essen et al. (2018) that could beautifully explain a number of

processes required for cerebral cortical and cerebellar folding, especially from the view of evolution. It is likely that these and other ideas (Na(V), Smith et al., 2018; extracellular matrix, Long et al., 2018) will merge to unveil the full explanation for how neural tissue accomplishes its folding (Meng et al., 2018). In addition, perhaps it is time to consider new model systems (Matsumoto et al., 2017). Recent work used human microcephaly as a starting point for understanding cortical size and complexity. Knowing that mutations in the abnormal spindle-like microcephaly-associated (*Aspm*) gene are common in the human disease but have surprisingly little impact on mouse cortex, Johnson and colleagues developed an *Aspm* knockout ferret (Johnson et al., 2018). The rationale for choosing this model was the more complicated gryrification of the cerebral cortex compared to rodents and the greater diversity of neuronal progenitors. In the *Aspm* model, the approach proved fruitful as they uncovered essential roles for radial glia in controlling cortical expansion. It would be interesting to examine the role of *Aspm* in the ferret cerebellum, considering the milder, but evident cerebellar defects (Johnson et al., 2018).

Topography Relates to Function

Folds roughly correlate to functional domains. In the cerebral cortex, the four principle lobes each have a predominant set of functions. Different sensory, motor, and cognitive behaviors are mapped to distinct regions (a famous correlate was the removal of the hippocampi in patient HM and the resulting specific inability to form new memories), and in some cases, each with specific cytoarchitectures. A remarkable evolutionary adaptation reflecting the structure-function relationship is seen in star-nosed moles, which have 22 fleshy foraging appendages that ring their nostrils. Each appendage is represented in the somatosensory cortex, where they form a "cortical star" that mimics the structure (Catania, 2012). An equivalent topographical mapping of sensory representations onto the cortical surface is revealed in ocular dominance columns in the visual cortex (Hubel and Wiesel, 1979), barrels in the somatosensory cortex (Li and Crair, 2011), patch matrix compartments in the striatum (Bloem et al., 2017), and odorant maps in the olfactory system (Bozza et al., 2002). One of the best-studied examples of brain organization is the Purkinje cell zonal map (**Figure 2**; Miterko et al., 2018). The topographic inputs and outputs of Purkinje cell zones form functional modules (Ruigrok, 2011). Gene expression reveals patterns of stripes that demarcate the modules (cerebellar stripe patterns are obvious in Purkinje cells; **Figure 2**). Modules are derived from lineage patterning mechanisms that instruct specific classes of sensory afferents to target particular regions of the cerebellum (and to some extent particular folds). Modules are therefore comprised of neurons, glia, and terminals that are wired together with a specific topography. It is proposed that modules are organized into patterns that provide an efficient packaging framework for circuits to encode behaviors and that could allow parallel processing of information during complex behaviors (Horn et al., 2010). From a developmental perspective, one could ask what are the embryonic origins of two adjacent circuits that perform complementary functions during a given behavior? For instance, the hindlimb and forelimb cooperate during locomotion, and it is not a coincidence that limb sensory axons are placed side by side in the module map (Gebre et al., 2012). The wiring of the cerebellar map is genetically determined (Sillitoe et al., 2010) and sculpted to precision by activity (White et al., 2014), and the same is true for retinotopic maps in the visual cortex (Cang et al., 2008). The topographic structure of the input and output pathways as well as their internal maps (e.g., Purkinje cell patterns) is therefore intimately

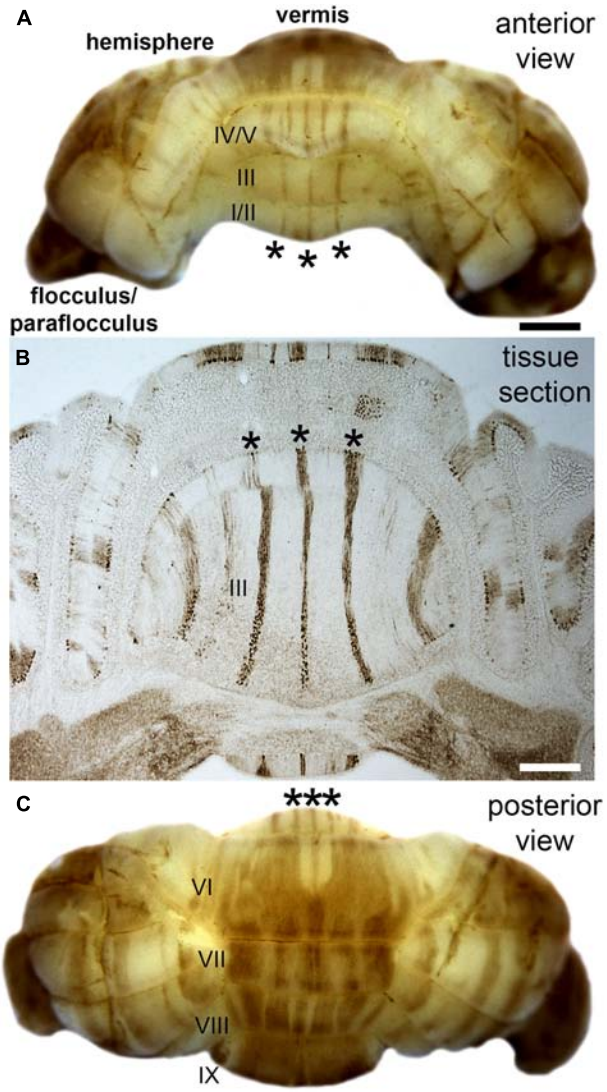

FIGURE 2 | Purkinje cell patterning in the adult mouse cerebellum. **(A)** Anterior view of the mouse cerebellum stained in wholemount with a monoclonal antibody to zebrin II/aldolaseC. **(B)** Coronal tissue section cut through the anterior cerebellum illustrating the pattern of zebrin II stripes in the anterior lobules (asterisks in all panels). Although the intervening stripes are not immunoreactive for zebrin II, they do express other markers that define this complementary set of stripes. **(C)** Posterior view of the mouse cerebellum stained in wholemount with zebrin II. The lobules in the vermis are labeled with Roman numerals according to the nomenclature of Larsell (Larsell, 1970). Scale bar in **A** = 1 mm (applies to **C**), and the scale bar in **B** = 500 μm. The images were modified with permission from White et al. (2012).

linked to circuit function and the behaviors that the circuits support.

Taking Shape in Space and Time

Besides folds, brain and region size is another important feature established during development that is thought to influence global and local function. As folds became increasingly more complex, and potentially co-evolving with the necessity for higher order brain functions, the need for larger mammalian brains possibly arose. Accompanying this increase in brain size is an increase in the number of neurons and glia, and an increase in the diversity within each cell class. More specifically, it is thought that the increase in the number of astrocytes is to preserve its roles of synaptogenesis and regulating metabolic demand in a more complex and robust neural environment (Nedergaard et al., 2003; Oberheim et al., 2006).

Individual brain regions also enlarged as a result of adaptation. For example, the neocortex in primates exponentially increased in size (Finlay and Darlington, 1995) and the hippocampus of foraging birds enlarged as the need for improved social interaction and spatial memory mounted (Sherry et al., 1992). Epigenetic events during development, such as loss of a sensory organ (Kahn and Krubitzer, 2002), have been shown to influence the size and function of cortical areas, though within limits established by genetic programs. The observation that magnification has accompanied the acquisition of complex behaviors raises the question of how regions expand during development, and with this process again comes the obligatory issue of folding. Genetic programs during development create balance between proliferation and cell death, and when genes such as *LIS1*, *DCX*, *ASPM*, *EMX2*, *FGF*, and *Gpr56* affect the normal processes of neuron and glia formation and migration, a host of conditions including lissencephaly and polymicrogyria ensue (Ronan and Fletcher, 2015). Interestingly, defective SHH signaling, one of the most powerful morphogens in mammalian development and an essential component of cerebellar folding during late embryogenesis and early postnatal development in mice (Corrales, 2006), also controls cerebral cortical growth and folding by modulating cell proliferation (Wang L. et al., 2016; Wang Y. et al., 2016). It should therefore not be surprising that the outcome of conditions with defective SHH signaling can be extremely severe, as is the case when the catalytic subunit of phosphoinositide 3-kinase (*PIK3CA*) is mutated causing brain and body overgrowth. In the brain, *PIK3CA*-induced overgrowth causes bilateral dysplastic megalencephaly, hemimegalencephaly, and focal cortical dysplasia, the most common cause of intractable pediatric epilepsy (Roy et al., 2015).

Clear behavioral symptoms also result from the reversed problem, i.e., when reduced growth is triggered, as in the case of *reeler* mutations, the result is a small brain with no folds. In this scenario, the organized layering of the cerebral cortex, hippocampus, and cerebellum is also disrupted (Sudarov et al., 2011; Guy and Staiger, 2017). A recent epidemic with similar consequences is Zika virus infection, which causes microcephaly with cognitive disability. The Zika virus impairs Musashi-1 function in neural progenitors, leading to decreased neurogenesis in both the cortex and the dentate gyrus and therefore an overall decrease in size (Chavali et al., 2017; Christian et al., 2018). Moreover, the Zika virus disorganizes the granule cell layer and strata, in addition to predisposes infants to brain calcifications (Christian et al., 2018). Accompanying these structural deficits to the brain are insults to neural circuit development. The Zika virus promotes gliosis, impairs myelination, disrupts synaptogenesis, and alters the levels of SHH and FGF (Christian et al., 2018; Thawani et al., 2018). But, during normal development it should be noted that even before secreted molecules such as SHH, FGF, and REELIN impact cell placement, lineage history and birthdate initiate a spatial and temporal order of cellular invasion of a territory (Sudarov et al., 2011). In addition, in the cerebral cortex, arealization maps the areas of invasion by a transcription factor-mediated process (O'Leary et al., 2007) that can also involve repurposed axon guidance cues in rodents and primates (Homman-Ludiye and Bourne, 2014).

Axon guidance itself plays a multitude of roles in shaping structures for function. For instance, functional systems are determined by how effective pioneer tracts are in setting up circuits, how guidepost cells mediate the proper trajectory of axons, and how chemoaffinity cues such EPH-EPHRIN and cadherin signaling establish circuit maps through axon-target recognition. Interestingly, progenitors not only drive proliferation for regional expansion, but recent evidence indicates that they also produce the NETRIN guidance cue for proper long-range targeting of axons (Dominici et al., 2017; Varadarajan et al., 2017). Remarkably, yet an additional role for SHH is to mediate axon-axon guidance to shape structure into the optic chiasm crossing (Peng et al., 2018), a necessary step in forming the precise retinotectal topography that underlies vision.

It is interesting to speculate that changes in these molecular processes and axon routing could account for the subtle but significant variations in the sizes of brain regions observed in different strains of inbred mice (Hikishima et al., 2017). To solve how this occurs, dissecting the impact of a large number of intersecting genetic pathways *in vivo* would be impractical. However, one could consider highlighting the relationship between structure and function, even within the context of folding, in a disease-relevant model using organoids. The cellular, molecular, and structural features of Zika, and the more basic mechanisms of brain folding, were rapidly worked out with organoids (Cugola et al., 2016; Garcez et al., 2016; Qian et al., 2017; Karzbrun et al., 2018). Perhaps human organoids could also be helpful in developmental conditions in which the structural defects are unclear yet function is perturbed. One example is hydrocephalus. Hydrocephalus is a severe developmental disorder characterized by an excessive build-up of CSF, which causes pressure on the surrounding tissue. In rare cases, the hydrocephalus may be spontaneously corrected such that brain scans no longer show the ventricular enlargement (Dreazen et al., 1989). This is surprising because hydrocephalus alters hindbrain shape, and if shape is no longer defective, then endogenous repair mechanisms could be at play. This is intriguing because recent work shows that a specific progenitor population in the cerebellum can rescue granule cells post-injury (Wojcinski et al., 2017).

More complicated are conditions such as autism with overt behavioral deficits and covert structural deficits. While a reduction in gray matter volume has been found in the cerebellum, hippocampus, amygdala, and parietal lobe of children with autism spectrum disorder (ASD), others have reported an overall increase in brain volume as a hallmark feature of ASD (Carlisi et al., 2017; Riddle et al., 2017). Studies on the underlying genes associated with ASD pathogenesis suggest that a range of functions are disrupted such as synaptic maintenance and motor control (Antoine et al., 2018; Golden et al., 2018; Tatavarty et al., 2018). However, inconsistent structural findings and the seemingly endless number or combination of genetic causes have complicated the process of studying function in autism and other diseases. As a result, the development of new therapeutic approaches has been modest. Recent methodological advances could hold promise.

Organoids and iPSC approaches could be tailor-made to address the mechanism of diseases with either structural or circuit-based defects. In their remarkable study, Orly Reiner and colleagues were inspired by physics and tackled the problem of cortical folding using organoids. They used "wrinkling" as a proxy for folding and uncovered that the process is driven by mechanical instability (Karzbrun et al., 2018). Furthermore, they showed in their organoid system that a *LIS1*$^{+/-}$ mutation reduced wrinkling, and at the cellular level, the defects arose through a combination of defects in nuclear motion, extracellular matrix, and cytoskeleton. A major question to answer—and model—is whether circuit function could be fully restored if the structure of the developing brain is rescued in time. In addressing this question, it could be that the regional differences in stem cell and progenitor population number and capabilities have to be considered. For instance, radial glia-like cells in the outer subventricular zone could promote cortical folding complexity (Fietz et al., 2010; Hansen et al., 2010; Wang et al., 2011). It would be interesting if the inner versus outer granule cell progenitors in the external granular layer have differential effects on cerebellar lobulation. Moreover, there may be a great number of genes, such as *ARHGAP11A* (which encodes a Rho guanosine triphosphatase-activating protein), that control the species-specific complexity of folding (Florio et al., 2015), not only in cortex but other regions as well. To disentangle whether function could be rescued if folding is corrected, the timing of when the activity of such progenitors or genes is initiated is critical.

Structure-Function Reciprocity

Evidently, injury to the brain and more specifically to regions such as the cortex and cerebellum has severe consequences on function (Dahlem et al., 2016). In addition to the direct consequences of missing an area, one has to consider that compensation for loss of function, even in long-range circuits such as the brain to spinal cord connectivity or cerebro-cerebellar connectivity, adds considerable complexity to the structure-function relationship (Hollis et al., 2016). In stroke, the functional improvements are dependent on structural plasticity that induces changes at the synapse (Cooperrider et al., 2014). Indeed, in the cerebellum, topographic molecular mechanisms determine spatial patterns of synaptic plasticity (Wadiche and Jahr, 2005). Synaptic connectivity also follow an architectural heterogeneity of the targets. For example, despite the textbook view of a canonical Purkinje cell, these cells vary in their form and function depending on where in the cerebellum they are located (Cerminara et al., 2015). Purkinje cells have different dendritic structures depending on where they are in a fold. And, at the action potential level, subsets of Purkinje cells have very unique functional (firing) properties that align almost perfectly with the modular stripe topography of the cerebellar cortex (Xiao et al., 2014; Zhou et al., 2014).

Similarly, one can imagine that that cellular diversity and the dense connectivity plan between cerebral cortical cells

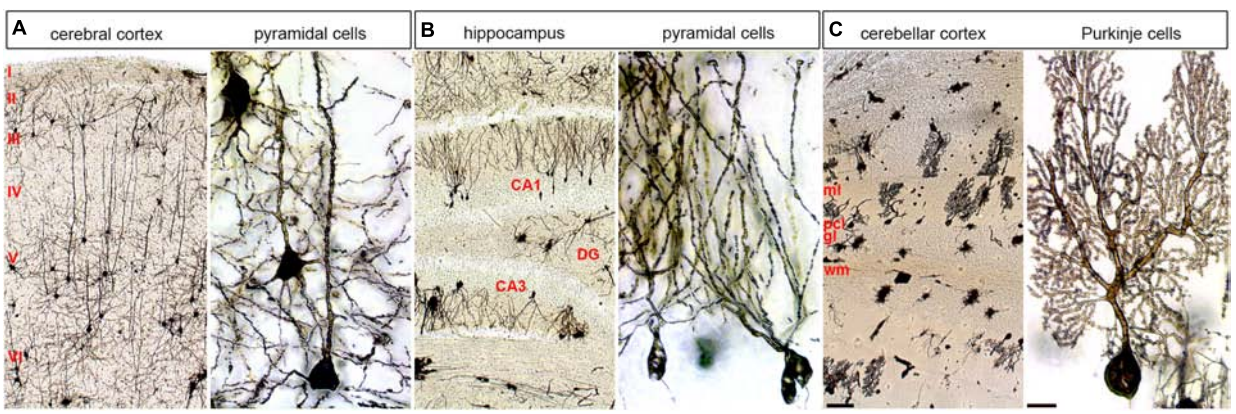

FIGURE 3 | Cellular diversity and specificity in different layered brain structures. The adult mouse brain was stained using a modified Golgi–Cox method. **(A)** Cerebral cortex shown at low and high power. **(B)** Hippocampus shown at low and high power shown at low and high power. **(C)** Cerebellum shown at low and high power shown at low and high power. Pyramidal cells are shown at high power for the cerebral cortex and hippocampus and Purkinje cells are shown for the cerebellum. ml, molecular layer; pcl, Purkinje cell layer; gl, granular layer; wm, white matter; DG, dentate gyrus. The six main layers of the cerebral cortex are labeled with Roman numerals. The scale bar in **C** (cerebellar cortex) = 100 μm and applies to all three low power images. The scale bar in **C** (Purkinje cells) = 20 μm and applies to all three high power images.

should impact computations (Jiang et al., 2015), especially when synaptic structural variations, such as size and neurotransmitter phenotype, are taken into account (Larramendi et al., 1967). We can also no longer ignore that glial diversity will shape synaptic output (John Lin et al., 2017). In the cerebellum, loss of AMPA receptors in Bergmann glia results in motor coordination defects (Saab et al., 2012). Bergmann glia are patterned according to Purkinje cell stripes (Reeber et al., 2018) and are critical for foliation (Ma et al., 2012; Li et al., 2014). It would therefore be interesting to consider whether the three-dimensional plan of the cerebellum with its Cartesian coordinate-like map (Sillitoe and Joyner, 2007) uses Bergmann glia heterogeneity and their influence over neuronal activity to help sculpt the folding and shape of the cerebellum. Could the anchor centers at the base of each fold be defined by particular stripe and zone features? And, are these features unique to each fold? Perhaps the glia-neuron heterogeneity plays a role in differentiating the vermis from hemisphere folds, which require additional curvature even seen in the mouse cerebellum. Certainly, in addition to the differences in functional roles of the vermis compared to the hemispheres, there exists developmental (Govek et al., 2018) as well as disease related distinctions (Tan et al., 2018) that drive shape. It is intriguing to speculate that the initiation and growth of the additional folia and sub-folia in higher order mammals could be facilitated by cellular and molecular heterogeneity in the highly conserved cerebellar map (Sillitoe et al., 2005; Marzban and Hawkes, 2011), and perhaps other classes of glia such as oligodendrocytes and NG2+ cells could in theory promote specific aspects of folding over time. Might there be equivalent features of heterogeneity in the cerebral cortex and hippocampus to support their folding? There is certainly enough heterogeneity for this to be possible.

Behavioral Implications

Considering the above findings together, we are reminded that cellular and structural heterogeneity, even in structures with as high a regional diversity as the cerebral cortex, map to a fundamental functional plan (Mountcastle, 1957). But there is a problem raised by this heterogeneity in that how do these different circuits work together to ultimately drive behavior? This problem is in part solved by neuronal synchrony. Whether it is in the cerebral cortex, cerebellum, or another area, circuits that are linked by cell lineage or connectivity can be synchronously activated in a manner that provides flexibility in controlling behavior (Welsh et al., 2002). But, does long-range connectivity between brain areas with different canonical circuit structures allow for different types of plasticity to work together to influence behavior (Caligore et al., 2017)? Such a model would provide one mechanism for increasing functional flexibility.

Also, localized cellular diversity in each cortical column or cerebellar module could add computational diversity (**Figure 3**). These discrete functional features are built into the brain, but some degree of structure has to be in place first. Though, it is intriguing that blocking neuronal function in the embryonic cerebellum causes lifelong changes in circuit function and behavior without changing structure (White and Sillitoe, 2017). This is consistent with findings that the wiring of topographic circuits–a proxy for arising function–is not strictly linked to the morphology of overlying folds (Sillitoe et al., 2008). Still, the intricate folding (cerebral cortex and cerebellum) and layering (cerebral cortex, cerebellum, hippocampus, and other regions; **Figure 3**) in the different regions of the brain are necessary developmental steps in establishing circuits.

SUMMARY

Regional differences in proliferation set up the structural flexibility that folds and shapes the brain. Genetic cascades control the process, but they also initiate the patterned wiring of circuits. Establishment of structure-function relationships is therefore dependent on topographic circuits, which define the connectivity patterns of networks of neurons with specific physiological properties, which jointly control particular behavioral outcomes. Cues such as SHH play multiple roles throughout development, tying several aspects of brain growth, patterning, wiring, and behavior together. But there is a still a major gap in our understanding of how the precise structure formed in one region relates to that in connected regions. For simplicity, we have discussed somewhat independently the cerebral cortex and cerebellum as models of two areas that are structurally vastly different but are massively interconnected (Bostan et al., 2013) with widely overlapping functional involvements. Moreover, conditions such as ASDs could involve long-range functional interactions from the cerebellum to cortex (Stoodley et al., 2017). Could coordinated inter-regional growth perform critical functions, with common spatial and temporal developmental features? And how would this get processed to impact behavior? The synchronous neuronal activity within structurally defined local circuits could be integrated with circuits of similar design in the connected regions. Proper network structures allow neural computations to actively harness the power of "communication through coherence" as a means of integrating multiple brain systems (Fries, 2015). Indeed, there is growing evidence that this may be how the cerebellum communicates with the hippocampus and the cerebral cortex during non-motor function (McAfee et al., 2017). To further resolve this, future studies could exploit the phenotypes of rare human diseases (Wangler et al., 2017) as a means to systematically define how developmental programs drive the coordinated assembly of structure and function in the brain.

ETHICS STATEMENT

Animal studies were performed under an approved Institutional Animal Care and Use Committee (IACUC) protocol at Baylor College of Medicine.

AUTHOR CONTRIBUTIONS

LM and RS wrote the first draft. LM, EL, DH, and RS edited the manuscript and finalized the paper.

FUNDING

RS was supported by funds from Baylor College of Medicine (BCM) and Texas Children's Hospital, the Hamill Foundation, BCM IDDRC Grant U54HD083092 from the Eunice Kennedy Shriver National Institute of Child Health and Human Development (The IDDRC Neuropathology Sub-Core contributed to the tissue staining), and the National Institutes of Neurological Disorders and Stroke (NINDS) R01NS089664 and R01NS100874. DH and RS were supported by National Institutes of Mental Health (NIMH) R01MH112143.

REFERENCES

Albus, J. S. (1971). A theory of cerebellar function. *Math. Biosci.* 10, 25–61. doi: 10.1016/0025-5564(71)90051-4

Altman, J., and Bayer, S. (1997). *Development of the Cerebellar System in Relation to its Evolution, Structure, and Function*. Boca Raton, FL: CRC Press.

Antoine, M. W., Schnepel, P., Langberg, T., and Feldman, D. E. (2018). Increased excitation-inhibition ratio stabilizes synapse and circuit excitability in four autism mouse models. *bioRxiv* [Preprint]. doi: 10.1101/317693

Apps, R., and Hawkes, R. (2009). Cerebellar cortical organization: a one-map hypothesis. *Nat. Rev. Neurosci.* 10, 670–681.

Apps, R., Hawkes, R., Aoki, S., Bengtsson, F., Brown, A. M., Chen, G., et al. (2018). Cerebellar modules and their role as operational cerebellar processing units. *Cerebellum* doi: 10.1007/s12311-018-0952-3 [Epub ahead of print].

Arbib, M. A., Érdi, P., and Szentágothai, J. (1998). *Neural Organization: Structure, Function, and Dynamics*. Cambridge, MA: The MIT Press.

Barron, D. H. (1950). An experimental analysis of some factors involved in the development of the fissure pattern of the cerebral cortex. *J. Exp. Zool.* 113, 553–581. doi: 10.1002/jez.140113034

Blaess, S., Stephen, D., and Joyner, A. L. (2008). Gli3 coordinates three-dimensional patterning and growth of the tectum and cerebellum by integrating Shh and Fgf8 signaling. *Development* 135, 2093–2103. doi: 10.1242/dev.015990

Bloem, B., Huda, R., Sur, M., and Graybiel, A. M. (2017). Two-photon imaging in mice shows striosomes and matrix have overlapping but differential reinforcement-related responses. *Elife* 6:e32353. doi: 10.7554/eLife.32353

Bolk, L. (1906). *Das Cerebellum der Säugetiere*. Jena: G. Fisher.

Bostan, A. C., Dum, R. P., and Strick, P. L. (2013). Cerebellar networks with the cerebral cortex and basal ganglia. *Trends Cogn. Sci.* 17, 241–254. doi: 10.1016/j.tics.2013.03.003

Bozza, T., Feinstein, P., Zheng, C., and Mombaerts, P. (2002). Odorant receptor expression defines functional units in the mouse olfactory system. *J. Neurosci.* 22, 3033–3043. doi: 10.1523/JNEUROSCI.22-08-03033.2002

Brodmann, K. (1909). *Vergleichende Lokalisationslehre der Grosshirnrinde in ihren Prinzipien dargestellt auf Grund des Zellenbaues*. Leipzig: J. A. Barth.

Caligore, D., Pezzulo, G., Baldassarre, G., Bostan, A. C., Strick, P. L., Doya, K., et al. (2017). Consensus paper: towards a systems-level view of cerebellar function: the interplay between cerebellum, basal ganglia, and cortex. *Cerebellum* 16, 203–229. doi: 10.1007/s12311-016-0763-3

Cang, J., Niell, C. M., Liu, X., Pfeiffenberger, C., Feldheim, D. A., and Stryker, M. P. (2008). Selective disruption of one cartesian axis of cortical maps and receptive fields by deficiency in ephrin-As and structured activity. *Neuron* 57, 511–523. doi: 10.1016/j.neuron.2007.12.025

Carlisi, C. O., Norman, L. J., Lukito, S. S., Radua, J., Mataix-Cols, D., and Rubia, K. (2017). Comparative multimodal meta-analysis of structural and functional brain abnormalities in autism spectrum disorder and obsessive-compulsive disorder. *Biol. Pyschiatry* 82, 83–102. doi: 10.1016/j.biopsych.2016.10.006

Catania, K. C. (2012). Tactile sensing in specialized predators: from behavior to the brain. *Curr. Opin. Neurobiol.* 22, 251–258. doi: 10.1016/j.conb.2011.11.014

Cerminara, N. L., Lang, E. J., Sillitoe, R. V., and Apps, R. (2015). Redefining the cerebellar cortex as an assembly of non-uniform Purkinje cell microcircuits. *Nat. Rev. Neurosci.* 16, 79–93. doi: 10.1038/nrn3886

Chavali, P. L., Stojic, L., Meredith, L. W., Joseph, N., Nahorski, M. S., Sanford, T. J., et al. (2017). Neurodevelopmental protein Musashi-1 interacts with the Zika genome and promotes viral replication. *Science* 357, 83–88. doi: 10.1126/science.aam9243

Christian, K. M., Song, H., and Ming, G.-L. (2018). A previously undetected pathology of Zika virus infection. *Nat. Med.* 24, 258–259. doi: 10.1038/nm.4510

Cooperrider, J., Furmaga, H., Plow, E., Park, H. J., Chen, Z., Kidd, G., et al. (2014). Chronic deep cerebellar stimulation promotes long-term potentiation, microstructural plasticity, and reorganization of perilesional cortical representation in a rodent model. *J. Neurosci.* 34, 9040–9050. doi: 10.1523/JNEUROSCI.0953-14.2014

Corrales, J. D. (2006). The level of sonic hedgehog signaling regulates the complexity of cerebellar foliation. *Development* 133, 1811–1821. doi: 10.1242/dev.02351

Cugola, F. R., Fernandes, I. R., Russo, F. B., Freitas, B. C., Dias, J. L. M., Guimarães, K. P., et al. (2016). The Brazilian Zika virus strain causes birth defects in experimental models. *Nature* 534, 267–271. doi: 10.1038/nature18296

Dahlem, K., Valko, Y., Schmahmann, J. D., and Lewis, R. F. (2016). Cerebellar contributions to self-motion perception: evidence from patients with congenital cerebellar agenesis. *J. Neurophysiol.* 115, 2280–2285. doi: 10.1152/jn.00763.2015

Dominici, C., Moreno-Bravo, J. A., Puiggros, S. R., Rappeneau, Q., Rama, N., Vieugue, P., et al. (2017). Floor-plate-derived netrin-1 is dispensable for commissural axon guidance. *Nature* 545, 349–354. doi: 10.1038/nature22331

Dreazen, E., Tessler, F., Sarti, D., and Crandall, B. F. (1989). Spontaneous resolution of fetal hydrocephalus. *J. Ultrasound Med.* 8, 155–157. doi: 10.7863/jum.1989.8.3.155

Eccles, J. (1965). Functional meaning of the patterns of synaptic connections in the cerebellum. *Perspect. Biol. Med.* 8, 289–310. doi: 10.1353/pbm.1965.0041

Fietz, S. A., Kelava, I., Vogt, J., Wilsch-Brauninger, M., Stenzel, D., Fish, J. L., et al. (2010). OSVZ progenitors of human and ferret neocortex are epithelial-like and expand by integrin signaling. *Nat. Neurosci.* 13, 690–699. doi: 10.1038/nn2553

Finlay, D., and Darlington, R. (1995). Linked regularities in the development and evolution of mammalian brains. *Science* 268, 1578–1584. doi: 10.1126/science.7777856

Florio, M., Albert, M., Taverna, E., Namba, T., Brandi, H., Lewitus, E., et al. (2015). Human-specific gene ARHGAP11B promotes basal progenitor amplification and neocortex expansion. *Science* 347, 1465–1470. doi: 10.1126/science.aaa1975

Fox, C. A., and Snider, R. S. (1967). *The Cerebellum*. Amsterdam: Elsevier.

Fries, P. (2015). Rhythms for cognition: communication through coherence. *Neuron* 88, 220–235. doi: 10.1016/j.neuron.2015.09.034

Garcez, P. P., Loiola, E. C., Da Costa, R. M., Higa, L. M., Trindade, P., Delvecchio, R., et al. (2016). Zika virus: Zika virus impairs growth in human neurospheres and brain organoids. *Science* 352, 816–818. doi: 10.1038/srep40780

Garcia, M. A., Nelson, J., and Chavez, N. (2018). Cell-cell junctions organize structural and signaling networks. *Cold Spring Harb. Perspect. Biol.* 10:a029181. doi: 10.1101/cshperspect.a029181

Gebre, S. A., Reeber, S. L., and Sillitoe, R. V. (2012). Parasagittal compartmentation of cerebellar mossy fibers as revealed by the patterned expression of vesicular glutamate transporters VGLUT1 and VGLUT2. *Brain Struct. Funct.* 217, 165–180. doi: 10.1007/s00429-011-0339-4

Gilbert, P. F. (1974). A theory of memory that explains the function and structure of the cerebellum. *Brain Res.* 70, 1–18. doi: 10.1016/0006-8993(74)90208-X

Golden, C. E., Buxbaum, J. D., and De Rubeis, S. (2018). Disrupted circuits in mouse models of autism spectrum disorder and intellectual disability. *Curr. Opin. Neurobiol.* 48, 106–112. doi: 10.1016/j.conb.2017.11.006

Govek, E.-E., Wu, Z., Acehan, D., Molina, H., Rivera, K., Zhu, X., et al. (2018). Cdc42 regulates neuronal polarity during cerebellar axon formation and glial-guided migration. *iScience* 1, 35–48. doi: 10.1016/j.isci.2018.01.004

Guy, J., and Staiger, T. F. (2017). The functioning of a cortex without layers. *Front. Neuroanat.* 11:54. doi: 10.3389/fnana.2017.00054

Hansen, D. V., Lui, J. H., Parker, P. R., and Kriegstein, A. R. (2010). Neurogenic radial glia in the outer subventricular zone of human neocortex. *Nature* 464, 554–561. doi: 10.1038/nature08845

Herculano-Houzel, S. (2014). The glia/neuron ratio: how it varies uniformly across brain structures and species and what that means for brain physiology and evolution. *Glia* 62, 1377–1391. doi: 10.1002/glia.22683

Herculano-Houzel, S., Collins, C. E., Wong, P., and Kaas, J. H. (2007). Cellular scaling for primate brains. *Proc. Natl. Acad. Sci. U.S.A.* 104, 3562–3567. doi: 10.1073/pnas.0611396104

Hevner, R. F. (2006). From radial glia to pyramidal-projection neuron: transcription factor cascades in cerebral cortex development. *Mol. Neurobiol.* 33, 33–50. doi: 10.1385/MN:33:1:033

Hikishima, K., Komaki, Y., Seki, F., Ohnishi, Y., Okano, H. J., and Okano, H. (2017). In vivo microscopic voxel-based morphometry with a brain template to characterize strain specific structures in the mouse brain. *Sci. Rep.* 7:85. doi: 10.1038/s41598-017-00148-1

Hitti, F. L., and Siegelbaum, S. A. (2014). The hippocampal CA2 region is essential for social memory. *Nature* 508, 88–92. doi: 10.1038/nature13028

Hollis, E. R., Ishiko, N., Yu, T., Lu, C. C., Haimovich, A., Tolentino, K., et al. (2016). Ryk controls remapping of motor cortex during functional recovery after spinal cord injury. *Nat. Neurosci.* 19, 697–705. doi: 10.1038/nn.4282

Homman-Ludiye, J., and Bourne, J. A. (2014). Mapping arealisation of the visual cortex of non-primate species: lessons for development and evolution. *Front. Neural Circuits* 8:79. doi: 10.3389/fncir.2014.00079

Horn, K. M., Pong, M., and Gibson, A. R. (2010). Functional relations of cerebellar modules of the cat. *J. Neurosci.* 30, 9411–9423. doi: 10.1523/JNEUROSCI.0440-10.2010

Howell, B. W., Hawkes, R., Soriano, P., and Cooper, J. A. (1997). Neuronal position in the developing brain is regulated by mouse disabled-1. *Nature* 389, 733–737. doi: 10.1038/39607

Hubel, D. H., and Wiesel, T. N. (1979). Brain mechanisms of vision. *Sci. Am.* 241, 150–162. doi: 10.1038/scientificamerican0979-150

Jiang, X., Shen, S., Cadwell, C. R., Berens, P., Sinz, F., Ecker, A. S., et al. (2015). Principles of connectivity among morphologically defined cell types in adult neocortex. *Science* 350:aac9462. doi: 10.1126/science.aac9462

John Lin, C. C., Yu, K., Hatcher, A., Huang, T. W., Lee, H. K., Carlson, J., et al. (2017). Identification of diverse astrocyte populations and their malignant analogs. *Nat. Neurosci.* 20, 396–405. doi: 10.1038/nn.4493

Johnson, M. B., Sun, X., Kodani, A., Borges-Monroy, R., Girskis, K. M., Ryu, S. C., et al. (2018). Aspm knockout ferret reveals an evolutionary mechanism governing cerebral cortical size. *Nature* 556, 370–375.

Kaas, J. H. (1982). "The segregation of function in the nervous system: why do sensory systems have so many subdivisions?," in *Contributions to Sensory Physiology*, Vol. 7, ed. W. P. Neff (New York, NY: Academic Press), 201–240.

Kaas, J. H. (2013). The evolution of brains from early mammals to humans. *Wiley Interdiscip. Rev. Cogn. Sci.* 4, 33–45. doi: 10.1002/wcs.1206

Kahn, D. M., and Krubitzer, L. (2002). Massive cross-modal cortical plasticity and the emergence of a new cortical area in developmentally blind mammals. *Proc. Natl. Acad. Sci. U.S.A.* 99, 11429–11434. doi: 10.1073/pnas.162342799

Karzbrun, E., Kshirsagar, A., Cohen, S. R., Hanna, J. H., and Reiner, O. (2018). Human brain organoids on a chip reveal the physics of folding. *Nat. Phys.* 14, 515–522. doi: 10.1038/s41567-018-0046-7

Kohara, K., Pignatelli, M., Rivest, A. J., Jung, H. Y., Kitamura, T., Suh, J., et al. (2014). Cell type-specific genetic and optogenetic tools reveal hippocampal CA2 circuits. *Nat. Neurosci.* 17, 269–279. doi: 10.1038/nn.3614

Kremer, M. C., Jung, C., Batelli, S., Rubin, G. M., and Gaul, U. (2017). The glia of the adult *Drosophila* nervous system. *Glia* 65, 606–638. doi: 10.1002/glia.23115

Larramendi, L. M., Fickenscher, N., and Lemkey-Johnston, N. (1967). Synaptic vesicles of inhibitory and excitatory terminals in the cerebellum. *Science* 156, 967–969. doi: 10.1126/science.156.3777.967

Larsell, O. (1970). *The Comparative Anatomy and Histology of the Cerebellum from Monotremes through Apes*. Minneapolis, MN: University of Minnesota Press.

Le Gros Clark, W. (1945). *Deformation Patterns on the Cerebral Cortex: Essays on Growth and Form*. London: Oxford University Press.

Legue, E., Riedel, E., and Joyner, A. L. (2015). Clonal analysis reveals granule cell behaviors and compartmentalization that determine the folded morphology of the cerebellum. *Development* 142, 1661–1671. doi: 10.1242/dev.120287

Li, H., and Crair, M. C. (2011). How do barrels form in somatosensory cortex? *Ann. N. Y. Acad. Sci.* 1225, 119–129. doi: 10.1111/j.1749-6632.2011.06024.x

Li, K., Leung, A. W., Guo, Q., Yang, W., and Li, J. Y. (2014). Shp2-dependent ERK signaling is essential for induction of Bergmann glia and foliation of the cerebellum. *J. Neurosci.* 34, 922–931. doi: 10.1523/JNEUROSCI.3476-13.2014

Long, K. R., Newland, B., Florio, M., Kalebic, N., Langen, B., Kolterer, A., et al. (2018). Extracellular matrix components HAPLN1, lumican, and collagen I cause hyaluronic acid-dependent folding of the developing human neocortex. *Neuron* 99, 702–719.e7. doi: 10.1016/j.neuron.2018.07.013

Ma, S., Kwon, H. J., and Huang, Z. (2012). Ric-8a, a guanine nucleotide exchange factor for heterotrimeric G proteins, regulates Bergmann glia-basement membrane adhesion during cerebellar foliation. *J. Neurosci.* 32, 14979–14993. doi: 10.1523/JNEUROSCI.1282-12.2012

Manto, M. (2008). The cerebellum, cerebellar disorders, and cerebellar research—two centuries of discoveries. *Cerebellum* 7, 505–516. doi: 10.1007/s12311-008-0063-7

Marr, D. (1969). A theory of cerebellar cortex. *J. Physiol.* 202, 437–470. doi: 10.1113/jphysiol.1969.sp008820

Marzban, H., and Hawkes, R. (2011). On the architecture of the posterior zone of the cerebellum. *Cerebellum* 10, 422–434. doi: 10.1007/s12311-010-0208-3

Matsumoto, N., Shinmyo, Y., Ichikawa, Y., and Kawasaki, H. (2017). Gyrification of the cerebral cortex requires FGF signaling in the mammalian brain. *Elife* 6:e29285. doi: 10.7554/eLife.29285

Mayer, C., Bandler, R. C., and Fishell, G. (2016). Lineage is a poor predictor of interneuron positioning within the forebrain. *Neuron* 92, 45–51. doi: 10.1016/j.neuron.2016.09.035

McAfee, S. S., Liu, Y., Sillitoe, R. V., and Heck, D. H. (2017). Cerebellar Purkinje cell simple spike activity in awake mice represents phase differences between oscillations in medial prefrontal cortex and hippocampus. *bioRxiv* [Preprint]. doi: 10.1101/173849

Meng, Y., Li, G., Wang, L., Lin, W., Gilmore, J. H., and Shen, D. (2018). Discovering cortical sulcal folding patterns in neonates using large-scale dataset. *Hum. Brain Mapp.* doi: 10.1002/hbm.24199 [Epub ahead of print].

Miterko, L. N., Sillitoe, R. V., and Hawkes, R. (2018). "Zones and stripes: development of cerebellar topography," in *Handbook of the Cerebellum and Cerebellar Disorders*, 2nd Edn, eds M. Manto, J. D. Schmahmann, F. Rossi, D. L. Gruol, and N. Koibuchi (Dordrecht: Springer), 43–59.

Mota, B., and Herculano-Houzel, S. (2015). BRAIN STRUCTURE. Cortical folding scales universally with surface area and thickness, not number of neurons. *Science* 349, 74–77. doi: 10.1126/science.aaa9101

Mountcastle, V. B. (1957). Modality and topographic properties of single neurons of cat's somatic sensory cortex. *J. Neurophysiol.* 20, 408–434. doi: 10.1152/jn.1957.20.4.408

Nedergaard, M., Ransom, B., and Goldman, S. A. (2003). New roles for astrocytes: redefining the functional architecture of the brain. *Trends Neurosci.* 26, 523–530. doi: 10.1016/j.tins.2003.08.008

Oberheim, N. A., Wang, X., Goldman, S., and Nedergaard, M. (2006). Astrocytic complexity distinguishes the human brain. *Trends Neurosci.* 29, 547–553. doi: 10.1016/j.tins.2006.08.004

Okuyama, T., Kitamura, T., Roy, D. S., Itohara, S., and Tonegawa, S. (2016). Ventral CA1 neurons store social memory. *Science* 353, 1536–1541. doi: 10.1126/science.aaf7003

O'Leary, D. D., Chou, S. J., and Sahara, S. (2007). Area patterning of the mammalian cortex. *Neuron* 56, 252–269. doi: 10.1016/j.neuron.2007.10.010

Ozol, K. O., and Hawkes, R. (1997). Compartmentation of the granular layer of the cerebellum. *Histol. Histopathol.* 12, 171–184.

Penfield, W. (1968). Engrams in the human brain: mechanisms of memory. *Proc. R. Soc. Med.* 61, 831–840.

Peng, J., Fabre, P. J., Dolique, T., Swikert, S. M., Kermasson, L., Shimogori, T., et al. (2018). Sonic hedgehog is a remotely produced cue that controls axon guidance trans-axonally at a midline choice point. *Neuron* 97, 326–340. doi: 10.1016/j.neuron.2017.12.028

Qian, X., Nguyen, H. N., Jacob, F., Song, H., and Ming, G. (2017). Using brain organoids to understand Zika virus-induced microcephaly. *Development* 144, 952–957. doi: 10.1242/dev.14707

Rakic, P., Ayoub, A. E., Breunig, J. J., and Dominguez, M. H. (2009). Decision by division: making cortical maps. *Trends Neurosci.* 32, 291–301. doi: 10.1016/j.tins.2009.01.007

Reeber, S. L., Arancillo, M., and Sillitoe, R. V. (2018). Bergmann glia are patterned into topographic molecular zones in the developing and adult mouse cerebellum. *Cerebellum* 17, 392–403. doi: 10.1007/s12311-014-0571-6

Richman, D., Stewart, R., Hutchinson, J., and Caviness, V. (1975). Mechanical model of brain convolutional development. *Science* 189, 18–21. doi: 10.1126/science.1135626

Riddle, K., Cascio, C. J., and Woodward, N. D. (2017). Brain structure in autism: a voxel-based morphometry analysis of the Autism Brain Imaging Database Exchange (ABIDE). *Brain Imaging Behav.* 11, 541–551. doi: 10.1007/s11682-016-9534-5

Ronan, L., and Fletcher, P. C. (2015). From genes to folds: a review of cortical gyrification theor. *Brain Struct. Funct.* 220, 2475–2483. doi: 10.1007/s00429-014-0961-z

Ronan, L., Voets, N., Rua, C., Alexander-Bloch, A., Hough, M., Mackay, C., et al. (2013). Differential tangential expansion as a mechanism for cortical gyrification. *Cereb. Cortex* 24, 2219–2228. doi: 10.1093/cercor.bht082

Roy, A., Skibo, J., Kalume, F., Ni, J., Rankin, S., Lu, Y., et al. (2015). Mouse models of human PIK3CA-related brain overgrowth have acutely treatable epilepsy. *eLife* 4:e12703. doi: 10.7554/eLife.12703

Ruigrok, T. J. H. (2011). Ins and outs of cerebellar modules. *Cerebellum* 10, 464–474. doi: 10.1007/s12311-010-0164-y

Ryan, K. E., Kim, P. S., Fleming, J. T., Brignola, E., Cheng, F. Y., Litingtung, Y., et al. (2017). Lkb1 regulates granule cell migration and cortical folding of the cerebellar cortex. *Dev. Biol.* 432, 165–177. doi: 10.1016/j.ydbio.2017.09.036

Saab, A. S., Neumeyer, A., Jahn, H. M., Cupido, A., Simek, A. A. M., Boele, H.-J., et al. (2012). Bergmann glial AMPA receptors are required for fine motor coordination. *Science* 337, 749–753. doi: 10.1126/science.1221140

Sarna, J. R., and Hawkes, R. (2003). Patterned Purkinje cell death in the cerebellum. *Prog. Neurobiol.* 70, 473–507. doi: 10.1016/S0301-0082(03)00114-X

Scoville, W. B., and Milner, B. (1957). Loss of recent memory after bilateral hippocampal lesions. *J. Neurol. Neurosurg. Psychiatry* 20, 11–21. doi: 10.1136/jnnp.20.1.11

Sherry, D. F., Jacobs, L. F., and Gaulin, S. J. C. (1992). Spatial memory and adaptive specialization of the hippocampus. *Trends Neurosci.* 15, 298–303. doi: 10.1016/0166-2236(92)90080-R

Sillitoe, R. V., and Joyner, A. L. (2007). Morphology, molecular codes, and circuitry produce the three-dimensional complexity of the cerebellum. *Annu. Rev. Cell Dev. Biol.* 23, 549–577. doi: 10.1146/annurev.cellbio.23.090506.123237

Sillitoe, R. V., Marzban, H., Larouche, M., Zahedi, S., Affanni, J., and Hawkes, R. (2005). Conservation of the architecture of the anterior lobe vermis of the cerebellum across mammalian species. *Prog. Brain Res.* 148, 283–297. doi: 10.1016/S0079-6123(04)48022-4

Sillitoe, R. V., Stephen, D., Lao, Z., and Joyner, A. L. (2008). Engrailed homeobox genes determine the organization of Purkinje cell sagittal stripe gene expression in the adult cerebellum. *J. Neurosci.* 28, 12150–12162. doi: 10.1523/JNEUROSCI.2059-08.2008

Sillitoe, R. V., Vogel, M. W., and Joyner, A. L. (2010). Engrailed homeobox genes regulate establishment of the cerebellar afferent circuit map. *J. Neurosci.* 30, 10015–10024. doi: 10.1523/JNEUROSCI.0653-10-2010

Smith, R. S., Kenny, C. J., Ganesh, V., Jang, A., Borges-Monroy, R., Partlow, J. N., et al. (2018). Sodium channel *SCN3A* (NaV1.3) regulation of human cerebral cortical folding and oral motor development. *Neuron* 99, 905–913.e7. doi: 10.1016/j.neuron.2018.07.052

Stoodley, C. J., D'Mello, A. M., Ellegood, J., Jakkamsetti, V., Liu, P., Nebel, M. B., et al. (2017). Altered cerebellar connectivity in autism and cerebellar-mediated rescue of autism-related behaviors in mice. *Nat. Neurosci.* 20, 1744–1751. doi: 10.1038/s41593-017-0004-1

Stoodley, C. J., and Schmahmann, J. D. (2009). Functional topography in the human cerebellum: a meta-analysis of neuroimaging studies. *Neuroimage* 44, 489–501. doi: 10.1016/j.neuroimage.2008.08.039

Sudarov, A., and Joyner, A. L. (2007). Cerebellum morphogenesis: the foliation pattern is orchestrated by multi-cellular anchoring centers. *Neural Dev.* 2:26. doi: 10.1186/1749-8104-2-26

Sudarov, A., Turnbull, R. K., Kin, E. J., Lebel-Potter, M., Guillemot, F., and Joyner, A. L. (2011). Ascl1 genetics reveals insights into cerebellum local circuit assembly. *J. Neurosci.* 31, 11055–11069. doi: 10.1523/JNEUROSCI.0479-11.2011

Sultan, K., Han, Z., Zhang, X. J., Xianyu, A., Li, Z., Huang, K., et al. (2016). Clonally related GABAergic interneurons do no randomly disperse but frequently form local clusters in the forebrain. *Neuron* 92, 31–44. doi: 10.1016/j.neuron.2016.09.033

Sun, T., and Hevner, R. F. (2016). Growth and folding of the mammalian cerebral cortex: from molecules to malformations. *Nat. Rev. Neurosci.* 15, 217–232. doi: 10.1038/nrn3707

Tan, G. H., Liu, Y. Y., Wang, L., Li, K., Zhang, Z. Q., Li, H. F., et al. (2018). PRRT2 deficiency induces paroxysmal kinesigenic dyskinesia by regulating synaptic transmission in cerebellum. *Cell Res.* 28, 90–110. doi: 10.1038/cr.2017.128

Tatavarty, V., Pacheco, A. T., Lin, H., Miska, N. J., Hengen, K. B., Wagner, F. F., et al. (2018). Autism-associated Shank3 is essential for homeostatic plasticity and neuronal circuit stability. *bioRxiv* [Preprint]. doi: 10.1101/365445

Thawani, A., Sirohi, D., Kuhn, R. J., and Fekete, D. M. (2018). Zika virus can strongly infect and disrupt secondary organizers in the ventricular zones of the embryonic chicken brain. *Cell* 23, 692–700. doi: 10.1016/j.celrep.2018.03.080

Uesaka, N., Uchigashima, M., Mikuni, T., Nakazawa, T., Nakao, H., Hirai, H., et al. (2014). Retrograde semaphoring signaling regulates synapse elimination in the developing mouse brain. *Science* 344, 1020–1023. doi: 10.1016/j.neuron.2018.01.018

Van Essen, D. C. (1997). A tension-based theory of morphogenesis and compact wiring in the central nervous system. *Nature* 385, 313–318. doi: 10.1038/385313a0

Van Essen, D. C., Donahue, C. J., and Glasser, M. F. (2018). Development and evolution of cerebral and cerebellar cortex. *Brain Behav. Evol.* 91, 158–169. doi: 10.1159/000489943

Varadarajan, S. G., Kong, J. H., Phan, K. D., Kao, T. J., Panaitof, S. C., Cardin, J., et al. (2017). Netrin1 produced by neural progenitors, not floor plate cells, is required for axon guidance in the spinal cord. *Neuron* 94, 790–799. doi: 10.1016/j.ydbio.2017.08.001

Voogd, J., and Ruigrok, T. J. (1997). Transverse and longitudinal patterns in the mammalian cerebellum. *Prog. Brain Res.* 114, 21–37. doi: 10.1016/S0079-6123(08)63356-7

Wadiche, J. I., and Jahr, C. E. (2005). Patterned expression of Purkinje cell glutamate transporters controls synaptic plasticity. *Nat. Neurosci.* 8, 1329–1334. doi: 10.1038/nn1539

Wang, L., Hou, S., and Han, Y. G. (2016). Hedgehog signaling promotes basal progenitor expansion and the growth and folding of the neocortex. *Nat. Neurosci.* 19, 888–896. doi: 10.1038/nn.4307

Wang, X., Tsai, J.-W., LaMonica, B., and Kriegstein, A. R. (2011). A new subtype of progenitor cell in the mouse embryonic neocortex. *Nat. Neurosci.* 14, 555–561. doi: 10.1038/nn.2807

Wang, Y., Wu, Q., Yang, P., Wang, C., Liu, J., Ding, W., et al. (2016). LSD1 co-repressor Rcor2 orchestrates neurogenesis in the developing mouse brain. *Nat. Commun.* 7:10481. doi: 10.1038/ncomms10481

Wangler, M. F., Yamamoto, S., Chao, H. T., Posey, J. E., Westerfield, J., Postlethwait, J., et al. (2017). Model organisms facilitate rare disease diagnosis and therapeutic research. *Genetics* 207, 9–27. doi: 10.1534/genetics.117.203067

Wasser, C. R., and Herz, J. (2017). Reelin: neurodevelopmental architect and homeostatic regulator of excitatory synapses. *J. Biol. Chem.* 292, 1330–1338. doi: 10.1074/jbc.R116.766782

Welker, W. (1990). "Why does cerebral cortex fissure and fold?," in *Cerebral Cortex*, Vol. 8B, eds E. G. Jones and A. Peters (Boston, MA: Springer), 3–136.

Welsh, J. P., Yuen, G., Placantonakis, D. G., Vu, T. Q., Haiss, F., O'Hearn, E., et al. (2002). Why do Purkinje cells die so easily after global brain ischemia? Aldolase C, EAAT4, and the cerebellar contribution to posthypoxic myoclonus. *Adv. Neurol.* 89, 331–359.

White, J. J., Arancillo, M., Stay, T. L., George-Jones, N. A., Levy, S. L., Heck, D. H., et al. (2014). Cerebellar zonal patterning relies on Purkinje cell

neurotransmission. *J. Neurosci.* 34, 8231–8245. doi: 10.1523/JNEUROSCI.0122-14.2014

White, J. J., Reeber, S. L., Hawkes, R., and Sillitoe, R. V. (2012). Wholemount immunohistochemistry for revealing complex brain topography. *J. Vis. Exp.* 5:e4042. doi: 10.3791/4042

White, J. J., and Sillitoe, R. V. (2013). Development of the cerebellum: from gene expression patterns to circuit maps. *Wiley Interdiscip. Rev. Dev. Biol.* 2, 149–164. doi: 10.1002/wdev.65

White, J. J., and Sillitoe, R. V. (2017). Genetic silencing of olivocerebellar synapses causes dystonia-like behaviour in mice. *Nat. Commun.* 8:14912. doi: 10.1038/ncomms14912

Wojcinski, A., Lawton, A. K., Bayin, N. S., Lao, Z., Stephen, D. N., and Joyner, A. L. (2017). Cerebellar granule cell replenishment postinjury by adaptive reprogramming of Nestin + progenitors. *Nat. Neurosci.* 20, 1361–1370. doi: 10.1038/nn.4621

Xiao, J., Cerminara, N. L., Kotsurovskyy, Y., Aoki, H., Burroughs, A., Wise, A. K., et al. (2014). Systematic regional variations in Purkinje cell spiking patterns. *PLoS One* 9:e105633. doi: 10.1371/journal.pone.0105633

Zhou, H., Lin, Z., Voges, K., Ju, C., Gao, Z., Bosman, L. W., et al. (2014). Cerebellar modules operate at different frequencies. *eLife* 3:e02536. doi: 10.7554/eLife.02536

Conflict of Interest Statement: The authors declare that the research was conducted in the absence of any commercial or financial relationships that could be construed as a potential conflict of interest.

frontiers in Cellular Neuroscience

ORIGINAL RESEARCH
published: 13 November 2018
doi: 10.3389/fncel.2018.00417

TRH Analog, Taltirelin Improves Motor Function of Hemi-PD Rats Without Inducing Dyskinesia via Sustained Dopamine Stimulating Effect

*Cong Zheng[1†], Guiqin Chen[2†], Yang Tan[1], Weiqi Zeng[1], Qiwei Peng[1], Ji Wang[1], Chi Cheng[1], Xiaoman Yang[1], Shuke Nie[2], Yan Xu[1], Zhentao Zhang[2], Stella M. Papa[3,4], Keqiang Ye[5] and Xuebing Cao[1]**

[1] Department of Neurology, Union Hospital, Tongji Medical College, Huazhong University of Science and Technology, Wuhan, China, [2] Department of Neurology, Renmin Hospital of Wuhan University, Wuhan, China, [3] Yerkes National Primate Research Center, Emory University School of Medicine, Atlanta, GA, United States, [4] Department of Neurology, Emory University School of Medicine, Atlanta, GA, United States, [5] Department of Pathology and Laboratory Medicine, Emory University School of Medicine, Atlanta, GA, United States

Thyrotropin-releasing hormone (TRH) and its analogs are able to stimulate the release of the endogenic dopamine (DA) in the central nervous system. However, this effect has not been tested in the Parkinson's disease (PD), which is characterized by the DA deficiency due to the dopaminergic neurons loss in the substantia nigra. Here, we investigated the therapeutic effect of Taltirelin, a long-acting TRH analog on 6-hydroxydopamine-lesioned hemi-Parkinsonian rat model. 1–10 mg/kg Taltirelin i.p. administration significantly improved the locomotor function and halted the electrophysiological abnormities of PD animals without inducing dyskinesia even with high-dose for 7 days treatment. Microdialysis showed that Taltirelin gently and persistently promoted DA release in the cortex and striatum, while L-DOPA induced a sharp rise of DA especially in the cortex. The DA-releasing effect of Taltirelin was alleviated by reserpine, vanoxerine (GBR12909) or AMPT, indicating a mechanism involving vesicular monoamine transporter-2 (VMAT-2), dopamine transporter (DAT) and tyrosine hydroxylase (TH). The *in vivo* and *in vitro* experiments further supported that Taltirelin affected the regulation of TH expression in striatal neurons, which was mediated by p-ERK1/2. Together, this study demonstrated that Taltirelin improved motor function of hemi-PD rats without inducing dyskinesia, thus supporting a further exploration of Taltirelin for PD treatment.

Keywords: Parkinson's disease, TRH, Taltirelin, L-DOPA, dopamine, tyrosine hydroxylase

OPEN ACCESS

Edited by:
Jing-Ning Zhu,
Nanjing University, China

Reviewed by:
Paolo Calabresi,
University of Perugia, Italy
Camino Fidalgo,
University of Zaragoza, Spain

****Correspondence:***
Xuebing Cao
caoxuebing@126.com

† These authors have contributed equally to this work

Received: *11 August 2018*
Accepted: *25 October 2018*
Published: *13 November 2018*

Citation:
Zheng C, Chen G, Tan Y, Zeng W, Peng Q, Wang J, Cheng C, Yang X, Nie S, Xu Y, Zhang Z, Papa SM, Ye K and Cao X (2018) TRH Analog, Taltirelin Improves Motor Function of Hemi-PD Rats Without Inducing Dyskinesia via Sustained Dopamine Stimulating Effect. Front. Cell. Neurosci. 12:417. doi: 10.3389/fncel.2018.00417

INTRODUCTION

Parkinson's disease (PD) is a neurodegenerative disease with the second high incidence among elderly over the age of 65. The main "Off" symptoms of PD patients, such as bradykinesia and rigidity, are closely associated with oscillation at the high β band (25–35 Hz) between the motor cortex and the basal ganglia (Jenkinson and Brown, 2011; Li et al., 2012; Dupre et al., 2016),

which is usually accompanied by a pathological burst firing pattern of projecting neurons in the motor cortex or striatum (Singh et al., 2016). These abnormal electrophysiological features are the prominent manifestation of disordered basal ganglia neural circuits as a result of the significant loss of dopaminergic neurons in the substantia nigra (SN) and accordingly dopamine (DA) deficiency in the striatum. Thus, the symptoms not only can be halted by deep brain stimulation (DBS) (Li et al., 2012), which directly targets the oscillation, but also can be largely alleviated by pharmacological DA substitution, such as the administration of DA precursor, L-DOPA (Dupre et al., 2016; Kuhn et al., 2017). L-DOPA is a classic medicine used in relieving the symptoms of PD, however, it is gradually recognized that sub-chronic use of L-DOPA is toxic to dopaminergic neurons (Burbulla et al., 2017), and what's more worrying, L-DOPA-induced dyskinesia (LID) severely damages the life quality of patients and is hard to managed once appears (Calabresi et al., 2010). Thus, novel targets and drugs for the treatment of PD are in urgent need.

Thyrotropin-releasing hormone (TRH) is widely known as a metabolism-regulating endocrine hormone acting through the hypothalamus–pituitary–thyroid axis (HPT axis). However, another role of TRH as a neuropeptide is underestimated (Gary et al., 2003; Khomane et al., 2011). Multiple studies have reported that TRH could promote DA release both *in vitro* (Nishikawa et al., 1993) and *in vivo* (Crespi et al., 1986; Kalivas et al., 1987; Puga et al., 2016). A single injection of TRH increased DA release in striatum by 240% (Kreutz et al., 1990). In addition, a study once shown that subcutaneous injection of TRH sustained-release microparticles significantly improved motor function of encephalitis-induced PD model rats (Ogata et al., 1998). However, TRH has the intrinsic shortcomings such as short half-life, poor lipophilicity and strong HPT axis stimulating effect, which severely restrict its application (Kinoshita et al., 1998). Taltirelin (TA-0910, Ceredist®), an oral-effective TRH analog, has 10 to 100 times more potent central nervous system (CNS) stimulant activity and eight times longer duration than TRH. More importantly, Taltirelin has been approved in the treatment of spinocerebellar degeneration (SCD), which makes it highly promising in exploring more applications of TRH family (Kinoshita et al., 1994, 1998). In addition to the anti-ataxic (Nakamura et al., 2005), neuroprotective (Urayama et al., 2002; Veronesi et al., 2007) and analgesic effect (Tanabe et al., 2009), Taltirelin is also able to stimulate DA release (Fukuchi et al., 1998). Is there any benefit or any superiorities over L-DOPA of Taltirelin in treating PD model animals, and what are the possible underlying mechanisms? These issues all await further investigations.

In this study, we established steady *in vivo* electrophysiological recording system of PD model animals to explore and compare the efficacy of Taltirelin and L-DOPA, *in vivo* and *ex vivo*. Our study showed that Taltirelin gently and persistently promoted DA release in the CNS thus alleviated the locomotor disorder and related abnormal electrical activities of PD rats, without inducing dyskinesia even in sub-chronic or high-dose use, thus providing the theoretical basis for a novel PD therapy with Taltirelin.

MATERIALS AND METHODS

Animals

Seven-week-old male Sprague-Dawley (SD) rats (Beijing HFK Bioscience Co., Ltd., China) weighing 230–250 g were used in this experiment. The animals were housed with food and water provided *ad libitum*, 12 h light/dark cycle, constant temperature and humidity. Animal use and care were conformed to the recommendations of the Guidelines of Laboratory Animals Ethics of Tongji Medical College, Huazhong University of Science and Technology. The protocol was approved by the Ethics Committee of Huazhong University of Science and Technology.

Stereotaxic Surgery

6-OHDA Lesion

Rats were anesthetized with chloral hydrate (7%, 5 ml/kg, i.p.) and secured on the stereotaxic apparatus (RWD Life Science Co., Ltd., China). A temperature controller system was used to maintain body temperature at 37°C. A total dose of 16 μg of 6-hydroxydopamine (6-OHDA, Sigma, United States) dissolved in 4 μl of sterile 0.9% saline and 0.02% ascorbic acid was injected into the right medial forebrain bundle (MFB) via a 10-μl microsyringe at a rate of 0.5 μl/min at the following stereotactic coordinates: anteroposterior (AP), −4.4 mm; mediolateral (ML), −1.5 mm; and dorsoventral (DV), 7.8 mm from dura (Chen et al., 2017). The microsyringe was maintained in place for 5 min before retracting. After 2 weeks of recovery, apomorphine-induced contralateral rotation behavior was assessed.

Microelectrode Implantation

After apomorphine induced rotation test, eight near-complete lesioned rats and two intact rats received the implantation surgery. Two multichannel microwire electrode recording arrays, each constructed of eight stainless steel microwires (Stablohm 675, 35 μm in diameter, heavy formvar coated, arranged in 4*2, Bio-Signal Technologies, McKinney, TX, United States) were targeted at the layer V of the primary motor cortex (MI, center coordinates: AP, +2.5 mm; ML, −3 mm; DV, −1.6 mm from dura) (Li et al., 2012) and dorsolateral striatum (DLS, center coordinates: AP, +0.2 mm; ML, −3.8 mm; DV, −3.5 mm from the dura) (Halje et al., 2012) in the lesioned side. Four stainless steel screws were firmly attached to the skull for electrode anchoring, and an additional ground wire was connected to one of them for reference. At the end of the procedure, the whole electrode array was secured with dental cement.

Behavioral Assessment

Apomorphine-Induced Rotation Test

The efficacy of the dopaminergic lesion was tested by measuring contralateral turning behavior with an acute subthreshold dose of apomorphine (0.05 mg/kg s.c.) 2 weeks post surgery. Rats that exhibited more than 200 turns contralateral to the lesion side in

30 min were considered to be compatible with the model of near-complete lesion and were selected for further study (Boldry et al., 1995).

Adjusting Step Test

The hindlimbs and contralateral forelimb were slightly lifted up, with only the to-be-examined forelimb touching the table. The rat was moved slowly along the table with speed of 90 cm in 5 s. The number of adjusting steps of each forelimb in the forward directions was counted for three times and took the average (Pinna et al., 2007; Chen et al., 2017).

Abnormal Involuntary Movements (AIMs) Score

After injection of L-DOPA (12 mg/kg + benserazide 6 mg/kg, i.p.) or Taltirelin (1 or 5 mg/kg), AIMs were evaluated for 1 min every 20 min for a total 140 min following L-DOPA treatment, using the validated AIMs scale. Axial, limb and orofacial (ALO) dyskinesia were graded, respectively, from score 0 to 4: 0 = absent; 1 = occasional, present during less than half min; 2 = frequent, present during more than half min; 3 = continuous but interrupted by strong sensory distraction; 4 = continuous, not interrupted by strong sensory distraction. All the scores were graded by one experienced researcher during each experiment, while behaviors of animals were also recorded using a video camera for necessary reviews (Lundblad et al., 2004; Chen et al., 2017).

In vivo Electrophysiological Recordings and Analysis

Data Recordings

Both the local field potentials (LFPs) and extracellular single-unit activity in MI and DLS were recorded simultaneously using 16-channel Zeus® system (Bio-Signal Technologies, McKinney, TX, United States). Broadband (0.3 Hz–7.5 kHz) neural signals were simultaneously recorded (16 bits @ 30 kHz). Spike and LFP bands were extracted with high-pass (300 Hz) and low-pass (200 Hz) filters, respectively. Real-time spike sorting was performed using principal component analysis (PCA). LFP were down sampled to 1 kHz. Data recorded from intact rats contained 10 min of free moving state. For the hemi-Parkinsonian rats, the recorded data included 10 min of basal line, 120 min continuous data post administration of L-DOPA or at least 10 min data at different time point during 8 h observation period after Taltirelin administration.

Spectral Analysis of LFP

Local field potential in MI and DLS was assessed in two frequency ranges: high β (25–35 Hz) and high γ (70–110 Hz) using NeuroExplorer 5.107 software (Nex Technologies, Littleton, MA, United States) as previously described with modification (Li et al., 2012). Briefly, epochs of 120 s, representative of each sample and free of major artifacts, were used to calculate LFP power. The spectrum value was normalized as log of raw power spectral density (PSD) from 0.5 to 200 Hz, which was calculated using Fast Fourier Transform with Hanning window function, shifting each 0.05 s with 50% window overlap. The frequency block was set at 512 at 0.2 Hz resolution.

Single-Unit Spike Sorting and Classification

Single-unit spike sorting was performed with Off-Line Spike Sorter 2.8.5 software (Plexon Inc., Dallas, TX, United States) using a combination of automatic and manual sorting techniques. The first three principal components (PCs) of all waveforms recorded from each channel were depicted in 3-dimensional (3D) space. Automatic clustering techniques (K-means clustering and valley seeking methods) were used to produce an initial separation of waveforms into individual cluster. Each cluster was then checked manually to ensure that the cluster boundaries were well separated and spike waveforms were consistent. Pyramidal projection neurons (PNs) and interneurons (INs) in MI (Li et al., 2012), and striatal projection neurons (SPNs), tonically active interneurons (TANs), and fast spiking interneurons (FSIs) in DLS (Singh et al., 2018) were distinguished according as described previously (**Supplementary Figure S1**).

Discharge Pattern Analysis

Burst discharge was quantified using Legendy surprise (probability) method with the Poisson surprise threshold at 5 using NeuroExplorer. Parameters for burst detection were based on typical short epochs of spiking that could be unequivocally classified as burst activity. Limits were as follows: maximal interval to start (10 ms), maximal interval to end bursts (10 ms), minimal interburst interval (20 ms), and minimal number of spikes or burst duration (three spikes and 20 ms) (Singh et al., 2016).

Assessing Neurotransmitters Release by Microdialysis

A self-made concentric circular microdialysis probe (dialysis membrane, RC, cut-off molecular weight: 20 kDa, Union Carbide; membrane length: 3 mm, outside diameter 1.5 mm) (**Supplementary Figure S2**) was inserted into the lesioned DLS (center coordinates: AP, +0.2 mm; ML, −3.8 mm; DV, −3.5 mm from the dura) under anesthesia with isoflurane (1.5%) (Yan et al., 2016). The sterile artificial cerebrospinal fluid (aCSF) (140 mM NaCl, 3 mM KCl, 1.3 mM, $CaCl_2$, 0.9 mM $MgCl_2$, 0.27 mM NaH_2PO4, 1.2 mM Na_2HPO4, 3.4 mM D-glucose, pH 7.4) were perfused through the microdialysis probe with a constant flow rate of 2.0 μl/ml using a CMA 402 infusion pump (Harvard Apparatus, Holliston, MA, United States). After a stabilization period of 1 h perfusion, two baseline samples of dialysate (0 h) were obtained and then animals were injected i.p. with either saline, 250 mg/kg α-methyl-dl-tyrosine (AMPT, Sigma, United States) (Butcher et al., 1988), 5 mg/kg reserpine (MedChemExpress, United States) (Butcher et al., 1988; Kannari et al., 2000) or 20 mg/kg vanoxerine dihydrochloride (GBR12909; MedChemExpress, United States) (Budygin et al., 2000). Two hours later, 5 mg/kg Taltirelin was injected. Samples were collected at 0.5 h, 2 h, and 3 h of the whole microdialysis experiment. One part of the antioxidative mixture (100 mM acetic acid, 3.3 mM L-cysteine, 0.27 mM Na_2EDTA, 12.5 μM ascorbic acid, pH 3.2) is added to four parts of dialysate (Van Schoors et al., 2015), which was immediately stored at −20°C until DA and its metabolites measurement by HPLC.

High Performance Liquid Chromatography Coupled With Electrochemical Detection (HPLC-ECD) Analysis of Neurotransmitters

The level of DA, its metabolites 3,4-dihydroxyphenylacetic acid (DOPAC), or homovanillic acid (HVA) and another monoamine neurotransmitter norepinephrine (NE) of rat tissues or dialysates were analyzed by HPLC-ECD as following: For tissue samples, at different timepoint (0, 0.5, 1, and 2 h) after the i.p. injection of L-DOPA (12 mg/kg, with benserazide 6 mg/kg) or 5 mg/kg Taltirelin. Cortex or striatum of each animal were hand-dissected and tissues of 30–80 mg were homogenized in 300 μl of 0.1 M $HClO_4$ (0.1% L-cysteine) and centrifuged at 18,000 × *g* for 15 min at 4°C; supernatants were collected and stored at −20°C. The mixed standards of DA, DOPAC and NE were prepared by diluting each stock solutions (1 mg/ml, in 0.1 M $HClO_4$ with 0.1% L-cysteine) with the mobile phase (3 mM sodium heptanesulfonate, 100 mM sodium acetate, 85 mM citric acid, 0.2 mM EDTA, and 8% methanol) into 2.1, 6.2, 18.5, 55.6, 166.7 or 500 ng/ml. For dialysate samples, mixed standards (2.5, 5, and 10 ng/ml) of DA, DOPAC and HVA are prepared by diluting the stock standard solutions (1 mg/ml, aCSF: antioxidative mixture = 4:1) with the mobile phase. Samples and standards (30 μl) were injected into the Waters 510 HPLC system equipped with HPLC column (Zorbax C18, 4.6 mm*25 cm, particle size 5 μm; Agilent, Germany). The mobile phase was delivered at 1 ml/min flow rate; column temperature was 17°C; electrodes potential was 700 mV. Detection of compounds was performed with HP1049i ECD detector. The concentration of each sample was obtained from the standard curve generated by plotting concentration of the standards against respective peak area.

Serum Thyroid Hormone Measurement

Blood was collected at 2 h post-administration of drugs and placed in 4°C overnight. Then the blood was centrifugated at 3,000 rpm for 15 min, and serum was collected for further analysis. The levels of thyroid stimulating hormone (TSH), free and total thyroxine (T4) or triiodothyronine (T3) were measured using ELISA kit, respectively (ALPCO) according to the manufacturer's protocol. Briefly, 50 μL of serum samples or reference was pipetted into the assigned wells, followed by T3/T4 enzyme-conjugated solution with 1 h of incubation. The mixture was removed, and the plate was washed several times with water; then, working substrate solution was added to each well for reaction, and after 20 min in the dark, the reaction was stopped by adding 3 M HCl. Absorbance was read at 450 nm. The corresponding concentrations were calculated based on the standard curve.

Primary Neonatal Rat Striatal and Cortex Neurons Culture

Primary rat striatal and cortex cultures were prepared as described previously (Beaudoin et al., 2012). In brief, the striatum and cortex was dissected from P1-3 mouse pups. The isolated tissues were then chemically and mechanically dissociated into single cell suspensions. Cells were plated into 6-well plates coated with 0.5 mg/ml poly-L-lysine at a density of 5.5–6 × 10^5/well. Incubate the cells with plating medium: DMEM/F-12 medium (Hyclone, United States) with 20% FBS (Gibco, United States) and 100 units/ml of penicillin and streptomycin for 4 h and replace the medium with maintenance medium: Neurobasal medium (Gibco, United States) with 2% B-27 supplement (Gibco, United States), 2 mM glutamine (Gibco, United States) and 100 units/ml of penicillin and streptomycin. Cultures were maintained in a humidified incubator at 37°C/5% CO_2 for 3 days *in vitro* prior to further studies.

Western Blot Analysis

For animal brain tissues, striatum was dissected and homogenized with micro-tissue-grinders (Tiangen, OSE-Y30) in ice-cold enhanced RIPA lysis buffer [50 mM Tris, pH 7.4, 150 mM NaCl, 1% Triton X-100, 1% sodium deoxycholate, 0.1% SDS, 5 mM EDTA, 2 mM Na3VO4, 1 mM PMSF, 10 mM NaF, and a cocktail of protease inhibitors (Roche, United States)]. For cellular culture, cells were scraped down by a cell scraper and lysed in lysis buffer. Brain or cellular lysates were centrifuged at 12,000 × *g* at 4°C for 15 min and the protein concentrations were determined by a BCA assay kit (Pierce, Rockford). The supernatants were boiled for 10 min with 1% SDS loading buffer. After SDS-PAGE, the samples are transferred to a PVDF membrane (Millipore, United States), blocked with 5% non-fat milk for 1 h at room temperature, and incubated overnight at 4°C with primary antibodies against following proteins: tyrosine hydroxylase (TH) (1:1000, Proteintech, 25859-1-AP), p44/42 MAPK (ERK1/2) (1:2000, Cell Signaling, #4695), phospho-p44/42 MAPK (ERK1/2) (1:2000, Cell Signaling, #4370), ΔFosB (1:500, Cell Signaling, #9890), GAPDH (1:2000, AntGene, ANT012). The membranes were washed with TBST, then incubated with HRP-conjugated anti-rabbit secondary antibody (1:3000, AntGene, ANT020) for 1 h at room temperature. After washing, the membrane was visualized with an ECL detection kit (Thermo Scientific) in the Bio-Rad imaging system. Bands intensities were analyzed with ImageJ software.

Immunohistochemical and Immunofluorescent Staining

Immunohistochemical Staining (IHC)

Animals were deeply anesthetized and transcardially perfused with 0.9% saline, followed by 4% paraformaldehyde (PFA) in 0.1 M PBS (pH 7.4). Brain were dissected and fixed in 4% PFA overnight at 4°C. After fixation, tissues were transferred to 70% ethanol and processed for paraffin sectioning (4 μm/section). Sections were mounted on glass slides, deparaffinized by xylene, dehydrated in graded ethanol solutions, baked in the basic antigen retrieval buffer (pH = 6.0), and washed with phosphate buffer (pH 7.4). After washing, sections were blocked with 3% bovine serum albumin (BSA) and then incubated with diluted primary antibody in a humidified chamber overnight at 4°C. The following primary antibodies were used: anti-FosB antibody (1:100, Santa Cruz, sc-48, detecting FosB-ΔFosB), anti-TH antibody (1:750, Abcam, ab112). Sections were washed and subsequently incubated with biotinylated goat anti-rabbit

IgG, then HRP labeled streptavidin fluid, followed by DAB solutions, counterstained with Harris hematoxylin, dehydrated in graded ethanol solutions, and eventually cover slipped. Images were collected through an Olympus camera connected to the microscope at the same light intensity, and analyzed using Image-Pro Plus software.

Immunofluorescent Staining (IF)

For brain slices, immunofluorescent staining shared a same procedure with immunohistochemistry staining before secondary antibodies incubation. For cellular cultures, sterile coverslips were placed in 24-well plates and coated with PLL before cells were plated on the coverslips. After intervention, cells were first washed with PBS and fixed with 4% PFA. Then cells were permeablized with 0.2% Triton X-100 and blocked with 5% BSA. Incubate brain slices or cell slides with following primary antibodies overnight at 4°C: anti-DOPA decarboxylase (AADC) antibody (1:250, Abcam, ab3905), anti-dopamine transporter (DAT) antibody (1:50, Santa Cruz, sc-32258), anti-TH antibody (1:750, Abcam, ab129991), anti-MAP2 antibody (1:500, Servicebio, Wuhan), anti-GABA antibody (1:200, Abcam, ab8891), anti-dynorphin antibody (1:50, Santa Cruz, sc-46313), anti-enkephalin (1:100, Abcam, ab150346). After being washed, sections were incubated in dark with an appropriately diluted Alexa 488- or Cyanine 3-coupled secondary antibodies followed by DAPI staining nucleus for 10 min. Coverslips were mounted on slides with one drop per coverslip of antifade mounting medium (Beyotime, China). Images were collected using fluorescence microscopy with image manipulation software, and analyzed using Image-Pro Plus software.

Statistic Analysis

Data were analyzed using one-way analysis of variance (ANOVA) followed by Tukey HSD or LSD *post hoc* tests for multiple comparisons between groups, and Student's *t*-test for comparing two groups. All statistical analyses were performed in SPSS 21.0 software. The significance level was set at $p < 0.05$. Data are presented as mean ± SEM for all results.

RESULTS

Taltirelin Improved Motor Function and Normalized Aberrant Electrical Activity of 6-OHDA-Lesioned Rats

The *in vivo* multi-channel electrophysiological recording technology, of good time and spatial resolution, allows real-time recording and analysis of electrophysiological data and animal behavior simultaneously, which makes it a unique tool in studying mechanisms of motor diseases. After the apomorphine-induced rotation tests, complete-depleted (TH-positive dopaminergic terminals in striatum, **Figures 1A,B**, or dopaminergic neurons in the SN, **Supplementary Figure S3**, were reduced by more than 90%, $p < 0.001$) animals were implanted with electrodes targeting MI and DLS (**Figures 1C–E**). When spikes and LFP could be steadily recorded in most of the channels, behavior assessments were performed. In the adjusting step test, the number of steps of the lesioned forelimb of the PD rats significantly decreased compared with the intact forelimb (1.39 ± 0.23 vs. 9.97 ± 0.28, $p < 0.001$), indicating an impaired locomotor function. After Taltirelin 1–10 mg/kg i.p. injection, the bradykinesia of lesioned forelimb was relieved at as early as 0.5 h after injection (5.75 ± 1.5 of 1 mg/kg, 9.50 ± 2.38 of 5 mg/kg, 11.00 ± 1.00 of 10 mg/kg vs. 2.75 ± 0.50 of control, $p < 0.01$). The improving effect maintained for at least 10 h and was dose-dependent (**Figure 1F**).

Next, the LFP PSD analysis showed that free-moving PD rats exhibited high β band oscillation (25–35 Hz) in the MI and DLS ipsilateral to the lesion, which is a characteristic abnormal electrical activity associated with bradykinesia. Administration of 1 mg/kg or 5 mg/kg Taltirelin caused a significant reduction of the power of the β band oscillation, which approached the normal level 2 h later ($86.15 \pm 3.94\%$, $84.27 \pm 3.15\%$, respectively, compared with their baseline, **Figures 1G,H**). Furthermore, a total of 75 discharge units in the MI and 78 discharge units in the DLS were recorded from 10 rats in this experiment. 32 PNs (44%) and 36 SPNs (46%) were classified for following single unit firing pattern analysis. Consistent with previous studies, there was an increase of burst firing rather a random firing mode of neurons at the lesioned side of the PD rat. Similarly, Taltirelin (1 or 5 mg/kg) significantly reduced the total number of spikes in burst discharge of PNs by 17.06% and 12.32%, or of SPNs by 14.29% and 16.03%, respectively (**Figures 1I–K**, $p < 0.05$). Therefore, the alleviation of abnormal electrophysiological indicators further supported the finding that Taltirelin relieved the bradykinesia of 6-OHDA-PD rats.

Acute or Sub-Chronic Administration of Taltirelin Relieved Bradykinesia Without Inducing Dyskinesia

L-DOPA-induced dyskinesia is one of the main drawbacks of long-term L-DOPA therapy, which are characterized by involuntary, repetitive orofacial, limb and axial movements. Interestingly, no dyskinesia-related behaviors were observed in the animals treated with Taltirelin even at high, toxic dose (10 mg/kg). In order to confirm the difference between Taltirelin and L-DOPA, we chose a relative high dose (5 mg/kg) of Taltirelin and a high dose (12 mg/kg, with benserazide 6 mg/kg) of L-DOPA which usually induces dyskinesia at first dose. As expected, animals injected i.p. with L-DOPA exhibited obvious dyskinesia as early as 20 min post-administration. Meanwhile, the power of β oscillation decreased with the release of bradykinesia, while the dyskinesia-associated high γ band oscillation (70–110 Hz) arose and intensified as dyskinesia aggravated (increased by 126% compared with baseline at 1 h, $p < 0.05$). On the contrary, the animals injected with Taltirelin did not show any abnormal behaviors or high γ oscillation (**Figures 2A–C** and **Supplementary Figures S4A,B**).

ΔFosB is a classic marker of LID, whose level in the DA-deprived striatum is positively related to the severity of LID (Cao et al., 2010) (**Supplementary Figures S4C,D**). The animals treated with Taltirelin for 7 days showed no signs of dyskinesia, however, there was a moderate but significant elevation of ΔFosB

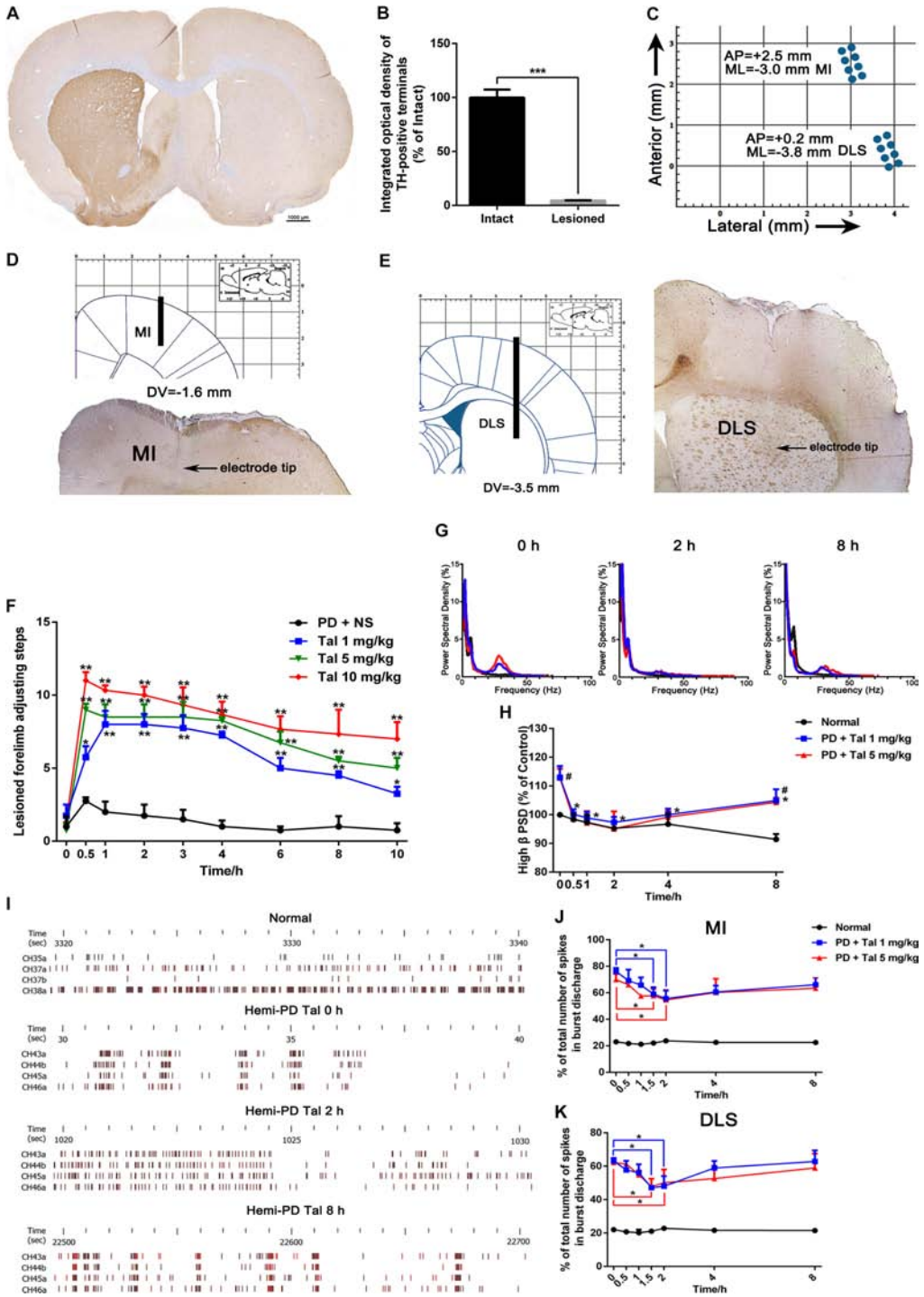

FIGURE 1 | Taltirelin improved motor function and normalized aberrant electrical activity of 6-OHDA-lesioned rats. **(A)** Tyrosine hydroxylase (TH) immunostaining in the striatum of 6-OHDA lesioned rat model. **(B)** Integrated optical density of TH-positive terminals in the intact and lesioned side. $N = 3$. **(C)** Schematics illustrating horizontal positioning of recording electrodes targeting primary motor cortex (MI) or dorsolateral striatum (DLS) relative to bregma. **(D,E)** Coronal plane indicating schematic vertical positions for MI and DLS together with AP positions (left). Typical brain slice showed actual electrode position (right). Electrodes were implanted in the right (lesioned) side. **(F)** Adjusting step tests of PD rats treated with saline or Taltirelin (Tal 1, 5 or 10 mg/kg, i.p.). $N = 6$. **(G)** Typical example of power spectral distribution of local field potential (LFP) after treatment of Taltirelin (1 or 5 mg/kg, i.p.). **(H)** Power of high β oscillation changed with time (a total of 128 LFP data from two intact rats and six hemi-Parkinsonian rats). **(I)** Typical examples of raster plots showing the neuronal discharge patterns of normal or 6-OHDA-lesioned rats. **(J,K)** The % of total number of spikes in burst discharge of PNs or striatal projection neurons (SPNs) (a total of 75 PNs and 78 SPNs from two intact rats and eight hemi-parkinsonian rats). $^{\#}p < 0.05$ vs. control; $^{*}p < 0.05$; $^{**}p < 0.01$; $^{***}p < 0.001$. Error bars denote SEM.

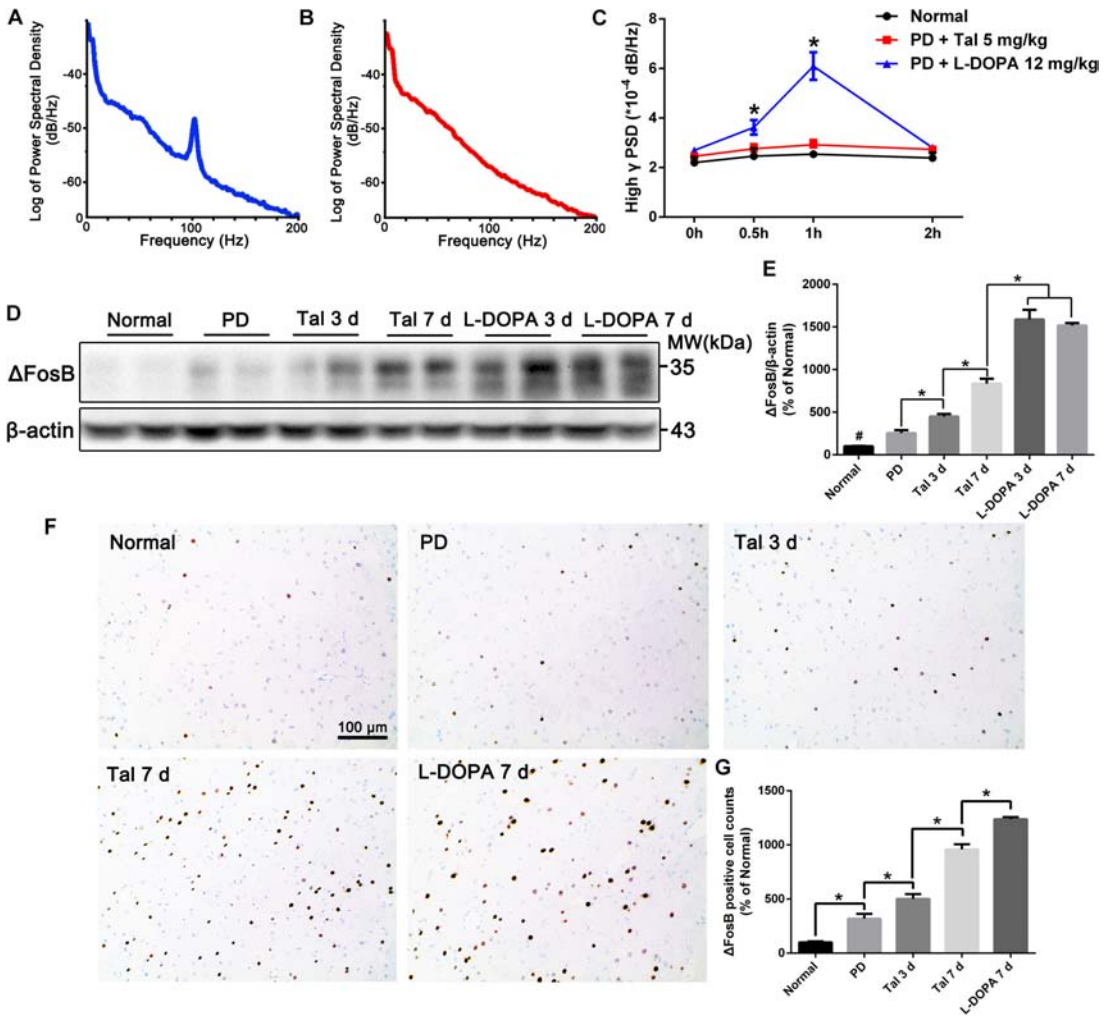

FIGURE 2 | Acute or sub-chronic administration of Taltirelin relieved bradykinesia without inducing dyskinesia. **(A,B)** Power spectral distribution of local field potential (LFP) after treatment of L-DOPA (12 mg/kg, with benserazide 6 mg/kg) or Taltirelin (5 mg/kg, i.p.). **(C)** Power of high γ oscillation changed with time (32 LFP data in MI and DLS of two intact rats and 96 LFP records in six lesioned rats). **(D,E)** Western blot analysis of ΔFosB in the DA-denervated striatum of each group (normal, PD, Tal 5 mg/kg or L-DOPA 12 mg/kg treated for 3 or 7 days). $N = 3$. **(F)** Immunostaining of ΔFosB of lesioned striatum. **(G)** Counts of ΔFosB-positive cells in each group. $N = 3$. $^{\#}p < 0.01$ vs. intact or other groups; $^{*}p < 0.05$; $^{**}p < 0.01$. $N = 3$. Error bars represent SEM.

in the lesion striatum (834.40 ± 58.46% of the normal) compared with the short-term (3 days) Taltirelin (449.70 ± 29.15%) or PD control (254.7 ± 34.46%). However, the ΔFosB levels in Taltirelin groups were still lower than the levels in L-DOPA (12 mg/kg) group of 3 days (1588.00 ± 84.70%) or of 7 days (1515.00 ± 30.94%) (**Figures 2D,E**, $p < 0.05$). The counts of ΔFosB-positive cells in the striatum confirmed the observation in Western blot (PD < Tal 3 days < Tal 7 days < L-DOPA, 318.18 ± 40.45%, 511 ± 32.28%, 957.58 ± 48.48%, 1236.36 ± 21.00%, respectively) (**Figures 2F,G**, $p < 0.05$).

We further assessed the levels of DA, its metabolite, DOPAC and another monoamine neurotransmitter NE in the cortex and striatum of PD rats (**Figures 3A–F**). As expected, the basal level of DA in the lesioned cortex (0.13 ± 0.02 ng/mg vs. 0.37 ± 0.06 ng/mg, $p < 0.01$) and striatum (0.25 ± 0.03 ng/mg vs. 26.31 ± 2.96 ng/mg, $p < 0.01$) was significantly lower than the intact side. Similarly, DOPAC (0.19 ± 0.02 ng/mg vs. 1.54 ± 0.34 ng/mg, $p < 0.05$) and NE (3.35 ± 0.15 ng/mg vs. 3.98 ± 0.23 ng/mg, $p < 0.05$) also decreased significantly in the striatum. After injection of L-DOPA, DA, DOPAC and NE in both the cortex and striatum increased significantly ($p < 0.05$). However, the concentrations of DA in the lesioned striatum peaked at 0.5 h (1.14 ± 0.46 ng/mg) post-injection, which then decreased with time, while the DA in the cortex peaked at 1 h (0.33 ± 0.10 ng/mg), which was in a better correlation with the LID behaviors and CNS abnormal electrical activities (**Figure 2C**). On the contrary, Taltirelin induced a slight reduction of DA and elevation of DOPAC in the cortex and striatum, while the trend of NE level is similar to the L-DOPA group though at a lower level. The results in the Taltirelin group seemed contradictory but was consistent with previous studies (Puga et al., 2016). Since the tissue homogenates were mainly composed of intracellular

fluids, a decrease in content may suggest the release of these neurotransmitters into the extracellular spaces. To confirm this, we then examined the DA-releasing effect of Taltirelin through microdialysis.

Taltirelin Elevated Dopamine Level in a DA-Releasing Dependent Manner

Here, we used microdialysis and three DA-releasing-related drugs to confirm the DA-releasing function of Taltirelin and investigate the possible underlying mechanisms. TH inhibitor, AMPT and vesicular monoamine transporter-2 (VMAT-2) inhibitor, reserpine both causes DA depletion and results in very low level of both intracellular and extracellular DA in the striatum. Vanoxerine (GBR12909) is a DA reuptake inhibitor, which elevates DA in striatum after administration but would also deplete DA pool. Results showed that the basal extracellular levels of DA, DOPAC and HVA in the lesioned striatum of rats were too low to detect. As expected, vanoxerine (20 mg/kg, i.p.) caused a sharp increase (6.55 ± 1.07 ng/ml, $p < 001$) and then fall of DA, while AMPT (250 mg/kg, i.p.) and reserpine (5 mg/kg, i.p.) produced no undetectable alteration of DA. As the level of DA stabilized 2 h later, Taltirelin (5 mg/kg, i.p.) was administrated, and DA was elevated to different levels in each groups: N.S. > reserpine > AMPT > vanoxerine (8.54 ± 2.94 ng/ml, 4.51 ± 0.73 ng/ml, 1.36 ± 0.22 ng/ml, 0 ng/ml) (**Figure 3G**). Thus, the results supported the fact that Taltirelin promotes DA release in DA-depleted striatum. In addition, the lower or even absent DA in groups with pre-treatment further suggested that intracellular DA pool made up a large part of DA released by Taltirelin. As for the metabolites of DA, DOPAC: reserpine > N.S. > vanoxerine > AMPT (75.06 ± 12.22 ng/ml, 38.97 ± 12.67 ng/ml, 22.75 ± 3.70 ng/ml, 4.35 ± 1.09 ng/ml) (**Figure 3H**); HVA: reserpine > N.S. > vanoxerine > AMPT (27.25 ± 12.22 ng/ml, 22.22 ± 7.34 ng/ml, 0.83 ± 0.13 ng/ml, 0.06 ± 0.01 ng/ml) (**Figure 3I**). Since inhibition of VMAT-2 by reserpine led to more chances for DA to be exposed and metabolized in the cytoplasm, more DA metabolites were generated accordingly. Interestingly, incomplete blockade by the above DA-releasing inhibitors and less DA in group treated with TH-inhibitors AMPT suggested the existence of a newly synthesized DA pool induced by Taltirelin, which is more meaningful as the number of residual dopaminergic neurons, i.e., the storage of DA, diminishes as the disease progresses, and new source of DA would be very in need. Thus, we next examined the possible ability of Taltirelin to manipulate DA synthesis.

Taltirelin Elevated the Level of TH Both *in vivo* and *in vitro* in a p-ERK/1/2-Dependent Manner

It was once reported that TRH could elevate the activity of TH (Yokoo et al., 1983), but whether the expression of TH could be manipulated by TRH was not reported. We thus stained the DA-deprived striatum slices with TH and found significantly increased TH-positive neurons in animals injected with Taltirelin (5 mg/kg) for continuous 7 days but not in animals with 3-day injection (350.00 ± 28.87%, 183.33 ± 44.10%, respectively, **Figures 4A–C**; $p < 0.05$). We then quantified the level of TH in animals injected with different doses of Taltirelin for 3 days, but there was no obvious elevation of TH even at high dose such as 10 mg/kg (**Figures 4D,E**). In contrast, the TH level in the animals injected with Taltirelin (5 mg/kg) for 7 days (27.36 ± 4.58%) was significantly higher than other groups, including Taltirelin (1 mg/kg, 7 days) (7.12 ± 4.43%) (**Figures 4F,G**; $p < 0.05$). The above results showed that sub-chronic, high-dose Taltirelin could elevate TH level in the lesioned striatum of PD rats. Besides, we also conducted double-staining of TH with other dopaminergic neurons markers, such as AADC and DAT, but found no double-positive neurons (data not shown), indicating that those Taltirelin-induced TH-positive neurons were non-dopaminergic neurons.

We further verified our results *in vitro* using primary neurons. It was reported that there was a 4-fold increase in the activity of TH in the brain during rat embryonic development, while only a 2.5-fold increase after birth (Coyle and Axelrod, 1972). To ensure the consistency, we cultured the neonatal rats of 1–3 days (P1–3) primary striatal neurons. We found that primary striatal neurons cultured for 3 days had basal expression of TH, while the primary cortical neurons had a much lower level of TH. Studies have shown that *ex vivo* cultured itself could induce TH expression (Du and Iacovitti, 1997), which may act as compensation to the loss of DA. On the third day *in vitro*, the primary neurons were treated with Taltirelin (5 μM) for 24 h, and we found TH increased in the primary striatal neurons (136.20 ± 3.47%, $p < 0.05$) but not in the primary cortical neurons. In addition, p-ERK1/2 increased by 124.84% in the primary striatal neurons, but decreased by 15.52% in the primary cortical neurons (**Figures 4H,I**), indicating that the effect of Taltirelin on TH expression was neuronal species-specific.

The elevation of p-ERK1/2 along with the TH suggested that this signaling molecule may be involved in this process. Therefore, we pre-treated primary striatal neurons with U0126 (10 μM) for 2 h to inhibit MEK, the upstream kinase of ERK1/2, then incubated neurons with Taltirelin (5 μM) for 24 h. As expected, U0126 significantly decreased p-ERK1/2 by 76.28% and TH by 71.93% (**Figures 4J,K**; $p < 0.001$), indicating that Taltirelin-induced TH expression is p-ERK1/2-dependent. Next, after 24 h incubation of Taltirelin, we treated neurons with U0126 for further 2 h, 4 h, or 6 h. We found that p-ERK1/2 was almost completely blocked after treatment with U0126 for 2 h (7.28 ± 2.36% of control), accompanied by TH decreasing with time (2 h: 112.60 ± 8.97%, 4 h: 74.71 ± 8.67%, 6 h: 50.48 ± 5.29%) (**Figures 4L,M**; $p < 0.05$), indicating that down-regulating p-ERK1/2 interfered with the maintenance of the level of cellular TH.

In order to determine the species of neurons expressing TH *in vitro*, we co-stained the primary striatal neurons with TH and other markers, such as GABA, enkephalin, dynorphin or DAT. The results showed that the neurons treated with Taltirelin exhibited wider distribution and higher fluorescent intensity of TH, which is consistent with the above results. The SPNs are GABAergic neurons, and we found TH mainly co-located with GABA in neurons treated with or without Taltirelin, indicating that these TH-positive neurons are GABAergic (**Figure 5A**).

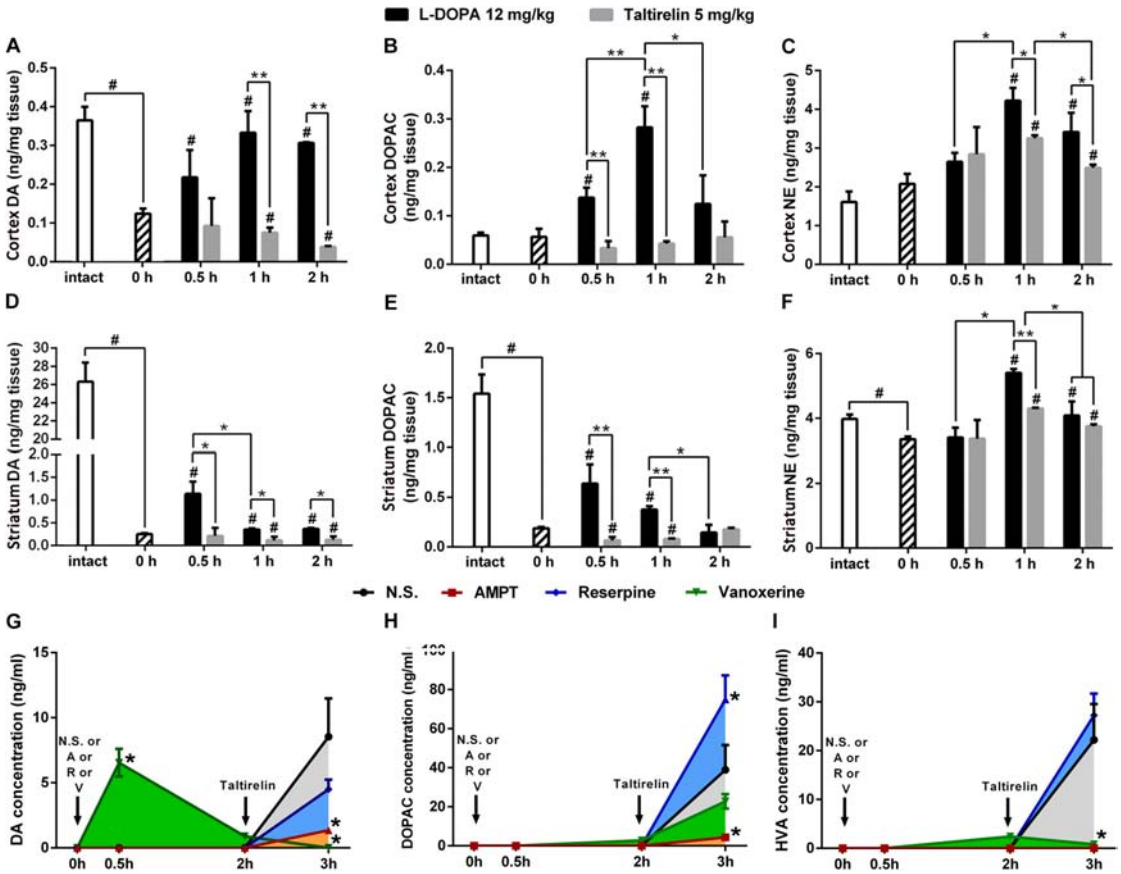

FIGURE 3 | Taltirelin elevated dopamine level in a DA-releasing dependent manner. **(A–F)** The high performance liquid chromatography coupled with electrochemical detection (HPLC-ECD) assessed the intracellular dopamine (DA), 3,4-dihydroxyphenylacetic acid (DOPAC) and norepinephrine (NE) in the cortex and striatum of 6-OHDA lesioned animals treated with L-DOPA or Taltirelin. $^{\#}p < 0.05$ vs. 0 h, $^{*}p < 0.05$ vs. indicated group, $^{**}p < 0.05$ vs. indicated group. **(G–I)** Effects of AMPT (250 mg/kg, i.p.), reserpine (5 mg/kg, i.p.) or vanoxerine dihydrochloride (20 mg/kg, i.p.) on Taltirelin-induced alterations of DA, its metabolites DOPAC and HVA in dialysates collected from lesioned DLS. Taltirelin (5 mg/kg) was injected 2 h after administration of three medications. $^{*}p < 0.05$ vs. other groups at the same time point. $N = 3$. Error bars represent SEM.

GABAergic neurons are divided into two main species: the enkephalin-positive and the dynorphin-positive, each plays different role in basal ganglia neural circuits. In our experiments, TH-enkephalin, but not TH-dynorphin double-positive neurons were observed, suggesting that TH was mainly expressed by enkephalin-positive GABAergic neurons (**Figures 5B,C**). DAT is another essential enzyme in the synthesis process of DA, but DAT-positive neurons were not found in this experiment (**Figure 5D**), which was consistent with the results *in vivo* that those new-emerging TH-positive cells were not dopaminergic neurons.

DISCUSSION

Thyrotropin-releasing hormone and its analogs have long been recognized as DA-releasing agents in CNS (Crespi et al., 1986; Fukuchi et al., 1998; Puga et al., 2016), however, their therapeutic potential toward PD, which is mainly characterized by insufficient DA in striatum, is rarely recognized or discussed thoroughly. Our results showed that Taltirelin (1–10 mg/kg) significantly improved the locomotor function of 6-OHDA-induced hemi-Parkinsonian rat model, alleviated the intensity of bradykinesia-associated high β oscillation and reversed the bursting firing form of projecting neurons in MI and DLS. The beneficial effect maintained for as long as 8 h, which was in consistency with the long half-life of Taltirelin (Kinoshita et al., 1998). Besides, animals exhibited involuntary shaking and repeated jaws action after the injection of Taltirelin above 5 mg/kg (**Supplementary video**), which may be related to the stimulation of 5-HT system (Miwa et al., 1995) by Taltirelin during high dose use. We also examined and found that Taltirelin (>5 mg/kg) elevated serum level of TT3, TT4, FT3, and FT4 in PD rats (**Supplementary Figure S5**). Compared with TRH, Taltirelin has much weaker peripheral stimulatory effect (Fukuchi et al., 1998), and it was once reported that prolonged oral administration of Taltirelin of 2.5–20 mg did not significantly alter the pituitary–thyroid axis in subjects with brain stroke (Miyashita et al., 1993). However, it has been reported that hyperthyroidism and hypothyroidism are more common in PD patients than in the general population

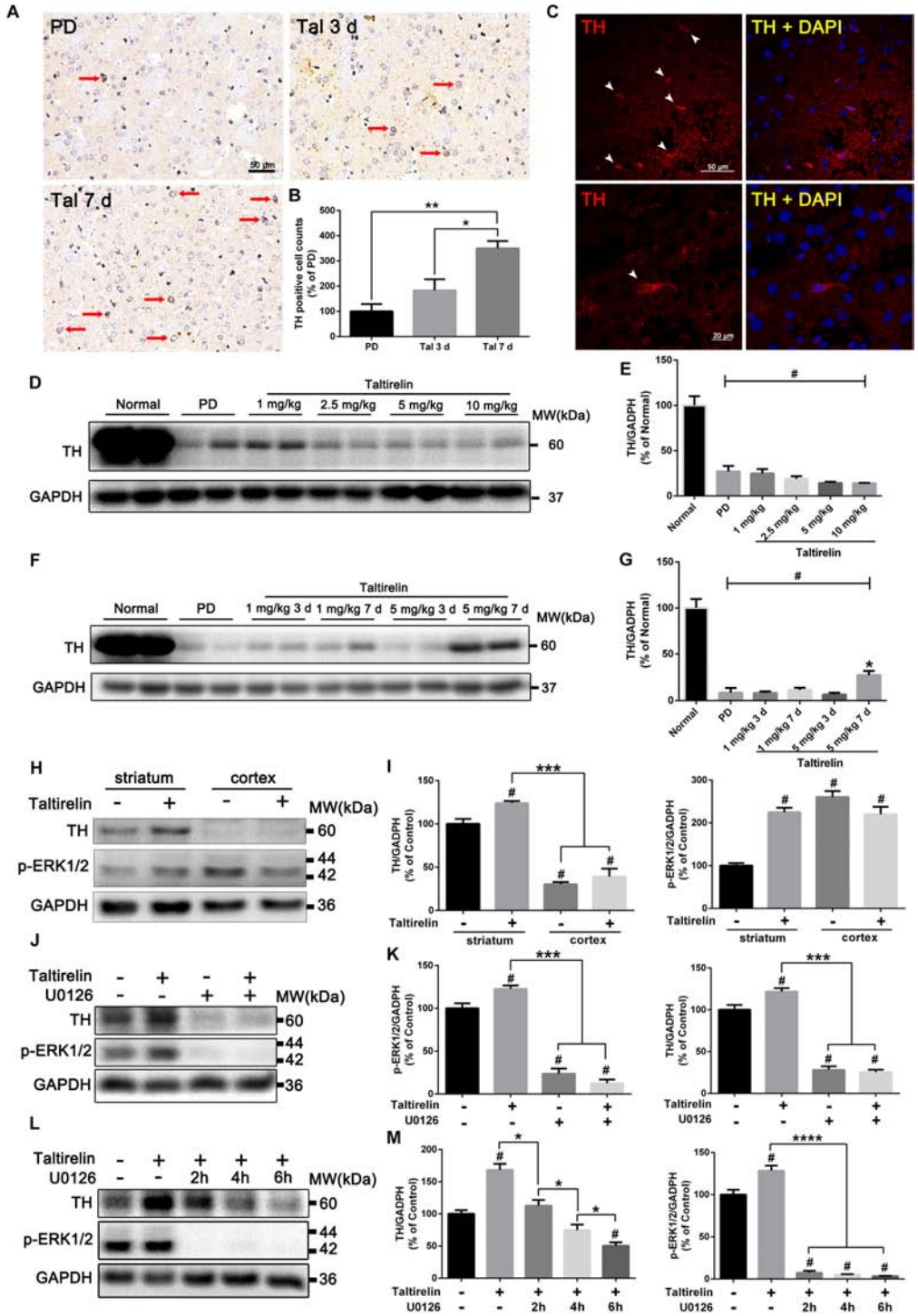

FIGURE 4 | Taltirelin elevated the level of TH both *in vivo* and *in vitro* in a p-ERK/1/2-dependent manner. **(A)** Immunostaining of tyrosine hydroxylase (TH) in the lesioned striatum of each group (PD, Tal 5 mg/kg for 3 days or 7 days). Red arrows indicated TH-positive cells. **(B)** Counts of TH-positive cells. **(C)** Immunofluorescent staining of TH in the lesioned striatum of animals treated with Tal 5 mg/kg for 7 days. White arrows indicated TH-positive cells (top). Higher-magnification photomicrographs of a TH-positive cell (down). **(D,E)** Western blot analysis of TH in the lesioned striatum of each group (normal, PD, Tal 1, 2.5, 5, or 10 mg/kg). **(F,G)** Western blot analysis of TH in the lesioned striatum of each group (normal, PD, Tal 1 or 5 mg/kg continuous administrated for 3 or 7 days). **(H,I)** Western blot analysis of intracellular TH and p-ERK1/2 of the primary rat striatal or cortical neurons treated with Tal 1, 5, or 10 μM. **(J,K)** Western blot analysis of intracellular TH and p-ERK1/2 of the primary rat striatal neurons pre-treated with MEK inhibitor U0126 (10 μM) for 2 h, then incubated with Tal (5 μM) for 24 h. **(L,M)** Western blot analysis of intracellular TH and p-ERK1/2 of the primary rat striatal neurons incubated with Tal (5 μM) for 24 h, then treated with U0126 (10 μM) for 2 h, 4 h, or 6 h. $^{\#}p < 0.01$ vs. normal or control; $^{*}p < 0.05$; $^{**}p < 0.01$; $^{***}p < 0.001$; $^{****}p < 0.0001$. $N = 3$. Error bars represent SEM.

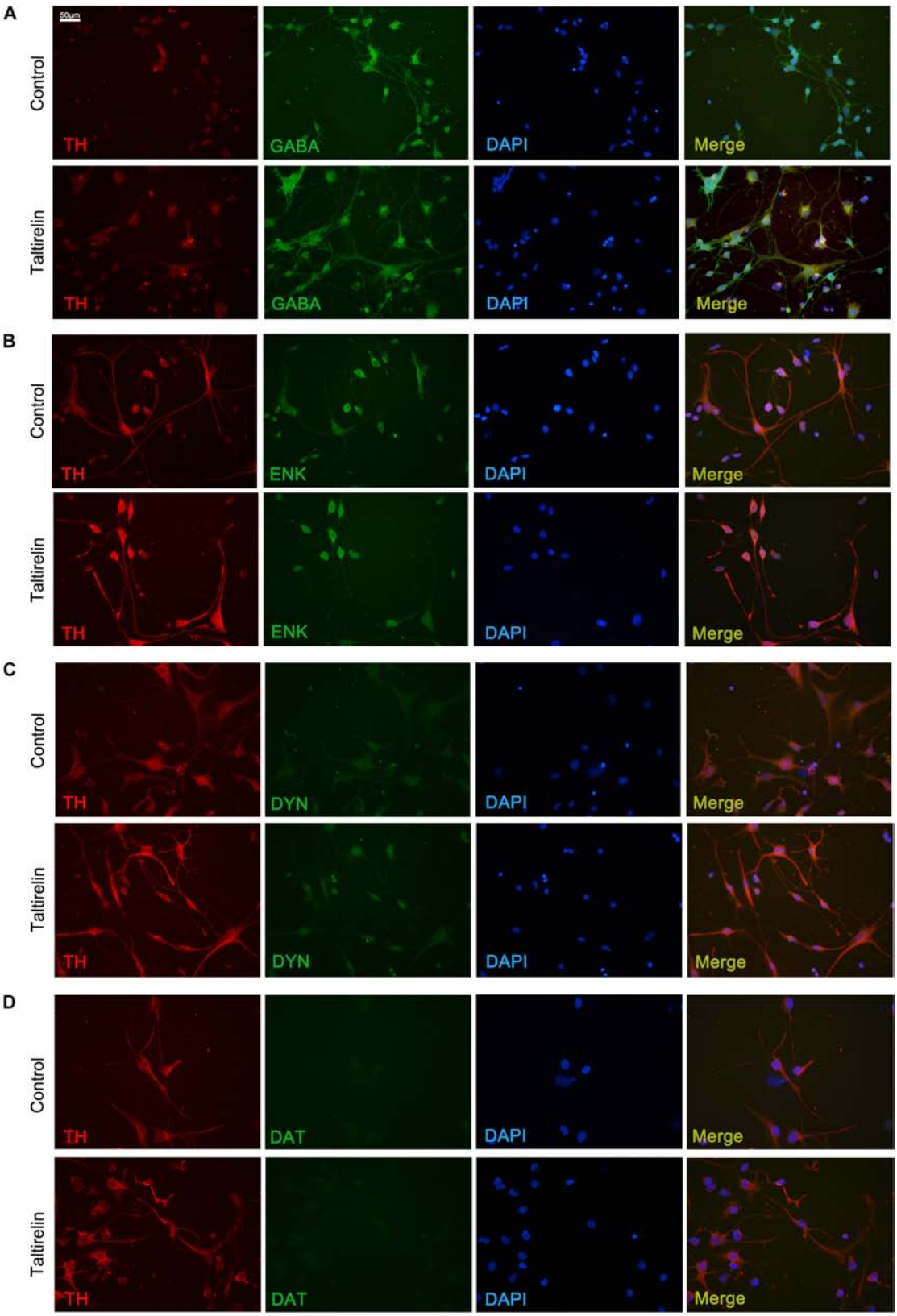

FIGURE 5 | Taltirelin elevated the level of TH in enkephalin-positive neurons *in vitro*. Double immunolabeling images showed co-localization of tyrosine hydroxylase (TH) with GABA **(A)**, enkephalin **(B)**, dynorphin **(C)** or dopamine transporter (DAT) **(D)** in control or Taltirelin treated rat primary striatal neurons. *N* = 3.

(Daimon et al., 2013). Thus, the thyroid function of patients should be thoroughly evaluated and adjusted accordingly before administration of Taltirelin if possible in the future.

Impressively, Taltirelin improved locomotor function without inducing dyskinesia-like behaviors for sub-chronic use, which was confirmed by the absence of LID-related high γ band oscillation (70–110 Hz) during the PD symptom-remitting period. Measurement of DA in the brain tissues and dialysates of PD rats by HPLC-ECD confirmed that Taltirelin promoted DA release in a mild and persistent manner. In contrast, after L-DOPA injection, DA sharply elevated in the cortex, and peaked at 1 h then maintained at high concentration, which was in good correlation with the severity of dyskinesia behaviors. Studies once showed that application of dopamine type 1 receptor (D1R) antagonists on the surface of the DA-depleted cortex immediately halted LID symptoms and terminated high γ band oscillation in PD rats (Halje et al., 2012). It is suggested that discontinuous drug delivery due to the short half-life of L-DOPA and the variability in its gastrointestinal absorption are responsible for the non-physiological pulsatile cortical dopamine receptor stimulation and the dopamine receptor hypersensitivity (Halje et al., 2012; Poewe and Antonini, 2015; Antonini et al., 2016). DA agonists, monoamine oxidase (MAO) and catechol-*O*-methyltransferase (COMT) inhibitors, and sustained-effective L-DOPA preparations under development are all aimed at achieving the goal of continuous dopamine receptor stimulation (Poewe et al., 2017). Thus, the long half-life and absence of dyskinesias in sub-chronic and high dose application of Taltirelin do bring benefit to PD treatments. However, the anti-parkinsonian effect of Taltirelin in longer period of time should be investigated in the future, for 7-day sub-chronic scheme is not enough to completely address the long-term impact of Taltirelin.

The mechanism by which TRH promotes the elevation of DA is still unclear so far (Yokoo et al., 1983; Prasad, 1991; Fukuchi et al., 1998). Reserpine irreversibly blocks the uptake of catecholamines (NE, DA and 5-HT) into synaptic vesicles by inhibiting the VMAT-2, and neurotransmitter in the cytoplasm are easily degraded by MAO, thus depleting the vesicular storage of catecholamines (Kannari et al., 2000). Pretreatment with reserpine produced 47.19% reduction in Taltirelin-derived extracellular DA levels, indicating that a large part of the Taltirelin-derived DA release is of vesicular origin. Vanoxerine (GBR12909) usually caused a slow and sustained elevation of extracellular DA by inhibiting DA uptake (Nakachi et al., 1995; Gagnaire and Micillino, 2006), however, in our study, DA increased by vanoxerine returned to their baseline 2 h after administration, which may be due to the deficiency of DA caused by 6-OHDA lesion. The interesting finding here was that vanoxerine almost totally blocked the ability of Taltirelin to increase extracellular DA. This result could be explained by two possible reasons: first, vanoxerine occupied DA transporters which were the same binding sites of Taltirelin and thereby blocked the similar releasing effect or the entrance of Taltirelin into the cells (Baumann et al., 1994). Second, depletion of already limited DA pool by vanoxerine prevented the storage pool-dependent actions of Taltirelin, which is supported by the findings with reserpine. What's more, we found that inhibition of DA synthesis using AMPT led to the reduction of Taltirelin-induced DA efflux by 84.08%. However, AMPT pre-treatment not only blocked the newly synthesis of DA, but also depleted the storage of DA (Butcher et al., 1988). Thus, the results supported the hypothesis that Taltirelin may have multiple action targets such as VMAT-2, DAT and TH, affecting DA efflux in multiple processes including the redistribution, uptake and synthesis of DA. Nevertheless, it is necessary to adopted more strategies such as genetic manipulation (Sulzer et al., 2005; Fleckenstein et al., 2007) to verified our hypothesis.

Our recent studies showed that Taltirelin raised TH levels in dyskinesia rats (unpublished), together with the results that AMPT blocked most DA-releasing action of Taltirelin, it is highly possible that Taltirelin could manipulate TH expression. Short-term (3 days) use of Taltirelin had no significant effect on TH level in the lesioned striatum of PD rats, whereas sub-chronic (7 days) injections significantly increased TH levels. In addition, incubation with Taltirelin (5 μM) for 24 h also greatly elevated the intracellular TH in primary striatal neurons, while TH remained unchanged in primary cortex neurons, indicating a neuron-type-dependent response or characteristic of Taltirelin actions. We further found that TH mainly co-localized with enkephalin in primary GABAergic neurons *in vitro*, whereas the dynorphin was almost undetectable. The sub-species of GABAergic neurons are directly related to the direct and indirect pathway model of PD (Calabresi et al., 2014), therefore, the influence of elevated TH on the basal ganglia neural circuits *in vivo* deserved further investigation. In addition, there are a small number of TH positive cells in the striatum under normal physiological conditions, which are in general identified as interneurons and do not contain AADC or DAT, i.e., non-dopaminergic neurons (Xenias et al., 2015). In our study, none of those TH-positive cells were stained with AADC or DAT either *in* or *ex vivo*, suggesting that Taltirelin did not induce the neuron type transformation at least in our experiment conditions. Regarding the functions of the TH-positive cells in the striatum, it has been proposed that those cells could co-synthesize DA with 5-HT neuronal terminals that contain ADDC (Keber et al., 2015; Kozina et al., 2017). Therefore, new-emerging TH-positive cells may help promoting DA synthesis and secretion in sub-chronic use of Taltirelin. ERK1/2 (or mitogen-activated protein kinase, MAPK) is a part of the Ras-Raf-MEK-ERK signaling pathway, participating in multiple important physiological activities (Jr, 2012). The activated form of ERK1/2, p-ERK1/2, is able to regulate the transcription and phosphorylation of TH (Tekin et al., 2014), and also could mediate the functions of TRH through TRH type 1 receptor (TRH-R1) (Choi et al., 2015), which is also the main action receptor of Taltirelin in the CNS (Thirunarayanan et al., 2013). In our study, p-ERK1/2 elevated after the treatment with Taltirelin, which could be blocked by MEK inhibitor U0126 (10 μM). However, p-ERK1/2 is a wide-functioning signaling factor and the expression of TH is subtly regulated by various factors, thus whether TRH or Taltirelin is able to increase phosphorylation level of TH or the affinity of

TH cofactors (Lenartowski and Goc, 2011) still need further investigation.

ΔFosB, a truncated isoform of transcription factor FosB, is an established hallmark of dyskinesia. Due to its stable nature and tendency to accumulate, the level of ΔFosB in the striatum is positively correlated with the severity and frequency of dyskinesia. We once showed that overexpression of ΔFosB in the striatum of PD rats was enough to induce LID (Cao et al., 2010). L-DOPA caused a significant elevation of ΔFosB and showed an accumulating effect with injection times increased. Taltirelin group also showed similar cumulative effects, but the level was significantly lower than that of L-DOPA group. Studies once showed that L-DOPA significantly increased the level of TH and ΔFosB in the striatum of normal mice (Keber et al., 2015). In addition, striatal emerging TH-positive neurons usually appeared in areas of near complete or partial deprivation of DA rather than completely destructed areas (Lopez-Real et al., 2003). It has been suggested that such increase in TH-positive cells may be associated with D1R (Espadas et al., 2012), whereas DA exposure *in vitro* is known to increase the number of TH-positive cells in primary cortical and striatal cultures (Zhou et al., 1996). Thus, we wondered if that high-dose extraneous DA itself is enough to increase TH and ΔFosB in a dose-dependent effect and independent from LID. If this hypothesis is true, elevated ΔFosB in sub-chronic administration of Taltirelin without dyskinesia could be explained by the increased DA stimulated by Taltirelin, and the increased DA may also help promoting TH expression in striatum (**Figure 6**).

Whether the endogenic DA-releasing effect of Taltirelin would recede with the degeneration of dopaminergic terminals still needs further assessment in PD patients. However, in addition to the continuous DA-releasing effect that could avoid the occurrence of dyskinesia, Taltirelin also has other advantages over L-DOPA. First, a study recently reported a

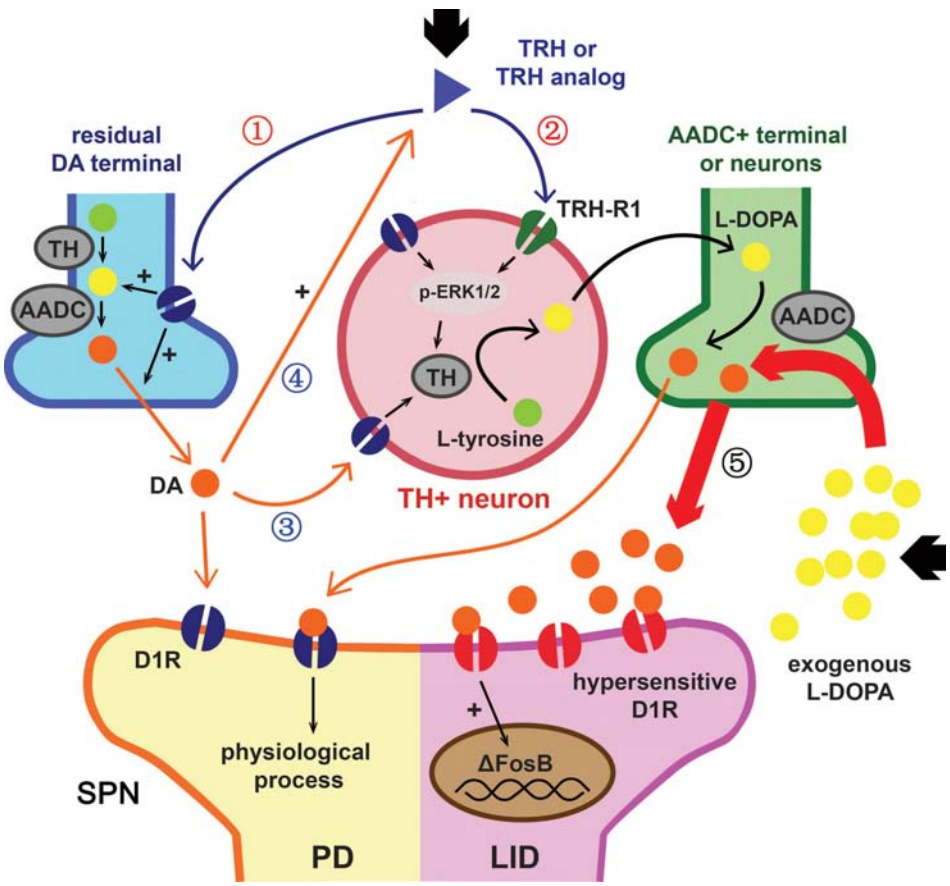

FIGURE 6 | Hypothetical action mechanism of TRH or Taltirelin in PD model animals. Based on our results and recent literature, this scheme illustrated how TRH or its analog, Taltirelin (Tal) worked in PD model animals (adapted from Keber et al., 2015). Post administration, Tal firstly acted on the dopaminergic neurons on soma in the substantia nigra (SN) or on residual nerve terminal in striatum, resulting in increased dopamine (DA) synthesis and release (①). Secondly, after sub-chronic application, Tal bound to TRH type 1 receptor (TRH-R1) of striatal neurons, leads to an increase in tyrosine hydroxylase (TH) expression or activity mediated by p-ERK1/2. Striatal TH-positive neurons co-synthesized DA with 5-HT nerve terminals or other DOPA decarboxylase (AADC)-positive neurons and further increased DA levels (②). Elevated DA in turn stimulated TH expression in striatal neurons via dopamine type 1 receptor (D1R) or D2R (③) and further increased endogenous TRH release (④) (Przegaliński et al., 1991). With such positive feedback, the level of DA in the striatum or cortex elevated slowly and steadily. On the contrary, exogenous L-DOPA usually caused a sudden increase of DA level in the striatum or cortex. Such pulse-like stimulus of DA caused hypersensitization of D1R and increased the expression of downstream ΔFosB, thus ultimately led to L-DOPA-induced dyskinesia (⑤).

human-specific time-dependent pathological cascade of DA oxidation, mitochondrial and lysosomal dysfunction. The selective accumulation of neuromelanin (a complex aggregate consisted of oxidized DA, proteins, and lipids) in human neurons and the exogenous L-DOPA increased cytosolic DA, which may contribute to elevated mitochondrial oxidant stress, leading to a vicious cycle of dopamine and mitochondrial oxidation in human midbrain neurons (Burbulla et al., 2017). Consistently, we also observed a strikingly high level of DA in the intracellular contents of cortex and striatum of PD rats injected with L-DOPA. On the contrary, Taltirelin not only avoids the neurotoxicity of high-dose DA (Kang et al., 2018) but also provides disease-modifying effect which helps reserving residual dopaminergic neurons (Veronesi et al., 2007; Jaworska-Feil et al., 2010), which may help delaying the development of PD thus provides long-term benefit for the patients. Second, non-motor symptoms of PD, such as depression, constipation and cognitive dysfunction manifest usually earlier and can be equally or more disabling than the motor symptoms. Many non-motor symptoms do not respond to DA replacement therapy and some are even aggravated by this treatment (Poewe et al., 2017). Fortunately, TRH has been proved effect in improving depression (Szuba et al., 1996; Marangell et al., 1997; Zeng et al., 2007), memory impairment (Molchan et al., 1990) and regulating sympathetic nervous system (Khomane et al., 2011). These benefits associated with the role of TRH plays as homeostatic regulator in both CNS and periphery. For example, when the organism is sedated, TRH is a stimulant, but when the body is convulsed, TRH is anticonvulsant. Therefore, TRH and its analogs have great potential in treating many nervous system diseases (Khomane et al., 2011). However, it is impossible to fully explore the therapeutic potential, without thorough understanding of the mechanisms of action of TRH and relevant clinical trials to demonstrate its effectiveness. Above all, our study showed that TRH analog Taltirelin promoted DA release in the CNS in a mild and persistent manner, thus improving the motor function and relieving the PD-related abnormal electrical activities of PD rats without inducing dyskinesia in sub-chronic or high-dose use. Therefore, we introduced a novel promising drug for treating Parkinson's disease.

AUTHOR CONTRIBUTIONS

CZ, GC, YX, ZZ, SP, KY, and XC conceived and designed the study. CZ, GC, YT, WZ, QP, JW, CC, XY, and SN performed the experiments. CZ and GC analyzed the data. CZ, GC, YX, SP, KY, and XC wrote the manuscript. All authors read and approved the final manuscript.

FUNDING

This work was supported by the National Natural Science Foundation of China (81171193, 81671108, and 81873734) and Natural Science Foundation of Hubei Province of China (2016CFB544).

ACKNOWLEDGMENTS

We would like to thank Pro. Jiangeng Huang from Department of Pharmaceutics, School of Pharmacy, Tongji Medical College, Huazhong University of Science and Technology for kindly providing microdialysis devices and technical guidance.

SUPPLEMENTARY MATERIAL

The Supplementary Material for this article can be found online at: https://www.frontiersin.org/articles/10.3389/fncel.2018.00417/full#supplementary-material

REFERENCES

Antonini, A., Fung, V. S., Boyd, J. T., Slevin, J. T., Hall, C., Chatamra, K., et al. (2016). Effect of levodopa-carbidopa intestinal gel on dyskinesia in advanced Parkinson's disease patients. *Mov. Disord.* 31, 530–537. doi: 10.1002/mds.26528

Baumann, M. H., Char, G. U., De Costa, B. R., Rice, K. C., and Rothman, R. B. (1994). GBR12909 attenuates cocaine-induced activation of mesolimbic dopamine neurons in the rat. *J. Pharmacol. Exp. Ther.* 271:1216.

Beaudoin, G. M. III, Lee, S. H., Singh, D., Yuan, Y., Ng, Y. G., Reichardt, L. F., et al. (2012). Culturing pyramidal neurons from the early postnatal mouse hippocampus and cortex. *Nat. Protoc.* 7, 1741–1754. doi: 10.1038/nprot.2012.099

Boldry, R. C., Papa, S. M., Kask, A. M., and Chase, T. N. (1995). MK-801 reverses effects of chronic levodopa on D1 and D2 dopamine agonist-induced rotational behavior. *Brain Res.* 692, 259–264. doi: 10.1016/0006-8993(95)00690-R

Budygin, E. A., Kilpatrick, M. R., Gainetdinov, R. R., and Wightman, R. M. (2000). Correlation between behavior and extracellular dopamine levels in rat striatum: comparison of microdialysis and fast-scan cyclic voltammetry. *Neurosci. Lett.* 281, 9–12. doi: 10.1016/S0304-3940(00)00813-2

Burbulla, L. F., Song, P., Mazzulli, J. R., Zampese, E., Wong, Y. C., Jeon, S., et al. (2017). Dopamine oxidation mediates mitochondrial and lysosomal dysfunction in Parkinson's disease. *Science* 357, 1255–1261. doi: 10.1126/science.aam9080

Butcher, S. P., Fairbrother, I. S., Kelly, J. S., and Arbuthnott, G. W. (1988). Amphetamine-induced dopamine release in the rat striatum: an in vivo microdialysis study. *J. Neurochem.* 50, 346–355. doi: 10.1111/j.1471-4159.1988.tb02919.x

Calabresi, P., Filippo, M. D., Ghiglieri, V., Tambasco, N., and Picconi, B. (2010). Levodopa-induced dyskinesias in patients with Parkinson's disease: filling the bench-to-bedside gap. *Lancet Neurol.* 9, 1106–1117. doi: 10.1016/S1474-4422(10)70218-0

Calabresi, P., Picconi, B., Tozzi, A., Ghiglieri, V., and Di Filippo, M. (2014). Direct and indirect pathways of basal ganglia: a critical reappraisal. *Nat. Neurosci.* 17, 1022–1030. doi: 10.1038/nn.3743

Cao, X., Yasuda, T., Uthayathas, S., Watts, R. L., Mouradian, M. M., Mochizuki, H., et al. (2010). Striatal overexpression of DeltaFosB reproduces chronic levodopa-induced involuntary movements. *J. Neurosci.* 30, 7335–7343. doi: 10.1523/JNEUROSCI.0252-10.2010

Chen, G., Nie, S., Han, C., Ma, K., Xu, Y., Zhang, Z., et al. (2017). Antidyskinetic effects of MEK inhibitor are associated with multiple neurochemical alterations in the striatum of hemiparkinsonian rats. *Front. Neurosci.* 11:112. doi: 10.3389/fnins.2017.00112

Choi, J., Kim, J. E., Kim, T. K., Park, J. Y., Lee, J. E., Kim, H., et al. (2015). TRH and TRH receptor system in the basolateral amygdala mediate stress-induced depression-like behaviors. *Neuropharmacology* 97, 346–356. doi: 10.1016/j.neuropharm.2015.03.030

Coyle, J. T., and Axelrod, J. (1972). Dopamine-β-hydroxylase in the rat brain: developmental characteristics. *J. Neurochem.* 19, 449–459. doi: 10.1111/j.1471-4159.1972.tb01354.x

Crespi, F., Keane, P. E., and Morre, M. (1986). In vivo evaluation by differential pulse voltammetry of the effect of thyrotropin-releasing hormone (TRH) on dopaminergic and serotoninergic synaptic activity in the striatum and nucleus accumbens of the rat. *Exp. Brain Res. Exp.* 62:329. doi: 10.1007/BF00238852

Daimon, C. M., Chirdon, P., Maudsley, S., and Martin, B. (2013). The role of thyrotropin releasing hormone in aging and neurodegenerative diseases. *Am, J. Alzheimers Dis.* 1. doi: 10.7726/ajad.2013.1003

Du, X., and Iacovitti, L. (1997). Multiple signaling pathways direct the initiation of tyrosine hydroxylase gene expression in cultured brain neurons. *Brain Res. Mol. Brain Res.* 50, 1–8. doi: 10.1016/S0169-328X(97)00149-6

Dupre, K. B., Cruz, A. V., Mccoy, A. J., Delaville, C., Gerber, C. M., Eyring, K. W., et al. (2016). Effects of L-dopa priming on cortical high beta and high gamma oscillatory activity in a rodent model of Parkinson's disease. *Neurobiol. Dis.* 86, 1–15. doi: 10.1016/j.nbd.2015.11.009

Espadas, I., Darmopil, S., Vergano-Vera, E., Ortiz, O., Oliva, I., Vicario-Abejon, C., et al. (2012). L-DOPA-induced increase in TH-immunoreactive striatal neurons in parkinsonian mice: insights into regulation and function. *Neurobiol. Dis.* 48, 271–281. doi: 10.1016/j.nbd.2012.07.012

Fleckenstein, A. E., Volz, T. J., Riddle, E. L., Gibb, J. W., and Hanson, G. R. (2007). New insights into the mechanism of action of amphetamines. *Annu. Rev. Pharmacol. Toxicol.* 47, 681–698. doi: 10.1146/annurev.pharmtox.47.120505.105140

Fukuchi, I., Asahi, T., Kawashima, K., Kawashima, Y., Yamamura, M., Matsuoka, Y., et al. (1998). Effects of taltirelin hydrate (TA-0910), a novel thyrotropin-releasing hormone analog, on in vivo dopamine release and turnover in rat brain. *Arzneimittelforschung* 48, 353–359.

Gagnaire, F., and Micillino, J. C. (2006). Effects of triadimefon on extracellular dopamine, DOPAC, HVA and 5-HIAA in adult rat striatum. *Toxicology* 217:91. doi: 10.1016/j.tox.2005.08.021

Gary, K. A., Sevarino, K. A., Yarbrough, G. G., Prange, A. J. Jr., and Winokur, A. (2003). The thyrotropin-releasing hormone (TRH) hypothesis of homeostatic regulation: implications for TRH-based therapeutics. *J. Pharmacol. Exp. Ther.* 305, 410–416. doi: 10.1124/jpet.102.044040

Halje, P., Tamte, M., Richter, U., Mohammed, M., Cenci, M. A., and Petersson, P. (2012). Levodopa-induced dyskinesia is strongly associated with resonant cortical oscillations. *J. Neurosci.* 32, 16541–16551. doi: 10.1523/JNEUROSCI.3047-12.2012

Jaworska-Feil, L., Jantas, D., Leskiewicz, M., Budziszewska, B., Kubera, M., Basta-Kaim, A., et al. (2010). Protective effects of TRH and its analogues against various cytotoxic agents in retinoic acid (RA)-differentiated human neuroblastoma SH-SY5Y cells. *Neuropeptides* 44, 495–508. doi: 10.1016/j.npep.2010.08.004

Jenkinson, N., and Brown, P. (2011). New insights into the relationship between dopamine, beta oscillations and motor function. *Trends Neurosci.* 34, 611–618. doi: 10.1016/j.tins.2011.09.003

Jr, R. R. (2012). ERK1/2 MAP kinases: structure, function, and regulation. *Pharmacol. Res.* 66:105. doi: 10.1016/j.phrs.2012.04.005

Kalivas, P. W., Stanley, D., and Prange, A. J. Jr. (1987). Interaction between thyrotropin-releasing hormone and the mesolimbic dopamine system. *Neuropharmacology* 26, 33–38. doi: 10.1016/0028-3908(87)90041-4

Kang, S. S., Ahn, E. H., Zhang, Z., Liu, X., Manfredsson, F. P., Sandoval, I. M., et al. (2018). α-Synuclein stimulation of monoamine oxidase-B and legumain protease mediates the pathology of Parkinson's disease. *EMBO J.* 37:e201798878. doi: 10.15252/embj.201798878

Kannari, K., Tanaka, H., Maeda, T., Tomiyama, M., Suda, T., and Matsunaga, M. (2000). Reserpine pretreatment prevents increases in extracellular striatal dopamine following L-DOPA administration in rats with nigrostriatal denervation. *J. Neurochem.* 74, 263–269. doi: 10.1046/j.1471-4159.2000.0740263.x

Keber, U., Klietz, M., Carlsson, T., Oertel, W. H., Weihe, E., Schafer, M. K., et al. (2015). Striatal tyrosine hydroxylase-positive neurons are associated with L-DOPA-induced dyskinesia in hemiparkinsonian mice. *Neuroscience* 298, 302–317. doi: 10.1016/j.neuroscience.2015.04.021

Khomane, K. S., Meena, C. L., Jain, R., and Bansal, A. K. (2011). Novel thyrotropin-releasing hormone analogs: a patent review. *Expert Opin. Ther. Pat.* 21, 1673–1691. doi: 10.1517/13543776.2011.623127

Kinoshita, K., Nagao, T., and Ono, H. (1994). Effects of TA-0910, an orally active TRH analog, on the spinal reflex in spinal rats. *Neuropharmacology* 33, 1183–1188. doi: 10.1016/S0028-3908(05)80008-5

Kinoshita, K., Yamamura, M., Sugihara, J., Suzuki, M., and Matsuoka, Y. (1998). Taltirelin hydrate (TA-0910): an orally active thyrotropin-releasing hormone mimetic agent with multiple actions. *CNS Drug Rev.* 4, 25–41. doi: 10.1111/j.1527-3458.1998.tb00039.x

Kozina, E. A., Kim, A. R., Kurina, A. Y., and Ugrumov, M. V. (2017). Cooperative synthesis of dopamine by non-dopaminergic neurons as a compensatory mechanism in the striatum of mice with MPTP-induced Parkinsonism. *Neurobiol. Dis.* 98, 108–121. doi: 10.1016/j.nbd.2016.12.005

Kreutz, M. R., Acworth, I. N., Lehnert, H., and Wurtman, R. J. (1990). Systemic administration of thyrotropin-releasing hormone enhances striatal dopamine release in vivo. *Brain Res.* 536:347. doi: 10.1016/0006-8993(90)90049-H

Kuhn, J., Haumesser, J. K., Beck, M. H., Altschuler, J., Kuhn, A. A., Nikulin, V. V., et al. (2017). Differential effects of levodopa and apomorphine on neuronal population oscillations in the cortico-basal ganglia loop circuit in vivo in experimental parkinsonism. *Exp. Neurol.* 298, 122–133. doi: 10.1016/j.expneurol.2017.09.005

Lenartowski, R., and Goc, A. (2011). Epigenetic, transcriptional and posttranscriptional regulation of the tyrosine hydroxylase gene. *Int. J. Dev. Neurosci.* 29, 873–883. doi: 10.1016/j.ijdevneu.2011.07.006

Li, Q., Ke, Y., Chan, D. C., Qian, Z. M., Yung, K. K., Ko, H., et al. (2012). Therapeutic deep brain stimulation in Parkinsonian rats directly influences motor cortex. *Neuron* 76, 1030–1041. doi: 10.1016/j.neuron.2012.09.032

Lopez-Real, A., Rodriguez-Pallares, J., Guerra, M. J., and Labandeira-Garcia, J. L. (2003). Localization and functional significance of striatal neurons immunoreactive to aromatic l-amino acid decarboxylase or tyrosine hydroxylase in rat Parkinsonian models. *Brain Res.* 969, 135–146. doi: 10.1016/S0006-8993(03)02291-1

Lundblad, M., Picconi, B., Lindgren, H., and Cenci, M. A. (2004). A model of L-DOPA-induced dyskinesia in 6-hydroxydopamine lesioned mice: relation to motor and cellular parameters of nigrostriatal function. *Neurobiol. Dis.* 16, 110–123. doi: 10.1016/j.nbd.2004.01.007

Marangell, L. B., George, M. S., Callahan, A. M., Ketter, T. A., Pazzaglia, P. J., L'herrou, T. A., et al. (1997). Effects of intrathecal thyrotropin-releasing hormone (protirelin) in refractory depressed patients. *Arch. Gen. Psychiatry* 54, 214–222. doi: 10.1001/archpsyc.1997.01830150034007

Miwa, Y., Koshikawa, N., Miyata, N., Koshida, Y., Kobayashi, M., and Cools, A. R. (1995). YM-14673, a thyrotropin-releasing hormone analogue, injected into the nucleus accumbens and the striatum produces repetitive jaw movements in rats. *Eur. J. Pharmacol.* 277, 63–69. doi: 10.1016/0014-2999(95)00066-T

Miyashita, K., Murakami, M., Satoh, T., Monden, T., Yamada, M., Iriuchuima, T., et al. (1993). Alteration by prolonged oral administration of a thyrotropin-releasing hormone analog, TA-0910, of the pituitary-thyroid axis in subjects with brain stroke. *Intern. Med.* 32, 681–685. doi: 10.2169/internalmedicine.32.681

Molchan, S. E., Mellow, A. M., Lawlor, B. A., Weingartner, H. J., Cohen, R. M., Cohen, M. R., et al. (1990). TRH attenuates scopolamine-induced memory impairment in humans. *Psychopharmacology* 100, 84–89. doi: 10.1007/BF02245795

Nakachi, N., Kiuchi, Y., Inagaki, M., Inazu, M., Yamazaki, Y., and Oguchi, K. (1995). Effects of various dopamine uptake inhibitors on striatal extracellular dopamine levels and behaviours in rats. *Eur. J. Pharmacol.* 281, 195–203. doi: 10.1016/0014-2999(95)00246-H

Nakamura, T., Honda, M., Kimura, S., Tanabe, M., Oda, S.-I., and Ono, H. (2005). Taltirelin improves motor ataxia independently of monoamine levels in rolling mouse nagoya, a model of spinocerebellar atrophy. *Biol. Pharm. Bull.* 28, 2244–2247. doi: 10.1248/bpb.28.2244

Nishikawa, Y., Ikegami, H., Jikihara, H., Koike, K., Masumoto, N., Kasahara, K., et al. (1993). Effects of thyrotropin-releasing hormone and phorbol ester on dopamine release from dispersed rat tuberoinfundibular dopaminergic neurons. *Peptides* 14:839. doi: 10.1016/0196-9781(93)90122-W

Ogata, A., Nagashima, K., Yasui, K., Matsuura, T., and Tashiro, K. (1998). Sustained release dosage of thyrotropin-releasing hormone improves experimental Japanese encephalitis virus-induced parkinsonism in rats. *J. Neurol. Sci.* 159, 135–139. doi: 10.1016/S0022-510X(98)00150-6

Pinna, A., Pontis, S., Borsini, F., and Morelli, M. (2007). Adenosine A2A receptor antagonists improve deficits in initiation of movement and sensory motor integration in the unilateral 6-hydroxydopamine rat model of Parkinson's disease. *Synapse* 61, 606–614. doi: 10.1002/syn.20410

Poewe, W., and Antonini, A. (2015). Novel formulations and modes of delivery of levodopa. *Mov. Disord.* 30, 114–120. doi: 10.1002/mds.26078

Poewe, W., Seppi, K., Tanner, C. M., Halliday, G. M., Brundin, P., Volkmann, J., et al. (2017). Parkinson disease. *Nat. Rev. Dis. Primers* 3:17013. doi: 10.1038/nrdp.2017.13

Prasad, C. (1991). Peptidergic regulation of striatal dopamine transporter complex. *Presynaptic Receptors Neuronal Transporters* 82, 207–211. doi: 10.1016/B978-0-08-041165-1.50073-9

Przegaliński, E., Jaworska, L., Konarska, R., and Gołembiowska, K. (1991). The role of dopamine in regulation of thyrotropin-releasing hormone in the striatum and nucleus accumbens of the rat. *Neuropeptides* 19, 189–195. doi: 10.1016/0143-4179(91)90118-3

Puga, L., Alcantara-Alonso, V., Coffeen, U., Jaimes, O., and De Gortari, P. (2016). TRH injected into the nucleus accumbens shell releases dopamine and reduces feeding motivation in rats. *Behav. Brain Res.* 306, 128–136. doi: 10.1016/j.bbr.2016.03.031

Singh, A., Jenkins, M. A., Burke, K. J. Jr., Beck, G., Jenkins, A., Scimemi, A., et al. (2018). Glutamatergic tuning of hyperactive striatal projection neurons controls the motor response to dopamine replacement in parkinsonian primates. *Cell Rep.* 22, 941–952. doi: 10.1016/j.celrep.2017.12.095

Singh, A., Mewes, K., Gross, R. E., Delong, M. R., Obeso, J. A., and Papa, S. M. (2016). Human striatal recordings reveal abnormal discharge of projection neurons in Parkinson's disease. *Proc. Natl. Acad. Sci. U.S.A.* 113, 9629–9634. doi: 10.1073/pnas.1606792113

Sulzer, D., Sonders, M. S., Poulsen, N. W., and Galli, A. (2005). Mechanisms of neurotransmitter release by amphetamines: a review. *Prog. Neurobiol.* 75, 406–433. doi: 10.1016/j.pneurobio.2005.04.003

Szuba, M., Fernando, A., Winokur, A., and Gary, K. (1996). "Nocturnal TRH administration acutely ameliorates bipolar depression," in *Conference Proceeding of the American College of Neuropsychopharmacology*, San Juan, 235.

Tanabe, M., Tokuda, Y., Takasu, K., Ono, K., Honda, M., and Ono, H. (2009). The synthetic TRH analogue taltirelin exerts modality-specific antinociceptive effects via distinct descending monoaminergic systems. *Br. J. Pharmacol.* 150, 403–414. doi: 10.1038/sj.bjp.0707125

Tekin, I., Roskoski, R. Jr., Carkaci-Salli, N., and Vrana, K. E. (2014). Complex molecular regulation of tyrosine hydroxylase. *J. Neural Transm.* 121, 1451–1481. doi: 10.1007/s00702-014-1238-7

Thirunarayanan, N., Nir, E. A., Raaka, B. M., and Gershengorn, M. C. (2013). Thyrotropin-releasing hormone receptor type 1 (TRH-R1), not TRH-R2, primarily mediates taltirelin actions in the CNS of mice. *Neuropsychopharmacology* 38, 950–956. doi: 10.1038/npp.2012.256

Urayama, A., Yamada, S., Kimura, R., Zhang, J., and Watanabe, Y. (2002). Neuroprotective effect and brain receptor binding of taltirelin, a novel thyrotropin-releasing hormone (TRH) analogue, in transient forebrain ischemia of C57BL/6J mice. *Life Sci.* 72, 601–607. doi: 10.1016/S0024-3205(02)02268-3

Van Schoors, J., Lens, C., Maes, K., Michotte, Y., Smolders, I., and Van Eeckhaut, A. (2015). Reassessment of the antioxidative mixture for the challenging electrochemical determination of dopamine, noradrenaline and serotonin in microdialysis samples. *J. Chromatogr. B Analyt. Technol. Biomed. Life Sci.* 99, 63–71. doi: 10.1016/j.jchromb.2015.06.010

Veronesi, M. C., Yard, M., Jackson, J., Lahiri, D. K., and Kubek, M. J. (2007). An analog of thyrotropin-releasing hormone (TRH) is neuroprotective against glutamate-induced toxicity in fetal rat hippocampal neurons *in vitro*. *Brain Res.* 1128, 79–85. doi: 10.1016/j.brainres.2006.10.047

Xenias, H. S., Ibanez-Sandoval, O., Koos, T., and Tepper, J. M. (2015). Are striatal tyrosine hydroxylase interneurons dopaminergic? *J. Neurosci.* 35, 6584–6599. doi: 10.1523/JNEUROSCI.0195-15.2015

Yan, X., Zhao, S., Zhu, W., Rao, J., Kang, L., Xu, J., et al. (2016). LC-MS/MS assay of ropinirole in rat biological matrices: elimination of lysoglycerophosphocholines-based matrix effect. *Bioanalysis* 8, 1823–1835. doi: 10.4155/bio-2016-0087

Yokoo, H., Nakahara, T., Uchimura, H., Matsumoto, T., and Hirano, M. (1983). Effect of a TRH analog (DN-1417) on tyrosine hydroxylase activity in discrete areas of rat brain. *Kurume Med. J.* 30(Suppl.), S37–S43. doi: 10.2739/kurumemedj.30.SUPPLEMENT_S37

Zeng, H., Schimpf, B. A., Rohde, A. D., Pavlova, M. N., Gragerov, A., and Bergmann, J. E. (2007). Thyrotropin-releasing hormone receptor 1-deficient mice display increased depression and anxiety-like behavior. *Mol. Endocrinol.* 21, 2795–2804. doi: 10.1210/me.2007-0048

Zhou, J., Bradford, H. F., and Stern, G. M. (1996). Induction of dopaminergic neurotransmitter phenotype in rat embryonic-cerebrocortex by the synergistic action of neurotrophins and dopamine. *Eur. J. Neurosci.* 8, 2328–2339. doi: 10.1111/j.1460-9568.1996.tb01196.x

Conflict of Interest Statement: The authors declare that the research was conducted in the absence of any commercial or financial relationships that could be construed as a potential conflict of interest.

frontiers in Cellular Neuroscience

MINI REVIEW
published: 22 November 2018
doi: 10.3389/fncel.2018.00456

Vestibular System and Self-Motion

Zhixian Cheng[1] *and Yong Gu*[2]*

[1]Department of Neuroscience, Yale School of Medicine, New Haven, CT, United States, [2]Key Laboratory of Primate Neurobiology, CAS Center for Excellence in Brain Science and Intelligence Technology, Institute of Neuroscience, Chinese Academy of Sciences, Shanghai, China

Detection of the state of self-motion, such as the instantaneous heading direction, the traveled trajectory and traveled distance or time, is critical for efficient spatial navigation. Numerous psychophysical studies have indicated that the vestibular system, originating from the otolith and semicircular canals in our inner ears, provides robust signals for different aspects of self-motion perception. In addition, vestibular signals interact with other sensory signals such as visual optic flow to facilitate natural navigation. These behavioral results are consistent with recent findings in neurophysiological studies. In particular, vestibular activity in response to the translation or rotation of the head/body in darkness is revealed in a growing number of cortical regions, many of which are also sensitive to visual motion stimuli. The temporal dynamics of the vestibular activity in the central nervous system can vary widely, ranging from acceleration-dominant to velocity-dominant. Different temporal dynamic signals may be decoded by higher level areas for different functions. For example, the acceleration signals during the translation of body in the horizontal plane may be used by the brain to estimate the heading directions. Although translation and rotation signals arise from independent peripheral organs, that is, otolith and canals, respectively, they frequently converge onto single neurons in the central nervous system including both the brainstem and the cerebral cortex. The convergent neurons typically exhibit stronger responses during a combined curved motion trajectory which may serve as the neural correlate for complex path perception. During spatial navigation, traveled distance or time may be encoded by different population of neurons in multiple regions including hippocampal-entorhinal system, posterior parietal cortex, or frontal cortex.

Keywords: vestibular, self-motion perception, heading, path trajectory, distance perception

OPEN ACCESS

Edited by:
Jing-Ning Zhu,
Nanjing University, China

Reviewed by:
Wu Zhou,
University of Mississippi Medical Center School of Dentistry, United States
Jean Laurens,
Baylor College of Medicine, United States

***Correspondence:**
Yong Gu
guyong@ion.ac.cn

Received: *07 September 2018*
Accepted: *12 November 2018*
Published: *22 November 2018*

Citation:
Cheng Z and Gu Y (2018) Vestibular System and Self-Motion. Front. Cell. Neurosci. 12:456. doi: 10.3389/fncel.2018.00456

INTRODUCTION

Accurate and precise detection of displacement of our head and body in space is critical for important functions including balance, posture control, gait, spatial orientation and self-motion perception. It can be accomplished through the vestibular pathway that starts from two small but elegant organs embedded in our inner ears: the otolith and semicircular canals, which detect linear and angular acceleration of our head, respectively (Goldberg and Fernandez, 1971; Fernández and Goldberg, 1976a,b). The encoded inertial motion signals in the peripheral system are propagated to the central nervous system for further processing. While the neural circuits mediating automatic process such as vestibulo-ocular reflex (VOR) for maintaining visual stability

and body balance are well known (Takakusaki, 2017), less is clear about how vestibular signals are coded by the brain for perception of self-motion and spatial orientation (Lopez, 2016). Recent neurophysiological studies have discovered that robust vestibular signals are distributed broadly in sensory cortices, suggesting that the vestibular system may be involved in higher cognitive functions (Gu, 2018).

In this review article, we summarized recent progress on the involvement of the vestibular system in higher cognitive functions, particularly for self-motion. We will focus on three topics: (1) how vestibular signals may contribute to estimating of one's heading direction through space; (2) how a more complex path trajectory may be coded by convergent translation and rotation signals arising independently from the otolith and horizontal canals; and (3) how traveled distance or time is possibly coded by the vestibular system. For each topic, we first reviewed results from psychophysical studies on humans and monkeys, and then pointed to the neurophysiological studies that may provide insights for the underlying neural mechanisms. We finally discussed remained issues that need to be addressed in future studies. Note that we have focused primarily on recent progress in the cortical system. Numerous studies conducted in subcortical areas including thalamus, hippocampus, and the limbic system including the entorhinal cortex, retrosplenial cortex can be referred elsewhere, and are only briefly mentioned in the current review article.

HEADING

Both human and monkey can judge heading directions accurately and precisely based on vestibular cues (Telford et al., 1995; Ohmi, 1996; Gu et al., 2007; Fetsch et al., 2009, 2011; Crane, 2012; Drugowitsch et al., 2014). The intact vestibular system is crucial for heading estimation. For example, bilateral labyrinthectomy led to dramatic increase in the psychophysical threshold in a vestibular heading discrimination task, in which the monkeys were instructed to report their perceived heading directions delivered through a motion platform under a two-alternative-forced-choice experimental paradigm (Gu et al., 2007). However, psychophysical threshold decreased gradually after labyrinthectomy, suggesting that the animals may learn to use other sensory inputs, for example, somatosensory or proprioceptive cues to compensate the deficiency in the vestibular system. This hypothesis is consistent with the phenomenon that the animals began to lean their hands against the wall of the cage when moving around after labyrinthectomy. Note that, the psychophysical threshold remained about 10 times worse than the baseline (i.e., before labyrinthectomy), demonstrating that the function of the vestibular system could not be fully compensated by other sensory systems (Gu et al., 2007).

Other sensory inputs, in particular, visual cues, do help the vestibular system for more accurate and precise heading estimate. Provided with congruent vestibular and visual optic flow cues, both humans (Butler et al., 2010, 2011, 2015; Crane, 2017; Ramkhalawansingh et al., 2018) and monkeys (Gu et al., 2008; Fetsch et al., 2009; Chen et al., 2013) can judge smaller heading directions compared to the condition when only one sensory input is available. Interestingly, the decrement in psychophysical threshold during cue combined condition is consistent with the prediction from the optimal cue integration theory (Ernst and Banks, 2002), indicating that our brain makes full use of the information when summing sensory evidence from different sensory modalities. The optimal performance is verified under conditions when a conflict heading angle between vestibular and visual cues is introduced (Fetsch et al., 2009; Butler et al., 2015), or when subjects performed a reaction-time version of the task in which they do not have to wait and accumulate sensory evidence for a long and fixed duration (Drugowitsch et al., 2014).

The neural substrate for heading perception has been extensively explored within the last three decades. Most of the studies have largely focused on areas within the cerebral cortex because neurons in many of these areas are modulated by complex optic flow that is typically experienced during natural navigation. For example, Duffy and colleagues have shown that neurons in the dorsal portion of the medial superior temporal sulcus (MSTd) are sensitive to global-field optic flow simulating real self-motion (Duffy and Wurtz, 1991, 1995), as well as to transient whole body movement in darkness (Duffy, 1998; Page and Duffy, 2003). Later on, Angelaki and DeAngelis further characterized heading selectivity of MSTd neurons in three-dimensional (3D) space using a six degree of freedom (6-DOF) motion platform (Gu et al., 2006; Takahashi et al., 2007; Morgan et al., 2008). They found that nearly all MSTd neurons are significantly modulated by optic flow and two thirds are significantly tuned to vestibular stimuli. Labyrinthectomy largely diminished the vestibular activity but not visual activity in MSTd, suggesting the responses measured during the physical motion condition in darkness really arise from the vestibular source (Gu et al., 2007; Takahashi et al., 2007). Interestingly, for neurons significantly modulated by both optic flow and inertial motion, about half prefers congruent heading direction, and these "congruent" neurons typically exhibit higher heading selectivity when both cues are provided in a congruent way, constituting an ideal substrate for more robust heading estimate during natural navigation. However, note that the other half neurons tend to carry conflict visual and vestibular heading information, producing weaker heading selectivity during cue combination. Thus, this population of neurons is unlikely to account for more robust heading estimate under congruent vestibular-visual inputs. The exact functional implications of these neurons remain a mystery at this stage.

Using the same paradigm, researchers have examined a number of areas in the cerebral sensory cortices and cerebellum. Many of these areas exhibit similar neuronal properties as those found in MSTd, including the ventral parietal area (VIP; Chen et al., 2011c), the smooth eye movement area of the frontal eye field (FEF_{sem}; Gu et al., 2016), the visual posterior sylvian area (VPS; Chen et al., 2011b), and the cerebellar nodulus and uvula (Yakusheva et al., 2013). However, some areas exhibit different properties. For example, most neurons in the posterior insular vestibular cortex (PIVC) are only tuned to vestibular stimuli, but not to optic flow (Chen et al., 2010). By contrast,

most neurons in the middle temporal area (MT; Chowdhury et al., 2009) and V6 (Fan et al., 2015) only respond to visual stimuli, but not to inertial motion. Taken together, we can sketch a map with each area serving as a node in the network for heading perception (**Figure 1A**; see review by Gu, 2018). Note in this map, sensory information is hypothesized to further transmit to decision-related areas such as the frontal and parietal lobes (e.g., FEF_{sac} and LIP) in which the evidence of sensory inputs is accumulated and transformed to form decision and generate motor output. How momentary vestibular evidence is accumulated during this process is still unverified. For example, is the vestibular acceleration accumulated for heading estimate (Drugowitsch et al., 2014)? Future physiological experiments need to be conducted to examine this hypothesis.

The exact information flow across the heading network is currently unknown. However, there are hints from some properties of the neurons recorded from these areas (**Figures 1B,C**). First, the strength of vestibular heading selectivity tends to increase from visual dominant areas (e.g., V6) to vestibular dominant areas (e.g., PIVC; **Figure 1B**). Second, the vestibular temporal dynamics are heterogeneous in the brain. In the peripheral otolith organs, vestibular signals predominantly encode the acceleration component of the inertial motion. Yet these signals are integrated more or less after propagating to the central nervous system, leading to temporal dynamics varied from acceleration to velocity dominant profiles (Laurens et al., 2017; see review by Gu, 2018). Across sensory cortices, the proportion of velocity dominant neurons tends to decrease gradually from area MSTd to PIVC, whereas the proportion of acceleration dominant neurons shows an opposite trend (Chen et al., 2011a). These results suggest that PIVC may lie most proximally to the vestibular periphery, followed by VPS and FEF_{sem}, and then VIP and MSTd.

Although the vestibular and visual heading signals are broadly distributed within the brain network, it is unclear about which areas are really involved in heading estimate. Recently some studies were conducted to address this issue. In these studies, animals were required to actively report their experienced heading directions (Gu et al., 2007, 2008; Fetsch et al., 2009, 2011; Liu et al., 2010; Chen et al., 2013). At the same time, neural activities in certain areas were artificially manipulated to test their causal roles in heading perception. For example, researchers injected chemical drugs (such as muscimol) into the brain to suppress neuronal activity, and found that inactivation of PIVC greatly diminishes the animals' heading performance based on vestibular cues, but not much in the optic flow condition (Chen et al., 2016). On contrary, inactivation of MSTd greatly diminishes the animals' heading performance based on optic flow, but not much in the vestibular condition (Gu et al., 2012). These results suggest that the vestibular-dominant area PIVC plays a critical role in heading perception based on inertial motion, whereas the visual-dominant area MSTd is key to heading based on optic flow.

Different from PIVC and MSTd, inactivation of area VIP does not generate significant effects on the animals' heading performance based on either the vestibular or visual cues (Chen et al., 2016). Such a result is surprising because VIP is similar to MSTd in many aspects (Britten, 2008; Maciokas and Britten, 2010). For example, both areas carry robust vestibular and visual heading signals (Chen et al., 2011c). In addition, neuronal activity in VIP also co-varies with the animal's choice on a trial to trial basis, and this choice-correlation effect is even larger compared to that in MSTd (Chen et al., 2013; Zaidel et al., 2017; Yu and Gu, 2018). Hence, the exact functional implications of the motion directional signals in VIP remain unclear and require further investigation, probably by using other techniques or other behavioral paradigms. For example, by delivering weak electrical currents into the brain to selectively activate a cluster of neurons, researchers examine whether the animals' perceptual judgments are biased in the direction that is predicted from the artificially stimulated neurons (e.g., Salzman et al., 1992). Such an effect implies that the examined area plays a sufficient role in the perceptual decision making task. Using this technique, researcher found that microstimulation in MSTd produces significant effects on the animals' heading performance based on optic flow (Gu et al., 2012; Yu and Gu, 2018; Yu et al., 2018), but not for VIP (Yu and Gu, 2018). However, this effect becomes significant when smooth eye movements were simultaneously accompanied the presented heading stimuli (Zhang and Britten, 2011). In another study, electrical stimulation in VIP could even directly evoke complex facial movements (Cooke et al., 2003). Thus, compared to other sensory cortices (e.g., MSTd), VIP seems to carry more motor-related signals and may causally contribute to behavior only when more complex behavior is involved.

TRAJECTORY OF SELF-MOTION

Our motion trajectory through the space can be complex, typically composed of both translation and rotation components rather than only one of them. For example, when animals run away from their predators, they may make turns while remain heading forward at the same time, resulting in a curved motion trajectory. Curved motion also frequently happens in human world, for example, vehicle driving, ski and running race in sports. How could complex motion trajectories be represented by the vestibular system?

Recent studies begin to address this issue by focusing on interactions of translation and rotation signals arising from otolith and semicircular canals respectively, particularly in the horizontal plane. For example, researcher have designed experiments in which human subjects were instructed to navigate along a curved motion trajectory through passive driving or active walking (Ivanenko et al., 1997; Israël et al., 2005; Nooij et al., 2016). The subjects were then required to reproduce the experienced path by drawing, walking or driving a vehicle. This is not a trivial task because to reproduce the exact profile of the experienced motion trajectory, the subjects need to discriminate the relative translation and rotation components over time during navigation (Li and Cheng, 2011). It showed that the blindfolded subjects were quite good at recovering the traveled path either under the straight or curved motion conditions, suggesting that similar to visual optic flow cues (Li and Cheng, 2011), vestibular signals could also be reliable enough for path perception. However, subjects could not effectively

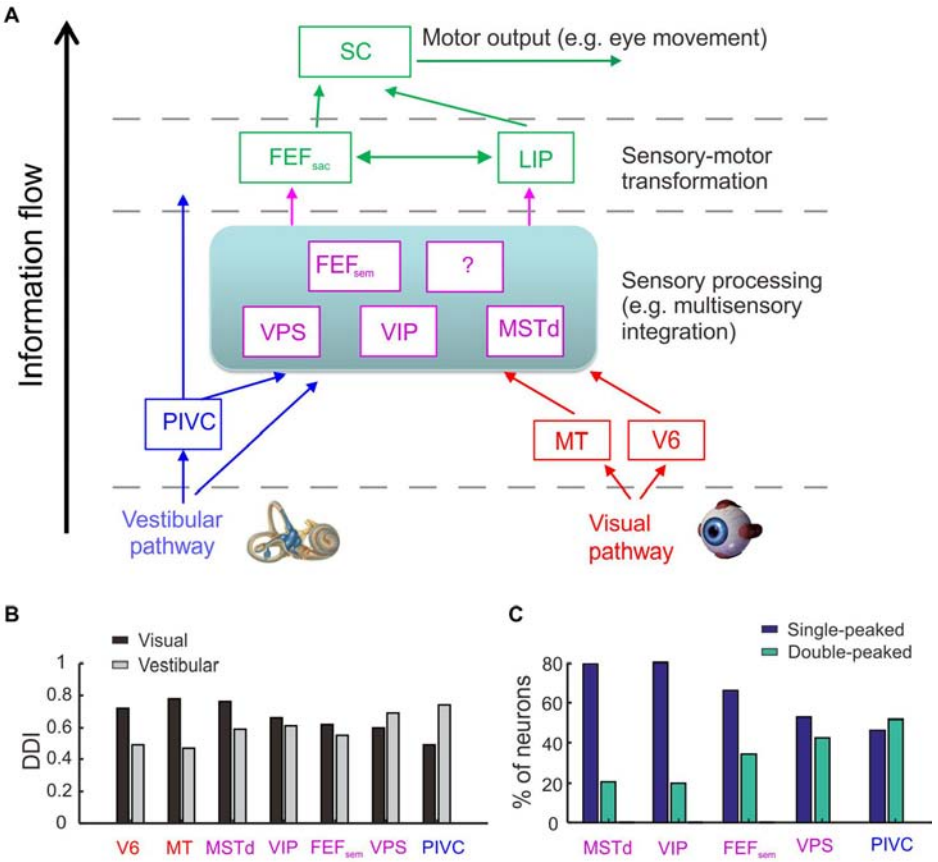

FIGURE 1 | Cortical regions involved in heading perception and their spatial and temporal tuning properties. **(A)** Possible cortical network involved in heading perception revealed by recording neurons in macaques during translating the whole body using a motion platform system. Arrows represent possible information flow based on previous neurophysiological findings. PIVC, parieto-insular vestibular cortex; VPS, visual posterior sylvian area; VIP, ventral intraparietal area; MSTd, the dorsal portion of medial superior temporal area; FEF_{sem}, smooth eye movement region of frontal eye field; FEF_{sac}, saccade region of frontal eye field; V6, area V6; MT, middle temporal area; LIP, lateral intraparietal area. Blue: vestibular dominant area or pathway; Red: visual dominant area or pathway; Magenta: areas with converged visual and vestibular signals; Green: sensory-motor transformation areas involved in oculomotor decision tasks. **(B)** The spatial tuning strength quantified by a direction discrimination index (DDI). DDI value ranges from 0 to 1, with 0 indicating no selectivity and 1 indicating high selectivity (Takahashi et al., 2007). Gray: DDI values measured under the vestibular condition; Black: DDI values measured under the visual condition. Redrew using data from Fan et al. (2015) and Gu et al. (2016). **(C)** The temporal tuning property under the vestibular condition quantified by the proportion of single-peaked neuron (navy blue) and double-peaked neuron (spring green). Redrew using data from Chen et al. (2010, 2011a,b,c) and Gu et al. (2016). The temporal dynamics of the single-peaked neurons follow more closely with the velocity profile of the vestibular stimuli, whereas temporal dynamics of the double-peaked neurons match more with the acceleration profile.

distinguish real curved self-motion from a straight motion trajectory accompanied by a yaw rotation of the head or whole body at the same time (i.e., illusorily perceived curved motion; Ivanenko et al., 1997; Israël et al., 2005). Thus, signals arising from horizontal canals seem to play a critical role in complex path perception. Indeed, a recent study examined the detection threshold for head translation and rotation respectively during combined, i.e., curvilinear motion (MacNeilage et al., 2010). It is found that the detection threshold for rotation was unaffected under the presence of translation, while the detection threshold for translation was significantly increased under the presence of rotation. In a different study, researcher found that yaw rotations could significantly bias the subjects' perceived sway of the body, but a reversed effect did not happen (Crane, 2016). Finally, when asked to reproduce a triangle path, some patients with vestibular deficits could replicate the traveled distance, but not the traveled angle (Glasauer et al., 2002), indicating a causal role of the vestibular signals, particularly for the rotation signals in complex path perception.

How do neurons in the brain carry out computations that could underlie the curvilinear self-motion perception? To address this issue, researchers recorded single-unit activity from neurons in the central nervous system of macaques under translation only, yaw rotation only and convergent translation plus yaw rotation conditions. In the vestibular nucleus (VN) in brainstem, neurons integrate translation and rotation inputs in a sub-additive (Carriot et al., 2015) or near additive way (Newlands et al., 2018) when both signals co-exist in the curvilinear motion condition. Researchers also have examined several cortical areas including MSTd, VIP and VPS, and found that a group of convergent neurons receiving both translation and

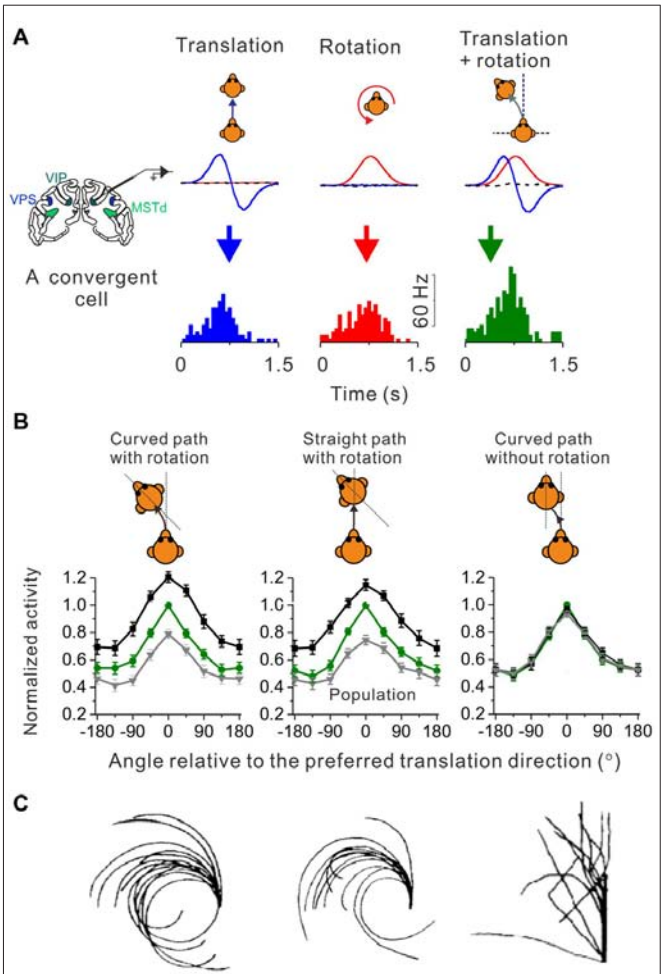

FIGURE 2 | Identify cortical neurons responding to curvilinear self-motion. **(A)** Top panel: schematic illustration for three types of self-motion; middle panel: measured linear acceleration (Blue curve) and angular velocity (Red curve) for forward translation, CCW rotation and their corresponding curvilinear motion; Bottom panel: PSTH to forward translation, counter-clockwise (CCW) rotation and curvilinear motion with combined forward translation and CCW from an example convergent neuron in area VPS. **(B)** Firing rate pattern of convergent neurons from areas VPS, VIP and MSTd during curved-path-with-rotation, straight-path-with-rotation, and curved-path-without-rotation. Green curves: the translation only condition; black curves: curvilinear condition with preferred rotation; gray curves: curvilinear conditions with non-preferred rotation. Plots were made and modified with permission from Cheng and Gu (2016). **(C)** Trajectories drew by blinded-folded subjects after experiencing curved-path-with-rotation, straight-path-with-rotation and curved-path-without rotation delivered by a vehicle. Plots were made and modified with permission from Ivanenko et al. (1997).

rotation inputs tended to integrate the two signals sub-additively (**Figure 2**), suggesting that this property may arise from the subcortical areas, e.g., the brainstem (Cheng and Gu, 2016). However, the weight assigned to the translation and rotation signals in cortices is not consistent with what has been reported in the brainstem, suggesting that additional integration may also happen when the vestibular signals are propagated to the cortex.

Curved motion trajectory in the horizontal plane would potentially produce centripetal force that may also mediate curvilinear self-motion perception. However, using a straight linear path with simultaneous head rotation paradigm (Ivanenko et al., 1997), researchers found that human subjects reported almost the same "curved" motion experience as in the curved path condition with head rotation (**Figure 2C**, middle panel vs. left panel). Because the magnitude of the centripetal force is quite different between these two experimental conditions, it is unlikely that the centripetal force would be a key to curved motion sensation. Indeed, in a third experimental conditions in which subjects experienced curved motion path but without head rotations, they did not report curved self-motion any more although the centrifugal force was now present as in the curved path condition with head rotation (**Figure 2C**, right panel vs. left panel). On the neural level, recently researcher recorded neurons in a number of cortical areas under a similar paradigm as in the above psychophysical study (Cheng and Gu, 2016). Interestingly, similar to the behavior, the firing patterns of the cortical neurons are analogous under the curved-path-with-rotation condition and straight-path-with-rotation condition, but are different from the condition when yaw rotation is absent (**Figure 2B**). Thus, neurons receiving inputs from both otolith and horizontal canals in the brain may mediate curvilinear self-motion perception. Note, that physiological properties including the proportion of different types of neurons, tuning strength and sensory summation rules are similar across the examined cortical areas, suggesting that the complex motion trajectory may be widely represented in the brain. However, future work is required to dissect the exact role of individual areas in self-motion.

TRAVEL DISTANCE

From the mathematical point of view, double integration of the vestibular acceleration signals provides information about the distance we have traveled, which appears to be more challenging than estimating heading direction during spatial navigation. Researchers have investigated the role of vestibular signals in distance perception by requiring blindfolded human subjects to report their linear or angular displacement of the body through a number of methods including pointing (Ivanenko et al., 1997; Nooij et al., 2016), saccade (Berthoz et al., 1987; Israël and Berthoz, 1989), pressing button (Israël et al., 1993; Harris et al., 2000), walking (Mittelstaedt and Mittelstaedt, 2001; Campos et al., 2010, 2012, 2014), or controlling vehicles (Grasso et al., 1999; Tremblay et al., 2013). Normal human subjects could accurately recover their traveled distance, as well as the motion velocity profile regardless of reporting methods. By contrast, performance from vestibulopathy subjects were typically impaired in estimating time and distance when they were instructed to walk forward and make turns at a particular point under a blindfolded condition (Cohen, 2000), suggesting a causal role of vestibular signals in distance perception.

Similar to heading perception, information from other sensory modalities such as visual and proprioceptive cues, also contribute to the estimation of traveled distance

(Jürgens et al., 2003; Jürgens and Becker, 2006). For example, a number of studies have illustrated that subjects can accurately estimate the traveled distance from optic flow (Bremmer and Lappe, 1999; Redlick et al., 2001; Frenz and Lappe, 2005; Dacke and Srinivasan, 2007). When different sensory inputs are provided at the same time, information from different sources is summed with a weight that is proportional to the reliability of each cue (Sun et al., 2004; Campos et al., 2010, 2012, 2014; ter Horst et al., 2015). However, some work proposed that the vestibular signals could dominate the visual signals (Harris et al., 2000), similar to a prior of the vestibular signals as observed in heading discrimination tasks (Fetsch et al., 2011; Butler et al., 2015).

Unlike the extensive studies exploring the contribution of vestibular signals in heading perception, little is known about the role of vestibular signals underlying distance perception. There is evidence suggesting that the temporoparietal junction, which carries prominent vestibular signals, may be involved in distance perception. For example, patients with lesions in the temporoparietal region tended to underestimate the traveled distance and stimulus duration, whereas the ability to detect onset of motion was unaffected (Kaski et al., 2016). When using repetitive transcranial magnetic stimulation (rTMS) to interfere the temporoparietal junction, subjects could replicate the motion velocity profile, but could not replicate the traveled distance (Seemungal et al., 2008a,b, 2009; Ventre-Dominey, 2014). This result suggests that temporoparietal junction plays an important role in distance perception, and moreover, distance perception (related to integration of velocity information over time) and heading perception (related to detection of motion direction over time) are two separate processes implemented in the brain.

How exactly vestibular signals in cortex contribute to the estimation of traveled distance or time remains unclear. Recently a study characterizing the spatial-temporal properties of vestibular responses in MSTd found that nearly half of the neurons exhibited a statistically significant position component, yet it was much weaker compared to the velocity as well as the acceleration component (Chen et al., 2011a). More works need to be conducted in the future to characterize how neurons in different cortical areas (see **Figure 1**) may encode the moving distance. For example, neurons in the sensory-motor transformation areas including the parietal and frontal lobes exhibit ramping activity over time (Kim and Shadlen, 1999; Gold and Shadlen, 2000; Shadlen and Newsome, 2001; Ding and Gold, 2012), which may serve as a neural correlate for distance coding. Indeed, it has been indicated that parietal neurons may encode the elapsed time (Jazayeri and Shadlen, 2015), thus, these neurons may also encode the traveled distance as the product of the time and moving speed. Such neurons have also been reported in subcortical areas such as the rodents' hippocampus when the animals performed a spatial navigation task (Kraus et al., 2013).

In fact, via the anterior part of thalamus, vestibular peripheral inputs project to the limbic system which has been illustrated to be critical for self-motion based path integration (Cullen and Taube, 2017). For example, rotation signals arising from the semicircular canals are necessary for formation of head direction cells (Valerio and Taube, 2016). Translation signals from otolith may be critical for place cells, grid cells, and speed cells in the hippocampal-entorhinal system (Yoder and Kirby, 2014). It remains unclear how exactly the cortical self-motion system is connected with the subcortical and limbic systems, for example, through retrosplenial cortex (Vann et al., 2009). Future studies need to be conducted to fully understand how a complete neural network in the brain code self-motion during spatial navigation.

CONCLUSION

Convergent evidence from behavioral, neurophysiological and computational studies reveals that the vestibular system plays a critical role in different aspects of self-motion perception, such as heading, path, and traveled distance or time. Particularly for heading estimation, a series of physiological studies have been conducted in recent years to address the underlying neural mechanisms. These studies have provided us with valuable information about how the brain may code motion signals to guide spatial navigation. At the same time, these studies also provoke many important issues to be addressed in the future.

First, vestibular signals are widely distributed in the central nervous system. Recent studies have revealed many areas conveying robust vestibular signals in the cerebral cortex. It is likely that more areas will be continually discovered in the future. Thus, it is important to address both the homogeneity and heterogeneity of the functional implications of each area in self-motion perception.

Second, the temporal dynamics of vestibular signals, especially those arise from the otolith organs, vary broadly in the central nervous system. Future studies need to identify exact functions of the neurons with different temporal dynamics. For example, it has been proposed that the momentary vestibular acceleration evidence could be accumulated by decision making neurons e.g., LIP neuron to generate the final behavioral output for heading discrimination task (Drugowitsch et al., 2014). In contrast, velocity information may be used for other functions such as distance perception, or maintenance of visual stability during head or body movements.

Third, vestibular signals arising from the inner ears are encoded in a head-centered reference frame, yet spatial navigation in the environment is basically a body-centered behavior. Recent neurophysiological studies have provided evidence suggesting that vestibular reference frame may be gradually transformed along the signal propagation pathway, for example, from largely head-centered in the rostral regions of the VN (Shaikh et al., 2004), to mixed head- and body-centered in the cerebellar rFN (Kleine et al., 2004; Martin et al., 2018) and the cerebral PIVC (Chen et al., 2013a), and to predominantly body-centered in the cortical area of VIP (Chen et al., 2013a). Future studies need to explore the possible role of neurons with gain modulated activity in reference frame transformation (Zipser and Andersen, 1988; Siegel, 1998; Xing and Andersen, 2000; Gu et al., 2006; Pesaran et al., 2006; Fetsch et al., 2007; Chen et al., 2013b; Hadjidimitrakis et al., 2014; Fan et al., 2015; Yang and Gu, 2017).

Fourth, vestibular signals have been recently discovered in a number of sensory cortices that also carry robust visual motion signals, suggesting that interactions between sensory modalities may exist. It is possible that vestibular and visual signals are integrated by the brain for more robust heading estimate. In addition, it is also possible that these signals may interact with each other for other functions such as maintaining visual stability when smooth pursuit eye movements are accompanied during head or body movements. Future works need to explore these potential functions, as well as the computational rules underlying the integration or interaction process.

Finally, the current review article focuses data mainly collected in the passive self-motion conditions. However, researchers have shown that active self-motion largely diminishes vestibular activity in the brainstem and cerebellum (see review Cullen and Taube, 2017). Recent theoretical studies suggest that a single sensory internal model can combine motor commands with the vestibular and proprioceptive signals optimally to recover accurate self-motion during active head movements (Laurens and Angelaki, 2017). Thus, it would be important to explore the vestibular signals in the cerebral cortex, including sensory cortices, sensory-motor transformation areas, and motor areas under active self-motion conditions.

AUTHOR CONTRIBUTIONS

ZC and YG wrote, revised and finalized the manuscript.

FUNDING

This work was supported by grants from the National Key Basic Research Project (2016YFC1306801) and Ministry of Science and Technology of China, National Key R&D Program of China (1306801).

REFERENCES

Berthoz, A., Israël, I., Viéville, T., and Zee, D. (1987). Linear head displacement measured by the otoliths can be reproduced through the saccadic system. *Neurosci. Lett.* 82, 285–290. doi: 10.1016/0304-3940(87)90270-9

Bremmer, F., and Lappe, M. (1999). The use of optical velocities for distance discrimination and reproduction during visually simulated self motion. *Exp. Brain Res.* 127, 33–42. doi: 10.1007/s002210050771

Britten, K. H. (2008). Mechanisms of self-motion perception. *Annu. Rev. Neurosci.* 31, 389–410. doi: 10.1146/annurev.neuro.29.051605.112953

Butler, J. S., Campos, J. L., and Bülthoff, H. H. (2015). Optimal visual-vestibular integration under conditions of conflicting intersensory motion profiles. *Exp. Brain Res.* 233, 587–597. doi: 10.1007/s00221-014-4136-1

Butler, J. S., Campos, J. L., Bülthoff, H. H., and Smith, S. T. (2011). The role of stereo vision in visual-vestibular integration. *Seeing Perceiving* 24, 453–470. doi: 10.1163/187847511x588070

Butler, J. S., Smith, S. T., Campos, J. L., and Bülthoff, H. H. (2010). Bayesian integration of visual and vestibular signals for heading. *J. Vis.* 10:23. doi: 10.1167/10.11.23

Campos, J. L., Butler, J. S., and Bülthoff, H. H. (2012). Multisensory integration in the estimation of walked distances. *Exp. Brain Res.* 218, 551–565. doi: 10.1007/s00221-012-3048-1

Campos, J. L., Butler, J. S., and Bülthoff, H. H. (2014). Contributions of visual and proprioceptive information to travelled distance estimation during changing sensory congruencies. *Exp. Brain Res.* 232, 3277–3289. doi: 10.1007/s00221-014-4011-0

Campos, J. L., Byrne, P., and Sun, H. J. (2010). The brain weights body-based cues higher than vision when estimating walked distances. *Eur. J. Neurosci.* 31, 1889–1898. doi: 10.1111/j.1460-9568.2010.07212.x

Carriot, J., Jamali, M., Brooks, J. X., and Cullen, K. E. (2015). Integration of canal and otolith inputs by central vestibular neurons is subadditive for both active and passive self-motion: implication for perception. *J. Neurosci.* 35, 3555–3565. doi: 10.1523/jneurosci.3540-14.2015

Chen, A., DeAngelis, G. C., and Angelaki, D. E. (2010). Macaque parieto-insular vestibular cortex: responses to self-motion and optic flow. *J. Neurosci.* 30, 3022–3042. doi: 10.1523/jneurosci.4029-09.2010

Chen, A., DeAngelis, G. C., and Angelaki, D. E. (2011a). A comparison of vestibular spatiotemporal tuning in macaque parietoinsular vestibular cortex, ventral intraparietal area and medial superior temporal area. *J. Neurosci.* 31, 3082–3094. doi: 10.1523/jneurosci.4476-10.2011

Chen, A., DeAngelis, G. C., and Angelaki, D. E. (2011b). Convergence of vestibular and visual self-motion signals in an area of the posterior sylvian fissure. *J. Neurosci.* 31, 11617–11627. doi: 10.1523/JNEUROSCI.1266-11.2011

Chen, A., DeAngelis, G. C., and Angelaki, D. E. (2011c). Representation of vestibular and visual cues to self-motion in ventral intraparietal cortex. *J. Neurosci.* 31, 12036–12052. doi: 10.1523/jneurosci.0395-11.2011

Chen, A., DeAngelis, G. C., and Angelaki, D. E. (2013). Functional specializations of the ventral intraparietal area for multisensory heading discrimination. *J. Neurosci.* 33, 3567–3581. doi: 10.1523/jneurosci.4522-12.2013

Chen, X., DeAngelis, G. C., and Angelaki, D. E. (2013a). Diverse spatial reference frames of vestibular signals in parietal cortex. *Neuron* 80, 1310–1321. doi: 10.1016/j.neuron.2013.09.006

Chen, X., DeAngelis, G. C., and Angelaki, D. E. (2013b). Eye-centered representation of optic flow tuning in the ventral intraparietal area. *J. Neurosci.* 33, 18574–18582. doi: 10.1523/jneurosci.2837-13.2013

Chen, A., Gu, Y., Liu, S., DeAngelis, G. C., and Angelaki, D. E. (2016). Evidence for a causal contribution of macaque vestibular, but not intraparietal, cortex to heading perception. *J. Neurosci.* 36, 3789–3798. doi: 10.1523/jneurosci.2485-15.2016

Cheng, Z., and Gu, Y. (2016). Distributed representation of curvilinear self-motion in the macaque parietal cortex. *Cell Rep.* 15, 1013–1023. doi: 10.1016/j.celrep.2016.03.089

Chowdhury, S. A., Takahashi, K., DeAngelis, G. C., and Angelaki, D. E. (2009). Does the middle temporal area carry vestibular signals related to self-motion? *J. Neurosci.* 29, 12020–12030. doi: 10.1523/jneurosci.0004-09.2009

Cohen, H. S. (2000). Vestibular disorders and impaired path integration along a linear trajectory. *J. Vestib. Res.* 10, 7–15.

Cooke, D. F., Taylor, C. S., Moore, T., and Graziano, M. S. (2003). Complex movements evoked by microstimulation of the ventral intraparietal area. *Proc. Natl. Acad. Sci. U S A* 100, 6163–6168. doi: 10.1073/pnas.1031751100

Crane, B. T. (2012). Direction specific biases in human visual and vestibular heading perception. *PLoS One* 7:e51383. doi: 10.1371/journal.pone.0051383

Crane, B. T. (2016). Perception of combined translation and rotation in the horizontal plane in humans. *J. Neurophysiol.* 116, 1275–1285. doi: 10.1152/jn.00322.2016

Crane, B. T. (2017). Effect of eye position during human visual-vestibular integration of heading perception. *J. Neurophysiol.* 118, 1609–1621. doi: 10.1152/jn.00037.2017

Cullen, K. E., and Taube, J. S. (2017). Our sense of direction: progress, controversies and challenges. *Nat. Neurosci.* 20, 1465–1473. doi: 10.1038/nn.4658

Dacke, M., and Srinivasan, M. V. (2007). Honeybee navigation: distance estimation in the third dimension. *J. Exp. Biol.* 210, 845–853. doi: 10.1242/jeb.002089

Ding, L., and Gold, J. I. (2012). Neural correlates of perceptual decision making before, during and after decision commitment in monkey frontal eye field. *Cereb. Cortex* 22, 1052–1067. doi: 10.1093/cercor/bhr178

Drugowitsch, J., DeAngelis, G. C., Klier, E. M., Angelaki, D. E., and Pouget, A. (2014). Optimal multisensory decision-making in a reaction-time task. *Elife* 3:e03005. doi: 10.7554/eLife.03005

Duffy, C. J. (1998). MST neurons respond to optic flow and translational movement. *J. Neurophysiol.* 80, 1816–1827. doi: 10.1152/jn.1998.80.4.1816

Duffy, C. J., and Wurtz, R. H. (1991). Sensitivity of MST neurons to optic flow stimuli. I. A continuum of response selectivity to large-field stimuli. *J. Neurophysiol.* 65, 1329–1345. doi: 10.1152/jn.1991.65.6.1329

Duffy, C. J., and Wurtz, R. H. (1995). Response of monkey MST neurons to optic flow stimuli with shifted centers of motion. *J. Neurosci.* 15, 5192–5208. doi: 10.1523/jneurosci.15-07-05192.1995

Ernst, M. O., and Banks, M. S. (2002). Humans integrate visual and haptic information in a statistically optimal fashion. *Nature* 415, 429–433. doi: 10.1038/415429a

Fan, R. H., Liu, S., DeAngelis, G. C., and Angelaki, D. E. (2015). Heading tuning in macaque area V6. *J. Neurosci.* 35, 16303–16314. doi: 10.1523/jneurosci.2903-15.2015

Fernández, C., and Goldberg, J. M. (1976a). Physiology of peripheral neurons innervating otolith organs of the squirrel monkey: II. Directional selectivity and force-response relations. *J. Neurophysiol.* 39, 985–995. doi: 10.1152/jn.1976.39.5.985

Fernández, C., and Goldberg, J. M. (1976b). Physiology of peripheral neurons innervating otolith organs of the squirrel monkey: I. Response to static tilts and to long-duration centrifugal force. *J. Neurophysiol.* 39, 970–984. doi: 10.1152/jn.1976.39.5.970

Fetsch, C. R., Pouget, A., Deangelis, G. C., and Angelaki, D. E. (2011). Neural correlates of reliability-based cue weighting during multisensory integration. *Nat. Neurosci.* 15, 146–154. doi: 10.1038/nn.2983

Fetsch, C. R., Turner, A. H., DeAngelis, G. C., and Angelaki, D. E. (2009). Dynamic reweighting of visual and vestibular cues during self-motion perception. *J. Neurosci.* 29, 15601–15612. doi: 10.1523/jneurosci.2574-09.2009

Fetsch, C. R., Wang, S., Gu, Y., Deangelis, G. C., and Angelaki, D. E. (2007). Spatial reference frames of visual, vestibular and multimodal heading signals in the dorsal subdivision of the medial superior temporal area. *J. Neurosci.* 27, 700–712. doi: 10.1523/JNEUROSCI.3553-06.2007

Frenz, H., and Lappe, M. (2005). Absolute travel distance from optic flow. *Vision Res.* 45, 1679–1692. doi: 10.1016/j.visres.2004.12.019

Glasauer, S., Amorim, M. A., Viaud-Delmon, I., and Berthoz, A. (2002). Differential effects of labyrinthine dysfunction on distance and direction during blindfolded walking of a triangular path. *Exp. Brain Res.* 145, 489–497. doi: 10.1007/s00221-002-1146-1

Gold, J. I., and Shadlen, M. N. (2000). Representation of a perceptual decision in developing oculomotor commands. *Nature* 404, 390–394. doi: 10.1038/35006062

Goldberg, J. M., and Fernandez, C. (1971). Resting discharge and response to constant angular accelerations. *J. Neurophysiol.* 34, 635–660. doi: 10.1152/jn.1971.34.4.635

Grasso, R., Glasauer, S., Georges-Francois, P., and Israel, I. (1999). Replication of passive whole-body linear displacements from inertial cues. Facts and mechanisms. *Ann. N Y Acad. Sci.* 871, 345–366. doi: 10.1111/j.1749-6632.1999.tb09197.x

Gu, Y. (2018). Vestibular signals in primate cortex for self-motion perception. *Curr. Opin. Neurobiol.* 52, 10–17. doi: 10.1016/j.conb.2018.04.004

Gu, Y., Angelaki, D. E., and Deangelis, G. C. (2008). Neural correlates of multisensory cue integration in macaque MSTd. *Nat. Neurosci.* 11, 1201–1210. doi: 10.1038/nn.2191

Gu, Y., Cheng, Z., Yang, L., DeAngelis, G. C., and Angelaki, D. E. (2016). Multisensory convergence of visual and vestibular heading cues in the pursuit area of the frontal eye field. *Cereb. Cortex* 26, 3785–3801. doi: 10.1093/cercor/bhv183

Gu, Y., DeAngelis, G. C., and Angelaki, D. E. (2007). A functional link between area MSTd and heading perception based on vestibular signals. *Nat. Neurosci.* 10, 1038–1047. doi: 10.1038/nn1935

Gu, Y., DeAngelis, G. C., and Angelaki, D. E. (2012). Causal links between dorsal medial superior temporal area neurons and multisensory heading perception. *J. Neurosci.* 32, 2299–2313. doi: 10.1523/JNEUROSCI.5154-11.2012

Gu, Y., Watkins, P. V., Angelaki, D. E., and DeAngelis, G. C. (2006). Visual and nonvisual contributions to three-dimensional heading selectivity in the medial superior temporal area. *J. Neurosci.* 26, 73–85. doi: 10.1523/JNEUROSCI.2356-05.2006

Hadjidimitrakis, K., Bertozzi, F., Breveglieri, R., Fattori, P., and Galletti, C. (2014). Body-centered, mixed, but not hand-centered coding of visual targets in the medial posterior parietal cortex during reaches in 3D space. *Cereb. Cortex* 24, 3209–3220. doi: 10.1093/cercor/bht181

Harris, L. R., Jenkin, M., and Zikovitz, D. C. (2000). Visual and non-visual cues in the perception of linear self-motion. *Exp. Brain Res.* 135, 12–21. doi: 10.1007/s002210000504

Israël, I., and Berthoz, A. (1989). Contribution of the otoliths to the calculation of linear displacement. *J. Neurophysiol.* 62, 247–263. doi: 10.1152/jn.1989.62.1.247

Israël, I., Chapuis, N., Glasauer, S., Charade, O., and Berthoz, A. (1993). Estimation of passive horizontal linear whole-body displacement in humans. *J. Neurophysiol.* 70, 1270–1273. doi: 10.1152/jn.1993.70.3.1270

Israël, I., Crockett, M., Zupan, L., and Merfeld, D. (2005). Reproduction of ON-center and OFF-center self-rotations. *Exp. Brain Res.* 163, 540–546. doi: 10.1007/s00221-005-2323-9

Ivanenko, Y., Grasso, R., Israël, I., and Berthoz, A. (1997). The contribution of otoliths and semicircular canals to the perception of two-dimensional passive whole-body motion in humans. *J. Physiol.* 502, 223–233. doi: 10.1111/j.1469-7793.1997.223bl.x

Jazayeri, M., and Shadlen, M. N. (2015). A neural mechanism for sensing and reproducing a time interval. *Curr. Biol.* 25, 2599–2609. doi: 10.1016/j.cub.2015.08.038

Jürgens, R., and Becker, W. (2006). Perception of angular displacement without landmarks: evidence for Bayesian fusion of vestibular, optokinetic, podokinesthetic, and cognitive information. *Exp. Brain Res.* 174, 528–543. doi: 10.1007/s00221-006-0486-7

Jürgens, R., Nasios, G., and Becker, W. (2003). Vestibular, optokinetic, and cognitive contribution to the guidance of passive self-rotation toward instructed targets. *Exp. Brain Res.* 151, 90–107. doi: 10.1007/s00221-003-1472-y

Kaski, D., Quadir, S., Nigmatullina, Y., Malhotra, P. A., Bronstein, A. M., and Seemungal, B. M. (2016). Temporoparietal encoding of space and time during vestibular-guided orientation. *Brain* 139, 392–403. doi: 10.1093/brain/awv370

Kim, J. N., and Shadlen, M. N. (1999). Neural correlates of a decision in the dorsolateral prefrontal cortex of the macaque. *Nat. Neurosci.* 2, 176–185. doi: 10.1038/5739

Kleine, J. F., Guan, Y., Kipiani, E., Glonti, L., Hoshi, M., and Büttner, U. (2004). Trunk position influences vestibular responses of fastigial nucleus neurons in the alert monkey. *J. Neurophysiol.* 91, 2090–2100. doi: 10.1152/jn.00849.2003

Kraus, B. J., Robinson, R. J. II., White, J. A., Eichenbaum, H., and Hasselmo, M. E. (2013). Hippocampal "time cells": time versus path integration. *Neuron* 78, 1090–1101. doi: 10.1016/j.neuron.2013.04.015

Laurens, J., and Angelaki, D. E. (2017). A unified internal model theory to resolve the paradox of active versus passive self-motion sensation. *Elife* 6:e28074. doi: 10.7554/eLife.28074

Laurens, J., Liu, S., Yu, X. J., Chan, R., Dickman, D., DeAngelis, G. C., et al. (2017). Transformation of spatiotemporal dynamics in the macaque vestibular system from otolith afferents to cortex. *Elife* 6:e20787. doi: 10.7554/elife.20787

Li, L., and Cheng, J. C. K. (2011). Perceiving path from optic flow. *J. Vis.* 11:22. doi: 10.1167/11.1.22

Liu, S., Yakusheva, T., Deangelis, G. C., and Angelaki, D. E. (2010). Direction discrimination thresholds of vestibular and cerebellar nuclei neurons. *J. Neurosci.* 30, 439–448. doi: 10.1523/JNEUROSCI.3192-09.2010

Lopez, C. (2016). The vestibular system: balancing more than just the body. *Curr. Opin. Neurol.* 29, 74–83. doi: 10.1097/WCO.0000000000000286

Maciokas, J. B., and Britten, K. H. (2010). Extrastriate area MST and parietal area VIP similarly represent forward headings. *J. Neurophysiol.* 104, 239–247. doi: 10.1152/jn.01083.2009

MacNeilage, P., Turner, A., and Angelaki, D. (2010). Canal-otolith interactions and detection thresholds of linear and angular components during curved-path self-motion. *J. Neurophysiol.* 104, 765–773. doi: 10.1152/jn.01067.2009

Martin, C. Z., Brooks, J. X., and Green, A. M. (2018). Role of rostral fastigial neurons in encoding a body-centered representation of translation in three dimensions. *J. Neurosci.* 38, 3584–3602. doi: 10.1523/JNEUROSCI.2116-17.2018

Mittelstaedt, M. L., and Mittelstaedt, H. (2001). Idiothetic navigation in humans: estimation of path length. *Exp. Brain Res.* 139, 318–332. doi: 10.1007/s002210100735

Morgan, M. L., Deangelis, G. C., and Angelaki, D. E. (2008). Multisensory integration in macaque visual cortex depends on cue reliability. *Neuron* 59, 662–673. doi: 10.1016/j.neuron.2008.06.024

Newlands, S. D., Abbatematteo, B., Wei, M., Carney, L. H., and Luan, H. (2018). Convergence of linear acceleration and yaw rotation signals on non-eye movement neurons in the vestibular nucleus of macaques. *J. Neurophysiol.* 119, 73–83. doi: 10.1152/jn.00382.2017

Nooij, S. A., Nesti, A., Bülthoff, H. H., and Pretto, P. (2016). Perception of rotation, path and heading in circular trajectories. *Exp. Brain Res.* 234, 2323–2337. doi: 10.1007/s00221-016-4638-0

Ohmi, M. (1996). Egocentric perception through interaction among many sensory systems. *Cogn. Brain Res.* 5, 87–96. doi: 10.1016/s0926-6410(96)00044-4

Page, W. K., and Duffy, C. J. (2003). Heading representation in MST: sensory interactions and population encoding. *J. Neurophysiol.* 89, 1994–2013. doi: 10.1152/jn.00493.2002

Pesaran, B., Nelson, M. J., and Andersen, R. A. (2006). Dorsal premotor neurons encode the relative position of the hand, eye, and goal during reach planning. *Neuron* 51, 125–134. doi: 10.1016/j.neuron.2006.05.025

Ramkhalawansingh, R., Butler, J. S., and Campos, J. L. (2018). Visual-vestibular integration during self-motion perception in younger and older adults. *Psychol. Aging* 33, 798–813. doi: 10.1037/pag0000271

Redlick, F. P., Jenkin, M., and Harris, L. R. (2001). Humans can use optic flow to estimate distance of travel. *Vision Res.* 41, 213–219. doi: 10.1016/s0042-6989(00)00243-1

Salzman, C. D., Murasugi, C. M., Britten, K. H., and Newsome, W. T. (1992). Microstimulation in visual area MT: effects on direction discrimination performance. *J. Neurosci.* 12, 2331–2355. doi: 10.1523/JNEUROSCI.12-06-02331.1992

Seemungal, B. M., Rizzo, V., Gresty, M. A., Rothwell, J. C., and Bronstein, A. M. (2008a). Cortical processing in vestibular navigation. *Prog. Brain Res.* 171, 339–346. doi: 10.1016/S0079-6123(08)00650-X

Seemungal, B. M., Rizzo, V., Gresty, M. A., Rothwell, J. C., and Bronstein, A. M. (2008b). Posterior parietal rTMS disrupts human Path Integration during a vestibular navigation task. *Neurosci. Lett.* 437, 88–92. doi: 10.1016/j.neulet.2008.03.067

Seemungal, B. M., Rizzo, V., Gresty, M. A., Rothwell, J. C., and Bronstein, A. M. (2009). Perceptual encoding of self-motion duration in human posterior parietal cortex. *Ann. N Y Acad. Sci.* 1164, 236–238. doi: 10.1111/j.1749-6632.2009.03772.x

Shadlen, M. N., and Newsome, W. T. (2001). Neural basis of a perceptual decision in the parietal cortex (area LIP) of the rhesus monkey. *J. Neurophysiol.* 86, 1916–1936. doi: 10.1152/jn.2001.86.4.1916

Shaikh, A. G., Meng, H., and Angelaki, D. E. (2004). Multiple reference frames for motion in the primate cerebellum. *J. Neurosci.* 24, 4491–4497. doi: 10.1523/JNEUROSCI.0109-04.2004

Siegel, R. M. (1998). Representation of visual space in area 7a neurons using the center of mass equation. *J. Comput. Neurosci.* 5, 365–381. doi: 10.1023/A:1008844027878

Sun, H. J., Campos, J. L., and Chan, G. S. (2004). Multisensory integration in the estimation of relative path length. *Exp. Brain Res.* 154, 246–254. doi: 10.1007/s00221-003-1652-9

Takakusaki, K. (2017). Functional neuroanatomy for posture and gait control. *J. Mov. Disord.* 10, 1–17. doi: 10.14802/jmd.16062

Takahashi, K., Gu, Y., May, P. J., Newlands, S. D., DeAngelis, G. C., and Angelaki, D. E. (2007). Multimodal coding of three-dimensional rotation and translation in area MSTd: comparison of visual and vestibular selectivity. *J. Neurosci.* 27, 9742–9756. doi: 10.1523/JNEUROSCI.0817-07.2007

Telford, L., Howard, I. P., and Ohmi, M. (1995). Heading judgments during active and passive self-motion. *Exp. Brain Res.* 104, 502–510. doi: 10.1007/bf00231984

ter Horst, A. C., Koppen, M., Selen, L. P., and Medendorp, W. P. (2015). Reliability-based weighting of visual and vestibular cues in displacement estimation. *PLoS One* 10:e0145015. doi: 10.1371/journal.pone.0145015

Tremblay, L., Kennedy, A., Paleressompoulle, D., Borel, L., Mouchnino, L., and Blouin, J. (2013). Biases in the perception of self-motion during whole-body acceleration and deceleration. *Front. Integr. Neurosci.* 7:90. doi: 10.3389/fnint.2013.00090

Valerio, S., and Taube, J. S. (2016). Head direction cell activity is absent in mice without the horizontal semicircular canals. *J. Neurosci.* 36, 741–754. doi: 10.1523/JNEUROSCI.3790-14.2016

Vann, S. D., Aggleton, J. P., and Maguire, E. A. (2009). What does the retrosplenial cortex do? *Nat. Rev. Neurosci.* 10, 792–802. doi: 10.1038/nrn2733

Ventre-Dominey, J. (2014). Vestibular function in the temporal and parietal cortex: distinct velocity and inertial processing pathways. *Front. Integr. Neurosci.* 8:53. doi: 10.3389/fnint.2014.00053

Xing, J., and Andersen, R. A. (2000). Models of the posterior parietal cortex which perform multimodal integration and represent space in several coordinate frames. *J. Cogn. Neurosci.* 12, 601–614. doi: 10.1162/089892900562363

Yakusheva, T. A., Blazquez, P. M., Chen, A., and Angelaki, D. E. (2013). Spatiotemporal properties of optic flow and vestibular tuning in the cerebellar nodulus and uvula. *J. Neurosci.* 33, 15145–15160. doi: 10.1523/JNEUROSCI.2118-13.2013

Yang, L., and Gu, Y. (2017). Distinct spatial coordinate of visual and vestibular heading signals in macaque FEFsem and MSTd. *Elife* 6:e29809. doi: 10.7554/elife.29809

Yoder, R. M., and Kirby, S. L. (2014). Otoconia-deficient mice show selective spatial deficits. *Hippocampus* 24, 1169–1177. doi: 10.1002/hipo.22300

Yu, X., and Gu, Y. (2018). Probing sensory readout via combined choice-correlation measures and microstimulation perturbation. *Neuron* 100, 715.e5–727.e5. doi: 10.1016/j.neuron.2018.08.034

Yu, X., Hou, H., Spillmann, L., and Gu, Y. (2018). Causal evidence of motion signals in macaque middle temporal area weighted-pooled for global heading perception. *Cereb. Cortex* 28, 612–624. doi: 10.1093/cercor/bhw402

Zaidel, A., DeAngelis, G. C., and Angelaki, D. E. (2017). Decoupled choice-driven and stimulus-related activity in parietal neurons may be misrepresented by choice probabilities. *Nat. Commun.* 8:715. doi: 10.1038/s41467-017-00766-3

Zhang, T., and Britten, K. H. (2011). Parietal area VIP causally influences heading perception during pursuit eye movements. *J. Neurosci.* 31, 2569–2575. doi: 10.1523/JNEUROSCI.5520-10.2011

Zipser, D., and Andersen, R. A. (1988). A back-propagation programmed network that simulates response properties of a subset of posterior parietal neurons. *Nature* 331, 679–684. doi: 10.1038/331679a0

Conflict of Interest Statement: The authors declare that the research was conducted in the absence of any commercial or financial relationships that could be construed as a potential conflict of interest.

frontiers in Neural Circuits

ORIGINAL RESEARCH
published: 23 November 2018
doi: 10.3389/fncir.2018.00105

Response Properties of Interneurons and Pyramidal Neurons in Macaque MSTd and VPS Areas During Self-Motion

Yingying Zhang†, *Shasha Li*†, *Danqing Jiang* and *Aihua Chen**

Key Laboratory of Brain Functional Genomics (Ministry of Education), East China Normal University, Shanghai, China

To perceive self-motion perception, the brain needs to integrate multi-modal sensory signals such as visual, vestibular and proprioceptive cues. Self-motion perception is very complex and involves multi candidate areas. Previous studies related to self-motion perception during passive motion have revealed that some of the areas show selective response to different directions for both visual (optic flow) and vestibular stimuli, such as the dorsal subdivision of the medial superior temporal area (MSTd) and the visual posterior sylvian fissure (VPS), although MSTd is dominated by visual signals and VPS is dominated by vestibular signals. However, none of studies related to self-motion perception have distinguished the different neuron types with distinct neuronal properties in cortical microcircuitry, which limited our understanding of the local circuits for self-motion perception. In the current study, we classified the recorded MSTd and VPS neurons into putative pyramidal neurons and putative interneurons based on the extracellular action potential waveforms and spontaneous firing rates. We found that: (1) the putative interneurons exhibited obviously broader direction tuning than putative pyramidal neurons in response to their dominant (visual for MSTd; vestibular for VPS) stimulation type; (2) either in visual or vestibular condition, the putative interneurons were more responsive but with larger variability than the putative pyramidal neurons for both MSTd and VPS areas; and (3) the timing of vestibular and visual peak directional tuning was earlier in the putative interneurons than that of the putative pyramidal neurons for both MSTd and VPS areas. Based on these findings we speculated that, within the microcircuitry, several adjacent putative interneurons with broad direction tuning receive earlier strong but variable signals, which might act feedforward input to shape the direction tuning of the target putative pyramidal neuron, but each interneuron may participate in several microcircuitries, targeting different output neurons.

Keywords: interneuron, pyramidal neuron, self-motion, visual, vestibular, MSTd, VPS

OPEN ACCESS

Edited by:
Jing-Ning Zhu,
Nanjing University, China

Reviewed by:
Mingsha Zhang,
Beijing Normal University, China
Shiyong Huang,
Hussman Institute for Autism, United States

***Correspondence:**
Aihua Chen
ahchen@brain.ecnu.edu.cn

†*These authors have contributed equally to this work*

Received: *16 September 2018*
Accepted: *05 November 2018*
Published: *23 November 2018*

Citation:
Zhang Y, Li S, Jiang D and Chen A (2018) Response Properties of Interneurons and Pyramidal Neurons in Macaque MSTd and VPS Areas During Self-Motion. Front. Neural Circuits 12:105. doi: 10.3389/fncir.2018.00105

INTRODUCTION

In everyday life, perception of self-motion is essential for navigation, spatial orientation and motor control. It is vital for our living and survival. To perceive self-motion, the brain needs to integrate information from visual, vestibular, auditory, kinesthetic and somatosensory sensors (Warren, 1990; Gottfried and Dolan, 2003; Pettorossi and Schieppati, 2014). Previous

researches in passive motion conditions have revealed that both visual (optic flow across the retina) and vestibular (sensed by otolith organs when the head is translating in space) provide powerful cues for the heading (here, referred as the direction of the self-motion) perception in human self-motion (Telford et al., 1995; Ohmi, 1996; Harris et al., 2000; Bertin and Berthoz, 2004; Butler et al., 2010). Meanwhile physiological studies have proved that many neurons in several cortical areas, including dorsal subdivision of the medial superior temporal (MSTd) area (Britten and van Wezel, 1998, 2002; Duffy, 1998; Bremmer et al., 1999; Gu et al., 2006; Britten, 2008; Fetsch et al., 2010; Angelaki et al., 2011) and visual posterior sylvian fissure (VPS) area (Jones and Burton, 1976; Guldin et al., 1992; Guldin and Grüsser, 1998; Dicke et al., 2008; Chen et al., 2011a), show selectivity for heading in response to both visual and vestibular self-motion stimuli, although the responses to visual and vestibular stimuli varies across different cortical areas. MSTd area shows visual-dominant heading tuning while VPS area shows vestibular-dominant heading tuning (Chen et al., 2011b). These studies have enriched our knowledge about the self-motion perception in passive motion conditions and advanced our understanding of the underlying neural mechanism.

However, none of these self-motion related studies considered the diversity of cell types within local microcircuits, which are known to exist in cortex (Ramon and Cajal, 1899) and have been studied widely *in vitro* (Peters and Jones, 1984; Toledo-Rodriguez et al., 2003; Markram et al., 2004). Intracellular recordings in cortical slices have shown that action potentials produced by GABAergic inhibitory interneurons were shorter in duration than that produced by glutamatergic excitatory pyramidal cells (McCormick et al., 1985; Connors and Gutnick, 1990; Nowak et al., 2003). Since intracellular characteristics determine the extracellular waveform (Henze et al., 2000; Gold et al., 2006), duration of extracellular spike is usually used as a basic parameter in distinguishing inhibitory interneurons (narrow-spiking, NS) from pyramidal neurons (broad-spiking, BS). Based on the waveform, a number of recent studies have begun to explore the role of these two classes of neurons in cortical microcircuits in visual cortex (Gur et al., 1999; Mitchell et al., 2007; Chen et al., 2008; Woloszyn and Sheinberg, 2012), somatosensory cortex (Mountcastle et al., 1969), auditory cortex (Tsunada et al., 2012), motor cortex (Kaufman et al., 2010, 2013), parietal cortex (Yokoi and Komatsu, 2010) prefrontal cortex (Wilson et al., 1994; Rao et al., 1999; Constantinidis and Goldman-Rakic, 2002; Diester and Nieder, 2008; Hussar and Pasternak, 2009, 2012; Johnston et al., 2009), and the hippocampus (Csicsvari et al., 1999; Kuang et al., 2010), and have demonstrated a differential functional role of interneurons and pyramidal neurons. For instance, in macaque area V4, putative interneurons are modulated stronger than pyramidal neurons by attention during multiple-object tracking task (Mitchell et al., 2007). Thus, it is imperative to comprehend how inhibitory interneurons and pyramidal neurons play different roles during self-motion perception? Is the difference of the roles reflected by the spatio-temporal direction tuning properties between interneurons and pyramidal neurons? To test these hypotheses, we classified the recorded neurons into BS neurons (putative pyramidal neurons) and NS neurons (putative interneurons) based on their known differences in extracellular action potential waveform, and compared their heading response properties based on visual and vestibular stimuli.

MATERIALS AND METHODS

Subjects

Physiological data were obtained from five adult male monkeys (Macaca mulatta), whose weights ranged from 6 kg to 10 kg. A circular plastic ring was chronically implanted on the head of each monkey for head restraint; a magnetic field coil was also chronically implanted on the sclera of each monkey for monitoring eye-movement; and a plastic grid was fixed in the circular ring for positioning the electrode (for details, see Gu et al., 2006). After sufficient recovery, animals were trained using standard operant conditioning to receive liquid reward for fixation to visual targets. This study was carried out in accordance with the recommendations of the Institutional Animal Care and Use Committee at East China Normal University. The protocol was approved by the Institutional Animal Care and Use Committee at East China Normal University.

Apparatus and Motion Stimuli

A virtual reality system including a motion platform (6DOF2000E; Moog, East Aurora, NY, USA) and a monitor mounted on that was used to simulate the vestibular and visual stimulation during self-motion. During experiments, the monkey was sitting in a chair which is mounted on the platform. The monkey's head was fixed and was kept facing the center of the screen (**Figure 1A**). Vestibular stimuli were delivered by translation of the platform, and visual stimuli, simulated the identical translational self-motion through movements of random dots (optical flow) in a virtual 3D space of 100 cm wide, 100 cm tall, and 40 cm deep, were programmed in OpenGL and presented on the monitor (PHILIPS BDL4225, Royal Philips, Amsterdam, Netherlands). A magnetic field coil frame moved together with the animal as it was mounted on the platform. For more details, refer to previous studies (Gu et al., 2006; Chen et al., 2011a,b).

Experimental Protocol

Two stimulus conditions, the vestibular condition and visual condition were used in the present study. In each condition, there are 26 evenly sampled translation directions originated from the center of the sphere to the surface of the sphere, including all combinations of eight different azimuth angles from 0° to 315° in increments of 45° and three different elevation angles: 0° and ± 45° (elevation 0 indicates the horizontal plane), along with two another elevation angles: −90° and 90° corresponding to the upward and downward movement directions respectively (**Figure 1B**). Movement along one of the 26 directions lasted 2 s and its velocity varied with a Gaussian profile. The peak velocity was 30 cm/s and the peak acceleration was about 0.1 g (∼0.98 m/s^2; **Figure 1C**), thus the displace amplitude is 13 cm in total. In vestibular condition, the monkey was moved by translation of the platform in the absence of optical flow. In

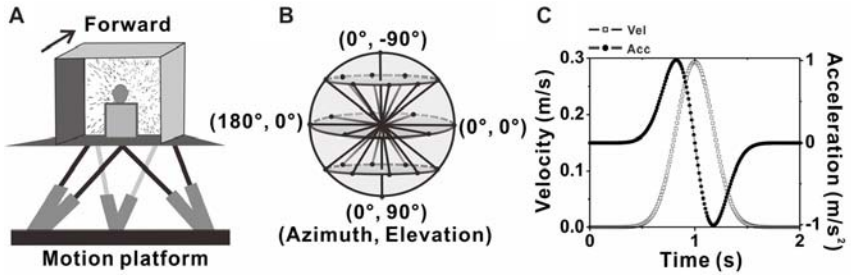

FIGURE 1 | Experimental setup and transient translation stimuli. **(A)** Schematic illustration of the virtual reality apparatus. Monkeys were seated on a motion platform, with six degrees of freedom, which provided the vestibular stimulus. Visual stimulus (optic flow) was displayed on the screen located in front of the monkey. **(B)** Illustration of the 26 movement trajectories used to measure 3D heading tuning curve, corresponding to all combinations of azimuth and elevation, in 45° increments from a sphere. **(C)** Motion Profile. All movements had a 2 s duration, originated from the center position, and had a Gaussian velocity profile (peak of 0.3m/s, dashed-square line) with a corresponding biphasic linear acceleration profile (peak of ± 1 m/s^2, dashed-dot line).

visual condition, only optic flow simulating self-motion through the cloud of random dots was presented on the monitor while the platform was kept stationary. All directions under both conditions were interleaved and delivered randomly in one block of trials. In each trial, the animal has to fix its eyes on a fixation point of 0.2° in diameter in the center of the monitor for 200 ms before stimulus onset (fixation windows were restricted to 1.5° ×1.5° of visual angle) and was rewarded with a drop of juice at the end of the trial for keeping fixation during the presentation of the stimulus (only vestibular or visual stimulus was given in each trail). Trials were aborted and data discarded when the animal broke fixation at any time during the stimulation.

Electrophysiological Recordings

Extracellular recordings from single neuron were performed using tungsten microelectrodes. The tip diameter of the electrode is 3 μm and the impedance is 1–2 MΩ at 1 kHz (Frederick Haer Company, Bowdoin, ME, USA). Through a transdural guide tube, the microelectrode was moving downward into the cortex driven by a hydraulic microdrive (Frederick Haer Company, Bowdoin, ME, USA). Electrical voltage signals from neurons were collected, amplified, filtered (400–5,000 Hz), and isolated with a metal microelectrode preamplifier (Bak Electronics, Mount Airy, MD, USA). The TEMPO system (Reflective Computing, Olympia, WA, USA) was used to control the experiment protocol and data acquisition including sending synchronous event signals to the recoding system (CED Power 1401; Cambridge Electronic Design, Cambridge, UK). The spike times and all behavioral events were sampled at 1 kHz in TEMPO system, while the raw neural signals were recorded at a rate of 25 kHz by CED. All these data were saved for off-line spike sorting. Area MSTd and VPS were identified by a combination of magnetic resonance imaging scans, stereotaxic coordinates, white/gray matter transitions, and physiological response properties, as described in detail previously (Gu et al., 2006; Chen et al., 2011a,b). Area MSTd is centered about 15 mm lateral to the midline and ∼3–6 mm posterior to the interaural plane, and area VPS is located posterior to PIVC and extends approximately 4–5 mm anterior to posterior, which were consistent with previous studies (Gu et al., 2006; Chen et al., 2011a).

Data Analysis

All the data analyses in the present study were performed using custom designed software running in Matlab (Mathworks, Natick, MA, USA). Isolated spike waveforms of every single neuron were obtained by offline spike sorting using Spike2 software (Cambridge Electronic Design, Cambridge, UK), from the raw data recorded by CED.

Neuron Classification

For each neuron, all spike waveforms were spline interpolated to give a resolution of 0.2 μs and then averaged. The spike duration was defined as the time from the negative trough to the succeeding positive peak of this average waveform. It has been demonstrated by intracellular studies that pyramidal neurons are regular-spiking (RS) neurons while inhibitory interneurons are fast spiking (FS) neurons, and one striking difference between these two kinds of neurons is that the extracellular waveform of RS neurons have longer and shallower peak following the initial trough (McCormick et al., 1985; Henze et al., 2000; Nowak et al., 2003; Hasenstaub et al., 2005). On the other hand, the baseline firing rate difference between inhibitory interneurons and excitatory pyramidal neurons is a common finding throughout numerous studies related to classification of these two neuronal groups in the last two decades (Gur et al., 1999; Frank et al., 2001; Constantinidis and Goldman-Rakic, 2002; Maurer et al., 2006; Mitchell et al., 2007; Viskontas et al., 2007; Chen et al., 2008; Diester and Nieder, 2008; Le Van Quyen et al., 2008; Hussar and Pasternak, 2009, 2012; Johnston et al., 2009; Kuang et al., 2010; Yokoi and Komatsu, 2010; Tsunada et al., 2012; Woloszyn and Sheinberg, 2012; Kaufman et al., 2013). Thus, in the present study, we used not only the parameters of spike duration but also the baseline firing rate (spontaneous firing rate, SponT) to classify the neurons into BS neurons and NS neurons, namely putative pyramidal neurons and putative inhibitory interneurons, respectively. SponT was calculated from the neuron's firing activities from 100 ms pre-stimulus onset to 300 ms post-stimulus onset, since stimulus velocity was still

very small at 300 ms and the response was still kept at a baseline (for details, see Gu et al., 2006; Chen et al., 2010). Different neuronal groups were further sorted by the k-means algorithms (k = 3, squared Euclidean distance) using the two parameters: spike duration and SponT (Barthó et al., 2004; Sakata and Harris, 2009; Tsunada et al., 2012). We designated the cluster of neurons fell in long spike duration and low SponT as BS neurons and those fell in short spike duration and high SponT as NS neurons. Neurons that fell between those two clusters were called Unclassified in the present study. We could specify the number of clusters in K-means cluster analysis. As shown in **Figures 2D,F**, by setting the cluster number as 3, we could exclude the neurons having short spike durations but high SponTs to minimize false commissions as much as possible.

Analysis of Tuning Properties

To measure the direction tuning of the neurons, translational responses for visual or vestibular were measured along 26 directions in 3D (see "Experimental Protocol" section for detail). For each isolated single neuronal activity, we used and a 400 ms slide window stepped at 25 ms to construct a smoothed peristimulus time histograms (PSTHs) for each direction of translation. Mean firing rates during the 400 ms time window centered at the peak time were transformed using the Lambert cylindrical equal-area projection (Snyder, 1987), and then plotted as a function of azimuth and elevation in color contour maps to visualize 3D spatial tuning (Chen et al., 2011c; as shown in right panels in **Figure 3**). In these plots, the abscissa represents azimuth and the ordinate represents a cosine-transformed version of elevation.

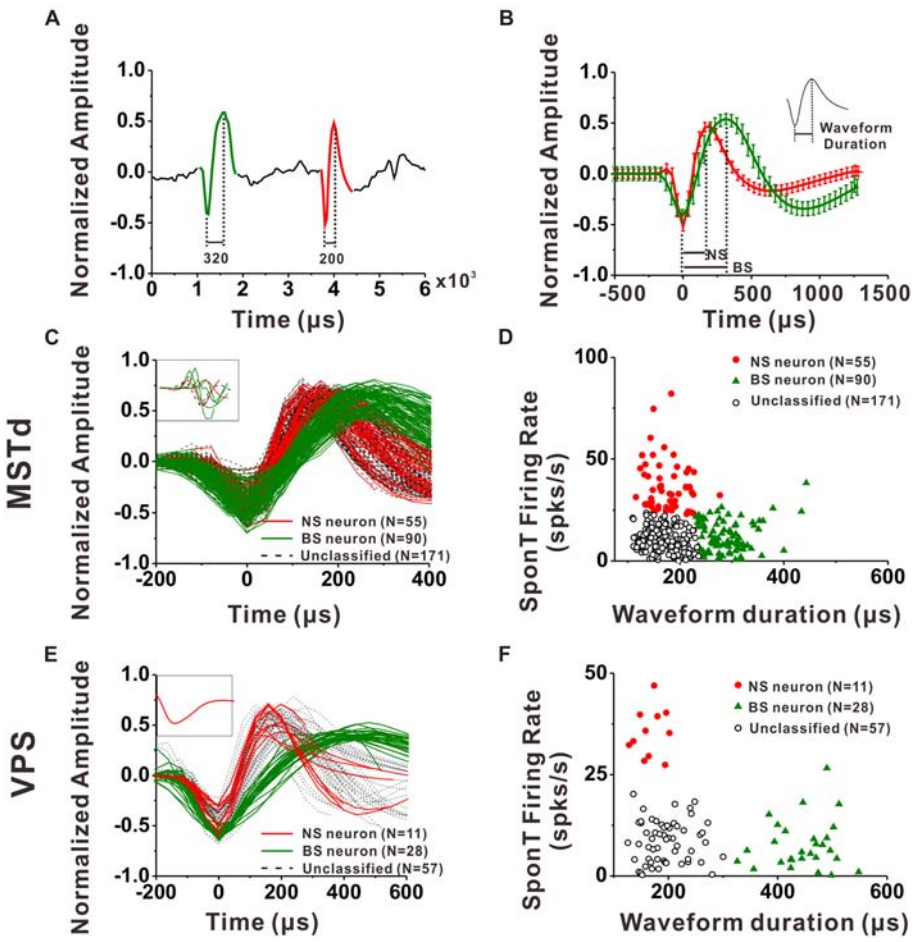

FIGURE 2 | Classification of narrow-spiking (NS) and broad-spiking (BS) neurons. **(A)** Original spike waveforms of two distinct neurons isolated from simultaneous recordings of one electrode. The trough to peak durations of these two neurons are 200 μs (red, NS) and 320 μs (green, BS), respectively. **(B)** Average spike waveforms (mean ± SD, normalized by dividing the difference between the peak value and the trough value) of two distinct neurons isolated from simultaneous recordings of one electrode. The two waveforms were aligned by their troughs. The trough to peak durations of these two neurons are 188 μs (red, NS) and 313 μs (green, BS) respectively. Inserted is the illustration of trough to peak duration of a standard waveform. **(C)** The average waveforms of every neuron in the group of dorsal subdivision of the medial superior temporal (MSTd) neurons. The waveforms of eight neurons without general biphasic shape are inserted in the top left corner. **(D)** Classification results of all the isolated MSTd neurons using K-means clustering analysis running on the distribution of spike durations and SponTs. **(E)** The average waveform of every neuron in the group of visual posterior sylvian fissure (VPS) neurons. The waveforms of the discarded neuron are inserted in the top left corner. **(F)** Classification results of all the isolated VPS neurons using K-means clustering analysis running on the distribution of spike durations and SponTs.

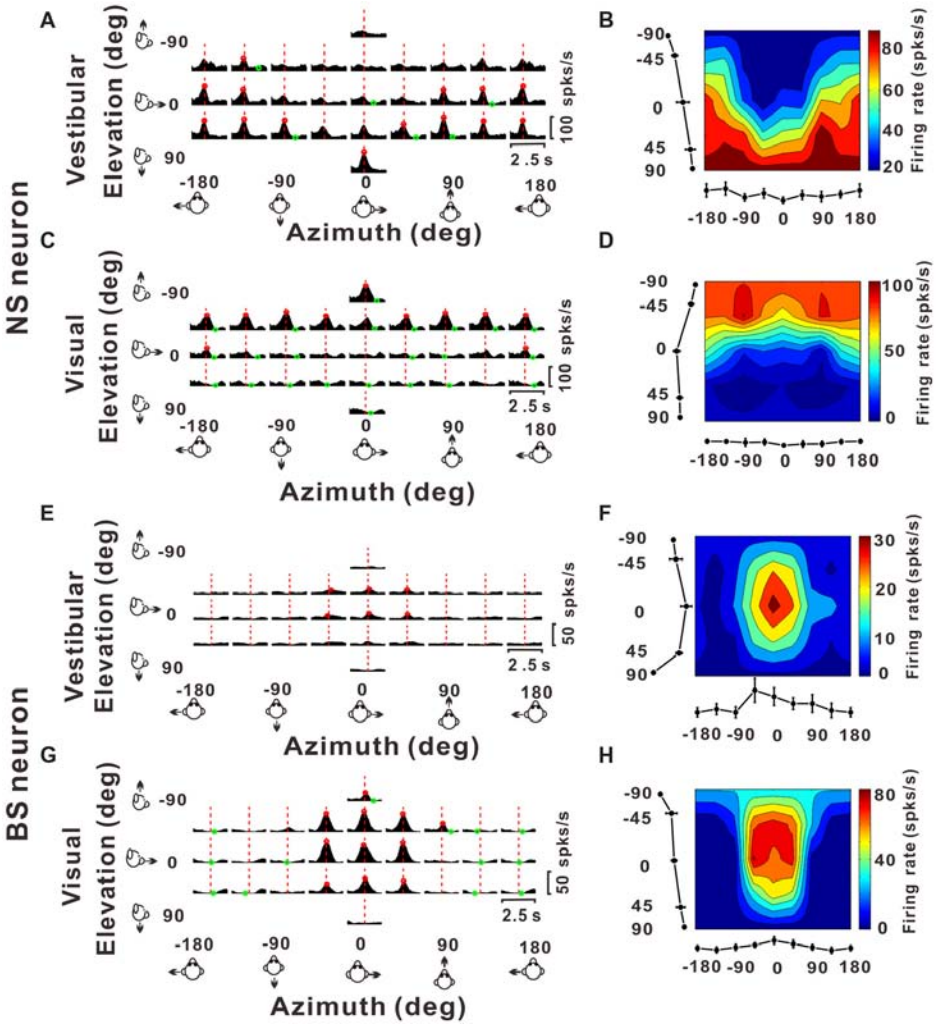

FIGURE 3 | Example responses from a NS neuron and a BS neuron. **(A,C,E,G)** Response peristimulus time histograms (PSTHs) for an example NS neuron (**A** for vestibular stimuli and **C** for visual stimuli) and an example BS neuron (**E** for vestibular stimuli and **G** for visual stimuli). The averaged PSTHs for all 26 directions of vestibular or visual translation arranged according to stimulus direction in spherical coordinates. Vertical dashed red lines indicate the peak time of the neuron. PSTHs were computed with sequential 25 ms bins and then smoothed with a 400 ms sliding window (see "Materials and Methods" section). **(B,D,F,H)** Color contour maps of the neurons at the peak time. The peak time was taken from the preferred direction. Tuning curves along the bottom and left sides of each color contour maps show the 3D tuning at the peak time indicated by the red dashed lines in panels **(A,C,E,G)**. Noted that because azimuth 180° (away from azimuth 0° anticlockwise) and azimuth −180° (away from azimuth 0° clockwise) are overlapped on the horizontal plane, so in panels **(A,C,E,G)**, the left-most three panels were just copied from the right-most three panels for symmetry and actually there were only 26 directions out of the 29 panels.

Temporal Modulation Analysis

To test whether the temporal modulation along each stimulus direction was significant, we first identified the 400 ms time windows containing the spike count distributions having the maximum and/or minimum values. Then we compared these distributions with SponT distribution to see whether they are significantly different from each other (Wilcoxon signed rank test, $p < 0.01$, for details, see Chen et al., 2010). At least four overlapping time windows (spaced 25 ms apart and including the maximum or minimum time window defined above) were required to have spike count distributions that differed significantly from the baseline distribution to avoid false positives. For each stimulus condition and direction of movement, we used this statistical test to identify whether there are a significant peak and/or trough in the PSTH, otherwise the cell was deemed not to be responsive to stimulation in that direction.

Peak Times

As reported previously, times of the local maximum or minima at which distinct epochs of directional tuning happened were defined as "peak times" (for details, see Chen et al., 2010). First, for each 25 ms time bin between 0.5 s and 2 s after stimulus onset, the maximum/minimum response of the neuron across directions was calculated. Then the statistical significance of direction selectivity for each time bin was further evaluated

by one-way ANOVA test (five repeats for each direction). By checking the statistical significance of direction tuning as a function of time, we decided whether there are multiple time periods in which a neuron shows distinct temporal peaks of directional tuning (see Chen et al., 2010). Cells without peak times were excluded from all the analyses in present study.

Preferred Direction

For each stimulus condition, the mean firing rate during the 400 ms window whose center aligned at peak response time in each trial was represented by the magnitude of a 3D vector whose direction defined by the elevation and azimuth angles (Gu et al., 2006). The preferred direction of this neuron under each condition was further computed from the vector sum's elevation and azimuth of each neuron's responses (spontaneous activity subtracted).

Half Tuning Width

To quantify the tuning characteristics of the neurons, we also constructed tuning width curves from the horizontal tuning curve. The mean firing rates of the neuron at its peak time in eight horizontal directions were shifted such that the maximum firing rate was aligned at 0°. Then the directional tuning curve was fitted by a Gaussian function, $r(\theta)$ (Chen et al., 2010):

$$r(\theta) = a \times \exp\langle -2\{[1-\cos(\theta-\theta_{\text{pref}})]/\sigma^2\}\rangle + b$$

where θ_{pref} indicates the preferred direction, σ represents the half peak width of the tuning curve, a indicates the tuning curve amplitude, and b denotes the baseline firing rate, σ is defined as the half tuning width.

Strength of Direction Tuning

The 3D directional tuning strength was defined using a direction discrimination index direction discrimination index (DDI), given by Takahashi et al. (2007):

$$DDI = \frac{R_{\max} - R_{\min}}{R_{\max} - R_{\min} + 2\sqrt{SSE/(N-M)}}$$

$R_{\max}$ and $R_{\min}$ are the maximum and minimum firing rate from the 3D tuning function, respectively. *SSE* represents the sum squared error around the mean response, N is for the total number of trials, and M denotes the number of directions (M = 26). Thus, the reliability of a neuron for discriminating the preferred motion direction from the null motion direction can be quantified by *DDI*, whose value ranges from 0 to 1, corresponding to response modulations that range from weak to strong.

RESULTS

We recorded MSTd and VPS neurons as monkey was passively translated in physical (vestibular) or simulated (visual) motion along 26 motion direction uniformly distributed in 3D space (**Figures 1A,B**). The movement along each direction followed a Gaussian velocity profile, as shown in **Figure 1C**. The corresponding acceleration profile is biphasic. For each block, we randomly give monkey vestibular or visual stimulus. A null condition was also contained for control, and monkey was asked to fixate at the target of head-centered position without any vestibular or visual condition during this trial. To exclude any multiunit activity that may average the waveforms and blur differences in the population, we only included units that had been clearly isolated from noise and other units by offline spike sorting based on clustering in the principal components of waveforms on that electrode (Spike2, Cambridge Electronic Design). In total, 324 single units from MSTd (three rhesus monkey) and 97 single units from VPS (two rhesus monkey) were isolated. We further divided these units into putative interneurons (NS neurons) and putative pyramidal neurons (BS neurons) according to the parameters of spike duration and base line firing rate, then compared the spatiotemporal response characteristics to 3D translation between these two groups of neurons.

Classification of Interneurons and Pyramidal Cells

An example of the classification of interneurons and pyramidal cells is shown in **Figures 2A,B**. **Figure 2A** shows 6 ms of filtered raw signals collected from one electrode. It is clear that there are two kinds of spike waveform beyond the noise. Thus, all the spikes from this electrode were further sorted into two isolated neurons according to the spike waveforms. The spikes recorded in each neuron were averaged after the alignment by troughs, and the mean waveforms (±1 SD) was shown in **Figure 2B** for two isolated neurons collected from the same electrode. In the current study, the spike duration of a neuron was calculated from the interval between the peak and trough of the mean spike waveform, as shown in the inserted figure at the top right corner in **Figure 2B**. **Figures 2C,E** show the mean spike waveforms from all the isolated MSTd and VPS neurons, respectively. Each curve representing the mean spike waveform from one neuron. From these figures, we can see that most of the recorded spike waveforms exhibited variations in duration although they have similar biphasic shape. It should be noted that the spike waveforms were normalized by the difference between their peak and trough values before calculating the spike durations. All except eight MSTd and one VPS neuron, exhibited in the inset, had waveforms with a negative trough followed by a clear positive peak. And these nine cells were excluded from further analysis.

Since the discharge frequencies and spike durations varied between pyramidal cells and interneurons (Mountcastle et al., 1969; McCormick et al., 1985; Rao et al., 1999; Constantinidis and Goldman-Rakic, 2002; Nowak et al., 2003; Likhtik et al., 2006), we used these two characters to discriminate principal excitatory units (putative pyramidal cells) and inhibitory units (putative interneurons; for details, see "Materials and Methods" section). As shown in **Figures 2D**, K-means cluster analysis (k = 3) was applied to the distribution of all isolated neurons' spike durations and SponTs, and the neurons were separated into three clusters (see "Materials and Methods" section for more information). Neurons fell in long spike duration and low SponT were assigned to putative pyramidal neurons and those fell in short spike duration and high SponT were deemed putative interneurons. Neurons that fell between those two

clusters were called "**Unclassified**" in the present study and were excluded from further analysis (**Figures 2D,F**). As a result, 55 neurons were classified as putative interneurons (Silhouette value = 0.43) and 90 neurons were classified as putative pyramidal neurons (Silhouette value = 0.45) in MSTd, while in VPS 11 putative interneurons (Silhouette value = 0.81) and 28 putative pyramidal neurons (Silhouette value = 0.82) were classified for the remaining analysis. Overall, the fraction of our recordings identified as NS putative interneurons among all the identified neurons (38% for MSTd; 28% for VPS) was similar to the fraction present in other physiological study (20%–30%; Connors and Gutnick, 1990).

Temporal Modulation for Putative Interneurons and Pyramidal Neurons

Once we classified the recorded responsive neurons into NS and BS neurons, we examined the 3D responses between these two neuronal groups under vestibular and visual stimuli. Example responses of a NS and a BS neuron from MSTd are illustrated in **Figure 3**. **Figure 3A** shows the averaged PSTHs for all 26 directions of vestibular translation arranged according to stimulus direction in spherical coordinates. The red circle represents a significant peak in that PSTH and the green circle indicates a significant trough in the PSTH. This NS neuron responds significantly to 13 motion directions during vestibular condition (**Figure 3A**) and 22 motion directions during visual condition (**Figure 3C**). These numbers are larger than that of the example BS neuron ($N = 7$ for vestibular stimuli and $N = 19$ for visual stimuli). The population summary of the number of significant responsive directions was shown in **Figure 4**. In MSTd, the number of significant responsive directions of NS neurons under the vestibular condition (**Figure 4A**, mean ± SE: 7.2 ± 1.0) was significantly higher than that of BS neurons (mean ± SE: 4.8 ± 0.8; $p < 0.05$, Wilcoxon rank-sum test). During visual condition, the difference was more obvious with the number of significant responsive directions being 15.9 ± 7.4 (mean ± SE) for NS neurons and 7.8 ± 0.9 (mean ± SE) for BS neurons (**Figure 4B**, $p < 0.001$, Wilcoxon rank-sum test). These results suggest putative interneurons are more broadly tuned by different directions across sphere than putative pyramidal neurons in MSTd. Weaker but similar results were observed in VPS, as shown in **Figures 4C,D**.

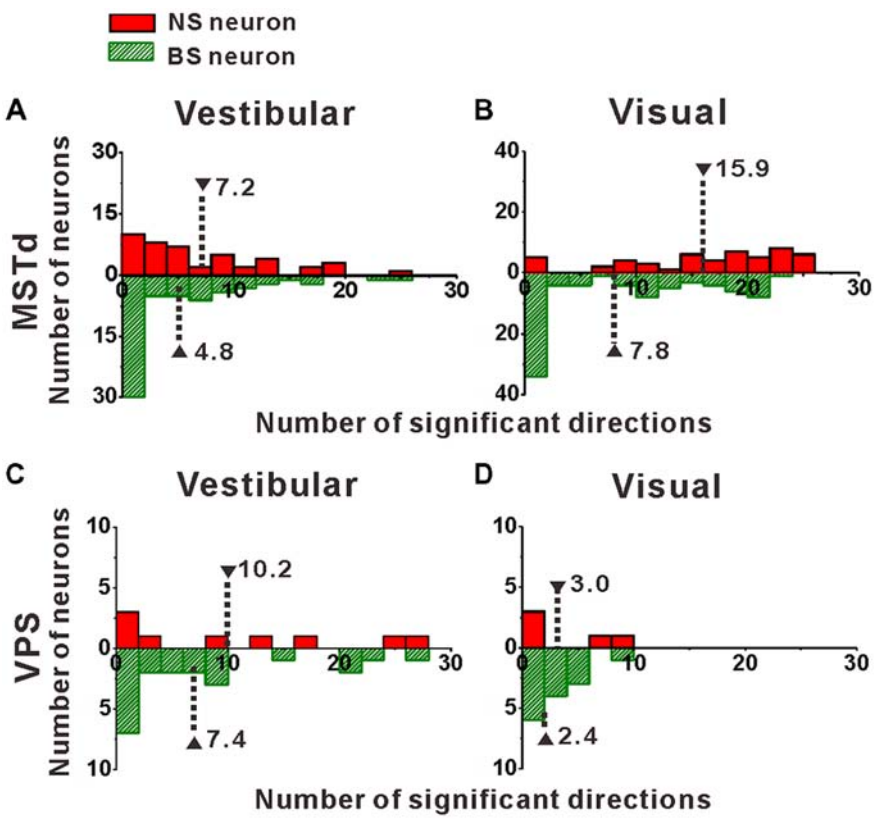

FIGURE 4 | Distribution of the number of significant directions. **(A,B)** Distribution histogram of the number of neurons that have a significant response to vestibular **(A)** and visual stimuli **(B)** for NS and BS neurons in MSTd. A total of 45 NS neurons and 61 BS neurons with significant directional tune to vestibular stimuli were selected (both $p < 0.05$, ANOVA test) and a total of 52 NS neurons and 83 BS neurons with significant directional tune to visual stimuli were selected (both $p < 0.05$, ANOVA test). **(C,D)** Distribution histogram of the number of neurons that have a significant response to vestibular **(C)** and visual stimuli **(D)** for NS and BS neurons in VPS. The neurons analyzed in the graph have a significant directional tune to vestibular or visual stimuli (both $p < 0.05$, ANOVA test). Vestibular tuning: NS neuron ($N = 13$), BS neuron ($N = 7$). Visual tuning: NS neuron ($N = 22$), BS ($N = 19$). Note that the number of significant direction distributions for BS neurons were plotted as downward projecting histograms simply for illustrative purposes.

Although there were no significant differences between these two classes of neurons (vestibular: $p = 0.56$; visual: $p = 0.99$, Wilcoxon rank-sum test), the average number of significant responsive directions for NS neurons (mean ± SE: 10.2 ± 3.5 in vestibular condition; 3.0 ± 1.8 in visual condition) was still larger than that for BS neurons (mean ± SE: 7.4 ± 1.8 in vestibular condition; 2.4 ± 0.7 in visual condition). However, in contrast to MSTd, the broader direction tuning of putative interneurons are more obvious for vestibular stimuli rather for visual stimuli in VPS. This might be caused by that MSTd is dominated by visual signals while VPS is dominated by vestibular signals.

3D Spatial Tuning for Putative Interneurons and Pyramidal Neurons

Above results showed that NS neurons were responsive to more direction in 3D. To address whether the larger number of significant responsive directions was caused by selective stronger inputs or evenly elevated responses along all the directions, we further quantified the neurons' 3D spatial tuning properties.

Figures 3B,D illustrate 3D tuning at the peak time by the color contour maps for the example NS neuron from MSTd under vestibular and visual stimuli, respectively. **Figures 3F,H** show an example of BS neuron. It should be noted that peak time that produces the largest firing rate comparing to the baseline response, is indicated by the red dashed lines in **Figure 3A**; and the 3D directional tuning of this neuron at this peak time (0.93 s) to the vestibular stimuli was shown as the color contour map in **Figure 3B**. In this map, mean firing rate (represented by color) is plotted as a function of azimuth and elevation. This neuron was significantly tuned during vestibular translation (one-way ANOVA for firing rates across 26 directions with five repeats for each direction, $p < 0.001$) and exhibited broad tuning with a preferred direction at 75° azimuth and 90° elevation, corresponding to a motion downward. For the visual condition, this neuron was also broadly tuned (one-way ANOVA for firing rates across 26 directions with five repeats for each direction, $p < 0.001$) at its peak time (1.18 s), with a preferred direction at 0° azimuth and −90° elevation (**Figure 3D**), corresponding to an upward motion trajectory. In contrast, the example BS neuron exhibited relatively sharp tuning for both vestibular and visual translation (one-way ANOVA for firing rates across 26 directions with five repeats for each direction, $p < 0.001$), with a preferred direction at 0° azimuth and 0° elevation, corresponding to a forward motion trajectory in horizontal plane under vestibular stimuli (**Figure 3F**, at the peak time of 1.45 s) and a preferred direction at 0° azimuth and −23° elevation, corresponding to a forward and slightly upward motion trajectory under visual stimuli (**Figure 3H**, at the peak time of 1.28 s). The example NS MSTd neuron was tuned more broadly than the example MSTd BS neuron both under vestibular and visual stimuli. To see whether this was a common difference between classes of NS and BS neurons, we further compared the tuning width distribution between these two groups of neurons in the following analyses.

Before comparing the tuning widths, we first looked at the distributions of the preferred directions of the population NS neurons and BS neurons across the spherical stimulus space, as shown in **Figure 5**. For both NS and BS neurons in MSTd, the preferred directions were distributed throughout the spherical stimulus space under either vestibular stimulus (**Figure 5A**) or visual stimulus (**Figure 5B**). Situation in VPS shown was same as in MSTd, as shown in **Figures 5C,D** for vestibular and visual condition, respectively. The preferred directions of the NS and BS neurons in VPS were also widely distributed throughout the spherical stimulus space in both stimulus conditions. All the distributions fitted the normal distribution (Shapiro-Wilk test, the minimal value of p was 0.36) and there is no clear difference for the direction preferences between interneurons and pyramidal neurons (T-test, the minimal value of p was 0.18).

Cumulative distributions of the half tuning widths in MSTd are summarized for vestibular and visual condition in **Figures 6A,B**, respectively. For vestibular condition (**Figure 6A**), the cumulative curve of the NS and BS neurons were nearly overlapping, indicating that in terms of tuning width, no significant difference between these two classes of neurons was observed (mean ± SE: 125.3° ± 7.0° for NS; 123.2 ± 5.4° for BS; $p = 0.61$, Kolmogorov–Smirnov test). However, the distributions for these two groups of neurons during visual condition showed obvious tendency to be different ($p = 0.09$, Kolmogorov–Smirnov test). As shown in **Figure 6B**, the cumulative curve of the MSTd NS neurons rises slowly than that of the BS neurons in visual condition, which means that the NS neurons had broader tuning width (mean ± SE: 140.4 ± 6.9°) than the MSTd BS neurons (mean ± SE: 121.8 ± 4.5°). In contrast, for VPS neurons, the difference of the tuning width for these two group neurons was observed in vestibular condition rather than visual condition, as shown in **Figures 6C,D**, respectively. In vestibular condition, the tuning width was obviously (although not very significantly) larger in NS neurons (mean ± SE: 156.2 ± 19.3°) than in BS neurons (mean ± SE: 113.5 ± 7.4°; $p = 0.05$, Kolmogorov–Smirnov test). However, in visual condition, these two distributions are almost overlapping, and the tuning widths are not significantly different from each other (mean ± SE: 101.3 ± 14.8° for NS neurons; 106.1 ± 9.2° for BS neurons; $p = 0.87$, Kolmogorov–Smirnov test). One possible explanation for the difference between MSTd and VPS is that the putative interneurons are more broadly tuned than the putative pyramidal neurons when they response to their dominant stimuli rather than non-dominant stimuli.

All the above analysis seems to demonstrate that the NS neurons showed more broadly direction tuning than BS neurons, Intuitively, the broader tuning curve might cause weaker tuning strength. To examine whether it is true, we further compared the direction tuning strength between the NS and BS neurons by using DDI (for details, see "Strength of Direction Tuning" in "Data Analysis" section and Takahashi et al., 2007). It can quantify the reliability of a neuron for discriminating the preferred motion direction from the null motion direction. The value of DDI

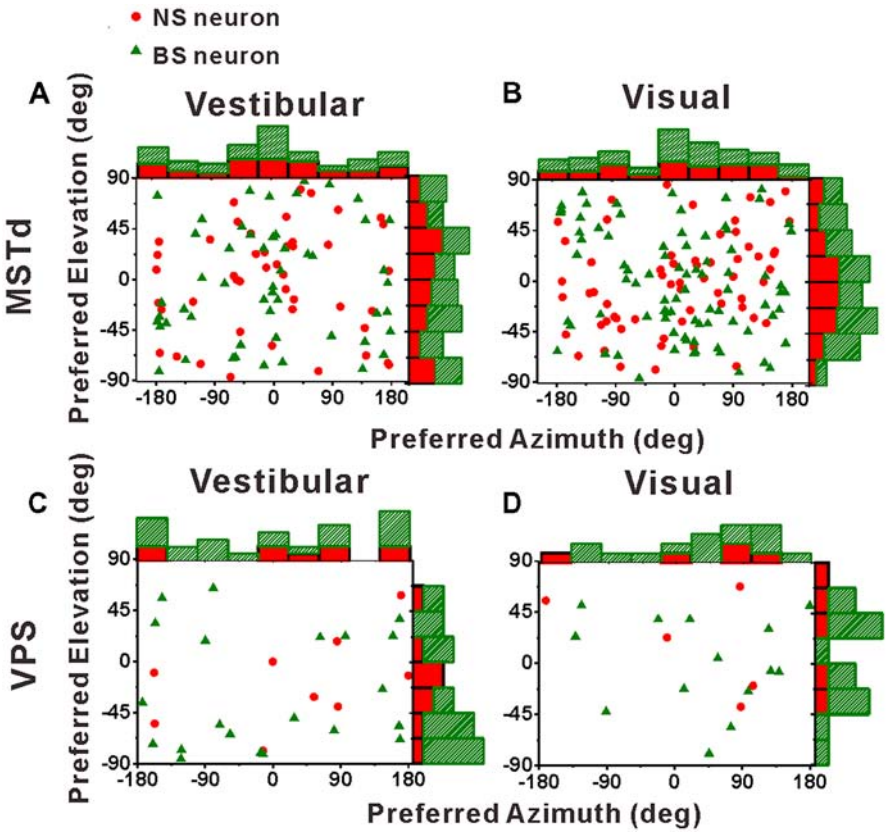

FIGURE 5 | Distributions of 3D heading preferences for NS (red) neurons and BS (green) neurons in areas MSTd **(A,B)** and VPS **(C,D)** in response to vestibular and visual stimuli. Each data point in the scatter plot corresponds to the preferred azimuth (abscissa) and elevation (ordinate) of a single neuron with significant heading tuning. Histograms along the top and right sides of each scatter plot show the marginal distributions. The neurons analyzed in the graph have a significant directional tune to vestibular or visual stimuli (both $p < 0.05$, ANOVA test). The number of neurons were same as in **Figure 4**.

ranges from 0 to 1, 0 represents the weakest direction discrimination, and one represents the strongest directional discrimination.

Figure 7A compares DDI values of the MSTd between NS neurons and BS neurons. For both NS (green) and BS (red) neurons, the majority of them were distributed above the diagonal, indicating that DDI values under visual condition are larger than that under vestibular condition (both $p < 0.001$, Wilcoxon rank-sum test) for both groups. The averaged DDI values were 0.60 ± 0.01 (mean ± SE) for NS neurons and 0.57 ± 0.01 (mean ± SE) for BS neurons in vestibular condition. There was no significant difference between these two groups ($p = 0.55$, Wilcoxon rank-sum test). However, the DDI values of the NS neurons was significantly larger than that of the BS neurons (mean ± SE: 0.77 ± 0.02 for NS neurons; mean ± SE: 0.71 ± 0.01 for BS neurons, $p < 0.01$, Wilcoxon rank-sum test) in visual condition. As larger DDI values usually indicate the stronger directional discrimination ability, the higher DDI values for NS neurons seems to be conflict with the broader tuning results. One possible explanation is that wider tuning curve was caused by the combination results of flat tuning curve and smaller response variability across different directions. Since DDI was affected both by $R_{max} - R_{min}$ (the difference between the maximum and the minimum firing rate across 26 directions) and SSE (the sum of squared error of the firing rates in 26 directions), the larger DDI values of the NS MSTd neurons in visual condition might be resulted from larger $R_{max} - R_{min}$ or smaller SSE. To examine it, **Figures 7B,C** compared the distribution of $R_{max} - R_{min}$ and SSE between the NS and BS neurons in vestibular and visual condition, respectively. For both vestibular and visual conditions, the distribution of the red dots (representing the NS neurons) was more inclined to have the larger values along the horizontal and longitudinal axis than that of the green triangles (represent the BS neurons). In the vestibular condition, the averaged response amplitude of the NS neurons (mean ± SE: 52.9 ± 4.1, spikes/s) was significantly higher than that of the BS neurons (mean ± SE: 33.5 ± 2.4; $p < 0.01$, Wilcoxon rank-sum test), meanwhile the SSE of the NS neurons (mean ± SE: 26.9 ± 3.4) was also significantly larger than that of the pyramidal neurons (mean ± SE: 18.8 ± 2.1; $p < 0.01$, Wilcoxon rank-sum test). Similar results were observed in the visual condition (**Figure 7C**): the $R_{max} - R_{min}$ of the NS neurons (mean ± SE: 30.0 ± 2.5) was significantly higher than that of the BS neurons (mean ± SE: 16.1 ± 1.3; $p < 0.01$, Wilcoxon signed rank test), and the SSE of the NS neurons (mean ± SE: 13.2 ± 0.9) was also

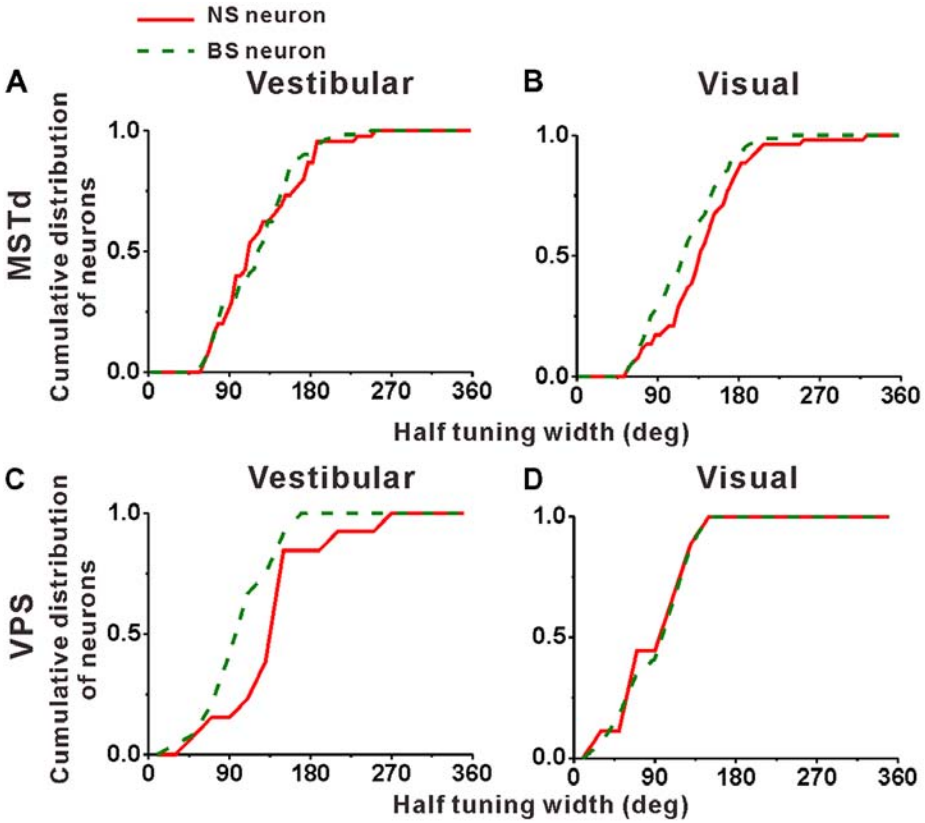

FIGURE 6 | Population summary of the half tuning width of the NS (red) neurons and BS (green) neurons in areas MSTd **(A,B)** and VPS **(C,D)** under the vestibular and visual conditions. Cumulative frequency distribution of the neurons on the half tuning widths, which were computed from each neuron's tuning curve in the horizontal plane, are given by the curves. The neurons analyzed in the graph have a significant directional tune to vestibular or visual stimuli (both $p < 0.05$, ANOVA test). The number of neurons were same as in **Figure 4**.

significantly larger than that of the BS neurons (mean ± SE: 9.9 ± 0.6; $p < 0.01$, Wilcoxon rank-sum test). Thus, the larger DDI values of the MSTd NS neurons for visual stimuli was mostly attributed to larger modulation depth compared with the response variability (SSE). This had no causal link to flat tuning curve or smaller response variability across different directions that account for broader tuning curves of MSTd NS neurons, thus the challenge of conflict did not exist here.

In contrast to MSTd, VPS is a vestibular-dominant area. Consequently, the direction tuning strength of both NS neurons and BS neurons for vestibular condition was significantly greater than those for visual condition (**Figure 7D**, $p < 0.001$, Wilcoxon rank-sum test). For both vestibular and visual condition, the DDI values of NS neurons were not significantly different from BS neurons, with averaged values 0.61 ± 0.04 (mean ± SE) for NS and 0.65 ± 0.02 (mean ± SE) for BS neurons during vestibular condition($p = 0.37$, Wilcoxon rank-sum test) while 0.53 ± 0.03 (mean ± SE) and 0.56 ± 0.02 (mean ± SE) for NS and BS neurons during visual condition ($p = 0.36$, Wilcoxon rank-sum test). However, the distribution of the $R_{max} - R_{min}$ and SSE between these two groups of neurons in VPS showed the same tendency as in MSTd. For vestibular condition (**Figure 7E**), the $R_{max} - R_{min}$ of the NS neurons was significantly higher than that of the BS neurons (mean ± SE: 54.7 ± 20.9 vs. 29.2 ± 5.1, $p < 0.01$, Wilcoxon rank-sum test). The SSE of the NS neurons was also significantly larger than that of the pyramidal neurons (mean ± SE: 16.6 ± 6.1 vs. 6.2 ± 1.3, $p < 0.01$, Wilcoxon rank-sum test). Results were similar for visual condition (**Figure 7F**): both the $R_{max} - R_{min}$ and SSE of the NS neurons were significantly higher than that of the BS neurons ($p < 0.01$, Wilcoxon rank-sum test). The averaged $R_{max} - R_{min}$ was 39.3 ± 13.1 (mean ± SE) for NS and 14.3 ± 6.4 (mean ± SE) for BS neurons, respectively, and the averaged SSE was 14.3 ± 6.4 (mean ± SE) for NS and 5.9 ± 1.5 (mean ± SE) for BS neurons respectively. Since in MSTd, the DDI values of NS neurons was significantly larger than that of BS neurons in visual condition, it was natural to expect that in VPS, the DDI values of the NS neurons was significantly larger than that of BS neurons in vestibular condition, however, it was not the case. We noted that the VPS neurons' $R_{max} - R_{min}$ and SSE were obviously larger than that of the MSTd, which indicate the relatively poorer and more diverse response of the VPS neurons upon stimulation and may account for the difference between MSTd and VPS.

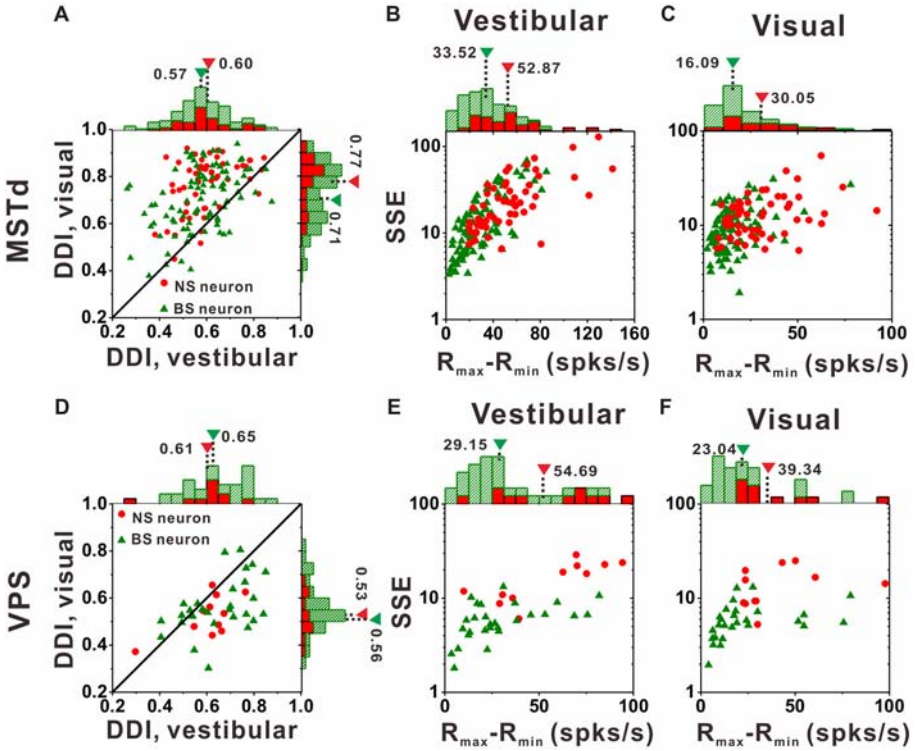

FIGURE 7 | Tuning strengths to the NS (red) neurons and BS (green) neurons in areas MSTd (upper panel) and VPS (lower panel) under the vestibular and visual conditions. **(A)** Scatter plots of direction discrimination index (DDI) values for the vestibular (abscissa) and visual (ordinate) conditions, respectively. **(B,C)** Scatter plots of each neuron's firing rate variabilities (standard deviation, SD) over the maximum difference of the neuron's firing rates ($R_{max} - R_{min}$) for the vestibular condition **(B)** and the visual condition **(C)**. The histograms on the top and right show the marginal distributions. **(D–F)** Same as **(A–C)** respectively but for area VPS.

Comparison of Peak Times Between Narrow-Spiking and Broad-Spiking Neurons

Interneurons are supposed to modulate the activities of output pyramidal neurons in local circuitry to fulfill information transmission to next stage through feedforward or feedback connections (Wilson, 2007; Suzuki and Bekkers, 2012), thus the response latency of the putative pyramidal and interneurons might be different from each other. In the present study, motion stimuli were dynamic and followed a Gaussian velocity profile with peak velocity of 30 cm/s at 1 s. The recorded neurons were not activated and kept the baseline response during the first several hundred milliseconds of the stimulus until the velocity increased large enough, and reached their peak firing rates around or after the timing of the peak velocity of the stimulus. So, it is impossible to measure the response latency of the neurons accurately in the present study, but we could measure the peak time of the response relative to the peak velocity of the stimulus instead. To test whether the peak times of the putative pyramidal and interneurons are different from each other, we further looked into the peak time distributions of these two neuronal populations as shown in **Figure 8**. In MSTd, peak times under vestibular stimuli averaged 0.04 ± 0.04 s (mean ± SE) relative to the peak velocity of the stimulus for NS neurons were significantly earlier than that for BS neurons (mean ± SE: 0.07 ± 0.03 s; **Figure 8A**, $p < 0.05$, Wilcoxon rank-sum test), meanwhile peak times under visual stimuli averaged —0.02 ± 0.04 s (mean ± SE) for NS neurons were also obviously earlier than that for BS neurons (mean ± SE: 0.01 ± 0.03 s; **Figure 8A**, $p < 0.05$, Wilcoxon rank-sum test). In VPS, peak times under vestibular stimuli averaged − 0.11 ± 0.10 s (mean ± SE) for NS neurons were earlier than that for BS neurons (mean ± SE: 0.12 ± 0.06 s; **Figure 8C**, $p < 0.05$, Wilcoxon rank-sum test). In visual condition, although peak times for NS neurons (mean ± SE: 0.06 ± 0.22 s) showed no significant difference from that for BS neurons (mean 26± SE: 0.17 ± 0.05 s; **Figure 8D**, $p = 0.46$, Wilcoxon rank-sum test), the mean value of NS neurons was still smaller than that of BS neurons. This result showed that in self-motion perception, the putative interneurons in the local circuits for both MSTd and VPS areas may receive the external information earlier than the putative pyramidal neurons, may suggesting feedforward modulation of the putative interneurons to pyramidal neurons.

DISCUSSION

We classified MSTd and VPS neurons into putative interneurons with narrow spikes and putative pyramidal neurons with broad spikes, then compared the spatiotemporal direction tuning properties between these two classes. Our main findings are that

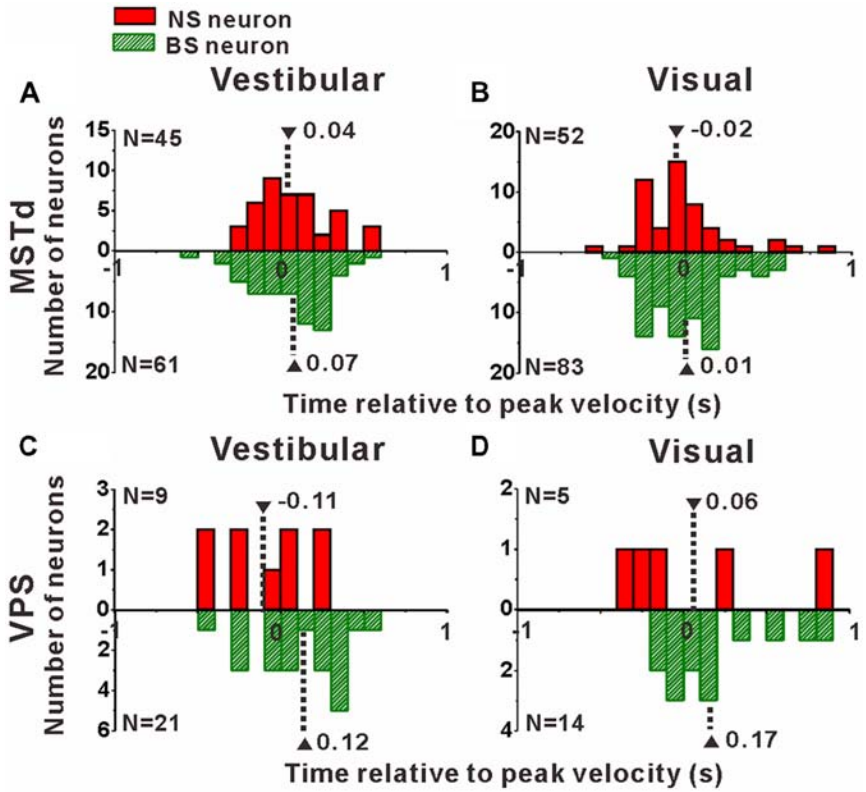

FIGURE 8 | Peak times of the NS (red) neurons and BS (green) neurons in areas MSTd **(A,B)** and VPS **(C,D)** under the vestibular and visual conditions. The neurons analyzed in the graph have a significant directional tune to vestibular or visual stimuli (both $p < 0.05$, ANOVA test). The number of neurons were same as in **Figure 4**. Note that the number of significant direction distributions for BS neurons were plotted as downward projecting histograms simply for illustrative purpose.

putative interneurons responded to visual or vestibular signals with earlier peak times, higher firing rates and greater variability, and the broader tuning of putative interneurons were more obviously observed for visual condition in MSTd and vestibular condition in VPS. These findings suggest a general functional distinction between inhibitory and excitatory neurons across cortex.

Comparison With Previous Neuron Classification

The fraction of our recordings identified as NS putative interneurons among all the identified neurons (38% for MSTd; 28% for VPS) was close to but a little bigger than the fraction present in an early physiological study (20%–30; Connors and Gutnick, 1990) and several previous studies that reported small proportions (10%–30) of NS neurons (Wilson et al., 1994; Markram et al., 2004; Mitchell et al., 2007; Atencio and Schreiner, 2008; Diester and Nieder, 2008; Isomura et al., 2009; Sakata and Harris, 2009; Yokoi and Komatsu, 2010; Ison et al., 2011). One possible reason is the cell classification criteria. Instead of using spike duration as the sole criteria as they do in some of the previous classifications (Barthó et al., 2004; González-Burgos et al., 2005; Krimer et al., 2005; Merchant et al., 2008; Le Van Quyen et al., 2008; Isomura et al., 2009), we used two parameters in the present study, spike durations (i.e., the trough-to-peak times) and baseline firing rates to classify the NS and BS neurons. Intracellular studies have demonstrated that GABAergic inhibitory interneurons produce spikes of much shorter duration than glutamatergic excitatory pyramidal neurons (McCormick et al., 1985; Connors and Gutnick, 1990; Nowak et al., 2003). The metric of spike duration, although there is still much place for perfection, appears to work reasonably well especially for extracellular recordings because: (1) the heterogeneous nature that lies in inhibitory interneurons (Kawaguchi and Kubota, 1997; Markram et al., 2004); it is a group in which some of them exhibit intermediate (González-Burgos et al., 2005; Krimer et al., 2005; Brill and Huguenard, 2009) or even broad (Merchant et al., 2008) waveforms, while spike waveforms exhibited by some of the neurons that tract to pyramidal cells can also be very narrow, which resembles inhibitory neurons (Vigneswaran et al., 2011); and (2) in extracellular recordings, spike durations have been demonstrated to vary, as much as 0.7 ms, with the distance between the exact position of the electrode and the recorded cell (Likhtik et al., 2006). It was shown in the rat hippocampus that, the combined criterion of three factors: baseline firing rate, duration of spikes and bursting characteristics, enabled the effective separation of cells into interneurons and pyramidal neurons (Ranck, 1973; Csicsvari et al., 1999), which has been further supported by *in vivo* intracellular labeling and through

recording simultaneously from the inside and outside of neurons of the same types (Henze et al., 2000; Klausberger et al., 2003) and even more studies support this by concurrent identification of either excitatory projection neurons through a method called antidromic stimulation (Likhtik et al., 2006; Johnston et al., 2009) or inhibitory interneurons by means of pairwise recordings and cross-correlation analysis (Barthó et al., 2004; Tamura et al., 2004). Additionally, the baseline firing rate difference between inhibitory interneurons and pyramidal neurons is a common exhibition throughout studies related with classification (Gur et al., 1999; Frank et al., 2001; Constantinidis and Goldman-Rakic, 2002; Maurer et al., 2006; Mitchell et al., 2007; Viskontas et al., 2007; Chen et al., 2008; Diester and Nieder, 2008; Le Van Quyen et al., 2008; Hussar and Pasternak, 2009; Johnston et al., 2009; Kuang et al., 2010; Yokoi and Komatsu, 2010; Tsunada et al., 2012; Woloszyn and Sheinberg, 2012; Kaufman et al., 2013). So in our study, we combined the criteria of spike duration and baseline firing rate to classify these two neuronal groups and excluded equivocal neurons between these two classes to minimize false commissions as much as possible. There may be some omission, but it will not alter the present findings.

Comparison With Previous Studies Testing Properties of Narrow-Spiking and Broad-Spiking Neurons

Our finding of broader tunings for NS neurons than BS neurons in MSTd and VPS during translational self-motion is consistent with previous studies of differential functional role for interneurons and pyramidal neurons in vision, audition, somato sensation and motor control (Wilson et al., 1994; Swadlow, 2003; Markram et al., 2004; Mitchell et al., 2007; Viskontas et al., 2007; Zoccolan et al., 2007; Diester and Nieder, 2008; Isomura et al., 2009; Johnston et al., 2009; Yokoi and Komatsu, 2010; Ison et al., 2011; Mruczek and Sheinberg, 2012; Tsunada et al., 2012). The broader tunings of putative interneurons were also found in monkey prefrontal cortex for spatial tuning (Constantinidis and Goldman-Rakic, 2002) and for number representations (Diester and Nieder, 2008), in cat primary visual cortex for orientation (Cardin et al., 2007) and direction representation (Nowak et al., 2008), in mouse primary visual cortex for orientation and spatial frequency tuning (Sohya et al., 2007; Niell and Stryker, 2008; Liu et al., 2009; Kerlin et al., 2010; Runyan et al., 2010), in mouse auditory cortex for frequency tuning (Lin and Liu, 2010), in the primate motor system for directional tuning (Merchant et al., 2008) and in primate inferior temporal cortex for images representation (Mruczek and Sheinberg, 2012).

The shorter response latencies (corresponding to our finding of earlier peak times) of putative interneurons were as well universal in some of these studies mentioned above and other studies across cortex areas and species (Wilson et al., 1994; Diester and Nieder, 2008; Merchant et al., 2008; Hussar and Pasternak, 2009; Lin and Liu, 2010; Yokoi and Komatsu, 2010; Murray and Keller, 2011; Mruczek and Sheinberg, 2012). One related question is why inhibitory interneurons fire earlier? There are several speculations: (1) maybe for the simple reason that a lower activation threshold is possible for inhibitory neurons (Connors and Gutnick, 1990) because of low-threshold Na+ channel subtypes (Li et al., 2014), which can also account for the higher spontaneous rates, since spiking initiation may requires very little input; (2) preferential input produced by "fast" signal pathways (Hernández-González et al., 1994; Chen et al., 2007) or top-down inputs oriented from prefrontal cortex (Bar, 2003) may be received by inhibitory neurons, both of which would likely convey coarser responses of less selectivity; whereas the traditional information conducting stream hierarchy may be the dominant input to excitatory neurons; and (3) it is possible that the recording positions of the inhibitory interneurons and excitatory pyramidal neurons were in different layers. Therefore, the peak time differences between putative inhibitory interneurons and pyramidal neurons could be explained by a local processing hierarchy.

Regional Differences and Network Implications for Self-Motion Perception

Although both MSTd and VPS putative interneurons show broader tuning and earlier peak times than putative pyramidal neurons, the differences between these two classes of neurons were not identical in MSTd and VPS. First, in MSTd, broader direction tunings of putative interneurons were found for visual stimuli but not for vestibular stimuli, while in VPS, putative interneurons were more broadly tuned to directions in vestibular condition instead of visual condition. Previous studies have demonstrated that MSTd area is dominated by visual stimuli and VPS area is dominated by vestibular stimuli although these two areas are multisensory for visual and vestibular self-motion stimuli (Gu et al., 2006; Chen et al., 2011b). Thus, we speculate that regional diversity of tuning width differences of the putative interneurons and pyramidal neurons between MSTd and VPS areas is very likely due to their dominant inputs. Second, significantly larger tuning strengths (defined as DDI values) of putative interneurons were only found in MSTd in visual condition. Analysis of the neurons' $R_{max} - R_{min}$ and SSE showed that the larger DDI values of MSTd putative interneurons in visual condition was mostly due to the greater discrepancy between the neurons' $R_{max} - R_{min}$ and SSE in visual condition as MSTd area is visual-dominant, while greater DDI values of VPS putative interneurons in vestibular condition did not occur because of the relatively poorer and more diverse response of the VPS neurons upon stimulation, reflected by the larger SE of the VPS neurons' $R_{max} - R_{min}$ and SSE. However, the larger SSE might be resulted from the smaller amount of VPS neurons in present study, thus it is too hasty to reject the possibility of the expectation that VPS putative interneurons may also have larger DDI values in vestibular condition. Thus so far, the regional differences across MSTd and VPS areas are mainly due to the difference of the dominant inputs.

Besides slight diversity between MSTd and VPS due to the difference of stimulus dominance and response variation, results in present study clarify the general points in basic response characteristics that differ in inhibitory and excitatory neurons in self-motion. Although the classification of neurons into putative

inhibitory interneurons and pyramidal neurons is oversimplified and the circuit mechanism still cannot be elucidated, it has important implications for us to understand the role these neuron classes play in self-motion perception. Self-motion perception is complicated and involves several cortical areas with diverse functions. What roles do different classes of neurons play in the whole network? Further studies extending to identify, position and trace different neuronal classes, and analyzing their functional properties will be useful and critical for understanding the neural mechanism underlying self-motion perception and information transmission across cortical areas.

AUTHOR CONTRIBUTIONS

AC designed research. YZ, SL and DJ performed research. YZ and SL analyzed data. YZ, SL and AC wrote the article.

FUNDING

This work was supported by grants from National Basic Research Program of China (31371029, 31571121, 31871089), and Shanghai education committee of scientific research innovation (15JC1400104, 16JC1400100, 18JC1412500).

REFERENCES

Angelaki, D. E., Gu, Y., and Deangelis, G. C. (2011). Visual and vestibular cue integration for heading perception in extrastriate visual cortex. *J. Physiol.* 589, 825–833. doi: 10.1113/jphysiol.2010.194720

Atencio, C. A., and Schreiner, C. E. (2008). Spectrotemporal processing differences between auditory cortical fast-spiking and regular-spiking neurons. *J. Neurosci.* 28, 3897–3910. doi: 10.1523/jneurosci.5366-07.2008

Bar, M. (2003). A cortical mechanism for triggering top-down facilitation in visual object recognition. *J. Cogn. Neurosci.* 15, 600–609. doi: 10.1162/089892903321662976

Barthó, P., Hirase, H., Monconduit, L., Zugaro, M., Harris, K. D., and Buzsaki, G. (2004). Characterization of neocortical principal cells and interneurons by network interactions and extracellular features. *J. Neurophysiol.* 92, 600–608. doi: 10.1152/jn.01170.2003

Bertin, R. J. V., and Berthoz, A. (2004). Visuo-vestibular interaction in the reconstruction of travelled trajectories. *Exp. Brain Res.* 154, 11–21. doi: 10.1007/s00221-003-1524-3

Bremmer, F., Kubischik, M., Pekel, M., Lappe, M., and Hoffmann, K. P. (1999). Linear vestibular self-motion signals in monkey medial superior temporal area. *Ann. N Y Acad. Sci.* 871, 272–281. doi: 10.1111/j.1749-6632.1999.tb09191.x

Brill, J., and Huguenard, J. R. (2009). Robust short-latency perisomatic inhibition onto neocortical pyramidal cells detected by laser-scanning photostimulation. *J. Neurosci.* 29, 7413–7423. doi: 10.1523/jneurosci.6098-08.2009

Britten, K. H. (2008). Mechanisms of self-motion perception. *Annu. Rev. Neurosci.* 31, 389–410. doi: 10.1146/annurev.neuro.29.051605.112953

Britten, K. H., and van Wezel, R. J. A. (1998). Electrical microstimulation of cortical area MST biases heading perception in monkeys. *Nat. Neurosci.* 1, 59–63. doi: 10.1038/259

Britten, K. H., and van Wezel, R. J. A. (2002). Area MST and heading perception in macaque monkeys. *Cereb. Cortex* 12, 692–701. doi: 10.1093/cercor/12.7.692

Butler, J. S., Smith, S. T., Campos, J. L., and Bülthoff, H. H. (2010). Bayesian integration of visual and vestibular signals for heading. *J. Vis.* 10:23. doi: 10.1167/10.11.23

Cardin, J. A., Palmer, L. A., and Contreras, D. (2007). Stimulus feature selectivity in excitatory and inhibitory neurons in primary visual cortex. *J. Neurosci.* 27, 10333–10344. doi: 10.1523/jneurosci.1692-07.2007

Chen, A., DeAngelis, G. C., and Angelaki, D. E. (2010). Macaque parieto-insular vestibular cortex: responses to self-motion and optic flow. *J. Neurosci.* 30, 3022–3042. doi: 10.1523/jneurosci.4029-09.2010

Chen, A., DeAngelis, G. C., and Angelaki, D. E. (2011a). Convergence of vestibular and visual self-motion signals in an area of the posterior sylvian fissure. *J. Neurosci.* 31, 11617–11627. doi: 10.1523/jneurosci.1266-11.2011

Chen, A., DeAngelis, G. C., and Angelaki, D. E. (2011b). Representation of vestibular and visual cues to self-motion in ventral intraparietal cortex. *J. Neurosci.* 31, 12036–12052. doi: 10.1523/jneurosci.0395-11.2011

Chen, A., DeAngelis, G. C., and Angelaki, D. E. (2011c). A comparison of vestibular spatiotemporal tuning in macaque parietoinsular vestibular cortex, ventral intraparietal area and medial superior temporal area. *J. Neurosci.* 31, 3082–3094. doi: 10.1523/jneurosci.4476-10.2011

Chen, C. M., Lakatos, P., Shah, A. S., Mehta, A. D., Givre, S. J., Javitt, D. C., et al. (2007). Functional anatomy and interaction of fast and slow visual pathways in macaque monkeys. *Cereb. Cortex* 17, 1561–1569. doi: 10.1093/cercor/bhl067

Chen, Y., Martinez-Conde, S., Macknik, S. L., Bereshpolova, Y., Swadlow, H. A., and Alonso, J. M. (2008). Task difficulty modulates the activity of specific neuronal populations in primary visual cortex. *Nat. Neurosci.* 11, 974–982. doi: 10.1038/nn.2147

Connors, B. W., and Gutnick, M. J. (1990). Intrinsic firing patterns of diverse neocortical neurons. *Trends Neurosci.* 13, 99–104. doi: 10.1016/0166-2236(90)90185-d

Constantinidis, C., and Goldman-Rakic, P. S. (2002). Correlated discharges among putative pyramidal neurons and interneurons in the primate prefrontal cortex. *J. Neurophysiol.* 88, 3487–3497. doi: 10.1152/jn.00188.2002

Csicsvari, J., Hirase, H., Czurko, A., Mamiya, A., and Buzsaki, G. (1999). Oscillatory coupling of hippocampal pyramidal cells and interneurons in the behaving rat. *J. Neurosci.* 19, 274–287. doi: 10.1523/jneurosci.19-01-00274.1999

Dicke, P. W., Chakraborty, S., and Thier, P. (2008). Neuronal correlates of perceptual stability during eye movements. *Eur. J. Neurosci.* 27, 991–1002. doi: 10.1111/j.1460-9568.2008.06054.x

Diester, I., and Nieder, A. (2008). Complementary contributions of prefrontal neuron classes in abstract numerical categorization. *J. Neurosci.* 28, 7737–7747. doi: 10.1523/jneurosci.1347-08.2008

Duffy, C. J. (1998). MST neurons respond to optic flow and translational movement. *J. Neurophysiol.* 80, 1816–1827. doi: 10.1152/jn.1998.80.4.1816

Fetsch, C. R., Rajguru, S. M., Karunaratne, A., Gu, Y., Angelaki, D. E., and DeAngelis, G. C. (2010). Spatiotemporal properties of vestibular responses in area MSTd. *J. Neurophysiol.* 104, 1506–1522. doi: 10.1152/jn.91247.2008

Frank, L. M., Brown, E. N., and Wilson, M. A. (2001). A comparison of the firing properties of putative excitatory and inhibitory neurons from CA1 and the entorhinal cortex. *J. Neurophysiol.* 86, 2029–2040. doi: 10.1152/jn.2001.86.4.2029

Gold, C., Henze, D. A., Koch, C., and Buzsaki, G. (2006). On the origin of the extracellular action potential waveform: a modeling study. *J. Neurophysiol.* 95, 3113–3128. doi: 10.1152/jn.00979.2005

González-Burgos, G., Krimer, L. S., Povysheva, N. V., Barrionuevo, G., and Lewis, D. A. (2005). Functional properties of fast spiking interneurons and their synaptic connections with pyramidal cells in primate dorsolateral prefrontal cortex. *J. Neurophysiol.* 93, 942–953. doi: 10.1152/jn.00787.2004

Gottfried, J. A., and Dolan, R. J. (2003). The nose smells what the eye sees: crossmodal visual facilitation of human olfactory perception. *Neuron* 39, 375–386. doi: 10.1016/s0896-6273(03)00392-1

Gu, Y., Watkins, P. V., Angelaki, D. E., and DeAngelis, G. C. (2006). Visual and nonvisual contributions to three-dimensional heading selectivity in the medial superior temporal area. *J. Neurosci.* 26, 73–85. doi: 10.1523/jneurosci.2356-05.2006

Guldin, W. O., Akbarian, S., and Grüsser, O. J. (1992). Corticocortical connections and cytoarchitectonics of the primate vestibular cortex–a study in squirrel-monkeys (*Saimiri-sciureus*). *J. Comp. Neurol.* 326, 375–401. doi: 10.1002/cne.903260306

Guldin, W. O., and Grüsser, O. J. (1998). Is there a vestibular cortex? *Trends Neurosci.* 21, 254–259. doi: 10.1016/S0166-2236(97)01211-3

Gur, M., Beylin, A., and Snodderly, D. M. (1999). Physiological properties of macaque V1 neurons are correlated with extracellular spike amplitude,

duration and polarity. *J. Neurophysiol.* 82, 1451–1464. doi: 10.1152/jn.1999.82.3.1451

Harris, L. R., Jenkin, M., and Zikovitz, D. C. (2000). Visual and non-visual cues in the perception of linear self motion. *Exp. Brain Res.* 135, 12–21. doi: 10.1007/s002210000504

Hasenstaub, A., Shu, Y., Haider, B., Kraushaar, U., Duque, A., and McCormick, D. A. (2005). Inhibitory postsynaptic potentials carry synchronized frequency information in active cortical networks. *Neuron* 47, 423–435. doi: 10.1016/j.neuron.2005.06.016

Henze, D. A., Borhegyi, Z., Csicsvari, J., Mamiya, A., Harris, K. D., and Buzsaki, G. (2000). Intracellular features predicted by extracellular recordings in the hippocampus *in vivo*. *J. Neurophysiol.* 84, 390–400. doi: 10.1152/jn.2000.84.1.390

Hernández-González, A., Cavada, C., and Reinoso-Suárez, F. (1994). The lateral geniculate nucleus projects to the inferior temporal cortex in the macaque monkey. *Neuroreport* 5, 2693–2696. doi: 10.1097/00001756-199412000-00071

Hussar, C. R., and Pasternak, T. (2009). Flexibility of sensory representations in prefrontal cortex depends on cell type. *Neuron* 64, 730–743. doi: 10.1016/j.neuron.2009.11.018

Hussar, C. R., and Pasternak, T. (2012). Memory-guided sensory comparisons in the prefrontal cortex: contribution of putative pyramidal cells and interneurons. *J. Neurosci.* 32, 2747–2761. doi: 10.1523/JNEUROSCI.5135-11.2012

Isomura, Y., Harukuni, R., Takekawa, T., Aizawa, H., and Fukai, T. (2009). Microcircuitry coordination of cortical motor information in self-initiation of voluntary movements. *Nat. Neurosci.* 12, 1586–1593. doi: 10.1038/nn.2431

Ison, M. J., Mormann, F., Cerf, M., Koch, C., Fried, I., and Quiroga, R. Q. (2011). Selectivity of pyramidal cells and interneurons in the human medial temporal lobe. *J. Neurophysiol.* 106, 1713–1721. doi: 10.1152/jn.00576.2010

Johnston, K., DeSouza, J. F., and Everling, S. (2009). Monkey prefrontal cortical pyramidal and putative interneurons exhibit differential patterns of activity between prosaccade and antisaccade tasks. *J. Neurosci.* 29, 5516–5524. doi: 10.1523/JNEUROSCI.5953-08.2009

Jones, E. G., and Burton, H. (1976). Areal differences in the laminar distribution of thalamic afferents in cortical fields of the insular, parietal and temporal regions of primates. *J. Comp. Neurol.* 168, 197–247. doi: 10.1002/cne.901680203

Kaufman, M. T., Churchland, M. M., Santhanam, G., Yu, B. M., Afshar, A., Ryu, S. I., et al. (2010). Roles of monkey premotor neuron classes in movement preparation and execution. *J. Neurophysiol.* 104, 799–810. doi: 10.1152/jn.00231.2009

Kaufman, M. T., Churchland, M. M., and Shenoy, K. V. (2013). The roles of monkey M1 neuron classes in movement preparation and execution. *J. Neurophysiol.* 110, 817–825. doi: 10.1152/jn.00892.2011

Kawaguchi, Y., and Kubota, Y. (1997). GABAergic cell subtypes and their synaptic connections in rat frontal cortex. *Cereb. Cortex* 7, 476–486. doi: 10.1093/cercor/7.6.476

Kerlin, A. M., Andermann, M. L., Berezovskii, V. K., and Reid, R. C. (2010). Broadly tuned response properties of diverse inhibitory neuron subtypes in mouse visual cortex. *Neuron* 67, 858–871. doi: 10.1016/j.neuron.2010.08.002

Klausberger, T., Magill, P. J., Márton, L. F., Roberts, J. D. B., Cobden, P. M., Buzsáki, G., et al. (2003). Brain-state- and cell-type-specific firing of hippocampal interneurons *in vivo*. *Nature* 421, 844–848. doi: 10.1038/nature01374

Krimer, L. S., Zaitsev, A. V., Czanner, G., Kröner, S., Gonzalez-Burgos, G., Povysheva, N. V., et al. (2005). Cluster analysis-based physiological classification and morphological properties of inhibitory neurons in layers 2-3 of monkey dorsolateral prefrontal cortex. *J. Neurophysiol.* 94, 3009–3022. doi: 10.1152/jn.00156.2005

Kuang, H., Lin, L., and Tsien, J. Z. (2010). Temporal dynamics of distinct CA1 cell populations during unconscious state induced by ketamine. *PLoS One* 5:e15209. doi: 10.1371/journal.pone.0015209

Le Van Quyen, M., Bragin, A., Staba, R., Crépon, B., Wilson, C. L., and Engel, J. (2008). Cell type-specific firing during ripple oscillations in the hippocampal formation of humans. *J. Neurosci.* 28, 6104–6110. doi: 10.1523/JNEUROSCI.0437-08.2008

Li, T., Tian, C. P., Scalmani, P., Frassoni, C., Mantegazza, M., Wang, Y. H., et al. (2014). Action potential initiation in neocortical inhibitory interneurons. *PLoS Biol.* 12:e1001944. doi: 10.1371/journal.pbio.1001944

Likhtik, E., Pelletier, J. G., Popescu, A. T., and Pare, D. (2006). Identification of basolateral amygdala projection cells and interneurons using extracellular recordings. *J. Neurophysiol.* 96, 3257–3265. doi: 10.1152/jn.00577.2006

Lin, F. G., and Liu, R. C. (2010). Subset of thin spike cortical neurons preserve the peripheral encoding of stimulus onsets. *J. Neurophysiol.* 104, 3588–3599. doi: 10.1152/jn.00295.2010

Liu, B. H., Li, P., Li, Y. T., Sun, Y. J., Yanagawa, Y., Obata, K., et al. (2009). Visual receptive field structure of cortical inhibitory neurons revealed by two-photon imaging guided recording. *J. Neurosci.* 29, 10520–10532. doi: 10.1523/JNEUROSCI.1915-09.2009

Markram, H., Toledo-Rodriguez, M., Wang, Y., Gupta, A., Silberberg, G., and Wu, C. Z. (2004). Interneurons of the neocortical inhibitory system. *Nat. Rev. Neurosci.* 5, 793–807. doi: 10.1038/nrn1519

Maurer, A. P., Cowen, S. L., Burke, S. N., Barnes, C. A., and McNaughton, B. L. (2006). Phase precession in hippocampal interneurons showing strong functional coupling to individual pyramidal cells. *J. Neurosci.* 26, 13485–13492. doi: 10.1523/JNEUROSCI.2882-06.2006

McCormick, D. A., Connors, B. W., Lighthall, J. W., and Prince, D. A. (1985). Comparative electrophysiology of pyramidal and sparsely spiny stellate neurons of the neocortex. *J. Neurophysiol.* 54, 782–806. doi: 10.1152/jn.1985.54.4.782

Merchant, H., Naselaris, T., and Georgopoulos, A. P. (2008). Dynamic sculpting of directional tuning in the primate motor cortex during three-dimensional reaching. *J. Neurosci.* 28, 9164–9172. doi: 10.1523/JNEUROSCI.1898-08.2008

Mitchell, J. F., Sundberg, K. A., and Reynolds, J. H. (2007). Differential attention-dependent response modulation across cell classes in macaque visual area V4. *Neuron* 55, 131–141. doi: 10.1016/j.neuron.2007.06.018

Mountcastle, V. B., Talbot, W. H., Sakata, H., and Hyvarinen, J. (1969). Cortical neuronal mechanisms in flutter-vibration studied in unanesthetized monkeys. Neuronal periodicity and frequency discrimination. *J. Neurophysiol.* 32, 452–484. doi: 10.1152/jn.1969.32.3.452

Mruczek, R. E. B., and Sheinberg, D. L. (2012). Stimulus selectivity and response latency in putative inhibitory and excitatory neurons of the primate inferior temporal cortex. *J. Neurophysiol.* 108, 2725–2736. doi: 10.1152/jn.00618.2012

Murray, P. D., and Keller, A. (2011). Somatosensory response properties of excitatory and inhibitory neurons in rat motor cortex. *J. Neurophysiol.* 106, 1355–1362. doi: 10.1152/jn.01089.2010

Niell, C. M., and Stryker, M. P. (2008). Highly selective receptive fields in mouse visual cortex. *J. Neurosci.* 28, 7520–7536. doi: 10.1523/JNEUROSCI.0623-08.2008

Nowak, L. G., Azouz, R., Sanchez-Vives, M. V., Gray, C. M., and McCormick, D. A. (2003). Electrophysiological classes of cat primary visual cortical neurons *in vivo* as revealed by quantitative analyses. *J. Neurophysiol.* 89, 1541–1566. doi: 10.1152/jn.00580.2002

Nowak, L. G., Sanchez-Vives, M. V., and McCormick, D. A. (2008). Lack of orientation and direction selectivity in a subgroup of fast-spiking inhibitory interneurons: cellular and synaptic mechanisms and comparison with other electrophysiological cell types. *Cereb. Cortex* 18, 1058–1078. doi: 10.1093/cercor/bhm137

Ohmi, M. (1996). Egocentric perception through interaction among many sensory systems. *Cogn. Brain Res.* 5, 87–96. doi: 10.1016/s0926-6410(96)00044-4

Peters, A., and Jones, E. G. (1984). *Cerebral Cortex. Volume 1. Cellular Components of the Cerebral Cortex.* New York, NY: Plenum Press.

Pettorossi, V. E., and Schieppati, M. (2014). Neck proprioception shapes body orientation and perception of motion. *Front. Hum. Neurosci.* 8:895. doi: 10.3389/fnhum.2014.00895

Ramon, Y., and Cajal, S. (1899). Estudios sobre la corteza cerebral humana. *Rev. Trimest. Micrographica* 4, 1–63.

Ranck, J. B. Jr. (1973). Studies on single neurons in dorsal hippocampal formation and septum in unrestrained rats: I. Behavioral correlates and firing repertoires. *Exp. Neurol.* 41, 461–531. doi: 10.1016/0014-4886(73)90290-2

Rao, S. G., Williams, G. V., and Goldman-Rakic, P. S. (1999). Isodirectional tuning of adjacent interneurons and pyramidal cells during working memory: evidence for microcolumnar organization in PFC. *J. Neurophysiol.* 81, 1903–1916. doi: 10.1152/jn.1999.81.4.1903

Runyan, C. A., Schummers, J., Van Wart, A., Kuhlman, S. J., Wilson, N. R., Huang, Z. J., et al. (2010). Response features of parvalbumin-expressing interneurons suggest precise roles for subtypes of inhibition in visual cortex. *Neuron* 67, 847–857. doi: 10.1016/j.neuron.2010.08.006

Sakata, S., and Harris, K. D. (2009). Laminar structure of spontaneous and sensory-evoked population activity in auditory cortex. *Neuron* 64, 404–418. doi: 10.1016/j.neuron.2009.09.020

Snyder, J. P. (1987). *Map Projections: A Working Manual*. Washington, DC: US Government Printing Office.

Sohya, K., Kameyama, K., Yanagawa, Y., and Tsumoto, T. (2007). Difference in response selectivity between inhibitory and excitatory neurons in visual cortex, as revealed by *in vivo* two-photon functional Ca^{2+} imaging. *Neurosci. Res.* 58:S63. doi: 10.1016/j.neures.2007.06.369

Suzuki, N., and Bekkers, J. M. (2012). Microcircuits mediating feedforward and feedback synaptic inhibition in the piriform cortex. *J. Neurosci.* 32, 919–931. doi: 10.1523/JNEUROSCI.4112-11.2012

Swadlow, H. A. (2003). Fast-spike interneurons and feedforward inhibition in awake sensory neocortex. *Cereb. Cortex* 13, 25–32. doi: 10.1093/cercor/13.1.25

Takahashi, K., Gu, Y., May, P. J., Newlands, S. D., DeAngelis, G. C., and Angelaki, D. E. (2007). Multimodal coding of three-dimensional rotation and translation in area MSTd: comparison of visual and vestibular selectivity. *J. Neurosci.* 27, 9742–9756. doi: 10.1523/JNEUROSCI.0817-07.2007

Tamura, H., Kaneko, H., Kawasaki, K., and Fujita, I. (2004). Presumed inhibitory neurons in the macaque inferior temporal cortex: visual response properties and functional interactions with adjacent neurons. *J. Neurophysiol.* 91, 2782–2796. doi: 10.1152/jn.01267.2003

Telford, L., Howard, I. P., and Ohmi, M. (1995). Heading judgments during active and passive self-motion. *Exp. Brain Res.* 104, 502–510. doi: 10.1007/bf00231984

Toledo-Rodriguez, M., Gupta, A., Wang, Y., Wu, C. Z., and Markram, H. (2003). "Neocortex: basic neuron types," in *The Handbook of Brain Theory and Neural Networks*, ed. M. A. Arbib (Cambridge, MA: The MIT Press), 719–725.

Tsunada, J., Lee, J. H., and Cohen, Y. E. (2012). Differential representation of auditory categories between cell classes in primate auditory cortex. *J. Physiol.* 590, 3129–3139. doi: 10.1113/jphysiol.2012.232892

Vigneswaran, G., Kraskov, A., and Lemon, R. N. (2011). Large identified pyramidal cells in macaque motor and premotor cortex exhibit "thin spikes": implications for cell type classification. *J. Neurosci.* 31, 14235–14242. doi: 10.1523/JNEUROSCI.3142-11.2011

Viskontas, I. V., Ekstrom, A. D., Wilson, C. L., and Fried, I. (2007). Characterizing interneuron and pyramidal cells in the human medial temporal lobe *in vivo* using extracellular recordings. *Hippocampus* 17, 49–57. doi: 10.1002/hipo.20241

Warren, R. (1990). "Preliminary questions for the study of egomotion," in *Resources for Ecological Psychology: Perception and Control of Self-Motion*, eds R. Warren and A. H. Wertheim (Hillsdale, NJ: Lawrence Erlbaum Associates), 3–32.

Wilson, C. J. (2007). GABAergic inhibition in the neostriatum. *Prog. Brain Res.* 160, 91–110. doi: 10.1016/s0079-6123(06)60006-x

Wilson, F. A., O'Scalaidhe, S. P., and Goldman-Rakic, P. S. (1994). Functional synergism between putative gamma-aminobutyrate-containing neurons and pyramidal neurons in prefrontal cortex. *Proc. Natl. Acad. Sci. U S A* 91, 4009–4013. doi: 10.1073/pnas.91.9.4009

Woloszyn, L., and Sheinberg, D. L. (2012). Effects of long-term visual experience on responses of distinct classes of single units in inferior temporal cortex. *Neuron* 74, 193–205. doi: 10.1016/j.neuron.2012.01.032

Yokoi, I., and Komatsu, H. (2010). Putative pyramidal neurons and interneurons in the monkey parietal cortex make different contributions to the performance of a visual grouping task. *J. Neurophysiol.* 104, 1603–1611. doi: 10.1152/jn.00160.2010

Zoccolan, D., Kouh, M., Poggio, T., and DiCarlo, J. J. (2007). Trade-off between object selectivity and tolerance in monkey inferotemporal cortex. *J. Neurosci.* 27, 12292–12307. doi: 10.1523/JNEUROSCI.1897-07.2007

Conflict of Interest Statement: The authors declare that the research was conducted in the absence of any commercial or financial relationships that could be construed as a potential conflict of interest.

frontiers in Cellular Neuroscience

ORIGINAL RESEARCH
published: 12 December 2018
doi: 10.3389/fncel.2018.00490

Contribution of Thyrotropin-Releasing Hormone to Cerebellar Long-Term Depression and Motor Learning

*Masashi Watanave[1], Yasunori Matsuzaki[1], Yasuyo Nakajima[2], Atsushi Ozawa[2], Masanobu Yamada[2] and Hirokazu Hirai[1,3]**

[1] Department of Neurophysiology and Neural Repair, Gunma University Graduate School of Medicine, Maebashi, Japan,
[2] Department of Medicine and Molecular Science, Gunma University Graduate School of Medicine, Maebashi, Japan,
[3] Research Program for Neural Signalling, Division of Endocrinology, Metabolism and Signal Research, Gunma University Initiative for Advanced Research, Maebashi, Japan

Thyrotropin-releasing hormone (TRH) regulates various physiological activities through activation of receptors expressed in a broad range of cells in the central nervous system. The cerebellum expresses TRH receptors in granule cells and molecular layer interneurons. However, the function of TRH in the cerebellum remains to be clarified. Here, using TRH knockout (KO) mice we studied the role of TRH in the cerebellum. Immunohistochemistry showed no gross morphological differences between KO mice and wild-type (WT) littermates in the cerebellum. In the rotarod test, the initial performance of KO mice was comparable to that of WT littermates, but the learning speed of KO mice was significantly lower than that of WT littermates, suggesting impaired motor learning. The motor learning deficit in KO mice was rescued by intraperitoneal injection of TRH. Electrophysiology revealed absence of long-term depression (LTD) at parallel fiber-Purkinje cell synapses in KO mice, which was rescued by bath-application of TRH. TRH was shown to increase cyclic guanosine monophosphate (cGMP) content in the cerebellum. Since nitric oxide (NO) stimulates cGMP synthesis in the cerebellum, we examined whether NO-cGMP pathway was involved in TRH-mediated LTD rescue in KO mice. Pharmacological blockade of NO synthase and subsequent cGMP production prevented TRH-induced LTD expression in KO mice, whereas increase in cGMP signal in Purkinje cells by 8-bromoguanosine cyclic 3',5'-monophosphate, a membrane-permeable cGMP analog, restored LTD without TRH application. These results suggest that TRH is involved in cerebellar LTD presumably by upregulating the basal cGMP level in Purkinje cells, and, consequently, in motor learning.

Keywords: thyrotropin-releasing hormone, motor learning, cerebellum, LTD, NO

OPEN ACCESS

Edited by:
Jing-Ning Zhu,
Nanjing University, China

Reviewed by:
Maria Concetta Miniaci,
University of Naples Federico II, Italy
Eriola Hoxha,
Università degli Studi di Torino, Italy

****Correspondence:***
Hirokazu Hirai
hirai@gunma-u.ac.jp

Received: *07 September 2018*
Accepted: *29 November 2018*
Published: *12 December 2018*

Citation:
Watanave M, Matsuzaki Y, Nakajima Y, Ozawa A, Yamada M and Hirai H (2018) Contribution of Thyrotropin-Releasing Hormone to Cerebellar Long-Term Depression and Motor Learning. Front. Cell. Neurosci. 12:490. doi: 10.3389/fncel.2018.00490

INTRODUCTION

The tripeptideamide pyroGlu-His-Pro-NH2 was originally isolated from mammalian hypothalami, and is released from the hypothalamus. It stimulates the synthesis and secretion of pituitary thyrotropin. Thus, this small peptide was named thyrotropin-releasing hormone (TRH). However, it became evident that the biological action of TRH extends far beyond the thyroid

hormone-associated pathway. TRH and TRH receptors are expressed in a wide range of cells in the central nervous system and are implicated in the regulation of various physiological activities including arousal, circadian rhythmicity, pain perception, and spinal motor function (Nillni and Sevarino, 1999; Yamada et al., 2003).

The cerebellum is a center of motor coordination and motor learning (Bellebaum and Daum, 2007; Peterburs and Desmond, 2016), and its impairment results in cerebellar ataxia and motor learning deficits (Bastian, 2011). Spinocerebellar degeneration is a major disorder that progressively affects cerebellar function. Its main symptoms include dysmetria, intention tremor, and dysarthria (Paulson et al., 2017). Currently, no fundamental cure has been identified for this disease. A synthetic TRH analog, taltirelin, was shown to ameliorate ataxic behavior in the hereditary rolling mouse Nagoya, a murine model of spinocerebellar ataxia (Nakamura et al., 2005). It is, thus, used mostly in Japan for the treatment of spinocerebellar degeneration. However, the mechanisms by which TRH and taltirelin mitigate cerebellar ataxia have not yet been fully clarified.

One known finding about an effect of TRH on the cerebellum is an increase in cyclic guanosine monophosphate (cGMP) content, following the systemic administration, without significant changes in other brain regions (Mailman et al., 1979). The cGMP content in the cerebellum is extremely high (about 10-fold than that in other brain regions) (Steiner et al., 1972). Previous studies have suggested primary presence of cGMP and cGMP-dependent protein kinase G (PKG) in Purkinje cells (PCs) (Mao et al., 1975; Schlichter et al., 1980), suggesting that cGMP and PKG play critical roles in PC function. Since the TRH receptor (subtype 2) is expressed in granule cells and molecular layer interneurons, but not in PCs (Heuer et al., 2000), it is assumed that TRH signals are first activated in granule cells and molecular layer interneurons, and then, transferred transsynaptically to PCs to increase the cGMP level. However, considering broad physiological activities of TRH in other brain regions (Yarbrough, 2003; Zhang and Van Den Pol, 2012; Zhang et al., 2013), TRH could have more divergent roles in the cerebellum. In this study, we examined TRH knockout (KO) mice to investigate the physiological role of TRH in cerebellar function.

MATERIALS AND METHODS

Animals

We used 10- to 16-week-old TRH KO mice, which were generated previously (Yamada et al., 1997). All procedures for the care and treatment of animals were performed according to the Japanese Act on the Welfare and Management of Animals, and the Guidelines for Proper Conduct of Animal Experiments as issued by the Science Council of Japan. The experimental protocol was approved by the Institutional Committee of Gunma University (No. 17-026; 17-034). All efforts were made to minimize suffering and to reduce the number of animals that were used.

Rotarod Test

The motor control ability of mice was evaluated using a rotarod test (MK-610A/RKZ; Muromachi Kikai, Tokyo, Japan). Mice were subjected to four trials separated by 30-min intervals on the rod while accelerating from 5 to 50 rpm in 5 min. For rescue experiments of motor ability, saline or TRH (Sigma Aldrich, St. Louis, MO, United States) was administered by intraperitoneal injection (30 mg/kg body weight [BW]) to KO mice 10 min before the first trial of the rotarod test.

Immunohistochemistry

Mice were deeply anesthetized and perfused intracardially with 4% paraformaldehyde in 0.1 M phosphate buffer (PB). The entire brain was removed and immersed in 4% paraformaldehyde in 0.1 M PB for 8 h at 4°C. Parasagittal cerebellar slices (50 μm thickness) were prepared using a vibratome (VT1200S; Leica, Wetzlar, Germany). The tissue slices were permeabilized and blocked with 0.1 M PB containing fivefold-diluted G-Block (GenoStaff, Tokyo, Japan), 0.5% (w/v) Triton X-100, and 0.025% NaN_3 (blocking solution). They were then incubated in blocking solution containing the following antibodies overnight at room temperature (26°C): rabbit monoclonal anti-calbindin D-28K (1:500; C2724; Merck, Darmstadt, Germany), mouse monoclonal anti-NeuN (1:1,000; MAB377; Merck), and goat polyclonal anti-parvalbumin (1:200; PV-Go-Af460; Frontier Institute, Hokkaido, Japan). After washing six times with 0.1 M PB, the slices were incubated for 4 h at room temperature (26°C) in the blocking solution containing the following secondary antibodies (1:1,000; all purchased from Thermo Fisher Scientific, Waltham, MA, United States): Alexa Fluor 488-conjugated donkey anti-rabbit immunoglobulin G, Alexa Fluor 568-conjugated donkey anti-mouse immunoglobulin G, and Alexa Fluor 647-conjugated donkey anti-goat immunoglobulin G. After washing six times with 0.1 M PB at RT, the slices were mounted on glass slides using ProLong Diamond Antifade Reagent (P36961; Thermo Fisher Scientific). Each specimen was observed using a fluorescent microscope (BZ-X700; Keyence, Osaka, Japan) or a confocal laser-scanning microscope (LSM 800; Carl Zeiss, Oberkochen, Germany).

Molecular layer thickness was measured using ZEN 2 (blue edition) software (Carl Zeiss). Sagittal slices from the cerebellar vermis (±0.5 μm from the median) were immunostained with the anti-calbindin D-28K antibody and mounted. Twenty-four hours after the mounting, images were obtained from lobules 4/5 – 6 including the primary fissure and lobules 8 – 9 including the secondary fissure, using a confocal microscope (LSM800). The molecular layer thickness was measured 100 μm (primary) or 200 μm (secondary) from the inner end of the fissure (see **Figure 1B**). The molecular layer thickness of both sides of the fissure was measured using ZEN2, and the sum was defined as molecular layer thickness.

Patch Clamp Recording

Parasagittal cerebellar slices (250 μm in thickness) were prepared from mice. Briefly, mice were anesthetized deeply by inhalation of isoflurane (3%) and killed by decapitation. The whole brain

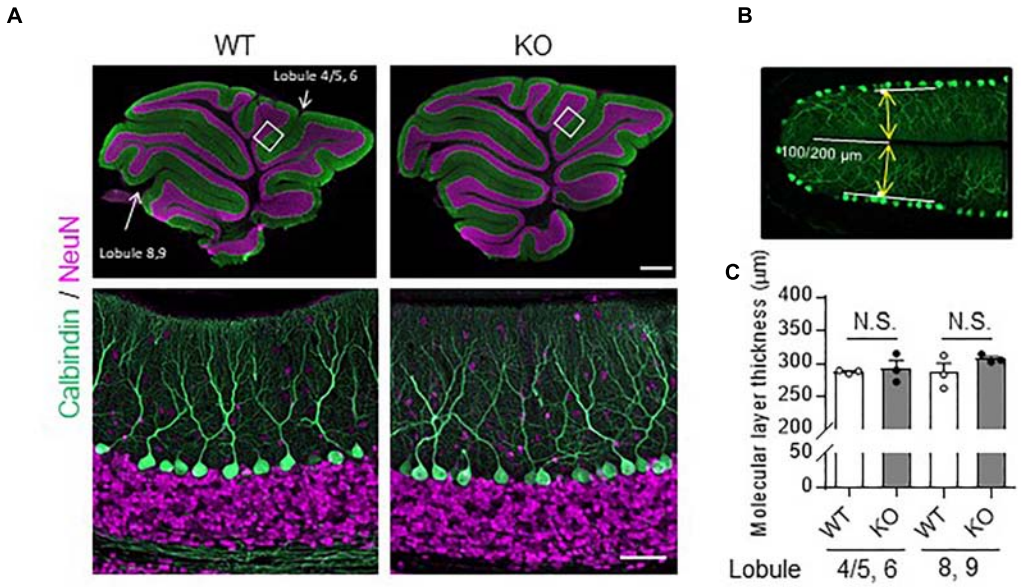

FIGURE 1 | No obvious morphological differences in the cerebellum were found between TRH-KO mice and their WT littermates. Immunohistochemistry was used to compare sagittal cerebellar sections from TRH-KO mice to those from their WT littermates. Slices were double-immunostained for calbindin, a marker of PCs (green), and NeuN, a marker of granule cells (magenta). **(A)** Sagittal sections of the WT (left) and TRH-KO (right) cerebellum. The boxed areas in upper panels are enlarged. Scale bar: 500 μm (upper right) and 50 μm (lower right). KO, knock-out; WT, wild-type. **(B,C)** Quantitative analysis of the molecular layer thickness. The molecular layer thickness was measured at two different points on the sagittal section of the cerebellar vermis: lobule 4/5 and lobule 6 at 100 μm from the end of the primary fissure, and lobule 8 and lobule 9 at 200 μm from the end of the secondary fissure **(B)**. The molecular layer thickness of both sides of the fissure was measured, and the sum was defined as molecular layer thickness. There are no significant differences at both two points between genotypes **(C)**. KO, knock-out; N.S., not significant; WT, wild-type.

was quickly dissected out and immersed for a 2–3 min in an ice-cold solution containing the following (in mM): 234 sucrose, 26 $NaHCO_3$, 2.5 KCl, 1.25 NaH_2PO_4, 11 glucose, 10 $MgSO_4$, and 0.5 $CaCl_2$ (pH 7.4 when bubbled with 95% O_2 and 5% CO_2). Parasagittal slices of the cerebellar vermis were obtained using a microslicer (ZERO1; Dosaka-EM, Kyoto, Japan). The slices were maintained in an extracellular solution containing (in mM): 125 NaCl, 2.5 KCl, 2 $CaCl_2$, 1 $MgCl_2$, 1.25 NaH_2PO_4, 26 $NaHCO_3$, 10 D-glucose, and 0.1 picrotoxin, bubbled continuously with a mixture of 95% O_2 and 5% CO_2 at room temperature (26°C) for at least 1 h before commencing recording. PCs were visualized using a 40× water-immersion objective attached to an upright microscope (Axioskop, Carl Zeiss). Whole-cell recordings were made from PCs at room temperature (26°C) and the slices were continuously perfused with the extracellular solution during the experiment. The extracellular solution contained 0.1 mM picrotoxin, except for the solution used to record spontaneous and miniature inhibitory postsynaptic currents (sIPSCs and mIPSCs, respectively). The resistance of the patch pipette was 3–6 MΩ when filled with intracellular solution containing (in mM): 122.5 Cs methane sulfonate, 17.5 CsCl, 8 NaCl, 2 Mg adenosine triphosphate, 0.3 Na guanosine triphosphate, 10 4-(2-hydroxyethyl)-1-piperazineethanesulfonic acid, 0.2 ethylene glycol-bis(β-aminoethyl ether)-N,N,N',N'-tetraacetic acid, and 5 sucrose (pH 7.2, adjusted with CsOH). The intracellular solution used for IPSC recording contained (in mM): 127.5 CsCl, 2 $CaCl_2$, 1 $MgCl_2$, 2 MgATP, 0.3 NaGTP, 10 HEPES (pH 7.3, adjusted with CsOH).

Stimulation pipettes were filled with the extracellular solution and placed in the molecular and granule layer to activate parallel fibers (PFs) and climbing fibers (CFs), respectively. PCs were clamped at −70 mV or −10 mV to record PF- or CF-evoked excitatory postsynaptic currents (EPSCs), respectively. Liquid junction potentials were not corrected. To estimate the passive electrical properties of the recorded PCs, we applied 10-mV hyperpolarizing voltage pulses (from −70 mV to −80 mV, 200 ms duration). The averaged trace of the 10 current responses was used for the estimation. Membrane capacitance and input resistance were calculated from the integral of the capacitive charging current, and from the steady-state current amplitude measured late during the pulse, respectively.

Selective stimulation of PFs and CFs was confirmed by paired-pulse facilitation (PPF) and paired-pulse depression (PPD) of EPSC amplitudes with a 50 ms inter-stimulus interval, respectively. To isolate metabotropic glutamate receptor type 1 (mGluR1)-mediated slow EPSCs, repetitive PF stimuli (100 Hz) were applied in the presence of 20 μM 2,3-dioxo-6-nitro-1,2,3,4-tetrahydrobenzo[f]quinoxaline-7-sulfonamide, which is a highly selective competitive antagonist of α-amino-3-hydroxy-5-methyl-4-isoxazolepropionic acid (AMPA)-type glutamate receptors (Libbey et al., 2016).

For analysis of long-term depression (LTD), PF EPSCs were monitored every 10 s. We always confirmed the stability of

PF EPSCs for at least 10 min before LTD induction. Series resistance was continuously monitored every 10 s by applying small hyperpolarizing pulses. Data were discarded when the resistance values changed by >20% of the basal value during the course of the experiment. To induce LTD, we applied conjunctive stimulation consisting of 30 single PF stimuli paired with single 200-ms depolarizing pulses (−70 mV to +10 mV) repeated at 1 Hz. Amplitudes of PF EPSCs were averaged every minute (six traces) and normalized by the averaged value of the responses over 10 min immediately before the conjunctive stimulation. Some LTD recordings were made in the presence of 100 nM TRH (Sigma-Aldrich), 30 μM 8-bromoguanosine 3',5'-cyclic monophosphate (8-bromo-cGMP) (Sigma-Aldrich) or 100 μM N^G-Nitro-L-arginine methyl ester hydrochloride (L-NAME) (Dojindo Laboratory, Kumamoto, Japan) (**Figures 5–7**).

Inhibitory postsynaptic currents were recorded in the presence of 25 μM D-2-amino-5-phosphonopentanoic acid (D-APV) and 20 μM NBQX to block excitatory inputs. mIPSCs were recorded in the presence of 1 μM tetrodotoxin (TTX) to block action potentials, and events were detected using a semiautomatic event detector (Clampfit software, San Jose, CA, United States). mIPSC events whose were amplitudes less than 10 pA were discarded.

Statistical Analysis

Significant differences were analyzed using Welch's *t*-test and repeated-measures analysis of variance using GraphPad Prism 7 (GraphPad Software, San Diego, CA, United States). The data are expressed as the mean ± standard error of the mean.

RESULTS

No Gross Morphological Changes in the Cerebellum in TRH-Deficient Mice

The cerebella of 14-week-old TRH-KO mice were compared morphologically to those of wild-type (WT) littermates. After perfusion fixation, the cerebella were cut into 50-μm-thick sections and double-immunostained for calbindin, a PC marker, and NeuN, a granule cell marker. The morphology of the cerebellar cortex was almost indistinguishable between the KO mice and WT littermates (**Figure 1A**). We measured molecular layer thickness quantitatively, and confirmed no significant differences between the KO mice and WT littermates (**Figures 1B,C**, Lobule 4/5, 6; $P = 0.272$, Lobule 8, 9; $P = 0.728$). Thus, TRH deficiency had no overt influence on cerebellar morphology.

TRH-Deficient Mice Show Motor Learning Deficits

As the behavior of TRH-KO mice in the home cages was indistinguishable from that of their WT littermates, we analyzed their motor ability more carefully using a rotarod apparatus. Numbers of males and females for the rotarod were adjusted between KO and WT mouse groups. However, since BW affects the rotarod performance, we compared the BW of 10- to 12-week-old KO mice with that of their WT littermates. The results showed no significant differences between genotypes (**Figure 2A**, $P = 0.757$). In the rotarod test, 10- to 14-week-old TRH-KO mice had similar performance to their WT littermates on the first trial. During the following trials, mice of both genotypes learned the task, and the time on the rod gradually increased. However, learning was significantly slower in the KO mice [**Figure 2B**, $F(1,22) = 5.22$, $P = 0.032$]. These results suggest that motor coordination was normal in TRH-KO mice, but that motor learning ability was significantly impaired.

Rescue of Motor Learning Defect by Exogenous TRH

As revealed in the rotarod test, TRH-KO mice had impaired motor learning. This might be due to a developmental abnormality or merely the absence of TRH-triggered signaling. To address this issue, we administered TRH (6 ml/kg BW, 5 mg/ml) or similar volume of saline intraperitoneally to TRH-KO mice and assessed the effects of TRH on motor learning 10 min after the injection (**Figure 2C**). TRH-injected KO mice had significantly better performance than saline-injected KO mice in the rotarod test [**Figure 2D**, $F(1,14) = 9.44$, $P = 0.008$]. WT mice were treated similarly with TRH or saline, but, TRH, like saline, had no significant influence on the rotarod performance (**Supplementary Figure S1**). Notably, TRH-administered KO mice showed favorable rotarod performance, almost comparable to that of TRH-treated WT mice. These results suggest that the motor learning deficit was likely due to an absence of TRH signaling, which was restored by application of exogenous TRH.

Normal Fast Synaptic Transmission at PF- and CF-PC Synapses in TRH-Deficient Mice

We next examined synaptic transmission at PF- and CF-PC synapses using the whole cell patch-clamp technique. Fast PF and CF EPSCs were elicited in PCs by electrical stimulation of PFs or CFs, respectively. Membrane capacitance (**Figure 3A**, KO: 1053.0 ± 68.5 pF, WT: 903.8 ± 88.9 pF, $P = 0.19$), and rise time and decay time constants of the fast PF and CF EPSCs (**Table 1**) were comparable between the KO mice and their WT littermates. We then examined the relationship between stimulus intensity and evoked PF EPSC amplitude, and found no difference between the KO mice and their WT littermates (**Figure 3B**). Moreover, there were no significant differences in short-term synaptic plasticity, as assessed based on the ratio of PPF in PF EPSCs and the ratio of PPD in CF EPSCs, between the KO mice and their WT littermates (**Figures 3C,D**).

Absence of LTD at PF-PC Synapses in TRH-Deficient Mice

Long-term depression at PF-PC synapses is thought to be a cellular basis of motor learning. We thus examined whether LTD could be induced at PF-PC synapses in TRH-KO mice. After recording stable PF-EPSCs for at least 10 min,

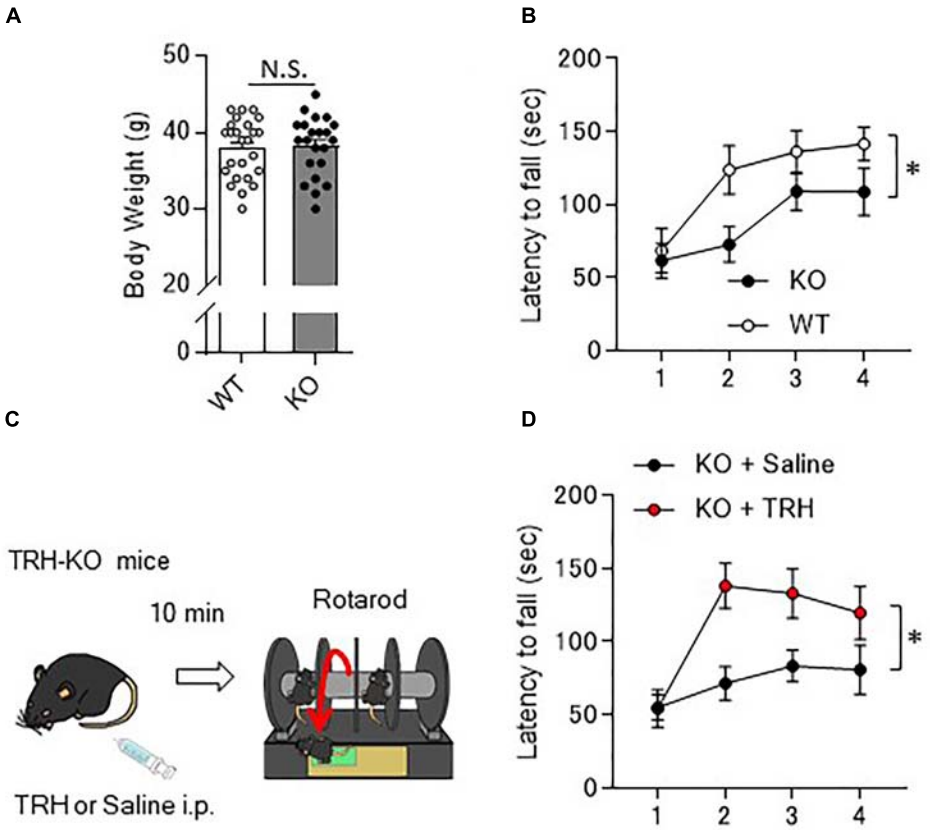

FIGURE 2 | Motor learning deficits in TRH-KO mice and the restoration by exogenous TRH. **(A)** No difference in the body weights between genotypes. Body weight of 10- to 14-week-old TRH-KO mice and their WT littermates were measured [WT: n = 25 (male: 14, female: 12), KO: n = 22 (male: 12, female: 10)]. N.S., not significant. **(B)** Graph showing the averaged results of four rotarod trials [n = 12 (male: 8, female: 4) for both KO and WT mice], and the average time on the rod was plotted. KO, knock-out; WT, wild-type. **(C)** Schema showing the experimental procedure. Littermate TRH-KO mice received TRH (6 ml/kg BW, 5 mg/ml, n = 8 mice, male: 3, female: 5) or the same volume of saline (n = 8 mice, male: 3, female: 5) intraperitoneally (i.p.). The effects of the treatment were tested 10 min after the injection using the rotarod test. **(D)** Results of the rotarod test. Mice were subjected to four trials. *$P < 0.05$, as determined using repeated-measures analysis of variance. KO, knock-out; WT, wild-type.

conjunctive stimulation (electrical stimulation to PFs combined with depolarization of the recording PC) induced LTD at PF-PC synapses in WT mice. However, similar stimulation failed to induce LTD in TRH-KO mice (**Figures 4A,B**, KO: 108.0 ± 9.3%, WT: 82.1 ± 4.5%, $P = 0.039$).

Repetitive PF stimulation leads to glutamate spillover from the synaptic clefts between the PF terminals and the dendritic spines of PCs. This in turn leads to activation of Gq/11 protein-coupled mGluR1, which is localized postsynaptically at perisynaptic sites of PC dendritic spines (Hirai and Kano, 2018). Activation of mGluR1 leads to production of diacylglycerol and inositol-triphosphate, the latter of which triggers calcium release from the endoplasmic reticulum. The elevated calcium together with diacylglycerol activates protein kinase C (PKC), which plays a key role in LTD induction (Matsuda et al., 2000; Hirai, 2001; Chung et al., 2003). Thus, activation of mGluR1 and downstream signaling is indispensable for LTD at these synapses. To confirm proper mGluR1 activation following repetitive PF stimulation in TRH-KO mouse PCs, we assessed the generation of slow EPSCs. PFs were stimulated with five pulses at 100 Hz in the presence of NBQX to block AMPA receptor-mediated fast EPSCs. The amplitude of the evoked slow EPSC was plotted against the increasing electrical stimulation (**Figure 4C**). There were no statistically significant differences in the slow EPSC amplitude between TRH-KO mice and their WT littermates. These results suggest that TRH deficiency had no influence on the activation of mGluR1 in PCs.

Rescue of Cerebellar LTD Defects by Exogenous TRH

Next, we examined whether failure of LTD induction in TRH-KO mice could be restored by exogenous TRH. Bath application of TRH (100 μM) to cerebellar slices from TRH-KO mice did not influence the PF EPSC amplitude (**Figures 5A,B**). However, PF stimulation paired with depolarization of the PC recording effectively induced LTD (**Figures 5C,D**, KO + TRH: 72.7 ± 5.9%, P = 0.011). Similar bath application of TRH to cerebellar slices from WT mice had no significant effect on LTD expression and the degree of PF EPSC depression (**Figures 5C,D**, WT: 82.2 ± 4.5%, WT + TRH: 74.7 ± 10.3%,

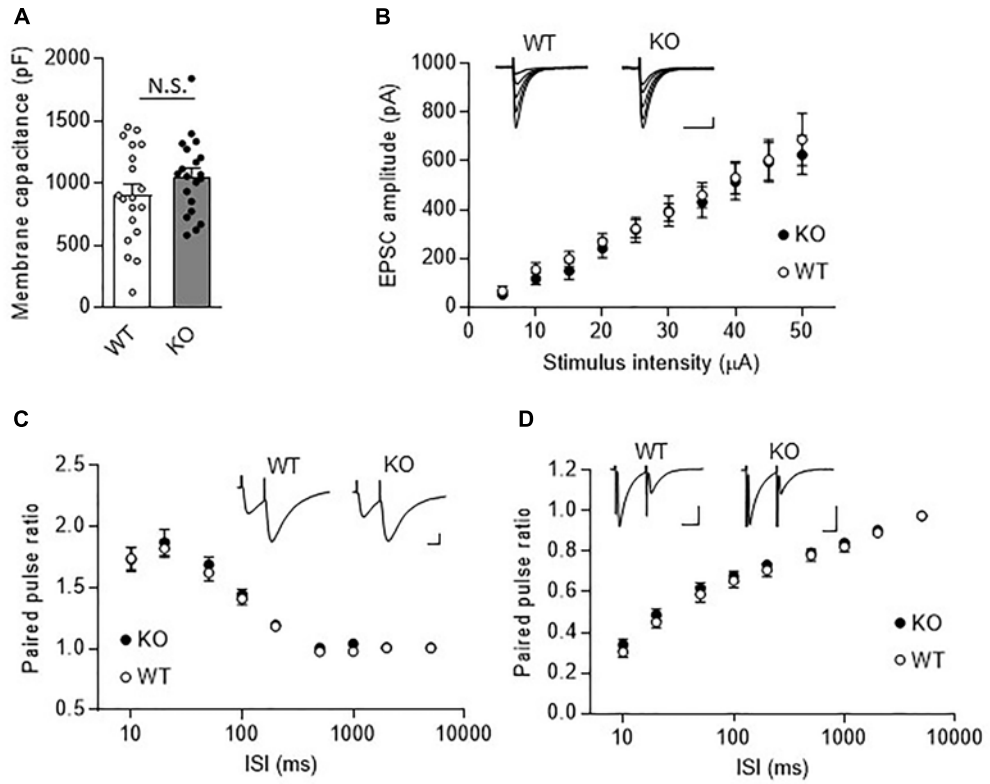

FIGURE 3 | Normal fast synaptic transmission and short-term synaptic plasticity in TRH-KO mouse PCs. **(A)** Membrane capacitance in PCs from TRH-KO mice and their WT littermates (KO: 20 PCs from four mice, WT: 19 PCs from four mice). N.S., no significant difference as determined using Welch's *t*-test. **(B)** Graph depicting the average sizes of PF EPSC amplitudes against the intensity of stimulus delivered to PFs (KO: 9 PCs from four mice, WT: 10 PCs from four mice). Representative traces of EPSCs at various stimulus intensities (5–50 μA) are presented above the graph. Scale bar: 100 pA, 50 ms. **(C,D)** Averaged graphs showing the PPF ratios of PF EPSCs **(C)** and the PPD ratios of CF EPSCs **(D)** determined based on the responses evoked by two stimuli with various interstimulus intervals. The PPF and PPD ratios were measured as the second EPSC amplitude normalized to the first EPSC amplitude. Representative traces for stimulation with a 20-ms interstimulus interval are presented above the graph. CF, climbing fiber; EPSC, excitatory postsynaptic current; KO, knock-out; PF, parallel fiber; PPD, paired-pulse depression; PPF, paired-pulse facilitation; WT, wild-type.

TABLE 1 | PF and CF EPSC kinetics were normal in TRH-KO mouse PCs.

	PF EPSC		CF EPSC	
	Rise (ms)	**Decay (ms)**	**Rise (ms)**	**Decay (ms)**
WT	2.59 ± 0.13	14.25 ± 1.15	0.65 ± 0.08	9.29 ± 1.04
KO	2.69 ± 0.16	16.25 ± 1.09	0.61 ± 0.05	8.40 ± 0.47
P-value	0.65	0.22	0.72	0.45

Statistically significant differences were determined using Welch's t-test. EPSC, excitatory postsynaptic current; KO, knock-out; PF, parallel fiber; WT, wild-type.

P = 0.528). These results suggest that absence of LTD in the TRH-KO mice were likely due to an absence of TRH signaling, which was restored by application of exogenous TRH.

Involvement of NO-cGMP Pathway in TRH-Mediated Rescue of LTD

In the cerebellar cortex, TRH receptors (TRH-R2) are expressed in granule cells and molecular layer interneurons, but not in PCs (Heuer et al., 2000), while TRH was shown to increase cGMP in PCs (Mao et al., 1975; Mailman et al., 1979; Schlichter et al., 1980). NO is a possible mediator of the trans-synaptic event. NO is synthesized by neuronal NO synthase, which is selectively expressed in granule cells and molecular layer interneurons (Vincent and Kimura, 1992; Rodrigo et al., 1994; Schilling et al., 1994; Ihara et al., 2006). Thus, it is assumed that NO, which is produced in these cells upon TRH receptor activation, diffuses into dendritic spines of PCs, and activates a guanylyl cyclase to synthesize cGMP. However, considering the highly bioactive nature of TRH, different mechanisms may contribute to the rescue of cerebellar LTD by exogenous TRH in TRH-KO mice. To clarify this, TRH was perfused to cerebellar slices, with NO production blocked by L-NAME, a cell-permeable NO synthase blocker. Bath application of L-NAME (100 μM) did not affect the amplitude of PF EPSC (**Figures 6A,B**). However, TRH-mediated rescue of LTD was completely blocked by L-NAME (**Figures 6C,D**). Next, we applied 30 μM 8-bromo-cGMP, a cell permeable analog of cGMP to cerebellar slices in the absence of exogenous TRH. This concentration of 8-bromo-cGMP did not affect PF EPSC amplitude (**Figures 7A,B**). Conjunctive

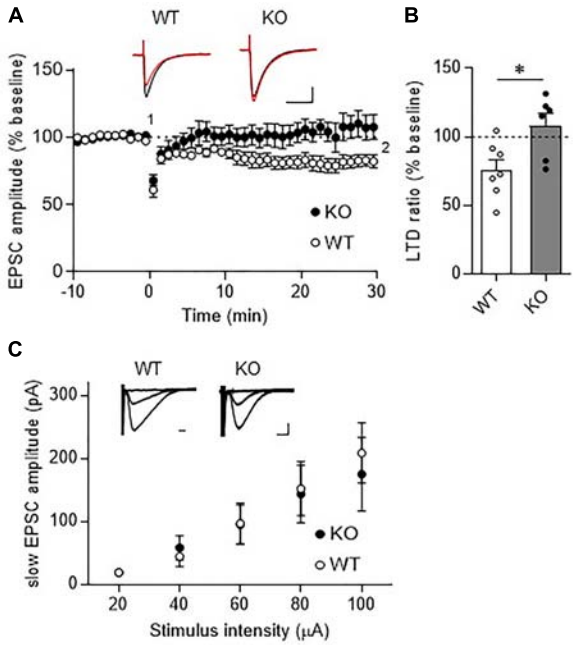

FIGURE 4 | Absence of LTD in TRH-KO mice. **(A)** Time course depicting PF EPSC amplitudes before and after a conjunctive stimulation (KO: six PCs from four mice, WT: eight PCs from five mice). Representative traces before (1) and 30 min after (2) the conjunctive stimulation is shown as black and red lines. Scale bar: 100 pA, 50 ms. **(B)** Percent ratios of PF EPSC amplitudes 30 min after a conjunctive stimulation relative to those before the conjunctive stimulation. Asterisks indicate statistically significant differences as determined using Welch's *t*-test (*$P < 0.05$). **(C)** Input–output graph showing slow EPSC amplitudes against the intensity of stimulus delivered to PFs. Representative traces of slow EPSCs at 20 μA, 60 μA, and 100 μA stimulus intensity are presented above the graph. Scale bar: 100 pA, 200 ms (WT: eight PCs from four mice, KO: seven PCs from three mice). EPSC, excitatory postsynaptic current; KO, knock-out; LTD, long-term depression; PF, parallel fiber; WT, wild-type.

stimulation was then applied to induce LTD, resulting in robust LTD without application of exogenous TRH (**Figures 7C,D**, KO + 8-bromo-cGMP: 78.9 ± 9.0%, $P = 0.048$). These results suggest the involvement of the NO-cGMP pathway in the TRH-mediated rescue of cerebellar LTD in TRH-KO mice.

No Significant Alteration in sIPSCs and mIPSCs in TRH-KO Mice

Previous studies have shown that TRH increased the frequency of $GABA_A$ receptor-mediated sIPSCs without affecting mIPSCs in the hippocampus (Deng et al., 2006) and lateral hypothalamus (Zhang and Van Den Pol, 2012). Since TRH receptors are expressed in molecular layer interneurons (Heuer et al., 2000), inhibitory synaptic transmission from molecular layer interneurons to PCs may be altered in TRH-KO mice. To test this possibility, we recorded sIPSCs and mIPSCs from PCs, and compared the amplitudes and frequencies between KO mice and their WT littermates. However, there were no significant differences in both the amplitudes ($P = 0.437$) and frequencies ($P = 0.893$) of sIPSCs between the genotypes ($n = 3$ mice, 9 PCs in each group) (**Supplementary Figures S2A–C**). Next, we recorded mIPSCs after perfusing TTX. Again, there were no significant differences in both the amplitudes ($P = 0.687$) and frequencies ($P = 0.966$) of mIPSCs between the genotypes ($n = 3$ mice, 7 PCs in each group) (**Supplementary Figures S2D–F**).

DISCUSSION

Here, we report that TRH-KO mice have cerebellar LTD and motor learning deficits, without obvious morphological changes in the cerebellum. Notably, these impairments were significantly rescued by treatment with exogenous TRH. These results suggest that TRH-KO mouse cerebella lack TRH signaling, but are structurally normal. Therefore, supplementation to replace the missing TRH reliably reconstitutes defective signaling, resulting in restoration of the aberrant phenotypes.

Thyrotropin-releasing hormone triggers cellular signaling by binding to TRH receptors (Engel and Gershengorn, 2007). There are two types of TRH receptors that have been identified so far (TRH R1 and TRH R2) (O'dowd et al., 2000; Harder et al., 2001). The cerebellar cortex has been reported to contain only TRH R2, which is expressed in granule cells and molecular layer interneurons (Heuer et al., 2000). Systemic administration of TRH was demonstrated to increase the cerebellar cGMP level (Mailman et al., 1979). Since soluble guanylyl kinase, which is required for production of cGMP, is present in PCs, areas of the brain containing TRH receptors (granule cells and molecular layer interneurons) are separate from those of cGMP production (PCs). One idea proposed to reconcile the cellular inconsistency is that NO, which is produced following TRH R2 activation, acts as an anterograde messenger.

Neuronal NO synthetase is expressed in both granule cells and molecular layer interneurons (Vincent and Kimura, 1992; Rodrigo et al., 1994; Schilling et al., 1994; Ihara et al., 2006). NO produced in these cells has been shown to diffuse into neighboring PC dendrites, where it activates soluble guanylyl cyclase, leading to production of cGMP and subsequent activation of PKG in PCs (Contestabile, 2012).

Long-term depression at PF-PC synapses is caused by stimulation of PFs coupled with that of a CF. Since CFs convey error signals associated with inappropriate motor performance to PCs (Maekawa and Simpson, 1973), LTD is thought to contribute to motor learning by suppressing PF-PC synaptic transmissions that are related to inappropriate actions (Ito, 2001). Conjunctive stimulation for LTD induction leads to spillover of glutamate from the synaptic cleft between a PF and a PC, which in turn leads to activation of mGluR1 and PKC activation (**Figure 8**) (Hirai and Kano, 2018). CF-mediated depolarization leads to striking increases in the intracellular Ca^{2+} level through activation of voltage-gated Ca^{2+} channels and strengthens PKC activity. Activated PKC in turn phosphorylates the intracellular domain of the GluA2 subunit at Ser880 (Matsuda et al., 1999), leading to endocytosis of postsynaptic AMPA receptors and attenuation of synaptic strength (LTD) (**Figure 8**) (Matsuda et al., 2000; Hirai, 2001; Chung et al., 2003). It has been reported that NO

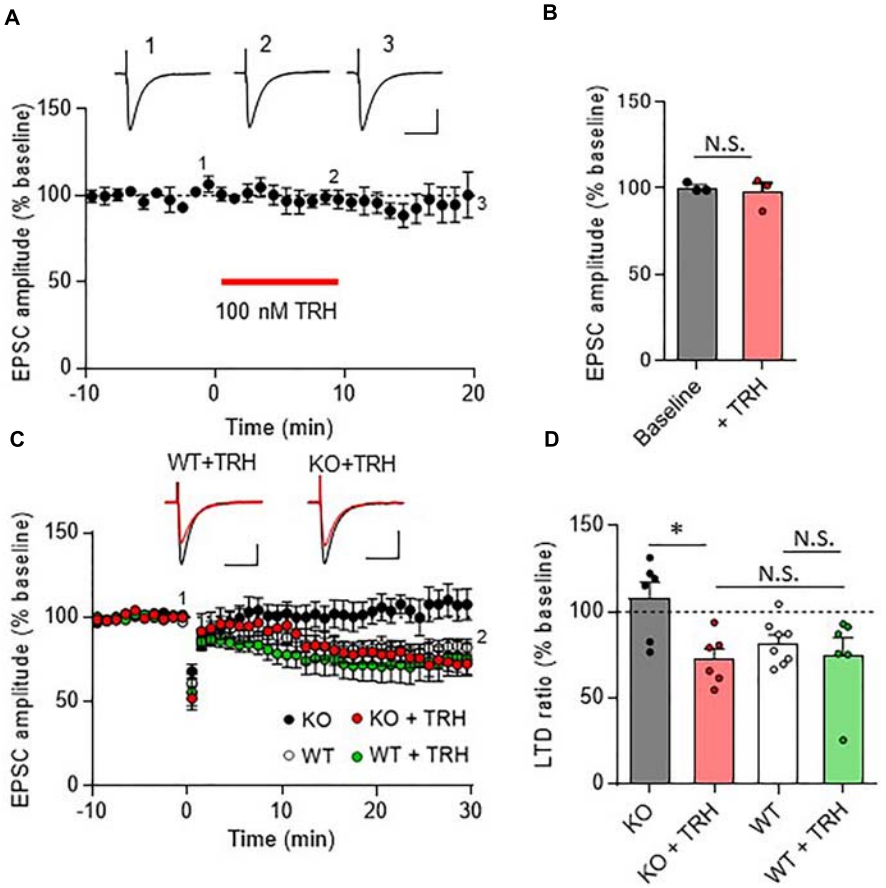

FIGURE 5 | Rescue of cerebellar LTD in TRH-deficient mice following treatment with exogenous TRH. **(A)** No influence of TRH on the amplitudes of PF EPSCs elicited in TRH-KO mouse PCs. TRH (100 nM) was bath-applied to cerebellar slices for 10 min, as indicated by the red horizontal bar (n = 3 PCs from three TRH-KO mice). Representative traces before (1) and 10 min after (2) the TRH application and washout (3) are shown. Scale bar: 100 pA, 50 ms. **(B)** Summary graph showing the effects of TRH on EPSCs, which were calculated by dividing the averaged EPSC amplitude values obtained from –5 to 0 min or 5 to 10 min by those obtained from –10 to 0 min. **(C)** Cerebellar LTD in the presence of TRH (100 nM). Conjunctive stimulation used for LTD induction was performed at time 0 (KO: six PCs from four mice, WT: eight PCs from five mice, KO + TRH: six PCs from four mice, WT + TRH: six PCs from three mice). Representative traces before (1) and 30 min after (2) the conjunctive stimulation is shown as black and red lines, respectively. Scale bar: 100 pA, 50 ms. **(D)** Summary graph showing PF EPSC amplitudes 30 min after conjunctive stimulation relative to the baseline (100%). Data from the control KO mice and those from the control WT mice **(C,D)**, which are the same as those shown in other figures, are presented for comparison. $^*P < 0.05$, as determined using Welch's t-test. EPSC, excitatory postsynaptic current; KO, knock-out; LTD, long-term depression; N.S., not significant; PF, parallel fiber; WT, wild-type.

is indispensable for cerebellar LTD (Ito and Karachot, 1990; Lev-Ram et al., 1995; Contestabile, 2012).

As discussed above, NO, which is produced by neuronal NO synthase-positive neurons (granule cells and some molecular layer interneurons), readily diffuses into PCs and activates PKG via production of cGMP (**Figure 8**). A previous study has proposed that G-substrate, which is abundantly and exclusively expressed in PCs, is the primary substrate for PKG (Detre et al., 1984). G-substrate phosphorylation by PKG then leads to suppression of protein phosphatase 2A (PP2A) activity (**Figure 8**) (Endo et al., 1999). Since PP2A dephosphorylates AMPA receptors and counteracts PKC, suppression of PP2A eventually enhances AMPA receptor phosphorylation, leading to LTD (Launey et al., 2004). Thus, NO-cGMP-PKG pathway plays a critical role in LTD by damping the PP2A activity, and consequently, facilitating AMPA receptor phosphorylation.

In conjunction with previous studies that TRH increased cGMP in the cerebellum (Mao et al., 1975; Mailman et al., 1979; Schlichter et al., 1980), we propose that TRH has a role to upregulate the basal cGMP content in PCs. In our proposed model, loss of TRH results in decreased cGMP content in PCs, and therefore, conjunctive stimulation is not sufficient to exceed a threshold of cGMP for LTD induction. Exogenous TRH or 8-bromo-cGMP compensates the loss of cGMP in KO mouse PCs, and thus, additional increase in cGMP by subsequent conjunctive stimulation can reach the threshold, and rescue LTD. However, exogenous TRH with conjunctive stimulation in the presence of L-NAME fails to upregulate cGMP content in KO PCs, because of the inhibition of NO production, resulting in failure of LTD expression.

Insufficient activation of PKC and the resultant failure of LTD has been reported in mouse models of spinocerebellar ataxia type

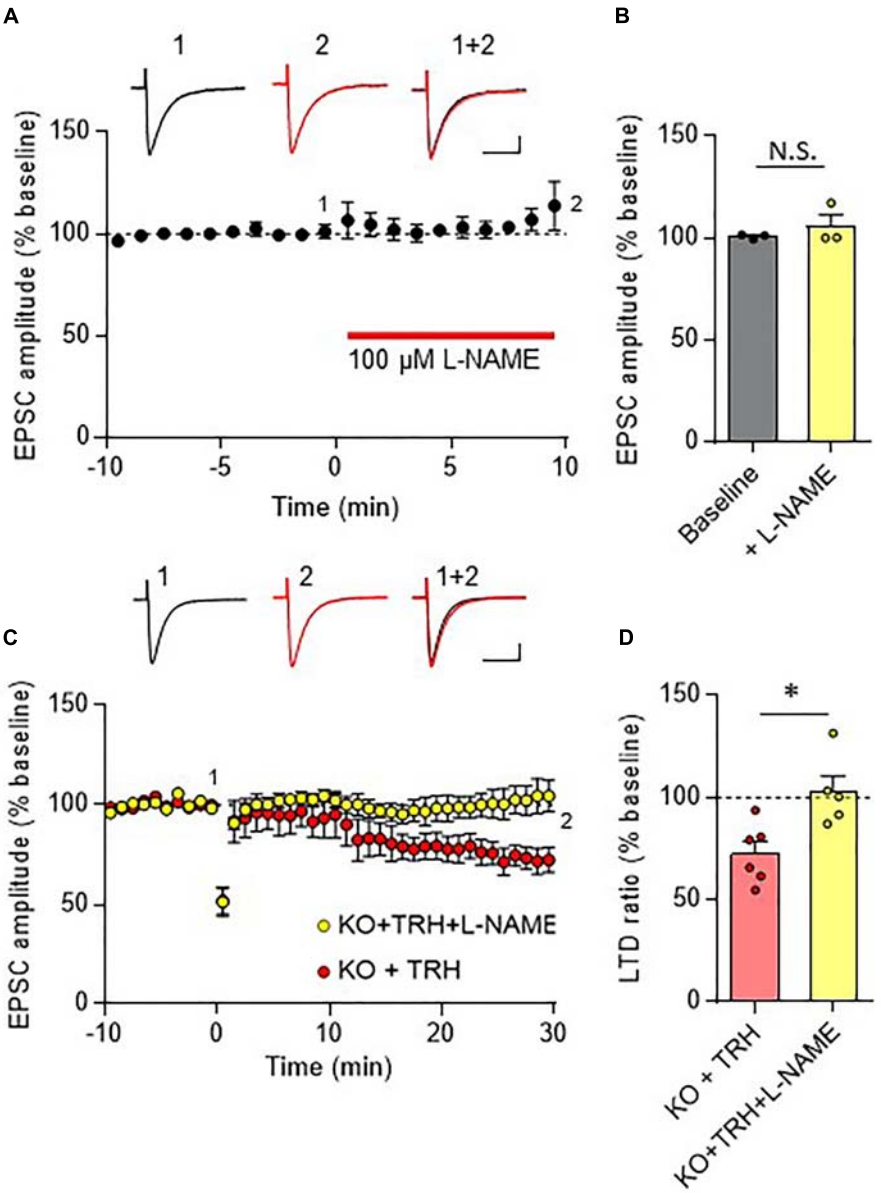

FIGURE 6 | Inhibition of the NO synthase eliminates the TRH-mediated rescue of cerebellar LTD. **(A)** Bath application of L-NAME, a cell-permeable NO synthase inhibitor, had no influence on PF EPSC. Representative traces before (1) and 10 min after (2) the L-NAME treatment are shown as black and red lines, respectively. Superimposed images (1 + 2) are also shown. Scale bar: 100 pA, 50 ms. **(B)** Summary graph showing the effects of 8-bromo-cGMP on EPSCs, which were calculated by dividing the averaged EPSC amplitude values obtained from –5 to 0 min or 5 to 10 min by those obtained from –10 to 0 min. **(C)** TRH fails to induce LTD in PCs from KO mice in the presence of 100 μM L-NAME. Representative traces before (1) and 30 min after (2) the conjunctive stimulation is shown as black and red lines, respectively. Superimposed images (1 + 2) are also shown. Scale bar: 100 pA, 50 ms. **(D)** Summary graph showing depression ratios, which were calculated by dividing the averaged EPSC amplitude values obtained from 25 to 30 min by those obtained from –10 to 0 min (KO + TRH: six PCs from four mice, KO + TRH + L-NAME: five PCs from three mice). Data from KO mouse cerebellum treated only with TRH (KO + TRH) **(C,D)**, which are the same as those shown in the other figures, are presented for comparison. Asterisks indicate statistically significant differences, as determined using Welch's *t*-test. $^*P < 0.05$. EPSC, excitatory postsynaptic current; KO, knock-out; L-NAME, *N*-nitro-L-arginine methyl ester; LTD, long-term depression; PF, parallel fiber.

1 (SCA1) (Shuvaev et al., 2017) and SCA14 (Shuvaev et al., 2011). In addition, a number of previous studies have suggested that impairment of the mGluR1-PKC pathway (and aberrant PKC activation) underlie the pathologies of different types of SCAs, such as SCA3, SCA5, and SCA15/16, as reviewed recently (Hirai and Kano, 2018). It is therefore likely that treatment with TRH, which was suggested to enhance the NO-cGMP-PKG pathway in PCs, could restore cerebellar LTD by suppressing PP2A activity and eventually restoring AMPA receptor phosphorylation. In this context, it would be intriguing to investigate whether treatment with exogenous TRH or taltirelin, which is a synthetic TRH analog, could restore cerebellar LTD in mouse models of SCA

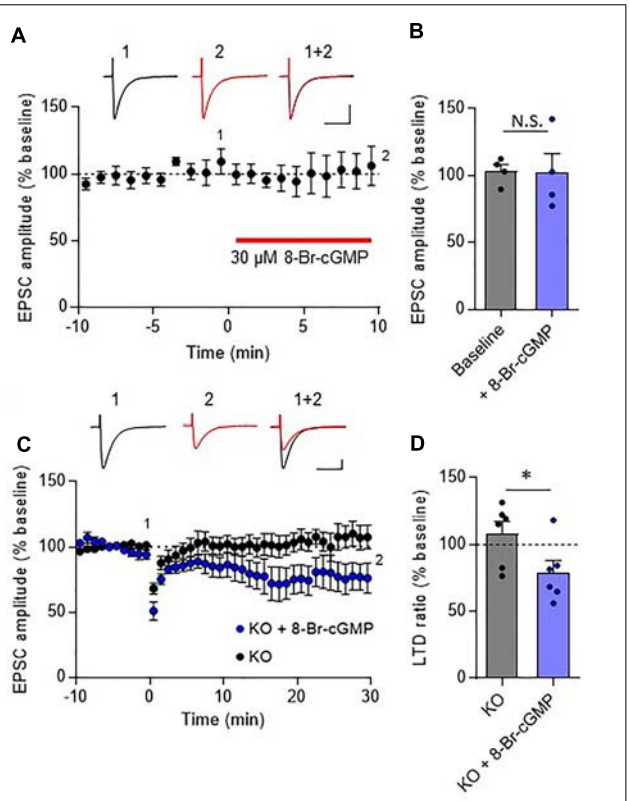

FIGURE 7 | Rescue of cerebellar LTD in TRH-deficient mice by 8-bromo-cGMP treatment. **(A)** Effects of 8-bromo-cGMP on baseline PF EPSCs. Thirty micromolar 8-bromo-cGMP was bath-applied to cerebellar slices for 10 min, as indicated using the red horizontal bar (n = 4 PCs from three mice). Representative traces before (1) and 10 min after (2) the 8-bromo-cGMP treatment are shown as black and red lines, respectively. Superimposed images (1 + 2) are also shown. Scale bar: 100 pA, 50 ms. **(B)** Summary graph showing the effects of 8-bromo-cGMP on EPSCs, which were calculated by dividing the averaged EPSC amplitude values obtained from –5 to 0 min or 5 to 10 min by those obtained from –10 to 0 min. **(C)** Robust LTD in PCs from KO mice in the presence of 30 μM 8-bromo-cGMP. Representative traces before (1) and 30 min after (2) the conjunctive stimulation is shown as black and red lines, respectively. Superimposed images (1 + 2) are also shown. Scale bar: 100 pA, 50 ms. **(D)** Summary graph showing depression ratios, which were calculated by dividing the averaged EPSC amplitude values obtained from 25 to 30 min by those obtained from –10 to 0 min (KO: six PCs from four mice, KO + 8-bromo-cGMP: six PCs from three mice). Data from control KO mice **(C,D)**, which are the same as those shown in the other figures, are presented for comparison. Asterisks indicate statistically significant differences, as determined using Welch's t-test. *$P < 0.05$. EPSC, excitatory postsynaptic current; KO, knock-out; LTD, long-term depression; PF, parallel fiber.

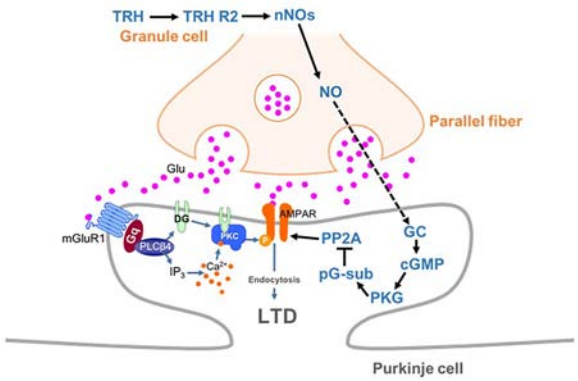

FIGURE 8 | Schema depicting proposed signaling cascades regulating cerebellar LTD. AMPA receptors are phosphorylated by PKC in mGluR1-dependent manner. TRH produces NO in granule cells (and molecular layer interneurons), which diffuses into PCs. NO produces cGMP via activation of the guanylyl cyclase, leading to activation of PKG. Activated PKG phosphorylates G-substrate, which in turn suppresses PP2A. Since PP2A counteracts PKC in terms of AMPA receptor phosphorylation, suppression of PP2A facilitates LTD through enhancement of AMPA receptor phosphorylation. cGMP, cyclic guanosine monophosphate; GC, guanylyl cyclase; LTD, long-term depression; nNOs, neuronal NO synthase; pG-sub, phosphor-G-substrate; PP2A, protein phosphatase 2A; PKG, cGMP-dependent protein kinase G; TRH, thyrotropin-releasing hormone; TRH R2, TRH receptor 2.

demonstrated to exhibit defects in cerebellar LTD (Shuvaev et al., 2011, 2017).

In addition to LTD at PF to PC synapses, recent studies have proposed a significant contribution of two different forms of synaptic plasticity to cerebellar motor learning, long-term potentiation (LTP) at PF to PC synapses (Grasselli and Hansel, 2014; Gutierrez-Castellanos et al., 2017) and rebound potentiation (RP) at molecular layer interneurons to PC synapses (Hirano and Kawaguchi, 2014; Hirano, 2018). Since NO is also involved in the induction of postsynaptic LTP (Lev-Ram et al., 2002; Kakegawa and Yuzaki, 2005), LTP may be impaired in TRH-KO mouse cerebellum. Meanwhile, since the mild tertiary hypothyroidism was observed in the TRH-KO mice (Yamada et al., 1997), lower levels of thyroid hormone likely alter the intrinsic excitability of PCs, which could affect LTP and/or RP. Moreover, it cannot be excluded that rescue of motor learning in TRH-KO mice by exogenous TRH was attained by upregulation of thyroid hormone. Thus, considering a wide variety of physiological actions of TRH, mechanisms other than cerebellar LTD may underlie the motor learning deficit observed in TRH-KO mice. Further studies will be necessary for extensive understanding of TRH functions in the cerebellum.

AUTHOR CONTRIBUTIONS

MW designed and performed the experiments, analyzed the data, and drafted the manuscript. YM performed immunohistochemistry. YN, AO, and MY provided the TRH KO mice, contributed to the behavioral experiments, and discussed the study design. HH designed and supervised the experiments and wrote the manuscript.

FUNDING

This work was supported by JSPS KAKENHI (Grant Nos. 15H04254, 16K15477, and 18H02521 to HH, and 17K14929 to YM) and Research on Measures for Intractable Diseases (Ataxic

Diseases and Neurodegenerative Diseases) from the Ministry of Health, Labor and Welfare (to HH).

SUPPLEMENTARY MATERIAL

The Supplementary Material for this article can be found online at: https://www.frontiersin.org/articles/10.3389/fncel.2018.00490/full#supplementary-material

FIGURE S1 | Systemic application of TRH restores rotarod performance of TRH-KO mice to the level comparable to that of their WT littermates. **(A)** Schema showing the experimental procedure. TRH-KO and WT mice received TRH (6 ml/kg BW, 5 mg/ml) or the same volume of saline intraperitoneally (i.p.). The effects of the treatment were tested 10 min after the injection using the rotarod test. **(B)** Results of the rotarod test. Mice were subjected to four trials (n = 9 mice in each group). There are statistically no significant differences among four groups, as determined using repeated-measures analysis of variance. KO, knock-out; WT, wild-type.

FIGURE S2 | No significant difference in the amplitude and frequency of both sIPSCs and mIPSCs recorded in PCs between KO mice and their WT littermates. **(A)** sIPSC traces recorded from WT mouse (left) or KO (right) mouse PCs. **(B,C)** Graphs showing averaged medial amplitudes **(B)** and inter event intervals **(C)** of sIPSCs recorded from TRH-KO mice and their WT littermates (both genotypes, n = 9 PCs from three mice). **(D)** mIPSC traces recorded from WT mouse (left) or KO (right) mouse PCs in the absence (upper) and presence (lower) of picrotoxin (100 μM). **(E,F)** Graphs showing averaged medial amplitudes **(E)** and inter event intervals **(F)** of mIPSCs recorded from TRH-KO mice and their WT littermates (both genotypes, n = 7 PCs from three mice). No statistically significant difference was detected using the Welch's t-test. Scale bar: 50 pA and 1 s for **(A,D)**. KO, knock-out; mIPSCs, miniature inhibitory postsynaptic currents; N.S., not significant; PTX, picrotoxin; sIPSCs, spontaneous inhibitory postsynaptic currents; WT, wild-type.

REFERENCES

Bastian, A. J. (2011). Moving, sensing and learning with cerebellar damage. *Curr. Opin. Neurobiol.* 21, 596–601. doi: 10.1016/j.conb.2011.06.007

Bellebaum, C., and Daum, I. (2007). Cerebellar involvement in executive control. *Cerebellum* 6, 184–192. doi: 10.1080/14734220601169707

Chung, H. J., Steinberg, J. P., Huganir, R. L., and Linden, D. J. (2003). Requirement of AMPA receptor GluR2 phosphorylation for cerebellar long-term depression. *Science* 300, 1751–1755. doi: 10.1126/science.1082915

Contestabile, A. (2012). Role of nitric oxide in cerebellar development and function: focus on granule neurons. *Cerebellum* 11, 50–61. doi: 10.1007/s12311-010-0234-1

Deng, P. Y., Porter, J. E., Shin, H. S., and Lei, S. (2006). Thyrotropin-releasing hormone increases GABA release in rat hippocampus. *J. Physiol.* 577, 497–511. doi: 10.1113/jphysiol.2006.118141

Detre, J. A., Nairn, A. C., Aswad, D. W., and Greengard, P. (1984). Localization in mammalian brain of G-substrate, a specific substrate for guanosine 3',5'-cyclic monophosphate-dependent protein kinase. *J. Neurosci.* 4, 2843–2849. doi: 10.1523/JNEUROSCI.04-11-02843.1984

Endo, S., Suzuki, M., Sumi, M., Nairn, A. C., Morita, R., Yamakawa, K., et al. (1999). Molecular identification of human G-substrate, a possible downstream component of the cGMP-dependent protein kinase cascade in cerebellar Purkinje cells. *Proc. Natl. Acad. Sci. U.S.A.* 96, 2467–2472. doi: 10.1073/pnas.96.5.2467

Engel, S., and Gershengorn, M. C. (2007). Thyrotropin-releasing hormone and its receptors–a hypothesis for binding and receptor activation. *Pharmacol. Ther.* 113, 410–419. doi: 10.1016/j.pharmthera.2006.09.004

Grasselli, G., and Hansel, C. (2014). Cerebellar long-term potentiation: cellular mechanisms and role in learning. *Int. Rev. Neurobiol.* 117, 39–51. doi: 10.1016/B978-0-12-420247-4.00003-8

Gutierrez-Castellanos, N., Da Silva-Matos, C. M., Zhou, K., Canto, C. B., Renner, M. C., Koene, L. M. C., et al. (2017). Motor learning requires purkinje cell synaptic potentiation through activation of AMPA-receptor subunit GluA3. *Neuron* 93, 409–424. doi: 10.1016/j.neuron.2016.11.046

Harder, S., Lu, X., Wang, W., Buck, F., Gershengorn, M. C., and Bruhn, T. O. (2001). Regulator of G protein signaling 4 suppresses basal and thyrotropin releasing-hormone (TRH)-stimulated signaling by two mouse TRH receptors, TRH-R(1) and TRH-R(2). *Endocrinology* 142, 1188–1194. doi: 10.1210/endo.142.3.8019

Heuer, H., Schafer, M. K., O'donnell, D., Walker, P., and Bauer, K. (2000). Expression of thyrotropin-releasing hormone receptor 2 (TRH-R2) in the central nervous system of rats. *J. Comp. Neurol.* 428, 319–336. doi: 10.1002/1096-9861(20001211)428:2<319::AID-CNE10>3.0.CO;2-9

Hirai, H. (2001). Modification of AMPA receptor clustering regulates cerebellar synaptic plasticity. *Neurosci. Res.* 39, 261–267. doi: 10.1016/S0168-0102(00)00237-6

Hirai, H., and Kano, M. (2018). Type 1 metabotropic glutamate receptor and its signaling molecules as therapeutic targets for the treatment of cerebellar disorders. *Curr. Opin. Pharmacol.* 38, 51–58. doi: 10.1016/j.coph.2018.02.002

Hirano, T. (2018). Regulation and interaction of multiple types of synaptic plasticity in a purkinje neuron and their contribution to motor learning. *Cerebellum* [Epub ahead of print] doi: 10.1007/s12311-018-0963-0.

Hirano, T., and Kawaguchi, S. Y. (2014). Regulation and functional roles of rebound potentiation at cerebellar stellate cell-Purkinje cell synapses. *Front. Cell. Neurosci.* 8:42. doi: 10.3389/fncel.2014.00042

Ihara, H., Kuwamura, M., Atsuta, M., Nihonmatsu, I., Okada, T., Mukamoto, M., et al. (2006). Expression of neuronal nitric oxide synthase variant, nNOS-mu, in rat brain. *Nitric Oxide* 15, 13–19. doi: 10.1016/j.niox.2005.11.011

Ito, M. (2001). Cerebellar long-term depression: characterization, signal transduction, and functional roles. *Physiol. Rev.* 81, 1143–1195. doi: 10.1152/physrev.2001.81.3.1143

Ito, M., and Karachot, L. (1990). Messengers mediating long-term desensitization in cerebellar purkinje cells. *Neuroreport* 1, 129–132. doi: 10.1097/00001756-199010000-00012

Kakegawa, W., and Yuzaki, M. (2005). A mechanism underlying AMPA receptor trafficking during cerebellar long-term potentiation. *Proc. Natl. Acad. Sci. U.S.A.* 102, 17846–17851. doi: 10.1073/pnas.0508910102

Launey, T., Endo, S., Sakai, R., Harano, J., and Ito, M. (2004). Protein phosphatase 2A inhibition induces cerebellar long-term depression and declustering of synaptic AMPA receptor. *Proc. Natl. Acad. Sci. U.S.A.* 101, 676–681. doi: 10.1073/pnas.0302914101

Lev-Ram, V., Makings, L. R., Keitz, P. F., Kao, J. P., and Tsien, R. Y. (1995). Long-term depression in cerebellar Purkinje neurons results from coincidence of nitric oxide and depolarization-induced Ca2+ transients. *Neuron* 15, 407–415. doi: 10.1016/0896-6273(95)90044-6

Lev-Ram, V., Wong, S. T., Storm, D. R., and Tsien, R. Y. (2002). A new form of cerebellar long-term potentiation is postsynaptic and depends on nitric oxide but not cAMP. *Proc. Natl. Acad. Sci. U.S.A.* 99, 8389–8393. doi: 10.1073/pnas.122206399

Libbey, J. E., Hanak, T. J., Doty, D. J., Wilcox, K. S., and Fujinami, R. S. (2016). NBQX, a highly selective competitive antagonist of AMPA and KA ionotropic glutamate receptors, increases seizures and mortality following picornavirus infection. *Exp. Neurol.* 280, 89–96. doi: 10.1016/j.expneurol.2016.04.010

Maekawa, K., and Simpson, J. I. (1973). Climbing fiber responses evoked in vestibulocerebellum of rabbit from visual system. *J. Neurophysiol.* 36, 649–666. doi: 10.1152/jn.1973.36.4.649

Mailman, R. B., Frye, G. D., Mueller, R. A., and Breese, G. R. (1979). Change in brain guanosine 3', 5'-monophosphate (cGMP) content by thyrotropin-releasing hormone. *J. Pharmacol. Exp. Ther.* 208, 169–175.

Mao, C. C., Guidotti, A., and Landis, S. (1975). Cyclic GMP: reduction of cerebellar concentrations in "nervous" mutant mice. *Brain Res.* 90, 335–339. doi: 10.1016/0006-8993(75)90316-9

Matsuda, S., Launey, T., Mikawa, S., and Hirai, H. (2000). Disruption of AMPA receptor GluR2 clusters following long-term depression induction in cerebellar Purkinje neurons. *EMBO J.* 19, 2765–2774. doi: 10.1093/emboj/19.12.2765

Matsuda, S., Mikawa, S., and Hirai, H. (1999). Phosphorylation of serine-880 in GluR2 by protein kinase C prevents its C terminus from binding with glutamate receptor-interacting protein. *J. Neurochem.* 73, 1765–1768. doi: 10.1046/j.1471-4159.1999.731765.x

Nakamura, T., Honda, M., Kimura, S., Tanabe, M., Oda, S., and Ono, H. (2005). Taltirelin improves motor ataxia independently of monoamine levels in rolling mouse nagoya, a model of spinocerebellar atrophy. *Biol. Pharm. Bull.* 28, 2244–2247. doi: 10.1248/bpb.28.2244

Nillni, E. A., and Sevarino, K. A. (1999). The biology of pro-thyrotropin-releasing hormone-derived peptides. *Endocr. Rev.* 20, 599–648. doi: 10.1210/er.20.5.599

O'dowd, B. F., Lee, D. K., Huang, W., Nguyen, T., Cheng, R., Liu, Y., et al. (2000). TRH-R2 exhibits similar binding and acute signaling but distinct regulation and anatomic distribution compared with TRH-R1. *Mol. Endocrinol.* 14, 183–193. doi: 10.1210/me.14.1.183

Paulson, H. L., Shakkottai, V. G., Clark, H. B., and Orr, H. T. (2017). Polyglutamine spinocerebellar ataxias - from genes to potential treatments. *Nat. Rev. Neurosci.* 18, 613–626. doi: 10.1038/nrn.2017.92

Peterburs, J., and Desmond, J. E. (2016). The role of the human cerebellum in performance monitoring. *Curr. Opin. Neurobiol.* 40, 38–44. doi: 10.1016/j.conb.2016.06.011

Rodrigo, J., Springall, D. R., Uttenthal, O., Bentura, M. L., Abadia-Molina, F., Riveros-Moreno, V., et al. (1994). Localization of nitric oxide synthase in the adult rat brain. *Philos. Trans. R. Soc. Lond. B Biol. Sci.* 345, 175–221. doi: 10.1098/rstb.1994.0096

Schilling, K., Schmidt, H. H., and Baader, S. L. (1994). Nitric oxide synthase expression reveals compartments of cerebellar granule cells and suggests a role for mossy fibers in their development. *Neuroscience* 59, 893–903. doi: 10.1016/0306-4522(94)90293-3

Schlichter, D. J., Detre, J. A., Aswad, D. W., Chehrazi, B., and Greengard, P. (1980). Localization of cyclic GMP-dependent protein kinase and substrate in mammalian cerebellum. *Proc. Natl. Acad. Sci. U.S.A.* 77, 5537–5541. doi: 10.1073/pnas.77.9.5537

Shuvaev, A. N., Horiuchi, H., Seki, T., Goenawan, H., Irie, T., Iizuka, A., et al. (2011). Mutant PKCgamma in spinocerebellar ataxia type 14 disrupts synapse elimination and long-term depression in purkinje cells in vivo. *J. Neurosci.* 31, 14324–14334. doi: 10.1523/JNEUROSCI.5530-10.2011

Shuvaev, A. N., Hosoi, N., Sato, Y., Yanagihara, D., and Hirai, H. (2017). Progressive impairment of cerebellar mGluR signalling and its therapeutic potential for cerebellar ataxia in spinocerebellar ataxia type 1 model mice. *J. Physiol.* 595, 141–164. doi: 10.1113/JP272950

Steiner, A. L., Ferrendelli, J. A., and Kipnis, D. M. (1972). Radioimmunoassay for cyclic nucleotides. 3. effect of ischemia, changes during development and regional distribution of adenosine 3',5'-monophosphate and guanosine 3',5'-monophosphate in mouse brain. *J. Biol. Chem.* 247, 1121–1124.

Vincent, S. R., and Kimura, H. (1992). Histochemical mapping of nitric oxide synthase in the rat brain. *Neuroscience* 46, 755–784. doi: 10.1016/0306-4522(92)90184-4

Yamada, M., Saga, Y., Shibusawa, N., Hirato, J., Murakami, M., Iwasaki, T., et al. (1997). Tertiary hypothyroidism and hyperglycemia in mice with targeted disruption of the thyrotropin-releasing hormone gene. *Proc. Natl. Acad. Sci. U.S.A.* 94, 10862–10867. doi: 10.1073/pnas.94.20.10862

Yamada, M., Satoh, T., and Mori, M. (2003). Mice lacking the thyrotropin-releasing hormone gene: what do they tell us? *Thyroid* 13, 1111–1121.

Yarbrough, G. G. (2003). Fundamental molecular mechanism of the CNS effects of TRH. *Trends Pharmacol. Sci.* 24, 617–618. doi: 10.1016/j.tips.2003.10.001

Zhang, L., Kolaj, M., and Renaud, L. P. (2013). GIRK-like and TRPC-like conductances mediate thyrotropin-releasing hormone-induced increases in excitability in thalamic paraventricular nucleus neurons. *Neuropharmacology* 72, 106–115. doi: 10.1016/j.neuropharm.2013.04.023

Zhang, X., and Van Den Pol, A. N. (2012). Thyrotropin-releasing hormone (TRH) inhibits melanin-concentrating hormone neurons: implications for TRH-mediated anorexic and arousal actions. *J. Neurosci.* 32, 3032–3043. doi: 10.1523/JNEUROSCI.5966-11.2012

Conflict of Interest Statement: The authors declare that the research was conducted in the absence of any commercial or financial relationships that could be construed as a potential conflict of interest.

frontiers in Cellular Neuroscience

MINI REVIEW
published: 12 December 2018
doi: 10.3389/fncel.2018.00492

Biological Sex, Estradiol and Striatal Medium Spiny Neuron Physiology: A Mini-Review

Amanda A. Krentzel[1,2]* *and John Meitzen*[1,2,3,4]

[1] Department of Biological Sciences, North Carolina State University, Raleigh, NC, United States, [2] W. M. Keck Center for Behavioral Biology, North Carolina State University, Raleigh, NC, United States, [3] Center for Human Health and the Environment, North Carolina State University, Raleigh, NC, United States, [4] Comparative Medicine Institute, North Carolina State University, Raleigh, NC, United States

The caudate-putamen, nucleus accumbens core and shell are important striatal brain regions for premotor, limbic, habit formation, reward, and other critical cognitive functions. Striatal-relevant behaviors such as anxiety, motor coordination, locomotion, and sensitivity to reward, all change with fluctuations of the menstrual cycle in humans and the estrous cycle in rodents. These fluctuations implicate sex steroid hormones, such as 17β-estradiol, as potent neuromodulatory signals for striatal neuron activity. The medium spiny neuron (MSN), the primary neuron subtype of the striatal regions, expresses membrane estrogen receptors and exhibits sex differences both in intrinsic and synaptic electrophysiological properties. In this mini-review, we first describe sex differences in the electrophysiological properties of the MSNs in prepubertal rats. We then discuss specific examples of how the human menstrual and rat estrous cycles induce differences in striatal-relevant behaviors and neural substrate, including how female rat MSN electrophysiology is influenced by the estrous cycle. We then conclude the mini-review by discussing avenues for future investigation, including possible roles of striatal-localized membrane estrogen receptors and estradiol.

Keywords: female, estradiol, estrous cycle, spiny projection neurons, caudate-putamen, dorsal striatum, nucleus accumbens, aromatase

OPEN ACCESS

Edited by:
Ying Shen,
Zhejiang University, China

Reviewed by:
Nicola Berretta,
Fondazione Santa Lucia (IRCCS), Italy
Constance Hammond,
Institut National de la Santé et de la Recherche Médicale (INSERM), France
Carola Sales-Carbonell,
B&A Therapeutics, France, in collaboration with reviewer CH

***Correspondence:**
Amanda A. Krentzel
aakrentz@ncsu.edu

Received: *11 September 2018*
Accepted: *30 November 2018*
Published: *12 December 2018*

Citation:
Krentzel AA and Meitzen J (2018) Biological Sex, Estradiol and Striatal Medium Spiny Neuron Physiology: A Mini-Review. Front. Cell. Neurosci. 12:492. doi: 10.3389/fncel.2018.00492

INTRODUCTION

Sex differences in brain structure and function have been described at all levels of biological analysis, from differences in neuronal gene expression to the output of the nervous system, behavior (McCarthy, 2010; Forger, 2016; Arnold, 2017; Grabowska, 2017). Sex is a compelling biological variable that must be considered from single neuron analysis all the way to clinical trials. The striatal regions, including the caudate-putamen and nucleus accumbens core and shell (**Figure 1A**), are sensitive to biological sex and sex steroid hormone fluctuations and signaling in both animals and humans. Although striatal sex and hormone-specific differences have long been documented, the mechanisms by which hormones and sex influence caudate-putamen and accumbens physiology remain active research areas. In this mini-review, we first describe the known sex differences in the physiology of the output neuron of the striatal brain regions, the medium spiny neuron (MSN), in prepubertal rats. We then broaden the discussion to address aspects of how the menstrual cycle in adult female humans and estrous cycle in adult female rats influences striatal-relevant behaviors, and feature select studies providing mechanistic insight. This includes recent data demonstrating

that the estrous cycle modulates MSN physiology. We then end the mini-review by presenting two challenge hypotheses for future investigation, namely, the possible roles of striatal-localized membrane estrogen receptors and neuroestrogen production.

CAUDATE-PUTAMEN AND NUCLEUS ACCUMBENS CORE MSNs EXHIBIT SEX DIFFERENCES BEFORE PUBERTY

MSNs (or alternatively, spiny projection neurons) consist of ∼95% of striatal neurons (Kemp and Powell, 1971; Graveland and DiFiglia, 1985; Gerfen and Surmeier, 2011) and are the major efferent projection neurons. MSNs do not exhibit gross sex differences in soma size or neuron density (Meitzen et al., 2011), and the overall volume of the striatal brain regions does not robustly differ between males and females (Wong et al., 2016). MSNs do exhibit functional electrophysiological properties that differ by striatal subregion and developmental period (**Table 1**). Before puberty, sex differences are present in both intrinsic and synaptic properties of MSNs that is specific to striatal region in rats. Here we define intrinsic properties are those being related to single action potential properties such as threshold, multiple action potential properties such as action potential firing rate as evoked by excitatory current injection, and passive membrane properties such as input resistance. All of these properties are unified in that they help determine how a neuron responds to synaptic input, in other words, the input-output process of the individual neuron. Regarding synaptic properties, here we focus on properties that have been directly investigated in MSN with regards to sex, such as miniature excitatory postsynaptic currents (mEPSC), which provides insight into the strength, number, and sensitivity of glutamatergic synapse. In rat caudate-putamen, MSN excitability is increased in females compared to males, as indicated by an increased evoked action potential to excitatory current injection slope, hyperpolarized threshold, and decreased after hyperpolarization magnitude in females compared to males. There are no differences in mEPSC properties, including frequency, amplitude, and decay (Dorris et al., 2015). Conversely, in the nucleus accumbens core, mEPSC frequency is increased in prepubertal females compared to males and this sex difference exist both pre-puberty and in adults (Cao et al., 2016). This sex difference is organized during the postnatal critical window (P0–P1) and in females can be eliminated by postnatal 17β-estradiol (estradiol) or testosterone exposure (Cao et al., 2016). Estradiol is a type of estrogen, which binds to estrogen receptors. Testosterone can either bind to androgen receptors or be metabolized via the enzyme aromatase into estradiol to in turn act on estrogen receptors. Prepubertal recordings from nucleus accumbens shell did not show any sex differences in MSN electrical properties (Willett et al., 2016), however environmental influences such as stress engender sex differences in synapse markers in adult rodents (Brancato et al., 2017). Together, these studies illustrate heterogeneity of sex-specific mechanisms across the subregions of the striatum (Cao et al., 2018b). Interestingly, sex differences in MSN properties detected in prepubertal rat are different than those detected in prepubertal mouse nucleus accumbens core (Cao et al., 2018a), indicating that sex differences in the development of MSN electrophysiological properties can be species-specific or perhaps mouse strain-dependent. It is also unknown how sex differences and sex steroid sensitivity present across MSN subtypes. This question is an important avenue for future investigations, as differential sensitivity to biological sex across MSN subtypes may have important functional consequences.

THE MENSTRUAL AND ESTROUS CYCLES INFLUENCE STRIATAL-RELATED BEHAVIORS AND DISORDERS IN ADULT FEMALES

In adult female humans, the cyclical fluctuation of estradiol, progesterone, and other hormones is called the menstrual cycle and is ∼28 days long. Plasma estradiol levels peak during the follicular phase, while progesterone levels peak during the luteal phase (Sherman and Korenman, 1975). In adult female rats and mice, this cycle is called the estrous cycle and likewise features repeated hormone changes, but across a ∼4–5 day period (Cora et al., 2015). In rats, plasma estradiol levels rapidly peak during proestrus, after which progesterone levels peak, leading to ovulation and a resulting estrus phase. The diestrus phase, during which hormone levels are generally low, follows the estrus phase (**Figure 1B**).

Regarding behaviors associated with the striatal regions, changes in motor coordination and severity of Parkinson's symptoms, which are controlled by the caudate-putamen, have been associated with the menstrual cycle. The luteal phase, when estradiol and progesterone are high, is associated with more coordination, manual skills, and less L-DOPA-induced dyskinesia (Quinn and Marsden, 1986; Hampson and Kimura, 1988; Hampson, 1990). These findings in menstrual cycle-related behavioral changes generalize to other movement disorders with worsening of symptoms occurring just before and during menses when estradiol and progesterone are lowest (Castrioto et al., 2010). Additionally, changes in anxiety-related behaviors and anxiety-related symptoms which are controlled, in part, by the nucleus accumbens, also occur across the menstrual cycle (Nillni et al., 2011). In general, the extent of documented changes in motor skills and cognitive functions across the human menstrual cycle differs across population characteristics and sampled task-type (Souza et al., 2012).

DOPAMINE AND ESTRADIOL ARE PART OF THE MECHANISM UNDERLYING FEMALE CYCLE-DEPENDENT DIFFERENCES

Animal studies have provided more controlled designs and techniques to understand the mechanisms underlying these sex differences. It has long been documented that the dopamine and estrogen systems interact to influence striatal function (Yoest et al., 2018b). Here we highlight some select pieces of evidence. In female monkeys, during the luteal phase, D2 receptor availability is increased in the caudate-putamen and nucleus accumbens

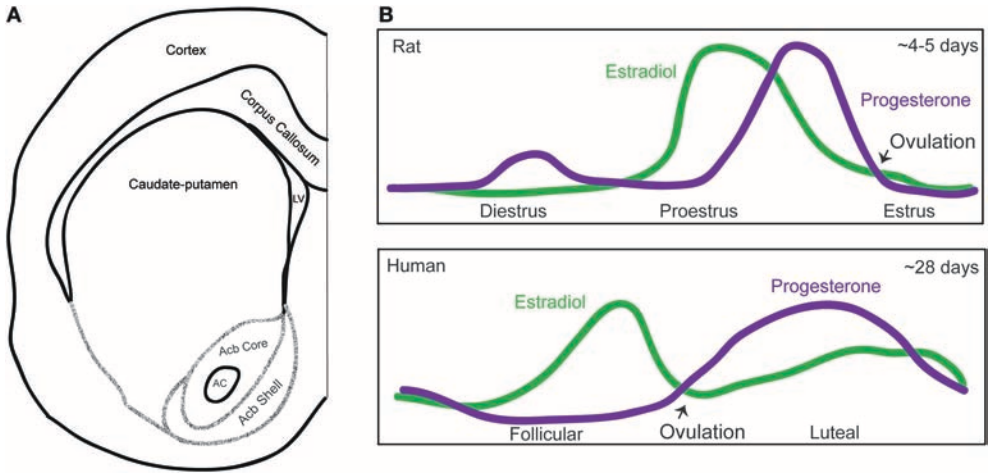

FIGURE 1 | Map of the striatal subregions and female hormone cycling. **(A)** Schematic of a coronal section of one hemisphere of the rat brain depicting the striatal subregions, including the caudate-putamen, nucleus accumbens core, and shell (Interaural ∼10.92–10.80 mm, Bregma ∼1.92–1.80 mm). Acronyms: AC, anterior commissure; Acb, nucleus accumbens; LV, lateral ventricle. The extensive afferent and efferent circuitry of the striatal subregions is not depicted in this schematic, and we refer the reader to the following articles for a review of this topic (Russo and Nestler, 2013; Scofield et al., 2016) **(B)** Graphical depictions of the adult female rat estrous and human menstrual cycle. Purple line indicates progesterone levels and the green line estradiol levels. Over a span of about 4–5 days, rats exhibit a diestrus, proestrus, and estrus phase. There is also a metestrus phase between estrus and diestrus (not pictured). In rats, estradiol levels peak the morning of proestrus, as progesterone levels are rising, and behavioral estrus begins roughly when progesterone levels peak. The human cycle lasts about 28 days, and exhibits a follicular and luteal phase. In humans, estradiol peaks during the follicular phase, and progesterone peaks during the luteal phase.

(Czoty et al., 2009) suggesting that gonadal hormones may influence dopamine (DA) transmission and sensitivity which can promote movement coordination. In rats, females during proestrus and estrus (comparable to luteal phase in humans and monkeys) have higher extracellular DA concentrations than diestrus and ovariectomized females (Xiao and Becker, 1994). Estrous cycle-dependent changes in dopamine signaling have also been observed in mice (Calipari et al., 2017). This may be a mechanism that contributes to changes in locomotion (Becker et al., 1987) and anxiety (Marcondes et al., 2001; Sayin et al., 2014) across estrous cycle in rodents. Gonad-intact and castrated males do not differ, indicating that gonadal hormone influences on striatal release of dopamine are sex-specific (Xiao and Becker, 1994). Estradiol has been proposed as a major hormone to facilitate sex differences. Specific to the caudate-putamen, estradiol promotes motor coordination (Becker et al., 1987; Schultz et al., 2009) and its enhancement of dopamine action is specific to females (Becker, 1990; Xiao and Becker, 1994; Yoest et al., 2014, 2018a). The role of dopamine in regulating MSN electrical properties suggests that MSN properties would likewise differ between males, females, and across the adult female hormone cycle (Nicola et al., 2000).

CYCLICAL FEMALE HORMONE FLUCTUATIONS INDUCE SEX DIFFERENCES IN ADULT MSN ELECTRICAL PROPERTIES

Intrinsic and synaptic electrophysiological properties of MSNs of the caudate-putamen and nucleus accumbens core change with the estrous cycle (Arnauld et al., 1981; Tansey et al., 1983; Proaño et al., 2018). In the caudate-putamen, classic experiments first demonstrated that spontaneous action potential firing rates recorded *in vivo* increased in ovariectomized female rats exogenously exposed to estradiol compared to vehicle-exposed females and males (Arnauld et al., 1981). Later on, using *in vivo* extracellular recording, it was found that nigrostriatal MSNs increased spontaneous action potential generation in female rats during the phases of the estrous cycle associated with high levels of estradiol, or in ovariectomized females exposed to exogenous estradiol compared to animals with low levels of estradiol (Tansey et al., 1983). Other MSN subtypes and striatal interneurons were not tested in this study. The exact electrophysiological, endocrine, and molecular mechanisms driving these changes in electrical activity in the caudate-putamen remain to be elucidated, although this is an area of active research. More detailed data is available for MSNs in the adult female rat nucleus accumbens. In the nucleus accumbens core, during diestrus, when both progesterone and estradiol are low, MSN excitatory synaptic input properties decrease in magnitude while intrinsic excitability increases (Proaño et al., 2018). Specifically, mEPSC frequency and amplitude are decreased compared to other estrous cycle phases, while properties such as action potential rheobase, action potential threshold, input resistance, and resting membrane potential change to increase cellular excitability. Conversely, during proestrus and estrus, which are when estradiol and progesterone increase, and females are sexually receptive, excitatory synaptic input increases and intrinsic excitability decreases. mEPSC frequency and amplitude are increased compared to other estrous cycle phases, aligning with previous work examining excitatory synapse anatomy in

TABLE 1 | Sex differences of electrophysiological properties of medium spiny neurons across striatal subregions in rats.

Electrophysiological property	Developmental stage	Caudate-putamen	Nucleus accumbens core	Nucleus accumbens shell
Intrinsic excitability	Prepubertal	F > M	F = M	F = M
	Adult	?[d]	Cycle determines sex difference[a]	?
Excitatory synaptic input	Prepubertal	F = M	F > M[b]	F = M
	Adult	?	Cycle determines sex difference[a]	?[c]

Gray fill indicates sex and/or cycle dependent differences. Inequality signs indicate relative differences between sexes. "?" indicates complex or no evidence.

[a] Estrous cycle stage determined directionality of sex difference and difference between female estrous stages. Gonadectomy eliminates sex differences.

[b] This sex difference has been shown to be organized by estradiol during masculinization window.

[c] Examination of synapse properties shows divergent evidence of sex differences in non-stressed animals, but an electrophysiological approach in adult animals has not yet been done to our knowledge (as reviewed by Cao et al., 2018b). The adult nucleus accumbens shell exhibits variable sex differences, likely indicating interactions with other environmental influences such as stress (i.e., Brancato et al., 2017).

[d] In adult caudate-putamen, estrous-cycle induced differences in select rat medium spiny neuron action potential generation rates have been reported in vivo, but the underlying cellular electrophysiological mechanisms are not yet documented.

females in these estrous cycle phases solely compared to males (Forlano and Woolley, 2010; Wissman et al., 2012). In contrast, cellular properties such as action potential rheobase, action potential threshold, input resistance, and resting membrane potential change to decrease cellular excitability. When analyzing these properties in gonadectomized males and females, all sex differences disappear (Proaño et al., 2018). This study indicates that adult female hormone cycles are necessary to induce sex differences in adult MSN properties, including excitatory synapse function. Changes in excitatory synaptic properties are consistent with previous anatomical studies in adult rats (Forlano and Woolley, 2010; Staffend et al., 2011; Wissman et al., 2011, 2012; Martinez et al., 2016; Peterson et al., 2016). Whether these properties differ by MSN subtype is still unknown. Given that accumbens core MSNs exhibit divergent sex differences across development, sexual differentiation of MSNs likely occur across multiple developmental periods. Puberty may be one such period (Ernst et al., 2006; Kuhn et al., 2010; Manitt et al., 2011; Matthews et al., 2013; Staffend et al., 2014; Kopec et al., 2018).

CHALLENGE HYPOTHESIS #1: HOW DO MEMBRANE ESTROGEN RECEPTORS INFLUENCE STRIATAL NEURON PHYSIOLOGY?

Although there is ample evidence that estradiol is an important and sex-specific hormonal regulator of striatal behavior, dopamine systems, and MSN function, the exact mechanisms by which estradiol exerts its actions requires further research. An increasing body of work strongly implicates membrane estrogen receptor action. Adult female rats exclusively express membrane estrogen receptors (GPER1, membrane-associated ERα, and membrane-associated ERβ) in MSNs of the caudate-putamen and accumbens (Almey et al., 2012). However, to our knowledge a thorough analysis of estrogen receptors across development, MSN subtype, and species has not been accomplished and nuclear estrogen receptors may be expressed at early developmental stages. Sex-specific differences in membrane estrogen receptor facilitation of changes in neuronal activity have been reported in other brain regions (Oberlander and Woolley, 2016; Krentzel et al., 2018). Importantly, sex differences in function can exist even when receptor expression is similar between males and females (Krentzel et al., 2018), indicating that the sex-specific sensitivity and functionality of estrogen receptors are more complicated than indicated by anatomical analyses alone.

Membrane estrogen receptors are expressed both on axon terminals, MSN somas and dendritic spines (Almey et al., 2012, 2015, 2016), and there is evidence that estradiol has both pre- and post-synaptic mechanisms for altering dopaminergic signaling which promotes locomotion (Becker and Beer, 1986). Estrogen receptors associated in the membrane with metabotropic glutamate receptors have also been shown to facilitate locomotor sensitization to cocaine (Martinez et al., 2014), involved in drug addiction (Tonn Eisinger et al., 2018), and change dendritic spine morphology in the nucleus accumbens (Peterson et al., 2015). Application of estradiol increases dopamine (DA) rapidly in the accumbens and caudate-putamen (Becker, 1990; Pasqualini et al., 1996), as well as decreases GABA production (Hu et al., 2006). This suggests that estradiol may indirectly act on dopamine signaling by first releasing inhibition from GABAergic signaling, and perhaps also directly upon dopamine-producing regions. In striatal MSNs, estradiol acting through ERα, ERβ, and mGluR rapidly decreases L-type calcium currents and phosphorylates the transcription factor CREB (Mermelstein et al., 1996; Grove-Strawser et al., 2010).

One proposed model for estradiol actions on striatal networks builds upon these and other findings, positing that estradiol binds to membrane estrogen receptors on MSNs to decrease neuronal excitation, therefore leading to less GABA release and a "disinhibition" of dopaminergic signaling either through a collateral synapse upon dopamine fibers from the substantia nigra pars compacta or the VTA (Yoest et al., 2014, 2018b). Direct evidence that estradiol rapidly acts on MSNs to decrease intrinsic neuronal excitability or excitatory post synaptic currents remains unknown, although this is an active area of research. This model also predicts that MSNs synapse upon either dopaminergic fibers from the

substantia nigra pars compacta, the VTA, or perhaps tyrosine-hydroxylase positive striatal interneurons. Alternatively, estradiol may potentially act on striatal interneurons, such as the cholinergic subtype, which synapses upon both dopamine terminals and MSNs (Chuhma et al., 2011). Cholinergic interneurons express membrane estrogen receptors and have been implicated in estradiol-induced shifting between hippocampal and striatal-based learning behaviors, suggesting interactions been estrogen, cholinergic, and dopamine-systems (Euvrard et al., 1979; Davis et al., 2003; Almey et al., 2012). These models are not necessarily mutually exclusive. They also do not exclude direct actions of estradiol on MSNs independent of dopaminergic signaling, perhaps instead targeting glutamatergic systems. Consistent with this speculation, glutamatergic systems have been implicated in sex differences in psychiatric diseases such as anxiety (Wickens et al., 2018).

WHAT IS THE RELATIONSHIP BETWEEN MEMBRANE ESTROGEN RECEPTORS AND THE ESTROUS CYCLE?

Gonadal hormone fluctuations related to the estrous cycle correlate with changes in both caudate-putamen and accumbens dependent behaviors and with the electrical properties of MSNs. This conclusion raises questions regarding the potential relationship between the estrous cycle and the actions of rapid estradiol signaling to modulate striatal neuron activity. To date, one study has shown that after 3 days of estradiol priming to artificially mimic estradiol-high proestrus of females, locomotion and DA release is potentiated after an acute estradiol injection and amphetamine (Becker and Rudick, 1999). This work is one piece of evidence that females may exhibit cycle-dependent rapid estradiol mechanisms. Estradiol-mediated signaling in MSNs may alter depending on estrous cycle phase, though little work has tested this hypothesis, much less uncovered the mechanistic details of how this may occur. It is unknown how cycle stage changes sensitivity to estradiol, estrogen receptor expression, and synapse functionality. However, proestrus (higher estradiol and progesterone) females exhibit more and larger dendritic spines than males (Forlano and Woolley, 2010; Wissman et al., 2011). Other estrous cycle phases were not examined. This anatomical work from Woolley and colleagues is consistent with electrophysiological findings which indicate strong sex differences during the proestrus phase (Proaño et al., 2018).

CHALLENGE HYPOTHESIS #2: DOES LOCAL PRODUCTION OF ESTRADIOL INFLUENCE CAUDATE-PUTAMEN AND NUCLEUS ACCUMBENS FUNCTION?

Another component of rapid estradiol signaling is the dynamic production of localized estradiol. Evidence of aromatase activity and fluctuations in local estradiol content have been shown across vertebrate brains (Callard et al., 1978) especially in songbirds (Saldanha et al., 2000; Remage-Healey et al., 2008, 2012; Ikeda et al., 2017). Low levels of aromatase, the enzyme that synthesizes estradiol from testosterone, has been observed in processes and cell bodies of rat striatum (Jakab et al., 1993; Wagner and Morrell, 1996; Horvath et al., 1997) but a thorough analysis and comparison across subregions has not been performed. It is unknown how aromatase expression differs based on age, sex, cell compartment, or cell subtype, thus overly-definitive statements regarding striatal aromatase should be avoided. It is still speculative exactly what role aromatase plays in striatal neuron physiology. For the caudate-putamen, there is evidence that inhibition of aromatase prevents the induction of LTP in male rat MSNs (Tozzi et al., 2015) suggesting that local production of estradiol plays a role in striatal neuronal physiology. Inhibition of aromatase in the caudate-putamen of males proceeding a chemical lesion is neuroprotective (McArthur et al., 2007). To our knowledge, central administration of aromatase inhibitors has not been performed in females in studies examining striatal function.

Thus, the evidence for estradiol action in the striatal subregions is robust, but the source of that estradiol has not been directly tested in both sexes. One major question is the relationship between gonadal/peripheral vs. brain production of steroid sex hormones. The precursor to estradiol, testosterone, can increase the presence of aromatase expression and activity in rodent male brain (Roselli et al., 1984; Roselli and Klosterman, 1998), which is compelling evidence for the relationship of gonads and brain estradiol production in males. In male rats, long term testosterone exposure can influence MSN dendritic spine density (Wallin-Miller et al., 2016), and the nucleus accumbens is known to regulate the rewarding-aspects of testosterone exposure in males (Frye et al., 2002). It is unclear how castration and testosterone directly affect striatal aromatase activity and expression in males. For females, one study measuring estradiol content in both brain and blood of rodents across estrous stages found that estradiol content in the striatum was highest during late proestrus and far exceeded blood concentration (Morissette et al., 1992). However, at this point there remains a lack of corroborating evidence, especially when considered in light of the lack of differences in aromatase activity detected in other rat brain regions (Roselli et al., 1984). Continued research into how hormonal state and sex interact with possible aromatase activity is essential to grasp how steroid signaling modulates striatal neuron function.

AUTHOR CONTRIBUTIONS

AK wrote the initial manuscript draft. AK and JM revised and approved the manuscript.

FUNDING

We acknowledge NIH MH109471 to JM and P30ES025128 (Center for Human Health and the Environment).

REFERENCES

Almey, A., Filardo, E. J., Milner, T. A., and Brake, W. G. (2012). Estrogen receptors are found in glia and at extranuclear neuronal sites in the dorsal striatum of female rats: evidence for cholinergic but not dopaminergic colocalization. *Endocrinology* 153, 5373–5383. doi: 10.1210/en.2012-1458

Almey, A., Milner, T. A., and Brake, W. G. (2015). Estrogen receptors in the central nervous system and their implication for dopamine-dependent cognition in females. *Horm. Behav.* 74, 125–138. doi: 10.1016/j.yhbeh.2015.06.010

Almey, A., Milner, T. A., and Brake, W. G. (2016). Estrogen receptor alpha and G-protein coupled estrogen receptor 1 are localized to GABAergic neurons in the dorsal striatum. *Neurosci. Lett.* 622, 118–123. doi: 10.1016/j.neulet.2016.04.023

Arnauld, E., Dufy, B., Pestre, M., and Vincent, J. D. (1981). Effects of estrogens on the responses of caudate neurons to microiontophoretically applied dopamine. *Neurosci. Lett.* 21, 325–331. doi: 10.1016/0304-3940(81)90225-1

Arnold, A. P. (2017). A general theory of sexual differentiation. *J. Neurosci. Res.* 95, 291–300. doi: 10.1002/jnr.23884

Becker, J. B. (1990). Direct effect of 17 beta-estradiol on striatum: sex differences in dopamine release. *Synapse* 5, 157–164. doi: 10.1002/syn.890050211

Becker, J. B., and Beer, M. E. (1986). The influence of estrogen on nigrostriatal dopamine activity: behavioral and neurochemical evidence for both pre- and postsynaptic components. *Behav. Brain Res.* 19, 27–33. doi: 10.1016/0166-4328(86)90044-6

Becker, J. B., and Rudick, C. N. (1999). Rapid effects of estrogen or progesterone on the amphetamine-induced increase in striatal dopamine are enhanced by estrogen priming: a microdialysis study. *Pharmacol. Biochem. Behav.* 64, 53–57. doi: 10.1016/S0091-3057(99)00091-X

Becker, J. B., Snyder, P. J., Miller, M. M., Westgate, S. A., and Jenuwine, M. J. (1987). The influence of estrous cycle and intrastriatal estradiol on sensorimotor performance in the female rat. *Pharmacol. Biochem. Behav.* 27, 53–59. doi: 10.1016/0091-3057(87)90476-X

Brancato, A., Bregman, D., Ahn, H. F., Pfau, M. L., Menard, C., Cannizzaro, C., et al. (2017). Sub-chronic variable stress induces sex-specific effects on glutamatergic synapses in the nucleus accumbens. *Neuroscience* 350, 180–189. doi: 10.1016/j.neuroscience.2017.03.014

Calipari, E. S., Juarez, B., Morel, C., Walker, D. M., Cahill, M. E., Ribeiro, E., et al. (2017). Dopaminergic dynamics underlying sex-specific cocaine reward. *Nat. Commun.* 8:13877. doi: 10.1038/ncomms13877

Callard, G. V., Petro, Z., and Ryan, K. J. (1978). Phylogenetic distribution of aromatase and other androgen-converting enzymes in the central nervous system. *Endocrinology* 103, 2283–2290. doi: 10.1210/endo-103-6-2283

Cao, J., Dorris, D. M., and Meitzen, J. (2016). Neonatal masculinization blocks increased excitatory synaptic input in female rat nucleus accumbens core. *Endocrinology* 157, 3181–3196. doi: 10.1210/en.2016-1160

Cao, J., Dorris, D. M., and Meitzen, J. (2018a). Electrophysiological properties of medium spiny neurons in the nucleus accumbens core of prepubertal male and female Drd1a-tdTomato line 6 BAC transgenic mice. *J. Neurophysiol.* 120, 1712–1727. doi: 10.1152/jn.00257.2018

Cao, J., Willett, J. A., Dorris, D. M., and Meitzen, J. (2018b). Sex differences in medium spiny neuron excitability and glutamatergic synaptic input: heterogeneity across striatal regions and evidence for estradiol-dependent sexual differentiation. *Front. Endocrinol.* 9:173. doi: 10.3389/fendo.2018.00173

Castrioto, A., Hulliger, S., Poon, Y. Y., Lang, A. E., and Moro, E. (2010). A survey on the impact of the menstrual cycle on movement disorders severity. *Can. J. Neurol. Sci.* 37, 478–481. doi: 10.1017/S0317167100010490

Chuhma, N., Tanaka, K. F., Hen, R., and Rayport, S. (2011). Functional connectome of the striatal medium spiny neuron. *J. Neurosci.* 31, 1183–1192. doi: 10.1523/JNEUROSCI.3833-10.2011

Cora, M. C., Kooistra, L., and Travlos, G. (2015). Vaginal cytology of the laboratory rat and mouse: review and criteria for the staging of the estrous cycle using stained vaginal smears. *Toxicol. Pathol.* 43, 776–793. doi: 10.1177/0192623315570339

Czoty, P. W., Riddick, N. V., Gage, H. D., Sandridge, M., Nader, S. H., Garg, S., et al. (2009). Effect of menstrual cycle phase on dopamine D2 receptor availability in female cynomolgus monkeys. *Neuropsychopharmacology* 34, 548–554. doi: 10.1038/npp.2008.3

Davis, S., Bozon, B., and Laroche, S. (2003). How necessary is the activation of the immediate early gene zif268 in synaptic plasticity and learning? *Behav. Brain Res.* 142, 17–30. doi: 10.1016/S0166-4328(02)00421-7

Dorris, D. M., Cao, J., Willett, J. A., Hauser, C. A., and Meitzen, J. (2015). Intrinsic excitability varies by sex in prepubertal striatal medium spiny neurons. *J. Neurophysiol.* 113, 720–729. doi: 10.1152/jn.00687.2014

Ernst, M., Pine, D. S., and Hardin, M. (2006). Triadic model of the neurobiology of motivated behavior in adolescence. *Psychol. Med.* 36, 299–312. doi: 10.1017/S0033291705005891

Euvrard, C., Labrie, F., and Boissier, J. R. (1979). Effect of estrogen on changes in the activity of striatal cholinergic neurons induced by DA drugs. *Brain Res.* 169, 215–220. doi: 10.1016/0006-8993(79)90392-5

Forger, N. G. (2016). Epigenetic mechanisms in sexual differentiation of the brain and behaviour. *Philos. Trans. R. Soc. Lond. B. Biol. Sci.* 371:20150114. doi: 10.1098/rstb.2015.0114

Forlano, P. M., and Woolley, C. S. (2010). Quantitative analysis of pre- and postsynaptic sex differences in the nucleus accumbens. *J. Comp. Neurol.* 518, 1330–1348. doi: 10.1002/cne.22279

Frye, C. A., Rhodes, M. E., Rosellini, R., and Svare, B. (2002). The nucleus accumbens as a site of action for rewarding properties of testosterone and its 5alpha-reduced metabolites. *Pharmacol. Biochem. Behav.* 74, 119–127. doi: 10.1016/S0091-3057(02)00968-1

Gerfen, C. R., and Surmeier, D. J. (2011). Modulation of striatal projection systems by dopamine. *Annu. Rev. Neurosci.* 34, 441–466. doi: 10.1146/annurev-neuro-061010-113641

Grabowska, A. (2017). Sex on the brain: are gender-dependent structural and functional differences associated with behavior? *J. Neurosci. Res.* 95, 200–212. doi: 10.1002/jnr.23953

Graveland, G. A., and DiFiglia, M. (1985). The frequency and distribution of medium-sized neurons with indented nuclei in the primate and rodent neostriatum. *Brain Res.* 327, 307–311. doi: 10.1016/0006-8993(85)91524-0

Grove-Strawser, D., Boulware, M. I., and Mermelstein, P. G. (2010). Membrane estrogen receptors activate the metabotropic glutamate receptors mGluR5 and mGluR3 to bidirectionally regulate CREB phosphorylation in female rat striatal neurons. *Neuroscience* 170, 1045–1055. doi: 10.1016/j.neuroscience.2010.08.012

Hampson, E. (1990). Estrogen-related variations in human spatial and articulatory-motor skills. *Psychoneuroendocrinology* 15, 97–111. doi: 10.1016/0306-4530(90)90018-5

Hampson, E., and Kimura, D. (1988). Reciprocal effects of hormonal fluctuations on human motor and perceptual-spatial skills. *Behav. Neurosci.* 102, 456–459. doi: 10.1037/0735-7044.102.3.456

Horvath, T. L., Roa-Pena, L., Jakab, R. L., Simpson, E. R., and Naftolin, F. (1997). Aromatase in axonal processes of early postnatal hypothalamic and limbic areas including the cingulate cortex. *J. Steroid Biochem. Mol. Biol.* 61, 349–357. doi: 10.1016/S0960-0760(97)80032-5

Hu, M., Watson, C. J., Kennedy, R. T., and Becker, J. B. (2006). Estradiol attenuates the K+-induced increase in extracellular GABA in rat striatum. *Synapse* 59, 122–124. doi: 10.1002/syn.20221

Ikeda, M. Z., Krentzel, A. A., Oliver, T. J., Scarpa, G. B., and Remage-Healey, L. (2017). Clustered organization and region-specific identities of estrogen-producing neurons in the forebrain of Zebra Finches (*Taeniopygia guttata*). *J. Comp. Neurol.* 525, 3636–3652. doi: 10.1002/cne.24292

Jakab, R. L., Horvath, T. L., Leranth, C., Harada, N., and Naftolin, F. (1993). Aromatase immunoreactivity in the rat brain: gonadectomy-sensitive hypothalamic neurons and an unresponsive "limbic ring" of the lateral septum-bed nucleus-amygdala complex. *J. Steroid Biochem. Mol. Biol.* 44, 481–498. doi: 10.1016/0960-0760(93)90253-S

Kemp, J. M., and Powell, T. P. (1971). The structure of the caudate nucleus of the cat: light and electron microscopy. *Philos. Trans. R. Soc. Lond. B. Biol. Sci.* 262, 383–401. doi: 10.1098/rstb.1971.0102

Kopec, A. M., Smith, C. J., Ayre, N. R., Sweat, S. C., and Bilbo, S. D. (2018). Microglial dopamine receptor elimination defines sex-specific nucleus accumbens development and social behavior in adolescent rats. *Nat. Commun.* 9:3769. doi: 10.1038/s41467-018-06118-z

Krentzel, A. A., Macedo-Lima, M., Ikeda, M. Z., and Remage-Healey, L. (2018). A membrane g-protein coupled estrogen receptor is necessary but not

sufficient for sex-differences in zebra finch auditory coding. *Endocrinology* 159, 1360–1376. doi: 10.1210/en.2017-03102

Kuhn, C., Johnson, M., Thomae, A., Luo, B., Simon, S. A., Zhou, G., et al. (2010). The emergence of gonadal hormone influences on dopaminergic function during puberty. *Horm. Behav.* 58, 122–137. doi: 10.1016/j.yhbeh.2009.10.015

Manitt, C., Mimee, A., Eng, C., Pokinko, M., Stroh, T., Cooper, H. M., et al. (2011). The netrin receptor DCC is required in the pubertal organization of mesocortical dopamine circuitry. *J. Neurosci.* 31, 8381–8394. doi: 10.1523/JNEUROSCI.0606-11.2011

Marcondes, F. K., Miguel, K. J., Melo, L. L., and Spadari-Bratfisch, R. C. (2001). Estrous cycle influences the response of female rats in the elevated plus-maze test. *Physiol. Behav.* 74, 435–440. doi: 10.1016/S0031-9384(01)00593-5

Martinez, L. A., Gross, K. S., Himmler, B. T., Emmitt, N. L., Peterson, B. M., Zlebnik, N. E., et al. (2016). Estradiol facilitation of cocaine self-administration in female rats requires activation of mGluR5. *eNeuro* 3:ENEURO.0140-16.2016. doi: 10.1523/ENEURO.0140-16.2016

Martinez, L. A., Peterson, B. M., Meisel, R. L., and Mermelstein, P. G. (2014). Estradiol facilitation of cocaine-induced locomotor sensitization in female rats requires activation of mGluR5. *Behav. Brain Res.* 271, 39–42. doi: 10.1016/j.bbr.2014.05.052

Matthews, M., Bondi, C., Torres, G., and Moghaddam, B. (2013). Reduced presynaptic dopamine activity in adolescent dorsal striatum. *Neuropsychopharmacology* 38, 1344–1351. doi: 10.1038/npp.2013.32

McArthur, S., Murray, H. E., Dhankot, A., Dexter, D. T., and Gillies, G. E. (2007). Striatal susceptibility to a dopaminergic neurotoxin is independent of sex hormone effects on cell survival and DAT expression but is exacerbated by central aromatase inhibition. *J. Neurochem.* 100, 678–692. doi: 10.1111/j.1471-4159.2006.04226.x

McCarthy, M. M. (2010). How it's made: organisational effects of hormones on the developing brain. *J. Neuroendocrinol.* 22, 736–742. doi: 10.1111/j.1365-2826.2010.02021.x

Meitzen, J., Pflepsen, K. R., Stern, C. M., Meisel, R. L., and Mermelstein, P. G. (2011). Measurements of neuron soma size and density in rat dorsal striatum, nucleus accumbens core and nucleus accumbens shell: differences between striatal region and brain hemisphere, but not sex. *Neurosci. Lett.* 487, 177–181. doi: 10.1016/j.neulet.2010.10.017

Mermelstein, P. G., Becker, J. B., and Surmeier, D. J. (1996). Estradiol reduces calcium currents in rat neostriatal neurons via a membrane receptor. *J. Neurosci.* 16, 595–604. doi: 10.1523/JNEUROSCI.16-02-00595.1996

Morissette, M., Garcia-Segura, L. M., Bélanger, A., and Di Paolo, T. (1992). Changes of rat striatal neuronal membrane morphology and steroid content during the estrous cycle. *Neuroscience* 49, 893–902. doi: 10.1016/0306-4522(92)90365-9

Nicola, S. M., Surmeier, J., and Malenka, R. C. (2000). Dopaminergic modulation of neuronal excitability in the striatum and nucleus accumbens. *Annu. Rev. Neurosci.* 23, 185–215. doi: 10.1146/annurev.neuro.23.1.185

Nillni, Y. I., Toufexis, D. J., and Rohan, K. J. (2011). Anxiety sensitivity, the menstrual cycle, and panic disorder: a putative neuroendocrine and psychological interaction. *Clin. Psychol. Rev.* 31, 1183–1191. doi: 10.1016/j.cpr.2011.07.006

Oberlander, J. G., and Woolley, C. S. (2016). 17beta-estradiol acutely potentiates glutamatergic synaptic transmission in the hippocampus through distinct mechanisms in males and females. *J. Neurosci.* 36, 2677–2690. doi: 10.1523/JNEUROSCI.4437-15.2016

Pasqualini, C., Olivier, V., Guibert, B., Frain, O., and Leviel, V. (1996). Rapid stimulation of striatal dopamine synthesis by estradiol. *Cell. Mol. Neurobiol.* 16, 411–415. doi: 10.1007/BF02088105

Peterson, B. M., Martinez, L. A., Meisel, R. L., and Mermelstein, P. G. (2016). Estradiol impacts the endocannabinoid system in female rats to influence behavioral and structural responses to cocaine. *Neuropharmacology* 110(Pt A), 118–124. doi: 10.1016/j.neuropharm.2016.06.002

Peterson, B. M., Mermelstein, P. G., and Meisel, R. L. (2015). Estradiol mediates dendritic spine plasticity in the nucleus accumbens core through activation of mGluR5. *Brain Struct. Funct.* 220, 2415–2422. doi: 10.1007/s00429-014-0794-9

Proaño, S., Morris, H. J., Kunz, L. M., Dorris, D. M., and Meitzen, J. (2018). Estrous cycle-induced sex differences in medium spiny neuron excitatory synaptic transmission and intrinsic excitability in adult rat nucleus accumbens core. *J. Neurophysiol.* 120, 1356–1373. doi: 10.1152/jn.00263.2018

Quinn, N. P., and Marsden, C. D. (1986). Menstrual-related fluctuations in Parkinson's disease. *Mov. Disord.* 1, 85–87. doi: 10.1002/mds.870010112

Remage-Healey, L., Dong, S. M., Chao, A., and Schlinger, B. A. (2012). Sex-specific, rapid neuroestrogen fluctuations and neurophysiological actions in the songbird auditory forebrain. *J. Neurophysiol.* 107, 1621–1631. doi: 10.1152/jn.00749.2011

Remage-Healey, L., Maidment, N. T., and Schlinger, B. A. (2008). Forebrain steroid levels fluctuate rapidly during social interactions. *Nat. Neurosci.* 11, 1327–1334. doi: 10.1038/nn.2200

Roselli, C. E., Ellinwood, W. E., and Resko, J. A. (1984). Regulation of brain aromatase activity in rats. *Endocrinology* 114, 192–200. doi: 10.1210/endo-114-1-192

Roselli, C. E., and Klosterman, S. A. (1998). Sexual differentiation of aromatase activity in the rat brain: effects of perinatal steroid exposure. *Endocrinology* 139, 3193–3201. doi: 10.1210/endo.139.7.6101

Russo, S. J., and Nestler, E. J. (2013). The brain reward circuitry in mood disorders. *Nat. Rev. Neurosci.* 14, 609–625. doi: 10.1038/nrn3381

Saldanha, C. J., Tuerk, M. J., Kim, Y. H., Fernandes, A. O., Arnold, A. P., and Schlinger, B. A. (2000). Distribution and regulation of telencephalic aromatase expression in the zebra finch revealed with a specific antibody. *J. Comp. Neurol.* 423, 619–630. doi: 10.1002/1096-9861(20000807)423:4andlt;619::AID-CNE7andgt;3.0.CO;2-U

Sayin, A., Derinöz, O., Yüksel, N., Sahin, S., and Bolay, H. (2014). The effects of the estrus cycle and citalopram on anxiety-like behaviors and c-fos expression in rats. *Pharmacol. Biochem. Behav.* 124, 180–187. doi: 10.1016/j.pbb.2014.06.002

Schultz, K. N., von Esenwein, S. A., Hu, M., Bennett, A. L., Kennedy, R. T., Musatov, S., et al. (2009). Viral vector-mediated overexpression of estrogen receptor-alpha in striatum enhances the estradiol-induced motor activity in female rats and estradiol-modulated GABA release. *J. Neurosci.* 29, 1897–1903. doi: 10.1523/JNEUROSCI.4647-08.2009

Scofield, M. D., Heinsbroek, J. A., Gipson, C. D., Kupchik, Y. M., Spencer, S., Smith, A. C., et al. (2016). The nucleus accumbens: mechanisms of addiction across drug classes reflect the importance of glutamate homeostasis. *Pharmacol. Rev.* 68, 816–871. doi: 10.1124/pr.116.012484

Sherman, B. M., and Korenman, S. G. (1975). Hormonal characteristics of the human menstrual cycle throughout reproductive life. *J. Clin. Invest.* 55, 699–706. doi: 10.1172/JCI107979

Souza, E. G., Ramos, M. G., Hara, C., Stumpf, B. P., and Rocha, F. L. (2012). Neuropsychological performance and menstrual cycle: a literature review. *Trends Psychiatry Psychother.* 34, 5–12. doi: 10.1590/S2237-60892012000100003

Staffend, N. A., Loftus, C. M., and Meisel, R. L. (2011). Estradiol reduces dendritic spine density in the ventral striatum of female Syrian hamsters. *Brain Struct. Funct.* 215, 187–194. doi: 10.1007/s00429-010-0284-7

Staffend, N. A., Mohr, M. A., DonCarlos, L. L., and Sisk, C. L. (2014). A decrease in the addition of new cells in the nucleus accumbens and prefrontal cortex between puberty and adulthood in male rats. *Dev. Neurobiol.* 74, 633–642. doi: 10.1002/dneu.22160

Tansey, E. M., Arbuthnott, G. W., Fink, G., and Whale, D. (1983). Oestradiol-17 beta increases the firing rate of antidromically identified neurones of the rat neostriatum. *Neuroendocrinology* 37, 106–110. doi: 10.1159/000123527

Tonn Eisinger, K. R., Gross, K. S., Head, B. P., and Mermelstein, P. G. (2018). Interactions between estrogen receptors and metabotropic glutamate receptors and their impact on drug addiction in females. *Horm. Behav.* 104, 130–137. doi: 10.1016/j.yhbeh.2018.03.001

Tozzi, A., de Iure, A., Tantucci, M., Durante, V., Quiroga-Varela, A., Giampa, C., et al. (2015). Endogenous 17beta-estradiol is required for activity-dependent long-term potentiation in the striatum: interaction with the dopaminergic system. *Front. Cell. Neurosci.* 9:192. doi: 10.3389/fncel.2015.00192

Wagner, C. K., and Morrell, J. I. (1996). Distribution and steroid hormone regulation of aromatase mRNA expression in the forebrain of adult male and female rats: a cellular-level analysis using in situ hybridization. *J. Comp. Neurol.* 370, 71–84. doi: 10.1002/(SICI)1096-9861(19960617)370:1andlt;71::AID-CNE7andgt;3.0.CO;2-I

Wallin-Miller, K., Li, G., Kelishani, D., and Wood, R. I. (2016). Anabolic-androgenic steroids decrease dendritic spine density in the nucleus accumbens of male rats. *Neuroscience* 330, 72–78. doi: 10.1016/j.neuroscience.2016.05.045

Wickens, M. M., Bangasser, D. A., and Briand, L. A. (2018). Sex differences in psychiatric disease: a focus on the glutamate system. *Front. Mol. Neurosci.* 11:197. doi: 10.3389/fnmol.2018.00197

Willett, J. A., Will, T., Hauser, C. A., Dorris, D. M., Cao, J., and Meitzen, J. (2016). No evidence for sex differences in the electrophysiological properties and excitatory synaptic input onto nucleus accumbens shell medium spiny neurons. *eNeuro* 3:e0147-15.2016. doi: 10.1523/ENEURO.0147-15.2016

Wissman, A. M., May, R. M., and Woolley, C. S. (2012). Ultrastructural analysis of sex differences in nucleus accumbens synaptic connectivity. *Brain Struct. Funct.* 217, 181–190. doi: 10.1007/s00429-011-0353-6

Wissman, A. M., McCollum, A. F., Huang, G. Z., Nikrodhanond, A. A., and Woolley, C. S. (2011). Sex differences and effects of cocaine on excitatory synapses in the nucleus accumbens. *Neuropharmacology* 61, 217–227. doi: 10.1016/j.neuropharm.2011.04.002

Wong, J. E., Cao, J., Dorris, D. M., and Meitzen, J. (2016). Genetic sex and the volumes of the caudate-putamen, nucleus accumbens core and shell: original data and a review. *Brain Struct. Funct.* 221, 4257–4267. doi: 10.1007/s00429-015-1158-9

Xiao, L., and Becker, J. B. (1994). Quantitative microdialysis determination of extracellular striatal dopamine concentration in male and female rats: effects of estrous cycle and gonadectomy. *Neurosci. Lett.* 180, 155–158. doi: 10.1016/0304-3940(94)90510-X

Yoest, K. E., Cummings, J. A., and Becker, J. B. (2014). Estradiol, dopamine and motivation. *Cent. Nerv. Syst. Agents Med. Chem.* 14, 83–89. doi: 10.2174/1871524914666141226103135

Yoest, K. E., Cummings, J. A., and Becker, J. B. (2018a). Estradiol influences on dopamine release from the nucleus accumbens shell: sex differences and the role of selective estradiol receptor subtypes. *Br. J. Pharmacol.* doi: 10.1111/bph.14531. [Epub ahead of print].

Yoest, K. E., Quigley, J. A., and Becker, J. B. (2018b). Rapid effects of ovarian hormones in dorsal striatum and nucleus accumbens. *Horm. Behav.* 104, 119–129. doi: 10.1016/j.yhbeh.2018.04.002

Conflict of Interest Statement: The authors declare that the research was conducted in the absence of any commercial or financial relationships that could be construed as a potential conflict of interest.

frontiers in Cellular Neuroscience

REVIEW
published: 17 December 2018
doi: 10.3389/fncel.2018.00484

Neuronal Migration During Development of the Cerebellum

Maryam Rahimi-Balaei[1,2], *Hugo Bergen*[1], *Jiming Kong*[1] *and Hassan Marzban*[1,2]*

[1]Department of Human Anatomy and Cell Science, Max Rady College of Medicine, Rady Faculty of Health Sciences, University of Manitoba, Winnipeg, MB, Canada, [2]The Children's Hospital Research Institute of Manitoba (CHRIM), Max Rady College of Medicine, Rady Faculty of Health Sciences, University of Manitoba, Winnipeg, MB, Canada

Neuronal migration is a fundamental process in central nervous system (CNS) development. The assembly of functioning neuronal circuits relies on neuronal migration occurring in the appropriate spatio-temporal pattern. A defect in the neuronal migration may result in a neurological disorder. The cerebellum, as a part of the CNS, plays a pivotal role in motor coordination and non-motor functions such as emotion, cognition and language. The excitatory and inhibitory neurons within the cerebellum originate from different distinct germinal zones and migrate through complex routes to assemble in a well-defined neuronal organization in the cerebellar cortex and nuclei. In this review article, the neuronal migration modes and pathways from germinal zones to the final position in the cerebellar cortex and nuclei will be described. The cellular and molecular mechanisms involved in cerebellar neuronal migration during development will also be reviewed. Finally, some diseases and animal models associated with defects in neuronal migration will be presented.

Keywords: neuron, migration, cerebellum, development, mechanism

OPEN ACCESS

Edited by:
Jing-Ning Zhu,
Nanjing University, China

Reviewed by:
Takaki Miyata,
Nagoya University, Japan
Salvador Martinez,
Universidad Miguel Hernández de Elche, Spain
Roy Vincent Sillitoe,
Baylor College of Medicine, United States

***Correspondence:**
Hassan Marzban
hassan.marzban@umanitoba.ca

Received: *06 July 2018*
Accepted: *27 November 2018*
Published: *17 December 2018*

Citation:
Rahimi-Balaei M, Bergen H, Kong J and Marzban H (2018) Neuronal Migration During Development of the Cerebellum. Front. Cell. Neurosci. 12:484. doi: 10.3389/fncel.2018.00484

INTRODUCTION

The structural and functional development of the central nervous system (CNS) depends on neurogenesis, neuronal migration and circuit formation. This is a complex sequence of events involving a variety of molecular pathways. Neuronal migration is an essential phenomenon for normal development as it brings cells into appropriate spatial relationships with other cells

Abbreviations: Acp2, lysosomal acid phosphatase 2; ApoER2, apolipoprotein E receptor 2; Astn, astrotactin 1; Atoh1, atonal homolog 1; BDNF, brain-derived neurotrophic factor; CAMs, cell adhesion molecules; CN, cerebellar nuclei; CNN, cerebellar nuclei neuron; CNS, central nervous system; CXCL12, chemokine ligand 12; CXCR4, chemokine receptor 4; Dab1, disabled-1; DCC, deleted in colorectal cancer; DCX, doublecortin; E, embryonic day; EAAT1, excitatory amino acid transporter; EGF, epidermal growth factor; ErbB4, Erb-B2 receptor tyrosine kinase 4; FoxP2, forkhead box protein P2; GABA, gamma amino butyric acid; GC, granule cell; GCP, granule cell precursor; GFAP, glial fibrillary acidic protein; GLASTs, glutamate receptors and transporters; HGF/SF, hepatocyte growth factor/scatter factor; i, isthmus; IN, interneuron; IZ, intermediate zone; KCC2, potassium-chloride co-transporter; LIS1, lissencephaly-1 homolog; Lmx1a, LIM homeobox transcription factor 1 alpha; m, mesencephalon; MAP, microtubule-associated protein; MDM2, mouse double minute 2 homolog; MZ, marginal zone; *Nf1*, neurofibromatosis type 1; NRG1, neuregulin-1; NTZ, nuclear transitory zone; P, postnatal day; Pax2, paired homeobox gene 2; Pax6, paired homeobox gene 6; PC, purkinje cell; PCC, purkinje cell cluster; PCP, purkinje cell plate; Pex2, peroxisomal biogenesis factor 2; Ptf1a, pancreas specific transcription factor 1a; RL, rhombic lip; Rp58, 58 KDa repressor protein; SDF-1, stromal derived factor 1; Sema3A, semaphorin 3a; Sema6A, semaphorin 6A; Shh, sonic hedgehog; SmoA2, smoothened A2; SVZ, subventricular zone; Tbr1, T-box, brain, 1; Tbr2, T-box, brain, 2; UBC, unipolar brush cells; uPAR, urokinase-type plasminogen activator receptor; VLDLR, very-low-density lipoprotein receptor; VPS18, vacuole protein sorting 18; VZ, ventricular zone.

(Marín et al., 2010). During development, newborn neurons form within the neuroepithelium, a proliferative layer of the neural tube. Under tightly controlled conditions, the newborn neurons migrate from their germinal zone and disperse throughout the CNS to reach their final destination where they subsequently become part of an appropriate lamination and neuronal circuit (Cooper, 2013). Cell polarity is required for neuronal migration which is dependent on cytoskeletal changes in concert with cell adhesion receptor systems that are regulated by a wide variety of molecules (Govek et al., 2011). Neuronal locomotion can be divided to three phases: (1) extension of the leading process; (2) nucleokinesis; and (3) retraction of the trailing process (Tsai and Gleeson, 2005). The main mode of neuronal migration is somal translocation which uses extracellular matrix components (Nadarajah and Parnavelas, 2002), glial fibers (Hatten, 1990), blood vessels (Tsai et al., 2016), axons (Takei et al., 2000) and possibly pia mater (Komuro and Yacubova, 2003) as substrates. Neuronal migration follows either a radial or a tangential migratory pathway, depending on the area of the developing nervous system in which the neurons originate. In radial migration, nascent neurons follow a track that is perpendicular to the neuroepithelial surface and the neurons proceed alongside radial glial fibers (Marín and Rubenstein, 2001). In contrast, the tangential migration of neurons is parallel to the pial surface (Nadarajah et al., 2001). There is also a dual phase neuronal migration referred to as a switching migration, which is a combination of tangential and radial migration (Kawaji et al., 2004).

In this article, the neuronal migration modes and the direction and pathways from origin to the final position during CNS development will be reviewed. Then, we will review the migration of cerebellar neurons with an emphasis on Purkinje cells (PCs). Finally, we will describe some diseases and animal models associated with defects in neuronal migration.

THE CELLULAR AND MOLECULAR MECHANISMS INVOLVED IN NEURONAL MIGRATION

During neuronal migration, neuronal precursor cells move forward, switch their direction, or change their migration mode to reach their final position, which is fundamental for nervous system function. All of these processes are under an elaborate control system and have been studied extensively (**Table 1**). In this section, we will describe the main molecular and cellular mechanisms involved in neuronal migration during CNS development and then the migration of each cerebellar neuronal type will be described.

Migrating neurons exhibit highly polarized cell morphology in the direction of their movement. The polarized neurons are defined as having a leading process and a trailing process. The leading process is a structure that is similar to the growth cones of growing axons, whereas the trailing process is a short process at the posterior part of the cell. The formation of these processes is regulated by precise cellular and molecular mechanisms through which extrinsic and intrinsic signaling pathways change the cytoskeleton resulting in pulling and pushing forces (Matsuki et al., 2013; Nguyen and Hippenmeyer, 2013). The major structures that define the leading edge activity of migrating neurons are lamellipodia and filopodia (Kurosaka and Kashina, 2008). Initially a lamellipodium-like network forms and then filopodia form through the addition of monomers to filaments and assembly with adjacent filaments (Davies, 2013). Lamellipodia are broad membrane protrusions at the leading edge of cells that arise as a result of actin polymerization. Lamellipodia are dynamic structures that include protrusion and retraction activities (Krause and Gautreau, 2014). On the other hand, filopodia are thin protrusions of the lamellipodium plasma-membrane. The formation of filopodia is a highly dynamic process and these structures function as antennae to navigate and direct cell migration. The initiation and elongation of filopodia depends on the precise regulation of polymerization, crosslinking and assembly by various actin-associated proteins (Mattila and Lappalainen, 2008).

The movements of neurons are controlled by the generation, maintenance and remodeling of a leading process. The leading process of the neuron marks the direction of neuronal migration, followed by movement of the cell somata (somal translocation) along with the translocation of the nucleus (nucleokinesis), and finally the migrating neuron eliminates its trailing process. Leading processes interact with the surrounding microenvironment to guide neuronal movements (Nguyen and Hippenmeyer, 2013). The remodeling of the leading process will repeatedly initiate new migratory cycles until it reaches its final destination (Nguyen and Hippenmeyer, 2013). Cytoskeletal proteins such as microtubules, actin and actomyosin play important roles in nucleokinesis and cell locomotion. The centrosome is the main microtubule organizing center and as it moves forward, it pulls forward the longitudinal array of microtubules in association with the Golgi apparatus, which is followed by the movement of the nucleus. The absence of microtubules at the trailing part of the cell may initiate

TABLE 1 | Methods to study neuronal migration (Mannan et al., 2004; Baubet et al., 2012; Rahimi-Balaei et al., 2016).

Techniques for progenitor differentiation and neuronal migration	
Traditional	a) Analysis of fixed tissue
	b) *in vitro*: culture of individual cells
Advanced	a) Electron microscopy
	b) Autoradiography
	c) Tissue culture methods
	d) Chimeras
	e) X-ray crystallography
	f) Genetic labeling
Recent	a) Live imaging techniques
	b) Genetic labeling of distinct cell types in developing brain
	c) *In vitro* migration assay using dissociated neuronal cells migration (boyden chamber assays and gap closure assays)
	d) Real-time neuronal migration in embryonic brain slice assay (fluorescent dyes or XFP transgenes, lipophilic or vital dyes, such as DiI, DiO, CMTMR, Oregon Green plus dye- or transgene-coated gold particles *in utero* or *ex vivo* electroporation)
	e) Neuronal migration in embryonic brain explants in 3-D matrigel
	f) Embryonic culture
	g) Dynamic *in-silico* model for neuronal migration

contractions dependent on myosin II, and this pushing force on the nucleus results in moving forward and breaks adhesions at the trailing part of the cell. The role of actomyosin contraction at the back part of the cell also plays an important role in the migration of cortical interneurons (INs; Martini and Valdeolmillos, 2010). The somal translocation process is the main mode of neuronal migration during the early stage of embryonic development and includes the radially migrating neurons such as cerebellar granule cells (GCs) that move along the Bergmann glia fibers. A wide range of cellular events, including cell adhesion, modulate this migration (Hatten, 1999; Nadarajah et al., 2001; Sanada et al., 2004).

It has been shown that Lissencephaly-1 homolog, (LIS1, a member of the microtubule-associated proteins, MAPs) and doublecortin (DCX, a member of MAP that directly polymerizes purified tubulin into microtubules) are important in the translocation of the neuronal cell body during neuronal migration. Both molecules are components of an evolutionarily conserved pathway regulating microtubule function and cell migration (Gleeson et al., 1999; Feng and Walsh, 2001). In addition, the microtubule bundling that is accompanied by the action of dynein mediates coupling of the nucleus to the centrosome (modulating and stabilizing microtubules; Tanaka et al., 2004). In another study, it has been shown that LIS1 and dynein play a role in radial neuronal migration (Wynshaw-Boris and Gambello, 2001). In males, DCX mutations produce lissencephaly phenotypes similar to those associated with *LIS1* mutations (Gleeson et al., 1998). Recently, c-Jun N-terminal signaling pathway has gained attention as one of the critical regulators of neuronal mobility. Indeed, components of this pathway activate some specific brain proteins (e.g., by phosphorylation of the MAP1B and MAP2) which affect the stability of microtubules in neurons and neuronal migration (Tsai et al., 2016). In cerebellar GC migration, that is assisted by Bergmann glia, the majority of F-actin and myosin II is located at the front of the nucleus rather than the trailing end, suggesting these proteins may pull the soma forward (Solecki et al., 2009).

In addition to intrinsic factors discussed above, there are several extrinsic factors (also known as motogens) involved in neuronal migration. Gamma amino butyric acid (GABA) secreted by neurons themselves, acts as an extrinsic factor and accelerates their migration. In mice deficient in GABA, the migration rate of neurons is decreased, which is consistent with a role for GABA as a motogen (Inada et al., 2011). Hepatocyte growth factor/scatter factor (HGF/SF) is another extrinsic factor involved in migration. In mice lacking the urokinase-type plasminogen activator receptor (uPAR, a key component of HGF/SF activation), neurons exhibit abnormal migration from the ganglionic eminence, which leads to a reduced number of neurons in the frontal and parietal cortices (Powell et al., 2001).

The rate of cerebellar GC migration is controlled positively through the frequency of the intracellular calcium fluctuation and negatively regulates the rate of the extension of axonal growth cones. In cortical migratory interneurons, their motility is stimulated by the activation of GABA and glutamate receptors. An up-regulation of the potassium-chloride co-transporter (KCC2) plays a key role in reducing interneuron motility through its ability to reduce membrane potential upon gamma-aminobutyric acid A($GABA_A$) receptor activation, and decrease the frequency of intracellular calcium transients. Subsequently, during early postnatal weeks the expression of KCC2 is increased and early-born interneurons express higher levels of KCC2 compared to late-born interneurons (Bortone and Polleux, 2009).

The control of the specific direction of the migration in cortical neurons originating from the subventricular zone (SVZ) is a combination of the leading process and the use of scaffolds (such as the radial glia; Marín et al., 2010). However, there are additional factors such as semaphorin 3A (Sema3A), which acts like an attractant and is expressed in descending gradients across cortical layers, that guide newborn cortical neurons to the upper cortical layers (Chen et al., 2008). During development of pontine nuclei in the hindbrain, neurons reach the midline and Netrin-1 acts as a midline attractant and these neurons themselves express deleted in colorectal cancer (DCC), a Netrin-1 receptor), to assist these neurons to reach the midline (Yee et al., 1999). Neuregulin-1 (NRG1) is a member of the NRG family of proteins that contains an epidermal growth factor (EGF)-like motif that activates EGF receptor. It is expressed in the developing cortex and acts as a chemoattractant. Erb-B2 Receptor Tyrosine Kinase 4 (ErbB4), the NRG1 receptor, is expressed in migrating interneurons (Flames et al., 2004).

It is clear that several intrinsic and extrinsic factors are involved in the regulating neuronal migration. The mode of the neuronal migration, its direction, and finally the positioning of the neurons, which is important for neuronal circuit formation and function, are regulated by a complex molecular pathway that is currently not fully understood and need to be addressed in future. In the next section, we discuss direction of neuronal migration. The orientation and directionality of cell migration can be classified into two basic axes (radial and tangential) that use different types of substrates such as glial processes or neuronal axons (Rakic, 1990).

Radial Migration

Radial migration occurs in two opposite directions: (1) pial-directed migration in which neurons migrate toward the pial surface (or the outer neural tube surface); and (2) radially inward migration in which neurons migrate away from the pial surface. In the pial-directed radial migration, the neural progenitors or neuroepithelial derived cells migrate from their site of origin toward the pial surface to reach the mantle zone. Radial glial cells, which express glial fibrillary acidic protein (GFAP), play an important role in promoting the generation of neuronal progenitors and providing the migratory substrate during the neuronal migration (Tabata and Nakajima, 2003). Although pyramidal cells of the cerebral cortex are the classical example of pial-directed radial migration, a recent study has demonstrated this movement is not as straight forward as previously thought. Recently, it has been described that neurons may switch the mode of their migratory pathway (in the intermediate and subventricular zone, IZ/SVZ) before starting radial migration (Tabata and Nakajima, 2003).

During inward radial migration, neurons move away from the pial layer after their tangential migration. The typical examples for this mode of migration are cerebellar GCs and pontine nuclei neurons (Kawauchi et al., 2006).

Tangential Migration

Tangential migration occurs in two different manners: (1) directed; and (2) non-directed. In the directed manner of migration, many neurons and interneurons migrate tangentially from their site of origin toward a specific direction. This includes cerebellar granule cell precursors (GCPs), interneurons of the cerebral cortex, neurons of the pontine nuclei, Cajal Retzius cells, neurons of the lateral reticular nucleus, and neuronal migration from the telencephalon to the olfactory bulb. The interneurons of the cerebral cortex migrate between the pallium and subpallium and the neurons of the pontine nuclei migrate between rhombomeres (Nóbrega-Pereira and Marin, 2009). Cajal-Retzius cells play an important role during neuronal migration as they secrete Reelin to guide the radial migration of the projection neurons of the neocortex. These cells originate from the discrete pallium and by tangential migration they will colonize the surface of the entire cortex (Bielle et al., 2005; Gil-Sanz et al., 2013).

The non-directed manner of tangential migration is more complicated than other modes of the migration, in that some groups of neurons exhibit migrations in all directions of the tangential plane. For example, interneurons of the marginal zone (MZ) of the cerebral cortex migrate tangentially in different directions, or change their direction repeatedly, which is referred to as random walk (Tanaka et al., 2009).

Switching Migration (Mode and Direction)

Although many neurons migrate simply to reach their final destinations, for some neurons the migration is more complicated and involves a type of migration referred to as switching migration (random walk). Switching migration can occur dynamically and includes switching from radial to tangential migration or directed to non-directed manner, and vice versa. For example, tangentially migrating cerebellar GCPs in the external germinal zone place a leading and a trailing process oriented horizontally and then orient these processes vertically to the putative molecular layer from the cell body (Komuro and Yacubova, 2003). After a stationary period following the tangential migration, the GCs switch to radial migration and migrate to the direction of their descending processes (Komuro and Yacubova, 2003). Similarly, pontine nuclei neurons also switch their mode of migration from tangential to radial as they approach the region of the pontine nuclei. The leading processes of pontine nuclei neurons divert their direction radially and start radial migration. In some neurons of the pontine nuclei, the new-born process initially elongates radially and subsequently results in the radial migration of their soma (Hatten, 1990).

The basic mechanisms and principles of neuronal migration during development that are described above are general and similar for most of the neuronal types in the CNS. However, depending on the area of the developing CNS, diverse classes of neurons follow different strategies and may use distinct molecular cues and substrate during migration from their origin to their final position. Based on this, the following sections will focus on neuronal migration in the cerebellum.

THE NEURONAL MIGRATION IN THE DEVELOPING CEREBELLUM

Similar to the other regions of the brain, neuronal migration plays a substantial role in the development of cerebellar circuits (Hoshino et al., 2005). Relatively few cell types are aggregated to form the cerebellar gray matter, which includes the cerebellar cortex and the cerebellar nuclei (CN). The neurons that reside within the cerebellum are derived from two distinct germinal zones: the VZ and the rostral rhombic lip (RL). The VZ is the neuroepithelium of the alar plate of rhombomere 1 that will form the roof of the 4th ventricle. The neurons derived from the VZ includes PCs, Golgi cells, stellate cells and basket cells (Butts et al., 2014). All of these neurons are derived from neural progenitors that express pancreas specific transcription factor 1a (Ptf1a) and use GABA as a neurotransmitter (Hoshino et al., 2005). The cerebellar neurons derived from the RL at the dorsal edge of the cerebellar primordium, include the large neurons of the CN (which provide the output of the cerebellum), unipolar brush cells (UBCs), and the GCs (the most numerous cell in the brain; Elsen et al., 2013). All of these neurons originate from neuronal progenitors that express Atonal homolog 1 (Atoh1, formerly known as Math1) and use glutamate as their neurotransmitter (Manto et al., 2013).

The cerebellar cortex segregates into three layers: the molecular layer (stellate and basket cells), the PC layer (PCs and candelabrum cells) and the granular cell layer (GCs, Golgi cells, UBCs and Lugaro cells). The two most distinctive cells in the cerebellar cortex are the large PCs and the small GCs. PCs are the principal neurons of the cerebellar cortex, and the sole output of the cerebellar cortex projecting an axon to the CN. The molecular layer of the cerebellar cortex contains inhibitory interneurons, but is dominated by PC dendrites and parallel fibers which are the axons of GCs (Butts et al., 2014). PCs develop earlier and initially secrete sonic hedgehog (Shh) which is essential for proliferation of GCPs (Wallace, 1999). Under an intricate regulatory system, the appropriate numbers, migration and positioning of these cells is required in order for synapse formation and assembly of the cerebellar cortical circuitry.

The cerebellar cortex, which is the location of the most of cerebellar neurons, is compartmentalized and the cytoarichtecture is the most elaborately patterned circuit of all the CNS structures (White and Sillitoe, 2013; Beckinghausen and Sillitoe, 2019). The molecular expression patterns, afferent/efferent fibers, and birthdates divide the cerebellar cortex into an array of parasagittal stripes (e.g., Voogd, 1967; Hashimoto and Mikoshiba, 2003; Sugihara and Shinoda, 2004; Pijpers et al., 2006; Apps and Hawkes, 2009; Marzban and Hawkes, 2011; Bailey et al., 2013; Rahimi-Balaei et al., 2016) and

is further subdivided into four transverse zones (Sillitoe et al., 2005; Marzban et al., 2008; Marzban and Hawkes, 2011; Bailey et al., 2013, 2014; Rahimi-Balaei et al., 2016). The most extensive study of cerebellar cortex compartmentation was performed on PCs using zebrin II and phospholipase C beta 4, and resulted in a striking map of topographic stripes (Plcβ4) e.g., (Marzban et al., 2007; Kim et al., 2009; Bailey et al., 2014). The cerebellar cortical interneurons are also organized and restricted to the same zone and stripes pattern (Consalez and Hawkes, 2013). In addition, stripes of the cerebellar cortex align with the terminal fields of the two major cerebellar afferent types; mossy fibers and climbing fibers (Akintunde and Eisenman, 1994; Sugihara and Shinoda, 2004; Sugihara and Quy, 2007; Rahimi-Balaei et al., 2015; Sillitoe, 2016). Remarkably, an interesting birth dating study has revealed that the zone and stripe pattern is established before migration of cerebellar neurons. It was found that, the fate of PC topography is already specified according to their birth date during E10.5–12.5 (Hashimoto and Mikoshiba, 2003). Recently, it has been shown that the CN neurons (CNNs) are organized with molecular heterogeneity that may mirror the molecular complexity of the cerebellar cortex (Sugihara and Shinoda, 2007; Chung et al., 2009a; Sugihara, 2011).

Underlying the complex cerebellar cytoarchitecture with a few neuronal types is an intricate sequence of events in which neurons that originate from different germinal zones migrate via a complicated migratory pathway to their final position and establish elaborate cerebellar compartmentation and circuits (**Figure 1**). The cerebellar glial cells migration are not included in this review because of complexity and the molecular processes involved and need to be discussed in a specific focused review article.

Purkinje Cells Origin, Migration and Final Organization

PCs, which are key neurons in the cerebellar cortex networking, complete their final mitotic division at E10.5–12.5 in mice (Hashimoto and Mikoshiba, 2003, 2004; Minaki et al., 2008). Once in the postmitotic stage, they start a short distance radial migration along the radial glial fibers (scaffold/substrate) from their site of origin in the VZ (Rakic and Sidman, 1970; Yuasa et al., 1996; Hatten, 1999). PCs exhibit an elongated morphology consistent with axonogenesis at E12.5, which is directed toward the mantle zone where they accumulate as an irregular multilayer of cells called the cerebellar plate, or PC plate (PCP) at E14.5 (Miyata et al., 2010). However, PC axons project to the CN by around E16 (in mice; Sillitoe et al., 2009) and around E18 (in rat; Eisenman et al., 1991). During the early stage of PC migration, PCs initially have a leading apical neurite and trailing process, and the cell's position changes during cerebellar primordium expansion and morphological development (Hatten and Heintz, 1995; Sotelo and Dusart, 2009). At E13, the somata of cerebellar radial glial cells—the precursor of Bergmann glia—are aligned along the surface of the 4th ventricle, and extend processes up to the pial surface of the cerebellar plate. Along with translocation of the radial glial somata from VZ, the PCs undergo delamination and migration which is quickly followed by the detachment of the trailing process of the radial glia from the VZ (Yuasa et al., 1996). The migration of PCs along radial glia has not been documented in live preparations and this assumption is based on still images. However, it is believed that the newborn Purkinje cells from the VZ migrate radially, along the processes of radial glia. Recently it was shown that those Purkinje cells originate from caudolateral VZ migrate tangentially and cross the radial glial fibers but not along with them (Miyata et al., 2010; Sotelo, 2017; Schilling, 2018). With this evidence it can be speculated that despite the tangentially oriented PCs, some of these cells use radial glial fibers for their migration. The fast proliferating VZ neuroepithelium leads to prominent bulging toward the 4th ventricle and the caudal appearance of the cerebellar primordium seems oriented horizontally. However, radial glial fibers are connected from the neuroepithelium to the subpial surface and provide substrates for the PCs that originated from the caudal VZ.

After ∼E14.5 the PCP, a multi-cell-thick immature PC layer, is expanded in orchestra with the cerebellum development and aggregated in several PC clusters (PCCs) that become well established around E17.5 (Fujita et al., 2012). It appears that there is no migratory activity during this stage, but rather a small displacement of Purkinje cell groups following expansion of the developing cerebellum. The second wave of PC migration/displacement is initiated after formation of the PCCs. PCs disperse and arrange in a single regularly spaced monolayer during cerebellar expansion and simultaneously grow their axon and dendrites (Butts et al., 2014). During PC differentiation, they collapse their apical neurite (at P0) and form numerous short neurites at ∼P6 which develop ramified dendrites at ∼P8 (Armengol and Sotelo, 1991). In humans, PC progenitors start their migration from the VZ at stages18 and 19 of the development (∼44–48 days; Müller and O'Rahilly, 1990). They form a monolayer at 16–28 weeks of the gestation, and start the cerebellar enlargement with the development of more dendritic branches, which is associated with an increase in synapse formation (Müller and O'Rahilly, 1990).

It is not clear how PCs disperse from the cluster stage to the monolayer position (**Figure 1**). One of the most studied molecules that is involved in controlling PC migration is the Reelin pathway (Larouche and Hawkes, 2006). During mouse cerebellar development, the expression of Reelin (*Reln* mRNA and glycoprotein) is first detected at E13, along the dorsal cerebellar surface corresponding to the RL-derived cells and the nuclear transitory zone (NTZ; Fink et al., 2006). It has been shown that the delamination of postmitotic lateral Purkinje cells (at around E10.5) from the ventricular neuroepithelium and their initial migration is independent on Reelin signaling because at this time-point Reelin expression in the cerebellum has not yet started (Yuasa et al., 1993). By the first week of postnatal life, Reelin expression disappears from the deep areas but is maintained in GCPs, and the expression of Reelin may continue in some GCs of adult mice (Fink et al., 2006). Dispersal of Purkinje cells from the clusteric stage is

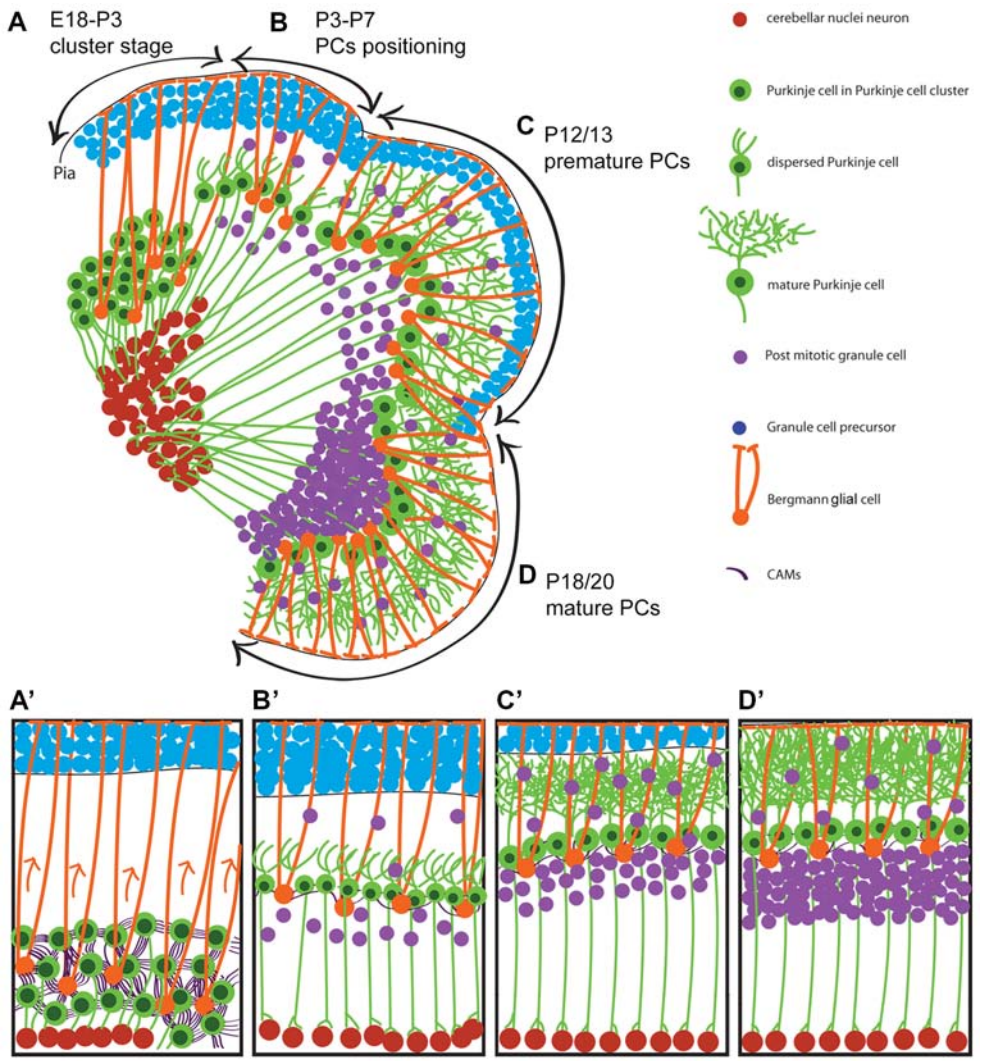

FIGURE 1 | Neuronal migration during postnatal cerebellar development. A schematic illustration of cerebellar development at sagittal section of postnatal mice. It shows that Purkinje cells (PCs) cluster disperse to establish PC monolayer and start maturation while granular layer form from external germinal zone (E18–P20). **(A,A')** Around E18 to P3, PCs are in clusteric stage and show high CAMs connections between PCs-PCs and PCs-Bergmann glial cell body which is located beside PCs during clusteric stage and extend their fibers to the cerebellar pia surface. **(B,B')** PCs in dispersal situation and positioning process (P3–P7) with less CAMs connections and show shortened Bergmann glial fibers. **(C,C')** It shows how premature PCs (P12/13) arborized (maturation process) while granule cell precursors (GCPs) migrate to the developing granular layer and become mature GCs. **(D,D')** At around P18/20 is end stage of the PCs maturation and GCPs inward migration. P, postnatal day; E, embryonic day; CAMs, cell adhesion molecules.

dependent on Reelin expression and its downstream molecules apolipoprotein E receptor 2 (ApoER2) and very-low-density lipoprotein receptor (VLDLR). Reelin binds with similar affinity to ApoER2 and VLDLR. Disabled-1 (Dab1) which is a key molecule in the Reelin pathway, is expressed by Purkinje cells, as they settle underneath the Reelin-expressing cells of the external germinal zone (Fatemi, 2005; Miyata et al., 2010). Mutations in the *Reelin* gene (*reeler* mouse; D'Arcangelo et al., 1995), *dab1* gene (*scrambler* and *yotari* mouse; Howell et al., 1997; Sheldon et al., 1997), and targeted deletion of the genes for both *Apoer2* and *Vldlr* (Trommsdorff et al., 1999) all result in a similar phenotype of ectopic Purkinje cells due to a lack of dispersal from the cluster. These findings have placed Reelin, ApoER2, VLDLR and Dab1 into a common signaling pathway. It has been shown that the Reelin protein resembles extracellular matrix proteins that are involved in cell adhesion (D'Arcangelo et al., 1995) and regulate cadherin function via Dab1.

Cadherins are a group of transmembrane proteins that mediate cell–cell adhesion during tissue morphogenesis (Maitre and Heisenberg, 2013). Cadherin-6B (also known as cadherin-7) is overexpressed in Purkinje cell progenitors and is involved in guiding migrating neurons along neurites that express the same cadherin during their radial migration. These findings indicate that cadherin adhesive mechanisms are involved in neuronal guidance (Takei et al., 2000). It has also been

shown that Dab1 signaling controls the adhesive property of neurons to radial glia. The newborn neurons in the cortex of *scrambler* mice remain attached to the process of their parental radial glia during the entire course of radial migration and this abnormal neuronal-glial adhesion is highly linked to the positional abnormality of neurons in *scrambler* mice. Additionally, the phosphorylation of tyrosine residues of Dab1 regulates α3 integrin levels in migrating neurons and their timely detachment from the radial glial fibers (Sanada et al., 2004). Furthermore, direct interaction of phosphorylated Dab1 with other intracellular proteins such as members of Crk (adapter molecule crk also known as proto-oncogene c-Crk or p38) family might connect the Reelin pathway to integrin-mediated adhesion and migration of neurons (Ballif et al., 2004; Mayer et al., 2006). It has been shown that abnormal migration of neurons in *scrambler* mice is associated with an impaired detachment of neurons from clonally related radial glial cells. This abnormal neuronal-glial adhesion depends on α3 integrin signaling that is regulated by Dab1 (Sanada et al., 2004). However, a major challenge still remains: how do Purkinje cells from the clusteric stage disperse to their position in a monolayer?

It has been suggested that the PCC position changes during cerebellar surface development, which is extended rostrocaudally and mediolaterally and becomes arranged in a monolayer due to cerebellar expansion (Butts et al., 2014). In addition, GCs have been proposed to be a major player in the positioning of Purkinje cells postnatally (Jensen et al., 2002). However, several reports have shown that, Purkinje cells respond differently to different GC defects (such as hypoplasia, agenesis). In most cases, each affected cerebellum comprises several small percentages of Purkinje cells population, which are either in different ectopic locations, or arranged in the monolayer position. For example, a study of the *math1* null-mutant mouse in which the external germinal zone does not form, three populations of ectopic Purkinje cells have been described (Jensen et al., 2002). In the *scrambler* (mutation in *Dab1*, Reelin adaptor protein), the cerebellum is small because the size of the GC population is severely diminished by ∼80% and approximately 95% of Purkinje cells (not all) fail to complete their migration (Goldowitz et al., 1997; Reeber et al., 2013). Chemokine receptor 4 (*Cxcr4*) deficiency results in a lower number of GCs in the cerebellum and partially disorganized ectopic Purkinje cells (Huang et al., 2014), which is very similar to the phenotype described in *Weaver* mice (Smeyne and Goldowitz, 1989; Chen et al., 2009). It has been suggested that protein tyrosine phosphatase, non-receptor type 11 (Ptpn11) regulates formation of the laminar cerebellar cortex by controlling GC migration via the Cxcl12/Cxcr4 signaling (Hagihara et al., 2009), although removing *Ptpn11* in the external germinal zone has no distinct effect on cerebellar corticogenesis (Li et al., 2014). These results indicate that GCs are not the main player driving Purkinje cell organization in the cerebellum. Such an elaborate Purkinje cell monolayer organization cannot be explained by surface expansion and GC development. The development of this monolayer organization must be precisely regulated by active cellular and molecular processes rather than by a passive expansion.

Do PCs use any substrates or cells such as Bergmann glia cells to disperse from the clusteric stage to their final destination? Sudarov and Joyner (2007) introduced the role of GCs and Bergmann glia during formation of the base of each fissure (as an anchoring center) and proposed that this dictates the shape of the folia. Bergmann glia are defined as PC-associated astrocytes and are a specific type of astrocyte, which are zonally organized in the cerebellar cortex (Reeber et al., 2018). Bergmann glial cells originate from radial glia within the VZ. The radial glia transform to Bergmann glial cells during E14.5–E18.5 (in mice) under control of Ptpn11, which maintains the basal processes of the radial glia and relocates somata from the VZ to the nascent PCCs (Yuasa, 1996; Li et al., 2014). It is well documented that Bergmann fibers are associated with GCs in migration during cerebellar postnatal development, and this is the origin of the concept of glia-guided neuronal migration (Hatten, 1990). Recently, it was suggested that Bergmann glial cells are essential in cerebellar corticogenesis, especially through monolayer formation of Purkinje cells, dendritogenesis, migration of GCs, and circuit formation (Cajal, 1911; Rakic, 1971; Altman and Bayer, 1997; De Zeeuw and Hoogland, 2015; Leung and Li, 2018). Yamada et al. (2000) showed that not only are Bergmann glial cells associated with Purkinje cells in the adult cerebellum but they are also associated with Purkinje cells during their migration, dendritogenesis, synaptogenesis and maturation (Yamada and Watanabe, 2002). It is still controversial whether Bergmann glia regulate Purkinje cell monolayer formation through Notch-RBP-J signaling and notch ligand, Delta-like 1 (Komine et al., 2007; Hiraoka et al., 2013), since ablation of genes from Bergmann glia does not affect Purkinje cell monolayer formation while ablation of *Dner* (delta/notch-like EGF receptor containing) from Purkinje cells results in Bergman glia disruption (Eiraku et al., 2005; Tohgo et al., 2006; Greene et al., 2016). Bergman glia are rich in glutamate receptors and transporters [SLC1A3 (GLASTs) or the excitatory amino acid transporter, EAAT1] that are involved in Purkinje cell synapse formation (O'Hearn and Molliver, 1997). In fetal and neonatal stages, SLC1A3 is expressed ubiquitously in cerebellar radial glia or astrocytes and excessively in Bergmann glia at the postnatal stage (Yamada et al., 2000). It has been shown that the dendrites of the growing Purkinje cells ascend through the $GFAP^{+}/SLC1A3^{+}$ rod—like Bergmann fibers to reach the external granular layer (Yamada et al., 2000; Yamada and Watanabe, 2002). Studies on the *reeler* and *weaver* mutants has shown that SLC1A3 is down regulated in cerebellar astrocytes associated with Purkinje cells (Fukaya et al., 1999).

Reelin is also important for GFAP positive glial cell differentiation, process extension and orientation (Forster et al., 2006). In comparison to wild type mice, *reeler* mutant mice have unusual, numerous and heavily stained astrocytes with GFAP (Benjelloun-Touimi et al., 1985). Interestingly, in *scrambler* mutant mice, the cerebellum is small with no foliation, with GCs placed normally but their number reduced, and Purkinje

cell numbers decreased and placed ectopically (Goldowitz et al., 1997). Goldowitz et al. (1997) showed that the effects of Reelin on Purkinje cells could also be mediated indirectly by Bergmann glia. Although these studies indicate the role of the Reelin pathway in neuronal migration and Bergmann glia cell development, there is no evidence that Purkinje cells are using somal transduction or glial guided migration (Schilling, 2018). Therefore, it is possible that Purkinje cells utilize a different mode of migration in which they disperse passively with the assistance of a pulling force from the Bergmann glia by regulating cell adhesion molecules to form a Purkinje cell monolayer (**Figure 1**). This should be examined in future studies.

GABAergic Interneurons (Stellate/Basket and Golgi Cells)

Precursors of stellate and basket cells are generated within the VZ prenatally (when they express the paired homeobox gene, *Pax2*) and then migrate from the cerebellar plate to the developing white matter and postnatally (in mice) through the folial white matter while continuing to undergo cell division (Wefers et al., 2018). Thereafter, they migrate radially towards the molecular layer to accumulate at the inner border of the external granular layer and then migrate tangentially before settling at their final position within the molecular layer. A new study published by Wefers et al. (2018) document that the movement of cerebellar interneurons, basket cells and stellate cells, are highly directed and rerouted to the molecular layer during their transit through the nascent cerebellar cortex. They also showed that both the speed and directional persistence of basket cells and stellate cells are larger in the nascent GC layer than in the molecular layer (Wefers et al., 2018).

Golgi cell precursors are GC layer inhibitory interneurons and are born prenatally within the VZ. From the cerebellar plate these cells migrate to developing white matter while continuing proliferation during the migration until around P4 (Zhang and Goldman, 1996; Weisheit et al., 2006). During the perinatal development, Golgi cell precursors continue the migration through the developing folial white matter and terminate migration postnatally within the developing granular layer (Maricich and Herrup, 1999). In addition, a subset of Golgi cells are derived from the external germinal zone (Chung et al., 2011). These cells migrate within the white matter and become postmitotic postnatally and then migrate to position within the granular layer (Yamanaka et al., 2004; Wefers et al., 2018).

Although the mode and direction of migration of the GABAergic interneurons of the cerebellar cortex is a complex process and not entirely clear from origin to final position. However, based on the evidence the migration within the cerebellar cortex could be in the random walk mode.

Granule Cell Origin, Migration and Final Destination

The GCPs that originate in the RL (Atoh1 expressing progenitors) migrate tangentially through a subpial stream pathway, and over the cortical surface to form the external germinal zone, similar to the rostral migratory stream from the ganglionic eminences to the olfactory bulb (Komuro and Yacubova, 2003; Stenman et al., 2003; Machold and Fishell, 2005). Simultaneously, GCPs co-express *Pax6, Meis1, Zic1/2* and *Barhl1* while post mitotic (mature) GCs do not express *Atoh1* (Stoykova and Gruss, 1994; Ackerman et al., 1997; Miyata et al., 1999; Morales and Hatten, 2006). Although the existence of a substrate or scaffold in tangential migration has not been confirmed, it is possible that the pial meninges have this role as these processes are present underneath the pial surface (Komuro and Yacubova, 2003). In addition, the external germinal zone is unique among proliferative germinal zones of the CNS as it is adjacent to the pial surface rather than the ventricular surface. The cells in this layer are highly proliferative, generating an enormous number of granule cell progeny, thereby greatly increasing the thickness of the external germinal zone. In mice at E12.5 to E17, GCPs are born and migrate to establish the external germinal zone (postmitotic GCs typically sojourn for 1–2 days within the lower layers of the external germinal zone) and give rise to GCs during the first two postnatal weeks (**Figure 1**; Komuro et al., 2001; Wang and Zoghbi, 2001). In humans, the external germinal zone is distinguished as a distinct layer between 10 weeks gestation to 2 month postnatally and will disappear by about year one and a half (Marzban et al., 2015). GCs initially follow a tangential migration and after proliferation in the external germinal zone, the cells migrate radially. The GCs situated in the inner layers of the external germinal zone start redial migration along Bergmann glial fiber to form the granular layer while expressing *NeuroD1* (an early marker of the differentiated GCs). The expression of *Unc5h3* and *Pax6* continues throughout the life span (Komuro and Yacubova, 2003). The granule cells also change from a round cell to a more horizontal-oriented shape as they begin to extend axons tangential to the cortical surface. The CXCR4, a G-protein-coupled chemokine receptor, is broadly expressed in cells of the CNS and can mediate migration in response to its ligand, stromal derived factor 1 (SDF-1; also known as chemokine ligand 12, CXCL12). The CXCR4/CXCL12 signaling pathway is involved in the migration of GCPs in the rostral migratory stream from the RL. The alterations in this pathway result in the movement of GCPs toward deeper positions away from the meninges, i.e., the inward radial migration, to form the granular layer (Leto et al., 2016). In the GC migration pathway, Sema6A functions in the switch from tangential migration in the external germinal zone to radial migration along Bergmann glia (Leto et al., 2016).

These postmitotic GCs migrate radially inward from the external germinal zone and pass by the developing Purkinje cell layer, to generate the granular layer. The cells migrate along the processes of the Bergmann glia, which is only present in the cortex of the cerebellum (**Figure 1**). Electron microscopic studies have detected Bergmann fibers in the external germinal zone by E15.5 in mice, and by 9 weeks gestation in humans (Choi and Lapham, 1980). The radial migration of the cerebellar granule neurons depends on actomyosin of the leading-process which coordinates organelle positioning and adhesion receptor dynamics (Ballif et al., 2004). During cerebellar development,

DCX is strongly expressed by migratory GCs (as occurs in Purkinje cells) to mediate coupling of the nucleus to the centrosome (Gleeson and Walsh, 2000; Deutsch et al., 2010). Shh which is expressed by Purkinje cells plays a key role in GC proliferation, and may also provide a stop signal for GC proliferation and the beginning of the terminal differentiation as these cells migrate toward the source of Shh in Purkinje cell layer (Lewis et al., 2004). On the other hand, it is possible that the migration and maturation of GCs is not associated with Shh pathway signaling, but rather the subsequent loss of precursor cells from the external germinal zone limits the period over which postmitotic GCPs are generated (Lewis et al., 2004). The cellular and molecular mechanisms of cerebellar GC migration is reviewed by Yacubova and Komuro (2003).

Cerebellar Nuclei Neurons Origin, Migration and Final Destination

During the early stages of the cerebellar development *Atoh1*-expressing neural progenitors, which arise from the RL at around E9.5–12.5, give rise to the excitatory (glutamatergic) CN projection neurons (Manto et al., 2013; Marzban et al., 2015). The CNN precursors migrate tangentially from the RL through the rostral migratory stream to midway of the cerebellar primordium and then change direction toward the NTZ, a transient cell mass that is subsequently partitioned and organized to form the medial, interposed and lateral CN (Fink et al., 2006; Kurosaka and Kashina, 2008). During development of the glutamatergic CNNs, transcription factors *Pax6*, *Tbr2*, *Tbr1 and Lmx1a* are expressed sequentially within the neurons of the RL and the NTZ (Fink et al., 2006). It has been shown that *Tbr1* knockout mice have a similar number of CNNs, but the boundaries are not properly delineated (Fink et al., 2006). Neuroblasts that express Pax6/Reelin move radially to become Tbr2 positive cells (Fink et al., 2006). The formation of the dentate nucleus (the largest and most lateral cerebellar nucleus) begins by stage 20 (52 days in humans) when precursors (interneurons INs and projection neurons) migrate radially from the VZ and rostromedially from the RL (Marzban et al., 2015). In mice, projection neurons of CN originate from the RL and unipolar neuroblasts migrate in the subpial stream toward the NTZ under the guidance of both diffusible Netrin (a family of laminin-related secreted proteins) and Slit (an extracellular matrix protein; Fink et al., 2006; Guerrini and Parrini, 2010; Matsuki et al., 2013; Qin et al., 2017). Interestingly, a study using quail-chick chimeras has shown that the rostromedial end of the cerebellar primordium originates from the alar plate of the caudal mesencephalon (Hallonet and Alvarado-Mallart, 1996). By mapping the Ptf1a promoter with a reporter, it was shown that the VZ only gives rise to inhibitory neurons of the CN. Thus the CNNs are assembled in a coordinated fashion through integration of $PTF1a^{+}$ and $ATOH1^{+}$ lineages in local circuits that migrate from two different germinal zones (Leto et al., 2016). Nichols and Bruce (2006) hypothesized that the mesencephalic neural crest is the source of several migratory streams and it is the dorsal intermediate stream that gives rise to the neurons of the CN.

During brain development, in the majority of brain regions (including CN) the CXCR4/CXCL12 signaling pathway is the most important signaling pathway that regulates neuronal migration. This receptor first appears in immature neurons in the RL at E12.5 (Tissir et al., 2004) and the expression of this receptor continues in the RL-derived CN precursors during the rostral subpial migratory stream pathway to the NTZ. Their ligand CXCL12 is expressed simultaneously in the meninges overlying this migratory pathway. Similar to tangential migration of GCPs, this indicates the potential interaction of CXCR4- and CXCL12-expressing cells in the rostral migratory stream. This may facilitate the rostral migration of RL-derived neurons and also change the direction of the migration toward the NTZ. This occurs through the detachment of neurons in this region from the pial surface to descend toward deeper positions in the NTZ (Tissir et al., 2004).

Although there is some evidence for tangential migration of CNNs from the RL subpially to the midway of the cerebellar primordium, the mode of the migration and the substrate utilized during the change of the direction from the pial surface of the cerebellar primordium to the NTZ are not known. Furthermore, the mode of migration and the substrate pathway for the putative subset of mesencephalic derived cerebellar nuclear neurons are also not clear and need to be addressed.

Unipolar Brush Cell Origin, Migration, Final Position

UBCs project directly to GCs and amplify vestibular inputs to the cerebellum. In mice, the UBCs are generated from E13.5 to the early neonatal period (P0.5; Marzban et al., 2015). These cells originate from the RL and migrate through the developing white matter before settling in the GC layer of the cerebellar cortex (Hevner et al., 2006). The translocation of the UBCs from white matter to GC layer occurs between P3 to P10 and these cells sojourn in white matter for a period of time (Englund et al., 2006). Loss of the neurofibromatosis type 1 (*Nf1*) gene leads to imbalance in generating the appropriate numbers of glial cells, GC/UBC fate-specification/differentiation and GC/UBC migration (Kim et al., 2014). Studies have also shown a role for DCX in the neurogenesis and migration of UBCs (Manohar et al., 2012; Paolone et al., 2014). Furthermore, Wnt1 glycoprotein expression in the upper RL and UBCs is related to molecular identity and cell migration in cerebellar development (Hagan and Zervas, 2012). A previous study by Englund et al. (2006), reported that Tbr2 positive UBCs migrated from RL explants directly into the developing white matter of adjacent cerebellar slices (Hevner et al., 2006).

ANIMAL MODELS IN NEURONAL MIGRATION

The use of animal models is a powerful approach to understand both human disease and basic biology (Schofield et al., 2012). Several human developmental malformations have been attributed to defects in neuronal migration and have been

TABLE 2 | Mutant mice models with cerebellar neuronal migration defects.

Mouse model	Gene	Function	Defect	Reference
Reeler (like lissencephaly 2 or Norman-Robert syndrome in human)	*Reln*	Neuronal migration (Purkinje cells in cerebellum and pyramidal cells in cerebral cortex)	Ectopic Purkinje cell cluster (~80%), no foliation, cerebellar hypoplasia	Goffinet (1983), Yuasa et al. (1993) and Miyata et al. (2010)
Scrambler	*Dab1*	The Reelin-Dab1 signaling pathway involves in neuronal migration and also in lamination	Ectopic Purkinje cell cluster, no foliation, cerebellar hypoplasia	Chung et al. (2007, 2009b)
VLDLR/ApoE2	*VLDLR/ApoE2*	Reelin receptors involves in neuronal migration and also in lamination	Ectopic Purkinje cell cluster, no foliation, cerebellar hypoplasia	Reddy et al. (2011)
Src/Fyn	*Src/Fyn*	Downstream molecules of Reelin signaling pathway involves in neuronal migration and also in lamination	Ectopic Purkinje cell cluster, no foliation, cerebellar hypoplasia	Kuo et al. (2005)
Staggerer	*RORa*	RORa is a gene expressed only in Purkinje cells in the olivocerebellar circuit	Purkinje cells are small, ectopic, possess rudimentary dendritic arbors and their number is reduced by about 75%. All of the granule cells and 60% of the inferior olivary neurons die during the first postnatal month.	Hadj-Sahraoui et al. (1997)
Pten	*Pten*	Pten express in Bergmann glia (scaffold)	Ectopic Purkinje cells and Purkinje cell dendritic arborization	Yue et al. (2005)
SmoA2	*SmoA2*	Member of SHH pathway	Ectopic clusters of Purkinje cells with disorganized dendritic arbors and axonal collaterals	Armengol and Sotelo (1991) and Dey et al. (2012)
Naked Ataxic (*nax*)	*Acp2*	Lysosomal acid phosphatase 2	Excessive migration of Purkinje cells to the molecular layer, no Purkinje cell monolayer formation, cerebellar hypoplasia, reduced granule cells proliferation	Mannan et al. (2004); Bailey et al. (2013, 2014); Rahimi-Balaei et al. (2016, 2018) and unpublished data
p35/Cdk5	*p35/Cdk5*	Cyclin-dependent kinase 5 and its regulator, p35 involve in neuronal migration, proliferation and neurite outgrowth	Normal gross morphology, folia and lamination. Molecular layer with more cell density (GCs) and ectopic PCs in granular layer	Chae et al. (1997)
Weaver	*Girk2*	G protein-activated inward rectifier potassium channel 2	Beside PCs and GCs death, neuronal migration defect as a result of Bergman glia abnormality	Rakic and Sidman (1973)
Rp58	*Rp58*	GABAergic and Glutamatergic neuron development	Severe cerebellar hypoplasia and developmental failure of Purkinje cells, Bergmann glia and granule cells	Baubet et al. (2012)
CXCR4- and *SDF-1* deficient	*CXCR4*- and *SDF-1(*aka *CXCL12*)	The chemokine receptor 4 (CXCR4)–chemokine ligand 12 signaling pathway involve in neuronal migration and proliferation	Abnormal cerebellum, ectopic PCs, irregular external germinal zone	Ma et al. (1998), Larouche and Hawkes (2006) and Huang et al. (2014)
Astn or *Pex2*	*Astn* or *Pex2*	Genes for glial-guided neuronal migration	Ectopic granule cells precursors, abnormal Purkinje cell dendrite development, and external germinal zone present until late childhood cerebellum	Faust (2003)
BDNF	*BDNF*	Purkinje cells provide BDNF and promote granule cells precursors to differentiate and migrate along Bergmann glia fibers	Defects in cerebellar patterning such as ectopic granule cells precursors	Borghesani et al. (2002)
Rb/p107	*Rb/p107*	Survival of granule cells	Purkinje cells are disarranged with dystrophic dendrites	Marino et al. (2003) and Sotelo and Dusart (2009)
VPS18	*VPS18*	Disrupting multiple vesicle transport pathways to lysosomes	Neurodegeneration and impaired neuronal migration	Peng et al. (2012) and Davies (2013)
MDM2	*MDM2*	Link between p53 and Shh signaling pathways in granular neuronal precursors	Reduced levels of MDM2 and increased levels of p53 have small cerebella with shortened folia, reminiscent of deficient Shh signaling	Malek et al. (2011) and Gil-Sanz et al. (2013)
Tbr1	*Tbr1*	Cerebellar nuclei migration	Defect in medial cerebellar nuclei plus lateral and interpose	Fink et al. (2006)

confirmed in mouse models in which a gene mutation results in abnormal neuronal migration (**Table 2**).

In *reeler* knockout mice, the first manifestation of PCP malformation is at E14.5 and is prominent during cerebellar foliation at around E17.5 (Goffinet, 1983; Yuasa et al., 1993; Hadj-Sahraoui et al., 1997). This is mutation produces severe disorders in cellular migration throughout the brain and in the cerebellum it results in defects in Purkinje cell positioning, decreased proliferation and migration of GCs, and abnormality in foliation (Trommsdorff et al., 1999). The reduction and migratory defects observed in GCs could be due to Shh insufficiency caused by ectopically located Purkinje cells, which is far away from external germinal zone. The number of UBCs is also decreased and the cells are not positioned correctly (Trommsdorff et al., 1999). Interestingly, while there is no abnormality in the development of the NTZ in *reeler* knockout mice, the CN are significantly affected. The organization within the CN is especially disrupted in the lateral and medial CN. However, it has also been reported that alterations in the expression of the genes encoding the proteins in the Reelin signaling pathway do not change the morphology of the CN in mice. These components of Reelin pathway are cell surface receptor molecules VDLR/ApoER2, and intracellular signaling molecules Dab1, and tyrosine kinases Src and Fyn. In *Dab-1* mutant, *scrambler* mice, neurons show increased adhesion to radial glia which prevents them from reaching their final destination. These mice are ataxic and exhibit several neuroanatomical defects reminiscent of *reeler* mice. These findings indicate that abnormalities in the regulation of Reelin pathway result in cerebellar cortex anomalies which also result in defects in the development of CN (Fatemi, 2005).

In mice with a point mutation in the Lysosomal Acid phosphatase 2 (Acp2) gene, the result is a cerebellar defect with excessive migration of Purkinje cells to the molecular layer (Bailey et al., 2013, 2014; Rahimi-Balaei et al., 2016, 2018). We have recently investigated the role of Reelin-Dab1 signaling and its relationship to Erk1/2 (a member of mitogen activated kinases family) during Purkinje cell monolayer formation in the *Acp2* mutant cerebellum. Our findings indicate that down regulation of Reelin together with up regulation of phospho-Dab1 leads to the excessive and incorrect Purkinje cell migration in the *Acp2* mutant mice (under revision; Ashtari, 2017). In addition, it has been shown that the vacuole protein sorting 18 (VPS18), a core protein in intracellular vesicle transport, is involved in neuronal survival and CNS development. Genetic deletion of VPS18 leads to neurodegeneration and impaired neuronal migration as a result of disruption of multiple vesicle transport pathways that produce lysosomes. These findings indicate the importance of lysosomes in neuronal migration (Peng et al., 2012).

It is known that mouse double minute 2 homolog (MDM2), also known as E3 ubiquitin-protein ligase is a link between p53 and Shh. Using a p53 inhibitor it was shown that MDM2 is part of a signaling pathway in the development of GCs. It was reported that mice with reduced levels of MDM2 and increased levels of p53 have small cerebella with shortened folia, and Purkinje cells remained multi-layered and disorganized and exhibit stunted dendritic arborizations (Malek et al., 2011).

It has been shown that the lack of either *Astn* or *Pex2* (genes for glial-guided neuronal migration) produces a slowed migration pattern of GCPs which results in the formation of ectopic GCPs, abnormal Purkinje cell dendrite development, and the external germinal zone remains present until late childhood (Faust, 2003). Purkinje cells are an important source of brain-derived neurotrophic factor (BDNF) which promotes GCPs to differentiate and migrate along Bergmann glial fibers. Indeed, mice lacking BDNF have defects in cerebellar patterning such as ectopic GCPs (Borghesani et al., 2002). Finally, the deletion of CXCR4 leads to the premature migration of GCPs away from the proliferative zone of the external germinal zone, and small numbers of GCPs are found ectopically outside of the external germinal zone (Ma et al., 1998). Mouse models of fetal alcohol spectrum disorders and Minamata disease (a result of exposure to alcohol or methyl mercury during development) are also associated with deficits in GC migration related to interruption of a Ca^{2+}/cyclic nucleotide signaling pathway (Komuro et al., 2015).

Another study by Baubet et al. (2012) has shown that the ablation of 58 KDa repressor protein (Rp58) results in severe cerebellar hypoplasia and failure of Purkinje cells, Bergmann glia and granule cells to develop properly which leads to a delay in the formation of the primary fissure, number of folia and defective lamination of the cerebellar cortex. Marino et al. (2003) have investigated the role of Rb/p107 in the development of the cerebellum; and have shown that it is involved in the survival of granule cells. In Rb-deficient and Rb/p107 double mutants, Purkinje cells are disarranged with dystrophic dendrites. In Phosphatase and tensin homolog (*Pten*) mutant mice ectopic Purkinje cells are present (Yue et al., 2005). Similarly in mice with a genetic deletion of either smoothened (*SmoA2*, member of Shh pathway) or *Cxcr4*, ectopic clusters of Purkinje cells are present with disorganized dendritic arbors and axonal collaterals (Dey et al., 2012; Huang et al., 2014).

Early postnatal mice with a mutation in *Tbr1*, have abnormal morphogenesis of the medial CN suggesting that migration defects are associated with malformation of this region of cerebellum. It is important to note that *Tbr1* mutation is associated with the irregular formation of medial CN, as well as irregular formation of interposed and lateral nuclei. Interestingly, although there are some histologic malformations following *Tbr1* mutation, these changes are not correlated with the neuronal loss, cell death, or axonal abnormalities (Fink et al., 2006).

NEURONAL MIGRATION DISORDERS

Neuronal migration and positioning are critical processes during CNS development and circuitry formation, and defects in neuronal migration can lead to devastating brain diseases (Manto et al., 2013). It is well known that malfunctioning of the migratory process causes neuronal migration disorders (NMDs). NMDs are a heterogeneous group of birth defects with the same etiopathological mechanisms caused by the abnormal migration of neurons in the developing brain. This can result in neurological disorders with clinical manifestations including schizophrenia, autism, ataxia and epilepsy (Gleeson and Walsh,

2000; Nadarajah et al., 2003; Deutsch et al., 2010; Guerrini and Parrini, 2010; Demkow and Ploski, 2015; Marzban et al., 2015; Qin et al., 2017). The role of the Reelin pathway in neuronal migration has been extensively studied and in humans homozygous mutations in the *RELN* gene are associated with ataxia, cognitive abnormalities and cerebellar hypoplasia. In this context it has been also shown that the abnormal migration of cortical neurons is associated with reduced number of cortical gyri (lissencephaly). These results suggest an important role for Reelin in neuronal migration during the development. It should be noted that decreased levels of *RELN* expression have severe negative effects on the development of the human brain and may result in psychiatric diseases. For instance, patients who suffered from schizophrenia had reduced levels of *RELN* expression in the inhibitory neurons of their cortical areas. Additionally, decreased expression of Reelin has been observed in patients with other mental diseases, such as autistic-like disorders, bipolar disorder and major depressive disorder. Together these results suggest that Reelin has an important role in neuronal migration and synapse formation and deficits in Reelin expression may contribute to the pathophysiology of these disorders (Fatemi, 2005).

CONCLUSION

Neuronal migration is all about: where do neurons come from (origin), where do they go (neuronal migration pathway), and what are they going to become (differentiated neurons and positioning)? Given that different subsets of neurons may migrate long or short distances in different modes and directions before the positioning, there is no doubt that an accurate and precise regulation of neuronal migration is necessary in order to establish the appropriate neuronal architecture and perturbations during development can result in neuronal migration disorders. During the development of the brain, proliferative germinal zones have two important tasks which are: (1) to produce the right number of cells for the particular brain region (either too many or too few will result in abnormalities); and (2) to produce the right class of cells that need to migrate to the right position. The delineation of the regulation of these two tasks is a major goal of developmental neuroscience. In this review we have examined neuronal migration and its different modes with a focus on cerebellar cell types.

AUTHOR CONTRIBUTIONS

All authors listed have made a substantial, direct and intellectual contribution to the work, and approved it for publication.

FUNDING

This study was supported by grants from the Natural Sciences and Engineering Research Council of Canada (HM: NSERC Discovery Grant # RGPIN-2018-06040) and the ALS Canada-Brain Canada Arthur J. Hudson Translational Team Grant (JK, HM).

REFERENCES

Ackerman, S. L., Kozak, L. P., Przyborski, S. A., Rund, L. A., Boyer, B. B., and Knowles, B. B. (1997). The mouse rostral cerebellar malformation gene encodes an UNC-5-like protein. *Nature* 386, 838–842. doi: 10.1038/386838a0

Akintunde, A., and Eisenman, L. M. (1994). External cuneocerebellar projection and Purkinje cell zebrin II bands: a direct comparison of parasagittal banding in the mouse cerebellum. *J. Chem. Neuroanat.* 7, 75–86. doi: 10.1016/0891-0618(94)90009-4

Altman, J., and Bayer, S. A. (1997). *Development of the Cerebellar System: in Relation to Its Evolution, Structure and Functions*. New York, NY: CRC Press.

Apps, R., and Hawkes, R. (2009). Cerebellar cortical organization: a one-map hypothesis. *Nat. Rev. Neurosci.* 10, 670–681. doi: 10.1038/nrn2698

Armengol, J.-A., and Sotelo, C. (1991). Early dendritic development of Purkinje cells in the rat cerebellum. a light and electron microscopic study using axonal tracing in '*in vitro*' slices. *Dev. Brain Res.* 64, 95–114. doi: 10.1016/0165-3806(91)90213-3

Ashtari, N. (2017). Cerebellar corticogenesis in the lysosomal acid phosphatase (acp2) mutant mice: purkinje cell migration disorder. Available online at: http://hdl.handle.net/1993/32254

Bailey, K., Rahimi Balaei, M., Mannan, A., Del Bigio, M. R., and Marzban, H. (2014). Purkinje cell compartmentation in the cerebellum of the lysosomal acid phosphatase 2 mutant mouse (nax-naked-ataxia mutant mouse). *PLoS One* 9:e94327. doi: 10.1371/journal.pone.0094327

Bailey, K., Rahimi Balaei, M., Mehdizadeh, M., and Marzban, H. (2013). Spatial and temporal expression of lysosomal acid phosphatase 2 (ACP2) reveals dynamic patterning of the mouse cerebellar cortex. *Cerebellum* 12, 870–881. doi: 10.1007/s12311-013-0502-y

Ballif, B. A., Arnaud, L., Arthur, W. T., Guris, D., Imamoto, A., and Cooper, J. A. (2004). Activation of a Dab1/CrkL/C3G/Rap1 pathway in Retzius cells instruct neuronal. *Curr. Biol.* 14, 606–610. doi: 10.1016/j.cub.2004.03.038

Baubet, V., Xiang, C., Molczan, A., Roccograndi, L., Melamed, S., and Dahmane, N. (2012). Rp58 is essential for the growth and patterning of the cerebellum and for glutamatergic and GABAergic neuron development. *Development* 139, 1903–1909. doi: 10.1242/dev.075606

Beckinghausen, J., and Sillitoe, R. V. (2019). Insights into cerebellar development and connectivity. *Neurosci. Lett.* 688, 2–13. doi: 10.1016/j.neulet.2018.05.013

Benjelloun-Touimi, S., Jacque, C. M., Derer, P., De Vitry, F., Maunoury, R., and Dupouey, P. (1985). Evidence that mouse astrocytes may be derived from the radial glia. an immunohistochemical study of the cerebellum in the normal and reeler mouse. *J. Neuroimmunol.* 9, 87–97. doi: 10.1016/s0165-5728(85)80009-6

Bielle, F., Griveau, A., Narboux-Nême, N., Vigneau, S., Sigrist, M., Arber, S., et al. (2005). Multiple origins of Cajal-Retzius cells at the borders of the developing pallium. *Nat. Neurosci.* 8, 1002–1012. doi: 10.1038/nn1511

Borghesani, P. R., Peyrin, J. M., Klein, R., Rubin, J., Carter, A. R., Schwartz, P. M., et al. (2002). BDNF stimulates migration of cerebellar granule cells. *Development* 129, 1435–1442.

Bortone, D., and Polleux, F. (2009). KCC2 expression promotes the termination of cortical interneuron migration in a voltage-sensitive calcium-dependent manner. *Neuron* 62, 53–71. doi: 10.1016/j.neuron.2009.01.034

Butts, T., Green, M. J., and Wingate, R. J. (2014). Development of the cerebellum: simple steps to make a 'little brain'. *Development* 141, 4031–4041. doi: 10.1242/dev.106559

Cajal, S. R. (1911). *Histologie Du Systéme Nerveux De L'homme & Des Vertébrés*. Paris: Maloine.

Chae, T., Kwon, Y. T., Bronson, R., Dikkes, P., Li, E., and Tsai, L.-H. (1997). Mice lacking p35, a neuronal specific activator of Cdk5, display cortical lamination defects, seizures, and adult lethality. *Neuron* 18, 29–42. doi: 10.1016/s0896-6273(01)80044-1

Chen, K. A., Lanuto, D., Zheng, T., and Steindler, D. A. (2009). Transplantation of embryonic and adult neural stem cells in the granuloprival cerebellum of the weaver mutant mouse. *Stem Cells* 27, 1625–1634. doi: 10.1002/stem.83

Chen, G., Sima, J., Jin, M., Wang, K.-Y., Xue, X.-J., Zheng, W., et al. (2008). Semaphorin-3A guides radial migration of cortical

neurons during development. *Nat. Neurosci.* 11, 36–44. doi: 10.1038/nn2018

Choi, B. H., and Lapham, L. W. (1980). Evolution of bergman glia in developing human fetal cerebellum: a golgi, electron microscopic and immunofluorescent study. *Brain Res.* 190, 369–383. doi: 10.1016/0006-8993(80)90280-2

Chung, S. H., Marzban, H., Aldinger, K., Dixit, R., Millen, K., Schuurmans, C., et al. (2011). Zac1 plays a key role in the development of specific neuronal subsets in the mouse cerebellum. *Neural Dev.* 6:25. doi: 10.1186/1749-8104-6-25

Chung, S.-H., Marzban, H., and Hawkes, R. (2009a). Compartmentation of the cerebellar nuclei of the mouse. *Neuroscience* 161, 123–138. doi: 10.1016/j.neuroscience.2009.03.037

Chung, S.-H., Sillitoe, R. V., Croci, L., Badaloni, A., Consalez, G., and Hawkes, R. (2009b). Purkinje cell phenotype restricts the distribution of unipolar brush cells. *Neuroscience* 164, 1496–1508. doi: 10.1016/j.neuroscience.2009.09.080

Chung, S., Zhang, Y., Van Der Hoorn, F., and Hawkes, R. (2007). The anatomy of the cerebellar nuclei in the normal and scrambler mouse as revealed by the expression of the microtubule-associated protein kinesin light chain 3. *Brain Res.* 1140, 120–131. doi: 10.1016/j.brainres.2006.01.100

Consalez, G. G., and Hawkes, R. (2013). The compartmental restriction of cerebellar interneurons. *Front. Neural Circuits* 6:123. doi: 10.3389/fncir.2012.00123

Cooper, J. A. (2013). Mechanisms of cell migration in the nervous system. *J. Cell Biol.* 202, 725–734. doi: 10.1083/jcb.201305021

D'Arcangelo, G., Miao, G. G., Chen, S. C., Soares, H. D., Morgan, J. I., and Curran, T. (1995). A protein related to extracellular matrix proteins deleted in the mouse mutant reeler. *Nature* 374, 719–723. doi: 10.1038/374719a0

Davies, J. (2013). *Mechanisms of Morphogenesis*. San Diego, CA: Academic Press.

De Zeeuw, C. I., and Hoogland, T. M. (2015). Reappraisal of Bergmann glial cells as modulators of cerebellar circuit function. *Front. Cell. Neurosci.* 9:246. doi: 10.3389/fncel.2015.00246

Demkow, U., and Ploski, R. (2015). *Clinical Applications for Next-Generation Sequencing*. Cambridge, MA: Academic Press.

Deutsch, S. I., Burket, J. A., and Katz, E. (2010). Does subtle disturbance of neuronal migration contribute to schizophrenia and other neurodevelopmental disorders? potential genetic mechanisms with possible treatment implications. *Eur. Neuropsychopharmacol.* 20, 281–287. doi: 10.1016/j.euroneuro.2010.02.005

Dey, J., Ditzler, S., Knoblaugh, S. E., Hatton, B. A., Schelter, J. M., Cleary, M. A., et al. (2012). A distinct smoothened mutation causes severe cerebellar developmental defects and medulloblastoma in a novel transgenic mouse model. *Mol. Cell. Biol.* 32, 4104–4115. doi: 10.1128/mcb.00862-12

Eiraku, M., Tohgo, A., Ono, K., Kaneko, M., Fujishima, K., Hirano, T., et al. (2005). DNER acts as a neuron-specific notch ligand during Bergmann glial development. *Nat. Neurosci.* 8, 873–880. doi: 10.1038/nn1492

Eisenman, L. M., Schalekamp, M. P., and Voogd, J. (1991). Development of the cerebellar cortical efferent projection: an *in-vitro* anterograde tracing study in rat brain slices. *Brain Res. Dev.* 60, 261–266. doi: 10.1016/0165-3806(91)90055-n

Elsen, G. E., Juric-Sekhar, G., Daza, R. A., and Hevner, R. F. (2013). "Development of cerebellar nuclei," in *Handbook of the Cerebellum and Cerebellar Disorders*, eds M. Manto, D. Gruol, J. Schmahmann, N. Koibuchi and F. Rossi (Heidelberg: Springer), 179–205.

Englund, C., Kowalczyk, T., Daza, R. A., Dagan, A., Lau, C., Rose, M. F., et al. (2006). Unipolar brush cells of the cerebellum are produced in the rhombic lip and migrate through developing white matter. *J. Neurosci.* 26, 9184–9195. doi: 10.1523/jneurosci.1610-06.2006

Fatemi, S. H. (2005). Reelin glycoprotein: structure, biology and roles in health and disease. *Mol. Psychiatry* 10, 251–257. doi: 10.1038/sj.mp.4001613

Faust, P. L. (2003). Abnormal cerebellar histogenesis in PEX2 zellweger mice reflects multiple neuronal defects induced by peroxisome deficiency. *J. Comp. Neurol.* 461, 394–413. doi: 10.1002/cne.10699

Feng, Y., and Walsh, C. A. (2001). Protein-protein interactions, cytoskeletal regulation and neuronal migration. *Nat. Rev. Neurosci.* 2, 408–416. doi: 10.1038/35077559

Fink, A. J., Englund, C., Daza, R. A., Pham, D., Lau, C., Nivison, M., et al. (2006). Development of the deep cerebellar nuclei: transcription factors and cell migration from the rhombic lip. *J. Neurosci.* 26, 3066–3076. doi: 10.1523/jneurosci.5203-05.2006

Flames, N., Long, J. E., Garratt, A. N., Fischer, T. M., Gassmann, M., Birchmeier, C., et al. (2004). Short-and long-range attraction of cortical GABAergic interneurons by neuregulin-1. *Neuron* 44, 251–261. doi: 10.1016/j.neuron.2004.09.028

Forster, E., Jossin, Y., Zhao, S., Chai, X., Frotscher, M., and Goffinet, A. M. (2006). Recent progress in understanding the role of reelin in radial neuronal migration, with specific emphasis on the dentate gyrus. *Eur. J. Neurosci.* 23, 901–909. doi: 10.1111/j.1460-9568.2006.04612.x

Fujita, H., Morita, N., Furuichi, T., and Sugihara, I. (2012). Clustered fine compartmentalization of the mouse embryonic cerebellar cortex and its rearrangement into the postnatal striped configuration. *J. Neurosci.* 32, 15688–15703. doi: 10.1523/jneurosci.1710-12.2012

Fukaya, M., Yamada, K., Nagashima, M., Tanaka, K., and Watanabe, M. (1999). Down-regulated expression of glutamate transporter GLAST in purkinje cell-associated astrocytes of reeler and weaver mutant cerebella. *Neurosci. Res.* 34, 165–175. doi: 10.1016/s0168-0102(99)00052-8

Gil-Sanz, C., Franco, S. J., Martinez-Garay, I., Espinosa, A., Harkins-Perry, S., and Müller, U. (2013). Cajal-Retzius cells instruct neuronal migration by coincidence signaling between secreted and contact-dependent guidance cues. *Neuron* 79, 461–477. doi: 10.1016/j.neuron.2013.06.040

Gleeson, J. G., Allen, K. M., Fox, J. W., Lamperti, E. D., Berkovic, S., Scheffer, I., et al. (1998). Doublecortin, a brain-specific gene mutated in human X-linked lissencephaly and double cortex syndrome, encodes a putative signaling protein. *Cell* 92, 63–72. doi: 10.1016/s0092-8674(00)80899-5

Gleeson, J. G., Lin, P. T., Flanagan, L. A., and Walsh, C. A. (1999). Doublecortin is a microtubule-associated protein and is expressed widely by migrating neurons. *Neuron* 23, 257–271. doi: 10.1016/s0896-6273(00)80778-3

Gleeson, J. G., and Walsh, C. A. (2000). Neuronal migration disorders: from genetic diseases to developmental mechanisms. *Trends Neurosci.* 23, 352–359. doi: 10.1016/s0166-2236(00)01607-6

Goffinet, A. (1983). The embryonic development of the cerebellum in normal and reeler mutant mice. *Anat. Embryol.* 168, 73–86. doi: 10.1007/bf00305400

Goldowitz, D., Cushing, R. C., Laywell, E., D'Arcangelo, G., Sheldon, M., Sweet, H. O., et al. (1997). Cerebellar disorganization characteristic of reeler in scrambler mutant mice despite presence of reelin. *J. Neurosci.* 17, 8767–8777. doi: 10.1523/jneurosci.17-22-08767.1997

Govek, E. E., Hatten, M. E., and Van Aelst, L. (2011). The role of rho GTPase proteins in CNS neuronal migration. *Dev. Neurobiol.* 71, 528–553. doi: 10.1002/dneu.20850

Greene, M., Lai, Y., Pajcini, K., Bailis, W., Pear, W. S., and Lancaster, E. (2016). Delta/notch-like EGF-related receptor (DNER) is not a notch ligand. *PLoS One* 11:e0161157. doi: 10.1371/journal.pone.0161157

Guerrini, R., and Parrini, E. (2010). Neuronal migration disorders. *Neurobiol. Dis.* 38, 154–166. doi: 10.1016/j.nbd.2009.02.008

Hadj-Sahraoui, N., Frederic, F., Zanjani, H., Herrup, K., Delhaye-Bouchaud, N., and Mariani, J. (1997). Purkinje cell loss in heterozygous staggerer mutant mice during aging. *Dev. Brain Res.* 98, 1–8. doi: 10.1016/s0165-3806(96)00153-8

Hagan, N., and Zervas, M. (2012). Wnt1 expression temporally allocates upper rhombic lip progenitors and defines their terminal cell fate in the cerebellum. *Mol. Cell. Neurosci.* 49, 217–229. doi: 10.1016/j.mcn.2011.11.008

Hagihara, K., Zhang, E. E., Ke, Y. H., Liu, G., Liu, J. J., Rao, Y., et al. (2009). Shp2 acts downstream of SDF-1α/CXCR4 in guiding granule cell migration during cerebellar development. *Dev. Biol.* 334, 276–284. doi: 10.1016/j.ydbio.2009.07.029

Hallonet, M., and Alvarado-Mallart, R.-M. (1996). The chick/quail chimeric system: a model for early cerebellar development. *Perspect. Dev. Neurobiol.* 5, 17–31.

Hashimoto, M., and Mikoshiba, K. (2003). Mediolateral compartmentalization of the cerebellum is determined on the "birth date" of Purkinje cells. *J. Neurosci.* 23, 11342–11351. doi: 10.1523/jneurosci.23-36-11342.2003

Hashimoto, M., and Mikoshiba, K. (2004). Neuronal birthdate-specific gene transfer with adenoviral vectors. *J. Neurosci.* 24, 286–296. doi: 10.1523/jneurosci.2529-03.2004

Hatten, M. E. (1990). Riding the glial monorail: a common mechanism for glial-guided neuronal migration in different regions of the developing

mammalian brain. *Trends Neurosci.* 13, 179–184. doi: 10.1016/0166-2236(90)90044-b

Hatten, M. E. (1999). Central nervous system neuronal migration. *Annu. Rev. Neurosci.* 22, 511–539. doi: 10.1146/annurev.neuro.22.1.511

Hatten, M. E., and Heintz, N. (1995). Mechanisms of neural patterning and specification in the development cerebellum. *Annu. Rev. Neurosci.* 18, 385–408. doi: 10.1146/annurev.ne.18.030195.002125

Hevner, R. F., Hodge, R. D., Daza, R. A., and Englund, C. (2006). Transcription factors in glutamatergic neurogenesis: conserved programs in neocortex, cerebellum and adult hippocampus. *Neurosci. Res.* 55, 223–233. doi: 10.1016/j.neures.2006.03.004

Hiraoka, Y., Komine, O., Nagaoka, M., Bai, N., Hozumi, K., and Tanaka, K. (2013). Delta-like 1 regulates Bergmann glial monolayer formation during cerebellar development. *Mol. Brain* 6:25. doi: 10.1186/1756-6606-6-25

Hoshino, M., Nakamura, S., Mori, K., Kawauchi, T., Terao, M., Nishimura, Y. V., et al. (2005). Ptf1a, a bHLH transcriptional gene, defines GABAergic neuronal fates in cerebellum. *Neuron* 47, 201–213. doi: 10.1016/j.neuron.2005.06.007

Howell, B. W., Hawkes, R., Soriano, P., and Cooper, J. A. (1997). Neuronal position in the developing brain is regulated by mouse disabled-1. *Nature* 389, 733–737. doi: 10.1038/39607

Huang, G.-J., Edwards, A., Tsai, C.-Y., Lee, Y.-S., Peng, L., Era, T., et al. (2014). Ectopic cerebellar cell migration causes maldevelopment of Purkinje cells and abnormal motor behaviour in Cxcr4 null mice. *PLoS one* 9:e86471. doi: 10.1371/journal.pone.0086471

Inada, H., Watanabe, M., Uchida, T., Ishibashi, H., Wake, H., Nemoto, T., et al. (2011). GABA regulates the multidirectional tangential migration of GABAergic interneurons in living neonatal mice. *PLoS One* 6:e27048. doi: 10.1371/journal.pone.0027048

Jensen, P., Zoghbi, H. Y., and Goldowitz, D. (2002). Dissection of the cellular and molecular events that position cerebellar Purkinje cells: a study of the math1 null-mutant mouse. *J. Neurosci.* 22, 8110–8116. doi: 10.1523/jneurosci.22-18-08110.2002

Kawaji, K., Umeshima, H., Eiraku, M., Hirano, T., and Kengaku, M. (2004). Dual phases of migration of cerebellar granule cells guided by axonal and dendritic leading processes. *Mol. Cell. Neurosci.* 25, 228–240. doi: 10.1016/j.mcn.2003.10.006

Kawauchi, D., Taniguchi, H., Watanabe, H., Saito, T., and Murakami, F. (2006). Direct visualization of nucleogenesis by precerebellar neurons: involvement of ventricle-directed, radial fibre-associated migration. *Development* 133, 1113–1123. doi: 10.1242/dev.02283

Kim, J. Y., Marzban, H., Chung, S. H., Watanabe, M., Eisenman, L. M., and Hawkes, R. (2009). Purkinje cell compartmentation of the cerebellum of microchiropteran bats. *J. Comp. Neurol.* 517, 193–209. doi: 10.1002/cne.22147

Kim, E., Wang, Y., Kim, S. J., Bornhorst, M., Jecrois, E. S., Anthony, T. E., et al. (2014). Transient inhibition of the ERK pathway prevents cerebellar developmental defects and improves long-term motor functions in murine models of neurofibromatosis type 1. *Elife* 3:3:e05151. doi: 10.7554/elife.05151

Komine, O., Nagaoka, M., Watase, K., Gutmann, D. H., Tanigaki, K., Honjo, T., et al. (2007). The monolayer formation of Bergmann glial cells is regulated by Notch/RBP-J signaling. *Dev. Biol.* 311, 238–250. doi: 10.1016/j.ydbio.2007.08.042

Komuro, Y., Galas, L., Lebon, A., Raoult, E., Fahrion, J. K., Tilot, A., et al. (2015). The role of calcium and cyclic nucleotide signaling in cerebellar granule cell migration under normal and pathological conditions. *Dev. Neurobiol.* 75, 369–387. doi: 10.1002/dneu.22219

Komuro, H., and Yacubova, E. (2003). Recent advances in cerebellar granule cell migration. *Cell. Mol. Life Sci.* 60, 1084–1098. doi: 10.1007/s00018-003-2248-z

Komuro, H., Yacubova, E., Yacubova, E., and Rakic, P. (2001). Mode and tempo of tangential cell migration in the cerebellar external granular layer. *J. Neurosci.* 21, 527–540. doi: 10.1523/jneurosci.21-02-00527.2001

Krause, M., and Gautreau, A. (2014). Steering cell migration: lamellipodium dynamics and the regulation of directional persistence. *Nat. Rev. Mol. Cell Biol.* 15, 577–590. doi: 10.1038/nrm3861

Kuo, G., Arnaud, L., Kronstad-O'Brien, P., and Cooper, J. A. (2005). Absence of Fyn and Src causes a reeler-like phenotype. *J. Neurosci.* 25, 8578–8586. doi: 10.1523/jneurosci.1656-05.2005

Kurosaka, S., and Kashina, A. (2008). Cell biology of embryonic migration. *Birth Defects Res. C Embryo Today* 84, 102–122. doi: 10.1002/bdrc.20125

Larouche, M., and Hawkes, R. (2006). From clusters to stripes: the developmental origins of adult cerebellar compartmentation. *Cerebellum* 5, 77–88. doi: 10.1080/14734220600804668

Leto, K., Arancillo, M., Becker, E. B., Buffo, A., Chiang, C., Ding, B., et al. (2016). Consensus paper: cerebellar development. *Cerebellum* 15, 789–828. doi: 10.1007/s12311-015-0724-2

Leung, A. W., and Li, J. Y. H. (2018). The molecular pathway regulating bergmann glia and folia generation in the cerebellum. *Cerebellum* 17, 42–48. doi: 10.1007/s12311-017-0904-3

Lewis, P. M., Gritli-Linde, A., Smeyne, R., Kottmann, A., and McMahon, A. P. (2004). Sonic hedgehog signaling is required for expansion of granule neuron precursors and patterning of the mouse cerebellum. *Dev. Biol.* 270, 393–410. doi: 10.1016/j.ydbio.2004.03.007

Li, K., Leung, A. W., Guo, Q., Yang, W., and Li, J. Y. (2014). Shp2-dependent ERK signaling is essential for induction of Bergmann glia and foliation of the cerebellum. *J. Neurosci.* 34, 922–931. doi: 10.1523/jneurosci.3476-13.2014

Müller, F., and O'Rahilly, R. (1990). The human brain at stages 18–20, including the choroid plexuses and the amygdaloid and septal nuclei. *Anat. Embryol.* 182, 285–306. doi: 10.1007/bf00185521

Ma, Q., Jones, D., Borghesani, P. R., Segal, R. A., Nagasawa, T., Kishimoto, T., et al. (1998). Impaired B-lymphopoiesis, myelopoiesis and derailed cerebellar neuron migration in CXCR4-and SDF-1-deficient mice. *Proc. Natl. Acad. Sci. U S A* 95, 9448–9453. doi: 10.1073/pnas.95.16.9448

Machold, R., and Fishell, G. (2005). Math1 is expressed in temporally discrete pools of cerebellar rhombic-lip neural progenitors. *Neuron* 48, 17–24. doi: 10.1016/j.neuron.2005.08.028

Maitre, J. L., and Heisenberg, C. P. (2013). Three functions of cadherins in cell adhesion. *Curr. Biol.* 23, R626–R633. doi: 10.1016/j.cub.2013.06.019

Malek, R., Matta, J., Taylor, N., Perry, M. E., and Mendrysa, S. M. (2011). The p53 inhibitor MDM2 facilitates sonic hedgehog-mediated tumorigenesis and influences cerebellar foliation. *PLoS One* 6:e17884. doi: 10.1371/journal.pone.0017884

Mannan, A. U., Roussa, E., Kraus, C., Rickmann, M., Maenner, J., Nayernia, K., et al. (2004). Mutation in the gene encoding lysosomal acid phosphatase (Acp2) causes cerebellum and skin malformation in mouse. *Neurogenetics* 5, 229–238. doi: 10.1007/s10048-004-0197-9

Manohar, S., Paolone, N. A., Bleichfeld, M., Hayes, S. H., Salvi, R. J., and Baizer, J. S. (2012). Expression of doublecortin, a neuronal migration protein, in unipolar brush cells of the vestibulocerebellum and dorsal cochlear nucleus of the adult rat. *Neuroscience* 202, 169–183. doi: 10.1016/j.neuroscience.2011.12.013

Manto, M., Gruol, D. L., Schmahmann, J. D., Koibuchi, N., and Rossi, F. (2013). *Handbook of the Cerebellum and Cerebellar Disorders.* (Vol. 4), Netherlands: Springer.

Maricich, S. M., and Herrup, K. (1999). Pax-2 expression defines a subset of GABAergic interneurons and their precursors in the developing murine cerebellum. *J. Neurobiol.* 41, 281–294. doi: 10.1002/(sici)1097-4695(19991105)41:2<281::aid-neu10>3.0.co;2-5

Marín, O., and Rubenstein, J. L. (2001). A long, remarkable journey: tangential migration in the telencephalon. *Nat. Rev. Neurosci.* 2, 780–790. doi: 10.1038/35097509

Marín, O., Valiente, M., Ge, X., and Tsai, L.-H. (2010). Guiding neuronal cell migrations. *Cold Spring Harb. Perspect. Biol.* 2:a001834. doi: 10.1101/cshperspect.a001834

Marino, S., Hoogervoorst, D., Brandner, S., and Berns, A. (2003). Rb and p107 are required for normal cerebellar development and granule cell survival but not for Purkinje cell persistence. *Development* 130, 3359–3368. doi: 10.1242/dev.00553

Martini, F. J., and Valdeolmillos, M. (2010). Actomyosin contraction at the cell rear drives nuclear translocation in migrating cortical interneurons. *J. Neurosci.* 30, 8660–8670. doi: 10.1523/jneurosci.1962-10.2010

Marzban, H., Chung, S., Watanabe, M., and Hawkes, R. (2007). Phospholipase Cβ4 expression reveals the continuity of cerebellar topography through development. *J. Comp. Neurol.* 502, 857–871. doi: 10.1002/cne.21352

Marzban, H., Del Bigio, M. R., Alizadeh, J., Ghavami, S., Zachariah, R. M., and Rastegar, M. (2015). Cellular commitment in the developing cerebellum. *Front. Cell. Neurosci.* 8:450. doi: 10.3389/fncel.2014.00450

Marzban, H., and Hawkes, R. (2011). On the architecture of the posterior zone of the cerebellum. *Cerebellum* 10, 422–434. doi: 10.1007/s12311-010-0208-3

Marzban, H., Kim, C. T., Doorn, D., Chung, S. H., and Hawkes, R. (2008). A novel transverse expression domain in the mouse cerebellum revealed by a neurofilament-associated antigen. *Neuroscience* 153, 1190–1201. doi: 10.1016/j.neuroscience.2008.02.036

Matsuki, T., Chen, J., and Howell, B. W. (2013). Acute inactivation of the serine-threonine kinase Stk25 disrupts neuronal migration. *Neural Dev.* 8:21. doi: 10.1186/1749-8104-8-21

Mattila, P. K., and Lappalainen, P. (2008). Filopodia: molecular architecture and cellular functions. *Nat. Rev. Mol. Cell Biol.* 9, 446–454. doi: 10.1038/nrm2406

Mayer, H., Duit, S., Hauser, C., Schneider, W. J., and Nimpf, J. (2006). Reconstitution of the reelin signaling pathway in fibroblasts demonstrates that Dab1 phosphorylation is independent of receptor localization in lipid rafts. *Mol. Cell. Biol.* 26, 19–27. doi: 10.1128/mcb.26.1.19-27.2006

Minaki, Y., Nakatani, T., Mizuhara, E., Inoue, T., and Ono, Y. (2008). Identification of a novel transcriptional corepressor, Corl2, as a cerebellar Purkinje cell-selective marker. *Gene Expr. Patterns* 8, 418–423. doi: 10.1016/j.gep.2008.04.004

Miyata, T., Maeda, T., and Lee, J. E. (1999). NeuroD is required for differentiation of the granule cells in the cerebellum and hippocampus. *Genes Dev.* 13, 1647–1652. doi: 10.1101/gad.13.13.1647

Miyata, T., Ono, Y., Okamoto, M., Masaoka, M., Sakakibara, A., Kawaguchi, A., et al. (2010). Migration, early axonogenesis and reelin-dependent layer-forming behavior of early/posterior-born Purkinje cells in the developing mouse lateral cerebellum. *Neural Dev.* 5:23. doi: 10.1186/1749-8104-5-23

Morales, D., and Hatten, M. E. (2006). Molecular markers of neuronal progenitors in the embryonic cerebellar anlage. *J. Neurosci.* 26, 12226–12236. doi: 10.1523/JNEUROSCI.3493-06.2006

Nadarajah, B., Alifragis, P., Wong, R. O., and Parnavelas, J. G. (2003). Neuronal migration in the developing cerebral cortex: observations based on real-time imaging. *Cereb. Cortex* 13, 607–611. doi: 10.1093/cercor/13.6.607

Nadarajah, B., Brunstrom, J. E., Grutzendler, J., Wong, R. O., and Pearlman, A. L. (2001). Two modes of radial migration in early development of the cerebral cortex. *Nat. Neurosci.* 4, 143–150. doi: 10.1038/83967

Nadarajah, B., and Parnavelas, J. G. (2002). Modes of neuronal migration in the developing cerebral cortex. *Nat. Rev. Neurosci.* 3, 423–432. doi: 10.1038/nrn845

Nguyen, L., and Hippenmeyer, S. (2013). *Cellular and Molecular Control of Neuronal Migration*. Dordrecht: Springer Science & Business Media.

Nichols, D. H., and Bruce, L. L. (2006). Migratory routes and fates of cells transcribing the Wnt-1 gene in the murine hindbrain. *Dev. Dyn.* 235, 285–300. doi: 10.1002/dvdy.20611

Nóbrega-Pereira, S., and Marin, O. (2009). Transcriptional control of neuronal migration in the developing mouse brain. *Cereb. Cortex* 19, i107–i113. doi: 10.1093/cercor/bhp044

O'Hearn, E., and Molliver, M. E. (1997). The olivocerebellar projection mediates ibogaine-induced degeneration of Purkinje cells: a model of indirect, transsynaptic excitotoxicity. *J. Neurosci.* 17, 8828–8841. doi: 10.1523/jneurosci.17-22-08828.1997

Paolone, N., Manohar, S., Hayes, S. H., Wong, K. M., Salvi, R. J., and Baizer, J. S. (2014). Dissociation of doublecortin expression and neurogenesis in unipolar brush cells in the vestibulocerebellum and dorsal cochlear nucleus of the adult rat. *Neuroscience* 265, 323–331. doi: 10.1016/j.neuroscience.2014.01.026

Peng, C., Ye, J., Yan, S., Kong, S., Shen, Y., Li, C., et al. (2012). Ablation of vacuole protein sorting 18 (Vps18) gene leads to neurodegeneration and impaired neuronal migration by disrupting multiple vesicle transport pathways to lysosomes. *J. Biol. Chem.* 287, 32861–32873. doi: 10.1074/jbc.M112.384305

Pijpers, A., Apps, R., Pardoe, J., Voogd, J., and Ruigrok, T. J. (2006). Precise spatial relationships between mossy fibers and climbing fibers in rat cerebellar cortical zones. *J. Neurosci.* 26, 12067–12080. doi: 10.1523/JNEUROSCI.2905-06.2006

Powell, E. M., Mars, W. M., and Levitt, P. (2001). Hepatocyte growth factor/scatter factor is a motogen for interneurons migrating from the ventral to dorsal telencephalon. *Neuron* 30, 79–89. doi: 10.1016/s0896-6273(01)00264-1

Qin, R., Cao, S., Lyu, T., Qi, C., Zhang, W., and Wang, Y. (2017). CDYL deficiency disrupts neuronal migration and increases susceptibility to epilepsy. *Cell Rep.* 18, 380–390. doi: 10.1016/j.celrep.2016.12.043

Rahimi-Balaei, M., Afsharinezhad, P., Bailey, K., Buchok, M., Yeganeh, B., and Marzban, H. (2015). Embryonic stages in cerebellar afferent development. *Cerebellum Ataxias* 2:7. doi: 10.1186/s40673-015-0026-y

Rahimi-Balaei, M., Jiao, X., Ashtari, N., Afsharinezhad, P., Ghavami, S., and Marzban, H. (2016). Cerebellar expression of the neurotrophin receptor p75 in naked-ataxia mutant mouse. *Int. J. Mol. Sci.* 17:115. doi: 10.3390/ijms17010115

Rahimi-Balaei, M., Jiao, X., Shabanipour, S., Dixit, R., Schuurmans, C., and Marzban, H. (2018). Zebrin II is ectopically expressed in microglia in the cerebellum of neurogenin 2 null mice. *Cerebellum* doi: 10.1007/s12311-018-0944-3 [Epub ahead of print].

Rakic, P. (1971). Neuron-glia relationship during granule cell migration in developing cerebellar cortex. a golgi and electonmicroscopic study in macacus rhesus. *J. Comp. Neurol.* 141, 283–312. doi: 10.1002/cne.901410303

Rakic, P. (1990). Principles of neural cell migration. *Experientia* 46, 882–891. doi: 10.1007/bf01939380

Rakic, P., and Sidman, R. L. (1970). Histogenesis of cortical layers in human cerebellum, particularly the lamina dissecans. *J. Comp. Neurol.* 139, 473–500. doi: 10.1002/cne.901390407

Rakic, P., and Sidman, R. (1973). Weaver mutant mouse cerebellum: defective neuronal migration secondary to abnormality of Bergmann glia. *Proc. Natl. Acad. Sci. U S A* 70, 240–244. doi: 10.1073/pnas.70.1.240

Reddy, S. S., Connor, T. E., Weeber, E. J., and Rebeck, W. (2011). Similarities and differences in structure, expression and functions of VLDLR and ApoER2. *Mol. Neurodegener.* 6:30. doi: 10.1186/1750-1326-6-30

Reeber, S. L., Arancillo, M., and Sillitoe, R. V. (2018). Bergmann glia are patterned into topographic molecular zones in the developing and adult mouse cerebellum. *Cerebellum* 17, 392–403. doi: 10.1007/s12311-014-0571-6

Reeber, S. L., Loeschel, C. A., Franklin, A., and Sillitoe, R. V. (2013). Establishment of topographic circuit zones in the cerebellum of scrambler mutant mice. *Front. Neural Circuits* 7:122. doi: 10.3389/fncir.2013.00122

Sanada, K., Gupta, A., and Tsai, L. H. (2004). Disabled-1-regulated adhesion of migrating neurons to radial glial fiber contributes to neuronal positioning during early corticogenesis. *Neuron* 42, 197–211. doi: 10.1016/S0896-6273(04)00222-3

Schilling, K. (2018). Moving into shape: cell migration during the development and histogenesis of the cerebellum. *Histochem. Cell Biol.* doi: 10.1007/s00418-018-1677-6 [Epub ahead of print].

Schofield, P. N., Hoehndorf, R., and Gkoutos, G. V. (2012). Mouse genetic and phenotypic resources for human genetics. *Hum. Mutat.* 33, 826–836. doi: 10.1002/humu.22077

Sheldon, M., Rice, D. S., D'Arcangelo, G., Yoneshima, H., Nakajima, K., Mikoshiba, K., et al. (1997). Scrambler and yotari disrupt the disabled gene and produce a reeler-like phenotype in mice. *Nature* 389, 730–733. doi: 10.1038/39601

Sillitoe, R. V. (2016). Mossy fibers terminate directly within purkinje cell zones during mouse development. *Cerebellum* 15, 14–17. doi: 10.1007/s12311-015-0712-6

Sillitoe, R. V., Gopal, N., and Joyner, A. L. (2009). Embryonic origins of ZebrinII parasagittal stripes and establishment of topographic Purkinje cell projections. *Neuroscience* 162, 574–588. doi: 10.1016/j.neuroscience.2008.12.025

Sillitoe, R. V., Marzban, H., Larouche, M., Zahedi, S., Affanni, J., and Hawkes, R. (2005). Conservation of the architecture of the anterior lobe vermis of the cerebellum across mammalian species. *Prog. Brain Res.* 148, 283–297. doi: 10.1016/s0079-6123(04)48022-4

Smeyne, R. J., and Goldowitz, D. (1989). Development and death of external granular layer cells in the weaver mouse cerebellum: a quantitative study. *J. Neurosci.* 9, 1608–1620. doi: 10.1523/JNEUROSCI.09-05-01608.1989

Solecki, D. J., Trivedi, N., Govek, E.-E., Kerekes, R. A., Gleason, S. S., and Hatten, M. E. (2009). Myosin II motors and F-actin dynamics drive the coordinated movement of the centrosome and soma during CNS glial-guided neuronal migration. *Neuron* 63, 63–80. doi: 10.1016/j.neuron.2009.05.028

Sotelo, C. (2017). "Cerebellar transplantation: a potential model to study repair and development of neurons and circuits in the cerebellum," in *Development of the Cerebellum from Molecular Aspects to Diseases*, ed. H. Marzban (Cham: Springer), 465–493. doi: 10.1007/978-3-319-59749-2_22

Sotelo, C., and Dusart, I. (2009). Intrinsic versus extrinsic determinants during the development of Purkinje cell dendrites. *Neuroscience* 162, 589–600. doi: 10.1016/j.neuroscience.2008.12.035

Stenman, J., Toresson, H., and Campbell, K. (2003). Identification of two distinct progenitor populations in the lateral ganglionic eminence: implications for striatal and olfactory bulb neurogenesis. *J. Neurosci.* 23, 167–174. doi: 10.1523/JNEUROSCI.23-01-00167.2003

Stoykova, A., and Gruss, P. (1994). Roles of Pax-genes in developing and adult brain as suggested by expression patterns. *J. Neurosci.* 14, 1395–1412. doi: 10.1523/jneurosci.14-03-01395.1994

Sudarov, A., and Joyner, A. L. (2007). Cerebellum morphogenesis: the foliation pattern is orchestrated by multi-cellular anchoring centers. *Neural Dev.* 2:26. doi: 10.1186/1749-8104-2-26

Sugihara, I. (2011). Compartmentalization of the deep cerebellar nuclei based on afferent projections and aldolase C expression. *Cerebellum* 10, 449–463. doi: 10.1007/s12311-010-0226-1

Sugihara, I., and Quy, P. N. (2007). Identification of aldolase C compartments in the mouse cerebellar cortex by olivocerebellar labeling. *J. Comp. Neurol.* 500, 1076–1092. doi: 10.1002/cne.21219

Sugihara, I., and Shinoda, Y. (2004). Molecular, topographic, and functional organization of the cerebellar cortex: a study with combined aldolase C and olivocerebellar labeling. *J. Neurosci.* 24, 8771–8785. doi: 10.1523/jneurosci.1961-04.2004

Sugihara, I., and Shinoda, Y. (2007). Molecular, topographic, and functional organization of the cerebellar nuclei: analysis by three-dimensional mapping of the olivonuclear projection and aldolase C labeling. *J. Neurosci.* 27, 9696–9710. doi: 10.1523/jneurosci.1579-07.2007

Tabata, H., and Nakajima, K. (2003). Multipolar migration: the third mode of radial neuronal migration in the developing cerebral cortex. *J. Neurosci.* 23, 9996–10001. doi: 10.1523/jneurosci.23-31-09996.2003

Takei, Y., Teng, J., Harada, A., and Hirokawa, N. (2000). Defects in axonal elongation and neuronal migration in mice with disrupted *tau* and *map1b* genes. *J. Cell Biol.* 150, 989–1000. doi: 10.1083/jcb.150.5.989

Tanaka, T., Serneo, F. F., Higgins, C., Gambello, M. J., Wynshaw-Boris, A., and Gleeson, J. G. (2004). Lis1 and doublecortin function with dynein to mediate coupling of the nucleus to the centrosome in neuronal migration. *J. Cell Biol.* 165, 709–721. doi: 10.1083/jcb.200309025

Tanaka, D. H., Yanagida, M., Zhu, Y., Mikami, S., Nagasawa, T., and Miyazaki, J. (2009). Random walk behavior of migrating cortical interneurons in the marginal zone: time-lapse analysis in flat-mount cortex. *J. Neurosci.* 29, 1300–1311. doi: 10.1523/jneurosci.5446-08.2009

Tissir, F., Wang, C.-E., and Goffinet, A. M. (2004). Expression of the chemokine receptor Cxcr4 mRNA during mouse brain development. *Dev. Brain Res.* 149, 63–71. doi: 10.1016/j.devbrainres.2004.01.002

Tohgo, A., Eiraku, M., Miyazaki, T., Miura, E., Kawaguchi, S.-Y., Nishi, M., et al. (2006). Impaired cerebellar functions in mutant mice lacking DNER. *Mol. Cell. Neurosci.* 31, 326–333. doi: 10.1016/j.mcn.2005.10.003

Trommsdorff, M., Gotthardt, M., Hiesberger, T., Shelton, J., Stockinger, W., Nimpf, J., et al. (1999). Reeler/disabled-like disruption of neuronal migration in knockout mice lacking the VLDL receptor and ApoE receptor 2. *Cell* 97, 689–701. doi: 10.1016/s0092-8674(00)80782-5

Tsai, L.-H., and Gleeson, J. G. (2005). Nucleokinesis in neuronal migration. *Neuron* 46, 383–388. doi: 10.1016/j.neuron.2005.04.013

Tsai, H.-H., Niu, J., Munji, R., Davalos, D., Chang, J., Zhang, H., et al. (2016). Oligodendrocyte precursors migrate along vasculature in the developing nervous system. *Science* 351, 379–384. doi: 10.1126/science.aad3839

Voogd, J. (1967). Comparative aspects of the structure and fibre connexions of the mammalian cerebellum. *Prog. Brain Res.* 25, 94–134. doi: 10.1016/s0079-6123(08)60963-2

Wallace, V. A. (1999). Purkinje-cell-derived sonic hedgehog regulates granule neuron precursor cell proliferation in the developing mouse cerebellum. *Curr. Biol.* 9, 445–448. doi: 10.1016/s0960-9822(99)80195-x

Wang, V. Y., and Zoghbi, H. Y. (2001). Genetic regulation of cerebellar development. *Nat. Rev. Neurosci.* 2, 484–491. doi: 10.1038/35081558

Wefers, A. K., Haberlandt, C., Surchev, L., Steinhäuser, C., Jabs, R., and Schilling, K. (2018). Migration of interneuron precursors in the nascent cerebellar cortex. *Cerebellum* 17, 62–71. doi: 10.1007/s12311-017-0900-7

Weisheit, G., Gliem, M., Endl, E., Pfeffer, P. L., Busslinger, M., and Schilling, K. (2006). Postnatal development of the murine cerebellar cortex: formation and early dispersal of basket, stellate and golgi neurons. *Eur. J. Neurosci.* 24, 466–478. doi: 10.1111/j.1460-9568.2006.04915.x

White, J. J., and Sillitoe, R. V. (2013). Postnatal development of cerebellar zones revealed by neurofilament heavy chain protein expression. *Front. Neuroanat.* 7:9. doi: 10.3389/fnana.2013.00009

Wynshaw-Boris, A., and Gambello, M. J. (2001). LIS1 and dynein motor function in neuronal migration and development. *Genes Dev.* 15, 639–651. doi: 10.1101/gad.886801

Yacubova, E., and Komuro, H. (2003). Cellular and molecular mechanisms of cerebellar granule cell migration. *Cell Biochem. Biophys.* 37, 213–234. doi: 10.1385/cbb:37:3:213

Yamada, K., Fukaya, M., Shibata, T., Kurihara, H., Tanaka, K., Inoue, Y., et al. (2000). Dynamic transformation of Bergmann glial fibers proceeds in correlation with dendritic outgrowth and synapse formation of cerebellar Purkinje cells. *J. Comp. Neurol.* 418, 106–120. doi: 10.1002/(sici)1096-9861(20000228)418:1<106::aid-cne8>3.3.co;2-e

Yamada, K., and Watanabe, M. (2002). Cytodifferentiation of Bergmann glia and its relationship with Purkinje cells. *Anat. Sci. Int.* 77, 94–108. doi: 10.1046/j.0022-7722.2002.00021.x

Yamanaka, H., Yanagawa, Y., and Obata, K. (2004). Development of stellate and basket cells and their apoptosis in mouse cerebellar cortex. *Neurosci. Res.* 50, 13–22. doi: 10.1016/j.neures.2004.06.008

Yee, K. T., Simon, H. H., Tessier-Lavigne, M., and O'Leary, D. D. (1999). Extension of long leading processes and neuronal migration in the mammalian brain directed by the chemoattractant netrin-1. *Neuron* 24, 607–622. doi: 10.1016/s0896-6273(00)81116-2

Yuasa, S. (1996). Bergmann glial development in the mouse cerebellum as revealed by tenascin expression. *Anat. Embryol.* 194, 223–234. doi: 10.1007/bf00187133

Yuasa, S., Kawamura, K., Kuwano, R., and Ono, K. (1996). Neuron-glia interrelations during migration of Purkinje cells in the mouse embryonic cerebellum. *Int. J. Dev. Neurosci.* 14, 429–438. doi: 10.1016/0736-5748(96)00021-4

Yuasa, S., Kitoh, J., Oda, S.-I., and Kawamura, K. (1993). Obstructed migration of Purkinje cells in the developing cerebellum of the reeler mutant mouse. *Anat. Embryol.* 188, 317–329. doi: 10.1007/bf00185941

Yue, Q., Groszer, M., Gil, J. S., Berk, A. J., Messing, A., Wu, H., et al. (2005). PTEN deletion in Bergmann glia leads to premature differentiation and affects laminar organization. *Development* 132, 3281–3291. doi: 10.1242/dev.01891

Zhang, L., and Goldman, J. E. (1996). Generation of cerebellar interneurons from dividing progenitors in white matter. *Neuron* 16, 47–54. doi: 10.1016/s0896-6273(00)80022-7

Conflict of Interest Statement: The authors declare that the research was conducted in the absence of any commercial or financial relationships that could be construed as a potential conflict of interest.

frontiers in Cellular Neuroscience

ORIGINAL RESEARCH
published: 20 December 2018
doi: 10.3389/fncel.2018.00485

TRH Analog, Taltirelin Protects Dopaminergic Neurons From Neurotoxicity of MPTP and Rotenone

*Cong Zheng[1†], Guiqin Chen[2†], Yang Tan[1], Weiqi Zeng[1], Qiwei Peng[1], Ji Wang[1], Chi Cheng[1], Xiaoman Yang[1], Shuke Nie[2], Yan Xu[1], Zhentao Zhang[2], Stella M. Papa[3,4], Keqiang Ye[5] and Xuebing Cao[1]**

[1]Department of Neurology, Union Hospital, Tongji Medical College, Huazhong University of Science and Technology, Wuhan, China, [2]Department of Neurology, Renmin Hospital, Wuhan University, Wuhan, China, [3]Yerkes National Primate Research Center, Emory University School of Medicine, Atlanta, GA, United States, [4]Department of Neurology, Emory University School of Medicine, Atlanta, GA, United States, [5]Department of Pathology and Laboratory Medicine, Emory University School of Medicine, Atlanta, GA, United States

Dopaminergic neurons loss is one of the main pathological characters of Parkinson's disease (PD), while no suitable neuroprotective agents have been in clinical use. Thyrotropin-releasing hormone (TRH) and its analogs protect neurons from ischemia and various cytotoxins, but whether the effect also applies in PD models remain unclear. Here, we showed that Taltirelin, a long-acting TRH analog, exhibited the neuroprotective effect in both cellular and animal models of PD. The *in vitro* study demonstrated that Taltirelin (5 μM) reduced the generation of reactive oxygen species (ROS) induced by MPP+ or rotenone, alleviated apoptosis and rescued the viability of SH-SY5Y cells and rat primary midbrain neurons. Interestingly, SH-SY5Y cells treated with Taltirelin also displayed lower level of p-tau (S396) and asparagine endopeptidase (AEP) cleavage products, tau N368 and α-synuclein N103 fragments, accompanied by a lower intracellular monoamine oxidase-B (MAO-B) activity. In the subacute MPTP-induced and chronic rotenone-induced PD mice models, we found Taltirelin (1 mg/kg) significantly improved the locomotor function and preserved dopaminergic neurons in the substantia nigra (SN). In accordance with the *in vitro* study, Taltirelin down-regulated the levels of p-tau (S396), p-α-synuclein (S129) tau N368 and α-synuclein N103 fragments in SN and striatum. Together, this study demonstrates that Taltirelin may exert neuroprotective effect *via* inhibiting MAO-B and reducing the oxidative stress and apoptosis, preventing AEP activation and its subsequent pathological cleavage of tau and α-synuclein, thus provides evidence for Taltirelin in protective treatment of PD.

Keywords: Parkinson's disease, TRH, taltirelin, MPTP, rotenone, tau, α-synuclein, AEP

OPEN ACCESS

Edited by:
Jing-Ning Zhu,
State Key Laboratory of Pharmaceutical Biotechnology, School of Life Science, Nanjing University, China

Reviewed by:
Chen Ling,
Sun Yat-Sen University, China
Beisha Tang,
Central South University, China

***Correspondence:**
Xuebing Cao
caoxuebing@126.com

[†]These authors have contributed equally to this work

Received: *11 August 2018*
Accepted: *28 November 2018*
Published: *20 December 2018*

Citation:
Zheng C, Chen G, Tan Y, Zeng W, Peng Q, Wang J, Cheng C, Yang X, Nie S, Xu Y, Zhang Z, Papa SM, Ye K and Cao X (2018) TRH Analog, Taltirelin Protects Dopaminergic Neurons From Neurotoxicity of MPTP and Rotenone. Front. Cell. Neurosci. 12:485. doi: 10.3389/fncel.2018.00485

INTRODUCTION

Thyrotropin-releasing hormone (TRH) is widely known as a metabolism-regulating endocrine hormone acting through the hypothalamus-pituitary-thyroid axis (HPT axis). However, another role of TRH as a neuropeptide is underestimated (Gary et al., 2003; Khomane et al., 2011). TRH has long ago been proved useful in multiple animal models of diseases such as brain/spinal cord

injuries (Faden et al., 1981; Pitts et al., 1995), depression (Szuba et al., 1995; Marangell et al., 1997), epilepsy (Jaworska-Feil et al., 2001; Kubek et al., 2009), schizophrenia (Wilson et al., 1973), amyotrophic lateral sclerosis (ALS; Hawley et al., 1987; Brooks, 1989), Alzheimer's disease (AD; Mellow et al., 1989; Molchan et al., 1990) and Parkinson's disease (PD; Ogata et al., 1998). However, TRH has the intrinsic shortcomings such as short half-life, poor lipophilicity and strong HPT axis stimulating effect, which severely restrict its application (Kinoshita et al., 1998). Taltirelin (TA-0910, Ceredist®), an oral-effective TRH analog, has 10–100 times more potent central nervous system (CNS) stimulant activity and eight times longer duration than TRH. More importantly, Taltirelin has been approved in the treatment of spinocerebellar degeneration (SCD), thus is highly promising in investigating other possible applications of TRH (Kinoshita et al., 1994, 1998).

PD is a neurodegenerative disease with the second high incidence among elderly over the age of 65 (Lee and Gilbert, 2016). Motor (such as bradykinesia, tremor and rigidity) and non-motor (such as depression and constipation) symptoms of PD are directly related to the significant loss of dopaminergic neurons in the substantia nigra (SN) and accordingly dopamine (DA) deficiency within the CNS. Although these symptoms are managed by pharmacological DA substitution, lack of the disease-modifying interventions, which could prevent further neuron loss thus slow or halt the progression of the disease, PD remains an incurable disease that causes severe disability and high mortality (Poewe et al., 2017). The death of dopaminergic neurons are caused by several factors, the most prominent one among which is the pathologically elevated intracellular α-synuclein, whose toxic forms (oligomers or fibrils) or deposition induces and exacerbates other neurotoxic events, such as mitochondrial function, oxidative stress and neuroinflammation, ultimately driving the neuron death in PD (Kalia and Lang, 2015). Nevertheless, growing evidence showed that α-synuclein and another pathologic protein tau could form hybrid oligomers and enhance their aggregation in the brains of PD and AD patients (Sengupta et al., 2015). The overlap of these proteinopathies not only emphasizes a similar structural characteristics of α-synuclein and tau (Moussaud et al., 2014), but also suggests the existence of a common upstream pathological trigger. Asparagine endopeptidase (AEP, or legumain), a pH-dependent endo-lysosomal cysteine protease, is found abnormally up-regulated in AD and PD. Once activated, AEP is able to cleave amyloid precursor protein (APP), tau and α-synuclein, whose protein fragments are more susceptible to hyperphosphorylation and aggregation, thus resulting in neurotoxicity (Zhang et al., 2014, 2016, 2017). Moreover, we have recently reported that the crosstalk among α-synuclein, monoamine oxidase-B (MAO-B), 3,4-dihydroxyphenylacetaldehyde (DOPAL) and AEP plays a central role in the pathogenesis of PD (Kang et al., 2018).

TRH and its analogs reveal neurotrophic and anti-apoptotic effects by counteracting the toxic effects of various cytotoxins in PD cellular models (Jaworska-Feil et al., 2010) *via* anti-apoptosis, inhibiting the activity of glycosynthase kinase-3β (GSK-3β), decreasing the phosphorylation level of tau (Luo and Stopa, 2004), protecting against Aβ toxicity and reducing the production of inflammatory cytokines TNF-α and IL-6 *in vitro* (Faden et al., 2005). However, the underlying mechanisms were still unclear. In this study, we showed that Taltirelin significantly reduced the toxicity of MPP+ and rotenone in SH-SY5Y cells and rat primary SN neurons, ameliorated the behavioral disturbance induced by MPTP or rotenone in PD mice *via* inhibiting MAO-B activity and reactive oxygen species (ROS) generation, reducing the abnormal phosphorylation of α-synuclein and tau, inhibiting the activation of AEP and its specific cleavage effect, thus provides evidence for Taltirelin in protective treatment of PD.

MATERIALS AND METHODS

Animals

Male C57/BL6 mice, 8–9 weeks old (Beijing HFK Bioscience Co., Ltd., Beijing, China) weighing 20–25 g were used in this experiment. The animals were housed with food and water provided *ad libitum*, 12 h light/dark cycle, constant temperature and humidity. This study was carried out in accordance with the recommendations of the Guidelines of Laboratory Animals Ethics of Tongji Medical College, Huazhong University of Science and Technology. The protocol was approved by the Ethics Committee of Huazhong University of Science and Technology.

Cell Culture

SH-SY5Y Neuroblastoma Cells Culture

SH-SY5Y neuroblastoma cells (Cell Resources Center of Shanghai Institutes for Biological Sciences) were grown in DMEM/F12 medium (Hyclone, South Logan, UT, USA) supplemented with 10% FBS (Gibco, Carlsbad, CA, USA) and 100 units/ml of penicillin and streptomycin. Cultures were maintained in a humidified incubator at 37°C/5% CO_2 with medium changed every 3 days. After reaching 80% confluence, cells were seeded onto appropriate multi-well plates at a density of 4×10^5 cells/ml.

Primary Neonatal Rat Midbrain Neurons Culture

Primary rat midbrain cultures were prepared as described previously (Beaudoin et al., 2012). In brief, the midbrain was dissected from P1–3 mouse pups. The isolated tissues were then chemically and mechanically dissociated into single cell suspensions. Cells were plated into 0.5 mg/ml PLL coated 6-well plates or glass coverslips at a density of $5.5–6 \times 10^5$ per well. Incubate the cells with plating medium (DMEM/F-12 medium with 20% FBS, 100 units/ml of penicillin and streptomycin) for 4 h and replace the medium with maintenance medium: Neurobasal medium (Gibco, Carlsbad, CA, USA) with 2% B-27 supplement (Gibco, Carlsbad, CA, USA), 2 mM glutamine (Gibco, Carlsbad, CA, USA) and 100 units/ml of penicillin and streptomycin. Cultures were maintained in a humidified incubator at 37°C/5% CO_2 for 3 days *in vitro* prior to functional studies.

MTT Assay

Cell viability was quantified by colorimetric assay with MTT (Beyotime, China) according to the manufacturer's protocol. Briefly, 20 μl MTT (5 mg/ml) was added to each well (100 μl medium each) and incubated for 3 h at 37°C, then the dye was solubilized by 150 μl DMSO and the absorbance of each sample was measured at 570 nm with 630 nm as reference in a microplate reader (BioTek, Winooski, VT, USA). Cell viability = [(drug-treated well OD − MTT-free well OD)/(vehicle-treated well OD − MTT-free well OD)] × 100%.

Measurement of Lactate Dehydrogenase (LDH) Release

In order to estimate cell death, the level of lactate dehydrogenase (LDH) released from damaged cells into the culture media was measured after intervention. 1 h before the incubation endpoint, LDH release reagent was added to intervention-free wells as the maximum enzyme activity control. Then culture supernatants were collected and incubated with the appropriate reagent mixture according to the supplier's instructions (LDH Cytotoxicity Assay Kit, Beyotime, China) at room temperature for 30 min. Absorbance of each well was measured at a wavelength of 490 nm with 630 nm as reference. The absorbance of MTT-free controls was subtracted from each value; Cell death rate = [(drug-treated well OD − vehicle-treated control well OD)/(maximum enzyme activity control well OD − vehicle-treated control well OD)] × 100%.

Identification of Apoptotic Cells

In order to visually assess DNA fragmentation in SH-SY5Y cells, Hoechst 33342 staining was applied after intervention. The cultures were washed with PBS and fixed for 20 min with 4% paraformaldehyde (PFA). After fixation, cultures were washed and exposed to Hoechst 33342 (5 μg/ml; Beyotime, Shanghai, China) for 15 min. After washing, coverslips were mounted on slides and images were recorded using inverted fluorescence microscope (Olympus, Japan) with excitation wavelength 350 nm (blue fluorescence). Cells with bright blue fragmented nuclei showing condensation of chromatin were identified as apoptotic cells and counted.

PD Mice Model

Subacute MPTP-Induced PD Mice Model and Intervention

Mice were randomly divided into five groups: normal, MPTP, Taltirelin 0.2 mg/kg, 1 mg/kg, 5 mg/kg ($N = 8$). The intervention (14 days) was divided into two sections (7 days each). In the first section (MPTP + drug intervention), MPTP group was injected i.p. with MPTP (Sigma, St. Louis, MO, USA) of 30 mg/kg/d and three Taltirelin groups were pre-treated with Taltirelin (i.p.) of respective doses 4 h before MPTP injection for 7 days. In the second section (drug intervention), the MPTP group was given saline (i.p.), while three Taltirelin groups continued Taltirelin administration for another 7 days. Behavioral assessments and weights measurement were conducted on day 1, day 7 and day 14 of intervention period.

Chronic Rotenone-Induced Mice Model and Intervention

Mice were randomly divided into four groups: normal, rotenone, Taltirelin 0.2 mg/kg, 1 mg/kg ($N = 8$). Rotenone (4% Tween-20, 0.5% CMC; Sigma, St. Louis, MO, USA) was administered orally once a day at a dose of 30 mg/kg for 56 days. The Taltirelin groups were given Taltirelin i.p. of respective doses before gavage. Behavioral assessments and weights measurement were conducted on day 1 and day 56 of the intervention period.

Behavioral Assessment

Rotarod Test

Mice were placed on a rotarod system (YLS-4C, Jinan Yiyan Technology Development Co., Ltd., China) that accelerated from 5 rpm to 40 rpm over a period of 90 s and 40 rpm was maintained for maximal 300 s. The length of time that animal was able to stay on the rod (latency time) was recorded. Test of each animal was repeated three times with at least 30 min interval between each experiment and the longest latency time was adopted. Before the formal experiments, adaptational trainings were conducted for 3 days and the animals were evenly divided into different groups based on their performances.

Pole Test

Mice in each group were placed head-up on the top of a vertical pole (50 cm tall and 1 cm in diameter). The base of the pole was placed in the home cage. The mice would turn its head downward and climb along the pole to the home cage. Time of the mouse head orient downward (time-turn) and total time from the top of the pole to home cage (time-down) as an indication of the locomotion activity was recorded. Each mouse received three successive trials and the average time was calculated. Before the formal experiments, mice in each group received training for 3 days.

Serum Thyroid Hormone Measurement

Blood was collected at 2 h post-administration of drugs and placed in 4°C overnight. Then the blood was centrifugated at 3,000 rpm for 15 min and serum was collected for further analysis. The levels of thyroid stimulating hormone (TSH), free and total thyroxine (T4) or triiodothyronine (T3) were measured using ELISA kit respectively (ALPCO) according to the manufacturer's protocol. Briefly, 50 μL of serum samples or reference was pipetted into the assigned wells, followed by T3/T4 enzyme-conjugated solution with 1 h of incubation. The mixture was removed, and the plate was washed several times with water; then, working substrate solution was added to each well for reaction, and after 20 min in the dark, the reaction was stopped by adding 3 M HCl. Absorbance was read at 450 nm. The corresponding concentrations were calculated based on the standard curve.

Western Blot Analysis

For animal brain tissues, striatum or midbrain was dissected and homogenized with micro-tissue-grinders (Tiangen, OSE-Y30) in ice-cold enhanced RIPA lysis buffer [50 mM Tris, pH 7.4, 150 mM NaCl, 1% Triton X-100, 1% sodium deoxycholate,

0.1% SDS, 5 mM EDTA, 2 mM Na_3VO_4, 1 mM PMSF, 10 mM NaF and a cocktail of protease inhibitors (Roche, Branchburg, NJ, USA)]. For cellular culture, cells were scraped down by a cell scraper and lysed in lysis buffer. Brain or cellular lysates were centrifuged at 12,000 *g* at 4°C for 15 min and the protein concentrations were determined by a BCA assay kit (Pierce, Rockford). The supernatants were boiled for 10 min with 1% SDS loading buffer. After SDS-PAGE, the samples were transferred to a PVDF membrane (Millipore, USA), blocked with 5% non-fat milk for 1 h at room temperature and incubated overnight at 4°C with primary antibodies against following proteins: tyrosine hydroxylase (TH; 1:1,000, Proteintech, 25859-1-AP), p44/42 MAPK (ERK1/2; 1:2,000, Cell Signaling, #4695), phospho-p44/42 MAPK (ERK1/2; 1:2,000, Cell Signaling, #4370), α-synuclein (1:1,000, Abcam, ab85862), phospho-α-synuclein (1:1,000, Cell Signaling, #23706), phospho-tau (S396; 1:10,000, Abcam, ab109390), cleaved Caspase-3 (1:1,000, Cell Signaling, #9661), GAPDH (1:2,000, AntGene, ANT012), tau N368 and α-synuclein N103 (1:1,000, provided by Professor Keqiang Ye of Emory University). The membranes were washed with TBST, and then incubated with HRP-conjugated anti-rabbit secondary antibody (1:3,000, Antgene, ANT020) for 1 h at room temperature. After washing, the membrane was visualized with an ECL detection kit (Thermo Scientific) in the Bio-Rad imaging system. Bands intensities were analyzed with ImagineJ software.

Immunohistochemistry and Immunofluorescent Staining

Immunohistochemistry Staining

Animals were deeply anesthetized and transcardially perfused with saline, followed by 4% PFA in 0.1 M PBS (pH 7.4). Brain were dissected and fixed in 4% PFA overnight at 4°C. After fixation, tissues were transferred to 70% ethanol and processed for paraffin sectioning (4 μm/section). The sections were mounted on glass slides, deparaffinized by xylene, dehydrated in graded ethanol solutions, baked in the basic antigen retrieval buffer (pH = 6.0) and washed with phosphate buffer (pH 7.4). After washing, sections were blocked with 3% bovine serum albumin (BSA) and then incubated with diluted primary antibody in a humidified chamber overnight at 4°C. Primary antibodies against following proteins were used: TH (1:1,000, Proteintech, 25859-1-AP), phospho-tau (S396; 1:10,000, Abcam, ab109390). The sections were washed and subsequently incubated with biotinylated goat anti-rabbit IgG, then HRP labeled streptavidin fluid, followed by DAB solutions, counterstained with Harris hematoxylin, dehydrated in graded ethanol solutions and eventually cover slipped. Images were collected through an Olympus camera connected to the microscope at the same light intensity, and analyzed using Image-Pro Plus software.

Immunofluorescent Staining

For brain slices, immunofluorescent staining shared a same procedure with immunohistochemistry staining before secondary antibodies incubation. For cellular cultures, sterile coverslips were placed in 24-well plates and coated with PLL before cells were plated on the coverslips. After intervention, cells were first washed with PBS and fixed with 4% PFA. Then cells were permeabilized with 0.2% Triton X-100 and blocked with 5% BSA. Incubate brain slices or cell slides with following primary antibodies overnight at 4°C: α-synuclein (1:1,000, Abcam, ab85862), tau N368 (1:1,000, provided by Professor Keqiang Ye of Emory University). After being washed, sections were incubated in dark with appropriately diluted Alexa 488- or Cyanine 3-coupled secondary antibodies followed by DAPI staining nucleus for 10 min. To stain nuclei, incubate with DAPI for 10 min. Coverslips were mounted on slides with one drop per coverslip of antifade mounting medium (Beyotime, China). Images were collected using fluorescence microscopy with image manipulation software, and analyzed using Image-Pro Plus software.

Flow Cytometric Analysis of Reactive Oxygen Species (ROS)

After pre-treatment of PBS or Taltirelin (5 μM) for 0.5 h, SH-SY5Y cells were incubated with MPP+ (1,000 μM) or rotenone (50 μM) for 24 h. Then cells were stained with 2′,7′-dichlorodihydrofluorescein diacetate (DCFH-DA; Beyotime, China) according to the protocol. Briefly, the culture medium was removed and cells were washed twice with serum-free culture medium. Next, the cells were loaded with DCFH-DA (10 μM) in serum-free culture medium for 20 min in 37°C. After being washed twice with PBS, cells were digested with trypsin, then washed once with PBS and finally collected. The samples were analyzed for the fluorescence (488 nm excitation and 525 nm emission) of DCF by flow cytometry (FACS LSR Fortessa System, BD Biosciences, San Jose, CA, USA).

Monoamine Oxidase-B (MAO-B) Activity Assay

After pre-treatment of PBS or Taltirelin (5 μM) for 0.5 h, SH-SY5Y cells were incubated with MPP+ (1,000 μM) or rotenone (50 μM) for 24 h. Next, cells were scraped down by a cell scraper and homogenized in PBS with cocktail of protease inhibitors. Large debris was then removed by weak centrifugation (1,000 *g*, 10 min). Next, the supernatant was collected and incubated with the working solution of 100 μl containing 400 μM Amplex Red reagent, 2 U/ml HRP and 2 mM benzylamine substrate (Molecular Probes, Eugene, OR, USA). The fluorescence of MAO-B activity was measured in a fluorescence plate reader (530–560 nm excitation and 590 nm emission).

Statistic Analysis

Data were analyzed using one-way analysis of variance (ANOVA) followed by Tukey HSD or LSD *post hoc* tests for multiple comparisons between groups, and Student's *t*-test for comparing two groups. All statistical analyses were performed in SPSS 21.0 software. The significance level was set at $p < 0.05$. Data are presented as Mean ± SEM for all results.

RESULTS

Taltirelin Protected Dopaminergic Neurons Against Apoptosis *in vitro*

The neuroblastoma SH-SY5Y cells are a well-established and widely-used *in vitro* model of dopaminergic neuron origin. We found 5 μM Taltirelin induced the highest proliferation (109.70 ± 2.41% of control, $p < 0.05$) of cells after 24-h-incubation, while higher concentration (10 μM) caused a decrease of cell viability (91.64 ± 1.90% of control, $p < 0.05$; **Figure 1D**). Thus, we adopted 5 μM for our following experiments.

Consistent with the previous studies, SH-SY5Y cells exposed to rotenone for 24 h underwent substantial reduction of viable cells and exhibited early apoptotic cell death morphology, such as cell shrinkage and disappearance of neurite processes (**Figure 1A**). In contrast, MPP+ caused the decrease of cell numbers, but morphological changes were not obvious (data not shown). Moreover, Hoechst 33342 staining showed that MPP+ (50 μM, 100 μM) and rotenone (25 μM, 50 μM) increased the number of bright staining nuclei which was due to chromatin condensation (14.37 ± 2.01%, 32.60 ± 4.33%, 39.91 ± 1.16%, 46.93 ± 2.49% respectively vs. 6.33 ± 0.88% of control, $p < 0.05$; **Figure 1B**). Consistently, we quantified the cell viability by MTT assay and LDH release assay. As expected, both MPP+ (50 μM, 100 μM) and rotenone (25 μM, 50 μM) induced a dose-dependent decrease of cell viability (86.76 ± 2.81%, 79.33 ± 2.42%; 36.96 ± 0.60%, 32.43 ± 1.20% of control, $p < 0.05$; **Figures 1E,F**) and increase of LDH release (126.39 ± 5.21%, 138.99 ± 2.69%; 162.63 ± 7.09%, 173.95 ± 5.31% of control, $p < 0.05$), which indicated an increase of cell death (**Figure 1G**).

Pre-treatment of Taltirelin (5 μM) for 2 h significantly alleviated the injury caused by MPP+ or rotenone. Taltirelin decreased nuclear condensation by 46.37% (100 μM MPP+), 36.52% and 42.99% (25 μM and 50 μM rotenone, respectively) and recovered cell viability by 13.58% and 11.06% (50 μM and 100 μM MPP+ respectively), 19.26% and 23.78% (25 μM and 50 μM rotenone respectively; **Figures 1A–G**). Besides, we conducted similar experiments using primary midbrain neurons and observed a similar viability-improving effect of Taltirelin against 10 μM MPP+ (81.17 ± 1.10% vs. 68.99 ± 4.26% of control, $p < 0.05$) and 1 μM rotenone (52.45 ± 3.06% vs. 71.93 ± 2.64% of control, $p < 0.05$; **Figures 1A–H**), which further confirmed the protective effect of Taltirelin in dopaminergic neurons *in vitro*.

Taltirelin Down-Regulated Tau and α-Synuclein-Related Pathology *in vitro*

After being cleaved by the upstream caspase, caspase-3 is activated and execute apoptosis by further cleaving targeted cellular proteins, thus the level of cleaved caspase-3 is positively correlated with the extent of apoptosis (Elmore, 2007). We found that the level of cleaved caspase-3 in SH-SY5Y cells was significantly elevated by MPP+ (50 μM, 100 μM) and rotenone (25 μM, 50 μM). However, Taltirelin (5 μM) pre-incubation effectively prevented the elevation of the cleaved caspase-3 (decreased by 33.41%, 58.62%, 28.11% and 45.23% respectively, $p < 0.05$; **Figures 2A,B**), which further confirmed that Taltirelin protected dopaminergic neurons against apoptosis and preserved the cell viability.

Since α-synuclein of human but not rodents contains residue N103 thus the α-synuclein N103 fragment is selectively cleaved by AEP (Zhang et al., 2017), we further examined the impact of Taltirelin on tau and α-synuclein pathologies in SH-SY5Y cells of human origin. As expected, MPP+ (1,000 μM) and rotenone (25 μM, 50 μM) significantly increased the levels of p-tau (S396) and AEP cleavage products: tau N368 and α-synuclein N103 fragments. Taltirelin (5 μM) co-incubation reduced p-tau (S396) by 17.13% (1,000 μM MPP+) and 10.12% (50 μM rotenone), tau N368 by 17.28% (1,000 μM MPP+), 25.22% (25 μM rotenone) and 23.40% (50 μM rotenone), α-synuclein N103 by 26.55% (1,000 μM MPP+), 9.49% (25 μM rotenone) and 23.01% (50 μM rotenone; **Figures 2C–F**, $p < 0.05$). Thus, these results suggested that Taltirelin had a neuroprotective effect involved reducing the phosphorylation of tau and inhibiting the activation of AEP induced by MPP+ and rotenone.

Taltirelin Protected Locomotor Functions of PD Model Mice

We further assessed the neuroprotective effects of Taltirelin in the subacute MPTP-induced PD mice model (**Figure 3A**). In the pilot test, we found that the mice injected with MPTP (30 mg/kg, i.p.) 2 h after Taltirelin (5 mg/kg, i.p.) would develop irritation, spasm and finally death, which may be due to the metabolism increased by Taltirelin aggravated the toxicity of MPTP. Therefore, the injection interval was adjusted to 4 h and similar death was prevented. Possibly due to the same reason, after 7 days of intervention with MPTP, the body weights of the mice injected with 5 mg/kg Taltirelin (23.04 ± 0.90 g) was lower than other groups (24.20 ± 1.31 g), but gradually recovered (25.47 ± 1.09 g) after following Taltirelin protective treatment (7 days), while the body weight of the MPTP group (23.43 ± 0.83 g), obviously decreased on the 14th day. However, there was no significance difference between MPTP and Taltirelin groups (**Figure 3C**). On the 7th day of the MPTP modeling, no obvious performance differences in the rotarod test were observed among groups, but on the 14th day, the latency times in the rotarod test in the MPTP group (179.33 ± 94.62 s, $p < 0.05$) significantly decreased, indicating impaired locomotor functions. Taltirelin 1 mg/kg (287.20 ± 28.62 s) successfully alleviated the impairment induced by MPTP. Besides, there was a trend of better performance of Taltirelin 0.5 mg/kg group (245.5 ± 77.25 s) or 5 mg/kg (239.20 ± 75.31 s) group compared with MPTP group (**Figure 3D**).

We also examined the impacts of Taltirelin in rotenone-induced chronic (**Figure 3B**) neurotoxicity mice models. After the chronic modeling (rotenone, 30 mg/kg, IG, 55 days), the weights of mice declined with different degrees compared with the normal mice. The mice injected with 1 mg/kg Taltirelin (26.20 ± 1.04 g vs. 23.03 ± 1.53 g of MPTP group, $p < 0.05$) had the least reduction (**Figure 3E**). In the rotarod test, mice

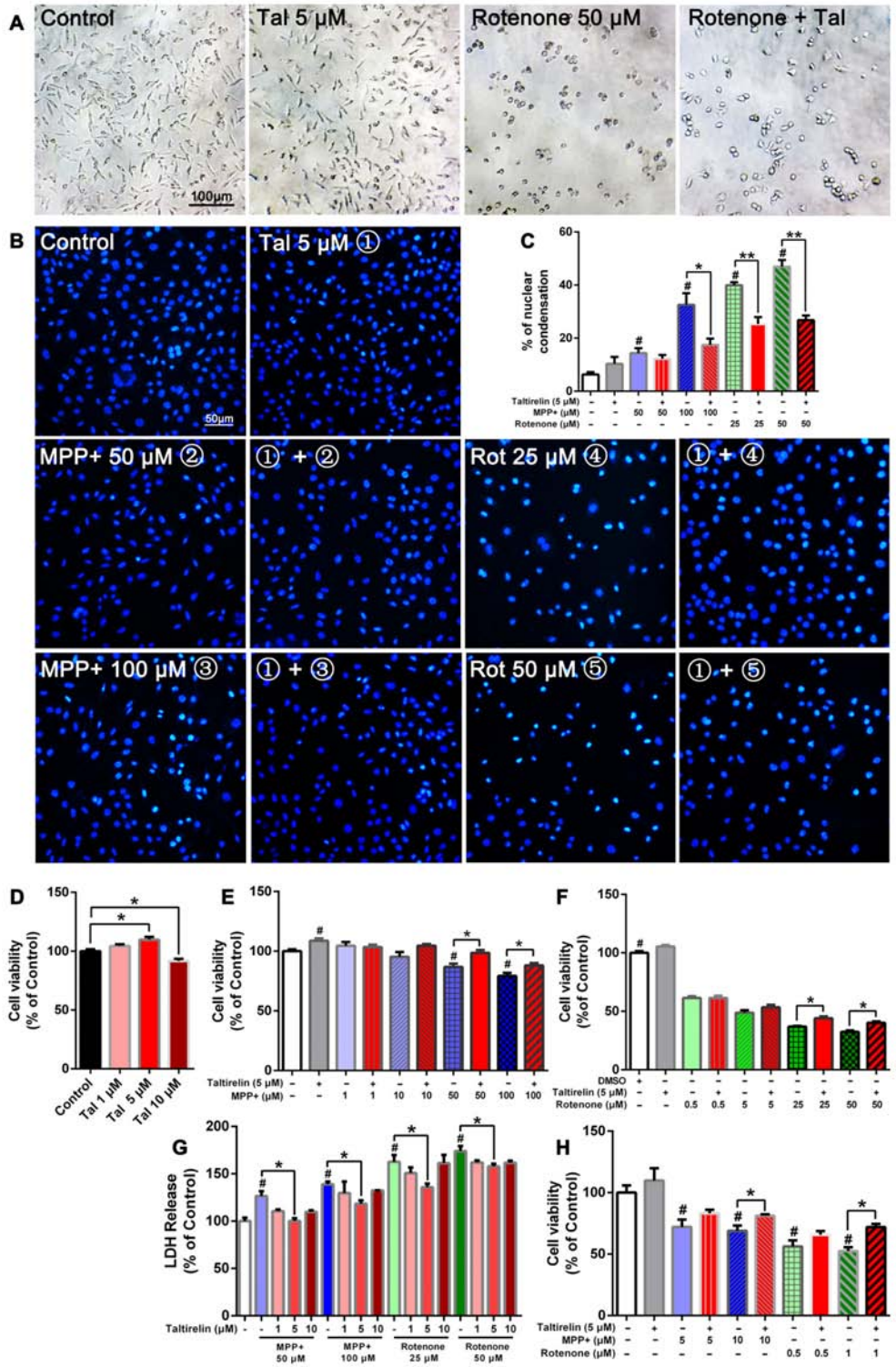

FIGURE 1 | Taltirelin protected dopaminergic neurons from toxicity of MPP+ and rotenone. SH-SY5Y cells were pre-treated with Taltirelin (5 μM) for 2 h and incubated another 24 h with MPP+ (1, 10, 50 or 100 μM) or rotenone (0.5, 5, 25 or 100 μM; **(A)** phase contrast micrograph of cultured SH-SY5Y cells exposed to rotenone (50 μM) for 24 h. **(B)** Hoechst 33342 staining of SH-SY5Y cells. **(C)** The percentage of nuclear condensation in total cell population as measured by Hoechst 33342 staining. **(D–F)** SH-SY5Y Cell viability was measured by MTT assay after intervention. **(G)** Lactate dehydrogenase (LDH) release assay was used to determine the cell death rate of SH-SY5Y cells. **(H)** Viability of primary midbrain neurons was assessed by MTT assay. $^{\#}p < 0.05$ vs. Control; $^{*}p < 0.05$; $^{**}p < 0.01$. $N = 6$. Error bars represent SEM.

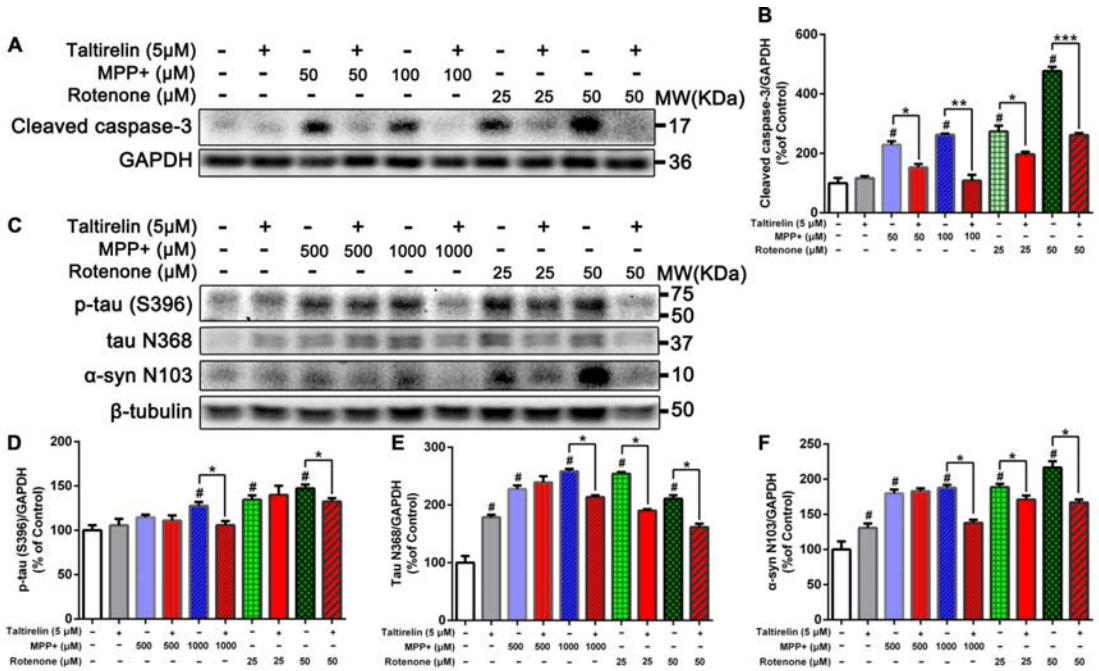

FIGURE 2 | Taltirelin down-regulating tau and α-synuclein-related pathology *in vitro*. **(A)** Western blot analysis showed the expression of cleaved caspase-3 in SH-SY5Y cells exposed to MPP+ (50 or 100 μM) or rotenone (25 or 50 μM), with or without 2 h pre-treatment of Taltirelin (5 μM). **(B)** Quantification of cleaved caspase-3 in different groups. **(C)** Western blot analysis showed the expression of p-tau (S396), tau N368 and α-synuclein N103 in SH-SY5Y cells exposed to MPP+ (500 or 1,000 μM) or rotenone (25 or 50 μM), with or without 2 h pre-treatment of Taltirelin (5 μM). **(D–F)** Analysis of p-tau (S396), tau N368 and α-synuclein N103 vs. β-tubulin in different groups. $^{\#}p < 0.05$ vs. control; $^{*}p < 0.05$, $^{**}p < 0.01$, $^{***}p < 0.001$. $N = 3$. Error bars represent SEM.

of 0.2 mg/kg Taltirelin group (193.78 ± 45.66 s) and 1 mg/kg Taltirelin (182.92 ± 56.64 s) performed much better than the rotenone group (124.92 ± 49.63 s; **Figure 3F**, $p < 0.05$). In addition, the mice of rotenone group (11.75 ± 3.81 s) in the pole test exhibited much slower decline speed or even declined in a rotatory manner, a sign of significant motor impairment. Both 0.2 mg/kg (7.70 ± 1.25 s) and 1 mg/kg Taltirelin (8.38 ± 1.92 s) rescued the time-down of the mice (**Figure 3G**, $p < 0.05$). However, there was no obvious difference of time-turn among different groups (**Figure 3H**). Anyhow, the above behavior assessments suggested a neuroprotective effect of Taltirelin in MPTP or rotenone PD mice models.

In addition, we also examined the motor improving effect of Taltirelin immediately after injections and found a time- and dose-dependent locomotor improvement of both MPTP and rotenone mice, which could maintain for at least 6 h ($p < 0.05$). This result was in consistency with our findings that Taltirelin could improve motor function of 6-OHDA lesioned PD rats (unpublished data).

Taltirelin Protected Dopaminergic Neurons and Reduced PD-Related Pathologies in MPTP-Induced PD Mice Model

In order to quantify the protective effect of Taltirelin, we stained the brain slices of SN with TH, the rate-limiting enzyme in DA synthesis which mainly expressed by dopaminergic neurons. We found that the numbers of TH positive neurons were much fewer in MPTP treated mice (36.66 ± 2.08% of normal) than that in 0.2 mg/kg (64.47 ± 3.91%) or 1 mg/kg (68.29 ± 4.45%) Taltirelin groups (**Figures 4A,B**, $p < 0.05$). We also quantified the level of TH in the striatum using western blot and the results validated the immunostaining observation (**Figures 4C,D**, $p < 0.05$).

We further examined the level of toxic forms of tau and α-synuclein in the SN and found that compared with the normal group, the levels of p-tau (S396), tau N368 and α-synuclein of the MPTP group were significantly higher, whereas the levels of the above proteins were reduced by Taltirelin of three doses by at least 55.43% (**Figures 4E–H**). Therefore, consistently with *in vitro* results, Taltirelin may have a protective effect against MPTP-induced neurotoxicity on dopaminergic neurons by decreasing the phosphorylation of tau and α-synuclein and down-regulating activation of AEP.

Taltirelin Down-Regulated Tau and α-Synuclein-Related Pathology in Rotenone-Induced PD Mice Model

Our previous studies have shown co-localization and increase of α-synuclein and tau N368 in the rotenone PD mice model (Nie et al., 2015). Thus, we also performed immunofluorescence double-labeling of the above two proteins in the SN, striatum, hippocampus and cortex of rotenone mice. The results showed that normal mice also had α-synuclein and tau N368 co-localized and evenly distributed within the neurons,

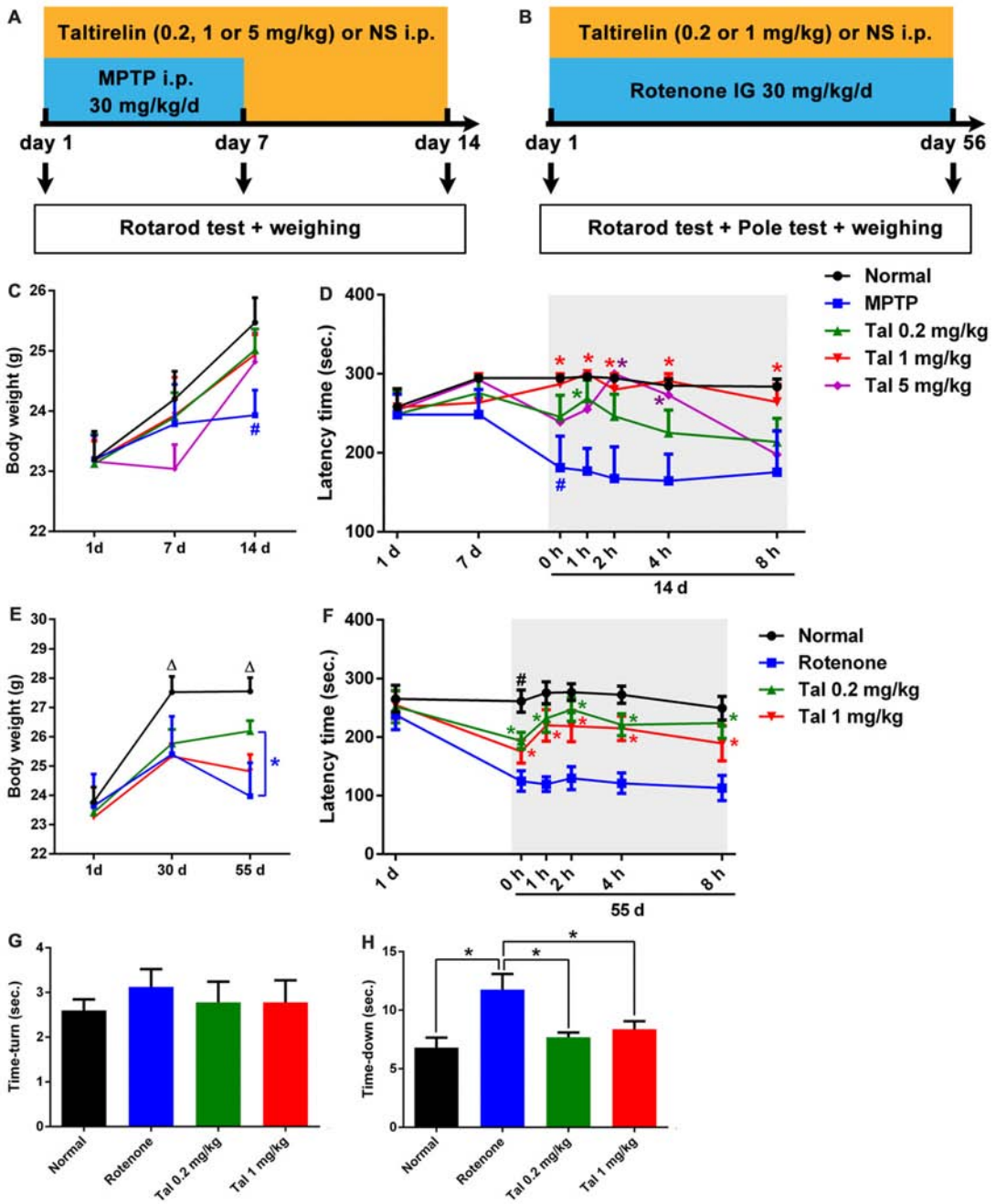

FIGURE 3 | Taltirelin protected locomotor functions of Parkinson's disease (PD) model mice. Schematic representation of the subacute MPTP-induced **(A)** and the chronic rotenone-induced **(B)** PD mice model experimental design. **(C)** Weight measurements on the first, 7th and 14th day of mice with MPTP (30 mg/kg, i.p.), with or without Taltirelin (Tal 0.2, 1 and 5 mg/kg). **(D)** Rotarod tests on the first, 7th and 14th day of MPTP modeling. **(E)** Weight measurements on the first, 30th and 55th day of mice with rotenone (30 mg/kg, IG), with or without Taltirelin (0.2 and 1 mg/kg). **(F)** Rotarod tests on the first and 55th day of rotenone modeling. **(G,H)** Pole tests on the 55th day of rotenone modeling. $^{\#}p < 0.05$ vs. normal; $^{*}p < 0.05$; $^{\triangle}p < 0.05$ vs. other groups. $N = 4$. Error bars represent SEM.

whereas in the rotenone group, intracellular α-synuclein and co-localized tau N368 exhibited higher and denser fluorescence with wider distribution in the cytoplasm, indicating increased and aggregation of α-synuclein and tau N368. In contrast, Taltirelin, especially 1 mg/kg group had much fewer and more dispersive distribution of α-synuclein and tau N368 in the SN (**Figure 5A**) and striatum (**Supplementary Figure S1**). However, similar difference among groups in the expression of two proteins was not significant in the hippocampus and cortex (**Supplementary Figures S2, S3**). Besides, we also stained p-tau (S396) in the SN and found an elevation of the number of p-tau (S396) positive cells in

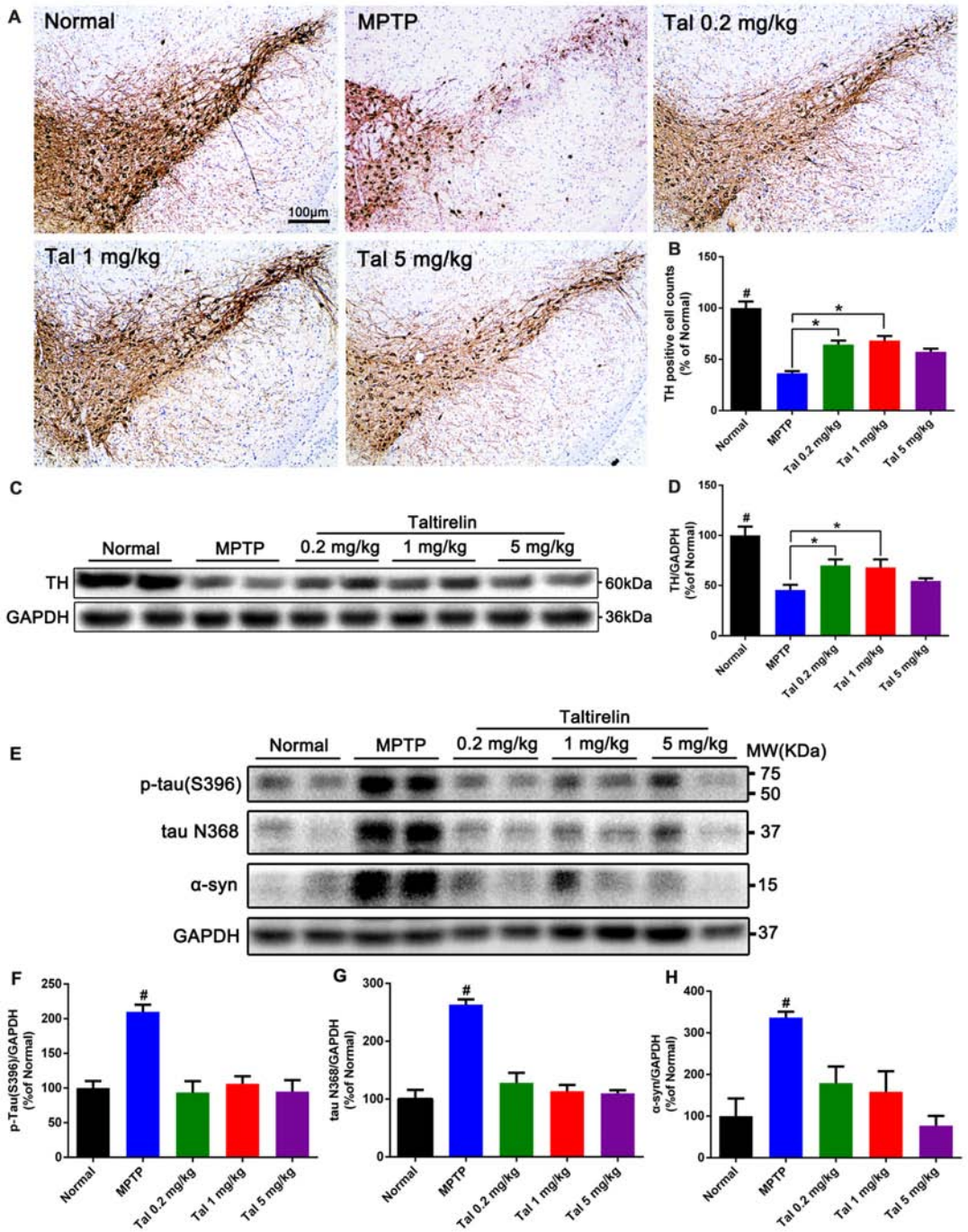

FIGURE 4 | Taltirelin protected dopaminergic neurons and reduced PD-related pathologies in MPTP-induced PD mice model. **(A)** Tyrosine hydroxylase (TH) immunostaining of the substantia nigra (SN) of mice treated with MPTP (30 mg/kg, i.p.), with or without Taltirelin (0.2 and 1 mg/kg). **(B)** Analysis of TH positive cells counts in each group. **(C)** Western blot analysis showed the levels of TH in the striatum of each group. **(D)** Quantification of the levels of TH. **(E)** WB showed the levels of p-tau (S396), tau N368 and α-synuclein in the SN of each group. **(F–H)** Quantification of WB of p-tau (S396), tau N368 or α-synuclein vs. GAPDH. $^{\#}p < 0.05$ vs. other groups; $^{*}p < 0.05$. $N = 3$. Error bars represent SEM.

the rotenone group (626.57 ± 66.31% of normal), in which immunostaining positive dense particles of aggregating p-tau (S396) could be easily spotted. In the 1 mg/kg Taltirelin group (175.44 ± 25.06%), both the number of p-tau (S396) positive cells and intracellular dense particles significantly decreased (**Figures 5B–D**, $p < 0.01$).

Similarly, we also examined the levels of p-ERK1/2 and tau N368, p-tau (S396), p-α-synuclein (S129) in the SN.

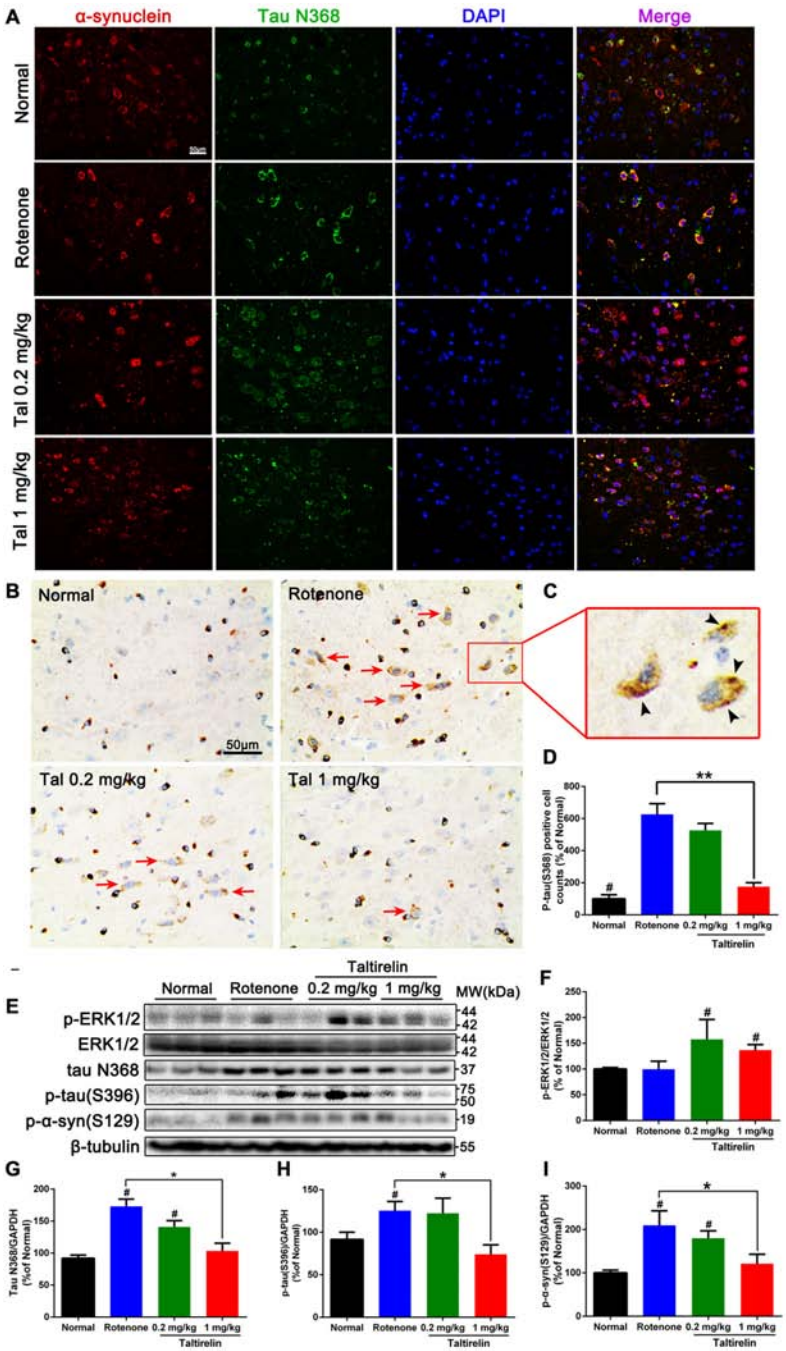

FIGURE 5 | Taltirelin down-regulated tau and α-synuclein-related pathology in rotenone-induced PD model mice. **(A)** Double-labeled immunofluorescence images showed co-localization of α-synuclein and tau N368 in the SN of each group (normal, rotenone, 0.2 or 1 mg/kg Taltirelin). **(B)** Immunostaining of p-tau (S396) in the SN. Red arrows indicated the positive cells. **(C)** The enlarged graph of indicated field. Black arrowheads indicated intracellular p-tau (S396) aggregation. **(D)** Analysis of p-tau (S396) positive cells counts in each group. **(E)** Western blot analysis of p-ERK1/2, tau N368, p-tau (S396) and p-α-synuclein (S129) in the SN of each group. **(F–I)** Quantification of WB showed the levels of p-ERK1/2, tau N368, p-tau (S396) and p-α-synuclein (S129). $^{\#}p < 0.05$ vs. other groups; $^{*}p < 0.05$; $^{**}p < 0.01$. $N = 3$. Error bars represent SEM.

Compared with the rotenone group, the levels of tau N368 (103.50 ± 11.86% vs. 173.10 ± 11.39%, $p < 0.05$), p-tau (S396; 74.01 ± 11.24% vs. 125.40 ± 10.71%, $p < 0.05$) and p-α-synuclein (S129; 121.20 ± 21.55% vs. 209.60 ± 33.19%, $p < 0.05$) were significantly lower in the 1 mg/kg Taltirelin group (**Figures 5E–I**), which further confirmed the immunostaining results above. In our previous study, we observed a rise of p-ERK1/2 after Taltirelin treatment both *in vivo* and

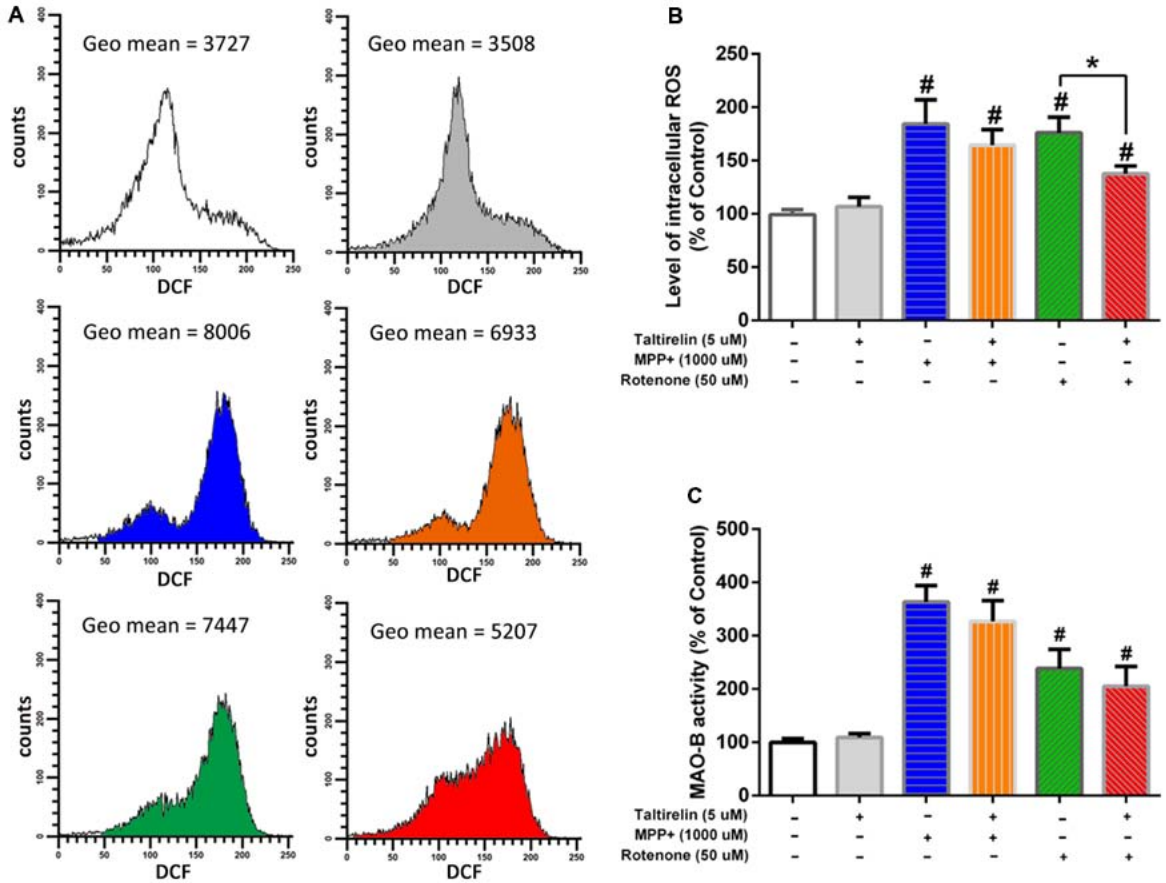

FIGURE 6 | Flow cytometry analysis of reactive oxygen species (ROS) generation and monoamine oxidase-B (MAO-B enzymatic assay. SH-SY5Y cells were pre-treated with PBS or Taltirelin (5 μM, 2 h), then incubated with MPP+ (1,000 μM, 24 h) or rotenone (50 μM, 24 h). **(A)** One typical experiments of Flow cytometry analysis. Geometric mean (Geo Mean) was used to calculate the total intensity of 2′,7′-dichlorofluorescein (DCF) fluorescence of cells. **(B)** Quantitative analysis of DCF fluorescence intensity in each treatment group. **(C)** MAO-B activity was assessed by Amplex® red monoamine oxidase assay kit. $^{\#}p < 0.05$ vs. control; $^{*}p < 0.05$. $N = 3$. Error bars represent SEM.

in vitro (unpublished data). Consistently, results showed that p-ERK1/2 increased in the SN and striatum of the 0.2 mg/kg (157.50 ± 38.55%, $p < 0.05$) and 1 mg/kg (136.8 ± 10.67%, $p < 0.05$) Taltirelin group, suggesting the involvement of p-ERK1/2 signaling in the actions of Taltirelin. Above all, the findings with rotenone mice further supported the observations in MPTP mice, indicating that Taltirelin has a neuroprotective effect associated with down-regulating AEP-related pathologies.

Taltirelin Reduced the Generation of ROS and the Activity of MAO-B

It is reported that oxidative stress facilitates accumulation (Conway et al., 2001) and oligomerization (Norris et al., 2003) of α-synuclein, which could be promoted by age-dependent activation of MAO-B (Kang et al., 2018). Thus, in order to get a further insight of the protective mechanisms of Taltirelin, we assessed the influence of Taltirelin on the ROS generation and MAO-B activity. Flow cytometry analysis showed that SH-SY5Y cells treated with MPP+ (1,000 μM) or rotenone (50 μM) for 24 h exhibited higher intracellular ROS (184.36 ± 22.63%, 176.16 ± 14.66%, respectively, $p < 0.05$). Pre-treatment with Taltirelin (5 μM) for 2 h significantly lowered the ROS elevated by rotenone by 38.65% ± 7.28% ($p < 0.05$) and decreased ROS induced by MPP+ by 19.83 ± 8.02%, though of no significance (**Figures 6A,B**). MPP+ (1,000 μM) and rotenone (50 μM) induced obvious increase of MAO-B activity (363 ± 30.58%, 238.41 ± 35.97%, respectively, $p < 0.05$) in SH-SY5Y cells. Cells pre-treated with Taltirelin (5 μM) exhibited a not significant but consistent decrease of the MAO-B activity elevated by MPP+ (by 36.15 ± 10.79%, $p > 0.05$) and rotenone (by 33.02 ± 6.71%, $p > 0.05$) (**Figure 6C**). Thus, these results suggested that Taltirelin may alleviate the neurotoxicity of MPTP and rotenone *via* reducing the generation of ROS and decreasing the activity of MAO-B.

DISCUSSION

TRH is stored in the releasable pool in the synaptic terminals and widely distributed in anatomically distinct pathways

throughout the neuroaxis (Gary et al., 2003), regulating a variety of physiological activities in the nervous system. The neuroprotective effects of TRH and its analogs have been showed in animal models of cerebral ischemia (Urayama et al., 2002), cellular models of PD (Jaworska-Feil et al., 2010) and AD (Luo and Stopa, 2004). Here, we report that Taltirelin, a TRH analog had neuroprotective effect in both cellular and animal models of PD.

MPP+ (metabolite of MPTP) and rotenone, highly lipophilic insecticide, both are mitochondrial complex I inhibitors which impair the mitochondrial respiration chain, increase ROS production and trigger apoptosis of dopaminergic neurons (Giordano et al., 2012; Xicoy et al., 2017). MTT assay and the LDH release assay showed that Taltirelin (5 μM) co-incubation for 24 h alleviated cytotoxicity induced by MPP+ or rotenone and rescued the viability of both SH-SY5Y cells and primary midbrain neurons. Hoechst 33342 staining and the level of cleaved caspase-3 further suggested that Taltirelin reduced the apoptosis caused by MPP+ and rotenone. Activation of ERK1/2 is found to be able to initiate a series of anti-apoptosis processes (Roskoski, 2012). We have demonstrated that the actions of Taltirelin both *in vitro* and *in vivo* were companied by an elevation of p-ERK1/2, which may mediate the resistance to apoptosis of Taltirelin. We further established the subacute MPTP-induced and chronic rotenone-induced PD mice models and found that Taltirelin significantly rescued the locomotor functions of these animals. However, long-term and high-dose administration of Taltirelin led to the loss of weight in animals, which is most likely due to an over-activation of HPT axis. We also measured the level of TSH and thyroid hormones in the serum of mice and found a significant increase of total T4 when the dose of Taltirelin exceeded 0.2 mg/kg, while free T4 or T3 had no significant alteration (**Supplementary Figure S4**). Since the total T4 is of the highest concentration among thyroid hormones and also the effector hormones, the results suggested that the thyroid function of patients should be thoroughly evaluated and adjusted accordingly before administration of Taltirelin if possible, in the future.

AEP, also known as legumain, is an endo-lysosomal cysteine protease activated under acidic conditions. The pH within the brain decreased with aging, while pH in the brains of patients of AD or PD is generally low and AEP is significantly elevated (Basurto-Islas et al., 2013). The cleaved products of AEP, tau N368 or α-synuclein N103 fragments are themselves highly neurotoxic and are prone to hyperphosphorylation and aggregation. We thus examined the influence of Taltirelin on these AEP-related pathologies both *in vitro* and *in vivo*. MPTP and rotenone caused an elevation of p-tau (S396), p-α-synuclein (S129), tau N368 and α-synuclein N103 fragments in SH-SY5Y cells and in the SN of PD mouse models, while Taltirelin successfully reduced the levels and aggregation of tau or α-synuclein in toxic forms. We recently reported that MPP+ could increase endogenous MAO-B, α-synuclein and AEP protein levels in SH-SY5Y cells in a time-dependent manner (Kang et al., 2018), while MAO-B activation is closely related with increase in free radical damage and ROS (Kang et al., 2018). In addition, rotenone administration may interfere with DA distribution and metabolism, leading to DA accumulated in the cytoplasm of PC12 cells, which may contribute to the ROS formation and cell death (Sai et al., 2008). Our results showed that Taltirelin decreased the generation of ROS induced by rotenone in SH-SY5Y cells though no significance was with MPP+. Taltirelin also moderately reduced activity of MAO-B, which was elevated by MPP+ and rotenone though the reduction was not significant. As for possible explanations for the insignificance: First, MAO-B mainly exists in glial cells, while SH-SY5Y cells as a neuron-origin species may contain low expression levels of MAO-B (Maruyama et al., 2003) to demonstrate the influence of Taltirelin. Second, previous studies showed that the amount of DA that SH-SY5Y cells could synthesize and release is barely detectable (Xicoy et al., 2017). However, MAO-B-induced DA metabolite, DOPAL, is neurotoxic *per se* and is able to activate and raise protein levels of both AEP and MAO-B (Kang et al., 2018). Since Taltirelin is a potent and sustained DA-releasing agent, which decreases the intracellular DA, this part of contribution to reducing MAO-B activity could not be elucidated under this condition. Thus, it is predictable that *in vivo* assessment of MAO-B activity or elevating MAO-B level with genetic manipulations could provide more insight into the mechanisms.

Besides, other possible explanations for the protective mechanism of Taltirelin may exist. First, Taltirelin mainly interacts with G-protein coupled receptors, TRH type 1 receptor (TRH-R1). As with many other rhodopsin-like GPCRs, the mitogen-activated protein kinase (MAPK; or Ras-Raf-MEK-ERK1/2) pathway has been found to be a downstream effector of TRH-R1 signaling (Smith et al., 2001; Oride et al., 2008). We also observed that Taltirelin caused a rise of p-ERK1/2 in the striatum and SN of mice after protective treatment. p-ERK1/2 participates in many signaling pathways and may therefore mediate the protective effects of Taltirelin. Second, TRH and its analogs are able to increase cerebral blood flow and metabolism which often decline with aging and in PD or AD (Farkas et al., 2000; Borghammer et al., 2010; Austin et al., 2011), thus achieve the protection by accelerating the elimination of toxins in the CNS and reducing the formation of anoxia or toxins-induced acidic micro-environment, which is a trigger in AEP activation. Finally, multiple studies have suggested that TRH acted as a regulator of homeostasis (Gary et al., 2003) involving immune and endocrine system, whereas imbalance of inflammation (Zheng et al., 2016) or diabetes (Arvanitakis et al., 2004) plays a recognized role in neurodegenerative diseases like PD or AD. Therefore, it will be interesting to investigate the interaction of TRH or Taltirelin with internal environment in PD or AD.

It is widely accepted that thyroid function has great impact on cognition. Deficiency of thyroid hormone in the critical period of brain development leads to severely stunted physical and mental growth, such as Cretinism. No surprise, functions of the HPT axis have been shown to undergo numerous changes with aging (Roelfsema and Veldhuis, 2013). Although there are still many controversies regarding the relationship between thyroid function and neurodegenerative disease (Villanueva et al., 2013), study showed that the free T3 level was significantly lower in

PD patients especially with akinetic-rigid motor subtype, while TSH level was lower in patients with tremor-dominant type or mixed type, suggesting a relation of the thyroid hormone level with PD motor symptoms (Umehara et al., 2015). TRH is decreased in the hippocampus of AD patients (Luo et al., 2002) and alterations in TSH (van Osch et al., 2004) or thyrotropin (Tan et al., 2008) have also been implicated as a risk factor for AD and dementia. Rat models of hypothyroidism exhibited increases of APP protein (Contreras-Jurado and Pascual, 2012), tau hyperphosphorylation, proinflammatory cytokines and spatial memory impairments (Chaalal et al., 2014), indicating that hypothyroidism represents an important risk factor of developing sporadic forms of AD. Since the regulatory functions in the nervous system of TRH are achieved in trace amount acting as a neuromodulator rather than endocrine hormones, even if the synthesis of TRH in the hypothalamus is disturbed or compensated, whether the total level of TRH in the brain is sufficient or excessive in maintaining its normal regulation functions is hard to assess. Therefore, the relationship between TRH and PD still needs further discussion. In conclusion, this study suggests TRH analog, Taltirelin possesses a protective effect on SH-SY5Y cells and rat primary midbrain neurons, as well as MPTP-induced subacute and rotenone-induced chronic PD mice models and this neuroprotective effect is associated with inhibition of apoptosis, ROS generation, phosphorylation of tau and α-synuclein, inhibition of AEP, thus providing evidence for applying a promising neuroprotective agent for treatment of PD.

AUTHOR CONTRIBUTIONS

CZ, GC, YX, ZZ, SP, KY and XC conceived and designed the study. CZ, GC, YT, WZ, QP, JW, CC, XY and SN performed the experiments. CZ and GC analyzed the data. CZ, GC, YX, SP, KY and XC wrote the manuscript. All authors read and approved the final manuscript.

FUNDING

This work was supported by the National Natural Science Foundation of China (81171193, 81671108 and 81873734) and Natural Science Foundation of Hubei Province of China (2016CFB544).

SUPPLEMENTARY MATERIAL

The Supplementary Material for this article can be found online at: https://www.frontiersin.org/articles/10.3389/fncel.2018.00485/full#supplementary-material

REFERENCES

Arvanitakis, Z., Wilson, R. S., Bienias, J. L., Evans, D. A., and Bennett, D. A. (2004). Diabetes mellitus and risk of Alzheimer disease and decline in cognitive function. *Arch. Neurol.* 61, 661–666. doi: 10.1001/archneur.61.5.661

Austin, B. P., Nair, V. A., Meier, T. B., Xu, G., Rowley, H. A., Carlsson, C. M., et al. (2011). Effects of hypoperfusion in Alzheimer's disease. *J. Alzheimers Dis.* 26, 123–133. doi: 10.3233/JAD-2011-0010

Basurto-Islas, G., Grundke-Iqbal, I., Tung, Y. C., Liu, F., and Iqbal, K. (2013). Activation of asparaginyl endopeptidase leads to tau hyperphosphorylation in Alzheimer disease. *J. Biol. Chem.* 288, 17495–17507. doi: 10.1074/jbc.m112.446070

Beaudoin, G. M. III., Lee, S. H., Singh, D., Yuan, Y., Ng, Y. G., Reichardt, L. F., et al. (2012). Culturing pyramidal neurons from the early postnatal mouse hippocampus and cortex. *Nat. Protoc.* 7, 1741–1754. doi: 10.1038/nprot.2012.099

Borghammer, P., Chakravarty, M., Jonsdottir, K. Y., Sato, N., Matsuda, H., Ito, K., et al. (2010). Cortical hypometabolism and hypoperfusion in Parkinson's disease is extensive: probably even at early disease stages. *Brain Struct. Funct.* 214, 303–317. doi: 10.1007/s00429-010-0246-0

Brooks, B. R. (1989). A summary of the current position of TRH in ALS therapy. *Ann. N. Y. Acad. Sci.* 553, 431–461. doi: 10.1111/j.1749-6632.1989.tb46664.x

Chaalal, A., Poirier, R., Blum, D., Gillet, B., Le Blanc, P., Basquin, M., et al. (2014). PTU-induced hypothyroidism in rats leads to several early neuropathological signs of Alzheimer's disease in the hippocampus and spatial memory impairments. *Hippocampus* 24, 1381–1393. doi: 10.1002/hipo.22319

Contreras-Jurado, C., and Pascual, A. (2012). Thyroid hormone regulation of APP (β-amyloid precursor protein) gene expression in brain and brain cultured cells. *Neurochem. Int.* 60, 484–487. doi: 10.1016/j.neuint.2012.01.027

Conway, K. A., Rochet, J. C., Bieganski, R. M., and Lansbury, P. T. Jr. (2001). Kinetic stabilization of the alpha-synuclein protofibril by a dopamine-alpha-synuclein adduct. *Science* 294, 1346–1349. doi: 10.1126/science.1063522

Elmore, S. (2007). Apoptosis: a review of programmed cell death. *Toxicol. Pathol.* 35, 495–516. doi: 10.1080/01926230701320337

Faden, A. I., Jacobs, T. P., and Holaday, J. W. (1981). Thyrotropin-releasing hormone improves neurologic recovery after spinal trauma in cats. *N. Engl. J. Med.* 305, 1063–1067. doi: 10.1056/NEJM198110293051806

Faden, A. I., Movsesyan, V. A., Knoblach, S. M., Ahmed, F., and Cernak, I. (2005). Neuroprotective effects of novel small peptides *in vitro* and after brain injury. *Neuropharmacology* 49, 410–424. doi: 10.1016/j.neuropharm.2005.04.001

Farkas, E., De Jong, G. I., de Vos, R. A., Jansen Steur, E. N., and Luiten, P. G. (2000). Pathological features of cerebral cortical capillaries are doubled in Alzheimer's disease and Parkinson's disease. *Acta Neuropathol.* 100, 395–402. doi: 10.1007/s004010000195

Gary, K. A., Sevarino, K. A., Yarbrough, G. G., Prange, A. J. Jr., and Winokur, A. (2003). The thyrotropin-releasing hormone (TRH) hypothesis of homeostatic regulation: implications for TRH-based therapeutics. *J. Pharmacol. Exp. Ther.* 305, 410–416. doi: 10.1124/jpet.102.044040

Giordano, S., Lee, J., Darley-Usmar, V. M., and Zhang, J. (2012). Distinct effects of rotenone, 1-methyl-4-phenylpyridinium and 6-hydroxydopamine on cellular bioenergetics and cell death. *PLoS One* 7:e44610. doi: 10.1371/journal.pone.0044610

Hawley, R. J., Kratz, R., Goodman, R. R., Mccutchen, C. B., Sirdofsky, M., and Hanson, P. A. (1987). Treatment of amyotrophic lateral sclerosis with the TRH analog DN-1417. *Neurology* 37, 715–717. doi: 10.1212/wnl.37.4.715

Jaworska-Feil, L., Jantas, D., Leskiewicz, M., Budziszewska, B., Kubera, M., Basta-Kaim, A., et al. (2010). Protective effects of TRH and its analogues against various cytotoxic agents in retinoic acid (RA)-differentiated human neuroblastoma SH-SY5Y cells. *Neuropeptides* 44, 495–508. doi: 10.1016/j.npep.2010.08.004

Jaworska-Feil, L., Kajta, M., Budziszewska, B., Leśkiewicz, M., and Lasoń, W. (2001). Protective effects of TRH and its stable analogue, RGH-2202, on kainate-induced seizures and neurotoxicity in rodents. *Epilepsy Res.* 43, 67–73. doi: 10.1016/s0920-1211(00)00178-9

Kalia, L. V., and Lang, A. E. (2015). Parkinson's disease. *Lancet* 386, 896–912. doi: 10.1016/S0140-6736(14)61393-3

Kang, S. S., Ahn, E. H., Zhang, Z., Liu, X., Manfredsson, F. P., Sandoval, I. M., et al. (2018). α-Synuclein stimulation of monoamine oxidase-B and legumain

protease mediates the pathology of Parkinson's disease. *EMBO J.* 37:e98878. doi: 10.15252/embj.201798878

Khomane, K. S., Meena, C. L., Jain, R., and Bansal, A. K. (2011). Novel thyrotropin-releasing hormone analogs: a patent review. *Expert Opin. Ther. Pat.* 21, 1673–1691. doi: 10.1517/13543776.2011.623127

Kinoshita, K., Nagao, T., and Ono, H. (1994). Effects of TA-0910, an orally active TRH analog, on the spinal reflex in spinal rats. *Neuropharmacology* 33, 1183–1188. doi: 10.1016/s0028-3908(05)80008-5

Kinoshita, K., Yamamura, M., Sugihara, J., Suzuki, M., and Matsuoka, Y. (1998). Taltirelin hydrate (TA-0910): an orally active thyrotropin-releasing hormone mimetic agent with multiple actions. *CNS Drug Rev.* 4, 25–41. doi: 10.1111/j.1527-3458.1998.tb00039.x

Kubek, M. J., Domb, A. J., and Veronesi, M. C. (2009). Attenuation of kindled seizures by intranasal delivery of neuropeptide-loaded nanoparticles. *Neurotherapeutics* 6, 359–371. doi: 10.1016/j.nurt.2009.02.001

Lee, A., and Gilbert, R. M. (2016). Epidemiology of Parkinson disease. *Neurol. Clin.* 34, 955–965. doi: 10.1016/j.ncl.2016.06.012

Luo, L., and Stopa, E. G. (2004). Thyrotropin releasing hormone inhibits tau phosphorylation by dual signaling pathways in hippocampal neurons. *J. Alzheimers Dis.* 6, 527–536. doi: 10.3233/jad-2004-6510

Luo, L., Yano, N., Mao, Q., Jackson, I. M., and Stopa, E. G. (2002). Thyrotropin releasing hormone (TRH) in the hippocampus of Alzheimer patients. *J. Alzheimers Dis.* 4, 97–103. doi: 10.3233/jad-2002-4204

Marangell, L. B., George, M. S., Callahan, A. M., Ketter, T. A., Pazzaglia, P. J., L'herrou, T. A., et al. (1997). Effects of intrathecal thyrotropin-releasing hormone (protirelin) in refractory depressed patients. *Arch. Gen. Psychiatry* 54, 214–222. doi: 10.1001/archpsyc.1997.01830150034007

Maruyama, W., Weinstock, M., Youdim, M. B., Nagai, M., and Naoi, M. (2003). Anti-apoptotic action of anti-Alzheimer drug, TV3326 [(*N*-propargyl)-(3*R*)-aminoindan-5-yl]-ethyl methyl carbamate, a novel cholinesterase-monoamine oxidase inhibitor. *Neurosci. Lett.* 341, 233–236. doi: 10.1016/s0304-3940(03)00211-8

Mellow, A. M., Sunderland, T., Cohen, R. M., Lawlor, B. A., Hill, J. L., Newhouse, P. A., et al. (1989). Acute effects of high-dose thyrotropin releasing hormone infusions in Alzheimer's disease. *Psychopharmacology* 98, 403–407. doi: 10.1007/bf00451695

Molchan, S. E., Mellow, A. M., Lawlor, B. A., Weingartner, H. J., Cohen, R. M., Cohen, M. R., et al. (1990). TRH attenuates scopolamine-induced memory impairment in humans. *Psychopharmacology* 100, 84–89. doi: 10.1007/bf02245795

Moussaud, S., Jones, D. R., Moussaud-Lamodière, E. L., Delenclos, M., Ross, O. A., and Mclean, P. J. (2014). Alpha-synuclein and tau: teammates in neurodegeneration? *Mol. Neurodegener.* 9:43. doi: 10.1186/1750-1326-9-43

Nie, S., Xu, Y., Chen, G., Ma, K., Han, C., Guo, Z., et al. (2015). Small molecule TrkB agonist deoxygedunin protects nigrostriatal dopaminergic neurons from 6-OHDA and MPTP induced neurotoxicity in rodents. *Neuropharmacology* 99, 448–458. doi: 10.1016/j.neuropharm.2015.08.016

Norris, E. H., Giasson, B. I., Ischiropoulos, H., and Lee, V. M. (2003). Effects of oxidative and nitrative challenges on alpha-synuclein fibrillogenesis involve distinct mechanisms of protein modifications. *J. Biol. Chem.* 278, 27230–27240. doi: 10.1074/jbc.m212436200

Ogata, A., Nagashima, K., Yasui, K., Matsuura, T., and Tashiro, K. (1998). Sustained release dosage of thyrotropin-releasing hormone improves experimental japanese encephalitis virus-induced parkinsonism in rats. *J. Neurol. Sci.* 159, 135–139. doi: 10.1016/s0022-510x(98)00150-6

Oride, A., Kanasaki, H., Mutiara, S., Purwana, I. N., and Miyazaki, K. (2008). Activation of extracellular signal-regulated kinase (ERK) and induction of mitogen-activated protein kinase phosphatase 1 (MKP-1) by perifused thyrotropin-releasing hormone (TRH) stimulation in rat pituitary GH3 cells. *Mol. Cell. Endocrinol.* 296, 78–86. doi: 10.1016/j.mce.2008.09.002

Pitts, L. H., Ross, A., Chase, G. A., and Faden, A. I. (1995). Treatment with thyrotropin-releasing hormone (TRH) in patients with traumatic spinal cord injuries. *J. Neurotrauma* 12, 235–243. doi: 10.1089/neu.1995.12.235

Poewe, W., Seppi, K., Tanner, C. M., Halliday, G. M., Brundin, P., Volkmann, J., et al. (2017). Parkinson disease. *Nat. Rev. Dis. Primers* 3:17013. doi: 10.1038/nrdp.2017.13

Roelfsema, F., and Veldhuis, J. D. (2013). Thyrotropin secretion patterns in health and disease. *Endocr. Rev.* 34, 619–657. doi: 10.1210/er.2012-1076

Roskoski, R. Jr. (2012). ERK1/2 MAP kinases: structure, function and regulation. *Pharmacol. Res.* 66, 105–143. doi: 10.1016/j.phrs.2012.04.005

Sai, Y., Wu, Q., Le, W., Ye, F., Li, Y., and Dong, Z. (2008). Rotenone-induced PC12 cell toxicity is caused by oxidative stress resulting from altered dopamine metabolism. *Toxicol. In Vitro* 22, 1461–1468. doi: 10.1016/j.tiv.2008.04.019

Sengupta, U., Guerrero-Muñoz, M. J., Castillo-Carranza, D. L., Lasagna-Reeves, C. A., Gerson, J. E., Paulucci-Holthauzen, A. A., et al. (2015). Pathological interface between oligomeric alpha-synuclein and tau in synucleinopathies. *Biol. Psychiatry* 78, 672–683. doi: 10.1016/j.biopsych.2014.12.019

Smith, J., Yu, R., and Hinkle, P. M. (2001). Activation of MAPK by TRH requires clathrin-dependent endocytosis and PKC but not receptor interaction with β-arrestin or receptor endocytosis. *Mol. Endocrinol.* 15, 1539–1548. doi: 10.1210/mend.15.9.0695

Szuba, M., Fernando, A., Winokur, A., and Gary, K. (1995). "Nocturnal TRH administration acutely ameliorates bipolar depression," in *Conference Proceeding of the American College of Neuropsychopharmacology* (San Juan, Peurto Rico).

Tan, Z. S., Beiser, A., Vasan, R. S., and Au, R. (2008). Thyroid function and the risk of alzheimer disease: the framingham study. *Arch. Intern. Med.* 168, 1514–1520. doi: 10.1001/archinte.168.14.1514

Umehara, T., Matsuno, H., Toyoda, C., and Oka, H. (2015). Thyroid hormone level is associated with motor symptoms in *de novo* Parkinson's disease. *J. Neurol.* 262, 1762–1768. doi: 10.1007/s00415-015-7780-x

Urayama, A., Yamada, S., Kimura, R., Zhang, J., and Watanabe, Y. (2002). Neuroprotective effect and brain receptor binding of taltirelin, a novel thyrotropin-releasing hormone (TRH) analogue, in transient forebrain ischemia of C57BL/6J mice. *Life Sci.* 72, 601–607. doi: 10.1016/s0024-3205(02)02268-3

van Osch, L. A. D. M., Hogervorst, E., Combrinck, M., and Smith, A. D. (2004). Low thyroid-stimulating hormone as an independent risk factor for Alzheimer disease. *Neurology* 62, 1967–1971. doi: 10.1212/01.wnl.0000128134.84230.9f

Villanueva, I., Alva-Sánchez, C., and Pacheco-Rosado, J. (2013). The role of thyroid hormones as inductors of oxidative stress and neurodegeneration. *Oxid. Med. Cell Longev.* 2013:218145. doi: 10.1155/2013/218145

Wilson, I., Lara, P., and Prange, A. Jr. (1973). Thyrotrophin-releasing hormone in schizophrenia. *Lancet* 302, 43–44. doi: 10.1016/s0140-6736(73)91979-x

Xicoy, H., Wieringa, B., and Martens, G. J. (2017). The SH-SY5Y cell line in Parkinson's disease research: a systematic review. *Mol. Neurodegener.* 12:10. doi: 10.1186/s13024-017-0149-0

Zhang, Z., Kang, S. S., Liu, X., Ahn, E. H., Zhang, Z., He, L., et al. (2017). Asparagine endopeptidase cleaves α-synuclein and mediates pathologic activities in Parkinson's disease. *Nat. Struct. Mol. Biol.* 24, 632–642. doi: 10.1038/nsmb.3433

Zhang, Z., Song, M., Liu, X., Kang, S. S., Kwon, I. S., Duong, D. M., et al. (2014). Cleavage of tau by asparagine endopeptidase mediates the neurofibrillary pathology in Alzheimer's disease. *Nat. Med.* 20, 1254–1262. doi: 10.1038/nm.3700

Zhang, Z., Xie, M., and Ye, K. (2016). Asparagine endopeptidase is an innovative therapeutic target for neurodegenerative diseases. *Expert Opin. Ther. Targets* 20, 1237–1245. doi: 10.1080/14728222.2016.1182990

Zheng, C., Zhou, X.-W., and Wang, J.-Z. (2016). The dual roles of cytokines in Alzheimer's disease: update on interleukins, TNF-α, TGF-β and IFN-γ. *Transl. Neurodegener.* 5:7. doi: 10.1186/s40035-016-0054-4

Conflict of Interest Statement: The authors declare that the research was conducted in the absence of any commercial or financial relationships that could be construed as a potential conflict of interest.

frontiers in Cellular Neuroscience

HYPOTHESIS AND THEORY
published: 20 December 2018
doi: 10.3389/fncel.2018.00506

Scaling Our World View: How Monoamines Can Put Context Into Brain Circuitry

Philipp Stratmann[1,2]*, *Alin Albu-Schäffer*[1,2] *and Henrik Jörntell*[3]

[1] *Sensor Based Robotic Systems and Intelligent Assistance Systems, Department of Informatics, Technical University of Munich, Garching, Germany,* [2] *German Aerospace Center (DLR), Institute of Robotics and Mechatronics, Weßling, Germany,* [3] *Neural Basis of Sensorimotor Control, Department of Experimental Medical Science, Lund University, Lund, Sweden*

Monoamines are presumed to be diffuse metabotropic neuromodulators of the topographically and temporally precise ionotropic circuitry which dominates CNS functions. Their malfunction is strongly implicated in motor and cognitive disorders, but their function in behavioral and cognitive processing is scarcely understood. In this paper, the principles of such a monoaminergic function are conceptualized for locomotor control. We find that the serotonergic system in the ventral spinal cord scales ionotropic signals and shows topographic order that agrees with differential gain modulation of ionotropic subcircuits. Whereas the subcircuits can collectively signal predictive models of the world based on life-long learning, their differential scaling continuously adjusts these models to changing mechanical contexts based on sensory input on a fast time scale of a few 100 ms. The control theory of biomimetic robots demonstrates that this precision scaling is an effective and resource-efficient solution to adapt the activation of individual muscle groups during locomotion to changing conditions such as ground compliance and carried load. Although it is not unconceivable that spinal ionotropic circuitry could achieve scaling by itself, neurophysiological findings emphasize that this is a unique functionality of metabotropic effects since recent recordings in sensorimotor circuitry conflict with mechanisms proposed for ionotropic scaling in other CNS areas. We substantiate that precision scaling of ionotropic subcircuits is a main functional principle for many monoaminergic projections throughout the CNS, implying that the monoaminergic circuitry forms a network within the network composed of the ionotropic circuitry. Thereby, we provide an early-level interpretation of the mechanisms of psychopharmacological drugs that interfere with the monoaminergic systems.

Keywords: monoamine neurotransmitter disorders, motor control, motor learning, neuromodulation, principal component analysis, raphe nuclei, serotonin, spinal cord

OPEN ACCESS

Edited by:
Jing-Ning Zhu,
Nanjing University, China

Reviewed by:
Jian Jing,
Nanjing University, China
Tjeerd V. Olde Scheper,
Oxford Brookes University, United Kingdom

***Correspondence:**
Philipp Stratmann
philipp.stratmann@tum.de

Received: *13 September 2018*
Accepted: *06 December 2018*
Published: *20 December 2018*

Citation:
Stratmann P, Albu-Schäffer A and Jörntell H (2018) Scaling Our World View: How Monoamines Can Put Context Into Brain Circuitry. Front. Cell. Neurosci. 12:506. doi: 10.3389/fncel.2018.00506

1. INTRODUCTION

Metabotropic neuromodulators are ubiquitous in the CNS. Together with acetylcholine (Picciotto et al., 2012), the four monoamines serotonin (5-HT), dopamine, noradrenaline, and histamine dominate neuromodulatory effects in the CNS (Cools et al., 2011; O'Donnell et al., 2012; Yu et al., 2015). These molecules are strongly implicated in mood and affective state, while their malfunction is tightly linked to cognitive disorders (Kurian et al., 2011; Howell and Cunningham, 2015; Ng et al., 2015; Mather and Harley, 2016). A common view is that brain function emanates

from signal processing of the ionotropic functional and anatomical connectome of the brain, which occurs with high topographic and temporal precision. In contrast to ionotropic neurotransmission, neuromodulation produces no direct excitatory or inhibitory effects mediated by the activation of the fast-acting ionotropic glutamate or GABA receptors. Instead, neuromodulation acts on G protein-coupled receptors and thereby changes the surface expression or efficacy of potassium, calcium, or sodium channels. This scales the general excitability, or gain, of the neuron (Haas et al., 2008; Rosenbaum et al., 2009; Beaulieu and Gainetdinov, 2011; Bargmann, 2012; Picciotto et al., 2012; Perrier et al., 2013; Husch et al., 2015; Perrier and Cotel, 2015). So far, monoamines are presumed to provide a diffuse general modulation of large connectome circuits (Fuxe et al., 2010). But knowledge of the specific functional contributions of monoaminergic neuromodulators to neuronal processing and the resulting integrative behavior is scarce.

In this paper, a novel functional principle is deduced for monoamines as temporal- and subcircuit-precise gain modulators. Whereas the ionotropic subcircuits can collectively signal predictive models of the world based on life-long learning, monoamines are shown to scale the influence of functionally distinct neuronal subcircuits individually. Hereby, their effects show just the right time constant to adjust the models to quickly changing contexts. By this precision scaling, monoamines provide an operation which may overcome functional limitations of ionotropic networks that apply under physiological conditions. The principle emerges from an analysis of monoaminergic effects in the specific context of locomotion, which integrates control theory of biomimetic robots, motor control neuroscience, and neurobiological findings on monoamine systems. Accordingly, serotonin must be assumed to scale motorpools of an individual joint when it shows particularly large movement, because this implies that the respective joint can be moved with smaller metabolic requirements. This precision scaling dramatically simplifies motor control adaptation in the face of gradually changing mechanical conditions which, for example, take place as one steps from a solid to a soft ground or lifts a load. But the principle of precision scaling is also tentatively applicable to general computational interactions between neuronal populations throughout the CNS and may thus support various high- and low-level functions.

Here we focus on the spinal motor circuitry to deduce if the CNS applies precision scaling. This focus has two reasons: First, it is comparatively easy to interpret how information is encoded and reconstruct how information is processed, because the spinal circuitry is the final motor output stage and the entry stage of low-level sensory feedback signals (Franklin et al., 2016). In contrast, higher-level systems operate by using more abstracted information that can be hard to interpret. Second, the control of body movement is widely assumed to be a major, if not the most important, factor for the evolution of the CNS (Wise and Shadmehr, 2002; Babič et al., 2016). This implies that cognitive levels evolved while being constrained by the spinal motor output and sensory input circuitry. Motor control can therefore be regarded as a basis to understand such higher integrative circuits.

In order to understand the spinal motor control, modern robotics control theory, which has been developed for robots with increasing functional similarity to biological locomotor systems, offers multiple advantages: Robotic control theory can provide comprehensive and well-tested analytical tools. If the major constraints of the CNS are taken into account, it further offers highly specific interpretational frames for understanding observations of sensorimotor control in the CNS. It goes without saying that early-stage testing of concepts for biological motor control is easier in robots than in biological systems.

In the present paper, we suggest that the mode of operation of various monoaminergic systems in the CNS is *precision scaling*, i.e., a topographically and temporally specific gain control of local neuronal operation. In the chain of argumentation that leads up to this prediction, we start out by comparing the functional operations within monoamine-driven metabotropic systems with those observed in ionotropic circuitry. Accordingly, the spinal ionotropic circuitry integrates descending motor commands and sensory signals and linearly processes them into muscle signals. By this function, it dominates the spinal generation of motor patterns, which has further contributions from gap junctions and diffuse metabotropic effects. Mathematically, the ionotropic circuitry transforms between the different representations, or the different "views," of the world as they are encoded by the individual processing stages (section 2). Nonlinear signal processing is required to adjust these transformations to changing contexts. Based on neurophysiological findings, these non-linear adjustments are ideally solved by neuromodulatory scaling of the ionotropic signals due to the properties of the serotonergic system (section 3). The scaling effect renders the metabotropic system functionally unique, given that ionotropic effects proposed for non-linear signal processing in other CNS areas are unlikely to apply to spinal circuitry conditions *in vivo* according to recent experimental studies (section 4). Subsequently, the spatial and temporal precision of the spinal serotonergic system is evaluated to see if it may perform tasks that cannot be obtained by ionotropic circuitry under the influence of exclusively diffuse neuromodulation. Insights from robotic control and motor neuroscience are combined to identify such a task and deduce how focused serotonin must act, both anatomically and temporally, in order to solve it (sections 5, 6). This functionally required precision is demonstrated to coincide with the neuroscientifically observed topographic and temporal precision of serotonergic effects in the spinal cord (section 7). Monoamines must therefore be considered, at least partly, subcircuit- and temporally-specific gain modulators of ionotropic circuitry, motivating the term *precision scaling*. As will be shown toward the end of this paper, precision scaling can potentially apply to multiple levels of CNS function and may explain the effects of psychopharmacological drugs that act on monoamine systems in the brain (section 8).

2. THE SPINAL CORD AS TRANSFORMER OF WORLD VIEWS

The function of the CNS emanates from the neurophysiological processes in the individual neurons and the precise network

of connections between them. In order to understand how monoaminergic neuromodulatory influences neuronal circuitry, it is important to first understand how functions arise in networks of ionotropic circuitry.

2.1. Linear Signal Processing Transforms How Spinal Neurons Encode the World

An individual neuron primarily works by integrating information in the form of the electrical signals it receives from other neurons by synaptic transmission. In response to the summated effect of those inputs, it issues electrical signals that reach other neurons. Hence, it can be said to process information. In the spinal cord, recent electrophysiological findings suggest that the neurons are hereby limited to linear processing of information encoded by ionotropic signals: Spinal interneurons which are subject to increasing single or multiple synaptic inputs respond linearly under physiological conditions *in vivo* (Prut and Perlmutter, 2003; Shalit et al., 2012; Spanne et al., 2014; Zelenin et al., 2015). In particular, they are active well before overt movement starts and do not saturate (Prut and Perlmutter, 2003), implying that they are in their linear regime during a movement. Investigations assign the same linear response to spinal motorneurons in anesthetized animals and *in vitro* (Powers and Binder, 1995, 2000; Hultborn et al., 2003; Cushing et al., 2005; Hyngstrom et al., 2008).

As the CNS forwards information from one group of neurons to another, it filters out irrelevant aspects, combines data of different origin, and adjusts the way the information is encoded. All CNS functions can be traced back to such basal neuronal circuitry mechanisms. These basal mechanisms can be cascaded and integrated to create interesting local functions. The local functions can to a large extent be shaped by learning and can be regarded as partial, often predictive, models of the world, e.g., describing how photoreceptors are distributed across the retina or what motor signals must be elicited to perform a particular task (Brown and Brüne, 2012; Bhanpuri et al., 2013). What model of the world a neuronal circuit contains is determined by an associated coordinate space. For motor control, illustrative examples of coordinate spaces are found in visual reaching tasks: The target position is initially encoded as a pixelated image mapped in a retinotopic reference frame (Heed et al., 2015). To reach the target, the incoming visual signal requires neuronal processing and merging with additional information represented in non-retinotopic reference frames (cf. **Figure 1**). Processing generates an appropriate movement intention and an according signal in a musculotopic coordinate space at the level of the spinal motorneurons (Graziano, 2006; Yanai et al., 2008). Describing how a neuronal circuit encodes its associated coordinate space requires knowledge of the set of qualitatively relevant categories of encoded information. The categories may in principle be directly linked to physical quantities (Franklin et al., 2016), such as the activation of different muscles. But at integrative stages, they may also be linked to more high-level quantities like the social status and familiarity that an animal takes into account before approaching a potential partner. They may even be linked to highly abstract quantities with no direct counterpart in the physical world. Given appropriate coordinates, it is convenient to describe the information encoded in a group of neurons as a vector,

$$\boldsymbol{x} = \begin{pmatrix} x_1 \\ x_2 \\ \vdots \end{pmatrix}. \tag{1}$$

Each coordinate x_1, x_2, ... would in the mentioned examples describe the motor signal driving a single muscle or a component of a higher-level quantity encoded by the CNS. It can be represented by the signal of individual, or groups of, neurons (Cunningham and Yu, 2014).

Between coordinate spaces, linear neurons as found in the spinal cord perform affine transformations. Affine transformations, which are exemplified in **Figure 1**, are heavily used by engineers since they often approximate general transformations involving arbitrary mathematical functions very well for a limited range of input values around an operating point (Cohen and Tan, 2012). In a network consisting of linear neurons, each neuron j receives sensory inputs from presynaptic neurons i, which is represented by a firing rate x_i for rate-coding neurons. The inputs are weighted by synaptic weights w_{ij} and subject to a neuron-specific firing threshold θ_j. In summary, the output firing rate y_j in neuron j can be described by the linear function

$$y_j(x_1, x_2, \ldots) = \sum_i w_{\mathrm{ij}} \cdot x_i - \theta_j. \tag{2}$$

Equation (2) can be represented in vector notation as

$$\boldsymbol{y}(\boldsymbol{x}) = \boldsymbol{W}_{\mathrm{xy}} \cdot \boldsymbol{x} - \boldsymbol{\theta}_{\mathrm{y}}. \tag{3}$$

It defines the affine transformation between two coordinate spaces in which the signal can be represented by coordinates $\boldsymbol{x}$ and $\boldsymbol{y}$, respectively.

A spinal ionotropic network consisting of linear neurons is limited to implement an affine transformation which can be described by Equation (3). Neither additional feedforward layers, nor recurrent synaptic connections can change this functional property. If the neuronal network is extended by intercalating further layers of linear neurons between the input and output layer, only the effective transformation weights $\boldsymbol{W}_{\mathrm{xy}}$ and threshold $\boldsymbol{\theta}_{\mathrm{y}}$ of the transformation will change. As shown in **Figure 2A**, the output firing rate will remain a linear function of the network input. If the network is extended by recurrent synaptic connections, it can memorize input and process time-series of data. Thereby, its output may vary non-linearly with time and, for example, converge to a steady state or oscillate (Dayan and Abbott, 2001). But at each time step, the network output $\boldsymbol{y}$ remains a linear function of its previous input $\boldsymbol{x}$ at previous time steps, as illustrated in **Figure 2B**.

2.2. Non-linear Signal Processing Is Required When the World Changes

Artificial neural networks have, with the enormous scientific and economical success of deep learning in particular and

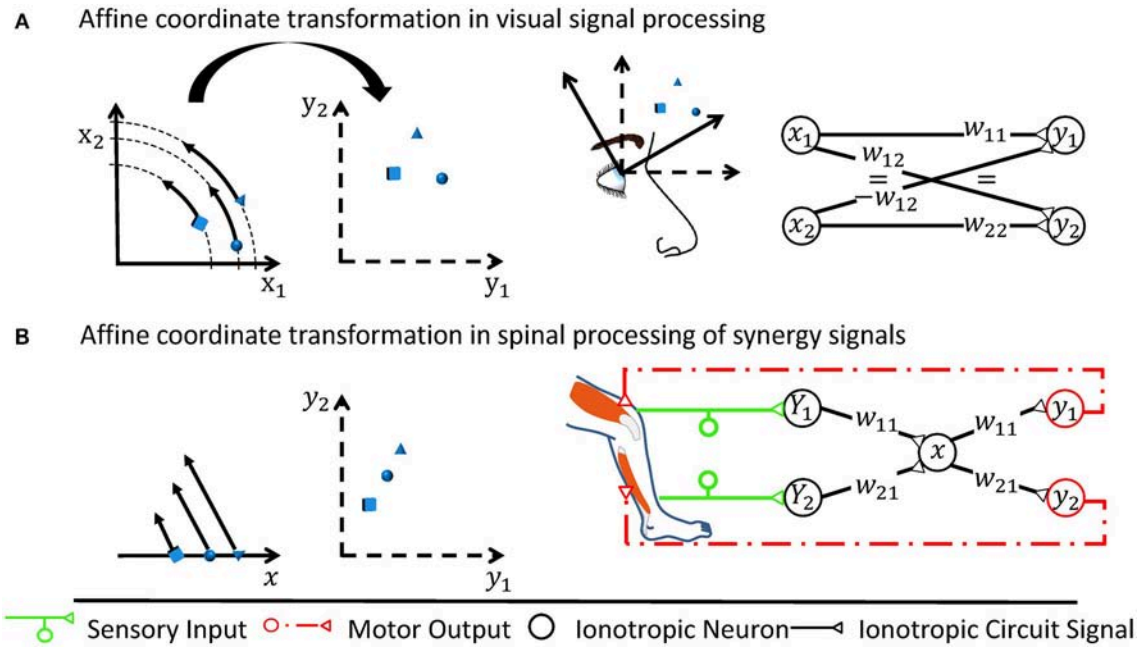

FIGURE 1 | Two examples of affine transformations and their simplest neuronal circuitry connectivity solution. Each transformation is made from a coordinate space represented by neuronal states (x_1, x_2) or x to a space represented by (y_1, y_2), respectively. For rate-coded models, these neuronal states would be equivalent to firing rates of neurons or neuron pools. Sketches of neuronal networks show the simplest possible way by which the CNS might implement each transformation. As illustrated for each panel, the networks in effect re-calculate individual signals encoded by the neuronal states into new individual neuronal states, where the re-calculation is the specific transformation made and is illustrated by arrows in the leftmost graph. **(A)** A rotation is assumed to occur when neurons transform retinotopic neuronal signals occurring at early visual processing stages to a head-centered representation at later stages (Heed et al., 2015). **(B)** Shown here is the transformation underlying a motor synergy, i.e., a spinal circuit which emits common ionotropic signals to actuate muscles that the neuronal synergy models as agonists (Santello et al., 2016). The low-dimensional synergy signal x is thereby transformed into the high-dimensional musculotopic space represented by coordinates (y_1, y_2). Signals (Y_1, Y_2), such as sensory signals, can be transformed into this low-dimensional synergistic subspace by orthogonal projections.

of artificial intelligence in general, strongly facilitated the view that also biological neuronal networks can approximate general transformations which adjust the output of the network to arbitrarily changing conditions (Chen et al., 2015). In mathematical terms, they are said to perform universal classification and function approximation. This view relies on the model of neurons as non-linear integrators of incoming signals (Cybenko, 1989; Hornik, 1991). While this contrasts the observed linear interaction of ionotropic signals for the specific example of the spinal circuitry, it must be assumed that also the spinal cord needs mechanisms which non-linearly combine external signals with the ionotropic inputs that the neuronal network processes. This becomes particularly obvious under quickly changing mechanical conditions of the environment and the locomotor system. Hereby, the changing context often requires that the CNS reacts differently to the same inputs. The multiplicative transformation weights of Equation (2) must therefore be context-dependent and change with a signal s which encodes the external cue,

$$y_j(x_1, x_2, \ldots, s) = \sum_i w_{ij}(s) \cdot x_i - \theta_j \,. \qquad (4)$$

This implies a non-linear integration of the signals s and x_i. In contrast, adding the signal s as an additional linear input, e.g., by a reflex loop that signals s and also converges onto the neurons j, would only additively increase the output of the network. In effect, it would only change its firing threshold θ_j.

By adjusting individual transformation weights independently from each other, the motor circuitry can gain a unique functionality. **Figure 3** illustrates this functionality based on the transformation of context-dependent motor signals from M1 onto the musculotopic motor output within spinal circuits. Hereby, pools of M1 neurons typically elicit a common motor command which is transformed into musculotopic signals as it is transmitted to spinal motorneurons either directly or through spinal interneurons (Yanai et al., 2008). The transformed motor command activates the spinal motorneuron pools of several muscles to produce a meaningful pattern of muscle contraction (Graziano, 2006; Overduin et al., 2012; Gallego et al., 2017). In this circuit, the transformation weights along the path between M1 and the motorneuron pools will need to be scaled in a pool-specific manner if a new mechanical condition necessitates that the involved muscles change their force output relative to each other. Similar examples for neuronal operations that require changing transformation weights can be found in integrative circuits such as the ventral intraparietal area. This area encodes an abstract representation of vestibular self-motion signals that is independent of head and eye position (Chen et al., 2013). To

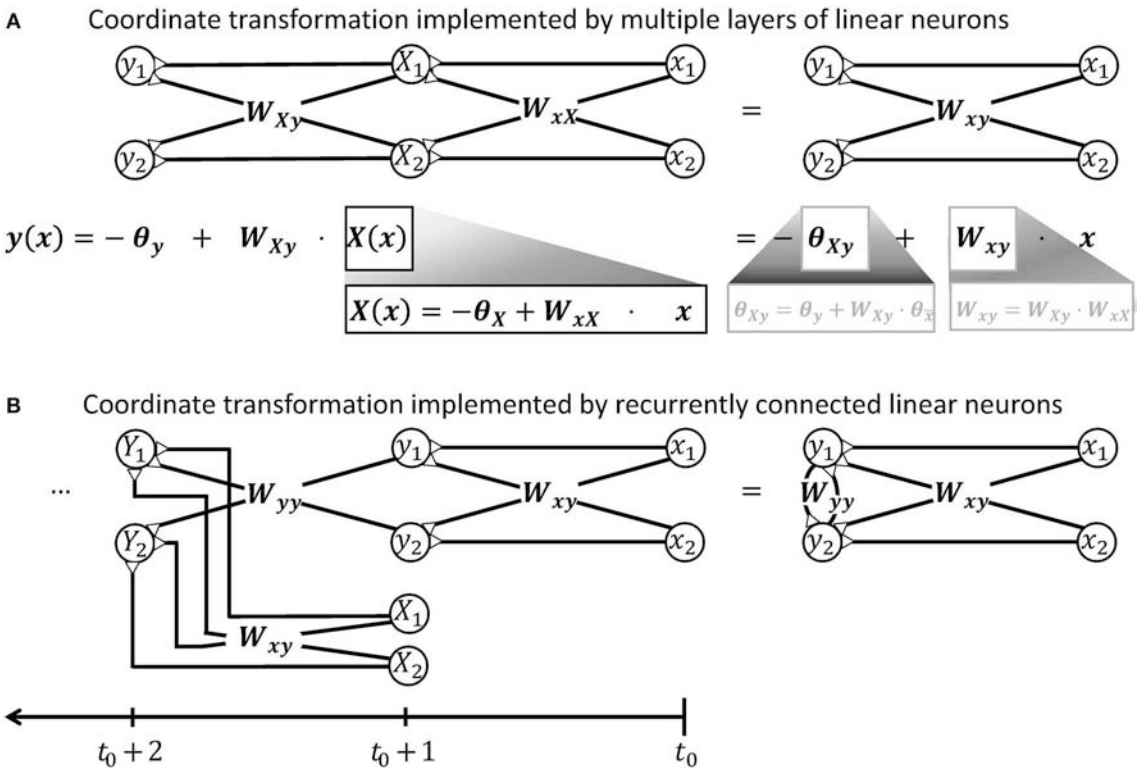

FIGURE 2 | Illustration demonstrating that a network of linear neurons is restricted to implement an affine coordinate transformation of the form $\boldsymbol{y}(\boldsymbol{x}) = \boldsymbol{W}_{\mathrm{xy}}\boldsymbol{x} - \boldsymbol{\theta}_{\boldsymbol{y}}$. **(A)** This relationship is independent of the number of incorporated neuronal feedforward layers. Adding additional layers of neurons changes the input-independent transformation weight $\boldsymbol{W}$ and the shift $\boldsymbol{\theta}$ of the basis, but the mathematical form remains. **(B)** Neuronal networks with recurrent connections are subject to the same limitation. To confirm this, it is advantageous to unfold the calculations performed by the recurrent network shown on the right hand side and deduce a hypothetical feedforward network that computes the same output. When the recurrent network receives an input signal $\boldsymbol{x}$ released at t_0, it will produce an output signal $\boldsymbol{y}$ like a simple feedforward network at $t_0 + 1$, i.e., after a short unitary transduction delay. At the next computational step $t_0 + 2$, the output signal $\boldsymbol{Y}$ is determined by the input signal $\boldsymbol{X}$ from time step $t_0 + 1$ and the previous output signal $\boldsymbol{y}$. The previous output signal is thereby feed back by recurrent synapses with weights $\boldsymbol{W}_{\mathrm{yy}}$. To model this recurrent calculation, one may extend the hypothetical feedforward network by a further layer of linear neurons as shown on the left hand side. These neurons receive the previous output $\boldsymbol{y}$ via synaptic weights $\boldsymbol{W}_{\mathrm{yy}}$. They also receive the further input signal $\boldsymbol{X}$ from time step $t_0 + 1$ from an additional pool of input neurons which synapse via synaptic weights $\boldsymbol{W}_{\mathrm{xy}}$. Further calculation steps $t_0 + 3, t_0 + 4, \ldots, t$ of the recurrent network can be modeled in the feedforward network by iteratively adding layers with the same properties. Thus, the output $\boldsymbol{y}$ of the recurrent network after t time steps is mathematically equivalent to the output produced by a hypothetical feedforward network with $t - 1$ intermediate and one output layers. According to the argument in the beginning of this caption, this multi-layered feedforward network implements an affine coordinate transformation. During each individual time step, also the recurrent network can thus only perform an affine coordinate transformation on its input.

decouple vestibular signals from head and eye movement, the transformation of vestibular signals onto intraparietal neurons must be adjusted according to time-varying signals encoding the motion (Salinas and Sejnowski, 2001). While the ionotropic signal processing is shaped by synaptic plasticity, it is important to notice that its non-linear adjustment during ongoing motor control inherently differs from synaptic plasticity rules in two ways. First, synaptic plasticity acts on a time scale of minutes to hours in motor circuitry (Nishimura et al., 2013), which is too slow for adjustments to changing mechanical contexts. Second, synaptic plasticity is typically local (Gerstner, 2016), whereas the external signal s modulates the transformation weights between multiple pre- and postsynaptic neurons that encode input signals x_i but not the signal s itself. The spinal cord needs to implement such a mechanism which non-linearly integrates signals in order to adjust transformations between neuronal information at different stages of processing, or abstraction, according to changing context.

3. MONOAMINES SCALE SIGNALS IN SPINAL MOTOR CIRCUITS

How would such a non-linear signal integration occur? Functional and anatomical evidence suggests that, in contrast to ionotropic receptors, metabotropic neuromodulation enables non-linear signal integration within spinal motor circuits. A serotonergic signal s is thereby a promising candidate for adjusting the spinal signal processing in line with Equation (4), as it can encode the changing context.

Serotonin (5-HT) released within the ventral spinal cord increases the gain or response of both spinal motorneurons (Hochman et al., 2001; Heckman et al., 2008) and ventral spinal

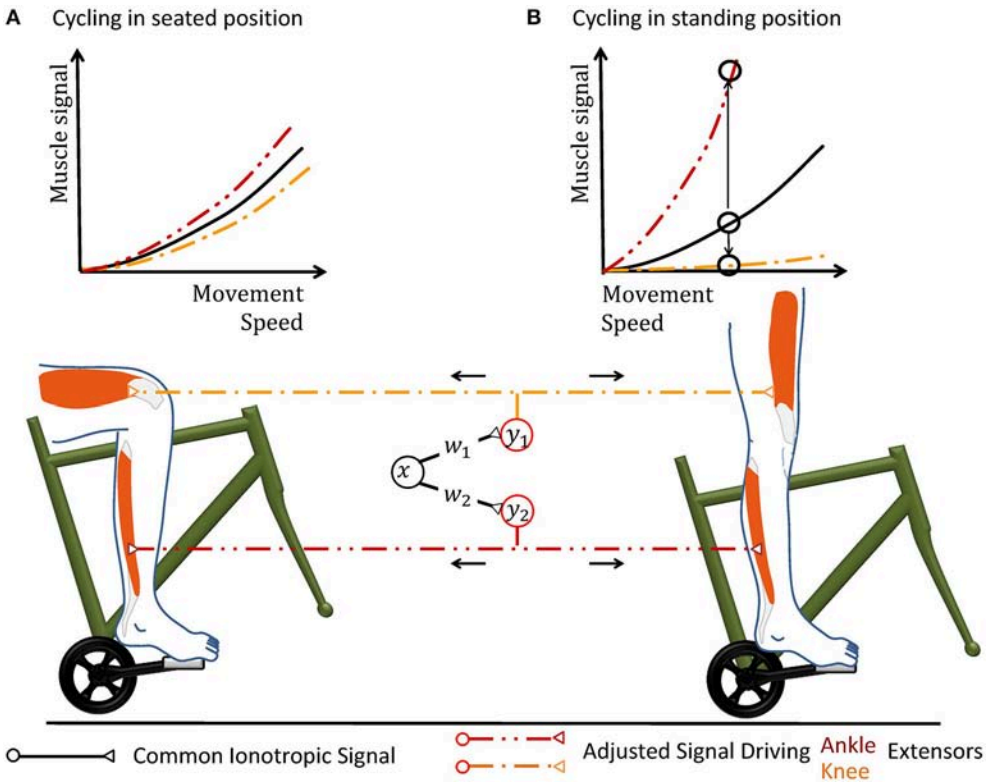

FIGURE 3 | Cycling can illustrate why a hypothetical coordinate transformation requires topographically precise non-linear scaling under varying conditions. The pedal forms a mechanical environment that constrains the movement and the muscular forces required to excite it in a particularly strict way. In the hypothetical neuronal circuit, a group of neurons carries a motor signal *x* that triggers several groups of muscles. As the motor signal is forwarded to spinal interneurons and motorneurons, it is transformed according to the transformation weights w_j. The resulting musculotopic signals y_j simultaneously actuate muscles involved in pushing the pedal, e.g., extensor muscles of the knee and ankle. Increasing the movement speed can be performed by an overall increase of the common motor signal. **(A)** When the person sits on the saddle, both knee and ankle extensors need to be actuated simultaneously. The weights of the synapses transferring the hypothetical motor signal *x* to the respective motorneuron pools are hereby chosen accordingly to achieve the required respective muscular signals. **(B)** When the mechanical properties of the environment changes during an ongoing movement, e.g., because the subject stands up to accelerate, the same muscle groups need to alter their output during the same phase of locomotion. In the standing position, knee actuation cannot exert force along the pedal trajectory. Thus, knee extensors should receive almost no muscle signal, while ankle extensors need to be activated more in order to keep up a given movement speed. Ankle and knee extensors thus need a scaling of different polarity, as illustrated by the upwards and downwards arrow in the graph. Under changing mechanical conditions, all motorneuron pools can thus still be actuated by the same abstract ionotropic motor signal from the hypothetical neuronal synergy, which just needs to be scaled differentially according to sensory information.

interneurons (Abbinanti and Harris-Warrick, 2012; Abbinanti et al., 2012; Husch et al., 2015; Perrier and Cotel, 2015) to ionotropic input, without affecting their baseline excitation. This effect is functionally equivalent to an increase of the transformation weights onto motorneurons. It results from a stimulation of 5-HT_2 receptors, which triggers a range of biochemical mechanisms as extensively reviewed previously (Abbinanti and Harris-Warrick, 2012; Perrier et al., 2013). Stimulating 5-HT_2 receptors by descending 5-HT is crucial in particular for the generation of rhythmic movement in mammals, such as whisking in rats (Hattox et al., 2003) and weight-supported locomotion (Slawińska et al., 2014). By activating 5-HT_{1A} receptors, the CNS can in turn divisively scale down the transformation weights of ionotropic circuitry converging onto motorneurons. The underlying decrease of motorneuronal gain has been suggested to occur during muscle fatigue, when 5-HT spills over its synaptic release site after prolonged release and diffuses to the axon initial segment (Cotel et al., 2013). Before fatigue occurs, the CNS can scale up the firing rate of spinal neurons monotonously and multiplicatively by a factor of up to 10 by increasing the concentrations of 5-HT (Heckman et al., 2008).

In the ventral spinal cord, neuromodulatory effects are dominated not only by 5-HT, but also by noradrenaline (Heckman et al., 2008) and neuropeptides (Thörn Pérez et al., 2015). Neuropeptides are co-released with monoamines and partly trigger similar biomechanic mechanisms (Thörn Pérez et al., 2015), but their predominant trophic effects are very slow (Svensson et al., 2001). In contrast to noradrenaline, 5-HT particularly stands out as candidate for multiplicative operations governed by a mechanical context, as serotonergic neurons receive proprioceptive information on a given movement and implement a distinct motor feedback loop as illustrated in **Figure 4**. About 90% of the 5-HT present within the spinal cord

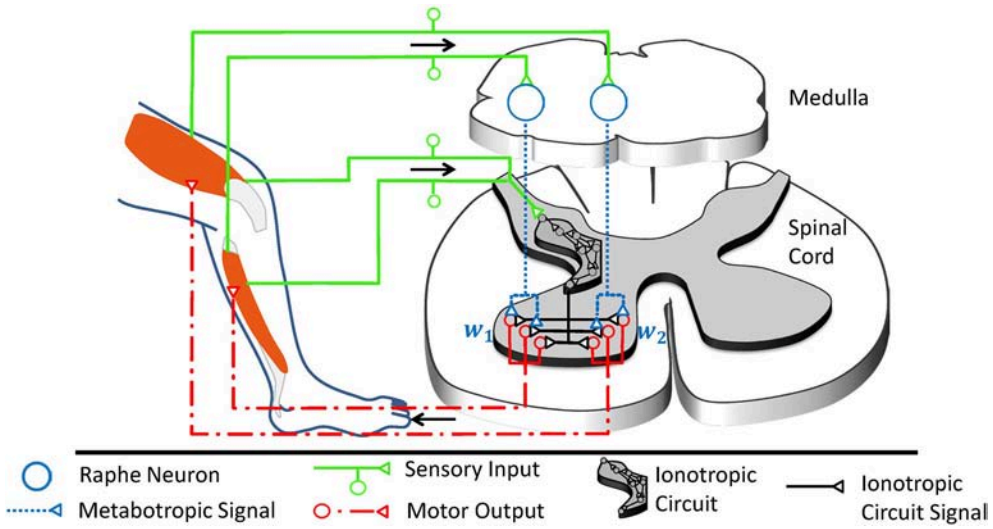

FIGURE 4 | The raphe nuclei obscurus and pallidus form a motor feedback loop. They receive proprioceptive signals and accordingly release serotonin into the ventral spinal cord. The resulting higher serotonin concentration metabotropically increases the excitability of spinal motorneurons as well as associated interneurons at the motor output stage. Collectively, these serotonergic raphe projections change the relative multiplicative weights w_j, which describe how ionotropic signals are transformed into musculotopic motor output. The serotonergic feedback loop acts in parallel to the ionotropic processing of sensory signals. Ionotropic circuitry could operate independently of the metabotropic weight adjustments at the motor output stage and could implement, for example, a low-dimensional control circuit as illustrated here and in **Figure 1B**. Those projections of the raphe nuclei obscurus and pallidus which target interneurons within the low-dimensional circuit will scale the overall spinal ionotropic motor signal without affecting the relative strength w_j of the signals actuating different muscles. In this figure, the ionotropic circuit and each motorneuron pool are represented by several neurons, which appear to be functionally redundant. However, neurons within a subcircuit may have dissimilar connections that assign them to different subcircuits during other tasks. Figure modified, with permission, from Stratmann et al. (2016).

originates from the raphe nuclei (ElBasiouny et al., 2010). In the ventral spinal cord, 5-HT originates primarily from the nucleus raphe obscurus (NRO) and pallidus (NRP), which in turn project almost exclusively to the ventral spinal motor circuitry (Martin et al., 1978; Loewy, 1981; Nieuwenhuys et al., 2008; Watson et al., 2012). These medullary nuclei receive proprioceptive inputs, potentially including inputs from cutaneous mechanoreceptors, and increase the firing rate of their serotonergic neurons accordingly (Springfield and Moolenaar, 1983; Veasey et al., 1995; Fornal et al., 1996). In agreement with the concept of a motor feedback loop, ionotropic motor output is functionally facilitated by 5-HT as an after-effect following strong muscle contraction (Crone et al., 1988; Wei et al., 2014).

There is one pivotal caveat to the presented concept of serotonin as the modulator of individual transformation weights in the ionotropic processing of information: Monoamines are typically considered to be slow and diffuse modulators of a spatially and temporally precise ionotropic circuitry. In fact, the ventral spinal serotonergic system will have a topographically diffuse effect on motor output for the reason that it partly projects to spinal interneurons, which often target several groups of muscles simultaneously (Santello and Lang, 2015; Pérez-Nombela et al., 2017; Takei et al., 2017). The diffuse component will scale the overall Spinal ionotropic motor signal without affecting the relative strength of signals actuating different muscles. But as will be detailed below, recent work suggests that the ventral spinal projections of the NRO and NRP have also a topographically specific component which performs precision scaling (Stratmann et al., 2016). In the following sections, the chain of argumentation will demonstrate that previous findings on the described serotonergic motor feedback loop are consistent with a role as a functionally specific multiplicative operator. By this precision scaling, the raphe nuclei accordingly overcome the limitations of ionotropic circuitry. The arguments run along three lines: First, metabotropic systems are shown to offer a unique functionality in the spinal cord, since ionotropic mechanisms cannot implement non-linear interaction of signals in this CNS region. Second, a fundamental motor control task is considered to define what spatial and temporal precision the serotonergic system needs in order to offer a meaningful functionality that cannot be obtained by diffuse neuromodulation. For this purpose, the particular affine transformation involved in synergy control is chosen as the system of study, as it is both likely implemented by spinal ionotropic circuits and solves motor tasks that would benefit from a subcircuit-specific gain-scaling mechanism. Third, the functionally required spatial and temporal precision will be compared with the experimentally observed precision of the serotonergic feedback loop.

4. LIMITATIONS OF IONOTROPIC SIGNAL INTERACTION *IN VIVO*

The adjustment of coordinate transformations to external signals could theoretically be performed by a neuronal network using

solely ionotropic synaptic currents. Based on neurophysiological findings, several mechanisms have previously been proposed for non-linear, particularly multiplicative, interactions of ionotropic signals. They are typically linked to specific respective CNS regions, have recently been reviewed in detail (Silver, 2010; Carandini and Heeger, 2012) and are summarized in **Table 1**. As mentioned before, the spinal interaction of ionotropic signals is known to be highly linear. This can be attributed to the properties of spinal neurons and signals, which make mechanisms suggested for other CNS regions physically implausible and typically even impossible.

Mechanisms of multiplicative signal interactions can be split into two groups (Silver, 2010): Some mechanisms work in neurons which show time-sparse encoding, i.e., which encode data in the correlations of spikes. Other mechanisms apply to neurons which show a rate-based encoding of information, implying that the neurons process information by exploiting a large range of firing rates.

For neuronal networks working in temporally sparse coding regimes with low firing rates, two main mechanisms for non-linear interaction have been proposed. The first is based on changing levels of synaptic noise emerging from balanced excitatory and inhibitory input (Berg et al., 2007), which can change the gain of the input-output function for neurons operating around their spiking threshold (Chance et al., 2002; Mitchell and Silver, 2003; Higgs et al., 2006). The second is based on shunting inhibition produced by inhibitory input in spatial proximity to the soma (Sherman and Koch, 1986; Isaacson and Scanziani, 2011). These mechanisms are unlikely to cause gain scaling in spinal circuitry, where the early sensory processing and motor output are dominated by rate-coded signals under normal behavior (Ahissar, 1998; Maier et al., 1998; Perlmutter et al., 1998; van Rossum et al., 2002; Stein et al., 2005; Shalit et al., 2012).

For neurons that work within a rate-coded regime, non-linear signal interaction can occur due to the short-term synaptic depression (STD) of synaptic efficacy. If a neuron transmits the sum of two excitatory signals, the second signal may push the firing rate into a regime where STD occurs and may therefore divisively scale the circuit response to the first signal (Carandini et al., 2002; Ozeki et al., 2009; Rothman et al., 2009; Carandini and Heeger, 2012). Using this mechanism is metabolically unfavorable compared to other possible non-linear mechanisms, as the neuronal network would transmit a particularly high number of metabolically expensive action and synaptic potentials (Magistretti and Allaman, 2015). In addition, recent recordings on rate-coding neurons which carry sensor and motor signals show that STD only takes place at the onset of a stimulation train (McElvain et al., 2015). During sustained firing, STD was found to saturate and remain constant for a wide range of firing rates. Thus, STD is unlikely to occur in spinal calculations during ongoing behavior. A second hypothesis originates from the mathematical fact that the multiplication of two signals turns into a pure addition when the logarithms of the signals are considered,

$$\log(x_1 \cdot x_2) = \log(x_1) + \log(x_2)\,. \tag{5}$$

For signals which are encoded logarithmically, such as specific quantities in the visual systems (Gabbiani et al., 2002; Jones and Gabbiani, 2012), multiplication thus becomes trivial (Jones and Gabbiani, 2012). However, many mechanical stimuli are known to be linearly encoded by sensory firing rates (Hensel, 1973; Davis, 1975; Rothwell, 1987; Muniak et al., 2007; Bensmaia, 2008). Furthermore, a neuronal network which implements this strategy would be restricted to implement exclusively either multiplicative or additive operations on its inputs. To implement both, it would need to implement an additional exponential function to extract the actual coordinates. The third possible non-linear mechanism uses active properties of dendrites. Voltage-dependent Na^+ and Ca^{2+} channels as well as NMDA receptors can individually induce supralinear and sublinear interaction of ionotropic signals (Oviedo and Reyes, 2002; Williams and Stuart, 2002; Mehaffey et al., 2005; Losonczy and Magee, 2006; Rhodes, 2006; Remy et al., 2009; Major et al., 2013). In concert, the non-linear effects can counteract the sublinear integration of signals caused either by passive dendritic properties (Segev et al., 1994) or by other voltage-dependent channels (Mehaffey et al., 2005; Rhodes, 2006; Palmer, 2014). The resulting overall effect is strongly determined by the clustering properties of converging synaptic inputs. Individual non-linear effects of unclustered inputs typically balance out to a linear signal summation (Priebe and Ferster, 2010). And indeed, *in vivo* mappings of the full dendritic tree of neurons at early sensory stages demonstrated that synaptic input is not clustered according to functional similarity, a finding which is consistent across different sensory systems (Jia et al., 2010; Varga et al., 2011). In agreement, other *in vivo* recordings showed that the individual non-linear effects of active dendrites are highly balanced and in effect facilitate a linear relationship between input current and output firing (Cash and Yuste, 1998, 1999). The same balance was found for spinal motorneurons in simulations (Cushing et al., 2005) and experiments (Hyngstrom et al., 2008) when neuromodulatory metabotropic input was removed. *In vivo* experiments on non-linear input summation of input from both eyes further emphasized that the CNS uses active dendritic properties not as a non-linear operation, but as a linearizing agent in sensory systems. The non-linear summation of individual signals was found to ensure that the output to binocular stimulation equals the linear summation of input during monocular stimulation (Longordo et al., 2013).

In conclusion, the specific physiological conditions of the spinal cord explain and emphasize that spinal neurons are linear integrators of incoming ionotropic signals. Therefore, the spinal cord needs to take advantage of the metabotropic serotonergic system in order to implement a non-linear interaction of signals.

5. LIGHTENING THE BURDEN OF FREEDOM

5.1. Synergies Simplify the Control of Redundant Locomotor Systems

In order to understand how serotonergic precision scaling can improve motor behavior, it is necessary to consider a typical

TABLE 1 | Overview of various mechanisms proposed for multiplicative interaction of neuronal signals.

Coding regime mechanism	Explanation	References
Time-sparse encoding		
Synaptic noise from balanced excitatory and inhibitory input	Noise triggers membrane voltage to cross threshold by chance and thus smooths input-output function around spiking threshold.	Pyramidal neurons from somatosensory cortex: Chance et al. (2002); Higgs et al. (2006). Motoneurons from spinal cord: Berg et al. (2007).
Shunting inhibition	Inhibitory input in proximity to the soma increases the membrane conductance, which divisively scales the postsynaptic potentials	Theoretical explanation: Isaacson and Scanziani (2011). Neurons from lateral geniculate nucleus: Sherman and Koch (1986). Granule neurons from cerebellum: Mitchell and Silver (2003).
Rate-based encoding		
Short-term synaptic depression	Divisively scales input when a further signal is added.	Neurons from V1: Carandini et al. (2002); Ozeki et al. (2009); Carandini and Heeger (2012). Granule cells from cerebellum: Rothman et al. (2009).
Logarithmic signals	Multiplication of signals x_i turns into a summation upon their logarithmic transformation: $\log(x_1 \cdot x_2) = \log(x_1) + \log(x_2)$.	Locust lobula giant motion detector: Jones and Gabbiani (2012).
Active dendrites	Voltage dependent channels can induce sub- or supralinear signal interaction.	Theoretical explanation: Segev et al. (1994); Rhodes (2006). Pyramidal neurons from sensorimotor cortex: Oviedo and Reyes (2002); Williams and Stuart (2002). Pyramidal neurons from hippocampus: Losonczy and Magee (2006); Remy et al. (2009). Pyramidal neurons from neocortex: Major et al. (2013).
Monoaminergic neuromodulation	Activation of G protein-coupled receptors changes neuronal excitability.	Review on general monoaminergic functions: Bargmann (2012). Review on dopamine receptors: Beaulieu and Gainetdinov (2011). Review on cholinergic receptors: Picciotto et al. (2012). Serotonergic receptors in the spinal cord: Perrier et al. (2013); Husch et al. (2015); Perrier and Cotel (2015); this paper.

coordinate transformations implemented by ionotropic spinal circuitry.

Synergies are an example of spinal transformations which neuroscientists have analyzed in detail. They are formed by interneurons that either receive many input signals or project to motoneurons of several muscles. As illustrated in **Figure 1B**, the CNS thereby transforms high-dimensional sensory information into the low-dimensional synergy space and transforms the motor output from the synergistic circuitry into the high-dimensional musculotopic space (Lacquaniti et al., 2012; Alessandro et al., 2013; Santello et al., 2016). The input sensory synergy filters out information which is unnecessary for a specific motor task. It therefore chooses a particular combination of sensory information from the infinite combinatorial possibilities of sensory signals. The output motor synergy predetermines coordinated activation of a group of muscles elicited by a single circuit. It allows the CNS to choose from an infinite number of possible movement patterns in a locomotor system with more degrees of freedom than is required for a specific task (Bernstein, 1967). The human hand is the most obvious example for such a redundant mechanical system (Santello et al., 2016). But also each lower human limb comprises more than 50 muscles which are to a major extent recruited together for locomotion (Lacquaniti et al., 2012). This redundancy provides a high versatility of possible movements.

Behaviorally, neuronal synergies become detectable as a spatiotemporal pattern of EMG signals emanating from different muscles. They can be extracted mathematically by linear source decomposition methods like principal component analysis (Naik et al., 2016). Human locomotion shows four to five basic patterns (Lacquaniti et al., 2012), which are reproducible when locomotion is perturbed (Chvatal and Ting, 2012). To change locomotion speed, their relative recruitment is shifted gradually (Hagio et al., 2015).

Neurophysiological analysis indicates that the spinal cord is an important basis for synergy control (Santello et al., 2013; Jörntell, 2016; Kiehn, 2016). The majority of spinal interneurons combine signals from different modalities into sensory synergies (Jankowska, 1992). In turn, groups of interneurons elicit a synergistic pattern of muscle activations (Clark et al., 2010; Levine et al., 2014; Danner et al., 2015; Santello and Lang, 2015; Pérez-Nombela et al., 2017; Takei et al., 2017). Synergy output is thereby transformed into the high-dimensional musculotopic space and may be further routed through a separate neuronal layer before it reaches the motoneurons (Zhong et al., 2012). The cerebellum links the individual synergies into more elaborate synergies or into sequential patterns (Bengtsson and Jörntell, 2014; Jörntell, 2017). Descending cortical motor commands may accordingly excite individual synergies to produce meaningful, complex behavior (Graziano, 2006; Overduin et al., 2012; Gallego et al., 2017). These commands may in fact be partly transferred by diffuse neuromodulation, which is known to activate movement patterns or increase the movement frequency (Jing et al., 2009; Harris-Warrick, 2011). In summary, the evidence implies that spinal interneurons often combine information in a low-dimensional synergy space, and the synergistic muscle output is transformed and forwarded to the redundant locomotor system.

Understanding synergies is essential for studies on integrative motor circuits. They can be regarded as a library of re-usable modular building blocks, which the brain combines in order to

construct a large range of complex learned and new movements from basic old ones. In the low-dimensional synergy space, the brain can integrate descending pathways, reflexes, and central pattern generators, i.e., neuronal circuits which produce rhythmic movement without rhythmic input (Ijspeert, 2008; Guertin, 2013; Ijspeert et al., 2013; Dzeladini et al., 2014; Kiehn, 2016; Minassian et al., 2017).

5.2. Robotics Control Theory Explains Synergistic Motor Control

Functional insights on the use of synergies can be obtained from robotics control theory. In recent work, an artificial neural network, which formed a similar network structure as a sensorimotor synergy, was trained to encode meaningful motor primitives within the intermediate synergy layer (Chen et al., 2015). The underlying type of artificial neural networks is called *autoencoder* and is typically used in in the field of deep learning to reduce the dimensionality of data (Hinton and Salakhutdinov, 2006). But while autoencoders in general deploy non-linear quasi-ionotropic mechanisms in the simulated neurons, also the use of more biologically plausible linear synergy spaces have been functionally well-examined for the control of biomimetic robotic hands (Bicchi et al., 2011; Santello et al., 2016) and legged systems (Aoi et al., 2017; Lakatos et al., 2017). The tools that have been developed in this endeavor are mathematically advanced and well-tested. Neuroscientists can thus use them to functionally explain or even predict a specific synergistic behavior.

For low movement speeds, the robotic control strategy of null space projections explains how several tasks, which are individually solved by a respective synergy, can be executed simultaneously (Dietrich et al., 2015). The top-priority command is executed using the full capability of the locomotor system, such as a synergy responsible to keep balance. If the locomotor system is redundant for that specific task, a lower-priority task, e.g., defined by a secondary synergy, can be executed to the greatest possible extent as long as it does not interfere with the top-priority task. For this purpose, an affine transformation projects the secondary task into a space formed by the redundant degrees of freedom, and the resulting motor signal is added to the signal of the top-priority command. The transformation weights depend on the current positions of the actuators, and their adjustments requires a precise model of the locomotor system and its environment (Featherstone and Khatib, 1997). The need for precise models applies to most strategies devised to control low movement speed (Braun et al., 2011). To adjust complex movements at low movement speed to changing conditions, it is therefore likely that human neuronal control circuits also require precise models of their locomotor system. Accordingly, the underlying circuits require high topographic precision. Since the fine-control of complex slow movements strongly relies on the supraspinal circuitry (MacKay-Lyons, 2002; Shemmell et al., 2009), it is reasonable to assume that the required precise models are encoded in the more sophisticated supraspinal neuronal networks. The slow movement speed allows for a heavy recruitment of these networks despite their long feedback delays.

5.3. Synergies for the Control of Highly Dynamic Movement

Here, we want to define a minimal precision that serotonergic effects need to show in order to perform a task that cannot be explained by diffuse neuromodulation. This suggests considering control strategies that require little model precision. It is likely that the CNS recruits such strategies more during fast and strong movements like running. These are strongly shaped by the inertia and elasticity of the system, i.e., quantities which can only be modeled with high inaccuracies and change over time (Nakanishi et al., 2008; Peters et al., 2008; Dietrich et al., 2015). Biomechanical locomotor systems are substantially more complex than robotic systems, as their dynamics critically depend on a particularly large range of parameters such as non-linear muscle elasticities, hysteresis effects, and the changing muscular 3D structure (Siebert and Rode, 2014). This emphasizes that control strategies which require a minimal model precision can control highly dynamic movements in biomechanical locomotor systems much more robustly than model-dependent strategies. A second advantage of considering the control of highly dynamic movement is the associated high consumption of metabolic energy within muscles. The metabolic demands can be drastically lowered by a control strategy utilizing elastic elements within tendons and muscles, as these elastic elements store kinetic energy during a ground impact and release it for recoil (Holmes et al., 2006; Sawicki et al., 2009; Lai et al., 2014). During the evolutionary development of the CNS, strategies for the energy-efficient control of this movement type were thus most likely a critical selection factor. For these reasons, control strategies for highly dynamic movements are likely to be implemented by the CNS. They require a minimum of model knowledge and are thus promising to estimate the minimum precision that serotonergic effects need to show.

For highly dynamic motion, robot control theory showed that a simple synergy controller can generate movement which is stable (Lakatos et al., 2013; Lakatos and Albu-Schäffer, 2014a,b) and makes optimal use of elastic elements in the locomotor system to minimize the consumption of metabolic energy (Stratmann et al., 2017). According to this control strategy, sensory information is linearly transformed into the one-dimensional synergy coordinate space, where it periodically drives a synergy controller (cf. **Figure 5**). Its output is reversely transformed into the musculotopic space using the transformation weights $\boldsymbol{w}$ to drive the joint actuators. Functionally, precise output weights are critical, whereas the input weights may strongly vary without relevant loss in movement performance (Stratmann et al., 2016). Within the synergy space, a circuit as simple as a pool of excitatory reflex interneurons can control the movement (Stratmann et al., 2016). This control law is a promising hypothesis for neuronal motor control for three reasons: First, it requires information about the number of degrees of freedom prior to movement onset and thus minimum model knowledge. Second, it requires only information about muscular deflections and forces during an ongoing movement, as provided by proprioceptive fibers. Third, a linear ionotropic synergy circuit can implement this controller for unchanging environments. To adjust the control law to

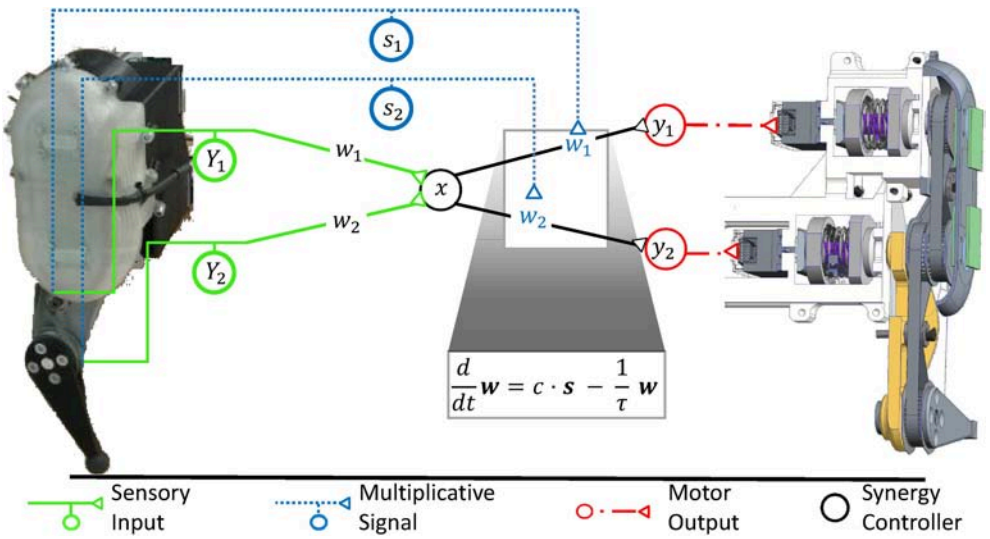

FIGURE 5 | The robotic controller, which was previously developed to maintain a stable, fast, and strong movement, is mathematically equivalent to a synergy controller as illustrated in **Figure 1B**. Sensory input (Y_1, Y_2) signals the movement of individual degrees of freedom of the mechanical system. It is transformed into the low-dimensional synergy space and adjusts the phase and frequency of a synergistic motor signal x. Since the different mechanical degrees of freedom move with high synchrony during fast locomotion, the input weights can be chosen arbitrarily without loss in movement performance (Stratmann et al., 2016). The motor signal x is reversely transformed along the weights (w_1, w_2) to drive the actuators of the same robot. These weights are functionally critical, as the relative forces (y_1, y_2) of different actuators determine, among others, how well the robot can take advantage of its elastic elements to store energy upon ground impact and release it for recoil. In robotic systems, springs typically dominate the elastic properties of the system, as shown on the right hand side of this figure in a cross-sectional illustration of the exemplary robot. As detailed in section 6, the synergy controller can maintain an elastic movement with optimal energy efficiency under changing mechanical conditions. For this purpose, the controller receives sensory inputs s_1 and s_2, which signal the deflections of the degrees of freedom such as joint angles. To adjust to changing mechanical conditions, the controller needs to multiplicatively scale the output transformation weights w_1 and w_2 according to these inputs s_1 and s_2, respectively (Stratmann et al., 2017). A common multiplicative factor c determines the jumping height or distance. To keep the weights bounded, they need to decay exponentially with a time constant τ. The ventral spinal serotonergic system forms a motor feedback loop, as illustrated in **Figure 4**, which functionally resembles the loop of the multiplicative signals presented here.

changing environments, multiplicative scaling of the neuronal gains $\boldsymbol{w}$ at the motor output stage is required, as will be explained in the following section. Since the number of degrees of freedom is the only required model knowledge, this control law is an ideal example to determine what minimal topographic precision serotonergic effects need at least in order to adjust synergies to changing contexts.

6. MULTIPLICATIVE GAIN SCALING MAINTAINS SYNERGIES IN CHANGING CONTEXTS

6.1. Gain Scaling Offers Unique Advantages to Neuronal Signal Processing

Mathematically, multiplicative gain scaling is a core principle for the extension of affine transformations. As will be shown, this principle can strongly enhance the presented robotic synergy controller. Thereby, it is possible to derive the spatial and temporal precision required by the serotonergic system to adjust synergic signal processing to changing contexts. Prior to that, it is important to consider how well multiplication can fulfill this task for realistic locomotor systems under arbitrary conditions. As will be shown, multiplication can in theory extend linear neuronal networks to fulfill this task arbitrarily well, because it allows them the implementation of arbitrary general transformations. Multiplication is furthermore a straightforward, functionally powerful operation for this task. These advantages of gain scaling are so fundamental that they apply to affine transformations in general, even beyond motor control. They motivate and help understand why precision scaling may have evolved during evolution.

Weierstrass and Stone (1948) have mathematically demonstrated that arbitrary continuous transformations $y(x)$ can be approximated to any desired precision for a restricted interval of possible input values $\boldsymbol{x}$ by the sum of exponentiation powers in the input,

$$\boldsymbol{y}(\boldsymbol{x}) = +(-\boldsymbol{\theta}_{\mathrm{y}}) + \boldsymbol{W}_{\mathrm{xy}}\boldsymbol{x}^1 + \ldots . \tag{6}$$

Each summand comprises a power of the input with increasing exponent. Engineers often use this finding since this sum can be used to approximate arbitrary transformations which cannot be derived mathematically or are changing unpredictably with time. An affine transformation implemented by a linear neuronal network, as described by Equation (3), is a first-order approximation. That means it includes a constant, i.e., a term proportional to the zeroth power $\boldsymbol{x}^0 = \mathbf{1}$ in the input, and a summand that is proportional to the first power $\boldsymbol{x}^1$ in the input. Taylors theorem, one of the basic theorems

in mathematical analysis, states that adding summands of higher exponent continuously improves the approximation. But given an approximation with summands up to a particular exponent, the benefit gained by adding further summands of higher exponent becomes increasingly negligible (Cohen and Tan, 2012). As affine transformations include terms up to the first power of the input, a linear neuronal network offers a general circuit scheme that captures a major portion of a general transformation. Linear neurons which are further able to multiply signals can be combined in several layers to calculate arbitrary powers of its inputs. In contrast to a purely linear neuronal network, such a network can implement Equation (6) and therefore perform each possible transformation on its inputs with arbitrary precision.

Deep learning shows that multiplication is only one out of many arithmetic operations which a neuronal network can implement in order to act as universal approximator of general transformations (Stone, 1948; Cybenko, 1989; Hornik, 1991; Chen et al., 2015). Hereby, the artificial networks typically implement a single function which seemingly resembles ionotropic signal processing, but may in fact represent the collective effect of ionotropic, metabotropic, and other mechanisms. While a multiplicative mechanism that parallels the ionotropic circuitry is not the only mechanism that allows implementing a universal approximator, it allows a particularly powerful, straightforward, and resource-efficient adjustment of an affine transformation to changing contexts. Adjusting an affine transformation,

$$y_j = \sum_i w_{\mathrm{ij}} x_i - \theta_j \,,$$

according to the external signal s encoding the context implies that individual transformation weights w_{ij} must change with s. If the CNS multiplies the inputs x_i with the external signal, it effectively performs an affine transformation with transformation weights

$$w_{\mathrm{ij}}(s) = w_{\mathrm{ij,c}} \cdot s \,, \tag{7}$$

which increase with the constant of proportionality $w_{\mathrm{ij,c}}$. The resulting affine transformation

$$y_{\mathrm{j}} = \sum_i w_{\mathrm{ij,c}} x_{\mathrm{i}} s - \theta_{\mathrm{j}} \tag{8}$$

can be seen as a Taylor approximation which models the interaction between inputs x_{i} and context s up to second order. As explained in the previous paragraph, such a second-order approximation captures a large portion of an arbitrary interaction, which eases the functional need for further resource-consuming neuronal operations. In agreement with this functional benefit, experiments typically link changing coordinate transformations to gain modulation, as reviewed by Salinas and Sejnowski (2001). For example, motor output following stimulations of M1 is multiplicatively modulated by proprioceptive information (Graziano et al., 2004), which can at least partly be attributed to serotonergic gain scaling at the level of spinal motorneurons (Wei et al., 2014).

6.2. How Gain Scaling Can Enhance Synergy Control

In the specific context of robotic synergies, it is possible to derive the spatial and temporal precision that the spinal serotonergic system needs for precision scaling. Scaling the gains of the output transformation hereby leverages the above-described robotic control law, as it decouples the synergy circuitry from changes in the mechanical context of the movement (Lakatos et al., 2013). The synergy itself is therefore unaffected, for example, when one runs from a solid to a soft ground or changes body posture during cycling (cf. **Figure 3**). The common synergistic motor signal can be individually scaled by separate output gains w_{j} to calculate the respective motor signal for each functional group j of muscles acting on a single degree of freedom. A degree of freedoms is thereby typically formed by an individual joint (Lakatos et al., 2013, 2017). The index i of the synaptic weights w_{ij} is neglected, as the synergy circuit functionally outputs only a single ionotropic signal x.

Robotic control theory predicts how the gains w_{j} within the biological neuronal network must be adjusted to changing mechanical contexts in order to minimize metabolic demands (Lakatos et al., 2013). To explore a given mechanical context, the ionotropic synergy circuitry provides input to all involved muscles and excites a non-optimal movement. As the controller adapts to the mechanical context, it increasingly optimizes the movement. The control approach derived for this purpose (cf. **Figure 5**) resembles the function performed by the serotonergic feedback loop (cf. **Figure 4**) in all of its three main characteristics: First, the controller receives sensory input about the resulting joint deflections, resembling the proprioceptive information converging onto the raphe nuclei. Second, the controller uses this information to update its model of the body and its environment. For this purpose, it adjusts the transformation weights from the motor synergy to groups of actuators driving the involved joints. The updated transformation weights improve the movement and recursively lead to updated sensory signals. Also this characteristic resembles the function of the raphe nuclei, which scale ionotropic synergy signals as they arrive on motorpools. Third, the multiplicative transformation weights $\boldsymbol{w}$ converge toward the dominant principal component of the sensory signals $\boldsymbol{s}$ encoding the deflections of individual joints. Based on work by Lakatos et al. (2013), Stratmann et al. (2016) demonstrated that the alignment can be achieved by multiplying the output of the synergy circuitry by weights that increase with the sensory signals. In order to keep the weights within a physiological regime, decay of the weights over time is required as counteracting mechanism. These two effects can be summarized as

$$\frac{d}{dt}\boldsymbol{w} = w_{\mathrm{c}} \cdot \boldsymbol{s} - \frac{1}{\tau}\boldsymbol{w} \,. \tag{9}$$

The constant factor w_{c} scales the overall force output. The time constant τ describes the gain decay and must be of the same order of magnitude as the typical cycle duration of biomechanical movement. This time scale guarantees constant gains throughout the movement cycle in a sustained context. Meanwhile, the dominant changes of transformation weights, and thus most of

the functional impact on metabolic costs, occurs already during the first step cycles, i.e., for quickly-changing contexts (Stratmann et al., 2017). Stratmann et al. (2016) demonstrated analytically and in neuromechanical simulations that previous models of the kinematics of released serotonin are fully consistent with Equation (9). But it remained unclear if the serotonergic feedback loops shows the same temporal and topographic precision as the controller.

The resemblance between the serotonergic motor feedback loop and the controller is remarkable, as the controller has been derived based purely on considerations about the dynamics of biomimetic systems. After controller convergence, the synergy controller makes optimal use of the energy saving capacity offered by the elastic elements within the mechanical locomotor system. This result was consistently obtained under the influence of physical noise, mechanical damping, and non-linear dynamics (Stratmann et al., 2017). This means that the actuators require a minimum of metabolic energy to sustain the highly dynamic locomotion. Throughout the adaptation, the mechanical system shows stable movement. This stability results from the weight decay and from the friction within the mechanical system. The friction implements a further negative feedback loop as it increases with higher movement velocity, i.e., a stronger motor signal (Lakatos and Albu-Schäffer, 2014b). Videos illustrating the emerging movement have been published previously for elastic robotic systems mimicking the leg of a small mammal (Stratmann et al., 2017), human legs (Löffl et al., 2016), and a human arm (Lakatos et al., 2013). Under the assumption that the raphe nuclei show sufficient topographic and temporal precision, also the simulated raphe nuclei optimized the energy efficiency of motion induced in a leg which was either mechanically constraint, resembling cycling as illustrated in **Figure 3**, or free to move along a trail (Stratmann et al., 2016).

The robotics control approach explains the functional advantage of a raphe motor feedback loop that shows precision scaling rather than a diffuse neuromodulation of motorpools. Thereby, it predicts that the serotonergic feedback loop must show gain scaling which acts on a time scale of hundreds of milliseconds to few seconds and which is at least joint-specific. In particular, it must amplify motorpools driving joints that show a large deflection throughout the movement and thus send out large proprioceptive signals s_i. With these characteristics, the raphe nuclei would ensure that simple ionotropic synergies can induce highly dynamic rhythmic movements with minimum metabolic demands under changing context.

7. SEROTONIN PROVIDES SUBCIRCUIT-SPECIFIC GAIN SCALING

The functional considerations offer a benchmark for the anatomical and functional precision that the serotonergic feedback loop requires to perform precision scaling.

Neuroscientific studies considering the topographic precision suggest that along the serotonergic feedback pathway, each processing step allows for a spatially focused signal transduction. Sensory signals are relayed to the NRP and NRO within 20 ms (Springfield and Moolenaar, 1983). This short delay indicates a monosynaptic or a strong oligosynaptic input from the peripheral sensors to the NRO and NRP. A likely candidate is disynaptically mediated input via spinal interneurons that typically targets the cerebellum (Jörntell, 2017) but that may also mediate peripheral inputs to brainstem nuclei (Johansson and Silfvenius, 1977) as illustrated in **Figure 6**. The efferent serotonergic projections of the approximately 19,000 serotonergic neurons comprised within the human NRP and NRO (Hornung, 2003) target almost exclusively the ventral spinal cord (Martin et al., 1978; Loewy, 1981; Nieuwenhuys et al., 2008; Watson et al., 2012). These projections have been suggested to comprise both an anatomically diffuse component and a separate topographically specific component (Huisman et al., 2011). The diffuse projections as well as projections to ventral interneurons within a neuronal synergy affect the overall gain like the factor w_c in Equation (9) and may additionally increase the overall leg stiffness by co-contraction of antagonistic muscles. Both effects have been suggested to underlie increases of the movement speed (Heglund and Taylor, 1988; Ferris et al., 1998). They explain functional findings demonstrating that the 5-HT released by the action of one limb amplifies motor signals that target the muscles in other limbs as well (Wei et al., 2014). Previous anatomical studies allow a quantification of the spatially focused projection onto spinal motorneurons and interneurons associated with specific motorneuron pools. Tracers inserted into the spinal cord showed that the location of the labeled serotonergic cells vary markedly with the region of injection, contrasting the more homogeneous labeling of non-serotonergic cells within the raphe nuclei (Skagerberg and Bjorklund, 1985). Dual retrograde tracers injected into different regions of the ventral horn of rats double-labeled about 50% of cells within the NRP (Cavada et al., 1984). This degree of collateralization resembles that of corticospinal axons, for which more than 40% of 156 neurons could be activated antidromically from several segments of the spinal cord in monkeys (Shinoda et al., 1979). In the ventral spinal cord, serotoninergic projections predominantly terminate in synaptic contacts and the release of 5-HT shows effects of high spatial precision (Brumley et al., 2007; Cotel et al., 2013; Perrier et al., 2013). In agreement with a topographically precise spinal serotonergic system, depletion of 5-HT and blockage of 5-HT_2 receptors in rats slackens locomotion due to adjustments in the motor signals which differentially affect muscles acting at different joints of the same limb or even the same joint (Myoga et al., 1995; Pflieger et al., 2002; Pearlstein et al., 2005). Evidence therefore suggests that the serotonergic system is able to induce effects which are at least joint-specific.

The time scale of metabotropic effects is slow in comparison to ionotropic signal transmission. Following sensory stimulation, the onset of the serotonergic multiplication effect was found to be delayed by tens of milliseconds after stimulus cessation in cats (Crone et al., 1988). It was shown to return back to baseline within a few seconds in turtles (Perrier and Delgado-Lezama, 2005), cats (Crone et al., 1988) and humans (Wei et al., 2014). This long time scale might impede fast neuronal calculations within the brain and may also have detrimental effects for motor control under rapidly changing conditions.

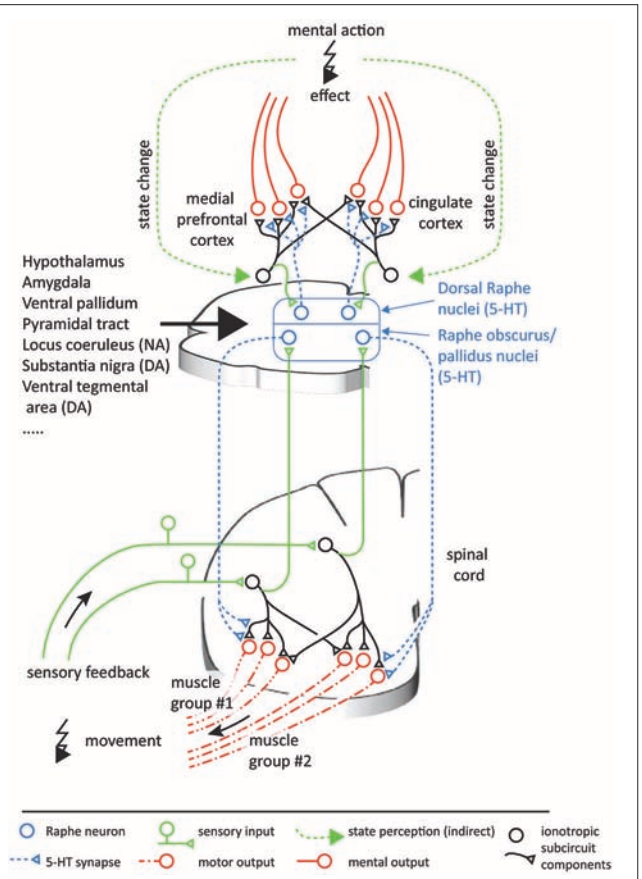

FIGURE 6 | Possible analogous organization of serotonergic function in the spinal cord and the neocortex. In both CNS areas, populations of serotonergic projections originating in the raphe nuclei can be assumed to multiplicatively scale the output of individual ionotropic subcircuits. In turn, the projecting raphe neurons receive feedback on the outcome of their effects, thus forming feedback loops. The ionotropic signals in the spinal cord can be interpreted relatively easily, as they are directly linked to physical muscles and sensors. As in the case of the spinal circuitry, neocortical circuitry operations likely involve integration of information from groups of neurons, which are innervated by different combinations of serotonergic neurons. In contrast, the information encoded in the neocortex can be expected to be more abstract and less directly intelligible, and at present it is therefore less clear what coordinate spaces the neocortex combines. Nevertheless, as a first-level descriptive model of the functional mechanisms monoamines have in neocortical systems, the functional principle presented here can help understand the principles of the effects elicited by psychopharmacological drugs.

For example, it may underlie the Kohnstam effect, where the arm involuntarily lifts following the abrupt end of a strong voluntary contraction. The Kohnstamm effect lasts for several seconds and originates in a persistent activation of the deltoid muscle, which is accompanied by higher motor evoked potentials. The underlying mechanisms are assumed to have a dominant spinal origin (Mathis et al., 1996; Ghosh et al., 2014). These properties are consistent with the idea that the excessive activity observed during the Kohnstamm effect is caused by serotonin that is released during a strong muscle contraction and increases the motoneuron gain of the deltoid specifically. Ongoing movements encountered in everyday life show less-abrupt and extreme switching between conditions. For such non-artificial movements, the time scale of serotonergic effects matches the time scale relevant to various motor behaviors.

To summarize, a joint-specific multiplicative effect which decreases on a time scale of seconds agrees well with the functional requirements determined for the stable and energy-efficient control of highly dynamic movement. The presented control-theoretical framework therefore links the previous experimental findings on monoamines into a new operational principle of temporally- and subcircuit-specific gain modulators. By this precision scaling, the serotoninergic projections to the ventral spinal cord can be assumed to strongly simplify motor control adaptation.

8. MONOAMINES SCALE SIGNALS THROUGHOUT THE CNS

8.1. A Principle Common Across Serotonergic Systems

The previous section considered the parts of the serotonergic system that target the spinal cord. But the functional interpretation developed so far may, in principle, also apply to the serotonergic innervation of other parts of the central nervous system. It may even apply to those CNS areas which may achieve precision scaling using non-linear ionotropic mechanisms, possibly by combining many non-linear neurons into a network that approximates more general transformations mediated by network effects. These CNS areas may take advantage of the parallel, resource-efficient implementation of precision scaling originating from monoaminergic systems. Serotonergic innervation is present in practically all parts of the CNS, including the striatum, amygdala, thalamus, and hippocampus (Vertes and Linley, 2008; Daubert and Condron, 2010). But in this paper, a specific interpretational example will be developed for the frontal and cingulate areas of the neocortex, where many researchers locate at least part of the effects caused by psychopharmacological drugs interfering with the serotonergic system.

The proposed framework suggests a generic function for 5-HT as a subcircuit- and temporally specific non-linear gain modulator which scales individual weights of transformations between different processing stages by postsynaptic effects. An important component of this framework is formed by the feedback connections which evaluate the contextual conditions to update the drive on the serotonergic gain modulation (cf. **Figure 4**). Because of the subcircuit-specificity, there is differential gain scaling. This is useful if changes in conditions require the transformation of different aspects of the overall information to be multiplied with different factors to correctly interact with the external world. For the 5-HT innervation of the prefrontal cortex (PFC), most of these requirements seem to be confirmed. First, there are topographically precise projections with well-defined synapses from the nucleus raphe dorsalis (NRD) to the PFC (Bang et al., 2012; Belmer et al., 2017). Second,

there is a topographically precise feedback inhibition from the PFC to the NRD (Jankowski and Sesack, 2004) and the NRD affects the neuronal gain in the layer V pyramidal cells of the PFC (Zhang and Arsenault, 2005). Considering these apparent functional homologies with the serotonergic innervation of the spinal circuitry, **Figure 6** illustrates a possible scenario for the functional organization of the serotonergic innervation of the PFC / cingulate areas.

In the spinal cord, the functional principle proposed for 5-HT is the multiplicative scaling of individual transformation weights in order to adjust transformations between different coordinate spaces. Whereas for the spinal circuitry one can speak in relatively concrete terms of what is being represented and on what bases the coordinates exist, the coordinates relevant to integrative neocortical systems are likely to have much more abstract bases and are anyway not well-known at the moment. However, there are studies of correlations between certain abstract measures and the activity of the neurons, which can serve as approximations of what kinds of representations are involved. Primate PFC neurons can encode at least in part the monitored actions (Yoshida et al., 2011) and the errors of action of other monkeys (Yoshida et al., 2012). In the anterior cingulate cortex, neurons strongly respond to rewards delivered to other monkeys, while orbitofrontal neurons are more biased toward rewards delivered to the recorded monkey (Chang et al., 2013). An effect of lesions in the orbitofrontal cortex is abnormal social and emotional judgements of facial expressions (Willis et al., 2010; Watson and Platt, 2012) possibly associated with autism or sociopathy (Chang et al., 2013). In rodents, an optogenetic stimulation of PFC neurons that project to the NRD creates abnormal avoidance behavior (Warden et al., 2012; Challis et al., 2014).

Consider the possibility that the neocortex, as we envisaged for the spinal circuitry organization around synergy control, consists of multiple subcircuits, or groups of neurons. Each subcircuit carries representations of specific parameters which are directly or indirectly relevant to dealing with situations arising mentally or in the social world. Because the subcircuits interact, the optimal weighting of each subcircuit will depend on context, similar to the relative muscle forces needed for locomotion across different terrains. In this case, the serotonergic system may scale the relative contributions of different subcircuits so that their contributions to the output become proportional to the required contributions which are imposed by the situation (cf. **Figure 6**).

Attempts toward more holistic models of the functional role of 5-HT have emerged from studies on lower animals, such as the lobster (Kravitz, 2000). In the social life of the lobster, 5-HT levels are assumed to gradually build up during encounters with other lobsters. Encounters typically end up in a gradually escalating demonstration of power in which the lobster with the most imposing body language, or, more rarely, physically proven superiority, will maintain high 5-HT levels and an imposing body posture. Conversely, the individual losing the social tete-a-tete will rapidly develop a subordinate body posture which is assumed to be associated with a dramatic decline in 5-HT levels. The subordinate will subsequently avoid engagement in social fighting for a long time. This acquired unwillingness to engage in fighting can be discharged, however, by an experimental manipulation of the 5-HT levels (Kravitz, 2000). In this model system with a low degree of behavioral diversification, 5-HT will hence affect social interactions and the level of 5-HT will also be a consequence of the behavioral outcome on the social stage. In mammals, possessing a more highly developed neocortex and hence a more diversified and richer understanding of the external world, one would expect a more complex set of feedback regulations of the serotonergic system. Still, the serotonergic system may abide the same principle, i.e., the serotonin level is a consequence of the actions we take and the effects we perceive them to produce. A high or a low level of 5-HT is not necessarily good or bad, but the level should rather be appropriate for how we perceive our position with respect to the external world.

Applying this type of functional model of 5-HT actions also to mental brain functions can offer a novel interpretational framework for the action of psychopharmacological drugs linked to malfunction of the monoaminergic system. Associated disorders include depression, melancholia, social anxiety disorder, obsessive compulsive disorders, panic disorders, posttraumatic stress syndrome, and generalized anxiety disorder. Drugs which are used against these disorders and interact with serotonin and monoamine synaptic transmission are sometimes viewed as pharmaceutical pushbuttons for specific emotional qualities, even though there seems to be no good support for assuming direct causality (Ruhe et al., 2007). However, as portrayed above, the cortical systems that can be expected to be ultimately responsible for the perception of our mood appear to provide feedback projections permitting them to regulate their own 5-HT release (Peyron et al., 1998). As in every negative feedback system, a set point of activity that the system strives toward will tend to arise. Temporary variations around that set point can be triggered by novel estimates of the prevailing conditions based on inputs from the ionotropic circuitry. Hence, according to this view, psychiatric disorders that are susceptible to treatment with drugs interfering with the 5-HT system may arise when the multiplicative coordination of activity for different subcircuits have fallen outside their normally functioning set points. If the scaling of the relative contributions of different subcircuits carrying mental models is out of order, the responses to a changing environment would become inadequate, which may start a vicious circle in which the system digresses further away from its functional set points. In principle, this could occur as a consequence of behavior and would thus be acquired, although internal predisposition factors could exist as well. Interference with 5-HT transmission by the clinical administration of seletive serotonin reuptake inhibitors (SSRIs) could theoretically push the set points of 5-HT in the different subcircuits to new ranges. In some patients, these emerging ranges turn out to be functionally operative. In many cases, however, the doses need to be individually adjusted over a long time. And for some patients SSRI treatment does not work irrespective of dose (Rush et al., 2006; Trivedi et al., 2006). Another feature of SSRI treatment that seems to indicate the existence of internal set points for 5-HT activity is that the therapeutic effect of SSRI is often delayed by some two weeks. One part of this delay has been hypothesized to be due to the autoreceptors on the synaptic terminal that releases

serotonin (Richardson-Jones et al., 2010). The autoreceptors exert a negative feedback on the amount of serotonin released by the terminal and thus forms another natural negative feedback system. However, a negative feedback acting across such a short diffusion range and with effects isolated to the own terminal would seem unlikely to normally take two weeks to find a new set point. But the long-range feedback connections back to the raphe nuclei, involving subcircuits of ionotropic neurons, where each neuron may be expected to have a differentially time-varying activity across different conditions, could well result in feedback systems with very long time constants. Hence, they seem to be a more logical explanatory model for such extremely delayed effects.

8.2. A Principle Common Across Monoaminergic Systems

Other monoaminergic systems than the raphe nuclei also function according to principles that strongly resemble the precision scaling function that is proposed here for serotonin in the spinal cord.

A beautiful and perhaps unexpected example comes from the apparent function of the dopaminergic innervation of the retina (Bargmann, 2012). Retinal processing is dominated by cone photoreceptors in bright light and by rod photoreceptors in low light. Both sensor types converge on cone bipolar cells, which receive direct input from cones as well as indirect input from rods relayed through intermediate rod bipolar cells and AII amacrine cells. When the light level is high, the responsible dopaminergic neurons are activated (Brainard and Morgan, 1987) and the gap junctions between AII amacrine cells and cone bipolar cells are uncoupled. This uncoupling is triggered by the action of dopamine at gates exclusively on the amacrine side, implying that it does not interfere with the processing of inputs from the cone photoreceptors (Xia and Mills, 2004). Uncoupling can be considered to be a multiplicative effect, in which the aim is to find the relative scaling that gives the best overall information for the current light level (Mills and Massey, 1995; Xia and Mills, 2004; Bargmann, 2012). This function is akin to the proposed effect of 5-HT in the ventral spinal cord, which scales the relative motor signals actuating individual groups of muscles according to sensory signals in order to optimize the overall force output.

In general, most monoaminergic systems share the principal features that underlie the model of serotonergic precision scaling presented in this paper. In particular, they are under the tight control of the hypothalamus (Veazey et al., 1982; Villalobos and Ferssiwi, 1987). In some cases, they are even part of the hypothalamic nuclear complex (Ugrumov, 1997), as for example the tuberomammillary nucleus of the hypothalamus in case of histaminergic neurons (Haas et al., 2008). The monoaminergic systems send dense projections to each other, suggesting that their respective activities are under mutual control (Ericson et al., 1989; Nakamura, 2013). They all have widespread terminations in most major structures of the CNS (Samuels and Szabadi, 2008; Vertes and Linley, 2008; Daubert and Condron, 2010; Nestler et al., 2015; Yu et al., 2015). They receive feedback connections from the structures they target and they have autoreceptors for the local feedback of their synaptic release (Douglas et al., 2001; Garcia et al., 2004; Richardson-Jones et al., 2010; Ford, 2014). The bulk of their projections go to the ionotropic circuitry where they act primarily by changing conductances which modulate gains (Foehring et al., 1989; Dong and White, 2003; Surmeier et al., 2007; Yu et al., 2015) in the targeted neurons. Among others, targets include the neocortex, thalamus, striatum, cerebellum, hippocampus, and amygdala. In many cases, there is support for a subcircuit-specific regulation (Blandina et al., 2012).

8.3. A Principle Preserved Across Phylogeny

The presented evidence suggests that precision scaling fundamentally extends the functions of the ionotropic circuitry. Therefore, it comes as no surprise that the monoaminergic systems have emerged very early in phylogeny (Parent, 1984) and that their effects have often been strikingly preserved in the course of natural selection. The serotonergic motor feedback loop, which we describe in detail for mammals, can for example be traced back to invertebrates. Also in these animals, serotonergic neurons strongly innervate motor circuits and receive corresponding feedback (Gillette, 2006). Once serotonin is released, motoneurons show equal reactions across species boundaries and increase their gain in Aplysia (Mackey et al., 1989) as well as in cats (Crone et al., 1988) and humans (Wei et al., 2014). In the lobster, it is known that serotonin can act with topographic precision and specifically increase the firing of flexor muscles. This increased flexor excitation induces the imposing body posture which was described above for dominant lobsters (Kravitz, 2000). Similar to the serotonergic motor feedback loop described here, the amacrine dopaminergic system in the retina has been found also in cartilaginous fishes and amphibians (Yamamoto and Vernier, 2011). A difference from the spinal circuitry is that the topographic precision of the population-integrated dopaminergic projection to the retina is not achieved by the distribution of presynaptic terminals and their amplification of ionotropic currents, but by acting on gap junctions. This reflects that gap junctions play a major role in retinal signal processing (Bloomfield and Volgyi, 2009), whereas the influence of electrical coupling within the spinal cord strongly decreases with developmental age (Li and Rekling, 2017). Thus, it is likely that precision scaling has independently emerged in different CNS regions based on the biochemical mechanisms that dominate the respective signal processing.

9. EXPERIMENTAL PREDICTIONS AND CONCLUSIONS

In order to test if the CNS takes advantage of monoaminergic precision scaling, it is most convenient to investigate the serotonergic motor feedback loop implemented by the raphe nuclei. For this circuit, the control of biomimetic robots clearly predicts the hypothesis that must be evaluated: The excitability of a motorpool actuating a specific joint must increase primarily after subjects have moved the respective

joint rather than other joints of the same limb. As serotonergic effects on motoneurons remain for several 100 ms, the increased excitability must be observable also after cessation of the movement and the motor signals that drive it. Given this predicted topographic precision, the raphe nuclei can adapt motor control to changing conditions and ensure highly-dynamic locomotion under minimum metabolic demands.

While this paper elaborates subcircuit-specific neuromodulation mainly for spinal circuitry, precision scaling presents a big picture which frames the ubiquitous monoaminergic neuromodulation across the CNS. Accordingly, monoaminergic systems represent a computational network within the network formed by the ionotropic circuitry. While subcircuits can collectively encode predictive models of the world, monoamines adapt these models to contextual changes by scaling the ionotropic output signals. This concept offers an attractive explanation of how metabotropic signal processing complements the ionotropic functional and anatomical connectome: By scaling individual ionotropic signals, monoamines can provide functionality that is powerful, resource-efficient and, at least in the spinal circuitry, unique. Furthermore, the slow time scale of metabotropic effect coincides with the time scale of many motor behaviors, rendering monoamines ideal candidates to bridge the fast ionotropic signals and slowly changing behavioral context. In turn, the long time scale of metabotropic mechanisms can impose testable detrimental limits on the speed of behavioral adaptation, as exemplarily observed in the persistent impairment of precision movements resulting from serotonergic effects after high muscular force production (Wei et al., 2014). Given these facts, it is not surprising that malfunction of monoaminergic systems is strongly implicated in motor and cognitive disorders. Conceptualizing monoaminergic systems as subcircuit-specific modulators of ionotropic circuitry thus helps scale our view on why diffuse psychopharmacological drugs often show unpredictable treatment outcomes in such disorders.

AUTHOR CONTRIBUTIONS

AA-S, HJ, and PS developed the structure of the paper. PS authored sections 1–7 and 9. HJ authored section 8. AA-S, HJ, and PS critically revised the paper.

REFERENCES

Abbinanti, M. D., and Harris-Warrick, R. M. (2012). Serotonin modulates multiple calcium current subtypes in commissural interneurons of the neonatal mouse. *J. Neurophysiol.* 107, 2212–2219. doi: 10.1152/jn.00768.2011

Abbinanti, M. D., Zhong, G., and Harris-Warrick, R. M. (2012). Postnatal emergence of serotonin-induced plateau potentials in commissural interneurons of the mouse spinal cord. *J. Neurophysiol.* 108, 2191–2202. doi: 10.1152/jn.00336.2012

Ahissar, E. (1998). Temporal-code to rate-code conversion by neuronal phase-locked loops. *Neural Comput.* 10, 597–650.

Alessandro, C., Delis, I., Nori, F., Panzeri, S., and Berret, B. (2013). Muscle synergies in neuroscience and robotics: from input-space to task-space perspectives. *Front. Comput. Neurosci.* 7:43. doi: 10.3389/fncom.2013.00043

Aoi, S., Manoonpong, P., Ambe, Y., Matsuno, F., and Wörgötter, F. (2017). Adaptive control strategies for interlimb coordination in legged robots: a review. *Front. Neurorobot.* 11:39. doi: 10.3389/fnbot.2017.00039

Babič, J., Oztop, E., and Kawato, M. (2016). Human motor adaptation in whole body motion. *Sci. Rep.* 6:32868. doi: 10.1038/srep32868

Bang, S. J., Jensen, P., Dymecki, S. M., and Commons, K. G. (2012). Projections and interconnections of genetically defined serotonin neurons in mice. *Eur. J. Neurosci.* 35, 85–96. doi: 10.1111/j.1460-9568.2011.07936.x

Bargmann, C. I. (2012). Beyond the connectome: how neuromodulators shape neural circuits. *Bioessays* 34, 458–465. doi: 10.1002/bies.201100185

Beaulieu, J.-M., and Gainetdinov, R. R. (2011). The physiology, signaling, and pharmacology of dopamine receptors. *Pharmacol. Rev.* 63, 182–217. doi: 10.1124/pr.110.002642

Belmer, A., Klenowski, P. M., Patkar, O. L., and Bartlett, S. E. (2017). Mapping the connectivity of serotonin transporter immunoreactive axons to excitatory and inhibitory neurochemical synapses in the mouse limbic brain. *Brain Struct. Funct.* 222, 1297–1314. doi: 10.1007/s00429-016-1278-x

Bengtsson, F., and Jörntell, H. (2014). Specific relationship between excitatory inputs and climbing fiber receptive fields in deep cerebellar nuclear neurons. *PLOS ONE* 9:e84616. doi: 10.1371/journal.pone.0084616

Bensmaia, S. J. (2008). Tactile intensity and population codes. *Behav. Brain Res.* 190, 165–173. doi: 10.1016/j.bbr.2008.02.044

Berg, R. W., Alaburda, A., and Hounsgaard, J. (2007). Balanced inhibition and excitation drive spike activity in spinal half-centers. *Science* 315, 390–393. doi: 10.1126/science.1134960

Bernstein, N. A. (1967). *The Co-ordination and Regulation of Movements, 1st english Edn.* Oxford: Pergamon Press.

Bhanpuri, N. H., Okamura, A. M., and Bastian, A. J. (2013). Predictive modeling by the cerebellum improves proprioception. *J. Neurosci.* 33, 14301–14306. doi: 10.1523/JNEUROSCI.0784-13.2013

Bicchi, A., Gabiccini, M., and Santello, M. (2011). Modelling natural and artificial hands with synergies. *Philos. Trans. R. Soc. Lond. B Biol. Sci.* 366, 3153–3161. doi: 10.1098/rstb.2011.0152

Blandina, P., Provensi, G., Munari, L., and Passani, M. B. (2012). Histamine neurons in the tuberomamillary nucleus: a whole center or distinct subpopulations? *Front. Syst. Neurosci.* 6:33. doi: 10.3389/fnsys.2012.00033

Bloomfield, S. A., and Volgyi, B. (2009). The diverse functional roles and regulation of neuronal gap junctions in the retina. *Nat. Rev. Neurosci.* 10, 495–506. doi: 10.1038/nrn2636

Brainard, G. C., and Morgan, W. W. (1987). Light-induced stimulation of retinal dopamine: a dose-response relationship. *Brain Res.* 424, 199–203. doi: 10.1016/0006-8993(87)91211-X

Braun, D., Howard, M., and Vijayakumar, S. (2011). "Exploiting variable stiffness in explosive movement tasks," in *Proceedings of Robotics: Science and Systems* (Los Angeles, CA).

Brown, E., and Brüne, M. (2012). The role of prediction in social neuroscience. *Front. Hum. Neurosci.* 6:147. doi: 10.3389/fnhum.2012.00147

Brumley, M. R., Hentall, I. D., Pinzon, A., Kadam, B. H., Blythe, A., Sanchez, F. J., et al. (2007). Serotonin concentrations in the lumbosacral spinal cord of the adult rat following microinjection or dorsal surface application. *J. Neurophysiol.* 98, 1440–1450. doi: 10.1152/jn.00309.2007

Carandini, M., and Heeger, D. J. (2012). Normalization as a canonical neural computation. *Nat. Rev. Neurosci.* 13, 51–62. doi: 10.1038/nrn3136

Carandini, M., Heeger, D. J., and Senn, W. (2002). A synaptic explanation of suppression in visual cortex. *J. Neurosci.* 22, 10053–10065. doi: 10.1523/JNEUROSCI.22-22-10053.2002

Cash, S., and Yuste, R. (1998). Input summation by cultured pyramidal neurons is linear and position-independent. *J. Neurosci.* 18, 10–15.

Cash, S., and Yuste, R. (1999). Linear summation of excitatory inputs by ca1 pyramidal neurons. *Neuron* 22, 383–394.

Cavada, C., Huisman, A. M., and Kuypers, H. G. (1984). Retrograde double labeling of neurons: the combined use of horseradish peroxidase and diamidino yellow dihydrochloride (DY·2HCl) compared with true blue and DY·2HCl in rat descending brainstem pathways. *Brain Res.* 308, 123–136.

Challis, C., Beck, S., and Berton, O. (2014). Optogenetic modulation of descending prefrontocortical inputs to the dorsal raphe bidirectionally bias socioaffective choices after social defeat. *Front. Behav. Neurosci.* 8:43. doi: 10.3389/fnbeh.2014.00043

Chance, F. S., Abbott, L. F., and Reyes, A. D. (2002). Gain modulation from background synaptic input. *Neuron* 35, 773–782. doi: 10.1016/S0896-6273(02)00820-6

Chang, S. W., Gariepy, J. F., and Platt, M. L. (2013). Neuronal reference frames for social decisions in primate frontal cortex. *Nat. Neurosci.* 16, 243–250. doi: 10.1038/nn.3287

Chen, N., Bayer, J., Urban, S., and van der Smagt, P. (2015). "Efficient movement representation by embedding dynamic movement primitives in deep autoencoders," in *2015 IEEE-RAS 15th International Conference on Humanoid Robots (Humanoids)* (Seoul), 434–440.

Chen, X., DeAngelis, G. C., and Angelaki, D. (2013). Diverse spatial reference frames of vestibular signals in parietal cortex. *Neuron* 80, 1310–1321. doi: 10.1016/j.neuron.2013.09.006

Chvatal, S. A., and Ting, L. H. (2012). Voluntary and reactive recruitment of locomotor muscle synergies during perturbed walking. *J. Neurosci.* 32, 12237–12250. doi: 10.1523/JNEUROSCI.6344-11.2012

Clark, D. J., Ting, L. H., Zajac, F. E., Neptune, R. R., and Kautz, S. A. (2010). Merging of healthy motor modules predicts reduced locomotor performance and muscle coordination complexity post-stroke. *J. Neurophysiol.* 103, 844–857. doi: 10.1152/jn.00825.2009

Cohen, M. A., and Tan, C. O. (2012). A polynomial approximation for arbitrary functions. *Appl. Math. Lett.* 25, 1947–1952. doi: 10.1016/j.aml.2012.03.007

Cools, R., Nakamura, K., and Daw, N. D. (2011). Serotonin and dopamine: unifying affective, activational, and decision functions. *Neuropsychopharmacology* 36, 98–113. doi: 10.1038/npp.2010.121

Cotel, F., Exley, R., Cragg, S. J., and Perrier, J.-F. (2013). Serotonin spillover onto the axon initial segment of motoneurons induces central fatigue by inhibiting action potential initiation. *Proc. Natl. Acad. Sci. U.S.A.* 110, 4774–4779. doi: 10.1073/pnas.1216150110

Crone, C., Hultborn, H., Kiehn, O., Mazieres, L., and Wigstrom, H. (1988). Maintained changes in motoneuronal excitability by short-lasting synaptic inputs in the decerebrate cat. *J. Physiol.* 405, 321–343.

Cunningham, J. P., and Yu, B. M. (2014). Dimensionality reduction for large-scale neural recordings. *Nat. Neurosci.* 17, 1500–1509. doi: 10.1038/nn.3776

Cushing, S., Bui, T., and Rose, P. K. (2005). Effect of nonlinear summation of synaptic currents on the input–output properties of spinal motoneurons. *J. Neurophysiol.*, 94(5):3465–3478. doi: 10.1152/jn.00439.2005

Cybenko, G. (1989). Approximation by superpositions of a sigmoidal function. *Math. Control Signals Syst.* 2, 303–314.

Danner, S. M., Hofstoetter, U. S., Freundl, B., Binder, H., Mayr, W., Rattay, F., et al. (2015). Human spinal locomotor control is based on flexibly organized burst generators. *Brain* 138, 577–588. doi: 10.1093/brain/awu372

Daubert, E. A., and Condron, B. G. (2010). Serotonin: a regulator of neuronal morphology and circuitry. *Trends Neurosci.* 33, 424–434. doi: 10.1016/j.tins.2010.05.005

Davis, J. N. (1975). The response to stretch of human intercostal muscle spindles studied *in vitro*. *J. Physiol.* 249, 561–579.

Dayan, P., and Abbott, L. (2001). "Chapter Network Models: Recurrent Networks," in *Theoretical Neuroscience: Computational and Mathematical Modeling of Neural Systems*, eds T. J. Sejnowski and T. Poggio (Cambridge, MA; London: Computational Neuroscience Series. Massachusetts Institute of Technology Press), 244–265.

Dietrich, A., Ott, C., and Albu-Schäffer, A. (2015). An overview of null space projections for redundant, torque-controlled robots. *Int. J. Robot. Res.* 34, 1385–1400. doi: 10.1177/0278364914566516

Dong, Y., and White, F. J. (2003). Dopamine d1-class receptors selectively modulate a slowly inactivating potassium current in rat medial prefrontal cortex pyramidal neurons. *J. Neurosci.* 23, 2686–2695. doi: 10.1523/JNEUROSCI.23-07-02686.2003

Douglas, C. L., Baghdoyan, H. A., and Lydic, R. (2001). M2 muscarinic autoreceptors modulate acetylcholine release in prefrontal cortex of c57bl/6j mouse. *J. Pharmacol. Exp. Ther.* 299, 960–966.

Dzeladini, F., Ijspeert, A., and van den Kieboom, J. (2014). The contribution of a central pattern generator in a reflex-based neuromuscular model. *Front. Hum. Neurosci.* 8:371. doi: 10.3389/fnhum.2014.00371

ElBasiouny, S. M., Schuster, J. E., and Heckman, C. J. (2010). Persistent inward currents in spinal motoneurons: Important for normal function but potentially harmful after spinal cord injury and in amyotrophic lateral sclerosis. *Clin. Neurophysiol.* 121, 1669-1679. doi: 10.1016/j.clinph.2009.12.041

Ericson, H., Blomqvist, A., and Köhler, C. (1989). Brainstem afferents to the tuberomammillary nucleus in the rat brain with special reference to monoaminergic innervation. *J. Comp. Neurol.* 281, 169–192. doi: 10.1002/cne.902810203

Featherstone, R., and Khatib, O. (1997). Load independence of the dynamically consistent inverse of the jacobian matrix. *Int. J. Robot. Res.* 16, 168–170.

Ferris, D. P., Louie, M., and Farley, C. T. (1998). Running in the real world: adjusting leg stiffness for different surfaces. *Proc. R. Soc. Lond. B Biol. Sci.* 265, 989–994.

Foehring, R. C., Schwindt, P. C., and Crill, W. E. (1989). Norepinephrine selectively reduces slow ca2+- and na+-mediated k+ currents in cat neocortical neurons. *J. Neurophysiol.* 61, 245–256.

Ford, C. P. (2014). The role of D2-autoreceptors in regulating dopamine neuron activity and transmission. *Neuroscience* 282, 13–22. doi: 10.1016/j.neuroscience.2014.01.025

Fornal, C. A., Metzler, C. W., Marrosu, F., do Valle, L. E. R., , and Jacobs, B. L. (1996). A subgroup of dorsal raphe serotonergic neurons in the cat is strongly activated during oral-buccal movements. *Brain Res.* 716, 123–133.

Franklin, D. W., Batchelor, A. V., and Wolpert, D. M. (2016). The sensorimotor system can sculpt behaviorally relevant representations for motor learning. *eNeuro* 3:ENEURO.0070-16.2016. doi: 10.1523/ENEURO.0070-16.2016

Fuxe, K., Dahlström, A. B., Jonsson, G., Marcellino, D., Guescini, M., Dam, M., Manger, P., et al. (2010). The discovery of central monoamine neurons gave volume transmission to the wired brain. *Prog. Neurobiol.* 90, 82–100. doi: 10.1016/j.pneurobio.2009.10.012

Gabbiani, F., Krapp, H. G., Koch, C., and Laurent, G. (2002). Multiplicative computation in a visual neuron sensitive to looming. *Nature* 420, 320–324. doi: 10.1038/nature01190

Gallego, J. A., Perich, M. G., Miller, L. E., and Solla, S. A. (2017). Neural manifolds for the control of movement. *Neuron* 94, 978–984. doi: 10.1016/j.neuron.2017.05.025

Garcia, A. S., Barrera, G., Burke, T. F., Ma, S., Hensler, J. G., and Morilak, D. A. (2004). Autoreceptor-mediated inhibition of norepinephrine release in rat medial prefrontal cortex is maintained after chronic desipramine treatment. *J. Neurochem.* 91, 683–693. doi: 10.1111/j.1471-4159.2004.02748.x

Gerstner, W. (2016). "Chapter 6: Hebbian learning and plasticity," in *From Neuron to Cognition Via Computational Neuroscience*, eds, M. A. Arbib and J. J. Bonaiuto (Cambridge, MA; London: Computational Neuroscience Series, MIT Press), 199–218.

Ghosh, A., Rothwell, J., and Haggard, P. (2014). Using voluntary motor commands to inhibit involuntary arm movements. *Proc. R. Soc. Lond. B Biol. Sci.* 281:20141139. doi: 10.1098/rspb.2014.1139

Gillette, R. (2006). Evolution and function in serotonergic systems. *Integr. Comp. Biol.* 46, 838–846. doi: 10.1093/icb/icl024

Graziano, M. (2006). The organization of behavioral repertoire in motor cortex. *Annu. Rev. Neurosci.* 29, 105–134. doi: 10.1146/annurev.neuro.29.051605.112924

Graziano, M. S. A., Patel, K. T., and Taylor, C. S. R. (2004). Mapping from motor cortex to biceps and triceps altered by elbow angle. *J. Neurophysiol.* 92, 395–407. doi: 10.1152/jn.01241.2003

Guertin, P. (2013). Central pattern generator for locomotion: anatomical, physiological, and pathophysiological considerations. *Front. Neurol.* 3:183. doi: 10.3389/fneur.2012.00183

Haas, H. L., Sergeeva, O. A., and Selbach, O. (2008). Histamine in the nervous system. *Physiol. Rev.* 88, 1183–1241. doi: 10.1152/physrev.00043.2007

Hagio, S., Fukuda, M., and Kouzaki, M. (2015). Identification of muscle synergies associated with gait transition in humans. *Front. Hum. Neurosci.* 9:48. doi: 10.3389/fnhum.2015.00048

Harris-Warrick, R. M. (2011). Neuromodulation and flexibility in central pattern generator networks. *Curr. Opin. Neurobiol.* 21, 685–692. doi: 10.1016/j.conb.2011.05.011

Hattox, A., Li, Y., and Keller, A. (2003). Serotonin regulates rhythmic whisking. *Neuron* 39, 343–352. doi: 10.1016/S0896-6273(03)00391-X

Heckman, C. J., Hyngstrom, A. S., and Johnson, M. D. (2008). Active properties of motoneurone dendrites: diffuse descending neuromodulation, focused local inhibition. *J. Physiol.* 586, 1225–1231. doi: 10.1113/jphysiol.2007.145078

Heed, T., Buchholz, V. N., Engel, A. K., and Röder, B. (2015). Tactile remapping: from coordinate transformation to integration in sensorimotor processing. *Trends Cogn. Sci.* 19, 251–258. doi: 10.1016/j.tics.2015.03.001

Heglund, N. C., and Taylor, C. R. (1988). Speed, stride frequency and energy cost per stride: how do they change with body size and gait? *J. Exp. Biol.* 138, 301–318.

Hensel, H. (1973). "Cutaneous thermoreceptors," in *Somatosensory System*, ed A. Iggo (Berlin; Heidelberg: Springer), 79–110.

Higgs, M. H., Slee, S. J., and Spain, W. J. (2006). Diversity of gain modulation by noise in neocortical neurons: regulation by the slow afterhyperpolarization conductance. *J. Neurosci.* 26, 8787–8799. doi: 10.1523/JNEUROSCI.1792-06.2006

Hinton, G. E., and Salakhutdinov, R. R. (2006). Reducing the dimensionality of data with neural networks. *Science* 313, 504–507. doi: 10.1126/science.1127647

Hochman, S., Garraway, S. M., Machacek, D. W., and Shay, B. L. (2001). "5-ht receptors and the neuromodulatory control of spinal cord function," in *Motor Neurobiology of the Spinal Cord*, ed T. Cope (Boca Raton, FL; London; New York, NY; Washington, DC), 47–88.

Holmes, P., Full, R. J., Koditschek, D., and Guckenheimer, J. (2006). The dynamics of legged locomotion: models, analyses, and challenges. *SIAM Rev.* 48, 207–304. doi: 10.1137/S0036144504445133

Hornik, K. (1991). Approximation capabilities of multilayer feedforward networks. *Neural Netw.* 4, 251–257.

Hornung, J.-P. (2003). The human raphe nuclei and the serotonergic system. *J. Chem. Neuroanat.* 26, 331–343. doi: 10.1016/j.jchemneu.2003.10.002

Howell, L. L., and Cunningham, K. A. (2015). Serotonin 5-HT2 receptor interactions with dopamine function: implications for therapeutics in cocaine use disorder. *Pharmacol. Rev.* 67, 176–197. doi: 10.1124/pr.114.009514

Huisman, A. M., Kuypers H. G. J. M., and Verburgh, C. A. (2011). "Differences in collateralization of the descending spinal pathways from red nucleus and other brain stem cell groups in cat and monkey," in *Descending Pathways to the Spinal Cord*, eds H. Kuypers and G. Martin (Amsterdam; New York, NY; Oxford: Elsevier Science), 185–218.

Hultborn, H., Denton, M. E., Wienecke, J., and Nielsen, J. B. (2003). Variable amplification of synaptic input to cat spinal motoneurones by dendritic persistent inward current. *J. Physiol.* 552(Pt 3), 945–952. doi: 10.1113/jphysiol.2003.050971

Husch, A., Dietz, S. B., Hong, D. N., and Harris-Warrick, R. M. (2015). Adult spinal v2a interneurons show increased excitability and serotonin-dependent bistability. *J. Neurophysiol.* 113, 1124–1134. doi: 10.1152/jn.00741.2014

Hyngstrom, A. S., Johnson, M. D., and Heckman, C. J. (2008). Summation of excitatory and inhibitory synaptic inputs by motoneurons with highly active dendrites. *J. Neurophysiol.* 99, 1643–1652. doi: 10.1152/jn.01253.2007

Ijspeert, A. J. (2008). Central pattern generators for locomotion control in animals and robots: a review. *Neural Netw.* 21, 642–653. doi: 10.1016/j.neunet.2008.03.014

Ijspeert, A. J., Nakanishi, J., Hoffmann, H., Pastor, P., and Schaal, S. (2013). Dynamical movement primitives: learning attractor models for motor behaviors. *Neural Comput.* 25, 328–373. doi: 10.1162/NECO_a_00393

Isaacson, J., and Scanziani, M. (2011). How inhibition shapes cortical activity. *Neuron* 72, 231–243. doi: 10.1016/j.neuron.2011.09.027

Jankowska, E. (1992). Interneuronal relay in spinal pathways from proprioceptors. *Prog. Neurobiol.* 38, 335–378.

Jankowski, M. P., and Sesack, S. R. (2004). Prefrontal cortical projections to the rat dorsal raphe nucleus: Ultrastructural features and associations with serotonin and gamma-aminobutyric acid neurons. *J. Comp. Neurol.* 468, 518–529. doi: 10.1002/cne.10976

Jia, H., Rochefort, N. L., Chen, X., and Konnerth, A. (2010). Dendritic organization of sensory input to cortical neurons *in vivo*. *Nature* 464, 1307–1312. doi: 10.1038/nature08947

Jing, J., Gillette, R., and Weiss, K. R. (2009). Evolving concepts of arousal: insights from simple model systems. *Rev. Neurosci.* 20, 405–427. doi: 10.1515/REVNEURO.2009.20.5-6.405

Johansson, H., and Silfvenius, H. (1977). Connexions from large, ipsilateral hind limb muscle and skin afferents to the rostral main cuneate nucleus and to the nucleus X region in the cat. *J. Physiol.* 265, 395–428.

Jones, P. W., and Gabbiani, F. (2012). Logarithmic compression of sensory signals within the dendritic tree of a collision-sensitive neuron. *J. Neurosci.* 32, 4923–4934. doi: 10.1523/JNEUROSCI.5777-11.2012

Jörntell, H. (2016). "Synergy control in subcortical circuitry: Insights from neurophysiology," in *Human and Robot Hands: Sensorimotor Synergies to Bridge the Gap Between Neuroscience and Robotics*, eds M. Bianchi and A. Moscatelli (Cham: Springer International Publishing), 61–68.

Jörntell, H. (2017). Cerebellar physiology: links between microcircuitry properties and sensorimotor functions. *J. Physiol.* 595, 11–27. doi: 10.1113/JP272769

Kiehn, O. (2016). Decoding the organization of spinal circuits that control locomotion. *Nat. Rev. Neurosci.* 17, 224–238. doi: 10.1038/nrn.2016.9

Kravitz, E. A. (2000). Serotonin and aggression: insights gained from a lobster model system and speculations on the role of amine neurons in a complex behavior. *J. Comp. Physiol. A* 186, 221–238. doi: 10.1007/s003590050423

Kurian, M. A., Gissen, P., Smith, M., Heales, S. J., and Clayton, P. T. (2011). The monoamine neurotransmitter disorders: an expanding range of neurological syndromes. *Lancet Neurol.* 10, 721–733. doi: 10.1016/S1474-4422(11)70141-7

Lacquaniti, F., Ivanenko, Y. P., and Zago, M. (2012). Patterned control of human locomotion. *J. Physiol.* 590, 2189–2199. doi: 10.1113/jphysiol.2011.215137

Lai, A., Schache, A. G., Lin, Y.-C., and Pandy, M. G. (2014). Tendon elastic strain energy in the human ankle plantar-flexors and its role with increased running speed. *J. Exp. Biol.* 217, 3159–3168. doi: 10.1242/jeb.100826

Lakatos, D., and Albu-Schäffer, A. (2014a). "Neuron model interpretation of a cyclic motion control concept," in *Biomedical Robotics and Biomechatronics, 2014 5th IEEE RAS EMBS International Conference* (Sao Paulo), 905–910.

Lakatos, D., and Albu-Schäffer, A. (2014b). "Switching based limit cycle control for compliantly actuated second-order systems," in *Proceedings of the IFAC World Congress, Vol. 19* (Cape Town), 6392–6399.

Lakatos, D., Friedl, W., and Albu-Schäffer, A. (2017). Eigenmodes of nonlinear dynamics: Definition, existence, and embodiment into legged robots with elastic elements. *IEEE Robot. Automat. Lett.* 2, 1062–1069. doi: 10.1109/LRA.2017.2658018

Lakatos, D., Görner, M., Petit, F., Dietrich, A., and Albu-Schäffer, A. (2013). "A modally adaptive control for multi-contact cyclic motions in compliantly actuated robotic systems," in *Intelligent Robots and Systems (IROS), 2013 IEEE International Conference on* (IEEE) (Tokyo), 5388–5395.

Levine, A. J., Hinckley, C. A., Hilde, K. L., Driscoll, S. P., Poon, T. H., Montgomery, J. M., et al. (2014). Identification of a cellular node for motor control pathways. *Nat. Neurosci.* 17, 586–593. doi: 10.1038/nn.3675

Li, W.-C., and Rekling, J. C. (2017). "Electrical coupling in the generation of vertebrate motor rhythms," in *Network Functions and Plasticity: Perspectives from Studying Neuronal Electrical Coupling in Microcircuits*, ed J. Jing (London; San Diego, CA; Cambridge, MA; Oxford: Elsevier Science), 243–264.

Loewy, A. (1981). Raphe pallidus and raphe obscurus projections to the intermediolateral cell column in the rat. *Brain Res.* 222, 129–133.

Löffl, F., Werner, A., Lakatos, D., Reinecke, J., Wolf, S., Burger, R., et al. (2016). "The dlr c-runner: Concept, design and experiments," in *2016 IEEE-RAS 16th International Conference on Humanoid Robots (Humanoids)* (Cancun), 758–765.

Longordo, F., To, M. S., Ikeda, K., and Stuart, G. J. (2013). Sublinear integration underlies binocular processing in primary visual cortex. *Nat. Neurosci.* 16, 714–723. doi: 10.1038/nn.3394

Losonczy, A., and Magee, J. C. (2006). Integrative properties of radial oblique dendrites in hippocampal ca1 pyramidal neurons. *Neuron* 50, 291–307. doi: 10.1016/j.neuron.2006.03.016

MacKay-Lyons, M. (2002). Central pattern generation of locomotion: a review of the evidence. *Phys. Ther.* 82, 69–83. doi: 10.1093/ptj/82.1.69

Mackey, S., Kandel, E., and Hawkins, R. (1989). Identified serotonergic neurons lcb1 and rcb1 in the cerebral ganglia of aplysia produce presynaptic facilitation of siphon sensory neurons. *J. Neurosci.* 9, 4227–4235.

Magistretti, P. J., and Allaman, I. (2015). A cellular perspective on brain energy metabolism and functional imaging. *Neuron* 86, 883–901. doi: 10.1016/j.neuron.2015.03.035

Maier, M. A., Perlmutter, S. I., and Fetz, E. E. (1998). Response patterns and force relations of monkey spinal interneurons during active wrist movement. *J. Neurophysiol.* 80, 2495–2513.

Major, G., Larkum, M. E., and Schiller, J. (2013). Active properties of neocortical pyramidal neuron dendrites. *Annu. Rev. Neurosci.* 36, 1–24. doi: 10.1146/annurev-neuro-062111-150343

Martin, R. F., Jordan, L. M., and Willis, W. D. (1978). Differential projections of cat medullary raphe neurons demonstrated by retrograde labelling following spinal cord lesions. *J. Comp. Neurol.* 182, 77–88. doi: 10.1002/cne.901820106

Mather, M., and Harley, C. W. (2016). The locus coeruleus: Essential for maintaining cognitive function and the aging brain. *Trends Cogn. Sci.* 20, 214–226. doi: 10.1016/j.tics.2016.01.001

Mathis, J., Gurfinkel, V., and Struppler, A. (1996). Facilitation of motor evoked potentials by postcontraction response (kohnstamm phenomenon). *Electroencephalogr. Clin. Neurophysiol.* 101, 289–297.

McElvain, L., Faulstich, M., Jeanne, J., Moore, J., and du Lac, S. (2015). Implementation of linear sensory signaling via multiple coordinated mechanisms at central vestibular nerve synapses. *Neuron.* 85, 1132–1144. doi: 10.1016/j.neuron.2015.01.017

Mehaffey, W. H., Doiron, B., Maler, L., and Turner, R. W. (2005). Deterministic multiplicative gain control with active dendrites. *J. Neurosci.* 25, 9968–9977. doi: 10.1523/JNEUROSCI.2682-05.2005

Mills, S. L., and Massey, S. C. (1995). Differential properties of two gap junctional pathways made by AII amacrine cells. *Nature* 377, 734–737.

Minassian, K., Hofstoetter, U. S., Dzeladini, F., Guertin, P. A., and Ijspeert, A. (2017). The human central pattern generator for locomotion: does it exist and contribute to walking? *Neuroscientist* 23, 649–663. doi: 10.1177/1073858417699790

Mitchell, S. J., and Silver, R. A. (2003). Shunting inhibition modulates neuronal gain during synaptic excitation. *Neuron* 38, 433–445. doi: 10.1016/S0896-6273(03)00200-9

Muniak, M. A., Ray, S., Hsiao, S. S., Dammann, J. F., and Bensmaia, S. J. (2007). The neural coding of stimulus intensity: linking the population response of mechanoreceptive afferents with psychophysical behavior. *J. Neurosci.* 27(43):11687–11699. doi: 10.1523/JNEUROSCI.1486-07.2007

Myoga, H., Nonaka, S., Matsuyama, K., and Mori, S. (1995). Postnatal development of locomotor movements in normal and para-chlorophenylalanine-treated newborn rats. *Neurosci. Res.* 21, 211 – 221.

Naik, G. R., Selvan, S. E., Gobbo, M., Acharyya, A., and Nguyen, H. T. (2016). Principal component analysis applied to surface electromyography: a comprehensive review. *IEEE Access* 4, 4025–4037. doi: 10.1109/ACCESS.2016.2593013

Nakamura, K. (2013). The role of the dorsal raphe nucleus in reward-seeking behavior. *Front. Integr. Neurosci.* 7:60. doi: 10.3389/fnint.2013.00060

Nakanishi, J., Cory, R., Mistry, M., Peters, J., and Schaal, S. (2008). Operational space control: a theoretical and empirical comparison. *Int. J. Robot. Res.* 27, 737–757. doi: 10.1177/0278364908091463

Nestler, E. J., Hyman, S. E., Holtzman, D. M., and Malenka, R. C. (eds.). (2015). "Chapter 6: Widely projecting systems: Monoamines, acetylcholine, and orexin," in *Molecular Neuropharmacology: A Foundation for Clinical Neuroscience, 3e* (New York, NY: McGraw-Hill Education), 149–183.

Ng, J., Papandreou, A., Heales, S., and Kurian, M. (2015). Monoamine neurotransmitter disorders - clinical advances and future perspectives. *Nat. Rev. Neurol.* 11, 567-84. doi: 10.1038/nrneurol.2015.172

Nieuwenhuys, R., Voogd, J., and van Huijzen, C. (eds.). (2008). "The reticular formation and the monoaminergic and cholinergic cell groups," in *The Human Central Nervous System* (Berlin; Heidelberg: Springer), 889–916.

Nishimura, Y., Perlmutter, S. I., Eaton, R. W., and Fetz, E. E. (2013). Spike-timing-dependent plasticity in primate corticospinal connections induced during free behavior. *Neuron* 80, 1301–1309. doi: 10.1016/j.neuron.2013.08.028

O'Donnell, J., Zeppenfeld, D., McConnell, E., Pena, S., and Nedergaard, M. (2012). Norepinephrine: A neuromodulator that boosts the function of multiple cell types to optimize cns performance. *Neurochem. Res.* 37, 2496–2512. doi: 10.1007/s11064-012-0818-x

Overduin, S. A., d'Avella, A., Carmena, J. M., and Bizzi, E. (2012). Microstimulation activates a handful of muscle synergies. *Neuron* 76, 1071–1077. doi: 10.1016/j.neuron.2012.10.018

Oviedo, H., and Reyes, A. (2002). Boosting of neuronal firing evoked with asynchronous and synchronous inputs to the dendrite. *Nat. Neurosci.* 5, 261–266. doi: 10.1038/nn807

Ozeki, H., Finn, I. M., Schaffer, E. S., Miller, K. D., and Ferster, D. (2009). Inhibitory stabilization of the cortical network underlies visual surround suppression. *Neuron* 62, 578–592. doi: 10.1016/j.neuron.2009.03.028

Palmer, L. M. (2014). Dendritic integration in pyramidal neurons during network activity and disease. *Brain Res. Bull.* 103(Suppl. C), 2–10. doi: 10.1016/j.brainresbull.2013.09.010

Parent, A. (1984). Functional anatomy and evolution of monoaminergic systems1. *Am. Zool.* 24, 783–790.

Pearlstein, E., Ben Mabrouk, F., Pflieger, J. F., and Vinay, L. (2005). Serotonin refines the locomotor-related alternations in the *in vitro* neonatal rat spinal cord. *Eur. J. Neurosci.* 21, 1338–1346. doi: 10.1111/j.1460-9568.2005.03971.x

Pérez-Nombela, S., Barroso, F., Torricelli, D., de Los Reyes-Guzman, A., Del-Ama, A. J., Gomez-Soriano, J., et al. (2017). Modular control of gait after incomplete spinal cord injury: differences between sides. *Spinal Cord* 55, 79–86. doi: 10.1038/sc.2016.99

Perlmutter, S. I., Maier, A. M., and Fetz, E. E. (1998). Activity of spinal interneurons and their effects on forearm muscles during voluntary wrist movements in the monkey. *J. Neurophysiol.* 80, 2475–2494.

Perrier, J.-F., and Cotel, F. (2015). Serotonergic modulation of spinal motor control. *Curr. Opin. Neurobiol.* 33, 1–7. doi: 10.1016/j.conb.2014.12.008

Perrier, J.-F., and Delgado-Lezama, R. (2005). Synaptic release of serotonin induced by stimulation of the raphe nucleus promotes plateau potentials in spinal motoneurons of the adult turtle. *J. Neurosci.* 25, 7993–7999. doi: 10.1523/JNEUROSCI.1957-05.2005

Perrier, J.-F., Rasmussen, H. B., Christensen, R. K., and Petersen, A. V. (2013). Modulation of the intrinsic properties of motoneurons by serotonin. *Curr. Pharmaceut. Design* 19, 4371–4384. doi: 10.2174/1381612811319990341

Peters, J., Mistry, M., Udwadia, F., Nakanishi, J., and Schaal, S. (2008). A unifying framework for robot control with redundant dofs. *Auton. Robots* 24, 1–12. doi: 10.1007/s10514-007-9051-x

Peyron, C., Petit, J. M., Rampon, C., Jouvet, M., and Luppi, P. H. (1998). Forebrain afferents to the rat dorsal raphe nucleus demonstrated by retrograde and anterograde tracing methods. *Neuroscience* 82, 443–468.

Pflieger, J.-F., Clarac, F., and Vinay, L. (2002). Postural modifications and neuronal excitability changes induced by a short-term serotonin depletion during neonatal development in the rat. *J. Neurosci.* 22, 5108–5117. doi: 10.1523/JNEUROSCI.22-12-05108.2002

Picciotto, M., Higley, M., and Mineur, Y. (2012). Acetylcholine as a neuromodulator: cholinergic signaling shapes nervous system function and behavior. *Neuron* 76, 116–129. doi: 10.1016/j.neuron.2012.08.036

Powers, R. K., and Binder, M. D. (1995). Effective synaptic current and motoneuron firing rate modulation. *J. Neurophysiol.* 74, 793–801.

Powers, R. K., and Binder, M. D. (2000). Summation of effective synaptic currents and firing rate modulation in cat spinal motoneurons. *J. Neurophysiol.* 83, 483–500. doi: 10.1152/jn.2000.83.1.483

Priebe, N. J., and Ferster, D. (2010). Neuroscience: each synapse to its own. *Nature* 464, 1290–1291. doi: 10.1038/4641290b

Prut, Y., and Perlmutter, S. I. (2003). Firing properties of spinal interneurons during voluntary movement. I. State-dependent regularity of firing. *J. Neurosci.* 23, 9600–9610. doi: 10.1523/JNEUROSCI.23-29-09600.2003

Remy, S., Csicsvari, J., and Beck, H. (2009). Activity-dependent control of neuronal output by local and global dendritic spike attenuation. *Neuron* 61, 906–916. doi: 10.1016/j.neuron.2009.01.032

Rhodes, P. (2006). The properties and implications of nmda spikes in neocortical pyramidal cells. *J. Neurosci.* 26, 6704–6715. doi: 10.1523/JNEUROSCI.3791-05.2006

Richardson-Jones, J. W., Craige, C. P., Guiard, B. P., Stephen, A., Metzger, K. L., Kung, H. F., et al. (2010). 5-HT1A autoreceptor levels determine vulnerability to stress and response to antidepressants. *Neuron* 65, 40–52.

Rosenbaum, D. M., Rasmussen, S. G., and Kobilka, B. K. (2009). The structure and function of G-protein-coupled receptors. *Nature* 459, 356–363. doi: 10.1016/j.neuron.2009.12.003

Rothman, J. S., Cathala, L., Steuber, V., and Silver, R. A. (2009). Synaptic depression enables neuronal gain control. *Nature* 457, 1015–1018. doi: 10.1038/nature07604

Rothwell, J. C. (ed.). (1987). "Proprioceptors in muscle, joint and skin," in *Control of Human Voluntary Movement* (Boston, MA: Springer), 74–104.

Ruhe, H. G., Mason, N. S., and Schene, A. H. (2007). Mood is indirectly related to serotonin, norepinephrine and dopamine levels in humans: a meta-analysis of monoamine depletion studies. *Mol. Psychiatry* 12, 331–359. doi: 10.1038/sj.mp.4001949

Rush, A. J., Trivedi, M. H., Wisniewski, S. R., Nierenberg, A. A., Stewart, J. W., Warden, D., et al. (2006). Acute and longer-term outcomes in depressed outpatients requiring one or several treatment steps: a star*d report. *Am. J. Psychiatry* 163, 1905–1917. doi: 10.1176/ajp.2006.163.11.1905

Salinas, E., and Sejnowski, T. J. (2001). Gain modulation in the central nervous system: where behavior, neurophysiology, and computation meet. *Neuroscientist* 7, 430–440. doi: 10.1177/107385840100700512

Samuels, E. R., and Szabadi, E. (2008). Functional neuroanatomy of the noradrenergic locus coeruleus: its roles in the regulation of arousal and autonomic function part I: principles of functional organisation. *Curr. Neuropharmacol.* 6, 235–253. doi: 10.2174/157015908785777229

Santello, M., Baud-Bovy, G., and Jörntell, H. (2013). Neural bases of hand synergies. *Front. Comput. Neurosci.* 7:23. doi: 10.3389/fncom.2013.00023

Santello, M., Bianchi, M., Gabiccini, M., Ricciardi, E., Salvietti, G., Prattichizzo, D.,et al. (2016). Hand synergies: Integration of robotics and neuroscience for understanding the control of biological and artificial hands. *Phys. Life Rev.* 17, 1–23. doi: 10.1016/j.plrev.2016.02.001

Santello, M., and Lang, C. E. (2015). Are movement disorders and sensorimotor injuries pathologic synergies? when normal multi-joint movement synergies become pathologic. *Front. Hum. Neurosci.* 8:1050. doi: 10.3389/fnhum.2014.01050

Sawicki, G. S., Lewis, C. L., and Ferris, D. P. (2009). It pays to have a spring in your step. *Exerc. Sport Sci. Rev.* 37, 130–138. doi: 10.1097/JES.0b013e31819c2df6

Segev, I., Rinzel, J., and Shepherd, G. (1994). *The Theoretical Foundation of Dendritic Function: Selected Papers of Wilfrid Rall with Commentaries*. Cambridge, MA; London: MIT Press.

Shalit, U., Zinger, N., Joshua, M., and Prut, Y. (2012). Descending systems translate transient cortical commands into a sustained muscle activation signal. *Cereb. Cortex* 22, 1904–1914. doi: 10.1093/cercor/bhr267

Shemmell, J., An, J. H., and Perreault, E. J. (2009). The differential role of motor cortex in stretch reflex modulation induced by changes in environmental mechanics and verbal instruction. *J. Neurosci.* 29, 13255–13263. doi: 10.1523/JNEUROSCI.0892-09.2009

Sherman, S. M., and Koch, C. (1986). The control of retinogeniculate transmission in the mammalian lateral geniculate nucleus. *Exp. Brain Res.* 63, 1–20.

Shinoda, Y., Zarzecki, P., and Asanuma, H. (1979). Spinal branching of pyramidal tract neurons in the monkey. *Exp. Brain Res.* 34, 59–72.

Siebert, T., and Rode, C. (2014). "Computational modeling of muscle biomechanics," in *Computational Modelling of Biomechanics and Biotribology in the Musculo-skeletal System, 1 Edn*, ed Z. Jin (Amsterdam; Boston, MA; Heidelberg; London; New York, NY; Oxford; Paris; San Diego CA; San Francisco CA; Singapore; Sydney, NSW; Tokyo: Woodhead Publishing; Elsevier), 173–204.

Silver, R. A. (2010). Neuronal arithmetic. *Nat. Rev. Neurosci.* 11, 474–489. doi: 10.1038/nrn2864

Skagerberg, G., and Bjorklund, A. (1985). Topographic principles in the spinal projections of serotonergic and non-serotonergic brainstem neurons in the rat. *Neuroscience* 15, 445–480.

Slawińska, U., Miazga, K., and Jordan, L. M. (2014). $[5\text{-HT}]_2$ and $[5\text{-HT}]_7$ receptor agonists facilitate plantar stepping in chronic spinal rats through actions on different populations of spinal neurons. *Front. Neural Circuits* 8:95. doi: 10.3389/fncir.2014.00095

Spanne, A., Geborek, P., Bengtsson, F., and Jörntell, H. (2014). Spike generation estimated from stationary spike trains in a variety of neurons *in vivo*. *Front. Cell. Neurosci.* 8:199. doi: 10.3389/fncel.2014.00199

Springfield, S. A., and Moolenaar, G.-M. (1983). Differences in the responses of raphe nuclei to repetitive somatosensory stimulation. *Exp. Neurol.* 79, 360–370.

Stein, R. B., Gossen, E. R., and Jones, K. E. (2005). Neuronal variability: noise or part of the signal? *Nat. Rev. Neurosci.* 6, 389–397. doi: 10.1038/nrn1668

Stone, M. H. (1948). The generalized weierstrass approximation theorem. *Math. Mag.* 21, 167–184. doi: 10.2307/3029750

Stratmann, P., Lakatos, D., and Albu-Schäffer, A. (2016). Neuromodulation and synaptic plasticity for the control of fast periodic movement: energy efficiency in coupled compliant joints via PCA. *Front. Neurorobot.* 10:2. doi: 10.3389/fnbot.2016.00002

Stratmann, P., Lakatos, D., Özparpucu, M. C., and Albu-Schäffer, A. (2017). "Legged elastic multibody systems: adjusting limit cycles to close-to-optimal energy efficiency," in *IEEE Robotics and Automation Letters*, 1–1.

Surmeier, D. J., Ding, J., Day, M., Wang, Z., and Shen, W. (2007). D1 and D2 dopamine-receptor modulation of striatal glutamatergic signaling in striatal medium spiny neurons. *Trends Neurosci.* 30, 228–235. doi: 10.1016/j.tins.2007.03.008

Svensson, E., Grillner, S., and Parker, D. (2001). Gating and braking of short- and long-term modulatory effects by interactions between colocalized neuromodulators. *J. Neurosci.* 21, 5984–5992. doi: 10.1523/JNEUROSCI.21-16-05984.2001

Takei, T., Confais, J., Tomatsu, S., Oya, T., and Seki, K. (2017). Neural basis for hand muscle synergies in the primate spinal cord. *Proc. Natl. Acad. Sci. U.S.A.* 114, 8643–8648. doi: 10.1073/pnas.1704328114

Thörn Pérez, C., Hill, R. H., and Grillner, S. (2015). Substance p depolarizes lamprey spinal cord neurons by inhibiting background potassium channels. *PLOS ONE* 10:e0133136. doi: 10.1371/journal.pone.0133136

Trivedi, M. H., Rush, A. J., Wisniewski, S. R., Nierenberg, A. A., Warden, D., Ritz, L., et al. (2006). Evaluation of outcomes with citalopram for depression using measurement-based care in star*d: Implications for clinical practice. *Am. J. Psychiatry* 163, 28–40. doi: 10.1176/appi.ajp.163.1.28

Ugrumov, M. V. (1997). Hypothalamic monoaminergic systems in ontogenesis: development and functional significance. *Int. J. Dev. Biol.* 41, 809–816.

van Rossum, M. C. W., Turrigiano, G. G., and Nelson, S. B. (2002). Fast propagation of firing rates through layered networks of noisy neurons. *J. Neurosci.* 22, 1956–1966. doi: 10.1523/JNEUROSCI.22-05-01956.2002

Varga, Z., Jia, H., Sakmann, B., and Konnerth, A. (2011). Dendritic coding of multiple sensory inputs in single cortical neurons *in vivo*. *Proc. Natl. Acad. Sci. U.S.A.* 108, 15420–15425. doi: 10.1073/pnas.1112355108

Veasey, S. C., Fornal, C. A., Metzler, C. W., and Jacobs, B. L. (1995). Response of serotonergic caudal raphe neurons in relation to specific motor activities in freely moving cats. *J. Neurosci.* 15(7 Pt 2), 5346–5359. doi: 10.1523/JNEUROSCI.15-07-05346.1995

Veazey, R. B., Amaral, D. G., and Cowan, W. M. (1982). The morphology and connections of the posterior hypothalamus in the cynomolgus monkey (macaca fascicularis). ii. efferent connections. *The J. Comp. Neurol.* 207, 135–156.

Vertes, R. P., and Linley, S. B. (2008). "Efferent and afferent connections of the dorsal and median raphe nuclei in the rat," in *Serotonin and Sleep: Molecular, Functional and Clinical Aspects* (Basel: Birkhäuser Basel), 69–102.

Villalobos, J., and Ferssiwi, A. (1987). The differential descending projections from the anterior, central and posterior regions of the lateral hypothalamic area: an autoradiographic study. *Neurosci. Lett.* 81, 95–99.

Warden, M. R., Selimbeyoglu, A., Mirzabekov, J. J., Lo, M., Thompson, K. R., Kim, S. Y., et al. (2012). A prefrontal cortex-brainstem neuronal projection that controls response to behavioural challenge. *Nature* 492, 428–432. doi: 10.1038/nature11617

Watson, C., Paxinos, G., and Puelles, L. (2012). *The Mouse Nervous System*. Amsterdam; Boston MA; Heidelberg; London; New York, NY; Oxford; Paris; San Diego, CA; San Francisco, CA; Singapore; Sydney, NSW; Tokyo: Academic Press; Elsevier Academic Press.

Watson, K., and Platt, M. (2012). Social signals in primate orbitofrontal cortex. *Curr. Biol.* 22, 2268–2273. doi: 10.1016/j.cub.2012.10.016

Wei, K., Glaser, J. I., Deng, L., Thompson, C. K., Stevenson, I. H., Wang, Q., et al. (2014). Serotonin affects movement gain control in the spinal cord. *J. Neurosci.* 34, 12690–12700. doi: 10.1523/JNEUROSCI.1855-14.2014

Williams, S. R., and Stuart, G. J. (2002). Dependence of epsp efficacy on synapse location in neocortical pyramidal neurons. *Science* 295, 1907–1910. doi: 10.1126/science.1067903

Willis, M. L., Palermo, R., Burke, D., McGrillen, K., and Miller, L. (2010). Orbitofrontal cortex lesions result in abnormal social judgements to emotional faces. *Neuropsychologia* 48, 2182 – 2187. doi: 10.1016/j.neuropsychologia.2010.04.010

Wise, S. P., and Shadmehr, R. (2002). "Motor control," in *Encyclopedia of the Human Brain, Vol. 3*, ed V. S. Ramachandran (Amsterdam; Boston MA; Heidelberg; London; New York, NY; Oxford; Paris; San Diego, CA; San Francisco, CA; Singapore; Sydney, NSW; Tokyo: Academic Press), 137–158.

Xia, X.-B., and Mills, S. L. (2004). Gap junctional regulatory mechanisms in the aii amacrine cell of the rabbit retina. *Vis. Neurosci.* 21, 791–805. doi: 10.1017/S0952523804215127

Yamamoto, K., and Vernier, P. (2011). The evolution of dopamine systems in chordates. *Front. Neuroanat.* 5:21. doi: 10.3389/fnana.2011.00021

Yanai, Y., Adamit, N., Israel, Z., Harel, R., and Prut, Y. (2008). Coordinate transformation is first completed downstream of primary motor cortex. *J. Neurosci.* 28, 1728–1732. doi: 10.1523/JNEUROSCI.4662-07.2008

Yoshida, K., Saito, N., Iriki, A., and Isoda, M. (2011). Representation of others' action by neurons in monkey medial frontal cortex. *Curr. Biol.* 21, 249–253. doi: 10.1016/j.cub.2011.01.004

Yoshida, K., Saito, N., Iriki, A., and Isoda, M. (2012). Social error monitoring in macaque frontal cortex. *Nat. Neurosci.* 15, 1307–1312. doi: 10.1038/nn.3180

Yu, X., Ye, Z., Houston, C., Zecharia, A., Ma, Y., Zhang, Z., et al. (2015). Wakefulness is governed by gaba and histamine cotransmission. *Neuron*, 87:164–178. doi: 10.1016/j.neuron.2015.06.003

Zelenin, P. V., Hsu, L. J., Lyalka, V. F., Orlovsky, G. N., and Deliagina, T. G. (2015). Putative spinal interneurons mediating postural limb reflexes provide a basis for postural control in different planes. *Eur. J. Neurosci.* 41, 168–181. doi: 10.1111/ejn.12780

Zhang, Z. W., and Arsenault, D. (2005). Gain modulation by serotonin in pyramidal neurones of the rat prefrontal cortex. *J. Physiol.* 566(Pt 2), 379–394. doi: 10.1113/jphysiol.2005.086066

Zhong, G., Shevtsova, N. A., Rybak, I. A., and Harris-Warrick, R. M. (2012). Neuronal activity in the isolated mouse spinal cord during spontaneous deletions in fictive locomotion: insights into locomotor central pattern generator organization. *J. Physiol.* 590, 4735–4759. doi: 10.1113/jphysiol.2012.240895

Conflict of Interest Statement: The authors declare that the research was conducted in the absence of any commercial or financial relationships that could be construed as a potential conflict of interest.

frontiers in Cellular Neuroscience

ORIGINAL RESEARCH
published: 21 December 2018
doi: 10.3389/fncel.2018.00500

Aberrant Development and Synaptic Transmission of Cerebellar Cortex in a VPA Induced Mouse Autism Model

*Ruanna Wang, Jiahui Tan, Junxiu Guo, Yuhan Zheng, Qing Han, Kwok-Fai So, Jiandong Yu and Li Zhang**

Joint International Research Laboratory of CNS Regeneration, Guangdong-Hong Kong-Macau Institute of CNS Regeneration, Jinan University, Guangzhou, China

Autistic spectral disorder (ASD) is a prevalent neurodevelopmental disease that affects multiple brain regions. Both clinical and animal studies have revealed the possible involvement of the cerebellum in ASD pathology. In this study, we generated a rodent ASD model through a single prenatal administration of valproic acid (VPA) into pregnant mice, followed by cerebellar morphological and functional studies of the offspring. Behavioral studies showed that VPA exposure led to retardation of critical motor reflexes in juveniles and impaired learning in a tone-conditioned complex motor task in adults. These behavioral phenotypes were associated with premature migration and excess apoptosis of the granular cell (GC) precursor in the cerebellar cortex during the early postnatal period, and the decreased cell density and impaired dendritic arborization of the Purkinje neurons. On acute cerebellar slices, suppressed synaptic transmission of the Purkinje cells were reported in the VPA-treated mice. In summary, converging evidence from anatomical, electrophysiological and behavioral abnormalities in the VPA-treated mice suggest cerebellar pathology in ASD and indicate the potential values of motor dysfunction in the early diagnosis of ASD.

Keywords: autism, cerebellum, environmental exposure, motor learning, postnatal development

OPEN ACCESS

Edited by:
Ying Shen,
Zhejiang University, China

Reviewed by:
Laurens Bosman,
Erasmus Medical Center, Netherlands
Simone Astori,
École Polytechnique Fédérale de Lausanne, Switzerland

***Correspondence:**
Li Zhang
zhangli@jnu.edu.cn

Received: *10 September 2018*
Accepted: *03 December 2018*
Published: *21 December 2018*

Citation:
Wang R, Tan J, Guo J, Zheng Y, Han Q, So K-F, Yu J and Zhang L (2018) Aberrant Development and Synaptic Transmission of Cerebellar Cortex in a VPA Induced Mouse Autism Model. Front. Cell. Neurosci. 12:500. doi: 10.3389/fncel.2018.00500

INTRODUCTION

The cerebellum has been recognized as the brain region mediating fine motor coordination and complex motor skill learning. Recent evidence however, has revealed the role of the cerebellum in psychiatric disorders including major depressive disorder (Su et al., 2014), schizophrenia (Mothersill et al., 2016) and autistic spectral disorder (ASD; Fatemi et al., 2012; Wang et al., 2014). Postmortem examinations of ASD patient brains reported cerebellar neuropathology (Hampson and Blatt, 2015). In particular, ASD children frequently present cerebellar associated motor disorders (McPhillips et al., 2014; Mosconi et al., 2015), which can occur at early age before the onset of language or social deficits (Lloyd et al., 2013). Currently, the potential value of motor dysfunction in the early diagnosis of ASD is being continuously discussed (Whyatt and Craig, 2013; Zwaigenbaum et al., 2013). It is thus necessary to further elaborate the cerebellar neuropathology associated with ASD.

ASD etiology can be attributed to genetic mutations and/or environmental exposures. Among the known ASD risk genes, *Pten* (Cupolillo et al., 2016) or *Shank2* (Peter et al., 2016) mutations in the cerebellar Purkinje cells lead to impaired cell morphology or synaptic transmission,

which are associated with motor learning and social deficits. These mouse studies support the involvement of the cerebellum in ASD pathogenesis. An alternative group of ASD risk factors consists of prenatal exposures of specific chemicals or drugs (Mandy and Lai, 2016). Valproic acid (VPA) is one anti-seizure drug and has been reported to dramatically elevate ASD risk in offspring (Ornoy, 2009; Roullet et al., 2013). Prenatal VPA exposure in rodents can replicate ASD-like symptoms including repetitive behaviors and social deficits (Markram et al., 2008; Yochum et al., 2008). Therefore, VPA overdosage has become one widely accepted model to elaborate the neurobiological mechanism of ASD (Nicolini and Fahnestock, 2018). The neurodevelopmental effects of VPA cover multiple brain regions including the prefrontal cortex (Codagnone et al., 2015), hippocampus (Bristot Silvestrin et al., 2013) and amygdala (Sosa-Díaz et al., 2014). In the cerebellum, previous studies have revealed an enhanced apoptosis in the external granular layer (EGL) after early postnatal VPA exposure in mice (Yochum et al., 2008) or rats (Kim et al., 2013). However, the effects of prenatal VPA exposure on the cerebellar development, or its correlation with motor deficits has not been reported yet.

In the current study, we utilized a single VPA injection in pregnant mice at embryonic day 10.5 (E10.5) and found that VPA exposure led to the retardation of motor reflexes in juveniles as well as deficits in complex motor learning tasks in adults. Those behavioral phenotypes were associated with premature migration and elevated apoptosis of granular cell (GC) precursors in the cerebellum during the first two postnatal weeks. The VPA-treated mice also had a decreased cell density and an impaired dendritic arborization of the cerebellar Purkinje neurons in both the juvenile and adult stages. Such structural deformation of the cerebellar cortex was accompanied with impaired excitatory and inhibitory synaptic transmission. In sum, our results describe both the structural and functional impairments of the cerebellum caused by prenatal VPA exposure, further elaborating the potential linkage between cerebellar pathology and ASD.

MATERIALS AND METHODS

Experimental Animals

Female C57BL/6 mice (7–8 weeks old) were mated with male mice at 8 pm. The vaginal plug was examined at 8 am the following morning. Those females having plugs were singly housed and denoted as embryonic at day 0.5 (E0.5). VPA (500 mg/kg body weight, in sodium salt, Sigma, Ronkonkoma, NY, USA) was prepared in 50 mg/mL sterile saline and injected into the peritoneal cavity of pregnant mice at E10.5. The control group received 0.1 mL sterile saline. Male offspring were used for further assays. The animal protocol was approved by the Jinan University Institutional Animal Care and Use Committee.

Developmental Examination

To characterize postnatal developmental patterns of mice, we utilized a test battery of developmental milestones as previously described (Zhang et al., 2014). Briefly speaking, juvenile mice from both VPA-treated and saline-treated groups were examined for different neural reflex and body development markers, including cliff avoidance (the avoidance behavior when the mouse' forepaws were approaching the edge of one platform), grasping reflex (to grasp one small metal bar with the forepaws), negative geotaxis (to recover from a head-down position on an inclined plane), surface righting (turning its body around from an upside-down position), air righting (recovering a normal prone position when releasing from the height in a supine position), bar holding (ability to hold a metal bar with the forepaws for more than 5 s), pinnae detachment and eye opening. The day of onset was recorded, and any positive reflexes were confirmed the following day. We examined two cerebellar associated motor reflexes: (1) negative geotaxis: the mouse was placed on a 30° inclined plane with its head facing downwards. The positive reflex was identified when the mouse could turn its body around to a head-up position within 30 s; and (2) air righting reflex: the mouse was released from a 30 cm height using an inverted supine position (with its belly facing upwards). The positive reflex was identified when the mouse could recover the normal prone position (belly facing downwards against the soft bedding) when landing.

Mouse Behavioral Assays

To validate the ASD phenotype of the VPA model, the 3-chamber sociability assay was employed first, as previously described (Peter et al., 2016). In brief, the mouse was first placed into the central zone to freely explore the three chambers (divided from a 60 cm × 45 cm clear box) for 15 min. During the second 15-min stage, one age-matched male mouse (S1) was placed into one chamber within a round wire cage. The time for the test mouse to explore and interact with the S1 mouse was recorded. For the third stage, a second stranger mouse (S2) was introduced to the other side of the chamber and the interaction time with both the S1 and S2 mice, was recorded during the 15-min session.

For the open field assay, a clear box (50 cm × 50 cm) was utilized to measure the locomotor activity of mice in a single 15 min session, during which the total distance of each mouse was analyzed.

The accelerating Rota-rod test was performed as previously described (Zhang et al., 2014). The mouse was trained on the rod in six consecutive daily sessions, with 5 rpm initial velocity and 80 rpm maximal at 5 min.

To further elaborate motor learning function, we employed the LadderScan apparatus (Clever System Inc., Reston, VA, USA; **Figure 1A**). The design of this learning paradigm was modified from a previous report (Vinueza Veloz et al., 2015). The whole apparatus consists of one runway and two side-chambers, which are equipped with LED lights and fans. The runway includes 37 rungs (metal rods, 2 mm diameter, in two lines) with a 15 mm interval. On one side, rungs with an odd number (1, 3, 5, . . ., 37) were at a high level, whilst even numbered rungs (2, 4, 6, . . ., 36) were located at a lower level. There were alternative patterns (odd number at low, even number at high level) on the other side. The vertical distance between high and low rungs was 6 mm in height, and mice typically walked on the high rungs only. During the middle segment (rung 7–31), each lower

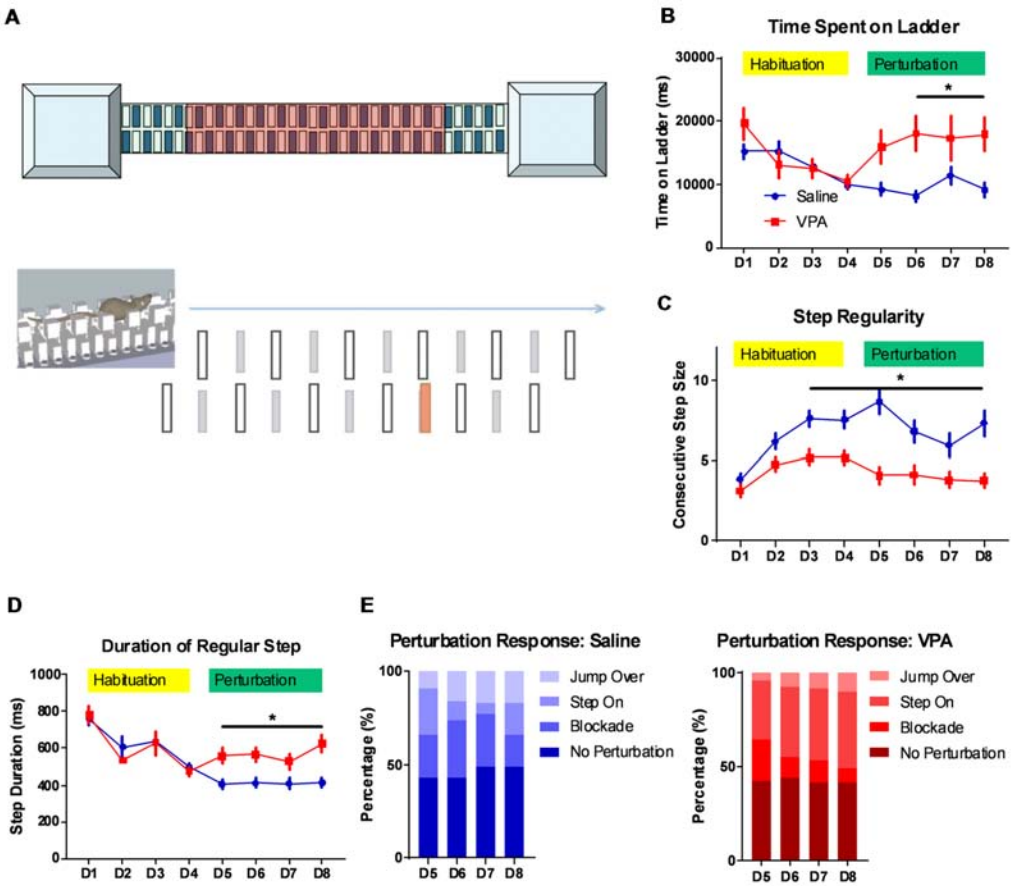

FIGURE 1 | Impaired complex motor learning in valproic acid (VPA)-treated mice. **(A)** Schematic diagram of the LadderScan apparatus (upper) and perturbation assays (lower). On day 1–4, the mouse was trained to run on the walkway between two chambers. Starting from day 5 to day 8, one lower-rung (red color) was randomly elevated before the mouse reached it, with a tone cue. **(B)** Total time spent running on the rung for each trial across training days. Both the saline-treated control and the VPA-treated group showed a similar and decreasing time during the habituation phase. Starting on perturbation day 5, VPA-treated mice presented an elevated total time ($F_{(1,1496)}$ = 18.88, $P < 0.0001$; Bonferroni *post hoc* comparison: $P < 0.05$ from day 6 to day 8). **(C)** Step regularity index, which is defined as the number of consecutive normal steps in each trial during a 4-day habituation followed by a 4-day perturbation. Saline-treated control mice showed gradually improved regularity, whilst VPA-treated mice showed no prominent learning effects [two-way analysis of variance (ANOVA) with respect to group effect: $F_{(1,1496)}$ = 77.92, $P < 0.0001$; Bonferroni *post hoc* comparison: $P < 0.05$ from day 3 to day 8]. **(D)** Duration of each regular step (in ms) of mice on rungs across 8-day test sessions. Similar to those for the total duration, the step duration of VPA-treated mice was significantly lower after introducing perturbation (two-way ANOVA with respect to group effect: $F_{(1,1496)}$ = 9.392, P = 0.0022; Bonferroni *post hoc* comparison: $P < 0.05$ from day 5 to day 8). **(E)** The percentage of distribution of responses toward perturbated rungs on each daily session, including jump over, step on, blockade and no perturbation. *$P < 0.05$; N = 125 trials from five mice in saline and VPA group.

rung was elevated by 18 mm to create one extra obstacle with a 12 mm height. All rungs were equipped with pressure sensors to time each gait. One single trial was initiated after placing the mouse into the chamber on either side. After a 9–12 s delay, light and air puffs were sequentially applied in the chamber to create negative stimuli, which forced the mouse to leave the chamber. The trial was terminated when the mouse successfully walked across the runway to reach the chamber on the other side. The whole behavioral paradigm started with a 4-day training run (25 daily trials for each mouse) to ensure the mouse ran smoothly on the runway. Starting on day 5 to day 8 (25 trials per day), one extra perturbation was introduced and consisted of one randomly "pop-up" rung ahead of the mouse. The elevation of rung occurred at any lower rung in the middle segment of the runway and was induced before a mouse approached, to avoid any spatial specific memory. The rung elevation was preceded by a tone cue (80 dB, 1,000 Hz, 250 ms duration, 250 ms before perturbation). The perturbation event occurred when the mouse performed at least three consecutive "regular steps," which were defined as having a step length with two or four rungs. All the gait parameters were recorded for each trial and were analyzed.

EdU Incorporation Assay

EdU assay was employed to describe the migration of the GC precursors. Following previously documented methods (Wang et al., 2017), EdU (50 mg/kg, from Click-iT EdU Alexa Fluor 594 Imaging Kit, Invitrogen, Waltham, MA, USA) was injected

into the peritoneal cavity of P7 mice. The whole brain was then harvested at 2 h or 72 h later and was prepared in 8 μm cryo-sections. The staining procedure followed manual instruction of the Click-iT EdU Alexa Fluor 594 Imaging Kit. A fluorescent microscope (Zeiss, Germany) was used to capture images. The number of EdU-positive cells in the EGL and internal granular layer (IGL) was counted by the ImageJ 1.48 (NIH, Bethesda, MD, USA).

TUNEL Assay

We used a terminal deoxynucleotidyl transferase (TdT) dUTP nick-end labeling (TUNEL) assay to measure the apoptosis of the cerebellar neurons and precursor cells. The assay was performed using an *in situ* Cell Death Detection Kit (Roche, Swiss) following its manual instructions. In brief, cryo-sections (8 μm thickness) were permeabilized using a 0.1 M sodium citrate buffer (with 0.1% Triton X-100), followed by PBS washing. A freshly prepared TUNEL reaction buffer (50 μL per slide) was added at 37°C incubation for 1 h. After PBS rinsing, the DAPI (Roche, Switzerland) was used for nuclei staining. Fluorescent images were captured as previously described.

Golgi Staining and Sholl Analysis

Golgi staining was performed using the Rapid Golgi Stain Kit (FD NeuroTech Inc., Ellicott City, MD, USA) according to the manual's instructions. The Purkinje cells at the apical region of the cerebellar lobule were imaged using a bright field microscope (Zeiss, Germany). NeuroLucida software (MBF Bioscience, Williston, VT, USA) was used to plot the soma and dendrites of the Purkinje cells under a manually assisted mode. The Sholl analysis was adopted using previous methods (Wang et al., 2017). Briefly, a series of concentric circles (10 μm interval) were plotted around the soma. The number of intersections of dendrites against each circle, and the total dendrite lengths within each 10 μm segment, were quantified using NeuroLucida software.

Immunofluorescence Staining

Mice were deeply anesthetized by isoflurane and were perfused with 4% paraformaldehyde (PFA). Whole brain tissues were extracted and were dehydrated in a 30% sucrose solution at 4°C overnight. Brain slices (30 μm thickness) were prepared using a cryostat (Leica, Germany). Slices were rinsed in 0.01 M PBS and blocked in 3% FBS (with 0.1% Triton X-100) for 1 h. Primary antibody against calbindin D-28K (Abcam, Cambridge, MA, USA) was added for 48 h incubation at 4°C. Donkey anti-rabbit Alexa 488 secondary antibody (Life Technology, Camarillo, CA, USA) was added at room temperature for 2 h incubation. After PBS rinsing, DAPI was added for nuclear staining. Fluorescent images were taken for cell enumeration by the ImageJ (NIH).

Western Blotting

The cerebellar tissues were homogenized by a RIPA buffer. Equal amounts of proteins were separated by an SDS-PAGE and were transferred to a PVDF membrane (GE Healthcare, Chicago, IL, USA). The membrane was blocked by a 5% bovine serum albumin (BSA) for 2 h and was incubated in a primary antibody against BDNF, p-TrkB (p-tyrosine kinase B), t-TrkB and β-actin (Cell Signaling Technology, Danvers, MA, USA) overnight at 4°C. The membrane was then incubated in horseradish peroxidase (HRP) conjugated anti-IgG antibody (Cell Signaling) for 2 h at room temperature. Protein bands were visualized by an ECL chemiluminescence substrate. A protein imaging system (Bio-Rad, Hercules, CA, USA) was used to capture images, and their integrated density was measured by the ImageJ (NIH).

Electrophysiological Recordings

Mice (P18–P21) were anesthetized with isoflurane and decapitated. Sagittal slices (300 μm) were prepared in ice-cold "cutting solution" containing (in mM): 240 sucrose, 2.5 KCl, 10 D-Glucose, 26 $NaHCO_3$, 1.25 Na_2HPO_4, 2 $MgCl_2$ and 1 $CaCl_2$, using a Leica VT1200S Vibratome. The slices were incubated in a submerged chamber containing an equal volume of cutting solution and recording solution, at 32 ± 1°C for 30 min and subsequently at room temperature. The recording solution contained (in mM): 126 NaCl, 26 $NaHCO_3$, 10 D-glucose, 1.25 NaH_2PO_4, 2.5 KCl, 2 $CaCl_2$ and 2 $MgCl_2$. All solutions were bubbled with 95% O_2 and 5% CO_2 and maintained at 7.4 pH. For the whole cell recordings, slices were perfused with the recording solution at room temperature. The Purkinje cells were visualized using an infrared differential interference contrast with a Nikon Eclipse FN-1 microscope with a 40× water-immersion objective. Recordings were performed using the MultiClamp 700B (Molecular Devices, San Jose, CA, USA). The recording electrodes (4–8 MΩ) were filled with an intracellular solution containing (in mM): 126 K-gluconate, 4 KCl, 10 HEPES, 4 Mg-ATP, 0.3 Na-GTP, 10 PO-creatinine (pH 7.25 with an osmolarity of 295 ± 5). Data were low-pass filtered at 3 kHz and digitized with the DigiData 1550B using a pClamp 10 at 10 kHz sampling frequency. Miniature excitatory postsynaptic currents (mEPSCs, in present of 1 μM tetrodotoxin) were recorded as inward currents at a holding potential of −70 mV and miniature inhibitory postsynaptic currents (mIPSCs) were recorded as outward currents at a holding potential of 0 mV. Both mEPSCs and mIPSCs were measured using automated event detection in the Clampfit software (Molecular Devices, San Jose, CA, USA) using 5.5 as the match threshold, followed by a manual inspection to exclude any artifacts. All events were extracted from the records with 2 min durations. For plotting the cumulative distribution curve, 40 events were extracted from the recording series of one neuron. The averaged amplitudes and frequencies were calculated from all events in each neuron.

Statistical Analysis

All data were presented as mean ± standard error of means (SEM), unless otherwise specified. Each group of data were first tested for normality using the KS test. Data that did not fit the Gaussian distribution, were compared by a non-parametric Mann-Whitney *U* test. For data with a normal distribution, a 2-sample student *t*-test was used for comparison between the two groups. A one-way or two-way analysis of variance (ANOVA), with repeated measures, was used for comparison among the

multiple groups, depending on the number of independent variables. The Tukey or Bonferroni *post hoc* comparison was used to compare means between two specific groups after one-way or two-way ANOVA, respectively.

RESULTS

Impaired Motor Learning Function by Prenatal VPA Exposure

The cerebellum is closely related with the acquisition of complex motor skills. We thus employed different motor learning paradigms to study the cerebellar associated motor functions on adult (P56) mice. The classical Rotarod assay showed that compared to the saline-treated controls, the VPA-treated group generally performed worse, especially at later training sessions (**Supplementary Figure 1A**). This impaired motor skill seems to not be caused by a general motor deficit, as the VPA-treated mice showed a similar movement distance in an open-field assay (**Supplementary Figure 1B**). However, as no significant difference was found in the learning ability on the Rota-rod (two-way ANOVA with repeated measures, interaction effect, $F_{(5,120)} = 0.9056$, $P = 0.4799$, **Supplementary Figure 1A**), more sensitive motor learning paradigms were expected. We thus introduced a tone-conditioned complex motor learning paradigm named the LadderScan (**Figure 1A**, see "Materials and Methods" section for detailed information) which was modified from a previous report (Vinueza Veloz et al., 2015). The whole test paradigm consisted of a 4-day habituation session followed by a second 4-day perturbation session. In general, VPA-treated mice showed a similar time duration completing a single trial compared to the saline-treated control group during the habituation stage (**Figure 1B**), and both groups showed decreased durations, indicating a normal motor function in the VPA-treated mice. After introducing the perturbation, however, the VPA-treated group showed a sharp increase in duration on the walkway, which was maintained at relatively low levels in the control group (two-way ANOVA, treatment × training day effect: $F_{(7,1496)} = 2.54$, $P = 0.0134$; Bonferroni *post hoc* comparison between VPA- and saline-treated group: $P = 0.0137$, 0.0479 and 0.0371 from day 6 to day 8; **Figure 1B**). Therefore, the VPA-treated mice seem to have deficits in the acquisition of this complex motor task with perturbation. When checking the step regularity index, which was defined as the number of consecutively regular steps in a single trial, the VPA-treated mice did not improve significantly with repeated training as compared to the control group (two-way ANOVA, treatment × training day effect: $F_{(7,1496)} = 2.232$, $P = 0.0294$; Bonferroni *post hoc* comparison: $P = 0.0018$, 0.0024, 0.0001, 0.0253, 0.0173 and 0.0005 from day 3 to day 8; **Figure 1C**). Similar results were obtained when checking the average duration of each regular step, which was continuously decreased in both the VPA-treated mice and the control group, with repeated training, but was re-elevated after perturbation introduction only in the VPA-treated group (two-way ANOVA, treatment × training day effect: $F_{(7,1496)} = 2.524$, $P = 0.0139$; Bonferroni *post hoc* comparison: $P = 0.0423$, 0.0374, 0.0109 and 0.0035 from day 5 to day 8; **Figure 1D**). We also analyzed the response of animals toward perturbation and found that the VPA-treated mice had a lower rate of successfully crossing the perturbation ("jump over") compared to the control group (4.8%–10.4% vs. 9.6%–16.8%, $t_{(6)} = 3.232$, $P = 0.0179$; **Figure 1E**). Moreover, the VPA-treated mice presented a higher rate of "step on" on the elevated rung (31.2%–40.8% of all sessions at day 5 to day 8) compared to the saline-treated control group (6.4%–24.0%, $t_{(6)} = 5.024$, $P = 0.0024$; **Figure 1E**). In summary, the LadderScan paradigm suggested that the VPA-treated mice developed motor incoordination when faced with unexpected perturbation, while they maintained normal motor function during relatively simple motor training. Such impairment in complex motor learning did not improve significantly with repeated training. These results supported the impaired motor learning after prenatal VPA exposure.

Retardation of Motor Function Development at Early Postnatal Stage in VPA-Treated Mice

Having observed the motor learning deficit in adult VPA-treated mice, we next explored if such impairment occurred at an early age. A series of developmental "milestones" was thus employed to describe both body development and motor reflex patterns during the first three postnatal weeks (Zhang et al., 2014). In examining two markers for the body development: pinnae detachment and eye opening, we found similar days of onset between the VPA- and saline-treated mice (**Figure 2A**), indicating unaltered general development. We further investigated the onset of several sensorimotor reflexes in juvenile mice including cliff avoidance, grasping, negative geotaxis, surface righting, air righting and bar holding. Among those markers, we found that prenatal exposure of VPA, led to the retardation of the negative geotaxis reflex, which is defined as the ability to turn the body around from a head-down position on an inclined plane. The VPA-treated mice also presented a late onset of the air righting reflex, in which the mouse can adjust its body to a prone position when landing on soft beddings, after releasing from a height in a supine posture. Statistical analysis showed the late onset of both reflexes in the VPA-treated group (Negative geotaxis: 5.9 ± 0.24 vs. 5.1 ± 0.20 days, Mann Whitney test, $U = 122.5$, $P = 0.0275$; Air-righting reflex: 12.6 ± 0.21 vs. 11.6 ± 0.32 days, $U = 114$, $P = 0.0139$; $n = 20$ in each group; **Figures 2B,C**). As previous reports have illustrated the impairment of the negative geotaxis (Holmes et al., 2006) and the air righting reflex (Wolf et al., 1996) in cerebellar developmental disorders, it is thus reasonable to speculate that prenatal VPA exposure may cause early postnatal developmental disorders of the cerebellum.

Aberrant Cerebellar Cortical Formation in a VPA-Treated Mouse

The abovementioned motor deficits and retardation of motor reflexes in the VPA-treated mice, indicate altered cerebellar

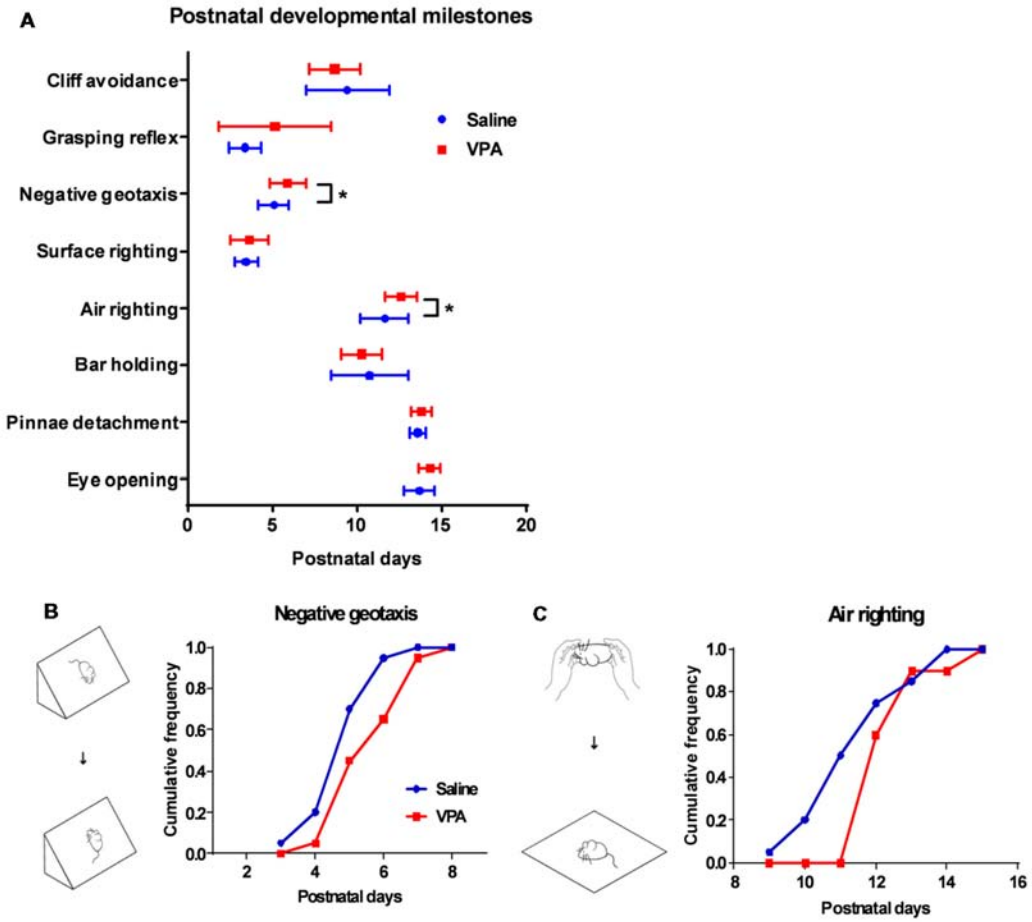

FIGURE 2 | Retardation of motor reflex onset in juvenile VPA-treated mice. **(A)** Days of onset for major developmental milestones in juvenile mice between the saline-treated control and the VPA-treated groups. In negative geotaxis (Mann Whitney test, $U = 122.5$, $P = 0.0275$) and air righting motor reflex ($U = 114$, $P = 0.0139$), VPA-treated mice showed delayed days of onset. **(B)** Schematic illustration for negative geotaxis (left). The juvenile mouse was placed on an inclined plane with the head facing down, and a positive reflex was defined when the mouse recovered to the head-up position. Right panel, cumulative frequency of mice having a positive reflex across the postnatal days. **(C)** Left panel, schematic illustration for air righting reflex, which is defined as turning around its body when the mouse was released in a supine position. Right panel, cumulative frequency of days of onset for air righting reflex. $^*P < 0.05$; $N = 20$ juveniles from the saline-treated and VPA-treated group.

development patterns. As the most abundant neuron type, the GC forms the major excitatory input to the Purkinje cells via a parallel fiber, in addition to a climbing fiber originating from the inferior olive nuclei. During early postnatal stage, GC precursors in the EGL undergo active proliferation followed by an inwardly radial migration to the IGL where they differentiate into mature GCs (Butts et al., 2014; Marzban et al., 2015). Using the EdU incorporation assay, we tracked the migration of newly generated GC precursors between P7 and P10 (**Figure 3A**). The VPA-treated mouse juveniles displayed significantly more EdU+ cells in the IGL at P7 (Mann Whitney test, $U = 104$, $P = 0.0191$; **Figures 3B,D**) but less cells in the EGL at P10 compared to the saline-treated control group ($t_{(53)} = 3.416$, $P = 0.0012$; **Figures 3C,E**). No difference was found in the P7 EGL or P10 IGL ($P = 0.3545$ and 0.8849). Since the GC precursors migrate from the EGL to the IGL, it indicates that VPA-treated mice presented premature inward migration. Newly formed cells also undergo programmed cell death if not undergoing migration or maturation. We further used a TUNEL assay and found that the VPA-treated mice showed elevated apoptosis at P9 in the EGL, but fewer deaths in the IGL (EGL: $t_{(16)} = 2.673$, $P = 0.0167$; IGL: $t_{(16)} = 3.75$, $P = 0.0017$; **Figures 3F,G**). Such accelerated apoptosis persisted until P15 in the EGL but not for the IGL (**Supplementary Figure S2**). Combining these results, prenatal VPA exposure leads to premature GC precursor migration in the cerebellar cortex during the second postnatal week, in association with higher apoptosis.

Purkinje Cell Deformation After Prenatal VPA Exposure

Cerebellar development is one well-orchestrated process involving neurogenesis, dendritic arborization and synaptogenesis. After demonstrating premature migration and excessed apoptosis of GC precursors, we next investigated

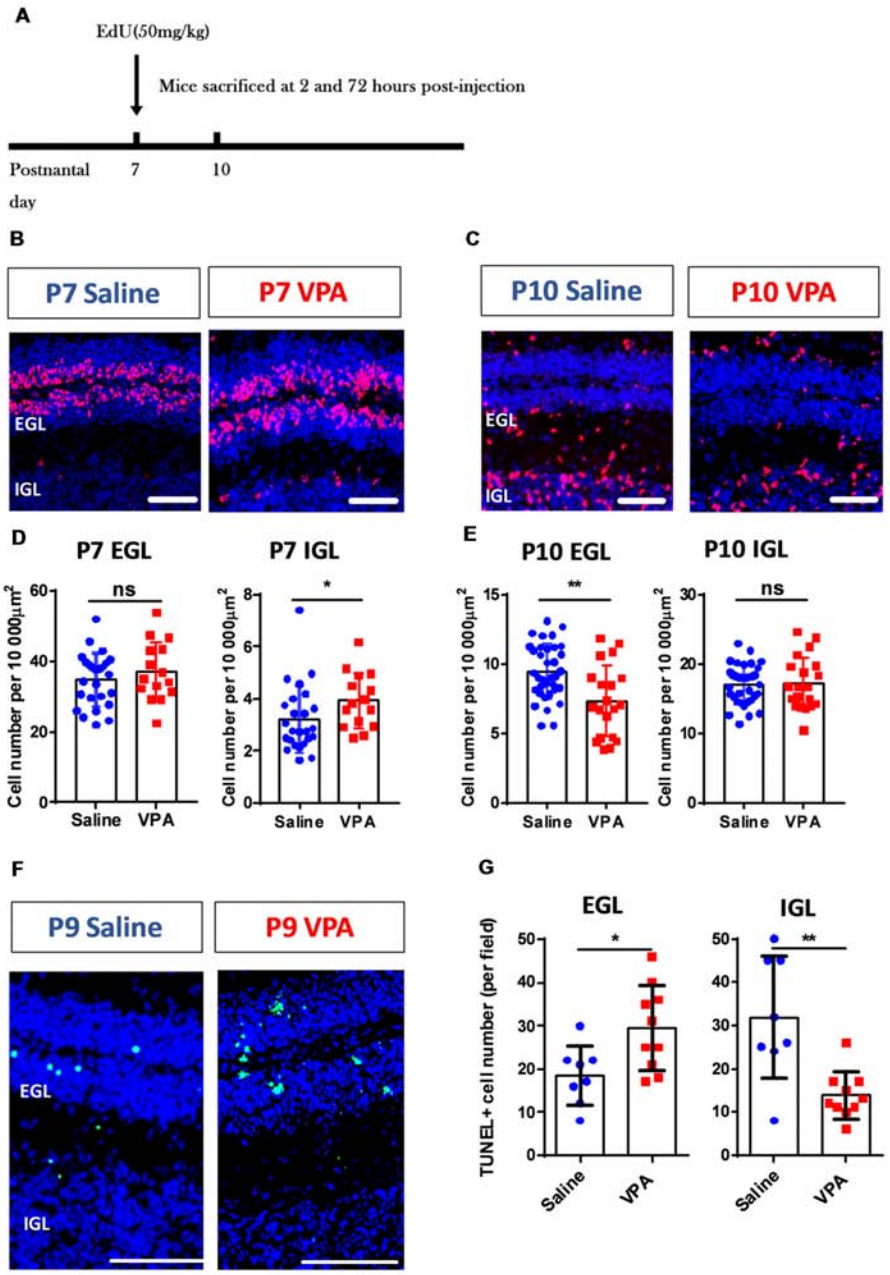

FIGURE 3 | Aberrant cerebellar cortical development in VPA-treated mice during the early postnatal phase. **(A)** Timelines for the EdU labeling and sampling schedule. **(B,C)** Representative images for the EdU+ cells (red) with DAPI (blue) staining in sagittal sections of the cerebellum at P7 **(B)** and P10 **(C)**. **(D,E)** Quantitative analysis for the density of the EdU+ cells (per 10,000 μm^2) in the external granular layer (EGL) and internal granular layer (IGL) on P7 **(D)** and P10 **(E)**. VPA-treated mice showed more EdU+ cells in P7 IGL (Mann Whitney test, $U = 104$, $P = 0.0191$) and fewer cells in P10 EGL (2-sample student t-test, $t_{(53)} = 3.416$, $P = 0.0012$), suggesting a pre-onset of the granular cell (GC) precursors migration. $N = 25$ slices from six mice in the saline-treated group, and 15 slices from five mice in the VPA-treated group. **(F)** Representative images for terminal deoxynucleotidyl transferase (TdT) dUTP nick-end labeling (TUNEL) staining to label apoptotic cells (green) at P9. **(G)** Quantitative analysis of apoptotic cells. VPA-treated mice showed more TUNEL+ cells in the EGL ($t_{(16)} = 2.673$ $P = 0.0167$) but less apoptosis in the IGL ($t_{(16)} = 3.75$). $N = 8$ slices from three mice in the saline-treated group, and 10 slices from four mice in the VPA-treated group. ns, no significant difference; $^*P < 0.05$; $^{**}P < 0.01$. Scale bar, 100 μm in **(B,C,F)**.

the Purkinje cells. In adult mice, we found a significantly decreased number of Purkinje neurons in most of the lobules (two-way ANOVA, group effect: $F_{(1,265)} = 248.5$, $P < 0.0001$; Bonferroni *post hoc* comparison: $P < 0.001$ for all lobules but lobule VII and lobule X, **Figures 4A,B**). On average, the Purkinje cell number was decreased by 15.3%–52.3% across the lobules in the VPA-treated mice, suggesting an impaired Purkinje cell population. Due to normal cerebellar size and

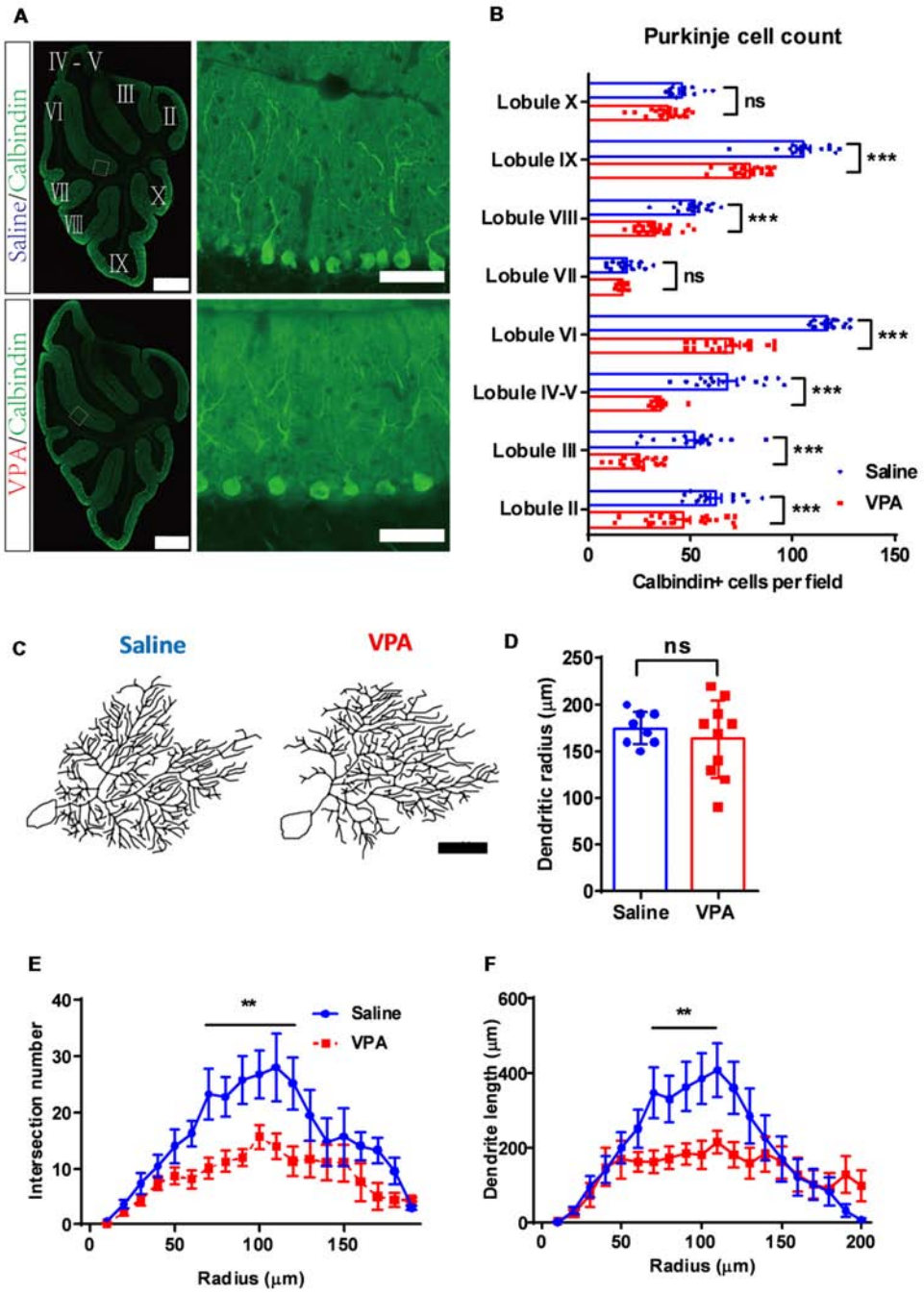

FIGURE 4 | Purkinje cell de-population and impaired dendritic arborization in VPA-treated mice. **(A)** Representative images for the whole cerebellum in a sagittal view (left panels) and high magnification images showing the cerebellar cortex (right panels) from the saline-treated control (upper) and the VPA-treated group (lower). Cerebellar lobules were labeled with Roman numbers. **(B)** Quantitative analysis for the Purkinje cell number in each lobule. Statistical analysis showed lower Purkinje cell numbers in most lobules examined (two-way ANOVA with respect to group effect: $F_{(1,265)} = 248.5$, $P < 0.0001$; Bonferroni *post hoc* comparison: $P < 0.001$ for all lobules but lobule VII and lobule X). $N = 16$ slices from four mice in the saline-treated group, and 22 slices from five mice in the VPA-treated group. **(C)** Re-plotting of the Purkinje cell dendritic trees at P30. **(D)** No significant difference of dendritic tree radius between the saline-treated control and VPA-treated group (2-sample student *t*-test, $t_{(16)} = 0.7583$, $P = 0.4593$). **(E,F)** Sholl analysis showed that VPA-treated mice had a decreased complexity of the dendritic trees in the middle segment, as suggested by fewer intersection numbers (two-way ANOVA with respect to group effect; intersection number: $F_{(1,235)} = 56.64$, $P < 0.0001$; Bonferroni *post hoc* comparison: $P < 0.05$ from 70 μm to 120 μm segment; **E**) and shorter dendrite length ($F_{(1,235)} = 17.85$, $P < 0.0001$; Bonferroni *post hoc* comparison: $P < 0.05$ from 70 μm to 100 μm segment; **F**). $N = 12$ cells from three mice in the saline-treated group, and 16 cells from four mice in the VPA-treated group. ns, no significant difference; $^{**}P < 0.01$; $^{***}P < 0.001$. Scale bar, 500 μm (low magnification) and 50 μm (high magnification) in **(A)**, and 50 μm in **(C)**.

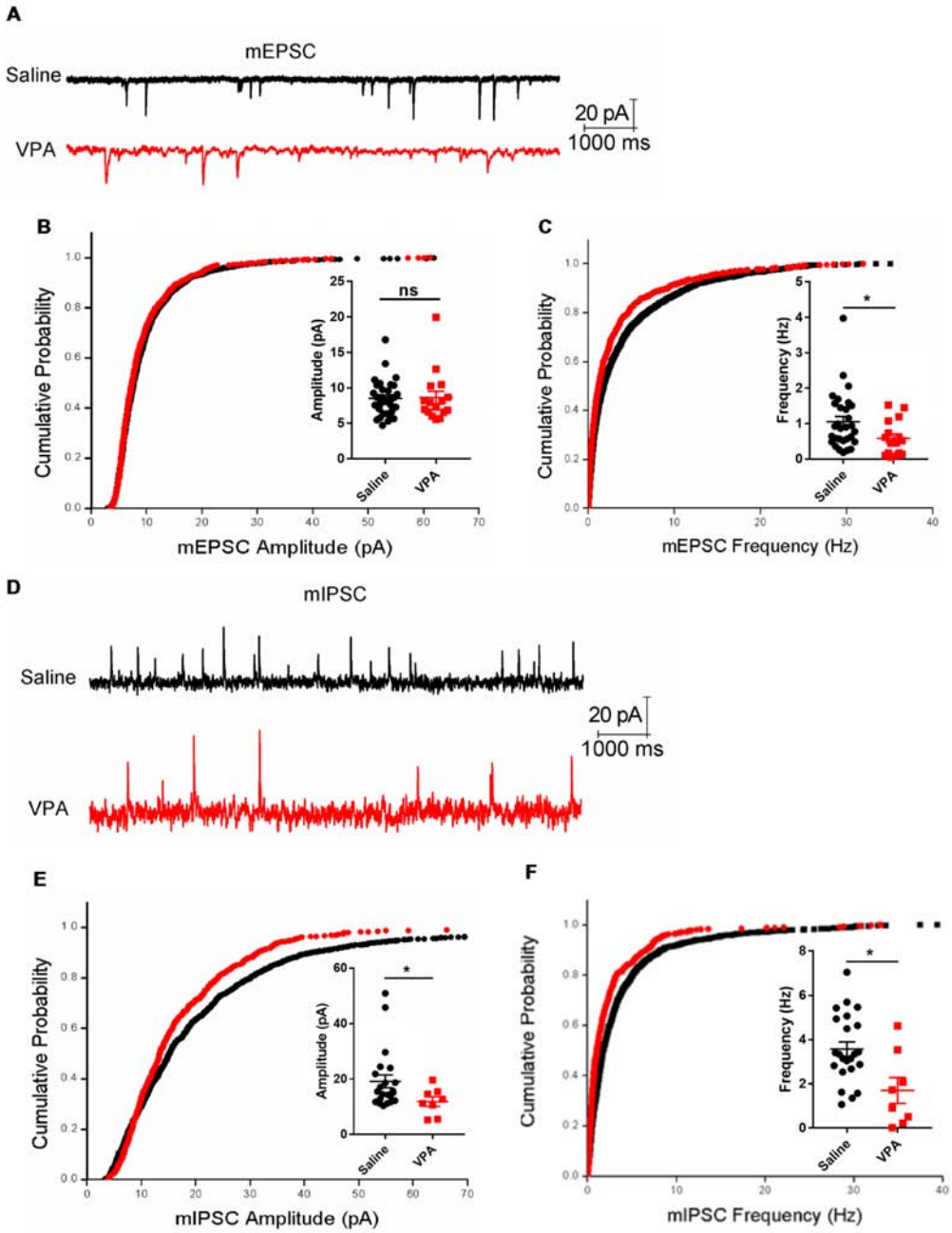

FIGURE 5 | Impaired synaptic transmission in the cerebellar cortex. **(A)** Representative traces from the whole-cell voltage-clamp recording of the miniature excitatory postsynaptic current (mEPSC) in the Purkinje neurons from a saline-treated (upper) and VPA-treated mouse (lower). **(B)** Cumulative distribution of mEPSC amplitude and plotted averaged amplitudes (insert figure) from each recorded neuron. **(C)** Same as **(B)** but for the instantaneous frequency of mEPSC. *N* = 33 neurons from five mice in the saline-treated group, and 16 neurons from four mice in the VPA-treated group. **(D)** Extracted traces for the miniature inhibitory postsynaptic current (mIPSC) recording. **(E)** Cumulative distribution of mIPSC amplitude and plotted averaged values. **(F)** Same as **(E)** but for mIPSC instantaneous frequency. *N* = 22 neurons from five mice in the saline-treated group, and eight neurons from four mice in the VPA-treated group. In all cumulative curves, 40 events were extracted from each neuron for statistical analysis. ns, no significant difference; $^*P < 0.05$ using Mann-Whitney nonparametric comparison.

lobular formation of the cerebellum (**Figure 4A**), VPA exposure decreased the Purkinje cell density. Moreover, we examined the dendritic formation of the Purkinje cells and found that at P9, the VPA-treated mice showed a lower dendritic field radius (**Supplementary Figure S3**). A Sholl analysis indicated altered dendritic arborization patterns at this stage, as indicated by the higher complexity in the proximal dendritic segment but fewer branches at the distal site (**Supplementary Figure S3**). At the adult stage (P30), the Purkinje cells in the VPA-treated group presented a similar dendritic field radius compared to

the control group ($t_{(16)}$ = 0.7583, P = 0.4593; **Figures 4C,D**). However, the dendritic arborization was remarkably impaired, especially at the middle-to-distal segment (70–120 μm from the soma) of the dendritic tree, as suggested by fewer intersections or shorter dendrite lengths (intersection number: two-way ANOVA, group effect; $F_{(1,235)}$ = 56.64, $P < 0.0001$; Bonferroni *post hoc* comparison: $P < 0.05$ from 70 μm to 120 μm segment; **Figures 4C,E**. Dendrite length: $F_{(1,235)}$ = 17.85, $P < 0.0001$; Bonferroni *post hoc* comparison: $P < 0.05$ from 70 μm to 100 μm segment; **Figures 4C,F**). The data therefore suggested that prenatal VPA exposure ablated the normal population and dendritic formation of the Purkinje neurons, in a progressive manner, from the juvenile until the adult stage.

Impaired Synaptic Transmission of Purkinje Neurons in the VPA Model

The Purkinje neurons receive excitatory synaptic inputs from the GCs via parallel fibers and from climbing fibers originating from the inferior olive nuclei, as well as inhibitory inputs from the interneurons in the molecular layers. Therefore, the impaired dendritic arborization of the Purkinje cell in the VPA-treated mouse model may lead to an aberrant synaptic transmission. To test this hypothesis, we prepared acute cerebellar slices from both VPA- and saline-treated mice and recorded the excitatory and inhibitory transmission on the Purkinje cells. When examining the mEPSC, the VPA-treated group had unchanged amplitudes (Mann Whitney test, U = 237, P = 0.5759; **Figures 5A,B**) but remarkably decreased frequencies compared to the control group (0.58 ± 0.12 Hz vs. 1.06 ± 0.15 Hz, U = 136, P = 0.0155; **Figure 5C**). This evidence strongly supports the impaired excitatory transmission in the cerebellar cortex. We also examined the mIPSC, which is evoked by the interneurons including the basket cells and stellate cells in the molecular layer. VPA-treated mice also showed decreased mIPSC amplitudes (11.88 ± 1.73 pA vs. 19.17 ± 2.28 pA, U = 45, P = 0.0446; **Figures 5D,E**) and suppressed frequencies (1.74 ± 0.53 Hz vs. 3.57 ± 0.32 Hz, U = 54, P = 0.0155; **Figure 5F**). In sum, prenatal VPA exposure led to suppressed excitatory and inhibitory transmission, which is consistent with the morphological alternations and motor learning deficits mentioned above.

DISCUSSION

The current study demonstrates the impaired postnatal development of the cerebellar cortex after prenatal VPA exposure, in association with motor deficits during both the juvenile and adult stages. Although having no prominent effect on the gross volume or foliation of the cerebellum, single prenatal VPA injection does lead to a premature GC precursor migration and an excess apoptosis, as well as a lower Purkinje cell density or an impaired dendritic arborization. These structural defects are associated with impaired synaptic transmission in the Purkinje cells. In order to validate ASD-like behaviors in our VPA model, we performed a 3-chamber assay, in which male VPA-treated mice showed an impaired sociability or social novelty (**Supplementary Figure S4**), as consistent with previous reports (Roullet et al., 2010). Furthermore, the retardation of motor reflexes occurred in our VPA-induced mouse ASD model, agreeing with clinical observations showing motor deficits in ASD children before the onset of social or verbal disorders (Lloyd et al., 2013). Our animal data thus supports the examination of early motor disorder as a marker in ASD screening (Brisson et al., 2012; Zwaigenbaum et al., 2013; Sacrey et al., 2015).

Deficits of motor coordination and motor learning have been reported after postnatal VPA exposure (Pragnya et al., 2014). Here, we showed similar phenotypes using prenatal VPA treatment, as suggested by both Rota-rod and LadderScan assays. Such consistent results from our prenatal exposure model as well as the postnatal models of other groups (Kim et al., 2013) suggest that VPA affects both the prenatal and postnatal development of the cerebellum. The tone-conditioned motor learning of a perturbation during walking paradigms, has been established as tightly associated with cerebellar functions (Van Der Giessen et al., 2008). Using similar behavioral approaches, a recent study reported neonatal hypoxia-induced aberrant cerebellar motor learning, as suggested by a higher percentage of irregular steps and longer step durations with the perturbation (Sathyanesan et al., 2018). Both of those phenotypes have been replicated in our VPA model and thus supports the cerebellar deformation and dysfunction. The motor deficits in hypoxic mice were further attributed to a decreased frequency of simple spike firings of the Purkinje cells (Sathyanesan et al., 2018). We consistently showed decreased mEPSC frequencies as well as lower mIPSC frequencies or amplitudes in VPA-treated mice, indicating impaired presynaptic inputs from the parallel fibers or climbing fibers, and from the inhibitory interneurons. The impaired synaptic transmissions may be caused by deficits of dendritic arborization of the Purkinje cells. Apart from those structural deformations, neurotransmitter imbalance may also be involved in ASD-induced cerebellar pathology. A previous study reported a decreased expression of 65 and 67 kDa enzymes of l-glutamic acid decarboxylase (GAD65/67) in a rat cerebellum after prenatal VPA exposure (Olexová et al., 2016). Hippocampal tissues in VPA-treated rats also have decreased glutamine synthesis and impaired glutamate uptake (Bristot Silvestrin et al., 2013). These two separate lines of evidence also supported our observations showing defects of presynaptic excitatory and inhibitory transmissions in the cerebellar cortex of VPA-treated mice. Our anatomical, electrophysiological and behavioral assays therefore provide consistent results showing disrupted cerebellar structures and functions after prenatal VPA exposure.

As a neurodevelopmental disorder, ASD influences neural circuit formation across various brain regions (Mohammad-Rezazadeh et al., 2016), among which the cerebellum has repeatedly been identified (Wang et al., 2014). Such evidence, however, mostly come from transgenic mouse models (Cupolillo et al., 2016; Peter et al., 2016) or ASD patients (Hampson and Blatt, 2015). For example, decreased gray matter volumes (D'Mello et al., 2015) and impaired microstructural connectivity (Hanaie et al., 2013) can be found in the cerebellum of ASD individuals. In mice carrying *Shank2* mutation in the Purkinje cells, potentiated postsynaptic inhibitory transmission as well

as impaired long-term potentiation (LTP) have been associated with motor learning and social deficits (Peter et al., 2016). Nevertheless, our understanding of the effects of ASD-related environmental factors on the cerebellum is far from complete. Prenatal VPA exposure is one commonly used rodent ASD model for mechanistic and therapeutic investigations (Nicolini and Fahnestock, 2018). Previous studies have reported elevated apoptosis of GC precursors (Yochum et al., 2008, 2010) and impaired motor functions (Pragnya et al., 2014) after postnatal VPA exposure. Our study, on the other hand, provides evidence showing interruptions of postnatal cerebellar development through prenatal VPA administration, including the premature migration and excess apoptosis of the GC precursors, and the deformation of the Purkinje cells. GC precursors are highly vulnerable to environmental stimuli. Ethanol exposure, for example, elevates GC apoptosis at an early postnatal stage (Oliveira et al., 2014) and causes motor dysfunctions (Valenzuela et al., 2010). Our VPA model also displayed higher GC apoptosis, as well as pre-onset of GC migration from the EGL to the IGL. The premature GCs migration was previously found to be associated with elevated cell apoptosis (Wang et al., 2017), probably due to an unfavorable micro-niche for the immature neuron precursors. More importantly, matured GCs form one of the two major excitatory inputs on the Purkinje cells. Therefore, GC survival and maturation is crucial for dendrite formation of the Purkinje cells in an activity-dependent manner (as reviewed in Tanaka, 2009). We thus expect that aberrant GC formation and maturation in VPA-treated mice can contribute to Purkinje cell deformation as suggested by morphological studies. Taken together, a decreased Purkinje cell number and dendrite arborization, as well as previously uncharacterized synaptic dysfunction, can help explain the impaired motor learning in VPA-treated mice.

The molecular mechanisms explaining VPA toxicity on the cerebellum are currently still inconclusive. Owing to its functional roles as one histone deacetylase (HDAC) inhibitor, VPA can mediate the expression of various target genes. Therefore, a wide spectrum of pathological phenotypes may co-exist after VPA injection. Some opinions state that a central inflammatory response is involved, as suggested by microglial activation (Suzuki et al., 2013) and elevated proinflammatory cytokines (Lucchina and Depino, 2014). VPA can also alter the endocannabinoid system (Kerr et al., 2013) or the androgen receptor (Perez-Pouchoulen et al., 2016) in the cerebellum. The neurotrophic factor may form an alternative explanation and we found an elevated expression of the brain derived neurotrophic factor (BDNF) in the P15 cerebellum but no change of its receptor TrkB (**Supplementary Figure S5**). In the VPA-treated mouse fetus (Almeida et al., 2014) and in ASD patients (Ricci et al., 2013), excess BDNF have been observed and may be related to ASD neuropathology. In addition to BDNF hypothesis, VPA also mediates the expression of the neurodevelopmental genes such as *Neuroligin1*, *Shank2* and *Shank3* to delay neuronal maturation (Kawanai et al., 2016). Further studies should thus be performed to investigate the major molecular pathways for postnatal cerebellar development such as *sonic hedgehog (Shh)*, to elaborate the developmental effects of VPA. In addition, the teratogenic effects of VPA on the cerebellum may not be limited to the cortical region, as embryonic VPA exposure disrupts normal cell population and nuclei morphology of the deep cerebellar nuclei (DCN; Mowery et al., 2015). More investigations on the effect of VPA on cerebellar circuitry formation could thus help to further elaborate the role of the cerebellum in ASD pathology.

In summary, the current study provides a series of systematic observations for morphological, electrophysiological and functional defects of the cerebellar cortex after prenatal VPA exposure. VPA effectively alters the migration pattern and survival of GC precursors, and leads to a lower Purkinje cell density and impaired dendritic arborizations. Such anatomical deficits are associated with impaired synaptic transmission, which probably lead to motor deficits from the early postnatal stages until the adult stages. This study illustrates the teratogenic effects of VPA on the cerebellum and helps to better characterize the cerebellar neuropathology of ASD. In a clinical perspective, the previously uncharacterized retardations of motor reflexes in VPA-treated juvenile mice supports the exploration of using motor examination in early ASD screening.

AUTHOR CONTRIBUTIONS

RW and JT designed and performed all the experiments. JG, YZ and QH performed the morphological works. JY designed and performed the electrophysiological studies. LZ and K-FS wrote the manuscript and supervised all the experiments. All authors revised and approved the manuscript.

FUNDING

This study was supported by the National Natural Science Foundation of China (#31500842, #81671288 and #81771455), the National Key Research and Development Program of China (2016YFC1306702) and the Natural Science Foundation of Guangdong Province (2016A030313082).

SUPPLEMENTARY MATERIAL

The Supplementary Material for this article can be found online at: https://www.frontiersin.org/articles/10.3389/fncel.2018.00500/full#supplementary-material

REFERENCES

Almeida, L. E., Roby, C. D., and Krueger, B. K. (2014). Increased BDNF expression in fetal brain in the valproic acid model of autism. *Mol. Cell. Neurosci.* 59, 57–62. doi: 10.1016/j.mcn.2014.01.007

Brisson, J., Warreyn, P., Serres, J., Foussier, S., and Adrien-Louis, J. (2012). Motor anticipation failure in infants with autism: a retrospective analysis of feeding situations. *Autism* 16, 420–429. doi: 10.1177/1362361311423385

Bristot Silvestrin, R., Bambini-Junior, V., Galland, F., Daniele Bobermim, L., Quincozes-Santos, A., Torres Abib, R., et al. (2013). Animal model of autism induced by prenatal exposure to valproate: altered glutamate metabolism in the hippocampus. *Brain Res.* 1495, 52–60. doi: 10.1016/j.brainres.2012.11.048

Butts, T., Green, M. J., and Wingate, R. J. (2014). Development of the cerebellum: simple steps to make a 'little brain'. *Development* 141, 4031–4041. doi: 10.1242/dev.106559

Codagnone, M. G., Podestá, M. F., Uccelli, N. A., and Reinés, A. (2015). Differential local connectivity and neuroinflammation profiles in the medial prefrontal cortex and hippocampus in the valproic acid rat model of autism. *Dev. Neurosci.* 37, 215–231. doi: 10.1159/000375489

Cupolillo, D., Hoxha, E., Faralli, A., De Luca, A., Rossi, F., Tempia, F., et al. (2016). Autistic-Like traits and cerebellar dysfunction in Purkinje cell PTEN knock-out mice. *Neuropsychopharmacology* 41, 1457–1466. doi: 10.1038/npp.2015.339

D'Mello, A. M., Crocetti, D., Mostofsky, S. H., and Stoodley, C. J. (2015). Cerebellar gray matter and lobular volumes correlate with core autism symptoms. *Neuroimage Clin.* 7, 631–639. doi: 10.1016/j.nicl.2015.02.007

Fatemi, S. H., Aldinger, K. A., Ashwood, P., Bauman, M. L., Blaha, C. D., Blatt, G. J., et al. (2012). Consensus paper: pathological role of the cerebellum in autism. *Cerebellum* 11, 777–807. doi: 10.1007/s12311-012-0355-9

Hampson, D. R., and Blatt, G. J. (2015). Autism spectrum disorders and neuropathology of the cerebellum. *Front. Neurosci.* 9:420. doi: 10.3389/fnins.2015.00420

Hanaie, R., Mohri, I., Kagitani-Shimono, K., Tachibana, M., Azuma, J., Matsuzaki, J., et al. (2013). Altered microstructural connectivity of the superior cerebellar peduncle is related to motor dysfunction in children with autistic spectrum disorders. *Cerebellum* 12, 645–656. doi: 10.1007/s12311-013-0475-x

Holmes, M. C., Sangra, M., French, K. L., Whittle, I. R., Paterson, J., Mullins, J. J., et al. (2006). 11β-Hydroxysteroid dehydrogenase type 2 protects the neonatal cerebellum from deleterious effects of glucocorticoids. *Neuroscience* 137, 865–873. doi: 10.1016/j.neuroscience.2005.09.037

Kawanai, T., Ago, Y., Watanabe, R., Inoue, A., Taruta, A., Onaka, Y., et al. (2016). Prenatal exposure to histone deacetylase inhibitors affects gene expression of autism-related molecules and delays neuronal maturation. *Neurochem. Res.* 41, 2574–2584. doi: 10.1007/s11064-016-1969-y

Kerr, D. M., Downey, L., Conboy, M., Finn, D. P., and Roche, M. (2013). Alterations in the endocannabinoid system in the rat valproic acid model of autism. *Behav. Brain Res.* 249, 124–132. doi: 10.1016/j.bbr.2013.04.043

Kim, J. E., Shin, M. S., Seo, T. B., Ji, E. S., Baek, S. S., Lee, S. J., et al. (2013). Treadmill exercise ameliorates motor disturbance through inhibition of apoptosis in the cerebellum of valproic acid-induced autistic rat pups. *Mol. Med. Rep.* 8, 327–334. doi: 10.3892/mmr.2013.1518

Lloyd, M., MacDonald, M., and Lord, C. (2013). Motor skills of toddlers with autism spectrum disorders. *Autism* 17, 133–146. doi: 10.1177/1362361311402230

Lucchina, L., and Depino, A. M. (2014). Altered peripheral and central inflammatory responses in a mouse model of autism. *Autism Res.* 7, 273–289. doi: 10.1002/aur.1338

Mandy, W., and Lai, M. C. (2016). Annual research review: the role of the environment in the developmental psychopathology of autism spectrum condition. *J. Child Psychol. Psychiatry* 57, 271–292. doi: 10.1111/jcpp.12501

Markram, K., Rinaldi, T., La Mendola, D., Sandi, C., and Markram, H. (2008). Abnormal fear conditioning and amygdala processing in an animal model of autism. *Neuropsychopharmacology* 33, 901–912. doi: 10.1038/sj.npp.1301453

Marzban, H., Del Bigio, M. R., Alizadeh, J., Ghavami, S., Zachariah, R. M., and Rastegar, M. (2015). Cellular commitment in the developing cerebellum. *Front. Cell. Neurosci.* 8:450. doi: 10.3389/fncel.2014.00450

McPhillips, M., Finlay, J., Bejerot, S., and Hanley, M. (2014). Motor deficits in children with autism spectrum disorder: a cross-syndrome study. *Autism Res.* 7, 664–676. doi: 10.1002/aur.1408

Mohammad-Rezazadeh, I., Frohlich, J., Loo, S. K., and Jeste, S. S. (2016). Brain connectivity in autism spectrum disorder. *Curr. Opin. Neurol.* 29, 137–147. doi: 10.1097/WCO.0000000000000301

Mosconi, M. W., Mohanty, S., Greene, R. K., Cook, E. H., Vaillancourt, D. E., and Sweeney, J. A. (2015). Feedforward and feedback motor control abnormalities implicate cerebellar dysfunctions in autism spectrum disorder. *J. Neurosci.* 35, 2015–2025. doi: 10.1523/JNEUROSCI.2731-14.2015

Mothersill, O., Knee-Zaska, C., and Donohoe, G. (2016). Emotion and theory of mind in schizophrenia-investigating the role of the cerebellum. *Cerebellum* 15, 357–368. doi: 10.1007/s12311-015-0696-2

Mowery, T. M., Wilson, S. M., Kostylev, P. V., Dina, B., Buchholz, J. B., Prieto, A. L., et al. (2015). Embryological exposure to valproic acid disrupts morphology of the deep cerebellar nuclei in a sexually dimorphic way. *Int. J. Dev. Neurosci.* 40, 15–23. doi: 10.1016/j.ijdevneu.2014.10.003

Nicolini, C., and Fahnestock, M. (2018). The valproic acid-induced rodent model of autism. *Exp. Neurol.* 299, 217–227. doi: 10.1016/j.expneurol.2017.04.017

Olexová, L., Štefánik, P., and Kršková, L. (2016). Increased anxiety-like behaviour and altered GABAergic system in the amygdala and cerebellum of VPA rats—an animal model of autism. *Neurosci. Lett.* 629, 9–14. doi: 10.1016/j.neulet.2016.06.035

Oliveira, S. A., Chuffa, L. G., Fioruci-Fontanelli, B. A., Lizarte Neto, F. S., Novais, P. C., Tirapelli, L. F., et al. (2014). Apoptosis of Purkinje and granular cells of the cerebellum following chronic ethanol intake. *Cerebellum* 13, 728–738. doi: 10.1007/s12311-014-0591-2

Ornoy, A. (2009). Valproic acid in pregnancy: how much are we endangering the embryo and fetus? *Reprod. Toxicol.* 28, 1–10. doi: 10.1016/j.reprotox.2009.02.014

Perez-Pouchoulen, M., Miquel, M., Saft, P., Brug, B., Toledo, R., Hernandez, M. E., et al. (2016). Prenatal exposure to sodium valproate alters androgen receptor expression in the developing cerebellum in a region and age specific manner in male and female rats. *Int. J. Dev. Neurosci.* 53, 46–52. doi: 10.1016/j.ijdevneu.2016.07.001

Peter, S., Ten Brinke, M. M., Stedehouder, J., Reinelt, C. M., Wu, B., Zhou, H., et al. (2016). Dysfunctional cerebellar Purkinje cells contribute to autism-like behaviour in Shank2-deficient mice. *Nat. Commun.* 7:12627. doi: 10.1038/ncomms12627

Pragnya, B., Kameshwari, J. S., and Veeresh, B. (2014). Ameliorating effect of piperine on behavioral abnormalities and oxidative markers in sodium valproate induced autism in BALB/C mice. *Behav. Brain Res.* 270, 86–94. doi: 10.1016/j.bbr.2014.04.045

Ricci, S., Businaro, R., Ippoliti, F., Lo Vasco, V. R., Massoni, F., Onofri, E., et al. (2013). Altered cytokine and BDNF levels in autism spectrum disorder. *Neurotox. Res.* 24, 491–501. doi: 10.1007/s12640-013-9393-4

Roullet, F. I., Lai, J. K., and Foster, J. A. (2013). *In utero* exposure to valproic acid and autism—a current review of clinical and animal studies. *Neurotoxicol. Teratol.* 36, 47–56. doi: 10.1016/j.ntt.2013.01.004

Roullet, F. I., Wollaston, L., Decatanzaro, D., and Foster, J. A. (2010). Behavioral and molecular changes in the mouse in response to prenatal exposure to the anti-epileptic drug valproic acid. *Neuroscience* 170, 514–522. doi: 10.1016/j.neuroscience.2010.06.069

Sacrey, L. A., Bennett, J. A., and Zwaigenbaum, L. (2015). Early infant development and intervention for autism spectrum disorder. *J. Child Neurol.* 30, 1921–1929. doi: 10.1177/0883073815601500

Sathyanesan, A., Kundu, S., Abbah, J., and Gallo, V. (2018). Neonatal brain injury causes cerebellar learning deficits and Purkinje cell dysfunction. *Nat. Commun.* 9:3235. doi: 10.1038/s41467-018-05656-w

Sosa-Díaz, N., Bringas, M. E., Atzori, M., and Flores, G. (2014). Prefrontal cortex, hippocampus, and basolateral amygdala plasticity in a rat model of autism spectrum. *Synapse* 68, 468–473. doi: 10.1002/syn.21759

Su, L., Cai, Y., Xu, Y., Dutt, A., Shi, S., and Bramon, E. (2014). Cerebral metabolism in major depressive disorder: a voxel-based meta-analysis of positron emission tomography studies. *BMC Psychiatry* 14:321. doi: 10.1186/s12888-014-0321-9

Suzuki, K., Sugihara, G., Ouchi, Y., Nakamura, K., Futatsubashi, M., Takebayashi, K., et al. (2013). Microglial activation in young adults with autism spectrum disorder. *JAMA Psychiatry* 70, 49–58. doi: 10.1001/jamapsychiatry.2013.272

Tanaka, M. (2009). Dendrite formation of cerebellar Purkinje cells. *Neurochem. Res.* 34, 2078–2088. doi: 10.1007/s11064-009-0073-y

Valenzuela, C. F., Lindquist, B., and Zamudio-Bulcock, P. A. (2010). A review of synaptic plasticity at Purkinje neurons with a focus on ethanol-induced cerebellar dysfunction. *Int. Rev. Neurobiol.* 91, 339–372. doi: 10.1016/s0074-7742(10)91011-8

Van Der Giessen, R. S., Koekkoek, S. K., van Dorp, S., De Gruijl, J. R., Cupido, A., Khosrovani, S., et al. (2008). Role of olivary electrical coupling in cerebellar motor learning. *Neuron* 58, 599–612. doi: 10.1016/j.neuron.2008.03.016

Vinueza Veloz, M. F., Zhou, K., Bosman, L. W., Potters, J. W., Negrello, M., Seepers, R. M., et al. (2015). Cerebellar control of gait and interlimb

coordination. *Brain Struct. Funct.* 220, 3513–3536. doi: 10.1007/s00429-014-0870-1

Wang, S. S., Kloth, A. D., and Badura, A. (2014). The cerebellum, sensitive periods, and autism. *Neuron* 83, 518–532. doi: 10.1016/j.neuron.2014.07.016

Wang, L., Zhang, L., and Chow, B. K. C. (2017). Secretin modulates the postnatal development of mouse cerebellar cortex Via PKA- and ERK-dependent pathways. *Front. Cell. Neurosci.* 11:382. doi: 10.3389/fncel.2017.00382

Whyatt, C., and Craig, C. (2013). Sensory-motor problems in Autism. *Front. Integr. Neurosci.* 7:51. doi: 10.3389/fnint.2013.00051

Wolf, L. W., LaRegina, M. C., and Tolbert, D. L. (1996). A behavioral study of the development of hereditary cerebellar ataxia in the shaker rat mutant. *Behav. Brain Res.* 75, 67–81. doi: 10.1016/0166-4328(96)00159-3

Yochum, C. L., Bhattacharya, P., Patti, L., Mirochnitchenko, O., and Wagner, G. C. (2010). Animal model of autism using GSTM1 knockout mice and early post-natal sodium valproate treatment. *Behav. Brain Res.* 210, 202–210. doi: 10.1016/j.bbr.2010.02.032

Yochum, C. L., Dowling, P., Reuhl, K. R., Wagner, G. C., and Ming, X. (2008). VPA-induced apoptosis and behavioral deficits in neonatal mice. *Brain Res.* 1203, 126–132. doi: 10.1016/j.brainres.2008.01.055

Zhang, L., Chung, S. K., and Chow, B. K. (2014). The knockout of secretin in cerebellar Purkinje cells impairs mouse motor coordination and motor learning. *Neuropsychopharmacology* 39, 1460–1468. doi: 10.1038/npp.2013.344

Zwaigenbaum, L., Bryson, S., and Garon, N. (2013). Early identification of autism spectrum disorders. *Behav. Brain Res.* 251, 133–146. doi: 10.1016/j.bbr.2013.04.004

Conflict of Interest Statement: The authors declare that the research was conducted in the absence of any commercial or financial relationships that could be construed as a potential conflict of interest.

frontiers in Cellular Neuroscience

ORIGINAL RESEARCH
published: 08 January 2019
doi: 10.3389/fncel.2018.00513

Electrophysiological Excitability and Parallel Fiber Synaptic Properties of Zebrin-Positive and -Negative Purkinje Cells in Lobule VIII of the Mouse Cerebellar Slice

Viet T. Nguyen-Minh[1], *Khoa Tran-Anh*[1], *Yuanjun Luo*[1] *and Izumi Sugihara*[1,2]*

[1]Department of Systems Neurophysiology, Graduate School of Medical and Dental Sciences, Tokyo Medical and Dental University, Tokyo, Japan, [2]Center for Brain Integration Research, Tokyo Medical and Dental University, Tokyo, Japan

Heterogeneous populations of cerebellar Purkinje cells (PCs) are arranged into separate longitudinal stripes, which have different topographic afferent and efferent axonal connections presumably involved in different functions, and also show different electrophysiological properties in firing pattern and synaptic plasticity. However, whether the differences in molecular expression that define heterogeneous PC populations affect their electrophysiological properties has not been much clarified. Since the expression pattern of many of such molecules, including glutamate transporter EAAT4, replicates that of aldolase C or zebrin II, we recorded from PCs of different "zebrin types" (zebrin-positive = aldolase C-positive = Z+; and Z−) in identified neighboring stripes in vermal lobule VIII, in which Z+ and Z− stripes occupy similar widths, in the Aldoc-Venus mouse cerebellar slice preparation. Regarding basic cellular electrophysiological properties, no significant differences were observed in input resistance or in occurrence probability of types of firing patterns between Z+ and Z− PCs. However, the firing frequency of the tonic firing type was higher in Z− PCs than in Z+ PCs. In the case of parallel fiber (PF)-PC synaptic transmission, no significant differences were observed between Z+ and Z− PCs in interval dependency of paired pulse facilitation or in time course of synaptic current measured without or with the blocker of glutamate receptor desensitization. These results indicate that different expression levels of the molecules that are associated with the zebrin type may affect the intrinsic firing property of PCs but not directly affect the basic electrophysiological properties of PF-PC synaptic transmission significantly in lobule VIII. The results suggest that the zebrin types of PCs in lobule VIII is linked with some intrinsic electrophysiological neuronal characteristics which affect the firing frequency of PCs. However, the results also suggest that the molecular expression differences linked with zebrin types of PCs does not much affect basic electrophysiological properties of PF-PC synaptic transmission in a physiological condition in lobule VIII.

Keywords: Purkinje cell, aldolase C, zebrin II, cerebellum, glutamate transporter, firing pattern, parallel fiber

OPEN ACCESS

Edited by:
Ying Shen,
Zhejiang University, China

Reviewed by:
De-Lai Qiu,
Yanbian University, China
Zhenyu Gao,
Erasmus University Rotterdam, Netherlands

***Correspondence:**
Izumi Sugihara
isugihara.phy1@tmd.ac.jp

Received: *14 September 2018*
Accepted: *10 December 2018*
Published: *08 January 2019*

Citation:
Nguyen-Minh VT, Tran-Anh K, Luo Y and Sugihara I (2019) Electrophysiological Excitability and Parallel Fiber Synaptic Properties of Zebrin-Positive and -Negative Purkinje Cells in Lobule VIII of the Mouse Cerebellar Slice. Front. Cell. Neurosci. 12:513. doi: 10.3389/fncel.2018.00513

INTRODUCTION

Purkinje cells (PCs), the sole output neuron of the cerebellar cortex, play an essential role in cerebellar motor and non-motor function through the integration of climbing fiber and parallel fiber (PF) excitatory inputs and inhibitory inputs from molecular layer inhibitory neurons (Ito, 2012). Although the local neuronal circuitry is uniform throughout the cerebellar cortex, PCs are organized into heterogeneous populations based on the expression profile of many molecules, which are distributed in longitudinally-striped patterns in the cerebellar cortex. The striped distribution pattern of heterogeneous populations of PCs is best clarified in the case of zebrin II or glycolytic enzyme aldolase C (Brochu et al., 1990; Fujita et al., 2014). Some 20 aldolase C-positive (Z+) and -negative (Z−) stripes (zebrin stripes) are topographically connected with different areas of the inferior olive and cerebellar nuclei (Voogd et al., 2003; Sugihara and Shinoda, 2004, 2007), and form parallel modules in the olivo-cortico-nuclear loop (Ruigrok, 2011). Expression of several molecules, including EAAT4, a neuronal glutamate transporter (Dehnes et al., 1998), exactly matches with that of aldolase C (Dehnes et al., 1998; Hawkes, 2014), high and low in Z+ and Z− PCs ("zebrin type"), respectively. Expression of other molecules is complementary or partially related to the zebrin type. Although the functional significance of the different expression profiles of these molecules are barely understood, it may be possible that differences in expression of these molecules affect the physiological properties of individual PCs.

Indeed, significant differences in physiological properties have also been reported among PC populations. Z− PCs have significantly higher firing frequencies of simple spikes (Xiao et al., 2014; Zhou et al., 2014), and show a more sustained increase in simple spike activity up to the time of the complex spike (Tang et al., 2017), relative to Z+ PCs in various areas of the cerebellar cortex in *in vivo* studies. In *in vitro* studies, PCs in lobules III-V have been shown to exhibit significantly higher input resistance as well as different variations of firing patterns relative to that of PCs in lobule X (Kim et al., 2012; Cerminara et al., 2015). Furthermore, PCs in lobule III show long term depression more robustly than PCs in lobule X (Wadiche and Jahr, 2005). Notwithstanding, the mechanisms underlying these differences have not been much clarified except for the last case, in which the EAAT4 expression rich in Z+ PCs, which is abundant in lobule X and sparse in lobule III, has been implicated in the rapid lowering of glutamate released by climbing fibers (Wadiche and Jahr, 2005). In the above *in vivo* studies, it is not clear whether these differences are brought about by the molecular expression profile of Z+ and Z− PCs or by specific afferent and local inputs to these PCs. In the seemingly sole *in vitro* study with direct identification of the zebrin type of recorded PCs in EAAT4-eGFP mice (Tsai et al., 2012), the authors reported no significant differences in PF-PC synaptic transmission between Z+ and Z− PCs in normal artificial cerebrospinal fluid (ACSF).

In the present study, we used Aldoc-Venus heterozygous mice (Fujita et al., 2014), in which Aldoc expression is visualized by fluorescent protein expression with a presumably clearer contrast between Z+ and Z− PCs than in EAAT4-eGFP mice, without any other obvious morphological or functional phenotypes. Since the zebrin striped pattern has been clarified in detail (Fujita et al., 2014; Sarpong et al., 2018), it was possible to identify zebrin stripes in longitudinal and transverse slice preparations, in which effects of cerebellar afferent activity are ignorable whereas PF innervation to neighboring Z+ and Z− stripes (Gao et al., 2006) is intact. We focused on lobule VIII, where Z+ and Z− PC populations are arranged into clearly-delineated similarly wide stripes (Fujita et al., 2014). By performing whole-cell patch clamp recording from Z+ and Z− PCs in neighboring stripes in lobule VIII, we made an experimental condition purposely suited to extract differences that are purely related to the zebrin type of PCs. Besides comparing basic electrophysiological properties of Z+ and Z− PCs, we also examined the differences in their PF-PC synaptic transmission, since the EAAT4 expression in PF-PC synapse is linked to the zebrin type and has been implicated in decay of the synaptic current through glutamate uptake (Yamada et al., 1997; Dehnes et al., 1998).

MATERIALS AND METHODS

Ethics Statements

Experimental protocols were approved by the Animal Care and Use Committee (A2017-060C4, A2018-148A) and Gene Recombination Experiment Safety Committee (2012-064C4, 2017-040A) of Tokyo Medical and Dental University.

Animals

Aldoc-Venus knock-in mouse line of C57BL/6N background (Fujita et al., 2014) was maintained by mating homozygotes. Heterozygotes were produced by mating Aldoc-Venus homozygous males with C57BL/6N females. Postnatal day (P) 18–32 male and female heterozygotes were used in experiments.

Slice Preparation

Animals were anesthetized with an intraperitoneal injection of an overdose of pentobarbital (0.1 mg/g, Abbott lab, Chicago, IL, USA) and xylazine (0.005 mg/g), and euthanized by cervical dislocation. The cerebellar block was dissected from the extracted brain under ice-cold cutting solution containing (in mM): 125 choline chloride, 3 KCl, 0.1 $CaCl_2$, 5 $MgCl_2$, 1.25 $NaH_2PO_4.2H_2O$, 10 D-glucose, 0.4 L-ascorbic acid, 25 $NaHCO_3$, 10 HEPES, pH 7.3 and saturated with 95% O_2 and 5% CO_2. 200–300 μm transversal and parasagittal slices were cut using a vibratome (PRO7, Dosaka, Osaka, Japan). Slices were initially allowed to recover in cutting solution at 34°C for 5–10 min, after which they were transferred into ACSF containing (in mM): 124 NaCl, 2.5 KCl, 2 $CaCl_2$, 1 $MgCl_2$, 1.2 NaH_2PO_4, 24 $NaHCO_3$, and 12.5 glucose and saturated with 95% O_2 and 5% CO_2 at 34°C for 30 min, and then allowed to recover in ACSF at room temperature for at least 1 h.

Identification of Zebrin Stripes in Slice

Slices were placed in the bottom of the recording chamber, soaked in ACSF, and mounted on the stage of a microscope (BX51IW, Olympus, Tokyo, Japan). In the case of a transversal section, the first section cut from lobule VIII was placed with the

apical surface facing the bottom such that the entire PC dendritic arbor was intact in the central part of the slice. Slices were then examined with a 10× objective and epifluorescence optics with a filter for appropriate wavelength selection (**Figure 1A**). In slices cut in the transversal orientation, it was straightforward in identifying zebrin stripes by referring to the reported aldolase C (zebrin) expression pattern in the Aldoc-Venus mouse (Fujita et al., 2014; see Figures 1, 3). In slices cut in the longitudinal orientation, the distance of the sliced plane from the midline, and location and tilt of Z+ stripes were carefully checked. Z+ stripes were clearly visible even in sagittal slices since Aldoc-Venus mice show a strong contrast of fluorescence expression between Z+ and Z− PCs. Stripes were then identified with reference to the aldolase C stripe pattern which has been mapped upon the unfolded scheme of the cerebellum (Sarpong et al., 2018). For example, stripe 1+ ran nearly in parallel with the plane of the slice throughout lobule VIII in the slice at the midsagittal section. Stripe 2+ ran more laterally in the rostral part and more medially in the caudal part of lobule VIII in the neighboring slice. Stripe 3+ ran medially in the apex of lobule VIII and laterally in the rostral and caudal part of lobule VIII in the same or next laterally neighboring slice. Stripe 4+ was thin and located more laterally in the rostral part, while it was wider and located more medially in the caudal part of lobule VIII, in the same or next laterally neighboring slice. With knowledge of these patterns, we could select a PC from an identified stripe. In a transversal slice, a PC located under a thin layer of granule cells was selected. The optics of the microscope were changed from epifluorescence to near-infrared Nomarski interference contrast system to approach the PC with the electrode.

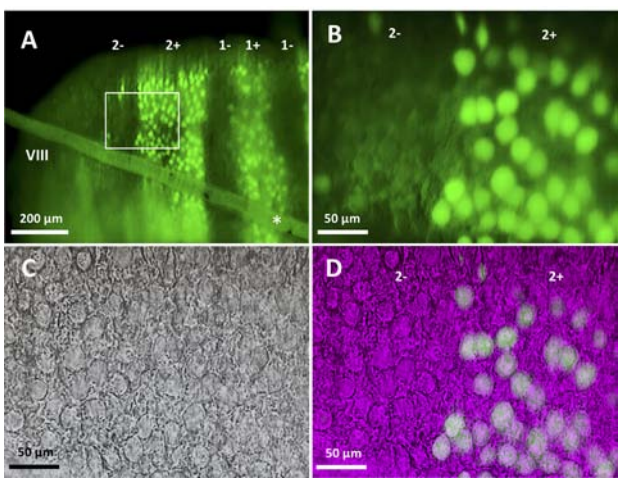

FIGURE 1 | Slice preparation from lobule VIII of the aldolase C-Venus mouse. **(A)** Epifluorescence image of a transverse slice with the 10× objective. The slanted object (asterisk) shows the thread used to hold the slice. Stripe names are indicated in the top. **(B–D)** An enlargement of the region outlined by the white square in **(A)**. Epifluorescence image with the 40× water-immersion objective **(B)**, near-infrared Nomarski interference contrast image **(C)** and superimposition of the epifluorescence and Nomarski images **(D)** showing identification of the zebrin type of individual Purkinje cells (PCs).

Electrophysiological Setups

Slices were constantly superfused with ACSF at room temperature (24°C). PCs were visualized for recording using a 40× water-immersion objective (**Figures 1B–D**). Patch pipettes had a resistance of 2–5 MΩ when filled with the internal solution consisting of the following (in mM): 120 K-gluconate, 6 NaCl, 10 HEPES, 12 Na_2-phosphocreatine, 5 EGTA, 1 $CaCl_2$, 2 $MgCl_2$, 2 MgATP, 0.5 NaGTP, pH 7.3, adjusted with KOH; osmolality ∼290 mosmol/kgH_2O. Signals from the patch pipette were recorded with a MultiClamp 700B amplifier (Molecular Devices, San Jose, CA, USA), digitized at 10–20 kHz and filtered at 2–5 kHz with a Digidata 1440A analog-to-digital converter (Molecular Devices). Whole-cell recording was made at a holding potential of −70 to 75 mV in current clamp and voltage clamp modes by injecting holding current <500 pA. Access resistance, which was monitored to check stability throughout the recording, was <10 MΩ. Experiments in which holding current was >500 pA or access resistance changed by >15% were not included for analysis. Recorded data were analyzed in Clampfit 10.7 (Molecular Devices).

Identification of the Spike Response Type

Sagittal and transverse slice preparations from P20 to P30 mice were used. Recording was done under current clamp mode with the membrane potential set to −70 to 75 mV by injecting holding current <500 pA in current clamp mode. ACSF containing 100 µm picrotoxin (C0375, Tokyo Chemical Industry Co., Tokyo, Japan) and 2 mM kynurenic acid (H0303, Tokyo Chemical Industry Co., Tokyo, Japan) was superfused to block spontaneous synaptic activities. Firing patterns were determined in response to depolarizing current pulses (100–1,000 pA) of 1,000 ms injected from hyperpolarized holding potentials.

Measurement of Input Resistance

Sagittal and transverse slice preparations from P20 to P30 mice were used. Recording was done under current clamp mode with the membrane potential set to −70–75 mV by injecting holding current <500 pA in current clamp mode. ACSF containing 100 µm picrotoxin and 2 mM kynurenic acid was superfused. Input resistance was obtained from the membrane potential response to the negative current injections of four different intensities (−600, −500, −400 and −300 pA) in current clamp mode.

Firing Property Analysis

Sagittal slice preparations were made from P20 to P30 mice. Recordings were made from Z+ and Z− PCs in stripes between 1+ and 3− in lobule VIII under current clamp mode with the membrane potential set to approximately −70 mV. ACSF containing 100 µm picrotoxin and 2 mM kynurenic acid was superfused. After identifying its response pattern as the tonic type, 20 current steps of 1,000 ms duration (20 pA incremental steps from 0 pA to 380 pA). The number of action potentials during the 1,000 ms period was obtained for each current injection step.

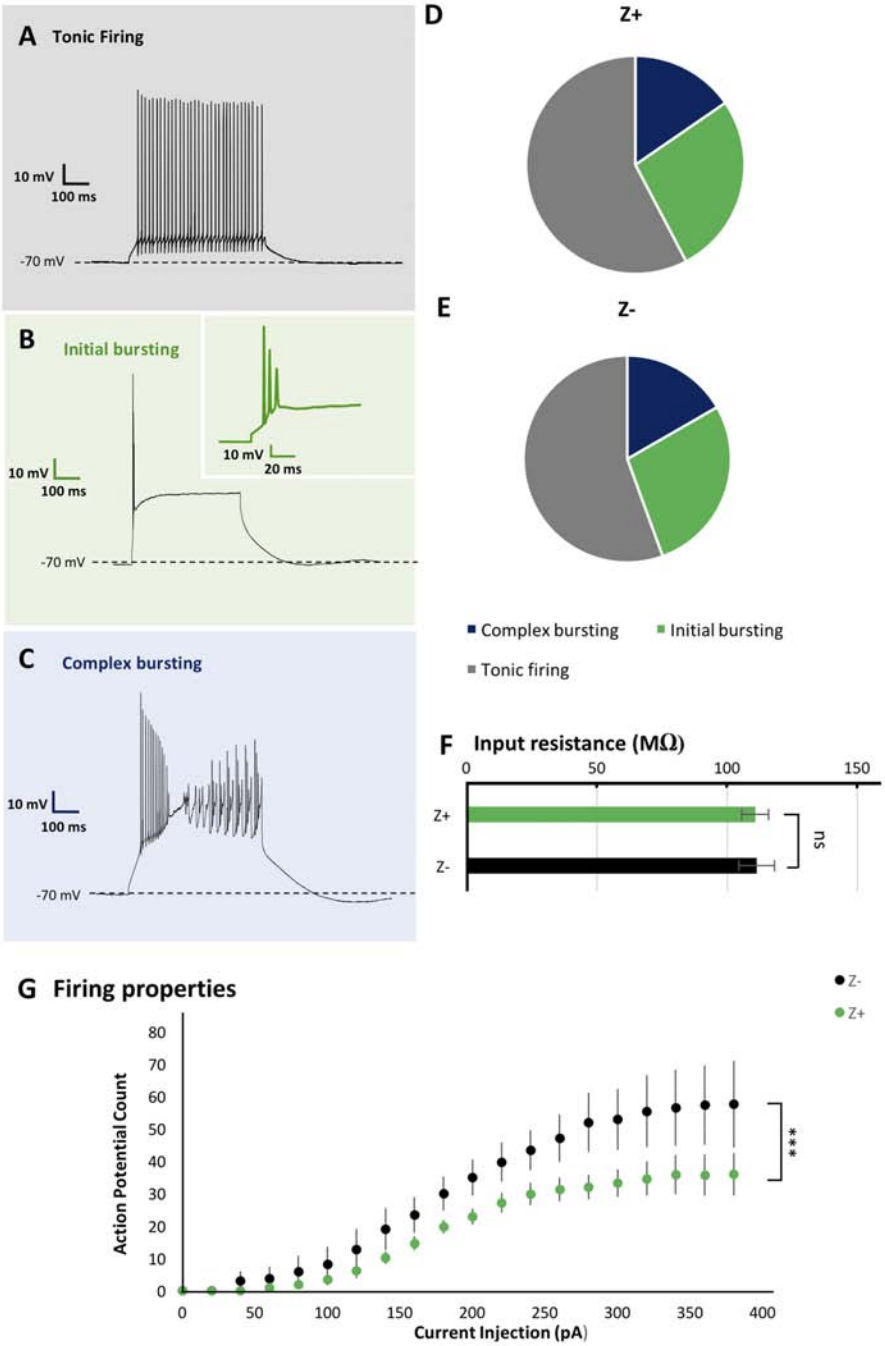

FIGURE 2 | Similar firing pattern variation and input resistance between Z+ and Z− PCs in lobule VIII. **(A–C)** Types of firing patterns in response to depolarizing current injection in three PCs. They represent tonic firing type **(A)**, initial bursting type **(B)** and complex bursting type **(C)**, respectively. **(D,E)** Pie charts show the relative proportion of each type of firing patterns Z+ (n = 24) and Z− (n = 19) PCs, respectively. **(F)** Comparison of input resistance between Z+ (n = 19) and Z− (n = 14) PCs. **(G)** Plot of the mean action potential count during the 1,000 ms current injection step against the current injection intensity, obtained for 10 Z+ (green) and 10 Z− (black) PCs of the tonic firing type (ns, not significant; ***p <0.001).

Recording PF-PC Synaptic Current

Sagittal slice preparations from P18 to P25 and P28–32 mice were used. Recording was done under voltage clamp mode at a holding potential of −70 mV. ACSF containing 100 μm picrotoxin was superfused to block activities of inhibitory synapses in some experiments. ACSF containing 100 μmol cyclothiazide (CTZ, ab120061, Abcam, Cambridge, UK) and 100 μm picrotoxin was superfused to block desensitization

of α-amino-3-hydroxy-5-methyl-4-isoxazolepropionic acid receptor (AMPAR) additionally in other experiments. Stimulation electrode (glass pipette with the tip diameter of 5–10 μm, filled with ACSF) was placed in the deep portion of the molecular layer (∼25–50 μm to the PC layer, Roth and Häusser, 2001) to obtain consistent fast decay time course of the synaptic current (half decay time of about 8 ms, see **Figure 4A**). For stimulation, negative pulses (duration, ∼0.1 ms) were given between stainless wires in the glass pipette and in the bath. Stimulus intensities were adjusted to observe an excitatory postsynaptic current (EPSC) amplitude of 100–150 pA from the whole-cell patch pipette. PF stimulation was confirmed by slow rising of EPSC, variable EPSC amplitude nearly linearly related to the stimulus intensity and paired-pulse facilitation (see **Figure 4B**).

Statistical Analysis

Measured values are shown with the mean ± standard error of the mean (SEM). The average and SEM were plotted in figures. Firing properties were analyzed using two-way ANOVA, while other statistical analyses were performed using one-way ANOVA. Differences were considered significant at $p < 0.05$. Single, double and triple asterisks indicate $p < 0.05$, $p < 0.01$, $p < 0.001$.

RESULTS

Firing Pattern of PC Was Not Correlated to the Zebrin Type and Location in Lobule VIII

In slice preparation obtained from Aldoc-Venus mice at the second and third postnatal week, fluorescence of individual PCs was clearly visible with 10× and 40× objectives, and consequently, it was straightforward to identify the longitudinally-arranged pattern of Z+ and Z− stripes of PC distribution (**Figure 1**). Whole-cell patch clamp recording was performed from single Z+ or Z− PCs within an identified stripe in lobule VIII.

As the basic electrophysiological property that may be correlated with regional difference or striped pattern, the type of spike response to step-wise current injection and input resistance were examined. These properties are reported to be significantly different between PCs in lobules III-V and lobule X (Kim et al., 2012) and thus suggested to be possibly correlated with the zebrin type (Cerminara et al., 2015). We investigated PC firing patterns in vermal area of lobule VIII. It was revealed that PCs generated a particular type of spike response, with suprathreshold current injection, which could be classified into multiple types as described previously (Kim et al., 2012; Cerminara et al., 2015). Among 44 PCs recorded in lobule VIII, tonic firing (**Figure 2A**), initial bursting (**Figure 2B**) and complex bursting (**Figure 2C**) types were found in 57% ($n = 25$), 16% ($n = 7$) and 27% ($n = 12$) PCs, respectively. However, no gap firing pattern, which has been observed in lobule X PCs (Kim et al., 2012), was observed.

The sample of 44 PCs included 26 Z+ and 18 Z− PCs. The tonic firing, initial bursting and complex bursting types were observed in 58% ($n = 15$), 27% ($n = 7$) and 15% ($n = 4$) of Z+ PCs (**Figure 2D**), and in 55% ($n = 10$), 28% ($n = 5$) and 17% ($n = 3$) of Z− PCs (**Figure 2E**). The results showed no clear differences in the occurrence of different types of spike response between Z+ and Z− PCs in lobule VIII. This was an indication that the zebrin type of PCs was not much correlated with the firing pattern of PCs in lobule VIII.

Since there are multiple Z+ and Z− stripes in lobule VIII, we mapped the location of the recorded PCs on the scheme of aldolase C stripes mapped on the unfolded mouse cerebellar cortex (Sugihara and Quy, 2007; Fujita et al., 2014; Sarpong et al., 2018) to further examine the distribution of PCs with respect to the different firing patterns. PCs with all of the three firing types were randomly distributed in various stripes as shown (**Figure 3**). We did not observe any particular relationship between the distribution of firing types and the location of Z+/Z− stripes or in the anterior-posterior/medial-lateral axes.

Input Resistance of PCs Was Not Correlated With the Zebrin Type

Input resistance relates to neuronal size, shape and resting membrane conductance. Previous studies have shown that PCs in lobules III-V have significantly larger input resistance that those in lobule X (Kim et al., 2012). However, it is not clear

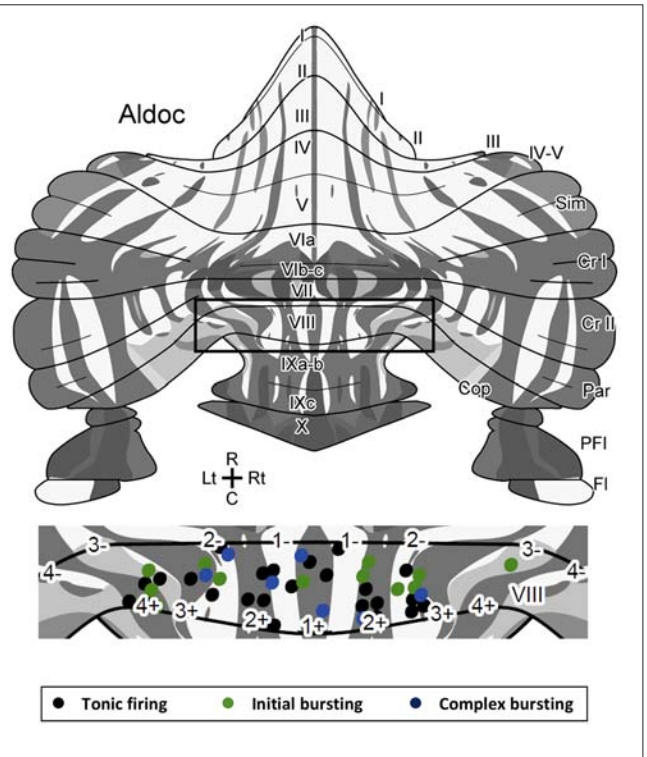

FIGURE 3 | Location of Z+ and Z− PCs with different types of firing patterns mapped on the unfolded scheme of the mouse cerebellar cortex with the zebrin stripe. Forty-three PCs are mapped in the lobule VIII area (center) of the scheme of the zebrin stripe of the mouse cerebellum (top, Sarpong et al., 2018) with a color coding of firing pattern types (bottom). Square in the top scheme indicates the lobule VIII area that is magnified in the center. Abbreviations, I–X, lobules I–X; a–c, sublobules a–c; Cop, copula pyramidis; Cr I, crus I; Cr II, crus II; Fl, flocculus; Par, paramedian lobule; PFl, paraflocculus; Sim, simple lobule.

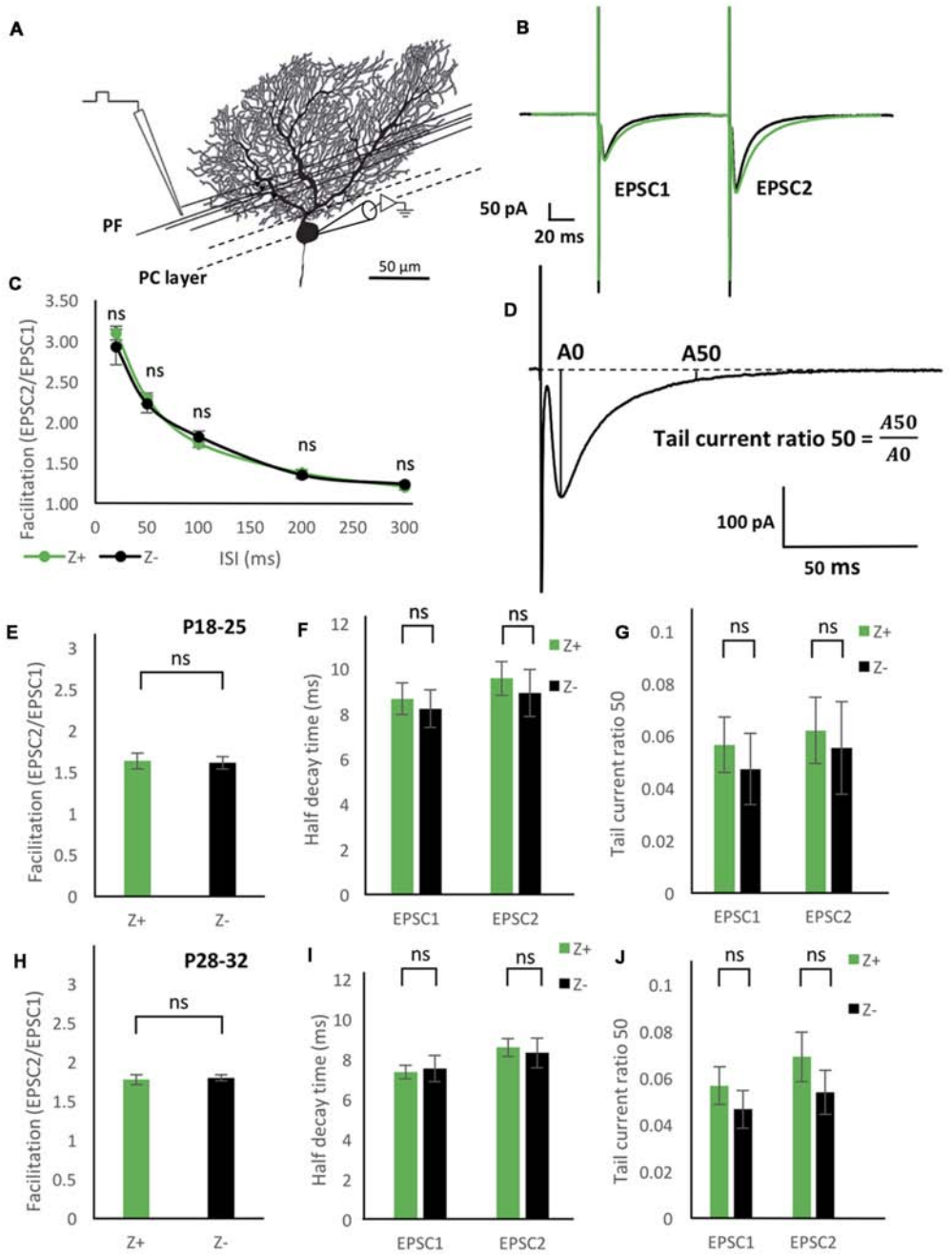

FIGURE 4 | Similar excitatory postsynaptic current (EPSC) properties of the parallel fiber (PF)-PC synapse between Z+ and Z− PCs. **(A)** Illustration of the experiment. The stimulation electrode was placed in the deep molecular layer 25–50 µm from the PC layer. **(B)** Average of PF-PC EPSCs recorded in Z+ (green, n = 8) and Z− (black, n = 8) PCs. **(C)** Time course of the facilitation, which was defined as the amplitude of the EPSC evoked by the second stimulus (EPSC2) divided by the amplitude of the EPSC evoked by the initial stimulus (EPSC1; n = 7 Z+ and 7 Z−). **(D)** Schematic showing definition of "tail current ratio 50," which is the ratio of the EPSP amplitude at 50 ms after the peak (A50) vs. the EPSC peak amplitude (A0). **(E–G)** Facilitation with the paired pulse interval of 100 ms **(E)**, half-decay time **(F)**, and tail current ratio 50 **(G)** of PF-PC EPSC in P18–25 mice (n = 8 Z+ and 8 Z−), respectively. In **(F,G)**, values for the EPSC1 and EPSC2 are shown. **(H–J)** Same measurements as **(E–G)** performed in P28–32 mice (n = 8 Z+ and 8 Z−; ns, not significant).

whether this difference is related to Z types of PCs, which are differently distributed in these lobules. Therefore, we measured the input resistance in 19 Z+ and 14 Z− PCs in lobule VIII. The obtained values, 110.8 ± 5.1 MΩ for Z+ PCs and 111.3 ± 6.8 MΩ for Z− PCs were not significantly different between the two populations ($F_{(1,31)}$ = 0.05, p = 0.95, one-way ANOVA). The result indicates that the input resistance of PCs were not correlated with the zebrin type in lobule VIII (**Figure 2F**).

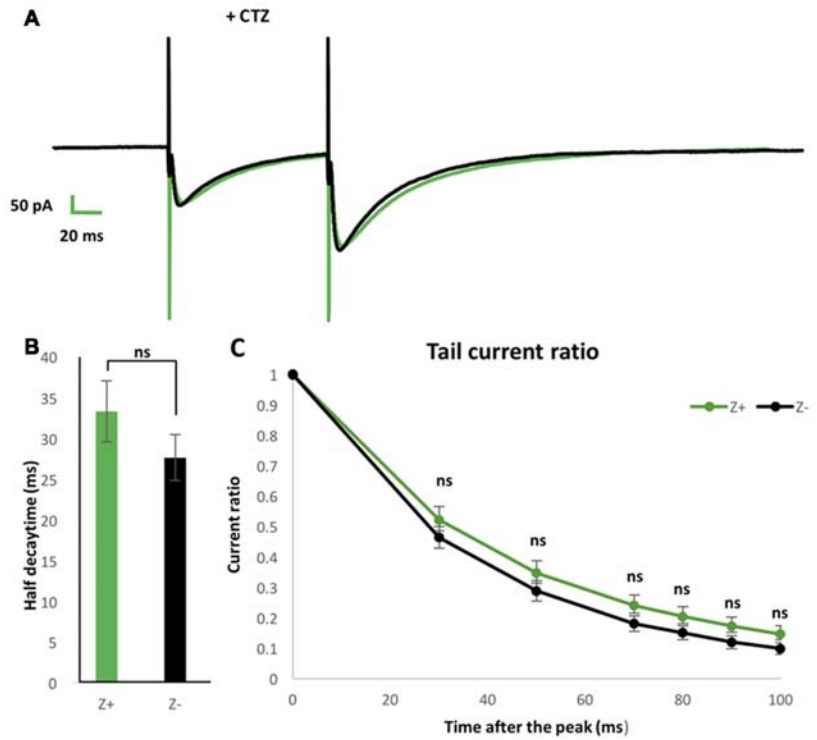

FIGURE 5 | Similar EPSCs decay kinetics of PF-PC synapse between Z+ and Z− PCs in the presence of blocker of α-amino-3-hydroxy-5-methyl-4-isoxazolepropionic acid receptor (AMPAR) desensitization 100 μmol cyclothiazide (CTZ). **(A)** Average of PF-PC EPSCs recorded in Z+ (green, $n = 9$) and Z− (black, $n = 9$) PCs in the presence of 100 μmol CTZ. **(B)** Half decay time of the EPSC evoked by the second stimulus. **(C)** Plots of tail current ratios, ratio of the EPSC amplitude at 30, 50, 70, 80, 90, 100 ms after the peak vs. the peak EPSC amplitude, of the EPSC evoked by the second stimulus. Interval of the paired stimuli was set at 100 ms (ns, not significant).

Comparison of Action Potential Count in Tonic Firing Type PCs

In vivo studies have reported higher firing frequency in Z− PCs than in Z+ PCs (Xiao et al., 2014; Zhou et al., 2014). Therefore, we examined the intrinsic firing properties of Z+ and Z− tonic firing type PCs in lobule VIII (10 Z+ and 10 Z− PCs in stripes 1+ to 3−), which comprised the largest population among the three types of firing patterns of Z+ and Z− PCs in lobule VIII (above), in a separate set of experiments with P22 and P23 mice. Although no differences were found in the rheobase, the lowest current intensity needed to produce firing between these Z+ and Z− PCs examined (data not shown), current injection steps produced a higher count of action potential firing in Z− PCs than in Z+ PCs in the input-output relationship (two-way repeated-measures ANOVA starting at 0 pA injection, factor zebrin type, $F_{(1,18)} = 37.41$; $p < 0.001$; **Figure 2G**).

Comparison of PF-PC EPSC Properties Between Z+ and Z− PCs

PFs run in the transverse plane along the major axis of a folium and excite PC dendrites along an extension of about 3 mm to cross multiple zebrin stripes and make excitatory synaptic connection to both Z+ and Z− PCs (Arata and Ito, 2004; Gao et al., 2006; Ito, 2006; Hoxha et al., 2016). Thus, PCs in neighboring zebrin stripes receive innervation from a similar population of PFs. Therefore, if there exist any differences in the property of PF-PC synapses between nearby Z+ and Z− PCs in the same lobule, they would indicate differences related to the zebrin type.

To study functional difference in PF-PC synaptic transmission between Z+ and Z− PCs, we first examined the degree of facilitation of EPSC of PF-PC synapse (**Figures 4A,B**), one of the essential plastic characteristics of synaptic transmission. The ratio of the amplitudes of the first and second EPSC evoked by paired pulse stimulation with an interval of 20 ms, 50 ms, 100 ms, 200 ms and 300 ms was measured in mice at P18–25. Results from 7 Z+ and 7 Z− PCs showed no significant differences at any paired pulse interval (**Figure 4C**). This indicated that PF-PC synapse exhibit similar degree and time course of facilitation between Z+ and Z− PCs (**Figure 4C**), suggesting that presynaptic mechanisms of PF-PC synapse were not much affected by the zebrin type of postsynaptic PCs.

Among the molecules that have expression pattern linked to the zebrin type, EAAT4, a glutamate transporter, is expressed in

PC dendritic spines, which form synaptic contact with PFs and are surrounded by astrocytes (Yamada et al., 1997; Dehnes et al., 1998; Lehre and Danbolt, 1998; Danbolt, 2001), and involved in the removal of low concentrations of glutamate (Takayasu et al., 2005). Therefore, we focused on the decay process of the EPSC of PF-PC synapse between Z+ and Z− PCs. We prepared two groups of different ages (P18–25 and P28–32) in another set of experiments of paired pulse stimulation of PFs (n = 8 Z+ and 8 Z− PCs at P18–25, n = 8 Z+ and 8 Z− PCs at P28–32), since EAAT expression level is dependent on postnatal date; effects of EAAT4 may be better observed at P28–32, when expression reaches the adult level, compared to P18–25, when it is still lower (Furuta et al., 1997). In this set of experiments, we did not observe significant differences in facilitation, i.e., the ratio of the amplitudes of EPSCs evoked by paired pulses with an interval of 100 ms, between Z+ and Z− PCs in the two age groups ($F_{(1,14)}$ = 0.03, p = 0.86; $F_{(1,14)}$ = 0.1, p = 0.76, one-way ANOVA respectively, **Figures 4E,H**). No significant difference was observed in "half decay time," time for the change of the amplitude from the peak to the half of the peak value, of the initial and second EPSC, between Z+ and Z− PCs in the two age groups ($F_{(1,14)}$ = 0.16, p = 0.7; $F_{(1,14)}$ = 0.06, p = 0.8, one-way ANOVA, respectively, **Figures 4F,I**). Finally, no significant difference was observed in "tail current ratio," the amplitude of EPSC 50 ms after the peak (**Figure 4D**; Takayasu et al., 2005), of the initial and second EPSC, between Z+ and Z− PCs in the two age groups ($F_{(1,14)}$ = 0.29, p = 0.60; $F_{(1,14)}$ = 0.77, p = 0.39; one-way ANOVA, respectively, **Figures 4G,J**). The results revealed that the different expression levels of EAAT4 between Z+ and Z− PCs do not affect the time course of PF-PC EPSC decay. This was against our original hypothesis that Z+ PCs might show faster EPSC decay because of higher expression of EAAT4, which uptakes low concentration glutamate (Takayasu et al., 2005).

Blocker of AMPAR Desensitization Did Not Distinguish PF-PC EPSCs Between Z+ and Z− PCs

To further examine possible EAAT4-dependent differences in PF-PC synaptic transmission between Z+ and Z− PCs, we added 100 μmol CTZ in the bath to reduce desensitization of AMPAR (Partin et al., 1994) in another set of experiments of paired pulse stimulation of PFs with slice cut from P28 to P32 mice (n = 9 Z+ and 9 Z− PCs). This condition was supposed to enable a sensitive detection of glutamate removal process in the PF-PC synapse, as observed with marked increase of EPSC tail current in EAAT4-deficient mice (Takayasu et al., 2005). Indeed, time course of the EPSC decay was significantly longer under CTZ application (half decay time about 30 ms) than in normal ACSF (about 9 ms, **Figures 4F,I**) both in Z+ and Z− PCs. The time course of decay of the second EPSC appeared slightly slower in Z+ PCs than Z− PCs (**Figure 5A**). However, statistical analysis showed no significant difference between them when the amplitude was compared at given times after the peak ($F_{(1,16)}$ = 1.09, p = 0.31; $F_{(1,16)}$ = 1.24, p = 0.28; $F_{(1,16)}$ = 1.99, p = 0.18; $F_{(1,16)}$ = 1.83, p = 0.19; $F_{(1,16)}$ = 2.16, p = 0.16; $F_{(1,16)}$ = 2.01, p = 0.17, one-way ANOVA, for 30, 50, 70, 80, 90, 100 ms after EPSC peak, respectively; **Figure 5C**). Half decay time measured in the second EPSC did not show significant difference between Z+ and Z− PCs, either ($F_{(1,16)}$ = 1.47, p = 0.24, one-way ANOVA, **Figure 5B**). The results further indicated that higher EAAT4 expression did not make EPSC decay faster in the PF-PC synapse in Z+ PCs.

DISCUSSION

The present study showed that there are no significant differences in input resistance, occurrence probability of types of firing patterns or in kinetics of PF-PC synaptic current between Z+ and Z− PCs in neighboring zebrin stripes in lobule VIII, in Aldoc-Venus mouse cerebellar slices. However, the intrinsic firing frequency of the tonic firing type was significantly higher in Z− negative PCs than Z+ PCs. The implications of the present results and possible functional significance of zebrin types in PCs are discussed.

Use of Aldoc-Venus Mice in Phenotype Study of Z+ and Z− PCs

Since many molecules are heterogeneously expressed in PC populations, it is an essential question what functional differences PC populations attain because of the heterogeneous molecular expression. However, this question is not simple to test, since the functional property of individual PCs is not solely dependent on their intrinsic molecular expression profiles but also on their cellular morphology, synaptic inputs from local circuits and afferent projections, and the environmental interaction between nearby extracellular and cellular components.

To address this question simply, we focused on a particular molecule, aldolase C or zebrin II, the expression pattern of which probably matches with the expression pattern of the largest number of other molecules. Aldoc-Venus mice facilitate a clear recognition of Z+ and Z− PCs, which are arranged in the longitudinal striped pattern at adult and at stages as early as the second postnatal week (Fujita et al., 2014).

By making slice preparations from Aldoc-Venus mice, we could sample identified Z+ and Z− PCs from identified stripes in an identified lobule. Lobule VIII, on which we focused in this study, contained a comparable number of Z+ and Z− PCs (**Figure 3**), different from lobules III or X. By sampling both Z+ and Z− PCs from neighboring stripes in lobule VIII, we eliminated the effects of environmental factors, if any. By using slice preparations, we excluded the effects of different inputs to Z+ and Z− PCs arising from climbing fibers. Thus, our preparation is better suited to detect electrophysiological properties that are directly related to the zebrin type of PCs than previously reported preparations.

Zebrin Type of PCs Is Linked to Some Aspects of Electrophysiological Excitability of PCs in Lobule VIII

Many types of heterogeneous electrophysiological properties have been reported among cerebellar PCs

(Cerminara et al., 2015). The main focus of this study was to clarify the properties that are tightly linked to the zebrin type of PCs.

Input resistance of PCs in lobules III-V is significantly higher than that of PCs in lobule X (Kim et al., 2012). This difference is even sharper when tonic firing PCs in these lobules are compared (Kim et al., 2012). Since the majority of PCs are Z− in lobules III-V while almost all PCs are Z+ in lobule X, their finding may suggest that Z− PCs have larger input resistance. However, the present results showed that the zebrin type of PCs was not tightly linked with different input resistances in lobule VIII, suggesting that differences in input resistance might reflect lobular organization and other factors. Recently, it has been reported that the morphology of PC dendritic arbor is significantly different among lobules and among locations in a lobule (Nedelescu et al., 2018). Such morphological differences may affect the PC input resistance rather than expression of molecules that is linked to the zebrin type.

PCs show different types of spiking activity in response to step-wise current injections (Kim et al., 2012). Two-thirds and one-third of PCs show tonic firing and complex bursting patterns in lobules III–V, while four groups of about one-fourth of PCs show tonic firing, complex bursting, initial bursting and gap firing patterns, respectively, in lobule X (Kim et al., 2012). Since the majority of PCs are Z− in lobules III-V while almost all PCs Z+ in lobule X, this difference may suggest that the occurrence probability of different spiking activity may be related to the zebrin type (Cerminara et al., 2015). However, the present results showed otherwise in lobule VIII. Although ionic conductance mechanisms that lead to the different spiking activity have not been fully understood, A-type K channels are responsible for the initial bursting response (Kim et al., 2012). However, we found that the firing frequency was higher in tonic firing type Z− PCs than in tonic firing type Z+ PCs. Although the underlying mechanisms for this difference is not clear, we speculate that some differences in expression level of voltage-dependent ion channels may be linked with the zebrin type of PCs. PC firing pattern is also related to intracellular Cl− concentration and expression of glutamate transporter, including EAAT4, which is highly expressed in Z+ PCs, that can affect intracellular Cl− concentration (Rabenstein et al., 2018). Our internal solution (K-gluconate-based solution) contained small fixed amounts of Cl−, which may have covered some effects mediated by Cl− between Z+ and Z− PCs.

Molecular Expression Differences in Zebrin Stripes Does Not Affect EPSC Kinetics in the PF-PC Synapse in Lobule VIII

In the present study, we made a systematic observation of PF-PC synaptic transmission between Z+ and Z− PCs in lobule VIII. A PF runs a few millimeters in the molecular layer. The experimental fact that the lateral spread of transverse beam activity evoked by PF stimulation to all parasagittal bands under suppression of inhibitory synaptic transmission (Gao et al., 2006) indicates that a PF makes synaptic contact to both Z+ and Z− PCs. Therefore, zebrin type-dependent electrophysiological differences in PF-PC synaptic transmission, if there are any, would be a result of the zebrin type-related property of postsynaptic PCs. On the contrary, zebrin type-dependent electrophysiological differences in climbing fiber-PC synaptic transmission may be a result of either different presynaptic property of climbing fibers (Paukert et al., 2010), since Z+ and Z− PCs are innervated by distinct population of climbing fibers (Voogd et al., 2003; Sugihara and Shinoda, 2004), or zebrin type-related property of postsynaptic PCs. Therefore, we are focused on the PF-PC synaptic transmission in the present study.

Among synaptic molecules, EAAT4 is expressed at a higher level in Z+ PCs than in Z− PCs, with a three-times difference in protein amount detected by gold particle counting in immunostaining under electron microscopy (Dehnes et al., 1998). EAAT4 expression is present in PCs at embryonic day 13 and increases to a maximum adult level at P26 in the mouse (Furuta et al., 1997; Yamada et al., 1997). EAAT4 is present in PCs at and around PF-PC and climbing fiber-PC synapses. It is located most densely at the side of the spine and on the dendritic membrane around the spine facing astrocytes or Bergmann glia, and less densely on the postsynaptic membrane of the spine (Dehnes et al., 1998; Danbolt, 2001). EAAT4 is involved in glutamate uptake from the extracellular cellular space (Takayasu et al., 2005) and glutamate-gated Cl− permeability (Fairman et al., 1995). In synaptic transmission, EAAT4 has been regarded to be responsible for the removal of low levels of glutamate that remains in the extrasynaptic region and hence for the time course of late decay of the EPSC (Takayasu et al., 2005).

In relation to the functional distinction between Z+ and Z− PCs, the properties of EAAT4 described above suggest that Z+ PCs may have faster decay of PC-PF EPSC, due to faster reuptake of glutamate from the synaptic cleft, than Z− PCs. However, kinetics of EPSC decay time course were not significantly different between Z+ and Z− PCs, in normal ACSF at P18–25, P28–32 and in ACSF with CTZ, a blocker of desensitization of AMPAR, at P28–32 in lobule VIII. These findings showed no evidence of faster glutamate removal or faster EPSC decay time course in Z+ PCs than in Z− PCs, even with the increased glutamate release by the paired stimulus and with the enhanced glutamate sensitivity of the glutamate receptor. This result generally agreed with that of Tsai et al. (2012), who have found similar release properties of PF-PC synapse in Z+ and Z− PCs and have concluded that the variation of endogenous EAAT4 expression does not alter the time course of EPSCs, presumably in lobules III and IV, although they have not explicitly identified the lobule. As a sole observed difference between Z+ and Z− PCs, Tsai et al. (2012) reported that the current required to evoke a half-maximum response was significantly greater in Z+ PCs with CTZ. We did not test half-maximum with CTZ response in the present study. As a whole, the results indicate that EAAT4-dependent clearance of glutamate occurs in a way that does not significantly affect the decay time course of EPSC in PF-PC synaptic activity in conjunct with other synaptic activity. Consequently, the results suggest that PF-PC synaptic transmission does not receive a crosstalk

from other PF-PC synapses (Lehre and Danbolt, 1998; Takayasu et al., 2005) through spill-over of glutamate in either Z+ or Z− PCs. Presumably, other glutamate transporters GLAST and GLT, which are expressed highly in astrocytes or Bergmann glia processes (Lehre and Danbolt, 1998) play the major role in the removal of glutamate in inconjunct PF-PC synaptic transmission. We speculate that the location of EAAT4 expression, mainly at the side of the dendritic spine facing astrocytes (Dehnes et al., 1998), is functionally too far to affect the glutamate level for AMPAR response in the PF-PC synapse. Our discussion above may be at variance with the results of *in vitro* experiments which showed a significant decrease in late EPSC amplitude of PF-PC synapse in EAAT4 knock-outs (Takayasu et al., 2005). This point may require further investigation concerning the localization of EAAT4, effects of its mutation, and intracellular storage (Dehnes et al., 1998) in a comparison between Z+ and Z− PCs.

Regarding the high affinity for glutamate by EAAT4 (Fairman et al., 1995), other functions may still be expected for the high EAAT4 expression in PF-PC synapse in Z+ PCs: (1) it may isolate the PF-PC synapse from spillover of glutamate released in other surrounding synapses, especially the climbing fiber-PC synapses (Szapiro and Barbour, 2007); (2) it may function as Cl− permeability (Fairman et al., 1995) that shunts inward current when it is exposed to spillover of glutamate; and (3) it may control extrasynaptic signaling to Bergmann glial cells (Tsai et al., 2012). Our recording condition was not tuned to detect Cl− permeability. Hence, further studies would be required to clarify these effects.

Possible Functional Significance of Zebrin Types in PCs

The present study showed that zebrin type was related with basic excitability of PCs to some extent, but not directly related with PF-PC synaptic transmission kinetics, in lobule VIII. The results suggest that the significantly higher simple spike firing frequency of Z− PCs relative to Z+ PCs, which has been observed in various cerebellar areas in *in vivo* preparation (Xiao et al., 2014; Zhou et al., 2014), may be partly because of the difference in intrinsic properties linked with the zebrin type. However, the other possibility such as different input patterns to Z− and Z+ PCs cannot be excluded. The present study did not cover differences in long term synaptic plasticities or inter-synaptic interactions between Z+ and Z− PCs, which remain to be clarified. Concerning interaction between the PF-CF synapse and the climbing fiber-PC synapse, the efficiency of occurrence of long term depression in the PF-PC synapse is dependent on zebrin types through EAAT4-dependent glutamate uptake (Wadiche and Jahr, 2005). Besides the long term depression, simple spike activity was modulated by occurrence of complex spikes and this modulation is larger in Z+ PCs than in Z− PCs (Tang et al., 2017). The mechanisms involved in this function are yet to be studied.

DATA AVAILABILITY

The raw data supporting the conclusions of this manuscript will be made available by the authors, without undue reservation, to any qualified researcher.

AUTHOR CONTRIBUTIONS

All authors had full access to all the data in the study and take responsibility for the integrity of the data and accuracy of the data analysis. VN-M and IS: study concept and design and critical revision of the manuscript for important intellectual content. VN-M: acquisition of data. VN-M, KT-A and IS: analysis and interpretation of data. VN-M, YL and IS: drafting of the manuscript.

FUNDING

This study was supported by Grant-in-Aid for Scientific Research (KAKENHI) from the Japan Society for the Promotion of Science (16K070025 to IS, and 18H06085 to YL). VN-M and KT-A are recipients of MEXT scholarship for foreign doctor course students.

ACKNOWLEDGMENTS

We thank Drs. Haruyuki Kamiya, Masashi Nagase, Fusao Kato, Taro Ishikawa and Moritoshi Hirono for their technical advice and experimental support, and Dr. Gideon Sarpong for proofreading the manuscript.

REFERENCES

Arata, A., and Ito, M. (2004). Purkinje cell functions in the *in vitro* cerebellum isolated from neonatal rats in a block with the pons and medulla. *Neurosci. Res.* 50, 361–367. doi: 10.1016/j.neures.2004.08.011

Brochu, G., Maler, L., and Hawkes, R. (1990). Zebrin II: a polypeptide antigen expressed selectively by Purkinje cells reveals compartments in rat and fish cerebellum. *J. Comp. Neurol.* 291, 538–552. doi: 10.1002/cne.902910405

Cerminara, N. L., Lang, E. J., Sillitoe, R. V., and Apps, R. (2015). Redefining the cerebellar cortex as an assembly of non-uniform Purkinje cell microcircuits. *Nat. Rev. Neurosci.* 16, 79–93. doi: 10.1038/nrn3886

Danbolt, N. C. (2001). Glutamate uptake. *Prog. Neurobiol.* 65, 1–105. doi: 10.1016/S0301-0082(00)00067-8

Dehnes, Y., Chaudhry, F. A., Ullensvang, K., Lehre, K. P., Storm-Mathisen, J., Danbolt, N. C., et al. (1998). The glutamate transporter EAAT4 in rat cerebellar Purkinje cells: a glutamate-gated chloride channel concentrated near the synapse in parts of the dendritic membrane facing astroglia. *J. Neurosci.* 18, 3606–3619. doi: 10.1523/JNEUROSCI.18-10-03606.1998

Fairman, W. A., Vandenberg, R. J., Arriza, J. L., Kavanaugh, M. P., and Amara, S. G. (1995). An excitatory amino-acid transporter with properties of a ligand-gated chloride channel. *Nature* 375, 599–603. doi: 10.1038/375599a0

Fujita, H., Aoki, H., Ajioka, I., Yamazaki, M., Abe, M., Oh-Nishi, A., et al. (2014). Detailed expression pattern of aldolase C (Aldoc) in the cerebellum, retina and other areas of the CNS studied in Aldoc-Venus knock-in mice. *PLoS One* 9:e86679. doi: 10.1371/journal.pone.0086679

Furuta, A., Rothstein, J. D., and Martin, L. J. (1997). Glutamate transporter protein subtypes are expressed differentially during rat CNS development.

J. Neurosci. 17, 8363–8375. doi: 10.1523/JNEUROSCI.17-21-08363.1997

Gao, W., Chen, G., Reinert, K. C., and Ebner, T. J. (2006). Cerebellar cortical molecular layer inhibition is organized in parasagittal zones. *J. Neurosci.* 26, 8377–8387. doi: 10.1523/JNEUROSCI.2434-06.2006

Hawkes, R. (2014). Purkinje cell stripes and long-term depression at the parallel fiber-Purkinje cell synapse. *Front. Syst. Neurosci.* 8:41. doi: 10.3389/fnsys.2014.00041

Hoxha, E., Tempia, F., Lippiello, P., and Miniaci, M. C. (2016). Modulation, plasticity and pathophysiology of the parallel fiber-Purkinje cell synapse. *Front. Synaptic Neurosci.* 8:35. doi: 10.3389/fnsyn.2016.00035

Ito, M. (2006). Cerebellar circuitry as a neuronal machine. *Prog. Neurobiol.* 78, 272–303. doi: 10.1016/j.pneurobio.2006.02.006

Ito, M. (2012). *The Cerebellum: Brain for An Implicit Self*. New Jersey, NJ: FT Press.

Kim, C. H., Oh, S. H., Lee, J. H., Chang, S. O., Kim, J., and Kim, S. J. (2012). Lobule-specific membrane excitability of cerebellar Purkinje cells. *J. Physiol.* 590, 273–288. doi: 10.1113/jphysiol.2011.221846

Lehre, K. P., and Danbolt, N. C. (1998). The number of glutamate transporter subtype molecules at glutamatergic synapses: chemical and stereological quantification in young adult rat brain. *J. Neurosci.* 18, 8751–8757. doi: 10.1523/JNEUROSCI.18-21-08751.1998

Nedelescu, H., Abdelhack, M., and Pritchard, A. T. (2018). Regional differences in Purkinje cell morphology in the cerebellar vermis of male mice. *J. Neurosci. Res.* 96, 1476–1489. doi: 10.1002/jnr.24206

Partin, K. M., Patneau, D. K., and Mayer, M. L. (1994). Cyclothiazide differentially modulates desensitization of α-amino-3-hydroxy-5-methyl-4-isoxazolepropionic acid receptor splice variants. *Mol. Pharmacol.* 46, 129–138.

Paukert, M., Huang, Y. H., Tanaka, K., Rothstein, J. D., and Bergles, D. E. (2010). Zones of enhanced glutamate release from climbing fibers in the mammalian cerebellum. *J. Neurosci.* 30, 7290–7299. doi: 10.1523/JNEUROSCI.5118-09.2010

Rabenstein, M., Peter, F., Rolfs, A., and Frech, M. (2018). Impact of reduced cerebellar EAAT expression on Purkinje cell firing pattern of NPC1-deficient mice. *Sci. Rep.* 8:3318. doi: 10.1038/s41598-018-21805-z

Roth, A., and Häusser, M. (2001). Compartmental models of rat cerebellar Purkinje cells based on simultaneous somatic and dendritic patch-clamp recordings. *J. Physiol.* 535, 445–472. doi: 10.1111/j.1469-7793.2001.00445.x

Ruigrok, T. J. (2011). Ins and outs of cerebellar modules. *Cerebellum* 10, 464–474. doi: 10.1007/s12311-010-0164-y

Sarpong, G. A., Vibulyaseck, S., Luo, Y., Biswas, M. S., Fujita, H., Hirano, S., et al. (2018). Cerebellar modules in the olivo-cortico-nuclear loop demarcated by pcdh10 expression in the adult mouse. *J. Comp. Neurol.* 526, 2406–2427. doi: 10.1002/cne.24499

Sugihara, I., and Quy, P. N. (2007). Identification of aldolase C compartments in the mouse cerebellar cortex by olivocerebellar labeling. *J. Comp. Neurol.* 500, 1076–1092. doi: 10.1002/cne.21219

Sugihara, I., and Shinoda, Y. (2004). Molecular, topographic, and functional organization of the cerebellar cortex: a study with combined aldolase C and olivocerebellar labeling. *J. Neurosci.* 24, 8771–8785. doi: 10.1523/JNEUROSCI.1961-04.2004

Sugihara, I., and Shinoda, Y. (2007). Molecular, topographic, and functional organization of the cerebellar nuclei: analysis by three-dimensional mapping of the olivonuclear projection and aldolase C labeling. *J. Neurosci.* 27, 9696–9710. doi: 10.1523/JNEUROSCI.1579-07.2007

Szapiro, G., and Barbour, B. (2007). Multiple climbing fibers signal to molecular layer interneurons exclusively via glutamate spillover. *Nat. Neurosci.* 10, 735–742. doi: 10.1038/nn1907

Takayasu, Y., Iino, M., Kakegawa, W., Maeno, H., Watase, K., Ozawa, S., et al. (2005). Differential roles of glial and neuronal glutamate transporters in Purkinje cell synapses. *J. Neurosci.* 25, 8788–8793. doi: 10.1523/JNEUROSCI.1020-05.2005

Tang, T., Xiao, J., Suh, C. Y., Burroughs, A., Cerminara, N. L., Jia, L., et al. (2017). Heterogeneity of Purkinje cell simple spike-complex spike interactions: zebrin- and non-zebrin-related variations. *J. Physiol.* 595, 5341–5357. doi: 10.1113/jp274252

Tsai, M. C., Tanaka, K., Overstreet-Wadiche, L., and Wadiche, J. I. (2012). Neuronal glutamate transporters regulate glial excitatory transmission. *J. Neurosci.* 32, 1528–1535. doi: 10.1523/JNEUROSCI.5232-11.2012

Voogd, J., Pardoe, J., Ruigrok, T. J., and Apps, R. (2003). The distribution of climbing and mossy fiber collateral branches from the copula pyramidis and the paramedian lobule: congruence of climbing fiber cortical zones and the pattern of zebrin banding within the rat cerebellum. *J. Neurosci.* 23, 4645–4656. doi: 10.1523/JNEUROSCI.23-11-04645.2003

Wadiche, J. I., and Jahr, C. E. (2005). Patterned expression of Purkinje cell glutamate transporters controls synaptic plasticity. *Nat. Neurosci.* 8, 1329–1334. doi: 10.1038/nn1539

Xiao, J., Cerminara, N. L., Kotsurovskyy, Y., Aoki, H., Burroughs, A., Wise, A. K., et al. (2014). Systematic regional variations in Purkinje cell spiking patterns. *PLoS One* 9:e105633. doi: 10.1371/journal.pone.0105633

Yamada, K., Wada, S., Watanabe, M., Tanakam, K., Wada, K., and Inoue, Y. (1997). Changes in expression and distribution of the glutamate transporter EAAT4 in developing mouse Purkinje cells. *Neurosci. Res.* 27, 191–198. doi: 10.1016/s0168-0102(96)01148-0

Zhou, H., Lin, Z., Voges, K., Ju, C., Gao, Z., Bosman, L. W., et al. (2014). Cerebellar modules operate at different frequencies. *Elife* 3:e02536. doi: 10.7554/elife.02536

Conflict of Interest Statement: The authors declare that the research was conducted in the absence of any commercial or financial relationships that could be construed as a potential conflict of interest.

frontiers in Cellular Neuroscience

ORIGINAL RESEARCH
published: 14 January 2019
doi: 10.3389/fncel.2018.00521

Chronic Ethanol Consumption Impairs the Tactile-Evoked Long-Term Depression at Cerebellar Molecular Layer Interneuron-Purkinje Cell Synapses *in vivo* in Mice

Da-Yong Li[1,2,3†], Yan-Hua Bing[1,4†], Chun-Ping Chu[1], Xun Cui[1], Song-Biao Cui[4], De-Lai Qiu[1,2] and Li-Da Su[5]**

[1]Key Laboratory of Cellular Function and Pharmacology of Jilin Province, Yanbian University, Yanji, China, [2]Department of Physiology and Pathophysiology, College of Medicine, Yanbian University, Yanji, China, [3]College of Basic Courses, Zhejiang Shuren University, Hangzhou, China, [4]Department of Neurology, Affiliated Hospital of Yanbian University, Yanji, China, [5]Neuroscience Care Unit, Second Affiliated Hospital of Zhe-Jiang University School of Medicine, Hangzhou, China

OPEN ACCESS

Edited by:
Jing-Ning Zhu,
State Key Laboratory of Pharmaceutical Biotechnology, School of Life Science, Nanjing University, China

Reviewed by:
Wei Lu,
Southeast University, China
Izumi Sugihara,
Tokyo Medical and Dental University, Japan

***Correspondence:**
De-Lai Qiu
dlqiu@ybu.edu.cn
Li-Da Su
sulida1001@zju.edu.cn

[†]These authors have contributed equally to this work

Received: 15 September 2018
Accepted: 13 December 2018
Published: 14 January 2019

Citation:
Li D-Y, Bing Y-H, Chu C-P, Cui X, Cui S-B, Qiu D-L and Su L-D (2019) Chronic Ethanol Consumption Impairs the Tactile-Evoked Long-Term Depression at Cerebellar Molecular Layer Interneuron-Purkinje Cell Synapses in vivo in Mice. Front. Cell. Neurosci. 12:521. doi: 10.3389/fncel.2018.00521

The cerebellum is sensitive to ethanol (EtOH) consumption. Chronic EtOH consumption impairs motor learning by modulating the cerebellar circuitry synaptic transmission and long-term plasticity. Under *in vitro* conditions, acute EtOH inhibits both parallel fiber (PF) and climbing fiber (CF) long-term depression (LTD). However, thus far it has not been investigated how chronic EtOH consumption affects sensory stimulation-evoked LTD at the molecular layer interneurons (MLIs) to the Purkinje cell (PC) synapses (MLI-PC LTD) in the cerebellar cortex of living animals. In this study, we investigated the effect of chronic EtOH consumption on facial stimulation-evoked MLI-PC LTD, using an electrophysiological technique as well as pharmacological methods, in urethane-anesthetized mice. Our results showed that facial stimulation induced MLI–PC LTD in the control mice, but it could not be induced in mice with chronic EtOH consumption (0.8 g/kg; 28 days). Blocking the cannabinoid type 1 (CB1) receptor activity with AM-251, prevented MLI-PC LTD in the control mice, but revealed a nitric oxide (NO)-dependent long-term potentiation (LTP) of MLI–PC synaptic transmission (MLI-PC LTP) in the EtOH consumption mice. Notably, with the application of a NO donor, S-nitroso-N-Acetyl-D, L-penicillamine (SNAP) alone prevented the induction of MLI–PC LTD, but a mixture of SNAP and AM-251 revealed an MLI-PC LTP in control mice. In contrast, inhibiting NO synthase (NOS) revealed the facial stimulation-induced MLI-PC LTD in EtOH consumption mice. These results indicate that long-term EtOH consumption can impair the sensory stimulation-induced MLI–PC LTD *via* the activation of a NO signaling pathway in the cerebellar cortex *in vivo* in mice. Our results suggest that the chronic EtOH exposure causes a deficit in the cerebellar motor learning function and may be involved in the impaired MLI–PC GABAergic synaptic plasticity.

Keywords: ethanol, cerebellar purkinje cell, molecular layer interneuron, sensory stimulation, plasticity, nitric oxide, *in vivo* cell-attached recording

INTRODUCTION

The cerebellum is an important organ controlling motor coordination, planning and fine regulating voluntary movement, and is also critical for cognitive functions, such as thought, behavior and emotion. The cerebellar cortex is composed of a molecular layer, a Purkinje cell (PC) layer and a granule layer, and these three layers mainly include PC, molecular layer interneurons (MLIs), granule cells (GCs) and Golgi cells (Palay and Chan-Palay, 1974). The PC is the focus of computation in the cerebellar cortex, receiving convergent projections from all other cortical neurons and providing the sole output from the cerebellar cortex to the deep cerebellar nuclei (Palay and Chan-Palay, 1974). The cerebellum is a target of the actions of ethanol (EtOH; Luo, 2012). EtOH consumption causes alterations of motor coordination, balance, behavior, speech, and certain cognitive functions. which are considered to be caused partly by impairment of cerebellar circuit functions and the modulation of synaptic transmissions (Schmahman and Sherman, 1997; Mameli et al., 2008). EtOH is known to enhance GABA–mediated synaptic transmission and to inhibit glutamatergic synaptic transmission (Lovinger, 1997; Woodward, 1999). It has been assumed that some of the behavioral actions of EtOH are mediated by enhancing the inhibitory action of GABA (Martz et al., 1983; Criswell and Breese, 2005; Weiner and Valenzuela, 2006; Botta et al., 2010). For instance, EtOH increases the frequency of miniature and spontaneous inhibitory postsynaptic currents at PCs and MLIs in rat cerebellar slices, *via* increasing the GABA release (Mameli et al., 2008; Hirono et al., 2009; Wadleigh and Valenzuela, 2012), and modulating facial stimulation-evoked GABAergic responses in the mouse cerebellar cortical molecular layer (Cui et al., 2014).

In cerebellar cortical circuits, long-term synaptic plasticity could be induced at the parallel fiber-PC (PF-PC), the PF-MLIs, mossy fiber-GC (MF-GC) and MLI-PC synapses under *in vitro* conditions, which has been proposed to provide a cellular mechanism for motor learning (Grasselli and Hansel, 2014). Both long-term potentiation (LTP) and long-term depression (LTD) of the PF-PC synapses have been demonstrated previously (Ito, 1989; D'Angelo et al., 2016; Hoxha et al., 2016). PF-PC LTD is the earliest characterized form of synaptic plasticity in the cerebellar cortex (Ito, 1989), while PF-PC LTP is latterly found and expressed both pre- and post-synoptically (Qiu and Knöpfel, 2007; Anggono and Huganir, 2012). Long-term synaptic plasticity has been induced by postsynaptic depolarization at MLI-PC synapses *via* activation of the cannabinoid type I receptor (CB1) and the N-methyl-D-aspartate (NMDA) receptor in cerebellar slices. The MLI-PC synaptic plasticity induced by excitatory inputs, express hetero-synoptically (Hirano, 2013; Hirano and Kawaguchi, 2014). However, there was no similar MLI-PC synaptic plasticity observed under *in vitro* conditions. The reason may be related to the difficulty of recording the electrical stimulation-evoked MLI-PC inhibitory postsynaptic currents in cerebellar slices. Therefore, MLI-PC synaptic plasticity induced by the MLIs inhibitory input is less known under *in vitro* conditions.

It has been reported that EtOH impaired long-term synaptic plasticity in the hippocampus (Zorumski et al., 2014) and the cerebellum (Chandler et al., 1998; Belmeguenai et al., 2008; Su et al., 2010; He et al., 2013). Administration of EtOH during standard stimulation inhibited both LTP and LTD in the CA1 region of a rat hippocampus (Izumi et al., 2005, 2007; Tokuda et al., 2011). The effects of EtOH on the hippocampal LTD were diminished by the blockade of NMDA receptors, while the effects of EtOH on the hippocampal LTP were involved in both NMDA receptors and GABAergic transmission (Izumi et al., 2007). Furthermore, chronic intermittent consumption of EtOH disrupts the NMDA receptor-associated post-synaptic proteins and specifically regulates group I mGlu receptor-dependent LTD in the mouse hippocampus (Wills et al., 2017). Moreover, chronic EtOH consumption induces a reduced-performance in a spatial recognition task in normal animals, but it attenuates spatial memory deficits and increases group I mGlu receptor expression in the rat hippocampus (Van Waes et al., 2009). In the cerebellum, it has been described that acute EtOH selectively blocked PF–LTD induction, whereas it did not change the amplitude of excitatory postsynaptic currents at the PF synapse *in vitro* in mice (Belmeguenai et al., 2008). Application of EtOH at a concentration of 50 mM inhibited LTD at the climbing fiber (CF) synapses onto PCs *via* inhibition of the NMDA receptors and the group I mGlu receptors (Carta et al., 2006; Belmeguenai et al., 2008; Su et al., 2010; He et al., 2013). However, it has been suggested that acute EtOH also impaired the induction of LTP, possibly through several other mechanisms that include the inhibition of the group I mGlu receptor-mediated potentiation of the NMDA receptor function and of the evoked dopamine release in the mouse nucleus accumbens (Mishra et al., 2012). Chronic EtOH exposure significantly reduced simple and complex spike frequencies of PCs, resulting in a depression of cerebellar motor coordination and ataxia in mice (Servais et al., 2005).

In addition, systemic administrations of EtOH resulted in a dose-dependent increase in nitric oxide (NO) levels, which was attenuated by the NO synthase (NOS) inhibitor, indicating that systemic administration of EtOH increased brain NO levels (Finnerty et al., 2015). Acute treatment with EtOH increased NOS activity and NO production in brain memory related regions, such as the prefrontal cortex, amygdala and the hippocampus in adult mice (Yu et al., 2013). Recently, it has been demonstrated that EtOH caused an increase in the level of glutamate, NO, and GABA in the rostral ventrolateral medulla during the hypotensive responses, suggesting that EtOH enhanced glutamatergic NMDA receptors /NO/GABA pathways in the rostral ventrolateral medulla and may participate in the hypotensive effects induced by acute administration of EtOH (Lo et al., 2018). NO also has been involved in cerebellar cortical PF-PC presynaptic LTP under *in vitro* (Qiu and Knöpfel, 2007) and *in vivo* conditions (Chu et al., 2014).

We previously found that facial stimulation evoked strong MLI-PC synaptic transmission *in vivo* in mice (Chu et al., 2011a,b, 2012). The facial stimulation evoked spike firing in MLIs, resulting in an inhibitory response in cerebellar PCs *via* a MF-GC pathway, but did not evoke complex spikes in

PCs *via* CFs. The facial stimulation evoked a simple spike firing in PCs only in the presence of the $GABA_A$ receptors antagonist (Chu et al., 2012). Furthermore, we found that facial stimulation induced LTD at MLI-PC synapses (MLI-PC LTD), accompanied with a decrease in the stimulation-evoked pause of spike firing in PCs *via* activation of NMDA receptors in the mouse cerebellar cortex, suggesting that sensory stimulation evoked MLI-PC GABAergic synaptic plasticity may play a critical role in motor learning of living animals (Bing et al., 2015). Moreover, acute application of EtOH inhibits the facial stimulation evoked MLI-PC synaptic transmission (Cui et al., 2014), and significantly depresses the MLI-PC synaptic transmission by activating presynaptic cannabinoid receptors *via* the protein kinase signaling pathway, suggesting that EtOH modulates GABA release from MLIs onto PCs (Wu et al., 2016). Our previous studies suggest that the cerebellar MLI-PC synapse is a target of EtOH, and EtOH consumption may impair the MLI-PC synaptic plasticity.

Altogether, EtOH exposure impaired long-term synaptic plasticity at PF-PC and CF-PC synapses in the cerebellar cortex, have been demonstrated under *in vitro* conditions. However, the effects of chronic EtOH exposure on the sensory stimulation-evoked MLI-PC LTD in the cerebellar cortex of living animals, are currently unknown. Therefore, we investigated the effects of chronic EtOH consumption on facial stimulation-evoked MLI-PC LTD, using electrophysiological techniques and pharmacological methods in urethane-anesthetized mice.

MATERIALS AND METHODS

Animals

A total of 56 (5-week-old) HA/ICR mice were used in this study. The mice were divided into the EtOH consumption group (29 mice) and the control group (27 mice). The experimental procedures were approved by the Animal Care and Use Committee of the Yanbian University and were in accordance with the animal welfare guidelines of the U.S. National Institutes of Health. The permit number is SYXK (Ji) 2011-006. All animals were housed under a 12-h light: 12-h dark cycle with free access to food and water in a colony room under constant temperature (23 ± 1°C) and humidity (50 ± 5%). Mice in the EtOH consumption group were intraperitoneally (i.p.) injected with EtOH (0.8 g/kg; 15% in saline), while mice in the control group were i.p. injected with the same volume of saline. The EtOH (95%) was diluted in saline for a final concentration of 15%. The electrophysiological recordings were performed after the i.p. injection of EtOH, for 28 days.

Anesthesia and Surgical Procedures

The anesthetic and surgical procedures have been described previously (Chu et al., 2011a,b). The mice were anesthetized with urethane (1.3 g/kg body weight, i.p.), and were tracheotomized to avoid respiratory obstruction. On a custom-made stereotaxic frame, soft tissue was retracted to gain access to the dorsal portion of the occipital bone. A watertight chamber was created and a 1–1.5 mm craniotomy was drilled to expose the cerebellar surface corresponding to Crus II. The brain surface was constantly superfused with oxygenated artificial cerebrospinal fluid (ACSF: 125 mM NaCl, 3 mM KCl, 1 mM $MgSO_4$, 2 mM $CaCl_2$, 1 mM NaH_2PO_4, 25 mM $NaHCO_3$, and 10 mM D-glucose) with a peristaltic pump (Gilson Minipulse 3; Villiers, Le Bel, France) at 0.4 ml/min. Rectal temperature was monitored and maintained at 37.0 ± 0.2°C using body temperature equipment.

Cell-Attached Recording and Facial Stimulation

Cell-attached recordings from cerebellar PCs were performed with an Axopatch-200B amplifier (Molecular Devices, Foster City, CA, USA). The signals of PC cell-attached recordings were acquired through a Digidata 1440 series analog-to-digital interface on a personal computer using Clampex 10.3 software (Molecular Devices). Patch pipettes were made with a puller (PB-10; Narishige, Tokyo, Japan) from thick-wall borosilicate glass (GD-1.5; Narishige). Recording electrodes were filled with ACSF, with a resistances of 3–5 MΩ. The cell-attached recordings from PCs were performed at depths of 200–300 μm under the pia mater membrane, and were identified by regular spontaneous simple spikes (SS) accompanied with irregular complex spikes.

Facial stimulation was performed by air-puff (10 ms, 60 psi) of the ipsilateral whisker pad through a 12-gauge stainless steel tube connected with a pressurized injection system (Picospritzer® III; Parker Hannifin Co., Pine Brook, NJ, USA). The air-puff stimuli were controlled by a personal computer, and were synchronized with the electrophysiological recordings and delivered at 0.05 Hz *via* a Master 8 controller (A.M.P.I., Jerusalem, Israel) and Clampex 10.3 software. The facial stimulation-evoked MLI–PC synaptic response has been demonstrated in our previous studies (Chu et al., 2011b; Bing et al., 2015), the response is expressed as a sequence of negative components (N1) followed by a positive component (P1) accompanied with a pause of SS firing (**Figure 1A**). N1 is identified as parallel fiber volley, while P1 is identified as MLI-PC synaptic transmission evoked by the facial stimulation through the MF-GC pathway (Chu et al., 2011b). For induction of MLI-PC synaptic plasticity, air-puff stimulation (10 ms, 60 psi; 240 pulses, 1 Hz) was delivered 10 min after the recording became stable.

Chemicals

The reagents, which included N-(piperidin-1-yl)-5-(4-iodophenyl)-1-(2,4-di-chlorophenyl)-4-methyl-1H-pyrazole-3-carboxamide (AM251), CB1 receptors antagonist; N^G-Nitro-L-arginine (L-NNA), NOS inhibitor; S-nitroso-N-Acetyl-D, L-penicillamine (SNAP), and NO donor. All chemicals were purchased from Sigma-Aldrich (Shanghai, China). For experiments with L-NNA and SNAP, the cerebellar surface was perfused with 200 μM L-NNA and 100 μM SNAP for 1 h before recordings were started, respectively. The drugs were dissolved in ACSF, and applied directly onto the cerebellar surface by a peristaltic pump (0.5 ml/min).

Data Analysis

The electrophysiological data were analyzed using Clampfit 10.3 software (Molecular Devices, Foster City, CA, USA). The

amplitude of P1 before and after 1 Hz facial stimulation was normalized by the mean value of the baseline. Values are expressed as the mean ± SEM. One-way analyses of variance (ANOVA; *post hoc* multiple comparison) and two-way ANOVA (SPSS Software) was used to determine the level of statistical significance among the groups of data. *P*-values below 0.05 were considered statistically significant.

RESULTS

Effect of Chronic EtOH Consumption on Facial Stimulation Induced MLI-PC LTD in the Cerebellar Cortex

Air-puff stimulation on the ipsilateral whisker pad (10 ms; 60 psi) evoked an inhibitory component (P1) followed by a pause of SS firing (**Figure 1A**). The mean latency of N1 was 16.4 ± 0.22 ms, while the mean latency of P1 was 19.1 ± 0.34 ms (n = 27 control mice). Application of the GABAA receptors antagonist, Gabazine (50 μM) abolished P1 and revealed the facial stimulation-evoked action potentials (**Figure 1B**). According to our previous studies (Chu et al., 2011b, 2012), P1 is identified as MLI-PC GABAergic synaptic transmission onto cerebellar PCs. Consistent with our previous study (Bing et al., 2015), facial stimulation at 1 Hz (240 pulses) produced an MLI-PC LTD, which was expressed as a decrease in P1 amplitude and a pause of SS for over 50 min in control mice (**Figures 2A,B**). The normalized amplitude of P1 was decreased to 75.5 ± 7.2% of the baseline for 40–50 min after 1 Hz facial stimulation (P < 0.05, n = 8, **Figure 2C**). The normalized value of the SS pause, at 40–50 min after 1 Hz facial stimulation, was decreased to 71.2 ± 7.6% of the baseline (100.0 ± 7.1%; P < 0.05, n = 7, **Figure 2D**). These results indicate that 1 Hz facial stimulation induces MLI-PC LTD in the cerebellar cortex of control mice.

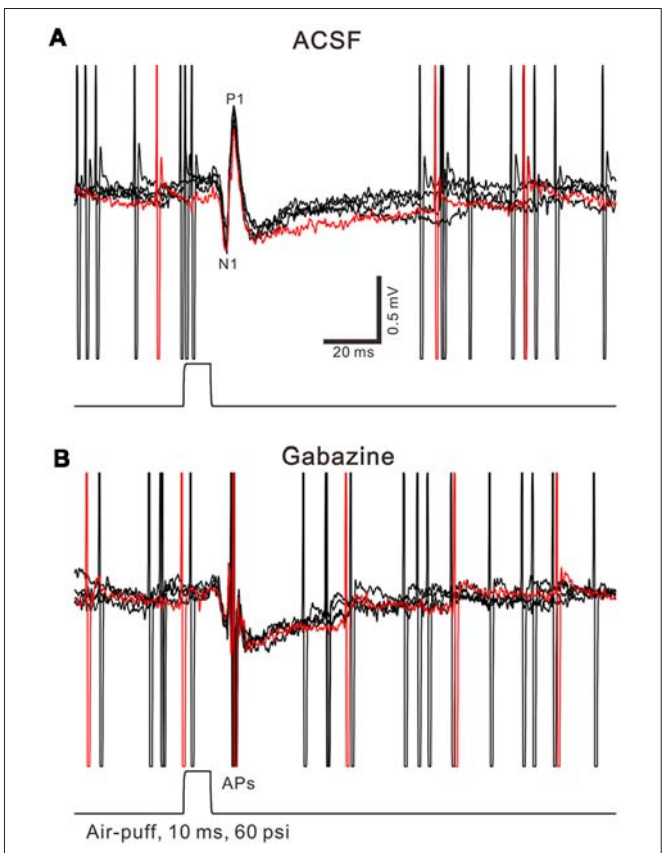

FIGURE 1 | Property of facial stimulation-evoked responses in cerebellar Purkinje cells (PCs). **(A)** Under cell-attached recording conditions (current-clamp mode; I = 0 pA), superposition of five sweeps shows a cerebellar PC in response to the tactile stimulation (bar, 10 ms) in artificial cerebrospinal fluid (ACSF). **(B)** The superposition of five sweeps shows the PC in response to the tactile stimulation (bar, 10 ms) in the presence of gabazine (50 μM). APs denote action potentials.

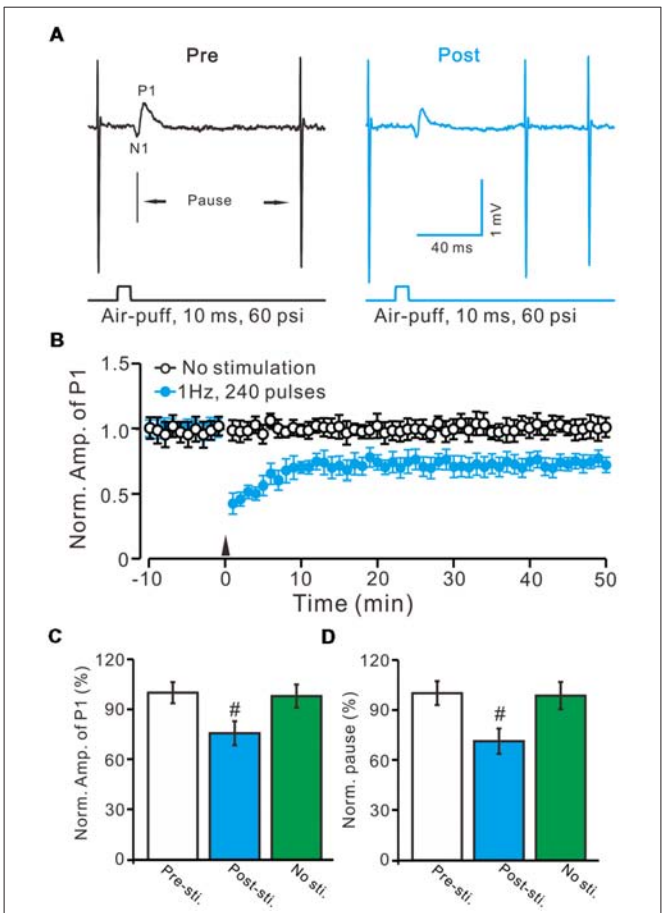

FIGURE 2 | Facial stimulation at 1 Hz induces molecular layer interneuron-PC long-term depression (MLI-PC) LTD in the cerebellar cortex of control mice. **(A)** Representative cell-attached recording traces, showing air-puff stimulation (10 ms, 60 psi)-evoked responses in a cerebellar PC before (Pre) and after (post) delivering 1 Hz (240 pulses) stimulation. **(B)** Summary of the normalized positive component (P1) amplitude under control conditions (No stimulation, open circle; n = 8 mice) and delivery of 1 Hz facial stimulation (arrow head; filled circles; n = 8 mice). **(C)** Bar graph (n = 8 mice) showing the normalized amplitude of P1 before (Pre sti.) and after (Post sti.) delivery of 1 Hz stimulation and no stimulation (No sti). **(D)** Summary of data (n = 8 mice) showing the normalized pause of a simple spike firing before (Pre sti.) and after (Post sti.) delivery of 1 Hz stimulation and no stimulation (No sti.). Note that facial stimulation at 1 Hz induced MLI-PC LTD in mouse cerebellar cortex. Data points are mean ± SEM. $^{\#}P$ < 0.05 vs. baseline (Pre-sti.).

Acute EtOH impairs long-term synaptic plasticity at PF-PC synapses (Belmeguenai et al., 2008; Su et al., 2010) and CF-PC synapses (He et al., 2013) have been described in rodent cerebellar slices, suggesting that long-term EtOH consumption might impair MLI-PC synaptic plasticity *in vivo* in mice. EtOH consumption for 28 days with facial stimulation at 1 Hz (240 pulses) failed to produce an MLI-PC LTD in the cerebellar cortex of mice (**Figures 3A,B**). The normalized amplitude of P1 was 97.6 ± 7.8% of the baseline for 40–50 min after 1 Hz facial stimulation ($P > 0.05$, $n = 7$, **Figure 3C**). The normalized value of the SS pause, at 40–50 min after 1 Hz facial stimulation was 95.2 ± 8.1% of the baseline (100.0 ± 6.7%; $P > 0.05$, $n = 7$, **Figure 3D**). These results indicate that 1 Hz facial stimulation fails to induce MLI-PC LTD in chronic EtOH consumption mice, suggesting that long-term consumption of EtOH impairs MLI-PC LTD *in vivo* in mice.

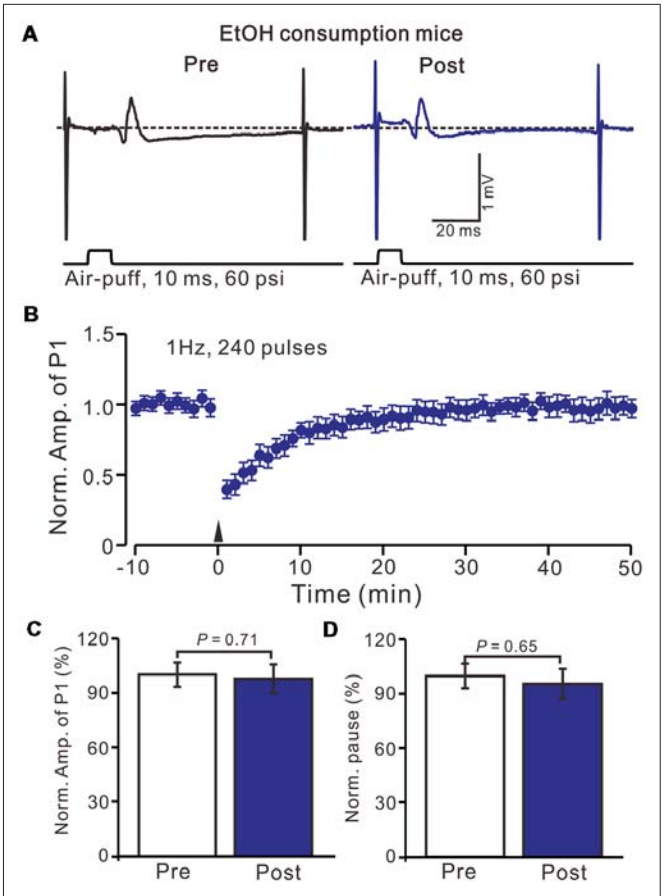

FIGURE 3 | Facial stimulation at 1 Hz failed to induce MLI-PC LTD in ethanol (EtOH) consumption mice. **(A)** Representative traces showing air-puff stimulation (10 ms, 60 psi)-evoked responses in a PC from an EtOH consumption mouse before (left) and after delivering 1 Hz stimulation. **(B)** Summary of the normalized P1 amplitude under delivery of 1 Hz facial stimulation (arrow head; $n = 8$ mice). **(C)** Bar graph ($n = 8$ mice) showing the normalized amplitude of P1 before (Pre) and after (Post) delivery of 1 Hz stimulation. **(D)** Summary of data ($n = 8$ mice) showing the normalized pause of a simple spike firing before (Pre) and after (Post) delivery of 1 Hz stimulation. Note that air-puff stimulation at 1 Hz failed to induce MLI-PC LTD in EtOH consumption mice. Data points are mean ± SEM.

MLI-PC LTD Is Dependent on CB1 Receptors Activity

In the cerebellar cortex, trains of PF stimulation can induce endocannabinoid (eCB) generation and release from PCs and MLIs through the activation of group I mGuR and NMDA receptors (Brown et al., 2003; Beierlein and Regehr, 2006; Soler-Llavina and Sabatini, 2006), which are considered to be involved in PF–PC presynaptic plasticity (Qiu and Knöpfel, 2009; Chu et al., 2014) and MLI–PC LTD (Bing et al., 2015). Therefore, we examined the effect of the CB1 receptor antagonist on the induction of 1 Hz facial stimulation-induced MLI-PC LTD in both the control mice and EtOH consumption mice. Blocking CB1 receptor activity with AM251, completely prevented the 1 Hz facial stimulation induced MLI–PC LTD in control mice. However, by blocking the CB1 receptors activity, facial stimulation induced a LTP of MLI-PC synaptic transmission (MLI-PC LTP) in EtOH consumption mice (**Figures 4A,B**). In the presence of AM251, the mean amplitude of P1 was 116.1 ± 7.8% ($n = 7$) of the baseline (100 ± 6.3%; **Figures 3A,C**; $P = 0.03$; $n = 7$) at 40–50 min after the trains of 1 Hz facial stimulation was delivered in the EtOH consumption mice. The mean normalized amplitude of P1 was significantly higher than that in the control mice (98.6 ± 6.1%; $n = 8$; **Figures 4A,C**; $P = 0.04$). Moreover, the mean pause of SS firing was 123.3 ± 8.4% ($n = 7$) of the baseline (100 ± 6.3%; **Figures 4A,D**; $P = 0.02$) at 40–50 min after the trains of 1 Hz facial stimulation was delivered in the EtOH consumption mice, which was significantly longer than that in the control mice (99.6 ± 6.5%; $n = 8$; **Figures 4A,D**; $P = 0.03$). These results indicate that by blocking the CB1 receptors activity, facial stimulation fails to induce MLI-PC LTD in control mice, but induces MLI-PC LTP in EtOH consumption mice.

NO Involves in the Facial Stimulation Induced MLI-PC Plasticity in EtOH Consumption Mice

We previously demonstrated that 4 Hz PF stimulation induced-PF-PC presynaptic LTP required activation of NOS under *in vitro* (Qiu and Knöpfel, 2007) and *in vivo* conditions (Chu et al., 2014), suggesting that NOS might be involved in the facial stimulation induced MLI-PC LTD under *in vivo* conditions. We then examined 1 Hz facial stimulation induced MLI-PC plasticity, in the presence of an NOS inhibitor, L-NNA (100 μM), in EtOH consumption mice. After the perfusion of L-NNA for 1 h, the 1 Hz facial stimulation induced MLI–PC LTD in EtOH consumption mice (**Figures 5A,B**). The mean amplitude of P1 was 76.8 ± 7.2% ($n = 7$) of the baseline (100 ± 6.2%; **Figure 5C**; $P = 0.032$; $n = 7$) at 40–50 min after the trains of 1 Hz facial stimulation were delivered in the EtOH consumption mice. The mean pause of SS firing was 77.2 ± 7.1% ($n = 7$) of the baseline (100 ± 5.6%; **Figures 5A,D**; $P = 0.036$) at 40–50 min after the trains of 1 Hz facial stimulation were delivered in the EtOH consumption mice. These results indicate that facial stimulation induces MLI-PC LTD in EtOH consumption mice when NOS is inhibited.

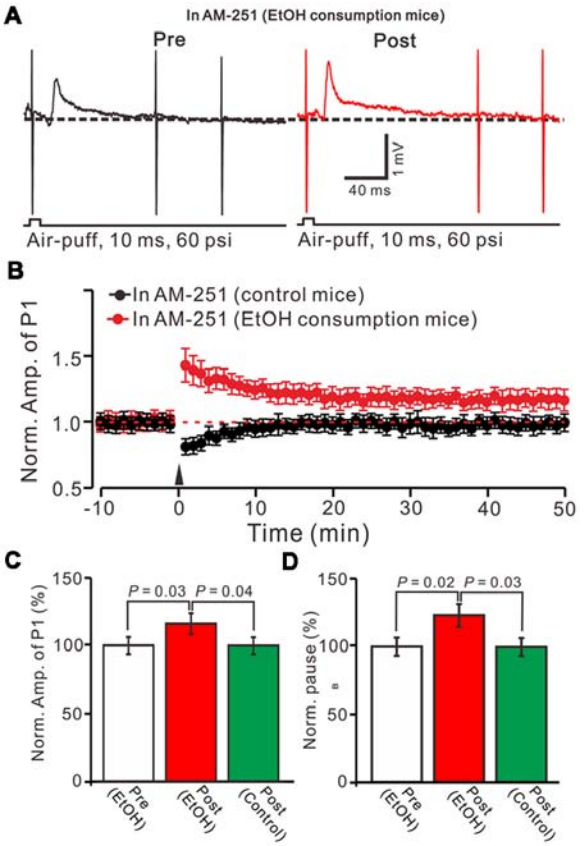

FIGURE 4 | Blocking cannabinoid type 1 (CB1) receptors activity, facial stimulation failed to induce MLI-PC LTD in control mice, but induced MLI-PC long-term potentiation (LTP) in EtOH consumption mice. **(A)** Representative cell-attached recording traces showing air-puff stimulation (10 ms, 60 psi)-evoked responses in a cerebellar PC from an EtOH consumption mouse before (left) and after delivering 1 Hz (240 pulses) stimulation in the presence of a CB1 antagonist, AM251 (5 μM). **(B)** Summary of the normalized P1 amplitude after delivery of 1 Hz facial stimulation (arrow head) in control mice (black; $n = 7$ mice) and EtOH consumption mice (Red; $n = 7$). **(C)** Bar graph ($n = 7$ mice) showing the normalized amplitude of P1 before (Pre EtOH) and after (Post, EtOH; Post control) delivery of 1 Hz stimulation in EtOH consumption and control mice. **(D)** Summary of data ($n = 7$ mice) showing the normalized pause of a simple spike firing before and after delivery of 1 Hz stimulation in EtOH consumption and control mice. Note that blocking by CB1 receptor activity, facial stimulation failed to induce MLI-PC LTD in control mice, but induced MLI-PC LTP in EtOH consumption mice.

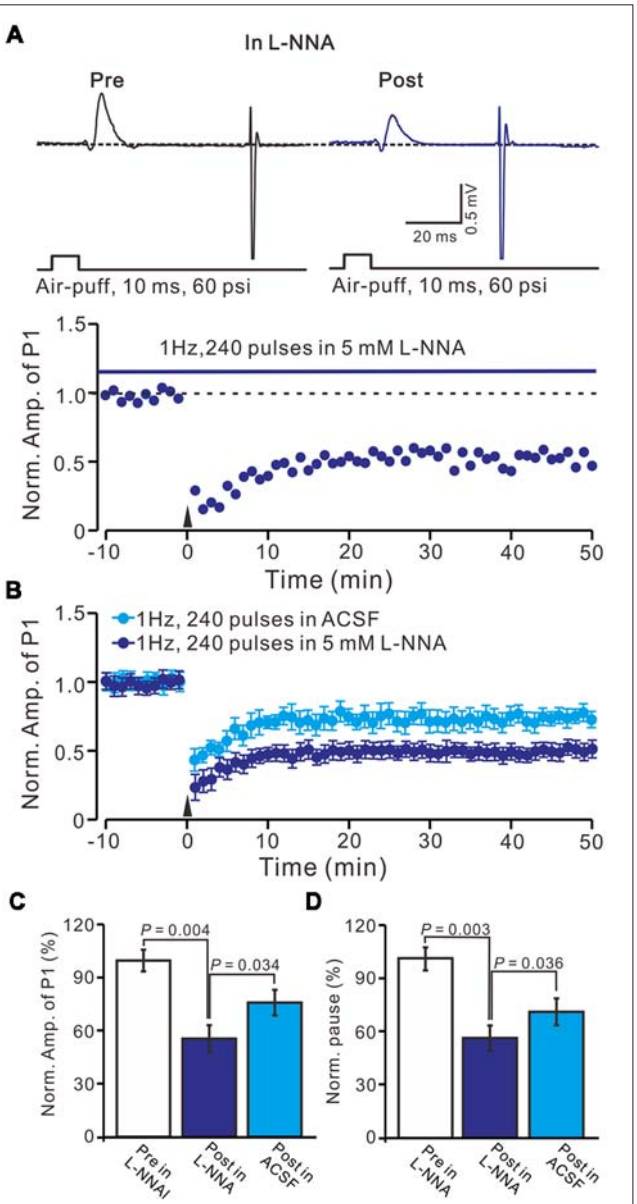

FIGURE 5 | Inhibition of nitric oxide synthase (NOS), facial stimulation induced MLI-PC LTD in EtOH consumption mice. **(A)** In the presence of the NOS inhibitor, representative traces showing air-puff stimulation (10 ms, 60 psi) evoked responses in a cerebellar PC from an EtOH consumption mouse before (Pre) and after (Post) delivering 1 Hz (240 pulses) stimulation. **(B)** Summary of the normalized P1 amplitude after delivery of 1 Hz facial stimulation (arrow head) in treatment with ACSF (blue) and the NOS inhibitor (purple; $n = 7$ mice). **(C)** Bar graph ($n = 7$ mice) showing the normalized amplitude of P1 before (Pre) and after (Post) delivery of 1 Hz stimulation. **(D)** Summary of data ($n = 7$ mice) showing the normalized pause of a simple spike firing before (Pre) and after (Post) delivery of 1 Hz stimulation. Note that at the inhibition of NOS, facial stimulation induced MLI-PC LTD, in EtOH consumption mice.

Furthermore, we examined the effect of the NO donor on facial stimulation induced MLI-PC LTD in control mice. As shown in **Figure 5**, after the perfusion of SNAP (100 μM) for 1 h, delivery of 1 Hz facial stimulation failed to induce MLI-PC LTD in control mice (**Figures 6A,B**). The mean amplitude of P1 was 103.6 ± 8.1% of the baseline (100 ± 5.6%; **Figure 6C**; $P = 0.67$; $n = 7$) at 40–50 min after the trains of facial stimulation was delivered in control mice. The mean pause of SS firing was 104.4 ± 8.4% of the baseline (100 ± 7.9%; **Figures 6A,D**; $P = 0.62$) at 40–50 min after the trains of facial stimulation were delivered in the control mice. These results indicate that application of the NO donor prevents the MLI-PC LTD in control mice.

We then observed the facial stimulation induced MLI-PC LTD, in the presence of the NO donor and the CB1 receptor blockers, in control mice. In the presence of SNAP and AM-251, 1 Hz facial stimulation induced MLI-PC LTP in control mice

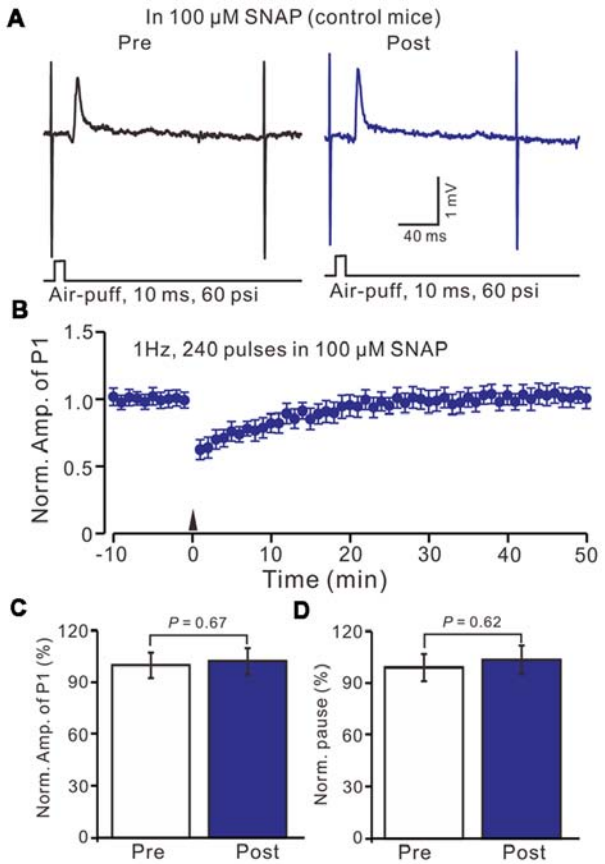

FIGURE 6 | In the presence of NO donor, S-nitroso-N-Acetyl-D, L-penicillamine (SNAP; 100 μM), facial stimulation failed to induce MLI-PC LTD in control mice. **(A)** In the presence of the NO donor, representative traces showing air-puff stimulation (10 ms, 60 psi) evoked responses in a cerebellar PC from a control mouse before and after delivering 1 Hz stimulation. **(B)** Summary of the normalized P1 amplitude after delivery of 1 Hz facial stimulation (arrow head) in the presence of the NO donor in control mice (n = 7 mice). **(C)** Bar graph (n = 7 mice) showing the normalized amplitude of P1 before (Pre) and after (Post) delivery of 1 Hz stimulation. **(D)** Summary of data (n = 7 mice) showing the normalized pause of a simple spike firing before (Pre) and after (Post) delivery of 1 Hz stimulation. Note that in the presence of the NO donor, facial stimulation failed to induce MLI-PC LTD in control mice.

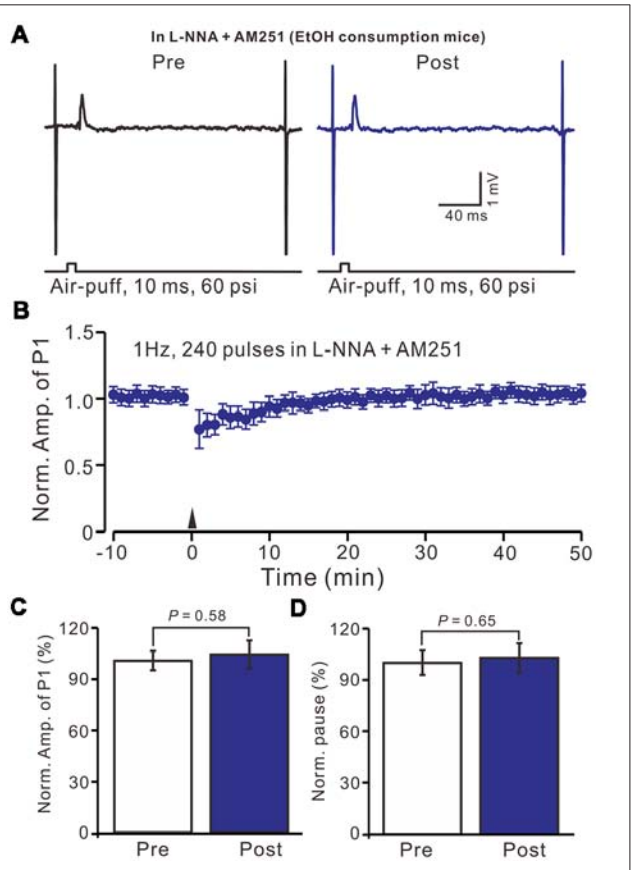

FIGURE 7 | In the presence of the NO donor, SNAP (100 μM) and the CB1 receptor blocker, AM-251 (5 μM), facial stimulation induced MLI-PC LTP in control mice. **(A)** In the presence of SNAP and AM-251, representative traces showing air-puff stimulation (10 ms, 60 psi) evoked responses a cerebellar PC from a control mouse before and after delivering 1 Hz stimulation. **(B)** Summary of the normalized P1 amplitude after delivery of 1 Hz facial stimulation (arrow head) in the presence of SNAP and AM-251 in control mice (n = 6 mice). **(C)** Bar graph (n = 6 mice) showing the normalized amplitude of P1 before (Pre) and after (Post) delivery of 1 Hz stimulation. **(D)** Summary of data (n = 6 mice) showing the normalized pause of a simple spike firing before (Pre) and after (Post) delivery of 1 Hz stimulation. Note that in the presence of SNAP and AM-251, facial stimulation induced MLI-PC LTP in control mice.

(**Figures 7A,B**). The mean amplitude of P1 was 114.6 ± 7.5% of the baseline (100 ± 8.2%; **Figure 7C**; P = 0.038; n = 6) at 40–50 min after 1 Hz facial stimulation. The mean pause of SS firing was 125.6 ± 9.3% of the baseline (100 ± 8.3%; **Figures 7A,D**; P = 0.024) at 40–50 min after 1 Hz facial stimulation in control mice. These results indicate that in the co-application of the NO donor and the CB1 receptor blockers, 1 Hz facial stimulation induces MLI-PC LTP rather than MLI-PC LTD, in control mice.

Moreover, we tested the facial stimulation induced MLI-PC LTD in the presence of the NOS inhibitor and the CB1 receptor blockers in EtOH consumption mice. In the presence of the NOS inhibitor and the CB1 receptor blockers, 1 Hz facial stimulation induced neither MLI-PC LTP nor MLI-PC LTD in EtOH consumption mice (**Figures 8A,B**). The mean amplitude of P1 was 102.3 ± 5.2% of the baseline (100 ± 7.3%; **Figure 8C**; P = 0.58; n = 7) at 40–50 min after the trains of 1 Hz facial stimulation were delivered in the EtOH consumption mice. The mean pause of SS firing was 103.1 ± 6.5% of the baseline (100 ± 7.6%; **Figures 8A,D**; P = 0.65) at 40–50 min after the facial stimulation were delivered in the EtOH consumption mice. These results indicate that inhibition of NOS and CB1 receptors activity, facial stimulation induces neither MLI-PC LTD nor MLI-PC LTP in EtOH consumption mice.

We also studied the effects of acute EtOH consumption on facial stimulation-induced MLI-PC synaptic plasticity. We found that acute EtOH consumption (1.6 g/kg) completely prevented MLI-PC LTD. However, by blocking CB1 receptor activity, neither MLI-PC LTD nor MLI-PC LTP was induced in acute EtOH consumption mice (not shown). These results indicated

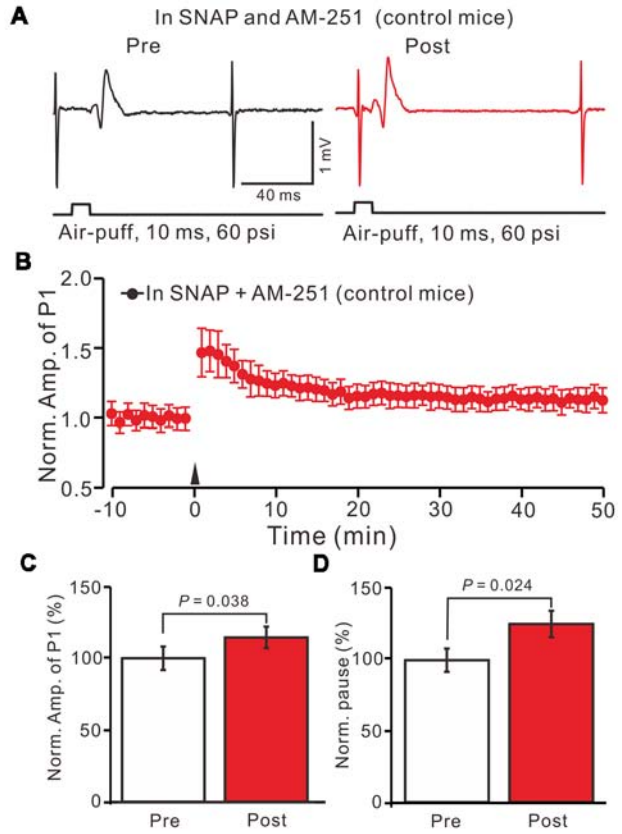

FIGURE 8 | Inhibition of NOS and CB1 receptor activity, facial stimulation induced neither LTD nor LTP at MLI-PC synapses in EtOH consumption mice. **(A)** In the presence of the NOS inhibitor and the CB1 receptor blocker, representative traces showing air-puff stimulation (10 ms, 60 psi)-evoked responses in a cerebellar PC of EtOH consumption mice before (left) and after delivering 1 Hz stimulation. **(B)** Summary of the normalized P1 amplitude after delivery of 1 Hz facial stimulation (arrow head) in EtOH consumption mice (n = 7 mice). **(C)** Bar graph (n = 7 mice) showing the normalized amplitude of P1 before and after delivery of 1 Hz stimulation in EtOH consumption mice. **(D)** Summary of data (n = 7 mice) showing the normalized pause of a simple spike firing before and after delivery of 1 Hz stimulation in EtOH consumption. Note that at the inhibition of NOS and CB1 receptor activity, facial stimulation failed to induce MLI-PC LTD/LTP in EtOH consumption mice.

that acute EtOH consumption blocked MLI-PC LTD, was mainly related to the CB1 receptor *in vivo* in mice.

DISCUSSION

EtOH consumption causes alterations of motor coordination and learning, balance, behavior, speech, and certain cognitive functions which are considered to be caused partly by the impairment of the cerebellar circuit function. The main finding of this study is that facial stimulation induced MLI-PC LTD in control mice, but not in EtOH consumption mice. However, inhibition of NOS revealed a facial stimulation induced MLI-PC LTD, while blocking CB1 receptor activity uncovered a NO dependent MLI-PC LTP in EtOH consumption mice. Our results indicate that long-term EtOH consumption impairs the sensory stimulation-induced MLI–PC LTD *via* the activation of the NO signaling pathway in the cerebellar cortical Crus II *in vivo* in mice.

EtOH Impairs the Facial Stimulation-Induced MLI-PC LTD *in vivo* in Mice

Cerebellar long-term synaptic plasticity has been proposed as a cellular mechanism for motor learning, which has been widely studied under *in vitro* conditions (Grasselli and Hansel, 2014). We previously found that facial stimulation at 1 Hz induced MLI-PC LTD *via* the activation of the NMDA receptor in a mouse cerebellar cortical Crus II, suggesting that the sensory stimulation evoked MLI-PC LTD, might contribute to motor learning in living animals (Bing et al., 2015). In this study, we showed that facial stimulation at 1 Hz induced MLI-PC LTD in control mice, but it failed to induce MLI-PC LTD in chronic EtOH consumption mice, suggesting that long-term consumption of EtOH impaired MLI-PC LTD *in vivo* in mice. The idea that EtOH impaired long-term synaptic plasticity in the central nervous system has been widely demonstrated (Izumi et al., 2005, 2007; Belmeguenai et al., 2008; Su et al., 2010; Tokuda et al., 2011; He et al., 2013; Zorumski et al., 2014). In the hippocampus CA1 region, acute administration of EtOH reversibly depresses LTD/LTP *via* modulating the NMDA and $GABA_A$ receptors (Izumi et al., 2005), as well as the GABAergic neurosteroids (Izumi et al., 2007; Tokuda et al., 2011). In the cerebellum, acute application of EtOH inhibits LTD at either CF-PC or PF-PC synapses *via* inhibition of the NMDA receptors and the group I mGlu receptors (Carta et al., 2006; Belmeguenai et al., 2008; Su et al., 2010; He et al., 2013).

Chronic application of EtOH impairing memory and synaptic plasticity, has also been demonstrated by previous studies (Van Waes et al., 2009; Mishra et al., 2012; Wills et al., 2017). Chronic EtOH exposure reduces performance in spatial recognition tasks in normal animals, but it attenuates spatial memory deficits and increases the mGlu1 receptor expression in the hippocampus of prenatal stress rats (Van Waes et al., 2009). Further, chronic intermittent exposure of EtOH disrupts the NMDA receptor-associated post-synaptic proteins and specifically regulates the group I mGlu receptor-dependent LTD in the mouse hippocampus (Wills et al., 2017). In addition, chronic EtOH consumption significantly reduces simple and complex spike frequencies of PCs, resulting in a depression of cerebellar motor coordination and ataxia in mice (Servais et al., 2005). Our present study is consistent with previous studies, indicating that chronic exposure to EtOH impairs facial stimulation-induced MLI-PC LTD, suggesting that long-term consumption of EtOH may cause a deficit in the cerebellar motor learning function *in vivo* in mice.

CB1 Receptors Play a Critical Role in the Facial Stimulation-Evoked MLI-PC Long-Term Synaptic Plasticity *in vivo* in Mice

In the cerebellar cortex, eCB is generated and released from cerebellar PCs and MLIs during the tetanus stimulation

(Brown et al., 2003; Beierlein and Regehr, 2006; Soler-Llavina and Sabatini, 2006). We previously found that CB1 receptor-dependent PF–PC presynaptic LTD was observed *in vivo* in the absence of a pharmacological blocker, suggesting that eCB signaling under *in vivo* conditions is stronger than that under *in vitro* conditions (Chu et al., 2014). In addition, CB 1 receptor-dependent presynaptic LTD was induced when presynaptic LTP was pharmacologically blocked in mouse cerebellar slices, suggesting that the eCB signaling pathway plays a critical role in cerebellar cortical neuronal plasticity (Qiu and Knöpfel, 2009) under control conditions. We recently found that blocking the CB1 receptors abolished facial stimulation evoked MLI–PC LTD, indicating that sensory stimulation induced MLI-PC LTD, *via* the eCB signaling pathway (Bing et al., 2015). Our present results showed that by blocking CB1 receptor activity, facial stimulation failed to induce MLI-PC LTD in control mice, but the stimulation induced a MLI-PC LTP in EtOH consumption mice, indicating that chronic EtOH consumption impaired MLI-PC LTD.

Chronic EtOH Exposure Impairs Facial Stimulation-Induced MLI-PC LTD *via* Enhancement of the NO Signaling Pathway

It is known that NO can either facilitate or suppress plasticity through biphasic effects on NMDA receptors and AMPA receptors insertion, presynaptic vesicle regulation, S-nitrosylation of synaptic proteins, and cyclic GMP (cGMP) generation (Reyes-Harde et al., 1999; Stanton et al., 2005; Ratnayaka et al., 2012; Selvakumar et al., 2013). In the cerebellar cortex, NO works as a retrograde signal, and has been implicated in presynaptically expressed LTP (Qiu and Knöpfel, 2007; Chu et al., 2014). In this study, facial stimulation induced MLI-PC LTP in the absence of CB1 receptor activity, which was blocked by the NOS inhibitor. However, facial stimulation induced MLI-PC LTD, in EtOH consumption mice in the absence of NOS activity. These results indicate that chronic EtOH consumption impairs MLI-PC LTD, may relate to the enhancement of NOS activity *in vivo* in mice Moreover, the application of the NO donor prevented the facial stimulation induced MLI-PC LTD in control mice, suggesting that an increase of NO levels inhibits the induction of MLI-PC LTD. Our results are supported by several previous studies (Yu et al., 2013; Finnerty et al., 2015; Lo et al., 2018), suggesting that EtOH consumption increases the NO level under *in vivo* conditions. First, systemic administration of EtOH resulted in a dose-dependent increase in NO levels, which was attenuated by administration of the NOS inhibitor (Finnerty et al., 2015). Furthermore, acute treatment with EtOH increased the NOS activity and NO production in the brain regions associated with memory, including the prefrontal cortex, amygdala and the hippocampus of adult mice (Yu et al., 2013). Moreover, EtOH consumption causes an increase in the level of glutamate, NO, and GABA in the rostral ventrolateral medulla during the hypotensive responses, suggesting that EtOH enhances the glutamatergic NMDA receptor/NO/GABA pathways in the rostral ventrolateral medulla and may participate in the hypotensive effects induced by acute administration of EtOH (Lo et al., 2018).

Altogether, our present study demonstrates that long-term EtOH consumption can impair the sensory stimulation-induced LTD at MLI–PC synapses, *via* the activation of the NO signaling pathway in the cerebellar cortical Crus II *in vivo* in mice, suggesting that the EtOH consumption attenuates motor coordination and motor learning, which may be involved in the impairment of MLI–PC synaptic plasticity *in vivo* in mice.

AUTHOR CONTRIBUTIONS

D-LQ, XC, L-DS conceived and designed the experiments. D-YL, Y-HB performed the experiments. C-PC, DL-Q analyzed the data. Y-HB contributed reagents, materials and analysis tools. C-PC, S-BC, D-LQ, L-DS wrote the manuscript.

FUNDING

This work was supported by the National Natural Science Foundation of China (81860219; 31460261; 31760273; 31660272), the international S and T cooperation program of China (2016YFE0128600), and the foundations from Jilin Provence (JJKH20180888KJ; 2017Q041).

REFERENCES

Anggono, V., and Huganir, R. L. (2012). Regulation of AMPA receptor trafficking and synaptic plasticity. *Curr. Opin. Neurobiol.* 22, 461–469. doi: 10.1016/j.conb.2011.12.006

Beierlein, M., and Regehr, W. G. (2006). Local interneurons regulate synaptic strength by retrograde release of endocannabinoids. *J. Neurosci.* 26, 9935–9943. doi: 10.1523/JNEUROSCI.0958-06.2006

Belmeguenai, A., Botta, P., Weber, J. T., Carta, M., De Ruiter, M., De Zeeuw, C. I., et al. (2008). Alcohol impairs long-term depression at the cerebellar parallel fiber-Purkinje cell synapse. *J. Neurophysiol.* 100, 3167–3174. doi: 10.1152/jn.90384.2008

Bing, Y. H., Wu, M. C., Chu, C. P., and Qiu, D. L. (2015). Facial stimulation induces long-term depression at cerebellar molecular layer interneuron-Purkinje cell synapses *in vivo* in mice. *Front. Cell. Neurosci.* 9:214. doi: 10.3389/fncel.2015.00214

Botta, P., de Souza, F. M., Sangrey, T., De Schutter, E., and Valenzuela, C. F. (2010). Alcohol excites cerebellar Golgi cells by inhibiting the Na^+/K^+ ATPase. *Neuropsychopharmacology* 35, 1984–1996. doi: 10.1038/npp.2010.76

Brown, S. P., Brenowitz, S. D., and Regehr, W. G. (2003). Brief presynaptic bursts evoke synapse-specific retrograde inhibition mediated by endogenous cannabinoids. *Nat. Neurosci.* 6, 1048–1057. doi: 10.1038/nn1126

Carta, M., Mameli, M., and Valenzuela, C. F. (2006). Alcohol potently modulates climbing fiber-Purkinje neuron synapses: role of metabotropic glutamate receptors. *J. Neurosci.* 26, 1906–1912. doi: 10.1523/JNEUROSCI.4430-05.2006

Chandler, L. J., Harris, R. A., and Crews, F. T. (1998). Ethanol tolerance and synaptic plasticity. *Trends Pharmacol. Sci.* 19, 491–495. doi: 10.1016/s0165-6147(98)01268-1

Chu, C. P., Bing, Y. H., Liu, Q. R., and Qiu, D. L. (2011a). Synaptic responses evoked by tactile stimuli in Purkinje cells in mouse cerebellar cortex. *PLoS One* 6:e22752. doi: 10.1371/journal.pone.0022752

Chu, C. P., Bing, Y. H., and Qiu, D. L. (2011b). Sensory stimulation evokes inhibition rather than excitation in cerebellar PCs *in vivo* in mice. *Neurosci. Lett.* 487, 182–186. doi: 10.1016/j.neulet.2010.10.018

Chu, C. P., Bing, Y. H., Liu, H., and Qiu, D. L. (2012). Roles of molecular layer interneurons in sensory information processing in mouse cerebellar cortex Crus II *in vivo*. *PLoS One* 7:e37031. doi: 10.1371/journal.pone.0037031

Chu, C. P., Zhao, G. Y., Jin, R., Zhao, S. N., Sun, L., and Qiu, D. L. (2014). Properties of 4 Hz stimulation-induced parallel fiber-Purkinje cell presynaptic long-term plasticity in mouse cerebellar cortex *in vivo*. *Eur. J. Neurosci.* 39, 1624–1631. doi: 10.1111/ejn.12559

Criswell, H. E., and Breese, G. R. (2005). A conceptualization of integrated actions of ethanol contributing to its GABAmimetic profile: a commentary. *Neuropsychopharmacology* 30, 1407–1425. doi: 10.1038/sj.npp.1300750

Cui, S. B., Cui, B. R., Liu, H., Wu, M. C., Xu, Y. H., Bian, J. H., et al. (2014). Effects of ethanol on sensory stimulus-evoked responses in the cerebellar molecular layer *in vivo* in mice. *Neurosci. Lett.* 577, 112–116. doi: 10.1016/j.neulet.2014.05.037

D'Angelo, E., Mapelli, L., Casellato, C., Garrido, J. A., Luque, N., Monaco, J., et al. (2016). Distributed circuit plasticity: new clues for the cerebellar mechanisms of learning. *Cerebellum* 15, 139–151. doi: 10.1007/s12311-015-0711-7

Finnerty, N., O'Riordan, S. L., Klamer, D., Lowry, J., and Pålsson, E. (2015). Increased brain nitric oxide levels following ethanol administration. *Nitric Oxide* 47, 52–57. doi: 10.1016/j.niox.2015.03.002

Grasselli, G., and Hansel, C. (2014). Cerebellar long-term potentiation: cellular mechanisms and role in learning. *Int. Rev. Neurobiol.* 117, 39–51. doi: 10.1016/B978-0-12-420247-4.00003-8

He, Q., Titley, H., Grasselli, G., Piochon, C., and Hansel, C. (2013). Ethanol affects NMDA receptor signaling at climbing fiber-Purkinje cell synapses in mice and impairs cerebellar LTD. *J. Neurophysiol.* 109, 1333–1342. doi: 10.1152/jn.00350.2012

Hirano, T. (2013). "GABA and synaptic transmission in the cerebellum," in *Handbook of the Cerebellum and Cerebellar Disorders*, eds M. Manto, J. D. Schmahmann, F. Rossi, D. L. Gruol and N. Koibuchi (Heidelberg: Springer), 881–893.

Hirano, T., and Kawaguchi, S. Y. (2014). Regulation and functional roles of rebound potentiation at cerebellar stellate cell-Purkinje cell synapses. *Front. Cell. Neurosci.* 8:42. doi: 10.3389/fncel.2014.00042

Hirono, M., Yamada, M., and Obata, K. (2009). Ethanol enhances both action potential-dependent and action potential-independent GABAergic transmission onto cerebellar Purkinje cells. *Neuropharmacology* 57, 109–120. doi: 10.1016/j.neuropharm.2009.04.012

Hoxha, E., Tempia, F., Lippiello, P., and Miniaci, M. C. (2016). Modulation, plasticity and pathophysiology of the parallel fiber-purkinje cell synapse. *Front. Synaptic Neurosci.* 8:35. doi: 10.3389/fnsyn.2016.00035

Ito, M. (1989). Long-term depression. *Annu. Rev. Neurosci.* 12, 85–102. doi: 10.1146/annurev.ne.12.030189.000505

Izumi, Y., Murayama, K., Tokuda, K., Krishnan, K., Covey, D. F., and Zorumski, C. F. (2007). GABAergic neurosteroids mediate the effects of ethanol on long-term potentiation in rat hippocampal slices. *Eur. J. Neurosci.* 26, 1881–1888. doi: 10.1111/j.1460-9568.2007.05809.x

Izumi, Y., Nagashima, K., Murayama, K., and Zorumski, C. F. (2005). Acute effects of ethanol on hippocampal long-term potentiation and long-term depression are mediated by different mechanisms. *Neuroscience* 136, 509–517. doi: 10.1016/j.neuroscience.2005.08.002

Lo, H., Lin, H. H., Chen, J. K., Situmorang, J. H., and Lai, C. C. (2018). Involvement of NMDA receptors, nitric oxide and GABA in rostral ventrolateral medulla in acute ethanol-induced cardiovascular responses in rats. *Alcohol. Clin. Exp. Res.* doi: 10.1111/acer.13800 [Epub ahead of print].

Lovinger, D. M. (1997). Alcohols and neurotransmitter gated ion channels: past, present and furture. *Naunyn Schmiedebergs Arch. Pharmacol.* 356, 267–282. doi: 10.1007/pl00005051

Luo, J. (2012). Mechanisms of ethanol-induced death of cerebellar granule cells. *Cerebellum* 11, 145–154. doi: 10.1007/s12311-010-0219-0

Mameli, M., Botta, P., Zamudio, P. A., Zucca, S., and Valenzuela, C. F. (2008). Ethanol decreases Purkinje neuron excitability by increasing GABA release in rat cerebellar slices. *J. Pharmacol. Exp. Ther.* 327, 910–917. doi: 10.1124/jpet.108.144865

Martz, A., Deitrich, R. A., and Harris, R. A. (1983). Behavioral evidence for the involvement of γ-aminobutyric acid in the actions of ethanol. *Eur. J. Pharmacol.* 89, 53–62. doi: 10.1016/0014-2999(83)90607-6

Mishra, D., Zhang, X., and Chergui, K. (2012). Ethanol disrupts the mechanisms of induction of long-term potentiation in the mouse nucleus accumbens. *Alcohol. Clin. Exp. Res.* 36, 2117–2125. doi: 10.1111/j.1530-0277.2012.01824.x

Palay, S. L., and Chan-Palay, V. (1974). *Cerebellar Cortex*. New York, NY: Springer-Verlag.

Qiu, D. L., and Knöpfel, T. (2007). An NMDA receptor/nitric oxide cascade in presynaptic parallel fiber-Purkinje neuron long-term potentiation. *J. Neurosci.* 27, 3408–3415. doi: 10.1523/JNEUROSCI.4831-06.2007

Qiu, D. L., and Knöpfel, T. (2009). Presynaptically expressed long-term depression at cerebellar parallel fiber synapses. *Pflugers Arch.* 457, 865–875. doi: 10.1007/s00424-008-0555-9

Ratnayaka, A., Marra, V., Bush, D., Burden, J. J., Branco, T., and Staras, K. (2012). Recruitment of resting vesicles into recycling pools supports NMDA receptor-dependent synaptic potentiation in cultured hippocampal neurons. *J. Physiol.* 590, 1585–1597. doi: 10.1113/jphysiol.2011.226688

Reyes-Harde, M., Empson, R., Potter, B. V., Galione, A., and Stanton, P. K. (1999). Evidence of a role for cyclic ADP-ribose in long-term synaptic depression in hippocampus. *Proc. Natl. Acad. Sci. U S A* 96, 4061–4066. doi: 10.1073/pnas.96.7.4061

Schmahman, J. D., and Sherman, J. C. (1997). Cerebellar cognitive affective syndrome. *Int. Rev. Neurobiol.* 41, 433–440. doi: 10.1016/S0074-7742(08)60363-3

Selvakumar, B., Jenkins, M. A., Hussain, N. K., Huganir, R. L., Traynelis, S. F., and Snyder, S. H. (2013). S-nitrosylation of AMPA receptor GluA1 regulates phosphorylation, single-channel conductance and endocytosis. *Proc. Natl. Acad. Sci. U S A* 110, 1077–1082. doi: 10.1073/pnas.1221295110

Servais, L., Bearzatto, B., Delvaux, V., Noël, E., Leach, R., Brasseur, M., et al. (2005). Effect of chronic ethanol ingestion on Purkinje and Golgi cell firing *in vivo* and on motor coordination in mice. *Brain Res.* 1055, 171–179. doi: 10.1016/j.brainres.2005.07.026

Soler-Llavina, G. J., and Sabatini, B. L. (2006). Synapse-specific plasticity and compartment- alized signaling in cerebellar stellate cells. *Nat. Neurosci.* 9, 798–806. doi: 10.1038/nn1698

Stanton, P. K., Winterer, J., Zhang, X. L., and Müller, W. (2005). Imaging LTP of presynaptic release of FM1–43 from the rapidly recycling vesicle pool of Schaffer collateral-CA1 synapses in rat hippocampal slices. *Eur. J. Neurosci.* 22, 2451–2461. doi: 10.1111/j.1460-9568.2005.04437.x

Su, L. D., Sun, C. L., and Shen, Y. (2010). Ethanol acutely modulates mGluR1-dependent long-term depression in cerebellum. *Alcohol. Clin. Exp. Res.* 34, 1140–1145. doi: 10.1111/j.1530-0277.2010.01190.x

Tokuda, K., Izumi, Y., and Zorumski, C. F. (2011). Ethanol enhances neurosteroidogenesis in hippocampal pyramidal neurons by paradoxical NMDA receptor activation. *J. Neurosci.* 31, 9905–9909. doi: 10.1523/JNEUROSCI.1660-11.2011

Van Waes, V., Enache, M., Zuena, A., Mairesse, J., Nicoletti, F., Vinner, E., et al. (2009). Ethanol attenuates spatial memory deficits and increases mGlu1a receptor expression in the hippocampus of rats exposed to prenatal stress. *Alcohol. Clin. Exp. Res.* 33, 1346–1354. doi: 10.1111/j.1530-0277.2009.00964.x

Wadleigh, A., and Valenzuela, C. F. (2012). Ethanol increases GABAergic transmission and excitability in cerebellar molecular layer interneurons from GAD67-GFP knock-in mice. *Alcohol Alcohol.* 47, 1–8. doi: 10.1093/alcalc/agr147

Weiner, J. L., and Valenzuela, C. F. (2006). Ethanol modulation of GABAergic transmission: the view from the slice. *Pharmacol. Ther.* 111, 533–554. doi: 10.1016/j.pharmthera.2005.11.002

Wills, T. A., Baucum, A. J., Holleran, K. M., Chen, Y., Pasek, J. G., Delpire, E., et al. (2017). Chronic intermittent alcohol disrupts the GluN2B-associated proteome and specifically regulates group I mGlu receptor-dependent long-term depression. *Addict Biol.* 22, 275–290. doi: 10.1111/adb.12319

Woodward, J. J. (1999). Ionotropic glutamate receptors as sites of action for ethanol in the brain. *Neurochem. Int.* 35, 107–113. doi: 10.1016/s0197-0186(99)00052-2

Wu, M. C., Bing, Y. H., Chu, C. P., and Qiu, D. L. (2016). Ethanol modulates facial stimulation-evoked outward currents in cerebellar Purkinje cells *in vivo* in mice. *Sci. Rep.* 6:30857. doi: 10.1038/srep 30857

Yu, S. Y., Gao, R., Zhang, L., Luo, J., Jiang, H., and Wang, S. (2013). Curcumin ameliorates ethanol-induced memory deficits and enhanced brain nitric oxide synthase activity in mice. *Prog. Neuropsychopharmacol. Biol. Psychiatry* 44, 210–216. doi: 10.1016/j.pnpbp.2013.03.001

Zorumski, C. F., Mennerick, S., and Izumi, Y. (2014). Acute and chronic effects of ethanol on learning-related synaptic plasticity. *Alcohol* 48, 1–17. doi: 10.1016/j.alcohol.2013.09.045

Conflict of Interest Statement: The authors declare that the research was conducted in the absence of any commercial or financial relationships that could be construed as a potential conflict of interest.

frontiers in Cellular Neuroscience

BRIEF RESEARCH REPORT
published: 21 January 2019
doi: 10.3389/fncel.2018.00509

Brain Derived Neurotrophic Factor (BDNF) Delays Onset of Pathogenesis in Transgenic Mouse Model of Spinocerebellar Ataxia Type 1 (SCA1)

Aaron Mellesmoen[1], *Carrie Sheeler*[1], *Austin Ferro*[1], *Orion Rainwater*[2] and *Marija Cvetanovic*[1,3]*

[1]Department of Neuroscience, University of Minnesota, Minneapolis, MN, United States, [2]Department of Lab Medicine and Pathology, University of Minnesota, Minneapolis, MN, United States, [3]Institute for Translational Neuroscience, University of Minnesota, Minneapolis, MN, United States

Spinocerebellar ataxia type 1 (SCA1) is a fatal neurodegenerative disease caused by an abnormal expansion of CAG repeats in the *Ataxin-1 (ATXN1)* gene and characterized by motor deficits and cerebellar neurodegeneration. Even though mutant ATXN1 is expressed from an early age, disease onset usually occurs in patient's mid-thirties, indicating the presence of compensatory factors that limit the toxic effects of mutant ATXN1 early in disease. Brain derived neurotrophic factor (BDNF) is a growth factor known to be important for the survival and function of cerebellar neurons. Using gene expression analysis, we observed altered BDNF expression in the cerebella of Purkinje neuron specific transgenic mouse model of SCA1, *ATXN1[82Q]* mice, with increased expression during the early stage and decreased expression in the late stage of disease. We therefore investigated the potentially protective role of BDNF in early stage SCA1 through intraventricular delivery of BDNF *via* ALZET osmotic pumps. Extrinsic BDNF delivery delayed onset of motor deficits and Purkinje neuron pathology in *ATXN1[82Q]* mice supporting its use as a novel therapeutic for SCA1.

Keywords: ATAXIN-1, BDNF, astroglia, neuroprotective, nuclear factor κb, cerebellum, neurodegeneration

OPEN ACCESS

Edited by:
Ying Shen,
Zhejiang University, China

Reviewed by:
Ruth M. Empson,
University of Otago, New Zealand
Laurens Bosman,
Erasmus University Rotterdam, Netherlands
Hong Jiang,
Central South University, China

***Correspondence:**
Marija Cvetanovic
mcvetano@umn.edu

Received: *11 September 2018*
Accepted: *10 December 2018*
Published: *21 January 2019*

Citation:
Mellesmoen A, Sheeler C, Ferro A, Rainwater O and Cvetanovic M (2019) Brain Derived Neurotrophic Factor (BDNF) Delays Onset of Pathogenesis in Transgenic Mouse Model of Spinocerebellar Ataxia Type 1 (SCA1). Front. Cell. Neurosci. 12:509. doi: 10.3389/fncel.2018.00509

INTRODUCTION

Spinocerebellar ataxia type 1 (SCA1) is a dominantly inherited and fatal neurodegenerative disease resulting from an overexpansion of CAG repeats within the *Ataxin-1 (ATXN1)* gene (Banfi et al., 1996; Zoghbi and Orr, 2009). SCA1 belongs to a group of polyglutamine (polyQ) disorders that also includes SCA2, 3, 6, 7, 17, spinobulbar muscular atrophy, Huntington's disease (HD), and dentatorubropallidoluysian atrophy (Genis et al., 1995; Gusella and MacDonald, 2000; La Spada and Taylor, 2010). Clinical onset of SCA1 is characterized by ataxia, or loss of motor coordination and balance, which typically presents during patient's mid-thirties (Genis et al., 1995; Orr and Zoghbi, 2007; Rüb et al., 2013; Matilla-Dueñas et al., 2014). Progressive degradation of motor function leads to death within 10–20 years following clinical onset (Rüb et al., 2013). Currently, no treatments exist for SCA1 (Paulson et al., 2017).

ATXN1 is expressed prior to birth in humans [**Figure 1A**, created using human developmental transcriptome data from BrainSpan (Miller et al., 2014)], yet the clinical phenotype of SCA1 emerges decades later. Similarly, in *ATXN1[82Q]* mice, Purkinje neuron specific transgenic mouse model of SCA1, mutant ATXN1 is expressed from postnatal day 10 (P10; Serra et al., 2006) yet they exhibit motor deficits and Purkinje neuron pathology earliest at 12 weeks of age, in our hands (Cvetanovic, 2015; Qu et al., 2017; Ferro et al., 2018). Neuroprotective factors may compensate for early mutant ATXN1-mediated neural toxicity, and gradual decline in compensation may contribute to late onset of disease. Indeed, pre-manifest carriers of SCA1 and other polyQ mutations demonstrate mild coordination deficits and brain abnormalities several years prior to estimated disease onset (Jacobi et al., 2013; Storey, 2013; Tabrizi et al., 2013; Espinoza et al., 2018;

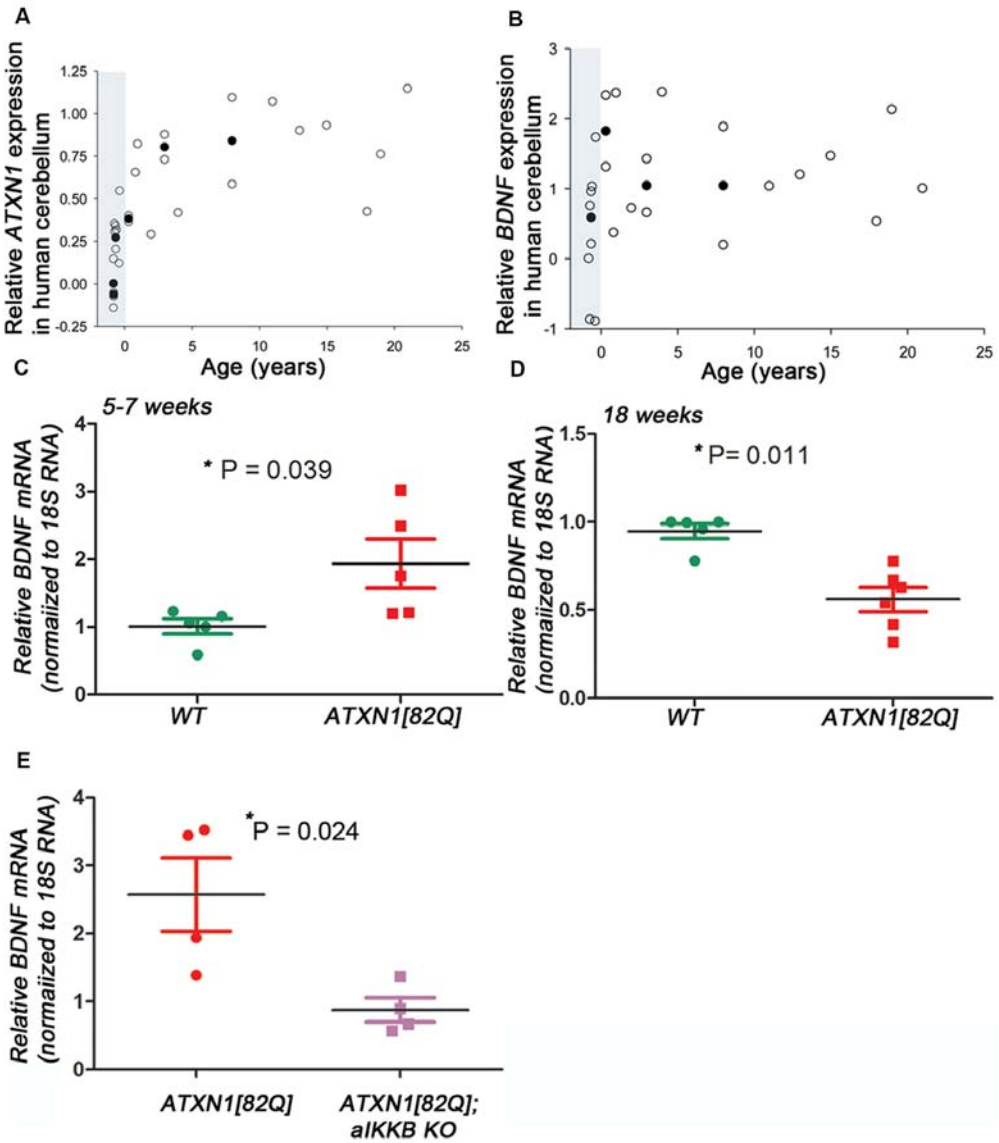

FIGURE 1 | Brain derived neurotrophic factor (BDNF) expression in transgenic spinocerebellar ataxia type 1 (SCA1) mice. **(A–B)** Relative *Ataxin-1* (ATXN1) **(A)** and BDNF **(B)** expression in the human cerebellar cortex [polyglutamine (polyQ) sequence/SCA1 status unknown] obtained from the transcriptome data at *Allen Brain Institute*. Raw reads per kilobase million (RPKM) values were normalized to the highest and lowest values and data was averaged when multiple patient samples fell within the same postnatal year or same post conception week. Open circles represent single patient samples and closed circles represent average expression (used when possible). Shaded areas mark pre-natal period. **(C–E)** Reverse transcription and quantitative polymerase chain reaction (RT-qPCR) using cerebellar extracts from **(C)** early stage (5–7 weeks) and **(D)** late stage (18–24 weeks old) *ATXN1[82Q]* mice. Results are normalized using 18S RNA and age-matched wild-type (WT) littermates. **(E)** RT-qPCR using cerebellar extracts from *ATXN1[82Q]* mice and mice in which astroglial nuclear factor κ-light-chain-enhancer of activated B cells (NF-κB) is inhibited early in disease [*ATXN1[82Q]*; aIKKβ KO]. Results are normalized using 18S RNA and age-matched WT littermates. For **(C–E)** error bars = SEM. Student's *t*-test *P* values. Each dot represents a biological sample.

Joers et al., 2018). We and others have observed cellular and molecular alterations that may compensate for neuronal dysfunction during the early stages of disease in *ATXN1[82Q]* mice (Dell'Orco et al., 2015; Kim et al., 2018). Here, we propose that increased expression of brain derived neurotrophic factor (BDNF) by reactive astroglia may be a part of this compensatory mechanism to delay disease onset in *ATXN1[82Q]* mice.

MATERIALS AND METHODS

Human RNAseq

Reads per kilobase million (RPKM) RNAseq data was obtained from the BrainSpan database[1] with permission (Miller et al., 2014). RPKM values were averaged over patients with equal ages and then normalized as follows:

$$Relative\,Expression = (RPKM_n - RPKM_y)/(RPKM_o - RPKM_n);$$

y, youngest datapoint; o, oldest datapoint.

Mice

The creation of the *ATXN1[82Q]* mice was previously described (Clark et al., 1997). Equal number of male and female mice were randomly allocated to BDNF (20 μg of human recombinant BDNF (R&D Systems Cat. 248-BD-250/CF) in 100 μl per micropump, ∼ 0.71μg/day) or control artificial cerebrospinal fluid (aCSF) groups. We surgically implanted ALZET pumps (Alzet Model 1004) into 8-week-old mice in a subcutaneous pocket in the back and the delivery cannula in the right lateral ventricle (A/P, 1.1; M/L, 0.5 D/V, −2.5 mm from Bregma) as we previously described (Cvetanovic et al., 2011).

In all the experiments investigators were blinded to the genotype/treatment.

Animal experimentation was approved by the Institutional Animal Care and Use Committee (IACUC) at the University of Minnesota and was conducted in accordance with the National Institutes of Health's (NIH) Principles of Laboratory Animal Care (86-23, revised 1985), and the American Physiological Society's Guiding Principles in the Use of Animals.

Mouse RNA Sequencing

Mouse RNA sequencing was done as previously described (Ingram et al., 2016).

Rotarod Analysis

Mice were tested on rotatod (#47600; Ugo Basile) to evaluate motor deficits as described previously (Kim et al., 2018). Rotarod paradigm consisted of acceleration from 5 rpm to 40 rpm over 0–5 min, followed by 40 rpm constant speed from 5 min to 10 min. Latency to fall was recorded.

Immunofluorescent (IF) Staining

Immunofluorescent (IF) was performed on floating 45 μm brain sections using primary antibodies [Calbindin #C9848, Sigma-Aldrich; vesicular glutamate transporter 2 (VGLUT2) #MAB5504, Millipore, Burlington, MA, USA] as previously described (Cvetanovic et al., 2011).

Quantitative analysis was performed using ImageJ National Institutes of Health's (NIH) as described previously. We quantified minimum of six different slices from each mouse. Per each slice we randomly chose two lobules and draw a line from the base of the Purkinje soma to the end of the dendrites to determine width of the molecular layer (length of the line) and average calbindin intensity. For assessing climbing fiber height, the distance from the Purkinje neuron soma to the end of VGLUT2 staining was measured (VGLUT2), and the extension of climbing fibers was depicted relative to the molecular layer thickness (VGLUT2/calbindin; Joers et al., 2018).

Reverse Transcription and Quantitative Polymerase Chain Reaction (RT-qPCR)

Total RNA was extracted from mouse cerebella using TRIzol (Life Technologies) and (reverse transcription and quantitative polymerase chain reaction (RT-qPCR) was performed as described previously (Kim et al., 2018).

Statistical Analysis

Wherever possible, sample sizes were calculated using power analyses based on the standard deviations from our previous studies, significance level of 5%, and power of 90%. Statistical tests were performed with GraphPad Prism. We have used one-way analyses of variance (ANOVA) followed by Bonferroni or Kruskal-Wallis *post hoc* tests (depending on the normality of the data) or two-tailed Student's *t*-test.

Data Availability

All the data from this study are available from the authors.

RESULTS

BDNF Expression Is Altered in *ATXN1[82Q]* Mice

We used unbiased RNA sequencing to examine gene expression changes during disease progression. We have found that expression of neuroprotective factor BDNF is increased early and decreased late in *ATXN1[82Q]* mice (Cvetanovic et al., 2015; **Supplementary Table S1**), 5-week-old *ATXN1[82Q]* mice 6.87 vs. 5.3 fragments per kilobase of exon per million reads mapped (FPKM) in wild-type (WT) littermates, $p = 0.00005$, adjusted $q = 0.0165$; 12-week-old *ATXN1[82Q]* mice 3.2 vs. 5.03 fragments per kilobase of exon per million reads mapped (FPKM) in WT littermates, $p = 0.00015$, adjusted $q = 0.0021$). Using RT-qPCR we have confirmed increased BDNF expression in the cerebella during early stage (**Figure 1C**, 1.934 ± 0.359 relative to WT littermates, $N = 5$ each, Student's *t*-test $P = 0.0394$) and later decrease (**Figure 1D**, 0.56 ± 006 relative to WT, $N = 6$ *ATXN1[82Q]* and $N = 5$ WT mice, Student's *t*-test $P = 0.0014$).

[1] http://www.brainspan.org/

Hallmark features of astrogliosis, the process by which astroglia react to neuronal dysfunction, are detectable early in SCA1 mice (Cvetanovic et al., 2015). We demonstrated that reducing astrogliosis early in SCA1, through inducible genetic inhibition of nuclear factor κ-light-chain-enhancer of activated B cells (NF-κB) signaling selectively in astroglia (astroglial IKKβ knock-out, aIKKβ KO), exacerbates motor deficits and neuropathology in *ATXN1[82Q]* mice (Kim et al., 2018). Inhibition of astroglial NF-κB prevented the early increase in BDNF expression (**Figure 1E**, 2.57 ± 0.11 increase in *ATXN1[82Q]* mice compared to 0.88 ± 0.17 in *ATXN1[82Q];aIKKB KO*, $N = 4$, *t*-test $P = 0.024$), indicating that astroglial NF-κB signaling may regulate increased BDNF expression early in SCA1 mice.

Delivery of BDNF Early in Disease Ameliorates SCA1

In our hands, *ATXN1[82Q]* mice demonstrate reproducible motor deficits and cerebellar pathology earliest at 12 weeks. However, as the onset of motor deficits has been observed earlier by others (Clark et al., 1997; Duvick et al., 2010; Hourez et al., 2011; Ibrahim et al., 2017), we refer to mice younger than 12 weeks as early stage instead of pre-symptomatic. To determine the neuroprotective effects of BDNF, we used osmotic ALZET pumps to deliver recombinant BDNF to 8-weeks-old SCA1 or WT littermate mice for a total of 4 weeks (∼0.71 μg/day). This study consisted of four experimental groups: WT and *ATXN1[82Q]* mice with pumps delivering BDNF, and control WT and *ATXN1[82Q]* mice with pumps delivering aCSF. Mice were tested on rotarod at 12 weeks and pathology was examined at 14 weeks (**Figure 2A**).

BDNF-treated *ATXN1[82Q]* mice performed significantly better on rotarod compared to control aCSF-treated *ATXN1[82Q]* mice (e.g., day 4 average latency to fall of BDNF-treated *ATXN1[82Q]* mice = 262.5 ± 24.3 s, $N = 10$; compared to aCSF-treated *ATXN1[82Q]* mice = 181 ± 16.73 s, $N = 11$, $P < 0.05$, one-way ANOVA with Kruskal-Wallis test $H = 15.74$, $P = 0.0013$; **Figure 2B**). Importantly, BDNF-treated *ATXN1[82Q]* mice were indistinguishable from BDNF- or aCSF-treated WT mice (aCSF- and BDNF-treated WT mice latency was 283 ± 36.7 s, $N = 12$, and 382 ± 39.78, $N = 13$, respectively, $P > 0.05$ for both comparisons one-way ANOVA with Kruskal-Wallis test).

We used immunofluorescence to determine whether BDNF ameliorates decreased calbindin expression and synaptic loss, two well-characterized hallmarks of Purkinje neuron pathology in SCA1 mice (Zu et al., 2004; Serra et al., 2006; Duvick et al., 2010; Barnes et al., 2011; Ebner et al., 2013; Ruegsegger et al., 2016; Ibrahim et al., 2017). BDNF-treated *ATXN1[82Q]* and WT mice were indistinguishable and both groups had significantly higher calbindin intensity of Purkinje neurons compared to aCSF-treated *ATXN1[82Q]* controls (**Figures 2C,D**, average relative intensity of aCSF-treated *ATXN1[82Q]* mice was 0.7417 ± 0.028 compared to 0.8989 ± 0.027 in BDNF-treated *ATXN1[82Q]* mice, $N = 6$ of each, $P < 0.05$ one-way ANOVA with *post hoc* Bonferroni test $F_{(3,20)} = 29.32$, $P < 0.0001$). BDNF also prevented loss of climbing fibers synapses on Purkinje neuron dendrites in *ATXN1[82Q]* mice as quantified with VGLUT2 staining (**Figures 2C,E**, average VGLUT2/CAL ratio for aCSF-treated *ATXN1[82Q]* mice was 0.7553 ± 0.009 compared to 0.8638 ± 0.02 in BDNF–treated *ATXN1[82Q]* mice, $N = 4$ each, one-way ANOVA $F_{(3,12)} = 3.878$ $P = 0.0071$, *post hoc* Bonferroni test $P < 0.05$). However, width of the molecular layer was not rescued (**Figure 2F**, average width for aCSF-treated *ATXN1[82Q]* mice was 132.1 ± 3.667 μm compared to 139 ± 6.1 in BDNF–treated *ATXN1[82Q]* mice, $N = 6$ each, one-way ANOVA with *post hoc* Bonferroni test $P > 0.05$).

We used RT-qPCR to demonstrate that BDNF treatment rescued expression of Purkinje neuron genes *Calbindin* (Ingram et al., 2016; **Figure 2G** left, aCSF-treated *ATXN1[82Q]* mice = 0.336 ± 0.065 compared to 0.648 ± 0.125 in BDNF-treated *ATXN1[82Q]* mice, $N = 5$, *t*-test, $P = 0.0296$) and *INNP5* (**Figure 2G** right, aCSF-treated *ATXN1[82Q]* mice = 0.404 ± 0.057 compared to 0.648 ± 0.115 in BDNF-treated *ATXN1[82Q]* mice, *t*-test, $P = 0.02872$, $N = 5$). Together, these results indicate that BDNF may be neuroprotective early in SCA1.

DISCUSSION

We report that early delivery of BDNF delays motor deficits and pathology of Purkinje neurons. In addition, we report an early increase in BDNF expression in SCA1 that may be regulated by astroglial NF-κB-signaling. Based on these results, we propose that early increase in BDNF expression may be neuroprotective and compensate for ATXN1 toxicity, thus delaying disease onset.

BDNF belongs to the family of neurotrophins (Barde et al., 1982) and is expressed in human cerebellum from early development (**Figure 1B**). Its cognate receptor, Tyrosine kinase B receptor (TrkB), is highly expressed on Purkinje neurons where BDNF signaling plays a host of neuroprotective and modulatory functions such as regulating dendritic branching and synaptic strength (Schwartz et al., 1997; Kafitz et al., 1999; Carter et al., 2002; Furutani et al., 2006; Huang et al., 2012). Purkinje neuron pathology in SCA1 includes shrinking of the dendritic arbor, loss of synapses, and altered evoked and spontaneous firing (Duvick et al., 2010; Cvetanovic et al., 2011; Hourez et al., 2011; Dell'Orco et al., 2015). It is possible that BDNF exerts its neuroprotective effect in SCA1 at least in part through prevention of these Purkinje neuron pathologies. Intriguingly, during postnatal cerebellar development BDNF signaling seems to promote elimination of climbing fiber synapses, and this may be regulated by temporal expression of short TrkB isoform (Bosman et al., 2006; Sherrard et al., 2009; Choo et al., 2017). Delivery of BDNF to WT mice at 8 weeks did not seem to affect climbing fiber synapses and these mice performed well on rotarod (**Figure 2B**) indicating that post-development extrinsic BDNF may not have obvious side effects on these tests. Since BDNF is delivered intracerebroventricularly, we cannot exclude the possibility of off-target BDNF effects. However, *ATXN1[82Q]* mice pathology

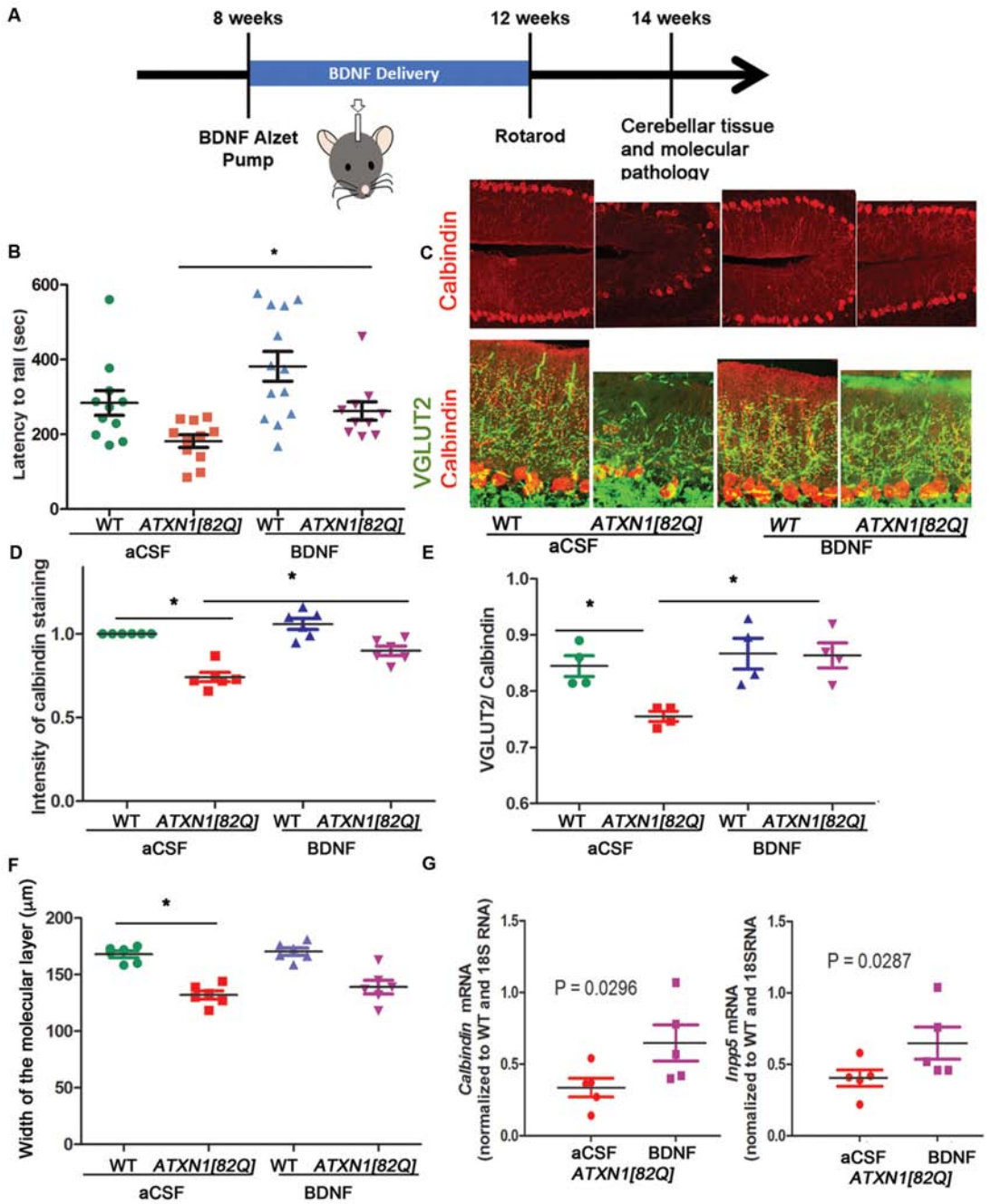

FIGURE 2 | BDNF delivery delays disease pathogenesis in *ATXN1[82Q]* mice. **(A)** Experimental scheme to test the role of BDNF early in SCA1. **(B)** Rotarod performance of mice at 12 weeks. *$P < 0.05$ using one-way ANOVA with Kruskal-Wallis test. **(C–F)** Cerebellar slices from 14-week-old mice were stained with antibody specific for Purkinje neuron-marker calbindin and vesicular glutamate transporter 2 (VGLUT2) to label climbing fiber synapses on Purkinje neurons. ImageJ was used to quantify **(D)** calbindin intensity in the Purkinje neurons, **(E)** length of climbing fiber synapses (VGLUT2 puncta) on Purkinje neuron dendrites (determined as VGLUT2/calbindin ratio), and **(F)** width of the molecular layer. *$P < 0.05$ using one-way ANOVA with Bonferroni's multiple comparison test. **(G)** RT-qPCR analysis of disease associated Purkinje neurons genes *calbindin* (left) and *Inpp5* (right). Student's *t*-test *P* values. For all error bars = SEM. Each dot represents a biological sample.

is limited to cerebellum (Burright et al., 1995) due to Purkinje neuron selective expression of mutant ATXN1.

BDNF expression is decreased in many neuropsychiatric and neurodegenerative diseases, including depression, bipolar disease, schizophrenia, Alzheimer's disease, HD, SCA6 and Parkinson's disease (Ferrer et al., 2000; Zuccato and Cattaneo, 2007; Takahashi et al., 2012; He et al., 2013; Shin et al., 2015). Moreover, beneficial treatments for these diseases

correlate with increased BDNF expression, and rescued BDNF expression ameliorates disease symptoms in mouse models (Willson et al., 2008; Nagahara et al., 2009; Giampà et al., 2013). While these studies underlie the importance of BDNF in brain pathology and pathophysiology, regulation of BDNF expression during disease is less understood. Recent studies indicate a link between BDNF and neuroinflammation (Lima Giacobbo et al., 2018), another phenomenon that is ubiquitously present in these diseases (Ilieva et al., 2009; Heneka et al., 2014; Pekny et al., 2016). NF-κB, a key regulator of neuroinflammation (Mincheva-Tasheva and Soler, 2013), modulates BDNF expression (Saha et al., 2006; Lima Giacobbo et al., 2018). Astroglia react to neuronal dysfunction by activating NF-κB (Barres, 2008), and our results implicate that astroglial NF-κB contributes to elevated BDNF levels early in SCA1 mice. Likewise, astroglia-derived BDNF delayed disease onset in a transgenic mouse model of HD (Giralt et al., 2011).

Previous studies indicate that reversibility of polyQ neurodegeneration diminishes with disease progression (Yamamoto and Lucas, 2000; Zu et al., 2004; Rubinsztein and Orr, 2016; Ibrahim et al., 2017), strongly supporting consideration of early stage treatments. Our results indicate that early BDNF treatment may delay disease onset in SCA1 carriers. We also observed decreased BDNF expression late in SCA1 that may contribute to disease severity (Hourez et al., 2011). Future work will examine the effects of late BDNF delivery on disease severity and progression in SCA1 mice.

AUTHOR CONTRIBUTIONS

MC conceived the study. AM, MC and CS performed the experiments and analyzed the data. AF analyzed data from BrainSpan database linked from Allen brain atlas. All authors prepared the figures and wrote the manuscript.

FUNDING

MC is supported by the funding from the National Institutes of Health 1R01NS107387-01 and Minnesota Regenerative Medicine RMM 101617 TR 001.

ACKNOWLEDGMENTS

We are grateful to Dr. Harry Orr for the generous gift of *ATXN1[82Q]* mice Katherine Hamel for help with data acquisition, and to all the members of Cvetanovic and Orr laboratories for suggestions.

SUPPLEMENTARY MATERIAL

The Supplementary Material for this article can be found online at: https://www.frontiersin.org/articles/10.3389/fncel.2018.00509/full#supplementary-material

TABLE S1 | BDNF expression from RNA sequencing of mouse cerebellar extracts.

REFERENCES

Banfi, S., Servadio, A., Chung, M., Capozzoli, F., Duvick, L. A., Elde, R., et al. (1996). Cloning and developmental expression analysis of the murine homolog of the spinocerebellar ataxia type 1 gene (Sca1). *Hum. Mol. Genet.* 5, 33–40. doi: 10.1093/hmg/5.1.33

Barde, Y., Edgar, D., and Thoenen, H. (1982). Purification of a new neurotrophic factor from mammalian brain. *EMBO J.* 1, 549–553. doi: 10.1002/j.1460-2075.1982.tb01207.x

Barnes, J. A., Ebner, B. A., Duvick, L. A., Gao, W., Chen, G., Orr, H. T., et al. (2011). Abnormalities in the climbing fiber-Purkinje cell circuitry contribute to neuronal dysfunction in ATXN1[82Q] mice. *J. Neurosci.* 31, 12778–12789. doi: 10.1523/jneurosci.2579-11.2011

Barres, B. A. (2008). The mystery and magic of glia: a perspective on their roles in health and disease. *Neuron* 60, 430–440. doi: 10.1016/j.neuron.2008.10.013

Bosman, L. W. J., Hartmann, J., Barski, J. J., Lepier, A., Noll-Hussong, M., and Reichardt, L. F. (2006). Requirement of TrkB for synapse elimination in developing cerebellar Purkinje cells. *Brain Cell Biol.* 35, 87–101. doi: 10.1007/s11068-006-9002-z

Burright, E. N., Clark, H. B., Servadio, A., Matilla, T., Feddersen, R. M., Yunis, W. S., et al. (1995). SCA1 transgenic mice: a model for neurodegeneration caused by an expanded CAG trinucleotide repeat. *Cell* 82, 937–948. doi: 10.1016/0092-8674(95)90273-2

Carter, A. R., Chen, C., Schwartz, P. M., and Segal, R. A. (2002). Brain-derived neurotrophic factor modulates cerebellar plasticity and synaptic ultrastructure. *J. Neurosci.* 22, 1316–1327. doi: 10.1523/jneurosci.22-04-01316.2002

Choo, M., Miyazaki, T., Yamazaki, M., Kawamura, M., Nakazawa, T., Zhang, J., et al. (2017). Retrograde BDNF to TrkB signaling promotes synapse elimination in the developing cerebellum. *Nat. Commun.* 8:195. doi: 10.1038/s41467-017-00260-w

Clark, H. B., Burright, E. N., Yunis, W. S., Larson, S., Wilcox, C., Hartman, B., et al. (1997). Purkinje cell expression of a mutant allele of SCA1 in transgenic mice leads to disparate effects on motor behaviors, followed by a progressive cerebellar dysfunction and histological alterations. *J. Neurosci.* 17, 7385–7395. doi: 10.1523/JNEUROSCI.17-19-07385.1997

Cvetanovic, M. (2015). Decreased expression of glutamate transporter GLAST in bergmann glia is associated with the loss of Purkinje neurons in the spinocerebellar ataxia type 1. *Cerebellum* 14, 8–11. doi: 10.1007/s12311-014-0605-0

Cvetanovic, M., Ingram, M., Orr, H., and Opal, P. (2015). Early activation of microglia and astrocytes in mouse models of spinocerebellar ataxia type 1. *Neuroscience* 289, 289–299. doi: 10.1016/j.neuroscience.2015.01.003

Cvetanovic, M., Patel, J. M., Marti, H. H., Kini, A. R., and Opal, P. (2011). Vascular endothelial growth factor ameliorates the ataxic phenotype in a mouse model of spinocerebellar ataxia type 1. *Nat. Med.* 17, 1445–1447. doi: 10.1038/nm.2494

Dell'Orco, J. M., Wasserman, A. H., Chopra, R., Ingram, M. A. C., Hu, Y.-S., Singh, V., et al. (2015). Neuronal atrophy early in degenerative ataxia is a compensatory mechanism to regulate membrane excitability. *J. Neurosci.* 35, 11292–11307. doi: 10.1523/jneurosci.1357-15.2015

Duvick, L., Barnes, J., Ebner, B., Agrawal, S., Andresen, M., Lim, J., et al. (2010). SCA1-like disease in mice expressing wild-type Ataxin-1 with a serine to aspartic acid replacement at residue 776. *Neuron* 67, 929–935. doi: 10.1016/j.neuron.2010.08.022

Ebner, B. A., Ingram, M. A., Barnes, J. A., Duvick, L. A., Frisch, J. L., Clark, H. B., et al. (2013). Purkinje cell ataxin-1 modulates climbing fiber synaptic input in developing and adult mouse cerebellum. *J. Neurosci.* 33, 5806–5820. doi: 10.1523/jneurosci.6311-11.2013

Espinoza, F. A., Turner, J. A., Vergara, V. M., Miller, R. L., Mennigen, E., Liu, J., et al. (2018). Whole-brain connectivity in a large study of Huntington's disease gene mutation carriers and healthy controls. *Brain Connect* 8, 166–178. doi: 10.1089/brain.2017.0538

Ferrer, I., Goutan, E., Marín, C., Rey, M. J., and Ribalta, T. (2000). Brain-derived neurotrophic factor in Huntington disease. *Brain Res.* 866, 257–261. doi: 10.1016/s0006-8993(00)02237-x

Ferro, A., Qu, W., Lukowicz, A., Svedberg, D., Johnson, A., and Cvetanovic, M. (2018). Inhibition of NF-κB signaling in IKKβF/F;LysM Cre mice

causes motor deficits but does not alter pathogenesis of Spinocerebellar ataxia type 1. *PLoS One* 13:e0200013. doi: 10.1371/journal.pone.0200013

Furutani, K., Okubo, Y., Kakizawa, S., and Iino, M. (2006). Postsynaptic inositol 1,4,5-trisphosphate signaling maintains presynaptic function of parallel fiber—Purkinje cell synapses via BDNF. *Proc. Natl. Acad. Sci. U S A* 103, 8528–8533. doi: 10.1073/pnas.0600497103

Genis, D., Matilla, T., Volpini, V., Rosell, J., Dávalos, A., Ferrer, I., et al. (1995). Clinical, neuropathologic and genetic studies of a large spinocerebellar ataxia type 1 (SCA1) kindred: (CAG)n expansion and early premonitory signs and symptoms. *Neurology* 45, 24–30. doi: 10.1212/wnl.45.1.24

Giampà, C., Montagna, E., Dato, C., Melone, M. A. B., Bernardi, G., and Fusco, F. R. (2013). Systemic delivery of recombinant brain derived neurotrophic factor (BDNF) in the R6/2 mouse model of Huntington's disease. *PLoS One* 8:e64037. doi: 10.1371/journal.pone.0064037

Giralt, A., Carretón, O., Lao-Peregrin, C., Martín, E. D., and Alberch, J. (2011). Conditional BDNF release under pathological conditions improves Huntington's disease pathology by delaying neuronal dysfunction. *Mol. Neurodegener.* 6:71. doi: 10.1186/1750-1326-6-71

Gusella, J. F., and MacDonald, M. E. (2000). Molecular genetics: unmasking polyglutamine triggers in neurodegenerative disease. *Nat. Rev. Neurosci.* 1, 109–115. doi: 10.1038/nrd1077

He, Y. Y., Zhang, X. Y., Yung, W. H., Zhu, J.-N., and Wang, J.-J. (2013). Role of BDNF in central motor structures and motor diseases. *Mol. Neurobiol.* 48, 783–793. doi: 10.1007/s12035-013-8466-y

Heneka, M. T., Kummer, M. P., and Latz, E. (2014). Innate immune activation in neurodegenerative disease. *Nat. Rev. Immunol.* 14, 463–477. doi: 10.1038/nri3705

Hourez, R., Servais, L., Orduz, D., Gall, D., Millard, I., and de Kerchove d'Exaerde, A. (2011). Aminopyridines correct early dysfunction and delay neurodegeneration in a mouse model of spinocerebellar ataxia type 1. *J. Neurosci.* 31, 11795–11807. doi: 10.1523/jneurosci.0905-11.2011

Huang, Y., Ko, H., Cheung, Z. H., Yung, K. K. L., Yao, T., Wang, J., et al. (2012). Dual actions of brain-derived neurotrophic factor on GABAergic transmission in cerebellar Purkinje neurons. *Exp. Neurol.* 233, 791–798. doi: 10.1016/j.expneurol.2011.11.043

Ibrahim, M. F., Power, E. M., Potapov, K., and Empson, R. M. (2017). Motor and cerebellar architectural abnormalities during the early progression of ataxia in a mouse model of SCA1 and how early prevention leads to a better outcome later in life. *Front. Cell. Neurosci.* 11:292. doi: 10.3389/fncel.2017.00292

Ilieva, H., Polymenidou, M., and Cleveland, D. W. (2009). Non-cell autonomous toxicity in neurodegenerative disorders: ALS and beyond. *J. Cell Biol.* 187, 761–772. doi: 10.1083/jcb.200908164

Ingram, M., Wozniak, E. A. L., Duvick, L., Yang, R., Bergmann, P., Carson, R., et al. (2016). Cerebellar transcriptome profiles of ATXN1 transgenic mice reveal SCA1 disease progression and protection pathways article cerebellar transcriptome profiles of ATXN1 transgenic mice reveal SCA1 disease progression and protection pathways. *Neuron* 89, 1194–1207. doi: 10.1016/j.neuron.2016.02.011

Jacobi, H., Reetz, K., du Montcel, S. T., Bauer, P., Mariotti, C., Nanetti, L., et al. (2013). Biological and clinical characteristics of individuals at risk for spinocerebellar ataxia types 1, 2, 3 and 6 in the longitudinal RISCA study: analysis of baseline data. *Lancet Neurol.* 12, 650–658. doi: 10.1016/S1474-4422(13)70104-2

Joers, J. M., Deelchand, D. K., Lyu, T., Emir, U. E., Hutter, D., Gomez, C. M., et al. (2018). Neurochemical abnormalities in premanifest and early spinocerebellar ataxias. *Ann. Neurol.* 83, 816–829. doi: 10.1002/ana.25212

Kafitz, K. W., Rose, C. R., Thoenen, H., and Konnerth, A. (1999). Neurotrophin-evoked rapid excitation through TrkB receptors. *Nature* 401, 918–921. doi: 10.1038/44847

Kim, J. H., Lukowicz, A., Qu, W., Johnson, A., and Cvetanovic, M. (2018). Astroglia contribute to the pathogenesis of spinocerebellar ataxia Type 1 (SCA1) in a biphasic, stage-of-disease specific manner. *Glia* 66, 1972–1987. doi: 10.1002/glia.23451

La Spada, A. R., and Taylor, J. P. (2010). Repeat expansion disease: progress and puzzles in disease pathogenesis. *Nat. Rev. Genet.* 11, 247–258. doi: 10.1038/nrg2748

Lima Giacobbo, B., Doorduin, J., Klein, H. C., Dierckx, R. A. J. O., Bromberg, E., and de Vries, E. F. J. (2018). Brain-derived neurotrophic factor in brain disorders: focus on neuroinflammation. *Mol. Neurobiol.* doi: 10.1007/s12035-018-1283-6 [Epub ahead of print].

Matilla-Dueñas, A., Ashizawa, T., Brice, A., Magri, S., McFarland, K. N., Pandolfo, M., et al. (2014). Consensus paper: pathological mechanisms underlying neurodegeneration in spinocerebellar ataxias. *Cerebellum* 13, 269–302. doi: 10.1007/s12311-013-0539-y

Miller, J. A., Ding, S., Sunkin, S. M., Smith, K. A., Ng, L., Szafer, A., et al. (2014). Transcriptional landscape of the prenatal human brain. *Nature* 508, 199–206. doi: 10.1038/nature13185

Mincheva-Tasheva, S., and Soler, R. M. (2013). NF-κB signaling pathways: role in nervous system physiology and pathology. *Neuroscientist* 19, 175–194. doi: 10.1177/1073858412444007

Nagahara, A. H., Merrill, D. A., Coppola, G., Tsukada, S., Schroeder, B. E., Shaked, G. M., et al. (2009). Neuroprotective effects of brain-derived neurotrophic factor in rodent and primate models of Alzheimer's disease. *Nat. Med.* 15, 331–337. doi: 10.1038/nm.1912

Orr, H. T., and Zoghbi, H. Y. (2007). Trinucleotide repeat disorders. *Annu. Rev. Neurosci.* 30, 575–621. doi: 10.1146/annurev.neuro.29.051605.113042

Paulson, H. L., Shakkottai, V. G., Clark, H. B., and Orr, H. T. (2017). Polyglutamine spinocerebellar ataxias—from genes to potential treatments. *Nat. Rev. Neurosci.* 18, 613–626. doi: 10.1038/nrn.2017.92

Pekny, M., Pekna, M., Messing, A., Steinhäuser, C., Lee, J. M., Parpura, V., et al. (2016). Astrocytes: a central element in neurological diseases. *Acta Neuropathol.* 131, 323–345. doi: 10.1007/s00401-015-1513-1

Qu, W., Johnson, A., Kim, J. H., Lukowicz, A., Svedberg, D., and Cvetanovic, M. (2017). Inhibition of colony-stimulating factor 1 receptor early in disease ameliorates motor deficits in SCA1 mice. *J. Neuroinflammation* 14:107. doi: 10.1186/s12974-017-0880-z

Rüb, U., Schöls, L., Paulson, H., Auburger, G., Kermer, P., Jen, J. C., et al. (2013). Clinical features, neurogenetics and neuropathology of the polyglutamine spinocerebellar ataxias type 1, 2, 3, 6 and 7. *Prog. Neurobiol.* 104, 38–66. doi: 10.1016/j.pneurobio.2013.01.001

Rubinsztein, D. C., and Orr, H. T. (2016). Diminishing return for mechanistic therapeutics with neurodegenerative disease duration?: there may be a point in the course of a neurodegenerative condition where therapeutics targeting disease-causing mechanisms are futile. *Bioessays* 38, 977–980. doi: 10.1002/bies.201600048

Ruegsegger, C., Stucki, D. M., Steiner, S., Angliker, N., Radecke, J., Keller, E., et al. (2016). Impaired mTORC1-dependent expression of homer-3 influences SCA1 pathophysiology. *Neuron* 89, 129–146. doi: 10.1016/j.neuron.2015.11.033

Saha, R. N., Liu, X., and Pahan, K. (2006). Up-regulation of BDNF in astrocytes by TNF-α: a case for the neuroprotective role of cytokine. *J. Neuroimmune Pharmacol.* 1, 212–222. doi: 10.1007/s11481-006-9020-8

Schwartz, P. M., Borghesani, P. R., Levy, R. L., Pomeroy, S. L., and Segal, R. A. (1997). Abnormal cerebellar development and foliation in BDNF$^{-/-}$ mice reveals a role for neurotrophins in CNS Patterning. *Neuron* 19, 269–281. doi: 10.1016/s0896-6273(00)80938-1

Serra, H. G., Duvick, L., Zu, T., Carlson, K., Stevens, S., Jorgensen, N., et al. (2006). ROR α-mediated purkinje cell development determines disease severity in adult SCA1 mice. *Cell* 127, 697–708. doi: 10.1016/j.cell.2006.09.036

Sherrard, R. M., Dixon, K. J., Bakouche, J., Rodger, J., Lemaigre-dubreuil, Y., and Mariani, J. (2009). Differential expression of TrkB isoforms switches climbing fiber-purkinje cell synaptogenesis to selective synapse elimination. *Dev. Neurobiol.* 69, 647–662. doi: 10.1002/dneu.20730

Shin, H. W., Kim, H., and Lee, K. J. (2015). Differences in BDNF serum levels in patients with Alzheimer's disease and mild cognitive impairment. *J. Psychiatry* 18:245. doi: 10.4172/psychiatry.1000245

Storey, E. (2013). Presymptomatic features of spinocerebellar ataxias. *Lancet Neurol.* 12, 625–626. doi: 10.1016/s1474-4422(13)70116-9

Tabrizi, S. J., Scahill, R. I., Owen, G., Durr, A., Leavitt, B. R., Roos, R. A., et al. (2013). Predictors of phenotypic progression and disease onset in premanifest and early-stage Huntington's disease in the TRACK-HD study: analysis of 36-month observational data. *Lancet Neurol.* 12, 637–649. doi: 10.1016/s1474-4422(13)70088-7

Takahashi, M., Ishikawa, K., Sato, N., Obayashi, M., Niimi, Y., Ishiguro, T., et al. (2012). Reduced brain-derived neurotrophic factor (BDNF) mRNA expression and presence of BDNF-immunoreactive granules in the spinocerebellar ataxia type 6 (SCA6) cerebellum. *Neuropathology* 6, 595–603. doi: 10.1111/j.1440-1789.2012.01302.x

Willson, M. L., McElnea, C., Mariani, J., Lohof, A. M., and Sherrard, R. M. (2008). BDNF increases homotypic olivocerebellar reinnervation and associated fine motor and cognitive skill. *Brain* 131, 1099–1112. doi: 10.1093/brain/awn024

Yamamoto, A., and Lucas, J. (2000). Reversal of neuropathology and motor dysfunction in a conditional model of Huntington's disease. *Cell* 101, 57–66. doi: 10.1016/s0092-8674(00)80623-6

Zoghbi, H. Y., and Orr, H. T. (2009). Pathogenic mechanisms of a polyglutamine-mediated neurodegenerative disease, spinocerebellar ataxia type 1. *J. Biol. Chem.* 284, 7425–7429. doi: 10.1074/jbc.R800041200

Zu, T., Duvick, L. A., Kaytor, M. D., Berlinger, M. S., Zoghbi, H. Y., Clark, H. B., et al. (2004). Recovery from polyglutamine-induced neurodegeneration in conditional SCA1 transgenic mice. *J. Neurosci.* 24, 8853–8861. doi: 10.1523/JNEUROSCI.2978-04.2004

Zuccato, C., and Cattaneo, E. (2007). Role of brain-derived neurotrophic factor in Huntington's disease. *Prog. Neurobiol.* 81, 294–330. doi: 10.1016/j.pneurobio.2007.01.003

Conflict of Interest Statement: The authors declare that the research was conducted in the absence of any commercial or financial relationships that could be construed as a potential conflict of interest.

frontiers in Cellular Neuroscience

ORIGINAL RESEARCH
published: 07 February 2019
doi: 10.3389/fncel.2019.00015

The Alteration of Intrinsic Excitability and Synaptic Transmission in Lumbar Spinal Motor Neurons and Interneurons of Severe Spinal Muscular Atrophy Mice

Jianli Sun[1,2]* *and Melissa A. Harrington*[1,2]*

[1]*Delaware Center for Neuroscience Research, Delaware State University, Dover, DE, United States,* [2]*Department of Biological Science, Delaware State University, Dover, DE, United States*

Spinal muscular atrophy (SMA) is the leading genetic cause of death in infants. Studies with mouse models have demonstrated increased excitability and loss of afferent proprioceptive synapses on motor neurons (MNs). To further understand functional changes in the motor neural network occurring in SMA, we studied the intrinsic excitability and synaptic transmission of both MNs and interneurons (INs) from ventral horn in the lumbar spinal cord in the survival motor neuron (SMN)Δ7 mouse model. We found significant differences in the membrane properties of MNs in SMA mice compared to littermate controls, including hyperpolarized resting membrane potential, increased input resistance and decreased membrane capacitance. Action potential (AP) properties in MNs from SMA mice were also different from controls, including decreased rheobase current, increased amplitude and an increased afterdepolarization (ADP) potential. The relationship between AP firing frequency and injected current was reduced in MNs, as was the threshold current, while the percentage of MNs showing long-lasting potentiation (LLP) in the intrinsic excitability was higher in SMA mice. INs showed a high rate of spontaneous firing, and those from SMA mice fired at higher frequency. INs from SMA mice showed little difference in their input-output relationship, threshold current, and plasticity in intrinsic excitability. The changes observed in both passive membrane and AP properties suggest greater overall excitability in both MNs and INs in SMA mice, with MNs showing more differences. There were also changes of synaptic currents in SMA mice. The average charge transfer per post-synaptic current of spontaneous excitatory and inhibitory synaptic currents (sEPSCs/sIPSCs) were lower in SMA MNs, while in INs sIPSC frequency was higher. Strikingly in light of the known loss of excitatory synapses

OPEN ACCESS

Edited by:
Jing-Ning Zhu,
Nanjing University, China

Reviewed by:
Wen-Chang Li,
University of St. Andrews, United Kingdom
Manuel Esteban Diaz-Rios,
University of Puerto Rico, Medical Sciences Campus, Puerto Rico

***Correspondence:**
Jianli Sun
jianlisun@desu.edu
Melissa A. Harrington
mharrington@desu.edu

Received: *14 August 2018*
Accepted: *16 January 2019*
Published: *07 February 2019*

Citation:
Sun J and Harrington MA (2019) The Alteration of Intrinsic Excitability and Synaptic Transmission in Lumbar Spinal Motor Neurons and Interneurons of Severe Spinal Muscular Atrophy Mice. Front. Cell. Neurosci. 13:15. doi: 10.3389/fncel.2019.00015

Abbreviations: ACSF, artificial cerebral spinal fluid; ADP, afterdepolarization; AHP, afterhyperpolarization; AMPA, α-amino-3-hydroxy-5-methyl-4-isoxazolepropionic acid; AP, action potential; CPG, central pattern generator; EPSC, excitatory postsynaptic current; F-I curve, frequency-current curve; GABA, γ-Aminobutyric Acid; IN, interneuron; IPSC, inhibitory postsynaptic current; LLD, long-lasting depression; LLP, long-lasting potentiation; MN, motor neuron; NMDA, N-Methyl-D-aspartic acid or N-Methyl-D-aspartate; SCI, spinal cord injury; SMA, spinal muscular atrophy; SMN, survival motor neuron; TTX, Tetrodotoxin; VAChT, Vesicular acetylcholine transporter; VGLUT, vesicular glutamate transporter.

on MNs, there was no difference in sEPSC frequency in MNs from SMA mice compared to controls. For miniature synaptic currents, mEPSC frequency was higher in SMA MNs, while for SMA INs, both mEPSC and mIPSC frequencies were higher. In SMA-affected mice we observed alterations of intrinsic and synaptic properties in both MNs and INs in the spinal motor network that may contribute to the pathophysiology, or alternatively, may be a compensatory response to preserve network function.

Keywords: spinal muscular atrophy, intrinsic excitability, synaptic transmission, motor neuron, interneuron

INTRODUCTION

The molecular genetics underlying spinal muscular atrophy (SMA) have been well established since 1995 with the discovery that it results from deletion or mutation of the *survival motor neuron 1* (*SMN1*) gene encoding the survival motor neuron (SMN) protein (Lefebvre et al., 1995). The human genome contains two SMN-coding genes, *SMN1* and *SMN2* (Lefebvre et al., 1995; Rochette et al., 2001). The telomeric *SMN1* expresses full-length SMN protein while the centromeric *SMN2* predominantly produces the unstable SMNΔ7 protein due to the aberrant splicing of exon 7 (Lorson et al., 1999; Monani et al., 2000). Deletion of, or mutations in *SMN1* are found in all types of SMA patients, with the severity of disease depending on the copy number of *SMN2*, which contributes different levels of residual SMN protein (Gennarelli et al., 1995; Lefebvre et al., 1995).

The SMN protein is ubiquitously expressed and localized in nuclear "gems" (Gubitz et al., 2004), in the cytoplasm (Liu and Dreyfuss, 1996), in neuronal growth cones (Fan and Simard, 2002), and neuronal axon (Fallini et al., 2010). The SMN protein plays an essential role in the assembly of the spliceosomal small nuclear ribonucleoproteins (Gubitz et al., 2004), regulates RNA metabolism (Li et al., 2014), actin cytoskeleton dynamics (Hensel and Claus, 2018), mRNA transport (Donlin-Asp et al., 2016), ubiquitin homeostasis (Groen and Gillingwater, 2015), bioenergetics pathways (Boyd et al., 2017) and synaptic vesicle release (Kong et al., 2009). Unfortunately, it is still not clear how low levels of SMN protein lead to the pathophysiology associated with SMA.

The most advanced clinical trials for SMA are focused on increasing SMN protein level by upregulating the production of full length protein from the *SMN2* gene (d'Ydewalle and Sumner, 2015), and the first, very costly, drug to specifically treat SMA was approved by the U.S. Food and Drug Administration in December 2016 (Aartsma-Rus, 2017), 125 years after the first description of this disease. However, we still lack a comprehensive therapy for SMA, since increasing SMN level does not abrogate but simply slows down the neurodegenerative process. Additional compounds or approaches that could slow the decline in neuromuscular function would be a major advance for SMA patients and their families. While current treatments and exploratory approaches seek to increase survival based on increasing SMN expression, the development of complementary approaches to preserving neuromuscular function will require a deeper understanding of the molecular pathology underlying the disease process.

Although planning and initiation of movement take place in the cortex, the basal ganglia, midbrain, and hindbrain, the generation of locomotion in vertebrates is mainly determined by neural networks in the spinal cord. Spinal circuits contain the basic instructions for coordinating the sequence of muscle activation during locomotion and are engaged by descending and ascending supraspinal systems for volitional tasks (Arber, 2012; Miri et al., 2013). With the combination of electrophysiology and mouse genetics to identify and manipulate the activity of components of the spinal locomotor networks, in the past two decades, great advances have been made in understanding of the organization of spinal networks in mammals, particularly those for locomotion (Kiehn, 2016).

This network appears to be active at birth, long before locomotion begins (Whelan et al., 2000; Juvin et al., 2007), and during a period when mouse models for SMA show minimal signs of pathology. Recent studies showed the impairment of proprioceptive synaptic input to motor neurons (MNs) observed in SMA mouse models occurs before neuronal loss (Mentis et al., 2011), and loss of vesicular glutamate transporter (VGLUT)1-labeled inputs to MNs has even been detected in embryos (Tarabal et al., 2014). In contrast, an increase of VGLUT1 and Vesicular acetylcholine transporter (VAChT) expression was found in calbindin-immunoreactive interneurons (INs)—Renshaw cells in a mouse model of SMA (Thirumalai et al., 2013). These studies suggest that spinal circuit dysfunction may be a feature of SMA, even though the locomotor activity appears to be normal in P4–6 SMA mice (Thirumalai et al., 2013), and the contribution of spinal motor network to the pathophysiology of SMA cannot be excluded without careful studies. In addition, there is substantial overlap and intermingling between spinal INs for different muscles and motor activities (Barthélemy et al., 2006; Levine et al., 2012).

SMA-related dysfunctions in sensory-motor pathways have been observed to occur prior to neuromuscular junction deficits or cell death, suggesting that there may be an early disease phase in which network function is altered while neurons remain viable. While alterations in MNs' intrinsic properties have been reported, whether there are changes in the intrinsic and synaptic properties of the various INs involved in the motor network is unknown.

In the current study, we investigated the passive membrane properties, action potentials (APs), long-lasting plasticity in intrinsic excitability, spontaneous and miniature synaptic currents in ventral horn alpha MNs and INs in spinal cord slices from SMA and control mice. We found increased excitability and synaptic abnormality in both types of neurons. The differences

in the long-lasting plasticity of the intrinsic excitability and spontaneous synaptic release in both neuron types suggests that there is a compensatory adjustment occurring in SMA. Whether this modulation is beneficial or harmful to the motor output and MN survival is yet to be determined.

MATERIALS AND METHODS

Animals

This study was carried out in accordance with the recommendations of the Institutional Animal Care and Use Committee of Delaware State University. The protocol was approved by the Institutional Animal Care and Use Committee of Delaware State University. Mice were maintained under a 14/10 h light/dark photoperiod with PMI rodent diet (Animal Specialties and Provisions) and water available *ad libitum*. *Smn1* heterozygotes male and female mice of the FVB.Cg-Grm7<Tg(SMN2)89Ahmb >Smn1<tm1Msd > Tg(SMN2*delta7)4299 strain obtained from Jackson Laboratory (stock#: 005025, Bar Harbor, ME, USA) were mated to produce pups for experiments. Postnatal pups from 6 to 10 days old were used in the experiment. Genotyping of mouse pups and adults was done by Transnetyx (Germantown, TN, USA). Pups were genotyped and assigned to experimental groups after recording and data analysis were completed. Wild type and heterozygous pups were pooled as control, pups with the homozygous mutation formed the SMA group as described previously (Zhang et al., 2010).

Chemicals and Solutions

Artificial cerebral spinal fluid (ACSF) contained (in mM): 126 NaCl, 3 KCl, 2 $MgCl_2$, 2 $CaCl_2$, 1.25 NaH_2PO_4, 10 glucose, and 26 $NaHCO_3$ (pH 7.2, 300–310 mOsm). Tissue slicing solution contained (in mM): 2.5 KCl, 10 $MgSO_4$, 0.5 $CaCl_2$, 1.25 NaH_2PO_4, 234 sucrose, 11 glucose, and 26 $NaHCO_3$ (pH 7.2, 310–330 mOsm). Intracellular solution contained (in mM): 130 K-gluconate, 10 Hepes, 11 EGTA, 2.0 $MgCl_2$, 2.0 $CaCl_2$, 4 Na-ATP, and 0.2 Na-GTP (pH 7.2–7.3 with KOH, 290–310 mOsm). Receptor antagonists (in μM) 10 CNQX (6-cyano-7-nitroquinoxaline), 50 LD-AP-5 [D-(–)-2-amino-5-phosphonovaleric acid], 10 bicuculline, and 10 strychnine were included in the ACSF to block AMPA, NMDA, $GABA_A$, and glycine receptors respectively. Tetrodotoxin (TTX; 1 μM) was applied to block AP for recording of miniature synaptic currents. All drugs were purchased from Tocris (Bristol, UK), except strychnine which was purchased from Sigma-Aldrich (St. Louis, MO, USA).

Spinal Cord Slice Preparation

A single mouse of postnatal day P6–P10 was anesthetized in a sealed chamber containing the inhalation anesthetic Isoflurane in an upward flowing Biological Safety Level (BSL) 2 cabinet. After decapitation, the skin and limbs were quickly removed leaving part of the hind limbs for insect pins, and the tissue was immersed in ice-cold oxygenated slicing solution. Two cuts through the shoulders and down the chest cage removed most tissue leaving just the vertebral column and enough ribs on each side for insect pins to hold. The cervical and top thoracic section of the cord were cut off to isolate the intact lumbar segment of the spinal cord. Remaining viscera and tissue around the vertebral column were removed on both dorsal and ventral sides to make it easier for laminectomy. The vertebral column was transferred to a silicon-filled petri dish, pinned dorsal side up with insect pins, and continuously perfused with carbogen-bubbled (5% CO_2, 95% O_2) ice-cold slicing solution. A laminectomy on the dorsal side exposed the spinal cord, using fine forceps the dura was peeled along the rostro-caudal axis, and the lumbar enlargement was isolated. Using a transfer pipet, the spinal cord was placed in a groove cut in a block of 5% agar to make a "hot dog". The surface was dried with filter paper, the agar block was glued onto the cutting chamber block, and 400 μM slices were cut with a LEICA VT1200S tissue slicer (Leica Microsystems, Wetzlar, Germany). Slices were moved into the incubation chamber with a transfer pipet and kept at 34°C for 30 min. Slices were left at room temperature for more than 30 min before recording.

Whole-Cell Patch-Clamp Recording

The recording chamber was continuously perfused with pre-heated 34°C ACSF at a rate of 2–3 ml/min. MNs and INs were identified using an IR-1000 infrared sensitive camera (DAGE MTI, Michigan City, IN, USA) coupled with a DIC-equipped BX51WI microscope from Olympus (Center Valley, PA, USA). Alpha MNs, which are selectively lost after SMA (Powis and Gillingwater, 2016), were recognized by their minimum soma diameter (>20 μM) and location (lamina IX). INs were distinguished by their smaller minimum soma diameter (<10 μM), high input resistance (>100 MΩ), and depolarized resting membrane potentials (≈ −50 mV). Most INs recorded were located in laminae VII and VIII. Cells were patched in the whole-cell configuration with patch pipettes (resistance of 2–4 MΩ) filled with intracellular solution. Current-clamp recordings were acquired with a MultiClamp 700B amplifier, low pass filtered at 10 kHz and digitized at 100 kHz with a Digidata 1440A (both from Molecular Devices; Sunnyvale, CA, USA). Spontaneous membrane potentials were recorded for 2 min to measure the resting membrane potential (Vrest) and firing frequency for neurons with spontaneous firing. To study AP properties, APs were evoked every 5 s with positive current injection step intervals of 20 pA and 200 pA for 5 ms for INs and MNs, respectively. To study the firing frequency vs. injected current (F-I) relationships, 500 ms negative and positive steps were applied every 10 s with the same step intervals as for AP activation. The membrane potential of the INs was held at −55 mV, and MNs at −65 mV by manually adjusted DC current injection.

Studies of models for neuronal plasticity suggested that memory traces can be supported not only by selective changes in the synaptic strength–synaptic plasticity, but that modifications in neuronal excitability—a plasticity in intrinsic properties, might also contribute to cellular substrates for memory. Long-lasting plasticity in intrinsic properties shares common features with synaptic plasticity which has been more extensively studied (Daoudal and Debanne, 2003). To study long-lasting plasticity in the intrinsic electrical properties of the spinal cord

neurons, INs were manually held at −50 mV, and MNs at −60 mV. The test protocol comprised 11 steps total, five negative and five positive, 500 ms duration at 10 s intervals, with the most positive step evoking 12–15 spikes. The conditioning protocol involved a 50 ms positive current injection to evoke three APs in each neuron. For the baseline before conditioning, three test trials were recorded with a 20 s delay, and a total recording of 6 min. For the conditioning stimulation, the conditioning protocol was delivered for 6 min at 2 Hz. Fifteen test trials totaling 30 min of time were recorded immediately after conditioning. For the baseline condition, 20 test trials totaling 40 min were recorded without conditioning stimulation.

Synaptic currents were recorded under voltage-clamp mode. Signals were digitized at 100 KHz, and low pass filtered at 4K and 6K Hz for INs and MNs, respectively. All neurons were clamped at −55 mV to record both excitatory and inhibitory postsynaptic currents (EPSCs and IPSCs) which were recorded from the same neuron simultaneously for 3 min. The outward IPSCs and inward EPSCs currents were confirmed by glutamatergic, GABAergic and glycinergic receptor antagonists (**Figure 8A**). The liquid junction potential (−13.5 mV) was compensated, and access resistance was continuously monitored and rechecked after each recording. If the series resistance increased by 20% at any time, the recording was terminated or data excluded from analysis.

Analysis

Current-clamp recordings were analyzed with Clampfit 10.4 (Molecular Devices; Sunnyvale, CA, USA). Membrane input resistance (Rin) was calculated from averaged voltage deflections during the last 50.75 ms of the 500 ms hyperpolarizing current pulse injection. The membrane time constant (Tau) was derived from an exponential decay fit applied to the beginning 173.29 ms of the 500 ms current-evoked hyperpolarization steps when onset of the hyperpolarization did not evoke channel activation (**Figures 1C,D**). The capacitance of the neuron (C) was calculated by the measurement of Rin and tau (Tau = C*Rin). AP amplitude was measured from the first AP evoked. AP threshold was defined as the membrane potential at which dV/dt first exceeds 10 V/s (Fricker et al., 1999). The minimum current to evoke an AP was defined as the rheobase current. The baseline for determining the afterdepolarization (ADP) and the afterhyperpolarization (AHP) was the membrane potential before AP activation (−55 mV for INs and −65 for MNs). F-I relationships were fit linearly to get the current threshold, and the slope was defined as neuronal gain. The degree of long-lasting potentiation (LLP) and depression (LLD) was calculated by the average percentage of firing frequency from 20 min to 40 min compared to the average frequency before conditioning stimulation. The one-tailed P value for the proportion of percentage comparison was calculated in Excel. Voltage-clamp synaptic currents were analyzed with MiniAnalysis6.0.7 (Synaptosoft, Decatur, GA, USA). The data distribution was tested by the ratio of Skewness and Kurtosis to their standard error in Excel. The normality was rejected if the ratio is less than −2 or greater than +2. Significance in synaptic currents was tested by Kolmogorov-Smirnov (K-S) test, other data was tested with student t-test unless otherwise noted. Statistical significance was set at $P < 0.05$. The data shown represent means ± SEM.

RESULTS

Resting Membrane Properties Suggest Increased Excitability in Both MNs and INs in SMNΔ7 Mice

A hyperexcitability of MNs has been reported in SMA mice (Mentis et al., 2011), in MNs derived from stem cell models of SMA (Simon et al., 2016), and iPSCs from severe SMA patients (Liu et al., 2015). Whether there are changes in the excitability of INs is unknown. In this study, we examined the excitability of both MNs and INs in the ventral horn of the lumbar spinal cords from post-natal day (P)6 to P10 SMNΔ7 mice (**Figure 1**). At rest, only 1 out of 31 MNs from control and no MNs (19) from SMNΔ7 mice showed spontaneous AP activity, while the majority of INs were spontaneously active (65% of control neurons and 71% of SMA neurons; **Figures 1A,B,G**). The frequency of spontaneous firing was higher in INs from SMNΔ7 mice compared to controls (9.7 ± 1.5 Hz vs. 6.5 ± 1.2 Hz, $P < 0.05$; **Figures 1B,H**). For MNs of SMNΔ7 mice, the resting membrane potential was hyperpolarized compared to control (−68.8 ± 1.0 mV vs. −64.3 ± 0.6 mV, $P < 0.01$; **Figures 1A,I**), while for INs, the resting potential was depolarized compared to MNs but was not significantly different in control compared to SMA (−52.1 ± 1.0 mV vs. −54.2 ± 1.0 mV; **Figure 1I**). The input resistance was significant higher in SMNΔ7 MNs compared to controls (44.2 ± 4.6 MΩ vs. 21.9 ± 2.0 MΩ, $P < 0.01$; **Figures 1C,E,K**) consistent with increased excitability, however the capacitance of SMNΔ7 MNs was lower compared to controls (264 ± 35 μF vs. 629 ± 84 μF, $P < 0.01$; **Figure 1L**). Current-voltage (I-V) curves used to calculate input resistance show the difference in intrinsic electrical properties in MNs from SMA mice and controls (**Figure 1E**), while INs show no difference (**Figure 1F**). The differences in input resistance and cell capacitance may have balanced out, as the membrane time constant was no different in MNs from SMNΔ7 mice compared to controls (10.5 ± 1.2 ms vs. 12.0 ± 0.1 ms; **Figures 1C,J**). For INs there was no difference between control and SMA neurons in input resistance (305 ± 33 MΩ vs. 304 ± 38 MΩ; **Figures 1D,F,K**), capacitance (control, 131 ± 27 μF; SMA, 127 ± 17 μF; **Figure 1L**) or time constant (control, 32 ± 4.6 ms; SMA, 34 ± 3.4 ms; **Figures 1D,J**). The input resistance of the INs in our recordings is somewhat lower than has been reported in other studies of the intrinsic properties of spinal INs (Zhong et al., 2006; Zhang et al., 2008). Possible reasons for this difference include the age of the animals (these recordings were made at P6–P10, while the earlier reports were of recordings made at P0–P3), the fact that in our studies fast synaptic transmission was not blocked as it was in the earlier studies, and differences in the populations of INs studied. Overall, our

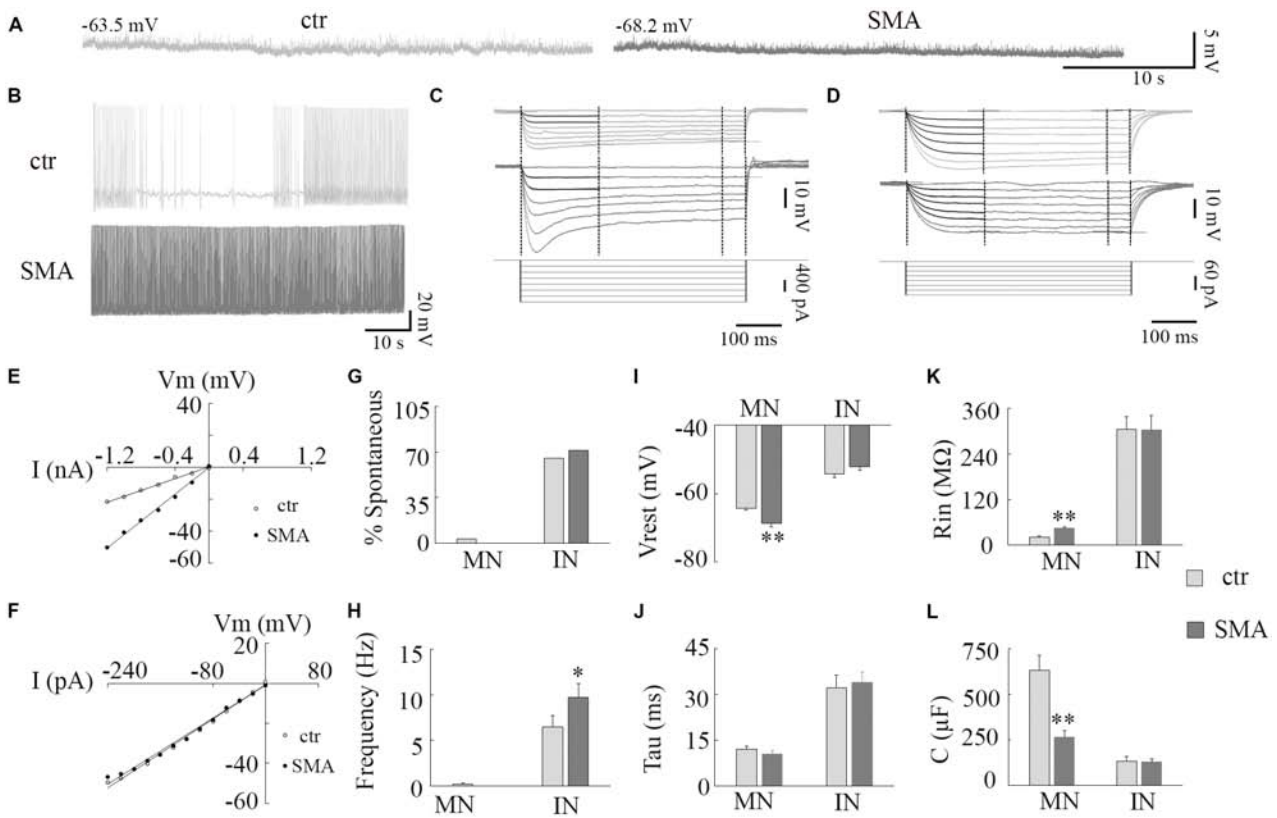

FIGURE 1 | Resting membrane properties of motor neurons (MNs) and interneurons (INs) in survival motor neuron (SMN)Δ7 mouse model mice. **(A)** Representative traces of spontaneous membrane potential in control (left) and spinal muscular atrophy (SMA; right) MNs. **(B)** Representative spontaneous firing in INs of control (top) and SMA (bottom). **(C,D)** Representative traces of membrane potentials evoked by hyperpolarization current pulses (bottom) for calculations of input resistance (Rin), time constant (Tau), and membrane capacitance (C) for control (top) and SMA (middle) MNs **(C)** and INs **(D)**. **(E,F)** Voltage/current relationship for MNs **(E)** and INs **(F)**. **(G)** Percent of neurons spontaneously firing at rest in MNs (n = 31 cells for control and 19 cells for SMA) and INs (n = 43 cells for control and n = 23 cells for SMA). **(H)** Frequency of spontaneous firing at rest for a single MN (from control) and INs (n = 28 cells for control and n = 23 cells for SMA). **(I)** Resting membrane potential for MNs (n = 31 cells for control and n = 19 cells for SMA) and INs (n = 43 cells for control and n = 31 cells for SMA). **(J–L)** Time constant (Tau, **J**), Input resistance (Rin, **K**), Membrane capacitance (C, **L**) in MNs and INs from control (n = 19 cells) and SMNΔ7 (n = 13 cells). $^*P < 0.05$, $^{**}P < 0.01$ with student t-test. Overall cells were recorded from spinal cords of eight SMA mice and 11 of their littermate controls.

results indicate that although it is manifested in different ways, by increased spontaneous firing in INs, and by changes in the membrane properties in MNs, the membrane excitability of both MNs and INs appears to be increased in SMA mice.

Action Potential Properties Are Different in SMA Motor Neurons Compared to Controls, While Interneurons Show Fewer Differences Between Control and SMA

Consistent with other studies (Mentis et al., 2011; Liu et al., 2015; Simon et al., 2016), we found many differences in the AP properties of MNs in SMNΔ7 mice compared to their littermate controls. These differences included a larger AP amplitude (110 ± 1.6 mV in SMA vs. 99 ± 2.3 mV in control, $P < 0.01$; **Figures 2A,C**), a lower rheobase current (1.2 ± 0.1 nA in SMA vs. 1.8 ± 0.1 nA in control, $P < 0.01$; **Figure 2E**), and a trend toward a more hyperpolarized voltage threshold for APs in SMA mice compared to controls (−48 ± 1.1 mV vs. −46 ± 0.7 mV; $P = 0.06$; **Figure 2F**). Further, we also found a larger AP half-width (0.72 ± 0.04 ms vs. 0.58 ± 0.02, $P < 0.01$; **Figures 2A,D**), and greater amplitude in the ADP potential in SMA MNs compared to control (13.6 ± 1.2 mV vs. 8.4 ± 1.2 mV, $P < 0.01$; **Figures 2B,G**). The amplitude of the AHP is very small in MNs, and there was no difference between SMA and control MNs (−1.5 ± 0.4 mV vs. −2.1 ± 0.4 mV; **Figures 2B,H**).

There were some differences in the AP properties of INs from SMA mice. AP amplitude was not different between control and SMA mice (87 ± 2.8 mV vs. 91 ± 2.3 mV; **Figures 2A,C**), neither was rheobase current (0.19 ± 0.02 nA vs. 0.19 ± 0.01 nA; **Figure 2E**), ADP (4.5 ± 1.5 mV vs. 4.2 ± 0.9 mV, **Figures 2B,G**), nor AHP (−7.5 ± 1.0 mV vs. −6.7 ± 0.7; **Figures 2B,H**). However, the AP half-width was significantly smaller in SMA INs compared to control (0.82 ± 0.04 ms vs. 1.02 ± 0.07 ms, $P < 0.01$; **Figures 2A,D**). In addition, the AP threshold voltage was hyperpolarized in SMA INs compared to control neurons (−41.5 ± 0.8 mV vs.

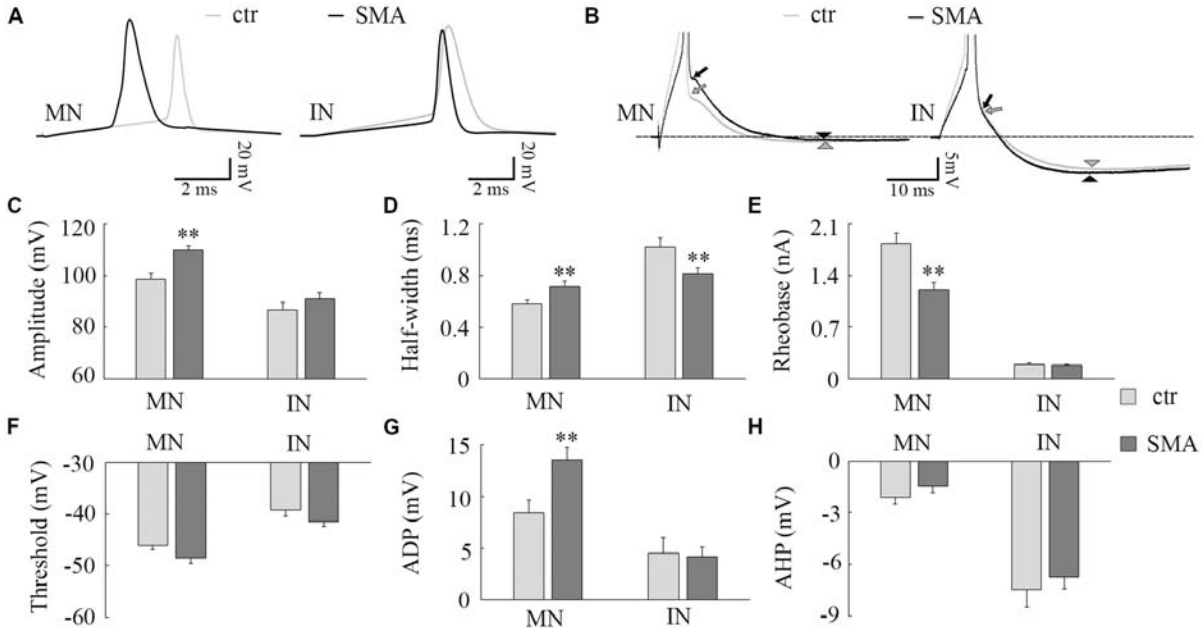

FIGURE 2 | Differences in action potential (AP) properties in MNs and INs from SMA mice. **(A)** Representative recordings of APs from MNs (left) and INs (right) from control (gray) and SMA (black) mice. **(B)** Truncated AP recording from the same neuron in **(A)**, showing the site of calculation of afterdepolarization (ADP; arrow) and afterhyperpolarization (AHP; arrowhead) amplitudes. **(C–H)** For MNs, n = 13 cells for control, n = 17 cells for SMA from seven SMA mice and seven littermate controls, while for INs, n = 17 cells for control, n = 13 cells for SMA from six SMA mice and 11 littermate control mice. **(C)** Peak amplitude of APs. **(D)** Half-with of APs. **(E)** Rheobase current from SMA mice and controls. **(F)** The AP threshold trends toward hyperpolarized in both MNs (P = 0.06) and INs (P = 0.06) of SMA mice compared to controls. **(G)** ADP and **(H)** AHP in MNs and INs from SMA and control mice. $^{**}P < 0.01$.

-39.2 ± 1.2 mV) although this trend did not reach significance (P = 0.06; **Figure 2F**).

These changes in AP properties indicate that there may be a difference in ion channel expression and/or function in SMA neurons (Liu et al., 2015). Overall, the differences in both passive membrane properties and the AP suggest an increased excitability of both MNs and INs in SMA model mice.

Changes in Input-Output Relationships in MNs and INs From SMNΔ7 Mice Compared to Controls

To assess how the changes in neuronal excitability in MNs and INs are expressed over a range of input currents, we studied the input-output relationships of MNs and INs in both control and SMA mice. The input-output (I-O) curve (also known as neuronal gain) was measured by the slope of a linear fit of the frequency-current (F-I) plot. In MNs, the frequency-current curve (F-I curve) was higher in SMA MNs compared to controls reflecting their increased excitability (**Figure 3B**). The threshold current was significantly lower in SMA mice compared to littermate controls (121 ± 70 pA vs. 635 ± 86 pA, $P < 0.01$; **Figure 3E**). However, the slope of the F-I relationship was lower in SMA (61.7 ± 3.5 Hz/nA in SMA vs. 79.6 ± 6.7 Hz/nA in control, $P < 0.05$; **Figure 3D**). The lower slope reflects the significantly higher firing frequency of SMA neurons compared to control at lower current injections (33.4 ± 3.0 Hz in SMA vs. 17.1 ± 4.6 Hz in control at 0.6 nA current injection, $P < 0.05$; 60.0 ± 5.5 Hz in SMA vs. 42.7 ± 7.2 Hz in control at 1.0 nA current injection, $P < 0.05$), but the differences were not significant at high current injections (**Figures 3A,B**). This is different from a previous study in P2 mice, that despite the increased input resistance, the firing rate was decreased in "SMA-affected MNs" (Fletcher et al., 2017). The reason for difference could be the age of the animals or/and the stage of SMA disease.

For INs there was no difference between the SMA mice and littermate controls in either F-I curve slope (242 ± 18 Hz/nA vs. 254 ± 21 Hz/nA; **Figures 3A,C,D**) or threshold current (-9.45 ± 5.2 nA vs. -6.37 ± 5.9 pA; **Figure 3E**). Since more than 65% of INs were spontaneously firing, the linearly fitted current threshold was slightly less than zero.

These results suggest that even though the excitability of MNs is greater in SMA mice, the input-output relationship is not as steep, so in SMA MNs firing frequency does not increase as much with increasing current as in control neurons. In contrast, the input-output relationship of INs was not different between control and SMA mice.

SMA Increases the Long-Lasting Potentiation in the Intrinsic Excitability of MNs

The plasticity in intrinsic properties has been identified as a cellular correlate of learning in various brain areas including the hippocampus, neocortex, and cerebellum (Daoudal and Debanne, 2003). A long-lasting plasticity of intrinsic excitability has been reported in neurons in layer 5 of mouse barrel

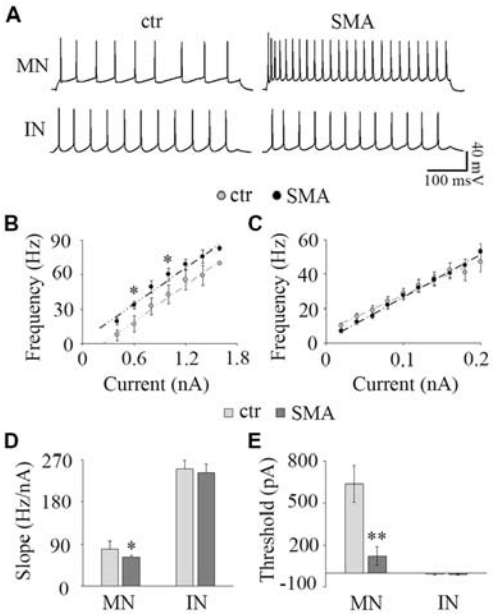

FIGURE 3 | Input-output relationship. **(A)** The representative repetitive firing by 1.0 nA current injection in MNs (top) and 40 pA in IN (bottom) in control (left) and SMA (right) mice. **(B)** Average F-I of MNs; $n = 15$ for control and $n = 15$ for SMA. The firing frequency was significant higher at 0.6 nA and 1.0 nA current injections in SMA mice. **(C)** Average F-I for INs; $n = 25$ for control, $n = 18$ for SMA. **(D)** The slope of F-I representing the gain of the neurons in MNs and INs. **(E)** The threshold current of firing in MNs and INs. $^{*}P < 0.05$, $^{**}P < 0.01$.

cortex neuron and plays a role in controlling sensory input efficiency (Mahon and Charpier, 2012). The mechanisms of the plasticity in intrinsic properties include changes in ion channel function (Beaumont and Zucker, 2000; Reyes, 2001), NMDAR (Daoudal et al., 2002), mGluR1 and mGluR5 (Sourdet et al., 2003; Ireland and Abraham, 2015), kainate receptors GluR6 (Melyan et al., 2002), CaMKII (Tsubokawa et al., 2000) and PKC (Ganguly et al., 2000). Long-lasting plasticity in intrinsic properties appears to share common features with the extensively studied synaptic plasticity. It is not known whether ventral horn neurons express a similar plasticity in intrinsic excitability and how it may be altered in SMA mice. To investigate this, we applied a 50 ms suprathreshold stimulation at 2 Hz frequency for 6 min to mimic sustained central pattern generator (CPG) activity in neonatal mouse spinal cord (Bonnot et al., 2002). This conditioning stimulus evoked three APs in each cycle (see "b" in **Figures 4A,B,D,E**). To measure the firing activity of the neuron while not distorting the neuronal activity by current injection, a test protocol of 10 equal current steps, five negative and five positive was applied. Before the 2 Hz conditioning stimulus ("a" in **Figures 4A,B,D,E**), the last step of positive current generated ∼15 APs. After the conditioning stimulus ("c" in **Figures 4A,B,D,E**) the last positive current step generated increased numbers of APs in some neurons (LLP; **Figures 4A,D**) while in others the last current step generated fewer APs (long-lasting depression, LLD; **Figures 4B,E**). In control mice 24% of MNs expressed LLP (5 of 21 cells), and 29% expressed LLD, while in SMA mice 58% of MNs expressed LLP (7 of 12 cells), and 17% expressed LLD (**Figure 4C**). There was no difference between the SMA mice and littermate controls in the degree of LLP (129.2 ± 0.6% for control vs. 134.5 ± 4.5% for SMA) and LLD (25.74 ± 13.2% for control vs. 30.74 ± 8.7% for SMA). For INs, 43% of control neurons expressed LLP (6 of 14 cells), and 29% of neuron expressed LLD; while 27% of SMA neurons expressed LLP, and 27% of neuron expressed LLD (**Figure 4F**). There was no difference between the SMA mice and littermate controls in the degree of LLP (122 ± 5.8% for control vs. 135 ± 7.4% for SMA); but the degree of LLD was reduced in SMA mice (9.84 ± 2.5% for control vs. 55.9 ± 6.3% for SMA, $P < 0.01$). In conclusion, MNs from SMA mice were much more likely to express LLP than controls (one-tailed distribution test, $P < 0.05$) after the 2 Hz 6 min stimulation. No significant differences were observed between SMA and control INs in the percentage of cells with either LLP or LLD.

Deficiencies in Presynaptic Inputs May Contribute to Excitability Changes and Trigger Compensatory Adjustments in Miniature Synaptic Current in Motor Neurons in SMA

Inhibitory Synaptic Input Is Reduced in MNs, but Increased in INs of SMNΔ7 Mice

While loss of excitatory synaptic input to MNs from proprioceptive afferents has been shown to be characteristic of SMN-deficient MNs (Mentis et al., 2011; Gogliotti et al., 2012; Martinez et al., 2012; McGovern et al., 2015), little is known about changes in synaptic transmission on other types of neurons. To investigate whether there are additional synaptic input impairments in MNs, and possibly synaptic changes in INs in SMNΔ7 mice, we used an approach to study both excitatory and inhibitory synaptic transmission simultaneously. By voltage clamping neurons at −55 mV, which is close to the resting membrane potential, it is possible to record both excitatory and inhibitory synaptic currents at the same time from the same neurons. This approach avoids the complex effects of receptor antagonists when receptor blockers are applied to isolate specific synaptic currents (Otis and Trussell, 1996; Brickley et al., 2001), and allows comparison of inhibitory and excitatory synaptic potentials in the same neurons.

Surprisingly given the known loss of proprioceptive excitatory inputs to MNs, for spontaneous excitatory post-synaptic potentials (sEPSCs) there was no difference between control and SMA MNs in frequency (7.88 ± 1.2 Hz vs. 6.71 ± 1.5 Hz) or amplitude (43 ± 2.5 pA vs. 41 ± 3.9 pA). For spontaneous inhibitory post-synaptic potentials (sIPSCs) the frequency was not different in SMA MNs compared to controls (2.71 ± 0.75 Hz vs. 4.37 ± 0.99 Hz), however the amplitude of sIPSCs trended smaller in SMA MNs compared to controls (44.9 ± 0.75 pA vs. 56.2 ± 4.2, $P = 0.07$; **Figures 5A–D**).

There were significant differences in the kinetics of the post-synaptic potentials. Rise time was significantly faster in

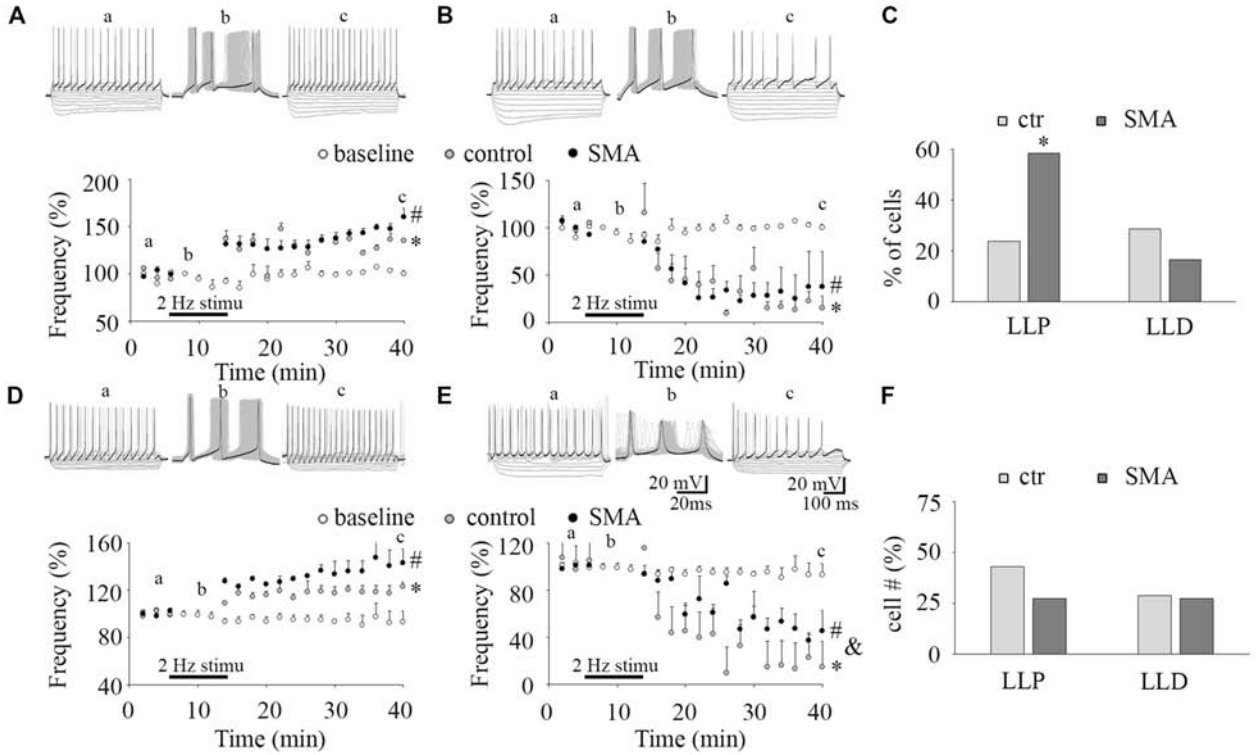

FIGURE 4 | Long-lasting plasticity in intrinsic excitability is altered in MNs from SMA mice. **(A,D)** Long-lasting potentiation of intrinsic excitability (LLP-IE) of MNs **(A)** and INs **(D)**, top, representative traces of before conditioning stimulation (a), 2 Hz conditioning stimulation (b) initially evoked 3 APs (black trace in b), and recording after conditioning (c), black traces in "a" and "c" were the last steps for analysis. Bottom: average firing frequency with time, open circles are a baseline without the conditioning stimulation (n = 4, two from control, two from SMA mice for MNs; n = 4, three from control, one from SMA mice for INs), gray circles are control neurons with the conditioning stimulation, and black circles are SMA neurons with the conditioning stimulation. One-way ANOVA with Bonfferoni *post hoc* test, * control group was significantly potentiated compared with baseline without conditioning, $P < 0.05$ at all time points except at 20 and 26 min in MNs, and except at 14 and 36 min in INs. # SMA group was compared with baseline, $P < 0.05$ at all time points except at 22 min in MNs, and at all time points in INs. **(B,E)** Long-lasting depression of intrinsic excitability (LLD-IE) of MNs **(B)** and INs **(E)** top, representative traces of before conditioning stimulation (a), 2 Hz conditioning stimulation (b) evoked 3 APs initially (the black trace in b), and recording after conditioning (c), black traces in "a" and "c" were the last steps for analysis. Bottom: summary of the firing frequency with time, without conditioning stimulation (open circles) is the baseline, control with conditioning stimulation in gray circle and SMA with conditioning stimulation is the black circles. One-way ANOVA with Bonfferoni *post hoc* test, * control group was significantly depressed compared with baseline without conditioning, $P < 0.05$ at all time points except at 14 min in MNs, $P < 0.01$ at all time points in INs. # SMA group was compared with baseline, $P < 0.05$ at all time points except at 14 and 16 min in MNs, and at time points except at 14, 16, 18, 22 and 26 min in INs; & SMA neurons were less depressed compared with control at all time points except at 40 min. **(C)** Percent of MNs expressing LLP-IE and LLD-IE in controls (n = 21 cells) and SMA mice (n = 12 cells) from a total of five control mice and five SMA mice. **(F)** Percent of INs expressing LLP-IE and LLD-IE in controls (n = 14 cells) and SMA mice (n = 11 cells) from a total of seven control mice and seven SMA mice. *One-tailed distribution test, $P < 0.05$.

SMA MNs for both sEPSCs (0.96 ± 0.07 ms vs. 1.15 ± 0.05 ms, $P < 0.05$) and sIPSCs (1.24 ± 0.06 Hz vs. 1.50 ± 0.05 ms, $P < 0.05$) compared to controls (**Figure 5E**). Similarly, the decay time was also significantly faster in SMA MNs for both sEPSCs (0.93 ± 0.07 ms vs. 1.19 ± 0.08 ms, $P < 0.05$) and sIPSCs (1.46 ± 0.11 ms vs. 2.21 ± 0.18 ms, $P < 0.01$) compared to controls (**Figure 5F**). Reflecting the faster rise and decay in MNs from SMA mice, the average charge transfer per post-synaptic current, as measured by the area of each synaptic current event, was lower in SMA MNs for both sEPSCs (52 ± 6.4 pA.ms vs. 69 ± 7.0 pA.ms, $P < 0.01$), and sIPSCs (85 ± 8.8 pA.ms vs. 150 ± 25 pA.ms, $P < 0.05$) compared to controls (**Figure 5G**).

For INs, there were fewer differences in spontaneous post-synaptic currents between SMA mice and controls. The frequency of sIPSCs was significantly higher in SMA INs (5.50 ± 1.3 Hz vs. 2.48 ± 0.66 Hz, $P < 0.01$; **Figures 6A,C**). There was no difference in the amplitude of sEPSCs in INs from SMA mice compared to controls (28.6 ± 1.7 pA vs. 28.4 ± 1.6 pA) or sIPSCs (control, 31.5 ± 2.4 pA; SMA, 35 ± 1.9 pA; **Figures 6A,B,D**). There was a faster rise time (0.89 ± 0.06 ms vs. 1.00 ± 0.05 ms, $P < 0.05$), but no change in the decay time (1.01 ± 0.09 ms vs. 1.22 ± 0.10 ms) in sEPSCs of SMA INs (**Figures 6B,E,F**). For sIPSCs, no differences were seen in INs from SMA mice vs. control mice for rise time (1.27 ± 0.06 ms vs. 1.34 ± 0.06 ms); decay time (1.97 ± 0.10 ms for control vs. 1.92 ± 0.12 ms for SMA). The charge transfer, as measured by the area of the synaptic currents, also was not different in INs from SMA mice for both sEPSCs (36.3 ± 4.5 pA.ms for SMA vs. 41.9 ± 4.5 pA.ms for control)

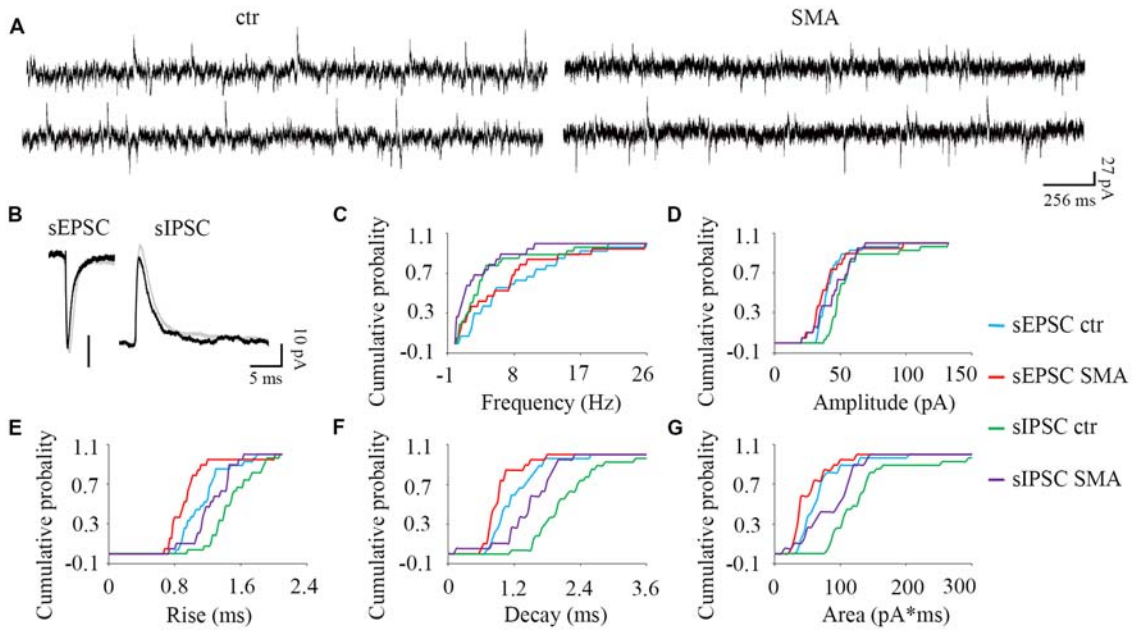

FIGURE 5 | MNs from SMA mice compared to controls show more differences in inhibitory post-synaptic currents than excitatory post-synaptic currents. **(A)** Example traces of MNs from control and SMA mice showing both excitatory and inhibitory postsynaptic currents (EPSCs and IPSCs). **(B)** Average traces of sEPSCs and sIPSCs from one representative recording for MNs from control (gray) and SMA (black) mice. **(C–G)** Cumulative probability plots of results from recordings from 19 control and 15 SMA MNs was compared with K-S test (from a total of 10 control and 7 SMA mice). **(C)** Frequency of sEPSCs and sIPSCs did not change. **(D)** Amplitude of sIPSCs trended toward a decrease ($P = 0.07$), but sEPSCs were no different. **(E)** Rise time was significantly faster in both sEPSCs ($P < 0.05$) and sIPSCs ($P < 0.05$). **(F)** Decay time was significantly faster in both sEPSCs ($P < 0.05$) and sIPSCs ($P < 0.01$). **(G)** The charge transfer (area) was significantly lower in both sEPSCs ($P < 0.01$) and sIPSCs ($P < 0.05$).

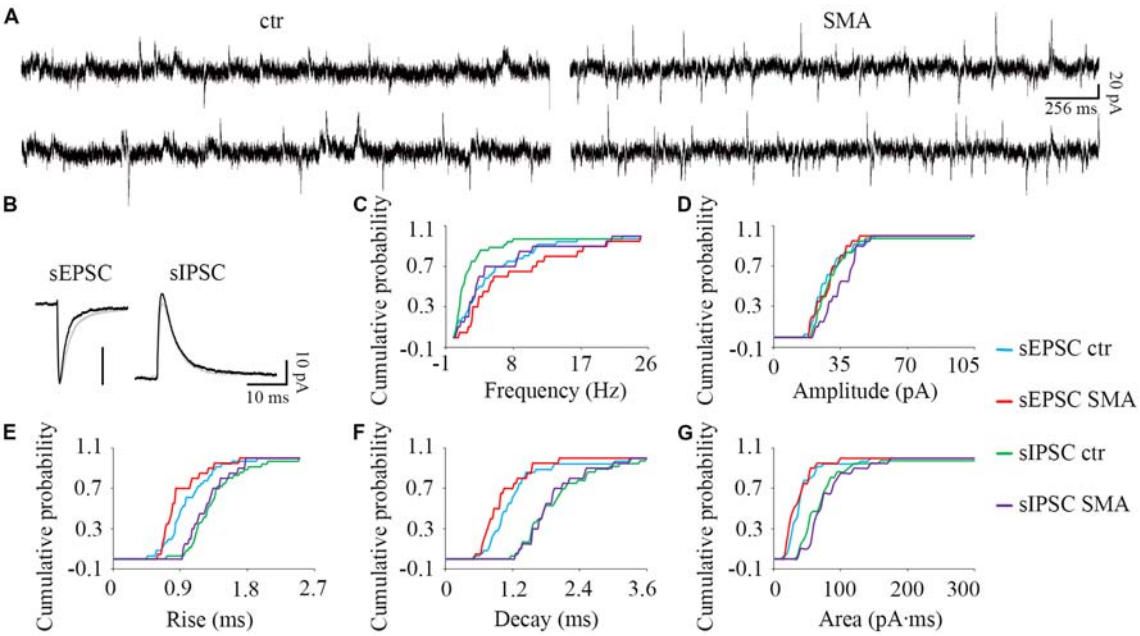

FIGURE 6 | For INs there are few differences in post-synaptic currents from SMA mice compared to controls. **(A)** Example traces of INs from control and SMA mice showing both EPSCs and IPSCs. **(B)** Average traces of sEPSCs and sIPSCs from one representative recording for INs from control (gray) and SMA (black) mice. **(C–G)** Cumulative probability plots of results from recordings from 36 control and 20 SMA INs was compared with K-S test (from a total of 12 control and 7 SMA mice). **(C)** Frequency was significantly higher in sIPSCs ($P < 0.01$), but not in sEPSCs. **(D)** Amplitude of sEPSCs and sIPSCs. **(E)** Rise time was significantly faster in sEPSCs ($P < 0.05$), with no change for sIPSCs. **(F)** Decay time and **(G)** The charge transfer (area) of sEPSCs and sIPSCs did not change.

and sIPSCs (77.6 ± 7.6 pA.ms for SMA vs. 78.7 ± 12 pA.ms for control; **Figure 6G**).

The Miniature Synaptic Transmission

To explore whether the changes we observe in synaptic transmission are due to changes in the presynaptic terminals or on the postsynaptic membrane, we recorded miniature synaptic currents in both MNs and INs with APs blocked by TTX (1 μM). Surprisingly, we found the frequency of mEPSCs was significantly increased in MNs from SMA mice compared to controls (2.07 ± 0.33 Hz vs. 1.06 ± 0.13 Hz, $P < 0.05$), although there was no difference in the frequency of mIPSCs (1.57 ± 0.67 Hz for SMA vs. 1.23 ± 0.37 Hz for control; **Figures 7A,C**). There were no significant differences in the amplitude or kinetics of mEPSCs between MNs from control and SMA mice (**Figure 7**; **Table 1**), however, for mIPSCs the decay time trended faster ($P = 0.07$; **Figure 7F**; **Table 1**) and the charge transfer for mIPSCs was significantly lower in SMA MNs ($P < 0.05$; **Figure 7G**; **Table 1**).

The higher frequency of miniature EPSCs in SMΔ7 MNs, and the minimal differences in their kinetics is in contrast to what was observed with sEPSCs where the frequency was essentially the same in SMNΔ7 MNs compared to controls, while the rise and decay time were faster. On the inhibitory side, sIPSCs had a lower amplitude, faster rise and decay times and lower charge transfer in SMA MNs compared to controls, but the differences in amplitude and rise time were not observed for miniature IPSCs. These results suggest that for miniature EPSCs there may be a homeostatic adjustment in MNs of SMA mice, as has been reported for AP-independent synaptic currents in other neurons (Kavalali, 2015). This could not be the homeostatic effect of TTX blockage, since the fastest synaptic scaling has been reported at 4 h after TTX application (Ibata et al., 2008).

To examine the relative contribution of network-driven inputs in control and SMA neurons, the ratio of miniature to spontaneous EPSCs and IPSCs (mEPSC/sEPSC and mIPSC/sIPSC) was calculated by the average frequency, since the spontaneous and miniature synaptic currents were recorded from different neurons. The ratio of the average frequencies of mEPSC/sEPSC and mIPSC/sIPSC was 13% and 28% for control MNs and 31% and 58% for SMA MNs. These results suggest that AP-dependent synaptic inputs, both excitatory and inhibitory are diminished in SMA MNs relative to control neurons even more than the results with spontaneous EPSCs and IPSCs suggest. The likely decrease in the effectiveness of inhibitory synaptic inputs to MNs in SMA may be related to the apparent hyperexcitability of MNs that is observed in SMNΔ7 mice.

For SMNΔ7 INs, significant differences were observed compared to controls in the frequency of both mEPSCs (2.36 ± 0.32 Hz for controls vs. 3.87 ± 0.58 Hz for SMA,

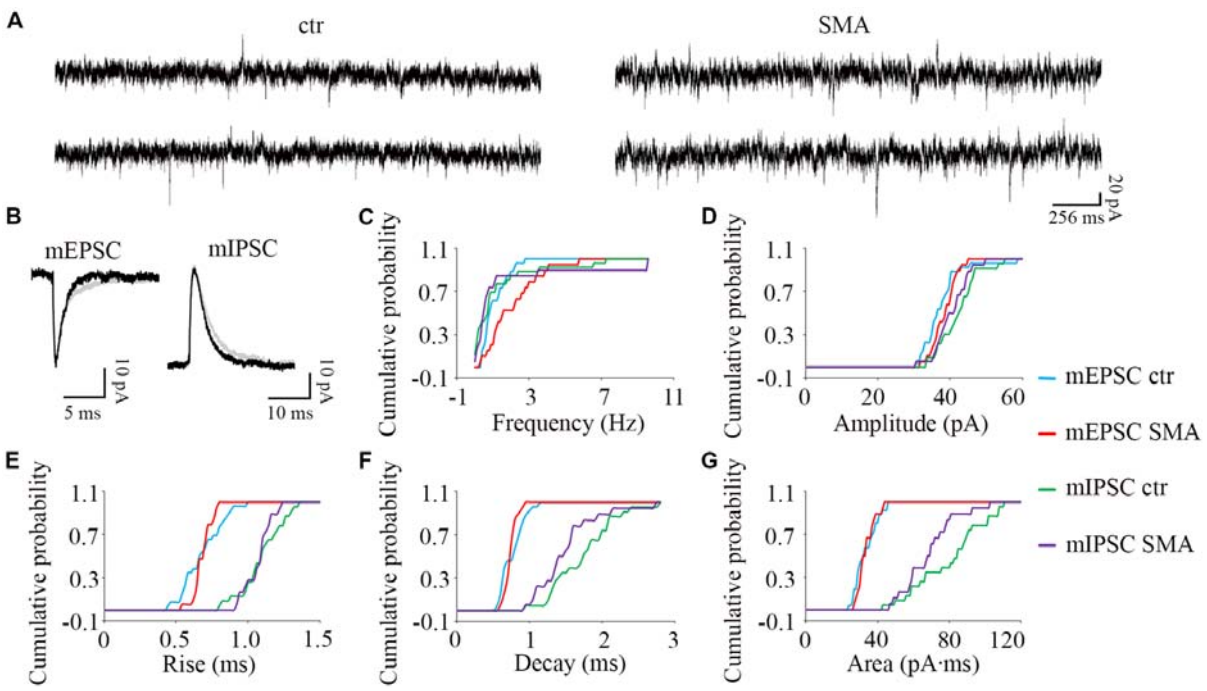

FIGURE 7 | Higher frequency of miniature excitatory post-synaptic currents (mEPSCs) in MNs from SMNΔ7 mice. **(A)** Sample traces of miniature post-synaptic currents in MNs from control and SMA mice. **(B)** Average traces of mEPSCs and mIPSCs from one representative recording from a MN from control (gray) and SMA (black) mice. **(C–G)** Cumulative probability plots of results from recordings from 26 control and 19 SMA MNs was compared with K-S test (from a total of 4 control and 4 SMA mice). **(C)** Frequency of mEPSCs was significantly higher ($P < 0.05$), but no difference for mIPSCs. **(D)** The amplitude and **(E)** rise time of mEPSCs and mIPSCs were not different. **(F)** The decay time of mIPSCs ($P = 0.07$) has a trend to be faster, with no change for mEPSCs. **(G)** The average charge transfer (area) of mIPSCs ($P < 0.05$) was lower, with no change for mEPSCs.

TABLE 1 | Amplitude and kinetics of miniature post-synaptic currents in motor neurons (MNs) and interneurons (INs).

Neuron type	Current type	Condition	Amplitude (pA)	Rise time (ms)	Decay time (ms)	Charge transfer (pA.ms)
Motor neurons	mEPSCs	Control	37 ± 1.1	0.68 ± 0.03	0.76 ± 0.03	33 ± 1.3
		SMA	38 ± 0.8	0.68 ± 0.01	0.74 ± 0.02	40 ± 7.1
	mIPSCs	Control	42 ± 1.2	1.09 ± 0.03	1.73 ± 0.09	80 ± 4.1
		SMA	40 ± 1.1	1.07 ± 0.02	1.50 ± 0.10	68 ± 3.5*
Inter-neurons	mEPSCs	Control	28 ± 0.9	0.63 ± 0.03	0.89 ± 0.04	26 ± 1.0
		SMA	30 ± 1.3	0.58 ± 0.02	0.77 ± 0.02*	25 ± 1.4
	mIPSCs	Control	30 ± 1.2	0.94 ± 0.04	1.89 ± 0.09	58 ± 2.5
		SMA	30 ± 1.3	1.06 ± 0.06	1.74 ± 0.14	57 ± 4.6

*Results from recordings from 26 control MNs and 19 SMA MNs, and 29 control INs and 19 SMA INs from a total of four control mice and four SMA mice. *P < 0.05.*

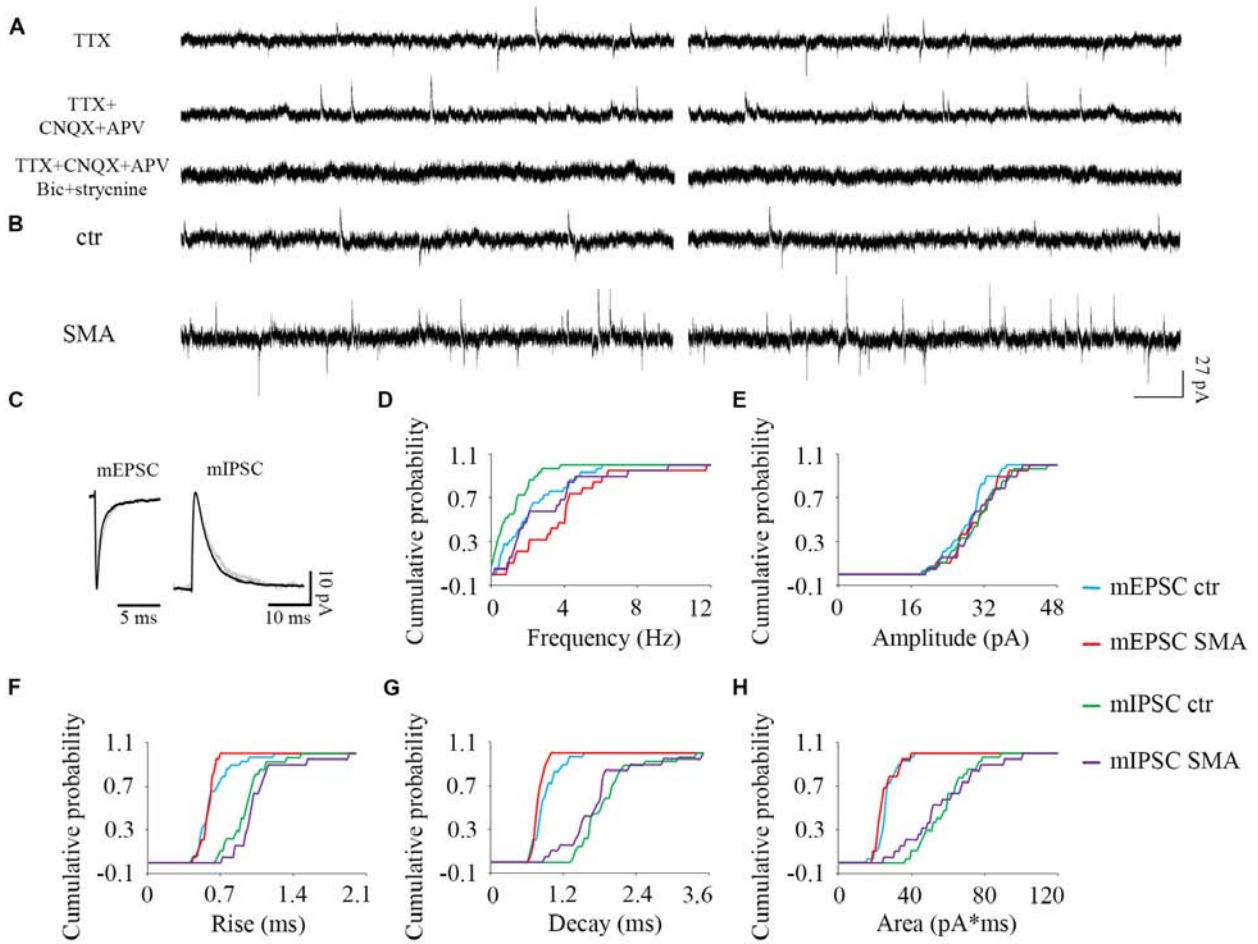

FIGURE 8 | Higher frequency of both excitatory and inhibitory miniature post-synaptic currents in INs from SMNΔ7 mice. **(A)** The outward and inward miniature synaptic currents (Tetrodotoxin, TTX 1 μM) were validated with glutamatergic (CNQX 10 μM, AP-5 50 μM), GABAergic (bicuculline 10 μM) and glycinergic (strychnine 10 μM) receptor antagonists. Two traces are shown for each condition. **(B)** Sample traces of miniature post-synaptic currents in INs from control and SMA mice. **(C)** Average traces of mEPSCs and mIPSCs from one representative recording from an IN from control (gray) and SMA (black) mice. Two traces are shown for each condition. **(D–H)** Cumulative probability plots of results from recordings from 29 control and 19 SMA INs was compared with K-S test (from a total of 4 control and 4 SMA mice). **(D)** Frequency was higher in both mEPSCs ($P < 0.05$) and mIPSCs ($P < 0.01$). **(E)** Amplitude and **(F)** rise time of mEPSCs and mIPSCs did not change. **(G)** Decay time of mEPSCs was faster ($P < 0.05$), with no change in mIPSCs. **(H)** The average charge transfer (area) of mEPSCs and mIPSCs did not change.

$P < 0.05$) and mIPSCs (1.08 ± 0.18 Hz for control vs. 2.95 ± 0.55 Hz for SMA, $P < 0.01$; **Figures 8B,D**). However, there were no differences in the amplitudes of either mEPSCs or mIPSCs (**Figures 8C,E**; **Table 1**). The rise times were not different for mEPSCs nor mIPSCs in SMNΔ7 INs compared to controls (**Figure 8F**; **Table 1**).The decay time was faster in SMNΔ7 INs for mEPSCs compared to controls ($P < 0.05$), but no differences were observed in mIPSCs (**Figure 8G**; **Table 1**). In spite of the differences observed in the rise and decay times of the mIPSCs and mEPSCs, no differences were observed between

INs of control and SMNΔ7 mice in charge transfer (**Figure 8H**; **Table 1**). The higher frequency of action-potential-independent synaptic release in INs from SMNΔ7 mice for both mEPSCs and mIPSCs suggests a greater number of presynaptic contacts or/and increased release probability, with little change in the miniature post-synaptic potentials themselves.

The ratio of the average frequency for mEPSC/sEPSC and mIPSC/sIPSC in INs was higher in SMA INs compared to controls (49% and 54% compared to 40% and 44%). The increase in frequency of sIPSCs in SMA INs suggests an increase in inhibitory synaptic inputs onto a subgroup of INs that may depress the activity of the preMNs, potentially contributing to MN hyperexcitability (Simon et al., 2016). Both AP-dependent and spontaneous release may contribute to this effect.

DISCUSSION

This study provides a detailed illustration of the membrane properties and synaptic currents of both MNs and ventral horn INs of SMNΔ7 mouse pups compared to littermate controls, and represents the first report of the electrophysiological properties of SMA-affected INs. Although we were not able to sort INs into different types based on their function, our results suggest that spinal motor neural networks are substantially altered in SMA mice compared to controls, and that the differences may contribute to the deficiencies in MN output that have been observed (Kong et al., 2009).

The Mechanisms Under Neuronal Intrinsic Property Change

The selective loss of alpha MNs in SMA has been confirmed in patients (Crawford and Pardo, 1996) and mouse models (Ling et al., 2010; Mentis et al., 2011; McGovern et al., 2015; Powis and Gillingwater, 2016), and MNs in mouse models also show a characteristic hyperexcitability (Mentis et al., 2011). Recent work with a stem cell-based model of the motor circuit suggests that, while neuronal death is a cell-autonomous effect of low SMN expression in MNs, the hyperexcitability likely results from the MN response to defects in premotor INs arising from low levels of SMN expression in those neurons (Simon et al., 2016). However, no other study has investigated alterations in the function of INs with low SMN expression. In our recordings from spinal cord slices we were not able to distinguish INs by type, inhibitory or excitatory, and this undoubtedly concealed and diluted differences in the activity of different types of INs. Still, we observed an overall increase in the activity of INs. The majority of ventral horn INs from control and SMA mice showed spontaneous activity, while the frequency of spontaneous AP firing was significantly higher in INs from SMA mice compared to controls. The smaller half-width of APs in the SMA INs compared to controls may contribute to their increased firing frequency. New tools and approaches to classify the different functional types of INs, might identify a specific type of IN whose activity and properties are substantially altered by low SMN expression.

We observed an increase of MN excitability in slices from SMA mice compared to controls, with a hyperpolarized AP threshold, increased input resistance and reduced rheobase current for initiation of APs, and this is also consistent with previous studies in mice (Mentis et al., 2011), stem cell models (Simon et al., 2016), and iPSC cells from severe SMA patients (Liu et al., 2015). While previous studies have suggested that the somatodendritic area of SMA MNs is not different from wild type (Mentis et al., 2011; Simon et al., 2016), we observed a significant decrease in membrane capacitance in SMA mice, suggesting a decrease in the soma area. The differences between our results and earlier findings could be related to differences in the age of the mice at the time of recording. At postnatal day four (P4), the average soma area was shown to be no different in MNs from SMA mice compared to controls (Mentis et al., 2011), but has been shown to be lower in SMA mice at P7–P8 (Tarabal et al., 2014). Our recordings were conducted in P6–P10 mice, and since MN loss is progressive with age (Kong et al., 2009; Tarabal et al., 2014) and it is likely that bigger MNs are lost earlier, the average somatodendritic area of the surviving MNs would be expected to decrease with age.

Interestingly, in spite of the MN hyperexcitability we observed, we also found that the resting membrane potential in SMA MNs was hyperpolarized compared to controls, while other studies have reported no change in resting membrane potential (Mentis et al., 2011; Simon et al., 2016). This difference could be related to the age of the mice at recording, and differences between mouse neurons and the stem cell model. The hyperpolarized membrane potential we observe may contribute to the increased amplitude of APs in SMA MNs, since more voltage-gated sodium channels will be released from voltage-dependent inactivation and in the channel pool that can readily open with depolarization. Greater availability of sodium channels may also contribute to the higher amplitude of APs as reported in SMN-deficient induced pluripotent stem cells (Liu et al., 2015). The widening of the AP and larger ADP in SMA MNs suggests that multiple channels play a role in the hyperexcitability of MNs in SMA, as has been observed in other types of neurons (Bean, 2007). Application of the quantitative polymerase chain reaction (q-PCR) technique in the stem cell model may validate changes in the specific channel expression in the future (Maeda et al., 2014; Liu et al., 2015; Simon et al., 2016). Surprisingly, in spite of the higher excitability of MNs in SMA, there is a decrease in the input-output relationship, so that the difference in firing frequency between SMA MNs and controls narrows at higher levels of injected current. This may be related to the deficiency of output from MN in SMA.

Differences in the Plasticity of Intrinsic Electrical Properties Hint at a Deficiency in the Motor Network in SMA Mice

Even though alterations in the plasticity in the intrinsic electrical properties of neurons can fundamentally alter the input-output properties of neuronal networks in CNS disorders, it receives limited attention (Beck and Yaari, 2008). Long-lasting plasticity in the intrinsic excitability of neurons has been reported

in the somatosensory cortex (Mahon and Charpier, 2012), hippocampus (Xu et al., 2005) and deep dorsal horn neurons (Kim et al., 2008). Excitability changes in MNs have been reported after chronic activity *in vivo* (Beaumont and Gardiner, 2003; Cormery et al., 2005; MacDonell et al., 2012) as well as after prolonged activation in slices (Lombardo et al., 2018), however LLP of the intrinsic excitability has not been studied in detail in spinal MNs. In this study, we investigated the expression of this form of plasticity and how it is altered in ventral horn neurons from SMA mice. For 6 min we applied a 2 Hz suprathreshold stimulation to mimic the spinal CPG activation in neonatal mice (Bonnot et al., 2002), producing three APs for each 50 ms stimulation. After this stimulation, the percentage of neuron expressing LLP of the intrinsic excitability was more than doubled in SMA MNs compared to controls, suggesting that the input-output gain of the neurons in response to this CPG activity-like conditioning stimulation is higher in SMA mice. In contrast, without the conditioning stimulation, the input-output relationship measured by the slope of the F-I curve is lower in SMA MNs. These results suggest that chronically deficient inputs may play a role in the decline of the MN output that has been observed in SMA mouse models (Kong et al., 2009), and is also is consistent with the finding that MN firing varies with afferents and descending inputs in rats (MacDonell et al., 2012). Interestingly, in INs, we observed a trend in the opposite direction for LLP in SMA neurons compared to controls. The percentage of INs expressing LLP trended lower in SMA than in controls, indicating that there may be a reduced input-output relationship in the IN network of SMA mice. These results suggest that there are additional impairments of the motor network in SMA involving the spinal IN network.

Changes in Presynaptic Inputs May Be Related to Deficient MN Output in Mouse Models of SMA

MN death is the histopathologic hallmark of SMA, while loss of afferent inputs to MN has been detected much earlier, even at embryonic stages (Tarabal et al., 2014). As early as P4, MNs from SMA mice have been shown to have reduced responsiveness to proprioceptive input and decreased number and function of glutamatergic synapses (Mentis et al., 2011). A decline in GABAergic inputs to MNs has been reported to start much later (P7–P8) than the glutamatergic loss (Tarabal et al., 2014), while in a stem cell model, SMN deficiency in INs caused a loss of glutamatergic but not GABAergic synapses on MNs (Simon et al., 2016). Interestingly, in spite of the loss of excitatory synapses on SMA MNs detected with immunohistochemistry, our electrophysiological recordings showed no difference in either the frequency or amplitude of AP-driven excitatory synaptic currents in SMA MNs. Our study of synaptic currents in MNs from P6–P10 mice showed more differences primarily in inhibitory synaptic currents in MNs of SMA mice compared to controls. We report a smaller reduction of excitatory synaptic currents compared with other studies that focused on proprioceptive synapses (Mentis et al., 2011; Fletcher et al., 2017). MNs in the spinal cord receive inputs from the local spinal network, descending pathways in addition to the sensory neurons, and they receive extensive projections from the brain stem (Rekling et al., 2000). The sEPSCs we record are the summation of all excitatory inputs to MNs. The lack of difference in overall sEPSC frequency suggests that excitatory inputs from other pathways either are not changed or change in the opposite direction that masks the reduction in input from proprioceptive synapses in SMA mice. For inhibitory post-synaptic currents, there was no decrease in frequency, but a reduction in their average amplitude as well as changes in their kinetics, that would have the effect of reducing the inhibitory tone of inputs to MNs.

The faster rise time and decay time in both excitatory and inhibitory post-synaptic potentials may be related to a decrease in the number of release sites or to changes in the type of receptor carrying post-synaptic current. For example, a change in NMDA vs. AMPA glutamatergic receptors (Rekling et al., 2000) or GABA vs. glycine receptors (González-Forero and Alvarez, 2005), would result in different kinetics for the current reflecting the differences in the underlying channels. For INs, the only significant difference between SMA neurons and controls for action-potential driven synaptic currents was in the frequency of inhibitory post-synaptic potentials, which were increased in SMA neurons. Along with the increase in spontaneous firing of INs, this suggests that inhibitory IN network may be more active in SMA mice.

For the miniature synaptic currents which are AP-independent, surprisingly, the frequency of excitatory currents was higher in SMA MNs. This suggests an increase in presynaptic release of glutamate, which is opposite what would be expected from the decrease in synaptic contact numbers reported in other studies (Mentis et al., 2011; Tarabal et al., 2014; Simon et al., 2016). This suggests that there is a compensatory adjustment in AP-independent glutamate release onto MNs. A similar increase in the frequency of miniature synaptic events vs. spontaneous synaptic events has been reported after traumatic injury in mossy cell of dentate gyrus (Howard et al., 2007). In addition, more studies are suggesting that spontaneous release is very different from AP-driven release with different machinery, vesicle release pools, even different postsynaptic receptor subtypes (for review see Kavalali, 2015). The loss of synaptic inputs to SMA MN may activate the homeostatic function of spontaneous release to compensate for declines in synaptic function, perhaps increasing release probability at the remaining excitatory release sites. This may also be related to the apparent preservation of the frequency of excitatory post-synaptic potentials in MNs even as excitatory synaptic contacts are lost.

For INs, the frequency of miniature synaptic currents was higher in SMA mice for both excitatory and inhibitory post-synaptic currents. Unlike for MNs, it is not clear if loss of synaptic inputs onto INs is part of the pathophysiology of SMA, so the increase in the frequency of miniature post-synaptic currents may be related either to an increase in release sites on the INs or a higher release probability in SMA neurons compared to controls. A higher number of release sites could arise from disease-related changes in INs other than the preMNs

that directly contact MNs. Our hypothesis is that one or more types of inhibitory activity are increased, which then limits both excitatory and inhibitory IN inputs to MNs after SMA. As mentioned earlier, new tools and approaches are necessary to dissect the neuron types that are altered in the SMA model.

The Adjustment of the Plasticity in Intrinsic Properties

Plasticity in the intrinsic electrical properties of neurons has been observed in many CNS disorders (Beck and Yaari, 2008). Changes in AP threshold have been observed in animal models of chronic pain (Wang et al., 2007), and the modification of somatic ion channels such as sodium, A-type of potassium, and T-type of calcium channels contribute to the increase of the excitability of DRG neurons (Hu et al., 2006; Tan et al., 2006; Jagodic et al., 2007; Wang et al., 2007). Similar mechanisms may be operating in SMA MNs, as the expression of Kv2.1 potassium channels has been shown to be reduced in MNs of SMA mice (Fletcher et al., 2017), while a Na^+ current was increased in an iPSC model for SMA MNs (Liu et al., 2015). Changes in sodium and potassium channels may also contribute to the differences in amplitude and half-width between the APs of SMA MNs and those of control animals.

Changes in neuronal firing mode have been reported in epilepsy (Sanabria et al., 2001), stress (Okuhara and Beck, 1998), chronic pain, (Cummins et al., 2007; Hains and Waxman, 2007) and experimental allergic encephalomyelitis (Saab et al., 2004). In addition, the large size of the AP ADP in SMA MNs has the potential to change the firing properties of the neurons. In other neurons, the interplay between axo-somatic persistent sodium channels and M-type potassium channels modulates the size of spike ADPs and the firing mode of the neurons (Beck and Yaari, 2008), and calcium channels that underlie the ADP contribute to the firing mode change of CA1 neurons in a chronic epilepsy animal model (Yaari et al., 2007). Our previous study of the contribution of M-type potassium channels to activity-dependent changes in the intrinsic properties of MNs (Lombardo et al., 2018) suggests that M-channels could be a target for plasticity in the intrinsic properties of MNs in SMA. The increased rate of LLP in SMA MNs, accompanied by the decrease in LLP in SMA INs suggests that changes in the plasticity of intrinsic properties may affect multiple types of neurons in SMA. These changes suggest that there is an adjustment in the intrinsic properties of neurons in the motor network that may either contribute to the pathophysiology of SMA or partially compensate for it.

CONCLUSION

Synaptic plasticity coexists and functionally interacts with the plasticity of intrinsic properties in most neurological disorders (Beck and Yaari, 2008). From this study, it is clear that a compensatory adjustment happens in both intrinsic properties and synaptic inputs of the MNs in SMA mice. The plasticity of the neuro-motor system in the context of spinal cord injury (SCI) has been studied extensively (Raineteau and Schwab, 2001), and activity-based, pharmacological and gene-delivery approaches to facilitate that plasticity are under intense investigation as a way to enhance the recovery after SCI (Onifer et al., 2011). However, the potential of plasticity mechanisms to aid the survival of MNs and sustain the function of the motor network in SMA has attracted much less attention. More research is needed to determine if changes that we have observed in the intrinsic and synaptic properties of MNs and INs contribute to the pathophysiology or are part of a compensatory response that helps preserve the function of the motor network. If the plasticity observed in SMA MNs is beneficial, it may be a useful target for novel therapeutic approaches (Bora et al., 2018). The combination of the current approaches that target increasing SMN levels (Bowerman et al., 2017) with other approaches that prolong the survival of MNs and enhance their output, may be of tremendous benefit to SMA patients.

AUTHOR CONTRIBUTIONS

JS and MH contributed to design of the experiment. JS performed all experiment and statistical data analysis. JS and MH contributed to writing of the manuscript.

FUNDING

This study was supported by the following grants: National Science Foundation (NSF)-#IOS1608147, National Institutes of Health (NIH)-#R15HD075207, P20GM103653, and R25NS095371.

REFERENCES

Aartsma-Rus, A. (2017). FDA approval of nusinersen for spinal muscular atrophy makes 2016 the year of splice modulating oligonucleotides. *Nucleic Acid Ther.* 27, 67–69. doi: 10.1089/nat.2017.0665

Arber, S. (2012). Motor circuits in action: specification, connectivity, and function. *Neuron* 74, 975–989. doi: 10.1016/j.neuron.2012.05.011

Barthélemy, D., Leblond, H., Provencher, J., and Rossignol, S. (2006). Nonlocomotor and locomotor hindlimb responses evoked by electrical microstimulation of the lumbar cord in spinalized cats. *J. Neurophysiol.* 96, 3273–3292. doi: 10.1152/jn.00203.2006

Bean, B. P. (2007). The action potential in mammalian central neurons. *Nat. Rev. Neurosci.* 8, 451–465. doi: 10.1038/nrn2148

Beaumont, E., and Gardiner, P. F. (2003). Endurance training alters the biophysical properties of hindlimb motoneurons in rats. *Muscle Nerve* 27, 228–236. doi: 10.1002/mus.10308

Beaumont, V., and Zucker, R. S. (2000). Enhancement of synaptic transmission by cyclic AMP modulation of presynaptic I(h) channels. *Nat. Neurosci.* 3, 133–141. doi: 10.1038/72072

Beck, H., and Yaari, Y. (2008). Plasticity of intrinsic neuronal properties in CNS disorders. *Nat. Rev. Neurosci.* 9, 357–369. doi: 10.1038/nrn2371

Bonnot, A., Whelan, P. J., Mentis, G. Z., and O'Donovan, M. J. (2002). Locomotor-like activity generated by the neonatal mouse spinal cord. *Brain Res. Rev.* 40, 141–151. doi: 10.1016/s0165-0173(02)00197-2

Bora, G., Subaşı-Yıldız, Ş., Yeşbek-Kaymaz, A., Bulut, N., Alemdaroğlu, İ., Tunca-Yılmaz, Ö., et al. (2018). Effects of arm cycling exercise in spinal

muscular atrophy type II patients: a pilot study. *J. Child Neurol.* 33, 209–215. doi: 10.1177/0883073817750500

Bowerman, M., Becker, C. G., Yáñez-Muñoz, R. J., Ning, K., Wood, M. J. A., Gillingwater, T. H., et al. (2017). Therapeutic strategies for spinal muscular atrophy: SMN and beyond. *Dis. Model. Mech.* 10, 943–954. doi: 10.1242/dmm.030148

Boyd, P. J., Tu, W. Y., Shorrock, H. K., Groen, E. J. N., Carter, R. N., Powis, R. A., et al. (2017). Bioenergetic status modulates motor neuron vulnerability and pathogenesis in a zebrafish model of spinal muscular atrophy. *PLoS Genet.* 13:e1006744. doi: 10.1371/journal.pgen.1006744

Brickley, S. G., Farrant, M., Swanson, G. T., and Cull-Candy, S. G. (2001). CNQX increases GABA-mediated synaptic transmission in the cerebellum by an AMPA/kainate receptor-independent mechanism. *Neuropharmacology* 41, 730–736. doi: 10.1016/s0028-3908(01)00135-6

Cormery, B., Beaumont, E., Csukly, K., and Gardiner, P. (2005). Hindlimb unweighting for 2 weeks alters physiological properties of rat hindlimb motoneurones. *J. Physiol.* 568, 841–850. doi: 10.1113/jphysiol.2005.091835

Crawford, T. O., and Pardo, C. A. (1996). The neurobiology of childhood spinal muscular atrophy. *Neurobiol. Dis.* 3, 97–110. doi: 10.1006/nbdi.1996.0010

Cummins, T. R., Sheets, P. L., and Waxman, S. G. (2007). The roles of sodium channels in nociception: implications for mechanisms of pain. *Pain* 131, 243–257. doi: 10.1016/j.pain.2007.07.026

Daoudal, G., and Debanne, D. (2003). Long-term plasticity of intrinsic excitability: learning rules and mechanisms. *Learn. Mem.* 10, 456–465. doi: 10.1101/lm.64103

Daoudal, G., Hanada, Y., and Debanne, D. (2002). Bidirectional plasticity of excitatory postsynaptic potential (EPSP)-spike coupling in CA1 hippocampal pyramidal neurons. *Proc. Natl. Acad. Sci. U S A* 99, 14512–14517. doi: 10.1073/pnas.222546399

Donlin-Asp, P. G., Bassell, G. J., and Rossoll, W. (2016). A role for the survival of motor neuron protein in mRNP assembly and transport. *Curr. Opin. Neurobiol.* 39, 53–61. doi: 10.1016/j.conb.2016.04.004

d'Ydewalle, C., and Sumner, C. J. (2015). Spinal muscular atrophy therapeutics: where do we stand? *Neurotherapeutics* 12, 303–316. doi: 10.1007/s13311-015-0337-y

Fallini, C., Bassell, G. J., and Rossoll, W. (2010). High-efficiency transfection of cultured primary motor neurons to study protein localization, trafficking, and function. *Mol. Neurodegener.* 5:17. doi: 10.1186/1750-1326-5-17

Fan, L., and Simard, L. R. (2002). Survival motor neuron (SMN) protein: role in neurite outgrowth and neuromuscular maturation during neuronal differentiation and development. *Hum. Mol. Genet.* 11, 1605–1614. doi: 10.1093/hmg/11.14.1605

Fletcher, E. V., Simon, C. M., Pagiazitis, J. G., Chalif, J. I., Vukojicic, A., Drobac, E., et al. (2017). Reduced sensory synaptic excitation impairs motor neuron function via Kv2.1 in spinal muscular atrophy. *Nat. Neurosci.* 20, 905–916. doi: 10.1038/nn.4561

Fricker, D., Verheugen, J. A. H., and Miles, R. (1999). Cell-attached measurements of the firing threshold of rat hippocampal neurones. *J. Physiol.* 517, 791–804. doi: 10.1111/j.1469-7793.1999.0791s.x

Ganguly, K., Kiss, L., and Poo, M. M. (2000). Enhancement of presynaptic neuronal excitability by correlated presynaptic and postsynaptic spiking. *Nat. Neurosci.* 3, 1018–1026. doi: 10.1038/79838

Gennarelli, M., Lucarelli, M., Capon, F., Pizzuti, A., Merlini, L., Angelini, C., et al. (1995). Survival motor-neuron gene transcript analysis in muscles from spinal muscular-atrophy patients. *Biochem. Biophys. Res. Commun.* 213, 342–348. doi: 10.1006/bbrc.1995.2135

Gogliotti, R. G., Quinlan, K. A., Barlow, C. B., Heier, C. R., Heckman, C. J., and DiDonato, C. J. (2012). Motor neuron rescue in spinal muscular atrophy mice demonstrates that sensory-motor defects are a consequence, not a cause, of motor neuron dysfunction. *J. Neurosci.* 32, 3818–3829. doi: 10.1523/JNEUROSCI.5775-11.2012

González-Forero, D., and Alvarez, F. J. (2005). Differential postnatal maturation of GABAA, glycine receptor and mixed synaptic currents in renshaw cells and ventral spinal interneurons. *J. Neurosci.* 25, 2010–2023. doi: 10.1523/jneurosci.2383-04.2005

Groen, E. J. N., and Gillingwater, T. H. (2015). UBA1: at the crossroads of ubiquitin homeostasis and neurodegeneration. *Trends Mol. Med.* 21, 622–632. doi: 10.1016/j.molmed.2015.08.003

Gubitz, A. K., Feng, W., and Dreyfuss, G. (2004). The SMN complex. *Exp. Cell Res.* 296, 51–56. doi: 10.1016/j.yexcr.2004.03.022

Hains, B. C., and Waxman, S. G. (2007). Sodium channel expression and the molecular pathophysiology of pain after SCI. *Prog. Brain Res.* 161, 195–203. doi: 10.1016/s0079-6123(06)61013-3

Hensel, N., and Claus, P. (2018). The actin cytoskeleton in SMA and ALS: how does it contribute to motoneuron degeneration? *Neuroscientist* 24, 54–72. doi: 10.1177/1073858417705059

Howard, A. L., Neu, A., Morgan, R. J., Echegoyen, J. C., and Soltesz, I. (2007). Opposing modifications in intrinsic currents and synaptic inputs in post-traumatic mossy cells: evidence for single-cell homeostasis in a hyperexcitable network. *J. Neurophysiol.* 97, 2394–2409. doi: 10.1152/jn.00509.2006

Hu, H. J., Carrasquillo, Y., Karim, F., Jung, W. E., Nerbonne, J. M., Schwarz, T. L., et al. (2006). The Kv4.2 potassium channel subunit is required for pain plasticity. *Neuron* 50, 89–100. doi: 10.1016/j.neuron.2006.03.010

Ibata, K., Sun, Q., and Turrigiano, G. G. (2008). Rapid synaptic scaling induced by changes in postsynaptic firing. *Neuron* 57, 819–826. doi: 10.1016/j.neuron.2008.02.031

Ireland, D. R., and Abraham, W. C. (2015). Group I mGluRs increase excitability of hippocampal CA1 pyramidal neurons by a PLC-independent mechanism. *J. Neurophysiol.* 88, 107–116. doi: 10.1152/jn.2002.88.1.107

Jagodic, M. M., Pathirathna, S., Nelson, M. T., Mancuso, S., Joksovic, P. M., Rosenberg, E. R., et al. (2007). Cell-specific alterations of T-type calcium current in painful diabetic neuropathy enhance excitability of sensory neurons. *J. Neurosci.* 27, 3305–3316. doi: 10.1523/jneurosci.4866-06.2007

Juvin, L., Simmers, J., and Morin, D. (2007). Locomotor rhythmogenesis in the isolated rat spinal cord: a phase-coupled set of symmetrical flexion-extension oscillators. *J. Physiol.* 583, 115–128. doi: 10.1113/jphysiol.2007.133413

Kavalali, E. T. (2015). The mechanisms and functions of spontaneous neurotransmitter release. *Nat. Rev. Neurosci.* 16, 5–16. doi: 10.1038/nrn3875

Kiehn, O. (2016). Decoding the organization of spinal circuits that control locomotion. *Nat. Rev. Neurosci.* 17, 224–238. doi: 10.1038/nrn.2016.9

Kim, D. K., Kwak, J., Kim, S. J., and Kim, J. (2008). Long-lasting enhancement in the intrinsic excitability of deep dorsal horn neurons. *Pain* 139, 181–189. doi: 10.1016/j.pain.2008.03.025

Kong, L., Wang, X., Choe, D. W., Polley, M., Burnett, B. G., Bosch-Marce, M., et al. (2009). Impaired synaptic vesicle release and immaturity of neuromuscular junctions in spinal muscular atrophy mice. *J. Neurosci.* 29, 842–851. doi: 10.1523/jneurosci.4434-08.2009

Lefebvre, S., Bürglen, L., Reboullet, S., Clermont, O., Burlet, P., Viollet, L., et al. (1995). Identification and characterization of a spinal muscular atrophy-determining gene. *Cell* 80, 155–165. doi: 10.1016/0092-8674(95)90460-3

Levine, A. J., Lewallen, K. A., and Pfaff, S. L. (2012). Spatial organization of cortical and spinal neurons controlling motor behavior. *Curr. Opin. Neurobiol.* 22, 812–821. doi: 10.1016/j.conb.2012.07.002

Li, D. K., Tisdale, S., Lotti, F., and Pellizzoni, L. (2014). SMN control of RNP assembly: from post-transcriptional gene regulation to motor neuron disease. *Semin. Cell Dev. Biol.* 32, 22–29. doi: 10.1016/j.semcdb.2014.04.026

Ling, K. K. Y., Lin, M. Y., Zingg, B., Feng, Z., and Ko, C. P. (2010). Synaptic defects in the spinal and neuromuscular circuitry in a mouse model of spinal muscular atrophy. *PLoS One* 5:e15457. doi: 10.1371/journal.pone.0015457

Liu, Q., and Dreyfuss, G. (1996). A novel nuclear structure containing the survival of motor neurons protein. *EMBO J.* 15, 3555–3565. doi: 10.1002/j.1460-2075.1996.tb00725.x

Liu, H., Lu, J., Chen, H., Du, Z., Li, X. J., and Zhang, S. C. (2015). Spinal muscular atrophy patient-derived motor neurons exhibit hyperexcitability. *Sci. Rep.* 5:12189. doi: 10.1038/srep12189

Lombardo, J., Sun, J., and Harrington, M. A. (2018). Rapid activity-dependent modulation of the intrinsic excitability through up-regulation of KCNQ/Kv7 channel function in neonatal spinal motoneurons. *PLoS One* 13:e0193948. doi: 10.1371/journal.pone.0193948

Lorson, C. L., Hahnen, E., Androphy, E. J., and Wirth, B. (1999). A single nucleotide in the SMN gene regulates splicing and is responsible for spinal muscular atrophy. *Proc. Natl. Acad. Sci. U S A* 96, 6307–6311. doi: 10.1073/pnas.96.11.6307

MacDonell, C. W., Button, D. C., Beaumont, E., Cormery, B., and Gardiner, P. F. (2012). Plasticity of rat motoneuron rhythmic firing properties with varying

levels of afferent and descending inputs. *J. Neurophysiol.* 107, 265–272. doi: 10.1152/jn.00122.2011

Maeda, M., Harris, A. W., Kingham, B. F., Lumpkin, C. J., Opdenaker, L. M., McCahan, S. M., et al. (2014). Transcriptome profiling of spinal muscular atrophy motor neurons derived from mouse embryonic stem cells. *PLoS One* 9:e106818. doi: 10.1371/journal.pone.0106818

Mahon, S., and Charpier, S. (2012). Bidirectional plasticity of intrinsic excitability controls sensory inputs efficiency in layer 5 barrel cortex neurons *in vivo*. *J. Neurosci.* 32, 11377–11389. doi: 10.1523/JNEUROSCI.0415-12.2012

Martinez, T. L., Kong, L., Wang, X., Osborne, M. A., Crowder, M. E., van Meerbeke, J. P., et al. (2012). Survival motor neuron protein in motor neurons determines synaptic integrity in spinal muscular atrophy. *J. Neurosci.* 32, 8703–8715. doi: 10.1523/JNEUROSCI.0204-12.2012

McGovern, V. L., Iyer, C. C., Arnold, W. D., Gombash, S. E., Zaworski, P. G., Blatnik, A. J., et al. (2015). SMN expression is required in motor neurons to rescue electrophysiological deficits in the SMNΔ7 mouse model of SMA. *Hum. Mol. Genet.* 24, 5524–5541. doi: 10.1093/hmg/ddv283

Melyan, Z., Wheal, H. V., and Lancaster, B. (2002). Metabotropic-mediated kainate receptor regulation of IsAHP and excitability in pyramidal cells. *Neuron* 34, 107–114. doi: 10.1016/s0896-6273(02)00624-4

Mentis, G. Z., Blivis, D., Liu, W., Drobac, E., Crowder, M. E., Kong, L., et al. (2011). Early functional impairment of sensory-motor connectivity in a mouse model of spinal muscular atrophy. *Neuron* 69, 453–467. doi: 10.1016/j.neuron.2010.12.032

Miri, A., Azim, E., and Jessell, T. M. (2013). Edging toward entelechy in motor control. *Neuron* 80, 827–834. doi: 10.1016/j.neuron.2013.10.049

Monani, U. R., Sendtner, M., Coovert, D. D., Parsons, D. W., Andreassi, C., Le, T. T., et al. (2000). The human centromeric survival motor neuron gene (SMN2) rescues embryonic lethality in $Smn^{-/-}$ mice and results in a mouse with spinal muscular atrophy. *Hum. Mol. Genet.* 9, 333–339. doi: 10.1093/hmg/9.3.333

Okuhara, D. Y., and Beck, S. G. (1998). Corticosteroids influence the action potential firing pattern of hippocampal subfield CA3 pyramidal cells. *Neuroendocrinology* 67, 58–66. doi: 10.1159/000054299

Onifer, S. M., Smith, G. M., and Fouad, K. (2011). Plasticity after spinal cord injury: relevance to recovery and approaches to facilitate it. *Neurotherapeutics* 8, 283–293. doi: 10.1007/s13311-011-0034-4

Otis, T. S., and Trussell, L. O. (1996). Inhibition of transmitter release shortens the duration of the excitatory synaptic current at a calyceal synapse. *J. Neurophysiol.* 76, 3584–3588. doi: 10.1152/jn.1996.76.5.3584

Powis, R. A., and Gillingwater, T. H. (2016). Selective loss of α motor neurons with sparing of γ motor neurons and spinal cord cholinergic neurons in a mouse model of spinal muscular atrophy. *J. Anat.* 228, 443–451. doi: 10.1111/joa.12419

Raineteau, O., and Schwab, M. E. (2001). Plasticity of motor systems after incomplete spinal cord injury. *Nat. Rev. Neurosci.* 2, 263–273. doi: 10.1038/35067570

Rekling, J. C., Funk, G. D., Bayliss, D. A., Dong, X. W., and Feldman, J. L. (2000). Synaptic control of motoneuronal excitability. *Physiol. Rev.* 80, 767–852. doi: 10.1152/physrev.2000.80.2.767

Reyes, A. (2001). Influence of dendritic conductances on the input-output properties of neurons. *Annu. Rev. Neurosci.* 24, 653–675. doi: 10.1146/annurev.neuro.24.1.653

Rochette, C. F., Gilbert, N., and Simard, L. R. (2001). SMN gene duplication and the emergence of the SMN2 gene occurred in distinct hominids: SMN2 is unique to Homo sapiens. *Hum. Genet.* 108, 255–266. doi: 10.1007/s004390100473

Saab, C., Craner, M., Kataoka, Y., and Waxman, S. (2004). Abnormal Purkinje cell activity *in vivo* in experimental allergic encephalomyelitis. *Exp. Brain Res.* 158, 1–8. doi: 10.1007/s00221-004-1867-4

Sanabria, E. R. G., Su, H., and Yaari, Y. (2001). Initiation of network bursts by Ca^{2+}-dependent intrinsic bursting in the rat pilocarpine model of temporal lobe epilepsy. *J. Physiol.* 532, 205–216. doi: 10.1111/j.1469-7793.2001.0205g.x

Simon, C. M., Janas, A. M., Lotti, F., Tapia, J. C., Pellizzoni, L., and Mentis, G. Z. (2016). A stem cell model of the motor circuit uncouples motor neuron death from hyperexcitability induced by SMN deficiency. *Cell Rep.* 16, 1416–1430. doi: 10.1016/j.celrep.2016.06.087

Sourdet, V., Russier, M., Daoudal, G., Ankri, N., and Debanne, D. (2003). Long-term enhancement of neuronal excitability and temporal fidelity mediated by metabotropic glutamate receptor subtype 5. *J. Neurosci.* 23, 10238LP–10248. doi: 10.1523/JNEUROSCI.23-32-10238.2003

Tan, Z., Donnelly, D. F., and LaMotte, R. H. (2006). Effects of a chronic compression of the dorsal root ganglion on voltage-gated Na^+ and K^+ currents in cutaneous afferent neurons. *J. Neurophysiol.* 95, 1115–1123. doi: 10.1152/jn.00830.2005

Tarabal, O., Caraballo-Miralles, V., Cardona-Rossinyol, A., Correa, F. J., Olmos, G., Llado, J., et al. (2014). Mechanisms involved in spinal cord central synapse loss in a mouse model of spinal muscular atrophy. *J. Neuropathol. Exp. Neurol.* 73, 519–535. doi: 10.1097/nen.0000000000000074

Thirumalai, V., Behrend, R. M., Birineni, S., Liu, W., Blivis, D., and O'Donovan, M. J. (2013). Preservation of VGLUT1 synapses on ventral calbindin-immunoreactive interneurons and normal locomotor function in a mouse model of spinal muscular atrophy. *J. Neurophysiol.* 109, 702–710. doi: 10.1152/jn.00601.2012

Tsubokawa, H., Offermanns, S., Simon, M., and Kano, M. (2000). Calcium-dependent persistent facilitation of spike backpropagation in the CA1 pyramidal neurons. *J. Neurosci.* 20, 4878–4884. doi: 10.1523/JNEUROSCI.20-13-04878.2000

Wang, J.-G., Strong, J. A., Xie, W., and Zhang, J.-M. (2007). Local inflammation in rat dorsal root ganglion alters excitability and ion currents in small-diameter sensory neurons. *Anesthesiology* 107, 322–332. doi: 10.1097/01.anes.0000270761.99469.a7

Whelan, P., Bonnot, A., and O'Donovan, M. J. (2000). Properties of rhythmic activity generated by the isolated spinal cord of the neonatal mouse. *J. Neurophysiol.* 84, 2821–2833. doi: 10.1152/jn.2000.84.6.2821

Xu, J., Kang, N., Jiang, L., Nedergaard, M., and Kang, J. (2005). Activity-dependent long-term potentiation of intrinsic excitability in hippocampal CA1 pyramidal neurons. *J. Neurosci.* 25, 1750–1760. doi: 10.1523/JNEUROSCI.4217-04.2005

Yaari, Y., Yue, C., and Su, H. (2007). Recruitment of apical dendritic T-type Ca^{2+} channels by backpropagating spikes underlies *de novo* intrinsic bursting in hippocampal epileptogenesis. *J. Physiol.* 580, 435–450. doi: 10.1113/jphysiol.2007.127670

Zhang, Y., Narayan, S., Geiman, E., Lanuza, G. M., Velasquez, T., Shanks, B., et al. (2008). Article V3 spinal neurons establish a robust and balanced locomotor rhythm during walking. *Neuron* 60, 84–96. doi: 10.1016/j.neuron.2008.09.027

Zhang, H., Robinson, N., Wu, C., Wang, W., and Harrington, M. A. (2010). Electrophysiological properties of motor neurons in a mouse model of severe spinal muscular atrophy: *in vitro* versus *in vivo* development. *PLoS One* 5:e11696. doi: 10.1371/journal.pone.0011696

Zhong, G., Díaz-Ríos, M., and Harris-Warrick, R. M. (2006). Intrinsic and functional differences among commissural interneurons during fictive locomotion and serotonergic modulation in the neonatal mouse. *J. Neurosci.* 26, 6509–6517. doi: 10.1523/JNEUROSCI.1410-06.2006

Conflict of Interest Statement: The authors declare that the research was conducted in the absence of any commercial or financial relationships that could be construed as a potential conflict of interest.

frontiers in Cellular Neuroscience

BRIEF RESEARCH REPORT
published: 12 February 2019
doi: 10.3389/fncel.2019.00032

Delayed Spine Pruning of Direct Pathway Spiny Projection Neurons in a Mouse Model of Parkinson's Disease

Steven M. Graves[1] *and D. James Surmeier*[2]*

[1]Department of Pharmacology, University of Minnesota, Minneapolis, MN, United States, [2]Department of Physiology, Feinberg School of Medicine, Northwestern University, Chicago, IL, United States

In animal models of Parkinson's disease (PD), principal striatal spiny projection neurons (SPNs) lose axospinous synapses. However, there has been a disagreement about whether this loss is restricted to a specific type of SPN or not, as some studies have reported pruning in both direct pathway SPNs and indirect pathway SPNs, while others have found this pruning to be restricted to indirect pathway SPNs. One possible explanation for the discrepancy is the period between the induction of the parkinsonian state and the assessment of spine loss. To test this hypothesis, transgenic mice were subjected to unilateral 6-hydroxydopamine (6-OHDA) lesions of nigrostriatal dopaminergic neurons and then direct pathway SPNs examined in *ex vivo* brain slices using two photon laser scanning microscopy either one or 2 months afterwards. These studies revealed that 1 month after the lesion, there was no loss of spines in direct pathway SPNs. However, 2 months after the lesion, spine loss was significant in direct pathway SPNs. In addition to reconciling the existing literature on the impact of the parkinsonian state on axospinous synapse elimination in SPNs, our results suggest that the delayed spine loss in direct pathway SPNs is not driven by homeostatic mechanisms [as posited for indirect pathway (iSPNs)], but rather by network pathophysiology.

Keywords: striatum, spiny projection neurons, Parkinson's disease, spine density, excitability

OPEN ACCESS

Edited by:
Jing-Ning Zhu,
Nanjing University, China

Reviewed by:
Rosario Moratalla,
Spanish National Research Council (CSIC), Spain
Carmelo Sgobio,
German Center for Neurodegenerative Diseases (DZNE), Germany

***Correspondence:**
D. James Surmeier
j-surmeier@northwestern.edu

Received: *16 November 2018*
Accepted: *22 January 2019*
Published: *12 February 2019*

Citation:
Graves SM and Surmeier DJ (2019) Delayed Spine Pruning of Direct Pathway Spiny Projection Neurons in a Mouse Model of Parkinson's Disease. Front. Cell. Neurosci. 13:32. doi: 10.3389/fncel.2019.00032

INTRODUCTION

The striatum is the largest of the basal ganglia nuclei that control goal-directed movement and habit. The principal neurons of the striatum are GABAergic spiny projection neurons (SPNs). Approximately half of SPNs express D1 dopamine receptors (D1Rs) and project to the substantia nigra pars reticulata forming the direct pathway (dSPNs), whereas the remaining SPNs express D2 dopamine receptors (D2Rs) and project to the globus pallidus external segment forming the indirect pathway (iSPNs; Gerfen and Surmeier, 2011). Both SPN populations have dendritic arbors that are densely populated with spines forming cortical and thalamic glutamatergic synapses (Deng et al., 2013; Fieblinger et al., 2014).

In Parkinson's disease (PD), the dopaminergic innervation of the striatum is lost resulting in a range of adaptations (Zhai et al., 2018). One adaptation that is common to the striatum of PD patients (McNeill et al., 1988; Stephens et al., 2005; Zaja-Milatovic et al., 2005) as well as non-human primate (Villalba et al., 2009) and rodent PD models (Ingham et al., 1989; Day et al., 2006; Zhang et al., 2013; Fieblinger et al., 2014; Suarez et al., 2014, 2016, 2018; Toy et al., 2014; Ueno et al., 2014) is the loss of SPN axospinous synapses. However, it remains unclear whether spine pruning

occurs in both SPN populations. Several studies have argued that spine pruning occurs exclusively in iSPNs (Day et al., 2006; Fieblinger et al., 2014; Ueno et al., 2014), whereas other studies suggest that pruning occurs in iSPNs and dSPNs (Villalba et al., 2009; Suarez et al., 2014, 2016, 2018; Toy et al., 2014; Gagnon et al., 2017).

One variable that might account for the discrepancy is the length of time between the lesion and the assessment of spine loss. In most of the studies reporting selective pruning, this period was 1 month; but in many of the studies finding less selectivity, this period was considerably longer. The present study was designed to test this hypothesis by assaying dSPN excitability and dendritic spine density 30 and 60 days after a 6-hydroxydopamine (6-OHDA) lesion. Our results show that dSPN spines are pruned but that this occurs much more slowly than that reported in iSPNs (Fieblinger et al., 2014). This difference in time-course suggests that the mechanisms driving dSPN spine loss differ from those in iSPNs.

METHODS

Animals

Male mice (n = 27) with the TdTomato fluorescent reporter encoded under the *drd1a* receptor regulatory element to identify dSPNs were bred in-house; experimental subjects were hemizygous. Procedures were approved by the Northwestern University Animal Care and Use Committees and in accordance with the National Institutes of Health Guide for the Care and Use of Laboratory Animals. Animals were group housed on a 12-h light/dark cycle with free access to food and water. Mice were 6–10 weeks of age at the time of 6-OHDA lesion.

Unilateral 6-OHDA Lesion

Mice were anesthetized using an isoflurane vaporizer (Kent Scientific) and placed in a stereotaxic frame (David Kopf Instruments) with a Cunningham adaptor (Harvard Apparatus) while a small incision was made and a hole drilled overlying the medial forebrain bundle. A calibrated glass micropipette (Drummond Scientific Company) pulled on a P-97 micropipette puller (Sutter Instruments) was filled with 0.02% ascorbic acid in sterile saline (vehicle) or 6-OHDA (3.5 μg in vehicle) was lowered into the medial forebrain bundle (AP: −0.7, ML: 1.2, DV: −4.75) and 1 μl injected. After stereotaxic injection mice were monitored and provided saline injections and/or high-fat/high-sucrose food on an as needed basis.

Ex vivo Slices

Mice were anesthetized 30 or 60 days post stereotaxic injection with ketamine (100 mg/kg)/xylazine (7 mg/kg) and transcardially perfused with ice cold modified artificial cerebrospinal fluid (aCSF) containing in mM: 124.0 NaCl, 3.0 KCl, 1.0 $CaCl_2$, 2.0 $MgCl_2$, 26 $NaHCO_3$, 1.0 NaH_2PO_4, and 16.66 glucose. Saggital slices from the lesioned hemisphere containing the dorsolateral striatum (275 μm thick) were sectioned using a vibratome (Leica Biosystems) and transferred to a holding chamber (34 degrees Celsius) with aCSF containing in mM: 124.0 NaCl, 3.0 KCl, 2.0 $CaCl_2$, 1.0 $MgCl_2$, 26 $NaHCO_3$, 1.0 NaH_2PO_4, and 16.66 glucose for 30–40 min prior to experimentation; solutions were pH 7.4, 310–320 mOsm and continually bubbled with 95% O_2/5% CO_2.

Two-Photon Laser Scanning Microscopy (2PLSM) and Electrophysiology

Slices were placed in a recording chamber and dSPNs visualized by somatic tdTomato with a laser scanning microscope system (Bruker) using 810 nm excitation by a two-photon laser (Coherent Inc.). Identified dSPNs were patched under an Olympus 60×/0.9 NA lens using glass pipettes (3–4.5 MΩ resistance) filled with recording solution containing (in mM): 135.0 KMeSO4, 5.0 KCL, 10.0 HEPES, 2.0 Mg-ATP, 0.5 Na-GTP, 5 phosphocreatine-Tris, 5.0 phosphocreatine-Na, 0.1 spermine; pH was adjusted to 7.25–7.30 and osmolarity 270–280 mOsm. Alexa 568 (50 μM) and Fluo-4 (200 μM) dyes were included in recording pipettes. Whole-cell patch clamp recordings were obtained at 32–34 degrees Celsius using a Multiclamp 700B amplifier as previously described (Fieblinger et al., 2014). Intrinsic excitability was assessed in current clamp with 500 ms somatic current injections (25 pA steps). Dendritic excitability was determined by somatic current injection evoking back propagating action potentials (bAPs) and measuring Fluo-4 fluorescence signals in proximal (30–60 μm from the soma) and distal (>80 μm from the soma) dendrites and spines using 2PLSM (Day et al., 2008). Data are presented as the area of the fluorescence change in distal divided by the proximal fluorescence change; this ratio was called the dendritic index and was used to correct for differences in dye loading, laser power and optical path. After electrophysiological recordings, z-series were obtained of proximal and distal dendritic segments as previously described (Fieblinger et al., 2014). High magnification images were acquired with 0.15 μm × 0.15 μm resolution at 0.3 μm z-steps; images were processed using AutoQuant deconvolution software (Media Cybernetics) and semi-automated spine counting using NeuronStudio (CNIC). Whole cell z-series were acquired at 0.389 μm × 0.389 μm resolution with 0.5 μm steps for Sholl's analysis using Neurolucida (MBF Bioscience).

Statistical Analysis

Non-parametric statistics were used for displaying data and for hypothesis testing with GraphPad Prism (GraphPad Software). Kruskal-Wallis with Dunn's *post hoc* analysis was performed with data expressed as median, quartiles, and range unless otherwise stated; $\alpha = 0.05$.

RESULTS

Physiological Adaptations in dSPNs From Parkinsonian Mice

Previously it was reported that the intrinsic excitability of dSPNs was elevated 1 month after a unilateral 6-OHDA lesion, but dendritic excitability was unchanged (Fieblinger et al., 2014; Suarez et al., 2016, 2018). This finding was reproduced here. Thirty days after lesioning, the intrinsic excitability of dSPNs was increased (**Figures 1A,B**) and persisted 2 months

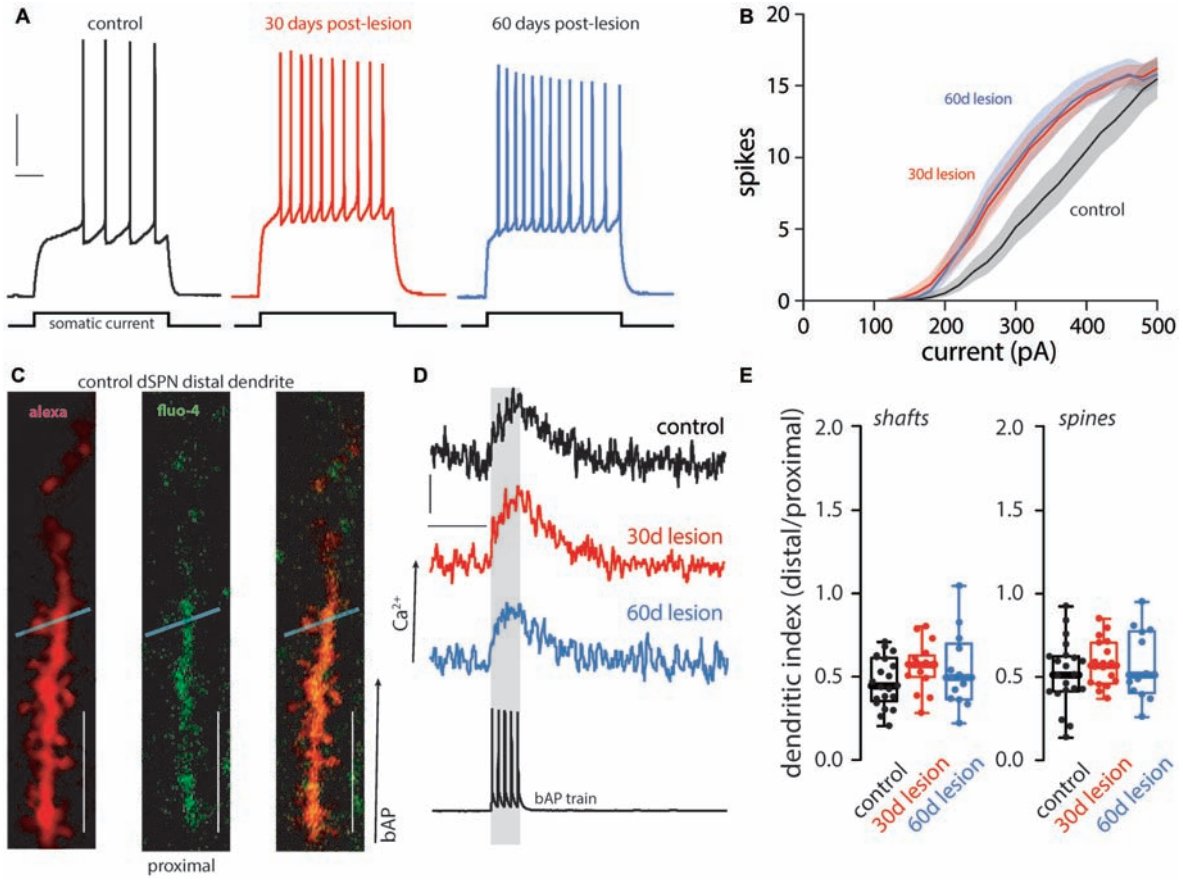

FIGURE 1 | Functional changes of direct pathway spiny projection neurons (dSPNs) in the 6-hydroxydopamine (6-OHDA) mouse model of Parkinson's disease (PD). Intrinsic and dendritic excitability was assessed in dSPNs in *ex vivo* slices from control mice and compared to slices prepared from mice 30 (30 day lesion) or 60 (60 days lesion) days post 6-OHDA lesion of the medial forebrain bundle. Intrinsic excitability was assessed by somatic current injection. **(A)** dSPN intrinsic excitability was increased in brain slices from parkinsonian mice at 30 and 60 days post-lesion. Sample traces at 300 pA current injection illustrating changes in excitability are provided with vertical and horizontal scale bars indicating 10 mV and 100 ms, respectively. **(B)** Current response curves (shaded regions depict SEM). Somatic excitability was increased in dSPNs from lesioned mice at 30 and 60 days post-lesion compared to controls (control n = 21 neurons, 30 days lesion n = 19 neurons, and 60 days lesion n = 10 neurons). **(C)** Dendritic excitability was determined by current injection and measurement of back propagating calcium signals using a fluorescent dye (fluo-4) at distal and proximal dendrites. Sample two-photon images are provided of a distal dendritic segment filled with an anatomical dye (alexa 568; left), calcium sensitive dye (fluo-4; middle), and the merged image (right). The light blue line depicts the region scanned to acquire fluorescent measurements in the dendritic shaft and spine; scale bar denotes 10 μm. **(D)** Sample traces illustrating the somatic voltage recording (bottom) and the corresponding calcium signal in a distal dendrite in dSPNs from control, 30 days lesion, and 60 days lesion subjects; scale bars denote 200 fluorescent units and 200 ms, respectively. **(E)** Data is presented as the polarization index (i.e., distal/proximal measurements; see methods). There was no difference in dendritic excitability in the shaft or spine (control n = 21 neurons, 30 days lesion n = 17 neurons, and 60 days lesion n = 13 neurons).

post-lesion (**Figures 1A,B**). In contrast, dendritic excitability as assessed by ratio of the distal Ca^{2+} transient evoked by back-propagating action potentials to that in the proximal dendrites (ratio = dendritic index), was unchanged, regardless of whether the measurement was made in dendritic shafts or spines (**Figures 1C–E**). Two months following the lesion, dendritic excitability remained similar to that of dSPNs from unlesioned mice (**Figures 1C–E**).

Dendritic Adaptations in dSPNs From Parkinsonian Mice

Following short-term (5-day) dopamine depletion using reserpine or 1 month after a unilateral 6-OHDA lesion, spine loss is restricted to iSPNs (Day et al., 2006; Fieblinger et al., 2014). In contrast, dSPN spine pruning has been seen in 1-methyl-4-phenyl-1,2,3,6-tetrahydropyridine (MPTP)-lesioned non-human primates and MPTP or 6-OHDA lesioned mice when examined at longer times after the insult (Villalba et al., 2009; Suarez et al., 2014, 2016; Toy et al., 2014; Gagnon et al., 2017). Here, there was no change in dSPN spine density when measured 1 month after the 6-OHDA lesion (**Figures 2A,B**). However, when spine density was measured 2 months after the lesion, the loss of dSPN spines was evident in both proximal and distal dendrites (**Figures 2A,B**). Approximately one third of dSPN spines were lost 2 months after lesioning, an effect size similar to that previously reported for iSPNs (Fieblinger et al., 2014).

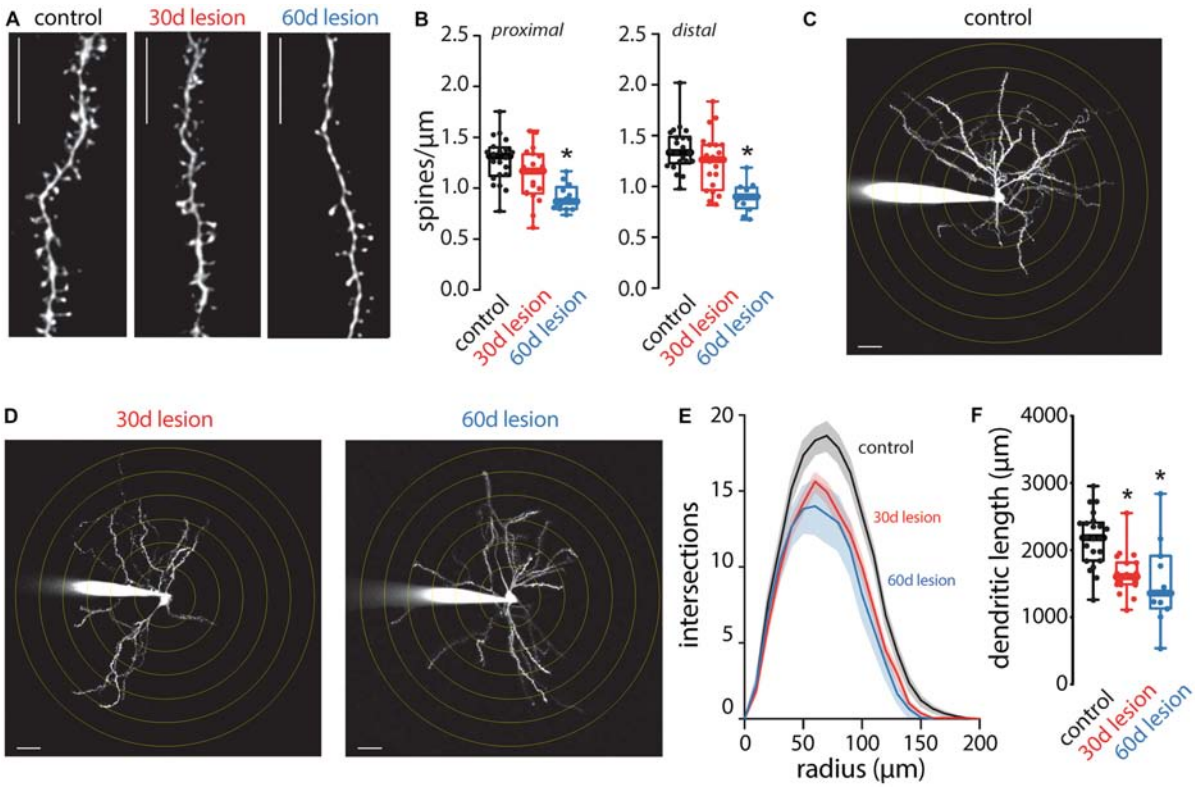

FIGURE 2 | Anatomical changes of dSPNs in the 6-OHDA lesion mouse model of PD. Spine density and dendritic arborization were measured in dSPNs in *ex vivo* slices obtained from control mice and compared to slices prepared from mice 30 (30 days lesion) or 60 (60 days lesion) days post 6-OHDA lesion of the medial forebrain bundle. **(A)** Sample two-photon images of distal dendritic segments illustrating reduced spine density at 60 days lesion compared to control but no change at 30 days lesion; scale bar denotes 10 µm. **(B)** Quantified spine densities from proximal and distal dendritic segments. dSPN spine density was decreased at 60 days post-lesion compared to control with no change at 30 days post lesion (proximal: control $n = 22$ neurons, 30 days lesion $n = 20$ neurons, and 60 days lesion $n = 13$ neurons; distal: control $n = 21$ neurons, 30 days lesion $n = 20$ neurons, and 60 days lesion $n = 12$ neurons). **(C)** Sample two-photon image of a dSPN from a control mouse. Concentric circles are spaced 10 µm apart and scale bar denotes 10 µm. **(D)** Sample two-photon images of dSPNs at 30 and 60 days post-lesion; dendritic arborization is reduced at both time points compared to control image presented in **(C)**. **(E)** Sholl analysis of dSPNs from control ($n = 22$ neurons), 30 days lesion ($n = 19$ neurons) and 60 days lesion ($n = 11$ neurons); solid lines represent the mean and shaded lines the SEM. **(F)** Total dendritic length was reduced in slices obtained from 30 days lesion and 60 days lesion mice compared to controls (control $n = 22$ neurons, 30 days lesion $n = 19$ neurons, and 60 days lesion $n = 11$ neurons); $^*p < 0.05$.

In contrast to the slowly developing pruning of dSPN spines, dSPN dendritic atrophy manifested rapidly. One month post-lesion, dendrites of dSPNs were reduced in complexity (**Figures 2C–F**), as reported previously (Fieblinger et al., 2014). It is important to note that although spine density was not changed 1 month post-lesion, the total number of spines would be reduced as a result of decreased total dendritic length as previously reported (Fieblinger et al., 2014). The dendritic atrophy was evident in both the Sholl plots, which measure branching, and in estimates of total dendritic length. Two months after lesioning, the deficit in dendritic branching and length was similar to that seen 1 month after lesioning (**Figures 2C–F**).

DISCUSSION

Our main finding is that dSPNs do lose spines in a mouse model of PD. However, this loss lags behind that reported for iSPNs (Fieblinger et al., 2014). It also lags behind changes in the physiology and global dendritic architecture of dSPNs. While our results argue that methodological differences, particularly the time post-lesion in which experiments are conducted, are responsible for the apparent discrepancy in the literature on PD-related spine loss in iSPNs and dSPNs, they also suggest that the biological determinants of spine loss in these two classes of striatal neurons are quite different with dSPN changes being partially homeostatic.

When the spike rate of neurons is pushed away from a phenotypically determined set point, homeostatic mechanisms are engaged to normalize the spike rate (Marder and Goaillard, 2006; Turrigiano, 2008). These homeostatic mechanisms are capable of up-regulating or down-regulating synaptic connections, as well as changing intrinsic ionic conductances that govern spiking. Dopamine depletion deprives dSPNs of D1R activation and intracellular signaling that serves to increase intrinsic excitability and promote long-term

potentiation (LTP) of axospinous glutamatergic synapses (Shen et al., 2008, 2015) resulting in a "dis-facilitation" that would reduce spike rate. Consistent with this there is a reduction in dSPN corticostriatal responses in lesioned rodents (Flores-Barrera et al., 2010; Escande et al., 2016). The up-regulation in intrinsic excitability of dSPNs in the following dopamine depletion (Fieblinger et al., 2014; Suarez et al., 2016) can thus be viewed as a homeostatic adaptation. What is lacking from a homeostatic response is an up-regulation of spine number. Why this is the case is not clear. It is possible that a homeostatic up-regulation in the number of glutamatergic synapses is counter-balanced by the loss of axospinous synapses that depend upon D1R signaling for maintenance (Plotkin et al., 2014). If this is the case, the afferent connectome of dSPNs would be expected to change in the parkinsonian state.

What accounts for the delayed loss of dSPN spines? In the parkinsonian striatum, the loss of D2R signaling dis-inhibits iSPNs and cholinergic interneurons that modulate both iSPN and dSPN function. In iSPNs cholinergic disinhibition increases dendritic excitability and spine pruning *via* M1 receptors (Shen et al., 2007). In dSPNs, M4 muscarinic receptors (M4Rs) oppose D1R signaling and promote cannabinoid-dependent LTD at axospinous synapses (Shen et al., 2015). Further study is needed to determine whether M4R signaling contributes to the loss of axospinous synapses in dSPNs. Moreover, it will be important to determine the functional properties of the synapses that are lost. In naïve dSPNs, approximately one-third of the axospinous synapses appear capable of undergoing D1R-dependent LTP (Plotkin et al., 2014)–precisely the percentage of axospinous synapses pruned by prolonged dopamine depletion. Investigation is needed to determine whether the spines lost are LTP capable or not in order to more fully understand the consequence of dopamine depletion on basal ganglia function and motor dysfunction.

Overall the loss of axospinous synapses in dSPNs would serve to exacerbate pathway imbalance underlying parkinsonian motor symptoms. The loss of D2R activation in iSPNs dis-inhibits them by shutting down intracellular signaling cascades that dampen intrinsic excitability and stimulate the production of endocannabinoids that diminish glutamate release and promote long-term depression (LTD) of axospinous glutamatergic synapses (Wang et al., 2006; Kreitzer and Malenka, 2007; Shen et al., 2008; Thiele et al., 2014). This dis-inhibition of the indirect pathway is thought to contribute to the hypokinetic symptoms of dopamine depletion. The "dis-facilitation" of dSPNs complements the dis-inhibition in iSPNs to promote the indirect pathway dominance thought to underlie bradykinesia and rigidity characteristic of PD.

DATA AVAILABILITY

Data presented in the manuscript are available from the corresponding author upon request.

AUTHOR CONTRIBUTIONS

SG performed experiments and data analysis. SG and DS designed the experiments, drafted and edited the manuscript. The final manuscript was read by and approved by both the authors.

FUNDING

This work was supported by a grant from the JPB Foundation and National Institutes of Health (NIH; NS 34696) to DS.

ACKNOWLEDGMENTS

We wish to thank Kyle Dombeck for his assistance in performing animal surgeries.

REFERENCES

Day, M., Wang, Z., Ding, J., An, X., Ingham, C. A., Shering, A. F., et al. (2006). Selective elimination of glutamatergic synapses on striatopallidal neurons in Parkinson disease models. *Nat. Neurosci.* 9, 251–259. doi: 10.1038/nn1632

Day, M., Wokosin, D., Plotkin, J. L., Tian, X., and Surmeier, D. J. (2008). Differential excitability and modulation of striatal medium spiny neuron dendrites. *J. Neurosci.* 28, 11603–11614. doi: 10.1523/jneurosci.1840-08.2008

Deng, Y. P., Wong, T., Bricker-Anthony, C., Deng, B., and Reiner, A. (2013). Loss of corticostriatal and thalamostriatal synaptic terminals precedes striatal projection neuron pathology in heterozygous Q140 Huntington's disease mice. *Neurobiol. Dis.* 60, 89–107. doi: 10.1016/j.nbd.2013.08.009

Escande, M. V., Taravini, I. R., Zold, C. L., Belforte, J. E., and Murer, M. G. (2016). Loss of homeostasis in the direct pathway in a mouse model of asymptomatic Parkinson's disease. *J. Neurosci.* 36, 5686–5698. doi: 10.1523/jneurosci.0492-15.2016

Fieblinger, T., Graves, S. M., Sebel, L. E., Alcacer, C., Plotkin, J. L., Gertler, T. S., et al. (2014). Cell type-specific plasticity of striatal projection neurons in parkinsonism and L-DOPA-induced dyskinesia. *Nat. Commun.* 5:5316. doi: 10.1038/ncomms6316

Flores-Barrera, E., Vizcarra-Chacon, B. J., Tapia, D., Bargas, J., and Galarraga, E. (2010). Different corticostriatal integration in spiny projection neurons from direct and indirect pathways. *Front. Syst. Neurosci.* 4:15. doi: 10.3389/fnsys.2010.00015

Gagnon, D., Petryszyn, S., Sanchez, M. G., Bories, C., Beaulieu, J. M., De Koninck, Y., et al. (2017). Striatal neurons expressing D_1 and D_2 receptors are morphologically distinct and differently affected by dopamine denervation in mice. *Sci. Rep.* 7:41432. doi: 10.1038/srep41432

Gerfen, C. R., and Surmeier, D. J. (2011). Modulation of striatal projection systems by dopamine. *Annu. Rev. Neurosci.* 34, 441–466. doi: 10.1146/annurev-neuro-061010-113641

Ingham, C. A., Hood, S. H., and Arbuthnott, G. W. (1989). Spine density on neostriatal neurones changes with 6-hydroxydopamine lesions and with age. *Brain Res.* 503, 334–338. doi: 10.1016/0006-8993(89)91686-7

Kreitzer, A. C., and Malenka, R. C. (2007). Endocannabinoid-mediated rescue of striatal LTD and motor deficits in Parkinson's disease models. *Nature* 445, 643–647. doi: 10.1038/nature05506

Marder, E., and Goaillard, J. M. (2006). Variability, compensation and homeostasis in neuron and network function. *Nat. Rev. Neurosci.* 7, 563–574. doi: 10.1038/nrn1949

McNeill, T. H., Brown, S. A., Rafols, J. A., and Shoulson, I. (1988). Atrophy of medium spiny I striatal dendrites in advanced Parkinson's disease. *Brain Res.* 455, 148–152. doi: 10.1016/0006-8993(88)90124-2

Plotkin, J. L., Day, M., Peterson, J. D., Xie, Z., Kress, G. J., Rafalovich, I., et al. (2014). Impaired TrkB receptor signaling underlies corticostriatal dysfunction in Huntington's disease. *Neuron* 83, 178–188. doi: 10.1016/j.neuron.2014.05.032

Shen, W., Flajolet, M., Greengard, P., and Surmeier, D. J. (2008). Dichotomous dopaminergic control of striatal synaptic plasticity. *Science* 321, 848–851. doi: 10.1126/science.1160575

Shen, W., Plotkin, J. L., Francardo, V., Ko, W. K., Xie, Z., Li, Q., et al. (2015). M4 muscarinic receptor signaling ameliorates striatal plasticity deficits in models of L-DOPA-induced dyskinesia. *Neuron* 88, 762–773. doi: 10.1016/j.neuron.2015.10.039

Shen, W., Tian, X., Day, M., Ulrich, S., Tkatch, T., Nathanson, N. M., et al. (2007). Cholinergic modulation of Kir2 channels selectively elevates dendritic excitability in striatopallidal neurons. *Nat. Neurosci.* 10, 1458–1466. doi: 10.1038/nn1972

Stephens, B., Mueller, A. J., Shering, A. F., Hood, S. H., Taggart, P., Arbuthnott, G. W., et al. (2005). Evidence of a breakdown of corticostriatal connections in Parkinson's disease. *Neuroscience* 132, 741–754. doi: 10.1016/j.neuroscience.2005.01.007

Suarez, L. M., Alberquilla, S., Garcia-Montes, J. R., and Moratalla, R. (2018). Differential synaptic remodeling by dopamine in direct and indirect striatal projection neurons in Pitx3(−/−) mice, a genetic model of Parkinson's disease. *J. Neurosci.* 38, 3619–3630. doi: 10.1523/JNEUROSCI.3184-17.2018

Suarez, L. M., Solis, O., Aguado, C., Lujan, R., and Moratalla, R. (2016). L-DOPA oppositely regulates synaptic strength and spine morphology in D1 and D2 striatal projection neurons in dyskinesia. *Cereb. Cortex* 26, 4253–4264. doi: 10.1093/cercor/bhw263

Suarez, L. M., Solis, O., Carames, J. M., Taravini, I. R., Solis, J. M., Murer, M. G., et al. (2014). L-DOPA treatment selectively restores spine density in dopamine receptor D2-expressing projection neurons in dyskinetic mice. *Biol. Psychiatry* 75, 711–722. doi: 10.1016/j.biopsych.2013.05.006

Thiele, S. L., Chen, B., Lo, C., Gertler, T. S., Warre, R., Surmeier, J. D., et al. (2014). Selective loss of bi-directional synaptic plasticity in the direct and indirect striatal output pathways accompanies generation of parkinsonism and l-DOPA induced dyskinesia in mouse models. *Neurobiol. Dis.* 71, 334–344. doi: 10.1016/j.nbd.2014.08.006

Toy, W. A., Petzinger, G. M., Leyshon, B. J., Akopian, G. K., Walsh, J. P., Hoffman, M. V., et al. (2014). Treadmill exercise reverses dendritic spine loss in direct and indirect striatal medium spiny neurons in the 1-methyl-4-phenyl-1,2,3,6-tetrahydropyridine (MPTP) mouse model of Parkinson's disease. *Neurobiol. Dis.* 63, 201–209. doi: 10.1016/j.nbd.2013.11.017

Turrigiano, G. G. (2008). The self-tuning neuron: synaptic scaling of excitatory synapses. *Cell* 135, 422–435. doi: 10.1016/j.cell.2008.10.008

Ueno, T., Yamada, J., Nishijima, H., Arai, A., Migita, K., Baba, M., et al. (2014). Morphological and electrophysiological changes in intratelencephalic-type pyramidal neurons in the motor cortex of a rat model of levodopa-induced dyskinesia. *Neurobiol. Dis.* 64, 142–149. doi: 10.1016/j.nbd.2013.12.014

Villalba, R. M., Lee, H., and Smith, Y. (2009). Dopaminergic denervation and spine loss in the striatum of MPTP-treated monkeys. *Exp. Neurol.* 215, 220–227. doi: 10.1016/j.expneurol.2008.09.025

Wang, Z., Kai, L., Day, M., Ronesi, J., Yin, H. H., Ding, J., et al. (2006). Dopaminergic control of corticostriatal long-term synaptic depression in medium spiny neurons is mediated by cholinergic interneurons. *Neuron* 50, 443–452. doi: 10.1016/j.neuron.2006.04.010

Zaja-Milatovic, S., Milatovic, D., Schantz, A. M., Zhang, J., Montine, K. S., Samii, A., et al. (2005). Dendritic degeneration in neostriatal medium spiny neurons in Parkinson disease. *Neurology* 64, 545–547. doi: 10.1212/01.wnl.0000150591.33787.a4

Zhai, S., Tanimura, A., Graves, S. M., Shen, W., and Surmeier, D. J. (2018). Striatal synapses, circuits, and Parkinson's disease. *Curr. Opin. Neurobiol.* 48, 9–16. doi: 10.1016/j.conb.2017.08.004

Zhang, Y., Meredith, G. E., Mendoza-Elias, N., Rademacher, D. J., Tseng, K. Y., and Steece-Collier, K. (2013). Aberrant restoration of spines and their synapses in L-DOPA-induced dyskinesia: involvement of corticostriatal but not thalamostriatal synapses. *J. Neurosci.* 33, 11655–11667. doi: 10.1523/jneurosci.0288-13.2013

Conflict of Interest Statement: The authors declare that the research was conducted in the absence of any commercial or financial relationships that could be construed as a potential conflict of interest.

frontiers in Cellular Neuroscience

ORIGINAL RESEARCH
published: 18 February 2019
doi: 10.3389/fncel.2019.00047

Stimulation of Single, Possible CHX10 Hindbrain Neurons Turns Swimming On and Off in Young *Xenopus* Tadpoles

Wen-Chang Li[1]* *and Stephen R. Soffe*[2]

[1]School of Psychology and Neuroscience, University of St Andrews, St Andrews, United Kingdom, [2]School of Biological Sciences, Tyndall Avenue, University of Bristol, Bristol, United Kingdom

Vertebrate central pattern generators (CPGs) controlling locomotion contain neurons which provide the excitation that drives and maintains network rhythms. In a simple vertebrate, the developing *Xenopus* tadpole, we study the role of excitatory descending neurons with ipsilateral projecting axons (descending interneurons, dINs) in the control of swimming rhythms. In tadpoles with both intact central nervous system (CNS) and transections in the hindbrain, exciting some individual dINs in the caudal hindbrain region could start swimming repeatedly. Analyses indicated the recruitment of additional dINs immediately after such evoked dIN spiking and prior to swimming. Excitation of dINs can therefore be sufficient for the initiation of swimming. These "powerful" dINs all possessed both ascending and descending axons. However, their axon projection lengths were not different from those of other excitatory dINs at similar locations. The dorsoventral position of dINs, as a population, significantly better matched that of cells marked by immunocytochemistry for the transcription factor CHX10 than other known neuron types in the ventral hindbrain and spinal cord. The comparison suggests that the excitatory interneurons including dINs are CHX10-positive, in agreement with CHX10 as a marker for excitatory neurons with ipsilateral projections in the spinal cord and brainstem of other vertebrates. Overall, our results further demonstrate the key importance of dINs in driving tadpole swimming rhythms.

Keywords: central pattern generator, swimming, excitatory interneurons, spinal cord, hindbrain, CHX10

OPEN ACCESS

Edited by:
Jing-Ning Zhu,
Nanjing University, China

Reviewed by:
Ole Kiehn,
Karolinska Institute (KI), Sweden
Jürg Streit,
University of Bern, Switzerland

***Correspondence:**
Wen-Chang Li
wl21@st-andrews.ac.uk

Received: *04 December 2018*
Accepted: *01 February 2019*
Published: *18 February 2019*

Citation:
Li W-C and Soffe SR (2019) Stimulation of Single, Possible CHX10 Hindbrain Neurons Turns Swimming On and Off in Young Xenopus Tadpoles. Front. Cell. Neurosci. 13:47. doi: 10.3389/fncel.2019.00047

INTRODUCTION

Vertebrate locomotion is directly controlled by the neuronal circuits in the spinal cord and brainstem. The conventional concept is that the spinal cord contains the basic circuit, termed central pattern generator (CPG), that can generate the locomotor rhythms by transforming excitatory commands descending from supraspinal centers like the reticulospinal nuclei (Dubuc et al., 2008; Kiehn, 2016). More recent studies in tadpoles (Li et al., 2006; Soffe et al., 2009), larval zebrafish (Kimura et al., 2013) and lamprey (Buchanan, 2018) suggest that the swimming CPG network may extend into the brainstem. Among CPG neurons, glutamatergic excitatory neurons, especially those with ipsilateral projecting axons, have been shown to

play cardinal roles in locomotion rhythm generation of both limbed and non-limbed animals (Jordan et al., 2008; Goulding, 2009; Roberts et al., 2010; Kiehn, 2016). In *Xenopus* tadpoles, as in lamprey, excitatory interneurons with ipsilateral projecting axons have been long identified in the CPG for axial swimming by their anatomy and physiology (Dale and Roberts, 1985; Dale and Grillner, 1986). Tadpole descending interneurons (dINs) in the caudal hindbrain and rostral spinal cord have been shown to be excitatory by coreleasing both glutamate and ACh (Li et al., 2004b). They form feedback excitatory connections among themselves (Li et al., 2006), are electrically coupled (Li et al., 2009) and their firing leads the activity of all other swimming CPG neurons (Soffe et al., 2009). Injecting large currents into dINs can change swimming frequencies (Li and Moult, 2012) and silencing dINs using large hyperpolarizing current injections can stop swimming within milliseconds (Moult et al., 2013). Although they are most easily recorded in the caudal hindbrain and rostral spinal cord region and there are reliable physiological and anatomical criteria to identify them, a molecular marker for the dIN population is still lacking.

The expression pattern of various transcription factors during early development has been used to trace the origin and to classify several groups of excitatory neurons (Goulding, 2009; Gosgnach, 2011; Kiehn, 2016). In mice, this has allowed manipulation of the function of these genetically identified groups of neurons to interrogate their roles in locomotor control. The V2a group of excitatory interneurons express ceh-10 homeodomain containing homolog (CHX10; Lundfald et al., 2007; Crone et al., 2008). Ablating V2a neurons affected the left-right alternation of locomotor rhythms in the high frequency range (Crone et al., 2008, 2009) and their role does not seem to be rhythm-generating (Kiehn, 2016). Ablation of V2a interneurons in the cervical spinal cord only disrupts forelimb reaching (Pivetta et al., 2014; Hayashi et al., 2018). The expression of short stature homeobox protein 2 (SHOX2) defines another excitatory interneuron group with ipsilateral axons (Dougherty et al., 2013), which partially overlaps with V2a CHX10-expressing neurons. V2a SHOX2+ neurons directly excite motoneurons (MNs) and the nonV2a SHOX2+ neurons may be part of the mammalian locomotor CPG. Neurons expressing basic helix-loop-helix domain containing, class B, 9 (HB9) transcription factor may also be part of the excitatory drive in mammalian CPG (Hinckley et al., 2005; Wilson et al., 2005), controlling the frequency of locomotion (Caldeira et al., 2017). These studies clearly show excitatory neuron types in mice belong to a number of diverse functional groups.

Transcription factor expression has also been studied in developing zebrafish where CHX10-expressing glutamatergic V2a interneurons (CiD) extend from the spinal cord into the hindbrain (Kimura et al., 2006, 2013). Optically exciting V2a neurons in the hindbrain could initiate swimming and inhibiting them could stop ongoing swimming in zebrafish larvae (Kimura et al., 2013). In the spinalized preparation, exciting V2a neurons could also induce fictive swimming bouts (Ljunggren et al., 2014). V2a firing during swimming in the hindbrain is phasic in the middle hindbrain region and more tonic in the caudal hindbrain, thus likely providing both tonic and phasic excitation in the swimming network (Eklöf-Ljunggren et al., 2012; Kimura et al., 2013). The anatomical and functional evidence strongly suggests that dINs in the tadpole swimming circuit are similar to V2a neurons identified in larval zebrafish (Kimura et al., 2006, 2013; Ljunggren et al., 2014) and might also, therefore, be expected to be of CHX10 origin.

In this study, we show that the activation of some individual, powerful dINs was sufficient to start swimming. We analyze the anatomical features of these neurons and show that their distribution suggests that they are, indeed, likely to be of CHX10 origin.

MATERIALS AND METHODS

Xenopus laevis tadpoles were raised from fertilized eggs after inducing mating between pairs of adult male and female by injecting human chorionic gonadotropin solution into the dorsal lymph sac. All experimental procedures were approved by the local Animal Welfare and Ethics Committee at the University of St Andrews and the University of Bristol and comply with UK Home Office regulations. At stage 37/38, ∼2 days post fertilization, tadpoles were briefly anesthetized with 0.1% MS-222 (3-aminobenzoic acid ester, sigma, UK). Then the tadpole was pinned down onto a Sylgard-lined stage in a bath to have its dorsal fin cut open with a fine tungsten needle. Saline contained (in mM): NaCl 115, KCl 3, $CaCl_2$ 4, $NaHCO_3$ 2.4, $MgCl_2$ 1, HEPES 10, with pH adjusted to 7.4 using 5 M NaOH. Next the animal was left in 10 μM α-bungarotoxin saline for immobilization. Afterwards, it was re-pinned onto the Sylgard stage to allow further dissections, which included removing some dorsal trunk skin and muscles over the spinal cord, exposing rostral spinal cord and caudal hindbrain, cutting open the dorsal roof of the exposed central nervous system (CNS) and removing some ependymal cells inside the spinal cord and hindbrain to provide access to neuronal somata for recordings.

Single or dual whole-cell patch clamp recordings were made in current clamp mode. Patch-clamp pipettes were filled with 0.1% neurobiotin in an intracellular solution (K-gluconate 100 mM, $MgSO_4$ 2 mM, EGTA 10 mM, HEPES 10 mM, Na_2ATP 3 mM, NaGTP 0.5 mM) and had resistances of ∼10 MΩ. Neurobiotin filling of neurons was achieved by passive diffusion during recordings. After experiments, tadpoles were fixed in 2% glutaraldehyde in 0.1 M phosphate buffer (pH 7.2) overnight in the fridge. After rinsing with 0.1 M phosphate buffered saline (PBS), tadpoles were treated with two changes of 1% triton-X100 in PBS for 15 min with agitation. Then they were incubated for 2–3 h in a 1:200 dilution of extravidin peroxidase conjugate (Sigma) in PBS containing 0.5% Triton-X100 with agitation. The animals were washed afterwards with a few changes of PBS. Then they were pre-soaked in 0.08% diaminobenzidine in PB (DAB solution) for 5 min and moved to a second pot with 0.03% hydrogen peroxide in DAB solution for five more minutes. The staining reaction was stopped by washing the preparations with tap water. Further dissections were carried out to free the brain and spinal cord with the notocord and some ventral muscles for slide-mounting using Depex after dehydration with alcohol and clearance with methyl benzoate and xylene.

For CHX10 staining, tadpoles were fixed in MEMFA (3.7% formaldehyde, 0.1 M MOPS, 2 mM EGTA, 1 mM $MgSO_4$) for 2 h, rinsed in two changes of methanol and stored overnight in methanol at −20°C. The spinal cord was exposed by dissection following rehydration and the tissues bleached in 15% hydrogen peroxide in 0.1 M PBS for 2 h. Then specimens were washed with three changes of PBT (PBS with 0.1% Triton X100 and 20 mg/ml bovine serum albumin) for 15 min each and then blocked in 10% normal goat serum in PBT. They were next transferred to primary antiserum CHX10 (1:1,000, kindly provided by Dr. Martyn Goulding) for 72 h, washed 5× 1 h in PBT, incubated overnight in secondary antibody (peroxidase conjugated F(ab)2 fragment goat anti-rabbit IgG (Jackson Immunoresearch, with 1:500 dilution in PBT). After washing 5× 45 min in PBT, the peroxidase was visualized using nickel-enhanced diaminobenzidine with glucose oxidase to generate the hydrogen peroxide. After two washes in PBS, specimens were cleared in Murrays Clear (2:1 Benzyl benzoate:benzyl alcohol) and mounted between coverslips.

Neurons were observed using a ×100 oil immersion objective to check the axon trajectories. Axons and soma positions were traced using a ×20 objective. All measurements were corrected for shrinkage during dehydration by multiplying by 1.28. Data distribution was routinely checked before comparisons were carried out using IBM SPSS Statistics 24. For normally distributed data, *t*-test or one way ANOVA were adopted and for other datasets, non-parametric tests were used. Figures were prepared using CorelDRAW Graphics Suite X6.

RESULTS

Hatchling *Xenopus* tadpoles at stage 37/38 (**Figure 1A**) swim forward when they are briefly touched on the trunk skin. The neuronal circuit responsible for generating the swimming rhythms has been located in the caudal hindbrain and spinal cord, comprising four types of neurons including MNs, dINs, commissural interneurons (cINs) and ascending interneurons (aINs, **Figure 1B**, aINs not shown for simplicity). Neuronal activity can be recorded once the animals are immobilized using α-bungarotoxin and dissections made to expose neuronal somata. The fictive swimming frequencies (10–25 Hz) are very similar to those for free swimming (Roberts et al., 2000). During fictive swimming, CPG neurons like dINs typically fire a single action potential on each swimming cycle, with firing alternating between the left and right sides coordinated by reciprocal

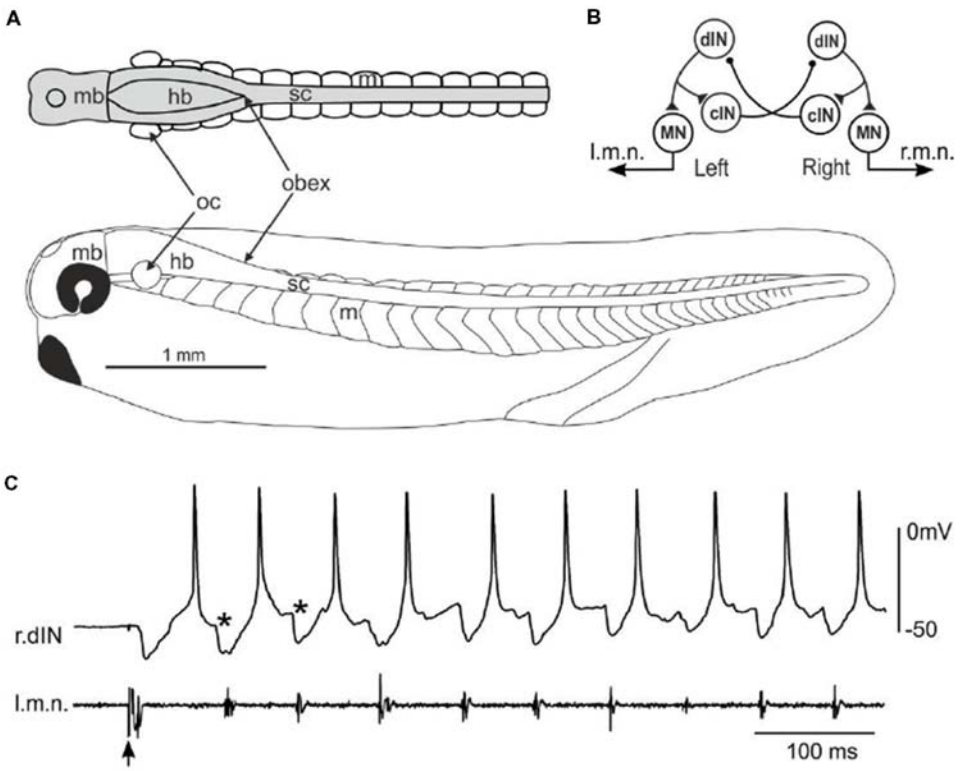

FIGURE 1 | Fictive swimming in a stage 37/38 tadpole and the neural circuit controlling swimming. **(A)** A side-view scale diagram of a developing tadpole at stage 37/38 with a top view of its central nervous system (CNS; gray) showing: m swimming myotomes; mb, midbrain; hb, hindbrain; sc, spinal cord; oc, otic capsule. Obex is where the hindbrain ventricle closes and the landmark separating hb and sc. **(B)** Diagram showing most critical neuron populations and their synaptic connections in tadpole swimming central pattern generator (CPG). Each circle represents a neuron population. dIN, descending interneuron; cIN, commissural interneuron; MN, motoneuron. l.m.n. and r.m.n.: left and right motor nerve. **(C)** Typical activity of a right side dIN (r.dIN) and simultaneous left motor nerve (l.m.n) activity at the beginning of an episode of fictive swimming started by electrical stimulation to the head skin (arrow). *Indicates cIN inhibition.

inhibitory coupling mediated by the cINs (**Figure 1C**). dINs can be physiologically identified by their single firing at the onset of step current injections, rebound-firing following phasic inhibition provided the membrane potential is held depolarized, their broad action potentials and one-spike-per-cycle firing in nearly all swimming cycles. Anatomically, dINs typically have ipsilateral descending axons and half of them in the caudal hindbrain and rostral spinal cord region also possess ascending branches (Li et al., 2006).

The Initiation of Swimming by Single dINs in Tadpoles With Hindbrain Transections

The importance of populations of neurons in a neuronal network can be demonstrated by their sufficiency and necessity for network activity. We previously showed that blocking dIN activity by injecting large hyperpolarizing current into individual dINs could stop ongoing swimming (Moult et al., 2013) possibly by currents spreading to other dINs *via* their electrical coupling, suggesting dINs are essential in swimming rhythmogenesis. We also reported that spiking in one dIN evoked by current injection could often initiate swimming, but only if magnesium was omitted from the saline to increase excitability by turning off the voltage dependency of NMDAR-mediated excitation (Li et al., 2006).

We have now made recordings from over 200 dINs and confirmed our previous finding that stimulating a single dIN in intact tadpoles rarely initiates swimming in normal saline (containing 1 mM magnesium). However, under some circumstances stimulating single dINs to fire was able to elicit episodes of swimming. All were cases in which the spinal cord and hindbrain were (partially) disconnected from higher brain areas. When one side of hindbrain and spinal cord were removed, single spiking in 2/48 dINs evoked rhythmic activity in 13/44 trials (**Figure 2A**). In preparations where one side of hindbrain was transected at the otic capsule level, spiking in

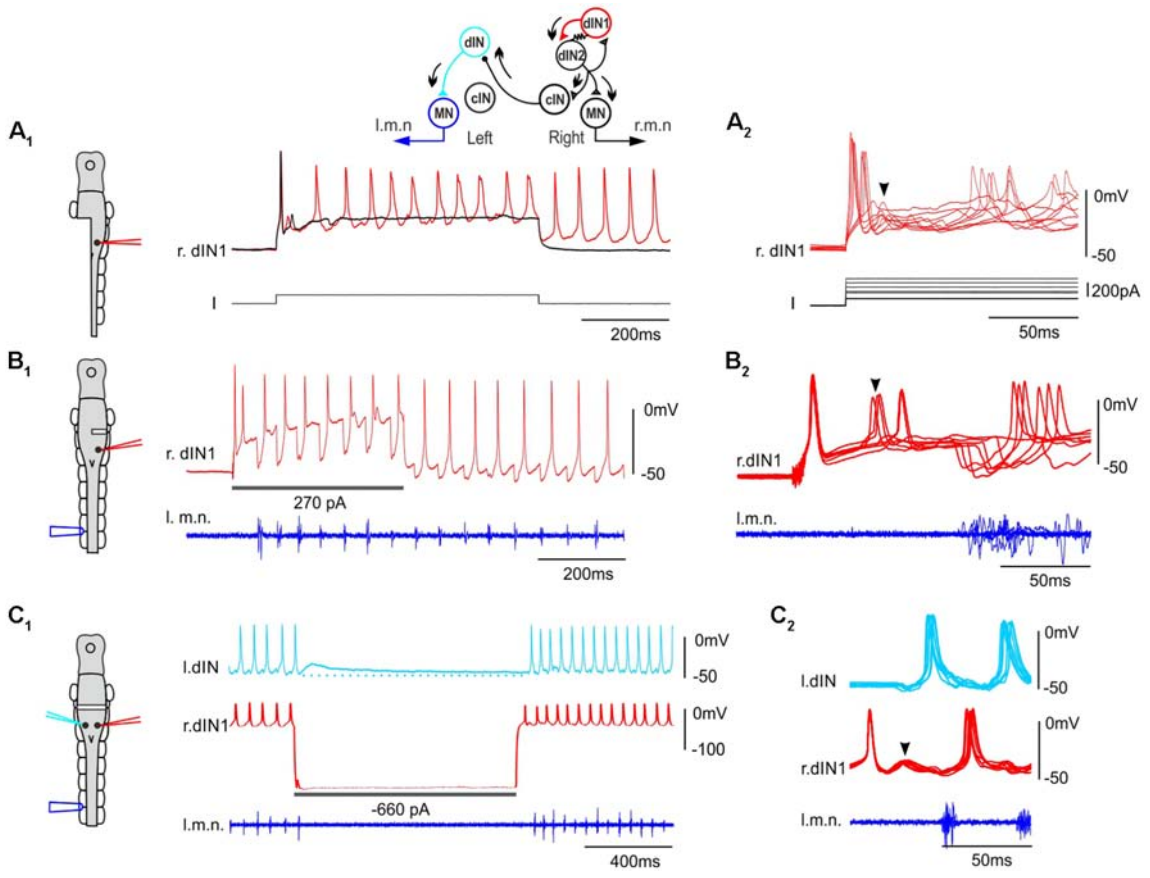

FIGURE 2 | Stimulating single dINs in tadpoles with hindbrain transections starts fictive swimming. **(A_1)** Step current injection into a right side dIN (r.dIN1) initiates swimming-like rhythms in a tadpole with the left side spinal cord and caudal hindbrain removed (black trace shows a failed trial). **(A_2)** Nine superimposed trials as in **(A_1)** but on a faster time scale and with different injected current levels. **(B_1)** Injecting depolarizing currents into a dIN in a tadpole with its right side hindbrain transected starts swimming. **(B_2)** Seven successful trials are overlapped on a faster time scale. **(C_1)** The rebound spiking of a right side dIN (r.dIN1) following the withdrawal of a hyperpolarizing current injection, which has stopped swimming for 1 s, re-starts swimming in a dual whole-cell recording. Dotted line indicates the resting membrane potential of l.dIN. **(C_2)** Eight superimposed trials. Traces are lined up to the rising phase of the first dIN spike in **(B_2,C_2)**. Diagrams on the left show CNS as in **Figure 1A** with location of lesions and electrodes (same color-coded as the recording traces). Arrowheads indicate secondary EPSPs and spiking following the initial dIN spiking. Inset shows sequence of activity in the CPG (arrows) with resistor sign representing electrical coupling among ipsilateral dINs.

1/39 dINs on the transected side initiated swimming multiple times (7/19 trials, **Figure 2B**). In addition, when the hindbrain was completely transected at the otic capsule level and large intracellular hyperpolarizing current injections were used to stop skin stimulation-evoked swimming in whole-cell dIN recordings (Moult et al., 2013), swimming could start again at the end of current pulse (1 s duration, swimming stopped for 400–1,000 ms) following rebound firing of the dIN (6/41 dINs, 45/97 trials, **Figure 2C**, depolarizing currents not tested). dINs typically receive tapering depolarization lasting for several seconds after swimming stops (for comparison, see hyperpolarization in other types of CPG neurons, Zhang and Sillar, 2012). A brief cessation of swimming would mean most dINs were still depolarized when the rebound spiking took place in the injected dIN, which should lower the swimming threshold. We measured the average depolarization levels in four non-injected dINs at the point of rebound spiking in paired recordings (**Figure 2C**$_1$). They were 2.5, 3, 6.2 and 9.8 mV, despite being electrically coupled to dINs injected with large hyperpolarizing currents.

Tadpole swimming is normally initiated by the activation of the mechanosensory pathway innervating the skin. We first asked whether swimming started directly by these powerful, individual dINs differed from swimming initiated by sensory stimulation. We compared three swimming parameters, motor nerve (m.n.) burst duration, swimming frequency and duty cycle, in the first 50 cycles of swimming evoked by powerful dINs or by skin stimulation (**Figure 3A**). All three parameters were lower in swimming episodes started by seven powerful dINs, in that swimming frequency was lower and with relatively shorter motor bursts ($p < 0.05$, all paired t-test, **Figure 3B**). However, basic form of the alternating swimming pattern was the same. These data show that activation of dINs is sufficient in inducing swimming activity.

We have previously shown that dINs fire relatively early on each swimming cycle and their activity drives all CPG neuronal activity on the same side (Soffe et al., 2009). However, the delay between an evoked spike in a powerful dIN and the first swimming motor burst was clearly longer than the delay for subsequent cycles (compare numbered events in **Figure 3C**). To quantify this difference, we simply compared the periods of the first two cycles, measured separately for dINs and motor bursts (**Figure 3D**). As expected, these matched closely for the second cycle (dINs 47.3 ± 5.8 ms, motor bursts 48 ± 6.6 ms; $p = 0.47$, paired t-test, $n = 7$). However, for the first cycle, dIN period was significantly longer than motor burst period (dIN 66.1 ± 8.4, motor bursts 47.3 ± 5.6 ms; Wilcoxon matched-pairs signed-ranks test, $p < 0.05$, $n = 7$). The first motor burst was therefore 18.9 ± 5.4 ms later than expected from the delay between dIN spikes and motor bursts on subsequent cycles. This additional delay indicates that the initial dIN spiking does not directly drive the first motor burst, but that some further step is involved.

Then what happens after the initial dIN spiking to initiate swimming only after a relatively long delay? In each of the 65 trials where dIN spiking evoked swimming, some clear EPSPs followed the initial dIN spiking with a latency of 15 ± 2.7 ms (**Figures 2A$_2$,C$_2$**). These EPSPs gave rise to secondary spikes in the stimulated dIN in 19 trials (**Figures 2B$_2$, 3C**). We previously

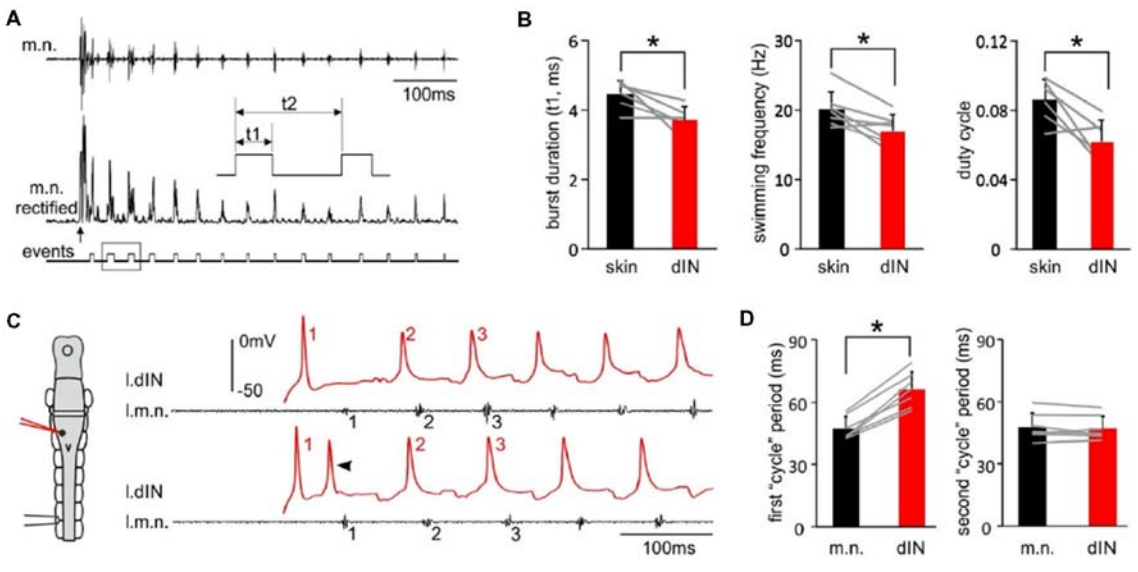

FIGURE 3 | The features of swimming evoked by powerful dINs. **(A)** The beginning of a swimming episode started by tail skin stimulation (arrow). m.n. trace is rectified and threshold set to trigger burst events. Box area is stretched in the inset to show burst duration (t1), swimming frequency (1/t2) and duty cycle (t1/t2). **(B)** Swimming burst durations, frequencies and duty cycles for the first 50 cycles are lower in the episodes evoked by powerful dINs (red) than those started by skin stimulation (black). **(C)** The beginning of two swimming episodes started by a powerful dIN (traces before the initial spiking is off scale). Numbers in red and black mark dIN spikes and m.n. bursts used for calculating spiking/cycle periods, respectively. Both dIN and m.n. are recorded from the left side (diagram, l.dIN, l.m.n.). Arrowhead points at secondary dIN spiking. **(D)** The first, but not the second dIN spiking period is longer than swimming cycle period measured using m.n. bursts. Gray lines link measurements from the same recordings in **(B,D)**. *Indicates $p < 0.05$.

revealed feedback excitation among dINs in the caudal hindbrain region (Li et al., 2006) and there was also widespread electrical coupling among dINs (Li et al., 2009). We suggest the most likely explanation for the events following an evoked dIN spike is that both types of synaptic connections act to recruit more dINs to amplify the initial excitation from this single spike. The sequence of event would therefore be that: the initial, evoked dIN firing would lead to excitation and recruitment of firing in a wider population of dINs; this in turn would produce the further EPSPs and secondary spiking seen in the recorded dIN; and firing across this wider dIN population would initiate the swimming rhythm (**Figure 2**, top diagram).

The Initiation of Swimming by a dIN in a Tadpole With Intact CNS

In one dIN from a tadpole with an intact CNS, swimming episodes were also reliably evoked by dIN current injections. From this example, we were able to estimate when the recruited dINs fired spikes by analyzing the timing of their EPSPs produced in the stimulated dIN. Injecting step currents of either 10 ms or 1,000 ms in duration evoked a single spike in this dIN and started swimming reliably (10/11 trials of 10 ms and 84/94 trials of 1,000 ms pulses, **Figure 4A**). Since the first two swimming cycle periods measured for motor bursts are similar (see above), we should expect similar spiking periods in the recruited dINs (dIN2, top right inset in **Figure 4**), which drive the motoneuron firing and motor nerve discharges. We measured the delay of three events relative to the first dIN spike after the first motor nerve burst (0 ms, **Figure 4B**): (a) the initial dIN spike; (b) onset of the first EPSP; and (c) the second dIN spike after the 1st motor nerve burst. In agreement with the analyses in **Figure 3**, event "a" had an average delay of 62.4 ± 5.1 ms, longer than the average delay of 52.7 ± 5.8 ms for event "c" ($p < 0.001$, $n = 94$, non-parametric median tests). The spike time for recruited dINs should be given by the delay for event "b" (50.1 ± 5.6 ms) plus the synaptic delay (∼1 ms). The deduced spiking time of (51.1 ± 5.6 ms) for the recruited dINs was similar to the delay for event "c" ($p = 0.13$, $n = 94$, non-parametric median tests, **Figure 4C**) as we expected. Therefore, these analyses illustrate how the powerful dINs may have started swimming (top right inset in **Figure 4**), i.e., by recruiting more dINs on the same side to amplify the excitation.

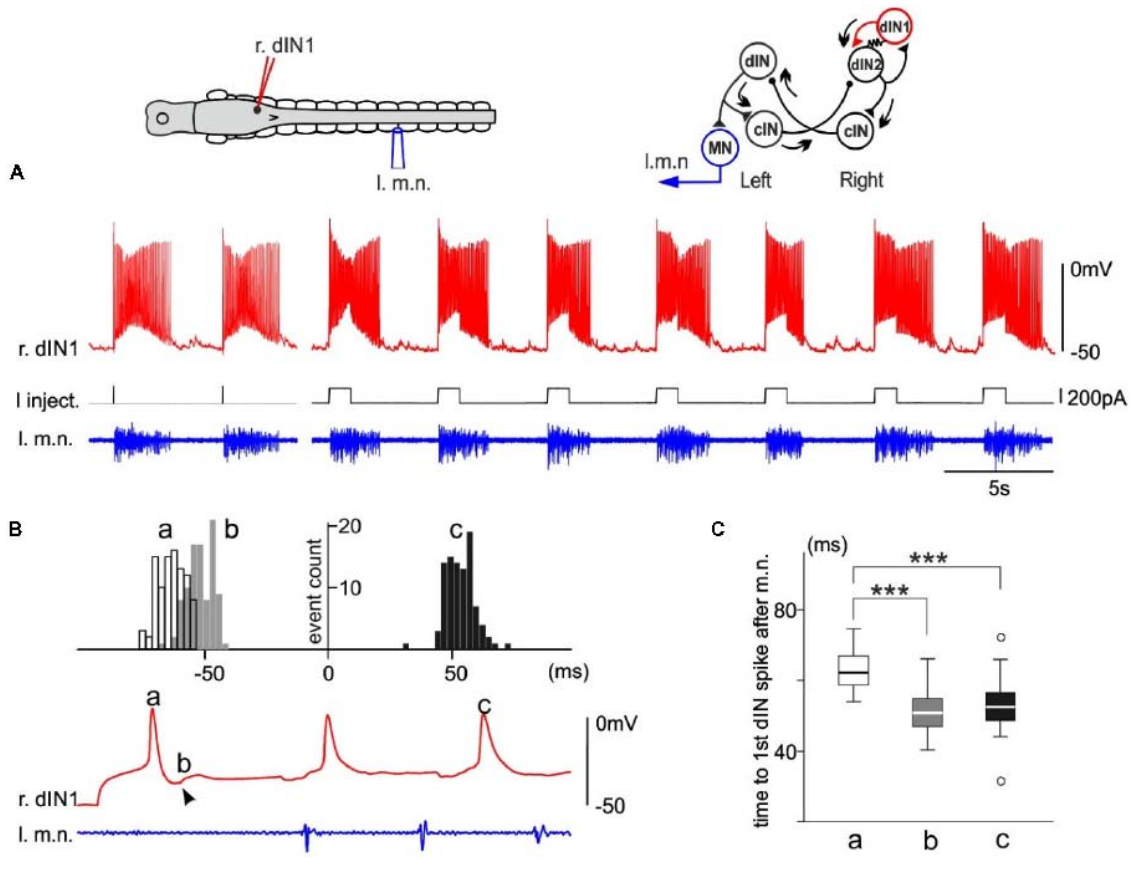

FIGURE 4 | Single spiking in a right side dIN (r.dIN1) in a tadpole with intact CNS reliably evokes fictive swimming (right inset drawing with arrows showing activity sequence). **(A)** In nine trials (two 10 ms and seven 1,000 ms current pulses), r.dIN1 spiking initiates swimming. **(B)** The distribution of r.dIN1 spike and EPSP time relative to the first spike after the first l.m.n. bursts (time 0, 94 trials for the histogram). The timing of three events (see the trace below for examples) are measured: initial r.dIN1 spike evoked by current injections ("a," unfilled histogram); onset of the first EPSP ("b," arrowhead, gray); 2nd r.dIN1 spike after m.n. bursts ("c," filled). **(C)** Comparison between the time of the three events in **(B)**. ***Indicates $p < 0.001$.

The Distributions and Axon Projections of Powerful dINs

We previously reported that about half of the dINs in the caudal hindbrain and rostral spinal cord area had ascending axon branches in addition to their primary descending axon (Li et al., 2006). All of the nine powerful dINs recorded in tadpoles with hindbrain transections (**Figure 2**) and the 1 dIN recorded in an intact CNS (**Figure 4**) were located in the caudal hindbrain region. We traced the axon trajectories of seven of these dINs whose anatomy was revealed clearly by neurobiotin staining (**Figure 5**). All of the seven powerful dINs possessed both ascending and descending axons. Four of them had additional branches and more extensive axon branching patterns. These axons tended to project throughout the caudal hindbrain and rostral spinal cord. This was compared to the anatomy of 12 other dINs, the excitation of which had failed to initiate swimming, at similar locations in tadpoles with transections in the hindbrain (**Figure 2C$_1$**, inset). Three of the 12 dINs did not have ascending axons and five of them possessed more than two axonal branches (3–6). Their total axon lengths (1,056 ± 367 μm) were similar to those of the seven powerful dINs (980 ± 340 μm, two-tailed independent *t*-test, $p = 0.65$, **Figure 5D**). The lack of distinctive anatomy of these powerful dINs suggests that they may have powerful synaptic excitation that allows them to evoke spiking in the remaining dINs in the swimming circuit to initiate swimming.

Is CHX10 Expressed by dINs?

In zebrafish, excitatory interneurons in the swimming circuit express the transcription factor CHX10. Is it possible that the dINs in the tadpole swimming network are also CHX10 positive? We previously used CHX10 antibody to stain the neurons in the tadpole CNS (**Figure 6A**, Roberts et al., 2012). The vast majority of the CHX10 positive cells are located in the ventral quarter of the hindbrain and ventral half of the spinal cord. Although there were many CHX10 positive cells in the rostral hindbrain region, the staining was relatively light. The density of CHX10 positive cells decreased at the caudal end of the hindbrain and further in the spinal cord. We compared the distributions of these CHX10 positive cells to those for neurons identified physiologically and anatomically within similar longitudinal regions. The somata of sensory interneurons in the mechanosensory pathways are very dorsal so we excluded them in this type of comparison (Roberts et al., 2010). CHX10 positive cells are more ventral than cINs ($n = 11$, $p < 0.01$) and aINs ($n = 7$, $p < 0.05$)

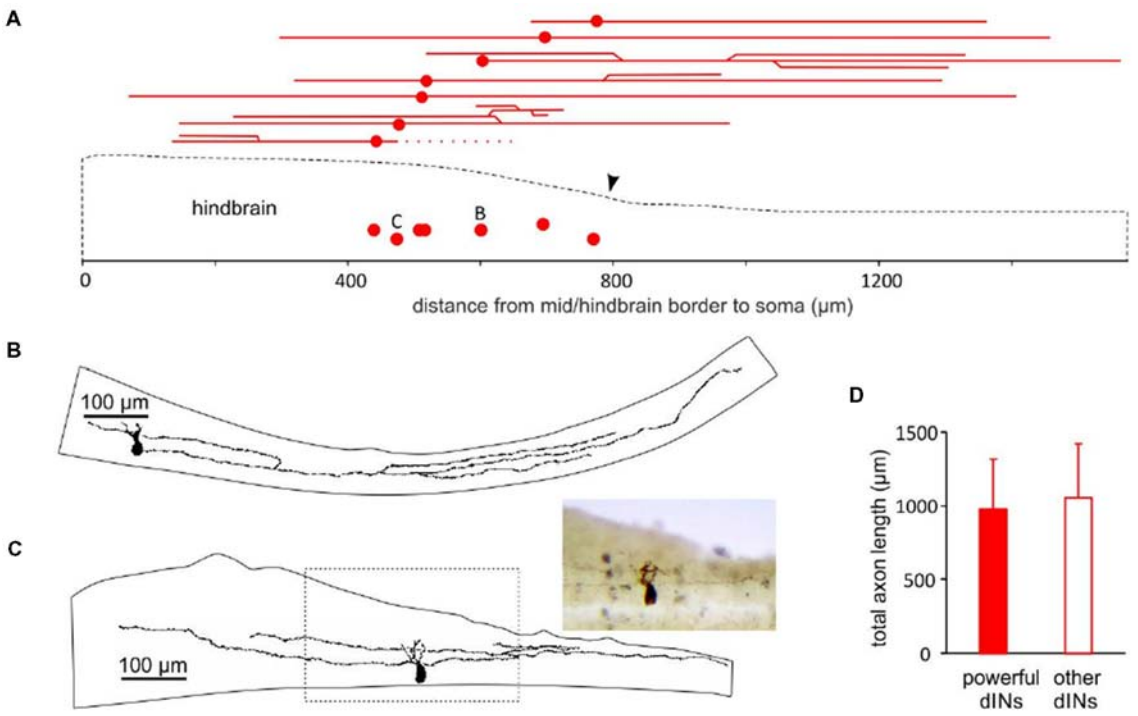

FIGURE 5 | The location of powerful dIN somata and longitudinal axonal projections. **(A)** A diagram of the tadpole hindbrain and rostral spinal cord outline (dashed) showing the location of seven somata of the 10 powerful dINs in **Figures 2**, **3**, **4** (red dots) relative to the mid/hindbrain border (0). The red lines above the sketch show the trajectories of their ascending and descending axons (dotted line indicates a broken axon). Arrowhead points at the obex. **(B)** Drawing of the axon branches and their trajectories in the CNS for dIN B marked in (**A**; also recording in **Figure 2B**). **(C)** Drawing of the axons and their trajectories for dIN C in (**A**; also recording in **Figure 4**). The area within the dashed box is photographed (inset). **(D)** Axon lengths of the seven powerful dINs are similar to those of other 12 dINs within the same region.

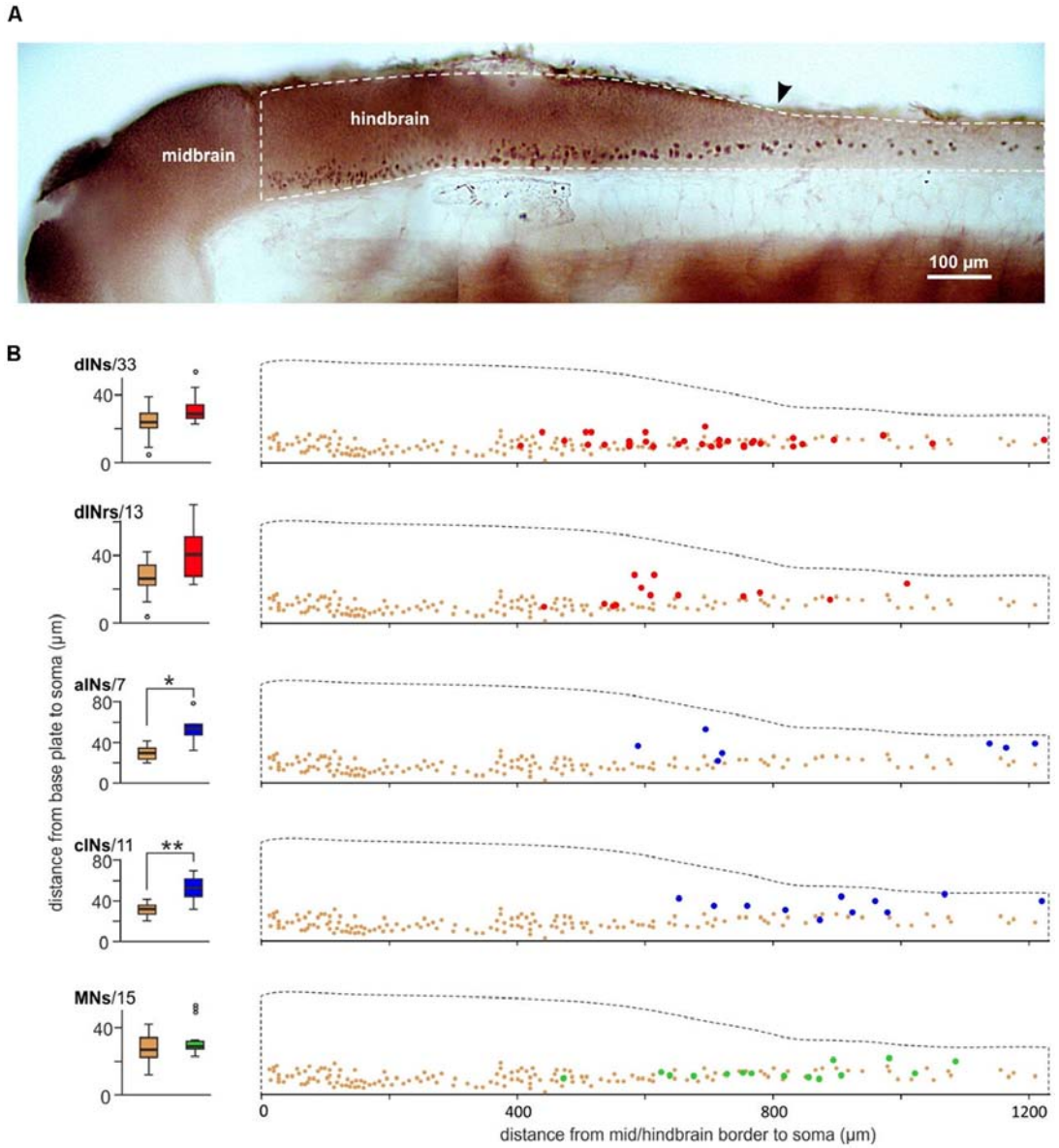

FIGURE 6 | Comparing the location of CHX10 immuno-positive cells and neurons identified by their anatomy and physiology. **(A)** Photograph of CHX10 immuno-positive cells in the right side CNS of a stage 37/38 tadpole (image flipped). The hindbrain and rostral spinal cord is outlined by the white dashed line. Arrowhead marks obex. **(B)** Comparing the dorsoventral soma positions of identified neuron groups [red: dINs, dINrs; blue: ascending interneurons (aINs), cINs; green: MNs, number of neurons given next to names] to the CHX10 immuno-positive cells (brown). The bottom of the hindbrain/spinal cord is set as 0 µm in the dorsoventral dimension and the mid/hindbrain border is set as 0 µm in the longitudinal dimension. *Indicates significance at $p < 0.05$ and ** at $p < 0.01$.

but have similar dorsoventral locations to that for dINs (n = 33), MNs (n = 15) and the repetitive-firing descending interneurons (dINrs, n = 13, all independent median test, **Figure 6B**), which are intensively active during tadpole struggling activity (Li et al., 2007). The CHX10 positive cells are unlikely to include the MNs since MNs have not been shown to be CHX10 positive in any vertebrate (Goulding, 2009; Gosgnach, 2011). However, these comparisons suggest that both dINs and dINrs may form part of the CHX10 distribution.

DISCUSSION

Interrogating the roles of individual groups of neurons in the vertebrate locomotor CPG has been difficult, even in model animals with largely identified neural circuits (Brownstone and Wilson, 2008). From a simple perspective, locomotion can be initiated by activating a single or a small number of "command" cells by sensory information, descending commands from higher brain regions or experimentally. Among invertebrates for example, the activation of serotonin command cells in the

marine Mollusc *Clione limacina* (Arshavsky et al., 1992), trigger cells in sea slug *Tritonia diomedea* (Frost et al., 2001), in leech (Brodfuehrer and Friesen, 1986) or in crayfish (Edwards et al., 1999) can all initiate swimming. These "command" cells receive and process sensory information and pass the swimming decision to the CPG to start locomotion. They then either remain silent or fire tonically during swimming.

In the relatively simple tadpole CNS we have recorded from several powerful dINs, among a large number of random recordings, whose activation showed behavior like that of invertebrate "command" cells by repeatedly leading to swimming. Almost invariably, this only occurred after removal of mid- and forebrain. The reason is unclear, but it may be that the transections in the hindbrain cut off a subpopulation of dINs located rostral to the transection, causing some homeostatic upregulation of dIN synaptic strengths or neuronal excitability (Cooke and Parker, 2009) that increased the likelihood of individual dINs showing powerful effects in the caudal end. Our analyses suggest that the ability of a single dIN to initiate swimming requires recruitment of a wider dIN population. We previously reported extensive electrical coupling among hindbrain dINs. However, the electrical coupling alone has never been strong enough to evoke postsynaptic dIN firing in paired recordings (Li et al., 2009). The initiation of swimming thus is very likely due to dIN chemical synapse connections (Li et al., 2004b). In this way, the initial dIN excitation can be amplified by the positive feedback connections among dINs (Li et al., 2006) allowing it to start swimming network activity. More detailed analyses of the recordings provided some indirect support for our explanation and the timing of what happens between the initial spiking of powerful dINs and the initiation of swimming: the recruitment of a population of dINs to drive the swimming CPG. However, unlike the silence or un-patterned activity of command cells during locomotion in invertebrates (Brodfuehrer and Friesen, 1986; Arshavsky et al., 1992; Frost et al., 2001), dINs fire very reliably on each swimming cycle (**Figure 1B**). Therefore, dINs are not like the invertebrate locomotor "command" cells in simply providing an initial command. Instead, dINs are the core CPG neurons in the tadpole swimming circuit. Swimming is initiated when the dIN population is recruited to fire and maintained dIN firing is essential for sustaining the swimming rhythm (Moult et al., 2013).

How the decision for swimming is made after sensory excitation, however, is not completely clear at this stage, although the dIN is a clear candidate (Koutsikou et al., 2018). Once the mechanosensory neurons innervating trunk or head skin are excited, they directly excite sensory interneurons in the dorsolateral part of the spinal cord or in the trigeminal nuclei (Roberts et al., 2010; Buhl et al., 2012, 2015). The broad distribution of EPSP delays that summate to threshold and give rise to the first synchronous dIN firing cannot be explained by the very brief and short-latency firing of sensory pathway neurons. This suggests the existence of some intermediate interneurons upstream to dINs, producing small EPSPs, which require significant summation to reach dIN firing threshold. Therefore, they should be physiologically different from the usually powerful "command" cells in invertebrates discussed above. In swimming started by powerful dINs, swimming frequency should be lower due to the absence of sensory excitation at the beginning of episodes (**Figure 3**, Li and Moult, 2012). In mammalian spinal circuit, locomotion central pattern generation is proposed to consist of two layers: rhythm generation and pattern-formation (e.g., see Brownstone and Wilson, 2008). There is evidence that some tadpole brainstem neurons have un-patterned firing following skin stimulation, which extends sensory pathway activity and underlie the initial excitation of dINs before swimming starts. However, these interneurons do not appear to be required in the maintenance of swimming rhythms. This is because they do not receive excitation from the rhythmically active dINs (Koutsikou et al., 2018) and we show in this article that dINs can initiate swimming without the activation of sensory pathways. Therefore, a rhythm generating layer is unlikely present between the sensory initiation pathway and the tadpole swimming CPG. Instead, both swimming rhythm-generation, which is based on rebound firing in dINs after reciprocal inhibition (Li et al., 2006; Soffe et al., 2009), and the basic left-right alternation of activity are mediated by the same identified CPG circuit (**Figure 1B**).

Like other types of CPG neurons, dINs fires in a one-spike-per-cycle manner during swimming. How do we determine that dINs drive the swimming rhythms rather than them driven by other neurons? We previously compared the timing of phasic EPSCs dINs received during swimming and their spiking time and found that in the caudal hindbrain and rostral spinal cord region, dIN spiking often preceded the onset of EPSCs. This suggests that dIN firing is not driven directly by the fast EPSPs they receive, but likely from the rebound following reciprocal inhibition (Soffe et al., 2009). In line with dINs driving the swimming CPG, dINs spike reliably earlier than other neurons at similar longitudinal positions. dINs' role as the driving force for swimming was further confirmed by silencing experiments where large hyperpolarizing currents were injected into individual dINs in the caudal hindbrain region (Moult et al., 2013). These currents likely spread into neighboring dINs through electrical coupling, inhibited more dINs and stopped swimming. Physiology and anatomical data also support that dINs form a continuous column extending into the caudal hindbrain, where their ascending axon branches provide feedback excitation critical for the maintenance of swimming (Li et al., 2006). Interestingly, some V2a neurons recorded in the middle hindbrain of zebrafish are rhythmically active during fictive swimming (Kimura et al., 2013). The caudal hindbrain of adult lamprey has also been recently demonstrated with swimming rhythm generating capacity (Buchanan, 2018). It is well known that locomotion rhythm generation lies in the spinal cord of vertebrates. It remains an interesting question if this wider distribution of swimming CPG in both spinal cord and hindbrain is just a feature of a developing motor circuit, or it is common for swimming vertebrates.

Do dINs potentially possess molecular characteristics that could be used to link them to similar excitatory interneurons

in the locomotion CPGs in other vertebrates? Apart from using immunocytochemical methods to reveal neurons with different neurotransmitters, several molecular markers have been used in the past to identify the sensory Rohon-Beard (RB) cells, MNs, the ascending inhibitory interneurons in *Xenopus* tadpoles (Borodinsky et al., 2004; Li et al., 2004a). Unfortunately, proper double-labeling was generally lacking to confirm the specificity for these markers in segregating neuronal groups defined anatomically or functionally, although the anatomical identification of RB cells is reliable. In this study, we have compared the dorsoventral location of CHX10 nuclei to the soma location for all known classes of ventrally located neurons. This has led to the conclusion that CHX10 is likely to be expressed in dINs and dINrs. Although MNs are located in similar, ventral locations, they have never been shown to express CHX10 in any vertebrate (Goulding, 2009; Gosgnach, 2011). Some dINrs are also located quite dorsally, implying the presence of some subgroups. Zebrafish CHX-10 expressing excitatory interneurons can be functionally divided into subgroups of bursting and regular-firing neurons based on their responses to intracellular current injections. Anatomically, the bursting subgroup only possesses descending axons (Song et al., 2018). Tadpole dINrs also only have descending axons but they fire repetitively. This may reflect differences among vertebrate species.

Unlike some invertebrate CPGs where inhibitory synapses and electrical synapses are common (Shepherd and Grillner, 2010), excitatory interneurons in the vertebrate locomotor CPG play critical roles. Such roles include providing the phasic and tonic excitation that drives the activity of the whole CPG, co-ordinating left-right motor activity, maintaining the locomotor rhythms (Kiehn, 2016) and potentially the propagation of rhythmic activity along the longitudinal body axis. In zebrafish, the CHX10-expressing interneurons also extend from the spinal cord into the hindbrain, although they appear to be more dorsally located in the hindbrain than the CHX10 positive cells in tadpoles (Kimura et al., 2006, 2013). Optogenetic tools have been developed in the fish to show that exciting V2a CHX10 neurons could start swimming and inhibiting them stopped swimming (Kimura et al., 2013; Ljunggren et al., 2014). A subpopulation of these CHX10 neurons in the ventromedial part of the hindbrain reticular formation appear be active only in the initial burst of swimming, contributing to the turning behavior in larval zebrafish (Huang et al., 2013). In mice, CHX10 have been shown to mark multiple functional groups of excitatory neurons in both the spinal cord and brainstem. Function of spinal CHX10 neurons in mouse seemed to be related to left-right motor activity alternation (Lundfald et al., 2007; Crone et al., 2008, 2009) and forelimb reaching (Pivetta et al., 2014). Surprisingly, optogenetically stimulating V2a neurons in the brainstem reticular formation in mice does not initiate locomotion, as suggested by an earlier study (Bretzner and Brownstone, 2013), but instead stops ongoing locomotion (Bouvier et al., 2015). Similar optogenetic tools to specifically target dINs as a neuronal group have not been developed. However, among a large number of recordings, we have fortunately found several examples of individual dINs, whose excitation could evoke swimming in this study. We previously showed that in many cases injecting large hyperpolarizing currents into individual dINs in the caudal hindbrain regions could slow down (Li and Moult, 2012) or stop ongoing swimming (Moult et al., 2013). Therefore, we conclude that dIN activity is both sufficient and necessary in tadpole swimming rhythms.

In conclusion, we have provided further evidence that hindbrain excitatory neurons, dINs, are vital in the initiation and maintenance of tadpole swimming. A key feature of the excitatory dIN population is that activity in some members or even, as here, single members, can recruit wider firing in the population. They also may express the transcription factor CHX10 in early development. There appears to be strong functional and anatomical similarity between CHX10 positive V2a neurons in zebrafish and dINs in tadpoles, i.e., swimming rhythm initiation and maintenance, but in mammals CHX10 neuronal functions in motor control have diversified.

DATA AVAILABILITY

The datasets generated for this study are available on request to the corresponding author.

AUTHOR CONTRIBUTIONS

W-CL collected and analyzed data. W-CL and SS contributed to writing.

FUNDING

This work was supported by Biotechnology and Biological Sciences Research Council (BBSRC, BB/L00111X), Wellcome Trust (089319) and the Royal Society.

ACKNOWLEDGMENTS

We thank Prof. Alan Roberts for critical comments on earlier versions of this manuscript.

REFERENCES

Arshavsky, Y. I., Deliagina, T. G., Orlovsky, G. N., Panchin, Y. V., Pavlova, G. A., and Pavlova, L. B. (1992). Interneurons mediating the escape reaction of the marine mollusc *Clione limacina*. *J. Exp. Biol.* 164, 307–314.

Borodinsky, L. N., Root, C. M., Cronin, J. A., Sann, S. B., Gu, X., and Spitzer, N. C. (2004). Activity-dependent homeostatic specification of transmitter expression in embryonic neurons. *Nature* 429, 523–530. doi: 10.1038/nature02518

Bouvier, J., Caggiano, V., Leiras, R., Caldeira, V., Bellardita, C., Balueva, K., et al. (2015). Descending command neurons in the brainstem that halt locomotion. *Cell* 163, 1191–1203. doi: 10.1016/j.cell.2015.10.074

Bretzner, F., and Brownstone, R. M. (2013). Lhx3-CHX10 reticulospinal neurons in locomotor circuits. *J. Neurosci.* 33, 14681–14692. doi: 10.1523/JNEUROSCI.5231-12.2013

Brodfuehrer, P. D., and Friesen, W. O. (1986). Initiation of swimming activity by trigger neurons in the leech subesophageal ganglion. II. Role of segmental swim-initiating interneurons. *J. Comp. Physiol. A* 159, 503–510. doi: 10.1007/bf00604170

Brownstone, R. M., and Wilson, J. M. (2008). Strategies for delineating spinal locomotor rhythm-generating networks and the possible role of Hb9 interneurones in rhythmogenesis. *Brain Res. Rev.* 57, 64–76. doi: 10.1016/j.brainresrev.2007.06.025

Buchanan, J. T. (2018). Swimming rhythm generation in the caudal hindbrain of the lamprey. *J. Neurophysiol.* 119, 1681–1692. doi: 10.1152/jn.00851.2017

Buhl, E., Roberts, A., and Soffe, S. R. (2012). The role of a trigeminal sensory nucleus in the initiation of locomotion. *J. Physiol.* 590, 2453–2469. doi: 10.1113/jphysiol.2012.227934

Buhl, E., Soffe, S. R., and Roberts, A. (2015). Sensory initiation of a co-ordinated motor response: synaptic excitation underlying simple decision-making. *J. Physiol.* 593, 4423–4437. doi: 10.1113/JP270792

Caldeira, V., Dougherty, K. J., Borgius, L., and Kiehn, O. (2017). Spinal Hb9::Cre-derived excitatory interneurons contribute to rhythm generation in the mouse. *Sci. Rep.* 7:41369. doi: 10.1038/srep41369

Cooke, R. M., and Parker, D. (2009). Locomotor recovery after spinal cord lesions in the lamprey is associated with functional and ultrastructural changes below lesion sites. *J. Neurotrauma* 26, 597–612. doi: 10.1089/neu.2008.0660

Crone, S. A., Quinlan, K. A., Zagoraiou, L., Droho, S., Restrepo, C. E., Lundfald, L., et al. (2008). Genetic ablation of V2a ipsilateral interneurons disrupts left-right locomotor coordination in mammalian spinal cord. *Neuron* 60, 70–83. doi: 10.1016/j.neuron.2008.08.009

Crone, S. A., Zhong, G., Harris-Warrick, R., and Sharma, K. (2009). In mice lacking V2a interneurons, gait depends on speed of locomotion. *J. Neurosci.* 29, 7098–7109. doi: 10.1523/JNEUROSCI.1206-09.2009

Dale, N., and Grillner, S. (1986). Dual-component synaptic potentials in the lamprey mediated by excitatory amino acid receptors. *J. Neurosci.* 6, 2653–2661. doi: 10.1523/jneurosci.06-09-02653.1986

Dale, N., and Roberts, A. (1985). Dual component amino-acid-mediated synaptic potentials: excitatory drive for swimming in *Xenopus* embryos. *J. Physiol.* 363, 35–59. doi: 10.1113/jphysiol.1985.sp015694

Dougherty, K. J., Zagoraiou, L., Satoh, D., Rozani, I., Doobar, S., Arber, S., et al. (2013). Locomotor rhythm generation linked to the output of spinal Shox2 excitatory interneurons. *Neuron* 80, 920–933. doi: 10.1016/j.neuron.2013.08.015

Dubuc, R., Brocard, F., Antri, M., Fénelon, K., Gariépy, J.-F., Smetana, R., et al. (2008). Initiation of locomotion in lampreys. *Brain Res. Rev.* 57, 172–182. doi: 10.1016/j.brainresrev.2007.07.016

Edwards, D. H., Heitler, W. J., and Krasne, F. B. (1999). Fifty years of a command neuron: the neurobiology of escape behavior in the crayfish. *Trends Neurosci.* 22, 153–161. doi: 10.1016/s0166-2236(98)01340-x

Eklöf-Ljunggren, E., Haupt, S., Ausborn, J., Dehnisch, I., Uhlén, P., Higashijima, S., et al. (2012). Origin of excitation underlying locomotion in the spinal circuit of zebrafish. *Proc. Natl. Acad. Sci. U S A* 109, 5511–5516. doi: 10.1073/pnas.1115377109

Frost, W. N., Hoppe, T. A., Wang, J., and Tian, L. M. (2001). Swim initiation neurons in *Tritonia diomedea*. *Am. Zool.* 41, 952–961. doi: 10.1093/icb/41.4.952

Gosgnach, S. (2011). The role of genetically-defined interneurons in generating the mammalian locomotor rhythm. *Integr. Comp. Biol.* 51, 903–912. doi: 10.1093/icb/icr022

Goulding, M. (2009). Circuits controlling vertebrate locomotion: moving in a new direction. *Nat. Rev. Neurosci.* 10, 507–518. doi: 10.1038/nrn2608

Hayashi, M., Hinckley, C. A., Driscoll, S. P., Moore, N. J., Levine, A. J., Hilde, K. L., et al. (2018). Graded arrays of spinal and supraspinal V2a interneuron subtypes underlie forelimb and hindlimb motor control. *Neuron* 97, 869.e5–884.e5. doi: 10.1016/j.neuron.2018.01.023

Hinckley, C. A., Hartley, R., Wu, L., Todd, A., and Ziskind-Conhaim, L. (2005). Locomotor-like rhythms in a genetically distinct cluster of interneurons in the Mammalian spinal cord. *J. Neurophysiol.* 93, 1439–1449. doi: 10.1152/jn.00647.2004

Huang, K. H., Ahrens, M. B., Dunn, T. W., and Engert, F. (2013). Spinal projection neurons control turning behaviors in zebrafish. *Curr. Biol.* 23, 1566–1573. doi: 10.1016/j.cub.2013.06.044

Jordan, L. M., Liu, J., Hedlund, P. B., Akay, T., and Pearson, K. G. (2008). Descending command systems for the initiation of locomotion in mammals. *Brain Res. Rev.* 57, 183–191. doi: 10.1016/j.brainresrev.2007.07.019

Kiehn, O. (2016). Decoding the organization of spinal circuits that control locomotion. *Nat. Rev. Neurosci.* 17, 224–238. doi: 10.1038/nrn.2016.9

Kimura, Y., Okamura, Y., and Higashijima, S. (2006). alx, a zebrafish homolog of CHX10, marks ipsilateral descending excitatory interneurons that participate in the regulation of spinal locomotor circuits. *J. Neurosci.* 26, 5684–5697. doi: 10.1523/JNEUROSCI.4993-05.2006

Kimura, Y., Satou, C., Fujioka, S., Shoji, W., Umeda, K., Ishizuka, T., et al. (2013). Hindbrain V2a neurons in the excitation of spinal locomotor circuits during zebrafish swimming. *Curr. Biol.* 23, 843–849. doi: 10.1016/j.cub.2013.03.066

Koutsikou, S., Merrison-Hort, R., Buhl, E., Ferrario, A., Li, W.-C., Borisyuk, R., et al. (2018). A simple decision to move in response to touch reveals basic sensory memory and mechanisms for variable response times. *J. Physiol.* 596, 6219–6233. doi: 10.1113/JP276356

Li, W.-C., Higashijima, S.-I., Parry, D. M., Roberts, A., and Soffe, S. R. (2004a). Primitive roles for inhibitory interneurons in developing frog spinal cord. *J. Neurosci.* 24, 5840–5848. doi: 10.1523/JNEUROSCI.1633-04.2004

Li, W.-C., Soffe, S. R., and Roberts, A. (2004b). Glutamate and acetylcholine corelease at developing synapses. *Proc. Natl. Acad. Sci. U S A* 101, 15488–15493. doi: 10.1073/pnas.0404864101

Li, W. C., and Moult, P. R. (2012). The control of locomotor frequency by excitation and inhibition. *J. Neurosci.* 32, 6220–6230. doi: 10.1523/JNEUROSCI.6289-11.2012

Li, W.-C., Roberts, A., and Soffe, S. R. (2009). Locomotor rhythm maintenance: electrical coupling among premotor excitatory interneurons in the brainstem and spinal cord of young *Xenopus* tadpoles. *J. Physiol.* 587, 1677–1693. doi: 10.1113/jphysiol.2008.166942

Li, W.-C., Soffe, S. R., Wolf, E., and Roberts, A. (2006). Persistent responses to brief stimuli: feedback excitation among brainstem neurons. *J. Neurosci.* 26, 4026–4035. doi: 10.1523/JNEUROSCI.4727-05.2006

Li, W.-C., Sautois, B., Roberts, A., and Soffe, S. R. (2007). Reconfiguration of a vertebrate motor network: specific neuron recruitment and context-dependent synaptic plasticity. *J. Neurosci.* 27, 12267–12276. doi: 10.1523/JNEUROSCI.3694-07.2007

Ljunggren, E. E., Haupt, S., Ausborn, J., Ampatzis, K., and El Manira, A. (2014). Optogenetic activation of excitatory premotor interneurons is sufficient to generate coordinated locomotor activity in larval zebrafish. *J. Neurosci.* 34, 134–139. doi: 10.1523/JNEUROSCI.4087-13.2014

Lundfald, L., Restrepo, C. E., Butt, S. J., Peng, C. Y., Droho, S., Endo, T., et al. (2007). Phenotype of V2-derived interneurons and their relationship to the axon guidance molecule EphA4 in the developing mouse spinal cord. *Eur. J. Neurosci.* 26, 2989–3002. doi: 10.1111/j.1460-9568.2007.05906.x

Moult, P. R., Cottrell, G. A., and Li, W.-C. (2013). Fast silencing reveals a lost role for reciprocal inhibition in locomotion. *Neuron* 77, 129–140. doi: 10.1016/j.neuron.2012.10.040

Pivetta, C., Esposito, M. S., Sigrist, M., and Arber, S. (2014). Motor-circuit communication matrix from spinal cord to brainstem neurons revealed by developmental origin. *Cell* 156, 537–548. doi: 10.1016/j.cell.2013.12.014

Roberts, A., Hill, N. A., and Hicks, R. (2000). Simple mechanisms organise orientation of escape swimming in embryos and hatchling tadpoles of *Xenopus laevis*. *J. Exp. Biol.* 203, 1869–1885.

Roberts, A., Li, W.-C., and Soffe, S. R. (2010). How neurons generate behavior in a hatchling amphibian tadpole: an outline. *Front. Behav. Neurosci.* 4:16. doi: 10.3389/fnbeh.2010.00016

Roberts, A., Li, W.-C., and Soffe, S. R. (2012). A functional scaffold of CNS neurons for the vertebrates: the developing *Xenopus* laevis spinal cord. *Dev. Neurobiol.* 72, 575–584. doi: 10.1002/dneu.20889

Shepherd, G. M., and Grillner, S. (2010). *Handbook of Brain Microcircuits*. New York, NY: Oxford University Press.

Soffe, S. R., Roberts, A., and Li, W.-C. (2009). Defining the excitatory neurons that drive the locomotor rhythm in a simple vertebrate: insights into the origin of reticulospinal control. *J. Physiol.* 587, 4829–4844. doi: 10.1113/jphysiol.2009.175208

Song, J., Dahlberg, E., and El Manira, A. (2018). V2a interneuron diversity tailors spinal circuit organization to control the vigor of locomotor movements. *Nat. Commun.* 9:3370. doi: 10.1038/s41467-018-05827-9

Wilson, J. M., Hartley, R., Maxwell, D. J., Todd, A. J., Lieberam, I., Kaltschmidt, J. A., et al. (2005). Conditional rhythmicity of ventral spinal interneurons defined by expression of the Hb9 homeodomain protein. *J. Neurosci.* 25, 5710–5719. doi: 10.1523/JNEUROSCI.0274-05.2005

Zhang, H. Y., and Sillar, K. T. (2012). Short-term memory of motor network performance via activity-dependent potentiation of Na^+/K^+ pump function. *Curr. Biol.* 22, 526–531. doi: 10.1016/j.cub.2012.01.058

Conflict of Interest Statement: The authors declare that the research was conducted in the absence of any commercial or financial relationships that could be construed as a potential conflict of interest.

frontiers in Neural Circuits

HYPOTHESIS AND THEORY
published: 21 February 2019
doi: 10.3389/fncir.2019.00010

The Functional Role of Striatal Cholinergic Interneurons in Reinforcement Learning From Computational Perspective

Taegyo Kim[1†], Robert A. Capps[2†], Khaldoun C. Hamade[1], William H. Barnett[3], Dmitrii I. Todorov[3], Elizaveta M. Latash[3], Sergey N. Markin[1], Ilya A. Rybak[1] and Yaroslav I. Molkov[2,3]*

[1] Department of Neurobiology and Anatomy, Drexel University College of Medicine, Philadelphia, PA, United States, [2] Neuroscience Institute, Georgia State University, Atlanta, GA, United States, [3] Department of Mathematics and Statistics, Georgia State University, Atlanta, GA, United States

In this study, we explore the functional role of striatal cholinergic interneurons, hereinafter referred to as tonically active neurons (TANs), via computational modeling; specifically, we investigate the mechanistic relationship between TAN activity and dopamine variations and how changes in this relationship affect reinforcement learning in the striatum. TANs pause their tonic firing activity after excitatory stimuli from thalamic and cortical neurons in response to a sensory event or reward information. During the pause striatal dopamine concentration excursions are observed. However, functional interactions between the TAN pause and striatal dopamine release are poorly understood. Here we propose a TAN activity-dopamine relationship model and demonstrate that the TAN pause is likely a time window to gate phasic dopamine release and dopamine variations reciprocally modulate the TAN pause duration. Furthermore, this model is integrated into our previously published model of reward-based motor adaptation to demonstrate how phasic dopamine release is gated by the TAN pause to deliver reward information for reinforcement learning in a timely manner. We also show how TAN-dopamine interactions are affected by striatal dopamine deficiency to produce poor performance of motor adaptation.

Keywords: striatum, reinforcement learning, striatal cholinergic interneurons, tonically active neurons, acetylcholine

OPEN ACCESS

Edited by:
Paul G. Mermelstein, University of Minnesota Twin Cities, United States

Reviewed by:
Julia C. Lemos, University of Minnesota Twin Cities, United States
John Meitzen, North Carolina State University, United States

***Correspondence:**
Taegyo Kim
ktgtech@gmail.com

†These authors have contributed equally to this work

Received: *22 November 2018*
Accepted: *30 January 2019*
Published: *21 February 2019*

Citation:
Kim T, Capps RA, Hamade KC, Barnett WH, Todorov DI, Latash EM, Markin SN, Rybak IA and Molkov YI (2019) The Functional Role of Striatal Cholinergic Interneurons in Reinforcement Learning From Computational Perspective. Front. Neural Circuits 13:10. doi: 10.3389/fncir.2019.00010

INTRODUCTION

It is widely accepted that the basal ganglia play an important role in action selection, the process by which contextually appropriate actions are chosen in response to presented stimuli. To determine the appropriateness of an action, in the basal ganglia perform reinforcement learning occurs to establish action-stimulus associations. This learning process is facilitated by dopaminergic activity in the striatum, where a reward prediction error is encoded by the dopamine concentration excursion from its baseline level. When a subject performs context-appropriate actions, there is a phasic increase in striatal dopamine if the received reward is above the expectation, which means a positive reward prediction error is computed. Over time, the synapses that correspond

to appropriate stimulus-action association in the striatal network are strengthened by long-term potentiation, and inappropriate actions are suppressed by long-term depression (Frank, 2005; Graybiel, 2008). Although this process is well understood from a behavioral perspective, there are still open questions about the underlying neural circuitry.

The neural populations within the striatum consist of GABAergic medium spiny neurons (MSNs), cholinergic interneurons, and GABAergic interneurons (Kita, 1993; Koós and Tepper, 1999; Tepper et al., 2010; Dautan et al., 2014; Yager et al., 2015). Many previous computational studies have focused on MSNs, which comprise a vast majority of the striatum and are heavily implicated in basal ganglia reinforcement learning (Smith et al., 1998; Kreitzer and Malenka, 2008; Wall et al., 2013). In contrast, cholinergic interneurons—also known as tonically active neurons (TANs)—comprise a small fraction of the striatal neurons and their functional role is not well understood. In this study, we integrate the results of previous studies into a computational model that includes TANs and highlight their role in propagating reward information during reinforcement learning.

Tonically active neurons (TANs) are so-called because they exhibit tonic firing activity (5∼10 Hz) (Tan and Bullock, 2008; Schulz and Reynolds, 2013). TANs receive glutamatergic inputs from the cortex and thalamus (Ding et al., 2010; Yager et al., 2015; Kosillo et al., 2016). These excitatory inputs convey sensory information during a salient event or the presentation of a reward (Cragg, 2006; Schultz, 2016). When a salient event occurs, TANs generate a short burst of action potentials, which is followed by a pause in TAN activity for several hundred milliseconds. After this pause, TANs undergo a postinhibitory rebound before returning to normal levels of activity (Aosaki et al., 1994; Morris et al., 2004; Joshua et al., 2008; Apicella et al., 2011; Schulz and Reynolds, 2013; Doig et al., 2014).

TANs project to various neighboring striatal neurons and affect them by releasing acetylcholine which binds to muscarinic and nicotinic cholinergic receptors present on postsynaptic neurons. Muscarinic receptors are widely expressed in the striatal medium spiny neurons (Galarraga et al., 1999; Franklin and Frank, 2015). The nicotinic receptors are present in striatal GABAergic interneurons and axon terminals of the dopaminergic substantia nigra pars compacta (SNc) neurons (Cragg, 2006; Franklin and Frank, 2015; Shin et al., 2017; Zhang et al., 2018).

The characteristic pause in TAN activity was previously suggested to be important for conveying reward information during reinforcement learning. The TAN pause duration depends on a change in striatal dopamine concentration, which is induced by dopaminergic inputs from SNc (Maurice et al., 2004; Straub et al., 2014). This dependence exists because TANs express type 2 dopamine receptors (D2) that have an inhibitory effect on TAN activity when activated (Deng et al., 2007; Ding et al., 2010).

After a stimulus, TANs develop a slow after-hyperpolarization (sAHP) that is mainly controlled by apamin-sensitive calcium dependent potassium current (I_{sAHP}). The sAHP lasts several seconds and induces a pause in tonic firing (Bennett et al., 2000; Reynolds et al., 2004; Wilson, 2005). Another current, the hyperpolarization-activated cation (h–) current (I_h), is involved in quick recovery from sAHP. Deng et al. showed that partially blocking I_h resulted in a prolonged TAN pause duration, and that I_h was modulated by dopamine primarily via D2 inhibitory receptors (Deng et al., 2007). Thus, the duration of the TAN pause is modulated by I_h activation, which in turn is dependent on striatal dopamine concentration.

In this study, we revisit previous experimental results to formulate the following interpretations. During baseline tonic firing TANs release acetylcholine, which binds to nicotinic receptors on dopaminergic axon terminals. Thus, during their tonic firing regime, TANs exclusively define the baseline concentration of dopamine in the striatum, independently of the firing frequency of dopaminergic neurons (Rice and Cragg, 2004; Cragg, 2006). This baseline dopamine concentration corresponds to the expected reward in the determination of the reward prediction error. Furthermore, during the TAN pause, TANs stop releasing acetylcholine, thereby temporarily returning control of striatal dopamine release to dopaminergic neurons. This phasic shift in dopamine concentration corresponds to the received reward; the reward prediction error is represented as the phasic increase/decrease in dopamine concentration from the TAN-defined baseline (Cragg, 2006). Importantly, this suggests that the TAN pause serves as a time window, during which the phasic release of dopamine encodes the reward prediction error.

In this paper, we introduce a mathematical model of the TAN activity-dopamine relationship that incorporates the sAHP- and h-currents in a rate-based description of the striatal TAN population. In the model, the I_h is modulated by striatal dopamine through D2 receptor activation. Our model provides a mechanistic interpretation of the TAN activity-dopamine concentration relationship; we use our model to elucidate the mechanism by which striatal dopamine modulates the TAN pause duration, and how TAN activity regulates dopamine release. Previously, we implemented a model of reward-based motor adaptation for reaching movements that incorporated reinforcement learning mechanisms in the basal ganglia (Kim et al., 2017; Teka et al., 2017). With that model, we reproduced several behavioral experiments that involved basal ganglia-focused motor adaptation (Kim et al., 2017). Presently, we integrate our new model of the TAN-dopamine relationship into our previous reinforcement learning model. We use the integrated model to simulate striatal dopamine deficiency, as occurs in Parkinson's Disease. Even though TANs are known to send cholinergic projections to other striatal neurons, e.g., medium spiny neurons, the model does not account for these projections and focuses exclusively on the implications of interactions between TAN activity and dopamine release in striatum.

RESULTS

Model of the TAN-Dopamine Relationship

Here we provide a short conceptual description of the model, sufficient for the qualitative understanding of the system dynamics. For equations and details please see Methods.

Rate-Based TAN Population

In the model, we assume that TANs comprise a homogeneous neuronal population, whose activity is described by a single variable representing the normalized firing rate of the population. We also assume that ACh release and the activation of all cholinergic receptors in the model are proportional to TAN activity.

TANs receive excitatory inputs from the cortex and thalamus (Ding et al., 2010; Yager et al., 2015; Kosillo et al., 2016). These inputs are implemented in the model as a binary input that—when activated—initiates a burst, followed by a pause in TAN activity.

TAN activity is attenuated by the slow after-hyperpolarization (sAHP) current. The sAHP current is activated by TAN depolarization—represented in the model as TAN activity in excess of a specified threshold. The kinetics of this current are defined on a timescale of hundreds of milliseconds. This mechanism—intrinsic to the TAN population—is responsible for generating the pause in TAN activity, following a stimulus from the cortex/thalamus.

TAN activity is also affected by a depolarizing hyperpolarization-activated *h*-current. This inward current activates when TANs are hyperpolarized, and the timescale of its kinetics is similar to the sAHP current. The *h*-current thus contributes to the recovery of TANs from the pause in activity. In the model, the *h*-current deactivates in response to an increase in the concentration of dopamine—an implementation of D2-receptor agonism, which serves as a dopamine-based modulation of TAN activity (Deng et al., 2007). This mechanism provides the basis for a positive correlation between TAN pause duration and dopamine concentration. **Figure 1** shows the above described mechanisms for TAN-dopamine release interaction in a diagram.

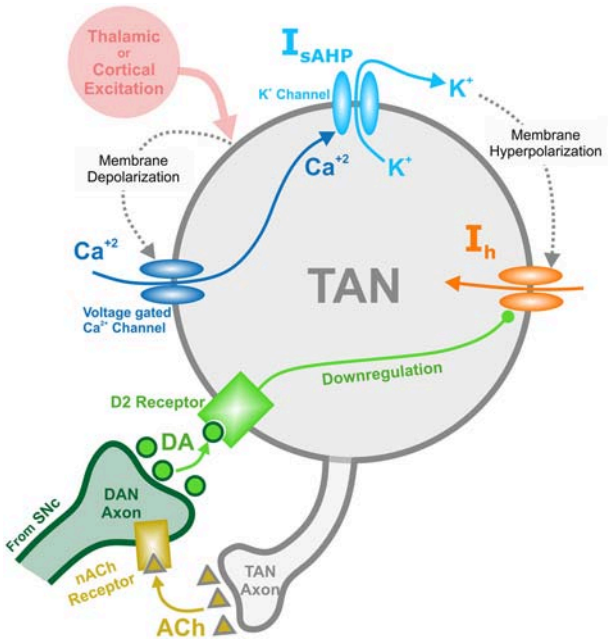

FIGURE 1 | Diagram of the mechanisms involved with the TAN-dopamine release interactions. Thalamic or cortical excitation leads to membrane depolarization in TANs. In response to depolarization, calcium ions enter through voltage dependent calcium channels, and the slow after-hyperpolarization current (I_{sAHP}) is activated via the efflux of potassium ions through calcium dependent potassium channels. Once the cortical/thalamic excitatory input ends, the efflux of potassium ions causes the membrane to hyperpolarize, which in turn activates the inward dopamine-dependent h-current (I_h) that increases the membrane potential. Furthermore, dopamine (DA) from dopaminergic neurons (DANs) in substantia nigra pars compacta (SNc) binds to D2 receptors on TANs, downregulating the h-current. In concert, TANs produce acetylcholine (ACh), which binds to nicotinic acetylcholine (nACh) receptors on DAN axonal terminals. This cholinergic pathway enables TANs to modulate the release of dopamine into the synaptic cleft. Importantly—since the h-current is downregulated via activation of dopamine D2 receptors—the DA concentration affects the refractory period of TANs.

Dynamics of Striatal Dopamine Concentration

In the model, the release of dopamine in striatum depends on the firing rate of SNc dopaminergic neurons, which receive cholinergic inputs through TAN-released acetylcholine. In the absence of acetylcholine—which occurs during a TAN pause—dopamine release is proportional to the firing rate of dopaminergic neurons. In contrast—during TAN tonic firing regimes—the release of dopamine is constant and corresponds to the baseline extracellular concentration of striatal dopamine. With increasing values of the cholinergic input to dopaminergic neurons, dopamine release becomes less dependent on the firing rate of dopaminergic neurons, and increasingly dependent on the magnitude of the TAN-provided cholinergic modulation (see Methods for mathematical description).

We also assume that the deviation of the firing rate of dopaminergic neurons from its baseline encodes the difference between the expected and received reward—the reward prediction error (Morris et al., 2004). Positive reward prediction errors correspond to increases in the firing rate of dopaminergic neurons, and negative reward prediction errors correspond to decreases in the firing rate of the dopaminergic neuron population. To constrain the model, we require that the baseline dopamine concentration is the same, whether it is defined by the baseline firing of the SNc neurons in absence of cholinergic inputs during the pause in TAN activity, or when controlled by those inputs during tonic TAN firing. We refer to deviations from the baseline dopamine concentration as "phasic dopamine release."

As follows from the above, for striatal dopamine dynamics to encode the reward prediction error—i.e., for reward information to be processed in the striatum (Calabresi et al., 2000; Zhou et al., 2002; Centonze et al., 2003; Pisani et al., 2003; Cragg, 2006; Joshua et al., 2008)—a pause in TAN activity must occur. In the model (see **Figure 2**), a thalamic stimulus produces an initial increase in the TAN firing rate. When the stimulus ends, due to activation of the sAHP current the TAN pause begins. During the pause, TANs stop releasing acetylcholine, resulting in a phasic dopamine release—proportional to the firing rate of dopaminergic neurons. While TAN activity is paused, the sAHP current slowly deactivates, and eventually TAN activity returns to baseline (Cragg, 2006; Aosaki et al., 2010).

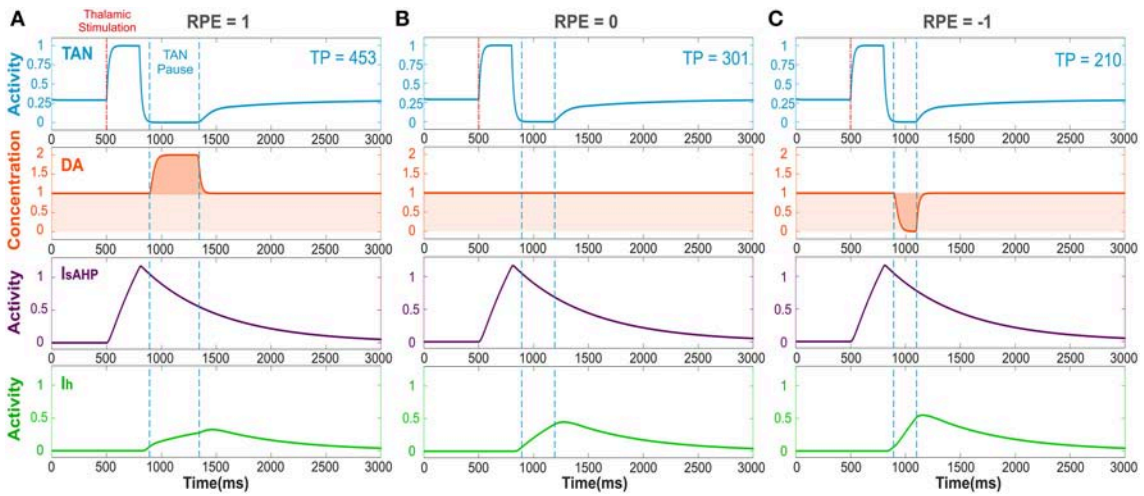

FIGURE 2 | The TAN pause duration positively correlates with the reward prediction error (RPE). Thalamic stimulus induces an initial burst of TAN activity, followed by a TAN pause. The blue curve is TAN activity; the orange curve is dopamine (DA) concentration; the purple curve is the slow after-hyperpolarization current I_{sAHP} and the green curve is the h-current I_h. **(A)** RPE = 1, the dopamine concentration increases during the TAN pause as a result of the positive RPE, which slows down I_h activation and thus prolong the pause. **(B)** For RPE = 0, the TAN pause is shorter, because there is no phasic change in dopamine release, so the concentration of dopamine remains at baseline during the TAN pause. **(C)** RPE = −1, the TAN pause is even shorter than for RPE = 0 because there is a net decrease in dopamine concentration during the pause, which provides the fastest I_h activation and hence, the shortest pause in TAN activity. Thalamic stimulation duration was 300 ms. TP stands for TAN pause duration in milliseconds.

Figure 2 depicts the dynamics of TAN activity and dopamine concentration in cases of positive, zero and negative reward prediction error, as generated by the model. If the reward prediction error is positive, the dopamine concentration increases above the baseline during the TAN pause (**Figure 2A**). Since the *h*-current in TANs is inactivated via D2 agonism, the increase in dopamine release during the TAN pause prolongs the pause by suppressing the *h*-current. If the reward prediction error is zero, the dopamine concentration does not change during the TAN pause (**Figure 2B**), which means the pause is shorter than in the case of a positive reward prediction error. Finally, when the reward prediction error is negative, the dopamine concentration falls below the baseline during the TAN pause (**Figure 2C**), which upregulates the *h*-current and thus results in an even shorter pause duration. In summary, the TAN pause duration positively correlates with the reward prediction error in the model.

Calibration of the Model

To calibrate the model, we first simulated the condition without phasic dopamine release and compared the results to those obtained by Ding et al. (2010). They experimentally studied changes in TAN activity, which were modulated pharmacologically with drugs affecting dopamine release, reuptake, and binding (**Figure 3**). We varied the model parameters to reproduce the experimental time course of TAN activity in control conditions as well as after application of sulpiride and cocaine (blue traces in **Figure 3**).

Sulpiride is a selective D2 receptor antagonist; thus, in the model administration of sulpiride corresponds to maximal activation of *h*-current in TANs (see section Methods), which in turn shortens the pause duration. Then—because cocaine is a dopamine transporter antagonist, which results in an increase in extracellular dopamine—we simulated the cocaine condition by increasing the tonic dopamine concentration in the model until the TAN pause duration matched the experimental results.

Additionally, we performed simulations of complete suppression of *h*-current (see **Figure 3D**) by setting the conductance of *h*-current to zero. This simulation qualitatively corresponds to the experimental results concerned with *h*-current blockade as described by Deng et al. (2007).

Striatal Dopamine Deficiency

Having calibrated the model, we further investigated the implications of the proposed TAN-dopamine interactions. We first simulated the condition of striatal dopamine deficiency, which may be caused, for example, by the degeneration of dopaminergic neurons in the Substantia Nigra pars compacta that occurs in Parkinson's Disease. Because dopaminergic signaling is critical for action selection and learning in the basal ganglia, dopamine deficiency adversely affects those functions.

We assumed that the degenerated Substantia Nigra pars compacta neuronal population releases less dopamine during both tonic and phasic modes. Accordingly, dopamine deficiency conditions were simulated by reducing the tonic dopamine concentration by a factor <1 and reducing the reward prediction error by the same factor (see section Materials and Methods). Thus, both tonic (baseline) and phasic dopamine levels are decreased by the same factor; **Figures 4A,B** show changes in TAN pause and dopamine dynamics in dopamine deficiency conditions. Noteworthy, in the dopamine deficiency conditions, the duration of the TAN pause decreases in response to the reduction in dopamine concentration (**Figure 4**).

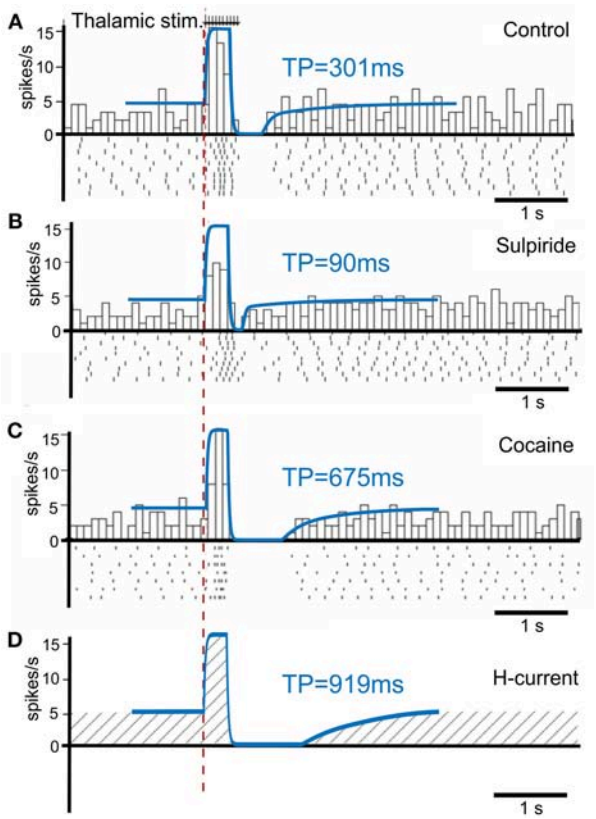

FIGURE 3 | TAN activity as simulated by the model against experimental data. **(A–C)** Peristimulus time histogram (PSTH) and raster plot from striatal cholinergic interneurons in response to a train (50 Hz, ten pulses) of thalamic stimulation. The background figures were reproduced from Ding et al. (2010) with permission. For easier comparison, all simulation results (blue lines) were rescaled down at the same ratio and overlaid on the figures of experiment results. **(A)** Simulation (blue) and data (gray bars) for control condition. **(B)** Simulation and data for sulpiride (D2 receptor blockade) condition. **(C)** Simulation and data for cocaine (dopamine reuptake blockade) condition. **(D)** Simulation of the hypothetical blockade of *h*-current. TP stands for TAN pause duration.

Effects of Levodopa Medication

Using the model, we investigated the mechanisms of levodopa-based treatments for dopamine deficiency. Levodopa (L-DOPA) is a common medication for Parkinson's Disease patients to increase overall dopamine concentration in the brain (Brooks, 2008; Kalia and Lang, 2015). Levodopa readily passes across the blood brain barrier and converted to dopamine (Wade and Katzman, 1975; Hyland and Clayton, 1992). This additional extracellular dopamine propagates nonspecifically throughout the brain. When simulating levodopa treatment conditions, we assume that levodopa administration increases the tonic (baseline) dopamine concentration but does not affect the phasic dopamine release.

In the model, the concentration of levodopa is represented as a constant added to the baseline dopamine concentration. **Figure 4C** shows the corresponding simulation results. Importantly, although phasic dopamine release is unaffected by levodopa, the increase in tonic dopamine prolongs the TAN pause duration.

Non-error-based Motor Adaptation During Dopamine Deficiency

In addition to our analysis of the local effects of dopamine deficiency on the striatal dopamine concentration, we also simulated the effects of dopamine deficiency on motor adaptation by incorporating the current model of TAN-dopamine interactions into our previously published model of reward-based motor adaptation (Kim et al., 2017) (see section Materials and Methods for details). Using this integrated BG model—including the TAN-dopamine interactions—we reproduced the non-error based motor adaptation experiments of Gutierrez-Garralda et al. (2013).

In these experiments, healthy subjects, Parkinson's Disease patients, and Huntington's Disease patients threw a ball at a target under different visual perturbation scenarios. In one scenario, each subject's vision was horizontally reversed using a Dove prism so that missing the target to the right was percived as missing to the left, and vice versa—corresponding to a sign change in the percieved error vs. the actual error. This perturbation rendered error-based motor adaptation useless. In these experiments, each session was comprized of 75 trials (25 trials before the perturbation, 25 trials with the pertubation, and 25 trials after the perturbation). Eight sessions per subject were performed and averaged. Subjects in the control group gradually overcame the visual perturbation and reduced the distance error, but Parkinson's Disease subjects showed poor learning performance (distance errors fluctuated without any sign of adaptation in 25 trials, **Figure 5A**).

In our simulations, we assumed that dopamine deficiency was the cause of Parkinson's Disease symptoms (Kalia and Lang, 2015). To see how much dopamine deficiency affects learning performance in the model, we performed multiple simulations with changing dopamine deficiency conditions from 0 to 90% (see section Methods for Details). The simulation of 0% dopamine deficiency (**Figure 5B,** control) shows a trend of decreasing errors, which accurately reproduces the experimental results of control subjects in Gutierrez-Garralda et al. (2013) (**Figure 5A,** control). As we can see in **Figure 5B** (Dopamine Deficiency), at 50% dopamine deficiency, learning performance is poor and is similar to the experimental results in Parkinson's Disease patients (**Figure 5A,** PD). For over 50% dopamine deficiency, average distance error remains at the initial level for all 25 trials, while error fluctuation and standard distance error decrease (result not shown). In summary, almost no learning occurs in the model when dopamine deficiency exceeds 50%.

Recovery of Non-error-based Motor Adaptation With Levodopa

To investigate the effects of levodopa medication on reinforcement learning in the striatum, again we simulated the same experimental settings. In the model, dopamine deficiency was set at 50% to simulate Parkinson's Disease conditions and simulations were performed with varying

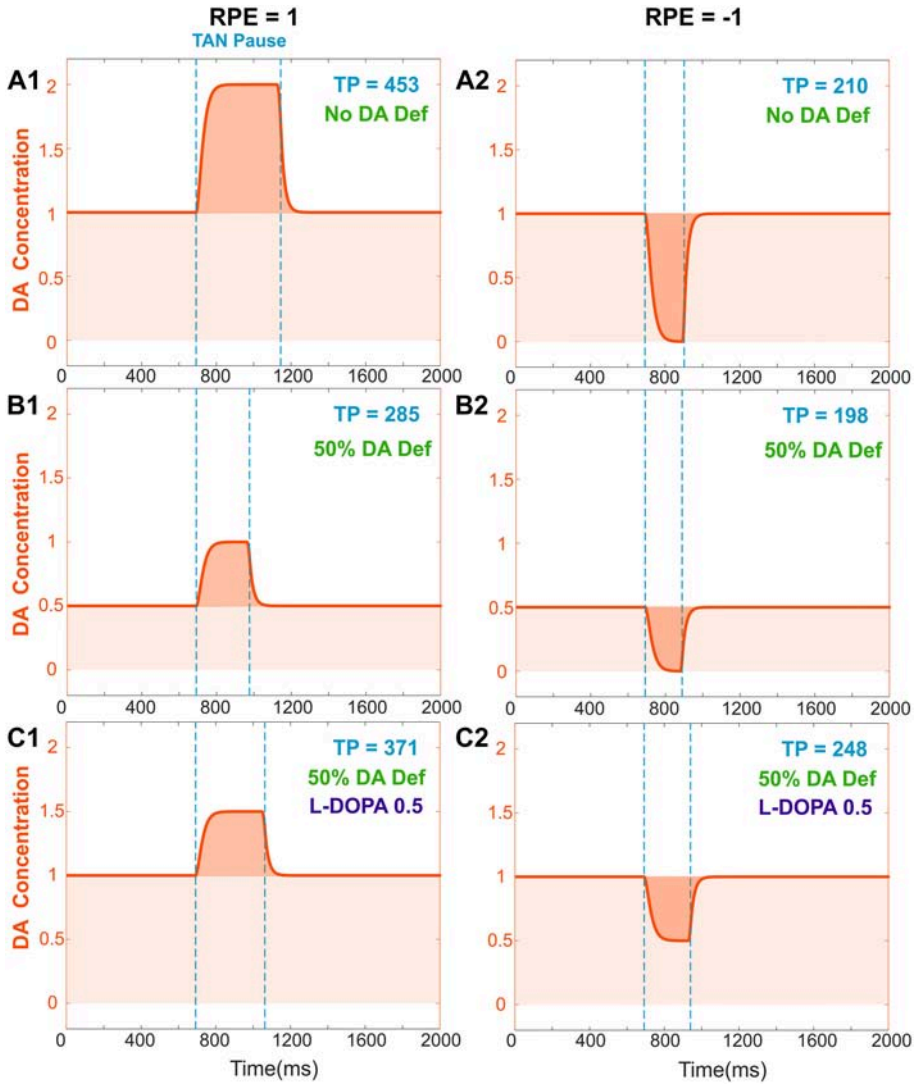

FIGURE 4 | Effects of dopamine deficiency on TAN pause duration (TP, area between two dotted blue lines) and changes in dopamine concentration (orange) with/without levodopa (L-DOPA). In these simulations, a 50% dopamine deficiency (DA Def) causes both the baseline dopamine concentration and the phasic dopamine release to decrease. **(A1–2)** RPE = 1 and −1, no dopamine deficiency for reference. **(B1)** RPE = 1, 50% dopamine deficiency. Normally, the baseline concentration of dopamine would be 1.0. With a deficiency of 50% of dopaminergic inputs, the baseline dopamine concentration is exactly halved; additionally, the phasic release of dopamine decreases in magnitude by 50%, and therefore the duration of the TAN pause also decreases. **(B2)** RPE = −1. The tonic and phasic release of dopamine are both reduced by the 50% due to dopamine deficiency. During the pause, dopamine concentration converges to zero, so the pause is similar (slightly shorter) to **(A2)**. **(C1)** RPE = 1. When levodopa (0.5) is applied, the baseline concentration of dopamine returns to normal (1.0) and the duration of the TAN pause duration increases, but it remains smaller than the one with no DA deficiency **(A1)**. This is because the magnitude of phasic dopamine release is unaffected by levodopa. **(C2)** RPE = −1. When levodopa (0.5) is applied, the baseline concentration of dopamine returns to normal (1.0) as for RPE = 1, but the duration of the TAN pause exceeds the one with no DA deficiency **(A2)**. This is due to the increased (non-zero) dopamine concentration during the pause.

levodopa values representing additional striatal dopamine converted from levodopa medication. **Figure 5B** (Levodopa) shows the simulation results.

At levodopa values corresponding to 100% recovery of the baseline dopamine concentration, the average error decreases siginificantly at the end of the perturbation trials (**Figure 5B,** Levodopa). Thus, the overall learning perfomance of the model significantly improves as a result of levodopa administration.

However—although the learning performance improves—the performance of levodopa-medicated patients is still noticably worse than in control subject simulations. This performance difference can be easily understood in the context of our model of TAN-dopamine interactions. In the model, when levodopa is introduced, the tonic concentration of dopamine returns to healthy baseline levels, but the amplitude of phasic dopamine release is not recovered (compare **Figures 4A1,C1**). Therefore, our integrated model simulations suggest that Parkinson's

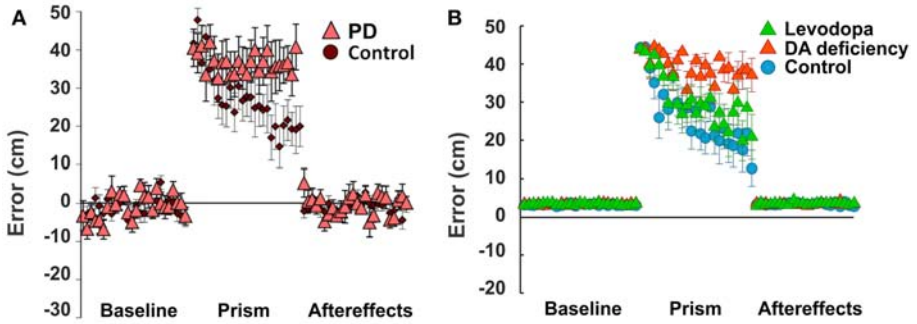

FIGURE 5 | Non-Error based motor adaptation in 50% of dopamine (DA) deficiency condition with/without levodopa medication. **(A)** Results of ball throwing tasks performed by healthy people and Parkinson's Disease (PD) patients. During experiment, a dove prism was used to horizontally flip subjects' vision as perturbation. This figure was adapted from Gutierrez-Garralda et al. (2013) with permission. **(B)** Simulation results with levodopa medication. Levodopa means the condition of 50% dopamine deficiency with levodopa medication ([LDOPA] = 1.0). Colored center markers (triangle or circle) are average error values of 8 sessions and error bars represent standard errors. 1 session = 75 trials (Baseline = 25 trials, Prism (visual perturbation) = 25 trials and Aftereffects = 25 trials).

patients can partially regain learning performance following levodopa administration—due to the increase in tonic dopamine concentration—but a full recovery is impossible without a corresponding increase in phasic dopamine release.

DISCUSSION

In this study we investigated the relationship between striatal dopamine and TAN activity; specifically, we elucidated the mechanism by which this interaction affects reinforcement learning in the striatum. Striatal TANs temporarily pause their tonic firing activity during sensory or reward events. During tonic firing regimes, TAN activity defines the baseline striatal dopamine concentration via nicotinic ACh receptors (nAChR) activation on dopaminergic axon terminals (Rice and Cragg, 2004); thus, the TAN pause enables a temporary variation of dopamine release. The duration of the TAN pause is important as it creates a window of opportunity for the dopaminergic neurons to transmit information about the reward prediction error by phasically modulating the dopamine concentration in the striatum. In turn, the concentration of dopamine determines the duration of the TAN pause by modulating the *h*-current via D2 receptors in TANs (Deng et al., 2007). Accordingly, in our model, the TAN pause enables the phasic release of dopamine, and the duration of the TAN pause varies with dopamine concentration.

One of the objectives of this study was to extend our previous model by adding details of the striatal circuit concerned with cholinergic modulation of dopamine release. By doing so, we were able to investigate how TAN activity contributes to reinforcement learning mechanisms in simulated behavioral experiments.

In the model, phasic dopamine levels are defined by the activity of dopaminergic neurons, which codes the reward prediction error. Deviations of striatal dopamine concentration from its baseline underlie the plasticity of cortico-striatal projections to medium spiny neurons, representing a basis for reinforcement learning in the striatum. These deviations last for the duration of the pause in TAN activity. Therefore, the magnitude of long-term potentiation or depression of cortico-striatal projections depends on the pause duration, which may affect learning performance.

TANs express D2 dopamine receptors, which are inhibitory. Through this mechanism, the duration of the pause in TAN activity positively correlates with striatal dopamine concentration. In conditions of dopamine deficiency, the baseline dopamine concentration is reduced, which also shortens the duration of the TAN pause.

Based on our model predictions, we speculate that levodopa medication improves learning performance in Parkinson's patients by increasing the baseline dopamine concentration and thus prolonging the pause in TAN activity—even though the magnitude of phasic dopamine excursions may be not affected by this medication.

Dopamine Release and Cholinergic Regulation

Within the Substantia Nigra pars compacta—a structure in the midbrain—are dopaminergic neurons that project to the striatum. These dopaminergic neurons are known to encode reward-related information by deviating from tonic baseline activity (Schultz, 1986; Hyland et al., 2002). Striatal dopamine release occurs via vesicles at local dopaminergic axon terminals (Sulzer et al., 2016). However, the amount of dopamine released is likely to be not always defined by the firing rate of the presynaptic neuron.

Cholinergic activity plays a major role in modulation of dopamine release in the striatum. For example, synchronized activity of striatal TANs directly evokes dopamine release at the terminals—regardless of the activity of dopaminergic neurons (Cachope et al., 2012; Threlfell et al., 2012). TANs release acetylcholine (ACh), which binds to nicotinic receptors on the axons of dopaminergic neurons—and when these cholinergic inputs are activated, dopamine release is independent of electrical stimulation frequency (Rice and Cragg, 2004). However, when these nicotinic receptors (nAChRs) are blocked, the magnitude

of dopamine release becomes proportional to the stimulation frequency (Rice and Cragg, 2004). Therefore, it is necessary for the cholinergic inputs to dopaminergic neurons to cease so that dopamine release reflects the firing activity of the presynaptic neurons.

Our model assimilates the above observations via the following assumptions. Baseline striatal dopamine concentration is determined by the presynaptic action of ACh on dopaminergic terminals (Threlfell et al., 2012) through nAChR desensitization. With no cholinergic inputs, e.g., when TAN activity ceases or nAChRs are blocked, the firing rates of dopaminergic neurons define the dopamine release. In other words, the phasic component of dopamine release is determined by Substantia Nigra pars compacta activity, which codes the reward prediction error. Therefore, the functional role of the pause in TAN activity is to allow the striatal dopamine concentration to vary, thus creating a window of opportunity for dopaminergic neurons to deliver the reward information to and enable reinforcement learning in the striatum.

Variations in the phasic release of dopamine reflect the reward prediction error (Hollerman and Schultz, 1998; Schultz, 1998, 1999); thus, in the case that the reward received is exactly the same as the expected reward—reward prediction error is zero—the dopamine concentration should not change during the TAN pause. In the model, as explained above, the baseline dopamine concentration is constrained by cholinergic inputs from TANs, and during the pause, dopamine release is controlled by the firing rate of dopaminergic neurons in the Substantia Nigra pars compacta. Therefore, we constrained the model by requiring that Substantia Nigra pars compacta firing corresponding to a reward prediction error value of zero (RPE = 0)—in absence of cholinergic input during the pause—leads to exactly the same dopamine release as during normal TAN activity. The exact homeostatic mechanisms responsible for such tuning remain open for speculation.

In our model, we did not differentiate between different parts of striatum in terms of cholinergic regulation of dopamine release. However, it was reported that the nucleus accumbens shell, the most ventral part of striatum, has a distinctive modulation mechanism of dopamine release with much higher activity of acetylcholinesterase minimizing nAChR desensitization, which is different from nucleus accumbens core and dorsal striatum (Shin et al., 2017). There is also evidence that DA release in nucleus accumbens is modulated by ACh not only through nicotinic but also via muscarinic receptors of several types activation of which has different effects on DA concentration (Shin et al., 2015). Our model does not account for this.

In our model, we focused on the functional role of TAN activity-dopamine interactions in reinforcement learning. Thus, we did not consider the effect of TANs on other striatal neuron types. For example, MSNs are known to receive cholinergic inputs via muscarinic M1 and M2 receptors. Functional role of these projections was discussed elsewhere. In particular, other computational models proposed that TANs might have a timing control function to hold and release MSNs (Ashby and Crossley, 2011; Franklin and Frank, 2015). Besides TANs and MSNs, many other types of interneurons have been identified in striatum, such as parvalbumin fast spiking interneurons, neuropeptide Y interneuron, calretinin interneurons, Tyrosine Hydroxylase interneurons (Tepper et al., 2010, 2018; Xenias et al., 2015). Functional roles of these interneurons and their relationships with cholinergic interneurons are not clearly understood. However, this does not rule out the possibility, that some of these neuron types interact with TANs and thus may play a role in TAN activity regulation.

TAN Pause Duration

In the model, the pause in TAN activity is initiated by transient excitatory corticothalamic inputs. Furthermore, the duration of the pause is dependent on the extracellular dopamine concentration (Deng et al., 2007; Oswald et al., 2009; Ding et al., 2010). To replicate this dependence, we calibrated the duration of TAN pause in the model to *in vitro* experimental data from Ding et al. (2010).

It is important to note that longer thalamic stimulation means stronger activation of the slow after-hyperpolarization (sAHP) current, and hence more time is required for its subsequent deactivation. This prediction is consistent with the *in vitro* studies by Oswald et al. In their experiments, a higher number of stimulation pulses did generate stronger after-hyperpolarization in TANs below their resting potential—and accordingly evoked a longer pause in TAN activity. In addition, several *in vitro* and *in vivo* experiments agree that the magnitude of thalamic input positively correlates with the TAN pause duration (Oswald et al., 2009; Schulz et al., 2011; Doig et al., 2014). Although we cannot directly compare our simulation results with their data, our TAN model exhibits a qualitatively similar relationship between input duration and pause duration.

To illustrate this relationship, we performed simulations, varying the duration of thalamic stimulation (from 100 to 400 ms) as shown in **Figure 6A**. The duration of the TAN pause increases non-linearly in response to increasing thalamic stimulation duration. Interestingly, this increase in the pause duration is stronger for higher reward prediction error values, which is because of the larger phasic dopamine concentration when the reward prediction error increases. The reward prediction error is independent of the thalamic stimulus duration, and the pause duration is sensitive to both variables. Thus, we manipulated each variable independently to show the dependence of the pause duration on both.

Furthermore, the TAN pause duration is dependent on any change in the extracellular dopamine concentration—not just the RPE-determined phasic dopamine release. Therefore, we also produced simulations demonstrating the effects of dopamine deficiency as well as the effect of levodopa administration on the TAN pause duration. Importantly, dopamine deficiency has almost no effect on the TAN pause duration when the reward prediction error is at a minimum (see the orange line in **Figure 6B**). This model behavior follows from the observation that the reward prediction error correlates with the magnitude of phasic dopamine release. If the reward prediction error is at its minimum possible value (in our model, RPE = −1),

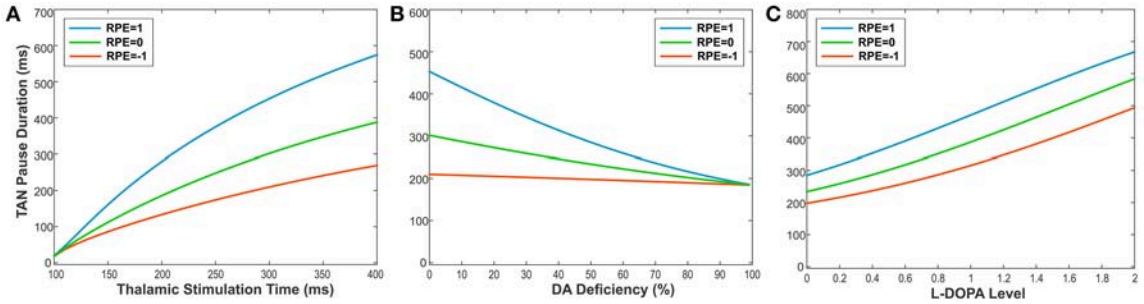

FIGURE 6 | (A-C) The changes in TAN pause (TP) duration by three different factors: the duration of thalamic stimulation, the percentage of dopamine (DA) deficiency, the L-DOPA level in 50% DA deficiency condition when RPE (Reward Prediction Error) = 1 (phasic, reward), 0 (tonic baseline), and −1 (phasic, aversive), respectively. **(A)** The changes in TP duration by the duration times of thalamic stimulation. The increment of thalamic stimulation duration increases TP duration for all RPE values. The difference of TP duration between RPE = 1 and RPE = −1 keeps increasing nonlinearly as increases in thalamic stimulation duration. **(B)** The changes in TP duration by the percentages of DA deficiency. The increased percentage of DA deficiency decreases TP duration when RPE = 1 and 0. For RPE = −1, the TP duration is nearly independent of the amount of DA deficiency, which is the result of RPE = −1 corresponding to the minimum possible DA concentration during the TP. Therefore, the TP duration for RPE = −1 is unaffected by the degradation of dopaminergic inputs. The deviation difference of TP duration from RPE = 0 between RPE = 1 and RPE = −1 keeps decreasing nonlinearly as increases in percentage of DA deficiency, which means minimizing the time difference between reward and aversive conditions for reinforcement learning and in turn deteriorating the learning performance. **(C)** The changes in TP duration by the levels of L-DOPA in 50% DA deficiency condition. In response to the administration of L-DOPA, the TP duration increases similarly for all RPE values. This follows from the fact that L-DOPA alters the baseline concentration of dopamine, but does not affect the phasic dopamine release.

then neither the amount of phasic dopamine nor the duration of the TAN pause can be decreased by dopamine deficiency conditions. In contrast, the administration of levodopa affects the TAN pause duration without any dependence on the reward prediction error. This follows from the fact that levodopa alters the baseline concentration of dopamine—not the phasic dopamine release—which is not dependent on the reward prediction error.

Comparisons With Other Models

The model presented here is not the first computational model of TAN activity. For example, Tan and Bullock previously developed a computational model incorporated *h*-current as an intrinsic property of TANs (Tan and Bullock, 2008). Their model was also a non-spiking model that focused on the generation mechanism of TAN-specific activity patterns, which the authors attributed to intrinsic TAN properties. Even though their model accounted for modulation of TAN activity by dopamine level, it did not include a mechanism that affects the dopamine release, which our model did.

Ashby and Crossley also developed a BG model that included Hodgkin-Huxley style spiking TANs with *h*-current (Ashby and Crossley, 2011). Their model emphasized the inhibitory effect of TAN activity on striatal medium spiny neurons (MSNs) through muscarinic receptors. They proposed that tonic TAN activity normally suppresses MSN firing, which is released during the TAN pause. Similar idea was exploited in the computational model of BG circuits by Franklin and Frank (2015) who proposed that the pause in TAN activity is formed by local striatal inhibition to code the uncertainty and regulate learning rates through cholinergic projections to MSNs. The model we propose significantly differs from these two models with respect to the gating function of the pause in TAN activity. Our model focuses on cholinergic dopamine regulation and does not incorporate direct cholinergic projections to—or GABAergic projections from—MSNs.

To the best of our knowledge, the model proposed here is the first that incorporates bidirectional effects of cholinergic and dopaminergic signaling in the striatum and explores the implications of these interactions by simulating real and hypothetical behavioral experiments in realistic settings. This was made possible by embedding our implementation of TAN-dopamine interactions into the model of reward-based motor adaptation we previously published (Kim et al., 2017).

Impaired Learning in Parkinsonians and the Effect of Levodopa Medication

Striatal dopamine deficiency in Parkinson's Disease is concerned with degeneration of dopaminergic neurons which results in smaller amounts of dopamine released. This affects both the baseline striatal dopamine concentration and phasic excursions of dopamine concentration that encode the reward prediction error. Our model predicts that lower dopamine concentration also leads to shortening of the pause in TAN activity, during which the phasic dopamine component drives reinforcement learning in the striatum. Using the model, we find that dopamine deficiency influences learning performance in the BG not only due to smaller magnitude of the learning signal, but also by decreasing the duration of the pause in TAN activity. From our simulation results, we found that 50% of dopamine deficiency in the model is sufficient to induce as poor learning performance as observed in Parkinsonians. This finding is consistent with the experimental data on striatal dopamine deficiency in Parkinson's Disease patients (Scherman et al., 1989) where it was reported that Parkinsonian symptoms appear when striatal dopamine deficiency exceeds 50%.

Levodopa is one of common treatments for early stage Parkinson's Disease patients (Brooks, 2008; Kalia and Lang, 2015). Levodopa administration increases Parkinson's Disease patient's UPDRS (Unified Parkinson's Disease Rating Scale) score by two or three times (Brooks, 2008; Beigi et al., 2016; Chen et al., 2016). In Gutierrez-Garralda et al.'s experiments (Gutierrez-Garralda et al., 2013), Parkinson's Disease patients were tested in the morning before taking their levodopa medicine to avoid levodopa effects on the results. According to a report, a standard dose of intravenous levodopa infusion increased the striatal dopamine level by 5–6 times (Zsigmond et al., 2014). Due to the lack of data, it is hard to know by how much the oral intake of levodopa increases dopamine concentration in the striatum. However, from the conventional dosage for Parkinson's Disease patients (Brooks, 2008), we can infer that oral levodopa may take more time to increase striatal dopamine levels and have less efficacy on striatal dopamine levels than intravenous levodopa infusion. In our simulations, levodopa 1.0 (2 times higher than baseline dopamine in 50% dopamine deficiency) caused the learning performance to recover close to the control levels (see **Figure 5B**). This effect is solely provided by the prolonged pause in TAN activity due to the levodopa-induced increase in baseline dopamine concentration. Interestingly, the extended pause duration at levodopa 1.0 is close to the one in control (no dopamine deficiency) conditions (see **Figure 6C**). The required increase of the baseline dopamine concentration by levodopa administration and the one predicted by the model is within a ballpark range.

Alternative TAN Pause Mechanisms

In our model, the pause in TAN activity is induced by a cortico-thalamic excitatory input which causes after-hyperpolarization. However, other mechanisms for TAN pause generation have been proposed. For example, there exist inhibitory projections from GABAergic neurons in ventral tegmental area (VTA) to the cholinergic interneurons in nucleus accumbens (Brown et al., 2012). Brown et al. (2012) were able to generate a pause of TANs in nucleus accumbens by optogenetically activating VTA GABAergic projection neurons and link this to potentiation of associative learning.

Interestingly, regardless of how the pause is generated, our model would exhibit the same qualitative features of interactions between TAN activity and DA release. Indeed, TAN recovery from the pause would still depend on activation of depolarizing h-current negatively modulated by DA through D2 receptors. Therefore, TAN pause duration would positively correlate with DA concentration thus providing the same basis for our conclusions.

On a side note, GABAergic inhibition of TANs has not been found in dorsal striatum (Zhang and Cragg, 2017), which means that external inhibition cannot represents the primary mechanism of the pause in dorsal striatal TAN activity. The same lab has recently provided further evidence that the pause in TAN activity is associated with intrinsic properties of striatal cholinergic interneurons, induced by an excitatory input, mediated by potassium currents, and modulated by dopamine (Zhang et al., 2018).

MATERIALS AND METHODS

The Model of TAN Activity

Our model describes the collective dynamics of a population of striatal tonically active neurons (TANs). The model represents the aggregate firing rate (activity) of the population treated as a smooth function of time t with TAN activity denoted by $V_{TAN}(t)$. The following differential equation governs its dynamics:

$$\tau_{TAN}\frac{dV_{TAN}(t)}{dt} + V_{TAN}(t) = \sigma\left(I_{TAN}(t)\right) \quad (1)$$

where τ_{TAN} is a time constant, $\sigma(x) = \Theta(x)\cdot\tanh(x)$ is a sigmoid function, $\Theta(x)$ is Heaviside's function, and $I_{TAN}(t)$ is a term representing an aggregate input composed of intrinsic current inputs and synaptic inputs to the TAN population:

$$I_{TAN}(t) = W_{Thal}\cdot V_{Thal}(t) + Drv_{TAN} + I_{sAHP}(t) + I_H(t) \quad (2)$$

Here $V_{Thal}(t)$ is a thalamic stimulus equal to 1 during stimulation and 0 otherwise, W_{Thal} is a synaptic weight of the thalamic input, Drv_{TAN} is a constant drive that defines the baseline firing rate, $I_{sAHP}(t)$ is a slow after-hyperpolarization current input, and $I_H(t)$ is an h-current input.

The slow after-hyperpolarization current $I_{sAHP}(t)$ is a hyperpolarizing current activated when the TAN activity exceeds certain threshold; the dynamics of this current are defined as

$$\tau_{sAHP}\frac{dI_{sAHP}(t)}{dt} + I_{sAHP}(t) = -g_{sAHP}\cdot\left(V_{TAN}(t) - \theta_{sAHP}\right)\cdot\Theta\left(V_{TAN}(t) - \theta_{sAHP}\right) \quad (3)$$

where τ_{sAHP} is a time constant, g_{sAHP} is the activation gain, and θ_{sAHP} is the threshold for activation.

In contrast to I_{sAHP}, the depolarizing h-current $I_H(t)$ is activated when the TAN activity is below certain threshold, and its activation is modulated by the dopamine concentration. Its dynamics is defined by the following equation.

$$\tau_H\frac{dI_H(t)}{dt} + I_H(t) = -g_H\cdot\exp\left(-W_{DA}\cdot[DA](t)\right)\cdot\left(V_{TAN}(t) - \theta_H\right)\cdot\Theta\left(\theta_H - V_{TAN}(t)\right) \quad (4)$$

where τ_H is a time constant, g_H is the activation gain, W_{DA} is the dopamine weight coefficient, $[DA]$ is the concentration of striatal dopamine, and θ_H is the h-current activation threshold.

The temporal dynamics of striatal dopamine are defined by

$$\tau_{DA}\frac{d[DA](t)}{dt} + [DA](t) = [DA]_0 + RPE\cdot\left(1 - \frac{V_{TAN}(t)}{\theta_{DA}}\right)\cdot\Theta\left(\theta_{DA} - V_{TAN}(t)\right) \quad (5)$$

where τ_{DA} is the time constant, RPE is the reward prediction error, θ_{DA} is the nicotinic receptor threshold, $[DA]_0$ is the baseline dopamine concentration.

To calibrate the model, we replicated experimental data published by Ding et al. (2010) who recorded TAN activity from sagittal slices of mice brains while stimulating either thalamic or

cortical neurons while blocking D2 receptors with sulpiride or increasing dopamine levels by cocaine (**Figure 3**). All parameters were tuned to fit the experimental data and their values are listed below:

$$\begin{aligned} \tau_{TAN} &= 20ms, W_{Thal} = 4, Drv_{TAN} = 0.3, \tau_{sAHP} = 700ms, \\ g_{sAHP} &= 5, \theta_{sAHP} = 0.3, \tau_H = 700ms, \\ g_H &= 20, \theta_H = 0.2, W_{DA} = 1, \\ \tau_{DA} &= 20, \theta_{DA} = 0.01, [DA]_0 = 1 \end{aligned}$$

To simulate the effect of sulpiride (**Figure 3B**) we set $W_{DA} = 0$ as sulpiride is a selective antagonist of dopamine D2 receptors. To simulate the effect of suppressed dopamine reuptake by cocaine (**Figure 3C**) we set $[DA]_0$ to three times its control value $[DA]_0 = 3$. We simulated blocking h-current (**Figure 3D**) by setting $g_H = 0$.

Simulation of Behavioral Experiments

Integration of TAN-Dopamine Interactions Into the Model of Reward-Based Motor Adaptation

Previously, we published a model able to reproduce key experiments concerned with non-error-based motor adaptation in the context of center-out reaching movements (Kim et al., 2017). The model included 3 modules: a 2 pathway (direct and indirect) BG module, a lower level spinal cord circuit module that integrated supra-spinal inputs with feedback from muscles, and a virtual biomechanical arm module executing 2D reaching movements in a horizontal plane (see Kim et al., 2017; Teka et al., 2017 for the details). The BG module was responsible for selection and reinforcement of the reaching movement based on reward provided. To study effects of TAN activities on dopaminergic signaling in the striatum, we integrated the model of TAN-dopamine interaction described above into the model of Kim et al. (2017). A schematic of the integrated model is shown in **Figure 7**.

The model of reinforcement learning in basal ganglia we used in this study was previously published and is described in details in Kim et al. (2017). Here, we only provide short qualitative description. Behavioral experiments studying reinforcement learning mechanisms assume that a choice must be made between several differentially rewarding behavioral options. Unlike decision-making tasks, motor learning does not imply a small or finite number of possible choices. The only constraint is the context of the task, e.g., reaching from a fixed initial position to an unknown destination. Our model has unlimited number of possible actions. As the context, we used center-out reaching movements performed in a horizontal plane. To calculate cortical activity corresponding to different movements, we explicitly solved an inverse problem based on the given arm kinematics. Accordingly, for every possible reaching movement we could calculate the corresponding motor program represented by the activity profiles of cortical inputs responsible for activation of different muscles. To describe different experiments, we define corresponding (arbitrarily large) sets of motor programs that define all possible behavioral choices (actions) in each experimental context.

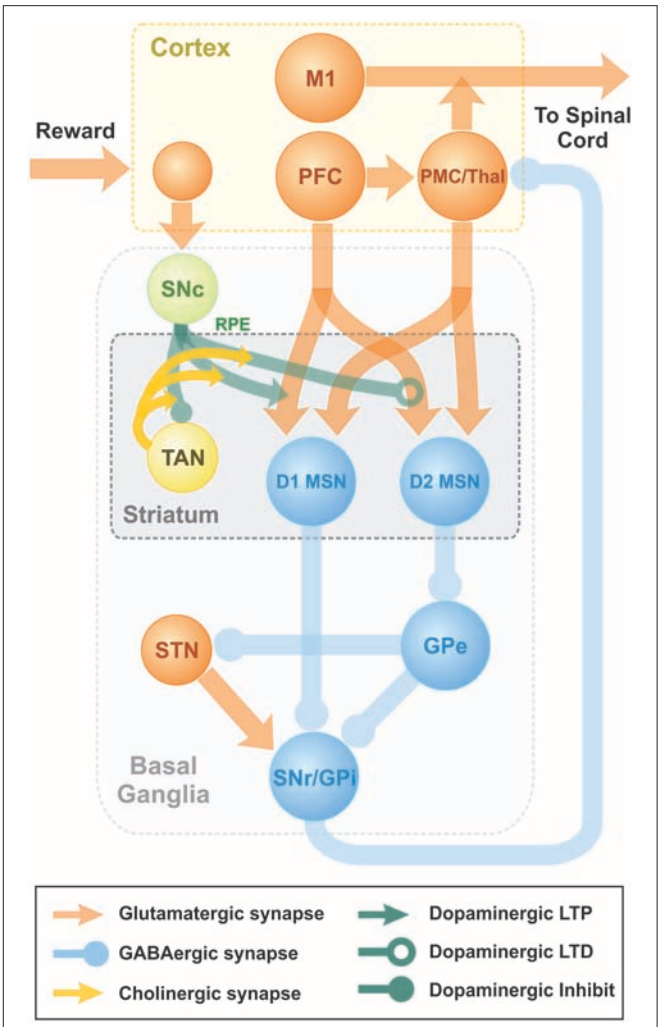

FIGURE 7 | Schematic diagram of two-pathway of basal ganglia integrated with TAN model. Dopaminergic Substantia Nigra pars compacta signal represents the reward prediction error (reward prediction error). PFC, PreFrontal Cortex; M1, Primary Motor Cortex; PMC, PreMotor Cortex; MSN, Medium Spiny Neuron; SNr, Substantia Nigra pars Reticulata; GPi, 0Globus Pallidus internal; GPe, Globus Pallidus external; Substantia Nigra pars compacta, Substantia Nigra pars Compacta; STN, SubThalamic Nucleus.

The classical view of action selection is that different motor actions are gated by thalamocortical relay neurons. In the presented model, we assume that relay neurons can be activated at different firing rates, and their firing rates define contributions of different motor programs to the resulting motor response. More specifically, in our model cortical input to the spinal network is implemented as a linear combination of all possible motor programs in the given context with coefficients defined by the firing rates of corresponding thalamocortical relay neurons. This linear combination can be viewed as an aggregate input to the spinal network from the cortical motoneurons exhibiting activity profiles corresponding to different motor behaviors, e.g., reaching movements in different directions.

The classical concept of BG function is that the BG network performs behavioral choice that maximizes reward. This action selection process results in activation of thalamic relay neurons corresponding to the selected action and suppression of neurons gating other behaviors. Per this concept, each action is dedicated to specific neurons in different BG nuclei. Their focused interconnections form action-related loops which start at the cortex, bifurcate in the striatum into direct and indirect pathways converging on the internal Globus Pallidus (GPi), and feed back to the cortex through the thalamus. Action preference is facilitated by increased excitatory projections from sensory cortical neurons representing the stimulus to direct pathway striatal neurons (D1 MSNs). Suppression of unwanted competing actions is assumed to occur because of lateral inhibition among the loops at some level of the network in a winner-takes-all manner.

In the model, novel cue-action associations are formed based on reinforcement learning in the striatum. Eventually, the preferable behavior is reliably selected due to potentiated projections from the neurons in prefrontal cortex (PFC), activated by the provided stimulus, to D1 MSNs, corresponding to the preferred behavior. In technical terms, the output of basal ganglia model is the activation levels of thalamocortical relay neurons in response to the input from PFC neurons activated by visual cues. Each cure represents one of the possible reaching targets. These levels are used as coefficients of the linear combination of all possible actions which represents the motor program selected for execution. The resulting motor program is used to calculate the endpoint of the movement using neuro-mechanical arm model (Teka et al., 2017). Depending on the distance between the movement endpoint and the target position, the reward is calculated as dictated by the experimental context. This reward value is used to calculate the reward prediction error as a temporal difference between the current and previous reward values. The reward prediction error is used as the reinforcement signal (positive or negative deviation of dopamine concentration from its baseline levels) to potentiate or depress synaptic projections from PFC neurons, activated by the visual cue provided, to the striatal neurons, representing the selected actions. See details in Kim et al. (2017).

In Kim et al. (2017), the reinforcement learning is described as a trial-to-trial change in the synaptic weights of prefrontal cortico-striatal projections as follows:

$$\Delta W_{ji}^{1} = \lambda_1 \cdot C_j \cdot D_i^1 \cdot RPE - d_w \cdot W_{ji}^{1} \quad (6)$$

$$\Delta W_{ji}^{2} = -\lambda_2 \cdot C_j \cdot D_i^2 \cdot RPE - d_w \cdot W_{ji}^{2} \quad (7)$$

where: ΔW_{ji}^{1} and ΔW_{ji}^{2} are the changes in synaptic weights between PFC neuron j and D1- and D2-MSNs i, respectively, λ_1 and λ_2 are the learning rates, RPE is the reinforcement signal equal to the reward prediction error, C_j is the firing rate of PFC neuron j; D_i^1 and D_i^2 are the firing rate of D1- and D2- MSNs i, respectively, and d_w is a degradation rate.

In the integrated model, we assume that learning in the striatum is a continuous process defined by the deviation of dopamine concentration from its baseline value. Therefore, we replace the difference equations above with their differential analogs with reward prediction error replaced with the phasic component of the dopamine level:

$$\frac{d}{dt} W_{ji}^{1} = \overline{\lambda}_1 \cdot C_j \cdot D_i^1 \cdot ([DA](t) - [DA]_0) - \overline{d}_w \cdot W_{ji}^{1} \quad (8)$$

$$\frac{d}{dt} W_{ji}^{2} = -\overline{\lambda}_2 \cdot C_j \cdot D_i^2 \cdot ([DA](t) - [DA]_0) - \overline{d}_w \cdot W_{ji}^{2} \quad (9)$$

Considering that dopamine concentration ($[DA]$) excurses from the baseline ($[DA]_0$) during a short pause in TAN activity only, while the degradation process occurs continuously on a lot longer timescale, we can approximately rewrite these equations in a difference form by integrating over the pause duration:

$$\Delta W_{ji}^{1} = \overline{\lambda}_1 \cdot C_j \cdot D_i^1 \cdot \int ([DA](t) - [DA]_0) dt - d_w \cdot W_{ji}^{1} \quad (10)$$

$$\Delta W_{ji}^{2} = -\overline{\lambda}_2 \cdot C_j \cdot D_i^2 \cdot \int ([DA](t) - [DA]_0) dt - d_w \cdot W_{ji}^{2} \quad (11)$$

Where $\lambda_{1,2} = \lambda_{1,2} \cdot 0.00125$ if $[DA] \geq [DA]_o$ or $\lambda_{1,2} = \lambda_{1,2} \cdot 0.0025$ if $[DA] < [DA]_o$.

All other parameters of BG model remain unchanged and can be found in Kim et al. (2017).

Dopamine Deficiency Simulation

Striatal dopamine deficiency is caused by degeneration of dopamine producing neurons as observed in Parkinson's Disease patients. Parkinson's Disease is a long-term neurodegenerative disorder of the central nervous system that mainly affects the motor system. Shaking, rigidity, slowness of movements and difficulty with walking are the most obvious Parkinson's Disease symptoms so called parkinsonism or parkinsonian syndrome (Kalia and Lang, 2015). Motor learning is also impaired (Gutierrez-Garralda et al., 2013). Aging is also often accompanied by death of midbrain Substantia Nigra pars compacta neurons which causes parkinsonism-like motor disorders (Kalia and Lang, 2015).

Based on the above, we assume that dopamine deficiency results from a reduced number of dopamine neurons which produce proportionally smaller amount of dopamine. To simulate this condition, we multiply the right-hand side of the equation describing dopamine concentration dynamics

$$\tau_{DA} \frac{d[DA](t)}{dt} + [DA](t) = \alpha \left(RPE \cdot \left(1 - \frac{V_{TAN}(t)}{\theta_{DA}} \right) \cdot \Theta(\theta_{DA} - V_{TAN}(t)) + [DA]_0 \right) \quad (12)$$

by a coefficient α between 0 and 1 with $\alpha = 1$ corresponding to 0% dopamine deficiency and $\alpha = 0$ meaning 100% dopamine deficiency, i.e., no dopamine is produced at all. Fifty percent dopamine deficiency used in our simulations assumes that the coefficient used is $\alpha = 0.5$, 30% deficiency corresponds to $\alpha = 0.7$, etc.

Levodopa Medication Simulation

Levodopa is an amino acid made by biosynthesis from the amino acid L-tyrosine (Knowles, 1986). Levodopa can

cross the blood brain barrier whereas dopamine itself cannot and so it is naturally transferred into the brain via blood circulation (Wade and Katzman, 1975). Then levodopa as a precursor to dopamine is converted to dopamine by the enzyme called DOPA decarboxylase (aromatic L-amino acid decarboxylase) in the central nervous system (Hyland and Clayton, 1992). Thus, levodopa application increases overall dopamine concentrations in the brain. Levodopa medication is a clinical treatment for Parkinson's Disease patients as dopamine replacement to compensate for the dopamine deficiency. It is unclear whether levodopa improves the function of remaining dopamine neurons or affects baseline levels of dopamine in the brain only.

Our objective was to investigate if increasing the baseline dopamine concentration by levodopa without affecting the phasic dopamine release can improve learning performance in simulated Parkinson's Disease conditions. Thus, we mathematically describe the effect of levodopa medication by adding a constant term to the right-hand side of the equation for dopamine concentration

$$\tau_{DA}\frac{d\left[DA\right](t)}{dt} + [DA]_0 = \alpha\left(RPE\cdot\left(1-\frac{V_{TAN}(t)}{\theta_{DA}}\right)\cdot\Theta\left(\theta_{DA}-V_{TAN}(t)\right)+[DA]_0\right)+LDOPA \tag{13}$$

where *LDOPA* is an increase in the baseline dopamine concentration due to levodopa administration. Correspondingly, to calculate the phasic component of dopamine dynamics in conditions of dopamine deficiency and/or levodopa medication for the baseline dopamine concentration, we use $\alpha\,[DA]_0 + LDOPA$ instead of $[DA]_0$.

SIMULATION ENVIRONMENT

Our basic TAN activity-DA release interaction model was developed and simulated in Matlab. Then the model was implemented in C++ to integrate it into our previous model of reward-based motor adaptation described in detail in Kim et al. (2017). All simulations for behavioral experiments were performed using custom software in C++. The simulated data were processed in Matlab to produce figures. For behavioral experiments, we performed 75 simulations (25 before perturbation, 25 with perturbation, 25 after perturbation) per session and results of 8 sessions were averaged (see Kim et al., 2017 for more details).

AUTHOR CONTRIBUTIONS

TK, SM, YM, and IR: conceptualization; TK, SM, and YM: methodology; TK, RC, KH, WB, DT, SM, EL, and YM: validation; TK, RC, SM, and YM: formal analysis and software; TK, RC, KH, SM, and YM: investigation; SM, IR, and YM: resources; TK, RC, KH, WB, DT, EL, and SM: data curation; TK, RC, and YM: writing (original draft preparation); TK, RC, KH, WB, DT, EL, SM, IR, and YM: writing (review and editing); TK, RC, and SM: visualization; IR, and YM: supervision, project administration, and funding acquisition.

ACKNOWLEDGMENTS

This work is supported by CHDI Foundation #A-8427.

REFERENCES

Aosaki, T., Miura, M., Suzuki, T., Nishimura, K., and Masuda, M. (2010). Acetylcholine-dopamine balance hypothesis in the striatum: an update. *Geriatr. Gerontol. Int.* 10(Suppl. 1), S148–S157. doi: 10.1111/j.1447-0594.2010.00588.x

Aosaki, T., Tsubokawa, H., Ishida, A., Watanabe, K., Graybiel, A. M., and Kimura, M. (1994). Responses of tonically active neurons in the primate's striatum undergo systematic changes during behavioral sensorimotor conditioning. *J. Neurosci.* 14, 3969–3984. doi: 10.1523/JNEUROSCI.14-06-03969.1994

Apicella, P., Ravel, S., Deffains, M., and Legallet, E. (2011). The role of striatal tonically active neurons in reward prediction error signaling during instrumental task performance. *J. Neurosci.* 31, 1507–1515. doi: 10.1523/JNEUROSCI.4880-10.2011

Ashby, F. G., and Crossley, M. J. (2011). A computational model of how cholinergic interneurons protect striatal-dependent learning. *J. Cogn. Neurosci.* 23, 1549–1566. doi: 10.1162/jocn.2010.21523

Beigi, M., Wilkinson, L., Gobet, F., Parton, A., and Jahanshahi, M. (2016). Levodopa medication improves incidental sequence learning in Parkinson's disease. *Neuropsychologia* 93, 53–60. doi: 10.1016/j.neuropsychologia.2016.09.019

Bennett, B. D., Callaway, J. C., and Wilson, C. J. (2000). Intrinsic membrane properties underlying spontaneous tonic firing in neostriatal cholinergic interneurons. *J. Neurosci.* 20, 8493–8503. doi: 10.1523/JNEUROSCI.20-22-08493.2000

Brooks, D. J. (2008). Optimizing levodopa therapy for Parkinson's disease with levodopa/carbidopa/entacapone: implications from a clinical and patient perspective. *Neuropsychiatr. Dis. Treat.* 4, 39–47. doi: 10.2147/NDT.S1660

Brown, M. T., Tan, K. R., O'Connor, E. C., Nikonenko, I., Muller, D., and Lüscher, C. (2012). Ventral tegmental area GABA projections pause accumbal cholinergic interneurons to enhance associative learning. *Nature* 492, 452–456. doi: 10.1038/nature11657

Cachope, R., Mateo, Y., Mathur, B. N., Irving, J., Wang, H. L., Morales, M., et al. (2012). Selective activation of cholinergic interneurons enhances accumbal phasic dopamine release: setting the tone for reward processing. *Cell Rep.* 2, 33–41. doi: 10.1016/j.celrep.2012.05.011

Calabresi, P., Centonze, D., Gubellini, P., Pisani, A., and Bernardi, G. (2000). Acetylcholine-mediated modulation of striatal function. *Trends Neurosci.* 23, 120–126. doi: 10.1016/S0166-2236(99)01501-5

Centonze, D., Gubellini, P., Pisani, A., Bernardi, G., and Calabresi, P. (2003). Dopamine, acetylcholine and nitric oxide systems interact to induce corticostriatal synaptic plasticity. *Rev. Neurosci.* 14, 207–216. doi: 10.1515/REVNEURO.2003.14.3.207

Chen, J., Ho, S. L., Lee, T. M., Chang, R. S., and Pang, S. Y. (2016). Visuomotor control in patients with Parkinson's disease. *Neuropsychologia* 80, 102–114. doi: 10.1016/j.neuropsychologia.2015.10.036

Cragg, S. J. (2006). Meaningful silences: how dopamine listens to the ACh pause. *Trends Neurosci.* 29, 125–131. doi: 10.1016/j.tins.2006.01.003

Dautan, D., Huerta-Ocampo, I., Witten, I. B., Deisseroth, K., Bolam, J. P., Gerdjikov, T., et al. (2014). A major external source of cholinergic innervation

of the striatum and nucleus accumbens originates in the brainstem. *J. Neurosci.* 34, 4509–4518. doi: 10.1523/JNEUROSCI.5071-13.2014

Deng, P., Zhang, Y., and Xu, Z. C. (2007). Involvement of I(h) in dopamine modulation of tonic firing in striatal cholinergic interneurons. *J. Neurosci.* 27, 3148–3156. doi: 10.1523/JNEUROSCI.5535-06.2007

Ding, J. B., Guzman, J. N., Peterson, J. D., Goldberg, J. A., and Surmeier, D. J. (2010). Thalamic gating of corticostriatal signaling by cholinergic interneurons. *Neuron* 67, 294–307. doi: 10.1016/j.neuron.2010.06.017

Doig, N. M., Magill, P. J., Apicella, P., Bolam, J. P., and Sharott, A. (2014). Cortical and thalamic excitation mediate the multiphasic responses of striatal cholinergic interneurons to motivationally salient stimuli. *J. Neurosci.* 34, 3101–3117. doi: 10.1523/JNEUROSCI.4627-13.2014

Frank, M. J. (2005). Dynamic dopamine modulation in the basal ganglia: a neurocomputational account of cognitive deficits in medicated and nonmedicated Parkinsonism. *J. Cogn. Neurosci.* 17, 51–72. doi: 10.1162/0898929052880093

Franklin, N. T., and Frank, M. J. (2015). A cholinergic feedback circuit to regulate striatal population uncertainty and optimize reinforcement learning. *Elife* 4:e12029. doi: 10.7554/eLife.12029

Galarraga, E., Hernández-López, S., Reyes, A., Miranda, I., Bermudez-Rattoni, F., Vilchis, C., et al. (1999). Cholinergic modulation of neostriatal output: a functional antagonism between different types of muscarinic receptors. *J. Neurosci.* 19, 3629–3638. doi: 10.1523/JNEUROSCI.19-09-03629.1999

Graybiel, A. M. (2008). Habits, rituals, and the evaluative brain, *Annu. Rev. Neurosci.* 31, 359–387. doi: 10.1146/annurev.neuro.29.051605.112851

Gutierrez-Garralda, J. M., Moreno-Briseño, P., Boll, M. C., Morgado-Valle, C., Campos-Romo, A., Diaz, R., et al. (2013). The effect of Parkinson's disease and Huntington's disease on human visuomotor learning. *Euro. J. Neurosci.* 38, 2933–2940. doi: 10.1111/ejn.12288

Hollerman, J. R., and Schultz, W. (1998). Dopamine neurons report an error in the temporal prediction of reward during learning. *Nat. Neurosci.* 1, 304–309. doi: 10.1038/1124

Hyland, B. I., Reynolds, J. N., Hay, J., Perk, C. G., and Miller, R. (2002). Firing modes of midbrain dopamine cells in the freely moving rat. *Neuroscience* 114, 475–492. doi: 10.1016/S0306-4522(02)00267-1

Hyland, K., and Clayton, P. T. (1992). Aromatic L-amino acid decarboxylase deficiency: diagnostic methodology. *Clin. Chem.* 38, 2405–2410.

Joshua, M., Adler, A., Mitelman, R., Vaadia, E., and Bergman, H. (2008). Midbrain dopaminergic neurons and striatal cholinergic interneurons encode the difference between reward and aversive events at different epochs of probabilistic classical conditioning trials. *J. Neurosci.* 28, 11673–11684. doi: 10.1523/JNEUROSCI.3839-08.2008

Kalia, L. V., and Lang, A. E. (2015). Parkinson's disease. *Lancet* 386, 896–912. doi: 10.1016/S0140-6736(14)61393-3

Kim, T., Hamade, K. C., Todorov, D., Barnett, W. H., Capps, R.A., Latash, E.M., et al. (2017). Reward based motor adaptation mediated by basal ganglia. *Front. Comput. Neurosci.* 11:19. doi: 10.3389/fncom.2017.00019

Kita, H. (1993). GABAergic circuits of the striatum. *Prog. Brain Res.* 99, 51–72. doi: 10.1016/S0079-6123(08)61338-2

Knowles, W. S. (1986). Application of organometallic catalysis to the commercial production of L-DOPA. *J. Chem. Edu.* 63:222. doi: 10.1021/ed063p222

Koós, T., and Tepper, J. M. (1999). Inhibitory control of neostriatal projection neurons by GABAergic interneurons. *Nat. Neurosci.* 2, 467–472. doi: 10.1038/8138

Kosillo, P., Zhang, Y., F., Threlfell, S., and Cragg, S. J. (2016). Cortical control of striatal dopamine transmission via striatal cholinergic interneurons. *Cereb. Cortex* 26, 4160–4169. doi: 10.1093/cercor/bhw252

Kreitzer, A. C., and Malenka, R. C. (2008). Striatal plasticity and basal ganglia circuit function. *Neuron* 60, 543–554. doi: 10.1016/j.neuron.2008.11.005

Maurice, N., Mercer, J., Chan, C. S., Hernandez-Lopez, S., and Held, J. (2004). D2 dopamine receptor-mediated modulation of voltage-dependent Na+ channels reduces autonomous activity in striatal cholinergic interneurons. *J. Neurosci.* 24, 10289–10301. doi: 10.1523/JNEUROSCI.2155-04.2004

Morris, G., Arkadir, D., Nevet, A., Vaadia, E., and Bergman, H. (2004). Coincident but distinct messages of midbrain dopamine and striatal tonically active neurons. *Neuron* 43, 133–143. doi: 10.1016/j.neuron.2004.06.012

Oswald, M. J., Oorschot, D. E., Schulz, J. M., and Lipski, J. (2009). IH current generates the afterhyperpolarisation following activation of subthreshold cortical synaptic inputs to striatal cholinergic interneurons. *J. Physiol.* 587, 5879–5897. doi: 10.1113/jphysiol.2009.177600

Pisani, A., Bonsi, P., Centonze, D., Gubellini, P., Bernardi, G., and Calabresi, P. (2003). Targeting striatal cholinergic interneurons in Parkinson's disease: focus on metabotropic glutamate receptors. *Neuropharmacology* 45, 45–56. doi: 10.1016/S0028-3908(03)00137-0

Reynolds, J. N., Hyland, B. I., and Wickens, J. R. (2004). Modulation of an afterhyperpolarization by the substantia nigra induces pauses in the tonic firing of striatal cholinergic interneurons. *J. Neurosci.* 24, 9870–9877. doi: 10.1523/JNEUROSCI.3225-04.2004

Rice, M. E., and Cragg, S. J. (2004). Nicotine amplifies reward-related dopamine signals in striatum. *Nat. Neurosci.* 7, 583–584. doi: 10.1038/nn1244

Scherman, D., Desnos, C., Darchen, F., Pollak, P., Javoy-Agid, F., and Agid, Y. (1989). Striatal dopamine deficiency in Parkinson's disease: role of aging. *Ann. Neurol.* 26, 551–557. doi: 10.1002/ana.410260409

Schultz, W. (1986). Activity of pars reticulata neurons of monkey substantia nigra in relation to motor, sensory, and complex events. *J. Neurophysiol.* 55, 660–677. doi: 10.1152/jn.1986.55.4.660

Schultz, W. (1998). Predictive reward signal of dopamine neurons. *J. Neurophysiol.* 80, 1–27. doi: 10.1152/jn.1998.80.1.1

Schultz, W. (1999). The reward signal of midbrain dopamine neurons. *News Physiol. Sci.* 14, 249–255. doi: 10.1152/physiologyonline.1999.14.6.249

Schultz, W. (2016). Reward functions of the basal ganglia. *J. Neural. Transm.* 123, 679–693. doi: 10.1007/s00702-016-1510-0

Schulz, J. M., Oswald, M. J., and Reynolds, J. N. (2011). Visual-induced excitation leads to firing pauses in striatal cholinergic interneurons. *J. Neurosci.* 31, 11133–11143. doi: 10.1523/JNEUROSCI.0661-11.2011

Schulz, J. M., and Reynolds, J. N. (2013). Pause and rebound: sensory control of cholinergic signaling in the striatum. *Trends Neurosci.* 36, 41–50. doi: 10.1016/j.tins.2012.09.006

Shin, J. H., Adrover, M. F., and Alvarez., V. A. (2017). Distinctive modulation of dopamine release in the nucleus accumbens shell mediated by dopamine and acetylcholine receptors. *J. Neurosci.* 37, 11166–11180. doi: 10.1523/JNEUROSCI.0596-17.2017

Shin, J. H., Adrover, M. F., Wess, J., and Alvarez, V. A. (2015). Muscarinic regulation of dopamine and glutamate transmission in the nucleus accumbens. *Proc. Natl. Acad. Sci. U S A.* 112, 8124–8129. doi: 10.1073/pnas.1508846112

Smith, Y., Bevan, M. D., Shink, E., and Bolam, J. P. (1998). Microcircuitry of the direct and indirect pathways of the basal ganglia. *Neuroscience* 86, 353–387.

Straub, C., Tritsch, N. X., Hagan, N. A., and Gu, C. (2014). Multiphasic modulation of cholinergic interneurons by nigrostriatal afferents. *J. Neurosci.* 34, 8557–8569. doi: 10.1523/JNEUROSCI.0589-14.2014

Sulzer, D., Cragg, S. J., and Rice, M. E. (2016). Striatal dopamine neurotransmission: regulation of release and uptake. *Basal. Ganglia.* 6, 123–148. doi: 10.1016/j.baga.2016.02.001

Tan, C. O., and Bullock, D. (2008). A dopamine-acetylcholine cascade: simulating learned and lesion-induced behavior of striatal cholinergic interneurons. *J. Neurophysiol.* 100, 2409–2421. doi: 10.1152/jn.90486.2008

Teka, W. W., Hamade, K. C., Barnett, W. H., and Kim, T. (2017). From the motor cortex to the movement and back again. *PLoS ONE* 12:e0179288. doi: 10.1371/journal.pone.0179288

Tepper, J. M., Koós, T., Ibanez-Sandoval, O., Tecuapetla, F., Faust, T. W., and Assous, M. (2018). Heterogeneity and diversity of striatal GABAergic interneurons: update 2018. *Front. Neuroanat.* 12:91. doi: 10.3389/fnana.2018.00091

Tepper, J. M., Tecuapetla, F., Koós, T., and Ibáñez-Sandoval, O. (2010). Heterogeneity and diversity of striatal GABAergic interneurons. *Front. Neuroanat.* 4:150. doi: 10.3389/fnana.2010.00150

Threlfell, S., Lalic, T., Platt, N. J., and Jennings, K. A. (2012). Striatal dopamine release is triggered by synchronized activity in cholinergic interneurons. *Neuron* 75, 58–64. doi: 10.1016/j.neuron.2012.04.038

Wade, L. A., and Katzman, R. (1975). Synthetic amino acids and the nature of L-DOPA transport at the blood-brain barrier. *J. Neurochem.* 25, 837–842. doi: 10.1111/j.1471-4159.1975.tb04415.x

Wall, N. R., De La Parra, M., Callaway, E. M., and Kreitzer, A. C. (2013). Differential innervation of direct- and indirect-pathway striatal projection neurons. *Neuron* 79, 347–360. doi: 10.1016/j.neuron.2013.05.014

Wilson, C. J. (2005). The mechanism of intrinsic amplification of hyperpolarizations and spontaneous bursting in striatal cholinergic interneurons. *Neuron* 45, 575–85. doi: 10.1016/j.neuron.2004.12.053

Xenias, H. S., Ibáñez-Sandoval, O., Koós, T., and Tepper, J. M. (2015). Are striatal tyrosine hydroxylase interneurons dopaminergic? *J. Neurosci.* 35, 6584–6599. doi: 10.1523/JNEUROSCI.0195-15.2015

Yager, L. M., Garcia, A. F., Wunsch, A. M., and Ferguson, S. M. (2015). The ins and outs of the striatum: role in drug addiction. *Neuroscience* 301, 529–541. doi: 10.1016/j.neuroscience.2015.06.033

Zhang, Y. F., and Cragg, S. J. (2017). Pauses in striatal cholinergic interneurons: what is revealed by their common themes and variations? *Front. Syst.* 11:80. doi: 10.3389/fnsys.2017.00080

Zhang, Y. F., Reynolds, J. N. J., and Cragg, S. J. (2018). Pauses in cholinergic interneuron activity are driven by excitatory input and delayed rectification, with dopamine modulation. *Neuron* 98, 918–925.e3. doi: 10.1016/j.neuron.2018.04.027t

Zhou, F. M., Wilson, C. J., and Dani, J. A. (2002). Cholinergic interneuron characteristics and nicotinic properties in the striatum. *J. Neurobiol.* 53, 590–605. doi: 10.1002/neu.10150

Zsigmond, P., Nord, M., Kullman, A., Diczfalusy, E., Wårdell, K., and Dizdar, N. (2014). Neurotransmitter levels in basal ganglia during levodopa and deep brain stimulation treatment in Parkinson's disease. *Neurol. Clin. Neurosci.* 2, 149–155. doi: 10.1111/ncn3.109

Conflict of Interest Statement: The authors declare that the research was conducted in the absence of any commercial or financial relationships that could be construed as a potential conflict of interest.

frontiers in Cellular Neuroscience

ORIGINAL RESEARCH
published: 12 March 2019
doi: 10.3389/fncel.2019.00088

Prediction of Forelimb Reach Results From Motor Cortex Activities Based on Calcium Imaging and Deep Learning

*Chunyue Li, Danny C. W. Chan, Xiaofeng Yang, Ya Ke and Wing-Ho Yung**

School of Biomedical Sciences and Gerald Choa Neuroscience Centre, Faculty of Medicine, The Chinese University of Hong Kong, Shatin, Hong Kong

Brain-wide activities revealed by neuroimaging and recording techniques have been used to predict motor and cognitive functions in both human and animal models. However, although studies have shown the existence of micrometer-scale spatial organization of neurons in the motor cortex relevant to motor control, two-photon microscopy (TPM) calcium imaging at cellular resolution has not been fully exploited for the same purpose. Here, we ask if calcium imaging data recorded by TPM in rodent brain can provide enough information to predict features of upcoming movement. We collected calcium imaging signal from rostral forelimb area in layer 2/3 of the motor cortex while mice performed a two-dimensional lever reaching task. Images of average calcium activity collected during motion preparation period and inter-trial interval (ITI) were used to predict the forelimb reach results. The evaluation was based on a deep learning model that had been applied for object recognition. We found that the prediction accuracy for both maximum reaching location and trial outcome based on motion preparation period but not ITI were higher than the probabilities governed by chance. Our study demonstrated that imaging data encompassing information on the spatial organization of functional neuronal clusters in the motor cortex is useful in predicting motor acts even in the absence of detailed dynamics of neural activities.

Keywords: motor cortex, two-photon imaging, movement prediction, deep learning, convolutional neural network

OPEN ACCESS

Edited by:
Ying Shen,
Zhejiang University, China

Reviewed by:
Rong Liu,
Dalian University of Technology (DUT), China
Kazuhiko Yamaguchi,
RIKEN, Japan

***Correspondence:**
Wing-Ho Yung
whyung@cuhk.edu.hk

Received: *28 September 2018*
Accepted: *20 February 2019*
Published: *12 March 2019*

Citation:
Li C, Chan DCW, Yang X, Ke Y and Yung W-H (2019) Prediction of Forelimb Reach Results From Motor Cortex Activities Based on Calcium Imaging and Deep Learning. Front. Cell. Neurosci. 13:88. doi: 10.3389/fncel.2019.00088

INTRODUCTION

A central question in neuroscience is how the motor cortex encodes movements (Georgopolous et al., 1988; Russo et al., 2018). One commonly used method to address this question is to implant one or several microelectrode arrays in the motor cortex and record electrophysiological signals while the subject repeats the same behavior task, such as center-out reach task and food reaching task (e.g., Sussillo et al., 2015; Li et al., 2017). Although in the past decades this approach has generated significant amount of information in understanding the relationship between motor cortex and behavior, the results obtained mainly describe the temporal evolution of neural activity during movement but provide limited spatial organization information of the neurons involved (O'Shea et al., 2017). Also, extracellular electrode recording is biased toward highly active neurons. On the other hand, two-photon microscopy (TPM) can record faithfully at single-cell spatial

resolution from a much larger population of neurons, regardless of their level of activities, and for an extended period of time spanning across weeks. These advantages make TPM a powerful tool to study fine spatial organization of neuronal ensemble in motor cortex in relation to behavior. Indeed, recent imaging studies have shown that micrometer-scale spatial organization may be a characteristic and plays crucial role in movement encoding. For example, ∼70 μm region-specific functional clusters in layer 2/3 of the motor cortex were revealed while mice conducted one-dimensional lever reaching task. Moreover, ensemble and individual activities of task-related cells within the cluster can more accurately reconstruct lever movement trajectories than those of task-related cells outside the cluster (Hira et al., 2013). A more recent study used retrograde pseudotyped lentivirus to label corticospinal neurons (CSNs) that send direct projection to the spinal cord, and found that subgroups of CSNs are activated in specific cortical locations and in precise temporal orders during a food reaching task (Wang et al., 2017).

In primates, premotor areas are involved in movement planning, whereas the primary motor cortex is more likely to be active during movement execution. It has been shown that unilateral lesion or inactivation of premotor areas during movement planning interferes with upcoming forelimb movements in the contralateral direction without impairing movements (Cisek and Kalaska, 2005; Churchland and Shenoy, 2007). Therefore, it may be feasible to predict features of upcoming movement by means of neural activity recorded in motor planning period (e.g., Filippini et al., 2017, 2018). In fact, such knowledge has been put into application in the field of brain-computer interface (Andersen et al., 2014). Several types of neuroimaging data, including functional magnetic resonance imaging (fMRI), functional near-infrared spectroscopy (fNIRS), and wide field calcium imaging, have been used to predict the motion intent or to infer the cognitive state. These imaging signals mainly reflect the input and intracortical processing of a given brain area, usually in the scale of millimeters or hundreds of micrometers (Logothetis et al., 2001). However, whether the spatial organization information in micrometer-scale during motor planning could be used to predict the upcoming motion states or motion dynamics has not been studied.

In rodents, the rostral forelimb area (RFA) has been considered to be a premotor area related to the planning and execution of forelimb movement (Rouiller et al., 1993). In this study, we trained mice to do a novel two-dimensional (2D) lever reaching task and simultaneously recorded calcium imaging signals from layer 2/3 of the contralateral RFA. We used the mean calcium image of movement planning period to predict the maximum reaching location and the reaching outcome, that is, success or failure. We employed a deep convolutional neural network (CNN) named Resnet, which has been shown to achieve outstanding performance in object recognition (He et al., 2016). Unlike the commonly used calcium signal analysis method, we did not extract calcium fluorescent activity ($\Delta F/F_0$). Rather, we let the CNN model to learn the spatial feature of the functional neuronal clusters directly from the data via a hierarchical layer-based structure. To the best of our knowledge, this is the first study to use deep learning method to analyze micrometer-scale calcium imaging data in motor task.

MATERIALS AND METHODS

Animals and Surgery

All procedures were in accordance with protocols approved by the Hong Kong Department of Health and the Chinese University of Hong Kong Animal Experimentation and Ethics Committee. Wild-type C57BL/6 mice were group housed in standard large cages under normal light cycle (12-h light/dark cycle and lights on at 7:00 am). The cages were each enriched with a plastic house, tunnel system, and low-profile running wheel. Behavioral experiments were performed in the light period.

Male adult mice (8–9 weeks old, $n = 4$) were anesthetized with isoflurane and intraperitoneally injected with ketamine (150 mg/kg) and xylazine (10 mg/kg). A subcutaneous injection of carprofen (5 mg/kg) is administered to reduce inflammation. A custom head-plate was glued to the skull and craniotomy (5 mm diameter) was performed over the left RFA. Adeno-associated viruses (AAV) carrying genes for the calcium indicator GCaMP6f (AAV1.Syn.GCaMP6f.WPRE.SV40, Penn Vector Core) were injected in the left RFA of the motor cortex around the coordinate of 1.0 mm anterior and 2.5 mm lateral from bregma (Hira et al., 2013). Two weeks after the AAV injection, a chronic glass imaging window was implanted. The procedures were separated to reduce the progression of bone regrowth under the window at the later stages of training. Gel superglue was applied at the gap between the glass plug and the skull. Buprenorphine and Baytril were injected subcutaneously at the end of surgery.

Behavior Training Paradigm

Three days after the window surgery, mice were food restricted and lasted throughout the whole experiment period, maintaining at 85% of their *ad libitum* body weight. Four mice were trained to perform a 2D lever reaching task daily over 17 days (**Figure 1A**). The lever trajectory was detected in real-time by an independent microcontroller at a rate of 90 Hz. Each trial began at a motor-enforced center position. After contact of the mouse limb with the lever was detected, the animal was required to hold the lever for 2.5 s to initiate an auditory cue. This PRECUE period allowed the mouse to prepare for its movements and the cue signaled the animal to start the task. After cue presentation, the animal was free to move the lever in any direction and was given a chocolate milk reward when the movement exceeded a predetermined threshold distance from the initial position, which increased with training days and was fixed at 3 mm when the expert level was reached. The mouse must complete the task within a fixed WINDOW period of 3 s. If successful, the state was preemptively changed to POST_SUCCESS for reward. On the other hand, the POST_FAILURE state was reached if the window period had elapsed, or if the distance threshold was met but the physical contact with the lever was lost. Generally, the inter-trial interval (ITI) was set as 6 s, and the trial initialization was conducted during this period. However, the ITI would become

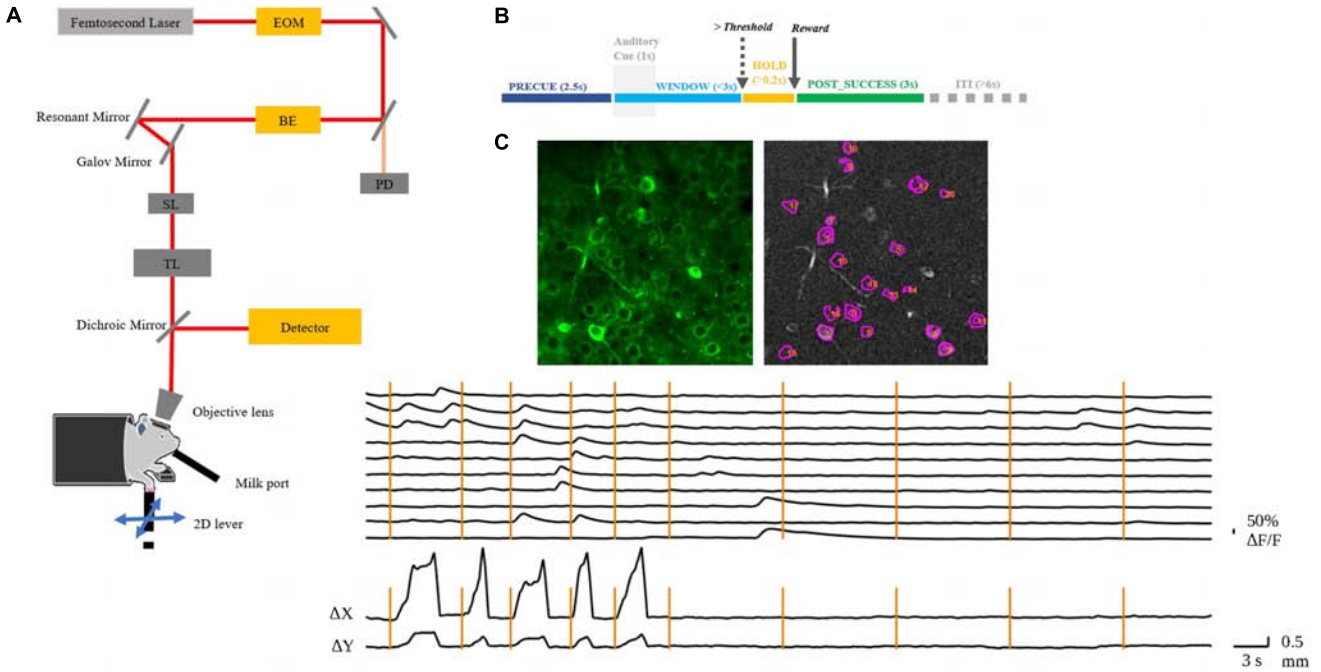

FIGURE 1 | (**A**) Layout of the custom-built TPM. EOM, electro-optic modulator; BE, beam expander; SL, scan lens; TL, tube lens. The mouse with craniotomy was head-fixed under the objective. (**B**) Behavior experiment schema. The mouse was required to hold the lever for 2.5 s to initiate an auditory cue. After the presentation of the auditory cue, the mouse could move the lever in any direction and would receive a chocolate milk reward when the reaching movement exceeded a preset threshold distance from the initial position. The WINDOW for mouse to complete the task was 3 s. If successful, the state was preemptively changed to POST_SUCCESS for reward. (**C**) A representative image of the left RFA with identified neurons in motor cortex layer 2/3 of mouse 9L (top); the normalized $\Delta F/F$ of the numbered neurons and the corresponding lever trajectory indicated as Δx and Δy (bottom). The vertical lines indicate the auditory cue of each trial.

longer if the mouse refused to touch the lever. The training paradigm is summarized in **Figure 1B**.

Two-Photon Calcium Imaging

In vivo imaging was conducted by a custom-built, resonant scanner-based TPM (**Figure 1A**). During the behavioral tests, the mouse was head-fixed under the microscope. Calcium fluorescent signals (512 × 512 pixels per frame) at layer 2/3 of the target RFA (**Figure 1C**) were acquired at 15 frames per second and were synchronized with the behavioral system by a data acquisition system. In the present study, motion artifacts in calcium imaging data were mainly caused by respiration and cardiac activity. Studies have shown that motion artifacts induced by these physiological processes are restricted mainly in the X-Y plane after using a glass coverslip and head-fixed device (Mohammed et al., 2016). We chose a commonly used method, TurboReg (Thevenaz et al., 1998), to reduce motion artifacts. For each trial, we took the averaged image as the template and registered each frame to the template image. After motion correction, we obtained the mean calcium image of the PRECUE period for each trial. The averaged images were used as the input of the prediction model. Pre-processing of imaging data included resizing and normalization to produce suitable input size and range of intensity required by the deep learning model. The calcium fluorescence changes ($\Delta F/F$) were detected by an open source toolbox available online based on a published paper (Pnevmatikakis et al., 2016).

Data Analysis and Prediction Model

The maximum reaching location (x_{end}, y_{end}) was defined as the end point of reaching trajectory during WINDOW period. In our study, each trial began at a motor-enforced center position. We collected (x^n_{end}, y^n_{end}), $n \in [1, N]$ from the n^{th} trial that received reward. N was the total trial number. For mouse 7N, we categorized the reaching locations into 4 clusters signifying 4 spatial territories. For mouse 9L, we categorized the reaching locations into 3 clusters. Then k-Means method, which is an iterative data-partitioning algorithm that assigns N observations to exactly one of k clusters defined by centroids (Lloyd, 1982), was applied on all data pairs. Here we set k as 4 for mouse 7N and 3 for mouse 9L to make trials that recorded in the same day could at least be separated into two clusters. We labeled each data pair (x^n_{end}, y^n_{end}), $n \in [1, N]$ according to their clustering results [label $\in \{1, 2, 3, 4\}$for 4 clusters, label $\in \{1, 2, 3\}$ for 3 clusters]. After collecting all trials' coordinates of the reach location and clustering all these coordinates by k-Means clustering algorithm, we then used the calcium imaging data of the motor planning period to predict each trial's maximum reach location category.

The calcium imaging data used in this study were recorded during the behavior training period, and the reward threshold

distance was adjusted during this period. For study on the prediction of trial outcome, we need to clearly separate the data sets for SUCCESS and FAILURE trials. Therefore, we applied the following exclusion criteria. First, we excluded a trial if the mouse pushed the lever beyond 0.5 mm during PRECUE period. Second, for trials that the animal did receive reward, we excluded the trial if the reaching distance during the WINDOW period was lower than 2 mm for Mice 7N and 1mm for Mice 9L. Third, for failed trials, we excluded the trial if the lever reaching distance during the WINDOW period was larger than 0.5 mm.

We built the deep learning prediction model based on a pre-trained Resnet18 (He et al., 2016). The whole set of data was subdivided into training set and testing set in the ratio of 4:1. The training set was used to train the prediction model. The testing set was used to evaluate the performance of the prediction model. **Figure 2** summarized the design of the data acquisition and analysis procedures.

Configuring the Convolutional Neural Network Model

We aimed to train a Resnet18 model to map each mean calcium image during the PRECUE period into the corresponding reaching result. When configuring this CNN model, we took into account some specific properties of our input data. First, the calcium imaging signals were collected across days, meaning that there might exist unique 3-dimensional (3D) displacement in the recording area of each recording day. Thus, to make sure that training dataset and test dataset have similar distributions, for each subject, we randomly partitioned the calcium imaging data recorded in each day, rather than all collected data, into 5 portions and took one portion as testing dataset and left all the others as training dataset. Experiments would be repeated for a total of 5 times and the results averaged. This specific five-fold data separation procedure is illustrated in **Figure 3**. Second, in view of the relatively small sample size available, the strategy of transfer learning was employed in our study. Transfer learning makes use of the knowledge gained while solving one task and applies it to a different task. In this study, Resnet18 was pre-trained on dataset ImageNet, which contains 1.2 million images with 1000 categories. Deep CNN discovers hierarchical feature representations such that higher-level features can be derived from lower-level features. Usually, lower CNN layers are used to extract abstract features like edges, and deeper CNN layers are used to find features that are informative for the target task (Shen et al., 2017). Thus, we froze the initial values of the first several CNN (first 6 layers for mouse 7N and first 13 layers for mouse 9L) and trained the remaining CNN layers with the training set. Also, the number of fully connected layer was adjustable, depending on the task involved.

After a series of testing and optimization, the structure of the specific Resnet18 model shown in **Figure 4** was used in the present study. This model started with one convolutional layer with 7×7 filters and one pooling layer, mapping 224×224 images to 56×56 feature maps. This was followed by a sequence of 4 convolutional layers with 3×3 filters, and then an average pooling layer and a fully connected layer. Each pair of 3×3 filters was added with a shortcut connection. We figured that the imaging data could be used by this CNN model in at least two different ways, namely, to predict the maximum reach location of the successful trials, and to distinguish the successful and failed outcome of the trials.

The optimization method used was Adam (Kingma and Ba, 2014) with a mini-batch size of 16. For mice 7N, the following parameters were used to predict maximum reach location: learning rate was set to 0.00001 and was divided by 10 every 150 epochs; the weight decay was set to 0.0001, and the total epoch number was 300. Moreover, for the outcome of the trials prediction, the weight decay was set to 0.0005, with other parameters remained the same. For mice 9L, the learning rate for maximum reach location was set to 0.00001 and was divided by 10 every 150 epochs, the weight decay was set to 0.00001, and the total epoch number was 300. Similarly, for reach outcome prediction, the weight decay was set to 0.0001, with other parameters are same as above.

Moreover, class activation mapping (CAM) technique (Zhou et al., 2016) was used to visualize the discriminative parts of different categories used by Resnet model for prediction. Let $f_k(x, y)$ be the task-specific feature map of filter k in the last convolutional layer at spatial location (x, y), and w_k be the corresponding weights of the fully connected layer, which indicates the importance of f_k for different categories. The CAM was calculated as follow:

$$M_{CAM}(x, y) = \sum_k f_k(x, y) \cdot w_k$$

Therefore, M_{CAM} could highlight the most informative regions in the image relevant to each category.

In addition, the calcium imaging data collected during the ITI period were used for comparison, as the motor cortical region was presumably in a relatively idle state during this period since the cue for movement task was not yet available. In fact, changes in behavior as a result of learning was obvious in the post-cue period including a reduction in delay in reaching action.

RESULTS

We trained four mice in total to do the 2D lever reaching task. Three of them successfully learned the 2D reaching task. However, we excluded the data from one mouse that was physically weaker resulting in insufficient number of trials number needed for deep learning analysis. Therefore, two mice (coded 7N and 9L) were included in the present study. The lever trajectory and the corresponding calcium fluorescent traces of individual neurons are shown as an example in **Figure 1C**.

Prediction of Maximum Reaching Location

We first used the calcium imaging data to predict the locations of the lever reach. The imaging data were collected from the two mice (7N and 9L) while they learned the 2D lever reaching task. In this analysis, we only included SUCCESS trials in which the animals received liquid reward, which is considered an

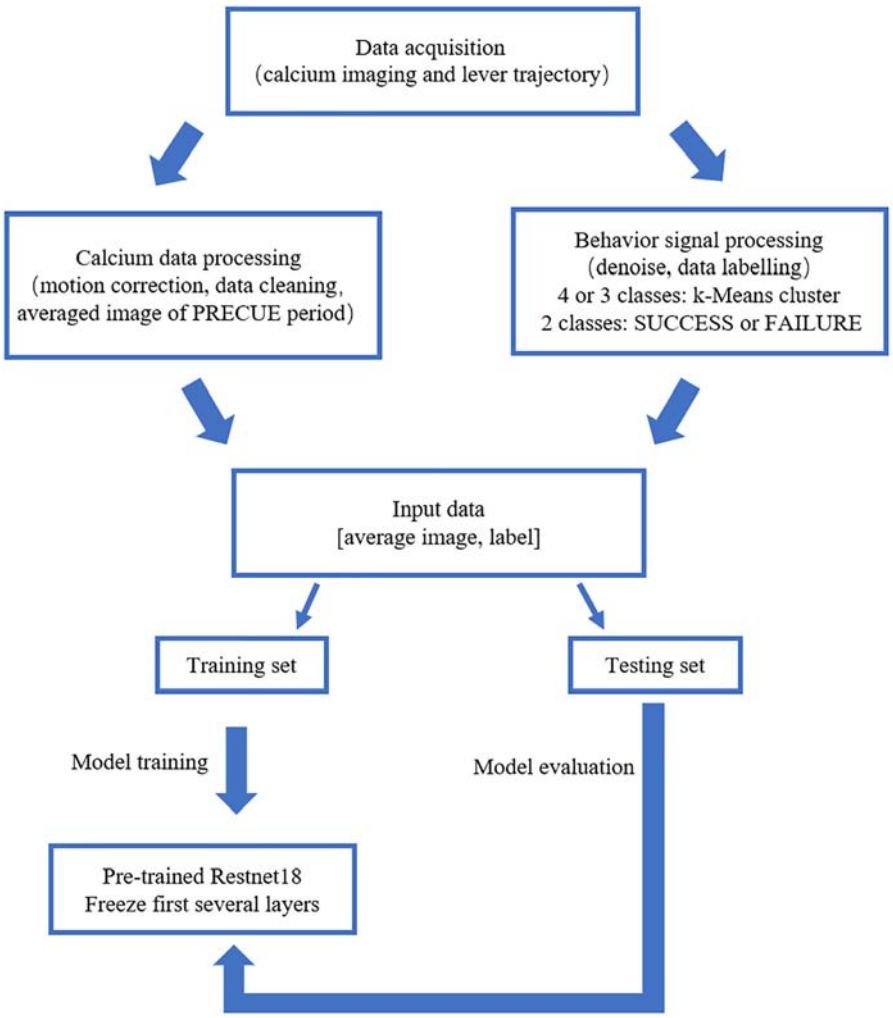

FIGURE 2 | Outline of the data analysis procedure. Calcium imaging data recorded in PRECUE period were collected in synchrony with forelimb movement parameters. TurboReg was used to remove motion artifacts of the imaging data within each trial. Behavioral data were denoised, labeled and k-Means algorithm was used to cluster maximum lever reaching position of all trials. The averaged calcium image were used to predict the result of each trial (SUCCESS or FAILURE) and the maximum lever reaching position. The prediction model was a pre-trained Resnet18. Transfer learning scheme was adopted due to the small sample size. The proportion of the training set and testing was set at a ratio of 4:1.

indicator of movement intention. At the same time, we could avoid including trials that did not involve planning leading to the failed result. To ensure that the calcium imaging data were from corresponding field and plane, we calculated the common neuron numbers across recording days with respect to neurons detected in the average image of all recording days and removed the recording days with percentages lower than 50%. As an example, the detected common neurons of mouse 9L are shown in **Figure 5**. There was a total of 320 trials for mouse 7N and 177 trials for mouse 9L

To facilitate the assessment of the CNN prediction model, we defined the maximum reach locations by the coordinates of the end point of the lever trajectories (see section "Materials and Methods"), and classified, i.e., labeled, them into different categories. We classified the reach locations of all included trials into 4 clusters for mouse 7N and 3 clusters for mouse 9L to make sure that trials that were recorded in the same day could at least be separated into two clusters. This was to avoid that the Resnet model categorized the results of trials according to the unique 3D displacement characteristics of each recording day. The classification of the maximum reach location was by means of the objective method k-Means clustering. The results of the clustering of the maximum reach locations are shown in **Figure 6**.

There was a total of 639 ITI for mouse 7N and a total of 516 ITI for mouse 9L. To reduce the impact from the adjacent trial on each ITI due to slow decay of the calcium reporter, we took the averaged image of calcium data collected during a middle 1s of each ITI as the input. For each mouse, the ITI images recorded in each day were chosen randomly into different groups with equal size, and each group is given different cluster labels (1, 2, 3, and 4 for mouse 7N; 1, 2, and 3 for mouse 9L) for maximum reach location prediction. Moreover, the same five-fold cross-validation

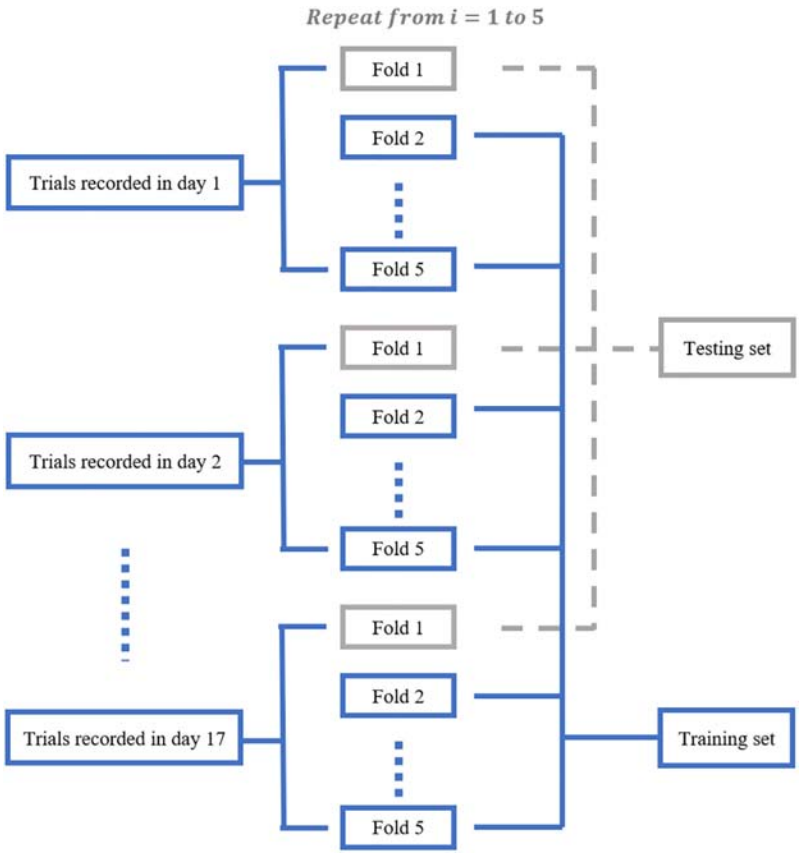

FIGURE 3 | The five-fold data separation procedure. The calcium imaging data recorded in each day was randomly partitioned into 5 portions. One portion was chosen as the testing dataset and the remaining data were used as training dataset. The classification experiments were repeated for 5 times.

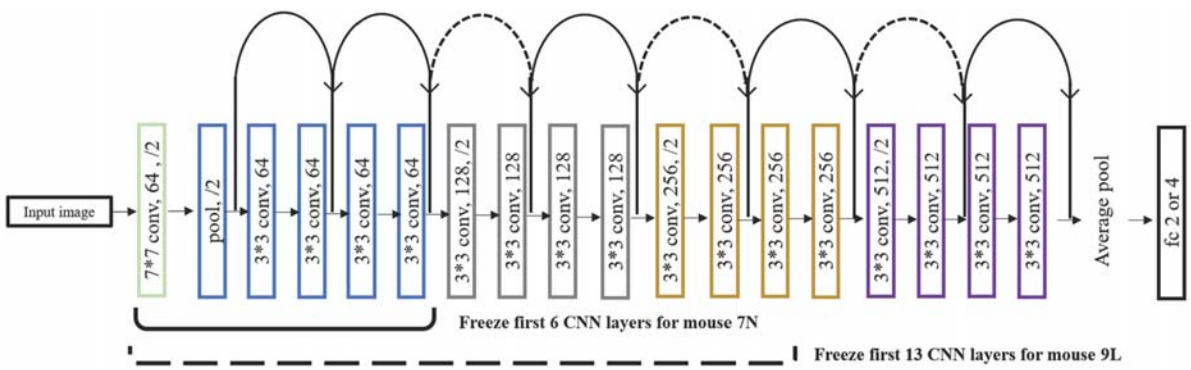

FIGURE 4 | The structure of the Resnet18 employed. Resnet18 was pretrained on the dataset ImageNet, which contains 1.2 million images with 1000 categories. The fully connected layer was changed to 2 to predict the outcome of the trial and to 3 and 4 to predict the maximum lever reaching position. We froze the initial values of the first several CNN (first 6 layers for mouse 7N and first 13 layers for mouse 9L) and trained the remaining CNN layers by using training set. Solid curves represent shortcut connections that performed identity mapping between feature maps that have the same dimensions. Dashed curves represent shortcut connections that performed identity mapping when feature maps have different dimensions.

procedure, transfer learning skill and model parameters were used in this analysis as those used in the RFA group.

The five-fold cross-validation results of the RFA group and ITI group are summarized in **Table 1**. The training data set for both mice of the RFA group achieved a high level of accuracy on average (>90%) in predicting the maximum reaching location clusters. At the same time, the accuracy for the test data of RFA group are 59.02% for mouse 7N and 64.26% for mouse 9L, while the F-score are 0.56 and 0.62, respectively. Since the probability governed by pure chance in correctly predicting the

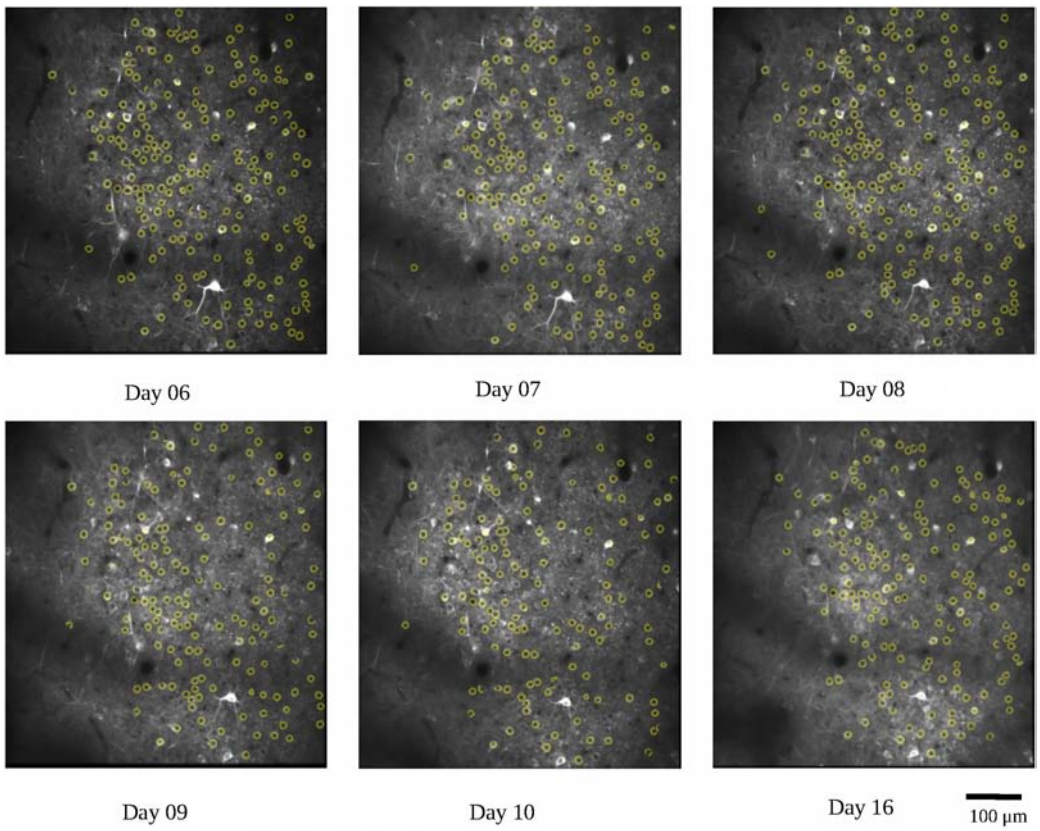

FIGURE 5 | Demonstration of the common neurons (yellow circles) detected in different recording days for mouse 9L. The detected common neurons were compared with neurons revealed in the average image of all recording days.

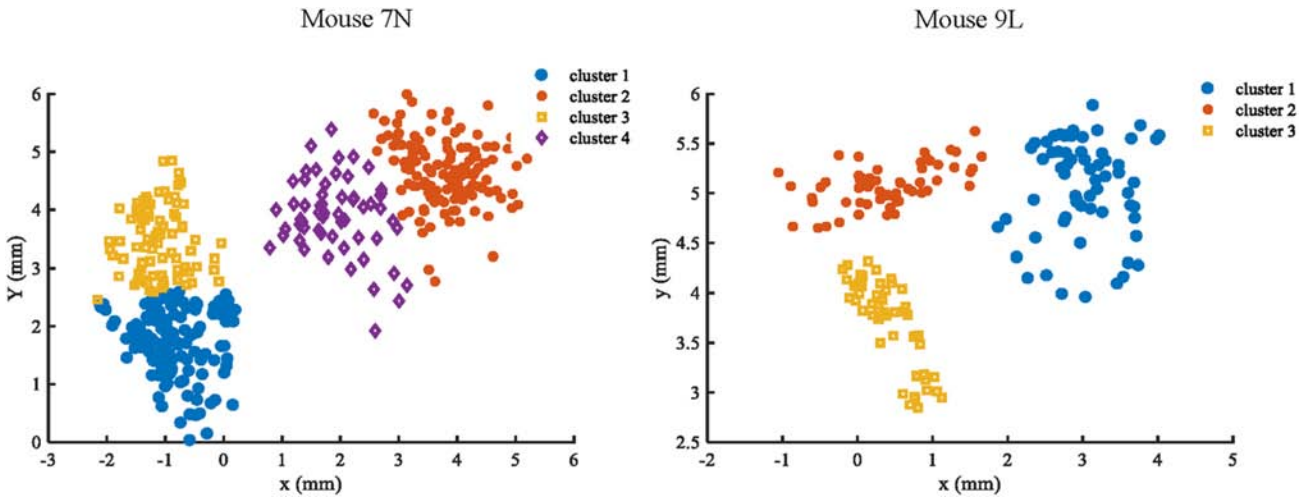

FIGURE 6 | Clustering results of mouse 7N (left) and mouse 9L (right) based on the k-Means method. Different clusters identified are represented by different colors.

reach location is 1 in 4, or 25% for mouse 7N and 1 in 3, or 33.3% for mouse 9L, these results indicate that the trained Resnet model possessed reasonably good ability in mapping averaged calcium activity of the RFA to the reaching location in the lever test. In contrast, the accuracy for the test data of ITI group is 23.28% for mouse 7N and 31.90% for mouse 9L, close to the probability of their respective chance level. In addition, we increased the total training epoch number to 600 to address whether the low

TABLE 1 | Five-fold cross validation results of maximum reach location prediction of the RFA post-cue and ITI group for mice 7N and 9L with epoch number equals to 300.

		RFA post-cue			RFA ITI		
	Fold No.	**Accuracy (Training) (%)**	**Accuracy (Test) (%)**	**F-score**	**Accuracy (Training) (%)**	**Accuracy (Test) (%)**	**F-score**
Mouse 7N	1st	94.05	61.67	0.58	77.76	24.22	0.23
	2nd	92.86	44.44	0.46	72.25	22.66	0.22
	3rd	91.97	60.56	0.57	70.97	22.65	0.22
	4th	90.91	64.18	0.62	70.22	21.87	0.21
	5th	90.77	63.33	0.59	74.96	25.00	0.24
	Mean	**92.11**	**59.02**	**0.56**	**73.23**	**23.28**	**0.22**
Mouse 9L	1st	96.43	52.00	0.51	59.92	32.20	0.32
	2nd	94.39	60.00	0.58	62.68	32.03	0.32
	3rd	93.58	67.86	0.63	60.81	35.24	0.34
	4th	93.40	80.64	0.79	62.63	30.47	0.30
	5th	89.47	60.87	0.57	62.95	29.56	0.29
	Mean	**93.45**	**64.26**	**0.62**	**61.80**	**31.90**	**0.31**

Bold values indicate data group names, performance matrices and mean results of five-fold cross validation.

TABLE 2 | Five-fold cross validation results of maximum reach location prediction of ITI group for mice 7N and 9L with epoch number equals to 600.

	Fold No.	**Accuracy (Training) (%)**	**Accuracy (Test) (%)**	**F-score**
Mouse 7N	1st	92.36	26.56	0.25
	2nd	92.64	29.68	0.26
	3rd	93.98	33.59	0.33
	4th	90.69	19.53	0.19
	5th	90.86	23.43	0.22
	Mean	**92.11**	**26.56**	**0.25**
Mouse 9L	1st	72.11	27.83	0.27
	2nd	75.77	32.81	0.32
	3rd	76.57	26.22	0.25
	4th	75.67	34.38	0.34
	5th	76.55	28.81	0.29
	Mean	**75.33**	**30.01**	**0.29**

Bold values indicate data group names, performance matrices and mean results of five-fold cross validation.

prediction accuracy for the ITI group was caused by under-fitting of the training data. The obtained five-fold cross-validation results of the ITI group for mice 7N and 9L are summarized in **Table 2**. As can be seen, the prediction accuracy of mice 7N and 9L are still close to chance level (26.56 and 30.01%, respectively), which do not increase with the rising training accuracy. Taken together, these results indicate that the averaged calcium imaging data of RFA during the preparation period contain specific information that is related to the maximum reach locations.

Prediction of Lever Reaching Outcome

We considered that a successful trial conducted by the subject was the result of motor planning driven by the motivation to move. In contrast, a failed outcome could reflect lack of sufficient motor planning or motivation. Thus, to provide some insight into these processes, we applied our deep learning model to analyze the activities of the RFA in successful and failed trials. Since the calcium imaging data used in the deep learning model were recorded during the training period, with the reward threshold distance adjusted during the training period, trials with the same reaching distance may result in different outcomes in different training phase. We eliminated such ambiguity by streamlining our data (see section "Materials and Methods") such that the two data sets were well segregated. The reaching distance of cleaned trials for the two mice are shown in **Figure 7**. For SUCCESS trials, the mean reaching distance in each recording day was greater than 2mm for mouse 7N and 1mm for mouse 9L. For FAILURE trials, the mean reaching distance in each recording day was lower than 0.5 mm for two mice. Moreover, we randomly deleted trials of each recording day to keep the ratio of successful and failed trials in the range of [1/2, 2], to make sure that the trials of each recording day were balancedly separated into two categories (SUCCESS and FAILURE), and that the Resnet model can learn useful features to distinguish successful and failed trials of each recording day. There was a total of 327 trials (SUCCESS: 186 trials, FAILURE: 141 trials) for mouse 7N, and 247 trials (SUCCESS: 149 trials, FAILURE: 98 trials) for mouse 9L.

The averaged image of calcium signals collected during the middle 1s of each ITI was used as the input for the ITI group. For each mouse, the ITI images recorded in each day were assigned randomly into different groups with equal size, and each group was given different labels (SUCCESS or FAILURE) for reaching outcome prediction. Moreover, the same five-fold cross-validation procedure, transfer learning skill and model parameters were used in the ITI group as in the RFA post-cue group.

Table 3 summarizes the five-fold cross-validation results of both RFA post-cue and ITI group. A high accuracy of prediction was achieved by the model based on the training data set for the RFA group of both mice. Also, the test accuracy is 72.26% for mouse 7N and 69.80% for mouse 9L. The prediction results of RFA group generated by our model are obviously higher than the probability of random guess or pure chance, i.e., 50%. This conclusion is also supported by the results of the sensitivity and

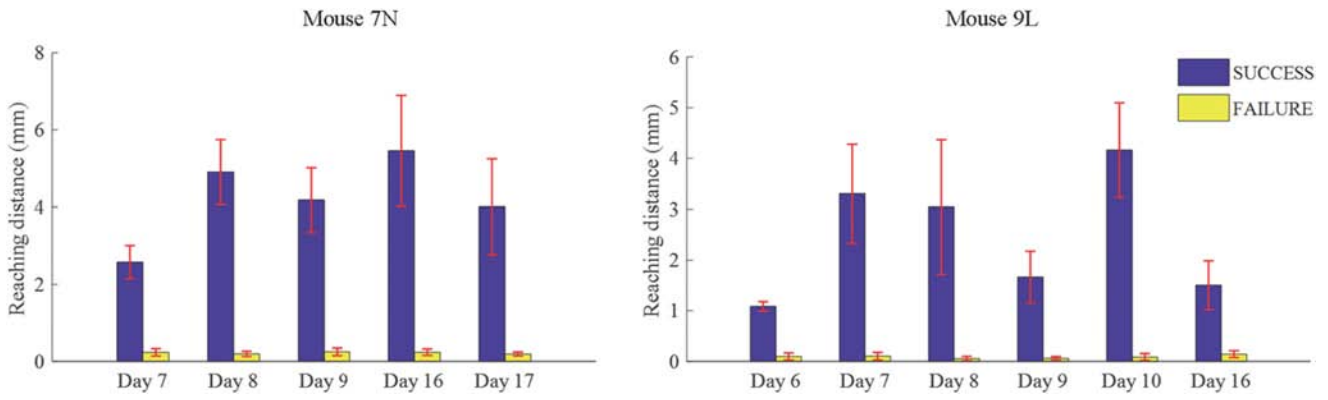

FIGURE 7 | Mean lever reaching distances in each used recording day of mouse 7N (left) and mouse 9L (right).

TABLE 3 | Five-fold cross validation results on the prediction of reaching outcome of RFA post-cue and ITI group for mice 7N and 9L with epoch number equals to 300.

		RFA post-cue					RFA ITI				
	Fold No.	**Accuracy (Training) (%)**	**Accuracy (Test) (%)**	**Sensitivity**	**Specificity**	**F1-score**	**Accuracy (Training) (%)**	**Accuracy (Test) (%)**	**Sensitivity**	**Specificity**	**F1-score**
Mouse 7N	1st	94.14	81.36	0.80	0.83	0.78	87.57	44.35	0.45	0.44	0.45
	2nd	93.87	71.42	0.75	0.67	0.67	88.39	46.09	0.42	0.50	0.47
	3rd	93.93	70.23	0.75	0.66	0.67	87.60	49.21	0.50	0.48	0.48
	4th	92.59	68.91	0.74	0.63	0.66	81.57	50.00	0.45	0.55	0.53
	5th	96.76	68.57	0.70	0.67	0.62	86.21	58.80	0.60	0.58	0.57
	Mean	**94.23**	**72.26**	**0.75**	**0.69**	**0.68**	**86.26**	**49.69**	**0.48**	**0.51**	**0.50**
Mouse 9L	1st	93.23	71.01	0.76	0.66	0.67	74.46	51.92	0.58	0.46	0.49
	2nd	92.35	67.80	0.79	0.54	0.60	75.00	50.00	0.48	0.52	0.51
	3rd	89.01	73.44	0.83	0.57	0.61	75.92	50.00	0.68	0.33	0.39
	4th	88.46	72.34	0.85	0.57	0.65	77.89	43.22	0.47	0.39	0.41
	5th	83.00	64.61	0.83	0.49	0.60	74.13	48.24	0.42	0.54	0.51
	Mean	**89.21**	**69.80**	**0.81**	**0.57**	**0.63**	**75.48**	**48.67**	**0.53**	**0.45**	**0.46**

Bold values indicate data group names, performance matrices and mean results of five-fold cross validation.

specificity of the prediction, as well as F-1 score. However, the accuracy for the test data of the ITI group are still chance level, 49.69 and 48.67% for mice 7N and 9L, respectively. Besides, the higher than pure chance accuracy was not obtained by using a higher epoch number for both two mice (**Table 4**).

Because information flow in broad cortical area was reported by using Ca-signal imaging in mouse cerebellar cortex (Kuroki et al., 2018), whether the motion-predictable Ca-signal is recorded only restricted region is crucially important. Thus, we explored what specific discriminative regions were used by the prediction model to predict SUCCESS and FAILURE. We employed a novel technique named CAM (Zhou et al., 2016, see section Materials and Methods), to detect the implicit attention of the prediction model on calcium imaging of the two groups. **Figure 8A** shows the example of activation maps derived from the prediction model. **Figure 8B** shows the corresponding raw average calcium images recorded in the same day (the 8th day). It could be observed that the most informative regions in the image relevant to the predicted class are confined to specific sub-regions of the image.

DISCUSSION

In this study, we recorded calcium signals from layer 2/3 of the RFA of the motor cortex while mice learned a 2D lever reaching task. The image representing the averaged calcium signal collected during the presumed motion planning period was used to predict the maximum reaching location and trial outcome. The prediction results, subject to five-fold cross-validation, are obviously higher than those governed by pure chance. Our study therefore demonstrated that imaging data containing spatial relationship of active neuronal clusters from motor planning region provide non-trivial information related to motion intent and movement target. Significantly, this can be achieved without the need to extract calcium transients, i.e., the usual $\Delta F/F_0$ signals that capture neuronal firing dynamics.

Large-scale neuroimaging techniques capable of recording wide areas of human cortex, such as fMRI and fNIRS, have been used to decode behavior, intent, or the cognitive processes (Hong et al., 2015; Zich et al., 2015). Similarly, in rodents, it has been demonstrated that widespread modulation of cortical

TABLE 4 | Five-fold cross validation results on the prediction of reaching outcome of ITI group for mice 7N and 9L with epoch number equals to 600.

	Fold No.	Accuracy (Training) (%)	Accuracy (Test) (%)	Sensitivity	Specificity	F1-score
Mouse 7N	1st	93.73	46.77	0.42	0.53	0.48
	2nd	96.27	50.00	0.48	0.52	0.51
	3rd	96.06	44.53	0.36	0.53	0.48
	4th	96.85	49.21	0.48	0.50	0.49
	5th	97.86	50.81	0.53	0.48	0.50
	Mean	**96.15**	**48.26**	**0.45**	**0.51**	**0.49**
Mouse 9L	1st	85.44	48.08	0.46	0.50	0.49
	2nd	86.54	45.00	0.48	0.42	0.43
	3rd	81.19	46.25	0.55	0.38	0.41
	4th	84.67	52.54	0.53	0.53	0.53
	5th	86.57	49.12	0.53	0.46	0.47
	Mean	**84.88**	**48.20**	**0.51**	**0.46**	**0.47**

Bold values indicate data group names, performance matrices and mean results of five-fold cross validation.

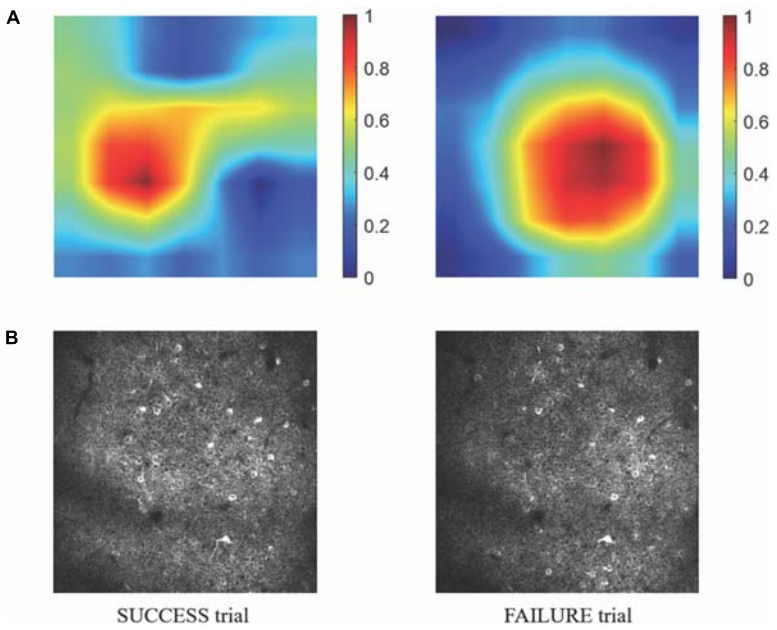

FIGURE 8 | (A) The specific discriminative regions used by the prediction model to predict SUCCESS (left) and FAILURE (right) are illustrated by the activation maps. The color indicates the relative value of M_{CAM}. The higher the M_{CAM} value, the more important the corresponding area is in prediction. The data are from mouse 9L. The corresponding raw average calcium images are shown in **(B)**.

activation could encode distinct behavior (e.g., Zhu et al., 2018). However, the imaging data recorded in these studies mainly reflect the input or intracortical processing of a given brain area and cannot provide fine scale information on the spatial organization of the microcircuits. Consequently, these techniques are usually used to distinguish very distinct gross motor behaviors or cognitive functions (Poldrack, 2006). At the same time, studies have found that micrometer-scale spatial organization of neurons are associated with both distinct motor activities and fine scale activities (Dombeck et al., 2009; Hira et al., 2013; Wang et al., 2017). Our study supports this notion as our model makes prediction mainly based on spatial features of active neurons at the micrometer scale through deep learning.

The present study also provides some insight into the neurobiology of motor control. In rodents, the functional role of CFA and RFA are still unclear. The classical view is that the CFA and RFA are analogous to the primate primary motor cortex and pre-motor area, respectively (Rouiller et al., 1993) although this view of hierarchical organization has been challenged (Wang et al., 2017). Although the full functional role of RFA is not entirely clear, our results do support the notion that RFA is involved in motor planning, and in line with a recent study suggesting transient and partially distributed neural processing of choice and execution across different subregions of the motor cortex (Morandell and Huber, 2017). It would be interesting to compare the abilities of CFA and

RFA activities as derived by TPM in decoding the motion intention and movement-related parameters, based on the deep learning approach, for a better understanding of their functions. One main advantage of TPM is that it can provide single-cell spatial resolution and can faithfully record a larger number of neurons across days. However, the need to combine with genetically calcium indicators limits its application in human, although similar viral delivery methods have already been used in humans for gene therapy (Dunbar et al., 2018; Roelfsema et al., 2018). Nevertheless, TPM has revealed that task-related neuronal groups are activated in specific cortical locations and in precise temporal orders during a learned movement (e.g., Wang et al., 2017). Therefore, studying the spatial activation sequence of movement-related neurons by TPM and its application in movement prediction represents a promising approach in unraveling the neurobiological basis of motor control and motor learning in the future.

Deep learning significantly improves the capability of classical artificial neural networks by incorporating more layers enabling higher levels of abstraction. The particular CNN model ResNet employed in this study is based on a residual learning framework and has been shown to outperform human in object identification (He et al., 2016). A core advantage of deep learning is that instead of using human designed features, it learns task-related features solely from data. In this study, we only resized and normalized all input calcium images to produce suitable input size for the pre-trained CNN model and the same range of intensity for each of the inputs before training the model. We did not provide any guidance except labels.

There are several technical issues that are worth pointing out. First, there were minor 3D displacements in the recording field across days, which may affect the learning by the CNN. To ensure comparisons were made among the same recording fields, we excluded the recording days in which the percentages of common neurons was lower than 50%. As a result, the data from some recording days were removed. Second, a major constraint of deep learning is that it requires a large amount of data to train the model. Consequently, the training process is also time-consuming and it is well-known that full training of a deep CNN is difficult. Thus, we used the scheme of transfer learning in our study. This learning scheme is particularly useful when sufficient data are not available. The pre-trained ResNet18 model with the comprehensively annotated ImageNet data was used for the present task, sparing the need to obtain a much larger volume of calcium imaging data. Third, although our calcium imaging data are different from ImageNet, earlier layers of the pretrained model are expected to extract features, e.g., circles or edges, that also exist in the calcium imaging data. However, the higher-level features of the pretrained model are more specific to the details contained in ImageNet. Therefore, it is necessary to fine-tune the latter CNN layers and derive features that are suitable for calcium imaging data. This approach has been used in medical imaging applications, such as nodule detection and chest pathology identification (Greenspan et al., 2016). Also, based on the results of transfer learning in medical image analysis, fine-tuned CNNs always show better performance than that of the CNNs trained from scratch when the size of training set is small (Tajbakhsh et al., 2016).

A major limitation of the present study is the lack of data in an indifferent brain region during the exact reaching trials for comparison. This is due to the constraint in our 2-photon imaging system preventing us to sample a bigger field of view, or from two fields of view simultaneously. Nevertheless, the spatial calcium activity of RFA during ITI period that was presumably irrelevant or less relevant to movement plan possessed no predictive power. Also, within the RFA, there was spatial sub-regions that were more relevant to prediction outcome. These observations are in line with the conclusion we made.

Despite the limitations of our approach and the modest performance of the prediction model, to the best of our knowledge, this proof-of-principle study is the first work demonstrating that it is possible to infer movement plan from the motor cortex by applying deep learning method on microscopic imaging data. This approach may find applications in different fields including brain machine interface (O'Shea et al., 2017; Pandarinath et al., 2017). Deep learning thus represents a promising direction for future studies. With respect to further development, increasing the sample size should improve the performance of prediction, and reduction of over-fitting of data, as reflected by the discrepancy between the predicting power of the training and testing data sets. Furthermore, since firing dynamics of neuronal ensemble play a significant role in encoding movements (Masamizu et al., 2014; Peters et al., 2014; Li et al., 2017), incorporating information in the time domain would be useful for generating more detailed information, such as the movement trajectory, which was not addressed in the present study. Since the CNN model can automatically learn high-level abstractions from the data, studying the feature map of the CNN layers may also provide insight into movement planning and coding processes.

AUTHOR CONTRIBUTIONS

CL, DC, YK, and W-HY designed the study. CL, YK, and W-HY analyzed the data and wrote the manuscript. DC and XY conducted the animal experiments.

FUNDING

This work was supported by a Faculty of Medicine Direct Grant (2017.075) of the Chinese University of Hong Kong and a Hong Kong UGC Area of Excellence Grant (AoE/M-604/16).

ACKNOWLEDGMENTS

We would like to thank Prof. Xiaogang Wang and Mr. Shaoshuai Shi of the Chinese University of Hong Kong for the useful suggestions about deep learning programming. We also would like to thank our lab members Dr. Jenny Zhang and Dr. Rongchao Peng for very useful discussion.

REFERENCES

Andersen, R. A., Kellis, S., Klaes, C., and Aflalo, T. (2014). Toward more versatileand intuitive cortical brain-machine interfaces. *Curr. Biol.* 24, R885–R897. doi: 10.1016/j.cub.2014.07.068

Churchland, M., and Shenoy, K. (2007). Delay of Movement Caused by Disruption of Cortical Preparatory Activity. *J. Neurophysiol.* 97, 348–359. doi: 10.1152/jn.00808.2006

Cisek, P., and Kalaska, J. (2005). Neural Correlates of Reaching Decisions in Dorsal Premotor Cortex: Specification of Multiple Direction Choices and Final Selection of Action. *Neuron* 45, 801–814. doi: 10.1016/j.neuron.2005.01.027

Dombeck, D., Graziano, M., and Tank, D. (2009). Functional Clustering of Neurons in Motor Cortex Determined by Cellular Resolution Imaging in Awake Behaving Mice. *Journal of Neuroscience* 29, 13751–13760. doi: 10.1523/jneurosci.2985-09.2009

Dunbar, E., High, A., Joung, K., Kohn, B., Ozawa, K., and Sadelain, M. (2018). Gene therapy comes of age. *Science* 359, eaan4672. doi: 10.1126/science.aan4672

Filippini, M., Breveglieri, R., Akhras, M. A., Bosco, A., Chinellato, E., and Fattori, P. (2017). Decoding information for grasping from the macaque dorsomedial visual stream. *J. Neurosci.* 37, 4311–4322. doi: 10.1523/JNEUROSCI.3077-16.2017

Filippini, M., Breveglieri, R., Hadjidimitrakis, K., Bosco, A., and Fattori, P. (2018). Prediction of Reach Goals in Depth and Direction from the Parietal Cortex. *Cell Reports* 23, 725–732. doi: 10.1016/j.celrep.2018.03.090

Georgopolous, A., Kettner, R., and Schwartz, A. (1988). Primate motor cortex and free arm movements to visual targets in three-dimensional space. *II. Coding of the direction of movement by a neuronal population. J. Neurosci.* 8, 2928–2937. doi: 10.1523/JNEUROSCI.08-08-02928.1988

Greenspan, H., van Ginneken, B., and Summers, R. (2016). Guest Editorial Deep Learning in Medical Imaging: Overview and Future Promise of an Exciting New Technique. *IEEE Trans. Med. Imaging* 35, 1153–1159. doi: 10.1109/tmi.2016.2553401

He, K., Zhang, X., Ren, S., and Sun, J. (2016). "Deep residual learning for image recognition," in *Proceedings of the IEEE conference on computer vision and pattern recognition*, (Las Vegas, NV), 770–778. doi: 10.1109/CVPR.2016.90

Hira, R., Ohkubo, F., Ozawa, K., Isomura, Y., Kitamura, K., Kano, M., et al. (2013). Spatiotemporal Dynamics of Functional Clusters of Neurons in the Mouse Motor Cortex during a Voluntary Movement. *Journal of Neuroscience* 33, 1377–1390. doi: 10.1523/jneurosci.2550-12.2013

Hong, K., Naseer, N., and Kim, Y. (2015). Classification of prefrontal and motor cortex signals for three-class fNIRS–BCI. *Neurosci. Lett.* 587, 87–92. doi: 10.1016/j.neulet.2014.12.029

Kingma, D., and Ba, J. (2014). Adam: A method for stochastic optimization*. *arXiv*

Kuroki, S., Yoshida, T., Tsutsui, H., Iwama, M., Ando, R., Michikawa, T., et al. (2018). Excitatory neuronal hubs configure multisensory integration of slow waves in association cortex. *Cell Reports* 22, 2873–2885. doi: 10.1016/j.celrep.2018.02.056

Li, Q., Ko, H., Qian, Z.-M., Yan, L. Y. C, Chan, D., Arbuthnott, G., et al. (2017). Refinement of learned skilled movement representation in motor cortex deep output layer. *Nature Communications* 8, 15834. doi: 10.1038/ncomms15834

Lloyd, S. (1982). Least squares quantization in PCM. *IEEE Transactions on Information Theory* 28, 129–137. doi: 10.1109/tit.1982.1056489

Logothetis, N., Pauls, J., Augath, M., Trinath, T., and Oeltermann, A. (2001). Neurophysiological investigation of the basis of the fMRI signal. *Nature* 412, 150–157. doi: 10.1038/35084005

Masamizu, Y., Tanaka, Y. R., Tanaka, Y. H., Hira, R., Ohkubo, F., Kitamura, K., et al. (2014). Two distinct layer-specific dynamics of cortical ensemblesduring learning of a motor task. *Nat. Neurosci.* 17, 987–994. doi: 10.1038/nn.3739

Mohammed, A., Gritton, H., Tseng, H., Bucklin, M., Yao, Z., and Han, X. (2016). An integrative approach for analyzing hundreds of neurons in task performing mice using wide-field calcium imaging. *Scientific Reports* 6, 20986. doi: 10.1038/srep20986

Morandell, K., and Huber, D. (2017). The role of forelimb motor cortex areas in goal directed action in mice. *Scientific Reports* 7, 15759. doi: 10.1038/s41598-017-15835-15832

O'Shea, D., Trautmann, E., Chandrasekaran, C., Stavisky, S., Kao, J., Sahani, M., et al. (2017). The need for calcium imaging in nonhuman primates: New motor neuroscience and brain-machine interfaces. *Exp. Neurol.* 287, 437–451. doi: 10.1016/j.expneurol.2016.08.003

Pandarinath, C., Nuyujukian, P., Blabe, C., Sorice, B., Saab, J., and Willett, F. (2017). High performance communication by people with paralysis using an intracortical brain-computer interface. *Elife* 6, e18554. doi: 10.7554/elife.18554

Peters, A. J., Chen, S. X., and Komiyama, T. (2014). Emergence of reproducible spatiotemporal activity during motor learning. *Nature* 510, 263–267. doi: 10.1038/nature13235

Pnevmatikakis, E., Soudry, D., Gao, Y., Machado, T., Merel, J., Pfau, D., et al. (2016). Simultaneous Denoising, Deconvolution, and Demixing of Calcium Imaging Data. *Neuron* 89, 285–299. doi: 10.1016/j.neuron.2015.11.037

Poldrack, R. (2006). Can cognitive processes be inferred from neuroimaging data? *Trends in Cognitive Sciences* 10, 59–63. doi: 10.1016/j.tics.2005.12.004

Roelfsema, P., Denys, D., and Klink, P. (2018). Mind Reading and Writing: The Future of Neurotechnology. *Trends in Cognitive Sciences* 22, 598–610. doi: 10.1016/j.tics.2018.04.001

Rouiller, E., Moret, V., and Liang, F. (1993). Comparison of the Connectional Properties of the Two Forelimb Areas of the Rat Sensorimotor Cortex: Support for the Presence of a Premotor or Supplementary Motor Cortical Area. *Somatosensory & Motor Research* 10, 269–289. doi: 10.3109/08990229309028837

Russo, A., Bittner, S., Perkins, S., Seely, J., London, B., and Lara, A. (2018). Motor Cortex Embeds Muscle-like Commands in an Untangled Population Response. *Neuron* 97, 953.e–966.e. doi: 10.1016/j.neuron.2018.01.004

Shen, D., Wu, G., and Suk, H. (2017). Deep Learning in Medical Image Analysis. *Annu. Rev. Biomed. Eng.* 19, 221–248. doi: 10.1146/annurev-bioeng-071516-044442

Sussillo, D., Churchland, M., Kaufman, M., and Shenoy, K. (2015). A neural network that finds a naturalistic solution for the production of muscle activity. *Nat. Neurosci.* 18, 1025–1033. doi: 10.1038/nn.4042

Tajbakhsh, N., Shin, J., Gurudu, S., Hurst, R., Kendall, C., Gotway, M., et al. (2016). Convolutional Neural Networks for Medical Image Analysis: Full Training or Fine Tuning? *IEEE Transactions on Medical Imaging* 35, 1299–1312. doi: 10.1109/tmi.2016.2535302

Thevenaz, P., Ruttimann, U., and Unser, M. (1998). A pyramid approach to subpixel registration based on intensity. *IEEE Transactions on Image Processing* 7, 27–41. doi: 10.1109/83.650848

Wang, X., Liu, Y., Li, X., Zhang, Z., Yang, H., and Zhang, Y. (2017). Deconstruction of Corticospinal Circuits for Goal-Directed Motor Skills. *Cell* 171, 440.e–455.e. doi: 10.1016/j.cell.2017.08.014

Zhou, B., Khosla, A., Lapedriza, A., Oliva, A., and Torralba, A. (2016). "Learning Deep Features for Discriminative Localization," in *Proceedings of The IEEE Conference on Computer Vision and Pattern Recognition*, (Las Vegas, NV), 2921–2929. doi: 10.1109/CVPR.2016.319

Zhu, L., Lee, C., Margolis, D., and Najafizadeh, L. (2018). Decoding cortical brain states from widefield calcium imaging data using visibility graph. *Biomedical Optics Express* 9, 3017. doi: 10.1364/boe.9.003017

Zich, C., Debener, S., Kranczioch, C., Bleichner, M., Gutberlet, I., and De Vos, M. (2015). Real-time EEG feedback during simultaneous EEG-fMRI identifies the cortical signature of motor imagery. *Neuroimage* 114, 438–447. doi: 10.1016/j.neuroimage.2015.04.020

Conflict of Interest Statement: The authors declare that the research was conducted in the absence of any commercial or financial relationships that could be construed as a potential conflict of interest.

frontiers in Neural Circuits

MINI REVIEW
published: 15 March 2019
doi: 10.3389/fncir.2019.00017

Spiny Projection Neuron Dynamics in Toxin and Transgenic Models of Parkinson's Disease

*Yijuan Du and Steven M. Graves**

Department of Pharmacology, University of Minnesota, Minneapolis, MN, United States

Parkinson's disease (PD) is the most common neurodegenerative movement disorder that results from the progressive degeneration of substantia nigra pars compacta (SNc) dopamine (DA) neurons. As a consequence of SNc degeneration, the striatum undergoes DA depletion causing the emergence of motor symptoms such as resting tremor, bradykinesia, postural instability and rigidity. The primary cell type in the striatum is the spiny projection neuron (SPN), which can be divided into two subpopulations, the direct and indirect pathway; the direct pathway innervates the substantia nigra pars reticulata and internal segment of the globus pallidus whereas the indirect pathway innervates the external segment of the globus pallidus. Proper control of movement requires a delicate balance between the two pathways; in PD dysfunction occurs in both cell types and impairments in synaptic plasticity are found in transgenic and toxin rodent models of PD. However, it is difficult to ascertain how the striatum adapts during different stages of PD, particularly during premotor stages. In the natural evolution of PD, patients experience years of degeneration before motor symptoms arise. To model premotor PD, partial lesion rodents and transgenic mice demonstrating progressive nigral degeneration have been and will continue to be assets to the field. Although, rodent models emulating premotor PD are not fully asymptomatic; modest reductions in striatal DA result in cognitive impairments. This mini review article gives a brief summary of SPN dynamics in animal models of PD.

Keywords: Parkinson's disease, striatum, direct pathway, indirect pathway, synaptic plasticity

OPEN ACCESS

Edited by:
Jing-Ning Zhu,
Nanjing University, China

Reviewed by:
M. Gustavo Murer,
Universidad de Buenos Aires, Argentina
Gordon William Arbuthnott,
Okinawa Institute of Science and Technology Graduate University, Japan

****Correspondence:***
Steven M. Graves
gravess@umn.edu

Received: *08 January 2019*
Accepted: *28 February 2019*
Published: *15 March 2019*

Citation:
Du Y and Graves SM (2019) Spiny Projection Neuron Dynamics in Toxin and Transgenic Models of Parkinson's Disease. Front. Neural Circuits 13:17. doi: 10.3389/fncir.2019.00017

INTRODUCTION

Parkinson's disease (PD) is the most common neurodegenerative movement disorder with more than six million patients worldwide (GBD 2016 Parkinson's Disease Collaborators, 2018). PD is largely characterized by the progressive degeneration of substantia nigra pars compacta (SNc) dopamine (DA) neurons that innervate the striatum. The striatum is a critical basal ganglia nucleus involved in initiating and regulating goal-directed movement; in PD, this region undergoes progressive DA depletion leading to the hallmark motor symptoms, i.e., resting tremor, bradykinesia, postural instability, and rigidity. The striatum itself entails a degree of cellular heterogeneity but is primarily dominated by GABAergic spiny projection neurons (SPNs). These SPNs have dendritic arbors heavily populated with spines chiefly consisting of corticostriatal and thalamostriatal circuitry (Bolam et al., 2000; Villalba et al., 2009; Smith et al., 2014). SPNs can

be subdivided into two distinct populations based on the DA receptor expression profile and projection patterns. SPNs that express D2 DA receptors project to the external segment of the globus pallidus forming the indirect pathway (iSPNs) and SPNs that express D1 DA receptors project to the substantia nigra pars reticulata and internal segment of the globus pallidus forming the direct pathway (dSPNs). DA effects on each SPN population are distinct; in iSPNs D2 receptor activation engages $G_{i/o}$ proteins, decreases intrinsic excitability and promotes long-term depression (LTD); in contrast D1 receptors in dSPNs couple to G_{olf}, increase intrinsic excitability, and promote long-term potentiation (LTP; Surmeier et al., 2007). Animal models of PD have shed light on a number of adaptations that arise in response to DA loss. In this concise review we focus on SPN dynamics in animal models of PD.

SPN DYNAMICS AND TRANSGENIC MODELS

Multiple genes have been implicated in PD (SNCA, LRRK2, PRKN, PINK1, and PARK7) and incorporated into transgenic rats and/or mice. A consistent finding across transgenic models of PD is impaired synaptic plasticity. Both dSPN and iSPNs are capable of undergoing forms of cellular learning and memory whereby synapses are weakened (LTD) or strengthened (LTP). In the striatum LTD is selective for corticostriatal circuits (Wu et al., 2015) and induction is achieved post-synaptically with presynaptic expression that is dependent on endocannabinoid signaling. LTD deficits are consistently reported in multiple transgenic models including PINK1 knockout (Kitada et al., 2007; Madeo et al., 2016), LRRK2 knockout (Chou et al., 2014) and A53T synuclein mouse models (Kurz et al., 2010; Tozzi et al., 2012). It is unclear whether the LTD deficit is specific to iSPNs or dSPNs. Some have argued that only iSPNs are capable of undergoing LTD, and thus the deficit only impacts iSPNs (Kreitzer and Malenka, 2007). However, others report LTD in iSPNs and dSPNs (Wang et al., 2006; Shen et al., 2008; Bagetta et al., 2011; Trusel et al., 2015; Wu et al., 2015). The disparity is likely a consequence of intrastriatal electrical stimulation evoking DA release that stimulates D1 receptors, thereby occluding LTD induction. Consistent with this, DA receptor activation uncovers SPN selectivity for LTD (Wu et al., 2015). The impairment of LTD in parkinsonian transgenic mice is a consequence of diminished D2 receptor stimulation resulting in reduced endocannabinoid production but also decreased CB1 receptor expression (Kurz et al., 2010; Madeo et al., 2016); boosting these impairments through CB1 recepetor agonism, increasing DA, or D2 agonism rescues LTD (Kitada et al., 2007; Chou et al., 2014; Madeo et al., 2016). The ability to rescue with D2 agonism may suggest selectivity for iSPNs; however, D2 receptor activation is also involved in dSPN LTD. D2 stimulation on cholinergic interneurons suppresses M1 receptor signaling to dis-inhibit L-type calcium channels allowing for LTD in dSPNs (Wang et al., 2006; Augustin et al., 2018). Nevertheless, based on the classical basal ganglia model it would hypothesize that this impairment is specific to iSPNs. This model posits that the dSPN circuit is the "go" pathway and the iSPN circuit is the "no-go" pathway; dSPN activity thus promotes and iSPN activity suppresses motor activity (Surmeier et al., 2007). In this framework it would be expected that the LTD deficit would be selective for iSPNs thereby biasing striatal output in favor of the indirect "no-go" pathway and motor suppression; consistent with this, deletion of D2 receptors, effectively removing DA-mediated inhibition, in iSPNs impairs motor activity (Lemos et al., 2016; Bello et al., 2017) as does optogenetic stimulation of iSPNs (Kravitz et al., 2010). Further supporting indirect pathway dominance in PD, corticostriatal responses in a lesion model are enhanced and diminished in iSPNs and dSPNs, respectively (Flores-Barrera et al., 2010; Escande et al., 2016), and optogenetic stimulation of dSPNs in parkinsonian mice improves motor function (Kravitz et al., 2010). However, more recent studies demonstrate that coordinated motor activity requires concurrent activation of both iSPN and dSPN populations (Cui et al., 2013; Freeze et al., 2013; Tecuapetla et al., 2014) making it less certain whether the LTD deficits would be pathway specific. Generating transgenic lines with SPN cell-type reporters will be necessary to further dissect circuit-specific changes but it is also important to compare with other PD models independent of genetic mutations.

The generation of genetic models has certainly advanced the understanding of PD; however, these models do not fully emulate the disease state and over 90% of PD cases (late onset) are idiopathic with no known genetic association (Puschmann, 2013). Moreover, transgenic models do not develop neurodegeneration with a few exceptions. In the G2019S LRRK2 model, SNc degeneration (∼40%–50%) is reported at 12–16 months of age (Chen et al., 2012) whereas others report no (Yue et al., 2015; Sloan et al., 2016) or very mild (∼20%) degeneration (Ramonet et al., 2011) even in 18–21-month-old animals. Reduced tyrosine hydroxylase staining in the SNc is observed in the α-synuclein A53T model at 12 months of age but the magnitude was not quantified (Yamasaki et al., 2016). In contrast, others report no degeneration in A53T mice (Gispert et al., 2003; Kurz et al., 2010). PINK1 animals show no degeneration at 8–9 months (Kitada et al., 2007). Similarly, Parkin deficient animals have no SNc cell loss even at 24 months of age (Goldberg et al., 2003) although animals expressing the Parkin-Q311X mutation show SNc DA neuron loss (40%) at 16 months of age (Lu et al., 2009). These reports support the notion that genetic perturbations increase the vulnerability of SNc DA neurons but are not sufficient for degeneration. SNc degeneration is also not necessary for parkinsonian symptoms. Neuroleptic treatment results in parkinsonism due to D2 receptor antagonism thereby disinhibiting iSPNs and cholinergic interneurons (Kharkwal et al., 2016); chronic neuroleptic treatment even manifests some of the same functional and anatomical changes (Sebel et al., 2017) observed in PD models (Fieblinger et al., 2014). Transgenic models have also not reproduced the changes in SPN dendritic arborization or spine density.

One of the most consistent and reproducible findings in rodent models, non-human primates, and post mortem tissue from patients is a robust loss of spines on SPNs (McNeill et al., 1988; Ingham et al., 1989; Stephens et al., 2005; Zaja-Milatovic et al., 2005; Day et al., 2006; Villalba et al., 2009; Zhang et al., 2013;

Anaya-Martínez et al., 2014; Fieblinger et al., 2014; Nishijima et al., 2014; Suárez et al., 2014; Toy et al., 2014; Suarez et al., 2016; Bentea et al., 2017; Gagnon et al., 2017; Gomez et al., 2019); this PD associated anatomical change has not been found (Matikainen-Ankney et al., 2016) or is yet to be reported in transgenic animals with the exception of the Pitx3$^{-/-}$ mouse (Suarez et al., 2018). Both dSPNs and iSPNs of Pitx3$^{-/-}$ mice have decreased spine density. However, Pitx3 is not a gene associated with PD; it is involved in the development of DA neurons. In Pitx3$^{-/-}$ animals, most SNc DA neurons fail to fully differentiate and do not innervate the striatum (Hwang et al., 2003). Thus it is rather a model with neurodevelopmental deficits as opposed to a parkinsonian model of degeneration. The absence of spine pruning in transgenic models of PD may relate to the fact that spine pruning seems to be associated with the severity of DA loss (Villalba et al., 2009; Suárez et al., 2014) and sufficient depletion may not be reached in transgenic mice. The models that reproducibly induce robust degeneration of SNc DA neurons are the toxin models. Toxin models such as the 6-OHDA and MPTP models of PD are far from perfect but comparison with evidence from transgenic models provides a means to determine what is consistent across PD models and thus most likely to be translatable to the human condition.

SPN DYNAMICS AND TOXIN MODELS

6-OHDA produces a near complete degeneration of DA neurons when injected into the medial forebrain bundle or SNc whereas the same result can be achieved with systemic injection of MPTP. Both toxins produce a rapid and robust loss of DA neurons with overt motor impairment that can be ameliorated by levodopa administration. Consistent with evidence from human post-mortem tissue (McNeill et al., 1988; Stephens et al., 2005; Zaja-Milatovic et al., 2005), both MPTP and 6-OHDA lesioned non-human primates and rodents (Ingham et al., 1989; Day et al., 2006; Villalba et al., 2009; Zhang et al., 2013; Anaya-Martínez et al., 2014; Fieblinger et al., 2014; Nishijima et al., 2014; Suárez et al., 2014; Toy et al., 2014; Ueno et al., 2014; Suarez et al., 2016; Gagnon et al., 2017; Graves and Surmeier, 2019) show reduced SPN dendritic arborization and robust spine pruning in the striatum. However, whether spine pruning is selective for iSPN or dSPNs is debatable. Some report selective spine pruning in iSPNs (Day et al., 2006; Fieblinger et al., 2014; Nishijima et al., 2014); others report decreased spine density in both iSPNs and dSPNs (Villalba et al., 2009; Suárez et al., 2014; Toy et al., 2014; Suarez et al., 2016; Gagnon et al., 2017; Gomez et al., 2019) and it remains to be seen what might account for the disparate findings. One potential variable is the time post-lesion at which investigations are conducted; dSPN spine density is unchanged 30 days post-6-OHDA lesion but decreased 60 days post-lesion (Graves and Surmeier, 2019). The spines of both iSPNs and dSPNs are the sites of glutamatergic axospinous circuitry; this is predominantly corticostriatal circuitry with the remaining subset of axospinous synapses belonging to thalamostriatal circuits. Spine pruning primarily reflects a loss of corticostriatal axospinous synapses (Zhang et al., 2013; Fieblinger et al., 2014; Bentea et al., 2017). Paradoxically, lesioning the motor cortex prevents and even reverses spine loss in 6-OHDA lesioned rats, an effect also achieved by mGluR2/3 antagonism (Garcia et al., 2010). In iSPNs M1 receptors increase dendritic excitability and contribute to spine pruning (Shen et al., 2007). In contrast, M4 signaling in dSPNs promotes LTD at axospinous synapses (Shen et al., 2015) but it is unclear whether this modulates dSPN spine dynamics in PD models. While the transgenic and toxin models disagree when it comes to SPN anatomical changes, consensus is found with synaptic plasticity. Similar to findings in transgenic models, LTD is impaired in both MPTP treated mice (Chen et al., 2008) and monkeys (Quik et al., 2006). LTD is also impaired in iSPNs from reserpinized and 6-OHDA lesioned mice (Kreitzer and Malenka, 2007; Shen et al., 2008; Thiele et al., 2014); rescuing iSPN LTD improves motor impairments (Kreitzer and Malenka, 2007). Based on the above data the LTD impairments in transgenic models are also likely specific to iSPNs. In contrast, LTP is impaired in dSPNs, consistent with a dis-inhibition of cholinergic interneurons and increased M4 stimulation; inhibition of cholinergic interneurons, M4 antagonism, or D1 agonism improves motor performance (Shen et al., 2008; Paille et al., 2010; Thiele et al., 2014; Ztaou et al., 2016). Agonism at D2 receptors also restores impaired LTD in iSPNs similar to the restoration in transgenic mice, whereas D1 receptor agonism restores LTP in dSPNs (Shen et al., 2008); restoring plasticity impairments in both SPN populations also improves motor function (Picconi et al., 2003; Thiele et al., 2014; Trusel et al., 2015).

In addition to spine pruning and impairments of synaptic plasticity, there is a rearrangement of excitatory synapse machinery. MPTP lesioning increases calcium permeable AMPA receptors in iSPNs (VanLeeuwen et al., 2010; Kintz et al., 2013). This is particularly intriguing given the problems with synaptic plasticity in parkinsonian animals; incorporation of calcium permeable AMPA receptors allows for an NMDA-independent form of LTP (Mameli et al., 2011). In this framework iSPNs would have a lower threshold to induce LTP and without sufficient DA to induce LTD this would contribute to indirect pathway dominance.

SPN DYNAMICS PRECEDING MOTOR DYSFUNCTION

By the time patients with PD are diagnosed and experiencing motor symptoms, >50% of SNc DA neurons have been lost and striatal levels of DA reduced by >60% (Tissingh et al., 1998; Hilker et al., 2005; Cheng et al., 2010). The premotor/prodromal phase is estimated to consist of a 4–6 year period prior to the emergence of motor symptoms and diagnosis (Fearnley and Lees, 1991; Morrish et al., 1998; Marek et al., 2001). During this premotor phase there are likely a number of adaptations occurring within the striatum to compensate for the loss of DA neurons. Human data demonstrate decreased DA reuptake and enhanced DA synthesis in early PD (Nandhagopal et al., 2011); how circuit function is altered and whether alterations are compensatory or pathological is much less clear and an important gap that needs to be addressed. Several groups have made efforts to investigate the premotor phase of PD

either through transgenic strategies or partial lesioning of the nigrostriatal system.

PINK1 knockout heterozygous mice are motorically asymptomatic despite having ∼40% reduction in extracellular DA (Madeo et al., 2014). These animals exhibit a selective deficit in LTP that is restored by drugs that increase striatal DA including amphetamine, tyramine and selegiline and partially restored by levodopa but not a D1 agonist (Madeo et al., 2014); however, D1 agonsim does restore LTP in homozygous knockout mice (Kitada et al., 2007). In partial 6-OHDA lesioned rats with modest motor impairments, LTP deficits and motor symptoms are also rescued by D1 agonism (Paille et al., 2010). It is unclear why in heterozygous PINK1 knockout LTP is not rescued by D1 stimulation but data support a DA-dependent deficit. Given that LTP in iSPNs utilizes A_{2A} receptors for LTP and D2 receptors promote LTD, it is likely that the LTP deficit is dSPN specific. If this is the case it indicates that the balance between iSPN and dSPN circuit function manifests well before motor symptoms. Consistent with this, in animals that receive a partial 6-OHDA lesion and do not present with motor dysfunction, there is a reduced response in dSPNs to cortical stimulation (Escande et al., 2016). In mice with motor impairment, iSPN corticostriatal responses are increased and dSPN corticostriatal responses further reduced (Escande et al., 2016). Taken together this suggests that dSPN circuits are the first to be impacted by moderate DA depletion and although there are not motor symptoms, animals with partial DA depletion show anxiety- and depression-like behaviors, as well as cognitive impairments (Tadaiesky et al., 2008, 2010; Bonito-Oliva et al., 2014a,b; Tozzi et al., 2016; Loiodice et al., 2018; Ztaou et al., 2018).

The 6-OHDA partial lesion model with 40% DA depletion exhibits impaired spatial object recognition (Ztaou et al., 2018) but with 75% DA depletion, novel object recognition is also impaired (Bonito-Oliva et al., 2014b; Loiodice et al., 2018). Hippocampal circuitry contributes to spatial and recognition memory and with partial lesions, hippocampal DA is reduced and hippocampal LTP impaired (Bonito-Oliva et al., 2014b). Levodopa or D1 agonism, but not D2 agonism rescues the deficits in novel object recognition and hippocampal LTP (Bonito-Oliva et al., 2014b; Loiodice et al., 2018) suggesting that early dysfunction not only occurs in dSPN circuits but are manifesting in D1-dependent systems that extend beyond the striatum. Similar cognitive deficits have also been observed in alpha-synuclein overexpression (Subramaniam et al., 2018). MitoPark mice have progressive degeneration of DA neurons (Ekstrand et al., 2007) with motor impairment beginning at 12 weeks of age (Galter et al., 2010). Preceding the onset of motor symptoms, 8-week-old MitoPark mice also perform poorly in the novel object recognition test and have impaired learning in a spatial task (Li et al., 2013). These cognitive impairments arise at a time when there is a DA deficit but well before the emergence of motor dysfunction.

Impaired striatal function may contribute to impaired spatial learning. MPTP partial lesioned animals are impaired in learning the constant-start version of the water maze task, which involves a cue-dependent navigation strategy within the striatum but performance is unaltered using a variable-start version of the task, which is more dependent on a hippocampal spatial navigation strategy (Da Cunha et al., 2006). The spatial task employed by Li et al. (2013) also used a constant start location paradigm. Therefore, the learning deficit could reflect a striatal dysfunction due to reduced D1 signaling in dSPNs.

CONCLUSION AND FUTURE DIRECTIONS

There is no perfect model system to study PD; by examining key findings from the diverse set of preclinical models two themes emerge. First, motorically impaired PD models have impaired synaptic function, particularly in the form of LTP and LTD and these impairments are cell-type specific with LTP being impaired in dSPNs and LTD impaired in iSPNs. Second, dSPNs appear to be the first SPN population to undergo functional alterations in response to moderate DA depletion. At this disease stage subjects are not motorically impaired but are cognitively impaired which may be a combination of dysfunction in dSPN circuits as well as extrastriatal D1 systems. Moving forward it will be important to better investigate changes during premotor phases to understand how the striatum and other DA reliant circuits adapt and deteriorate during disease progression. Moreover, it will be critical to determine what adaptations contribute to motor and non-motor symptoms and which, if any, are fighting to maintain normative function so that treatment strategies can be designed to directly target maladaptive plasticity and support or strengthen the compensatory changes.

AUTHOR CONTRIBUTIONS

SG and YD drafted and edited the manuscript. Both authors approved the final manuscript.

ACKNOWLEDGMENTS

We wish to thank the University of Minnesota Department of Pharmacology and Institute for Translational Neuroscience for financial support.

REFERENCES

Anaya-Martínez, V., Gutierrez-Valdez, A. L., Ordoñez-Librado, J. L., Montiel-Flores, E., Sánchez-Betancourt, J., Sánchez Vázquez del Mercado, C., et al. (2014). The presence of perforated synapses in the striatum after dopamine depletion, is this a sign of maladaptive brain plasticity? *Microscopy* 63, 427–435. doi: 10.1093/jmicro/dfu032

Augustin, S. M., Chancey, J. H., and Lovinger, D. M. (2018). Dual dopaminergic regulation of corticostriatal plasticity by cholinergic interneurons and indirect pathway medium spiny neurons. *Cell Rep.* 24, 2883–2893. doi: 10.1016/j.celrep.2018.08.042

Bagetta, V., Picconi, B., Marinucci, S., Sgobio, C., Pendolino, V., Ghiglieri, V., et al. (2011). Dopamine-dependent long-term depression is expressed in striatal spiny neurons of both direct and indirect pathways: implications for

Parkinson's disease. *J. Neurosci.* 31, 12513–12522. doi: 10.1523/JNEUROSCI.2236-11.2011

Bello, E. P., Casas-Cordero, R., Galiñanes, G. L., Casey, E., Belluscio, M. A., Rodriguez, V., et al. (2017). Inducible ablation of dopamine D2 receptors in adult mice impairs locomotion, motor skill learning and leads to severe parkinsonism. *Mol. Psychiatry* 22, 595–604. doi: 10.1038/mp.2016.105

Bentea, E., Moore, C., Deneyer, L., Verbruggen, L., Churchill, M. J., Hood, R. L., et al. (2017). Plastic changes at corticostriatal synapses predict improved motor function in a partial lesion model of Parkinson's disease. *Brain Res. Bull.* 130, 257–267. doi: 10.1016/j.brainresbull.2017.02.005

Bolam, J. P., Hanley, J. J., Booth, P. A., and Bevan, M. D. (2000). Synaptic organisation of the basal ganglia. *J. Anat.* 196, 527–542. doi: 10.1046/j.1469-7580.2000.19640527.x

Bonito-Oliva, A., Masini, D., and Fisone, G. (2014a). A mouse model of non-motor symptoms in Parkinson's disease: focus on pharmacological interventions targeting affective dysfunctions. *Front. Behav. Neurosci.* 8:290. doi: 10.3389/fnbeh.2014.00290

Bonito-Oliva, A., Pignatelli, M., Spigolon, G., Yoshitake, T., Seiler, S., Longo, F., et al. (2014b). Cognitive impairment and dentate gyrus synaptic dysfunction in experimental parkinsonism. *Biol. Psychiatry* 75, 701–710. doi: 10.1016/j.biopsych.2013.02.015

Chen, Y. H., Harvey, B. K., Hoffman, A. F., Wang, Y., Chiang, Y. H., and Lupica, C. R. (2008). MPTP-induced deficits in striatal synaptic plasticity are prevented by glial cell line-derived neurotrophic factor expressed via an adeno-associated viral vector. *FASEB J.* 22, 261–275. doi: 10.1096/fj.07-8797com

Chen, C. Y., Weng, Y. H., Chien, K. Y., Lin, K. J., Yeh, T. H., Cheng, Y. P., et al. (2012). (G2019S) LRRK2 activates MKK4-JNK pathway and causes degeneration of SN dopaminergic neurons in a transgenic mouse model of PD. *Cell Death Differ.* 19, 1623–1633. doi: 10.1038/cdd.2012.42

Cheng, H. C., Ulane, C. M., and Burke, R. E. (2010). Clinical progression in Parkinson disease and the neurobiology of axons. *Ann. Neurol.* 67, 715–725. doi: 10.1002/ana.21995

Chou, J. S., Chen, C. Y., Chen, Y. L., Weng, Y. H., Yeh, T. H., Lu, C. S., et al. (2014). (G2019S) LRRK2 causes early-phase dysfunction of SNpc dopaminergic neurons and impairment of corticostriatal long-term depression in the PD transgenic mouse. *Neurobiol. Dis.* 68, 190–199. doi: 10.1016/j.nbd.2014.04.021

Cui, G., Jun, S. B., Jin, X., Pham, M. D., Vogel, S. S., Lovinger, D. M., et al. (2013). Concurrent activation of striatal direct and indirect pathways during action initiation. *Nature* 494, 238–242. doi: 10.1038/nature11846

Da Cunha, C., Silva, M. H., Wietzikoski, S., Wietzikoski, E. C., Ferro, M. M., Kouzmine, I., et al. (2006). Place learning strategy of substantia nigra pars compacta-lesioned rats. *Behav. Neurosci.* 120, 1279–1284. doi: 10.1037/0735-7044.120.6.1279

Day, M., Wang, Z., Ding, J., An, X., Ingham, C. A., Shering, A. F., et al. (2006). Selective elimination of glutamatergic synapses on striatopallidal neurons in Parkinson disease models. *Nat. Neurosci.* 9, 251–259. doi: 10.1038/nn1632

Ekstrand, M. I., Terzioglu, M., Galter, D., Zhu, S., Hofstetter, C., Lindqvist, E., et al. (2007). Progressive parkinsonism in mice with respiratory-chain-deficient dopamine neurons. *Proc. Natl. Acad. Sci. U S A* 104, 1325–1330. doi: 10.1073/pnas.0605208103

Escande, M. V., Taravini, I. R., Zold, C. L., Belforte, J. E., and Murer, M. G. (2016). Loss of homeostasis in the direct pathway in a mouse model of asymptomatic Parkinson's disease. *J. Neurosci.* 36, 5686–5698. doi: 10.1523/JNEUROSCI.0492-15.2016

Fearnley, J. M., and Lees, A. J. (1991). Ageing and Parkinson's disease: substantia nigra regional selectivity. *Brain* 114, 2283–2301. doi: 10.1093/brain/114.5.2283

Fieblinger, T., Graves, S. M., Sebel, L. E., Alcacer, C., Plotkin, J. L., Gertler, T. S., et al. (2014). Cell type-specific plasticity of striatal projection neurons in parkinsonism and L-DOPA-induced dyskinesia. *Nat. Commun.* 5:5316. doi: 10.1038/ncomms6316

Flores-Barrera, E., Vizcarra-Chacón, B. J., Tapia, D., Bargas, J., and Galarraga, E. (2010). Different corticostriatal integration in spiny projection neurons from direct and indirect pathways. *Front. Syst. Neurosci.* 4:15. doi: 10.3389/fnsys.2010.00015

Freeze, B. S., Kravitz, A. V., Hammack, N., Berke, J. D., and Kreitzer, A. C. (2013). Control of basal ganglia output by direct and indirect pathway projection neurons. *J. Neurosci.* 33, 18531–18539. doi: 10.1523/JNEUROSCI.1278-13.2013

Gagnon, D., Petryszyn, S., Sanchez, M. G., Bories, C., Beaulieu, J. M., De Koninck, Y., et al. (2017). Striatal neurons expressing D_1 and D_2 receptors are morphologically distinct and differently affected by dopamine denervation in mice. *Sci. Rep.* 7:41432. doi: 10.1038/srep41432

Galter, D., Pernold, K., Yoshitake, T., Lindqvist, E., Hoffer, B., Kehr, J., et al. (2010). MitoPark mice mirror the slow progression of key symptoms and L-DOPA response in Parkinson's disease. *Genes Brain Behav.* 9, 173–181. doi: 10.1111/j.1601-183x.2009.00542.x

Garcia, B. G., Neely, M. D., and Deutch, A. Y. (2010). Cortical regulation of striatal medium spiny neuron dendritic remodeling in parkinsonism: modulation of glutamate release reverses dopamine depletion-induced dendritic spine loss. *Cereb. Cortex* 20, 2423–2432. doi: 10.1093/cercor/bhp317

GBD 2016 Parkinson's Disease Collaborators. (2018). Global, regional, and national burden of Parkinson's disease, 1990–2016: a systematic analysis for the Global Burden of Disease Study 2016. *Lancet Neurol.* 17, 939–953. doi: 10.1016/S1474-4422(18)30295-3

Gispert, S., Del Turco, D., Garrett, L., Chen, A., Bernard, D. J., Hamm-Clement, J., et al. (2003). Transgenic mice expressing mutant A53T human α-synuclein show neuronal dysfunction in the absence of aggregate formation. *Mol. Cell. Neurosci.* 24, 419–429. doi: 10.1016/s1044-7431(03)00198-2

Goldberg, M. S., Fleming, S. M., Palacino, J. J., Cepeda, C., Lam, H. A., Bhatnagar, A., et al. (2003). Parkin-deficient mice exhibit nigrostriatal deficits but not loss of dopaminergic neurons. *J. Biol. Chem.* 278, 43628–43635. doi: 10.1074/jbc.M308947200

Gomez, G., Escande, M. V., Suarez, L. M., Rela, L., Belforte, J. E., Moratalla, R., et al. (2019). Changes in dendritic spine density and inhibitory perisomatic connectivity onto medium spiny neurons in L-Dopa-induced dyskinesia. *Mol. Neurobiol.* doi: 10.1007/s12035-019-1515-4 [Epub ahead of print].

Graves, S. M., and Surmeier, D. J. (2019). Delayed spine pruning of direct pathway spiny projection neurons in a mouse model of Parkinson's disease. *Front. Cell. Neurosci.* 13:32. doi: 10.3389/fncel.2019.00032

Hilker, R., Schweitzer, K., Coburger, S., Ghaemi, M., Weisenbach, S., Jacobs, A. H., et al. (2005). Nonlinear progression of Parkinson disease as determined by serial positron emission tomographic imaging of striatal fluorodopa F 18 activity. *Arch. Neurol.* 62, 378–382. doi: 10.1001/archneur.62.3.378

Hwang, D. Y., Ardayfio, P., Kang, U. J., Semina, E. V., and Kim, K. S. (2003). Selective loss of dopaminergic neurons in the substantia nigra of Pitx3-deficient aphakia mice. *Mol. Brain Res.* 114, 123–131. doi: 10.1016/s0169-328x(03)00162-1

Ingham, C. A., Hood, S. H., and Arbuthnott, G. W. (1989). Spine density on neostriatal neurones changes with 6-hydroxydopamine lesions and with age. *Brain Res.* 503, 334–338. doi: 10.1016/0006-8993(89)91686-7

Kharkwal, G., Brami-Cherrier, K., Lizardi-Ortiz, J. E., Nelson, A. B., Ramos, M., Del Barrio, D., et al. (2016). Parkinsonism driven by antipsychotics originates from dopaminergic control of striatal cholinergic interneurons. *Neuron* 91, 67–78. doi: 10.1016/j.neuron.2016.06.014

Kintz, N., Petzinger, G. M., Akopian, G., Ptasnik, S., Williams, C., Jakowec, M. W., et al. (2013). Exercise modifies α-amino-3-hydroxy-5-methyl-4-isoxazolepropionic acid receptor expression in striatopallidal neurons in the 1-methyl-4-phenyl-1,2,3,6-tetrahydropyridine-lesioned mouse. *J. Neurosci. Res.* 91, 1492–1507. doi: 10.1002/jnr.23260

Kitada, T., Pisani, A., Porter, D. R., Yamaguchi, H., Tscherter, A., Martella, G., et al. (2007). Impaired dopamine release and synaptic plasticity in the striatum of PINK1-deficient mice. *Proc. Natl. Acad. Sci. U S A* 104, 11441–11446. doi: 10.1073/pnas.0702717104

Kravitz, A. V., Freeze, B. S., Parker, P. R., Kay, K., Thwin, M. T., Deisseroth, K., et al. (2010). Regulation of parkinsonian motor behaviours by optogenetic control of basal ganglia circuitry. *Nature* 466, 622–626. doi: 10.1038/nature09159

Kreitzer, A. C., and Malenka, R. C. (2007). Endocannabinoid-mediated rescue of striatal LTD and motor deficits in Parkinson's disease models. *Nature* 445, 643–647. doi: 10.1038/nature05506

Kurz, A., Double, K. L., Lastres-Becker, I., Tozzi, A., Tantucci, M., Bockhart, V., et al. (2010). A53T-α-synuclein overexpression impairs dopamine signaling and striatal synaptic plasticity in old mice. *PLoS One* 5:e11464. doi: 10.1371/journal.pone.0011464

Lemos, J. C., Friend, D. M., Kaplan, A. R., Shin, J. H., Rubinstein, M., Kravitz, A. V., et al. (2016). Enhanced GABA transmission drives bradykinesia following loss

of dopamine D2 receptor signaling. *Neuron* 90, 824–838. doi: 10.1016/j.neuron.2016.04.040

Li, X., Redus, L., Chen, C., Martinez, P. A., Strong, R., Li, S., et al. (2013). Cognitive dysfunction precedes the onset of motor symptoms in the MitoPark mouse model of Parkinson's disease. *PLoS One* 8:e71341. doi: 10.1371/journal.pone.0071341

Loiodice, S., Wing Young, H., Rion, B., Méot, B., Montagne, P., Denibaud, A. S., et al. (2018). Implication of nigral dopaminergic lesion and repeated L-dopa exposure in neuropsychiatric symptoms of Parkinson's disease. *Behav. Brain Res.* 360, 120–127. doi: 10.1016/j.bbr.2018.12.007

Lu, X. H., Fleming, S. M., Meurers, B., Ackerson, L. C., Mortazavi, F., Lo, V., et al. (2009). Bacterial artificial chromosome transgenic mice expressing a truncated mutant parkin exhibit age-dependent hypokinetic motor deficits, dopaminergic neuron degeneration, and accumulation of proteinase K-resistant α-synuclein. *J. Neurosci.* 29, 1962–1976. doi: 10.1523/JNEUROSCI.5351-08.2009

Madeo, G., Schirinzi, T., Maltese, M., Martella, G., Rapino, C., Fezza, F., et al. (2016). Dopamine-dependent CB1 receptor dysfunction at corticostriatal synapses in homozygous PINK1 knockout mice. *Neuropharmacology* 101, 460–470. doi: 10.1016/j.neuropharm.2015.10.021

Madeo, G., Schirinzi, T., Martella, G., Latagliata, E. C., Puglisi, F., Shen, J., et al. (2014). PINK1 heterozygous mutations induce subtle alterations in dopamine-dependent synaptic plasticity. *Mov. Disord.* 29, 41–53. doi: 10.1002/mds.25724

Mameli, M., Bellone, C., Brown, M. T., and Lüscher, C. (2011). Cocaine inverts rules for synaptic plasticity of glutamate transmission in the ventral tegmental area. *Nat. Neurosci.* 14, 414–416. doi: 10.1038/nn.2763

Marek, K., Innis, R., van Dyck, C., Fussell, B., Early, M., Eberly, S., et al. (2001). [123I]β-CIT SPECT imaging assessment of the rate of Parkinson's disease progression. *Neurology* 57, 2089–2094. doi: 10.1212/wnl.57.11.2089

Matikainen-Ankney, B. A., Kezunovic, N., Mesias, R. E., Tian, Y., Williams, F. M., Huntley, G. W., et al. (2016). Altered development of synapse structure and function in striatum caused by Parkinson's disease-Linked LRRK2–G2019S mutation. *J. Neurosci.* 36, 7128–7141. doi: 10.1523/JNEUROSCI.3314-15.2016

McNeill, T. H., Brown, S. A., Rafols, J. A., and Shoulson, I. (1988). Atrophy of medium spiny I striatal dendrites in advanced Parkinson's disease. *Brain Res.* 455, 148–152. doi: 10.1016/0006-8993(88)90124-2

Morrish, P. K., Rakshi, J. S., Bailey, D. L., Sawle, G. V., and Brooks, D. J. (1998). Measuring the rate of progression and estimating the preclinical period of Parkinson's disease with [18F]dopa PET. *J. Neurol. Neurosurg. Psychiatry* 64, 314–319. doi: 10.1136/jnnp.64.3.314

Nandhagopal, R., Kuramoto, L., Schulzer, M., Mak, E., Cragg, J., McKenzie, J., et al. (2011). Longitudinal evolution of compensatory changes in striatal dopamine processing in Parkinson's disease. *Brain* 134, 3290–3298. doi: 10.1093/brain/awr233

Nishijima, H., Suzuki, S., Kon, T., Funamizu, Y., Ueno, T., Haga, R., et al. (2014). Morphologic changes of dendritic spines of striatal neurons in the levodopa-induced dyskinesia model. *Mov. Disord.* 29, 336–343. doi: 10.1002/mds.25826

Paille, V., Picconi, B., Bagetta, V., Ghiglieri, V., Sgobio, C., Di Filippo, M., et al. (2010). Distinct levels of dopamine denervation differentially alter striatal synaptic plasticity and NMDA receptor subunit composition. *J. Neurosci.* 30, 14182–14193. doi: 10.1523/JNEUROSCI.2149-10.2010

Picconi, B., Centonze, D., Hakansson, K., Bernardi, G., Greengard, P., Fisone, G., et al. (2003). Loss of bidirectional striatal synaptic plasticity in L-DOPA-induced dyskinesia. *Nat. Neurosci.* 6, 501–506. doi: 10.1038/nn1040

Puschmann, A. (2013). Monogenic Parkinson's disease and parkinsonism: clinical phenotypes and frequencies of known mutations. *Parkinsonism. Relat. Disord.* 19, 407–415. doi: 10.1016/j.parkreldis.2013.01.020

Quik, M., Parameswaran, N., McCallum, S. E., Bordia, T., Bao, S., McCormack, A., et al. (2006). Chronic oral nicotine treatment protects against striatal degeneration in MPTP-treated primates. *J. Neurochem.* 98, 1866–1875. doi: 10.1111/j.1471-4159.2006.04078.x

Ramonet, D., Daher, J. P., Lin, B. M., Stafa, K., Kim, J., Banerjee, R., et al. (2011). Dopaminergic neuronal loss, reduced neurite complexity and autophagic abnormalities in transgenic mice expressing G2019S mutant LRRK2. *PLoS One* 6:e18568. doi: 10.1371/journal.pone.0018568

Sebel, L. E., Graves, S. M., Chan, C. S., and Surmeier, D. J. (2017). Haloperidol selectively remodels striatal indirect pathway circuits. *Neuropsychopharmacology* 42, 963–973. doi: 10.1038/npp.2016.173

Shen, W., Flajolet, M., Greengard, P., and Surmeier, D. J. (2008). Dichotomous dopaminergic control of striatal synaptic plasticity. *Science* 321, 848–851. doi: 10.1126/science.1160575

Shen, W., Plotkin, J. L., Francardo, V., Ko, W. K., Xie, Z., Li, Q., et al. (2015). M4 muscarinic receptor signaling ameliorates striatal plasticity deficits in models of L-DOPA-induced dyskinesia. *Neuron* 88, 762–773. doi: 10.1016/j.neuron.2015.10.039

Shen, W., Tian, X., Day, M., Ulrich, S., Tkatch, T., Nathanson, N. M., et al. (2007). Cholinergic modulation of Kir2 channels selectively elevates dendritic excitability in striatopallidal neurons. *Nat. Neurosci.* 10, 1458–1466. doi: 10.1038/nn1972

Sloan, M., Alegre-Abarrategui, J., Potgieter, D., Kaufmann, A. K., Exley, R., Deltheil, T., et al. (2016). LRRK2 BAC transgenic rats develop progressive, L-DOPA-responsive motor impairment, and deficits in dopamine circuit function. *Hum. Mol. Genet.* 25, 951–963. doi: 10.1093/hmg/ddv628

Smith, Y., Galvan, A., Ellender, T. J., Doig, N., Villalba, R. M., Huerta-Ocampo, I., et al. (2014). The thalamostriatal system in normal and diseased states. *Front. Syst. Neurosci.* 8:5. doi: 10.3389/fnsys.2014.00005

Stephens, B., Mueller, A. J., Shering, A. F., Hood, S. H., Taggart, P., Arbuthnott, G. W., et al. (2005). Evidence of a breakdown of corticostriatal connections in Parkinson's disease. *Neuroscience* 132, 741–754. doi: 10.1016/j.neuroscience.2005.01.007

Suarez, L. M., Alberquilla, S., García-Montes, J. R., and Moratalla, R. (2018). Differential synaptic remodeling by dopamine in direct and indirect striatal projection neurons in Pitx3$^{-/-}$ Mice, a genetic model of Parkinson's disease. *J. Neurosci.* 38, 3619–3630. doi: 10.1523/JNEUROSCI.3184-17.2018

Suarez, L. M., Solis, O., Aguado, C., Lujan, R., and Moratalla, R. (2016). L-DOPA oppositely regulates synaptic strength and spine morphology in D1 and D2 striatal projection neurons in dyskinesia. *Cereb. Cortex* 26, 4253–4264. doi: 10.1093/cercor/bhw263

Suárez, L. M., Solís, O., Caramés, J. M., Taravini, I. R., Solís, J. M., Murer, M. G., et al. (2014). L-DOPA treatment selectively restores spine density in dopamine receptor D2-expressing projection neurons in dyskinetic mice. *Biol. Psychiatry* 75, 711–722. doi: 10.1016/j.biopsych.2013.05.006

Subramaniam, S. R., Magen, I., Bove, N., Zhu, C., Lemesre, V., Dutta, G., et al. (2018). Chronic nicotine improves cognitive and social impairment in mice overexpressing wild type α-synuclein. *Neurobiol. Dis.* 117, 170–180. doi: 10.1016/j.nbd.2018.05.018

Surmeier, D. J., Ding, J., Day, M., Wang, Z., and Shen, W. (2007). D1 and D2 dopamine-receptor modulation of striatal glutamatergic signaling in striatal medium spiny neurons. *Trends Neurosci.* 30, 228–235. doi: 10.1016/j.tins.2007.03.008

Tadaiesky, M. T., Dombrowski, P. A., Da Cunha, C., and Takahashi, R. N. (2010). Effects of SR141716A on cognitive and depression-related behavior in an animal model of premotor Parkinson's disease. *Parkinsons Dis.* 2010:238491. doi: 10.4061/2010/238491

Tadaiesky, M. T., Dombrowski, P. A., Figueiredo, C. P., Cargnin-Ferreira, E., Da Cunha, C., and Takahashi, R. N. (2008). Emotional, cognitive and neurochemical alterations in a premotor stage model of Parkinson's disease. *Neuroscience* 156, 830–840. doi: 10.1016/j.neuroscience.2008.08.035

Tecuapetla, F., Matias, S., Dugue, G. P., Mainen, Z. F., and Costa, R. M. (2014). Balanced activity in basal ganglia projection pathways is critical for contraversive movements. *Nat. Commun.* 5:4315. doi: 10.1038/ncomms5315

Thiele, S. L., Chen, B., Lo, C., Gertler, T. S., Warre, R., Surmeier, J. D., et al. (2014). Selective loss of bi-directional synaptic plasticity in the direct and indirect striatal output pathways accompanies generation of parkinsonism and L-DOPA induced dyskinesia in mouse models. *Neurobiol. Dis.* 71, 334–344. doi: 10.1016/j.nbd.2014.08.006

Tissingh, G., Bergmans, P., Booij, J., Winogrodzka, A., van Royen, E. A., Stoof, J. C., et al. (1998). Drug-naive patients with Parkinson's disease in Hoehn and Yahr stages I and II show a bilateral decrease in striatal dopamine transporters as revealed by [^{123I}]β-CIT SPECT. *J. Neurol.* 245, 14–20. doi: 10.1007/s004150050168

Toy, W. A., Petzinger, G. M., Leyshon, B. J., Akopian, G. K., Walsh, J. P., Hoffman, M. V., et al. (2014). Treadmill exercise reverses dendritic spine loss in direct and indirect striatal medium spiny neurons in the 1-methyl-4-phenyl-1,2,3,6-tetrahydropyridine (MPTP) mouse model of Parkinson's disease. *Neurobiol. Dis.* 63, 201–209. doi: 10.1016/j.nbd.2013.11.017

Tozzi, A., Costa, C., Siliquini, S., Tantucci, M., Picconi, B., Kurz, A., et al. (2012). Mechanisms underlying altered striatal synaptic plasticity in old A53T-α synuclein overexpressing mice. *Neurobiol. Aging* 33, 1792–1799. doi: 10.1016/j.neurobiolaging.2011.05.002

Tozzi, A., de Iure, A., Bagetta, V., Tantucci, M., Durante, V., Quiroga-Varela, A., et al. (2016). α-synuclein produces early behavioral alterations via striatal cholinergic synaptic dysfunction by interacting With GluN2D N-methyl-D-aspartate receptor subunit. *Biol. Psychiatry* 79, 402–414. doi: 10.1016/j.biopsych.2015.08.013

Trusel, M., Cavaccini, A., Gritti, M., Greco, B., Saintot, P. P., Nazzaro, C., et al. (2015). Coordinated regulation of synaptic plasticity at striatopallidal and striatonigral neurons orchestrates motor control. *Cell Rep.* 13, 1353–1365. doi: 10.1016/j.celrep.2015.10.009

Ueno, T., Yamada, J., Nishijima, H., Arai, A., Migita, K., Baba, M., et al. (2014). Morphological and electrophysiological changes in intratelencephalic-type pyramidal neurons in the motor cortex of a rat model of levodopa-induced dyskinesia. *Neurobiol. Dis.* 64, 142–149. doi: 10.1016/j.nbd.2013.12.014

VanLeeuwen, J. E., Petzinger, G. M., Walsh, J. P., Akopian, G. K., Vuckovic, M., and Jakowec, M. W. (2010). Altered AMPA receptor expression with treadmill exercise in the 1-methyl-4-phenyl-1,2,3,6-tetrahydropyridine-lesioned mouse model of basal ganglia injury. *J. Neurosci. Res.* 88, 650–668. doi: 10.1002/jnr.22216

Villalba, R. M., Lee, H., and Smith, Y. (2009). Dopaminergic denervation and spine loss in the striatum of MPTP-treated monkeys. *Exp. Neurol.* 215, 220–227. doi: 10.1016/j.expneurol.2008.09.025

Wang, Z., Kai, L., Day, M., Ronesi, J., Yin, H. H., Ding, J., et al. (2006). Dopaminergic control of corticostriatal long-term synaptic depression in medium spiny neurons is mediated by cholinergic interneurons. *Neuron* 50, 443–452. doi: 10.1016/j.neuron.2006.04.010

Wu, Y. W., Kim, J. I., Tawfik, V. L., Lalchandani, R. R., Scherrer, G., and Ding, J. B. (2015). Input- and cell-type-specific endocannabinoid-dependent LTD in the striatum. *Cell Rep.* 10, 75–87. doi: 10.1016/j.celrep.2014.12.005

Yamasaki, T., Fujinaga, M., Kawamura, K., Furutsuka, K., Nengaki, N., Shimoda, Y., et al. (2016). Dynamic changes in striatal mGluR1 but not mGluR5 during pathological progression of Parkinson's disease in human α-synuclein A53T transgenic rats: a multi-PET imaging study. *J. Neurosci.* 36, 375–384. doi: 10.1523/JNEUROSCI.2289-15.2016

Yue, M., Hinkle, K. M., Davies, P., Trushina, E., Fiesel, F. C., Christenson, T. A., et al. (2015). Progressive dopaminergic alterations and mitochondrial abnormalities in LRRK2 G2019S knock-in mice. *Neurobiol. Dis.* 78, 172–195. doi: 10.1016/j.nbd.2015.02.031

Zaja-Milatovic, S., Milatovic, D., Schantz, A. M., Zhang, J., Montine, K. S., Samii, A., et al. (2005). Dendritic degeneration in neostriatal medium spiny neurons in Parkinson disease. *Neurology* 64, 545–547. doi: 10.1212/01.wnl.0000150591.33787.a4

Zhang, Y., Meredith, G. E., Mendoza-Elias, N., Rademacher, D. J., Tseng, K. Y., and Steece-Collier, K. (2013). Aberrant restoration of spines and their synapses in L-DOPA-induced dyskinesia: involvement of corticostriatal but not thalamostriatal synapses. *J. Neurosci.* 33, 11655–11667. doi: 10.1523/JNEUROSCI.0288-13.2013

Ztaou, S., Lhost, J., Watabe, I., Torromino, G., and Amalric, M. (2018). Striatal cholinergic interneurons regulate cognitive and affective dysfunction in partially dopamine-depleted mice. *Eur. J. Neurosci.* 48, 2988–3004. doi: 10.1111/ejn.14153

Ztaou, S., Maurice, N., Camon, J., Guiraudie-Capraz, G., Kerkerian-Le Goff, L., Beurrier, C., et al. (2016). Involvement of striatal cholinergic interneurons and M1 and M4 muscarinic receptors in motor symptoms of Parkinson's disease. *J. Neurosci.* 36, 9161–9172. doi: 10.1523/JNEUROSCI.0873-16.2016

Conflict of Interest Statement: The authors declare that the research was conducted in the absence of any commercial or financial relationships that could be construed as a potential conflict of interest.

frontiers in Cellular Neuroscience

HYPOTHESIS AND THEORY
published: 19 March 2019
doi: 10.3389/fncel.2019.00103

Mitochondrial Dysfunction in Huntington's Disease; Interplay Between HSF1, p53 and PGC-1α Transcription Factors

*Taylor A. Intihar[1], Elisa A. Martinez[2] and Rocio Gomez-Pastor[1]**

[1]Department of Neuroscience, School of Medicine, University of Minnesota, Minneapolis, MN, United States, [2]Department of Biochemistry and Molecular Biology, Dickinson College, Carlisle, PA, United States

Huntington's disease (HD) is a neurodegenerative disease caused by an expanded CAG repeat in the huntingtin (*HTT*) gene, causing the protein to misfold and aggregate. HD progression is characterized by motor impairment and cognitive decline associated with the preferential loss of striatal medium spiny neurons (MSNs). The mechanisms that determine increased susceptibility of MSNs to mutant HTT (mHTT) are not fully understood, although there is abundant evidence demonstrating the importance of mHTT mediated mitochondrial dysfunction in MSNs death. Two main transcription factors, p53 and peroxisome proliferator co-activator PGC-1α, have been widely studied in HD for their roles in regulating mitochondrial function and apoptosis. The action of these two proteins seems to be interconnected. However, it is still open to discussion whether p53 and PGC-1α dependent responses directly influence each other or if they are connected *via* a third mechanism. Recently, the stress responsive transcription factor HSF1, known for its role in protein homeostasis, has been implicated in mitochondrial function and in the regulation of PGC-1α and p53 levels in different contexts. Based on previous reports and our own research, we discuss in this review the potential role of HSF1 in mediating mitochondrial dysfunction in HD and propose a unifying mechanism that integrates the responses mediated by p53 and PGC-1α in HD *via* HSF1.

Keywords: heat shock factor 1 (HSF1), mitochondrial dysfunction, Huntington (disease), p53, PGC-1α

OPEN ACCESS

Edited by:
Jing-Ning Zhu,
Nanjing University, China

Reviewed by:
Simonetta Sipione,
University of Alberta, Canada
Michelle Gray,
University of Alabama at Birmingham, United States

****Correspondence:***
Rocio Gomez-Pastor
rgomezpa@umn.edu

Received: *26 November 2018*
Accepted: *28 February 2019*
Published: *19 March 2019*

Citation:
Intihar TA, Martinez EA and Gomez-Pastor R (2019) Mitochondrial Dysfunction in Huntington's Disease; Interplay Between HSF1, p53 and PGC-1α Transcription Factors. Front. Cell. Neurosci. 13:103. doi: 10.3389/fncel.2019.00103

INTRODUCTION

Mitochondria are critical organelles that control energy production, lipid metabolism, and Ca^{2+} signaling and buffering. Decreased mitochondrial function has been implicated in multiple cellular processes, linking dysfunctional mitochondria to a wide range of human diseases, including metabolic, cardiovascular, and neurological disorders (Ballinger, 2005; Lin and Beal, 2006; Bhatti et al., 2017). The specific role of mitochondrial dysfunction in the context of Huntington's disease (HD) has been the subject of numerous reviews in recent years (Quintanilla and Johnson, 2009; Reddy et al., 2009; Jin and Johnson, 2010; Oliveira, 2010; Costa and Scorrano, 2012; Dubinsky, 2017). Now, new findings have provided evidence for a novel role of Heat Shock transcription Factor 1 (HSF1) in directly regulating both mitochondrial function and HD pathology. Therefore, we discuss in this article the molecular mechanisms that contribute to mitochondrial dysfunction

in HD and speculate on the possible role of HSF1 in mediating this defect.

HD is an inherited neurodegenerative disease caused by a CAG triplet (encoding glutamine) repeat expansion in the huntingtin (*HTT*) gene that causes HTT protein to misfold and aggregate (MacDonald, 1993; DiFiglia et al., 1997). HD is manifested by progressive behavioral and motor impairment accompanied by cognitive decline. In HD, striatal GABAergic medium spiny neurons (MSNs) are particularly vulnerable. Progressive dysregulation of MSNs is strongly correlated with motor symptoms onset and severity (Ferrante et al., 1991).

Altered mitochondrial morphology is a hallmark of HD and different abnormalities can be seen in different cell types. In peripheral tissues (lymphoblast, myoblast and fibroblasts) mitochondria present an enlarged morphology, while neurons are characterized by increased mitochondrial fragmentation (Panov et al., 2002; Squitieri et al., 2006, 2010; Kim et al., 2010; Jin et al., 2013). Altered mitochondrial structure correlates with mitochondrial dysfunction in all HD cells which is manifested by decreased electron transport chain activity, oxygen consumption, Ca^{2+} buffering and decreased ATP and NAD+ production (Oliveira, 2010). It has been proposed that mutant HTT (mHTT)-mediated mitochondrial abnormalities significantly affect MSNs due to the high-energy demand of this neuronal subtype (Ferrante et al., 1991; Pickrell et al., 2011). This is one hypothesis that explains the increased vulnerability of MSNs in HD (Ferrante et al., 1991; Mitchell and Griffiths, 2003). In support of this hypothesis, mitochondria isolated from the striatum of adult rats showed higher sensitivity to Ca^{2+} induced membrane permeabilization than mitochondria from the cerebral cortex, suggesting that striatal neurons are selectively vulnerable to metabolic stress (Brustovetsky et al., 2003). Other factors that contribute to this cell-selective neuropathology include; cell-type specific processing or localization of mHTT (Li et al., 2000; Menalled et al., 2002), abnormal interactions between mHTT and brain region specific protein partners and tissue specific differences in CAG instability (Kennedy et al., 2003; Goula et al., 2012). All these processes play important roles in promoting MSN degeneration, and although they could also contribute to increase mitochondrial stress, they are not the subject of this review.

HD patients and mouse models of HD exhibit well-described metabolic defects (Mochel and Haller, 2011; Mochel et al., 2012; Dubinsky, 2017). Metabolic analysis in presymptomatic patients using positron emission tomography (PET) and proton nuclear magnetic resonance (1H-NMR) showed that striatal glucose uptake and pyruvate utilization were reduced years before the onset of the motor symptoms, suggesting that mitochondrial alteration may be an early cause of disease progression (Antonini et al., 1996; Feigin et al., 2001). Other studies conducted in HD mouse models showed that MSN dendritic alterations appear even before mitochondrial respiratory defects can be observed, thus suggesting that energy deficits are a consequence of neuropathological changes (Guidetti et al., 2001). It is agreed that, either as a cause or as consequence, mitochondrial dysfunction is a key player in HD pathogenesis and progression. In recent years there has been a tremendous effort in developing therapeutic strategies towards improving mitochondrial function such as those aimed to stabilize mitochondria by boosting the production of ATP, decreasing membrane permeability and/or preventing oxidative damage (Reddy and Reddy, 2011; Corona and Duchen, 2016).

One additional function of mitochondria is to act as a reservoir for pro-apoptotic factors and therefore regulating cell death (Suzuki et al., 1999; Dumollard et al., 2009). Mitochondrial dysfunction, Ca^{2+} overload, and accumulation of reactive oxygen species (ROS) causes the mitochondrial permeability transition pore (mPTP) to open. mPTP opening triggers the intrinsic apoptotic pathway associated with the mitochondrial outer membrane permeabilization, cytochrome c release, and activation of caspase-3 (Choo et al., 2004; Quintanilla et al., 2017). The dysregulation of two main transcription factors p53 and PGC-1α has been extensively studied in HD for their roles in mediating mitochondrial dysfunction, apoptosis, and neurodegeneration (reviewed by Oliveira, 2010). We will briefly review these mechanisms of action and their crosstalk and discuss the potential role of HSF1 as a converging mechanism that integrates the responses mediated by p53 and PGC-1α.

ROLE OF p53 AND PGC-1α IN MITOCHONDRIAL DYSFUNCTION

Transcriptional dysregulation and mitochondrial dysfunction are interconnected processes in HD governed by the crosstalk between p53 and the mitochondrial biogenesis factor PGC-1α (peroxisome proliferator-activated receptor γ co-activator 1α; Steffan et al., 2000; Jin and Johnson, 2010).

p53 is a transcription factor known for its role as a tumor suppressor through the regulation of several target genes with diverse biological functions including cell cycle arrest, DNA repair, metabolism, and apoptosis. p53 protein levels and activity are induced in the brain of HD patients and in cell and mouse models of HD^{33}, explaining at least in part, the low tumor incidence observed in HD patients (Sørensen et al., 1999; Bae et al., 2005). mHTT strongly interacts with p53, and it has been proposed that such interaction impairs the recruitment of the E3 ligase Mdm2, thus increasing p53 stabilization (Steffan et al., 2000; Bae et al., 2005). Up-regulation of p53 leads to induced expression of different mitochondria associated proteins (e.g., Bax and Puma, linked to mitochondrial depolarization) and activation of apoptosis (Chipuk et al., 2004; La Spada and Morrison, 2005). The role of p53 in mediating mitochondrial dysfunction in HD was confirmed when primary neurons expressing mHTT were treated with the p53 inhibitor pifithrin-α and showed improved mitochondrial membrane potential (MMP) and increased cell viability (Bae et al., 2005). Recently, p53 was shown to also participate in mediating mitochondrial related necrosis and fragmentation in HD *via* direct interaction with mitochondrial fission protein Drp1 (dynamin related protein; Guo et al., 2013, 2014). However, the molecular mechanism by which p53 inhibition exerts neuroprotection is still poorly understood.

PGC-1α represents another major player in the link between mHTT, transcriptional dysregulation, and mitochondrial dysfunction (Johri et al., 2013). PGC-1α is a transcriptional coactivator that governs the expression of nuclear-encoded mitochondrial genes and regulates several metabolic processes, including mitochondrial biogenesis and oxidative phosphorylation (Wu et al., 1999; Puigserver and Spiegelman, 2003). Strikingly, PGC-1α null mice manifest HD-like features including, striatal neuronal loss, hypothermia and motor alterations (Weydt et al., 2006; Lucas et al., 2012). The expression of PGC-1α is significantly downregulated in MSNs compared to other striatal cells in HD patients and transgenic mouse models (Cui et al., 2006; Weydt et al., 2006). PGC-1α expression impairment in HD is due, at least in part, to the interference of mHTT with the CREB/TAF4 signaling pathway (Cui et al., 2006), which is considered the major regulator of PGC-1α expression (Herzig et al., 2001). However, chromatin immunoprecipitation analysis conducted in murine striatal-like cells derived from WT (ST*Hdh*^{Q7}) and HD (ST*Hdh*^{Q111}) mice did not show differences in CREB/TAF4 binding to the PGC-1α promoter between the two cell types (Cui et al., 2006) suggesting that additional mechanisms may be involved in PGC-1α expression impairment (discussed elsewhere in this review).

Down-regulation of PGC-1α in HD is accompanied by decreased expression of several PGC-1α–dependent targets and MSN markers (Weydt et al., 2006; Lucas et al., 2012). Studies aimed to induce the expression of PGC-1α in transgenic models of HD showed that PGC-1α promoted not only mitochondrial biogenesis but also provided neuroprotective effects by activating autophagy and increasing the turnover of mHTT aggregates (Tsunemi et al., 2012). These studies demonstrated the important role of PGC-1α in HD, and have motivated the generation of several pharmacological activators due to its therapeutic potential (reviewed by Johri et al., 2013).

However, recent transcriptomic analyses comparing different HD mouse models with either PGC-1α null mice or mice lacking PGC-1α in MSNs revealed many differences between their transcriptional profiles, particularly in mitochondrial-related genes (Lucas et al., 2012; McMeekin et al., 2018). Unexpectedly, HD knock-in mice showed up-regulation of several PGC-1α-dependent genes in an age-dependent manner. These data suggest that further studies in other mouse models will be necessary to clarify the exact role of PGC-1a in regulating mitochondrial gene dysregulation in HD.

Different reports have suggested that p53 and PGC-1α may operate together in controlling mitochondrial function, although the relationship between these two transcription factors differs depending on the physiological context. Studies in transgenic mice overexpressing the mitochondrial monoamine oxidase-A (MAO-A), an enzyme related to cardiomyopathies, showed that transgenic hearts exhibited p53 accumulation and downregulation of PGC-1α (Villeneuve et al., 2013), similar to what is observed in HD neurons. However, additional studies conducted in SH-SY5Y neuroblastoma cells upon glutathione shortage, showed that p53 binds to the PGC-1α promoter and positively regulates its expression (Aquilano et al., 2013), while in liver carcinoma cells Hep2G, p53, and PGC-1α proteins interact with each other and modulate their transactivation functions (Sen et al., 2011). These studies highlight the complexity in the regulatory mechanisms of these two transcription factors and open up the possibility to alternative regulatory pathways not yet described.

HSF1 AS A PHYSIOLOGICAL REGULATOR OF MITOCHONDRIAL ACTIVITY

HSF1 is well known as the major transcriptional regulator of the heat shock response (Anckar and Sistonen, 2011). However, in the last decade a rising number of studies have proposed HSF1 to be a multifaceted factor involved in the regulation of many different cellular processes including but not limited to cell proliferation, inflammation, synapse formation, and energy metabolism (reviewed by Gomez-Pastor et al., 2017b). Here, we will discuss recent studies that have placed HSF1 in the spotlight for its role in mitochondrial function and neurodegeneration.

Benjamin and colleagues Yan et al. (2002) were the first to report a major role of HSF1 in regulating mitochondrial activity by studying the heart of Hsf1$^{-/-}$ mice. Their studies showed that lack of HSF1 results in increased mPTP and increased ROS production. Additional studies in Hsf1$^{-/-}$ oocytes confirmed the role of HSF1 in maintaining mitochondrial function and integrity by exhibiting mitochondrial ultrastructural abnormalities, functional defects, and activation of the apoptotic protein caspase-3 (Bierkamp et al., 2010). More recently, studies in Hsf1$^{-/-}$ hepatocytes also revealed decreased ATP and NAD+ production and mitochondrial abnormalities attributed to altered Drp1 function (Qiao et al., 2017). However, whether these mitochondrial alterations were directly regulated by HSF1 or indirectly as a result of chaperone down-regulation is somewhat unclear.

Very elegantly, Nakai and colleagues Tan et al. (2015) showed that in primary mouse embryonic fibroblasts (MEFs) exposed to proteotoxic stress conditions, HSF1 recruits the mitochondrial SSBP1 factor (involved in replication of mitochondrial DNA) to the nucleus where they both co-operate to control the expression of several cytoplasmic/mitochondrial genes. Further studies in cancer cells also revealed that HSF1 directly regulates the expression of SMAC (mitochondria-derived activator of caspase) and other mitochondrial genes inhibiting mitochondrial apoptosis (Liang et al., 2017). These studies propose HSF1 as a novel mitochondrial responsive transcription factor (Lee et al., 2015).

Lack of HSF1 has also been associated with reduced neurogenesis, neuronal demyelination, and severe astrogliosis, leading to motor and cognitive deficits in aged mice (Santos and Saraiva, 2004; Homma et al., 2007; Uchida et al., 2011). Viability studies conducted in primary cortical astrocytes and neurons isolated from Hsf1$^{-/-}$ mice exposed to different oxidative stress conditions revealed that both cell types were more sensitive than cells isolated from WT mice. Protein oxidation is also greater in Hsf1$^{-/-}$ primary cultures (Homma et al., 2007). These results suggest that mitochondrial function could be impaired

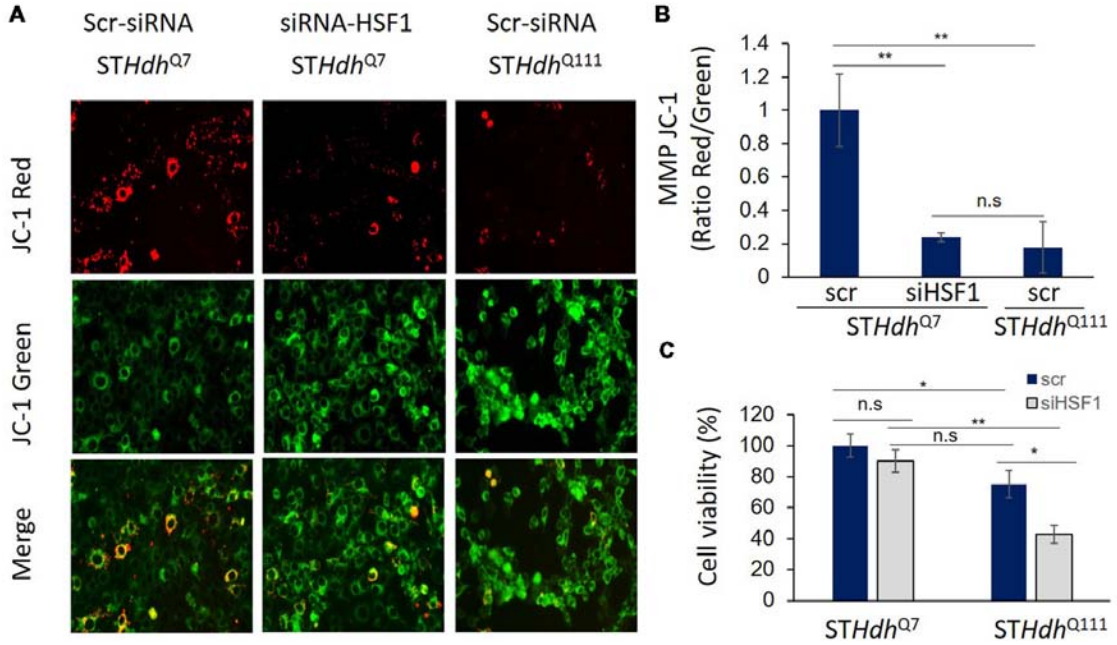

FIGURE 1 | Heat Shock transcription Factor 1 (HSF1) regulates mitochondrial membrane potential (MMP) in striatal cells. **(A,B)** Murine immortalized striatal ST*Hdh*^{Q7} and ST*Hdh*^{Q111} cells were transfected with scramble (Scr.; Santa Cruz, sc-37007) or 5 μM siHSF1 (Santa Cruz, sc-35612). After 24 h, cells were incubated with 5 μM JC-1 dye (Invitrogen T3168) for 30 min at 37°C in PBS. MMP was determined by measuring fluorescence intensity at excitation 550 nm, emission 600 nm for red fluorescence (energized mitochondria) and at excitation 485 nm and emission 535 nm for green fluorescence (depolarized mitochondria). Representative fluorescence images are shown. Ratio red/green fluorescence was calculated for each condition and levels were relative to ST*Hdh*^{Q7} cells. A total of three independent experiments were performed. **(C)** Cell viability was quantified using CYQUANT XTT (ThermoFisher, X12223) after 24 h of transfection with scr. or siHSF1 following manufacturer's instructions. Statistical analyses were performed using *T*-test, **p*-value < 0.05, **$p < 0.01$, n.s. (no significant).

in different cell types in the brain of Hsf1$^{-/-}$ mice, although no reports have addressed this issue yet. Whether the neuronal effects observed in HSF1 null mice are caused by mere chaperone depletion or directly related to HSF1-dependent regulation of mitochondrial gene transcription remains uncertain.

Recent studies conducted in adipose tissue revealed that HSF1 directly activates PGC-1α transcription by binding to a non-canonical Heat Shock Element (HSE) identified in its promoter sequence (Ma et al., 2015). This study highlighted the potential role of HSF1 in directly regulating mitochondrial function *via* regulation of PGC-1α. It is known that adipose tissue from HSF1 null-mice display mitochondrial gene expression deficits (Ma et al., 2015). However, lack of transcriptional studies in those cells impedes to determine whether lack of HSF1 specifically affects PGC-1α -dependent gene expression. In order to answer that question, further studies comparing the transcriptional profiles of HSF1 null mice and PGC-1 null mice will be necessary.

On the other hand, HSF1 and PGC-1α proteins interact and co-localize on several HSF1 target promoters co-operating in the regulation of different genes under hyperthermia (Xu et al., 2016). In fact, PGC-1α null cells showed down-regulation of several heat shock proteins, similar to those observed in HSF1-null mice (Trinklein et al., 2004; Xu et al., 2016). Intriguingly, PGC-1α also acts as a repressor of HSF1-mediated transcriptional program in hepatocytes and in cancer (Minsky and Roeder, 2015). Therefore, despite the evidence demonstrating the crosstalk between HSF1 and PGC-1α, the regulatory mechanisms that control PGC-1α and HSF1 interactions in different cell types or disease conditions is unclear.

HSF1 ROLE IN MEDIATING MITOCHONDRIAL DYSFUNCTION IN HD

HSF1 plays a fundamental role in HD pathogenesis (recently reviewed by Gomez-Pastor et al., 2017b). Studies where HSF1 null mice were crossbred with the R6/2 mice revealed that lack of HSF1 worsens neurodegeneration and disease progression (Hayashida et al., 2010) while HD transgenic mice overexpressing a constitutive active form of HSF1 significantly ameliorated HD symptoms (Fujimoto et al., 2005). The levels of HSF1 and its activity are strongly depleted in the striatum of patients with HD and in cell and mouse models of HD (Hay et al., 2004; Labbadia et al., 2011; Chafekar and Duennwald, 2012; Riva et al., 2012; Maheshwari et al., 2014; Gomez-Pastor et al., 2017a). HSF1 depletion is caused by inappropriate up-regulation of MSNs in two proteins, the Protein Kinase CK2α' and E3 ligase Fbxw7, that phosphorylate and ubiquitylate HSF1, respectively, signaling the protein for proteasomal degradation (Gomez-Pastor et al., 2017a). It is believed that decreased levels and activity of HSF1 contribute to neuronal dysfunction and

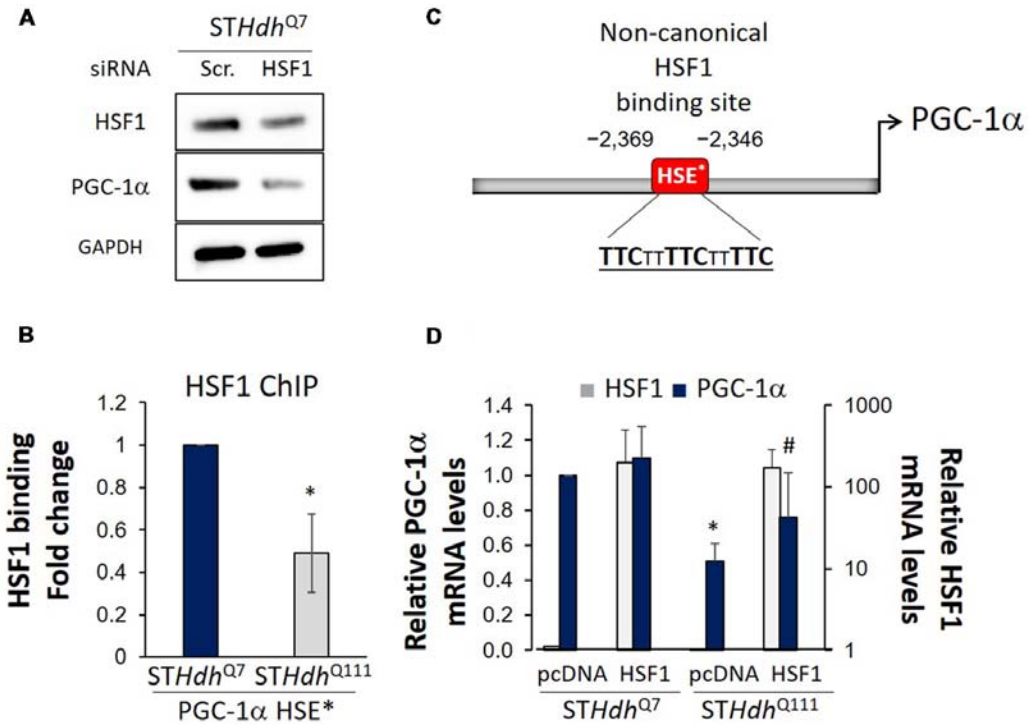

FIGURE 2 | HSF1 binds to PGC-1α promoter and regulates its expression in Huntington's disease (HD) cells. **(A)** Western blot analysis in ST*Hdh*^{Q7} cells treated with scramble (Scr.) or siRNA for 24 h. Cell lysates were prepared in lysis buffer (25 mM Tris pH 7.5, 150 mM NaCl, 1 mM EDTA, 1% Triton X-100, 0.1% SDS) and a total of 25 μg protein was loaded. **(B)** Diagram of PGC-1α promoter containing the non-canonical Heat Shock Element (HSE*; Ma et al., 2015). **(C)** HSF1 chromatin immunoprecipitation in ST*Hdh*^{Q7} and ST*Hdh*^{Q111} cells using 1 μg anti-HSF1 antibody (Bethyl Laboratories, A303-176A) and primers described by Ma et al. (2015; forward TTCATGGATGTGCTGGGTTA, reverse TTACAGATGGTTGCTTGCACT) for the PGC-1α promoter (Ma et al., 2015). Obtained values were normalized using % of input and fold enrichment over IgG (negative control) for each strain. Data was then expressed as fold change binding relative to ST*Hdh*^{Q7} cells. **(D)** qRT-PCR for PGC-1α expression (forward ATGTGTCGCCTTCTTGCTCT, reverse ATCTACTGCCTGGGGACCTT) performed 36 h after transfection with empty-pcDNA or HSF1-pcDNA overexpressing plasmid. At least three independent experiments were carried out for each analysis. Statistical analyses were performed using *T*-test, **p*-value < 0.05. **p*-value < 0.05 (compared to STHdhQ7-pcDNA), $^{\#}p$-value < 0.05 (compared to STHdhQ7-HSF1).

pathogenesis, suggesting HSF1 as a potential therapeutic target for HD intervention (Sittler et al., 2001; Neef et al., 2011). This hypothesis is supported by CK2α' allele knock-out studies in the HD KIQ175 mouse model, which resulted in increased HSF1 levels and neuronal chaperone expression, rescued MSNs morphology and synapse formation, and ameliorated weight loss associated to HD (Gomez-Pastor et al., 2017a).

Due to previous studies linking HSF1 to mitochondrial function and PGC-1α expression (described above), it is reasonable to hypothesize that depletion of HSF1 could also contribute to the mitochondrial dysfunction and abnormalities reported in HD. Current research in our lab supports this hypothesis. We present here unpublished data evaluating the effects of silencing HSF1 in the MMP of murine striatal ST*Hdh*^{Q7} cells and how MMP alterations under these conditions mirror the deficits observed in scramble ST*Hdh*^{Q111} treated cells (**Figure 1**). The effect on MMP was determined using the JC-1 assay, a fluorescence dye that distinguishes between energized (JC-1 red) and depolarized (JC-1 green) mitochondria. We observed increased mitochondrial depolarization (determined by the ratio JC-1 red/JC-1 green signals) in ST*Hdh*^{Q111} compared to ST*Hdh*^{Q7} cells, as previously described (Ruan et al., 2004; **Figure 1A**). More importantly, silencing HSF1 in ST*Hdh*^{Q7} cells resulted in a strong mitochondrial depolarization compared to scramble, similar to the results obtained in untreated ST*Hdh*^{Q111} cells. Cell viability analyses using CyQUANT XTT assay (Thermo Fisher X12223) demonstrated that decreased MMP in ST*Hdh*^{Q7} cells treated with siHSF1 is not secondary to cell death since no significant changes were observed between scramble and siHSF1 conditions (**Figure 1B**). On the contrary, cell viability was reduced in ST*Hdh*^{Q111} compared to ST*Hdh*^{Q7} cells, as previously described using similar assays (Singer et al., 2017). This defect was exacerbated upon silencing HSF1. This data suggests that mitochondrial dysfunction contributes to exacerbating the HD phenotype although it is not sufficient to cause cell death.

Decreased MMP in ST*Hdh*^{Q7} cells treated with siHSF1 was accompanied by a decrease in the levels of PGC-1α (**Figure 2A**). We then conducted HSF1 chromatin immunoprecipitation analysis on the promoter of PGC-1α. We demonstrated that HSF1 binds to the non-canonical HSE present in the promoter of PGC-1α in both ST*Hdh*^{Q7} and ST*Hdh*^{Q111} cells (**Figures 2B,C**). However, HSF1 binding was reduced in ST*Hdh*^{Q111} cells (**Figure 2C**) correlating with the previously reported depletion

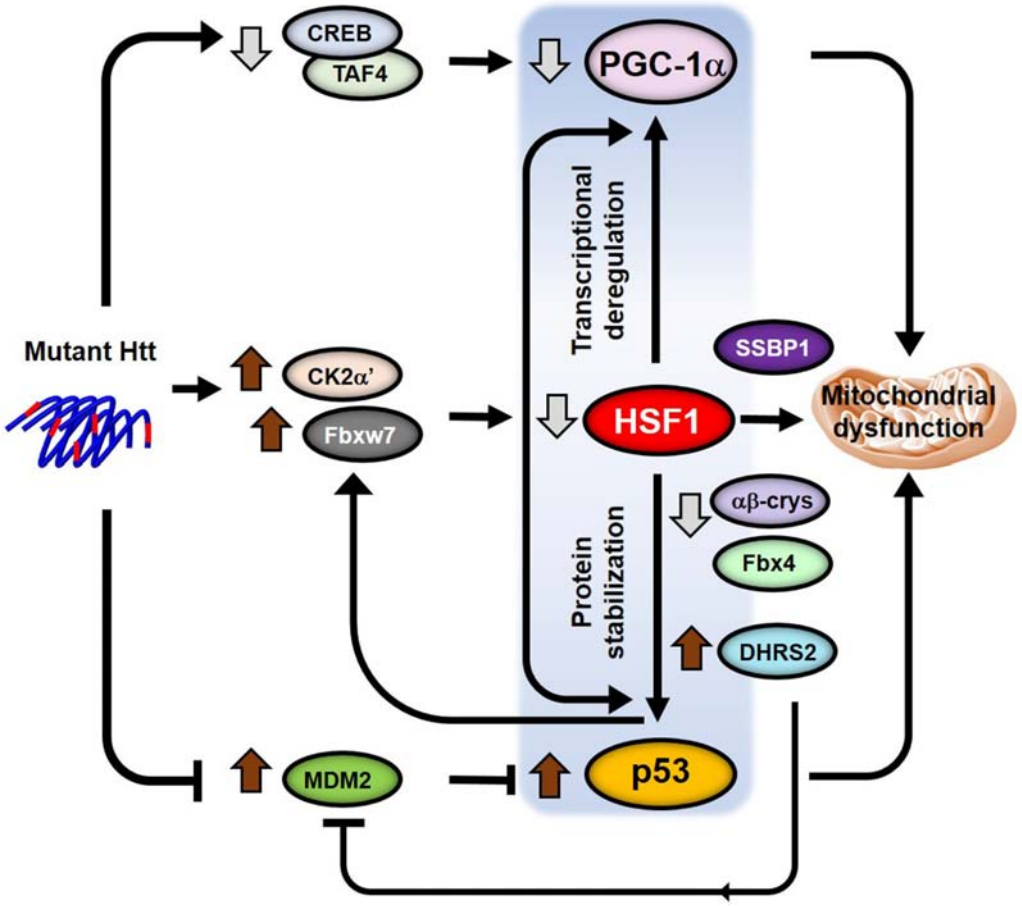

FIGURE 3 | Model for p53-HSF1-PGC1α integrated responses in HD. Crosstalk between the transcription factors p53, HSF1 and PGC-1α regulate transcription, protein homeostasis, mitochondrial function and apoptosis. Different pathways (CREB/TAF4, CK2α'/Fbxw7 and Mdm2) are altered in the presence of mutant HTT (mHTT) that independently lead to the deregulation of the levels and functions of all three transcription factors. However, HSF1 becomes a key player in the subsequent regulation of the levels of both p53 and PGC-1α by directly regulating transcription of PGC-1α and controlling p53 protein stability in HD. The potential role of p53 in the regulation of the HSF1 degradation pathway in HD would add a positive feedback into the p53-HSF1-PGC-1α axis triggering mitochondrial dysfunction and neuronal death.

of HSF1 and the reduced expression of PGC-1α in those same cells (Cui et al., 2006; Chafekar and Duennwald, 2012; Gomez-Pastor et al., 2017a). In line with HSF1 playing a role in the regulation of PGC-1α, overexpression of HSF1 in ST*Hdh*^{Q111} cells rescued the expression of PGC-1α (**Figure 2D**). These results suggest that depletion of HSF1 protein levels in HD (Gomez-Pastor et al., 2017a) could be responsible, at least in part, for the expression impairment of PGC-1α. In support of this hypothesis, we have previously observed that increasing HSF1 levels in the striatum of HD mice elevated the expression of PGC-1α and its downstream targets such as the cytochrome c and the mitochondrial transcription factor TFAM (Gomez-Pastor et al., 2017a). All this data provides evidence for the role of HSF1 degradation in contributing to mitochondrial dysregulation in HD. However, further experiments *in vivo* will be necessary to establish the direct connection between HSF1 depletion, mitochondrial impairment and PGC-1α down-regulation in HD.

CROSSTALK BETWEEN HSF1 AND p53-PGC1α AXIS

Different reports have revealed HSF1 crosstalk with the p53 pathway by directly regulating p53 stabilization and nuclear translocation (Li et al., 2008; Jin et al., 2009; Logan et al., 2009; Oda et al., 2018; **Figure 3**). In human diploid fibroblasts, acute depletion of HSF1 induces cellular senescence independent of chaperone-mediated protein homeostasis but dependent on activation of the p53-p21 pathway. This is partly because of the increased expression of dehydrogenase/reductase 2 (DHRS2), a putative MDM2 inhibitor. MDM2 regulates p53 degradation and its inhibition contributes to increased p53 levels and activation of apoptosis (Oda et al., 2018). A different study also reported increased levels of p53 in Hsf1$^{-/-}$ MEFs (Jin et al., 2009). However, the authors proposed an alternative HSF1 dependent mechanism for the up-regulation of p53 levels. They showed that αβ-crystallin, an HSF1-gene target, is necessary

to recruit the E3 ligase Fbx4 that ubiquitylates p53 and controls p53 degradation. In the absence of HSF1, reduced levels of αβ-crystallin results in the stabilization of p53.

On the other hand, p53 has been shown to directly regulate the expression of the human E3 ligase Fbxw7, by binding to regulatory elements contained within the Fbxw7 coding sequence (Kimura et al., 2003; Mao et al., 2004). Since Fbxw7 is involved in HSF1 ubiquitylation (Kourtis et al., 2015; Gomez-Pastor et al., 2017a) it is possible that increased p53 levels in HD participates in the degradation of HSF1 by up-regulating Fbxw7 during disease progression. If this hypothesis is correct, this would establish a vicious cycle where depletion of HSF1 contributes to the stabilization of p53 levels, which in turn potentiates HSF1 degradation (**Figure 3**).

As we previously discussed, p53 and PGC-1α pathways are also interconnected processes where the levels of one factor influences the levels and activity of the other (Sen et al., 2011; Aquilano et al., 2013; Villeneuve et al., 2013). Considering all the evidence that connects HSF1, p53, and PGC-1α, we speculate on the existence of a p53-HSF1-PGC-1α axis that integrates transcriptional dysregulation and mitochondrial dysfunction into one single pathway (**Figure 3**). However, it will be necessary to conduct further research to put together all the pieces of the puzzle and connect these three transcription factors in the context of HD.

FUTURE DIRECTIONS

Numerous studies now demonstrated the role of HSF1 in regulating mitochondrial dysfunction in different contexts including HD. However, many questions still remain unresolved. First, it would be necessary to uncover whether elevation of p53 is responsible for the degradation of HSF1 in HD and whether the neuroprotection exerted by p53 inhibition is indeed mediated *via* HSF1. On the other hand, the direct role of HSF1 in regulating the expression of PGC-1α in HD and the consequences of such regulation on mitochondrial dysfunction in neurons needs to be further validated in other systems. These studies will be critical to fully understand the causes and consequences of HSF1 degradation in HD and will help to develop more efficient therapeutic strategies for HD intervention.

DATA AVAILABILITY

All datasets generated for this study are included in the manuscript.

AUTHOR CONTRIBUTIONS

TI conducted experiments and contributed with writing, preparing literature and reviewing the manuscript. EM conducted experiments shown in **Figure 1** and contributed with reviewing the manuscript. RG-P contributed to the writing of the manuscript, preparing literature and designed the experiments shown in the manuscript.

FUNDING

We thank the University of Minnesota Undergraduate Research Opportunities Program (UROP; TI) and the R25 NS083059 University of Minnesota Summer Research in Neuroscience (EM) for their support and funding sources.

ACKNOWLEDGMENTS

We thank Dahyun Yu and Nicole Zarate for the technical support.

REFERENCES

Anckar, J., and Sistonen, L. (2011). Regulation of HSF1 function in the heat stress response: implications in aging and disease. *Annu. Rev. Biochem.* 80, 1089–1115. doi: 10.1146/annurev-biochem-060809-095203

Antonini, A., Leenders, K. L., Spiegel, R., Meier, D., Vontobel, P., Weigell-Weber, M., et al. (1996). Striatal glucose metabolism and dopamine D2 receptor binding in asymptomatic gene carriers and patients with Huntington's disease. *Brain* 119, 2085–2095. doi: 10.1093/brain/119.6.2085

Aquilano, K., Baldelli, S., Pagliei, B., Cannata, S. M., Rotilio, G., and Ciriolo, M. R. (2013). p53 orchestrates the PGC-1α-mediated antioxidant response upon mild redox and metabolic imbalance. *Antioxid. Redox Signal.* 18, 386–399. doi: 10.1089/ars.2012.4615

Bae, B. I., Xu, H., Igarashi, S., Fujimuro, M., Agrawal, N., Taya, Y., et al. (2005). p53 mediates cellular dysfunction and behavioral abnormalities in Huntington's disease. *Neuron* 47, 29–41. doi: 10.1016/j.neuron.2005.06.005

Ballinger, S. W. (2005). Mitochondrial dysfunction in cardiovascular disease. *Free Radic. Biol. Med.* 38, 1278–1295. doi: 10.1016/j.freeradbiomed.2005.02.014

Bhatti, J. S., Bhatti, G. K., and Reddy, H. (2017). Mitochondrial dysfunction and oxidative stress in metabolic disorders—A step towards mitochondria based therapeutic strategies. *Biochim. Biophys. Acta Mol. Basis Dis.* 1863, 1066–1077. doi: 10.1016/j.bbadis.2016.11.010

Bierkamp, C., Luxey, M., Metchat, A., Audouard, C., Dumollard, R., and Christians, E. (2010). Lack of maternal Heat Shock Factor 1 results in multiple cellular and developmental defects, including mitochondrial damage and altered redox homeostasis and leads to reduced survival of mammalian oocytes and embryos. *Dev. Biol.* 339, 338–353. doi: 10.1016/j.ydbio.2009.12.037

Brustovetsky, N., Brustovetsky, T., Purl, K. J., Capano, M., Crompton, M., and Dubinsky, J. M. (2003). Increased susceptibility of striatal mitochondria to calcium-induced permeability transition. *J. Neurosci.* 23, 4858–4867. doi: 10.1523/jneurosci.23-12-04858.2003

Chafekar, S. M., and Duennwald, M. L. (2012). Impaired heat shock response in cells expressing full-length polyglutamine-expanded huntingtin. *PLoS One* 7:e37929. doi: 10.1371/journal.pone.0037929

Chipuk, J. E., Kuwana, T., Bouchier-Hayes, L., Droin, N. M., Newmeyer, D. D., Schuler, M., et al. (2004). Direct activation of Bax by p53 mediates mitochondrial membrane permeabilization and apoptosis. *Science* 303, 1010–1014. doi: 10.1126/science.1092734

Choo, Y. S., Johnson, G. V., MacDonald, M., Detloff, P. J., and Lesort, M. (2004). Mutant huntingtin directly increases susceptibility of mitochondria to the calcium-induced permeability transition and cytochrome c release. *Hum. Mol. Genet.* 13, 1407–1420. doi: 10.1093/hmg/ddh162

Corona, J. C., and Duchen, M. R. (2016). PPARγ as a therapeutic target to rescue mitochondrial function in neurological disease. *Free Radic. Biol. Med.* 100, 153–163. doi: 10.1016/j.freeradbiomed.2016.06.023

Costa, V., and Scorrano, L. (2012). Shaping the role of mitochondria in the pathogenesis of Huntington's disease. *EMBO J.* 31, 1853–1864. doi: 10.1038/emboj.2012.65

Cui, L., Jeong, H., Borovecki, F., Parkhurst, C. N., Tanese, N., and Krainc, D. (2006). Transcriptional repression of PGC-1α by mutant huntingtin leads to mitochondrial dysfunction and neurodegeneration. *Cell* 127, 59–69. doi: 10.1016/j.cell.2006.09.015

DiFiglia, M., Sapp, E., Chase, K. O., Davies, S. W., Bates, G. P., Vonsattel, J. P., et al. (1997). Aggregation of huntingtin in neuronal intranuclear inclusions and dystrophic neurites in brain. *Science* 277, 1990–1993. doi: 10.1126/science.277.5334.1990

Dubinsky, J. M. (2017). Towards an understanding of energy impairment in Huntington's disease brain. *J. Huntingtons Dis.* 6, 267–302. doi: 10.3233/JHD-170264

Dumollard, R., Carroll, J., Duchen, M. R., Campbell, K., and Swann, K. (2009). Mitochondrial function and redox state in mammalian embryos. *Semin. Cell Dev. Biol.* 20, 346–353. doi: 10.1016/j.semcdb.2008.12.013

Feigin, A., Leenders, K. L., Moeller, J. R., Missimer, J., Kuenig, G., Spetsieris, P., et al. (2001). Metabolic network abnormalities in early Huntington's disease: an [(18)F]FDG PET study. *J. Nucl. Med.* 42, 1591–1595.

Ferrante, R. J., Kowall, N. W., and Richardson, E. P. (1991). Proliferative and degenerative changes in striatal spiny neurons in Huntington's disease: a combined study using the section-Golgi method and calbindin D28k immunocytochemistry. *J. Neurosci.* 11, 3877–3887. doi: 10.1523/jneurosci.11-12-03877.1991

Fujimoto, M., Takaki, E., Hayashi, T., Kitaura, Y., Tanaka, Y., Inouye, S., et al. (2005). Active HSF1 significantly suppresses polyglutamine aggregate formation in cellular and mouse models. *J. Biol. Chem.* 280, 34908–34916. doi: 10.1074/jbc.m506288200

Gomez-Pastor, R., Burchfiel, E. T., Neef, D. W., Jaeger, A. M., Cabiscol, E., McKinstry, S. U., et al. (2017a). Abnormal degradation of the neuronal stress-protective transcription factor HSF1 in Huntington's disease. *Nat. Commun.* 8:14405. doi: 10.1038/ncomms14405

Gomez-Pastor, R., Burchfiel, E. T., and Thiele, D. J. (2017b). Regulation of heat shock transcription factors and their roles in physiology and disease. *Nat. Rev. Mol. Cell Biol.* 19, 4–19. doi: 10.1038/nrm.2017.73

Goula, A. V., Stys, A., Chan, J. P., Trottier, Y., Festenstein, R., and Merienne, K. (2012). Transcription elongation and tissue-specific somatic CAG instability. *PLoS Genet.* 8:e1003051. doi: 10.1371/journal.pgen.1003051

Guidetti, P., Charles, V., Chen, E. Y., Reddy, P. H., Kordower, J. H., Whetsell, W. O.Jr, et al. (2001). Early degenerative changes in transgenic mice expressing mutant huntingtin involve dendritic abnormalities but no impairment of mitochondrial energy production. *Exp. Neurol.* 169, 340–350. doi: 10.1006/exnr.2000.7626

Guo, X., Disatnik, M. H., Monbureau, M., Shamloo, M., Mochly-Rosen, D., and Qi, X. (2013). Inhibition of mitochondrial fragmentation diminishes Huntington's disease-associated neurodegeneration. *J. Clin. Invest.* 123, 5371–5388. doi: 10.1172/jci70911

Guo, X., Sesaki, H., and Qi, X. (2014). Drp1 stabilizes p53 on the mitochondria to trigger necrosis under oxidative stress conditions *in vitro* and *in vivo*. *Biochem. J.* 461, 137–146. doi: 10.1042/bj20131438

Hay, D. G., Sathasivam, K., Tobaben, S., Stahl, B., Marber, M., Mestril, R., et al. (2004). Progressive decrease in chaperone protein levels in a mouse model of Huntington's disease and induction of stress proteins as a therapeutic approach. *Hum. Mol. Genet.* 13, 1389–1405. doi: 10.1093/hmg/ddh144

Hayashida, N., Fujimoto, M., Tan, K., Prakasam, R., Shinkawa, T., Li, L., et al. (2010). Heat shock factor 1 ameliorates proteotoxicity in cooperation with the transcription factor NFAT. *EMBO J.* 29, 3459–3469. doi: 10.1038/emboj.2010.225

Herzig, S., Long, F., Jhala, U. S., Hedrick, S., Quinn, R., Bauer, A., et al. (2001). CREB regulates hepatic gluconeogenesis through the coactivator PGC-1. *Nature* 413, 179–183. doi: 10.1038/35093131

Homma, S., Jin, X., Wang, G., Tu, N., Min, J., Yanasak, N., et al. (2007). Demyelination, astrogliosis and accumulation of ubiquitinated proteins, hallmarks of CNS disease in hsf1-deficient mice. *J. Neurosci.* 27, 7974–7986. doi: 10.1523/jneurosci.0006-07.2007

Jin, Y. N., and Johnson, G. (2010). The interrelationship between mitochondrial dysfunction and transcriptional dysregulation in Huntington disease. *J. Bioenerg. Biomembr.* 42, 199–205. doi: 10.1007/s10863-010-9286-7

Jin, X., Moskophidis, D., Hu, Y., Phillips, A., and Mivechi, N. F. (2009). Heat shock factor 1 deficiency via its downstream target gene αB-crystallin (Hspb5) impairs p53 degradation. *J. Cell. Biochem.* 107, 504–515. doi: 10.1002/jcb.22151

Jin, Y. N., Yu, Y. V., Gundemir, S., Jo, C., Cui, M., Tieu, K., et al. (2013). Impaired mitochondrial dynamics and Nrf2 signaling contribute to compromised responses to oxidative stress in striatal cells expressing full-length mutant huntingtin. *PLoS One* 8:e57932. doi: 10.1371/journal.pone.0057932

Johri, A., Chandra, A., and Flint Beal, M. (2013). PGC-1α, mitochondrial dysfunction and Huntington's disease. *Free Radic. Biol. Med.* 62, 37–46. doi: 10.1016/j.freeradbiomed.2013.04.016

Kennedy, L., Evans, E., Chen, C. M., Craven, L., Detloff, P. J., Ennis, M., et al. (2003). Dramatic tissue-specific mutation length increases are an early molecular event in Huntington disease pathogenesis. *Hum. Mol. Genet.* 12, 3359–3367. doi: 10.1093/hmg/ddg352

Kim, J., Moody, J. P., Edgerly, C. K., Bordiuk, O. L., Cormier, K., Smith, K., et al. (2010). Mitochondrial loss, dysfunction and altered dynamics in Huntington's disease. *Hum. Mol. Genet.* 19, 3919–3935. doi: 10.1093/hmg/ddq306

Kimura, T., Gotoh, M., Nakamura, Y., and Arakawa, H. (2003). hCDC4b, a regulator of cyclin E, as a direct transcriptional target of p53. *Cancer Sci.* 94, 431–436. doi: 10.1111/j.1349-7006.2003.tb01460.x

Kourtis, N., Moubarak, R. S., Aranda-Orgilles, B., Lui, K., Aydin, I. T., Trimarchi, T., et al. (2015). FBXW7 modulates cellular stress response and metastatic potential through HSF1 post-translational modification. *Nat. Cell Biol.* 17, 322–332. doi: 10.1038/ncb3121

La Spada, A. R., and Morrison, R. S. (2005). The power of the dark side: Huntington's disease protein and p53 form a deadly alliance. *Neuron* 47, 1–3. doi: 10.1016/j.neuron.2005.06.023

Labbadia, J., Cunliffe, H., Weiss, A., Katsyuba, E., Sathasivam, K., Seredenina, T., et al. (2011). Altered chromatin architecture underlies progressive impairment of the heat shock response in mouse models of Huntington disease. *J. Clin. Invest.* 121, 3306–3319. doi: 10.1172/jci57413

Lee, J. H., Lee, Y. K., Lim, J. J., Byun, H. O., Park, I., Kim, G. H., et al. (2015). Mitochondrial respiratory dysfunction induces claudin-1 expression via reactive oxygen species-mediated heat shock factor 1 activation, leading to hepatoma cell invasiveness. *J. Biol. Chem.* 290, 21421–21431. doi: 10.1074/jbc.m115.654913

Li, Q., Feldman, R. A., Radhakrishnan, V. M., Carey, S., and Martinez, J. D. (2008). Hsf1 is required for the nuclear translocation of p53 tumor suppressor. *Neoplasia* 10, 1138–1145. doi: 10.1593/neo.08430

Li, H., Li, S. H., Johnston, H., Shelbourne, P. F., and Li, X. J. (2000). Amino-terminal fragments of mutant huntingtin show selective accumulation in striatal neurons and synaptic toxicity. *Nat. Genet.* 25, 385–389. doi: 10.1038/78054

Liang, W., Liao, Y., Zhang, J., Huang, Q., Luo, W., Yu, J., et al. (2017). Heat shock factor 1 inhibits the mitochondrial apoptosis pathway by regulating second mitochondria-derived activator of caspase to promote pancreatic tumorigenesis. *J. Exp. Clin. Cancer Res.* 36:64. doi: 10.1186/s13046-017-0537-x

Lin, M. T., and Beal, M. F. (2006). Mitochondrial dysfunction and oxidative stress in neurodegenerative diseases. *Nature* 443, 787–795. doi: 10.1038/nature05292

Logan, I. R., McNeill, H. V., Cook, S., Lu, X., Meek, D. W., Fuller-Pace, F. V., et al. (2009). Heat shock factor-1 modulates p53 activity in the transcriptional response to DNA damage. *Nucleic Acids Res.* 37, 2962–2973. doi: 10.1093/nar/gkp180

Lucas, E. K., Dougherty, S. E., McMeekin, L. J., Trinh, A. T., Reid, C. S., and Cowell, R. M. (2012). Developmental alterations in motor coordination and medium spiny neuron markers in mice lacking pgc-1α. *PLoS One* 7:e42878. doi: 10.1371/journal.pone.0042878

Ma, X., Xu, L., Alberobello, A. T., Gavrilova, O., Bagattin, A., Skarulis, M., et al. (2015). Celastrol protects against obesity and metabolic dysfunction through activation of a HSF1-PGC1α transcriptional axis. *Cell Metab.* 22, 695–708. doi: 10.1016/j.cmet.2015.08.005

MacDonald, M. (1993). A novel gene containing a trinucleotide repeat that is expanded and unstable on Huntington's disease chromosomes. The Huntington's disease collaborative research group. *Cell* 72, 971–983. doi: 10.1016/0092-8674(93)90585-e

Maheshwari, M., Bhutani, S., Das, A., Mukherjee, R., Sharma, A., Kino, Y., et al. (2014). Dexamethasone induces heat shock response and slows down disease progression in mouse and fly models of Huntington's disease. *Hum. Mol. Genet.* 23, 2737–2751. doi: 10.1093/hmg/ddt667

Mao, J. H., Perez-Losada, J., Wu, D., Delrosario, R., Tsunematsu, R., Nakayama, K. I., et al. (2004). Fbxw7/Cdc4 is a p53-dependent, haploinsufficient tumour suppressor gene. *Nature* 432, 775–779. doi: 10.1038/nature03155

McMeekin, L. J., Li, Y., Fox, S. N., Rowe, G. C., Crossman, D. K., Day, J. J., et al. (2018). Cell-Specific Deletion of PGC-1? from Medium Spiny Neurons Causes Transcriptional Alterations and Age-Related Motor Impairment. *J. Neurosci.* 38, 3273–3286. doi: 10.1523/jneurosci.0848-17.2018

Menalled, L. B., Sison, J. D., Wu, Y., Olivieri, M., Li, X. J., Li, H., et al. (2002). Early motor dysfunction and striosomal distribution of huntingtin microaggregates in Huntington's disease knock-in mice. *J. Neurosci.* 22, 8266–8276. doi: 10.1523/JNEUROSCI.22-18-08266.2002

Minsky, N., and Roeder, R. G. (2015). Direct link between metabolic regulation and the heat-shock response through the transcriptional regulator PGC-1α. *Proc. Natl. Acad. Sci. U S A* 112, E5669–E5678. doi: 10.1073/pnas.15162 19112

Mitchell, I. J., and Griffiths, M. R. (2003). The differential susceptibility of specific neuronal populations: insights from Huntington's disease. *IUBMB Life* 55, 293–298. doi: 10.1080/1521654031000153012

Mochel, F., Durant, B., Meng, X., O'Callaghan, J., Yu, H., Brouillet, E., et al. (2012). Early alterations of brain cellular energy homeostasis in Huntington disease models. *J. Biol. Chem.* 287, 1361–1370. doi: 10.1074/jbc.m111.309849

Mochel, F., and Haller, R. G. (2011). Energy deficit in Huntington disease: why it matters. *J. Clin. Invest.* 121, 493–499. doi: 10.1172/jci45691

Neef, D. W., Jaeger, A. M., and Thiele, D. J. (2011). Heat shock transcription factor 1 as a therapeutic target in neurodegenerative diseases. *Nat. Rev. Drug Discov.* 10, 930–944. doi: 10.1038/nrd3453

Oda, T., Sekimoto, T., Kurashima, K., Fujimoto, M., Nakai, A., and Yamashita, T. (2018). Acute HSF1 depletion induces cellular senescence through the MDM2–p53-p21 pathway in human diploid fibroblasts. *J. Cell Sci.* 131:jcs210724. doi: 10.1242/jcs.210724

Oliveira, J. M. (2010). Nature and cause of mitochondrial dysfunction in Huntington's disease: focusing on huntingtin and the striatum. *J. Neurochem.* 114, 1–12. doi: 10.1111/j.1471-4159.2010.06741.x

Panov, A. V., Gutekunst, C. A., Leavitt, B. R., Hayden, M. R., Burke, J. R., Strittmatter, W. J., et al. (2002). Early mitochondrial calcium defects in Huntington's disease are a direct effect of polyglutamines. *Nat. Neurosci.* 5, 731–736. doi: 10.1038/nn884

Pickrell, A. M., Fukui, H., Wang, X., Pinto, M., and Moraes, C. T. (2011). The striatum is highly susceptible to mitochondrial oxidative phosphorylation dysfunctions. *J. Neurosci.* 31, 9895–9904. doi: 10.1523/JNEUROSCI.6223-10.2011

Puigserver, P., and Spiegelman, B. M. (2003). Peroxisome proliferator-activated receptor-γ coactivator 1 α (PGC-1 α): transcriptional coactivator and metabolic regulator. *Endocr. Rev.* 24, 78–90. doi: 10.1210/er.2002-0012

Qiao, A., Jin, X., Pang, J., Moskophidis, D., and Mivechi, N. F. (2017). The transcriptional regulator of the chaperone response HSF1 controls hepatic bioenergetics and protein homeostasis. *J. Cell Biol.* 216, 723–741. doi: 10.1083/jcb.201607091

Quintanilla, R. A., and Johnson, G. (2009). Role of mitochondrial dysfunction in the pathogenesis of Huntington's disease. *Brain Res. Bull.* 80, 242–247. doi: 10.1016/j.brainresbull.2009.07.010

Quintanilla, R. A., Tapia, C., and PÉrez, M. J. (2017). Possible role of mitochondrial permeability transition pore in the pathogenesis of Huntington disease. *Biochem. Biophys. Res. Commun.* 483, 1078–1083. doi: 10.1016/j.bbrc.2016.09.054

Reddy, H., Mao, P., and Manczak, M. (2009). Mitochondrial structural and functional dynamics in Huntington's disease. *Brain Res. Rev.* 61, 33–48. doi: 10.1016/j.expneurol.2009.03.042

Reddy, H., and Reddy, T. P. (2011). Mitochondria as a therapeutic target for aging and neurodegenerative diseases. *Curr. Alzheimer Res.* 8, 393–409. doi: 10.2174/156720511795745401

Riva, L., Koeva, M., Yildirim, F., Pirhaji, L., Dinesh, D., Mazor, T., et al. (2012). Poly-glutamine expanded huntingtin dramatically alters the genome wide binding of HSF1. *J. Huntingtons Dis.* 1, 33–45. doi: 10.3233/JHD-2012-1 20020

Ruan, Q., Lesort, M., MacDonald, M. E., and Johnson, G. V. (2004). Striatal cells from mutant huntingtin knock-in mice are selectively vulnerable to mitochondrial complex II inhibitor-induced cell death through a non-apoptotic pathway. *Hum. Mol. Genet.* 13, 669–681. doi: 10.1093/hmg/ddh082

Santos, S. D., and Saraiva, M. J. (2004). Enlarged ventricles, astrogliosis and neurodegeneration in heat shock factor 1 null mouse brain. *Neuroscience* 126, 657–663. doi: 10.1016/j.neuroscience.2004.03.023

Sen, N., Satija, Y. K., and Das, S. (2011). PGC-1α, a key modulator of p53, promotes cell survival upon metabolic stress. *Mol. Cell* 44, 621–634. doi: 10.1016/j.molcel.2011.08.044

Singer, E., Walter, C., Weber, J. J., Krahl, A. C., Mau-Holzmann, U. A., Rischert, N., et al. (2017). Reduced cell size, chromosomal aberration and altered proliferation rates are characteristics and confounding factors in the STHdh cell model of Huntington disease. *Sci. Rep.* 7:16880. doi: 10.1038/s41598-017-17275-4

Sittler, A., Lurz, R., Lueder, G., Priller, J., Lehrach, H., Hayer-Hartl, M. K., et al. (2001). Geldanamycin activates a heat shock response and inhibits huntingtin aggregation in a cell culture model of Huntington's disease. *Hum. Mol. Genet.* 10, 1307–1315. doi: 10.1093/hmg/10.12.1307

Sørensen, S. A., Fenger, K., and Olsen, J. H. (1999). Significantly lower incidence of cancer among patients with Huntington disease: an apoptotic effect of an expanded polyglutamine tract? *Cancer* 86, 1342–1346. doi: 10.1002/(sici)1097-0142(19991001)86:7<1342::aid-cncr33>3.0.co;2-3

Squitieri, F., Cannella, M., Sgarbi, G., Maglione, V., Falleni, A., Lenzi, P., et al. (2006). Severe ultrastructural mitochondrial changes in lymphoblasts homozygous for Huntington disease mutation. *Mech. Ageing Dev.* 127, 217–220. doi: 10.1016/j.mad.2005.09.010

Squitieri, F., Falleni, A., Cannella, M., Orobello, S., Fulceri, F., Lenzi, P., et al. (2010). Abnormal morphology of peripheral cell tissues from patients with Huntington disease. *J. Neural Transm.* 117, 77–83. doi: 10.1007/s00702-009-0328-4

Steffan, J. S., Kazantsev, A., Spasic-Boskovic, O., Greenwald, M., Zhu, Y. Z., Gohler, H., et al. (2000). The Huntington's disease protein interacts with p53 and CREB-binding protein and represses transcription. *Proc. Natl. Acad. Sci. U S A* 97, 6763–6768. doi: 10.1073/pnas.100110097

Suzuki, A., Tsutomi, Y., Yamamoto, N., Shibutani, T., and Akahane, K. (1999). Mitochondrial regulation of cell death: mitochondria are essential for procaspase 3–p21 complex formation to resist Fas-mediated cell death. *Mol. Cell. Biol.* 19, 3842–3847. doi: 10.1128/mcb.19.5.3842

Tan, K., Fujimoto, M., Takii, R., Takaki, E., Hayashida, N., and Nakai, A. (2015). Mitochondrial SSBP1 protects cells from proteotoxic stresses by potentiating stress-induced HSF1 transcriptional activity. *Nat. Commun.* 6:6580. doi: 10.1038/ncomms7580

Trinklein, N. D., Murray, J. I., Hartman, S. J., Botstein, D., and Myers, R. M. (2004). The role of heat shock transcription factor 1 in the genome-wide regulation of the mammalian heat shock response. *Mol. Biol. Cell* 15, 1254–1261. doi: 10.1091/mbc.e03-10-0738

Tsunemi, T., Ashe, T. D., Morrison, B. E., Soriano, K. R., Au, J., Roque, R. A., et al. (2012). PGC-1α rescues Huntington's disease proteotoxicity by preventing oxidative stress and promoting TFEB function. *Sci. Transl. Med.* 4:142ra97. doi: 10.1126/scitranslmed.3003799

Uchida, S., Hara, K., Kobayashi, A., Fujimoto, M., Otsuki, K., Yamagata, H., et al. (2011). Impaired hippocampal spinogenesis and neurogenesis and altered affective behavior in mice lacking heat shock factor 1. *Proc. Natl. Acad. Sci. U S A* 108, 1681–1686. doi: 10.1073/pnas.1016424108

Villeneuve, C., Guilbeau-Frugier, C., Sicard, P., Lairez, O., Ordener, C., Duparc, T., et al. (2013). p53-PGC-1α pathway mediates oxidative mitochondrial damage and cardiomyocyte necrosis induced by monoamine oxidase-A upregulation: role in chronic left ventricular dysfunction in mice. *Antioxid. Redox Signal.* 18, 5–18. doi: 10.1089/ars.2011.4373

Weydt, P., Pineda, V. V., Torrence, A. E., Libby, R. T., Satterfield, T. F., Lazarowski, E. R., et al. (2006). Thermoregulatory and metabolic defects in Huntington's disease transgenic mice implicate PGC-1α in Huntington's disease neurodegeneration. *Cell Metab.* 4, 349–362. doi: 10.1016/j.cmet.2006.10.004

Wu, Z., Puigserver, P., Andersson, U., Zhang, C., Adelmant, G., Mootha, V., et al. (1999). Mechanisms controlling mitochondrial biogenesis and respiration through the thermogenic coactivator PGC-1. *Cell* 98, 115–124. doi: 10.1016/s0092-8674(00)80611-x

Xu, L., Ma, X., Bagattin, A., and Mueller, E. (2016). The transcriptional coactivator PGC1α protects against hyperthermic stress via cooperation with the heat shock factor HSF1. *Cell Death Dis.* 7:e2102. doi: 10.1038/cddis.2016.22

Yan, L. J., Christians, E. S., Liu, L., Xiao, X., Sohal, R. S., and Benjamin, I. J. (2002). Mouse heat shock transcription factor 1 deficiency alters cardiac redox homeostasis and increases mitochondrial oxidative damage. *EMBO J.* 21, 5164–5172. doi: 10.1093/emboj/cdf528

Conflict of Interest Statement: The authors declare that the research was conducted in the absence of any commercial or financial relationships that could be construed as a potential conflict of interest.

frontiers in Cellular Neuroscience

ORIGINAL RESEARCH
published: 19 March 2019
doi: 10.3389/fncel.2019.00106

Wheel Running Improves Motor Function and Spinal Cord Plasticity in Mice With Genetic Absence of the Corticospinal Tract

*Wei Zhang[1†], Bin Yang[1†], Huandi Weng[1], Tao Liu[1], Lingling Shi[1], Panpan Yu[1], Kwok-Fai So[1], Yibo Qu[1] and Libing Zhou[1,2,3]**

[1]Guangdong-Hongkong-Macau Institute of CNS Regeneration, Ministry of Education CNS Regeneration Collaborative Joint Laboratory, Jinan University, Guangzhou, China, [2]Co-innovation Center of Neuroregeneration, Nantong University, Jiangsu, China, [3]Key Laboratory of Neuroscience, School of Basic Medical Sciences, Institute of Neuroscience, The Second Affiliated Hospital, Guangzhou Medical University, Guangzhou, China

Our previous studies showed that mutant mice with congenital absence of the corticospinal tract (CST) undergo spontaneous remodeling of motor networks to partially compensate for absent CST function. Here, we asked whether voluntary wheel running could further improve locomotor plasticity in CST-deficient mice. Adult mutant mice were randomly allocated to a "runners" group with free access to a wheel, or a "non-runners" group with no access to a wheel. In comparison with non-runners, there was a significant motor improvement including fine movement, grip strength, decreased footslip errors in runners after 8-week training, which was supported by the elevated amplitude of electromyography recording and increased neuromuscular junctions in the biceps. In runners, terminal ramifications of monoaminergic and rubrospinal descending axons were significantly increased in spinal segments after 12 weeks of exercise compared to non-runners. 5-ethynyl-2′-deoxyuridine (EDU) labeling showed that proliferating cells, 90% of which were Olig2-positive oligodendrocyte progenitors, were 4.8-fold more abundant in runners than in non-runners. In 8-week runners, RNAseq analysis of spinal samples identified 404 genes up-regulated and 398 genes down-regulated, and 69 differently expressed genes involved in signal transduction, among which the NF-κB, PI3K-Akt and cyclic AMP (cAMP) signaling were three top pathways. Twelve-week training induced a significant elevation of postsynaptic density protein 95 (PSD95), synaptophysin 38 and myelin basic protein (MBP), but not of brain derived neurotrophic factor (BDNF), glial cell line-derived neurotrophic factor (GDNF) and insulin like growth factor-1 (IGF-1). Thus, locomotor training activates multiple signaling pathways, contributes to neural plasticity and functional improvement, and might palliate locomotor deficits in patients.

Keywords: exercise, corticospinal tract, animal model, oligodendrogenesis, neural plasticity, transcriptomics

OPEN ACCESS

Edited by:
Ying Shen,
Zhejiang University, China

Reviewed by:
Xiaoming Jin,
Indiana University, Purdue University Indianapolis, United States
Yongjun Wang,
Nantong University, China

****Correspondence:***
Libing Zhou
tlibingzh@jnu.edu.cn

[†]These authors have contributed equally to this work

Received: *11 February 2019*
Accepted: *04 March 2019*
Published: *19 March 2019*

Citation:
Zhang W, Yang B, Weng H, Liu T, Shi L, Yu P, So K-F, Qu Y and Zhou L (2019) Wheel Running Improves Motor Function and Spinal Cord Plasticity in Mice With Genetic Absence of the Corticospinal Tract. Front. Cell. Neurosci. 13:106. doi: 10.3389/fncel.2019.00106

INTRODUCTION

The corticospinal tract (CST) is a main descending axonal bundle for motor control. Its axons originate from corticospinal motor neurons in cortical layer V and innervate different segments of the spinal cord. In the human, damage to the CST is a leading cause of motor disability in spinal cord injury (SCI), amyotrophic lateral sclerosis, cerebral palsy and related diseases. Although wiring by intact axons and re-innervation by axonal sprouting contributes to functional recovery, the limited growth ability of the adult central nervous system remains a formidable impediment to regeneration and treatment (Jin et al., 2015; Carmichael et al., 2017).

Motor training is used to improve motor skills in patients with SCI or cerebral palsy (Willerslev-Olsen et al., 2014, 2015; Wu et al., 2017; Kuczynski et al., 2018), and may assist in restoring locomotor ability by facilitating neural plasticity, attenuating inflammation and/or improving tolerance to physical activity (Cobianchi et al., 2017). There is some debate as to what animal models best mimics cerebral palsy and allow treatment evaluation (Clowry et al., 2014). Interestingly, an intrinsic plasticity of locomotor networks (Schulz, 2006) is known to persist through life in rodents (Kleim et al., 2003) and probably in human (Vahdat et al., 2015). Several studies confirm the benefit of specific locomotor training and/or stimulation of activity-dependent plasticity (Martin et al., 2007, 2011; Dunlop, 2008; Lynskey et al., 2008; Ilha et al., 2011). Others suggest that exercise induces an up-regulation of neurotrophins (NTs) such as brain derived neurotrophic factor (BDNF), nerve growth factor (NGF), NT-3, and NT-4, and thereby may facilitate neural plasticity and functional recovery, possibly through cyclic AMP (cAMP) signaling (Hannila and Filbin, 2008; Jung et al., 2014; Lee and Soya, 2017; Tian et al., 2018).

Using *Celsr3* conditional gene inactivation, we generated a mouse model in which the CST is congenitally absent (Zhou et al., 2008). Although wiring of alternative motor networks provides significant functional compensation, deficits in fine motor behavior and muscle tone are clearly present (Han et al., 2015). We wondered whether voluntary exercise training could increase further compensatory mechanisms in those mice. To test this, animals were trained in a running wheel for 8–12 weeks, after which we evaluated locomotor performances and studied changes in the spinal cord microenvironment, the morphological maturity of motor-related components, and the plastic changes of spinal networks. Our data provide rational arguments for therapy by exercise in patients with disorders of spinal cord or CST, such as in cerebral palsy.

MATERIALS AND METHODS

Animals

Animal procedures were approved by the Laboratory Animal Ethics Committee at Jinan University (ref file: 20150302007). *Emx1–Cre;Celsr3*$^{+/-}$ males were crossed with *Celsr3*$^{f/f}$ females to obtain *Emx1–Cre;Celsr3*$^{f/-}$ mice, thereafter referred as "mutant" (Zhou et al., 2008). Adult mutant mice (6–8 weeks old, 22–25 g) were individually housed and randomly allocated to runners and non-runners groups. Littermates with genotypes *Emx1–Cre;Celsr3*$^{f/+}$ or *Celsr3*$^{f/-}$ were used as controls. Females and males were used indiscriminately and all animals were kept under a 12-h light-dark cycle (light on at 7:00 a.m. and off at 7:00 p.m.) with *ad libitum* access to food and water. Mice were given free access to a silent spinner running wheel (diameter: 10.8 cm, width: 4.7 cm, rod spacing: 0.7 cm, rod diameter: 0.3 cm), which was locked in non runners. ER-4000 energizer/receivers (Mini Mitter, Bend, OR, USA) were placed above the cage to monitor motor activity, and the data were acquired using Vital View. Data were analyzed using Exceland Actiview to generate periodograms and actograms (Harkin et al., 2002; Eckel-Mahan and Sassone-Corsi, 2015).

Behavioral Tests

Mice underwent test sessions at approximately the same time each day, and eight animals were used in each group.

Grid Tests

The grid area (32 × 15 cm) has 11/11 mm openings. Behavior was recorded using a camera placed under the grid, in order to assess stepping errors (i.e., "footfaults"). Foot slips during the first 100 steps were scored when the paw missed a rung and the animal lost balance, or when the paw slipped off during weight bearing. For each limb, footfaults were counted and compared to the overall step number made by that limb.

Grip Strength Tests

Grip tests were performed every 4 weeks with a 47,200 Grip Strength Meter (Ugo Basile, Italy). This method consists of measuring the grip force using a dynamometer while the mouse is being pulled by the tail (Alamri et al., 2018). Mice were tested five times in succession, with a 3-min rest, and three best results were averaged.

Food-Pellet Taking Tests

Skilled motor function was assessed by testing food pellet handling. After fasting for 24 h, animals were videotaped to record food handling. Irvine, Beatties and Bresnahan (IBB) scores ranging from 0 to 9 were used to estimate forelimb usage, based on joint position, object support, digit movement and grasping technique (Irvine et al., 2010).

Home-Cage Tests

Walking distance was assessed by home-cage tests (Jhuang et al., 2010). At the end of the 12-week exercise period, runner and non-runner mice were placed for 5 days in individual cages (27 × 17 × 16 cm) inside cabinets with constant temperature and humidity, equipped with infrared cameras to monitor behavioral activity. The first 3 days served as an acclimatization period, and during the last 2 days, behavior was recorded and analyzed using the HomeCageScan 3.0 software.

Immunostaining

At the end of the 12-week experimental period, mice were deeply anesthetized with 4% tribromoethanol and perfused

intracardially with 4% paraformaldehyde in 0.01 M phosphate-buffered saline (PBS, pH 7.4). Spinal C5–C7 segments and biceps (six animals in each group) were collected and post-fixed in the same fixative overnight, and then immersed in 10%-20%-30% sucrose until they sank. Ten micrometer transverse spinal sections and 40-μm horizontal biceps sections were prepared with a sliding microtome (Leica). Sections were kept in 12-well plates at 4°C. After washing with PBS, sections were blocked in 10% goat serum plus 3% bovine serum albumin for 2 h, and incubated with the primary antibodies overnight at 4°C. The primary antibodies included: goat anti-choline acetyltransferase (anti-ChAT; 1:500; AB144p, Millipore), rabbit anti-oligodendrocyte transcription factor 2 (anti-Olig2; 1:2,000, AB9610, Millipore), mouse anti-serotonin (anti-5-HT; 1:500, ab6336, Abcam) and rabbit anti-tyrosine hydroxylase (anti-TH; 1:500; AB152, Millipore). Sections were rinsed in 0.01 M PBS and incubated with the secondary fluorescent antibodies (Alexa Fluor 488 or 546; 1:1,000, A21202/A21206/A11055, Thermo Fisher) for 2 h. α-bungarotoxin conjugated to Alexa Fluor 546 (α-BT; 1:1,000, T1175, Molecular Probes) was used to label acetylcholine receptor clusters.

Electrophysiology

To determine whether running wheel exercise modifies the properties of muscle, evoked electromyography was measured. At the end of the 12-week experimental period, an investigator blind to groups submitted mice to light sedation using propofol and inserted concentric needle electrodes in the biceps. A square pulse (50–100 μA stimulus of 100 μs at 0.13 Hz) was applied to musculocutaneous nerves and recordings were measured using Keypoint Portable (Dantec Biomed, Denmark). The stimulation was gradually increased from 50 μA to 100 μA until the maximal amplitude appeared just before large motor responses were evoked (typically between 80 μA and 100 μA). The maximum amplitude was measured and the latency was calculated from the initiation of pulse stimulus to the beginning of the response peak. The mean amplitude and wave width were calculated for each animal based on average tracing of more than 10 sweeps. Six animals were used in each group.

5-Ethynyl-2′-Deoxyuridine (EDU) Labeling *in vivo*

5-ethynyl-2′-deoxyuridine (EDU; Sigma, St. Louis, MI, USA) was dissolved at 10 mg/ml in 0.9% NaCl, and sterilized by filtration at 0.2 μm. Mice (n = 4 in each group) received one intraperitoneal injection of 50 mg/kg body weight per day for three consecutive days during the last of the 12 training weeks. Twenty-four hours after the last injection, mice were perfused with 4% paraformaldehyde and EDU was detected using the Alexa Fluor 555 Click-iT detection kit (Invitrogen). One of six series of adjacent C5–C7 spinal sections were used to count EDU-labeled cells.

Biotinylated Dextran Amine (BDA) Tracing

Animals (n = 3 in each group) were anesthetized and placed in a head holder (68004, RWD Life Science Co. Ltd., China). For anterograde tracing, 1 μl of biotinylated dextran amine (BDA; 10,000 MW, 10% in PBS, pH 7.4, Molecular Probes) was injected in the right red nucleus (3.49 mm posterior to the Bregma, 0.89 mm lateral to the midline, 3.94 mm ventral to the skull surface). Fourteen days later, animals were anesthetized and perfused with 4% paraformaldehyde. Spinal cords were postfixed overnight at 4°C. The distribution of BDA labeling was detected in 40 μm thick transverse sections of C5–C7 spinal segments using a BDA-10000 Neuronal Tracer kit (N-7167, molecular probes) and the density of axons was evaluated as described (Jin et al., 2015). Briefly, we drew a horizontal line through the central canal and across the lateral rim of the gray matter. Vertical lines were then drawn to divide the horizontal line into 100 μm intervals, starting from the central canal to the lateral rim. Crosses between axons and the vertical lines were counted in each section.

Bio-Plex Pro™ Cytokine Assays

After 12-week running, blood was collected from the retro-orbital sinus. Thereafter, the mice (n = 3 in each group) were killed by decapitation, and C5–C7 spinal segments and biceps were quickly collected. Lysates from biceps and spinal cords were prepared using RIPA solution containing Phenylmethanesulfonyl fluoride (PMSF; 1:100; P8340-1; Solarbio Bioscience and Technology), Protease Inhibitor Cocktail (1:100, 539137-10vlcn, Millipore) and Phosphatase Inhibitor Cocktail (1:100, 539131, Calbiochem). Bio-Plex Pro™ cytokine assays (BIO-RAD, Hercules, CA, USA) were used to measure cytokines in blood, spinal cords and muscles by using a 23-plex test kit, which included IL-1α, IL-1β, IL-2, IL-3, IL-4, IL-5, IL-6, IL-9, IL-10, IL-12 (p40), IL-12 (p70), IL-13, IL-17, Eotaxin, G-CSF, GM-CSF, IFN-γ, KC, MCP-1, MIP-1α, MIP-1β, RANTES and TNF-α.

Western Blotting

After 12-week exercise, animals (n = 3 in each group) were killed and proteins were extracted from C5 to C7 spinal segments, which were separated by 10% sodium dodecyl sulfate polyacrylamide gel electrophoresis. Proteins were then transferred to nitrocellulose and the blots were probed with anti-myelin basic protein (anti-MBP) rabbit polyclonal antibody (1:1,000, ab40390, Abcam), anti-TH rabbit polyclonal antibody (1:1,000, AB152, Millipore), anti-synaptophysin mouse polyclonal antibody (SY38; 1:500, ab8049, Abcam), anti-postsynaptic density-95 (anti-PSD-95) rabbit polyclonal antibody (1:500, 516900, Invitrogen), anti-insulin like growth factor-1 (anti-IGF-1) rabbit polyclonal antibody (1:2,000, ab9572, Abcam), anti-glial cell line-derived neurotrophic factor (anti-GDNF) rabbit polyclonal antibody (1:500, ab18956, Abcam), anti-BDNF (1:500, ab108319, Abcam), anti-β actin rabbit polyclonal antibody (1:5,000; ab8227, Abcam), anti-β tubulin rabbit polyclonal antibody (1:5,000; ab6046, Abcam). Peroxidase anti-rabbit IgG (1:5,000, ab6721, Abcam) and peroxidase anti-mouse IgG (1:10,000, Vector Laboratories) were used as secondary antibodies. Immunoreactivity was detected using an enhanced chemiluminescence (ECL) detection kit (1705061, Bio-Rad).

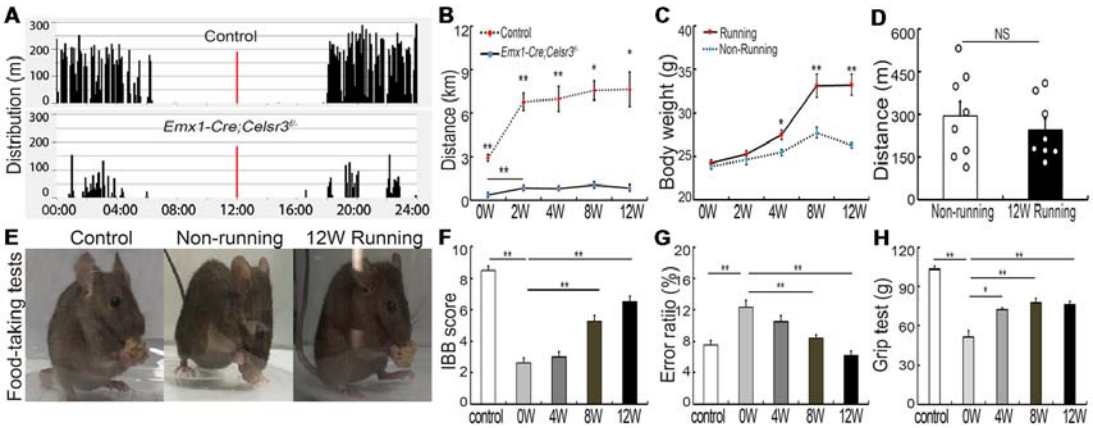

FIGURE 1 | Wheel running improves motor performance in *Emx1-Cre;Celsr3*$^{f/-}$ mutants. **(A)** Nycthemeral activity chart in control and mutant mice shows that mutants run during the dark period like controls, albeit less extensively. **(B)** Distance covered during 24 h by running in the wheel is lower in mutants than controls. $^{*}P < 0.05$; $^{**}P < 0.01$; $n = 8$. **(C)** Body weight increases in runners vs. non-runners after 8 weeks (8W) of exercise. $^{*}P < 0.05$; $^{**}P < 0.01$; $n = 8$. **(D)** Distance covered by walking in the cage is comparable in non-runners and runners after 12 weeks (12W) of running. Each circle represents the data from one animal. $P > 0.05$; $n = 8$; NS, not significant. **(E)** Examples of food-taking test performances in control, non-runner and runner mutants. Most 12-week runner mutants (6/8) could easily lift food pellets from the floor, like control animals (8/8), whereas non-runner mutants (0/8) failed to do so. **(F)** Irvine, Beatties and Bresnahan (IBB) scores in runners display a significant increase after 8 weeks (8W) of exercise and peak at 12 weeks (12W) compared to non-runners. $^{**}P < 0.01$; $n = 8$. **(G)** Gait coordination, estimated by grid tests, shows higher error rate in the mutant than in the control, with gradual improvement during exercise. $^{**}P < 0.01$; $n = 8$. **(H)** Muscle strength assessed by grasping tests. Forelimb strength in mutants is lower than in control mice and gradually increases with training. $^{*}P < 0.05$; $^{**}P < 0.01$; $n = 8$.

RNAseq Analysis

Eight-week runner and non-runner mutant mice (three animals from each group) were sacrificed and C5–C7 spinal segments were quickly dissected under a dissecting microscope. Total RNA from every six mice was extracted using a TRIzol Plus RNA Purification Kit (Cat. No. 12183018A, Invitrogen Life Technologies). The quality and quantity of the purified RNA were assessed using Agilent 2100 Bioanalyzer. RNA samples with high purity (28S/18S > 2.0) and high integrity (RIN > 8.0) were used for cDNA library construction. Eight microgram RNA from each sample was used for RNAseq (Illumina HiSeq^{TM} 2500, BGI) at the Schengen platform[1]. The method based on fragments per kilobase of exon per million fragments mapped (FPKM) was used to calculate gene expression. FPKM values were averaged for the three runners and three non-runners, and Poisson distribution analysis was performed to identify differentially expressed genes (DEGs) in the two groups. A FPKM filtering cutoff was taken as less than 0.5 in at least one of the six samples to remove genes with low abundance. Comparing the runner and the non-runner groups, transcripts were selected for further analysis by taking the cutoff of a fold change (FC) higher than 1.15 or less than 0.85 and the cutoff of *P*-value less than 0.05. The KEGG database was used to identify enriched pathways in DEGs relatively to the whole genome background (Kanehisa et al., 2008).

Statistical Analysis

Results are presented as mean ± SEM. Comparisons of different time points or groups were performed using the Student–Newman Keuls (*q* test) or Bonferroni correction. Single comparison between runner and non-runner animals at each time point was done using two-independent samples Student's *t*-test. Statistical significance was expressed as * or $^{**}P < 0.05$ or $P < 0.01$, respectively.

RESULTS

Mutant Mice Improve Motor Performances After Training

In contrast to free walking, voluntary wheel running implies a series of complex movements and motor-skill learning (Willuhn and Steiner, 2008). Control and mutant mice displayed comparable daily rhythms, with more activity in the dark than in the light (**Figure 1A**). After 2 weeks of running wheel exercise, the 24-h movement distance was significantly increased compared to that of the day of the experiment start in control (6,787.42 ± 601.47 m vs. 2,913.82 ± 238.07 m; $p = 0.001$, $t = 5.988$, $df = 14$) and mutant mice (855.75 ± 54.85 vs. 376.75 ± 66.17 m; $p = 0.001$, $t = 5.573$, $df = 14$), suggesting that both mice have the ability to learn this kind of complex movements. However, the total 24-h running distance in the wheel was significantly shorter in mutants than in control mice (**Figure 1B**), indicating a deficit of complex movements in mutants. In contrast to non-runner mutants, voluntary wheel running contributed to an increase of body weight, showing a significant difference in runner mutants after 4-week exercise (**Figure 1C**; $p = 0.011$, $t = 2.935$, $df = 14$). However, the 24-h moving distance was comparable between non-runner and runner mutants (295.33 ± 52.59 m vs. 247.28 ± 36.91 m; $p = 0.467$, $t = 0.748$, $df = 14$) at the end of 12-week exercise

[1]http://www.genomics.cn

assessed by home-cage tests (**Figure 1D**; $n = 8$ in each group), indicating running exercise cannot rescue hyperactivity in mutant animals as reported (Han et al., 2015).

Emx1-Cre;Celsr3$^{f/-}$ mutant mice have impaired skilled-motor function of forepaws (Han et al., 2015). To assess whether running exercise improves skilled movements, animals were submitted to food-pellet taking tests. At the end of 12-week exercise, most mutants (6/8) could easily grasp and lift small pellets away from the floor like control animals (8/8), whereas mutant non-runners (0/8) could not (**Figure 1E**). This was further confirmed by IBB scores: a significant increase appeared after 8 weeks running and peaked after 12 weeks running (6.50 ± 0.34, $n = 8$) compared to non-runner mutants (2.63 ± 0.32, $n = 8$), but still did not reach the scores of control animals (8.50 ± 0.27, $n = 8$; **Figure 1F**). In addition, wheel running improved gait coordination, as indicated by the significant decrease of the error ratios (falling steps to total steps) after 8 weeks running (**Figure 1G**; $p = 0.007$, $t = 3.146$, $df = 14$), a 31.4% decrease compared to mutants before running. In control animals, there were no significant changes in food-pellet taking

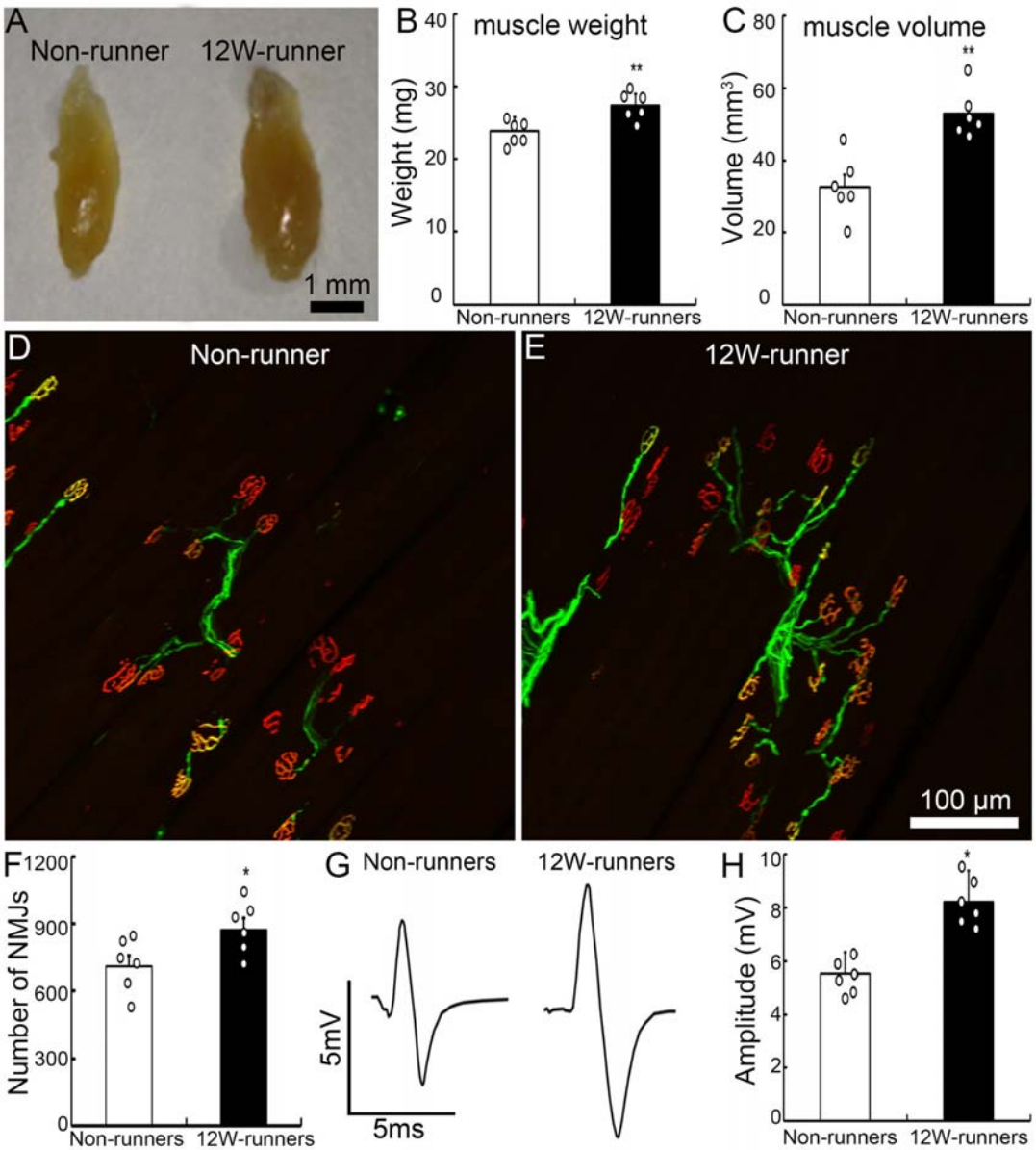

FIGURE 2 | Exercise fosters reorganization of neuromuscular junctions. **(A–C)** Twelve-week (12W) exercise increases the wet weight and volume of biceps in mutant mice. Each circle represents the data from one animal. $^{**}P < 0.01$; $n = 6$. **(D–F)** Examples of neuromuscular junctions in a non-runner **(D)** and a runner after 12-week exercise **(E)**, illustrating the higher number of nerve terminals (neurofilaments, green) and acetylcholine receptor clusters (α-BT, red) in runners, quantified in **(F)**. Each circle represents the data from one animal. $^{*}P < 0.05$; $n = 6$. **(G,H)** Electromyographic comparison. The peak-to-peak electromyography amplitude is increased in runners (**G**, right) vs. non-runners (**G**, left), as quantified in **(H)**. Each circle represents the data from one animal. $^{*}P < 0.05$; $n = 6$.

tests or grid tests after 12-week wheel running (data not shown), thus we focused our study in mutant animals thereafter.

Compared to control mice, the forelimb grasping strength was significantly lower in mutant mice, and it increased gradually after wheel running (**Figure 1H**, $n = 8$), with the increase of 39.68% ($p = 0.001$, $t = 4.34$, $df = 14$) at 4 weeks and 50.06% ($p = 0.001$, $t = 4.615$, $df = 14$) at 8 weeks compared to that before running exercise.

Forelimb function depends on elbow movements driven by the biceps brachii. After 12 weeks of exercise, the weight and volume of biceps brachii were significantly increased compared to mutant non-runners (**Figures 2A–C**; 23.93 ± 0.76 mg vs. 27.45 ± 0.63 mg, $p = 0.005$, $t = 3.549$, $df = 10$; 32.66 ± 3.51 mm^3 vs. 53.00 ± 2.65 mm^3, $p = 0.001$, $t = 4.619$). To test whether exercise triggers reorganization of spinal motor axons in muscles, we studied neuromuscular junctions by double staining with anti-neurofilament antibodies for axon terminals and α-BT for acetylcholine receptor clusters. After 12 weeks of exercise, the number of motor axonal termini surrounded by α-BT-positive acetylcholine receptor clusters was significantly increased in the runners compared to the non-runners group ($p = 0.04$, $t = 2.358$, $df = 10$; **Figures 2D,E**), and there was an increase of 22.8% of neuromuscular junctions compared to those in the non-runners group (**Figure 2F**). We recorded electromyography of biceps by stimulating the musculocutaneous nerve and found that the peak-to-peak electromyography amplitude was significantly increased in the runners after 12 weeks of exercise compared to the non-runners (**Figures 2G,H**; $p = 0.001$, $t = 6.374$, $df = 10$). Taken together, the data indicate that voluntary running fosters the reorganization of neuromuscular junctions and improves the electrophysiological function and skilled-motor performances.

Training Results in Increased Ramifications of Rubrospinal and Monoaminergic Descending Axons

To assess whether voluntary wheel running induces compensatory reorganization of rubrospinal axons in mutant spinal cords, we injected the anterograde tracer BDA in red nuclei and analyzed the density of labeled fibers in spinal C5–C7 segments. In transverse sections, well stained axons were widely distributed in the dorsolateral white matter and the gray matter contralateral to the injection side; some of them crossed the midline and innervated the ipsilateral gray matter, in samples from the runners and non-runners (**Figures 3A,B**). We quantified the fiber density as reported (Jin et al., 2015; **Figure 3C**) and found that, in runners after 12 weeks of exercise, crossing events were significantly increased contralaterally (indicated as −400, −300 and −100 μm away from the midline) and ipsilaterally (indicated as 200, 300 and 400 μm away from the midline) compared to non-runners (**Figure 3D**; $n = 3$ animals in each group).

Besides corticospinal and rubrospinal projections, spinal segments receive serotonergic inputs from the pons and dopaminergic inputs from the midbrain (Jordan et al., 2008).

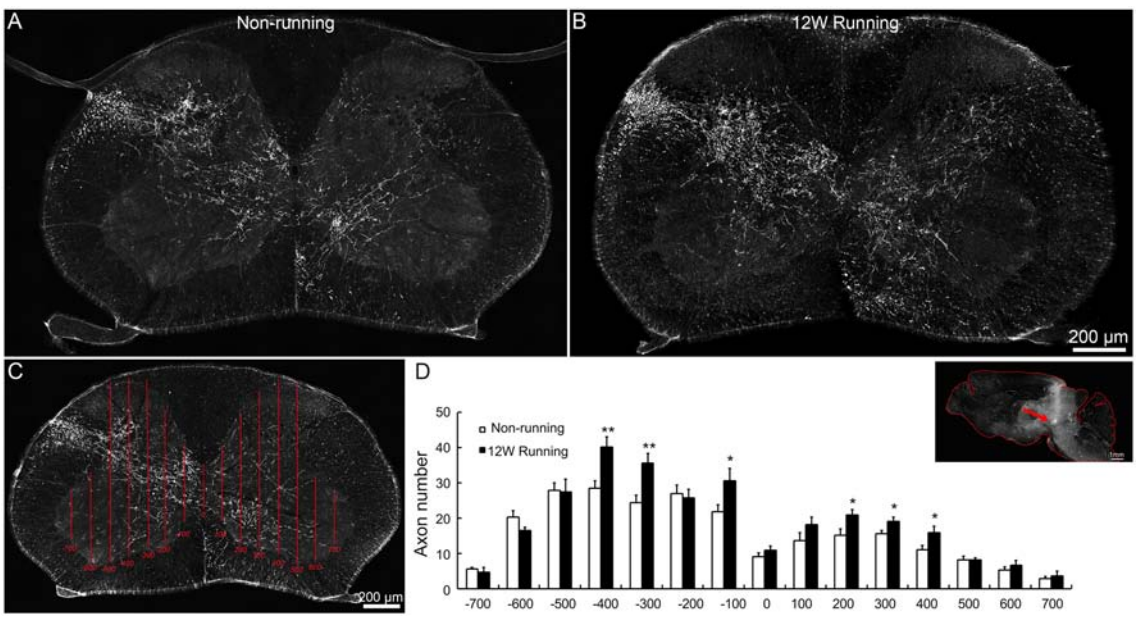

FIGURE 3 | Projections of red nuclei to the spinal cord are increased after training. **(A,B)** Upon biotinylated dextran amine (BDA) injections in the red nucleus, well stained axons are widely distributed in the dorsolateral white matter and the entire gray matter contralateral to the injection side, and some cross the midline and innervate the ipsilateral gray matter, both in runners **(A)** and non-runners **(B)**. **(C,D)** Quantitative assessment of axon extension shows that, after 12 weeks (12W) of training, the number of grid crossing is significantly increased at contralateral (indicated as −400, −300 and −100 μm away from the midline) and ipsilateral levels (indicated as 200, 300 and 400 μm away from the midline) in runners in comparison to non-runners. $^*P < 0.05$; $^{**}P < 0.01$; $n = 3$ for each group. The insert in **(D)** showed the injection site (arrow).

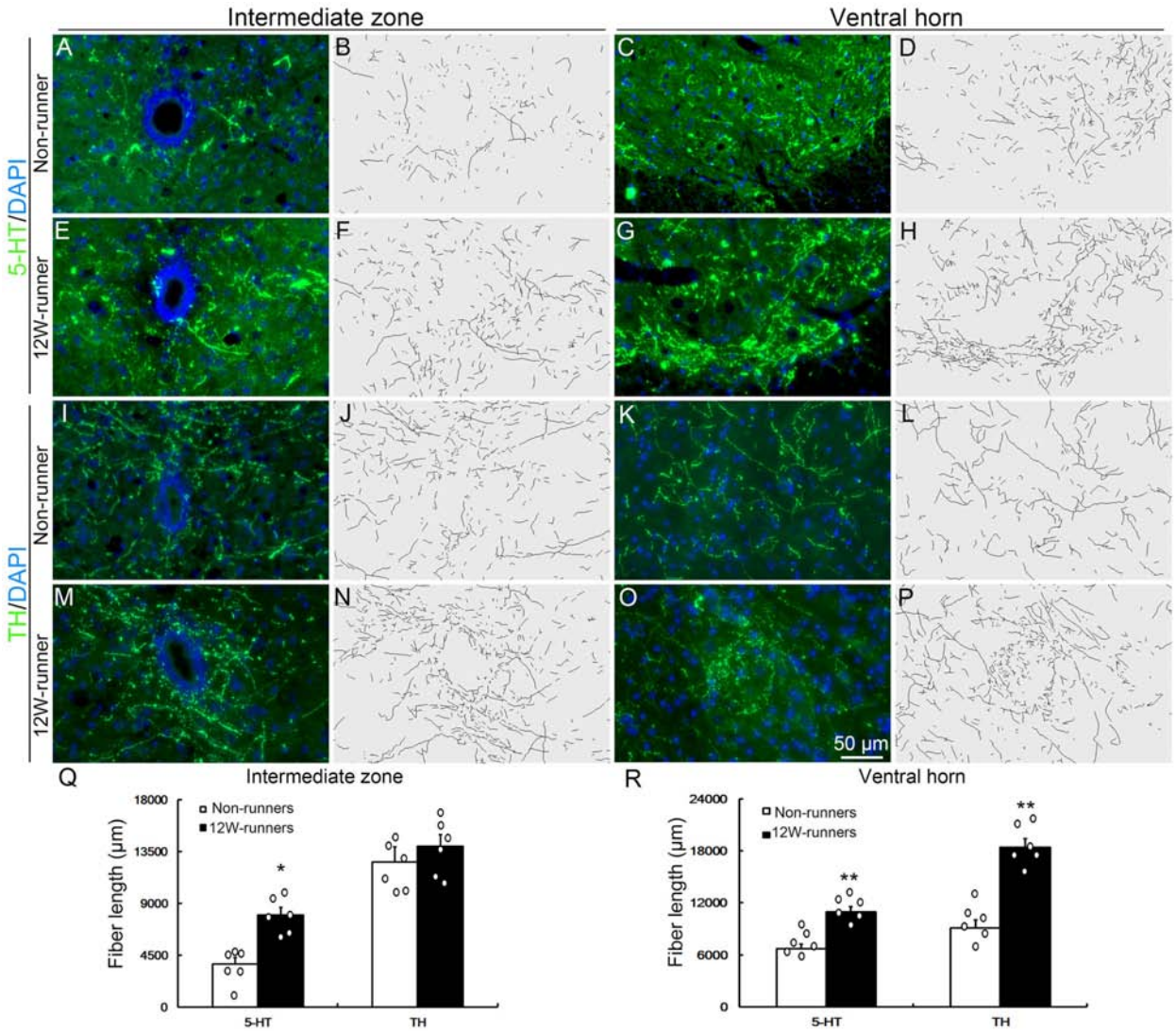

FIGURE 4 | Monoaminergic fibers in the spinal cord are increased after training. **(A–P)** Intermediate zone and ventral horn of spinal cord at C5–C7 segments, stained with anti-serotonin (anti-5-TH, **A–H**) and anti-tyrosine hydroxylase (anti-TH, **I–P**) antibodies, with outline of fiber patterns upon 3D reconstruction. **(Q,R)** Quantification of fiber length in intermediate zone and ventral horn. Each circle represents the data from one animal. $^{*}P < 0.05$; $^{**}P < 0.01$; $n = 6$ for each group.

The monoaminergic information is implicated in the initiation of locomotion under normal conditions, and the reorganization of their axons in the spinal cord contributes to functional recovery after SCI (Schmidt and Jordan, 2000; Carelli et al., 2017). To investigate whether voluntary wheel running influences monoaminergic innervation, C5−C7 transverse spinal sections were immunostained with anti-5-HT and anti-TH antibodies, followed with tri-dimensional reconstruction of fiber distribution. 5-HT- and TH-positive fibers were identified in the intermediate zone and the ventral horn in both groups (**Figures 4A–P**). In the intermediate zone, there was a significant increase of serotoninergic ($p = 0.01$, $t = 4.882$, $df = 10$), but not of dopaminergic fibers ($p = 0.230$, $t = 1.278$, $df = 10$) after 12 weeks of exercise in runners compared to non-runners (**Figures 4B,F,J,N,Q**). In the ventral horn, the density of serotoninergic and dopaminergic fibers was dramatically increased after 12-week running exercise (**Figures 4D,H,L,P,R**; $p = 0.001$, $t = 4.882$ and $p = 0.001$, $t = 6.857$, respectively).

To examine whether the increased monoaminergic projections make more contacts with spinal motor neurons, we performed double immunostaining with anti-ChAT antibodies to label spinal motor neurons, and anti-TH and anti-5-HT antibodies in C5–C7 transverse spinal sections. We did not observe more contacts between 5-HT-positive fibers and ChAT-positive cells (data not shown). By contrast, TH-positive fibers came into close proximity to spinal motor neurons, particularly in samples from runners (**Figures 5A,B**). We quantified the number of TH-positive varicosities adjacent to cholinergic motor neurons or dendrites. The criteria were

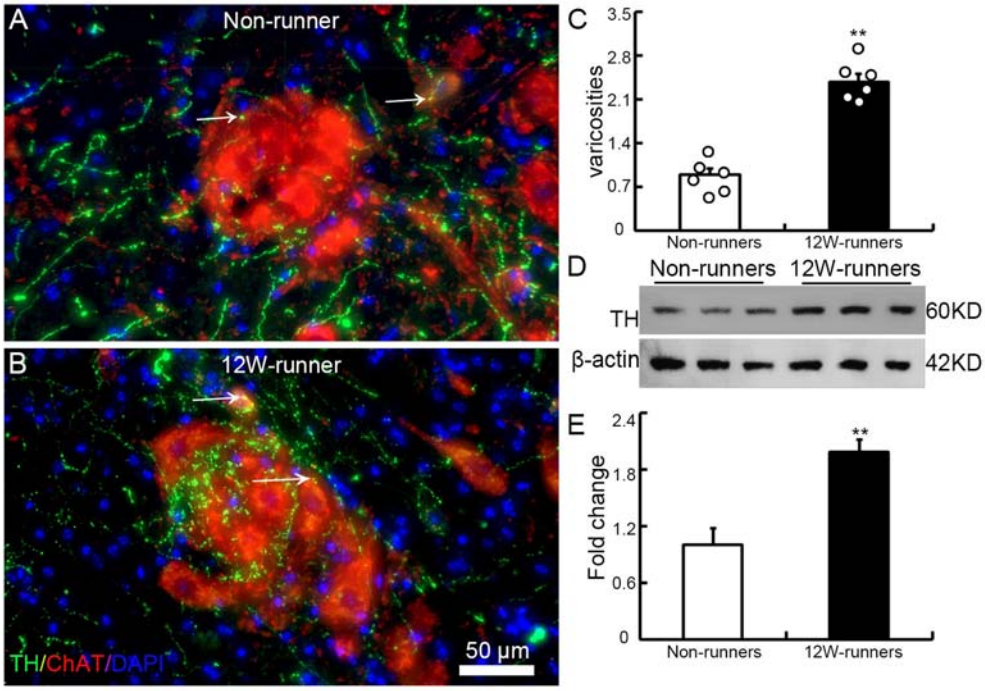

FIGURE 5 | Training induces increased contacts between dopaminergic axons and spinal motor neurons. **(A,B)** Illustration of contacts between TH-positive varicosities and cholinergic neurons in a non-runner **(A)** and a runner after training **(B)** the white arrows indicate "contacting varicosities between 5-HT fibers and ChAT-positive neurons". **(C)** Quantification of TH-positive varicosities. Each circle represents the data from one animal. $^{**}P < 0.01$; $n = 6$ for each group. **(D)** Western blot analysis of TH protein content in three non-runners and three runners, relatively to β-actin control, with quantification. **(E)** Statistics of protein levels. $^{**}P < 0.01$.

taken by visualizing an obvious varicose structure (more than 2-fold of axon diameter) along the axons and no visible space between the varicosity and the neuron when viewed at high magnification by confocal microscopy (Takeoka et al., 2009, 2010). In 12-week runner mutant mice, there was a significant increase of varicosities between TH-positive fibers and cholinergic spinal motor neurons (**Figure 5C**; $n = 6$ mice in each group). In agreement with this, western blot analysis showed that the TH protein level in runners' spinal cords was about 2-fold higher than in non-runners (**Figures 5D,E**; $p = 0.001$, $t = 7.84$, $df = 4$).

Training Activates Oligodendrogenesis in the Spinal Cord

BrdU studies showed the proliferation and differentiation of glial progenitors in the intact adult rat spinal cord (Horner et al., 2000). To assess whether running affects cell proliferation in spinal cords, we injected EDU to label newly-born cells in 12-week runner and non-runner mutant animals. In non-runners, a few EDU-labeled cells were scattered in the gray and white matter of C5–C7 spinal segments (**Figure 6A**). In contrast, the number of EDU-labeled cells was significantly increased after 12-week exercise (**Figure 6B**), about 4.8-folds higher than in non-runners (**Figure 6G**). To trace the lineage of these EDU-positive cells, we coupled EDU staining with immunostaining for neuronal, oligodendrocyte, astrocyte and microglial cell markers and found that more than 90% of EDU labeled cells were positive for Olig2, an oligodendrocyte marker (**Figures 6C–F**; $p = 0.001$; $t = 5.63$; $df = 6$).

Running Exercise Modifies Transcriptomic Profiles in the Spinal Cord

To further explore potential molecular mechanisms involved in exercise-induced neural plasticity in mutant animals, we compared gene expression of spinal C5–C7 segments in 8-week runners and matched non-runners, using RNAseq. mRNA libraries were generated from runners and non-runners mutant mice (three repeats for each group). High quality clean reads of 30, 851, 978 (97.23% of raw reads) were obtained for non-runners and 29, 818, 423 (97.47% of raw reads) for runners (**Figure 7A**). In the runner and non-runner groups, 88.30% and 88.60% of total clean reads were uniquely matched to gene-mapped reads, respectively. There were a total number of 17,951 co-expressed genes in runner and non-runner mutants, 441 unique genes in non-runners and 510 unique genes in runners (**Figure 7B**). Among them, 404 genes were up-regulated and 398 genes were down-regulated in the runner compared to the non-runner mutants (**Figure 7C**; $p < 0.05$). We then examined these 802 genes using pathway enrichment analysis and found that a total of 290 DEGs were annotated in the data bank (**Supplementary Table S1**). Some differentially activated pathways were related to neurodegenerative diseases (i.e., Parkinson's, Alzheimer's and

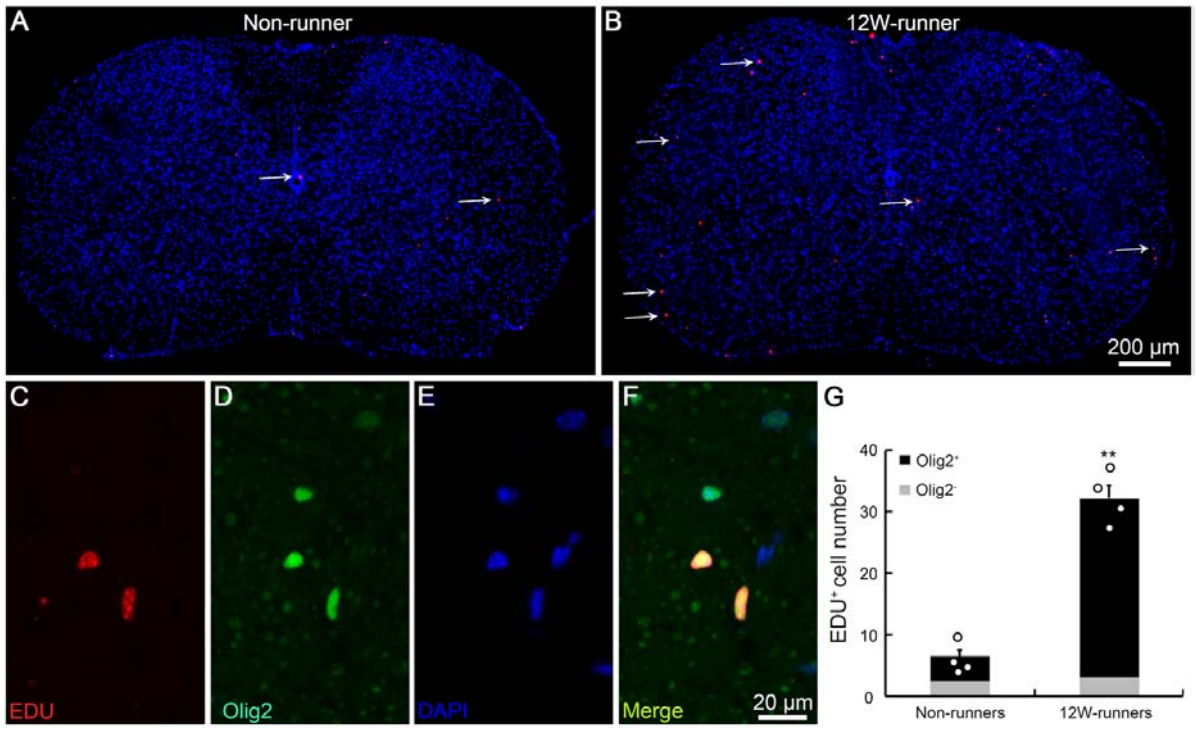

FIGURE 6 | Exercise activates neurogenesis in the spinal cord. **(A,B)** Overview of 5-ethynyl-2′-deoxyuridine (EDU) signal in spinal cords in non-runners **(A)** and runners **(B)**, and EDU-positive cells are indicated by arrows. **(C–G)** EDU-positive cells in runners are mostly Olig2-positive and about 4.8-fold more abundant in runners than in non-runners. Each circle represents the data from one animal. $^{**}P < 0.01$; $n = 4$ in each group.

Huntington's diseases) and energy metabolism (especially oxidative phosphorylation; **Figures 7D,E**). Sixty-nine DEGs were involved in signal transduction, and three top signaling pathways in the KEGG map were the NF-κB signaling pathway (10 DEGs, such as *Xiap*, *Tnfrsf1a*, *Relb* and *Tab3*), the PI3K-Akt signaling pathway (21 DEGs, such as *Fgf1*, *Igf1*, *Epor*, and *Thbs1*) and the cAMP signaling pathway (12 DEGs, such as *Gipr, PLD1*, *Rock1*, *Epac1* and *Gria1*; **Figures 7D,E**; **Supplementary Table S1**).

Exercise Induces Changes of Synaptic and Myelin-Related Proteins, but Not of Neurotrophins or Cytokines in Spinal Cords

Results mentioned above suggest that increased descending axons (rubrospinal and monoaminergic axons) may make more synapses with spinal neurons after training. To document this further, the levels of PSD95 and presynaptic protein synaptophysin (SY38) were analyzed by western blot in extracts from C5 to C7 spinal samples. After 12 weeks of exercise, PSD95 and SY38 proteins were significantly increased in runners compared to non-runners, respectively 1.37 and 1.60-fold (**Figures 8A,B**; $p = 0.015$, $t = 4.059$ and $p = 0.049$, $t = 2.79$, $df = 4$, respectively). Although this is somewhat controversial (Duncan et al., 2018), re-myelination of axonal sheaths may assist functional recovery after injury (Takase et al., 2018; Yang et al., 2018). In line with increased oligodendrogenesis after running exercise, we found that the protein level of MBP was significantly increased in 12-weeks runners, 2.01-folds of that in non-runners (**Figures 8C,D**; $p = 0.03$, $t = 6.71$, $df = 4$). In addition, Olig2 expression also showed an increased trend in runner animals (**Figures 8C,D**).

It is widely believed that neurotrophic factors play a significant role in neural plasticity and neurogenesis after exercise (Cobianchi et al., 2017). We therefore assessed the expression of a few neurotrophic factors including BDNF, GDNF and IGF1 in C5–C7 spinal samples from 12-week runners and non-runners. Quite unexpectedly, we did not find any significant difference in BDNF, GDNF and IGF1 protein levels in both groups (**Figures 8E,F**; $P > 0.05$; $n = 3$ animals in each group). To further identify whether running exercise induced changes of inflammatory cytokine levels, we compared samples from blood, muscles and C5–C7 spinal tissues in 12-week runner mice and matched non-runner mice, using Bioplex. There was a significant decrease of MIP-1β, TNF-α, IL-1β, MCP-1 and MIP-1α in blood of the running group, but not in muscles or spinal cord extracts (**Figure 9**; $n = 3$ animals in each group).

DISCUSSION

The present study was designed to determine whether voluntary exercise is beneficial and improves locomotor plasticity in

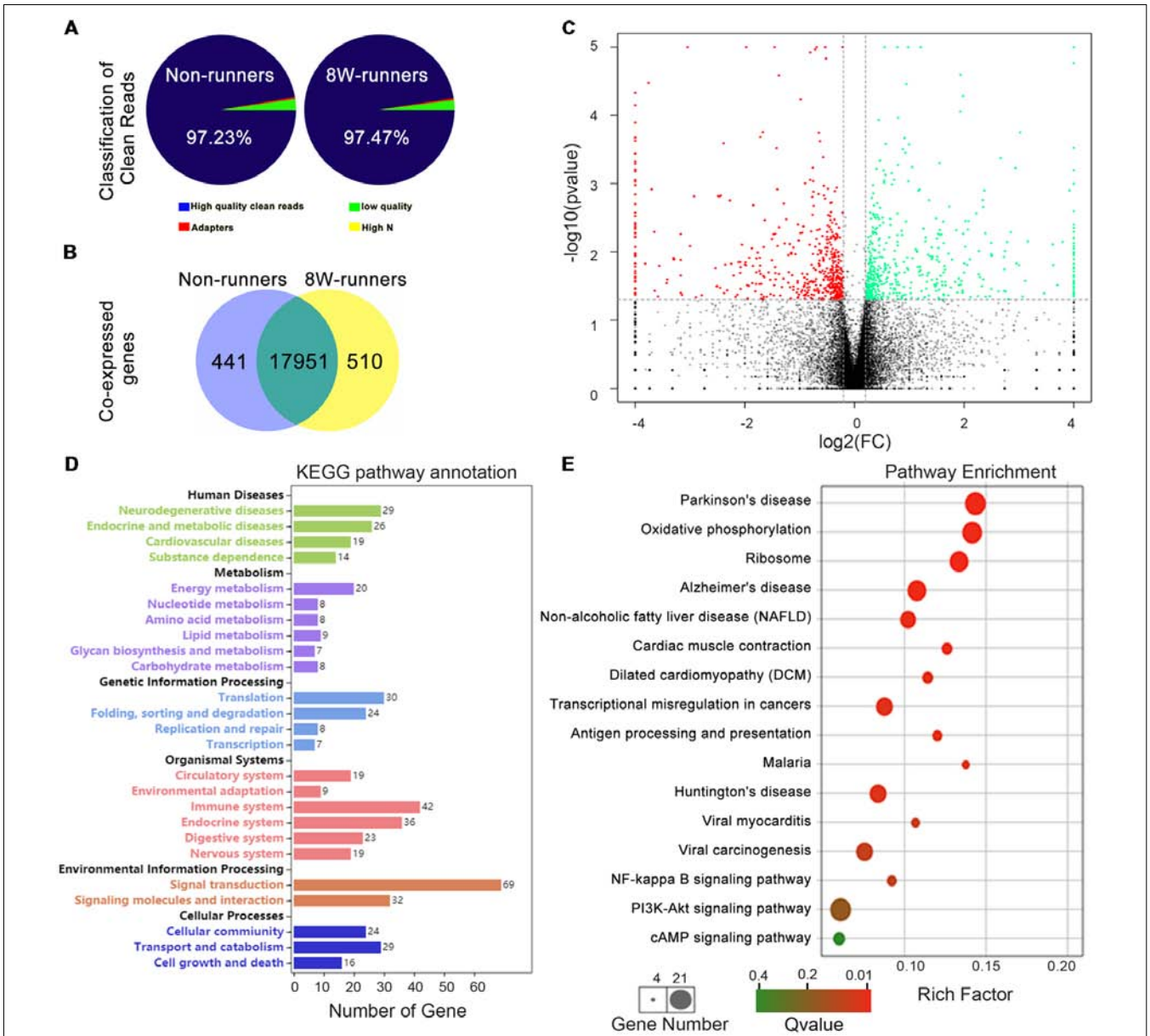

FIGURE 7 | Transcriptomic profiling of mutant mice after training. **(A)** Classification of clean reads in non-runner and 8-week (8W) runner mutants. **(B)** There are a total number of 17,951 co-expressed genes in runner and non-runner mutants, 441 unique genes in non-runners, and 510 unique genes in runners. **(C)** Scatter plots show co-expressed genes in runner and non-runner mutants. Green dots indicate down-regulated genes, and red dots represent up-regulated genes in the runner group, whereas brown dots show genes with no significant changes. Cutoffs of a fold change (FC) at 1.15, and *P*-value at less than 0.05 are considered significant. **(D)** Differentially expressed genes (DEGs) annotated in KEEG pathways. **(E)** KEGG pathway enrichment of the DEGs. The rich factor is calculated using the number of enriched genes divided by the number of all background genes in the corresponding pathway.

a mutant mouse model with congenital absence of the CST. Our results show that training for 8–12 consecutive weeks improves fine motor skills and muscle force. This is correlated with: (i) increased ramifications of rubrospinal and monoaminergic axons in the spinal cord, and increased contacts between dopaminergic varicosities and motor neurons; (ii) stimulation of spinal oligodendrogenesis and increased expression of synaptic and myelin marker proteins; (iii) modified expression of various genes and signaling pathways detected using transcriptomics analysis; and (iv) absence of detectable modifications of growth factors and cytokine expression in spinal cord.

The CST and rubrospinal tract are two most important descending axonal bundles that control spinal motor neurons to drive limb movements, and may partly palliate each other (Kennedy, 1990; Cheney et al., 1991). The observation that *Emx1-Cre;Celsr3*$^{f/-}$ mice have no CST and poor fine movement control shows that skilled motor function (such

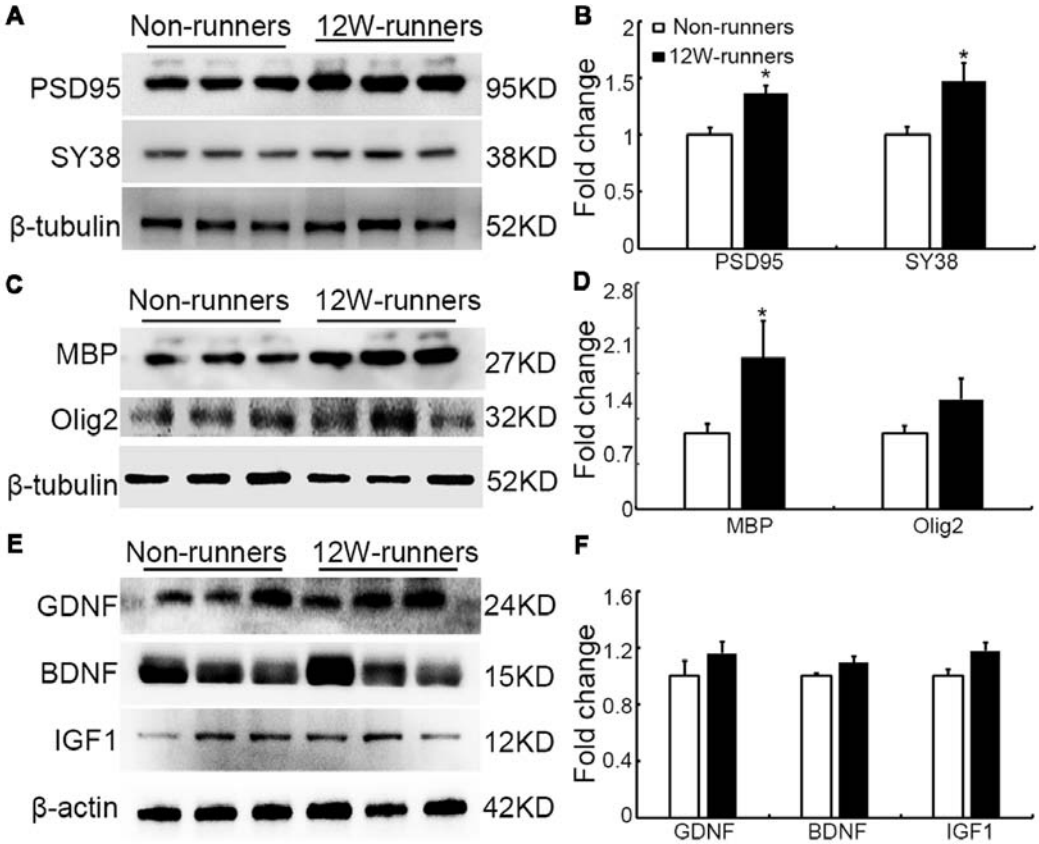

FIGURE 8 | Expression of synaptic and myelin-related proteins is increased after training. **(A,B)** Western blot analysis and quantification of postsynaptic density protein (PSD95) and the presynaptic protein synaptophysin (SY38). **(C,D)** Analysis of oligodendrocyte transcription factor-2 (Olig2) and myelin basic protein (MBP). **(E,F)** Neurotrophins glia-derived neurotrophic factor (GDNF), brain-derived neurotrophic factor (BDNF) and insulin like growth factor-1 (IGF-1). β-tubulin or β-actin is used as control as indicated. $^*P < 0.05$; three animals used in each group.

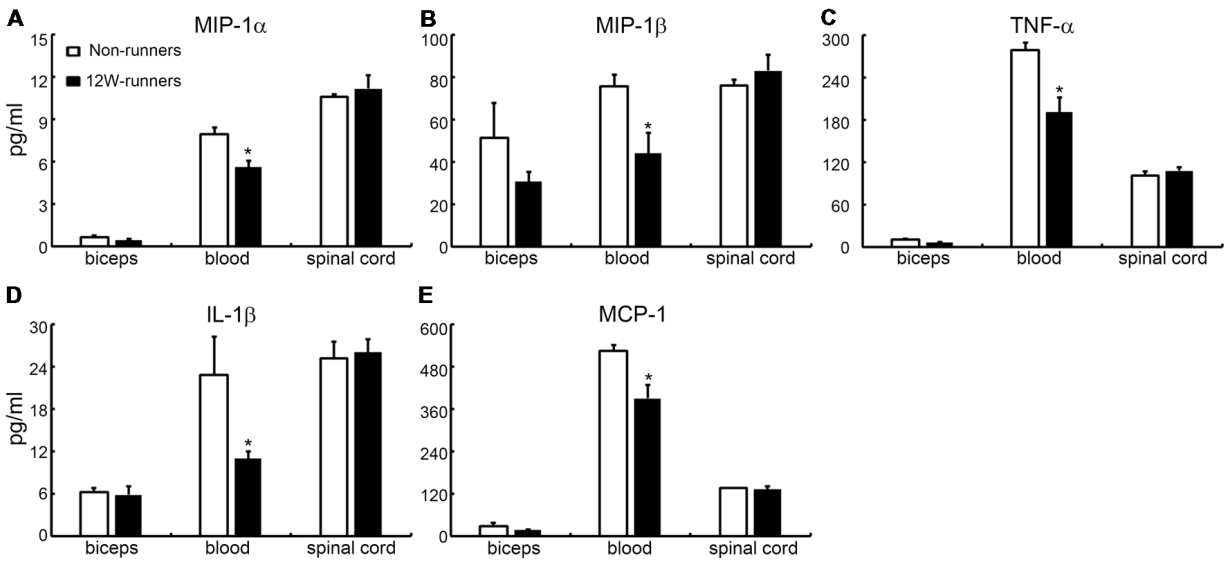

FIGURE 9 | Cytokine levels in spinal cord are unchanged by training. **(A–E)** Exercise can decrease the content of five inflammatory factors in the blood (MIP-1β; TNF-α; IL-1β; MCP-1; MIP-1α), but not in the muscle or spinal cord. $^*P < 0.05$; three animals used in each group.

as food pellet taking) is especially dependent on the CST and cannot be spontaneously compensated by rubrospinal input (Han et al., 2015). Here we provide evidence that voluntary wheel training can rescue fine movement control in CST-deficient mutant mice, thus providing evidence for intrinsic plasticity in the absence of lesion. Our results show a significant increase of rubrospinal terminals in spinal segments in runner compared to non-runner mutants, and exercise resulted in increased spinal cord expression of synaptic proteins PSD-95 and SY38. Exercise may thus trigger formation of additional synapses by rubrospinal axons, which could serve a function comparable to that of the CST in fine movement control. This should be confirmed using transynaptic labeling, for example using modified rabies virus (Callaway and Luo, 2015).

Fine movements of forelimbs are also dependent on coordinated monoaminergic inputs to spinal neurons. Serotoninergic inputs from parapyramidal raphe nuclei facilitate the initiation of movements (Jordan et al., 2008; Cabaj et al., 2017) and activate central pattern generators that produce rhythmic outputs, even after the loss of the CST (Schmidt and Jordan, 2000). Similarly, dopaminergic inputs from the A11 diencephalic region modulate locomotor function (Sharples et al., 2015), and motor skill learning is impaired upon inhibition of dopaminergic signaling (Willuhn and Steiner, 2008). In our study, the input of monoaminergic axons to spinal cord was increased and this may contribute to coordinating the activity of spinal motor neurons and/or segmental interneurons.

Spinal motor axons are the final pathway from upper motor neurons to muscles and drive muscle activity via neuromuscular junctions. After exercise, muscle strength and weight were augmented; neuromuscular junctions were increased in number, and muscle innervation became more efficient, as indicated in electromyographic recordings. These changes presumably reflect increased supraspinal inputs to spinal motor neurons (Ding et al., 2014), and/or a more efficient feedback loop between muscles and spinal motorneurons after wheel running training.

After wheel running, we found a significant increase of oligodendrogenesis with new myelin formation indicated by elevated MBP protein levels. Previous studies showed that, in rodents, active central myelination is required for skill motor learning (McKenzie et al., 2014). In mice submitted to wheel running, a secondary wave of oligodendrocyte precursor proliferation and differentiation is present in motor cortex (Xiao et al., 2016), and structural changes of the white matter were observed by MRI after learning a novel motor skill (Sampaio-Baptista et al., 2013). The role of re-myelination after SCI is somewhat controversial: some studies suggest that it is important for functional improvement (Karimi-Abdolrezaee et al., 2006; Biernaskie et al., 2007), whereas another work proposed that locomotor recovery does not require oligodendrocyte remyelination (Duncan et al., 2018). In intact adult spinal cords, cell proliferation is rare and restricted to the surrounding of the central canal (Barnabé-Heider et al., 2010; Becker et al., 2018). In runner mutants, we found EDU-labeled cells widely scattered in the gray and white matter, indicating that they undergo migration and may foster new myelin formation of long projecting and local spinal axons. Altogether, we propose that, in our mutant mice, running-induced myelination modulates neural spinal networks to foster skilled motor performance.

Several molecules and signaling mechanisms are thought to be involved in exercise-induced neural plasticity, such as neurotrophic factors (Zhao et al., 2012) or cAMP signaling (Ko et al., 2018). Here, we provide evidence that wheel-running influences the transcriptomic profile in the spinal cord. Wheel running is a moderate intervention and its effect may be highly dynamic. After 8-week running, expression of several genes was modified, and regulation of some signaling pathways were predicted, including pathways related to neuron degeneration (i.e., Parkinson's disease), oxidative phosphorylation, NF-κB signaling, PI3K-Akt signaling, and cAMP signaling. As described before, wheel running induces a significant elevation of dopaminergic fiber ramification and TH protein levels in spinal cord, and this may be a reason why some DEGs are associated with Parkinson's disease. Those data also suggest that the dopaminergic system might be implicated in exercise-induced neural plasticity. Oxidative phosphorylation is critical for ATP production by mitochondria, and increased mitochondrial metabolism contributes to neural plasticity and cell proliferation (Radak et al., 2007; Batty et al., 2017). The observed changes of oxidative phosphorylation-related genes presumably favor exercise-induced axonal ramification, new synapse formation and oligodendrogenesis.

We found 12 DEGs involved in the cAMP signaling pathway, among which *Gipr*, *PLD1*, *Rock1*, *Epac1* and *Gria1* are involved in neural plasticity and/or neurite growth (Mead and Stephens, 2003; Zhang et al., 2004; Faivre et al., 2011; Yang et al., 2012; Greathouse et al., 2018). In addition, 20 DEGs are involved in the PI3K/Akt pathway, and 10 DEGs in NF-κB signaling. These genes may point to potential mechanisms of exercise-induced locomotor plasticity that remain to be studied further.

Physical exercise results in increased production of neurotrophic factors and regulation of levels of some cytokines, cytokine inhibitors and chemokines, all of which may contribute to improving motor function and cognition in neurodegenerative disorders (Svensson et al., 2015; Wei et al., 2018). In SCI, local levels of cytokines critically influence the kinetics of neuron survival, axon degeneration and regeneration (Sun et al., 2016). Unexpectedly, we found a downregulation of pro-inflammatory cytokines including TNF-α, IL-1β, MCP-1, MIP-1α and MIP-1β after 12-week running only in serum but not in the spinal cord or muscles. Furthermore, we could not detect any differences in levels of classic neurotrophic factors including BDNF, GDNF and IGF1 after 12-week running exercise. The reasons for this apparent discrepancy are not clear. Spinal cord cytokine and growth factor levels may be more prone to change in the context of a lesion than upon exercise alone. Also, we measured cytokines and growth factors only at the end of the exercise period (12 weeks), whereas changes could follow a dynamic course.

In *Emx1-Cre;Celsr3*$^{f/-}$ mutant mice, the CST never develops, a situation which is different from experimental lesions. In that sense, those mice do not provide a fully relevant model for SCI or cerebral palsy (Clowry et al., 2014). With that reservation, our observations that motor-skill learning exercise can trigger intrinsic motor plasticity, even in the absence of lesion, is strong indication that similar procedures should be helpful in lesion cases. Our results suggest that skilled motor learning training, used as a complement to treadmill training, should be beneficial to patients with SCI, cerebral palsy and related conditions.

DATA AVAILABILITY

The datasets generated for this study can be found in SRA accession, PRJNA521582.

AUTHOR CONTRIBUTIONS

LZ, YQ and K-FS designed the experiment. WZ, BY, HW, TL and PY performed the research. WZ and LS analyzed the data. WZ and LZ wrote the manuscript.

FUNDING

This work was supported by the following grants: National Natural Science Foundation of China (81571186), National Basic Research Program of China (973 Program, 2014CB542205), Programme of Introducing Talents of Discipline to Universities (B14036), Science & Technology Planning and Key Technology Innovation Projects of Guangdong (2014B050504006), Health and Medical Collaborative Innovation Major Projects of Guangzhou (201803040016) and Guangzhou City-University Research Cooperative Innovation Major Project (20164046028).

ACKNOWLEDGMENTS

We wish to thank Andre Goffinet for help with manuscript edition, and Meizhi Wang for technical assistance.

SUPPLEMENTARY MATERIAL

The Supplementary Material for this article can be found online at: https://www.frontiersin.org/articles/10.3389/fncel.2019.00106/full#supplementary-material

REFERENCES

Alamri, F. F., Shoyaib, A. A., Biggers, A., Jayaraman, S., Guindon, J., and Karamyan, V. T. (2018). Applicability of the grip strength and automated von Frey tactile sensitivity tests in the mouse photothrombotic model of stroke. *Behav. Brain Res.* 336, 250–255. doi: 10.1016/j.bbr.2017.09.008

Barnabé-Heider, F., Göritz, C., Sabelström, H., Takebayashi, H., Pfrieger, F. W., Meletis, K., et al. (2010). Origin of new glial cells in intact and injured adult spinal cord. *Cell Stem Cell* 7, 470–482. doi: 10.1016/j.stem.2010.07.014

Batty, N. J., Fenrich, K. K., and Fouad, K. (2017). The role of cAMP and its downstream targets in neurite growth in the adult nervous system. *Neurosci. Lett.* 652, 56–63. doi: 10.1016/j.neulet.2016.12.033

Becker, C. G., Becker, T., and Hugnot, J. P. (2018). The spinal ependymal zone as a source of endogenous repair cells across vertebrates. *Prog. Neurobiol.* 170, 67–80. doi: 10.1016/j.pneurobio.2018.04.002

Biernaskie, J., Sparling, J. S., Liu, J., Shannon, C. P., Plemel, J. R., Xie, Y., et al. (2007). Skin-derived precursors generate myelinating Schwann cells that promote remyelination and functional recovery after contusion spinal cord injury. *J. Neurosci.* 27, 9545–9559. doi: 10.1523/JNEUROSCI.1930-07.2007

Cabaj, A. M., Majczynski, H., Couto, E., Gardiner, P. F., Stecina, K., Slawinska, U., et al. (2017). Serotonin controls initiation of locomotion and afferent modulation of coordination via 5-HT$_7$ receptors in adult rats. *J. Physiol.* 595, 301–320. doi: 10.1113/jp272271

Callaway, E. M., and Luo, L. (2015). Monosynaptic circuit tracing with glycoprotein-deleted rabies viruses. *J. Neurosci.* 35, 8979–8985. doi: 10.1523/JNEUROSCI.0409-15.2015

Carelli, S., Giallongo, T., Gombalova, Z., Merli, D., Di Giulio, A. M., and Gorio, A. (2017). EPO-releasing neural precursor cells promote axonal regeneration and recovery of function in spinal cord traumatic injury. *Restor. Neurol. Neurosci.* 35, 583–599. doi: 10.3233/rnn-170750

Carmichael, S. T., Kathirvelu, B., Schweppe, C. A., and Nie, E. H. (2017). Molecular, cellular and functional events in axonal sprouting after stroke. *Exp. Neurol.* 287, 384–394. doi: 10.1016/j.expneurol.2016.02.007

Cheney, P. D., Fetz, E. E., and Mewes, K. (1991). Neural mechanisms underlying corticospinal and rubrospinal control of limb movements. *Prog. Brain Res.* 87, 213–252. doi: 10.1016/s0079-6123(08)63054-x

Clowry, G. J., Basuodan, R., and Chan, F. (2014). What are the best animal models for testing early intervention in cerebral palsy? *Front. Neurol.* 5:258. doi: 10.3389/fneur.2014.00258

Cobianchi, S., Arbat-Plana, A., Lopez-Alvarez, V. M., and Navarro, X. (2017). Neuroprotective effects of exercise treatments after injury: the dual role of neurotrophic factors. *Curr. Neuropharmacol.* 15, 495–518. doi: 10.2174/1570159x14666160330105132

Ding, Y., Qu, Y., Feng, J., Wang, M., Han, Q., So, K. F., et al. (2014). Functional motor recovery from motoneuron axotomy is compromised in mice with defective corticospinal projections. *PLoS One* 9:e101918. doi: 10.1371/journal.pone.0101918

Duncan, G. J., Manesh, S. B., Hilton, B. J., Assinck, P., Liu, J., Moulson, A., et al. (2018). Locomotor recovery following contusive spinal cord injury does not require oligodendrocyte remyelination. *Nat. Commun.* 9:3066. doi: 10.1038/s41467-018-05473-1

Dunlop, S. A. (2008). Activity-dependent plasticity: implications for recovery after spinal cord injury. *Trends Neurosci.* 31, 410–418. doi: 10.1016/j.tins.2008.05.004

Eckel-Mahan, K., and Sassone-Corsi, P. (2015). Phenotyping circadian rhythms in mice. *Curr. Protoc. Mouse Biol.* 5, 271–281. doi: 10.1002/9780470942390.mo140229

Faivre, E., Gault, V. A., Thorens, B., and Hölscher, C. (2011). Glucose-dependent insulinotropic polypeptide receptor knockout mice are impaired in learning, synaptic plasticity and neurogenesis. *J. Neurophysiol.* 105, 1574–1580. doi: 10.1152/jn.00866.2010

Greathouse, K. M., Boros, B. D., Deslauriers, J. F., Henderson, B. W., Curtis, K. A., Gentry, E. G., et al. (2018). Distinct and complementary functions of rho kinase isoforms ROCK1 and ROCK2 in prefrontal cortex structural plasticity. *Brain Struct. Funct.* 223, 4227–4241. doi: 10.1007/s00429-018-1748-4

Han, Q., Cao, C., Ding, Y., So, K. F., Wu, W., Qu, Y., et al. (2015). Plasticity of motor network and function in the absence of corticospinal projection. *Exp. Neurol.* 267, 194–208. doi: 10.1016/j.expneurol.2015.03.008

Hannila, S. S., and Filbin, M. T. (2008). The role of cyclic AMP signaling in promoting axonal regeneration after spinal cord injury. *Exp. Neurol.* 209, 321–332. doi: 10.1016/j.expneurol.2007.06.020

Harkin, A., O'Donnell, J. M., and Kelly, J. P. (2002). A study of VitalView for behavioural and physiological monitoring in laboratory rats. *Physiol. Behav.* 77, 65–77. doi: 10.1016/s0031-9384(02)00810-7

Horner, P. J., Power, A. E., Kempermann, G., Kuhn, H. G., Palmer, T. D., Winkler, J., et al. (2000). Proliferation and differentiation of progenitor cells throughout the intact adult rat spinal cord. *J. Neurosci.* 20, 2218–2228. doi: 10.1523/JNEUROSCI.20-06-02218.2000

Ilha, J., Centenaro, L. A., Broetto Cunha, N., de Souza, D. F., Jaeger, M., do Nascimento, P. S., et al. (2011). The beneficial effects of treadmill step training on activity-dependent synaptic and cellular plasticity markers after complete spinal cord injury. *Neurochem. Res.* 36, 1046–1055. doi: 10.1007/s11064-011-0446-x

Irvine, K. A., Ferguson, A. R., Mitchell, K. D., Beattie, S. B., Beattie, M. S., and Bresnahan, J. C. (2010). A novel method for assessing proximal and distal forelimb function in the rat: the Irvine, Beatties and Bresnahan (IBB) forelimb scale. *J. Vis Exp.* 46:2246. doi: 10.3791/2246

Jhuang, H., Garrote, E., Mutch, J., Yu, X., Khilnani, V., Poggio, T., et al. (2010). Automated home-cage behavioural phenotyping of mice. *Nat. Commun.* 1:68. doi: 10.1038/ncomms1399

Jin, D., Liu, Y., Sun, F., Wang, X., Liu, X., and He, Z. (2015). Restoration of skilled locomotion by sprouting corticospinal axons induced by co-deletion of PTEN and SOCS3. *Nat. Commun.* 6:8074. doi: 10.1038/ncomms9074

Jordan, L. M., Liu, J., Hedlund, P. B., Akay, T., and Pearson, K. G. (2008). Descending command systems for the initiation of locomotion in mammals. *Brain Res. Rev.* 57, 183–191. doi: 10.1016/j.brainresrev.2007.07.019

Jung, S. Y., Kim, D. Y., Yune, T. Y., Shin, D. H., Baek, S. B., and Kim, C. J. (2014). Treadmill exercise reduces spinal cord injury-induced apoptosis by activating the PI3K/Akt pathway in rats. *Exp. Ther. Med.* 7, 587–593. doi: 10.3892/etm.2013.1451

Kanehisa, M., Araki, M., Goto, S., Hattori, M., Hirakawa, M., Itoh, M., et al. (2008). KEGG for linking genomes to life and the environment. *Nucleic Acids Res.* 36, D480–D484. doi: 10.1093/nar/gkm882

Karimi-Abdolrezaee, S., Eftekharpour, E., Wang, J., Morshead, C. M., and Fehlings, M. G. (2006). Delayed transplantation of adult neural precursor cells promotes remyelination and functional neurological recovery after spinal cord injury. *J. Neurosci.* 26, 3377–3389. doi: 10.1523/JNEUROSCI.4184-05.2006

Kennedy, P. R. (1990). Corticospinal, rubrospinal and rubro-olivary projections: a unifying hypothesis. *Trends Neurosci.* 13, 474–479. doi: 10.1016/0166-2236(90)90079-p

Kleim, J. A., Bruneau, R., Calder, K., Pocock, D., VandenBerg, P. M., MacDonald, E., et al. (2003). Functional organization of adult motor cortex is dependent upon continued protein synthesis. *Neuron* 40, 167–176. doi: 10.1016/s0896-6273(03)00592-0

Ko, I. G., Kim, S. E., Hwang, L., Jin, J. J., Kim, C. J., Kim, B. K., et al. (2018). Late starting treadmill exercise improves spatial leaning ability through suppressing CREP/BDNF/TrkB signaling pathway following traumatic brain injury in rats. *J. Exerc. Rehabil.* 14, 327–334. doi: 10.12965/jer.1836248.124

Kuczynski, A. M., Dukelow, S. P., Hodge, J. A., Carlson, H. L., Lebel, C., Semrau, J. A., et al. (2018). Corticospinal tract diffusion properties and robotic visually guided reaching in children with hemiparetic cerebral palsy. *Hum. Brain Mapp.* 39, 1130–1144. doi: 10.1002/hbm.23904

Lee, M., and Soya, H. (2017). Effects of acute voluntary loaded wheel running on BDNF expression in the rat hippocampus. *J. Exerc. Nutrition Biochem.* 21, 52–57. doi: 10.20463/jenb.2017.0034

Lynskey, J. V., Belanger, A., and Jung, R. (2008). Activity-dependent plasticity in spinal cord injury. *J. Rehabil. Res. Dev.* 45, 229–240. doi: 10.1682/jrrd.2007.03.0047

Martin, J. H., Chakrabarty, S., and Friel, K. M. (2011). Harnessing activity-dependent plasticity to repair the damaged corticospinal tract in an animal model of cerebral palsy. *Dev. Med. Child Neurol.* 53, 9–13. doi: 10.1111/j.1469-8749.2011.04055.x

Martin, J. H., Friel, K. M., Salimi, I., and Chakrabarty, S. (2007). Activity- and use-dependent plasticity of the developing corticospinal system. *Neurosci. Biobehav. Rev.* 31, 1125–1135. doi: 10.1016/j.neubiorev.2007.04.017

McKenzie, I. A., Ohayon, D., Li, H., de Faria, J. P., Emery, B., Tohyama, K., et al. (2014). Motor skill learning requires active central myelination. *Science* 346, 318–322. doi: 10.1126/science.1254960

Mead, A. N., and Stephens, D. N. (2003). Selective disruption of stimulus-reward learning in glutamate receptor gria1 knock-out mice. *J. Neurosci.* 23, 1041–1048. doi: 10.1523/JNEUROSCI.23-03-01041.2003

Radak, Z., Kumagai, S., Taylor, A. W., Naito, H., and Goto, S. (2007). Effects of exercise on brain function: role of free radicals. *Appl. Physiol. Nutr. Metab.* 32, 942–946. doi: 10.1139/h07-081

Sampaio-Baptista, C., Khrapitchev, A. A., Foxley, S., Schlagheck, T., Scholz, J., Jbabdi, S., et al. (2013). Motor skill learning induces changes in white matter microstructure and myelination. *J. Neurosci.* 33, 19499–19503. doi: 10.1523/JNEUROSCI.3048-13.2013

Schmidt, B. J., and Jordan, L. M. (2000). The role of serotonin in reflex modulation and locomotor rhythm production in the mammalian spinal cord. *Brain Res. Bull.* 53, 689–710. doi: 10.1016/s0361-9230(00)00402-0

Schulz, D. J. (2006). Plasticity and stability in neuronal output via changes in intrinsic excitability: it's what's inside that counts. *J. Exp. Biol.* 209, 4821–4827. doi: 10.1242/jeb.02567

Sharples, S. A., Humphreys, J. M., Jensen, A. M., Dhoopar, S., Delaloye, N., Clemens, S., et al. (2015). Dopaminergic modulation of locomotor network activity in the neonatal mouse spinal cord. *J. Neurophysiol.* 113, 2500–2510. doi: 10.1152/jn.00849.2014

Sun, X., Jones, Z. B., Chen, X. M., Zhou, L., So, K. F., and Ren, Y. (2016). Multiple organ dysfunction and systemic inflammation after spinal cord injury: a complex relationship. *J. Neuroinflammation* 13:260. doi: 10.1186/s12974-016-0736-y

Svensson, M., Lexell, J., and Deierborg, T. (2015). Effects of physical exercise on neuroinflammation, neuroplasticity, neurodegeneration, and behavior: what we can learn from animal models in clinical settings. *Neurorehabil. Neural Repair* 29, 577–589. doi: 10.1177/1545968314562108

Takase, H., Washida, K., Hayakawa, K., Arai, K., Wang, X., Lo, E. H., et al. (2018). Oligodendrogenesis after traumatic brain injury. *Behav. Brain Res.* 340, 205–211. doi: 10.1016/j.bbr.2016.10.042

Takeoka, A., Kubasak, M. D., Zhong, H., Kaplan, J., Roy, R. R., and Phelps, P. E. (2010). Noradrenergic innervation of the rat spinal cord caudal to a complete spinal cord transection: effects of olfactory ensheathing glia. *Exp. Neurol.* 222, 59–69. doi: 10.1016/j.expneurol.2009.12.008

Takeoka, A., Kubasak, M. D., Zhong, H., Roy, R. R., and Phelps, P. E. (2009). Serotonergic innervation of the caudal spinal stump in rats after complete spinal transection: effect of olfactory ensheathing glia. *J. Comp. Neurol.* 515, 664–676. doi: 10.1002/cne.22080

Tian, J., Yu, T., Xu, Y., Pu, S., Lv, Y., Zhang, X., et al. (2018). Swimming training reduces neuroma pain by regulating neurotrophins. *Med. Sci. Sports Exerc.* 50, 54–61. doi: 10.1249/mss.0000000000001411

Vahdat, S., Lungu, O., Cohen-Adad, J., Marchand-Pauvert, V., Benali, H., and Doyon, J. (2015). Simultaneous brain-cervical cord fMRI reveals intrinsic spinal cord plasticity during motor sequence learning. *PLoS Biol.* 13:e1002186. doi: 10.1371/journal.pbio.1002186

Wei, Y., Fang, C. L., Liu, S. J., Yang, W. Q., Wei, L. S., Lei, X. J., et al. (2018). Long-term moderate exercise enhances specific proteins that constitute neurotrophin signaling pathway: a TMT-based quantitative proteomic analysis of rat plasma. *J. Proteomics* 185, 39–50. doi: 10.1016/j.jprot.2018.06.017

Willerslev-Olsen, M., Lorentzen, J., and Nielsen, J. B. (2014). Gait training reduces ankle joint stiffness and facilitates heel strike in children with cerebral palsy. *NeuroRehabilitation* 35, 643–655. doi: 10.3233/NRE-141180

Willerslev-Olsen, M., Petersen, T. H., Farmer, S. F., and Nielsen, J. B. (2015). Gait training facilitates central drive to ankle dorsiflexors in children with cerebral palsy. *Brain* 138, 589–603. doi: 10.1093/brain/awu399

Willuhn, I., and Steiner, H. (2008). Motor-skill learning in a novel running-wheel task is dependent on D1 dopamine receptors in the striatum. *Neuroscience* 153, 249–258. doi: 10.1016/j.neuroscience.2008.01.041

Wu, M., Kim, J., Gaebler-Spira, D. J., Schmit, B. D., and Arora, P. (2017). Robotic resistance treadmill training improves locomotor function in children with cerebral palsy: a randomized controlled pilot study. *Arch. Phys. Med. Rehabil.* 98, 2126–2133. doi: 10.1016/j.apmr.2017.04.022

Xiao, L., Ohayon, D., McKenzie, I. A., Sinclair-Wilson, A., Wright, J. L., Fudge, A. D., et al. (2016). Rapid production of new oligodendrocytes is required in the earliest stages of motor-skill learning. *Nat. Neurosci.* 19, 1210–1217. doi: 10.1038/nn.4351

Yang, Y., Shu, X., Liu, D., Shang, Y., Wu, Y., Pei, L., et al. (2012). EPAC null mutation impairs learning and social interactions via aberrant regulation of miR-124 and Zif268 translation. *Neuron* 73, 774–788. doi: 10.1016/j.neuron.2012.02.003

Yang, J., Xiong, L. L., Wang, Y. C., He, X., Jiang, L., Fu, S. J., et al. (2018). Oligodendrocyte precursor cell transplantation promotes functional recovery following contusive spinal cord injury in rats and is associated with altered microRNA expression. *Mol. Med. Rep.* 17, 771–782. doi: 10.3892/mmr.2017.7957

Zhang, Y., Huang, P., Du, G., Kanaho, Y., Frohman, M. A., and Tsirka, S. E. (2004). Increased expression of two phospholipase D isoforms during experimentally induced hippocampal mossy fiber outgrowth. *Glia* 46, 74–83. doi: 10.1002/glia.10322

Zhao, T., Qi, Y., Li, Y., and Xu, K. (2012). PI3 Kinase regulation of neural regeneration and muscle hypertrophy after spinal cord injury. *Mol. Biol. Rep.* 39, 3541–3547. doi: 10.1007/s11033-011-1127-1

Zhou, L., Bar, I., Achouri, Y., Campbell, K., De Backer, O., Hebert, J. M., et al. (2008). Early forebrain wiring: genetic dissection using conditional Celsr3 mutant mice. *Science* 320, 946–949. doi: 10.1126/science.1155244

Conflict of Interest Statement: The authors declare that the research was conducted in the absence of any commercial or financial relationships that could be construed as a potential conflict of interest.

frontiers in Cellular Neuroscience

ORIGINAL RESEARCH
published: 24 April 2019
doi: 10.3389/fncel.2019.00153

Ionic Mechanisms Underlying the Excitatory Effect of Orexin on Rat Subthalamic Nucleus Neurons

Guang-Ying Li†, Qian-Xing Zhuang†‡, Xiao-Yang Zhang†, Jian-Jun Wang and Jing-Ning Zhu**

State Key Laboratory of Pharmaceutical Biotechnology and Department of Physiology, School of Life Sciences, Nanjing University, Nanjing, China

OPEN ACCESS

Edited by:
Yosef Yarom, Hebrew University of Jerusalem, Israel

Reviewed by:
Jessica R. Barson, Drexel University College of Medicine, United States
Paul Geoffrey Overton, University of Sheffield, United Kingdom
Constance Hammond, Institut National de la Santé et de la Recherche Médicale (INSERM), France

***Correspondence:**
Jian-Jun Wang
jjwang@nju.edu.cn
Jing-Ning Zhu
jnzhu@nju.edu.cn

†These authors have contributed equally to this work

‡Present address:
Qian-Xing Zhuang, Department of Physiology, School of Medicine, and Co-innovation Center of Neuroregeneration, Nantong University, Nantong, China

Received: *11 December 2018*
Accepted: *08 April 2019*
Published: *24 April 2019*

Citation:
Li G-Y, Zhuang Q-X, Zhang X-Y, Wang J-J and Zhu J-N (2019) Ionic Mechanisms Underlying the Excitatory Effect of Orexin on Rat Subthalamic Nucleus Neurons. Front. Cell. Neurosci. 13:153. doi: 10.3389/fncel.2019.00153

Central orexinergic system deficiency results in cataplexy, a motor deficit characterized with a sudden loss of muscle tone, highlighting a direct modulatory role of orexin in motor control. However, the neural mechanisms underlying the regulation of orexin on motor function are still largely unknown. The subthalamic nucleus (STN), the only excitatory structure of the basal ganglia, holds a key position in the basal ganglia circuitry and motor control. Previous study has revealed a wide distribution of orexinergic fibers as well as orexin receptors in the basal ganglia including the STN. Therefore, in the present study, by using whole-cell patch clamp recording and immunostaining techniques, the direct effect of orexin on the STN neurons in brain slices, especially the underlying receptor and ionic mechanisms, were investigated. Our results show that orexin-A elicits an excitatory effect on STN neurons in rats. Tetrodotoxin (TTX) does not block the orexin-induced excitation on STN neurons, suggesting a direct postsynaptic action of the neuropeptide. The orexin-A-induced inward current on STN neurons is mediated by the activation of both OX1 and OX2 receptors. Immunofluorescence result shows that OX1 and OX2 receptors are co-expressed and co-localized in STN neurons. Furthermore, Na^+-Ca^{2+} exchangers (NCXs) and inward rectifier K^+ channels co-mediate the excitatory effect of orexin-A on STN neurons. These results demonstrate a dual receptor in conjunction with the downstream ionic mechanisms underlying the excitatory action of orexin on STN neurons, suggesting a potential modulation of the central orexinergic system on basal ganglia circuitry as well as its related motor control and motor diseases.

Keywords: orexin, subthalamic nucleus, motor control, neuronal excitability, ionic mechanisms

INTRODUCTION

Orexin (also known as hypocretin) is a neuropeptide first identified in 1998 (de Lecea et al., 1998; Sakurai et al., 1998). There are two splice variants of orexin, orexin-A and orexin-B, both of which exert their physiological functions *via* two types of G-protein coupled receptors, OX1 and OX2 receptors (Tyree et al., 2018). Orexin-A binds to both receptor subtypes with approximately equal affinity, whilst orexin-B shows a 10-fold selectivity for OX2 receptor (Zhang et al., 2013).

In the central nervous system, orexin receptors produce excitation by postsynaptic depolarization *via* activation of non-selective cation channels, inhibition of K^+ channels and activation of Na^+-Ca^{2+} exchangers (NCXs), as well as presynaptic action through regulation of the release of other neurotransmitters (Kukkonen and Leonard, 2014; Leonard and Kukkonen, 2014). Although originating exclusively from the lateral hypothalamus/perifornical area, the central orexinergic system projects widely throughout almost the whole brain (Broberger et al., 1998; Peyron et al., 1998; Cutler et al., 1999). Accumulating studies have revealed that the central orexinergic system plays a key position in many basic physiological functions, including the sleep-wakefulness cycle, feeding, energy homeostasis and reward processes (Sakurai, 2007; Matsuki and Sakurai, 2008; Zhang et al., 2013; Giardino et al., 2018). Intriguingly, deficit in the orexinergic system in animals and humans results in cataplexy, a motor dysfunction characterized by sudden loss of muscle tone (Chemelli et al., 1999; Sakurai, 2007). The phenotype indicates that orexin may be directly involved in the somatic motor control. However, the knowledge about orexinergic modulation on motor control is still limited.

The basal ganglia is an essential subcortical center responsible for motor initiation and motor learning, within which the subthalamic nucleus (STN) is the sole structure mainly consisting of excitatory glutamatergic projection neurons. Through widespread innervation on other basal ganglia components, STN provides a powerful driving force for the whole basal ganglia circuitry (Plenz and Kital, 1999). In addition, STN is not only a crucial node in the "indirect" fronto-striatal-pallidal-subthalamic pathway, but also forms the "hyperdirect" fronto-subthalamic pathway which directly connects the cortex (Nambu et al., 2002; Kravitz et al., 2010; Chu et al., 2015; Zhuang et al., 2018a). *Via* sending excitatory input to the internal globus pallidus, the STN balances the activity of the "direct" fronto-striatal-pallidal pathway and thus contributes to modulate an appropriate initiation and execution of voluntary movement. Lesion of the STNs leads to ballism (Barlas et al., 2001), a syndrome characterized by continuous, violent, involuntary, wild, and flinging movements of the proximal parts of the limbs. Moreover, a series of recent studies have documented that STN also holds a key position in action selection, response vigor, reinforcement learning, as well as cognitive, emotional, and motivational functions (Wagenbreth et al., 2015; Zavala et al., 2015; Dunovan and Verstynen, 2016; Zénon et al., 2016; Fischer et al., 2017).

Notably, orexinergic cell bodies are localized adjacent to the STN, which send a high-density of projections to the nucleus (Peyron et al., 1998; Sakurai et al., 1998), and even orexin mRNAs can be detected in the STN, indicating a modulatory role of orexin on STN neurons. Moreover, *in situ* hybridization and immunohistochemical studies have illustrated that the OX1/OX2 receptor mRNAs and proteins are expressed in the STN (Trivedi et al., 1998; Hervieu et al., 2001; Cluderay et al., 2002). By using *in vivo* electrophysiological recordings, the effect of orexin-A and orexin-B on STN neuronal firing rate has been reported recently (Sheng et al., 2018). However, the ionic mechanisms underlying the excitatory effect of orexin on STN neurons remain unknown. Therefore, in the present study, by using whole-cell patch clamp recording and immunostaining techniques, we showed that orexin directly excited STN neurons *via* postsynaptic OX1 and OX2 receptors, and the two orexin receptor subtypes co-expressed and co-localized on the same STN neurons. Also, a dual ionic mechanism involving both NCXs and inward rectifier K^+ channels was found to mediate the orexin-induced excitation on STN neurons.

MATERIALS AND METHODS

Animals

The experiments were conducted on Sprague-Dawley rats of either sex, housed under controlled conditions with a lighting schedule of 12 h light and 12 h darkness at 22 ± 2°C. Standard food and water were provided *ad libitum*. Rats aged about 14–21 days were used for whole-cell patch clamp recordings since the central orexinergic system seems to reach adult-like levels around P21 in rats and change only slightly in the post-weaning development in Eastern gray kangaroos (Steininger et al., 2004; Yamamoto et al., 2006). Rats aged about 8 weeks were used for immunohistochemical study. All animal experiments were approved by the Experimental Animal Care and Use Committee of Nanjing University and were conducted in accordance with the US National Institutes of Health Guide for the Care and Use of Laboratory Animals (NIH Publication 85-23, revised 2011). All efforts were made to minimize the number of animals used and their suffering.

Whole-Cell Patch Clamp Recordings

Whole-cell patch clamp recordings were performed as previously described (Zhang et al., 2011; Wang et al., 2017; Zhuang et al., 2018a,b; Ji et al., 2019) on STN neurons on brain slices to assess the effect of orexin and the underlying receptor and ionic mechanisms. According to the rat brain atlas of Paxinos and Watson (2014), sagittal slices (300 μm in thickness) containing the STN were cut (**Figure 1A**) with a vibroslicer (VT 1200S, Leica) at 4°C. The slices were incubated in artificial cerebrospinal fluid (ACSF, composition in mM: 124 NaCl, 2.5 KCl, 1.25 NaH_2PO_4, 1.3 $MgSO_4$, 26 $NaHCO_3$, 2 $CaCl_2$ and 10 D-glucose) equilibrated with 95% O_2 and 5% CO_2 at 35°C ± 0.5°C for at least 1 h and then maintained at room temperature. During recording sessions, the slices were transferred to a submerged chamber and continuously superfused with 95% O_2 and 5% CO_2 oxygenated ACSF at a rate of 2 ml/min maintained at room temperature.

Whole-cell recordings were performed on STN neurons with borosilicate glass pipettes (3–5 MΩ) filled with an internal solution (composition in mM: 135 K-methylsulfate, 5 KCl, 2 $MgCl_2$, 10 HEPES, 5 EGTA, 0.5 $CaCl_2$, 4 Na_2-ATP, 0.4 GTP-Tris, adjusted to pH 7.25 with 1 M KOH). Recordings of STN neurons were carried out in slices that were superfused with ACSF. STN neurons were visualized with an Olympus BX51WI microscope (Olympus, Tokyo, Japan) equipped with infrared differential interference contrast. Patch-clamp recordings were acquired with an Axopatch-700B amplifier (Axon Instruments, Sunnyvale, CA, USA) and the signals were fed into a computer

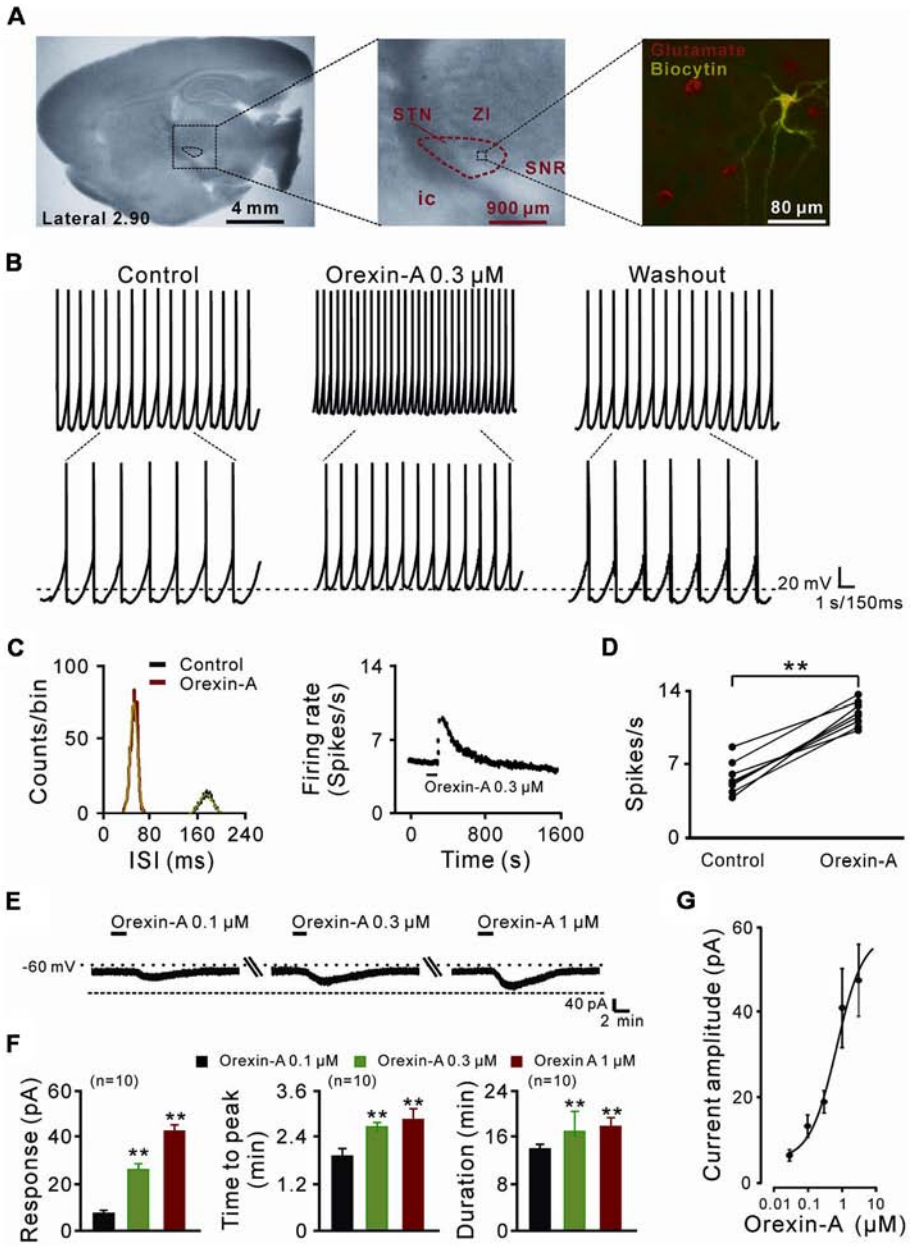

FIGURE 1 | The direct excitatory effect of orexin on the subthalamic nucleus (STN) neurons. **(A)** Microscope image of a STN which centrally located in a 300 μm thick brain sagittal slice (observed with Olympus BX51WI, using a 40× water immersed objective) and a glutamatergic STN neuron labeled with biocytin after patch-clamp recording. **(B)** Orexin-A (300 nM) excited a STN spontaneous firing neuron in current clamp recording. **(C)** Orexin changed the distribution of inter-spike intervals (the red curve is Gaussian fit to the data) and increased firing rate of the STN neuron presented in **(B)**. **(D)** Group data of the effect of orexin-A on firing rate of STN neurons (n = 8). **(E)** Orexin-A concentration-dependently elicited the inward current and increased time to peak and duration of response of the recorded STN neuron. **(F)** A group of data recorded from 10 STN neurons. **(G)** Concentration-response curve for orexin-A on STN neurons show mean EC50 value of 29.0 ± 14.3 nM (n = 8). Data are presented as mean ± SEM; $^{**}P < 0.01$. In this and the following figures, the short horizontal bars above the experimental records indicate the 1 min period of application of orexin-A, and the long horizontal bars indicate the exposure of the slice to tetrodotoxin (TTX), antagonists or blockers of receptors, ion exchangers or channels.

through a Digidata-1440A interface (Axon Instruments) for data capture and analysis (pClamp 10.5, Axon Instruments). Neurons were held at a membrane potential of −60 mV and characterized by injection of rectangular voltage pulses (5 mV, 50 ms) to monitor the whole-cell membrane capacitance, series resistance, and membrane resistance. Neurons were excluded from the study if the series resistance was not stable or exceeded 20 MΩ.

We bathed the slices with orexin-A (0.03–3 μM, Tocris, Bristol, UK) to stimulate the recorded neurons. Tetrodotoxin

(TTX, Alomone Labs, Israel), NBQX (AMPA/kainate receptor antagonist, 20 μM; Tocris), D-AP5 (NMDA receptor antagonist, 50 μM; Tocris) and gabazine ($GABA_A$ receptor antagonist, 50 μM; Tocris) were used to examine the direct postsynaptic effect of orexin-A. SB334867 (10 μM, Tocris) and JNJ10397049 (10 μM, Tocris), high selective antagonists for OX1 and OX2 receptor respectively, were applied to assess the underlying receptor mechanism. Selective NCX blocker KB-R7943 (50 μM, Alomone Labs, Israel), broad spectrum K^+ channel blocker $BaCl_2$ (1 mM) and selective inward-rectifier K^+ channel blocker tertiapin-Q (100 nM, Tocris) were used to explore the underlying ionic mechanism. Moreover, to determine the characteristic of whole cell current induced by orexin-A, in voltage-clamp recordings, current-voltage plots (*I-V* curves) were obtained before and during application of orexin-A using a slow ramp command (dV/dt = −10 mV/s, ranged from −60 to −120 mV) to allow for attainment of steady-state conditions.

Immunohistochemistry and Imaging

The experimental procedures for immunostaining followed our previous work (Li et al., 2017; Wang et al., 2017; Zhuang et al., 2018a,b). Rats were deeply anesthetized with sodium pentobarbital (65 mg/kg) and perfused transcardially with 100 ml normal saline, followed by 250–300 ml 4% paraformaldehyde in 0.1 M phosphate buffer. Subsequently, the brain was removed, trimmed and postfixed in the same fixative for 12 h at 4°C, and then cryoprotected with 30% sucrose for 48 h. Frozen coronal sections (25 μm thick) containing the STN were obtained by using a freezing microtome (CM1860, Leica, Wetzlar, Germany) and mounted on gelatin-coated slides. The slices were rinsed with PBS containing 0.1% Triton X-100 and then incubated in 10% normal bovine serum in PBS containing 0.1% Triton X-100 for 30 min. Sections were incubated overnight at 4°C with primary antibody/antibodies, as follows: mouse anti-glutamate (1:1,000; Millipore Sigma, St. Louis, MO, USA; Cat# MAB5304, RRID:AB_94698), chicken anti-OX1 receptor (1:200; Acris Antibodies GmbH, Germany; Cat# BP4012, RRID:AB_1005881), rabbit anti-OX2 receptor (1:100; Millipore Sigma; Cat# AB3094, RRID:AB_91358). After a complete wash in PBS, the sections for single or double immunostaining were incubated in the related secondary antibodies (1:2,000; Life Technologies Carlsbad, CA, USA) conjugated to Alexa Fluor 488 and/or Alexa Fluor 594 (1:2,000, Life Technologies) for 2 h at room temperature in the dark. The slides were washed and mounted in Fluoromount-G mounting medium (Southern Biotech, Birmingham, AL, USA). Incubations replacing the primary antiserum with control immunoglobulins and/or omitting the primary antiserum were used as negative controls. All micrographs were taken with an inverted laser scanning confocal FluoView FV1000 microscope (Olympus, Tokyo, Japan), equipped with Plan-Apochromat ×60/1.42 NA oil, ×40/0.9 NA dry, ×20/0.75 NA dry, and ×10/0.4 NA dry objective lenses. Digital images from the microscope were recorded with FV10-ASW 3.1 Viewer Software (Olympus) and image processing was done with Photoshop (Adobe Systems Inc., San Jose, CA, USA).

Statistics

All data were analyzed with SPSS 17.0 (SPSS, Chicago, IL, USA) and presented as mean ± SEM Shapiro-Wilk test was used for testing the normality of data. Two-tailed Student's *t*-test was employed for statistical analysis. *P*-values of < 0.05 were considered to be significant.

RESULTS

Orexin-A Excites STN Neurons *via* a Direct Postsynaptic Effect

In the present study, a total of 70 STN neurons with the input resistance higher than 150 MΩ were recorded. All the glutamatergic neurons we patched had a diameter >25 μm (**Figure 1A**) and showed spontaneous firing, which was in agreement with the previous reports (Baufreton et al., 2005; Atherton et al., 2010). In current clamp experiments, brief bath application of orexin-A (0.3 μM, 1 min) elicited a significant increase in the discharge rate of STN neurons (8/11, 72.72%) from 6.0 ± 0.5 spikes/s to 12.0 ± 0.4 spikes/s (n = 8, $P < 0.01$; **Figures 1B,D**). The inter-spike intervals and peri-stimulus time histograms showed that orexin-A largely changed the distribution of inter-spike intervals and increased the firing rate of the STN neurons (**Figure 1C**). On the other hand, in voltage-clamp experiments, 0.1, 0.3, and 1 μM orexin-A induced an inward current (from 7.2 ± 3.7 pA to 24.6 ± 5.2 pA and 43.5 ± 4.8 pA, respectively, n = 10, $P < 0.001$, respectively), increased the time to peak (from 1.8 ± 0.6 min to 2.5 ± 0.2 min and 2.7 ± 0.8 min, respectively, n = 10, $P < 0.01$, respectively), and prolonged the duration of response (from 14.8 ± 0.3 min to 17.3 ± 1.0 min and 17.9 ± 0.4 min, respectively, n = 10, $P < 0.01$, respectively) on STN neurons in a dose-dependent manner (**Figures 1E,F**). Fitting the concentration-response curve from eight STN neurons yielded that the concentration of orexin-A required for half-maximal activation (EC_{50}) was 28.3 ± 11.6 nM (**Figure 1G**).

Moreover, combined application of TTX (0.3 μM), NBQX (20 μM, a potent AMPA receptor antagonist), D-AP5 (50 μM, a potent NMDA receptor antagonist) and SR95531 (50 μM, a $GABA_A$ receptor antagonist) did not block the orexin-A-elicited inward current on the recorded neurons (44.3 ± 2.1 pA vs. 42.3 ± 1.9 pA, n = 8, $P > 0.05$; **Figures 2A,B**), strongly indicating that orexin excites STN neurons *via* a direct postsynaptic effect.

Orexin-A Excites STN Neurons by Activation of Both OX1 and OX2 Receptors

Orexin-A exerts its physiological actions *via* two G protein-coupled orexin receptors, OX1 and OX2 receptor (Sakurai et al., 1998; Marcus et al., 2001). Therefore, in the present study, we used SB334867 (selective OX1 receptor antagonist) and JNJ10397049 (selective OX2 receptor antagonist) to examine which receptor(s) mediated the orexin-induced excitation on STN neurons (**Figure 3**). The orexin-A-elicited inward current was partly blocked by separate application of SB334867 (10 μM; from 44.5 ± 2.5 pA to 23.6 ± 1.4 pA, n = 8, $P < 0.01$;

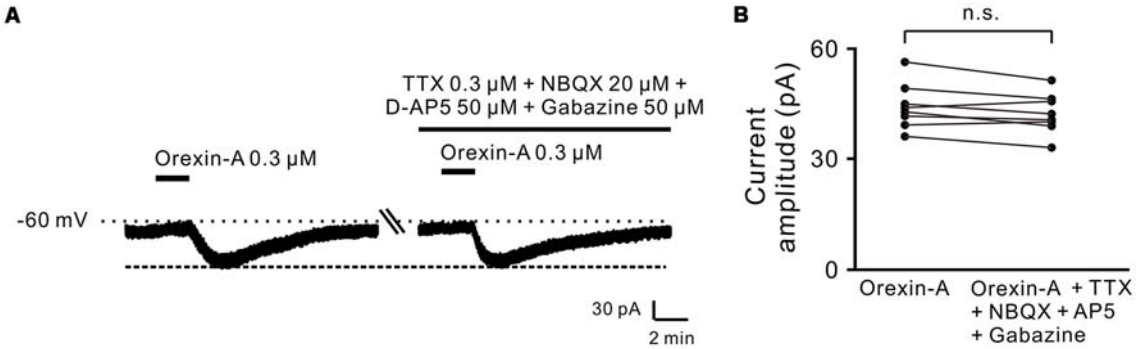

FIGURE 2 | Orexin-A excited the recorded STN neurons with a postsynaptic manner. **(A)** TTX, NBQX, D-AP5 and gabazine did not block the inward currents induced by orexin-A on a recorded STN neuron. **(B)** Group data of the recorded STN neurons (n = 8). Data are presented as mean ± SEM; n.s., no statistical difference.

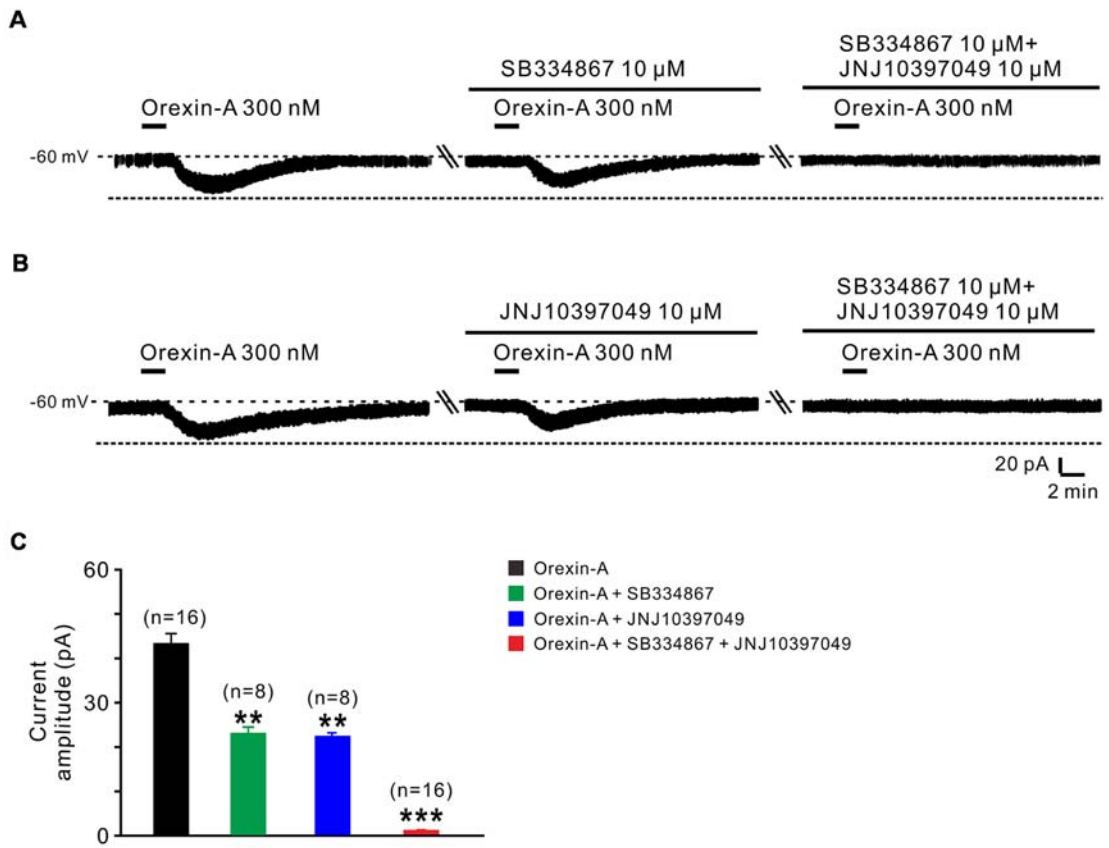

FIGURE 3 | OX1 and OX2 receptors co-mediate the excitation of orexin on STN neurons. **(A)** Orexin-A (300 nM) elicited an inward current in a STN neuron, SB334867 (10 μM), a selective antagonist for OX1 receptor, partly blocked the current induced by orexin-A and SB334867 combined with JNJ10397049, a selective antagonist for OX2 totally abolished the orexin-A-induced inward current. **(B)** Orexin-A (300 nM) elicited an inward current in a STN neuron, JNJ10397049 (10 μM) partly blocked the current induced by orexin-A and JNJ10397049 combined with SB334867 totally abolished the orexin-A-induced inward current. **(C)** Group data of the tested STN neurons under orexin-A induced inward current as present in (**A**, n = 8) and (**B**, n = 8). Data are presented as mean ± SEM, $^{**}P < 0.01$, $^{***}P < 0.001$.

Figures 3A,C) or JNJ10397049 (10 μM; from 44.6 ± 2.5 pA to 22.6 ± 0.5 pA, n = 8, $P < 0.01$; **Figures 3B,C**). Moreover, combined application of SB334867 and JNJ10397049 nearly totally antagonized the orexin-A-induced excitation from 44.6 ± 2.5 pA to 1.2 ± 0.1 pA on STN neurons (n = 16, $P < 0.001$; **Figures 3A–C**). All these results suggest that OX1 and OX2 receptors co-mediate the excitatory effect induced by orexin-A on STN neurons.

Furthermore, the distribution of OX1 and OX2 receptors was mapped in the STN by double immunofluorescence staining. We found that for all the stained sections (five rats and 10 sections for each) both of the orexin receptor subtypes were not only co-expressed in the STN (**Figures 4A1–A3,B1–B3**) but also co-localized in the same neurons (**Figures 4C1–C3**), which was consistent with the electrophysiological results mentioned above.

Orexin-A Excites the STN Neurons *via* Activation of NCXs and Closure of Inward Rectifier K^+ Channels

Next, we applied slow-ramp command tests and determined the *I-V* curves in response to orexin-A to investigate the underlying ionic mechanisms of orexin on STN neurons. We observed three types of the orexin-A-induced changes on the *I-V* curves from STN neurons (n = 15; **Figures 5A1–A3**). The diversity of the orexin-A-induced changes in *I-V* relationships implies that more than one ionic mechanism is involved in the orexin-A-induced excitation on STN neurons. In 8 of 15 neurons, the *I-V* curves in the absence and presence of orexin-A were apart more at −130 mV as compared with −55 mV, indicating that ion channels/exchangers with the reversal potential depolarized than −60 mV may be involved in the orexin-A-induced net current (**Figure 5A1**). Considering NCXs were reported to be coupled to orexin receptors in many different brain regions and have a more positive reversal potential (Wu et al., 2004; Zhang et al., 2011), we thus speculated that the activation

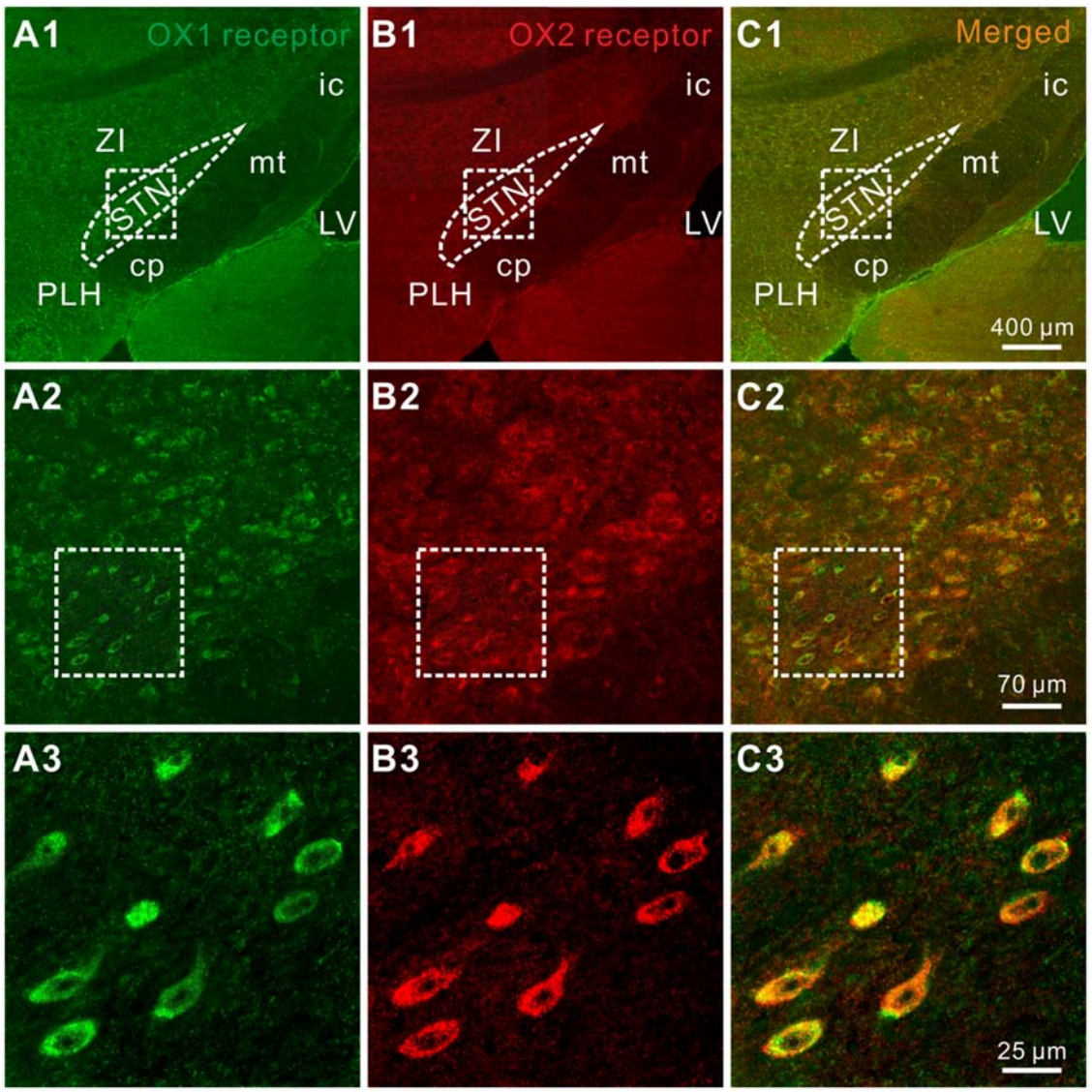

FIGURE 4 | Double-labeled immunofluorescence staining for OX1 (green) and OX2 (red) receptors in rat STN. **(A1–A3)** OX1 receptor staining. **(B1–B3)** OX2 receptor staining. **(C1–C3)** Merged images showing colocalization of OX1 and OX2 receptors in the same STN neurons. STN, subthalamic nucleus; ZI, zona incerta; 3V, 3th ventricle; 4V, 4th ventricle; cp, cerebral peduncle; ic, internal capsule; mt, mammillothalamic tract; PLH, peduncular part of the lateral hypothalamus.

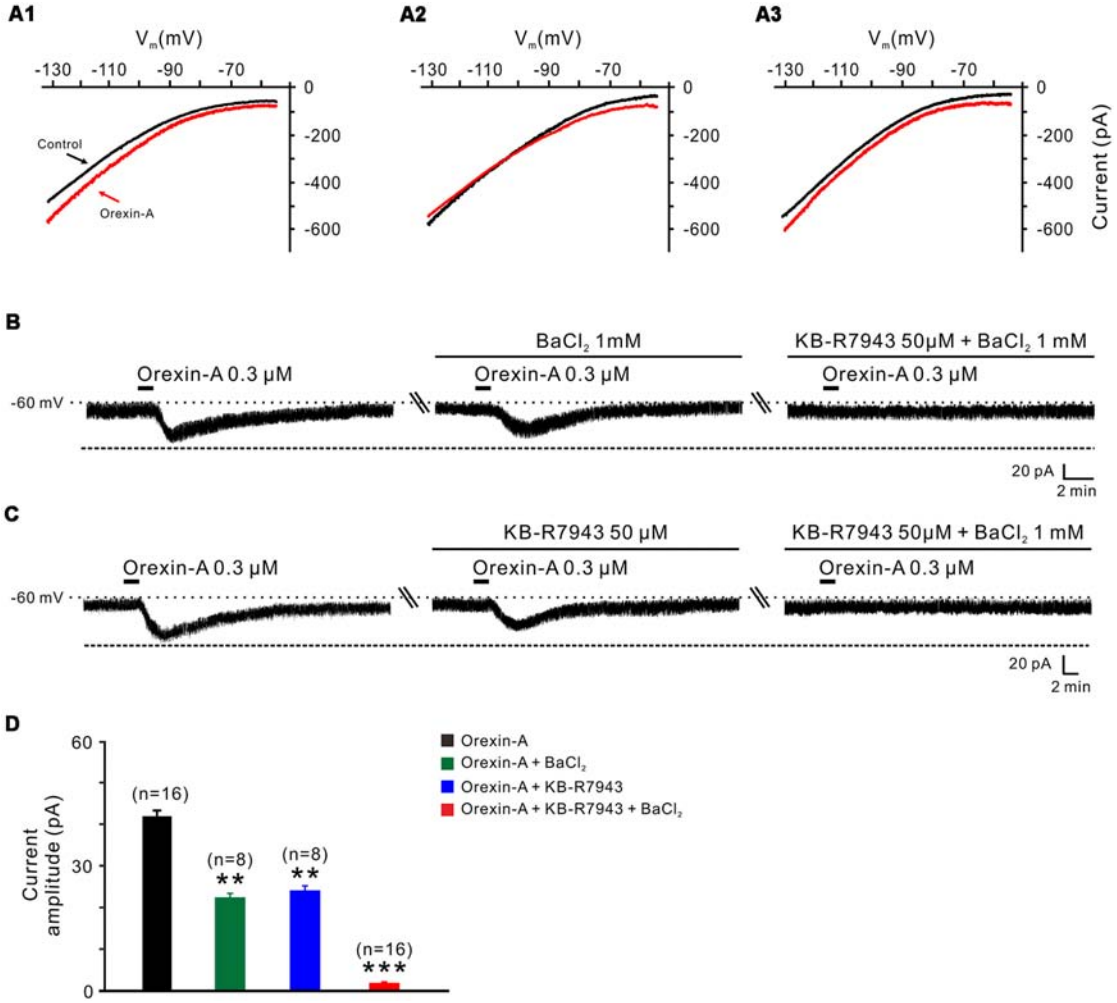

FIGURE 5 | Na^+-Ca^{2+} exchangers (NCXs) and K^+ channels co-mediate the excitation of orexin on STN neurons. **(A1–A3)** *I-V* relationships of STN neurons in the absence and presence of orexin. In 63.8% of the neurons tested, the orexin A-induced inward current was larger at the more hyperpolarized potential of −130 mV than at −55 mV **(A1)**; in 22.4% of these neurons tested, the orexin A-induced inward current reversed near the calculated Ek of −105 mV **(A2)**; in 13.8% neurons, the orexin A-induced inward current first decreased then increase amplitude along with the holding potential hyperpolarization, and was similar in magnitude at −55 and −130 mV **(A3)**. **(B)** Orexin-A (300 nM) elicited an inward current in a STN neuron. $BaCl_2$, a broad spectrum blocker of K^+ channels, partly blocked the effect of orexin-A on STN neurons and combined application of the NCX blocker KB-R7943 totally abolished the orexin-A-induced inward current (n = 8). **(C)** Orexin-A (300 nM) elicited an inward current in a STN neuron. KB-R7943 partly blocked the effect of orexin-A on STN neurons and combined application of the $BaCl_2$ totally abolished the orexin-A-induced inward current (n = 8). **(D)** Group data of the 16 tested STN neurons under orexin-A induced inward current as present in **(B,C)**. Data are presented as mean ± SEM, $^{**}P < 0.01$, $^{***}P < 0.001$.

of NCXs may mediate the orexin-induced change in the *I-V* relationships. Furthermore, in 5 of 15 recorded STN neurons, the *I-V* curves in the absence and presence of orexin-A intersected at the −105 mV (**Figure 5A2**), which means that the orexin-A-induced inward current reverses near the calculated E_k of −105 mV, thus indicating that K^+ channels may be involved in the effect of orexin-A on STN neurons. In the remaining two neurons, the orexin-A-elicited change in the *I-V* curves was similar in amplitudes at −55 and −130 mV (**Figure 5A3**), although the amplitude first decreased then increased along with the hyperpolarization.

To further confirm the results of slow-ramp command tests, we applied Ba^{2+} (a broad spectrum blocker for K^+ channels) and KB-R7943 (a potent and selective inhibitor for NCXs) to determine whether K^+ channels and NCXs are involved in the effect of orexin-A on STN neurons. We found a partial inhibition of the orexin-A-induced inward current either by Ba^{2+} (1 mM; from 41.0 ± 1.3 pA to 22.2 ± 0.5 pA, n = 8, $P < 0.01$; **Figures 5B,D**) or by KB-R7943 application (50 μM; from 42.5 ± 1.7 pA to 24.5 ± 0.7 pA, n = 8, $P < 0.01$; **Figures 5C,D**). Moreover, the orexin-A-induced inward current was totally blocked from 41.8 ± 1.5 pA to 1.6 ± 0.2 pA by combined application of Ba^{2+} and KB-R7943 (n = 16, $P < 0.001$; **Figures 5B–D**), suggesting that the closure of K^+ channels as well as activation of NCXs co-mediated the excitation of orexin-A on STN neurons.

In order to clarify which kind of K^+ channels contributes to the excitatory effect of orexin on STN neurons, we further analyzed the characteristics of the orexin-A-induced K^+ current component. Under a condition of blockage of NCXs by continuously perfusing the slice with KB-R7943, we used slow ramp command tests to obtain the *I-V* curves in the absence and presence of orexin-A (**Figures 6A1,A2**). The results showed that the difference current had a reversal potential of −100 mV that was near the calculated E_k and exhibited a characterization of strongly outwardly rectifying (**Figure 6A2**). Since, the closure of K^+ channels is responsible for depolarization, the result indicates that the K^+ channels blocked by orexin-A are the inward rectifier K^+ channels. As shown in **Figures 6B,C**, the orexin-A induced inward current on STN neurons was partly blocked by separate application of specific inward rectifier K^+ channels antagonist tertiapin-Q (100 nM; from 49.3 ± 6.8 pA to 27.9 ± 3.8 pA, $n = 10$, $P < 0.01$; **Figures 6B,C**) or KB-R7943 (50 μM; from 49.3 ± 6.8 to 26.5 ± 4.6 pA, $n = 10$, $P < 0.01$; **Figures 6B,C**), and totally blocked by combined application of KB-R7943 and tertiapin-Q (from 49.3 ± 6.8 to 2.5 ± 0.6 pA, $n = 10$, $P < 0.001$; **Figures 6B,C**). All these results strongly indicate that the excitatory effect of orexin-A on STN neurons is mediated by a dual ionic mechanism including both activation of the NCXs and blockage of the inward rectifier K^+ channels.

DISCUSSION

As a driving force for the integrated function of basal ganglia circuitry, the STN plays a key role in the motor initiation and execution. However, little is known about the endogenous factors modulating STN neuronal activity. In the present study, we report that orexin, a hypothalamic neuropeptide, directly excites STN neurons *via* postsynaptic OX1 and OX2 receptors. And a dual ionic mechanism including activation of the NCXs and closure of the inward rectifier K^+ channels mediates the excitatory effect of orexin-A on STN neurons.

Previous studies from our laboratory and others have revealed an extensive regulation of orexin on the neuronal activity within the basal ganglia nuclei. It has been documented that there is a selective excitation of orexin-A on the GABAergic neurons in the substantia nigra pars reticulata instead of the dopaminergic neurons in the substantia nigra pars compacta (Korotkova et al., 2002). Moreover, orexin-A directly enhances

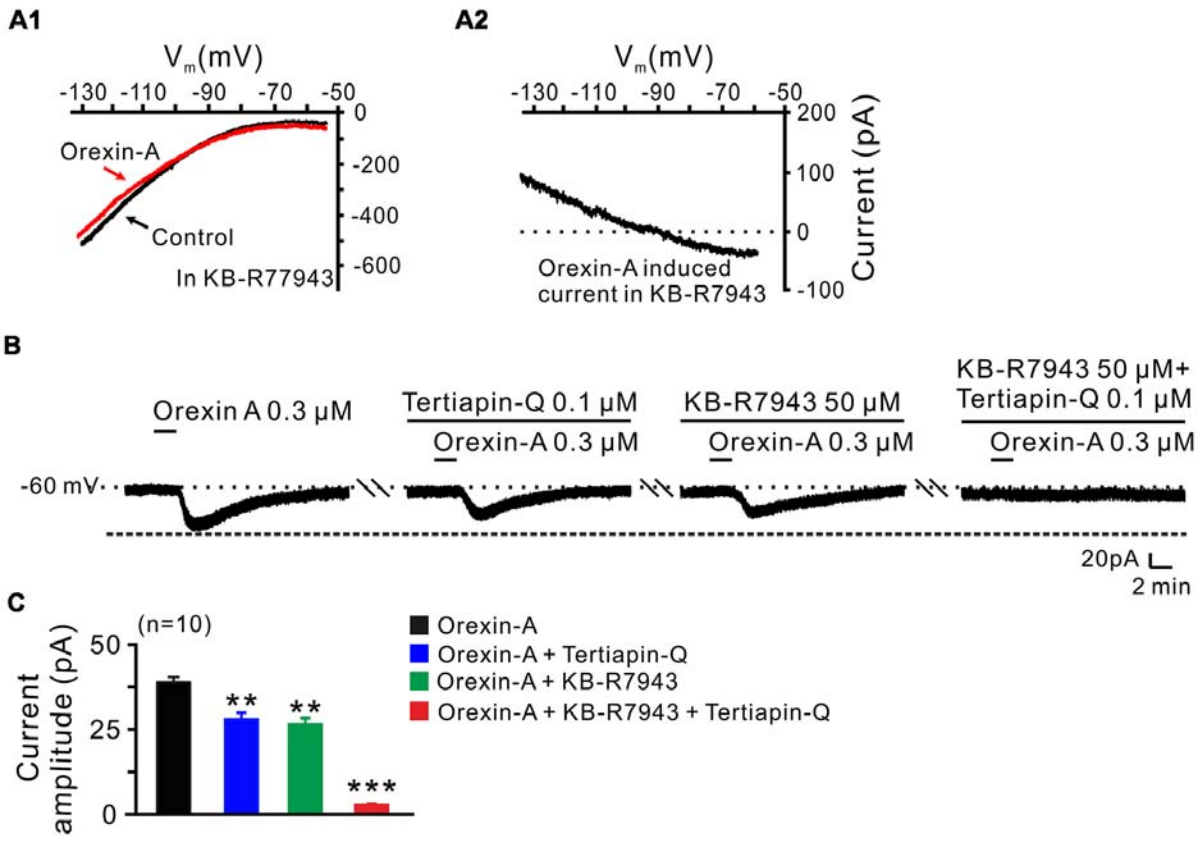

FIGURE 6 | Inward rectifier K^+ channels and NCXs contribute to the excitatory effect of orexin on STN neurons. **(A1,A2)** *I-V* relationship shows an outward rectifier K^+ current was exposed after KB-R7943 inhibited the activation of the NCX. **(B)** Orexin-A (300 nM) elicited an inward current in a STN neuron. KB-R7943 partly blocked the effect of orexin-A on STN neurons and combined application of the inward rectifier K^+ channel antagonist tertiapin-Q totally abolished the orexin-A-induced inward current. **(C)** Group data of the 10 tested STN neurons under orexin-A induced inward current as present in **(B)**. Data are presented as mean ± SEM, $^{**}P < 0.01$, $^{***}P < 0.001$.

the excitability of globus pallidus internus neurons and ventral pallidal GABAergic neurons by direct activation of OX1 and OX2 receptors (Gao et al., 2016; Ji et al., 2019). However, in the striatum, instead of a direct postsynaptic effect, orexin-A potentiates the AMPA-mediated synaptic transmission on the corticostriatal synapses (Shin et al., 2009). In this study, we demonstrate an excitatory action of orexin on neurons in the STN *via* postsynaptic OX1 and OX2 receptors, which is in accordance with the previous neuropharmacological studies *in vivo*, previous and present immunohistochemical studies as well as the *in situ* hybridization on the distribution of orexinergic fibers and receptors (Peyron et al., 1998; Trivedi et al., 1998; Hervieu et al., 2001; Cluderay et al., 2002; Sheng et al., 2018). These results suggest that the central orexinergic system may modulate the major components in the basal ganglia circuitry in parallel and subsequently participate in regulation of motor behaviors, such as biased swing behavior (Sheng et al., 2018).

Several types of ionic channels/exchangers including K^+ channels, nonselective cation channels and/or electrogenic NCXs have been reported to be linked to orexin receptors (Lytton, 2007; Kukkonen, 2011; Kukkonen and Leonard, 2014; Ji et al., 2019). *In situ* hybridization and immunocytochemical studies have revealed the distribution of NCX and inward rectifier K^+ channel mRNAs in the basal ganglia (Karschin et al., 1994; Murer et al., 1997; Canitano et al., 2002; Jeon et al., 2008). Here, we find that both the NCXs and inward rectifier K^+ channels are involved in the excitation of STN neurons induced by the activation of orexin receptors. Because of the highly positive reversal potential (Wu et al., 2004), NCXs activation can provide a powerful force for neuronal depolarization. On the other hand, by extruding Ca^{2+} from the cytoplasm, NCXs prevent Ca^{2+} overload in the highly excited neurons. Nevertheless, distinct from the NCXs, the activation of inward rectifier K^+ channels are responsible for the repolarization of membrane action potentials, and their shutoff help to generate a spike (Hille, 2001; Nishida and MacKinnon, 2002). Thus, through activation of NCXs and closure of inward rectifier K^+ channels, orexin strongly depolarizes and increases the discharge of spontaneous firing STN neurons. We speculate that *via* the dual ionic mechanism, orexin/central orexinergic system may subsequently bias the excitability of the STN neurons and actively participate in the regulation of STN mediated motor control, action selection, response vigor, reinforcement learning, as well as other cognitive, emotional, and motivational functions (Wagenbreth et al., 2015; Zavala et al., 2015; Dunovan and Verstynen, 2016; Zénon et al., 2016; Fischer et al., 2017).

The STN holds a key position not only in normal function of the basal ganglia but also in the pathological processes of basal ganglia disorders (Wang et al., 2018). A change in firing rate and/or firing patterns as well as an excess of neuronal synchronization of STN is a well-recognized hallmark in the parkinsonian state, and lesions of the STN have been reported to alleviate the parkinsonian motor symptoms (Bergman et al., 1990; Limousin et al., 1998; Rodriguez et al., 1998). Here, we report a direct excitation of orexin on STN neurons *via* both OX1 and OX2 receptors and the coupled NCXs and inward rectifier K^+ channels. Intriguingly, parkinsonian patients show an increasing loss of orexin cells with disease progression and a decrease in orexin level in the cerebrospinal fluid (Fronczek et al., 2007; Thannickal et al., 2007). Therefore, the role of the central orexinergic system in the basal ganglia circuitry including the STN, especially the contribution of endogenous orexin to the basal ganglia motor functions and dysfunctions, needs to be further assessed. The ion channels and exchangers coupled to orexin receptors in the STN might be potential effective targets for the treatment of basal ganglia motor diseases such as Parkinson disease.

ETHICS STATEMENT

All animal experiments were approved by the Experimental Animal Care and Use Committee of Nanjing University and were conducted in accordance with the US National Institutes of Health Guide for the Care and Use of Laboratory Animals (NIH Publication 85-23, revised 2011). All efforts were made to minimize the number of animals used and their suffering.

AUTHOR CONTRIBUTIONS

G-YL, Q-XZ and X-YZ performed experiments, analyzed data, and prepared figures and the draft manuscript. J-NZ and J-JW designed research and wrote the article.

FUNDING

This work was supported by the National Natural Science Foundation of China (grants 31330033, 31471112, 81671107, 31600834, 31771143, and NSFC/RGC Joint Research Scheme 31461163001); the Ministry of Education of China (Fundamental Research Funds for the Central Universities 020814380091); and the Natural Science Foundation of Jiangsu Province, China (grant BK20151384).

REFERENCES

Atherton, J. F., Kitano, K., Baufreton, J., Fan, K., Wokosin, D., Tkatch, T., et al. (2010). Selective participation of somatodendritic HCN channels in inhibitory but not excitatory synaptic integration in neurons of the subthalamic nucleus. *J. Neurosci.* 30, 16025–16040. doi: 10.1523/JNEUROSCI.3898-10.2010

Barlas, O., Hanağasi, H. A., Imer, M., Sahin, H. A., Sencer, S., and Emre, M. (2001). Do unilateral ablative lesions of the subthalamic nucleu in parkinsonian patients lead to hemiballism? *Mov. Disord.* 16, 306–310. doi: 10.1002/mds.1051

Baufreton, J., Atherton, J. F., Surmeier, D. J., and Bevan, M. D. (2005). Enhancement of excitatory synaptic integration by GABAergic inhibition in the subthalamic nucleus. *J. Neurosci.* 25, 8505–8517. doi: 10.1523/JNEUROSCI.1163-05.2005

Bergman, H., Wichmann, T., and Delong, M. R. (1990). Reversal of experimental parkinsonism by lesions of the subthalamic nucleus. *Science* 249, 1436–1438. doi: 10.1126/science.2402638

Broberger, C., De Lecea, L., Sutcliffe, J. G., and Hökfelt, T. (1998). Hypocretin/orexin- and melanin-concentrating hormone-expressing cells form distinct populations in the rodent lateral hypothalamus: relationship to

the neuropeptide Y and agouti gene-related protein systems. *J. Comp. Neurol.* 402, 460–474. doi: 10.1002/(sici)1096-9861(19981228)402:4<460::aid-cne3>3.3.co;2-j

Canitano, A., Papa, M., Boscia, F., Castaldo, P., Sellitti, S., Taglialatela, M., et al. (2002). Brain distribution of the Na^+/Ca^{2+} exchanger-encoding genes NCX1, NCX2, and NCX3 and their related proteins in the central nervous system. *Ann. N Y Acad. Sci.* 976, 394–404. doi: 10.1111/j.1749-6632.2002.tb04766.x

Chemelli, R. M., Willie, J. T., Sinton, C. M., Elmquist, J. K., Scammell, T., Lee, C., et al. (1999). Narcolepsy in orexin knockout mice: molecular genetics of sleep regulation. *Cell* 98, 437–451. doi: 10.1016/S0092-8674(00)81973-X

Chu, H. Y., Atherton, J. F., Wokosin, D., Surmeier, D. J., and Bevan, M. D. (2015). Heterosynaptic regulation of external globus pallidus inputs to the subthalamic nucleus by the motor cortex. *Neuron* 85, 364–376. doi: 10.1016/j.neuron.2014.12.022

Cluderay, J. E., Harrison, D. C., and Hervieu, G. J. (2002). Protein distribution of the orexin-2 receptor in the rat central nervous system. *Regul. Pept.* 104, 131–144. doi: 10.1016/s0167-0115(01)00357-3

Cutler, D. J., Morris, R., Sheridhar, V., Wattam, T. A., Holmes, S., Patel, S., et al. (1999). Differential distribution of orexin-A and orexin-B immunoreactivity in the rat brain and spinal cord. *Peptides* 20, 1455–1470. doi: 10.1016/s0196-9781(99)00157-6

de Lecea, L., Kilduff, T. S., Peyron, C., Gao, X., Foye, P. E., Danielson, P. E., et al. (1998). The hypocretins: hypothalamus-specific peptides with neuroexcitatory activity. *Proc. Natl. Acad. Sci. U S A* 95, 322–327. doi: 10.1073/pnas.95.1.322

Dunovan, K., and Verstynen, T. (2016). Believer-skeptic meets actor-critic: rethinking the role of basal ganglia pathways during decision-making and reinforcement learning. *Front. Neurosci.* 10:106. doi: 10.3389/fnins.2016.00106

Fischer, P., Pogosyan, A., Herz, D. M., Cheeran, B., Green, A. L., Fitzgerald, J., et al. (2017). Subthalamic nucleus γ activity increases not only during movement but also during movement inhibition. *Elife* 6:e23947. doi: 10.7554/elife.23947

Fronczek, R., Overeem, S., Lee, S. Y., Hegeman, I. M., van Pelt, J., van Duinen, S. G., et al. (2007). Hypocretin (orexin) loss in Parkinson's disease. *Brain* 130, 1577–1585. doi: 10.1093/brain/awm090

Gao, H. R., Zhuang, Q. X., Li, B., Li, H. Z., Chen, Z. P., Wang, J. J., et al. (2016). Corticotropin releasing factor excites neurons of posterior hypothalamic nucleus to produce tachycardia in rats. *Sci. Rep.* 6:20206. doi: 10.1038/srep20206

Giardino, W. J., Eban-Rothschild, A., Christoffel, D. J., Li, S. B., Malenka, R. C., and de Lecea, L. (2018). Parallel circuits from the bed nuclei of stria terminalis to the lateral hypothalamus drive opposing emotional states. *Nat. Neurosci.* 21, 1084–1095. doi: 10.1038/s41593-018-0198-x

Hervieu, G. J., Cluderay, J. E., Harrison, D. C., Roberts, J. C., and Leslie, R. A. (2001). Gene expression and protein distribution of the orexin-1 receptor in the rat brain and spinal cord. *Neuroscience* 103, 777–797. doi: 10.1016/s0306-4522(01)00033-1

Hille, B. (2001). *Ionic Channels of Excitable Membranes.* 3rd Edn. Sunderland, MA: Sinauer Associates, Inc.

Jeon, D., Chu, K., Jung, K. H., Kim, M., Yoon, B. W., Lee, C. J., et al. (2008). Na^+/Ca^{2+} exchanger 2 is neuroprotective by exporting Ca^{2+} during a transient focal cerebral ischemia in the mouse. *Cell Calcium* 43, 482–491. doi: 10.1016/j.ceca.2007.08.003

Ji, M. J., Zhang, X. Y., Chen, Z., Wang, J. J., and Zhu, J. N. (2019). Orexin prevents depressive-like behavior by promoting stress resilience. *Mol. Psychiatry* 24, 282–293. doi: 10.1038/s41380-018-0127-0

Karschin, C., Schreibmayer, W., Dascal, N., Lester, H., Davidson, N., and Karschin, A. (1994). Distribution and localization of a G protein-coupled inwardly rectifying K^+ channel in the rat. *FEBS Lett.* 348, 139–144. doi: 10.1016/0014-5793(94)00590-7

Korotkova, T. M., Haas, H. L., and Brown, R. E. (2002). Histamine excites GABAergic cells in the rat substantia nigra and ventral tegmental area *in vitro*. *Neurosci. Lett.* 320, 133–136. doi: 10.1016/s0304-3940(02)00050-2

Kravitz, A. V., Freeze, B. S., Parker, P. R., Kay, K., Thwin, M. T., Deisseroth, K., et al. (2010). Regulation of parkinsonian motor behaviours by optogenetic control of basal ganglia circuitry. *Nature* 466, 622–666. doi: 10.1038/nature09159

Kukkonen, J. P. (2011). A ménage à trois made in heaven: G-protein-coupled receptors, lipids and TRP channels. *Cell Calcium* 50, 9–26. doi: 10.1016/j.ceca.2011.04.005

Kukkonen, J. P., and Leonard, C. S. (2014). Orexin/hypocretin receptor signalling cascades. *Br. J. Pharmacol.* 171, 314–331. doi: 10.1111/bph.12324

Leonard, C. S., and Kukkonen, J. P. (2014). Orexin/hypocretin receptor signalling: a functional perspective. *Br. J. Pharmacol.* 171, 294–313. doi: 10.1111/bph.12296

Li, B., Zhuang, Q. X., Gao, H. R., Wang, J. J., and Zhu, J. N. (2017). Medial cerebellar nucleus projects to feeding-related neurons in the ventromedial hypothalamic nucleus in rats. *Brain Struct. Funct.* 222, 957–971. doi: 10.1007/s00429-016-1257-2

Limousin, P., Krack, P., Pollak, P., Benazzouz, A., Ardouin, C., Hoffmann, D., et al. (1998). Electrical stimulation of the subthalamic nucleus in advanced Parkinson's disease. *N. Engl. J. Med.* 339, 1105–1111. doi: 10.1056/NEJM199810153391603

Lytton, J. (2007). Na^+/Ca^{2+} exchangers: three mammalian gene families control Ca^{2+} transport. *Biochem. J.* 406, 365–382. doi: 10.1042/bj20070619

Marcus, J. N., Aschkenasi, C. J., Lee, C. E., Chemelli, R. M., Saper, C. B., Yanagisawa, M., et al. (2001). Differential expression of orexin receptors 1 and 2 in the rat brain. *J. Comp. Neurol.* 435, 6–25. doi: 10.1002/cne.1190

Matsuki, T., and Sakurai, T. (2008). Orexins and orexin receptors: from molecules to integrative physiology. *Results Probl. Cell Differ.* 46, 27–55. doi: 10.1007/400_2007_047

Murer, G., Adelbrecht, C., Lauritzen, I., Lesage, F., Lazdunski, M., Agid, Y., et al. (1997). An immunocytochemical study on the distribution of two G-protein-gated inward rectifier potassium channels (GIRK2 and GIRK4) in the adult rat brain. *Neuroscience* 80, 345–357. doi: 10.1016/s0306-4522(97)00001-8

Nambu, A., Tokuno, H., and Takada, M. (2002). Functional significance of the cortico-subthalamo-pallidal 'hyperdirect' pathway. *Neurosci. Res.* 43, 111–117. doi: 10.1016/S0168-0102(02)00027-5

Nishida, M., and MacKinnon, R. (2002). Structural basis of inward rectification: cytoplasmic pore of the G protein-gated inward rectifier GIRK1 at 1.8 A resolution. *Cell* 111, 957–965. doi: 10.1016/S0092-8674(02)01227-8

Paxinos, G., and Watson, C. (2014). *The Rat Atlas in Stereotaxic Coordinates.* 7th Edn. San Diego, CA: Academic Press.

Peyron, C., Tighe, D. K., van den Pol, A. N., de Lecea, L., Heller, H. C., Sutcliffe, J. G., et al. (1998). Neurons containing hypocretin (orexin) project to multiple neuronal systems. *J. Neurosci.* 18, 9996–10015. doi: 10.1523/JNEUROSCI.18-23-09996.1998

Plenz, D., and Kital, S. T. (1999). A basal ganglia pacemaker formed by the subthalamic nucleus and external globus pallidus. *Nature* 400, 677–682. doi: 10.1038/23281

Rodriguez, M. C., Guridi, O. J., Alvarez, L., Mewes, K., Macias, R., Vitek, J., et al. (1998). The subthalamic nucleus and tremor in Parkinson's disease. *Mov. Disord.* 13, 111–118. doi: 10.1002/mds.870131320

Sakurai, T. (2007). The neural circuit of orexin (hypocretin): maintaining sleep and wakefulness. *Nat. Rev. Neurosci.* 8, 171–181. doi: 10.1038/nrn2092

Sakurai, T., Amemiya, A., Ishii, M., Matsuzaki, I., Chemelli, R. M., Tanaka, H., et al. (1998). Orexins and orexin receptors: a family of hypothalamic neuropeptides and G protein-coupled receptors that regulate feeding behavior. *Cell* 92:696. doi: 10.1016/S0092-8674(00)80949-6

Sheng, Q., Xue, Y., Wang, Y., Chen, A. Q., Liu, C., Liu, Y. H., et al. (2018). The subthalamic neurons are activated by both orexin-A and orexin-B. *Neuroscience* 369, 97–108. doi: 10.1016/j.neuroscience.2017.11.008

Shin, H. S., Cho, H. S., Sung, K. W., and Yoon, B. J. (2009). Orexin-A increases cell surface expression of AMPA receptors in the striatum. *Biochem. Biophys. Res. Commun.* 378, 409–413. doi: 10.1016/j.bbrc.2008.11.051

Steininger, T. L., Kilduff, T. S., Behan, M., Benca, R. M., and Landry, C. F. (2004). Comparison of hypocretin/orexin and melanin-concentrating hormone neurons and axonal projections in the embryonic and postnatal rat brain. *J. Chem. Neuroanat.* 27, 165–181. doi: 10.1016/j.jchemneu.2004.02.007

Thannickal, T. C., Lai, Y. Y., and Siegel, J. M. (2007). Hypocretin (orexin) cell loss in Parkinson's disease. *Brain* 130, 1586–1595. doi: 10.1093/brain/awm097

Trivedi, P., Yu, H., MacNeil, D. J., Van der Ploeg, L. H., and Guan, X. M. (1998). Distribution of orexin receptor mRNA in the rat brain. *FEBS Lett.* 438, 71–75. doi: 10.1016/s0014-5793(98)01266-6

Tyree, S. M., Bomiger, J. C., and de Lecea, L. (2018). Hypocretin as a hub for arousal and motivation. *Front. Neurol.* 9:413. doi: 10.3389/fneur.2018.00413

Wagenbreth, C., Zaehle, T., Galazky, I., Voges, J., Guitart-Masip, M., Heinze, H. J., et al. (2015). Deep brain stimulation of the subthalamic nucleus modulates reward processing and action selection in Parkinson patients. *J. Neurol.* 262, 1541–1547. doi: 10.1007/s00415-015-7749-9

Wang, Y., Chen, Z. P., Zhuang, Q. X., Zhang, X. Y., Li, H. Z., Wang, J. J., et al. (2017). Role of corticotropin-releasing factor in cerebellar motor control and ataxia. *Curr. Biol.* 27, 2661.e5–2669.e5. doi: 10.1016/j.cub.2017.07.035

Wang, Y., Wang, Y., Liu, J., and Wang, X. (2018). Electroacupuncture alleviates motor symptoms and up-regulates vesicular glutamatergic transporter 1 expression in the subthalamic nucleus in a unilateral 6-hydroxydopamine-lesioned hemi-parkinsonian rat model. *Neurosci. Bull.* 34, 476–484. doi: 10.1007/s12264-018-0213-y

Wu, M., Zaborszky, L., Hajszan, T., van den Pol, A. N., and Alreja, M. (2004). Hypocretin/orexin innervation and excitation of identified septohippocampal cholinergic neurons. *J. Neurosci.* 24, 3527–3536. doi: 10.1523/JNEUROSCI.5364-03.2004

Yamamoto, Y., McKinley, M. J., Nakazato, M., Yamashita, H., Shirahata, A., and Ueta, Y. (2006). Postnatal development of orexin-A and orexin-B like immunoreactivities in the Eastern grey kangaroo (Macropus giganteus) hypothalamus. *Neurosci. Lett.* 392, 124–128. doi: 10.1016/j.neulet.2005.09.014

Zavala, B., Zaghloul, K., and Brown, P. (2015). The subthalamic nucleus, oscillations, and conflict. *Mov. Disord.* 30, 328–338. doi: 10.1002/mds.26072

Zénon, A., Duclos, Y., Carron, R., Witjas, T., Baunez, C., Régis, J., et al. (2016). The human subthalamic nucleus encodes the subjective value of reward and the cost of effort during decision-making. *Brain* 139, 1830–1843. doi: 10.1093/brain/aww075

Zhang, J., Li, B., Yu, L., He, Y. C., Li, H. Z., Zhu, J. N., et al. (2011). A role for orexin in central vestibular motor control. *Neuron* 69, 793–804. doi: 10.1016/j.neuron.2011.01.026

Zhang, X. Y., Yu, L., Zhuang, Q. X., Zhu, J. N., and Wang, J. J. (2013). Central functions of the orexinergic system. *Neurosci. Bull.* 29, 355–365. doi: 10.1007/s12264-012-1297-4

Zhuang, Q. X., Li, G. Y., Li, B., Zhang, C. Z., Zhang, X. Y., Xi, K., et al. (2018a). Regularizing firing patterns of rat subthalamic neurons ameliorates parkinsonian motor deficits. *J. Clin. Invest.* 128, 5413–5427. doi: 10.1172/jci99986

Zhuang, Q. X., Xu, H. T., Lu, X. J., Li, B., Yung, W. H., Wang, J. J., et al. (2018b). Histamine excites striatal dopamine D1 and D2 receptor-expressing neurons via postsynaptic H1 and H2 receptors. *Mol. Neurobiol.* 55, 8059–8070. doi: 10.1007/s12035-018-0976-1

Conflict of Interest Statement: The authors declare that the research was conducted in the absence of any commercial or financial relationships that could be construed as a potential conflict of interest.

frontiers in Cellular Neuroscience

ORIGINAL RESEARCH
published: 05 June 2019
doi: 10.3389/fncel.2019.00184

Onecut Factors and Pou2f2 Regulate the Distribution of V2 Interneurons in the Mouse Developing Spinal Cord

*Audrey Harris[1], Gauhar Masgutova[1], Amandine Collin[1], Mathilde Toch[1], Maria Hidalgo-Figueroa[1†], Benvenuto Jacob[2], Lynn M. Corcoran[3], Cédric Francius[1†] and Frédéric Clotman[1]**

[1] Laboratory of Neural Differentiation, Institute of Neuroscience, Université catholique de Louvain, Brussels, Belgium, [2] Institute of Neuroscience, System and Cognition Division, Université catholique de Louvain, Brussels, Belgium, [3] Molecular Immunology Division and Immunology Division, The Walter and Eliza Hall Institute of Medical Research, Parkville, VIC, Australia

Acquisition of proper neuronal identity and position is critical for the formation of neural circuits. In the embryonic spinal cord, cardinal populations of interneurons diversify into specialized subsets and migrate to defined locations within the spinal parenchyma. However, the factors that control interneuron diversification and migration remain poorly characterized. Here, we show that the Onecut transcription factors are necessary for proper diversification and distribution of the V2 interneurons in the developing spinal cord. Furthermore, we uncover that these proteins restrict and moderate the expression of spinal isoforms of *Pou2f2*, a transcription factor known to regulate B-cell differentiation. By gain- or loss-of-function experiments, we show that Pou2f2 contribute to regulate the position of V2 populations in the developing spinal cord. Thus, we uncovered a genetic pathway that regulates the diversification and the distribution of V2 interneurons during embryonic development.

Keywords: embryonic spinal cord, V2 interneurons, Onecut, Pou2f2, neuronal migration, differentiation

OPEN ACCESS

Edited by:
Jing-Ning Zhu,
Nanjing University, China

Reviewed by:
Lyandysha Zholudeva,
Drexel University, United States
Tuan Vu Bui,
University of Ottawa, Canada

****Correspondence:***
Frédéric Clotman
frederic.clotman@uclouvain.be

†Present address:
Maria Hidalgo-Figueroa,
Neuropsychopharmacology and Psychobiology Research Group, Area of Psychobiology, Department of Psychology, University of Cádiz, Cádiz, Spain;
Instituto de Investigación e Innovación en Ciencias Biomédicas de Cádiz (INiBICA), Cádiz, Spain
Cédric Francius,
PAREXEL International, Paris, France

Specialty section:
This article was submitted to Cellular Neurophysiology, a section of the journal Frontiers in Cellular Neuroscience

Received: *14 January 2019*
Accepted: *12 April 2019*
Published: *05 June 2019*

Citation:
Harris A, Masgutova G, Collin A, Toch M, Hidalgo-Figueroa M, Jacob B, Corcoran LM, Francius C and Clotman F (2019) Onecut Factors and Pou2f2 Regulate the Distribution of V2 Interneurons in the Mouse Developing Spinal Cord. Front. Cell. Neurosci. 13:184. doi: 10.3389/fncel.2019.00184

INTRODUCTION

Neuronal migration is a critical feature of CNS development. It enables neurons to reach an adequate location in the nervous parenchyma and to properly integrate into neural circuits. The mechanisms that regulate neuronal migration have been extensively studied in the developing brain, particularly for cortical interneurons (INs) (Guo and Anton, 2014; Barber and Pierani, 2016). In contrast, the factors that control IN migration in the developing spinal cord remain almost totally unknown.

In the embryonic spinal cord, distinct neuronal populations are generated from different progenitor domains orderly distributed along the dorso-ventral axis of the ventricular zone. These progenitors produce motor neurons and multiple populations of ventral or dorsal INs

(Lu et al., 2015; Lai et al., 2016). Although spinal IN populations do not organize into columns along the anteroposterior axis of the spinal cord, they each migrate according to a stereotyped pattern and settle down at specific focused or diffuse locations in the spinal parenchyma (Grossmann et al., 2010). Recent studies demonstrated that proper neuronal distribution is critical for adequate formation of spinal circuits. Indeed, the clustering and dorso-ventral settling position of motor neuron pools critically pattern sensory input specificity (Surmeli et al., 2011). Position of dorsal INs along the medio-lateral axis in lamina V determines their connectivity with sensory afferents (Hilde et al., 2016) while extensor and flexor premotor INs segregate along the medio-lateral axis of the spinal cord (Tripodi et al., 2011). Positional distinctions among premotor INs additionally correlate with their output to different motor columns (Goetz et al., 2015) and differential distribution of V1 IN subsets constrain patterns of input from sensory and from motor neurons (Bikoff et al., 2016). Consistently, distinct ventral IN subsets are differentially distributed along the anteroposterior axis of the spinal cord (Francius et al., 2013; Bikoff et al., 2016; Hayashi et al., 2018) and integrate into specific local microcircuit modules (Hayashi et al., 2018). However, the molecular mechanisms that regulate proper distribution of spinal INs remain elusive.

During their migration, cardinal populations of spinal neurons undergo progressive diversification into distinct subsets that exert specific functions in spinal circuits (Catela et al., 2015; Lu et al., 2015; Lai et al., 2016). For example, V2 INs divide into major V2a and V2b and minor V2c and V2d populations characterized by the expression of Chx10, Gata3, Sox1, and Shox2, respectively. V2a and V2d are excitatory neurons that participate in left–right alternation at high speed and contribute to rhythmic activation of locomotor circuits, respectively (Crone et al., 2008; Dougherty and Kiehn, 2010; Dougherty et al., 2013). V2b cells are inhibitory INs that participate in alternation of flexor vs. extensor muscle contraction (Britz et al., 2015). As observed for V1 INs (Bikoff et al., 2016), V2 cells further diversify into more discrete subpopulations differentially distributed along the anteroposterior axis of the spinal cord (Francius et al., 2013; Hayashi et al., 2018). However, specific functions of these IN subsets have not been investigated yet, and the mechanisms that govern their production remain currently unknown.

Recently, we identified Onecut (OC) transcription factors as regulators of neuronal diversification (Roy et al., 2012; Francius and Clotman, 2014; Kabayiza et al., 2017) and of dorsal IN migration (Kabayiza et al., 2017) in the developing spinal cord. OC factors, namely Hepatocyte Nuclear Factor-6 (HNF-6, or OC-1), OC-2, and OC-3, are transcriptional activators present in the digestive tract and in the CNS during embryonic development (Lemaigre et al., 1996; Landry et al., 1997; Jacquemin et al., 1999; Vanhorenbeeck et al., 2002; Jacquemin et al., 2003b). In neural tissue, they regulate production (Espana and Clotman, 2012a), diversification (Roy et al., 2012; Francius and Clotman, 2014; Kabayiza et al., 2017), distribution (Espana and Clotman, 2012a,b; Audouard et al., 2013; Kabayiza et al., 2017), and maintenance (Espana and Clotman, 2012a,b; Stam et al., 2012) of specific neuronal populations, as well as the formation of neuromuscular junctions (Audouard et al., 2012). Here, we demonstrate that OC factors regulate the diversification and the distribution of V2 INs during spinal cord development. Analyzes of OC-deficient embryos showed defective production of specific subpopulations of V2a INs, as well as abnormal distribution of V2a and V2b cells in the developing spinal cord. Furthermore, we uncovered that OC proteins act upstream of specific spinal isoforms of Pou2f2, a POU family transcription factor. Using gain- or loss-of-function experiments, we demonstrated that, as observed for OC factors, Pou2f2 regulates the distribution of V2 INs in the developing spinal cord. Thus, we uncovered a genetic pathway that regulates the diversification and the distribution of V2 INs during embryonic development.

RESULTS

OC Factors Are Present in Multiple Subsets of Spinal V2 INs

In the developing spinal cord, OC factors contribute to diversification, migration, and maintenance of different neuronal populations (Roy et al., 2012; Stam et al., 2012; Kabayiza et al., 2017). To study V2 IN diversification, we previously established a repertoire of markers that divide embryonic V2 cells into multiple subpopulations (Francius et al., 2013). Although OC factors have been detected in V2 INs (Francius and Clotman, 2010; Francius et al., 2013) and are similarly distributed at distinct antero-posterior levels (Francius et al., 2013), their production in V2 subsets has not been investigated yet. Therefore, we first determined the presence of each OC in these V2 subpopulations at e12.5.

V2a INs include neuronal subsets characterized by the presence of Shox2, MafA, cMaf, Bhlhb5, or Prdm8 (Francius et al., 2013). Only Hnf6 was detected in few Shox2+ V2a cells (**Figures 1A–C"** and **Table 1**). In contrast, the three OC proteins were detected in MafA+ and cMaf+ V2a subpopulations (**Figures 1D–I"** and **Table 1**), but not in Bhlhb5+ or Prdm8+ cells (**Table 1**; data not shown). V2b INs include similar subsets except for Shox2+ and cMaf+ cells, and contain an additional MafB+ subpopulation (Francius et al., 2013). OC were present in MafA+ but not in MafB+, Bhlhb5+, or Prdm8+ V2b subsets (**Figures 1J–L"** and **Table 1**; data not shown). In addition, OC were detected in V2c (non-progenitor Sox1+ cells; **Figures 1M–O"** and **Table 1**) but not in V2d (Shox2+Chx10-) cells (**Figures 1A–C"** and **Table 1**). Thus, OC factors are present in multiple subpopulations of V2 INs.

OC Factors Regulate the Diversification of Spinal V2 INs

To determine whether OC proteins contribute to the development of V2 IN subsets, we characterized the phenotype of these cells in *Hnf6/Oc2* double-mutant embryos, which lack the three OC factors in the developing spinal cord (Roy et al., 2012; Kabayiza et al., 2017). Given that the number and the distribution of cells in each IN subpopulation vary along the anteroposterior axis of the spinal cord (Francius et al., 2013; Hayashi et al., 2018;

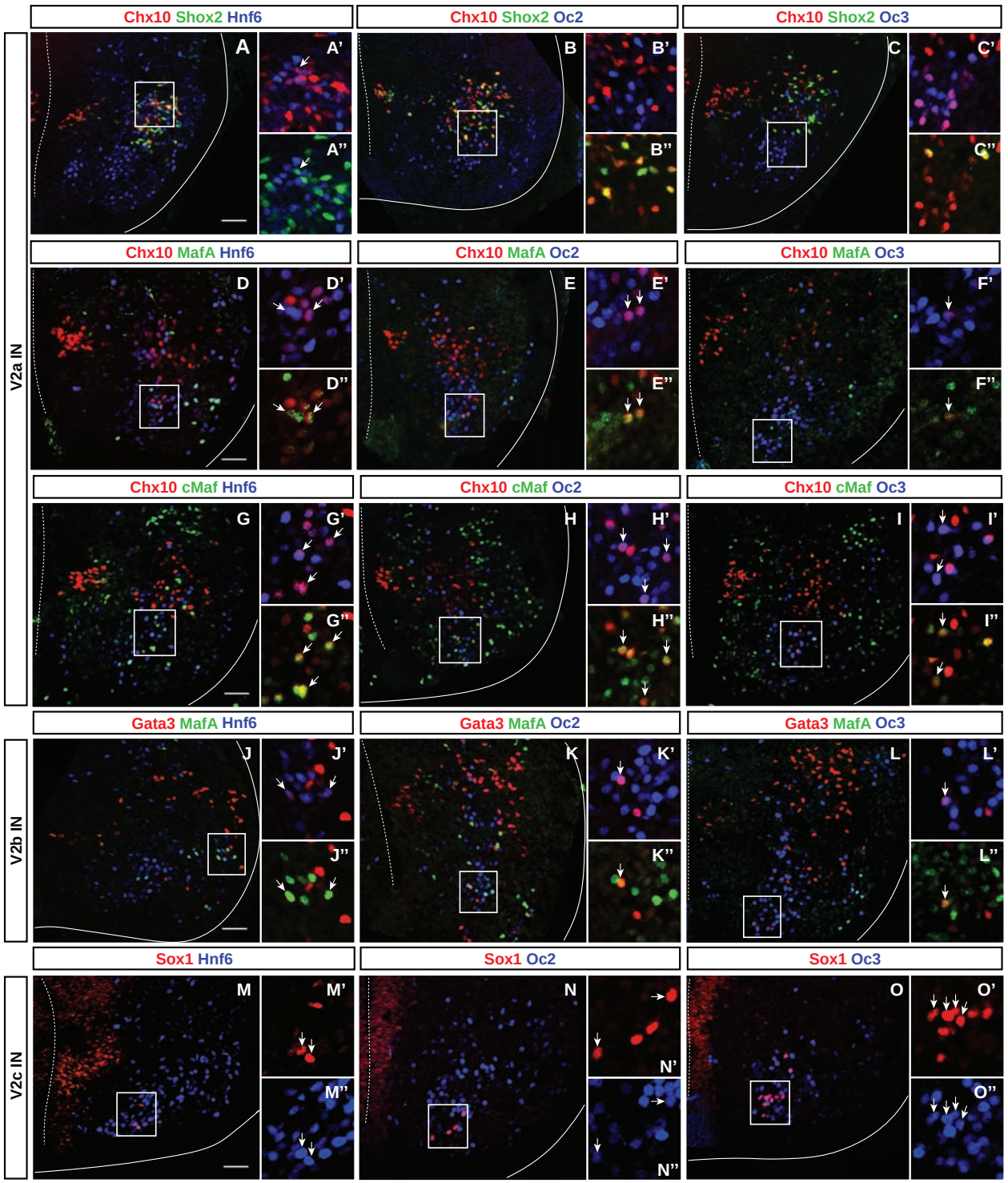

FIGURE 1 | Onecut factors are present in multiple subsets of V2 interneurons. **(A–I")** Immunolabelings for OC, the V2a generic marker Chx10 and markers of V2a subpopulations (Francius et al., 2013) on transverse spinal cord sections (brachial or thoracic levels) of e12.5 wild-type mouse embryos. In each figure, the right ventral quadrant of the spinal cord is shown. Only HNF-6 is detected in Shox2+ V2a cells (arrow in **A–C"**), whereas the three OC are present in the MafA+ and in the cMaf+ V2a subsets (arrows in **D–I"**). **(J–L")** Immunolabelings for OC, the V2b generic marker Gata3 and MafA. The three OC proteins are detected in MafA+ V2b interneurons (arrows). **(M–O")** Immunolabelings for OC and the V2c marker Sox1 demonstrate that OC factors are present in a majority of V2c interneurons (arrows). Sox1 in the ventricular zone labels neural progenitors. Scale bar = 50 μm.

TABLE 1 | Onecut factors are present in specific populations and subpopulations of V2 interneurons.

		V2-e12.5		
Populations	**Subpopulations**	**HNF-6**	**OC-2**	**OC-3**
V2a-Chx10		+	+	+
	Shox2	+	–	–
	MafA	+	+	+
	cMaf	+	+	+
	Bhlhb5	–	–	–
	Prdm8	–	–	–
V2b-Gata3		+	+	+
	MafA	+	+	+
	MafB	–	–	–
	Bhlhb5	–	–	–
	Prdm8	–	–	–
V2c-Sox1		+	+	+
V2d-Shox2		–	–	–

The V2 populations, including V2a, V2b, V2c, and V2d, are subdivided in smaller subpopulations characterized by differential expression of transcription factors (Francius et al., 2013). OC factors are detected in specific populations and subpopulations of V2 interneurons.

Sweeney et al., 2018), this analysis was systematically performed at brachial, thoracic and lumbar levels at e12.5 and e14.5.

In the absence of OC factors, the total number of Chx10+ INs was not significantly changed (**Figures 2A–D** and **Supplementary Figures S1A,B**), although a trend toward reduction was detected at brachial level at e12.5 (**Figure 2C**). Consistently, the number of Chx10+Shox2+ INs was not changed (**Figures 2E–H** and **Supplementary Figures S1C–D"**). These observations suggest that OC are not necessary for V2a IN production. In contrast, the smaller V2a subpopulations wherein OC factors were detected in control embryos, characterized by the presence of MafA (**Figures 1D–F"**) or cMaf (**Figures 1G–I"**), were almost completely lost in OC mutant embryos (**Figures 2I–P** and **Supplementary Figures S1E–H"**). As the total number of Chx10+ and of Shox2+ V2a was not changed (**Figures 2A–H** and **Supplementary Figures S1A–D"**), the loss of the MafA+ or cMaf+ subsets may be compensated for by expansion of other V2a subpopulations, markers of which remain to be identified. Nevertheless, our data indicate that OC factors are required either for the expression of V2 subpopulation markers or for the differentiation of specific V2a IN subsets.

To discriminate between these possibilities and to evaluate the contribution of OC factors to V2b diversification, we characterized the phenotype of V2b INs and of their MafA+ subpopulation in the absence of OC proteins. As observed for V2a INs, the total number of V2b cells was not changed in OC mutant embryos (**Figures 2Q–T** and **Supplementary Figures S1I,J**), although a trend toward reduction was observed at brachial level at e12.5 (**Figure 2S**). However, in contrast to V2a, the MafA+ V2b INs were present in normal number in OC mutant embryos (**Figures 2U–X** and **Supplementary Figures S1K–L"**). Hence, OC factors are not necessary for the production of the MafA+ V2b subset, although they are required for proper differentiation of the MafA+ and of the cMaf+ V2a subpopulations.

Finally, we assessed the requirement for OC in the production of V2c INs, a V2 population strongly related to V2b cells (Panayi et al., 2010). Although weak production of Sox1 in spinal progenitors was preserved, V2c cells characterized by high Sox1 levels were scarcely detectable in OC mutant embryos at e12.5 (arrows in **Figures 2Y–AA**). However, the number of V2c was normal at e14.5 (**Figure 2BB** and **Supplementary Figures S1M,N**), suggesting that the absence of OC delays the differentiation of V2c INs without affecting the V2b population. Taken together, these observations demonstrate that OC proteins are not required for V2 IN production but regulate the diversification of V2 INs into multiple subpopulations.

OC Factors Regulate the Distribution of Spinal V2 INs

Although the total number of V2a or V2b INs was not affected by the absence of OC factors, careful examination of immunofluorescence labelings suggested that, as observed for spinal dorsal INs (Kabayiza et al., 2017), OC proteins may regulate the distribution of V2 INs in the developing spinal cord (**Figures 2A,B,Q,R**). Therefore, quantitative distribution analyses (Kabayiza et al., 2017) were performed for each V2 population at brachial, thoracic or lumbar levels at e12.5, namely in the course of ventral IN migration, and at e14.5, i.e., when ventral IN migration in the transverse plane of the spinal cord is completed. Absence of the MafA+ and cMaf+ V2a subpopulations in OC mutants and the small size of other V2 subsets prevented analysis of subpopulation distribution.

At e12.5 in control embryos, V2a INs distributed in two connected clusters, a major central group and a minor medial group, at each level of the spinal cord (**Figures 3A–C**). In mutant embryos, V2a cells similarly distributed in connected central and medial groups. However, the relative cell distribution between the two clusters was altered, with less central cells at brachial level and less medial cells at lumbar levels (**Figures 3D–L**). Altered V2a distribution on the medio-lateral axis was confirmed at e14.5. In control embryos, the two V2a groups did coalesce in a more evenly distributed population that occupied ∼70% of the medio-lateral axis (**Figures 3M–O**). In mutant embryos, V2a INs remained segregated into two distinct, although connected, clusters with a majority of cells in medial position (**Figures 3P–X**). Thus, absence of OC factors perturbs proper distribution of the V2a INs and restricts at e14.5 migration of a fraction of V2a cells in a medial position.

To assess whether OC also regulate the position of other V2 populations, we studied the distribution of V2b INs. At e12.5 in control embryos, V2b cells distributed in a major central (brachial level) or lateral (thoracic and lumbar levels) cluster with minor subsets located more medially (arrows in **Figures 4A–C**) or ventrally (arrowheads in **Figures 4A–C**). In OC mutant embryos at e12.5, the major population was more compact, more centrally located and slightly more ventral. In addition, the ventral V2b subset was significantly depleted (**Figures 4D–L**). Consistently, at e14.5, V2b INs in the central

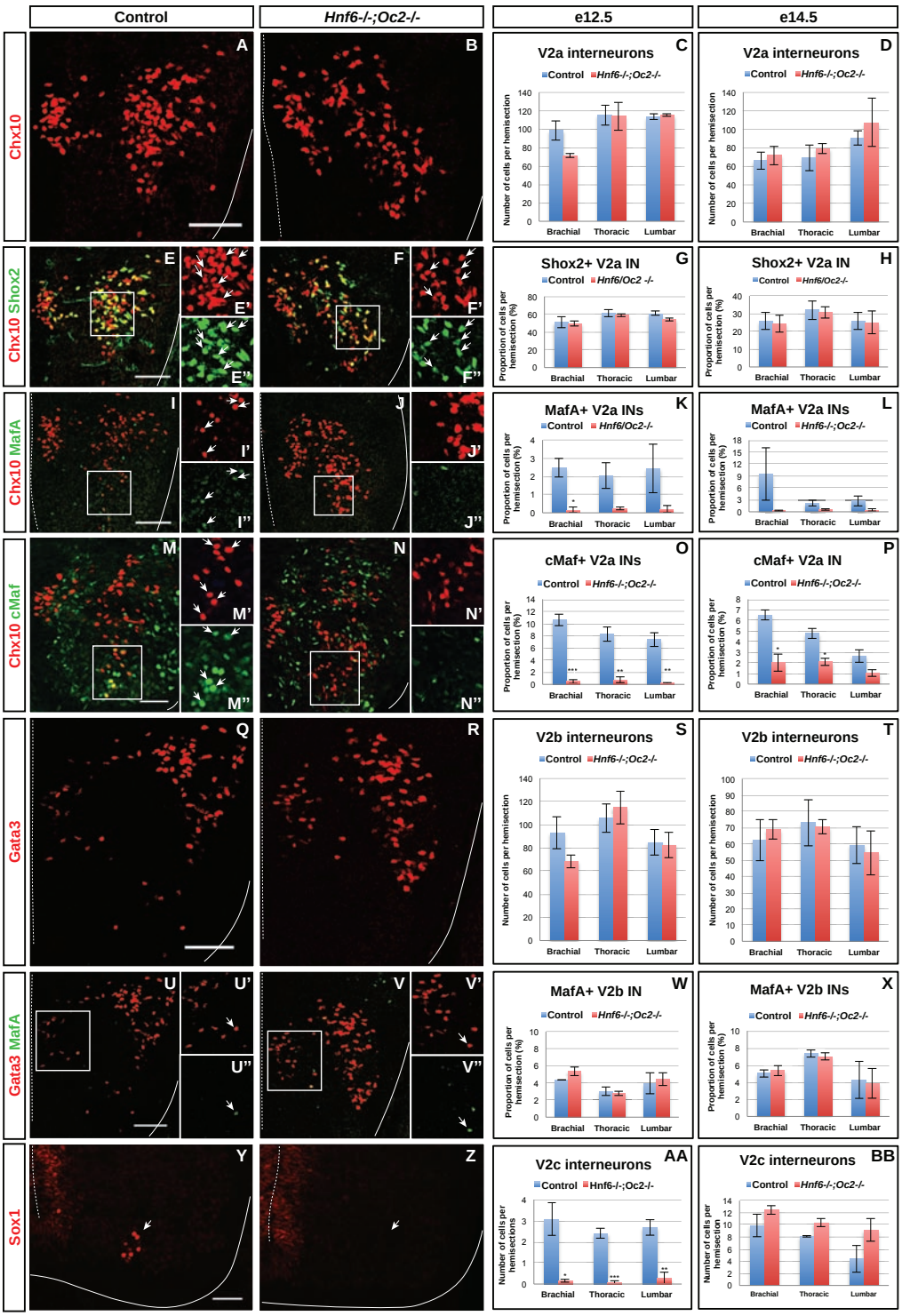

FIGURE 2 | Onecut factors regulate the diversification of the V2 interneurons. Immunolabelings on transverse spinal cord sections (brachial or thoracic levels) of control or *Hnf6*$^{-/-}$;*Oc2*$^{-/-}$ double-mutant embryos. At e12.5 **(A–C)** and e14.5 **(D)**, the production of the V2a Chx10+ interneurons is not altered in the absence of OC factors. Similarly, the number of Shox2+ V2a is affected neither at e12.5 **(E–G)** nor at e14.5 **(H)**. In contrast, quantitative analysis of control or *Hnf6*$^{-/-}$;*Oc2*$^{-/-}$ littermates at e12.5 **(I–K)** and at e14.5 **(L)** shows reduction in MafA+ V2a interneurons in double mutants as compared to control embryos. Similarly, the number of cMaf+ V2a interneurons is significantly reduced at e12.5 **(M–O)** and e14.5 **(P)** in the absence of OC factors. At e12.5 **(Q–S)** and e14.5 **(T)**, the production of the V2b interneurons is not affected in *Hnf6*$^{-/-}$;*Oc2*$^{-/-}$ embryos. The generation of the MafA+ V2b interneurons is also unchanged at e12.5 **(U–W)** or e14.5 **(X)**. At e12.5 **(Y–AA)**, the number of V2c interneurons is dramatically reduced in the absence of OC factors (Sox1 in the ventricular zone labels neural progenitors). However, this is no longer the case at e14.5 **(BB)**. Mean values ± SEM. *$p \leq 0.05$; **$p \leq 0.01$; ***$p \leq 0.001$. Scale bar = 50 μm.

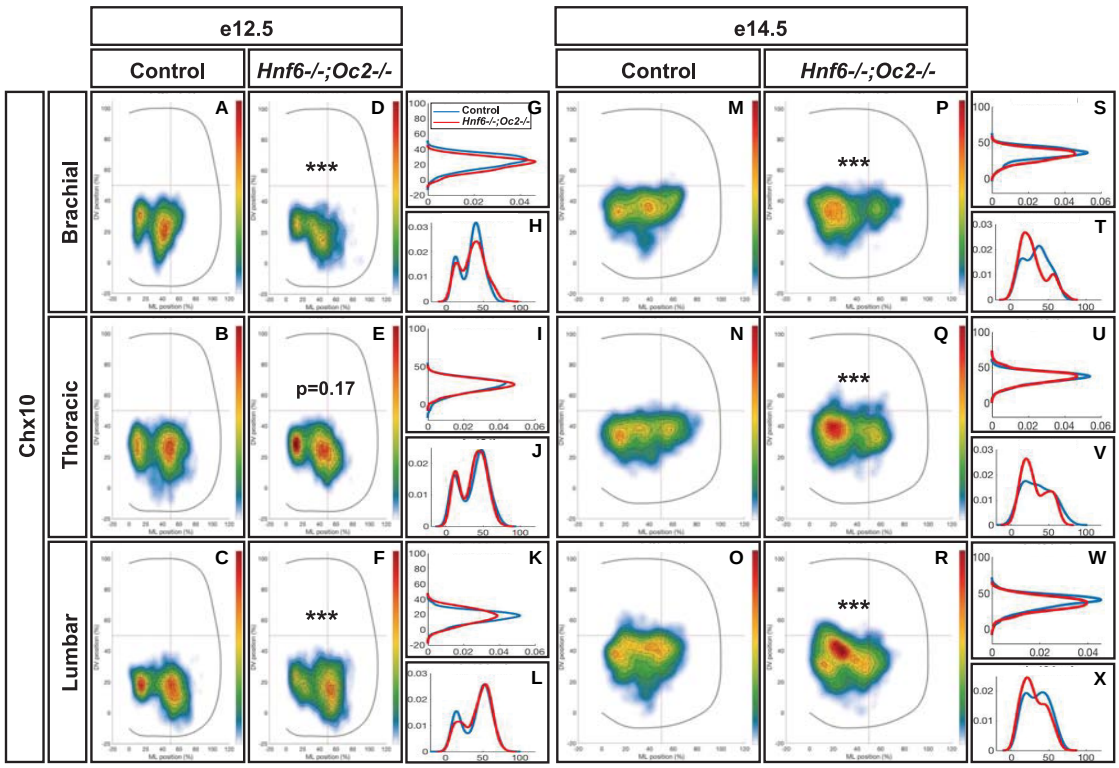

FIGURE 3 | Onecut factors regulate the distribution of V2a interneurons. Distribution of V2a interneurons on the transverse plane of the spinal cord in control or *Hnf6*$^{-/-}$;*Oc2*$^{-/-}$ double-mutant embryos at brachial, thoracic, or lumbar level (only the right hemisection is shown). Two-dimension distribution graphs (left) show integration of cell distribution from multiple sections of multiple embryos of each genotype. One-dimension graphs (right) compare density distribution in control (blue) and in double-mutant embryos (red) on the dorso-ventral (upper) or the medio-lateral (lower) axis of the spinal cord (see section "Materials and Methods" for details). **(A–C)** At e12.5 in control embryos, V2a interneurons distribute in two connected clusters, a major central group and a minor medial group, at each level of the spinal cord. **(D–L)** In mutant embryos, the relative cell distribution between the two clusters seems altered, with relatively less central cells at brachial level and less medial cells at lumbar levels (n = 3, $p \leq 0.001$ at brachial and lumbar levels; p = 0.17 at thoracic level). **(M–X)** Altered V2a distribution on the medio-lateral axis is confirmed at e14.5. **(M–O,S–X)** In control embryos, the two V2a groups coalesce in a more evenly distributed population that occupied ~70% of the medio-lateral axis. **(P–X)** In mutant embryos, V2a interneurons remain segregated into two distinct, although connected, clusters with a majority of cells in medial position (n = 3, $p \leq 0.001$).

cluster remained significantly more compact at thoracic level in the absence of OC factors, and identical trends were observed at brachial and lumbar levels (**Figures 4M–X**). In addition, a small contingent of V2b migrating toward the medio-dorsal spinal cord in control embryos (arrowheads in **Figures 4N,O**) was missing in OC mutant littermates (**Figures 4Q–X**). Taken together, these observations demonstrate that, in addition to V2 diversification, the OC transcription factors regulate proper distribution of V2 INs during spinal cord development.

OC Factors Control Expression of Neuronal-Specific Isoforms of *Pou2f2*

To identify genes downstream of OC that may contribute to V2 IN differentiation and distribution, we performed a microarray comparison of control and of OC-deficient spinal cord transcriptome at e11.5, namely at the stage when significant numbers of V2 cells have been generated and are initiating migration (GEO repository accession number: GSE117871). Among genes showing a differential expression level in the OC mutant spinal cord (**Supplementary Table S1**), *Pou2f2* was significantly upregulated (1.57-fold increase). Pou2f2 (previously named Oct-2) is a transcription factor containing a POU-specific domain and a POU-type homeodomain (**Figure 5A**) that binds an octamer motif (consensus sequence ATGCAAAT) (Latchman, 1996). *Pou2f2* expression has been detected in B lymphocytes, in neuronal cell lines and in neural tissues including the developing CNS (Hatzopoulos et al., 1990; Lillycrop and Latchman, 1992; Camos et al., 2014). Pou2f2 is required for differentiation of B lymphocytes and for postnatal survival (Corcoran et al., 1993; Konig et al., 1995; Corcoran et al., 2004; Hodson et al., 2016), and is able to modulate neuronal differentiation of ES cells (Theodorou et al., 2009). However, its role in the developing spinal cord remains unknown.

Based on work in B cells, multiple *Pou2f2* isoforms generated by alternative splicing have been described (**Figure 5A**; Hatzopoulos et al., 1990; Wirth et al., 1991; Lillycrop and Latchman, 1992; Stoykova et al., 1992; Liu et al., 1995). Therefore, we first determined whether similar isoforms are found in the developing spinal cord. However, we systematically failed to obtain RT-PCR products using upstream primers in described exon 1 (asterisks in **Supplementary Figures S2A,B** and data not shown; **Table 2**) and amplifications encompassing exons 5 to 6 generated predominant amplicons larger than

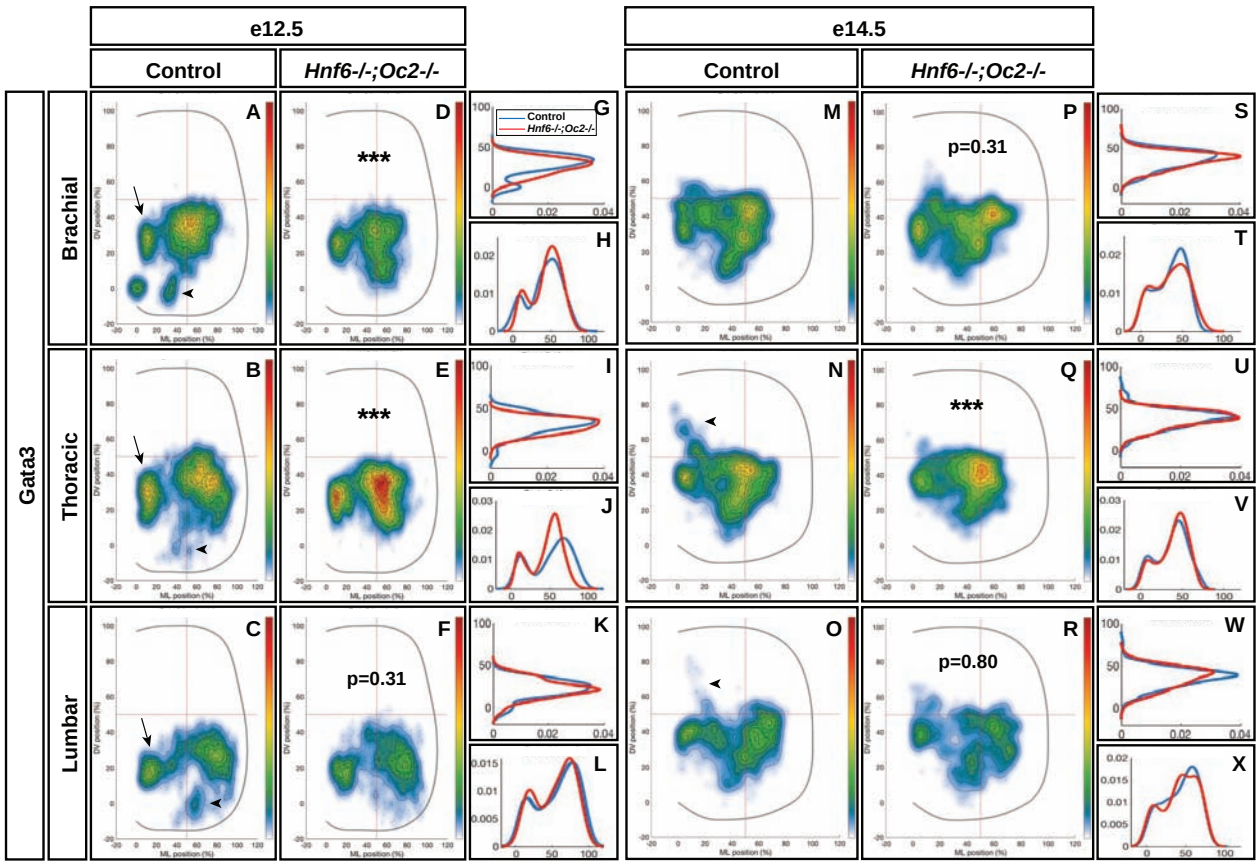

FIGURE 4 | Onecut factors regulate the distribution of V2b interneurons. **(A–C)** At e12.5 in control embryos, V2b cells are distributed in a major central (brachial level) or lateral (thoracic and lumbar levels) cluster with minor subsets located more medially (arrows) or ventrally (arrowheads). **(D–L)** In OC mutant embryos at e12.5, the major population remains more compact, more centrally located and slightly more ventral. In addition, the ventral V2b subset is significantly depleted (asterisks; $n = 3$, $p \leq 0.001$ at brachial and thoracic levels; $p = 0.31$ at brachial level). **(M–X)** Consistently, at e14.5, V2b interneurons in the central cluster are more compact in the absence of OC factors at thoracic level, and a small contingent of V2b migrating toward the medio-dorsal spinal cord in control embryos (arrowheads) is missing in OC mutant littermates ($n = 3$, $p \leq 0.001$ at thoracic level; $p = 0.31$ and 0.80 at thoracic and lumbar levels, respectively).

expected (arrowheads in **Supplementary Figure S2B** and **Table 2**), suggesting the existence of alternative exons in *Pou2f2* embryonic spinal cord transcripts (**Figure 5A**). Data mining the NCBI Nucleotide database for *Pou2f2* sequences identified a predicted murine *Pou2f2* isoform (X6 sequence, accession number XM_006539651.3) with a different exon 1 (E1X) and an additional sequence between exons 5 and 6, the size of which (279 bp) corresponded to the size differences estimated in our amplifications encompassing exons 5 to 6 (arrowheads in **Supplementary Figure S2B** and **Table 2**). Using PCR primers in this predicted sequence, we were able to amplify a 5′ region of *Pou2f2* from the alternative E1X exon and an additional sequence between exons 5 and 6 (**Supplementary Figure S2C** and **Table 2**), suggesting that alternative isoforms similar to this predicted sequence are produced in the developing spinal cord. However, amplifications from E1X systematically produced two amplicons (arrowheads in **Supplementary Figure S2C** and **Table 2**), suggesting the existence of an alternative exon downstream to E1X. Sequencing of our PCR products and alignment to genomic DNA confirmed that predominant *Pou2f2* isoforms in the developing spinal cord contain the alternative E1X exon, an additional exon (E5b) between exons 5 and 6, and can undergo alternative splicing of a short (61bp) exon (E1b) between E1X and exon 2 (**Supplementary Figure S2D**). E5b exon maintains the reading frame. In contrast E1b exon disrupts it, imposing the use of the ATG located in exon 2 to generate a functional Pou2f2 protein, whereas the absence of E1b leaves open the use of an alternative upstream ATG located at the 3′ end of E1X (**Figure 5A** and **Supplementary Figure S2D**). Hence, our RT-PCR and sequencing data indicate that four neuronal *Pou2f2* isoforms different from the previously described B-cell or neural isoforms are produced in the developing spinal cord (**Figure 5A**).

However, minor transcripts corresponding to B-cell isoforms are also detected in the embryonic spinal cord (**Supplementary Figures S2A,B** and **Table 2**). To assess the relative abundance of each transcript type in this tissue and to evaluate the extent of their relative overexpression in the absence of OC factors, we quantified each isoform type in control and in OC-deficient spinal cord at e11.5. In control spinal cords, spinal *Pou2f2* isoforms were >30-fold more abundant than B-cell

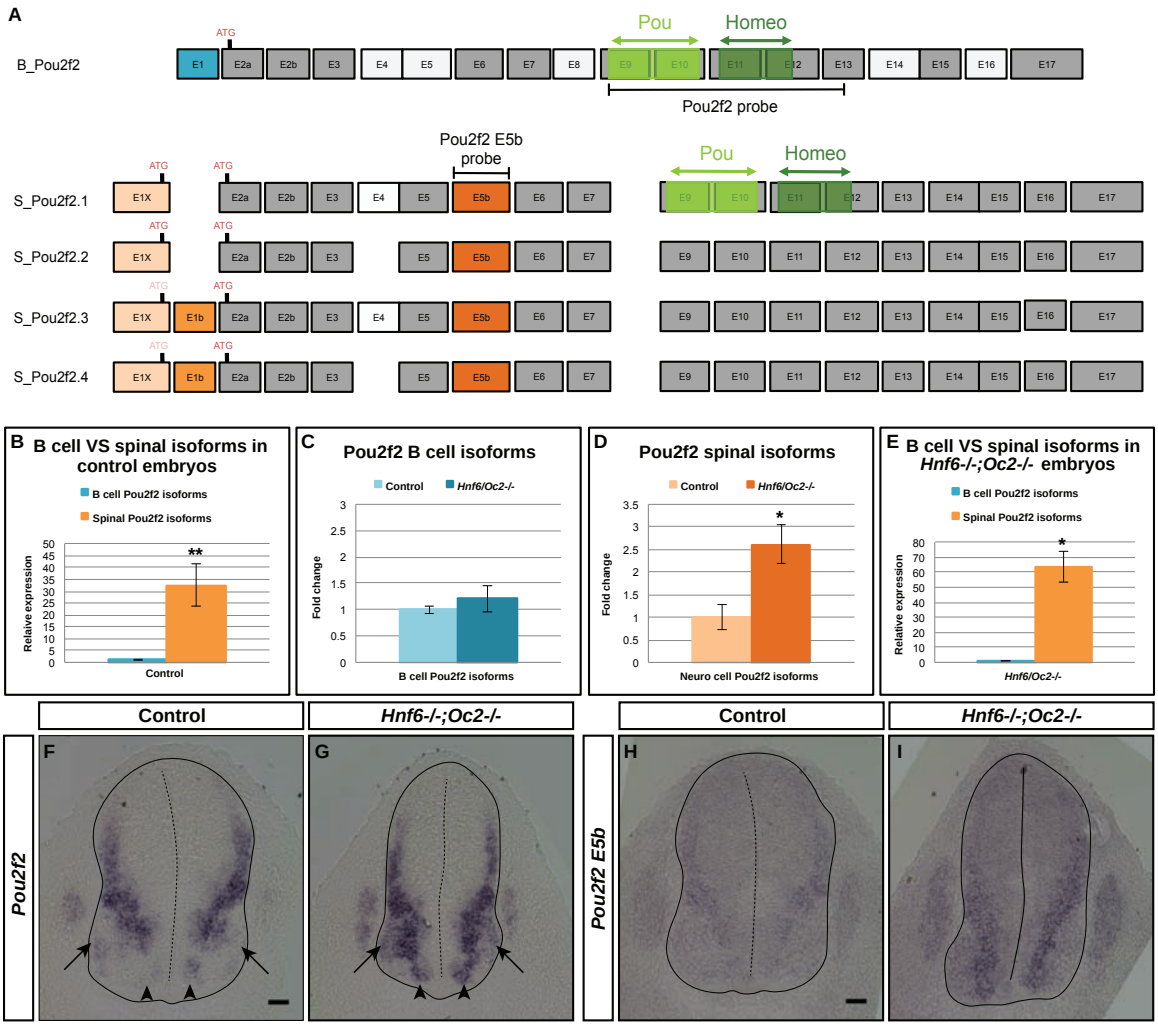

FIGURE 5 | Onecut factors control expression of spinal cord-specific isoforms of *Pou2f2*. **(A)** The different Pou2f2 isoforms present in the B cells (B_Pou2f2) are characterized by invariant exons (dark gray) and alternative exons 4, 5, 8, 14, or 16 (light gray). They contain a POU-specific domain (light green) encoded by exons 9 and 10 and a POU-type homeodomain (dark green) encoded by exons 11 and 12. The four spinal Pou2f2 isoforms (S_Pou2f2.1–S_Pou2f2.4) (identified in the spinal cord) are characterized by a distinct exon 1 (E1X in light orange), an additional exon E5b (dark orange) and alternative exons E1b and 4 (medium orange and light gray, respectively). The presence of E1b disrupts the reading frame and imposes the use of the ATG located in E2a, whereas the absence of E1b leaves open the use of the ATG located in E1X. The regions corresponding to the generic or to the E5b *in situ* hybridization probes are indicated. **(B–E)** Quantification of spinal Pou2f2 or B-cell isoforms by RT-qPCR. **(B)** In control spinal cords, spinal Pou2f2 isoforms are >30-fold more abundant than B-cell isoforms. **(C)** B cell Pou2f2 isoforms barely trend to increase in the absence of OC factors. **(D)** In contrast, spinal Pou2f2 isoforms are 2.6-fold overexpressed in *Hnf6*$^{-/-}$;*Oc2*$^{-/-}$ spinal cords. **(E)** In double mutant spinal cords, spinal Pou2f2 isoforms are >60-fold more abundant than B-cell isoforms. **(F–I)** *In situ* hybridization labelings on transverse sections (brachial level) of control or *Hnf6*$^{-/-}$;*Oc2*$^{-/-}$ spinal cords at e11.5 with **(F,G)** a generic *Pou2f2* probe complementary to spinal and to B-cell isoforms **(A)** or **(H,I)** a spinal isoform-specific probe corresponding only to exon E5b **(A)**. **(F,H)** In control embryos, *Pou2f2* is strongly expressed in ventral and in dorsal interneuron populations, and more weakly in the ventral motor neuron area. **(G,I)** In OC mutant embryos, *Pou2f2* is upregulated in interneuron populations and its expression is expanded in ventral populations (arrowheads) and in the motor neurons (arrows). *$p \leq 0.05$; **$p \leq 0.01$. Scale bars = 50 μm.

isoforms (**Figure 5B**), consistent with our RT-PCR observations (**Supplementary Figure S2**). In the absence of OC factors, spinal isoforms were ∼2.6-fold overexpressed whereas B-cell isoforms barely trended to increase (**Figures 5C–E**). Thus, OC factors repress expression of spinal *Pou2f2* isoforms in the developing spinal cord.

To confirm these data and to determine the expression pattern of *Pou2f2* in the ventral spinal cord, *in situ* hybridization was performed on sections from control or *Hnf6/Oc2* double-mutant spinal cords using either a generic *Pou2f2* probe complementary to spinal and to B-cell isoforms or a spinal isoform-specific probe corresponding only to exon E5b (**Figure 5A**). Using the generic *Pou2f2* probe on control tissue, we detected *Pou2f2* transcripts in the ventral region of the spinal cord, with lower expression levels in the location of the motor columns (arrows in **Figure 5F**). In OC mutant embryos, *Pou2f2* expression was globally increased and additionally expanded in the ventral area (arrowheads in **Figures 5F,G**) including the motor neuron territories (arrows in

TABLE 2 | Pou2f2 isoforms in the developing spinal cord are different from B-cell isoforms.

Amplification	Expected sizes	B cells	Control spinal cord
E1 → E6	272 bp 390 bp 456 bp	272 bp 390 bp 456 bp	No amplification[a]
E7 → E9	174 bp 222 bp	174 bp 222 bp	174 bp
E10 → E12	452 bp	452 bp	452 bp
E13 → E17	160 bp 296 bp 370 bp	160 bp 296 bp 370 bp	370 bp
E1 → E7	348bp 466 bp 532 bp	466 bp 532 bp	No amplification[a]
E2 → E7	284 bp 402 bp 468 bp	402 bp 468 bp	∼680 bp[a] ∼750 bp[a]
E3 → E6	154 bp 272 bp 378 bp	154 bp 272 bp 378 bp	272 bp[a] 378 bp[a] ∼550 bp[a] ∼650 bp[a]
E4 → E7	340 bp	340 bp	∼600 bp[a]
E5 → E7	201 bp	201 bp	201 bp[a] ∼480 bp[a]
E6 → E7	160 bp	160 bp	160 bp
E1X → E3	152 bp	No amplification[a]	152 bp[a] ∼220 bp[a]
E1X → E5b	554 bp 620 bp	N.D	554 bp 620 bp
E5b	234 bp	N.D	234 bp
E3 → E5b	429 bp 495 bp	N.D	429 bp 495 bp
E5b → E7	416 bp	N.D	416 bp

Regions covering B lymphocytes or predicted Pou2f2 isoforms (exons E1 or E1X to E17) were amplified by RT-PCR from lymphocyte or embryonic spinal cord RNA.
[a]*Unexpected results.*

Figures 5F,G). Similar observations were made with the spinal isoform-specific probe (**Figures 5H,I**). Thus, OC factors restrict and moderate *Pou2f2* expression in ventral spinal populations likely including V2 INs.

Pou2f2-Positive V2 INs Are Mislocated in the Absence of OC Factors

To assess whether increased *Pou2f2* expression in $Hnf6^{-/-};Oc2^{-/-}$ spinal cords corresponded to an expansion of Pou2f2 distribution in V2 INs or an upregulation in its endogenous expression territory, we first quantified the number and distribution of Pou2f2-containing Chx10+ cells at e12.5 and e14.5 (**Figure 6** and **Supplementary Figure S3**). Immunofluorescence experiments demonstrated that Pou2f2 is present in V2a INs in control embryos (**Figures 6A,C** and **Supplementary Figures S3A,D**), although it was only sparsely detected in MafA+ and cMaf+ V2a subsets (data not sown). Intensity of the labeling confirmed increased Pou2f2 production in the ventral regions of the spinal cord in OC mutant embryos (**Figures 6A–F**). However, the number in Pou2f2-positive V2a INs was not significantly different (**Figures 6E,F** and **Supplementary Figure S3**), suggesting that Pou2f2 is increased in its endogenous expression domain. In contrast, the distribution of Pou2f2-positive V2a INs was affected (**Figures 6A–D,G–DD**). At e12.5, cells in the central clusters were slightly reduced at brachial and at thoracic levels (**Figures 6G–R**). In contrast, at e14.5, a majority of V2a containing Pou2f2 settled in a medial position (**Figures 6S–DD**), reminiscent of the distribution defects observed for the whole V2a population (**Figure 3**). Similarly, Pou2f2 was detected in V2b INs in control embryos, although in a more restricted number of cells (**Figures 7A,B,E**). In the absence of OC factors, the number of Pou2f2-positive V2b cells was not significantly increased (**Figures 7C,D,F**) but, as observed for V2a, this subset of V2b INs was mislocated with cells more central at e12.5 and more clustered on the medio-lateral axis at e14.5 (**Figures 7G–DD**). Taken together, these observations suggest that Pou2f2 may contribute to control V2 IN migration during spinal cord development and could participate in alterations of V2 distribution in the absence of OC factors.

Pou2f2 Regulates the Distribution of Spinal V2 INs

To determine whether Pou2f2 is able to modulate V2 IN distribution, we mimicked increased expression of this transcription factor observed in OC mutant embryos by overexpressing *Pou2f2* in the chicken embryonic spinal cord (**Supplementary Figure S4**). Increased Pou2f2 did not impact on the number of V2a or V2b (**Figures 8A–F**). In contrast, it did alter V2 IN location. In HH27-28 control spinal cord, V2a INs were distributed in two closely connected clusters on the medio-lateral axis of the neuroepithelium (**Figure 8G**). In electroporated spinal cord, lateral migration was increased and a majority of V2a INs were clustered in a single group in a central position (**Figures 8H–J**) with ectopic lateral extensions (arrow in **Figure 8H**). In control spinal cord, V2b were distributed in two groups along the medio-lateral axis with a majority of cells in the lateral cluster (**Figure 8K**). In electroporated spinal cord, the V2b INs were equally distributed between these two clusters (**Figures 8L–N**). Thus, consistent with our observation in OC mutant embryos, increased Pou2f2 can modulate the distribution of V2 INs in the developing spinal cord.

To confirm the influence of Pou2f2 on V2 migration, we studied V2 distribution in mouse embryos devoid of Pou2f2 (Corcoran et al., 1993) at e12.5. Absence of Pou2f2 did not impact on the number of V2a INs (**Figures 9A–C**) nor on the Shox2+, cMaf+, or MafA+ V2a subsets (**Supplementary Figure S5**). In contrast, V2a distribution was affected in *Pou2f2* mutants. As compared to the two V2a clusters observed in control embryos, Chx10+ cells were more scattered in *Pou2f2* mutant embryos (**Figures 9D–O**). Furthermore, although the number of V2b, V2c, or MafA+ V2b cells was not changed in the absence of Pou2f2 (**Figures 10A–C** and **Supplementary Figure S6**), V2b cells remained more medial at brachial and thoracic levels and segregated more extensively on the medio-lateral axis at lumbar

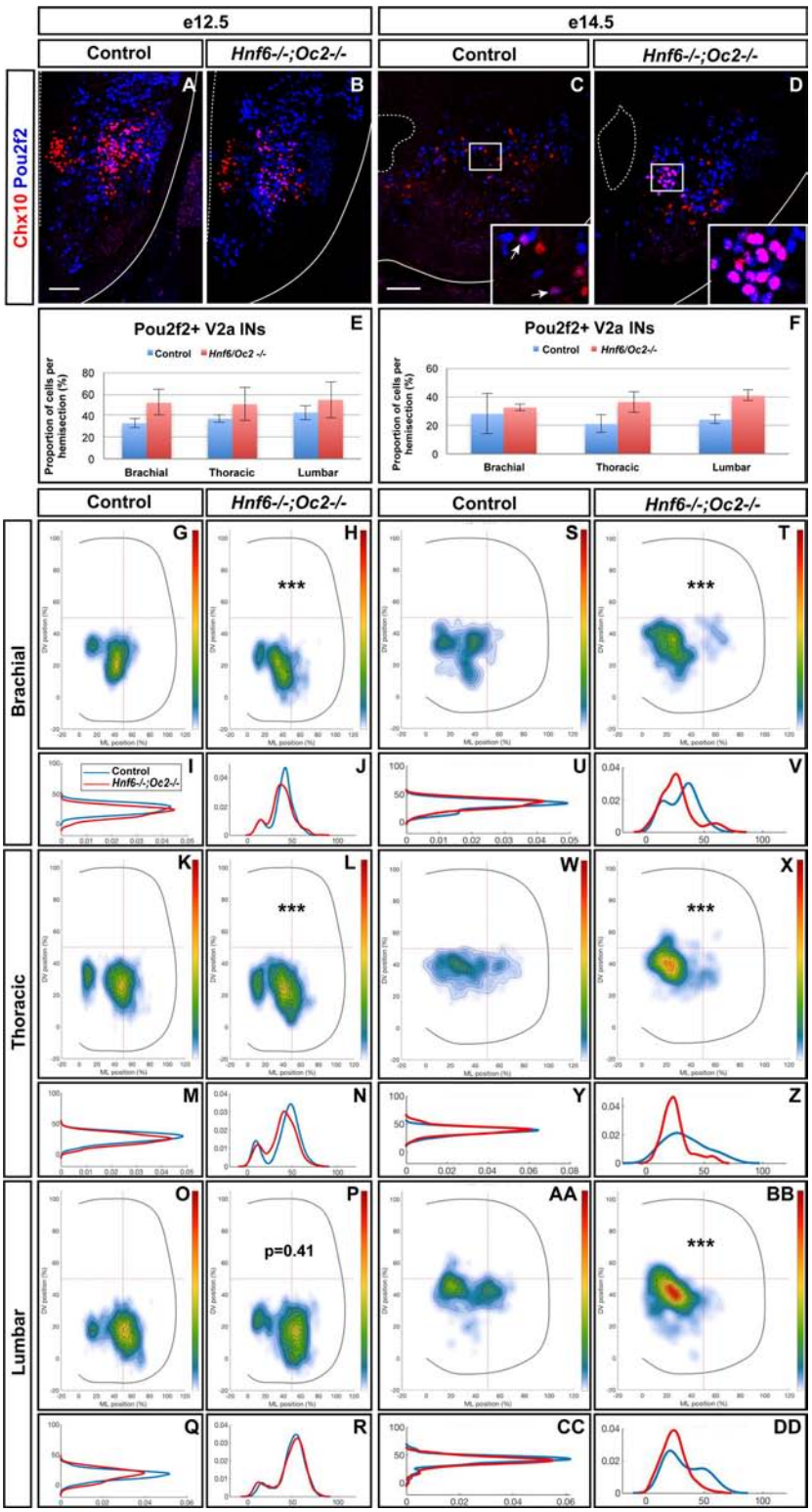

FIGURE 6 | The Pou2f2+ V2a interneurons are mislocated in the absence of OC factors. **(A–F)** Immunolabelings and quantification of Pou2f2+ V2a interneurons in control or *Hnf6*$^{-/-}$;*Oc2*$^{-/-}$ mutant embryos. At e12.5 **(A,B)** and e14.5 **(C,D)**, Pou2f2 is detected in V2a Chx10^{+} interneurons, and the number of Pou2f2-containing Chx10+ cells trends to increase but is not significantly different in the absence of OC factors **(E,F)**. **(G–DD)** Distribution of Pou2f2+ V2a interneurons on the transverse plane of the spinal cord in control or *Hnf6*$^{-/-}$;*Oc2*$^{-/-}$ double-mutant embryos. One-dimension graphs (lower) show density distribution on the dorso-ventral (left) or the medio-lateral (right) axis of the spinal cord. **(G–R)** At e12.5, cells in the central clusters are slightly reduced at brachial and at thoracic levels in the absence of OC factors ($n = 3$, $p \leq 0.001$ at brachial and thoracic levels; $p = 0.41$ at lumbar level). **(S–DD)** At e14.5, a vast majority of V2a containing Pou2f2 settles in a more medial position in *Hnf6*$^{-/-}$;*Oc2*$^{-/-}$ spinal cords ($n = 3$, $p \leq 0.001$). Mean values ± SEM. Scale bar = 50 μm.

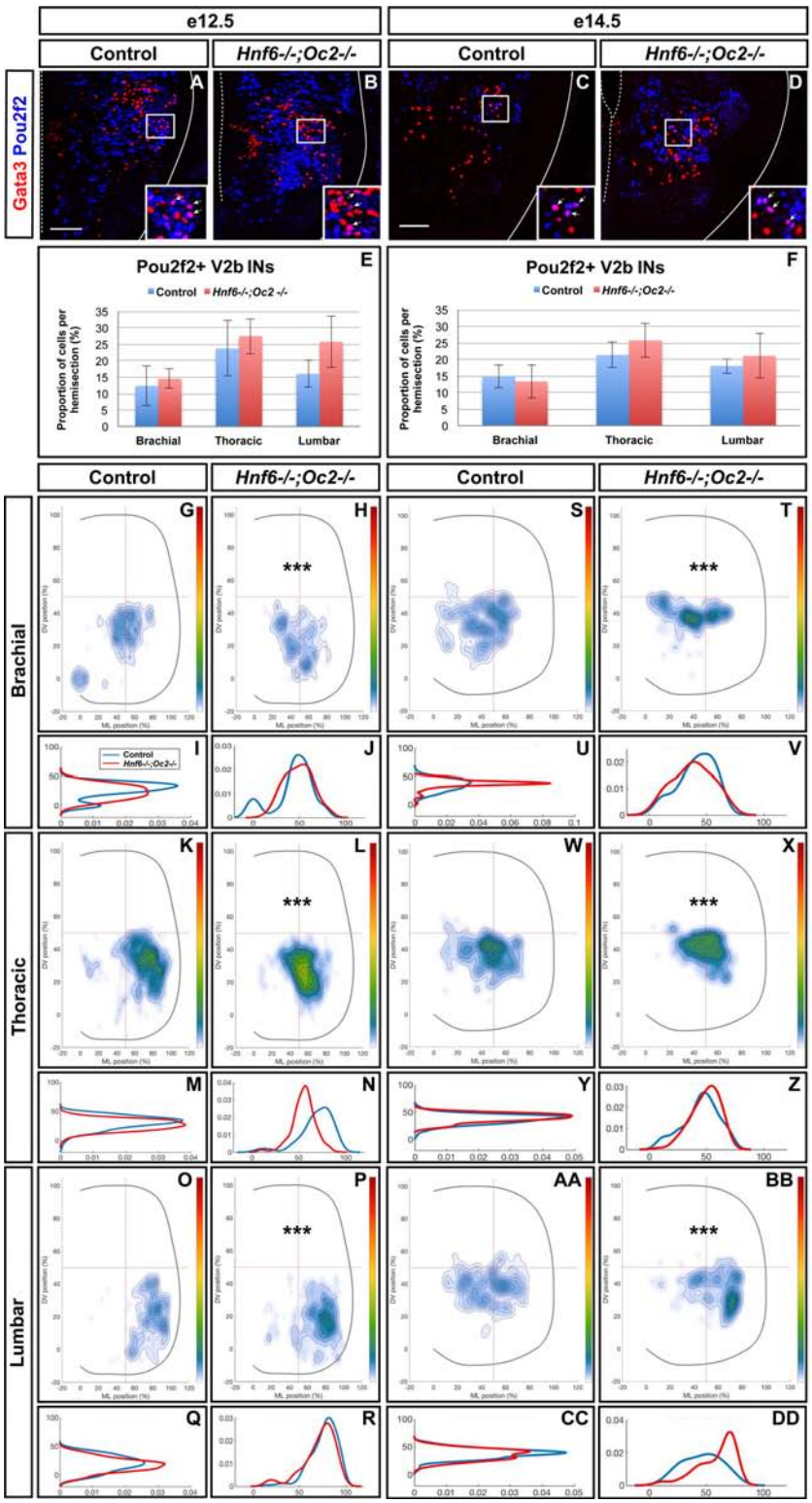

FIGURE 7 | The Pou2f2+ V2b interneurons are mislocated in the absence of OC factors. **(A–F)** Immunolabelings and quantification of Pou2f2+ V2b interneurons in control or *Hnf6*$^{-/-}$;*Oc2*$^{-/-}$ mutant embryos. At e12.5 **(A,B)** and e14.5 **(C,D)**, Pou2f2 is present in V2b Gata3+ interneurons, but the number of Pou2f2+ V2b cells was not significantly increased in the absence of OC factors **(E,F)**. **(G–DD)** Distribution of Pou2f2+ V2b interneurons on the transverse plane of the spinal cord in control or *Hnf6*$^{-/-}$;*Oc2*$^{-/-}$ double-mutant embryos. One-dimension graphs (lower) show density distribution on the dorso-ventral (left) or the medio-lateral (right) axis of the spinal cord. **(G–R)** At e12.5, Pou2f2-containing V2b are more central and slightly more ventral in the absence of OC factors ($n = 3$, $p \leq 0.001$). **(S–DD)** At e14.5, this subset of V2b interneurons is more clustered on the medio-lateral axis in *Hnf6*$^{-/-}$;*Oc2*$^{-/-}$ spinal cords ($n = 3$, $p \leq 0.001$). Mean values ± SEM. Scale bar = 50 μm.

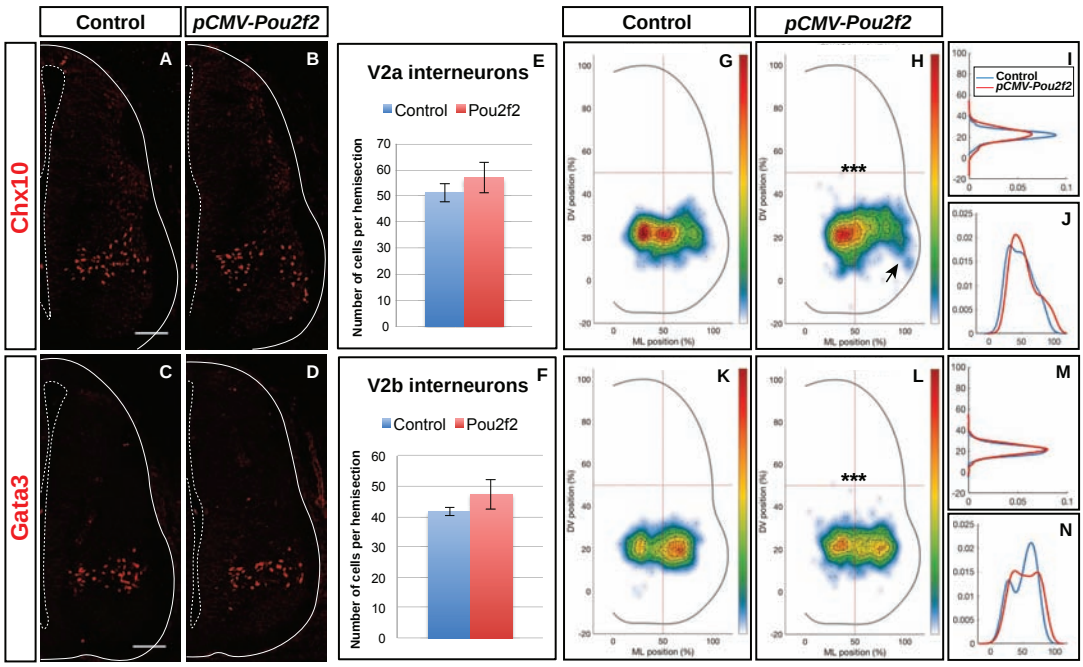

FIGURE 8 | V2 interneuron distribution is altered after misexpression of *Pou2f2*. Overexpression of *Pou2f2* in chick embryonic spinal cord after electroporation at HH14-16 and immunolabelings 72 h after electroporation. **(A–F)** At HH27-28, *Pou2f2* overexpression does not impact the number of V2a **(E)** or V2b **(F)** interneurons. In contrast, it alters V2 distribution. **(G–J)** In control spinal cord, V2a interneurons are distributed in two closely connected clusters on the medio-lateral axis of the neuroepithelium. In electroporated spinal cord, lateral migration is increased and a majority of V2a interneurons are clustered in a single central group with ectopic lateral extensions (arrows; $n = 3$, $p \leq 0.001$). **(K–N)** In control spinal cord, V2b are distributed in two groups along the medio-lateral axis with a majority of cells in the lateral cluster. In electroporated spinal cord, the V2b interneurons are equally distributed between these two clusters ($n = 3$, $p \leq 0.001$). Mean values ± SEM. Scale bar = 50 μm.

levels (**Figures 10D–O**). Taken together, these observations demonstrate that Pou2f2 regulate the distribution of V2 INs during spinal cord development.

DISCUSSION

In the recent years, several studies demonstrated that proper distribution of neuronal populations and subpopulations in the developing spinal cord is critical for adequate formation of spinal circuits (Surmeli et al., 2011; Tripodi et al., 2011; Goetz et al., 2015; Bikoff et al., 2016; Hilde et al., 2016; Hayashi et al., 2018). However, the genetic programs that control the diversification of spinal neuronal populations into specialized subpopulations and the proper settling of these neuronal subsets in the spinal parenchyma remain elusive. Here, we provide evidence that OC transcription factors regulate the diversification of spinal V2 INs, and that a genetic cascade involving OC factors and their downstream target Pou2f2 controls the distribution of V2 INs in the developing spinal cord.

Control of V2 IN Diversification by the OC Factors

Cardinal populations of spinal ventral INs have been well characterized, and their global contribution to the activity of motor circuits has been extensively studied (reviewed in (Gosgnach et al., 2017; Ziskind-Conhaim and Hochman, 2017; Boije and Kullander, 2018). However, more recently, the idea emerged that these cardinal populations are not homogeneous ensembles but rather contain multiple neuronal subsets with distinct molecular identities and functional properties (Borowska et al., 2013; Francius et al., 2013; Talpalar et al., 2013; Borowska et al., 2015; Bikoff et al., 2016; Sweeney et al., 2018). V2a INs comprise two major divisions, namely type I and type II V2a cells, that are arrayed in counter-gradients along the antero-posterior axis of the spinal cord and activate different patterns of motor output at brachial or lumbar levels. Furthermore, these two large divisions can themselves be fractionated at birth into 11 subsets characterized by distinct combinations of markers, differential segmental localization and specific distribution patterns on the medio-lateral axis of the spinal cord (Hayashi et al., 2018). In the zebrafish, three distinct subclasses of V2a INs participate in separate microcircuit modules driving slow, intermediate or fast motor neuron activity (Ampatzis et al., 2014). Taken together, these observations suggest that cardinal IN populations only constitute the first organization level of functionally distinct neuronal subsets that contribute to diversity and flexibility within spinal motor circuits.

We showed here that OC factors are present in subsets of V2 INs and contribute to their diversification. Normal numbers of cardinal V2a and V2b cells were generated in OC mutant embryos, suggesting that these factors do not contribute to the

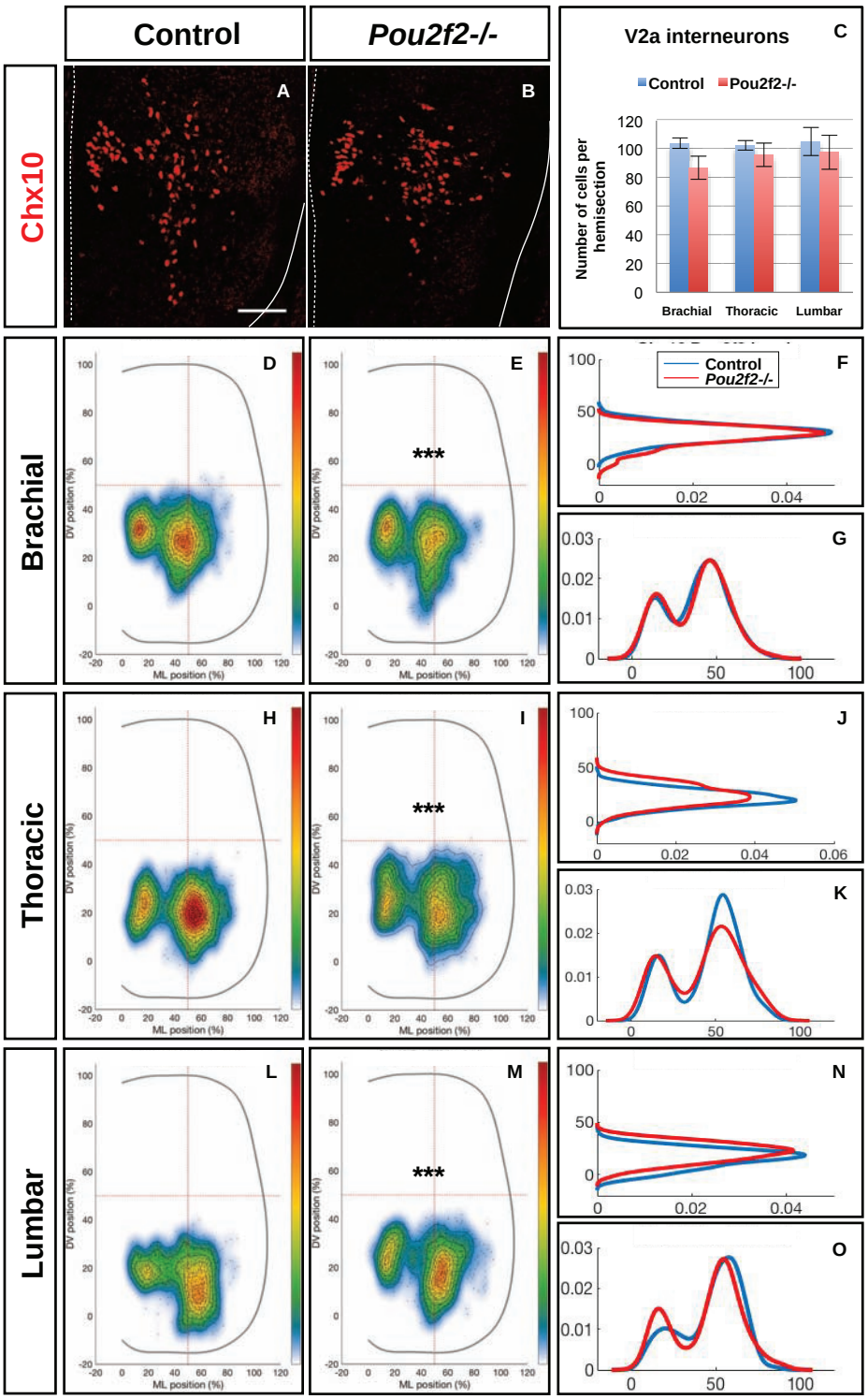

FIGURE 9 | Pou2f2 regulate the distribution of V2a interneurons. **(A–C)** Immunolabelings and quantification of V2a interneurons in control or *Pou2f2*$^{-/-}$ mutant embryos. At e12.5, the production of the Chx10+ V2a interneurons is not altered in absence of Pou2f2. **(D–O)** Distribution of V2a and Shox2+ V2a interneurons on the transverse plane of the spinal cord in control or *Pou2f2*$^{-/-}$ mutant embryos. One-dimension graphs (right) show density distribution on the dorso-ventral (upper) or the medio-lateral (lower) axis of the spinal cord. V2a distribution is affected in *Pou2f2*$^{-/-}$ mutants. As compared to the two V2a clusters observed in control embryos, Chx10+ cells are relatively more abundant in the medial cluster in *Pou2f2*$^{-/-}$ mutant embryos ($n = 3$, $p \leq 0.001$). Mean values ± SEM. Scale bar = 50 μm.

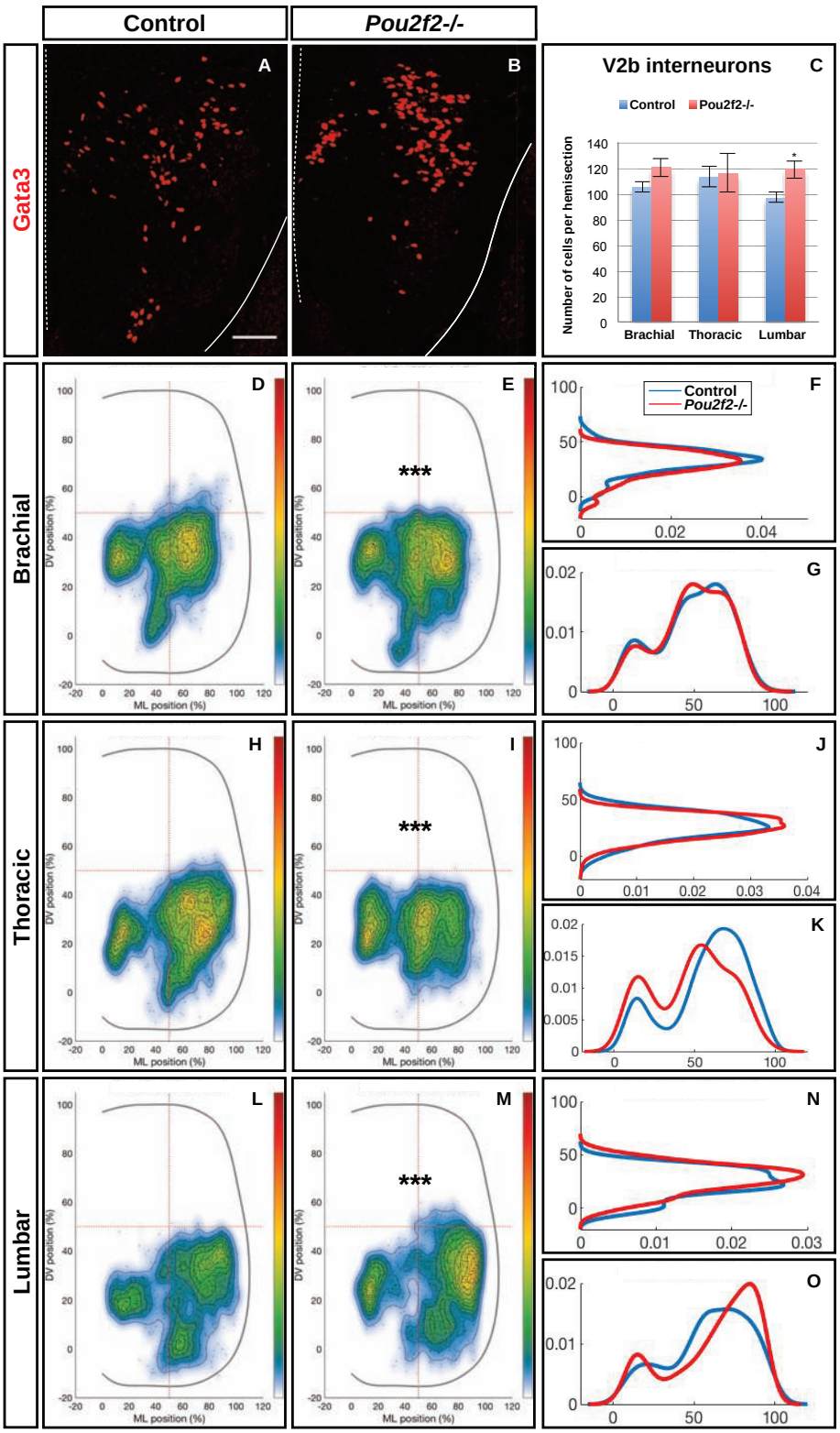

FIGURE 10 | Pou2f2 regulate the distribution of V2b interneurons. **(A–C)** Immunolabelings and quantification of V2b interneurons in control or *Pou2f2*$^{-/-}$ mutant embryos. At e12.5, the production of the Gata3+ V2b interneurons is not affected by the absence of Pou2f2. **(D–O)** Distribution of V2b interneurons on the transverse plane of the spinal cord in control or *Pou2f2*$^{-/-}$ mutant embryos. One-dimension graphs (right) show density distribution on the dorso-ventral (upper) or the medio-lateral (lower) axis of the spinal cord. The distribution of V2b cells is altered in *Pou2f2*$^{-/-}$ mutants, as V2b interneurons remained more medial at thoracic level and segregated more extensively on the medio-lateral axis at lumbar level ($n = 3$, $p \leq 0.001$). Mean values ± SEM. Scale bar = 50 μm.

production of V2 cells (Thaler et al., 2002; Lee et al., 2008; Clovis et al., 2016) nor to the segregation of the V2a and V2b lineages through differential activation of Notch signaling (Del Barrio et al., 2007; Peng et al., 2007; Joshi et al., 2009; Misra et al., 2014). In contrast, V2a subpopulations characterized by the presence of MafA or cMaf were strongly depleted in the absence of OC proteins. This observation results either from a loss of these V2a subsets or from a downregulation of *MafA* or *cMaf* expression in these cells. Incomplete knowledge of the whole collection of V2a subsets prevented to assess whether this apparent loss of specific subpopulations was compensated for by an expansion of neighboring subsets. Nevertheless, these data demonstrate altered differentiation of V2 IN subsets in the absence of OC factors, as previously observed for spinal motor neurons (Roy et al., 2012) and dorsal INs (Kabayiza et al., 2017). In addition, the production of V2c cells was delayed in OC mutant embryos, although V2b that are supposed to constitute the source of V2c (Panayi et al., 2010) were timely generated. This points to a specific contribution of OC protein to the development of V2c INs, the mechanism of which is currently unknown.

Control of V2 IN Distribution by the OC Factors

Beside diversification, the characterization of functionally distinct IN subpopulations unveiled a strong correlation between the distribution of each IN subset and their contribution to distinct microcircuit modules (Tripodi et al., 2011; Borowska et al., 2013; Goetz et al., 2015; Bikoff et al., 2016; Hilde et al., 2016; Hayashi et al., 2018). These data support a model wherein correct localization of spinal IN subsets is critical for proper formation of sensory and sensory-motor circuits, highlighting the importance of a strict regulation of short-distance neuronal migration in the developing spinal cord. However, genetic determinants that control spinal IN migration have only been sparsely identified. Sim1 regulate ventro-dorsal migration of the V3 IN subsets (Blacklaws et al., 2015). Similarly, SATB2 control the position of inhibitory sensory relay INs along the medio-lateral axis of the spinal cord (Hilde et al., 2016). Here, we provide evidence that the OC factors control a genetic program that regulates proper positioning of V2 INs during embryonic development. In the absence of OC proteins, a fraction of V2a INs remained in a more medial location, expanding the medial cluster containing locally projecting cells at the expanse of the lateral cluster that comprises the supraspinal-projecting V2a INs (Hayashi et al., 2018). V2b alterations were less spectacular, although ventral and dorsal contingents were reduced and the cell distribution in the central cluster was altered. Variability in the alterations observed at e12.5 and e14.5 highlights that spinal migration is not completed at e12.5 and suggests that distribution of earlier- or later-migrating neurons may be differently affected by the absence of OC proteins. In addition, migration along the anteroposterior axis, which can not be analyzed in our experimental setup, could also be perturbed. Alterations of the distribution of V2a and V2b interneurons likely correlate with alterations in their differentiation program. Indeed, the production of adequate clues to ensure proper cell positioning is an intrinsic component of any neuronal differentiation program (Blacklaws et al., 2015; Hilde et al., 2016; Hayashi et al., 2018). In any case, our observations are consistent with the contribution of OC factors to the migration of several populations of spinal dorsal INs (Kabayiza et al., 2017). This raises the question whether similar cues might be regulated by identical genetic programs and used by different IN populations to organize proper distribution of ventral and dorsal IN subsets in the developing spinal cord. Identification of the factors downstream of OC protein involved in the control of neuronal migration will be necessary to answer this question.

An OC-Pou2f2 Genetic Cascade Regulates the Migration of V2 INs

Therefore, we attempted to identify genes downstream of OC factors and possibly involved in the control of IN migration using a global approach comparing the transcriptome of whole spinal cords isolated from control or OC-deficient embryos. Absence of known regulators of neuronal migration among the most affected genes suggests that different actors may be active downstream of OC proteins in distinct IN populations to regulate proper neuronal distribution. In contrast, we uncovered that expression of the transcription factor *Pou2f2* is repressed by OC factors in different spinal populations. Surprisingly, our data demonstrated that variant *Pou2f2* isoforms are produced in the developing spinal cord as compared to B lymphocytes (Hatzopoulos et al., 1990; Wirth et al., 1991; Lillycrop and Latchman, 1992; Stoykova et al., 1992; Liu et al., 1995), and that these spinal variants are regulated by OC proteins. Spinal-enriched transcripts encode Pou2f2 proteins containing additional peptidic sequences upstream of the POU-specific domain and of the homeodomain. Furthermore, exon 1 is different and corresponds to sequences located ∼47kb upstream of the transcription initiation site used in B cells (data not shown) in the mouse genome, suggesting that OC regulate *Pou2f2* expression from an alternative promoter. However, we cannot exclude that additional exon(s) could be present upstream of the identified sequences, and determination of the regulating sequences targeted by the OC protein will require thorough characterization of the produced transcripts. In addition, we cannot rule out indirect regulation of *Pou2f2* expression by the OC factors, as OC are usually considered to be transcriptional activators rather than repressors (Jacquemin et al., 2000; Lannoy et al., 2000; Jacquemin et al., 2003a; Pierreux et al., 2004; Beaudry et al., 2006; Roy et al., 2012).

Nevertheless, our observations demonstrate that Pou2f2 is downstream of OC factors in the V2 INs and also contributes to regulate the distribution of V2 INs during embryonic development. The number of Pou2f2-containing V2 was not significantly increased in OC mutant spinal cords, suggesting that the absence of OC protein resulted in relaxing of Pou2f2 production in its endogenous expression domain rather that ectopic activation in other V2 subsets. Increased production of Pou2f2 in the chicken embryonic

spinal cord resulted in alterations in the localization of V2 populations without any change in cell number, pointing to a possible contribution of Pou2f2 to the regulation of V2 migration downstream of OC factors. However, spinal cord electroporation experiments are constrained by the developmental stage selected to target ventral INs and by the duration of the incubation to maintain viable embryos, which does not enable to compare IN migration in mouse and chicken at later developmental stages. These also limited chicken loss-of-function studies, which would additionally be hampered by incomplete inhibition of gene expression. Nevertheless, our observations suggested that Pou2f2 may regulate V2 IN migration.

Consistently, V2 distribution was perturbed in *Pou2f2* mutant embryos without any alteration in V2 population or subpopulation cell numbers, demonstrating the involvement of Pou2f2 in the control of V2 IN distribution. Alterations in V2 distribution after *Pou2f2* electroporation were not comparable to that observed in OC mutant embryos and were not strictly opposite to *Pou2f2* knockout phenotype because the developmental stages obtained after chicken embryo electroporation were much earlier than the developmental stages of analyzed mouse embryos. Nevertheless, our data demonstrate that a genetic cascade comprising OC and Pou2f2 transcription factors ensures proper distribution of V2 cells during spinal cord development. This program may not be restricted to V2 cells, as diversification and distribution of dorsal INs and of motor neurons are also altered in the absence of OC factors (Roy et al., 2012; Kabayiza et al., 2017) and as *Pou2f2* expression in the OC mutant spinal cord is increased in multiple neuronal populations.

MATERIALS AND METHODS

Ethics Statement and Mouse Lines

All experiments were strictly performed in accordance with the European Community Council directive of November 24, 1986 (86-609/ECC) and the decree of October 20,1987 (87-848/EEC). Mice were raised in our animal facilities and treated according to the principles of laboratory animal care, and experiments and mouse housing were approved by the Animal Welfare Committee of Université catholique de Louvain (Permit Number: 2013/UCL/MD/11 and 2017/UCL/MD/008). The day of vaginal plug was considered to be embryonic day (e) 0.5. A minimum of three embryos of the same genotype was analyzed in each experiment. The embryos were collected at e12.5 and e14.5. The *Hnf6;Oc2* and the *Pou2f2* mutant mice were previously described (Corcoran et al., 1993; Jacquemin et al., 2000; Clotman et al., 2005). In the $Hnf6^{-/-}Oc2^{-/-}$ embryos, expression of *Oc3* is completely downregulated in the developing spinal cord (Roy et al., 2012; Kabayiza et al., 2017), enabling to study spinal cord development in the absence of the three OC factors. The mice and the embryos were genotyped by PCR (primer information available on request).

In situ Hybridization (ISH) and Immunofluorescence Labelings

For ISH, the collected embryos were fixed in ice-cold 4% paraformaldehyde (PFA) in phosphate buffered-saline (PBS) overnight at 4°C, washed thrice in PBS for 10 min, incubated in PBS/30% sucrose solution overnight at 4°C, embedded and frozen in PBS/15% sucrose/7.5% gelatin. Fourteen µm section were prepared and ISH was performed as previously described (Beguin et al., 2013; Pelosi et al., 2014; Francius et al., 2016) with DIG-conjugated Pou2f2 (NM_011138.1, nucleotides 604-1187) or Pou2f2 exon 5b (XM_006539651.3, nucleotides 643-876) antisense RNA probes. Control and Onecut mutant sections were placed adjacent on the same histology slides to minimize inter-slide variations in ISH signals.

For immunofluorescence, collected embryos were fixed in 4% PFA/PBS for 25 or 35 min according to their embryonic stage and processed as for ISH. Immunolabeling was performed on 14 µm serial cryosections as previously described (Francius and Clotman, 2010). Primary antibodies against the following proteins were used: Chx10 (sheep; 1:500; Exalpha Biologicals #X1179P), Foxp1 (goat; 1:1000; R&D Systems #AF4534), Gata3 (rat; 1:50; Absea Biotechnology #111214D02), GFP (chick; 1:1000; Aves Lab #GFP-1020), HNF6 (guinea pig; 1:2000; (Espana and Clotman, 2012b); or rabbit; 1:100; Santa Cruz #sc-13050; or sheep; 1:1000 R&D Systems #AF6277), cMaf (rabbit; 1:3000; kindly provided by H. Wende), MafA (guinea pig; 1:500; kindly provide by T. Müller), OC2 (rat; 1:400; (Clotman et al., 2005); or sheep; 1:500; R&D Systems #AF6294), OC3 [guinea pig; 1:6000; (Pierreux et al., 2004)], Pou2f2 (rabbit; 1:2000; Abcam #ab178679), Shox2 (mouse; 1:500; Abcam #ab55740), Sox1 (goat; 1:500; Santa Cruz #sc-17318). Secondary antibodies donkey anti-guinea pig/AlexaFluor 488, 594 or 647, anti-mouse/AlexaFluor 488, 594, or 647, anti-rabbit/AlexaFluor 594 or 647, anti-goat/AlexaFluor 488, anti-rat/AlexaFluor 647, anti-sheep/AlexaFluor 594 or 647, and goat anti-mouse IgG2A specific/AlexiaFluor 488, purchased from ThermoFisher Scientific or Jackson Laboratories were used at dilution 1:2000 or 1:1000, respectively.

In ovo Electroporation

In ovo electroporations were performed at stage HH14-16, as previously described (Roy et al., 2012). The coding sequence of the S_Pou2f2.4 transcript was amplified by overlapping-PCR using: forward 5′ GCTCTGTCTGCCCAAGAGAAA 3′ and reverse 5′ GTTGGGACAAGGTGAGCTGT 3′ primers for the 5′ sequence, forward 5′ CCACCATCACAGCCTACCAG 3′ and reverse 5′ ATTATCTCGAGCCAGCCTCCTTACCCTCTCT 3′ (designed to enable integration at the *Xho*I restriction site of the pCMV-MCS vector) primers for the 3′ sequence. This sequence was first subcloned in a pCR®II-Topo® vector (Life Technologies, 45-0640) for sequencing then subcloned at the *Eco*RI (from the pCR®II-Topo® vector) and *Xho*I restriction sites of a pCMV-MCS vector for the *in ovo* electroporation. The pCMV-Pou2f2 (0.5 µg/ml) vector was co-electroporated with a pCMV-eGFP plasmid (0.25 µg/ml) to visualize electroporated cells. The embryos were collected 72 h

(HH27-28) after electroporation, fixed in PBS/4%PFA for 45 min and processed for immunofluorescence labelings as previously described (Francius and Clotman, 2010). The thoracic region of the electroporated spinal cord was used for analyzes. To minimize stage and experimental condition variations, the non-electroporated side of the spinal cord was used as control for quantification and distribution analyses.

Imaging and Quantitative Analyses

Immunofluorescence and ISH images of cryosections were acquired on an EVOS FL Auto Imaging System (Thermo Fisher Scientific) or a Confocal laser Scanning biological microscope FV1000 Fluoview with the FV10-ASW 01.02 software (Olympus). The images were processed with Adobe Photoshop CS5 software to match brightness and contrast with the observation. Quantifications were performed by subtractive method (Francius and Clotman, 2010). For each embryo ($n \geq 3$), one side of three to five sections at brachial, thoracic, or lumbar level were quantified using the count analysis tool of Adobe Photoshop CS5 software. Raw data were exported from Adobe Photoshop CS5 software to Sigma Plotv12.3 software to perform statistical analyses. The histograms were drawn with Microsoft Excel. Adequate statistical tests (standard Student's *t*-tests or Mann-Whitney *U* tests) were applied depending on the number of comparisons and on the variance in each group. Quantitative analyses were considered significant at $p \leq 0.05$.

Quantitative analyzes of IN spatial distribution were performed as previously described (Kabayiza et al., 2017). Statistical analyses of ventral IN distribution were performed using a two-sample Hotelling's T2, which is a two-dimensional generalization of the Student's *t*-test. The analysis was implemented using the NCSS software package.

Microarray Analyses

RNA was extracted from control or *Hnf6/Oc2* double-mutant spinal cords. The tissue was manually dissociated in Tripur isolation reagent (Roche, 11 667 165 001). After dissociation, chloroform (Merck Millipore, 1 02445 1000) was added to the sample, incubated at room temperature for 10 min and centrifugated for 10 min at 4°C. The aqueous phase was collected and the RNA was precipitated with isopropanol (VWR, 20880.310) and centrifugated for 15 min at 4°C. The pellet was washed in ethanol (Biosolve, 06250502) and centrifugated for 10 min at 4°C. The dried pellet was resuspended in RNAse free water. The integrity of the RNA was assessed using an Agilent RNA 6000 Nano assay procedure. For microarray analyzes, the RNA was converted in single-strand cDNA, labeled using the GeneChip® WT PLUS Reagent Kit (Affymetrix) and hybridized on the GeneChip® MoGene 2.0 ST array (Affymetrix, 90 2118) using Affymetrix devices: Genechip® Fluidics Station 450, Genechip® Hybridization oven 640, Affymetrix Genechip® scanner and the Expression Consol software. The analyzes were performed using the R software. Microarray data have been deposited in the GEO repository (accession number: GSE117871).

Amplification of *Pou2f2* Isoforms and Sequencing

Fragments of the different *Pou2f2* isoforms were amplified by RT-PCR from RNA of control B lymphocytes or embryonic spinal cords purified as described above using the iScript™ Reverse transcriptase and the 5x iScript™ reaction mix (BioRad). *Pou2f2* sequences (**Table 2**) were amplified using a GoTaq® Green master mix (Promega, M712) or a Q5® Hot Start High-Fidelity DNA Polymerase (New England BioLabs® Inc., M0493S) (primer information available on request). Sequencing of the spinal *Pou2f2* exons was outsourced to Genewiz.

Quantitative real-time PCR was performed on 1/100 of the retrotranscription reaction using iTaq™ universal SYBR® Green Supermix (BioRad, 172-5124) on a CFX Connect™ Real-Time System (BioRad) with the BioRad CFX Manage 3.1 software. Each reaction was performed in duplicate and relative mRNA quantities were normalized to the housekeeping gene RPL32 (primer information available on request). Relative expression changes between conditions were calculated using the $\Delta\Delta$Ct method. All changes are shown as fold changes.

AUTHOR CONTRIBUTIONS

AH, GM, CF, and FC designed the experiments. BJ generated Matlab routines for the distribution analyses of dorsal interneurons. LC provided Pou2f2+/− sperm to generate the Pou2f2 mutant mouse line. AH, GM, AC, MT, MH-F, and CF performed the experiments. All the authors discussed the data. AH and FC drafted the manuscript.

FUNDING

Work in the FC laboratory was supported by grants from the "Fonds spéciaux de recherche" (FSR) of the Université catholique de Louvain, by a "Projet de recherche (PDR)" #T.0117.13 and an "Equipement (EQP)" funding #U.N027.14 of the Fonds de la Recherche Scientifique (F.R.S.-FNRS, Belgium), by the "Actions de Recherche Concertées (ARC)" #10/15-026 and #17/22-079 of the "Direction générale de l'Enseignement non obligatoire et de la Recherche scientifique – Direction de la Recherche scientifique – Communauté française de Belgique" and granted by the "Académie Universitaire 'Louvain' and by the Association Belge contre les Maladies Neuro-Musculaires. LC acknowledges funding from the Australian Government (NHMRC IRIIS and research grants #637306 and #575500) and Victorian State Government Operational Infrastructure Support. AH and GM hold Ph.D. grants from the Fonds pour la Recherche dans l'Industrie et l'Agriculture (F.R.S.-FNRS, Belgium). MH-F was a Postdoctoral Researcher of the F.R.S.-FNRS. FC is a Senior Research Associate of the F.R.S.-FNRS.

ACKNOWLEDGMENTS

We thank members of the NEDI lab for material, technical support, and discussions. We are grateful to Drs. T. Müller and

H. Wende for kindly providing the guinea pig anti MafA and the rabbit anti cMaf antibodies, respectively, to Drs. F. Lemaigre and P. Jacquemin for the Hnf6/Oc2 double mutant mice, to Dr. C. Pierreux for the pCMV-MCS, to Dr. J. Ambroise for assistance with the microarray analyses, and to Dr. L. Dumoutier for cDNA of B lymphocytes. This manuscript has been released as a Pre-Print at BioRxiv (Harris et al., 2018).

SUPPLEMENTARY MATERIAL

The Supplementary Material for this article can be found online at: https://www.frontiersin.org/articles/10.3389/fncel.2019.00184/full#supplementary-material

FIGURE S1 | Onecut factors regulate the diversification of the V2 interneurons. **(A–H")** Immunolabelings of the V2a generic marker Chx10 and markers of V2a subpopulations on transverse spinal cord sections (brachial or thoracic levels) control or *Hnf6*$^{-/-}$*;Oc2*$^{-/-}$ mutant embryos at e14.5. Quantifications are shown in **Figure 1**. V2a **(A,B)**, Shox2+ V2a (arrows) and V2d interneurons (**C–D"**, arrowheads) are present in both control and double mutant embryos. **(E–E")** MafA is present in a V2a supbopulation in control embryos (arrows), **(F–F")** but is not detected in Chx10+ cells in the absence of OC factors. **(G–G")** Similarly, cMaf is present in a subpopulation of V2a interneurons in control embryos (arrows), **(H–H")** which is not the case in *Hnf6*$^{-/-}$*;Oc2*$^{-/-}$ embryos. **(I–L")** Immunolabelings of the V2b generic marker Gata3 and the marker of V2b subpopulation, MafA. V2b **(I–J")** and MafA+ V2b (**K–L"**, arrows) interneurons are present in control and in *Hnf6*$^{-/-}$*;Oc2*$^{-/-}$ embryos. **(M,N)** The number of V2c interneurons is unchanged is similarly detected in *Hnf6*$^{-/-}$*;Oc2*$^{-/-}$ embryos as compared to control embryos (delineated cells). Sox1 in the ventricular zone labels neural progenitors. Scale bar = 50 μm.

FIGURE S2 | Pou2f2 RT-PCR experiments and sequencing of exon 1b and exon 5b of the spinal Pou2f2 isoforms. Composite assembly of electrophoresis images of RT-PCR amplification products for *Pou2f2* isoform sequences on embryonic spinal cord or B-cell RNA samples. Water was used as a negative control (Ctl-). **(A)** Amplifications from exon 1 (E1) to E6 on embryonic spinal cord RNA samples (asterisk) fail to amplify the RNA isoforms detected in B cell samples. In contrast, amplifications from E7 to E9, from E10 to E12, and from E13 to E17 show at least one similar amplicon in spinal cord samples and in B cell samples. **(B)** Amplification from E1 (other forward primer) to E7 also fails to amplify *Pou2f2* spinal cord isoforms. In contrast, amplifications from E2, 3, 4, and 5 to E7 produce systematically longer amplicons in spinal cord samples (arrowheads) as compared to B cell samples. The E6 to E7 amplification is similar in both samples. **(C)** Amplifications from E1X (present in the X6 sequence) to E3 do not produce amplicon in B-cell samples (asterisk). Amplifications from E1X to E3 or to E5b on spinal cord samples systematically produce two amplicons (arrowheads). Amplifications of the E5b exon sequence, from E3 to E5b and from E5b to E7 produce expected amplicons in spinal cord samples. **(D)** Comparison of exon 1b and exon 5b sequences in the predicted X6 sequence and the sequenced embryonic spinal cord *Pou2f2* isoforms. Sequences of E1X, E2a, and E5b exons align (100% identity) with the predicted X6 sequence. Sequence of the additional alterative exon 1b is shown. SD, size standard; E, exon; SC, embryonic spinal cord; B, B lymphocytes.

FIGURE S3 | The number of Pou2f2+Shox2+ V2a interneurons is normal in *Hnf6*$^{-/-}$*;Oc2*$^{-/-}$ mutant embryos. Immunolabelings on transverse spinal cord sections (brachial or thoracic levels) of control or *Hnf6*$^{-/-}$*;Oc2*$^{-/-}$ mutant embryos. At e12.5 **(A–C)** and at e14.5 **(D–F)**, the number of V2a containing Shox2 and Pou2f2 is unchanged in the absence of OC factors. Mean values ± SEM. Scale bar = 50 μm.

FIGURE S4 | Efficacy of pCMV-eGFP and pCMV-Pou2f2 co-electroporation in the chicken embryonic spinal cord. **(A–C)** eGFP (green, **B**), and Pou2f2 (red, **C**) are present in a vast majority of cells along the dorso-ventral axis of the spinal cord. Scale bar = 50 μm.

FIGURE S5 | The number of MafA+ or cMaf+ V2a interneurons is normal in *Pou2f2*$^{-/-}$ mutant spinal cords. Immunolabelings on transverse spinal cord sections (brachial or thoracic levels) of control or *Pou2f2*$^{-/-}$ mutant embryos at e12.5. **(A–F)** Absence of Pou2f2 does not impact on the number of Shox2+ **(A–C),** cMaf+ **(D–F)**, or MafA+ **(G–I)** V2a interneurons. Mean values ± SEM. Scale bar = 50 μm.

FIGURE S6 | The number of MafA-positive V2b interneurons or of the V2c interneurons is normal in *Pou2f2*$^{-/-}$ mutant spinal cords. Immunolabelings on transverse spinal cord sections (brachial or thoracic levels) of control or *Pou2f2*$^{-/-}$ mutant embryos at e12.5. **(A,B,E)** The number of MafA+ V2b interneurons is not significantly altered in the absence of Pou2f2. **(C,D,F)** Similarly, the production of V2c interneurons is not affected in *Pou2f2* mutants. Mean values ± SEM. Scale bar = 50 μm.

TABLE S1 | Microarray comparison of control and of *Hnf6*$^{-/-}$*;Oc2*$^{-/-}$ spinal cords. The differential expression of selected candidates is shown as fold change in *Hnf6*$^{-/-}$*;Oc2*$^{-/-}$ vs. control spinal cords. Pval, *p*-value; adjpval, adjusted *p*-value.

REFERENCES

Ampatzis, K., Song, J., Ausborn, J., and El Manira, A. (2014). Separate microcircuit modules of distinct v2a interneurons and motoneurons control the speed of locomotion. *Neuron* 83, 934–943. doi: 10.1016/j.neuron.2014.07.018

Audouard, E., Schakman, O., Ginion, A., Bertrand, L., Gailly, P., and Clotman, F. (2013). The Onecut transcription factor HNF-6 contributes to proper reorganization of Purkinje cells during postnatal cerebellum development. *Mol. Cell. Neurosci.* 56, 159–168. doi: 10.1016/j.mcn.2013.05.001

Audouard, E., Schakman, O., Rene, F., Huettl, R. E., Huber, A. B., Loeffler, J. P., et al. (2012). The Onecut transcription factor HNF-6 regulates in motor neurons the formation of the neuromuscular junctions. *PLoS One* 7:e50509. doi: 10.1371/journal.pone.0050509

Barber, M., and Pierani, A. (2016). Tangential migration of glutamatergic neurons and cortical patterning during development: lessons from Cajal-Retzius cells. *Dev. Neurobiol.* 76, 847–881. doi: 10.1002/dneu.22363

Beaudry, J. B., Pierreux, C. E., Hayhurst, G. P., Plumb-Rudewiez, N., Weiss, M. C., Rousseau, G. G., et al. (2006). Threshold levels of hepatocyte nuclear factor 6 (HNF-6) acting in synergy with HNF-4 and PGC-1alpha are required for time-specific gene expression during liver development. *Mol. Cell. Biol.* 26, 6037–6046. doi: 10.1128/MCB.02445-05

Beguin, S., Crepel, V., Aniksztejn, L., Becq, H., Pelosi, B., Pallesi-Pocachard, E., et al. (2013). An epilepsy-related ARX polyalanine expansion modifies glutamatergic neurons excitability and morphology without affecting GABAergic neurons development. *Cereb. Cortex* 23, 1484–1494. doi: 10.1093/cercor/bhs138

Bikoff, J. B., Gabitto, M. I., Rivard, A. F., Drobac, E., Machado, T. A., Miri, A., et al. (2016). Spinal inhibitory interneuron diversity delineates variant motor microcircuits. *Cell* 165, 207–219. doi: 10.1016/j.cell.2016.01.027

Blacklaws, J., Deska-Gauthier, D., Jones, C. T., Petracca, Y. L., Liu, M., Zhang, H., et al. (2015). Sim1 is required for the migration and axonal projections of V3 interneurons in the developing mouse spinal cord. *Dev. Neurobiol.* 75, 1003–1017. doi: 10.1002/dneu.22266

Boije, H., and Kullander, K. (2018). Origin and circuitry of spinal locomotor interneurons generating different speeds. *Curr. Opin. Neurobiol.* 53, 16–21. doi: 10.1016/j.conb.2018.04.024

Borowska, J., Jones, C. T., Deska-Gauthier, D., and Zhang, Y. (2015). V3 interneuron subpopulations in the mouse spinal cord undergo distinctive postnatal maturation processes. *Neuroscience* 295, 221–228. doi: 10.1016/j.neuroscience.2015.03.024

Borowska, J., Jones, C. T., Zhang, H., Blacklaws, J., Goulding, M., and Zhang, Y. (2013). Functional subpopulations of V3 interneurons in the mature mouse spinal cord. *J. Neurosci.* 33, 18553–18565. doi: 10.1523/JNEUROSCI.2005-13.2013

Britz, O., Zhang, J., Grossmann, K. S., Dyck, J., Kim, J. C., Dymecki, S., et al. (2015). A genetically defined asymmetry underlies the inhibitory control of flexor-extensor locomotor movements. *eLife* 4:e04718. doi: 10.7554/eLife.04718

Camos, S., Gubern, C., Sobrado, M., Rodriguez, R., Romera, V. G., Moro, M. A., et al. (2014). Oct-2 transcription factor binding activity and expression up-regulation in rat cerebral ischaemia is associated with a diminution of neuronal damage in vitro. *Neuromol. Med.* 16, 332–349. doi: 10.1007/s12017-013-8279-1

Catela, C., Shin, M. M., and Dasen, J. S. (2015). Assembly and function of spinal circuits for motor control. *Annu. Rev. Cell Dev. Biol.* 31, 669–698. doi: 10.1146/annurev-cellbio-100814-125155

Clotman, F., Jacquemin, P., Plumb-Rudewiez, N., Pierreux, C. E., Van der Smissen, P., Dietz, H. C., et al. (2005). Control of liver cell fate decision by a gradient of TGF beta signaling modulated by onecut transcription factors. *Genes Dev.* 19, 1849–1854. doi: 10.1101/gad.340305

Clovis, Y. M., Seo, S. Y., Kwon, J. S., Rhee, J. C., Yeo, S., Lee, J. W., et al. (2016). Chx10 consolidates V2a interneuron identity through two distinct gene repression modes. *Cell Rep.* 16, 1642–1652. doi: 10.1016/j.celrep.2016.06.100

Corcoran, L. M., Karvelas, M., Nossal, G. J., Ye, Z. S., Jacks, T., and Baltimore, D. (1993). Oct-2, although not required for early B-cell development, is critical for later B-cell maturation and for postnatal survival. *Genes Dev.* 7, 570–582. doi: 10.1101/gad.7.4.570

Corcoran, L. M., Koentgen, F., Dietrich, W., Veale, M., and Humbert, P. O. (2004). All known in vivo functions of the Oct-2 transcription factor require the C-terminal protein domain. *J. Immunol.* 172, 2962–2969. doi: 10.4049/jimmunol.172.5.2962

Crone, S. A., Quinlan, K. A., Zagoraiou, L., Droho, S., Restrepo, C. E., Lundfald, L., et al. (2008). Genetic ablation of V2a ipsilateral interneurons disrupts left-right locomotor coordination in mammalian spinal cord. *Neuron* 60, 70–83. doi: 10.1016/j.neuron.2008.08.009

Del Barrio, M. G., Taveira-Marques, R., Muroyama, Y., Yuk, D. I., Li, S., Wines-Samuelson, M., et al. (2007). A regulatory network involving Foxn4, Mash1 and delta-like 4/Notch1 generates V2a and V2b spinal interneurons from a common progenitor pool. *Development* 134, 3427–3436. doi: 10.1242/dev.005868

Dougherty, K. J., and Kiehn, O. (2010). Firing and cellular properties of V2a interneurons in the rodent spinal cord. *J. Neurosci.* 30, 24–37. doi: 10.1523/JNEUROSCI.4821-09.2010

Dougherty, K. J., Zagoraiou, L., Satoh, D., Rozani, I., Doobar, S., Arber, S., et al. (2013). Locomotor rhythm generation linked to the output of spinal shox2 excitatory interneurons. *Neuron* 80, 920–933. doi: 10.1016/j.neuron.2013.08.015

Espana, A., and Clotman, F. (2012a). Onecut factors control development of the Locus Coeruleus and of the mesencephalic trigeminal nucleus. *Mol. Cell. Neurosci.* 50, 93–102. doi: 10.1016/j.mcn.2012.04.002

Espana, A., and Clotman, F. (2012b). Onecut transcription factors are required for the second phase of development of the A13 dopaminergic nucleus in the mouse. *J. Comp. Neurol.* 520, 1424–1441. doi: 10.1002/cne.22803

Francius, C., and Clotman, F. (2010). Dynamic expression of the onecut transcription factors HNF-6, OC-2 and OC-3 during spinal motor neuron development. *Neuroscience* 165, 116–129. doi: 10.1016/j.neuroscience.2009.09.076

Francius, C., and Clotman, F. (2014). Generating spinal motor neuron diversity: a long quest for neuronal identity. *Cell. Mol. Life Sci.* 71, 813–829. doi: 10.1007/s00018-013-1398-x

Francius, C., Harris, A., Rucchin, V., Hendricks, T. J., Stam, F. J., Barber, M., et al. (2013). Identification of multiple subsets of ventral interneurons and differential distribution along the rostrocaudal axis of the developing spinal cord. *PLoS One* 8:e70325. doi: 10.1371/journal.pone.0070325

Francius, C., Hidalgo-Figueroa, M., Debrulle, S., Pelosi, B., Rucchin, V., Ronellenfitch, K., et al. (2016). Vsx1 transiently defines an early intermediate V2 interneuron precursor compartment in the mouse developing spinal cord. *Front. Mol. Neurosci.* 9:145. doi: 10.3389/fnmol.2016.00145

Goetz, C., Pivetta, C., and Arber, S. (2015). Distinct limb and trunk premotor circuits establish laterality in the spinal cord. *Neuron* 85, 131–144. doi: 10.1016/j.neuron.2014.11.024

Gosgnach, S., Bikoff, J. B., Dougherty, K. J., El Manira, A., Lanuza, G. M., and Zhang, Y. (2017). Delineating the diversity of spinal interneurons in locomotor circuits. *J. Neurosci.* 37, 10835–10841. doi: 10.1523/JNEUROSCI.1829-17.2017

Grossmann, K. S., Giraudin, A., Britz, O., Zhang, J., and Goulding, M. (2010). Genetic dissection of rhythmic motor networks in mice. *Prog. Brain Res.* 187, 19–37. doi: 10.1016/B978-0-444-53613-6.00002-2

Guo, J., and Anton, E. S. (2014). Decision making during interneuron migration in the developing cerebral cortex. *Trends Cell Biol.* 24, 342–351. doi: 10.1016/j.tcb.2013.12.001

Harris, A., Masgutova, G., Collin, A., Toch, M., Hidalgo-Figueroa, M., Jacob, B., et al. (2018). Onecut factors and Pou2f2 regulate the distribution of V2 interneurons in the mouse developing spinal cord. *bioRxiv* [Preprint]. doi: 10.1101/413054

Hatzopoulos, A. K., Stoykova, A. S., Erselius, J. R., Goulding, M., Neuman, T., and Gruss, P. (1990). Structure and expression of the mouse Oct2a and Oct2b, two differentially spliced products of the same gene. *Development* 109, 349–362.

Hayashi, M., Hinckley, C. A., Driscoll, S. P., Moore, N. J., Levine, A. J., Hilde, K. L., et al. (2018). Graded arrays of spinal and supraspinal V2a interneuron subtypes underlie forelimb and hindlimb motor control. *Neuron* 97, 869–884.e5. doi: 10.1016/j.neuron.2018.01.023

Hilde, K. L., Levine, A. J., Hinckley, C. A., Hayashi, M., Montgomery, J. M., Gullo, M., et al. (2016). Satb2 is required for the development of a spinal exteroceptive microcircuit that modulates limb position. *Neuron* 91, 763–776. doi: 10.1016/j.neuron.2016.07.014

Hodson, D. J., Shaffer, A. L., Xiao, W., Wright, G. W., Schmitz, R., Phelan, J. D., et al. (2016). Regulation of normal B-cell differentiation and malignant B-cell survival by OCT2. *Proc. Natl. Acad. Sci. U.S.A.* 113, E2039–E2046. doi: 10.1073/pnas.1600557113

Jacquemin, P., Durviaux, S. M., Jensen, J., Godfraind, C., Gradwohl, G., Guillemot, F., et al. (2000). Transcription factor hepatocyte nuclear factor 6 regulates pancreatic endocrine cell differentiation and controls expression of the proendocrine gene ngn3. *Mol. Cell. Biol.* 20, 4445–4454. doi: 10.1128/mcb.20.12.4445-4454.2000

Jacquemin, P., Lannoy, V. J., Rousseau, G. G., and Lemaigre, F. P. (1999). OC-2, a novel mammalian member of the ONECUT class of homeodomain transcription factors whose function in liver partially overlaps with that of hepatocyte nuclear factor-6. *J. Biol. Chem.* 274, 2665–2671. doi: 10.1074/jbc.274.5.2665

Jacquemin, P., Lemaigre, F. P., and Rousseau, G. G. (2003a). The onecut transcription factor HNF-6 (OC-1) is required for timely specification of the pancreas and acts upstream of Pdx-1 in the specification cascade. *Dev. Biol.* 258, 105–116. doi: 10.1016/S0012-1606(03)00115-5

Jacquemin, P., Pierreux, C. E., Fierens, S., van Eyll, J. M., Lemaigre, F. P., and Rousseau, G. G. (2003b). Cloning and embryonic expression pattern of the mouse onecut transcription factor OC-2. *Gene Expr. Patterns* 3, 639–644. doi: 10.1016/S1567-133X(03)00110-8

Joshi, K., Lee, S., Lee, B., Lee, J. W., and Lee, S. K. (2009). LMO4 controls the balance between excitatory and inhibitory spinal V2 interneurons. *Neuron* 61, 839–851. doi: 10.1016/j.neuron.2009.02.011

Kabayiza, K. U., Masgutova, G., Harris, A., Rucchin, V., Jacob, B., and Clotman, F. (2017). The onecut transcription factors regulate differentiation and distribution of dorsal interneurons during spinal cord development. *Front. Mol. Neurosci.* 10:157. doi: 10.3389/fnmol.2017.00157

Konig, H., Pfisterer, P., Corcoran, L. M., and Wirth, T. (1995). Identification of CD36 as the first gene dependent on the B-cell differentiation factor Oct-2. *Genes Dev.* 9, 1598–1607. doi: 10.1101/gad.9.13.1598

Lai, H. C., Seal, R. P., and Johnson, J. E. (2016). Making sense out of spinal cord somatosensory development. *Development* 143, 3434–3448. doi: 10.1242/dev.139592

Landry, C., Clotman, F., Hioki, T., Oda, H., Picard, J. J., Lemaigre, F. P., et al. (1997). HNF-6 is expressed in endoderm derivatives and nervous system of the mouse embryo and participates to the cross-regulatory network of liver-enriched transcription factors. *Dev. Biol.* 192, 247–257. doi: 10.1006/dbio.1997.8757

Lannoy, V. J., Rodolosse, A., Pierreux, C. E., Rousseau, G. G., and Lemaigre, F. P. (2000). Transcriptional stimulation by hepatocyte nuclear factor-6. Target-specific recruitment of either CREB-binding protein (CBP) or p300/CBP-associated factor (p/CAF). *J. Biol. Chem.* 275, 22098–22103. doi: 10.1074/jbc.m000855200

Latchman, D. S. (1996). The Oct-2 transcription factor. *Int. J. Biochem. Cell Biol.* 28, 1081–1083.

Lee, S., Lee, B., Joshi, K., Pfaff, S. L., Lee, J. W., and Lee, S. K. (2008). A regulatory network to segregate the identity of neuronal subtypes. *Dev. Cell* 14, 877–889. doi: 10.1016/j.devcel.2008.03.021

Lemaigre, F. P., Durviaux, S. M., Truong, O., Lannoy, V. J., Hsuan, J. J., and Rousseau, G. G. (1996). Hepatocyte nuclear factor 6, a transcription factor that contains a novel type of homeodomain and a single cut domain. *Proc. Natl. Acad. Sci. U.S.A.* 93, 9460–9464. doi: 10.1073/pnas.93.18.9460

Lillycrop, K. A., and Latchman, D. S. (1992). Alternative splicing of the Oct-2 transcription factor RNA is differentially regulated in neuronal cells and B cells and results in protein isoforms with opposite effects on the activity of octamer/TAATGARAT-containing promoters. *J. Biol. Chem.* 267, 24960–24965.

Liu, Y. Z., Lillycrop, K. A., and Latchman, D. S. (1995). Regulated splicing of the Oct-2 transcription factor RNA in neuronal cells. *Neurosci. Lett.* 183, 8–12. doi: 10.1016/0304-3940(94)11102-o

Lu, D. C., Niu, T., and Alaynick, W. A. (2015). Molecular and cellular development of spinal cord locomotor circuitry. *Front. Mol. Neurosci.* 8:25. doi: 10.3389/fnmol.2015.00025

Misra, K., Luo, H., Li, S., Matise, M., and Xiang, M. (2014). Asymmetric activation of Dll4-Notch signaling by Foxn4 and proneural factors activates BMP/TGFbeta signaling to specify V2b interneurons in the spinal cord. *Development* 141, 187–198. doi: 10.1242/dev.092536

Panayi, H., Panayiotou, E., Orford, M., Genethliou, N., Mean, R., Lapathitis, G., et al. (2010). Sox1 is required for the specification of a novel p2-derived interneuron subtype in the mouse ventral spinal cord. *J. Neurosci.* 30, 12274–12280. doi: 10.1523/JNEUROSCI.2402-10.2010

Pelosi, B., Migliarini, S., Pacini, G., Pratelli, M., and Pasqualetti, M. (2014). Generation of Pet1210-Cre transgenic mouse line reveals non-serotonergic expression domains of Pet1 both in CNS and periphery. *PLoS One* 9:e104318. doi: 10.1371/journal.pone.0104318

Peng, C. Y., Yajima, H., Burns, C. E., Zon, L. I., Sisodia, S. S., Pfaff, S. L., et al. (2007). Notch and MAML signaling drives Scl-dependent interneuron diversity in the spinal cord. *Neuron* 53, 813–827. doi: 10.1016/j.neuron.2007.02.019

Pierreux, C. E., Vanhorenbeeck, V., Jacquemin, P., Lemaigre, F. P., and Rousseau, G. G. (2004). The transcription factor hepatocyte nuclear factor-6/Onecut-1 controls the expression of its paralog Onecut-3 in developing mouse endoderm. *J. Biol. Chem.* 279, 51298–51304. doi: 10.1074/jbc.M409038200M409038200

Roy, A., Francius, C., Rousso, D. L., Seuntjens, E., Debruyn, J., Luxenhofer, G., et al. (2012). Onecut transcription factors act upstream of Isl1 to regulate spinal motoneuron diversification. *Development* 139, 3109–3119. doi: 10.1242/dev.078501

Stam, F. J., Hendricks, T. J., Zhang, J., Geiman, E. J., Francius, C., Labosky, P. A., et al. (2012). Renshaw cell interneuron specialization is controlled by a temporally restricted transcription factor program. *Development* 139, 179–190. doi: 10.1242/dev.071134

Stoykova, A. S., Sterrer, S., Erselius, J. R., Hatzopoulos, A. K., and Gruss, P. (1992). Mini-Oct and Oct-2c: two novel, functionally diverse murine Oct-2 gene products are differentially expressed in the CNS. *Neuron* 8, 541–558. doi: 10.1016/0896-6273(92)90282-i

Surmeli, G., Akay, T., Ippolito, G. C., Tucker, P. W., and Jessell, T. M. (2011). Patterns of spinal sensory-motor connectivity prescribed by a dorsoventral positional template. *Cell* 147, 653–665. doi: 10.1016/j.cell.2011.10.012

Sweeney, L. B., Bikoff, J. B., Gabitto, M. I., Brenner-Morton, S., Baek, M., Yang, J. H., et al. (2018). Origin and segmental diversity of spinal inhibitory interneurons. *Neuron* 97, 341–355.e3. doi: 10.1016/j.neuron.2017.12.029

Talpalar, A. E., Bouvier, J., Borgius, L., Fortin, G., Pierani, A., and Kiehn, O. (2013). Dual-mode operation of neuronal networks involved in left-right alternation. *Nature* 500, 85–88. doi: 10.1038/nature12286

Thaler, J. P., Lee, S. K., Jurata, L. W., Gill, G. N., and Pfaff, S. L. (2002). LIM factor Lhx3 contributes to the specification of motor neuron and interneuron identity through cell-type-specific protein-protein interactions. *Cell* 110, 237–249. doi: 10.1016/S0092-8674(02)00823-1

Theodorou, E., Dalembert, G., Heffelfinger, C., White, E., Weissman, S., Corcoran, L., et al. (2009). A high throughput embryonic stem cell screen identifies Oct-2 as a bifunctional regulator of neuronal differentiation. *Genes Dev.* 23, 575–588. doi: 10.1101/gad.1772509

Tripodi, M., Stepien, A. E., and Arber, S. (2011). Motor antagonism exposed by spatial segregation and timing of neurogenesis. *Nature* 479, 61–66. doi: 10.1038/nature10538

Vanhorenbeeck, V., Jacquemin, P., Lemaigre, F. P., and Rousseau, G. G. (2002). OC-3, a novel mammalian member of the ONECUT class of transcription factors. *Biochem. Biophys. Res. Commun.* 292, 848–854. doi: 10.1006/bbrc.2002.6760

Wirth, T., Priess, A., Annweiler, A., Zwilling, S., and Oeler, B. (1991). Multiple Oct2 isoforms are generated by alternative splicing. *Nucleic Acids Res.* 19, 43–51. doi: 10.1093/nar/19.1.43

Ziskind-Conhaim, L., and Hochman, S. (2017). Diversity of molecularly defined spinal interneurons engaged in mammalian locomotor pattern generation. *J. Neurophysiol.* 118, 2956–2974. doi: 10.1152/jn.00322.2017

Conflict of Interest Statement: The authors declare that the research was conducted in the absence of any commercial or financial relationships that could be construed as a potential conflict of interest.

frontiers in Cellular Neuroscience

ORIGINAL RESEARCH
published: 11 June 2019
doi: 10.3389/fncel.2019.00250

MEA6 Deficiency Impairs Cerebellar Development and Motor Performance by Tethering Protein Trafficking

Xin-Tai Wang[1†], Xin-Yu Cai[1†], Fang-Xiao Xu[1], Lin Zhou[1], Rui Zheng[1], Kuang-Yi Ma[1], Zhi-Heng Xu[2] and Ying Shen[1*]*

[1] Department of Neurobiology, NHC and CAMS Key Laboratory of Medical Neurobiology, Zhejiang University School of Medicine, Hangzhou, China, [2] State Key Laboratory of Molecular Developmental Biology, CAS Center for Excellence in Brain Science and Intelligence Technology, Institute of Genetics and Developmental Biology Chinese Academy of Sciences, Beijing, China

OPEN ACCESS

Edited by:
Paul G. Mermelstein,
University of Minnesota Twin Cities,
United States

Reviewed by:
Marija Cvetanovic,
University of Minnesota Twin Cities,
United States
Laurens Bosman,
Erasmus University Rotterdam,
Netherlands

***Correspondence:**
Zhi-Heng Xu
zhxu@genetics.ac.cn
Ying Shen
yshen@zju.edu.cn

[†] These authors have contributed equally to this work

Specialty section:
This article was submitted to Cellular Neurophysiology, a section of the journal Frontiers in Cellular Neuroscience

Received: 03 December 2018
Accepted: 20 May 2019
Published: 11 June 2019

Citation:
Wang X-T, Cai X-Y, Xu F-X, Zhou L, Zheng R, Ma K-Y, Xu Z-H and Shen Y (2019) MEA6 Deficiency Impairs Cerebellar Development and Motor Performance by Tethering Protein Trafficking. Front. Cell. Neurosci. 13:250. doi: 10.3389/fncel.2019.00250

Meningioma expressed antigen 6 (MEA6), also called cutaneous T cell lymphoma-associated antigen 5 (cTAGE5), was initially found in tumor tissues. MEA6 is located in endoplasmic reticulum (ER) exit sites and regulates the transport of collagen, very low density lipoprotein, and insulin. It is also reported that MEA6 might be related to Fahr's syndrome, which comprises neurological, movement, and neuropsychiatric disorders. Here, we show that MEA6 is critical to cerebellar development and motor performance. Mice with conditional knockout of MEA6 (Nestin-Cre;MEA6$^{F/F}$) display smaller sizes of body and brain compared to control animals, and survive maximal 28 days after birth. Immunohistochemical and behavioral studies demonstrate that these mutant mice have defects in cerebellar development and motor performance. In contrast, PC deletion of MEA6 (pCP2-Cre;MEA6$^{F/F}$) causes milder phenotypes in cerebellar morphology and motor behaviors. While pCP2-Cre;MEA6$^{F/F}$ mice have normal lobular formation and gait, they present the extensive self-crossing of PC dendrites and damaged motor learning. Interestingly, the expression of key molecules that participates in cerebellar development, including Slit2 and brain derived neurotrophic factor (BDNF), is significantly increased in ER, suggesting that MEA6 ablation impairs ER function and thus these proteins are arrested in ER. Our study provides insight into the roles of MEA6 in the brain and the pathogenesis of Fahr's syndrome.

Keywords: MEA6, motor learning, Slit2, dendrite self-crossing, Fahr's syndrome

INTRODUCTION

Meningioma expressed antigen 6 (MEA6), also known as cutaneous T cell lymphoma-associated antigen 5 (CTAGE5), was found in tumor tissues and usually considered as a risk gene for the cancer (Heckel et al., 1997; Comtesse et al., 2002; Kalniņa et al., 2008). Recent studies show that MEA6 is also expressed in secretary organs (such as liver and pancreas), brain, spleen, lung, and intestine (Wang et al., 2016; Fan et al., 2017). Structurally, MEA6 is a coil-coiled protein with its main structure containing one transmembrane domain, two coiled-coil domains, and one proline-rich domain (Wang et al., 2016). Functionally, MEA6 localizes in endoplasmic reticulum (ER) exit

site and interacts with Golgi organization 1 (TANGO1) and Sec proteins to regulate the secretion of collagen, a large cargo (Saito et al., 2011, 2014). Surprisingly, recent studies demonstrate that MEA6 also regulates the transport of small cargos. MEA6 is involved in the transport and secretion of very low-density lipoprotein (VLDL) through the assembly of coat protein complex II (COPII) complex in the liver and insulin secretion through interacting with Sec22 in the pancreas (Wang et al., 2016; Fan et al., 2017).

Meningioma expressed antigen 6 is highly expressed in the central nervous system (CNS), however, its functions in cellular component trafficking of neurons, brain development and animal behaviors are poorly understood. Utilizing conditional knockout mice of MEA6 driven by Nestin-Cre, Zhang et al. (2018) recently show that MEA6 is important for brain development and function. The deletion of MEA6 in the brain leads to reduced brain size, early death of mice, and behavioral defects, including abnormal limb-clasping reflex and impaired motor performance in the rotarod test (Zhang et al., 2018). These phenotypes may be ascribed to the deficits in neural development, since the dendrite outgrowth and branching, spine formation and maintenance, and astrocytic activation are damaged in the cerebral cortex of Nestin-Cre;MEA6$^{F/F}$ mice (Zhang et al., 2018). Nevertheless, it is not yet answered how MEA6 affects the development of the cerebellum. Particularly, a loss-of-function mutation of MEA6 (P521A) might be associated with Fahr's syndrome (Lemos et al., 2011), an inheritance neurological disorder comprising neurological, movement, and neuropsychiatric disorders (Oliveira et al., 2007). The patients with Fahr's disease show severe degeneration in brain regions controlling movement and exhibit unsteady gaits (Moskowitz et al., 1971; Geschwind et al., 1999; Saleem et al., 2013). Thus, it is attractive to investigate how MEA6 knockout causes abnormal cerebellar development and dysfunctional motor behaviors, which will lead to more insights of the pathogenesis of Fahr's syndrome.

Here, we set out to establish the contribution of MEA6 in cerebellar development and motor functions using conditional approaches to generate specific deletion. We demonstrate that Nestin-Cre;MEA6$^{F/F}$ mice have defects in cerebellar development and motor performance. In contrast, mice with Purkinje cell (PC)-specific deletion of MEA6 (pCP2-Cre;MEA6$^{F/F}$) have normal lobular formation and walking gait, but display impaired self-avoidance of PC dendrites and motor learning. We further found that the expression of several molecules critical to cerebellar development, including Slit2, brain derived neurotrophic factor (BDNF) and Semaphorin 3A, is significantly increased in ER, suggesting that these proteins are tethered in ER, but not functionally expressed, by MEA6 ablation.

MATERIALS AND METHODS

Animals

All experiments were approved by the Animal Experimentation Ethics Committee of Zhejiang University and specifically designed to minimize the number of animals used. The construction of MEA6$^{F/F}$ mice was described previously (Wang et al., 2016). Nestin-Cre;MEA6$^{F/F}$ (N-Cre;MEA6$^{F/F}$) and pCP2-Cre;MEA6$^{F/F}$ (P-Cre;MEA6$^{F/F}$) mice were obtained by crossing MEA6$^{F/F}$ mice with Nestin-Cre and pCP2-Cre mice (Zhou et al., 2015, 2017), respectively. The resulting offspring were genotyped using PCR of genomic DNA, which were: MEA6 floxP fragment, F: 5′-GAC ACT TGA CCC CTC CTC TCC-3′; R: 5′-AAC GGC TCA TGC TTG CTA ACC-3′; Nestin-cre, F: 5′-GCG GTC TGG CAG TAA AAA CTA TCT-3′; R: 5′-GTG AAA CAG CAT TGC TGT CAC TT-3′; pCP2-cre, F: 5′-TGC CAC GAC CAA GTG ACA GCA ATG-3′; R: 5′-ACC AGA GAC GGA AAT CCA TCG CTC-3′. Mice were kept at the Experimental Animal Center of Zhejiang University under temperature-controlled condition on a 12:12 h light/dark cycle. All experiments were performed blind to genotypes in age-matched littermates of either sex.

Antibodies and Reagents

The antibody against γ-protocadherin (γ-Pcdh) was from Synaptic Systems (Gottingen, Germany). The antibody against VDAC was from Cell Signaling (Danvers, MA, United States). Antibodies against GAPDH, PSD95, Rab11, and TrkB were from Millipore (Billerica, MA, United States). Antibodies against Slit2 and γ-adaptin were was from Proteintech (Rosemont, IL, United States). Antibodies against MEA6 and calbindin were from Sigma (St. Louis, MO, United States). Antibodies against Bip, PDI, Robo2, and Semaphorin 3A were from Abcam (Cambridge, United Kingdom). Antibodies against β-actin, β-tubulin, YY1, and BDNF were from Santa Cruz (Dallas, TX, United States). Goat anti-mouse and anti-rabbit IgG horseradish peroxidase-conjugated were from Thermo Fisher Scientific (Waltham, MA, United States). The alexa fluor-conjugated secondary antibody was from Invitrogen (Carlsbad, CA, United States). Protease inhibitor cocktail was from Roche (Mannheim, Germany). Other chemicals were from Sigma unless stated otherwise.

Purification of ER

Endoplasmic reticulum fractions were purified according to Hammond et al. (2012). In brief, cerebellar tissues were homogenized in isotonic extraction buffer (10 mM HEPES, 250 mM sucrose, 25 mM KCl, 1 mM EGTA; pH 7.8) supplemented with protease inhibitors. A centrifugation (700 × *g*; 10 min) was used to remove nuclei and large cellular debris (P1). A subsequent 15,000 × *g* (10 min) of supernatant (S1) was performed to pellet mitochondria (P2). The resulting supernatant (S2) was loaded onto a three-layered sucrose gradient (2.0, 1.5, and 1.3 M) and centrifuged at 126,000 × *g* for 70 min on a ultracentrifuge. The upper supernatant was collected (S3) and the white band between the top and 1.3 M-sucrose layers was collected (P3), which was gently mixed by inversion with ice cold MTE solution (270 mM D-mannitol, 10 mM Tris-base, 0.1 mM EDTA; pH 7.4 with HCl) supplemented with protease inhibitors. This mixture was centrifuged at 126,000 × *g* for 45 min resulting in a large and translucent pellet (P4).

RT-PCR

The total RNA of the cerebellum was isolated using TRIzol Reagent (Thermo). cDNA was synthesized by reverse transcription using oligo (dT) as the primer using Revert Aid First Strand cDNA synthesis Kit (Thermo). For single-cell analysis, the contents of individual PCs (P21) were harvested as described in previous work (Zhou et al., 2015, 2017). The tip of a conventional patch-clamp pipette was placed tightly on the soma of a selected PC and a gentle suction was applied to the pipette. After complete incorporation of the soma, the negative pressure was released and the pipette was quickly removed from the bath. The harvested contents were subjected to RT-PCR using OneStep Kit (Qiagen, Germany). Forward (F) and reverse (R) primers used for amplification were as follows: MEA6, F: 5′-GTT GAA GGA TCA CAA ATA TC-3′; R: 5′-TCC TTT TTG AAA TAT CAG CC-3′; calbindin, F: 5′-GGC TTC ATT TCG ACG CTG AC-3′; R: 5′-ACG TGA GCC AAC TCT ACA ATT C-3′; GAPDH, F: 5′-GGT GAA GGT CGG TGT GAA CG-3′; R: 5′-CTC GCT CCT GGA AGA TGG TG-3′.

Western Blot

The protein concentration was determined using BCA protein assay. Equal quantities of proteins were loaded and fractionated on SDS–PAGE, transferred to PVDF membrane (Immobilon-P, Millipore), immunoblotted with antibodies, and visualized by enhanced chemiluminescence (Thermo Fisher Scientific). The dilutions of antibodies were MEA6 (1:4,000), Slit2 (1:1,000), Robo2 (1:1,000), β-tubulin (1:2,000), GAPDH (1:20,000), γ-Pcdh (1:2,000), BDNF (1:1,000), TrkB (1:1,000), PDI (1:1,000), Bip (1:5,000), γ-adaptin (1:1,000), YY1 (1:300), PSD95 (1:40,000), VDAC (1:1,000), Rab11 (1:1,000), Semaphorin 3A (1:1,000), and secondary antibodies (1:10,000). Film signals were digitally scanned and quantitated using ImageJ 1.42q (NIH).

Immunohistochemistry

Sagittal frozen sections (30 μm) were cut and placed in blocking solution for 1 h at room temperature (RT). After washing with PBS, sections were incubated with primary antibodies overnight at 4°C and incubated with secondary antibodies for 1 h at RT. Primary antibody dilutions used for immunohistochemistry were calbindin (1:500), NeuN (1:500), and MEA6 (1:250). Alexa Fluor 488-conjugated goat anti-mouse IgG, Alexa Fluor 594-conjugated goat anti mouse IgG and Alexa Fluor 488-conjugated goat anti-rabbit IgG antibody were diluted at 1:1,000. All antibodies were diluted in PBS containing 1% BSA and 1% normal goat serum. To offset weak staining ability of MEA6 antibody, we enhanced the excitation of confocal microscope (emission wavelength: 525 nm; excitation wavelength: 488 nm; pinhole radius: 22.99 μm; lser power: 13.84%, high voltage: 123).

H&E Staining

H&E staining was performed by using H&E staining Kit (Beyotime, Shanghai, China) (Xie et al., 2015). Sagittal cerebellar slices (30 μm) were immersed in hematoxylin staining solution for 5–10 min, rinsed with distilled water, and immersed in eosin staining solution for 2 min. The sections were then rinsed with distilled water, dehydrated in ethanol, and cleared in xylene. Images of cerebellar cortex were captured using a light microscope. For quantification, total cerebellar area, the thickness of lobule, the thicknesses of granule cell layer and molecular layer were calculated using ImageJ. The maximum width of a cerebellar lobule was defined as its thickness. The intermediate point of the long axis of a lobe was selected to measure the thicknesses of granule cell and molecular layers. The experimenter was blind to mouse genotypes during the measurement.

Nissl Staining

Nissl staining was performed using Nissl staining Kit (Beyotime) (Xie et al., 2015). Sagittal cerebellar slices (30 μm) were immersed in Nissl staining solution for 5 min, rinsed with distilled water, dehydrated in ethanol, and cleared in xylene. Images of the cerebellar cortex were captured using a light microscope. The quantification of cerebellar area, lobular thickness, and the thicknesses of granule cell and molecular layers in Nissl staining were measured as same as those in H&E staining.

Analysis of PC Dendrites

sUnder the anesthesia with an intraperitoneal injection of pentobarbital (30 mg/kg), mice (P21) were placed in a stereotaxic apparatus (Stoelting, Wood Dale, IL, United States) and multiple holes (∼1 × 1 mm^2) were opened above cerebellar vermis. According to stereotaxic coordinates (bregma: anteroposterior, −5.5 mm; mediolateral, −0.5 mm; dorsoventral, −1.2 mm), a Semliki Forest virus (SFV) solution (500 nl; 2.3E6 FFU/ml) containing mCherry or GFP was injected into lobules IV-V with the pressure of a glass pipette (30 μm in diameter). After injection, animals were put on an electric blanket for more than 30 min for recovery from the anesthesia, and then returned to their cages.

Injected animals were decapitated within 18 h after viral infection and cerebella were sectioned (20 μm). Optical sections were collected on a confocal microscope and analyzed using Imaris 9.0 (Bitplane, Concord, MA, United States). The z-distance between crossing branches was calculated from 3D reconstructions. Any two branches crossing over each other were marked and counted manually in z-projections. The number of self-crossing, total number of dendritic branches, and total dendrite length were calculated from 3D reconstruction according to previous work (Gibson et al., 2014). Total dendrite area was calculated from 2D reconstruction using Image-Pro Plus 6.0 (Media Cybernetics, Rockville, MD, United States).

Rotarod Test

Rotarod test was performed as previously described (Zhou et al., 2017). After the habituation to rotarod, N-Cre;$MEA6^{F/F}$ mice (P19-21) and P-Cre;$Mea6^{F/F}$ mice (2 month) were tested twice a day at a time interval of 8 h for 4 consecutive days. In each session, the velocity of rotation increased at a constant acceleration of 9 rpm/min starting from 5 rpm. Given the short lifetime, N-Cre;$Mea6^{F/F}$ mice at P19-21 were put on the rotarod at a fixed 20 rpm and the spent time on the rotarod was measured.

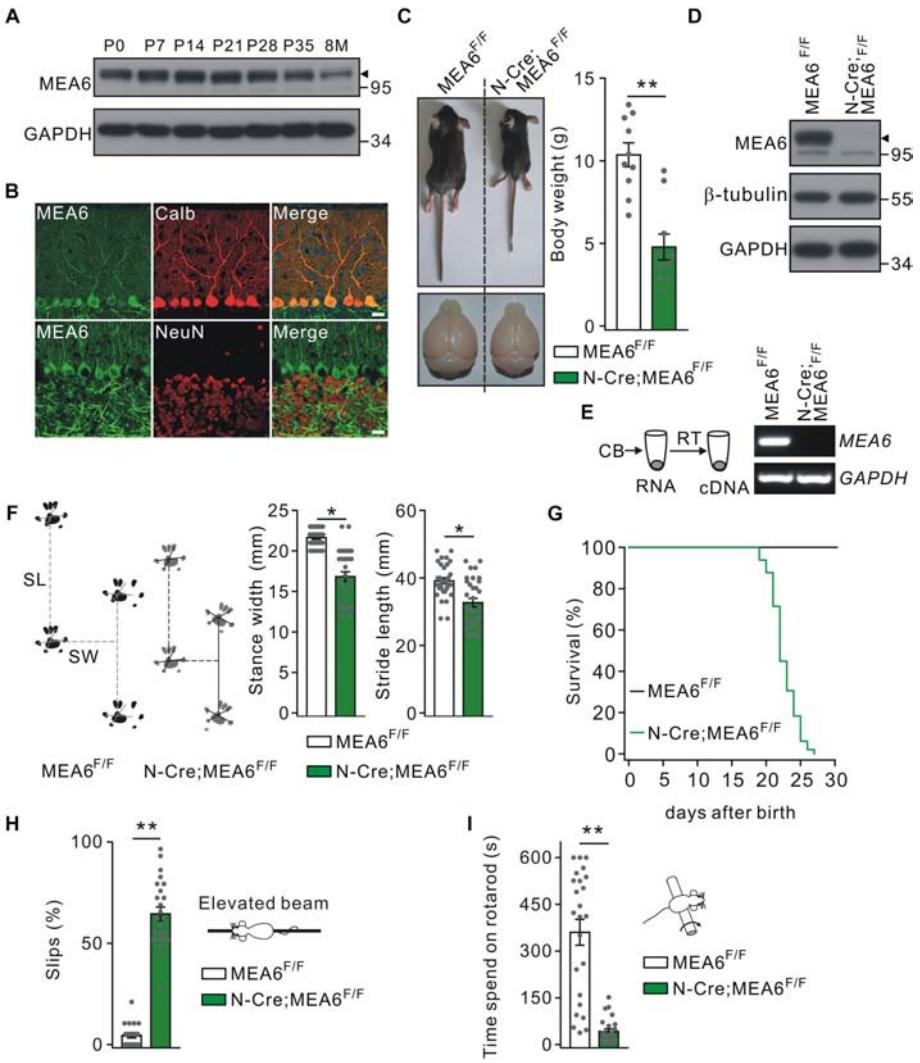

FIGURE 1 | Nestin-Cre;MEA6$^{F/F}$ mice display defects in motor performance. **(A)** MEA6 expression in the mouse cerebellum at different stages. Equal amounts of protein from cerebellar tissues were loaded onto SDS–PAGE and analyzed by Western blots using antibodies against MEA6 and GAPDH. The black triangle shows the bands of MEA6 protein. The experiment was performed three times. **(B)** Immunohistochemical staining for MEA6 (green), calbindin (Calb, red), and NeuN (red) in the cerebella from control mice. Scale bars: 20 μm. **(C)** The pictures of bodies and brains of MEA6$^{F/F}$ and N-Cre;MEA6$^{F/F}$ at P21. Average body weights were 10.4 ± 0.8 g (MEA6$^{F/F}$; n = 10 mice) and 4.8 ± 1.1 g (N-Cre;MEA6$^{F/F}$; n = 10 mice). Gray dots indicate individual data points. Unpaired t-test, $^{**}p < 0.01$. **(D)** Western blot detection of MEA6 expression in MEA6$^{F/F}$ and N-Cre;MEA6$^{F/F}$ mice (P21). The black triangle shows the band of MEA6 protein. **(E)** The cerebella (CB) of MEA6$^{F/F}$ and N-Cre;MEA6$^{F/F}$ mice (P21) were extracted in centrifuge tubes and subjected to RT-PCR. The electrophoresis of MEA6 (157 bp) and GAPDH (233 bp) is show in the right (n = 5 trials from one pair of mice). **(F)** Footprints of hind paws of MEA6$^{F/F}$ and N-Cre;MEA6$^{F/F}$ mice. The statistics shows abnormal gait with a shorter stride width (SW) and stance length (SL) in N-Cre;MEA6$^{F/F}$ (SW: 16.8 ± 0.8 mm, unpaired t-test, $^{*}p < 0.05$. SL: 32.7 ± 1.3 mm, unpaired t-test, $^{*}p < 0.05$. n = 32 trials from 5 mice), compared to MEA6$^{F/F}$ mice (SW: 21.6 ± 0.2 mm. SL: 39.1 ± 0.9 mm. n = 68 trials from 6 mice). Gray dots indicate individual data points. **(G)** Kaplan-Meier survival curves of MEA6$^{F/F}$ (n = 45 mice) and N-Cre;MEA6$^{F/F}$ mice (n = 49 mice). **(H)** The percentages of hindpaw slips during runs on an elevated horizontal beam. MEA6$^{F/F}$: 4.3 ± 1.0% (n = 24 trials from 6 mice). N-Cre;MEA6$^{F/F}$: 64.9 ± 4.8% (n = 24 trials from 6 mice). Gray dots indicate individual data points. Unpaired t-test, $^{**}p < 0.001$. **(I)** The time spent on the rotarod with a fixed speed for MEA6$^{F/F}$ and N-Cre;MEA6$^{F/F}$ mice at P19-21. MEA6$^{F/F}$: 359 ± 62 s (n = 24 trials from 6 mice); N-Cre;MEA6$^{F/F}$: 41 ± 8 s (n = 24 trials from 6 mice). Gray dots indicate individual data points. Unpaired t-test, $^{**}p < 0.001$.

Elevated Beam Test

This test was performed according to previous work (Hartmann et al., 2014; Zhou et al., 2017). The movement of mice on a round plastic beam (length 50 cm and diameter 1 cm) 40 cm above a surface with bedding was recorded and analyzed. The percentage of steps with hindpaw slips during runs on the beam was calculated.

Foot Print Test

To evaluate mice's walking gait we used footprint test according to previous work (Wang et al., 2017). Mice hindpaws were painted with non-toxic ink, and they were allowed to freely traverse a clear plexiglass tunnel (100 × 10 × 10 cm), with a sheet of white absorbent paper (100 × 10 cm) placed at the bottom of the track and a darkened cage at the end of the tunnel to encourage the

mouse to run toward a dark and safe environment. The resulting tracks provided the spatial relationship of consecutive footfalls, from which the stride length and stance width were measured. Measurements for three-step cycles were averaged, considering a cycle as the distance from one pair of hind prints to the next. Footprints at the start and the end of the tunnel were excluded from the analysis as they corresponded to the initiation and termination of the movement.

Statistical Analysis

Data were analyzed using GraphPad Prism 6.0 (GraphPad Software, San Diego, CA, United States), Excel 2003 (Microsoft, Seattle, WA, United States), and Igor Pro 6.0 (Wavemetrics, Lake Oswego, OR, United States). Data analysts were blind to experimental conditions until the data were integrated. Standard deviations for controls were calculated from the average of all control data. Statistical difference was determined using two-sided unpaired Student's *t*-test. The accepted level of significance was $p < 0.05$. *n* represents the number of preparations, cells, or animals. Data are presented as mean ± SEM.

RESULTS

MEA6 Deletion in the Cerebellum Impairs Motor Performance

The expression of MEA6 in the cerebellum was prominent and constant at postnatal stages but degraded a little after 8 month (**Figure 1A**). The expression pattern of MEA6 in the cerebellum was further examined using double immunostaining with cell-specific markers, showing that MEA6 was abundantly expressed in PCs and granule cells (**Figure 1B**). It should be noted that MEA6 antibody might be not so appropriate for staining because of its impurity. To assess the roles of MEA6 in the cerebellum, we generated conditional knockout of MEA6 in the brain by mating MEA6$^{F/F}$ mice with N-Cre transgenic mice, which affected MEA6 expression in most neural cells, including PCs, granule cells and glia. Compared with the control MEA6$^{F/F}$ mice, body weight and cerebellar size were significantly decreased in N-Cre;MEA6$^{F/F}$ mice (**Figure 1C**). The knockout of MEA6 in N-Cre;MEA6$^{F/F}$ mice was confirmed by Western blot (**Figure 1D**) and RT-PCR (**Figure 1E**) assays. N-Cre;MEA6$^{F/F}$ mice showed abnormal limb-clasping reflex in tail suspension test, in consistent with previous work (Zhang et al., 2018), and walked abnormally with shorter hindlimb stride length and stance width (**Figure 1F**), which might be related to their smaller body size. In fact, all N-Cre;MEA6$^{F/F}$ mice died before P28 (**Figure 1G**). Besides these degenerative phenotypes, we found that N-Cre;MEA6$^{F/F}$ mice displayed defective motor performance: (1) They performed poorly when walking on a narrow elevated beam with a remarkably higher number of hind-paw slips (**Figure 1H**); (2) They spent dramatically less time on the rotating rod in rotarod test (**Figure 1I**). These results indicate that MEA6 plays important roles in brain development.

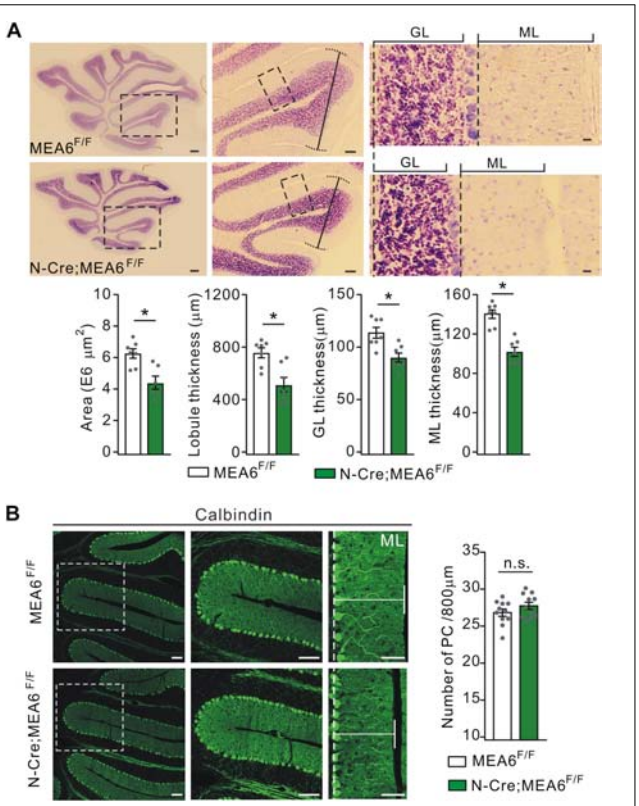

FIGURE 2 | Shrunken lobules in N-Cre;MEA6$^{F/F}$ mice. **(A)** The H&E staining of sagittal cerebellar sections from MEA6$^{F/F}$ and N-Cre;MEA6$^{F/F}$ mice at P25. The middle panel (Scale bars: 100 μm) is the higher magnification of left panel (Scale bars: 200 μm) and the right panel (Scale bars: 10 μm) is the higher magnification of middle panel, as indicated by black dashed boxes. Cerebellar area: 6.3 ± 0.4 E6 μm^2 (MEA6$^{F/F}$; $n = 7$ mice) and 4.5 ± 0.7 E6 μm^2 (N-Cre;MEA6$^{F/F}$; $n = 6$ mice), unpaired *t*-test, $^*p < 0.05$. Lobule III thickness: 758 ± 58 μm (MEA6$^{F/F}$; $n = 7$ mice) and 518 ± 71 μm (N-Cre;MEA6$^{F/F}$; $n = 7$ mice), unpaired *t*-test, $^*p < 0.05$. Thickness of granule cell layer (GL; lobule III): 110 ± 5 μm (MEA6$^{F/F}$; $n = 7$ mice) and 90 ± 4 μm (N-Cre;MEA6$^{F/F}$; $n = 7$ mice), unpaired *t*-test, $^*p < 0.05$. Thickness of molecular layer (ML; lobule III): 141 ± 4 μm (MEA6$^{F/F}$; $n = 7$ mice) and 101 ± 4 μm (N-Cre;MEA6$^{F/F}$; $n = 7$ mice), unpaired *t*-test, $^*p < 0.05$. Gray dots indicate individual data points. **(B)** The calbindin staining in MEA6$^{F/F}$ and N-Cre;MEA6$^{F/F}$ mice (P25), indicating that the number and arrangement of PCs are not changed by the deletion of MEA6. Average numbers of PCs per 800 μm were 26.8 ± 0.5 (MEA6$^{F/F}$; $n = 11$ mice) or 27.7 ± 0.5 (N-Cre;MEA6$^{F/F}$; $n = 11$ mice). Gray dots indicate individual data points. Unpaired *t*-test, $p > 0.05$ (n.s.).

MEA6 Deletion Reduces the Thicknesses of Lobules, Granule Cell Layer, and Molecular Layer

To examine the roles of MEA6 in the development of the cerebellum, the morphogenesis of N-Cre;MEA6$^{F/F}$ cerebella (P25) was observed in sagittal sections. While H&E staining showed that folia formation was grossly normal, there was an apparent reduction in the area of whole cerebellum and the thickness of lobules (**Figure 2A**). The averages of both area and thickness of lobule III shrunk by almost 60% in N-Cre;MEA6$^{F/F}$ mice compared to MEA6$^{F/F}$ mice (**Figure 2A**). Another phenotype was

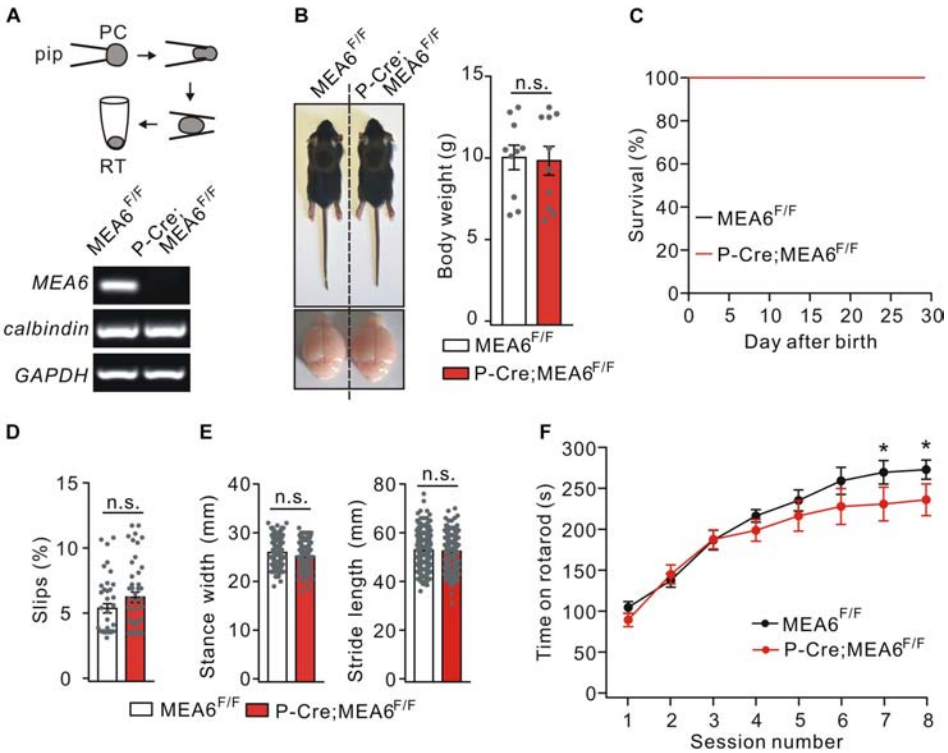

FIGURE 3 | The deletion of MEA6 in PCs does not affect gait but impairs motor learning. **(A)** PC contents of MEA6$^{F/F}$ and N-Cre;MEA6$^{F/F}$ mice (P21) were harvested using glass micropipettes (pip, OD 2 μm) and placed in centrifuge tubes. The contents collected from 10 cells were then subjected to RT-PCR. The electrophoresis of MEA6 (157 bp), calbindin (184 bp), and GAPDH (233 bp) is show in the lower panel (n = 5 trials). **(B)** Pictures of bodies and brains of MEA6$^{F/F}$ and P-Cre;MEA6$^{F/F}$ at P21. Average body weights were 10.4 ± 0.8 g (MEA6$^{F/F}$; n = 10 mice) and 10.2 ± 1.0 g (P-Cre;MEA6$^{F/F}$; n = 10 mice). Gray dots indicate individual data points. Unpaired t-test. **(C)** Kaplan-Meier survival curves of MEA6$^{F/F}$ (n = 15 mice) and P-Cre;MEA6$^{F/F}$ mice (n = 15 mice). **(D)** The percentages of hindpaw slips during runs on an elevated horizontal beam. MEA6$^{F/F}$: 5.3 ± 0.3% (n = 40 trials from 6 mice). P-Cre;MEA6$^{F/F}$: 6.2 ± 0.5% (n = 45 trials from 6 mice). Gray dots indicate individual data points. Unpaired t-test, $p > 0.05$. **(E)** The statistics of footprints of MEA6$^{F/F}$ and P-Cre;MEA6$^{F/F}$ mice shows normal gait with unchanged stride width (SW) and stance length (SL) in P-Cre;MEA6$^{F/F}$ (SW: 25.9 ± 0.4 mm, unpaired t-test, p = 0.69; SL: 45.4 ± 1.0 mm, unpaired t-test, p = 0.41; n = 172 trials from 16 mice), compared to MEA6$^{F/F}$ mice (SW: 25.2 ± 0.2 mm; SL: 44.7 ± 0.8 mm; n = 197 trials from 16 mice). Gray dots indicate individual data points. **(F)** Time spent on the accelerating rotarod for MEA6$^{F/F}$ (n = 8 mice) and P-Cre;MEA6$^{F/F}$ mice (n = 8 mice) at P60. Unpaired t-test, $^*p < 0.05$.

that the thicknesses of granule cell layer (GCL) and molecular layer (ML) were much reduced (lobule III; **Figure 2A**), resulting in an increased cell density in GCL of N-Cre;MEA6$^{F/F}$ mice.

Due to the remarkable expression of MEA6 in PCs (**Figure 1B**), we examined whether PC layer (PCL) is changed by the deletion of Mea6 in N-Cre;MEA6$^{F/F}$ mice. Unexpectedly, calbindin staining showed no abnormality in PCL, as the number and arrangement of PCs were comparable between N-Cre;MEA6$^{F/F}$ and MEA6$^{F/F}$ mice (**Figure 2B**). Still, we found that the dendritic branch of PCs was much reduced (**Figure 2B**), consistent with the reduced thickness of ML shown in **Figure 2A**.

PC-Specific Deletion of MEA6 Deletion Impairs Motor Learning but Not Walking Gait

To determine if motor defects in N-Cre;MEA6$^{F/F}$ mice are caused by PC abnormality and to study the function of MEA6 in PCs, MEA6$^{F/F}$ mice were mated with P-Cre transgenic mice. The knockout of MEA6 was confirmed by single-cell RT-PCR assay, showing that MEA6 mRNA was absent in P-Cre;MEA6$^{F/F}$ mouse PCs (**Figure 3A**). Different from N-Cre;MEA6$^{F/F}$ mice, P-Cre;MEA6$^{F/F}$ mice had no defects in the body and brain size (**Figure 3B**). Meanwhile, the lifetime of P-Cre;Mea6$^{F/F}$ mice was as long as that of MEA6$^{F/F}$ mice (**Figure 3C**). Regarding motor behavior, P-Cre;MEA6$^{F/F}$ mice did not show increased hind-paw slips during elevated beam test (**Figure 3D**) and had normal hindlimb stride length and stance width during the footprint test (**Figure 3E**), suggesting that PC deletion of MEA6 does not affect gait and that abnormal stance of N-Cre;Mea6$^{F/F}$ mice is related to smaller body size. In the accelerating rotarod test, P-Cre;MEA6$^{F/F}$ mice showed improvements as the sessions went by, but their time staying on the rod after six sessions was slightly reduced compared with that of controls (**Figure 3F**), implicating that MEA6 deficiency in PCs might impair motor learning.

MEA6 Deficiency in PCs Does Not Affect Cyto-Architecture

We continued to examine the morphogenesis of P-Cre;MEA6$^{F/F}$ cerebella at P21. Using Nissl staining of sagittal sections, we found

that the cyto-architecture of cerebella in P-Cre;MEA6$^{F/F}$ mice, including folia formation, the area of cerebella, the thickness of lobules, GCL thickness, and ML thickness, were not changed compared with those in MEA6$^{F/F}$ mice, as measured in lobule IV (**Figure 4A**). We also examined PCL in P-Cre;MEA6$^{F/F}$ mice at both P21 and P60 using calbindin staining. Similar to N-Cre;MEA6$^{F/F}$ mice, we failed to find any abnormality in PCL at two ages, shown by the unchanged number and arrangement of PCs (**Figure 4B**). These data indicate that cerebellar cyto-architecture grossly keeps intact in P-Cre;MEA6$^{F/F}$ mice.

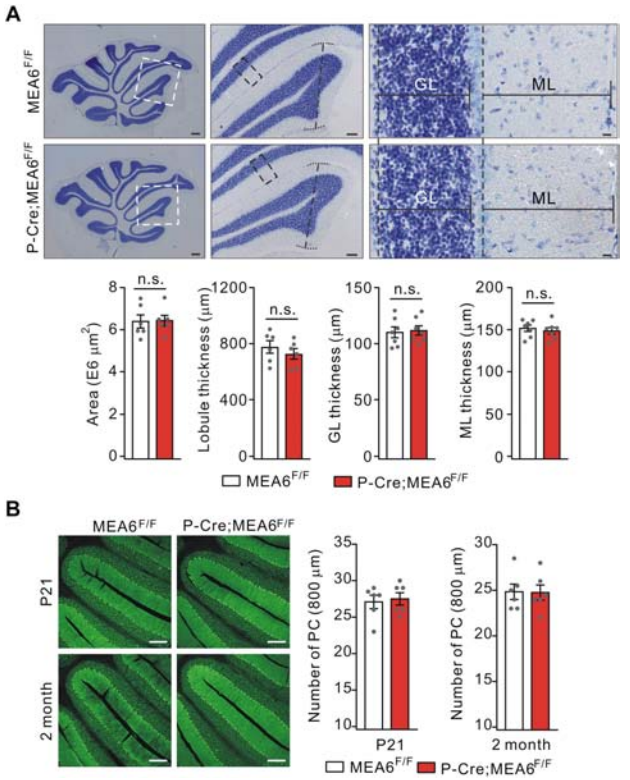

FIGURE 4 | Lobular formation is normal in P-Cre;MEA6$^{F/F}$ mice. **(A)** Nissl staining of cerebellar sections from MEA6$^{F/F}$ and P-Cre;MEA6$^{F/F}$ mice at P25. The middle panel (Scale bars: 100 μm) is the higher magnification of left panel (Scale bars: 200 μm) and the right panel (Scale bars: 10 μm) is the higher magnification of middle panel, as indicated by dashed boxes and lines. Cerebellar area: 6.4 ± 0.4 E6 μm^2 (MEA6$^{F/F}$; n = 6 mice) and 6.3 ± 0.3 E6 μm^2 (P-Cre;MEA6$^{F/F}$; n = 6 mice), unpaired t-test, $p > 0.05$. Lobule IV thickness: 774 ± 52 μm (MEA6$^{F/F}$; n = 6 mice) and 729 ± 48 μm (P-Cre;MEA6$^{F/F}$; n = 6 mice), unpaired t-test, $p > 0.05$. Thickness of granule cell layer (GL; lobule IV): 111 ± 5 μm (MEA6$^{F/F}$; n = 7 mice) and 112 ± 5 μm (P-Cre;MEA6$^{F/F}$; n = 7 mice), unpaired t-test, $p > 0.05$. Thickness of molecular layer (ML; lobule IV): 152 ± 5 μm (MEA6$^{F/F}$; n = 7 mice) and 149 ± 5 μm (P-Cre;MEA6$^{F/F}$; n = 7 mice), unpaired t-test, $p > 0.05$. Gray dots indicate individual data points. **(B)** The calbindin staining in MEA6$^{F/F}$ and P-Cre;MEA6$^{F/F}$ mice (P21 and P60), indicating that the number PCs is not changed by the deletion of MEA6. The average numbers of PCs per 800 μm were 27.1 ± 1.0 (MEA6$^{F/F}$; n = 6 mice), 27.4 ± 0.9 (P-Cre;MEA6$^{F/F}$; n = 6 mice), unpaired t-test, $p > 0.05$ at P21, and 24.8 ± 0.9 (MEA6$^{F/F}$; n = 6 mice), 24.7 ± 0.9 (P-Cre;MEA6$^{F/F}$; n = 6 mice), unpaired t-test, $p > 0.05$. Gray dots indicate individual data points. Scale bars: 200 μm.

PC Deletion of MEA6 Leads to Self-Crossing of PC Dendrites

Thus, a subsequent question is how PC deletion of MEA6 affects motor learning? It has been shown that neurons usually develop non-overlapping patterns by self-avoidance, an active process involving contact-dependent recognition and repulsion between neighboring sister branches (Grueber and Sagasti, 2010). Interestingly, the disruption in such self-avoidance is sufficient to produce a change in motor learning (Gibson et al., 2014). Therefore, we investigated if the motor behavior alteration in P-Cre;MEA6$^{F/F}$ mice is due to the self-avoidance of PC dendrites. To do so, we injected recombinant SFV expressing mCherry (SFV-mCherry) into the cerebellar midline of MEA6$^{F/F}$ and P-Cre;MEA6$^{F/F}$ mice at P21 (Jia et al., 2017), when PCs have developed nearly mature arbor morphology. This approach allowed us to visualize the entire dendritic arbor of single PCs because of the sparse expression of SFV (Jia et al., 2017). Single labeled PCs were imaged by confocal microscopy, traced and reconstructed from thin optical sections using Imaris software. In MEA6$^{F/F}$ mice, mCherry+ PC arbors consisted of smooth primary dendrites and spiny secondary branches restricted to and arborizing within ML (**Figure 5A**). These dendrites showed a strong tendency of self-avoidance with merely few crosses of sister dendrites (**Figure 5A**). In contrast, PCs with MEA6 deletion revealed extensive overlapping of sister branches (**Figure 5A**). The overlaps were mainly observed between high-order spiny branches and not between smooth primary dendrites (**Figure 5A**). By randomly selecting 100 μm^2 regions, which altogether cover ∼20% of each arbor (Gibson et al., 2014), we found that MEA6$^{F/F}$ PCs have only 0.9 ± 0.2 crosses per 100 μm^2 of dendrite length whereas P-Cre;MEA6$^{F/F}$ PCs have a significantly higher frequency of self-crossing with 2.5 ± 0.3 per 100 μm^2 (**Figure 5B**). Meanwhile, the number, total length, and total area of branches kept intact in P-Cre;MEA6$^{F/F}$ compared with MEA6$^{F/F}$ mice (**Figure 5B**). In addition, it was of interest to examine if abnormal self-avoidance of PC dendrites also occurs in N-Cre;MEA6$^{F/F}$ mice. We injected SFV expressing GFP (SFV-GFP) into the cerebellum to visualize the dendritic arbor of single PCs in MEA6$^{F/F}$ and N-Cre;MEA6$^{F/F}$ mice at P21. On one hand, PCs of N-Cre;MEA6$^{F/F}$ mice displayed extensive overlapping of sister branches (**Figure 5C**). On the other hand, total length and area of PC branches were decreased in N-Cre;MEA6$^{F/F}$ mice (**Figure 5C**). These results from P-Cre;MEA6$^{F/F}$ and N-Cre;MEA6$^{F/F}$ mice indicate that MEA6 is critical to self-avoidance of PC dendrites.

A number of cell-surface molecules have been identified to be required cell-autonomously for establishing non-overlapping dendrites in a 2D or 3D plane in mammals, including γ-Pcdh (Lefebvre et al., 2012), secreted molecule Slit2 and its receptor Robo2 (Gibson et al., 2014). Thus, we measured the protein expression of γ-Pcdh, Slit2, and Robo2, as well as PSD95, BDNF, and its receptor TrkB, which are responsible for the synaptogenesis and morphogenesis of PCs, respectively (Poo, 2011; Park and Poo, 2013; Choo et al., 2017). We found that the expressionlevels of γ-Pcdh, Robo2, BDNF, TrkB, and PSD95 were not changed by PC deletion of MEA6. In contrast, the

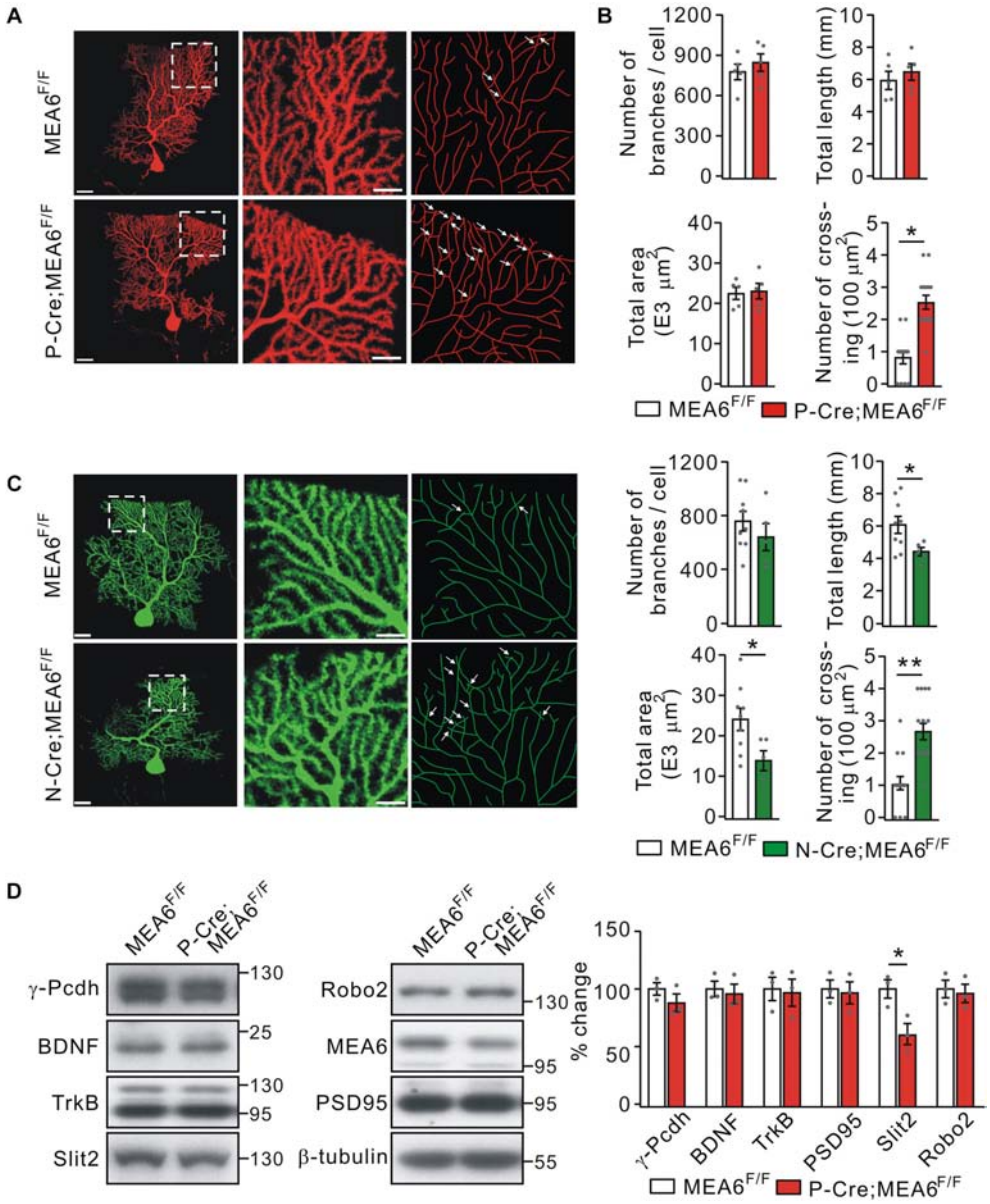

FIGURE 5 | Purkinje cell deletion of MEA6 impairs dendrite self-avoidance. **(A)** PCs from MEA6$^{F/F}$ and P-Cre;MEA6$^{F/F}$ mice (P21) are shown by z-projections of confocal images (left and middle panels) or skeletonized reconstructions (right panel). High magnification images shown in the middle panel correspond to the respective boxed regions in the left panel. White arrows indicate self-crossings. Scale bars: 50 μm (left panel) and 10 μm (middle panel). **(B)** Quantification of number of branches, total dendrite length, total area of dendritic arbor, and number of self-crossing per 100 μm^2 of dendrite area of labeled mCherry-expressing MEA6$^{F/F}$ (n = 5 from 5 mice) and P-Cre;MEA6$^{F/F}$ (n = 5 from 5 mice) PCs. Number of branches: 776 ± 63 per cell (MEA6$^{F/F}$) and 845 ± 70 per cell (P-Cre;MEA6$^{F/F}$), unpaired t-test, $p > 0.05$. Total dendrite length: 6.0 ± 0.6 mm (MEA6$^{F/F}$) and 6.5 ± 0.5 mm (P-Cre;MEA6$^{F/F}$), unpaired t-test, $p > 0.05$. Total area: 2.2 ± 0.2 E4 μm^2 (MEA6$^{F/F}$) and 2.4 ± 0.2 E4 μm^2 (P-Cre;MEA6$^{F/F}$), unpaired t-test, $p > 0.05$. Number of crossing: 0.9 ± 0.2 per 100 μm^2 (MEA6$^{F/F}$) and 2.5 ± 0.3 per 100 μm^2 (P-Cre;MEA6$^{F/F}$), unpaired t-test, $^*p < 0.05$. Gray dots indicate individual data points. **(C)** PCs from MEA6$^{F/F}$ and N-Cre;MEA6$^{F/F}$ mice (P21) are shown by z-projections of confocal images (left and middle panels) or skeletonized reconstructions (right panel). High magnification images shown in the middle correspond to the respective boxed regions in the left. White arrows indicate self-crossings. Scale bars: 50 μm (left panel) and 10 μm (middle panel). Bar graphs show the quantification of number of branches, total dendrite length, total area of dendritic arbor, and number of self-crossing per 100 μm^2 of dendrite area of MEA6$^{F/F}$ (n = 9 from 9 mice) and N-Cre;MEA6$^{F/F}$ (n = 5 from 9 mice) PCs. Number of branches: 752 ± 77 per cell (MEA6$^{F/F}$) and 639 ± 112 per cell (N-Cre;MEA6$^{F/F}$), unpaired t-test, $p > 0.05$. Total dendrite length: 6.0 ± 0.5 mm (MEA6$^{F/F}$) and 4.4 ± 0.3 mm (N-Cre;MEA6$^{F/F}$), unpaired t-test, $^*p < 0.05$. Total area: 2.4 ± 0.3 E4 μm^2 (MEA6$^{F/F}$) and 1.4 ± 0.3 E4 μm^2 (N-Cre;MEA6$^{F/F}$), unpaired t-test, $^*p < 0.05$. Number of crossing: 1.0 ± 0.2 per 100 μm^2 (MEA6$^{F/F}$) and 2.6 ± 0.3 per 100 μm^2 (N-Cre;MEA6$^{F/F}$), unpaired t-test, $^{**}p < 0.01$. Gray dots indicate individual data points. **(D)** Protein levels of γ-Pcdh, BDNF, TrkB, Slit2, Robo2, MEA6, and PSD95 in the MEA6$^{F/F}$ and P-Cre;MEA6$^{F/F}$ cerebellum at P20 were analyzed by Western blotting. The results were obtained from 3 pairs of mice. β-tubulin was used as the loading control. Gray dots indicate individual data points. $^*p < 0.05$.

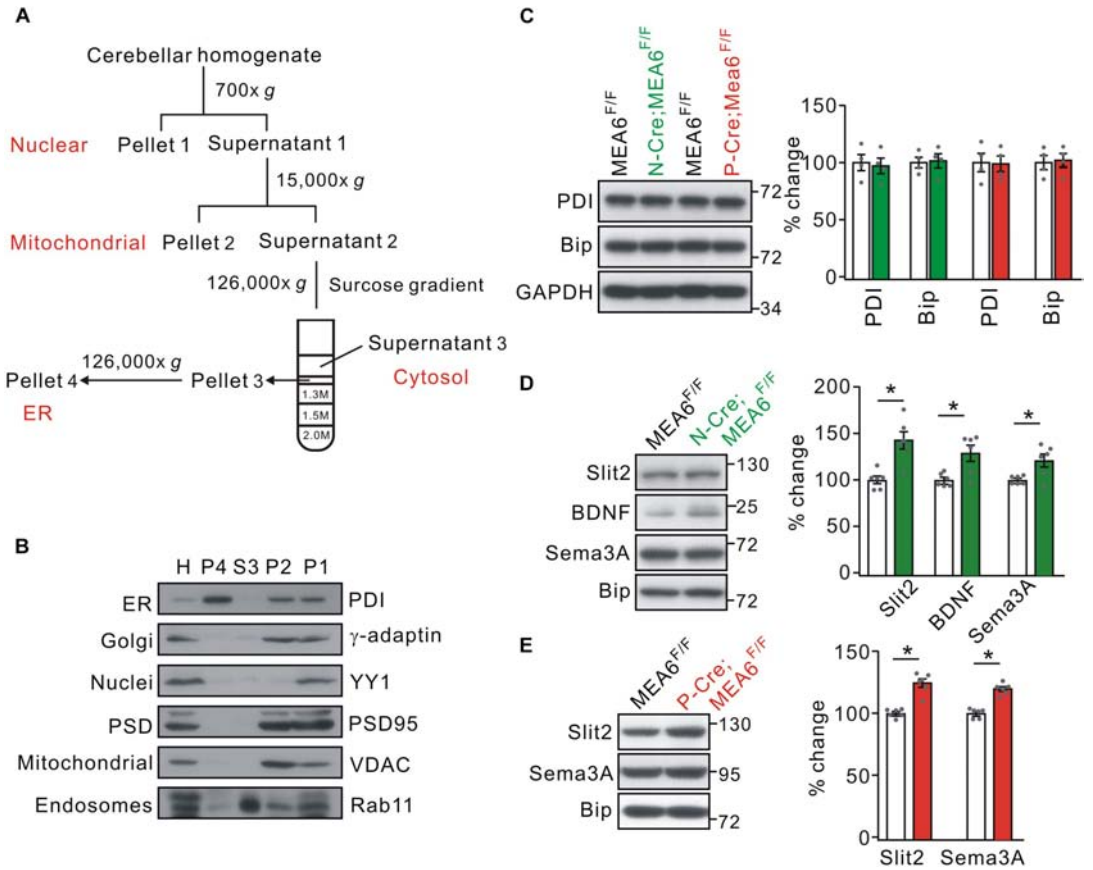

FIGURE 6 | MEA6 deficiency affects the transport of Slit2 from ER to Golgi apparatus. **(A)** A cartoon illustrating the procedures for the purification of subcellular organelles. More details are given in Experimental Procedures. **(B)** The purification of ER was confirmed by the Western blotting assay of marker proteins, including PDI, γ-adaptin, YY1, PSD95, VDAC, and Rab11. H, P1, P2, S3 and P4 refer to homogenate, pellet 1, pellet 2, supernatant 3, and pellet 4, respectively. The experiment was performed using 3 WT mice. **(C)** The protein levels of PDI and Bip were not changed in both N-Cre;MEA6$^{F/F}$ and P-Cre;MEA6$^{F/F}$ mice compared with corresponding control MEA6$^{F/F}$ mice. GAPDH was used as the loading control. The results were obtained from 4 pairs of mice. Gray dots indicate individual data points. **(D)** Western blotting assay of Slit2, BDNF, and Sema3A in ER purified from MEA6$^{F/F}$ and N-Cre;MEA6$^{F/F}$ mice cerebellum at P21. Bip was used as the internal control. Slit2: 100 ± 4% (MEA6$^{F/F}$) and 140 ± 11% (N-Cre;MEA6$^{F/F}$). BDNF: 100 ± 2% (MEA6$^{F/F}$) and 130 ± 10% (N-Cre;MEA6$^{F/F}$). Semaphorin 3A (Sema3A): 100 ± 2% (MEA6$^{F/F}$) and 121 ± 8% (N-Cre;MEA6$^{F/F}$). The results were obtained from 6 pairs of mice. Gray dots indicate individual data points. Unpaired *t*-test, $^*p < 0.05$. **(E)** Western assay of Slit2 and Sema3A in ER purified from MEA6$^{F/F}$ and P-Cre;MEA6$^{F/F}$ mice cerebellum at P21. Bip was used as internal control. Slit2: 100 ± 1% (MEA6$^{F/F}$) and 122 ± 4% (P-Cre;MEA6$^{F/F}$). Sema3A: 100 ± 1% (MEA6$^{F/F}$) and 120 ± 2% (P-Cre;MEA6$^{F/F}$). The results were obtained from 6 pairs of mice. Gray dots indicate individual data points. Unpaired *t*-test, $^*p < 0.05$.

expression of Slit2 was significantly decreased in P-Cre;MEA6$^{F/F}$ mice compared with MEA6$^{F/F}$ mice (**Figure 5D**). These results implicate that MEA6 deletion causes the self-crossing of dendrites via the downregulation of Slit2.

Slit2 Transport Is Interrupted in P-Cre;MEA6$^{F/F}$ Mice

Using tandem mass tag technique, Zhang et al. (2018) show that MEA6 is involved in protein trafficking between ER and Golgi apparatus in cultured cortical neurons, which might explain the reduced expression of Slit2 in P-Cre;MEA6$^{F/F}$ mice. We therefore inspected whether MEA6 ablation affects the forward protein transport in the cerebellum, taking advantage of a series of centrifugations to purify organelles (**Figure 6A**; also see Hammond et al., 2012). The purification of ER fraction was confirmed with distinct organelle markers, PDI (ER), γ-adaptin (Golgi apparatus), YY1 (nuclei), PSD95 (synapse), VDAC (mitochondria), and Rab11 (endosome) (**Figure 6B**). We first examined whether ER was affected by MEA6 deficiency by comparing the marker molecules for ER, PDI and Bip (Haefliger et al., 2011; Shimizu et al., 2017; McLelland et al., 2018). Our results indicated that both molecules were not changed in N-Cre;MEA6$^{F/F}$ and P-Cre;MEA6$^{F/F}$ mice compared with corresponding control mice (**Figure 6C**), suggesting that ER is not affected by PC deletion of MEA6. Second, we compared the subcellular expression of a number of secretary molecules, including Slit2, BDNF, and Semaphorin 3A between MEA6$^{F/F}$ and N-Cre;MEA6$^{F/F}$ mice. Interestingly, our results showed that the expression levels of these secretary molecules increased in ER fraction, which was indexed by the expression of Bip (**Figure 6D**). Finally, we compared the subcellular expression of Slit2 and

Semaphorin 3A between MEA6$^{F/F}$ and P-Cre;MEA6$^{F/F}$ mice. Similar to the results obtained from N-Cre;MEA6$^{F/F}$ mice, we found that the expression levels of Slit2 and Semaphorin 3A significantly increased in the ER fraction (**Figure 6E**). These results indicate that the deletion of MEA6 tethers secretary molecules in ER and then decreases their expression.

DISCUSSION

Meningioma expressed antigen 6 is important for the secretion of proteins including collagen, VLDL, and insulin (Saito et al., 2011, 2014; Wang et al., 2016; Fan et al., 2017). It also regulates the transport of cellular components in neurons, and its deficiency causes abnormal development in cerebral cortex (Zhang et al., 2018). In the present work, we provide new evidence for the functions of MEA6 in cerebellar development and motor behaviors by generating conditional knockout mice. We found that both N-Cre;MEA6$^{F/F}$ and P-Cre;MEA6$^{F/F}$ mice exhibit defects in cerebellar development and motor performance. N-Cre;MEA6$^{F/F}$ mice had a shrunken cerebellum and lobular layers and impaired gait behavior at P25, while P-Cre;MEA6$^{F/F}$ mice displayed extensive self-crossings of PC dendrites and impaired motor learning. It was apparent that the deletion of MEA6 driven by Nestin-Cre produced more profound influence on the development and the function of the cerebellum, suggesting that MEA6 deletion may affect other cells except PCs in the cerebellum. A phenotype, which both conditional knockout mice shared in common, was that the transport of Slit2, BDNF and Semaphorin 3A was interrupted and thus these proteins were tethered in ER. Combined with previous work showing impaired protein transport from ER to Golgi apparatus and the fragmentation of Golgi structure in cultured cortical neurons (Zhang et al., 2018), our result might explain why the development of PCs and the cerebellum was impaired in these conditional knockout mice. In addition, we found that Slit2 in cerebellar extracts of P-Cre;MEA6$^{F/F}$ mice was reduced, which might be ascribed to the retention of Slit2 in ER. Similar findings have been reported, i.e., total expression of AMPA receptors (AMPARs) is reduced because AMPARs are trapped in ER by Stargazin knockout (Tomita et al., 2003). Based on our findings showing the essential roles of MEA6 on the development and function of the cerebellum at early stage, it can be deduced that the absence or the loss-of-function of MEA6 may lead to severe neurodegeneration not only in the cerebellum but also in whole brain. Therefore, our study provides more insights into the pathogenesis of Fahr's syndrome, which includes neurological and movement disorders (Oliveira et al., 2007) and may be associated with MEA6 mutation (Lemos et al., 2011).

Meningioma expressed antigen 6 regulates ER-Golgi apparatus trafficking through the regulation of COPII complex formation in secretary cells and neurons (Saito et al., 2011, 2014; Wang et al., 2016; Fan et al., 2017; Zhang et al., 2018). COPII is composed of a small GTPase (SAR1) and coat proteins (Antonny and Schekman, 2001; Lee and Miller, 2007; Miller and Schekman, 2013). Zhang et al. (2018) demonstrate that MEA6 together with SAR1 is enriched in neuronal dendritic branch and the deletion of MEA6 in neurons alters the proper function of COPII through the disruption of SAR1 activity, which results in the downregulation of postsynaptic molecules critical to dendritic outgrowth and synaptic formation, such as PSD95, TrkB, CamKII, and membrane receptors and ion channels. In the present work, we found that MEA6 ablation reduced the trafficking and expression of several secretary proteins, such Slit2, BDNF, and Semaphorin 3A, but had no effects on γ-Pcdh, Robo2, TrkB, and PSD95, implicating that MEA6 deficiency has more influence on secretary proteins but not membrane proteins. This inconsistency with previous work may be due to the different regions of brain observed in each study, although the present results were closer to those findings obtained from secretary cells (Saito et al., 2011, 2014; Wang et al., 2016; Fan et al., 2017). Future study of MEA6 in neurons would need to define its biological functions on protein trafficking.

It has been discovered that two molecular pathways, γ-Pcdh and Slit2/Robo2, independently control self-recognition and self-avoidance of PC dendritic branch (Lefebvre et al., 2012; Gibson et al., 2014). We found that MEA6 ablation in PCs impaired Slit2 trafficking from ER to Golgi apparatus and reduced the expression of Slit2. In comparison, the transport and expression of Robo2 and γ-Pcdh were not affected. The impaired self-avoidance of PC dendrites in P-Cre;MEA6$^{F/F}$ mice may be caused by the reduced expression of Slit2, because the knockout of either Slit2 or Robo2 is sufficient to induce self-crossings in PCs (Gibson et al., 2014). Meanwhile, P-Cre;MEA6$^{F/F}$ mice displayed slight defective in motor learning without any alteration in gait, consistent with previous finding that Robo2, but not Slit2, in PCs is associated with gait alterations (Gibson et al., 2014). In summary, our results confirm the critical roles of Slit2/Robo2 signaling in self-avoidance of PC dendrites and motor performance. Little is known about the consequences of disrupting self-avoidance for circuit function or animal behavior, although the importance of local molecular interactions during dendritic development has been highlighted (Jan and Jan, 2010). PC dendritic branch is critical for integrating diverse synaptic inputs (Häusser et al., 2000) and normal motor behavior (Donald et al., 2008; Becker et al., 2009; Li et al., 2010; Sergaki et al., 2010). Interestingly, self-avoidance defect only occurs in spiny distal branches of parallel fiber, but not climbing fibers that only innervate with primary dendrites (Gibson et al., 2014), suggesting that the alteration in parallel fiber-PC innervations may underlie such motor deficits. We hypothesize that MEA6 may alter synapse distribution across branches or their connectivity transmission and further change the patter of neural circuits, which needs further investigation by electron microscopy and electrophysiology.

CONCLUSION

The deletion of MEA6 causes defects in cerebellar development and motor performance, including shrunken lobules, extensive self-crossings of PC dendrites, abnormal gait and motor learning.

All these phenotype may be associated with impaired transport of secretary proteins from ER to Golgi apparatus.

ETHICS STATEMENT

All experiments were approved by the Animal Experimentation Ethics Committee of Zhejiang University and specifically designed to minimize the number of animals used.

AUTHOR CONTRIBUTIONS

X-TW and YS designed the research and wrote the manuscript. X-TW, X-YC, F-XX, LZ, RZ, and K-YM performed the research. Z-HX provided the unpublished tools and techniques. X-TW, X-YC, and YS analyzed the data. All authors have read and approved the final manuscript.

FUNDING

This work was supported by the National Natural Science Foundation of China (81625006, 31820103005, and 31571051), Natural Science Foundation of Zhejiang Province (Z15C090001), and Chinese Ministry of Education Project 111 Program B13026 (YS).

ACKNOWLEDGMENTS

We thank the Core Facility of Zhejiang University, Institute of Neuroscience for technical assistance.

REFERENCES

Antonny, B., and Schekman, R. (2001). ER export: public transportation by the COPII coach. *Curr. Opin. Cell Biol.* 13, 438–443. doi: 10.1016/s0955-0674(00)00234-9

Becker, E. B., Oliver, P. L., Glitsch, M. D., Banks, G. T., Achilli, F., Hardy, A., et al. (2009). A point mutation in TRPC3 causes abnormal Purkinje cell development and cerebellar ataxia in moonwalker mice. *Proc. Natl. Acad. Sci. U.S.A.* 106, 6706–6711. doi: 10.1073/pnas.0810599106

Choo, M., Miyazaki, T., Yamazaki, M., Kawamura, M., Nakazawa, T., Zhang, J., et al. (2017). Retrograde BDNF to TrkB signaling promotes synapse elimination in the developing cerebellum. *Nat. Commun.* 8:195. doi: 10.1038/s41467-017-00260-w

Comtesse, N., Niedermayer, I., Glass, B., Heckel, D., Maldener, E., Nastainczyk, W., et al. (2002). MGEA6 is tumor-specific overexpressed and frequently recognized by patient-serum antibodies. *Oncogene* 21, 239–247. doi: 10.1038/sj.onc.1205005

Donald, S., Humby, T., Fyfe, I., Segonds-Pichon, A., Walker, S. A., Andrews, S. R., et al. (2008). P-Rex2 regulates Purkinje cell dendrite morphology and motor coordination. *Proc. Natl. Acad. Sci. U.S.A.* 105, 4483–4488. doi: 10.1073/pnas.0712324105

Fan, J., Wang, Y., Liu, L., Zhang, H., Zhang, F., Shi, L., et al. (2017). cTAGE5 deletion in pancreatic β cells impairs proinsulin trafficking and insulin biogenesis in mice. *J. Cell Biol.* 216, 4153–4164. doi: 10.1083/jcb.201705027

Geschwind, D. H., Loginov, M., and Stern, J. M. (1999). Identification of a locus on chromosome 14q for idiopathic basal ganglia calcification (Fahr disease). *Am. J. Hum. Genet.* 65, 764–772. doi: 10.1086/302558

Gibson, D. A., Tymanskyj, S., Yuan, R. C., Leung, H. C., Lefebvre, J. L., Sanes, J. R., et al. (2014). Dendrite self-avoidance requires cell-autonomous slit/robo signaling in cerebellar purkinje cells. *Neuron* 81, 1040–1056. doi: 10.1016/j.neuron.2014.01.009

Grueber, W. B., and Sagasti, A. (2010). Self-avoidance and tiling: Mechanisms of dendrite and axon spacing. *Cold Spring Harb. Perspect. Biol.* 2:a001750. doi: 10.1101/cshperspect.a001750

Haefliger, S., Klebig, C., Schaubitzer, K., Schardt, J., Timchenko, N., Mueller, B. U., et al. (2011). Protein disulfide isomerase blocks CEBPA translation and is up-regulated during the unfolded protein response in AML. *Blood* 117, 5931–5940. doi: 10.1182/blood-2010-08-304485

Hammond, J. C., Meador-Woodruff, J. H., Haroutunian, V., and McCullumsmith, R. E. (2012). AMPA receptor subunit expression in the endoplasmic reticulum in frontal cortex of elderly patients with schizophrenia. *PLoS One* 7:e39190. doi: 10.1371/journal.pone.0039190

Hartmann, J., Karl, R. M., Alexander, R. P., Adelsberger, H., Brill, M. S., Rühlmann, C., et al. (2014). STIM1 controls neuronal Ca2+ signaling, mGluR1-dependent synaptic transmission, and cerebellar motor behavior. *Neuron* 82, 635–644. doi: 10.1016/j.neuron.2014.03.027

Häusser, M., Spruston, N., and Stuart, G. J. (2000). Diversity and dynamics of dendritic signaling. *Science* 290, 739–744. doi: 10.1126/science.290.5492.739

Heckel, D., Brass, N., Fischer, U., Blin, N., Steudel, I., Türeci, O., et al. (1997). cDNA cloning and chromosomal mapping of a predicted coiled-coil proline-rich protein immunogenic in meningioma patients. *Hum. Mol. Genet.* 6, 2031–2041. doi: 10.1093/hmg/6.12.2031

Jan, Y. N., and Jan, L. Y. (2010). Branching out: mechanisms of dendritic arborization. *Nat. Rev. Neurosci.* 11, 316–328. doi: 10.1038/nrn2836

Jia, F., Miao, H., Zhu, X., and Xu, F. (2017). Pseudo-typed semliki forest virus delivers EGFP into neurons. *J. Neurovirol.* 23, 205–215. doi: 10.1007/s13365-016-0486-8

Kalniņa, Z., Silioà, K., Meistere, I., Zayakin, P., Rivosh, A., Abols, A., et al. (2008). Evaluation of T7 and lambda phage display systems for survey of autoantibody profiles in cancer patients. *J. Immunol. Methods* 334, 37–50. doi: 10.1016/j.jim.2008.01.022

Lee, M. C., and Miller, E. A. (2007). Molecular mechanisms of COPII vesicle formation. *Semin. Cell Dev. Biol.* 18, 424–434. doi: 10.1016/j.semcdb.2007.06.007

Lefebvre, J. L., Kostadinov, D., Chen, W. V., Maniatis, T., and Sanes, J. R. (2012). Protocadherins mediate dendritic self-avoidance in the mammalian nervous system. *Nature* 488, 517–521. doi: 10.1038/nature11305

Lemos, R. R., Oliveira, D. F., Zatz, M., and Oliveira, J. R. (2011). Population and computational analysis of the MGEA6 P521A variation as a risk factor for familial idiopathic basal ganglia calcification (Fahr's disease). *J. Mol. Neurosci.* 43, 333–336. doi: 10.1007/s12031-010-9445-7

Li, J., Gu, X., Ma, Y., Calicchio, M. L., Kong, D., Teng, Y. D., et al. (2010). Nna1 mediates Purkinje cell dendritic development via lysyl oxidase propeptide and NF-kappaB signaling. *Neuron* 68, 45–60. doi: 10.1016/j.neuron.2010.08.013

McLelland, G. L., Goiran, T., Yi, W., Dorval, G., Chen, C. X., Lauinger, N. D., et al. (2018). Mfn2 ubiquitination by PINK1/parkin gates the p97-dependent release of ER from mitochondria to drive mitophagy. *eLife* 20:7. doi: 10.7554/eLife.32866

Miller, E. A., and Schekman, R. (2013). COPII-A flexible vesicle formation system. *Curr. Opin. Cell Biol.* 25, 420–427. doi: 10.1016/j.ceb.2013.04.005

Moskowitz, M. A., Winickoff, R. N., and Heinz, E. R. (1971). Familial calcification of the basal ganglions: a metabolic and genetic study. *N. Engl. J. Med.* 285, 72–77. doi: 10.1056/NEJM197107082850202

Oliveira, J. R., Sobrido, M. J., Spiteri, E., Hopfer, S., Meroni, G., Petek, E., et al. (2007). Analysis of candidate genes at the IBGC1 locus associated with idiopathic basal ganglia calcification ("Fahr". Disease'). *J. Mol. Neurosci.* 33, 151–154. doi: 10.1007/s12031-007-0030-7

Park, H., and Poo, M. M. (2013). Neurotrophin regulation of neural circuit development and function. *Nat. Rev. Neurosci.* 14, 7–23. doi: 10.1038/nrn3379

Poo, M. M. (2011). Neurotrophins as synaptic modulators. *Nat. Rev. Neurosci.* 2, 24–32. doi: 10.1038/35049004

Saito, K., Yamashiro, K., Ichikawa, Y., Erlmann, P., Kontani, K., Malhotra, V., et al. (2011). cTAGE5 mediates collagen secretion through interaction with TANGO1 at endoplasmic reticulum exit sites. *Mol. Biol. Cell* 22, 2301–2308. doi: 10.1091/mbc.E11-02-0143

Saito, K., Yamashiro, K., Shimazu, N., Tanabe, T., Kontani, K., and Katada, T. (2014). Concentration of Sec12 at ER exit sites via interaction with cTAGE5 is required for collagen export. *J. Cell Biol.* 206, 751–762. doi: 10.1083/jcb.201312062

Saleem, S., Aslam, H. M., Anwar, M., Anwar, S., Saleem, M., Saleem, A., et al. (2013). Fahr's syndrome: literature review of current evidence. *Orphanet J. Rare Dis.* 8:156. doi: 10.1186/1750-1172-8-156

Sergaki, M. C., Guillemot, F., and Matsas, R. (2010). Impaired cerebellar development and deficits in motor coordination in mice lacking the neuronal protein BM88/Cend1. *Mol. Cell Neurosci.* 44, 15–29. doi: 10.1016/j.mcn.2010.01.011

Shimizu, A., Kaira, K., Yasuda, M., Asao, T., and Ishikawa, O. (2017). Clinical and pathological significance of ER stress marker (BiP/GRP78 and PERK) expression in malignant melanoma. *Pathol. Oncol. Res.* 23, 111–116. doi: 10.1007/s12253-016-0099-9

Tomita, S., Chen, L., Kawasaki, Y., Petralia, R. S., Wenthold, R. J., Nicoll, R. A., et al. (2003). Functional studies and distribution define a family of transmembrane AMPA receptor regulatory proteins. *J. Cell Biol.* 161, 805–816. doi: 10.1083/jcb.200212116

Wang, Y., Chen, Z. P., Zhuang, Q. X., Zhang, X. Y., Li, H. Z., Wang, J. J., et al. (2017). Role of corticotropin-releasing factor in cerebellar motor control and ataxia. *Curr. Biol.* 27, 2661–2669. doi: 10.1016/j.cub.2017.07.035

Wang, Y., Liu, L., Zhang, H., Fan, J., Zhang, F., Yu, M., et al. (2016). Mea6 controls VLDL transport through the coordinated regulation of COPII assembly. *Cell Res.* 26, 787–804. doi: 10.1038/cr.2016.75

Xie, Y. J., Zhou, L., Jiang, N., Zhang, N., Zou, N., Zhou, L., et al. (2015). Essential roles of leucine-rich glioma inactivated 1 in the development of embryonic and postnatal cerebellum. *Sci. Rep.* 5:7827. doi: 10.1038/srep07827

Zhang, F., Wang, Y., Wang, T., Yao, L., Lam, S. M., Huang, X., et al. (2018). cTAGE5/MEA6 plays a critical role in neuronal cellular components trafficking and brain development. *Proc. Natl. Acad. Sci. U.S.A.* 115, E9449–E9458. doi: 10.1073/pnas.1804083115

Zhou, J. H., Wang, X. T., Zhou, L., Zhou, L., Xu, F. X., Su, L. D., et al. (2017). Ablation of TFR1 in Purkinje cells inhibits mGlu1 trafficking and impairs motor coordination, but not autistic-like behaviors. *J. Neurosci.* 37, 11335–11352. doi: 10.1523/JNEUROSCI.1223-17.2017

Zhou, L., Yang, D., Wang, D. J., Xie, Y. J., Zhou, J. H., Zhou, L., et al. (2015). Numb deficiency in cerebellar Purkinje cells impairs synaptic expression of metabotropic glutamate receptor and motor coordination. *Proc. Natl. Acad. Sci. U.S.A.* 112, 15474–15479. doi: 10.1073/pnas.1512915112

Conflict of Interest Statement: The authors declare that the research was conducted in the absence of any commercial or financial relationships that could be construed as a potential conflict of interest.

The handling Editor is currently editing co-organizing a Research Topic with one of the authors YS, and confirms the absence of any other collaboration.

frontiers in Cellular Neuroscience

ORIGINAL RESEARCH
published: 17 December 2019
doi: 10.3389/fncel.2019.00539

Rack1 Controls Parallel Fiber–Purkinje Cell Synaptogenesis and Synaptic Transmission

Haihong Yang[1,2†], Chaojuan Yang[3†], Qian Zhu[1], Mengping Wei[3], Ying Li[1], Juanxian Cheng[1], Fengjiao Liu[1], Yan Wu[1], Jiyan Zhang[4], Chen Zhang[3] and Haitao Wu[1,5,6]**

[1] Department of Neurobiology, Beijing Institute of Basic Medical Sciences, Beijing, China, [2] Department of Anesthesiology, The General Hospital of Western Theater Command, Chengdu, China, [3] Department of Neurobiology, School of Basic Medical Sciences, Capital Medical University, Beijing, China, [4] Department of Neuroimmunology and Antibody Engineering, Beijing Institute of Basic Medical Sciences, Beijing, China, [5] Chinese Institute for Brain Research, Beijing, China, [6] Key Laboratory of Neuroregeneration, Co-innovation Center of Neuroregeneration, Nantong University, Nantong, China

Purkinje cells (PCs) in the cerebellum receive two excitatory afferents including granule cells-derived parallel fiber (PF) and the climbing fiber. Scaffolding protein Rack1 is highly expressed in the cerebellar PCs. Here, we found delayed formation of specific cerebellar vermis lobule and impaired motor coordination in PC-specific Rack1 conditional knockout mice. Our studies further revealed that Rack1 is essential for PF–PC synapse formation. In addition, Rack1 plays a critical role in regulating synaptic plasticity and long-term depression (LTD) induction of PF–PC synapses without changing the expression of postsynaptic proteins. Together, we have discovered Rack1 as the crucial molecule that controls PF–PC synaptogenesis and synaptic plasticity. Our studies provide a novel molecular insight into the mechanisms underlying the neural development and neuroplasticity in the cerebellum.

Keywords: parallel fiber, Purkinje cell, Rack1, LTD, synaptic plasticity

OPEN ACCESS

Edited by:
Ying Shen,
Zhejiang University, China

Reviewed by:
Zhenyu Gao,
Erasmus Medical Center, Netherlands
De-Lai Qiu,
Yanbian University, China

****Correspondence:***
Chen Zhang
czhang@ccmu.edu.cn
Haitao Wu
wuht@bmi.ac.cn

† These authors have contributed equally to this work

Specialty section:
This article was submitted to Cellular Neurophysiology, a section of the journal Frontiers in Cellular Neuroscience

Received: *20 August 2019*
Accepted: *20 November 2019*
Published: *17 December 2019*

Citation:
Yang H, Yang C, Zhu Q, Wei M, Li Y, Cheng J, Liu F, Wu Y, Zhang J, Zhang C and Wu H (2019) Rack1 Controls Parallel Fiber–Purkinje Cell Synaptogenesis and Synaptic Transmission. Front. Cell. Neurosci. 13:539. doi: 10.3389/fncel.2019.00539

INTRODUCTION

The multiple functions of the brain depend on the precise communication between distinct types of neurons. Communication between neurons is achieved at synapses by the process of synaptic transmission within neuronal networks (Jones, 2005; Cohen and Greenberg, 2008). Therefore, deciphering the molecular mechanisms underlying the development and function of synapses is the key aspect of cellular and molecular neuroscience. Owing to the unique patterned foliation, typical "three-layer" cortex, and relatively simple cell types, the cerebellum serves as an ideal model for studying the development and function of synapses and brain circuits (Middleton and Strick, 1998).

As the only efferent neurons in the cerebellar cortex, Purkinje cells (PCs) receive two types of excitatory synaptic inputs: climbing fibers and parallel fibers (PFs), and integrate cortical information for the deep cerebellar nuclei (Brown et al., 2012; Duguid et al., 2015; Nietz et al., 2017). The interaction between climbing fiber and PF inputs into PCs is critical for motor learning (Ito, 2002, 2006). Particularly, PF–PC synapses are the fundamental connections in the cerebellar cortex, which play an essential role in cerebellar synaptic plasticity and motor coordination (Guan et al., 2014). PF–PC synapses are generally viewed as a uniform population with homogeneous postsynaptic properties. PCs express several types of ionotropic and metabotropic glutamate

receptors (mGluRs) including α-amino-3-hydroxy-5-methyl-4-isoxazole propionic acid receptor (AMPA), *N*-methyl-D-aspartate receptor (NMDAR), mGluR, etc., which comprise different combinations of receptor subunits (Okubo et al., 2004; Jin et al., 2007). Several works have demonstrated the formation and maintenance of PF–PC synapses depending on distinct sets of molecules and synaptic organizers. Till now, the identification of novel molecules that modulate PF–PC synapse formation and synaptic transmission remains a critical open question.

The receptor for activated C kinase 1 (Rack1) is a multifaceted scaffolding protein with seven conserved WD40-repeat domains, which was originally identified as an anchoring protein for the conventional protein kinase C (PKC) (Adams et al., 2011; Li and Xie, 2015). Increasing evidence suggests that Rack1 was involved in the regulation of neural development and brain functions (Wang and Friedman, 2001; McGough et al., 2004; Sklan et al., 2006; Wehner et al., 2011; Kershner and Welshhans, 2017a,b). Our previous work has demonstrated that Rack1 controlled the mammalian cerebellar development by opposite regulation of Wnt/β-catenin and Sonic hedgehog (Shh) signaling pathways in neural stem cells and granule cell progenitors (G), respectively (Yang et al., 2019). Previous studies and our latest work both indicate the enriched expression of Rack1 in the cerebellum, especially in PCs (Ashique et al., 2006; Yang et al., 2019). Interestingly, Rack1 binds and negatively regulates NMDAR subunit NMDAR subtype 2B by inhibition of non-receptor protein tyrosine kinase Fyn phosphorylation in the hippocampus (Yaka et al., 2002; Thornton et al., 2004). However, whether Rack1 in PCs participates in PF–PC synapse formation and function is still elusive.

To understand the role of Rack1 in the regulation of cerebellar synaptogenesis and long-term depression (LTD) at PF–PC synapses, we first generated PC-specific Rack1 knockout mice. Morphological and ultrastructural studies demonstrate that Rack1 mutant mice exhibit delayed formation of cerebellar vermis specifically to lobule VII as well as significantly decreased number of PF–PC synapses. Induction of PF–PC LTD was also severely impaired in Rack1 mutant mice. Consistently, Rack1 mutant mice also showed significant motor coordination defects. Together, our studies demonstrated that Rack1 in PCs is responsible for PF–PC synaptogenesis and synaptic transmission.

MATERIALS AND METHODS

Animals

The *Rack1*$^{F/F}$ lines were generated as previously described, in which exon 2 of *Rack1* gene was flanked by loxP sites (Zhao et al., 2015). Homozygous *Rack1*$^{F/F}$ mice were crossed with mice expressing a transgene encoding Cre recombinase driven by *Pcp2* promoter (Barski et al., 2000). Conditional knockout mice were generated by the second generation, and *Rack1*$^{F/F}$ littermates served as wild-type controls. All experiments with animals were performed in accordance with protocols approved by the Institutional Animal Care and Use Committee of Beijing Institute of Basic Medical Sciences. Mice were housed in specific pathogen-free conditions with 12/12-h light/dark cycles at Beijing Institute of Basic Medical Sciences.

Immunofluorescent Staining

It was performed as previously described (Wu et al., 2015; Yang et al., 2019). Briefly, frozen sections were washed 10 min with 0.5% phosphate-buffered saline with Tween 20 (PBS-T) for three times and then blocked with 3% bovine serum albumin for 1 hr. After that, sections were incubated overnight at 4°C with the primary antibodies as follows: Calbindin (C9848, Sigma, 1:400), NeuN (MAB377, Millipore, 1:400), brain lipid binding protein (BLBP) (ab32423, Abcam, 1:500), Rack1 (R1905, Sigma, 1:400). The sections were washed 10 min with 0.5% PBS-T for three times again and subsequently subjected to Alexa Fluor-conjugated secondary antibodies (Biotium, 1:500). Nuclear staining was visualized with a mounting medium with 4′,6-diamidino-2-phenylindole (ZSGB-BIO). All images were taken from a laser scanning confocal microscope (Olympus FV1200) and then were processed and analyzed by FV10-ASW or Image Pro Plus 6.0 software.

Nissl Staining

The sections (12 μm) of cerebellum mounted on gelatin-coated slides were washed 10 min with 0.5% PBS-T for three times and then immersed into 0.5% tar-violet solution for 20 min. The slices were then quickly rinsed in distilled water and differentiated in 95% ethanol for 2 min. Then, they were dehydrated in 75% ethanol twice, 3 min each. Finally, the slices were sealed with neutral resin.

Transmission Electron Microscopy

The cerebellum were taken from mice at postnatal day 21 (P21) and then fixed in 2% formaldehyde and 2.5% glutaraldehyde in 0.1 M sodium cacodylate buffer (pH 7.4). After 12 h, the cerebellum were washed thoroughly and soaked in 0.1 M sodium dimethylarsenate buffer. The cerebellum was embedded in 4% agar and trimmed with a conventional microtome. After that, sections were fixed in 1% osmium tetroxide/1.5% potassium ferrocyanide solution for 1 h, washed three times in distilled water, incubated in 1% uranium peroxide acetate for 1 hr, washed twice in distilled water, and then dehydrated with gradient alcohol (50, 70, and 90%, 10 min each time; 100%, 10 min twice). Finally, the samples were incubated with propylene oxide for 1 h and then percolated overnight in a 1:1 mixture of propylene oxide and Epon (TAAB, United Kingdom). Next day, the samples were embedded in Epon and polymerized for 48 h at 60°C. Ultrathin sections (about 60–80 nm) were cut on Reichert Ultracut-S microtome sagittally and picked up on to a copper mesh stained with lead citrate. The formation of PF–PC synapses was observed by a transmission electron microscopy (Hitachi, H-7650) with an AMT 2k CCD camera.

Golgi Staining

Golgi staining was administrated with FD Rapid GolgiStain™ Kit (PK401). Briefly, mice were deeply anesthetized before killing, and cerebellum was removed from the skull as quickly as possible,

but handled carefully to avoid damaging or pressing of the tissue. Tissue was immersed in the impregnation solution made by mixing equal volumes of solutions A and B and was put aside at room temperature for at least 2 weeks in the dark, and then, tissue was transferred into solution C followed by storage at room temperature in the dark for 72 h. The 100-μm sections were cut on a vibrating slicer (Leica, VT1200 S). Each section was mounted on gelatin-coated microscope slides with solution C and dried naturally at room temperature. Sections were rinsed in double-distilled water twice, 4 min each, and then placed in a mixture consisting of one part solution D, one part of solution E, and two parts of double-distilled water for 10 min. Sections were dehydrated in 50, 75, 95, and 100% ethanol successively, 4 min each. Lastly, sections were cleared in xylene for three times, 4 min each, and finally sealed with neutral resin.

Electrophysiology

Brain Slice Preparation

At 21 days, mice were decapitated, and the brain was removed to an ice-cold solution containing 213 mM sucrose, 26 mM $NaHCO_3$, 10 mM glucose, 5 mM $MgCl_2$, 3 mM KCl, 1 mM NaH_2PO_4, and 0.5 mM $CaCl_2$. Sagittal slices of cerebellar vermis (250 μm) were prepared using a vibrating blade microtome (VT-1200s, Leica) and were incubated in artificial cerebrospinal fluid containing 125 mM NaCl, 26 mM $NaHCO_3$, 10 mM glucose, 5 mM KCl, 2.6 mM $CaCl_2$, 2 mM NaH_2PO_4, and 1.3 mM $MgCl_2$, at a pH of 7.3–7.4, bubbled with 95% O_2 and 5% CO_2, for 1 h at room temperature.

Whole-Cell Recordings

Whole-cell recordings were obtained with an EPC10 Patch Clamp Amplifier (HEKA, Lambrecht, Germany). Microelectrodes filled with internal solution (3–4 MΩ) were used. The internal solution contained 135 Cs-methanesulfonate, 10 CsCl, 10 4-(2-hydroxyethyl)-1-piperazineethanesulfonic acid, 0.2 ethylene glycol tetraacetic acid, 4 adenosine 5'-triphosphate disodium salt trihydrate, and 0.4 guanosine 5'-triphosphate sodium salt hydrate, pH 7.3, osmolality of 290. For miniature excitatory postsynaptic current (mEPSC) recordings, the slice was then transferred to a chamber perfused with artificial cerebrospinal fluid containing 50 μM picrotoxin (PTX) and 1 μM tetrodotoxin. Evoked EPSCs were pharmacologically isolated by adding 50 μM PTX to the bath solution. The stimulus was delivered to PFs through a concentric bipolar electrode (CBBEB75, FHC, Bowdoin, ME, United States). For LTD of PF-EPSCs recordings, we recorded the baseline for 10 min and then applied five pulse at 100-Hz stimulus and depolarizing the neurons to 0 mV for 100 ms while clamping the cell (30 pulse, 0.5 Hz), followed by 35 min of recording (Zhou et al., 2017). Synaptic responses were collected every 15 s. Somatic whole-cell current-clamp recordings were obtained from PCs in lobule VI or VII of the cerebellar vermis, and series resistances of >20 MΩ were rejected. The electrophysiological data were analyzed using Igor 4.0 (WaveMetrics), and Prism 5 (GraphPad Software).

Isolation of the Postsynaptic Density Fraction

Cerebellum was removed on ice and placed in a homogenate tube. Homogenate buffer (0.5 g tissue/5 ml homogenate, 0.32 M sucrose, 10 mM 4-(2-hydroxyethyl)-1-piperazineethanesulfonic acid–NaOH, pH 7.4) was added and placed under an electric homogenizer for 20 times. The whole protein fraction was centrifuged at 1,000 × *g*/4°C for 10 min. Then, 4 ml of 1.2 M sucrose solution was added into the ultracentrifuge tube in advance, and the previously obtained supernatant was poured in the top. The ultracentrifuge tube was centrifuged at 160,000 × *g*/4°C for 15 min. The synaptic layer (between 1.2 M sucrose solution and homogenate buffer) was carefully aspirated, and 4 ml of homogenate buffer was added to mix it well. Four milliliters of 0.8 M sucrose solution was added into the ultracentrifuge tube, and the solution obtained in the previous step was slowly added above the 0.8 M sucrose solution. Similarly, the ultracentrifuge tube was centrifuged at 160,000 × *g*/4°C for 15 min. The supernatant was discard, and the pellet was resuspend with 1.6 ml of the resuspension buffer (0.5% Triton X-100, 0.16 M sucrose, 6 mM Tris–HCl, pH 8.1). The synaptic component was centrifuged at 32,800 × *g* for 20 min. The supernatant was thrown away, and 0.4 ml resuspension buffer was added to the pellet to centrifuge for 1 h at 200,000 × *g*. The precipitate obtained after centrifugation was the postsynaptic density (PSD) component.

Western Blot

The experiments were performed as previously described (Wu et al., 2012). Briefly, PSD fraction isolated from cerebellum tissues was supplemented with 1 × protease and phosphatase inhibitor mixture. Protein concentration was measured using the BCA Protein Assay Kit. Samples (20–50 μg, including 5 μl of prestained protein standards) were loaded into the sodium dodecyl sulfate–polyacrylamide gel electrophoresis gel, and electrophoresis was conducted at constant voltage (120 V) at 4°C and then transferred to polyvinylidene difluoride membranes. The membranes were then blocked with 5% skim milk in 0.1% Tris–buffered saline/Tween-20 for 1 h and incubated overnight at 4°C with indicated primary antibodies. In each experiment, horseradish peroxidase and enhanced chemiluminescence were used to image protein bands on film. The film signal was electronically scanned and statistically analyzed by Image Pro Plus software.

Behavioral Tests

Balance Beam

The device consists of a strong light on the starting side and a safety platform (RWD, R-LBB) on the dark side. Each mouse was acclimated three times with an interval of 10 min before the formal test. The time of mice passing through the 50-cm long balance beam was recorded.

Accelerating Rotarod

Following adaptation to the stick (Ugo Basile, 47650), mice were measured every 8 h for eight consecutive times. In each test, the

speed was accelerated from 4 to 60 rpm over a 5-min period, and the deadline was 300 s.

Open Field

To analyze general locomotion and exploratory behavior in a novel environment, the open field test was performed. Open field apparatus comprised of a transparent plexiglas (40 cm × 40 cm × 40 cm) arena with a white floor virtually (SLY-ETS) divided into two zones: periphery and center. Every mouse was able to explore the novel environment for 5 min. Total distance and center distance traveled by the animal were calculated and analyzed, respectively. Room illumination was kept at 60 lx. Mice position were determined by automatic video tracking (ANY-maze technology).

Morphometric Analysis of Cerebellar Lobules and PCs

Serial cerebellar coronal cryostat sections were stained with cresyl violet. Golgi-stained brain slices of the whole PCs were taken with an Olympus microscope. One-micrometer-spaced Z-stack brightfield images for dendritic spines were taken with an Olympus BX60 microscope with Axiocam MRc Zeiss camera and Axiovision 4.8 Software (Zeiss, Germany). All images are processed and quantified using Adobe Photoshop CS6 version and ImageJ Software. Spine morphology was determinated based on previous studies (Lee et al., 2004). Spine density was evaluated as the relative spine number over 10-μm dendritic fragments with NeuronStudio software.

Statistical Analysis

The data between the two independent groups were shown as mean ± SEM of at least three independent experiments. p-values were determined by Student's t-test or non-parametric test, and $p < 0.05$ was considered statistically significant.

RESULTS

Ablation of *Rack1* in PCs Delays Cerebellar Lobule VII Formation

Expression of Rack1 protein was fairly rich in mice at birth but decreased gradually at approximately postnatal day P14 and remained constant thereafter (Yang et al., 2019). Immunofluorescent colocalization revealed that Rack1 protein was mainly expressed in PCs at P21 cerebellum. To investigate the potential function of Rack1 in PCs *in vivo*, the conditional knockout mice were generated with hybridization between *Pcp2-Cre* transgenic lines and *Rack1* loxP mice. At first, the *Pcp2-Cre* recombinase was visualized by Ai9 reporter mice. It exhibited that abundant *Pcp2-Cre* recombinase was specifically expressed in PCs (**Figures 1A,B**). Selective deletion of *Rack1* in PCs were confirmed by both Western blot from isolated synaptic fraction (**Figure 1C**) and immunofluorescence staining (**Figure 1F**). It showed robust Rack1 protein decline in Rack1 mutants (**Figure 1D**, 32.8 ± 1.96 in mutant vs. 100.0 ± 2.78 in control, $p = 0.0009$, $n = 5$). In general, *Rack1* mutant mice appeared normal at P21, as shown by similar body weight and cerebellar surface fissure compared to wild-type littermates (**Figure 1E**).

Next, we further precisely examined the cerebellar size by quantitative histological analysis. Nissl staining of cerebellar sections indicated that the foliation of *Pcp2-Cre;Rack1*$^{F/F}$ mutant mice was similar to that of the control littermates postnatally except for lobule VII until P60 (**Figure 1G**). Sagittal sections of cerebellar vermis indicates that the area of lobule VII but not other lobules was significantly smaller in *Pcp2-Cre;Rack1*$^{F/F}$ mutant mice compared to control littermates at P14 (0.18 ± 0.02 mm^2 in mutants vs. 0.29 ± 0.02 mm^2 in wild-type controls, $p = 0.007$, $n = 5$) and P21 (0.21 ± 0.05 mm^2 in mutants vs. 0.31 ± 0.02 mm^2 in wild-type controls, $p = 0.008$, $n = 5$), but not P60 (0.33 ± 0.02 mm^2 in mutants vs. 0.35 ± 0.02 mm^2 in wild-type controls, $p = 0.55$, $n = 5$), suggesting that the ablation of *Rack1* in PCs causes the delayed foliation and morphogenesis most specifically restricted to lobule VII, but not other lobules in vermis (**Figure 1H**). Interestingly, it should be noted that the alterations are only restricted to the vermis subregion but not other cerebellar hemispheres for some unknown reason. Since, the expansion of GNPs is crucial for cerebellar foliation formation, this phenotype is probably due to defects in delayed GNPs proliferation and migration at specific subregion in mutant mice.

Impaired Motor Coordination and Hyperactivity in *Rack1* cKO Mice

To further evaluate the effect of Rack1 knockout in PCs on locomotion, 8-week-old *Pcp2-Cre;Rack1*$^{F/F}$ and control mice were selected for balance-related behavioral testing. *Pcp2-Cre;Rack1*$^{F/F}$ mice did not show obvious ataxia in standard cages. However, they performed poorly, with a remarkably longer time when walking on a narrow elevated beam (**Figure 2A**, 3.6 ± 0.22 s in mutant vs. 8.0 ± 0.86 s in control, $p < 0.0001$, $n = 10$), which indicated that the balance ability of mutant mice was significantly decreased. In addition, the time of *Pcp2-Cre;Rack1*$^{F/F}$ mice staying on the accelerating rotarod was significantly shorter than that of the control mice (**Figure 2B**, 211.4 ± 20.11 s in mutant vs. 298.1 ± 1.81 s in control, $p < 0.0001$, $n = 11$), indicating the deficits in fine motor coordination skills in *Pcp2-Cre;Rack1*$^{F/F}$ mutants. Moreover, *Rack1* mutant mice also showed impaired motor learning, in which mutant mice exhibited declined improvement after multiple sessions on the accelerating rotarod compared with controls (**Figure 2B**).

In addition to motor function, the cerebellum has been implicated in various cognitive and social behaviors. The dysfunction of PCs have been observed in autism and schizophrenia (Andreasen and Pierson, 2008; Yeganeh-Doost et al., 2011; Peter et al., 2016). Thus, a series of behavioral tests were performed to assess whether Rack1 ablation in PCs would affect different domains of mouse behavioral repertoire. In the open field tests, Rack1 mutant mice exhibited dramatic hyperactivity (**Figure 2C**). In a limited time (5 min), the mutant mice travel more distances compared to controls (**Figure 2D**, 53.6 ± 8.6 cm in mutant vs. 35.2 ± 9.6 cm in control, $p = 0.0062$, $n = 8$), especially at the center zone of the place (**Figure 2E**,

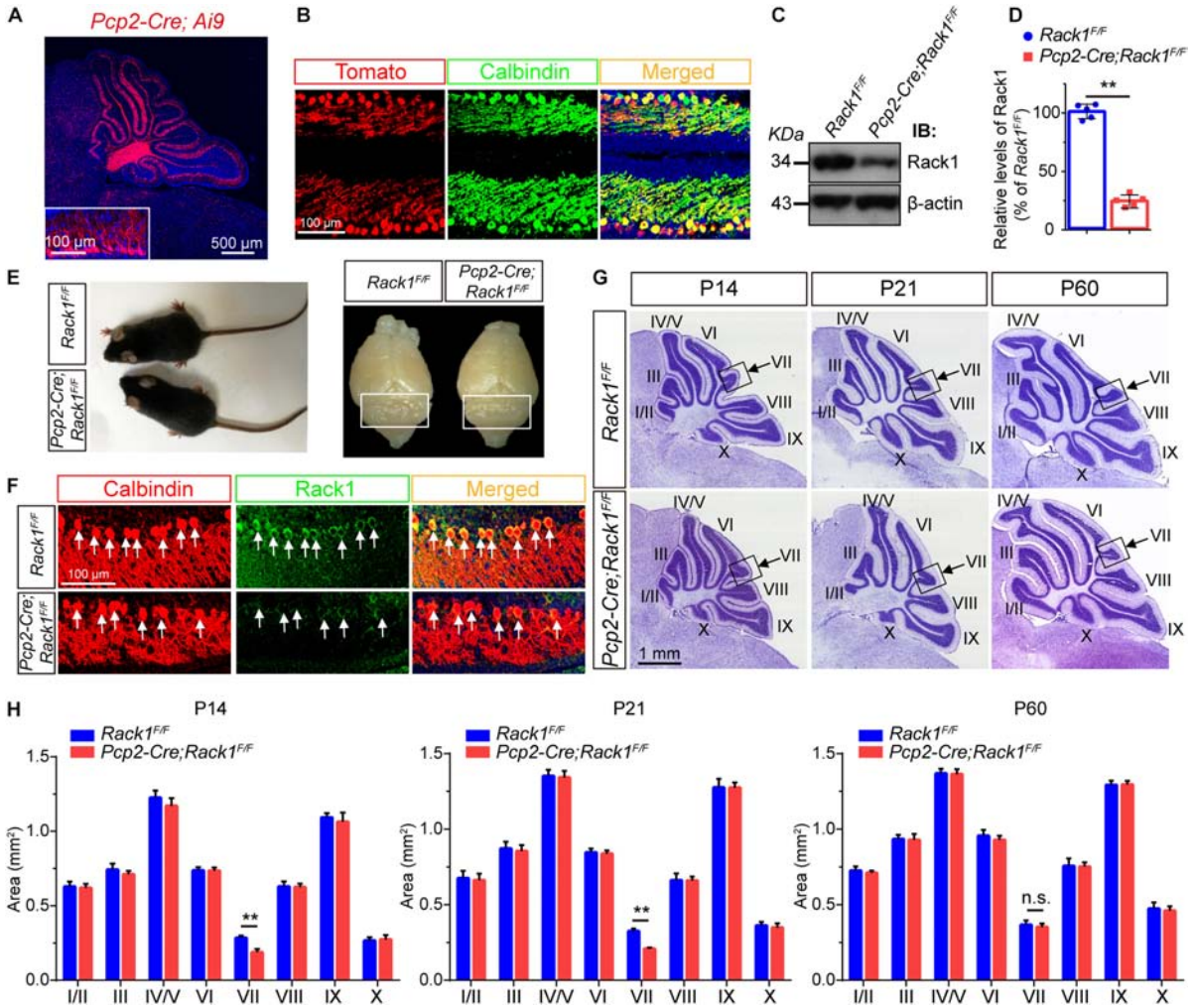

FIGURE 1 | Ablation of *Rack1* in Purkinje cells (PCs) delays cerebellar lobule VII formation. **(A)** Ai9 reporter mice showed that *Pcp2*-Cre is specifically expressed in the PC layer of cerebellar cortex. Scale bar = 500 μm. **(B)** The expression of *Pcp2*-Cre was determined in the offspring of *Pcp2*-Cre;Ai9 mice. Cerebellar sections were counterstained with Calbindin antibody. Scale bar = 100 μm. **(C)** Representative Western blot shows the expression of Rack1 in the postsynaptic density (PSD) fraction of cerebellar lysates from P7 wild-type and *Pcp2-Cre*;$Rack1^{F/F}$ mutant mice. **(D)** Quantitative analysis of Western blot displays significant decreased expression of Rack1 in *Pcp2-Cre*;$Rack1^{F/F}$ mutants compared to control littermates. Mean ± SEM, $^{**}p = 0.0009$, $n = 5$. **(E)** The body size of *Pcp2-Cre*;$Rack1^{F/F}$ mutant mice was indistinguishable compared to control littermates at P30. **(F)** Coimmunofluorescent staining with Rack1 and Calbindin antibodies show the significantly decreased expression of Rack1 in Purkinje cells in *Pcp2-Cre*;$Rack1^{F/F}$ mutants compared to control littermates. Scale bar = 100 μm. **(G)** Nissl staining of sagittal sections of the cerebellar vermis shows specific deficiency in cerebellar lobule VII foliation in *Pcp2-Cre*;$Rack1^{F/F}$ mutants compared to control littermates at P14, P21 but not at P60. Scale bar = 1 mm. **(H)** Quantitative analysis of the area of each individual lobule of the vermis in *Pcp2-Cre*;$Rack1^{F/F}$ mutant mice and control littermates at indicated developmental stages. $^{**}p = 0.007$ and 0.008, at P14 and P21, respectively; $p = 0.55$ at P60, $n = 5$, n.s. = not significant.

8.3 ± 4.2 cm in mutant vs. 3.6 ± 1.9 cm in control, $^{**}p = 0.0096$, $n = 8$; **Figure 2F**, 65.6 ± 18.6 s in mutant vs. 45.2 ± 19.4 s in control, $^{**}p = 0.0624$, $n = 8$). Together, these results indicate that *Pcp2-Cre;*$Rack1^{F/F}$ mice exhibit hyperactivity and a significant deficit in motor coordination.

Decreased PF–PC Synaptogenesis in *Rack1* cKO Mice

Moreover, immunofluorescence staining was employed to identify PCs and Bergmann glial cells using Calbindin and BLBP antibodies, respectively, to analyze the fine lamination and morphological differences in mutant cerebellum. As was shown in **Figure 3A**, in the mutant cerebellum, the Calbindin^{+} PCs and BLBP^{+} Bergmann glial cells were both well and neatly organized, with a single layer of polarization distributed in the PC layer, suggesting the normal cerebellar cortex stratification in Rack1 mutant mice. Nevertheless, due to the excessive number of Calbindin^{+} PCs in the brain slices, it was almost impossible to accurately count the number of dendritic branches and dendritic spines of PCs. Therefore, the Golgi staining method was adopted to sparsely illustrate the morphology of PCs. In general, it showed that there is no obvious distinction of dendritic branches and spine density in the PCs between control and Rack1 mutant mice

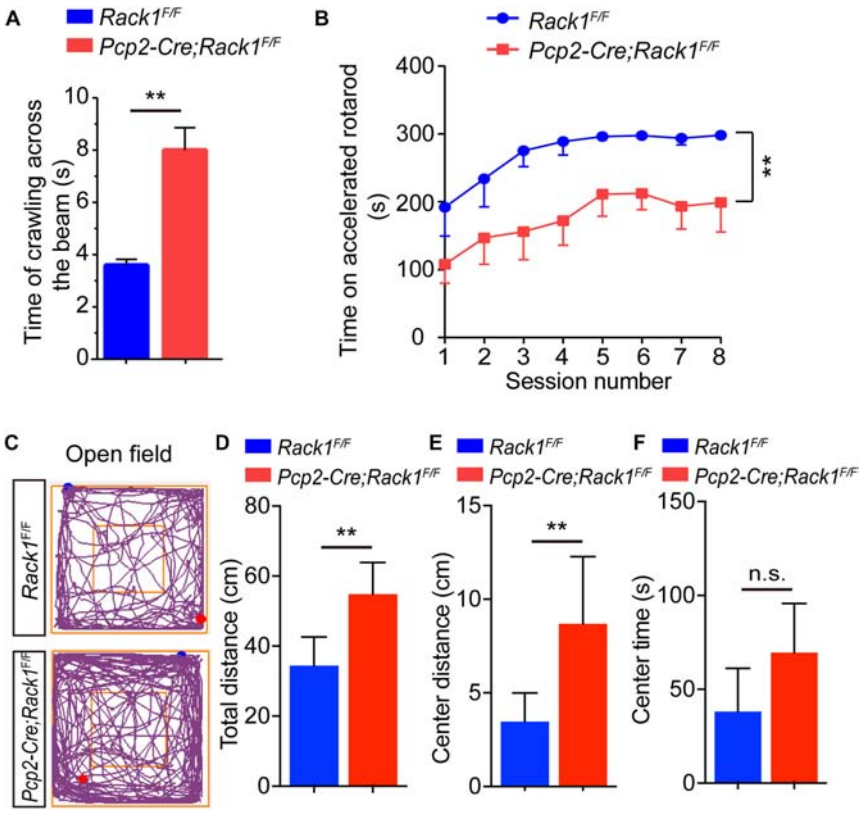

FIGURE 2 | *Pcp2-Cre;Rack1*$^{F/F}$ mutant mice show impaired motor coordination and hyperactivity. **(A)** Balanced beam experiment shows impaired motor balance in *Pcp2-Cre;Rack1*$^{F/F}$ mutant mice. Mean ± SEM, $^{**}p < 0.0001$, $n = 10$. **(B)** Time spent on the accelerating rotarod for *Rack1*$^{F/F}$ control and *Pcp2-Cre;Rack1*$^{F/F}$ mutant mice. Mean ± SEM, $^{**}p < 0.0001$, $n = 11$. **(C)** Traces of locomotor activity in *Rack1*$^{F/F}$ control and *Pcp2-Cre;Rack1*$^{F/F}$ mutant mouse in an open field test (OFT). **(D)** Averaged group data of total distance traveled in control and mutant mice in the OFT. Mean ± SEM, $^{**}p = 0.0062$, $n = 8$. **(E)** Averaged group data of center distance traveled in control and mutant mice in the OFT. Mean ± SEM, $^{**}p = 0.0096$, $n = 8$. **(F)** Averaged group data of the time spent in the central zone in control and mutant mice. Mean ± SEM, $^{**}p = 0.0624$, $n = 8$, n.s. = not significant.

(**Figure 3B**). Statistical results also confirmed that dendritic spine density was comparable to that of control littermates (**Figure 3C**, 13.3 ± 0.39/10 μm in mutant vs. 15.0 ± 1.15/10 μm in control, $p = 0.1878$, $n = 5$). Thus, specific deletion of Rack1 in PCs does not impair its morphogenesis and cytoarchitecture.

Owing to the fact that PC dendrites could convert excitatory PF input from granule cells into signals, they play an important role in synaptic plasticity and motor learning (Rowan et al., 2018). Next, we asked whether the impaired motor coordination in Rack1 mutant mice was caused by the synaptogenesis deficiency or synaptic dysfunction. Therefore, we assessed the effect of Rack1 ablation in PCs on the synapse formation between PCs dendrites and PFs from granule cells by electronic microscope analysis. As shown in **Figure 3D**, the black high-density postsynaptic materials marked by the red asterisks was the excitatory synapse formed by PCs and PFs. Quantitative analysis shows that the density of presynaptic PF boutons in Rack1 mutant mice was substantially lower than that of control (**Figure 3E**, 5.4 ± 0.56/μm^2 in mutant, $n = 17$, vs. 7.8 ± 0.69/μm^2 in control, $n = 22$, $p < 0.001$). We also found there were more free or mismatched spines in Rack1 mutant cerebellum, suggesting the defective synaptogenesis in mutant mice. Together, these ultrastructural results suggest that Rack1 is able to promote synaptogenesis between PC dendrites and PFs in the cerebellar cortex.

Decreased Synaptic Transmission and Impaired LTD in *Rack1* cKO Mice

The requirement for the Rack1 in synaptogenesis in the cerebellar cortex led to the postulation that synaptic transmission at PF–PC synapses might be affected in Rack1 mutants. Our electrophysiological analysis in acute cerebellar slices revealed that the amplitude of evoked EPSC at PC–PF synapses was normal between *Pcp2-Cre;Rack1*$^{F/F}$ and *Rack1*$^{F/F}$ mice (**Figures 4A,B**, 280.2 ± 44.45 pA, $n = 10$ in mutant vs. 279.2 ± 28.63 pA, $n = 14$ in control, $p = 0.9855$). However, the ratio of paired-pulse facilitation measured at an interval of 80 ms was reduced nearly 20% (**Figures 4C,D**, 1.7 ± 0.10 in mutant vs. 2.2 ± 0.14, $p = 0.0078$, $n = 12$), suggesting that the presynaptic glutamate release was impaired. Moreover, there was no difference in the amplitude of the presynaptic volley in mice between *Pcp2-Cre;Rack1*$^{F/F}$ mutant and *Rack1*$^{F/F}$ control mice, illustrating that the impairment of evoked EPSC in *Rack1*

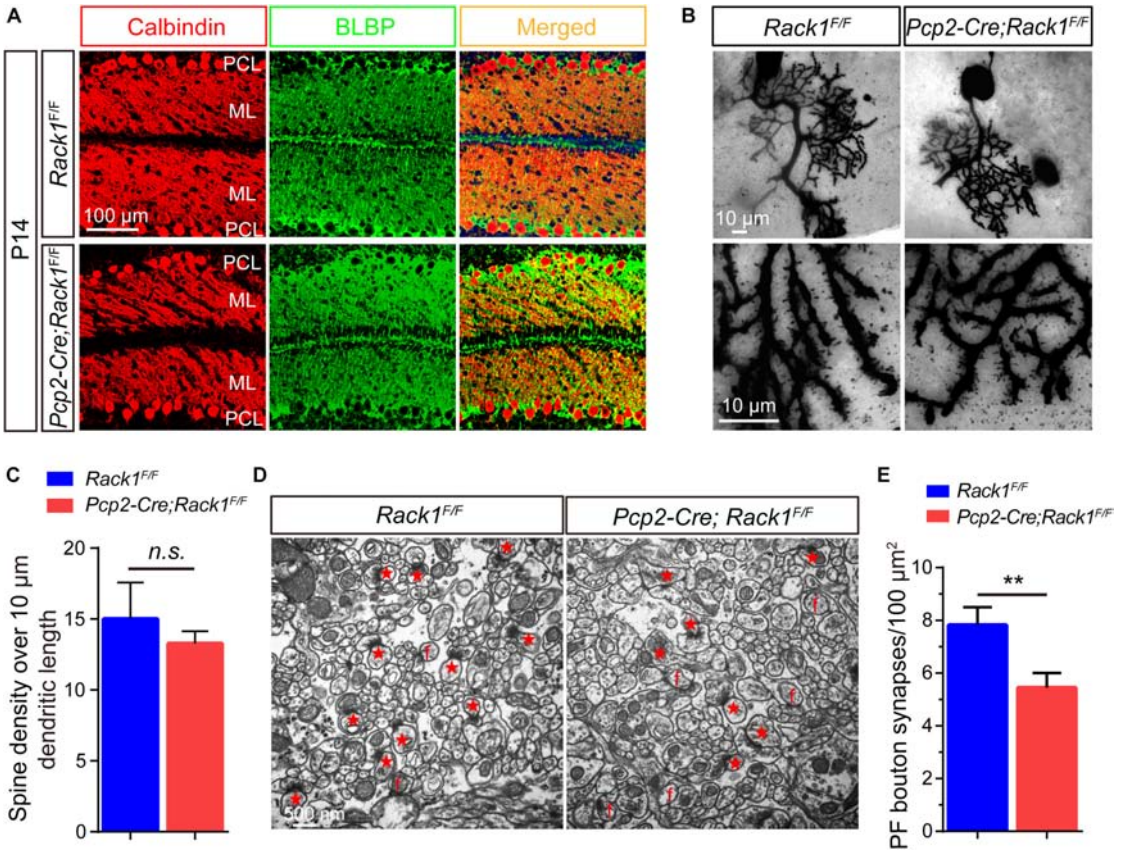

FIGURE 3 | Decreased parallel fiber (PF)–Purkinje cell (PC) synaptogenesis in *Pcp2-Cre;Rack1*$^{F/F}$ mutant mice. **(A)** Coimmunofluorescent staining of cerebellar sections with anti-Calbindin and anti-BLBP antibodies displayed the normally polarized distribution of PCs in *Pcp2-Cre;Rack1*$^{F/F}$ mutant mice compared to control littermates. Scale bar = 100 μm. **(B)** The morphology of dendritic spines of PCs in control and mutant mice was illustrated by Golgi staining. Scale bar = 10 μm. **(C)** The statistical result shows no significant difference between *Rack1*$^{F/F}$ control and *Pcp2-Cre;Rack1*$^{F/F}$ mutant mice in terms of the density of PC dendritic spines. Mean ± SEM, $p = 0.1878$, $n = 5$, n.s. = not significant. **(D)** Representative electron micrographs of the molecular layer within the cerebellar cortex from *Rack1*$^{F/F}$ control and *Pcp2-Cre;Rack1*$^{F/F}$ mutant mice at P21. Synapses comprising of presynaptic PF terminal boutons opposed to postsynaptic PC spines are marked with red asterisks. Free spines and mismatched synapses are indicated by f. Scale bar = 500 nm. **(E)** Quantification of the density of PF–PC synapses shows the reduction in *Pcp2-Cre;Rack1*$^{F/F}$ mutant mice compared to that of the control *Rack1*$^{F/F}$ littermates. Mean ± SEM, $^{**}p < 0.001$.

mutant mice is not due to the difference in axon excitability (data not shown).

Then, we asked whether the neurotransmission defects in *Rack1* mutant mice might be due to the secondary effect of the changed synapse numbers. As expected, the frequency of mEPSCs in PCs was reduced in acute cerebellar slices from *Pcp2-Cre;Rack1*$^{F/F}$ mice compared to *Rack1*$^{F/F}$ mice (**Figure 4F**, 0.14 ± 0.02 pA, $n = 17$ in mutant vs. 0.30 ± 0.03 pA, $n = 20$ in control, $p = 0.0002$), consistent with the previous conclusion that synapse number is reduced in *Rack1* mutants. The amplitude of mEPSCs was hardly reduced in *Rack1* knockout mice (**Figure 4E**, 11.99 ± 0.54 pA, $n = 17$ in mutant vs. 12.02 ± 0.55 pA, $n = 20$ in control, $p = 0.9724$), suggesting that the reactivity of the postsynaptic membrane was normal. Collectively, our electrophysiological and electronic microscope results suggest that the deficiency of synaptic transmission between PF-PCs in *Rack1* mutants might be due to the impaired synaptogenesis.

Long-term depression has been proposed as a potential factor contributing to motor learning in the cerebellar cortex (Kakegawa et al., 2018; Zamora Chimal and De Schutter, 2018). Given that *Pcp2-Cre;Rack1*$^{F/F}$ mutant mice showed impaired motor coordination and hyperactive locomotion, we next examined the LTD at PF–PC synapses with voltage-clamp mode both in control and *Rack1* mutants (**Figure 4G**). Our results showed that PCs in *Rack1*$^{F/F}$ mice performed robust PF-LTD induction (**Figure 4H**, last 5 min, 47.4 ± 5.73% of baseline; $n = 9$) in response to repetitive PF stimulation. However, the induction of LTD in PCs was significantly impaired in *Pcp2-Cre;Rack1*$^{F/F}$ mutant cerebellum (**Figure 4H**, last 5 min, 82.6 ± 7.14% of baseline; $n = 8$, $p = 0.0015$).

The Expression of Major Postsynaptic Components Were Not Affected in *Rack1* cKO Mice

Motor PF-LTD deficits may result from altered ion channel or glutamatergic-transmission-associated protein. Thus, the expression of ionotropic glutamate receptors were

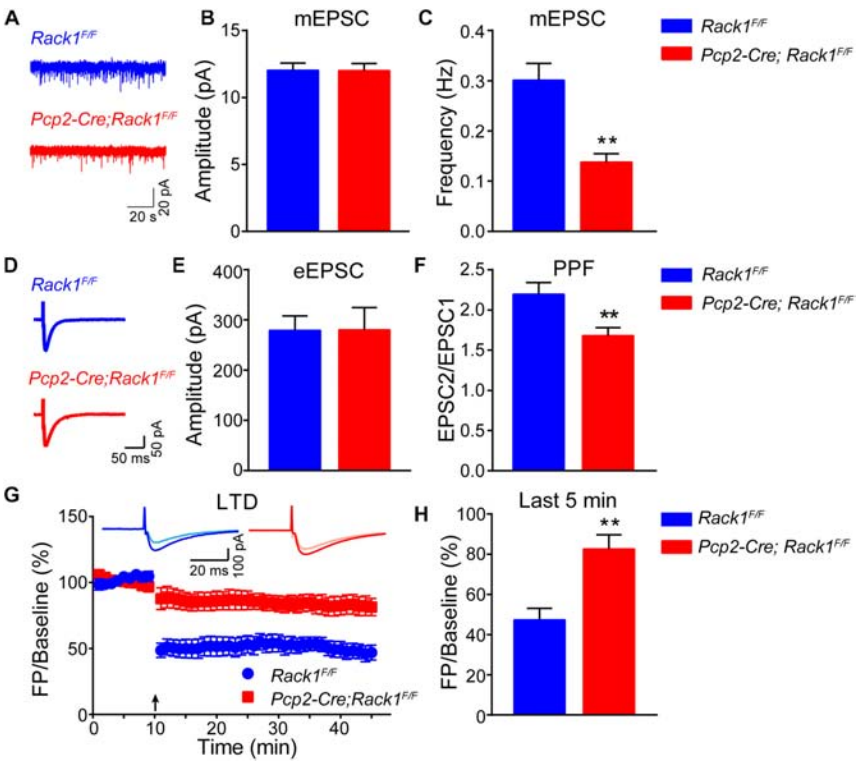

FIGURE 4 | Altered synaptic transmission and long-term depression (LTD) in *Pcp2-Cre*;*Rack1*$^{F/F}$ mice. **(A)** Representative traces of miniature excitatory postsynaptic currents (mEPSCs) recorded in the presence of 1 μM tetrodotoxin and 0.1 mM picrotoxin (PTX). **(B)** Summary graphs of the amplitudes of mEPSCs (*Rack1*$^{F/F}$: n = 20 cells/4 mice; *Pcp2-Cre*;*Rack1*$^{F/F}$: n = 17/4 mice). **(C)** Summary graphs of the frequency of mEPSCs (*Rack1*$^{F/F}$: n = 20 cells/4 mice; *Pcp2-Cre*;*Rack1*$^{F/F}$: n = 17/4 mice). $^{**}p$ = 0.0078, n = 12. **(D)** Representative traces of action potential-evoked EPSCs recorded in 0.1 mM picrotoxin. **(E)** The graphs of the amplitudes of action potential-evoked EPSCs (*Rack1*$^{F/F}$: n = 14/4 mice; *Pcp2-Cre*;*Rack1*$^{F/F}$: n = 10/3 mice). **(F)** The graphs of paired-pulse facilitation (*Rack1*$^{F/F}$: n = 12/4 mice; *Pcp2-Cre*;*Rack1*$^{F/F}$: n = 12/3 mice). $^{**}p$ = 0.0002. **(G)** Parallel fiber-LTD in *Rack1*$^{F/F}$ (filled blue circles) and *Pcp2-Cre*;*Rack1*$^{F/F}$ (filled red squares) mice. Each data point represents the average of four consecutive responses evoked at every 15 s. Representative traces before (light) and after (dark) LTD induction are shown. **(H)** Summary graphs of average amplitude of parallel fiber-LTD of the last 5 min (*Rack1*$^{F/F}$: n = 9/4 mice; *Pcp2-Cre*;*Rack1*$^{F/F}$: n = 8/4 mice). $^{**}p$ = 0.0015.

examined. We found that the level of AMPA-associated proteins such as GluA1/2/4 and transmembrane AMPA-receptor-regulated protein γ2/8 were not altered significantly in relation to those of PSD95 and GAD65 (**Figures 5A,B**, $p > 0.05$). Glutamatergic-transmission-associated protein such as membrane-associated guanylate kinase, Dynamin1, and Synapsin were also indistinguishable between *Rack1*$^{F/F}$ control and *Pcp2-Cre;Rack1*$^{F/F}$ mutant cerebellum (**Figures 5A,B**, $p > 0.05$), suggesting that deletion of Rack1 in PCs has no significant effects on the expression of synaptic proteins.

Our previous work has shown that Rack1 promotes the development of granule cells via regulating the stability of HDAC1/2 in GCPs (Yang et al., 2019). Here, we also found that the expression of HDAC1/2 proteins were significantly decreased in *Pcp2-Cre*;*Rack1*$^{F/F}$ mutant cerebellum compared to *Rack1*$^{F/F}$ control (**Figures 5A,B**, 93.5 ± 1.37% in mutant vs. 100.0 ± 1.58% in control, n = 3, p = 0.0092). Interestingly, previous work has shown that HDAC1/2 together with Chd4, RbAp48, Mbd3, and Mta1/2 constitute the remodeling of nucleosome and deacetylation complex, which programs the differentiation of presynaptic sites and triggers synaptic connectivity in the PF–PCs (Yamada et al., 2014). Thus, the decreased expression of HDAC1/2 in PCs might be responsible for the malformation of PF–PCs synaptogenesis.

DISCUSSION

Germline deletion of Rack1 in *Drosophila* or mice both causes their death at embryonic stage (Kadrmas et al., 2007; Volta et al., 2013). Our previous work shows that deletion of Rack1 in neuronal precursor cells does not cause embryonic lethality but severe neural developmental deficiency, indicating that the early death in Rack1 null mutants is not due to brain abnormalities (Yang et al., 2019). We have shown that ablation of Rack1 in either neural stem cells or GCPs disrupts cerebellar morphogenesis (Yang et al., 2019). Here, we show that specific deletion of Rack1 in PCs in mice causes delayed formation of specific vermis lobule as well as defective motor coordination and motor learning. Given that PC-derived Shh plays a critical role in promoting the proliferation of GCPs by disinhibition of its coreceptor smoothened and activation of transcriptional factors Gli1/2 (Lee et al., 2010; Shi et al., 2014). We assume that ablation of Rack1 in PCs might caused the decreased secretion of Shh, which

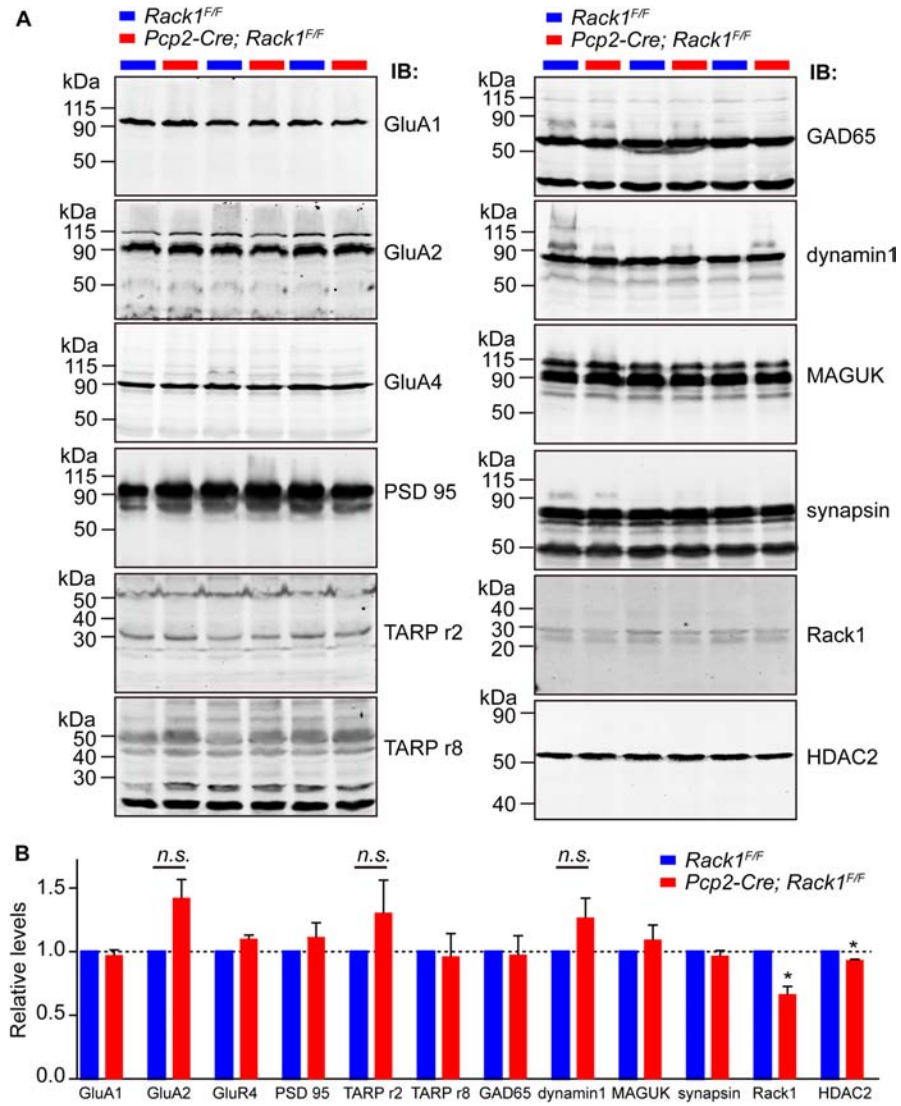

FIGURE 5 | The expression of major synaptic components was not affected in *Pcp2-Cre*;*Rack1*$^{F/F}$ mutant mice. **(A)** Representative Western blots examining the expression of major postsynaptic components in *Rack1*$^{F/F}$ control and *Pcp2-Cre*;*Rack1*$^{F/F}$ mutant cerebellum at postnatal day 21 (P21). **(B)** Quantitative analysis indicates normal levels of postsynaptic components but reduced level of HDAC2 expression in *Pcp2-Cre*;*Rack1*$^{F/F}$ mutants, $*p = 0.0092$, $n = 3$. Reduced expression of Rack1 was confirmed in *Pcp2-Cre*;*Rack1*$^{F/F}$ mutant compared to control littermates. Mean ± SEM, $*p = 0.0056$, $n = 3$. The expression of GluA2, TARPr2, and dynamin 1 in mutant mice is not significant compared to control littermates, $p = 0.0962$, 0.1346, and 0.1125, respectively.

might delay the development of cerebellar foliation in *Pcp2-Cre;Rack1*$^{F/F}$ mutants. Another interesting phenotype of mutant mice was hyperactivity in the open field test. The PCs are considered the principal neurons in the cerebellar cortex which provide their sole outputs by projecting to the deep cerebellar nuclei and the vestibular nuclei (Sillitoe and Joyner, 2007). This circuit is critical in controlling the ongoing execution as well as coordinating the planning of limb movement. Previously, Waite et al. have demonstrated that selectively ablation of PCs in rats resulted in hyperactivity in open field (Waite et al., 1999). Thus, it is possible that the inhibitory output of the cerebellar cortex was reduced in *Pcp2-Cre;Rack1*$^{F/F}$ mutants, leading to an elevated locomotive activity.

The cerebellum is important for movement control, which is tightly regulated by precise cerebellar circuits (Fetz, 1993; Voogd and Glickstein, 1998). PCs integrate signals from two major excitatory inputs including the climbing fibers and PFs that convey signals of the inferior olive or the mossy fiber relay system, respectively (Sillitoe and Joyner, 2007). Our finding that specific ablation of Rack1 in PCs caused significantly impaired PF–PC synaptogenesis and LTD induction suggest that Rack1 is essential for the development and function of PF–PC synapses. Thus, these findings provide another interesting aspect of Rack1 function in the cerebellar circuits. Owing to the fact that PF–PC circuits play important roles in movement control, motor learning, and non-motor functions such as language, social interaction,

and expectation of reward (Strick et al., 2009; Wagner et al., 2017), our studies provide a novel evidence how dysfunction of Rack1 in PCs may cause the movement and motor coordination disorders in mutant mice.

Interestingly, Rack1 has been shown to inhibit the NMDAR-mediated activity by preventing the phosphorylation of NR2B mediated by the tyrosine kinase Fyn (Yaka et al., 2002). Another interesting result of our work is that the reduction in the frequency but not the amplitude of the mEPSCs was identified in *Pcp2-Cre;Rack1*$^{F/F}$ mutant mice. Although we did not find significant changes of synaptic protein expression in the *Rack1* mutant mice, the finding that the PC-specific deletion of Rack1 selectively affected excitatory presynaptic transmission suggests an important role of Rack1 in synaptic homeostasis. Moreover, neuroadaptation is thought as one of the mechanisms that contributes to the synaptic changes in response to sustained morphine exposure (De Vries and Shippenberg, 2002), and Rack1 has been exactly implicated in this process by activation of extracellular signal-regulated kinase–cAMP response element binding signaling in hippocampus (Liu et al., 2016). However, whether this pathway is involved in Rack1-mediated PF-PC synaptic transmission is still elusive.

The climbing fiber innervation of PCs has been shown to be important for normal motor behavior in mice, and PF-mediated mGluR1 and PKCγ activation is essential for LTD and late-phase climbing fiber elimination (Kano et al., 1995, 1997; Ichise et al., 2000). The bidirectional plasticity of the PF–PC synapses has been nicely demonstrated, which shows that climbing fiber activity can reverse the PF–PC synapse long-term potentiation (LTP) into LTD (Coesmans et al., 2004). Moreover, the presynaptic LTP and LTD of PF–PC synaptic plasticity also have been elegantly demonstrated *in vitro* and *in vivo* in mice (Qiu and Knopfel, 2009; Chu et al., 2014; Wang et al., 2014; Bing et al., 2015). PKCα and CaMKII activation has been shown to be essential for PF–PC synapse LTD (Leitges et al., 2004; Hansel et al., 2006; van Woerden et al., 2009). However, how CaMKII and PKCs regulate the LTD induction is still poorly understood.

Notably, as a scaffolding protein, Rack1 serves as an intracellular receptor for activated PKC, which is responsible for subcellular localization of PKC (Ron et al., 1994). PKC has been shown to be important for AMPA receptor internalization by phosphorylation of GluR2 subunit (Chung et al., 2003). PKCα also regulates the AMPA receptor clustering by phosphorylation of GluR2 at Ser880 and thereby reducing their binding to glutamate receptor interacting proteins (Matsuda et al., 1999). Although in our study, we do not find the expression changes of GluR2 in *Pcp2-Cre;Rack1*$^{F/F}$ mutant mice, we cannot rule out the possibility that the phosphorylation of GluR2 is altered in the absence of Rack1 in PCs. Therefore, the impaired motor coordination and PF–PC synaptic transmission in PC-specific Rack1 knockout mice is presumably mediated by the deficiency in Rack1-dependent synaptic plasticity. In addition, LTP but not LTD at PF–PC is also known to be related to cerebellar motor learning (Schonewille et al., 2011; Gao et al., 2012). Previous study shows that PF–PC synaptic plasticity is regulated by a kinase/phosphatase switch. Protein phosphatase 1 (PP1), PP2A, and PP2B (calcineurin) play important roles in PF–PC LTP (Belmeguenai and Hansel, 2005; Schonewille et al., 2010). Additional studies will be necessary to fully elucidate the role of Rack1 in PF–PC LTP/LTD, at least in part because of its influence on the presynaptic function of PF–PCs and its relative roles in the regulation of NMDAR in PCs.

It should be noted that the synaptic plasticity in the cerebellum is not only observed for the excitatory PF–PC synapses but also for inhibitory synapses formed by basket and stellate interneurons with PCs in the molecular layer (Sillitoe and Joyner, 2007). In this study, we mainly focus on the impact of Rack1 on the PF–PCs synaptogenesis and synaptic transmission. Given that GABAergic synapses of PCs is also important for cerebellar motor learning (Tanaka et al., 2013; Hirano and Kawaguchi, 2014), it would be of interest to investigate whether Rack1 is also involved in the regulation of GABA receptor activity in PCs in the near future.

DATA AVAILABILITY STATEMENT

The raw data supporting the conclusions of this manuscript will be made available by the authors, without undue reservation, to any qualified researcher.

ETHICS STATEMENT

The animal study was reviewed and approved by the Institutional Animal Care and Use Committee of Beijing Institute of Basic Medical Sciences.

AUTHOR CONTRIBUTIONS

HW designed the research and wrote the manuscript. HY, CY, QZ, MW, YL, JC, FL, and YW performed the research. JZ and CZ contributed the reagents, mice, and analytic tools. CZ and HW analyzed data.

FUNDING

This study was supported by the National Natural Science Foundation of China (Grants 31522029, 31770929, 31670842, 81925011, and 31371149), the National Basic Research Program of China (Grants 2014CB542203 and 2017YFA0105201), the Beijing Municipal Science and Technology Commission (Grants Z181100001518001 and Z161100000216154), the Youth Beijing Scholars Program (015), and the Key Realm R&D Program of Guangdong Province (2019B030335001).

ACKNOWLEDGMENTS

The authors thank Dr. Ying Shen at Zhejiang University for generously providing the *Pcp2*-Cre line.

REFERENCES

Adams, D. R., Ron, D., and Kiely, P. A. (2011). RACK1, A multifaceted scaffolding protein: structure and function. *Cell Commun. Signal* 9:22. doi: 10.1186/1478-811X-9-22

Andreasen, N. C., and Pierson, R. (2008). The role of the cerebellum in schizophrenia. *Biol. Psychiatry* 64, 81–88. doi: 10.1016/j.biopsych.2008.01.003

Ashique, A. M., Kharazia, V., Yaka, R., Phamluong, K., Peterson, A. S., and Ron, D. (2006). Localization of the scaffolding protein RACK1 in the developing and adult mouse brain. *Brain Res.* 1069, 31–38. doi: 10.1016/j.brainres.2005.11.018

Barski, J. J., Dethleffsen, K., and Meyer, M. (2000). Cre recombinase expression in cerebellar Purkinje cells. *Genesis* 28, 93–98. doi: 10.1002/1526-968x(200011/12)28:3/4<93::aid-gene10>3.3.co;2-n

Belmeguenai, A., and Hansel, C. (2005). A role for protein phosphatases 1, 2A, and 2B in cerebellar long-term potentiation. *J. Neurosci.* 25, 10768–10772. doi: 10.1523/JNEUROSCI.2876-05.2005

Bing, Y. H., Wu, M. C., Chu, C. P., and Qiu, D. L. (2015). Facial stimulation induces long-term depression at cerebellar molecular layer interneuron-Purkinje cell synapses in vivo in mice. *Front. Cell Neurosci.* 9:214. doi: 10.3389/fncel.2015.00214

Brown, K. M., Sugihara, I., Shinoda, Y., and Ascoli, G. A. (2012). Digital morphometry of rat cerebellar climbing fibers reveals distinct branch and bouton types. *J. Neurosci.* 32, 14670–14684. doi: 10.1523/JNEUROSCI.2018-12.2012

Chu, C. P., Zhao, G. Y., Jin, R., Zhao, S. N., Sun, L., and Qiu, D. L. (2014). Properties of 4 Hz stimulation-induced parallel fiber-Purkinje cell presynaptic long-term plasticity in mouse cerebellar cortex in vivo. *Eur. J. Neurosci.* 39, 1624–1631. doi: 10.1111/ejn.12559

Chung, H. J., Steinberg, J. P., Huganir, R. L., and Linden, D. J. (2003). Requirement of AMPA receptor GluR2 phosphorylation for cerebellar long-term depression. *Science* 300, 1751–1755. doi: 10.1126/science.1082915

Coesmans, M., Weber, J. T., De Zeeuw, C. I., and Hansel, C. (2004). Bidirectional parallel fiber plasticity in the cerebellum under climbing fiber control. *Neuron* 44, 691–700. doi: 10.1016/j.neuron.2004.10.031

Cohen, S., and Greenberg, M. E. (2008). Communication between the synapse and the nucleus in neuronal development, plasticity, and disease. *Annu. Rev. Cell Dev. Biol.* 24, 183–209. doi: 10.1146/annurev.cellbio.24.110707.175235

De Vries, T. J., and Shippenberg, T. S. (2002). Neural systems underlying opiate addiction. *J. Neurosci.* 22, 3321–3325. doi: 10.1523/jneurosci.22-09-03321.2002

Duguid, I., Branco, T., Chadderton, P., Arlt, C., Powell, K., and Hausser, M. (2015). Control of cerebellar granule cell output by sensory-evoked Golgi cell inhibition. *Proc. Natl. Acad. Sci. U.S.A.* 112, 13099–13104. doi: 10.1073/pnas.1510249112

Fetz, E. E. (1993). Cortical mechanisms controlling limb movement. *Curr. Opin. Neurobiol.* 3, 932–939. doi: 10.1016/0959-4388(93)90165-u

Gao, Z., van Beugen, B. J., and De Zeeuw, C. I. (2012). Distributed synergistic plasticity and cerebellar learning. *Nat. Rev. Neurosci.* 13, 619–635. doi: 10.1038/nrn3312

Guan, X., Duan, Y., Zeng, Q., Pan, H., Qian, Y., Li, D., et al. (2014). Lgr4 protein deficiency induces ataxia-like phenotype in mice and impairs long term depression at cerebellar parallel fiber-Purkinje cell synapses. *J. Biol. Chem.* 289, 26492–26504. doi: 10.1074/jbc.M114.564138

Hansel, C., de Jeu, M., Belmeguenai, A., Houtman, S. H., Buitendijk, G. H., Andreev, D., et al. (2006). alphaCaMKII Is essential for cerebellar LTD and motor learning. *Neuron* 51, 835–843. doi: 10.1016/j.neuron.2006.08.013

Hirano, T., and Kawaguchi, S. Y. (2014). Regulation and functional roles of rebound potentiation at cerebellar stellate cell-Purkinje cell synapses. *Front. Cell Neurosci.* 8:42. doi: 10.3389/fncel.2014.00042

Ichise, T., Kano, M., Hashimoto, K., Yanagihara, D., Nakao, K., Shigemoto, R., et al. (2000). mGluR1 in cerebellar Purkinje cells essential for long-term depression, synapse elimination, and motor coordination. *Science* 288, 1832–1835. doi: 10.1126/science.288.5472.1832

Ito, M. (2002). Historical review of the significance of the cerebellum and the role of Purkinje cells in motor learning. *Ann. N. Y. Acad. Sci.* 978, 273–288. doi: 10.1111/j.1749-6632.2002.tb07574.x

Ito, M. (2006). Cerebellar circuitry as a neuronal machine. *Prog. Neurobiol.* 78, 272–303. doi: 10.1016/j.pneurobio.2006.02.006

Jin, Y., Kim, S. J., Kim, J., Worley, P. F., and Linden, D. J. (2007). Long-term depression of mGluR1 signaling. *Neuron* 55, 277–287. doi: 10.1016/j.neuron.2007.06.035

Jones, E. (2005). Nerve endings - the discovery of the synapse. *Science* 309, 1018–1019. doi: 10.1126/science.1116404

Kadrmas, J. L., Smith, M. A., Pronovost, S. M., and Beckerle, M. C. (2007). Characterization of RACK1 function in Drosophila development. *Dev. Dyn.* 236, 2207–2215. doi: 10.1002/dvdy.21217

Kakegawa, W., Katoh, A., Narumi, S., Miura, E., Motohashi, J., Takahashi, A., et al. (2018). Optogenetic control of synaptic AMPA receptor endocytosis reveals roles of LTD in motor learning. *Neuron* 98:e986. doi: 10.1016/j.neuron.2018.07.034

Kano, M., Hashimoto, K., Chen, C., Abeliovich, A., Aiba, A., Kurihara, H., et al. (1995). Impaired synapse elimination during cerebellar development in PKC gamma mutant mice. *Cell* 83, 1223–1231. doi: 10.1016/0092-8674(95)90147-7

Kano, M., Hashimoto, K., Kurihara, H., Watanabe, M., Inoue, Y., Aiba, A., et al. (1997). Persistent multiple climbing fiber innervation of cerebellar Purkinje cells in mice lacking mGluR1. *Neuron* 18, 71–79. doi: 10.1016/s0896-6273(01)80047-7

Kershner, L., and Welshhans, K. (2017a). RACK1 is necessary for the formation of point contacts and regulates axon growth. *Dev. Neurobiol.* 77, 1038–1056. doi: 10.1002/dneu.22491

Kershner, L., and Welshhans, K. (2017b). RACK1 regulates neural development. *Neural. Regen. Res.* 12, 1036–1039. doi: 10.4103/1673-5374.211175

Lee, E. Y., Ji, H., Ouyang, Z., Zhou, B., Ma, W., Vokes, S. A., et al. (2010). Hedgehog pathway-regulated gene networks in cerebellum development and tumorigenesis. *Proc. Natl. Acad. Sci. U.S.A.* 107, 9736–9741. doi: 10.1073/pnas.1004602107

Lee, K. J., Kim, H., Kim, T. S., Park, S. H., and Rhyu, I. J. (2004). Morphological analysis of spine shapes of Purkinje cell dendrites in the rat cerebellum using high-voltage electron microscopy. *Neurosci. Lett.* 359, 21–24. doi: 10.1016/j.neulet.2004.01.071

Leitges, M., Kovac, J., Plomann, M., and Linden, D. J. (2004). A unique PDZ ligand in PKCalpha confers induction of cerebellar long-term synaptic depression. *Neuron* 44, 585–594. doi: 10.1016/j.neuron.2004.10.024

Li, J. J., and Xie, D. (2015). RACK1, a versatile hub in cancer. *Oncogene* 34, 1890–1898. doi: 10.1038/onc.2014.127

Liu, L., Zhu, J., Zhou, L., and Wan, L. (2016). RACK1 promotes maintenance of morphine-associated memory via activation of an ERK-CREB dependent pathway in hippocampus. *Sci. Rep.* 6:20183. doi: 10.1038/srep20183

Matsuda, S., Mikawa, S., and Hirai, H. (1999). Phosphorylation of serine-880 in GluR2 by protein kinase C prevents its C terminus from binding with glutamate receptor-interacting protein. *J. Neurochem.* 73, 1765–1768. doi: 10.1046/j.1471-4159.1999.731765.x

McGough, N. N., He, D. Y., Logrip, M. L., Jeanblanc, J., Phamluong, K., Luong, K., et al. (2004). RACK1 and brain-derived neurotrophic factor: a homeostatic pathway that regulates alcohol addiction. *J. Neurosci.* 24, 10542–10552. doi: 10.1523/JNEUROSCI.3714-04.2004

Middleton, F. A., and Strick, P. L. (1998). The cerebellum: an overview. *Trends Neurosci.* 21, 367–369. doi: 10.1016/s0166-2236(98)01330-7

Nietz, A. K., Vaden, J. H., Coddington, L. T., Overstreet-Wadiche, L., and Wadiche, J. I. (2017). Non-synaptic signaling from cerebellar climbing fibers modulates Golgi cell activity. *eLife* 6:e29215. doi: 10.7554/eLife.29215

Okubo, Y., Kakizawa, S., Hirose, K., and Iino, M. (2004). Cross talk between metabotropic and ionotropic glutamate receptor-mediated signaling in parallel fiber-induced inositol 1,4,5-trisphosphate production in cerebellar Purkinje cells. *J. Neurosci.* 24, 9513–9520. doi: 10.1523/JNEUROSCI.1829-04.2004

Peter, S., Ten Brinke, M. M., Stedehouder, J., Reinelt, C. M., Wu, B., Zhou, H., et al. (2016). Dysfunctional cerebellar Purkinje cells contribute to autism-like behaviour in Shank2-deficient mice. *Nat. Commun.* 7:12627. doi: 10.1038/ncomms12627

Qiu, D. L., and Knopfel, T. (2009). Presynaptically expressed long-term depression at cerebellar parallel fiber synapses. *Pflugers Arch.* 457, 865–875. doi: 10.1007/s00424-008-0555-9

Ron, D., Chen, C. H., Caldwell, J., Jamieson, L., Orr, E., and Mochly-Rosen, D. (1994). Cloning of an intracellular receptor for protein kinase C: a homolog of the beta subunit of G proteins. *Proc. Natl. Acad. Sci. U.S.A.* 91, 839–843. doi: 10.1073/pnas.91.3.839

Rowan, M. J. M., Bonnan, A., Zhang, K., Amat, S. B., Kikuchi, C., Taniguchi, H., et al. (2018). Graded control of climbing-fiber-mediated plasticity and learning by inhibition in the cerebellum. *Neuron* 99:e1016. doi: 10.1016/j.neuron.2018.07.024

Schonewille, M., Belmeguenai, A., Koekkoek, S. K., Houtman, S. H., Boele, H. J., van Beugen, B. J., et al. (2010). Purkinje cell-specific knockout of the protein phosphatase PP2B impairs potentiation and cerebellar motor learning. *Neuron* 67, 618–628. doi: 10.1016/j.neuron.2010.07.009

Schonewille, M., Gao, Z., Boele, H. J., Veloz, M. F., Amerika, W. E., Simek, A. A., et al. (2011). Reevaluating the role of LTD in cerebellar motor learning. *Neuron* 70, 43–50. doi: 10.1016/j.neuron.2011.02.044

Shi, X., Zhang, Z., Zhan, X., Cao, M., Satoh, T., Akira, S., et al. (2014). An epigenetic switch induced by Shh signalling regulates gene activation during development and medulloblastoma growth. *Nat. Commun.* 5:5425. doi: 10.1038/ncomms6425

Sillitoe, R. V., and Joyner, A. L. (2007). Morphology, molecular codes, and circuitry produce the three-dimensional complexity of the cerebellum. *Annu. Rev. Cell Dev. Biol.* 23, 549–577. doi: 10.1146/annurev.cellbio.23.090506.123237

Sklan, E. H., Podoly, E., and Soreq, H. (2006). RACK1 has the nerve to act: structure meets function in the nervous system. *Prog. Neurobiol.* 78, 117–134. doi: 10.1016/j.pneurobio.2005.12.002

Strick, P. L., Dum, R. P., and Fiez, J. A. (2009). Cerebellum and nonmotor function. *Annu. Rev. Neurosci.* 32, 413–434. doi: 10.1146/annurev.neuro.31.060407.125606

Tanaka, S., Kawaguchi, S. Y., Shioi, G., and Hirano, T. (2013). Long-term potentiation of inhibitory synaptic transmission onto cerebellar Purkinje neurons contributes to adaptation of vestibulo-ocular reflex. *J. Neurosci.* 33, 17209–17220. doi: 10.1523/JNEUROSCI.0793-13.2013

Thornton, C., Tang, K. C., Phamluong, K., Luong, K., Vagts, A., Nikanjam, D., et al. (2004). Spatial and temporal regulation of RACK1 function and N-methyl-D-aspartate receptor activity through WD40 motif-mediated dimerization. *J. Biol. Chem.* 279, 31357–31364. doi: 10.1074/jbc.M402316200

van Woerden, G. M., Hoebeek, F. E., Gao, Z., Nagaraja, R. Y., Hoogenraad, C. C., Kushner, S. A., et al. (2009). betaCaMKII controls the direction of plasticity at parallel fiber-Purkinje cell synapses. *Nat. Neurosci.* 12, 823–825. doi: 10.1038/nn.2329

Volta, V., Beugnet, A., Gallo, S., Magri, L., Brina, D., Pesce, E., et al. (2013). RACK1 depletion in a mouse model causes lethality, pigmentation deficits and reduction in protein synthesis efficiency. *Cell Mol. Life Sci.* 70, 1439–1450. doi: 10.1007/s00018-012-1215-y

Voogd, J., and Glickstein, M. (1998). The anatomy of the cerebellum. *Trends Neurosci.* 21, 370–375.

Wagner, M. J., Kim, T. H., Savall, J., Schnitzer, M. J., and Luo, L. (2017). Cerebellar granule cells encode the expectation of reward. *Nature* 544, 96–100. doi: 10.1038/nature21726

Waite, J. J., Wardlow, M. L., and Power, A. E. (1999). Deficit in selective and divided attention associated with cholinergic basal forebrain immunotoxic lesion produced by 192-saporin; motoric/sensory deficit associated with Purkinje cell immunotoxic lesion produced by OX7-saporin. *Neurobiol. Learn. Mem.* 71, 325–352. doi: 10.1006/nlme.1998.3884

Wang, D. J., Su, L. D., Wang, Y. N., Yang, D., Sun, C. L., Zhou, L., et al. (2014). Long-term potentiation at cerebellar parallel fiber-Purkinje cell synapses requires presynaptic and postsynaptic signaling cascades. *J. Neurosci.* 34, 2355–2364. doi: 10.1523/JNEUROSCI.4064-13.2014

Wang, H., and Friedman, E. (2001). Increased association of brain protein kinase C with the receptor for activated C kinase-1 (RACK1) in bipolar affective disorder. *Biol. Psychiatr.* 50, 364–370. doi: 10.1016/s0006-3223(01)01147-7

Wehner, P., Shnitsar, I., Urlaub, H., and Borchers, A. (2011). RACK1 is a novel interaction partner of PTK7 that is required for neural tube closure. *Development* 138, 1321–1327. doi: 10.1242/dev.056291

Wu, H., Barik, A., Lu, Y., Shen, C., Bowman, A., Li, L., et al. (2015). Slit2 as a beta-catenin/Ctnnb1-dependent retrograde signal for presynaptic differentiation. *eLife* 4:e07266. doi: 10.7554/eLife.07266

Wu, H., Lu, Y., Barik, A., Joseph, A., Taketo, M. M., Xiong, W. C., et al. (2012). beta-Catenin gain of function in muscles impairs neuromuscular junction formation. *Development* 139, 2392–2404. doi: 10.1242/dev.080705

Yaka, R., Thornton, C., Vagts, A. J., Phamluong, K., Bonci, A., and Ron, D. (2002). NMDA receptor function is regulated by the inhibitory scaffolding protein, RACK1. *Proc. Natl. Acad. Sci. U.S.A.* 99, 5710–5715. doi: 10.1073/pnas.062046299

Yamada, T., Yang, Y., Hemberg, M., Yoshida, T., Cho, H. Y., Murphy, J. P., et al. (2014). Promoter decommissioning by the NuRD chromatin remodeling complex triggers synaptic connectivity in the mammalian brain. *Neuron* 83, 122–134. doi: 10.1016/j.neuron.2014.05.039

Yang, H., Zhu, Q., Cheng, J., Wu, Y., Fan, M., Zhang, J., et al. (2019). Opposite regulation of Wnt/beta-catenin and Shh signaling pathways by Rack1 controls mammalian cerebellar development. *Proc. Natl. Acad. Sci. U.S.A.* 116, 4661–4670. doi: 10.1073/pnas.1813244116

Yeganeh-Doost, P., Gruber, O., Falkai, P., and Schmitt, A. (2011). The role of the cerebellum in schizophrenia: from cognition to molecular pathways. *Clinics* 66(Suppl. 1), 71–77. doi: 10.1590/s1807-59322011001300009

Zamora Chimal, C. G., and De Schutter, E. (2018). Ca(2+) requirements for long-term depression are frequency sensitive in purkinje cells. *Front. Mol. Neurosci.* 11:438. doi: 10.3389/fnmol.2018.00438

Zhao, Y., Wang, Q., Qiu, G., Zhou, S., Jing, Z., Wang, J., et al. (2015). RACK1 promotes autophagy by enhancing the Atg14L-Beclin 1-Vps34-Vps15 complex formation upon phosphorylation by AMPK. *Cell Rep.* 13, 1407–1417. doi: 10.1016/j.celrep.2015.10.011

Zhou, J. H., Wang, X. T., Zhou, L., Zhou, L., Xu, F. X., Su, L. D., et al. (2017). Ablation of TFR1 in Purkinje cells inhibits mGlu1 trafficking and impairs motor coordination, but not autistic-like behaviors. *J. Neurosci.* 37, 11335–11352. doi: 10.1523/JNEUROSCI.1223-17.2017

Conflict of Interest: The authors declare that the research was conducted in the absence of any commercial or financial relationships that could be construed as a potential conflict of interest.

frontiers in Neural Circuits

ORIGINAL RESEARCH
published: 27 February 2020
doi: 10.3389/fncir.2020.00001

Fictive Scratching Patterns in Brain Cortex-Ablated, Midcollicular Decerebrate, and Spinal Cats

*Irene Guadalupe Aguilar Garcia[1], Judith Marcela Dueñas-Jiménez[2], Luis Castillo[3], Laura Paulina Osuna-Carrasco[4], Braniff De La Torre Valdovinos[4], Rolando Castañeda-Arellano[5], Jose Roberto López-Ruiz[6], Carmen Toro-Castillo[4], Mario Treviño[7], Gerardo Mendizabal-Ruiz[4] and Sergio Horacio Duenas-Jimenez[6]**

[1]Departamento de Biología Molecular y Genómica, CUCS, Universidad de Guadalajara, Guadalajara, Mexico, [2]Departamento de Fisiología, CUCS, Universidad de Guadalajara, Guadalajara, Mexico, [3]Centro Básico, Universidad de Aguascalientes, Aguascalientes, Mexico, [4]Departmento de Electrónica y Computación, CUCEI, Universidad de Guadalajara, Guadalajara, Mexico, [5]Departmento de Ciencias Biomédicas, CUTonala, Universidad de Guadalajara, Guadalajara, Mexico, [6]Departmento de Neurociencias, CUCS, Universidad de Guadalajara, Guadalajara, Mexico, [7]Laboratorio de Plasticidad Cortical y Aprendizaje Perceptual, Instituto de Neurociencias, Universidad de Guadalajara, Guadalajara, Mexico

Background: The spinal cord's central pattern generators (CPGs) have been explained by the symmetrical half-center hypothesis, the bursts generator, computational models, and more recently by connectome circuits. Asymmetrical models, at odds with the half-center paradigm, are composed of extensor and flexor CPG modules. Other models include not only flexor and extensor motoneurons but also motoneuron pools controlling biarticular muscles. It is unknown whether a preferred model can explain some particularities that fictive scratching (FS) in the cat presents. The first aim of this study was to investigate FS patterns considering the aiming and the rhythmic periods, and second, to examine the effects of serotonin (5HT) on and segmental inputs to FS.

Methods: The experiments were carried out first in brain cortex-ablated cats (BCAC), then spinalized (SC), and for the midcollicular (MCC) preparation. Subjects were immobilized and the peripheral nerves were used to elicit the Monosynaptic reflex (MR), to modify the scratching patterns and for electroneurogram recordings.

Results: In BCAC, FS was produced by pinna stimulation and, in some cases, by serotonin. The scratching aiming phase (AP) initiates with the activation of either flexor or extensor motoneurons. Serotonin application during the AP produced simultaneous extensor and flexor bursts. Furthermore, WAY 100635 (5HT1A antagonist) produced a brief burst in the tibialis anterior (TA) nerve, followed by a reduction in its electroneurogram (ENG), while the soleus ENG remained silent. In SC, rhythmic phase (RP) activity was recorded in the soleus motoneurons. Serotonin or WAY produced FS bouts. The electrical stimulation of Ia afferent fibers produced heteronymous MRes waxing and waning during the scratch cycle. In MCC, FS began with flexor activity. Electrical stimulation of either deep peroneus (DP) or superficial peroneus (SP) nerves increased the duration of the TA electroneurogram. Medial gastrocnemius (MG) stretching or MG nerve electrical stimulation produced a reduction in the TA electroneurogram and an initial MG extensor burst. MRes waxed and waned during the scratch cycle.

OPEN ACCESS

Edited by:
Jing-Ning Zhu, Nanjing University, China

Reviewed by:
Jianren Song, Tongji University, China
Jesus Angel Tapia-Lopez, Meritorious Autonomous University of Puebla, Mexico

***Correspondence:**
Sergio Horacio Duenas-Jimenez
sduenas@cucs.udg.mx

Received: *12 September 2019*
Accepted: *03 January 2020*
Published: *27 February 2020*

Citation:
Aguilar Garcia IG, Dueñas-Jiménez JM, Castillo L, Osuna-Carrasco LP, De La Torre Valdovinos B, Castañeda-Arellano R, López-Ruiz JR, Toro-Castillo C, Treviño M, Mendizabal-Ruiz G and Duenas-Jimenez SH (2020) Fictive Scratching Patterns in Brain Cortex-Ablated, Midcollicular Decerebrate, and Spinal Cats. Front. Neural Circuits 14:1. doi: 10.3389/fncir.2020.00001

Conclusion: Descending pathways and segmental afferent fibers, as well as 5-HT and WAY, can change the FS pattern. To our understanding, the half-center hypothesis is the most suitable for explaining the AP in MCC.

Keywords: fictive scratching, motor patterns, decerebrate cat, spinal cat, monosynaptic reflex

INTRODUCTION

The central pattern generators (CPGs) in the spinal cord were first studied by Brown and Sherrington (1911), who proposed the symmetrical half-center hypothesis. The burst generator concept emerged many decades later (Anderssson and Grillner, 1981) and was followed by the development of computational models (Shevtsova and Rybak, 2016; Ausborn et al., 2018, 2019). Recently, connectome circuits have been reported in genetically identified interneurons (for a comprehensive review, see Rybak et al., 2015).

Asymmetrical models are conformed by extensor and flexor CPG modules working independently but are at odds with the half-center paradigm (Hägglund et al., 2013). Other concepts that include not only flexor and extensor motoneurons but also motoneuron pools controlling bi-articular muscles are being developed (Barardi et al., 2014). There are other models based on a two-layer longitudinal architecture of the CPG that propose a theoretical circuit that reproduces the sinusoidal shape of the dorsal cord potentials (Pérez et al., 2009). Interneurons within extensor module circuits that possess rhythmic properties could be sufficient to perform different rhythmic motor tasks (Frigon and Gossard, 2010).

During fictive locomotion (FL) or fictive scratching (FS), flexor and extensor commissural interneurons share both motor tasks (Trejo et al., 2015). Moreover, the spinal cord CPG seems to be composed of neural elements in two levels: one generates the rhythm and the other produces several motor patterns in the hindlimb extensor and flexor motoneurons (Rybak et al., 2006a,b). These levels are related to the interneurons that generate the motor pattern such as the aiming phase (AP) and rhythmic phase (RP) during scratching. The segmental peripheral and descending inputs could affect the scratching motor task during the two different phases. Descending serotoninergic inputs increase the excitability of the CPG's spinal extensor motoneurons. These serotoninergic pathways could originate either from brainstem neurons giving rise to the descending tracts (Jordan et al., 2008) or from propriospinal interneurons (Cabaj et al., 2017). Some studies have reported that monoamines are strong modulators and/or activators of the spinal locomotor networks (Noga et al., 2009, 2017), although they are not necessary to evoke locomotion (Steeves et al., 1980). Sustained monoamine release activates receptors in neurons within the spinal cord, suggesting sustained extrasynaptic transmission (Noga et al., 2017). FS activity is also facilitated by topical d-tubocurarine spinal cord application induced by pinna stimulation (Domer and Feldberg, 1960). Numerous studies of spinal cord locomotor circuits' pharmacological modulation in decerebrated or in spinal cord-injured cats have provided insight into the roles of monoamines in posture and stepping (Barbeau and Rossignol, 1991; Rossignol et al., 1998, 2001; Brustein and Rossignol, 1999). Modulation of the monoaminergic system in cats, rats, and turtles has allowed the observation of motoneuron excitability regardless of the use of typical facilitation mechanisms to affect membrane potential (Hornby et al., 2002; Fedirchuk and Dai, 2004; Gilmore and Fedirchuk, 2004). It is important to emphasize that the scratching phenomenon in fictive motor preparations has not been deeply investigated to establish the afferent and descendent pathway producing FS in cats. A relevant work was made in a mice model, which exhibits the pathways related to itch and their relationship to periaqueductal gray glutamatergic neurons (Gao et al., 2019).

In brain cortex-ablated cats (BCAC), the AP in FS could initiate with either extensor or flexor tonic activity and is followed by the RP (Duenas-Jimenez et al., 2017). Interestingly, the AP in most midcollicular cats (MCC) starts with flexor tonic activity (Berkinblit et al., 1978). In BCAC, it remains unclear whether extensor motoneurons are inhibited during the AP as postulated by the half-center hypothesis. Therefore, one of the purposes of this work was to clarify whether the activation of the extensor half center during the AP in BCAC inhibits the flexor one, and vice versa, as the half center hypothesis predicts. Balanced excitation–inhibition and irregular firing modified by serotonin (5HT) are fundamental motifs in certain spinal network functions (Berg et al., 2007; Guzulaitis et al., 2016). It is also known that increased synaptic fluctuations in membrane potential, irregular firing, and increased conductance occur in spinal motoneurons during scratching network activity. Serotonin produces irregular firing in turtle motoneurons and modifies the actions between flexor and extensor half centers; however, its effect in cats is not known. Motoneuron activation is a general feature of spinal motor network activity (Guzulaitis et al., 2016); thus, we can conjecture that motoneurons that do not fire during FS could be driven by a different spinal cord oscillator. In the BCAC, it is unknown whether a different subthreshold rhythm could be elicited during FS in silent soleus (SOL) motoneurons.

Several recent studies have assessed the relationship between brainstem and spinal cord motoneurons to evaluate the neural circuits involved in the rhythm generator for FS. Therefore, an additional goal was to evaluate the effect of injecting 5HT in the caudal brainstem on the FS patterns generation in BCAC that were not induced by d-tubocurarine and pinna stimulation. The 5HT1A receptor is implicated in other rhythmic activities such as swimming in *Xenopus laevis* (Wedderburn and Sillar, 1994) and in the respiratory rhythm of mice. Therefore, the 1A receptor antagonist drug WAY 100635 can be used to study 5HT effects on FS patterns (Dhingra et al., 2016). Systemic

and focal 5HT1a receptor blockade with WAY100635 increased the occurrence of spontaneous apneas and rhythm variability. 5HT1aR-dependent synaptic transmission in the dorsolateral pontine nucleus modulates respiratory network stability through 5HT1a receptors, regulating the frequency of spontaneous apneas; hence, there is intrinsic respiratory variability in response to extrinsic chemosensory perturbations (Dhingra et al., 2016).

In BCAC, the heteronymous monosynaptic reflex (HeMR) produced by Ia afferent fibers acting in motoneurons of the same joint has been previously analyzed (Duenas-Jimenez et al., 2017). However, these reflexes were not fully analyzed among the Ia afferent fibers and motoneurons innervating the hindlimb muscles acting in different joints. Here, we studied whether Ia afferent fibers are producing HeMR in the semitendinosus (ST), lateral gastrocnemius (LG), and flexor hallucis longus (FHL) motoneurons by posterior biceps (PB) stimulation and whether medial gastrocnemius (MG) electrical stimulation of Ia afferent fibers evoke HeMR in FHL motoneurons. The effects of electrical stimulation of deep peroneus (DP), superficial peroneus (SP), and MG nerves in MCC were also evaluated to find support for either the half center or the asymmetrical hypothesis.

MATERIALS AND METHODS

General Procedures

All procedures were performed in accordance with the ethical guidelines of the Mexican Official Norm (NOM-062-ZOO-1999) and the National Institutes of Health Guide NIH Publication No. 8023 (1996) for the Care and Use of Laboratory Animals. All experimental experiments in 39 cats produced the total data set (preparations and protocols listed in **Table 1**). Protocols were approved by the Institutional Animal Care and Use Committee (IACUC). Some of the data presented come from experiments previously made in 32 cats for answering other scientific questions. However, this dataset optimizes the scientific output of every animal experiment. Animals were raised and housed in separate cages.

TABLE 1 | Treatment and stimulation applied in the different cats' preparations for ENG recordings during FS.

Preparation	Treatment	NC	NE	Stimulation
BCAC-SC	-	32		-
BCAC	d-tubocurarine	4	6	-
BCAC	d-tubocurarine	5	11	Pinna + PB/MG nerves
BCAC	BS 5-HT	2	3	Pinna
BCAC	IS 5-HT	21*	45	Pinna
BCAC	IS WAY	21*	27	Pinna
SC	IS 5-HT	21*	40	Pinna
SC	IS WAY	21*	9	Pinna
MCC	-	7		Pinna + GS muscle stretching
MCC	-	7*		Pinna + MG stimulation
MCC	-	7*		Pinna + SP stimulation
MCC	-	7*		Pinna + DP stimulation

BCAC-SC, brain cortex-ablated cats, later spinalized; BS: brainstem; DP: deep peroneus nerve; ENG: electroneurogram; FS: fictive scratching; 5HT: serotonin; IS: intra-spinal cord injection; MCC: midcollicular cats; MG, medial gastrocnemius; NC: number of cats used in the experiment; NE: number of episodes; PB: posterior biceps; SC: spinal cord; SP: superficial peroneus. The asterisk indicates the same subjects as BCAC-SC or MCC.

Immobilized BCAC with a mass of 3–3.5 kg each were used to study FS. Brain cortex and suprathalamic structure ablation, as well as damage in some thalamic nuclei, was performed under ketamine (20 mg/kg) and brevital (20–40 mg/kg) as previously described (López Ruiz et al., 2017). For SC, the spinal cord was cut at C1–C2 segments. Some were injected with 7 μM 5HT solution (0.5 ml at 2 μl/min) in the spinal cord during brain cortex-ablated status or in the same cats after spinalization; other cats were microinjected in the spinal cord with WAY-100635 (N-[2-[4-(2-methoxyphenyl)-1-piperazinyl] ethyl]-N-(2-pyridyl) cyclohexanecarboxamide, 0.2–5 nM throughout the course of 5–20 min) during brain cortex-ablated status and 3–4 h after spinalization preparation. Some cats were injected with 5HT in the brainstem, 1 mm down the obex to evoke FS (**Table 1**). In MCC, following a craniotomy, the cortex was removed, and all tissue rostral to the inferior colliculi and mammillary bodies was removed. At this point, the animals were considered painless, so anesthesia was discontinued. All cats were paralyzed with pancuronium bromide injections (1 mg/kg) administered through the radial veins every 60 min until the end of the experiment. Paralysis is required for the study of centrally generated FS and the effects of specific sensory inputs, so the animals were artificially ventilated (sustained expiratory CO_2 level from 4% to 5%) throughout the experiment. A lethal injection of pentobarbital anesthetic was administered through the jugular vein at the end of the experiment.

FS

FS in immobilized BCAC, MCC, and SC was evoked by light and continuous pressure in the pinna after topical d-tubocurarine application (0.01–0.025%) in C1–C2 spinal cord segments (Domer and Feldberg, 1960). In two cases, 5HT was injected in brainstem to achieve FS; in four other cats, FS appeared after local d-tubocurarine application.

ENG Recordings

ENG data acquisition and analysis from two to nine nerves was performed using AxoScope 7 software. The signal was amplified in differential alternating current. The sampling rates per channel varied from 16 to 2 kHz depending on the number of simultaneous recorded channels. FS episodes were divided into tonic AP and RP with extensor and flexor activity constituting a scratching cycle.

In MCC, the MG muscle was stretched 3–6 mm by applying force to the posterior surface of the calcaneus (calcaneus-tibial, angle 50–90°). In these experiments, the MG and LG nerves and spinal roots were kept intact except for a thin MG filament, which was dissected, sectioned, and used for recording. The DP, SP, or MG nerves were electrically stimulated with single shocks; the threshold of the most excitable nerve was determined by recording afferent volleys in the L7 or S1 using a ball electrode with a reference lead placed in the skin or back muscle.

Electrical high frequency (30–300 Hz) and variable duration were also used. Monosynaptic reflex (MR) discharges were elicited in the MG and flexor tibialis anterior (TA) nerves by electrical stimulation at 1.2–1.5 times the threshold for the most excitable fibers of the L7 or S1 dorsal roots.

HeMRs in BCAC

The time of each scratch cycle was normalized and divided in 10 bins to increase the temporal resolution of the statistical analysis (Alaburda, 2005). The means and standard deviations (SDs) of all the peak-to-peak HeMR amplitudes corresponding to each bin of the pre- and bursting period were computed and evaluated for statistical differences using one-way analysis of variance (alpha = 0.05). An adjustment was made for the degree of freedom (Bonferroni corrections for multiple comparisons, alpha = 0.05, $n = 10$ (Welch and Ting, 2009). The obtained HeMR means (circles) and SDs (vertical lines) prior to scratching are shown in **Figures 3A–D**. All scratching cycles that did not differ >15% from the mean cycle duration were plotted and indicated under the abscissa; the durations of the cycle phases are also shown (extensor: E and flexor: F).

Direct Current Potential in the BCAC Spinal Cord During Scratching

In cats, where FS only appeared after only d-tubocurarine applications, the DC potentials were measured by a microelectrode filled with sodium chloride (2 M) placed in the intermediate nucleus of the L6 spinal cord segment. A ball electrode was placed in the L6–L7 segment to record dorsal root potentials (DRPs) and the incoming potential evoked by PB or MG stimulation.

RESULTS

FS Patterns in Ablated Cats

In BCAC, we analyzed FS in several conditions. In four BCAC subjects, FS appeared after topical application of d-tubocurarine to the spinal cord. **Figure 1A** shows the rectified and integrated FDL, FHL, SOL, and LG ENGs from one of these experiments. It is clear that most SOL motoneurons did not exhibit ENG activity during scratching. FHL and LG activity occurred in phase. In two of these subjects, phasic DRP and a sustained DC potential appeared during RP activity (**Figure 1B**). This point is very important since actual models do not consider the electrical and the companying magnetic field related to the RP. The absence of activity in most SOL motoneurons is also noteworthy, since these silent motoneurons could be used by the locomotor CPG to act in some segregated motoneurons.

In BCAC, FS episodes were observed in FHL and PB nerves following pinna stimulation, and foot pad (FP) mechanical stimulation (indicated by an arrow) produced FL in the SOL nerve, thus concurring both rhythms (**Figure 2A**). During spontaneous FL recorded in the MG ENG, pinna stimulation produced FS (5 Hz) concurrent with the spontaneous low-frequency rhythm (2 Hz; **Figure 2B**), likely indicating a possible coupling between slow and fast oscillators (Ausborn et al., 2018; Frigon and Gossard, 2010). We did not record alternating activity between TA and MG or SOL; it seems possible that bursting activity occurs in some extensor motoneurons but not rhythmic activity in flexor motoneurons of the same joint. Then, we decided to study the HeMR between Ia afferent fibers to clarify if spinal scratching generator modulates the motoneuron activity simultaneously in distal joints.

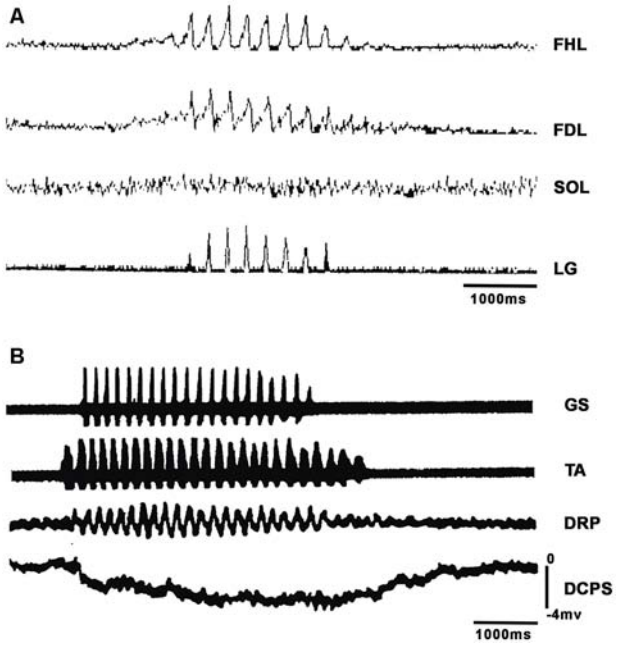

FIGURE 1 | Short episodes of fictive scratching (FS) appeared after d-tubocurarine application with two characteristics: absence of SOL electroneurographic activity and DC shifts in spinal cord intermediate nucleus. **(A)** Traces: flexor hallucis longus (FHL), lateral gastrocnemius (LG), flexor digitorum longus (FDL) and soleus (SOL). The ENGs were integrated and rectified. **(B)** DC potential during FS scratching. Traces: first, gastrocnemius soleus (GS); second, tibial anterior (TA). Traces 1 and 2 are raw electroneurograms. Third trace: dorsal root potential (DRP), fourth trace: DC potential shift.

Heteronymous Monosynaptic Reflex in BCAC During FS Produced by Pinna Stimulation

In five cats treated with d-tubocurarine, FS occurred after pinna stimulation. In these cats, we analyzed the HeMR produced in the motoneurons innervating muscles acting in different joints by stimulating the group Ia afferent fibers (**Figure 3**). MG stimulation produced HeMR in FHL motoneurons, waxing and waning during the scratch cycle (**Figure 3A**). PB electrical stimulation produced HeMR in the ST, FHL, and LG. These reflexes also waxed and waned during the scratch cycle (**Figures 3B–D**).

FS Patterns in BCAC and SC With Serotonin and WAY Application

When pinna stimulation did not produce FS (**Figure 4A**), 5HT brainstem microinjection did (**Figure 4B**). In 5HT-treated cats, the AP sometimes started with flexor activity (**Figure 5A**) as seen in cats that were not treated with 5HT. In other subjects, the AP initiated with simultaneous flexor and extensor ENG activity (**Figure 5C**) or with a short burst in the extensor nerves (**Figure 5B**, arrows). In BCAC, the SOL ENG remained silent, but activity occurred in SC; also, there was a notable reduction in TA and MG ENG activity in SC compared with BCAC, statistically significant as shown in the graph figure (**Figures 6A–C**). In

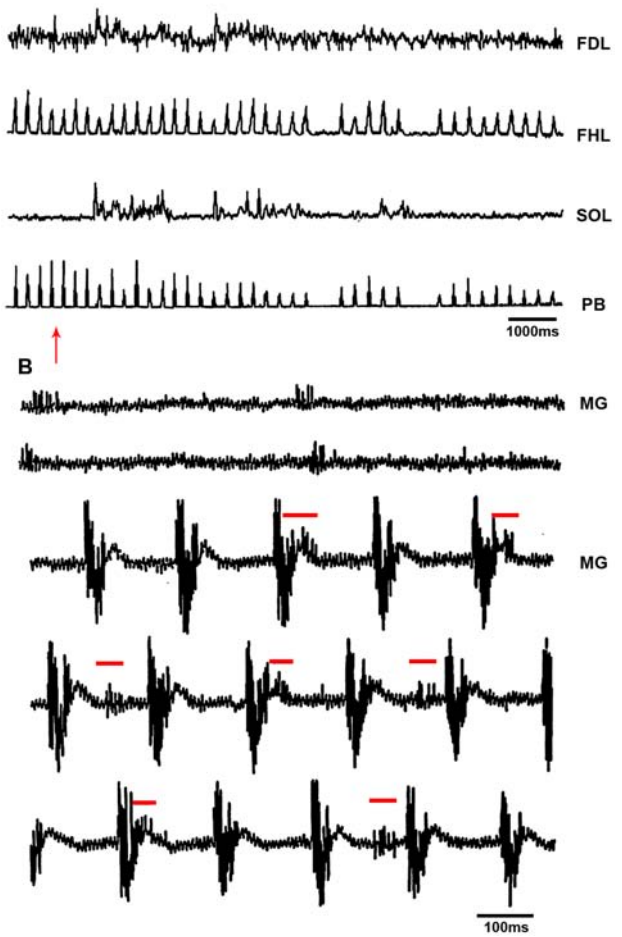

FIGURE 2 | **(A)** FS produced by pinna stimulation and bursting activity with a slower frequency in SOL ENG; FS was rectified and integrated ENG in FHL, FDL and SOL ENG exhibits a slow frequency rhythm produced by FP mechanical stimulation. Traces as indicated. **(B)** Slow frequency spontaneous rhythmic activity in the MG ENG. After pinna stimulation, slow frequency rhythmic activity concurred with FS frequency in the MG ENG. The red arrow indicates FP stimulation.

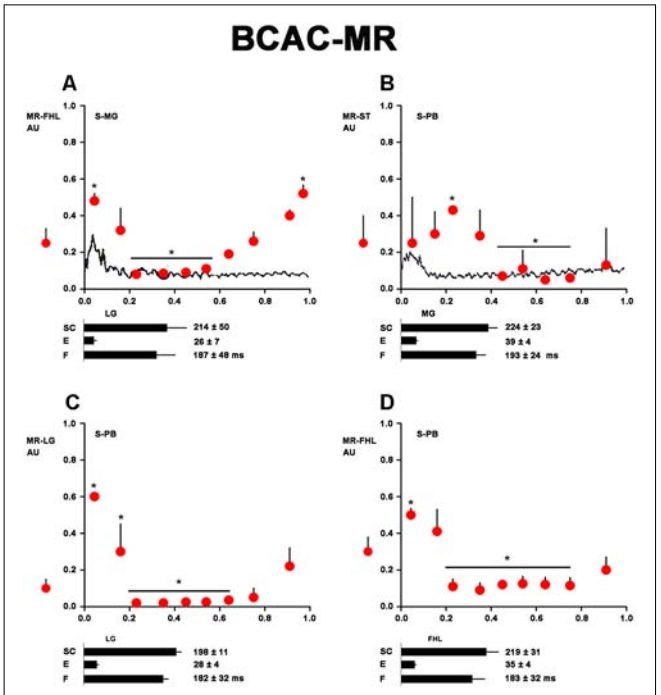

FIGURE 3 | Heteronymous Monosynaptic reflex (MR) modulation in brain cortex-ablated cats (BCAC) during the rhythmic phase (RP) of the FS. **(A)** HeMR amplitude changes in FHL motoneurons (ordinate), produced by electrical MG nerve stimulation (S-MG) plotted in relation to the normalized FHL scratch cycle (abscissa). Upper bar below the abscissa (SC) denotes cycle duration as measured in the FHL ENG. Second and third bars below the abscissa are the extensor and flexor phase durations, respectively. The dot with the vertical line on the left of the ordinate indicates the HeMR amplitude and standard deviation (SD) before the scratching episode. **(B–D)** HeMR amplitude changes in ST, LG, and FHL motoneurons in relation to normalized ST, LG, and FHL scratch cycles, respectively. Electrical stimulation was given to the PB nerve (1.3 T). In B, ST-HeMR amplitude changes (ordinate) in relation to the ST scratch cycle (abscissa). The continuous line in panel **(B)** represents the averaged and rectified ST ENG. The extensor phase is indicated. The mean scratching cycle duration and its SD were measured in the ST ENG. Asterisk in **(A–D)** denotes $P < 0.05$. In **(C,D)**, the HeMR was recorded in LG and FHL nerves, respectively. Other indications as in **(A)**.

five cats, when pinna stimulation induced FS, FP stimulation produced FL (**Figure 7**). Microinjection of WAY-100635 into the spinal cord produced a FS episode after a short TA ENG burst, which was followed by a TA ENG amplitude reduction (**Figure 8A**). In two cases, the initial TA burst was followed by tonic activity in the extensor ENG that continued until RP onset (**Figure 8B**). In SC, spinal cord 5HT microinjections produced bouts of FS (**Figure 9A**). WAY-100635 intraspinal cord injections also elicited FS (**Figure 9B**) that began with activity in the extensor motoneurons, although AP patterns was variable in other scratching episodes (**Figures 10A–C**).

FS Patterns and the MR in MCC

In MCC, FS began in the TA, 1–5 s after mechanical pinna stimulation. No changes were noted in this pattern after ipsilateral L5–L7 dorsal root sectioning. The duration of the initial TA ENG during the AP ranged from 0.5 to 2.5 s among different animals. The AP period concluded 20–40 ms before the RP onset. The average scratch cycle frequency was 5.5 ± 0.3 Hz, and the durations of the flexor and extensor bursts were 136 ± 35 ms and 17 ± 8 ms, respectively (**Figure 11A**). MRs in the TA and MG nerves were evaluated to study the MG and TA motoneuron excitability by L7 dorsal root electrical stimulation. The results in **Figure 11B** illustrate depolarization of the MG before the approach period, which could be subthreshold activity in the MG ENG. MR's amplitude increased 200 ms before the AP period, and the TA reflex increased several times during the AP. In contrast, the MG reflex decreased before TA activity's onset and the reflex was depressed (almost abolished). During the RP, TA and MG reflex activity amplitudes varied cyclically from facilitation to depression, almost matching temporarily with the MG or TA's activity (**Figure 11C**). Stretching the triceps surae muscle at 3 mm induced a short duration burst

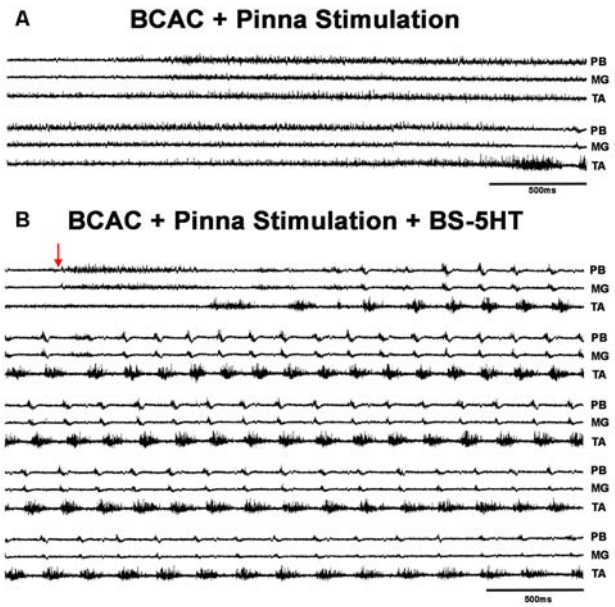

FIGURE 4 | FS episode elicited by pinna stimulation plus 5HT in a BCAC. **(A)** Pinna stimulation without 5HT (traces as indicated MG, TA, and PB). **(B)** After brainstem 5HT microinjection indicated with an arrow (traces as indicated PB, MG, and TA). The traces are consecutive recordings. In **(B)**, the ENG activity before RP onset occurred in PB and MG. The red arrow indicates pinna stimulation.

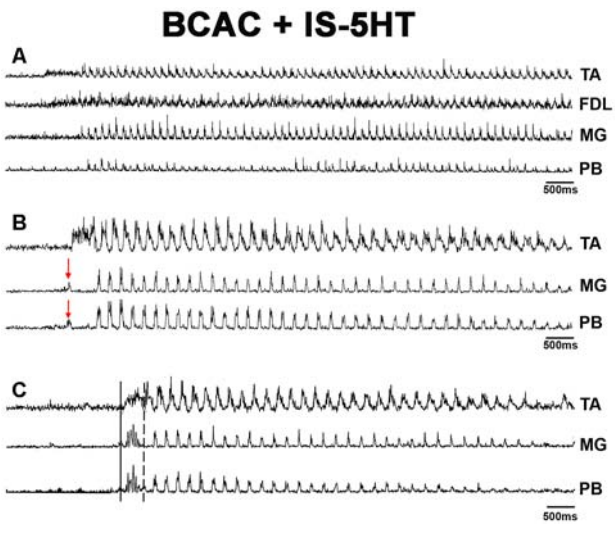

FIGURE 5 | Different FS patterns in BCAC produced by pinna stimulation plus 5HT. **(A)** The AP commences with flexor activity in the TA ENG. **(B)** FS in a different cat after spinal cord 5HT microinjection. The AP commences with ENG activity in the MG and PB ENG. **(C)** FS episode showing tonic AP with simultaneous activity on flexor and extensor ENG. FS episodes **(A–C)** were recorded in three different cats. ENGs, integrated and rectified. The red arrow indicates burst activity in MG and PB, ENG before TA-ENG activity during the AP.

in the MG sectioned nerve, and the AP in TA nerve was reduced (**Figures 12A,B**). When the MG tendon was pulled to 6 mm, the TA approach period duration was reduced even further; RP was also reduced and ceased in association with a prolonged MG ENG discharge (**Figure 12C**). In two experiments, thin filaments of the MG nerve were sectioned and used for electrical stimulation (30–300 Hz). When the pinna and nerves were stimulated simultaneously, the approach period in the TA nerve did not occur (**Figure 12E**). Instead, prolonged activity in the MG ENG was observed. When electrical stimulus was applied during the RP, the TA burst duration decreased, whereas the MG ENG duration increased (**Figure 12F**). This occurred when the stimulus was three to five times the threshold for the more excitable fibers. Electrical stimulation of SP nerves ($2 \times$ T, 30–300 Hz) prolonged the AP duration in the TA ENG (**Figures 13A,B**). Electrical stimulation of the DP nerve during the RP by more than three to four times the threshold of the most excitable fibers also prolonged the TA approach period based on stimulus duration, with concomitant abolishment of extensor ENG (**Figure 13C**). The extensor's activity in the MG nerve resumed after a prolonged TA activity. Short duration of electrical stimulus prolonged TA bursts and the MG ENG appeared after the TA post-discharges (**Figure 13D**). These results indicate that the half-center hypothesis prevails in the RP of MCC.

DISCUSSION

The presence of scratching rhythmic activity without pinna stimulation occurred in four BCAC. Thus, d-tubocurarine application to C1 affected the rhythmic scratching generator activation. It is important to note that the AP did not appear in these scratching patterns and the RP ranged from 6 to 20 cycles. There was a clear segregation between the AP and RP. Tubocurarine changes the state of the segmental scratching circuit apparatus, particularly, the activity of interneurons and flexor and extensor motoneurons. Flexor associated interneurons that are related to AP were inhibited maybe by a direct action of d-tubocurarine in interneurons with cholinergic receptors, this point deserves further investigation. The short duration of the RP could be attributed to a postural action, where the limbs of the subject are extended (Degtyarenko et al., 1992). The presence of DRPs is indicative of primary afferent depolarization (PAD) in some type of afferent fibers. PAD was not observed in group Ia afferents during scratching (Gossard, 1996; López Ruiz et al., 2017). The presence of DC potentials during the RP could be related to an increase in extracellular potassium (Jiménez et al., 1983) or it also could be produced by electrical coupling between neuronal elements (astroglia or neurons of the scratching generator; Kiehn et al., 2000; Wendy Bautista et al., 2012, 2014). Electrical coupling can generate synchronized oscillations to promote rhythmic firing (Bennett and Zukin, 2004; Connors and Long, 2004); this phenomenon has been described in the mammalian spinal cord (Rash et al., 1996; Kiehn et al., 2000; Lemieux et al., 2010), including among motoneurons in the adult cat (Gogan et al., 1977). DC-induced magnetic fields could probably alter the neuronal excitability by acting in potassium channels (Bączyk and Jankowska, 2018; Kaczmarek and Jankowska, 2018). Magnetic fields have been used to study

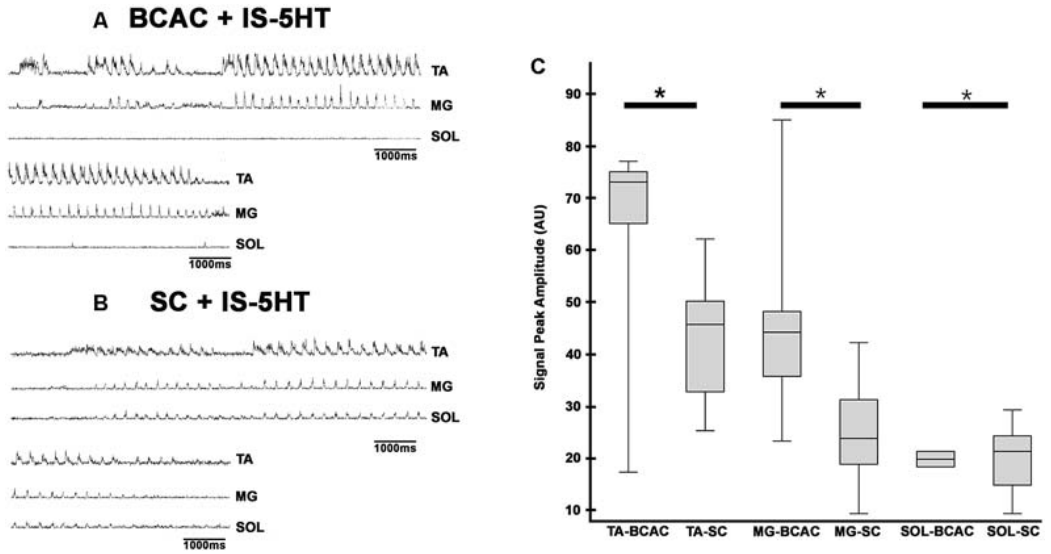

FIGURE 6 | FS episode elicited by pinna stimulation in a BCAC and SC after intraspinal cord 5HT microinjection. **(A)** BCAC, traces as indicated (TA, MG, and SOL). **(B)** SC, traces as indicated (TA, MG, and SOL), note the scratching SOL ENG activity. ENGs rectified and integrated. **(C)** The graph insert shows the peak amplitude means values of TA, MG, and SOL, $P < 0.05$.

its effects in motor circuitry activation, such as locomotion initiation with spinal cord stimulation (Avelev et al., 2009); they can also affect cell migration by increasing intracellular calcium and activating signaling pathways (Zhang et al., 2018).

The presence of two rhythms in different and the same motoneuron pools suggests the existence a two-level scratching CPG: one for the rhythm generation and the other for pattern formation (Rybak et al., 2006a,b). It also indicates motoneuron segregation. The slow rhythm (0.5–2 Hz) in SOL motoneurons following FP mechanical stimulation contrasts with the fast rhythm (5–6 Hz) induced by mechanical pinna stimulation. Thus, different pathways converge on a specific set of interneurons for either FS or FL. The activation of silent SOL motoneurons by mechanical FP stimulation in BCAC indicates increased excitability in extensor motoneurons (Power et al., 2010). This is probably mediated by 5HT, which can predominate in specific segregated neurons and produces asymmetrical oscillation. A segregation at the rhythmic level of the spinal cord's CPG is also possible. However, we did not find alternation between TA flexor motoneurons and MG motoneurons with simultaneous scratching alternating activity in neurons of the same or distal joints.

The descending control activating the rhythm generator could be related to the reticular formation–spinal cord pathway since tonic activity is sufficient to effectively drive motor activity. This includes pacemakers for gait initiation, speed regulation, and their descending targets in the pontine reticular formation of mammals, including humans (Kozlov et al., 2014; Brownstone and Chopek, 2018). In mice, an activation of brainstem interneurons by periventricular glutamatergic neurons that were active by itch and modify the scratching patterns was observed (Gao et al., 2019).

In BCAC, HeMRs produced by PB or MG Ia afferent fibers activate motoneurons innervating muscles acting in different joints. It is not known whether there is a synaptic connection between PB Ia afferents and FHL MG motoneurons. Ephaptic

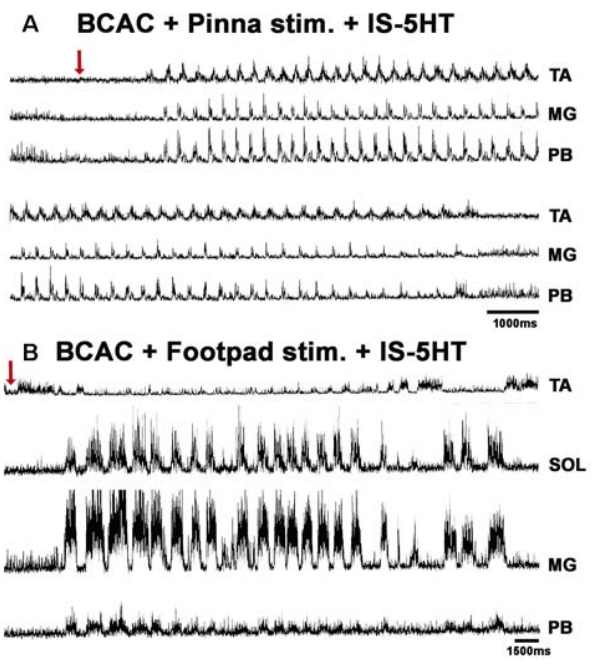

FIGURE 7 | FS and fictive locomotion (FL) evoked in a BCAC by pinna stimulation and mechanical FP stimulation with 5HT applied in the spinal cord. **(A)** An episode of FS evoked by pinna stimulation in a 5HT-treated cat. The red arrow indicates pinna stimulation. **(B)** An episode of FL evoked by FP stimulation in a 5HT-treated cat. The red arrow indicates FP stimulation.

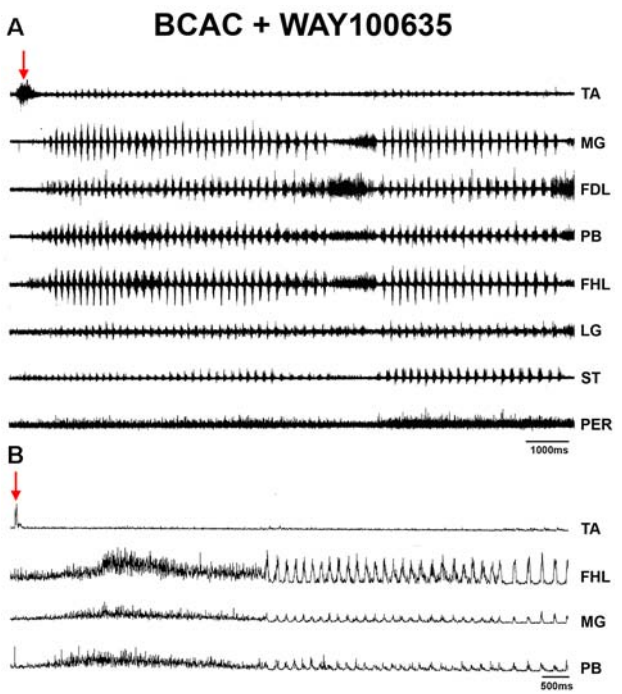

FIGURE 8 | (A) ENGs of eight hindlimb nerves during an episode of FS evoked by pinna stimulation after WAY-100635 microinjection in the L4 spinal cord in a BCAC. Traces as indicated (TA, MG, FDL, PB, FHL, LG, ST, and PER). **(B)** FS in a different cat produced by pinna stimulation and WAY-100635 in the L5 segment in the spinal cord of a BCAC. Traces as indicated (TA, FHL, GM, and PB). Note the TA ENG activity at the onset of the FS episode, also a sustained reduction in TA ENG during the RP. The red arrows indicates pinna stimulation with a burst in the TA-ENG.

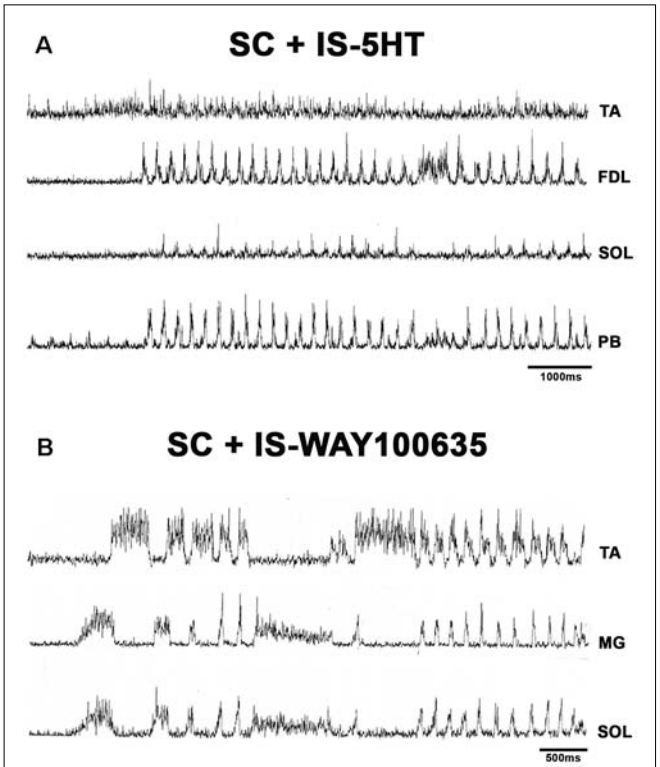

FIGURE 9 | (A) FS in spinal cat after 5HT microinjection. Traces as indicated (TA, FDL, SOL, and PB). 5HT produces rhythmic ENG activity in the SOL nerve. **(B)** FS in an SC after microinjection of WAY-100635. Traces as indicated (TA, GM, and SOL). EMG traces were integrated and rectified.

interactions between nerve fibers traversing the lumbar dorsal roots under control conditions and with nerve fiber stimulation have been demonstrated (Bolzoni and Jankowska, 2019). The excitability of these fibers increased coincident with the nerve impulses evoked by a conditioning stimulation. The increase in the excitability lasted 1–2 min (Bolzoni and Jankowska, 2019). We do not know whether there is an ephaptic connection between MG, PB, and FHL Ia afferent fibers. If so, HeMRs could be produced by either MG or PB in FHL motoneurons by FHL Ia afferents ephaptic effects. However, it is interesting that HeMR in distal joints behaves as HeMR in motoneurons of the same joint. This indicates an activation of the scratching generator, which is spread along several segments in the spinal cord (Pérez et al., 2009).

The effects of 5HT on scratching behavior remain unclear. In some experiments, 5HT application to the brainstem produced AP and RP after pinna stimulation, but neither occurred only with pinna stimulation. Thus, neurons with 5HT receptors placed down the obex are elements in the circuit to produce FS by pinna stimulation. This pathway and the circuit should be studied in further experiments. Previous studies have demonstrated the modulation of the locomotor behavior activation by 5HT receptors (5HT7, 5HT2A, and 5HT1A) in the cat spinal cord. 5HT also facilitates neuronal recruitment with the same receptors in neonatal rat spinal cord preparation (Gilmore and Fedirchuk, 2004). In this study, 5HT neuromodulatory mechanisms were described for the first time in cat scratching behavior, particularly during the AP. Increased extensor motoneuron's excitability through serotoninergic pathways could favor synaptic effects in the extensor motoneurons (Duenas-Jimenez et al., 2017). This 5HT-mediated excitability increase was also seen in studies addressing firing properties, depolarization, hyperpolarization, plateau potentials, and neuronal recruitment during the cat stretch reflex (Hounsgaard et al., 1988). Balanced excitation and inhibition and irregular firing are fundamental motifs in certain spinal network functions (Berg et al., 2007). Therefore, 5HT can modify the FS patterns. Others have reported similar results in turtle and rat spinal cord neurons (Hornby et al., 2002; Gilmore and Fedirchuk, 2004). These points deserve further investigation in cats.

Several computational models based on spinal cord neuronal circuits were developed to explain rhythm and pattern formation during locomotion with two or four limbs (Rybak et al., 2015; Shevtsova et al., 2015; Shevtsova and Rybak, 2016; Ausborn et al., 2018, 2019). Scratching in the cat is performed by one hindlimb, and its pattern consists of a tonic period to move the hindlimb to the scratching area and a rhythmic (5–6 Hz bursting) phase. In many 5HT-treated BCAC, the AP starts with tonic activation of either the extensor and/or flexor. Thus, in the BCAC preparation, the AP initiation appeared without

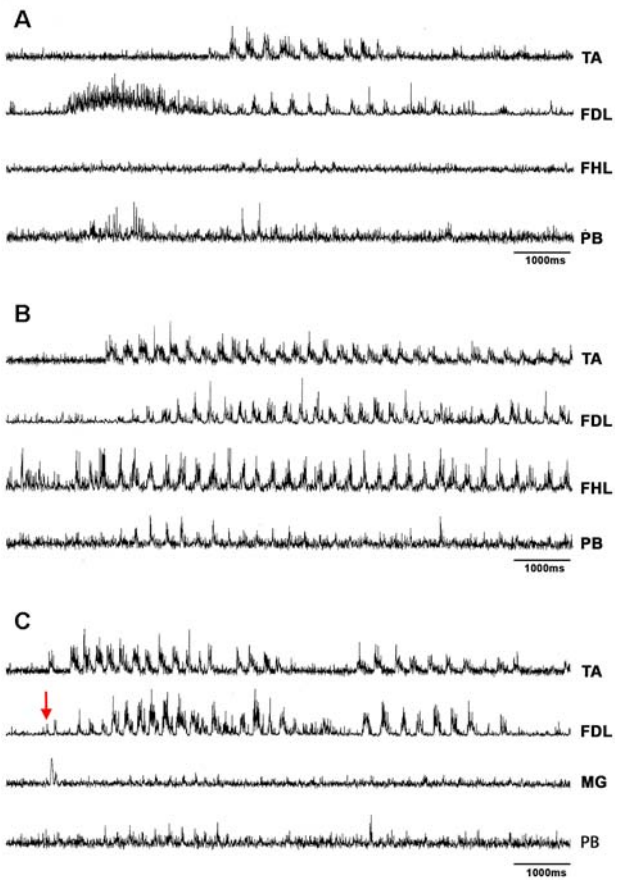

FIGURE 10 | FS bouts in spinal cats produced by WAY-100635, FS commences with long duration bursts in FDL and PB ENGs **(A)**, with a burst in FHL **(B)**, or short bursts in TA, FDL, and MG nerves **(C)**. ENG amplitude varied for different bouts of FS (TA, FDL, MG, and PB). EMG traces were integrated and rectified. The red arrow indicates pinna stimulation and the FS episode begun with a short burst of activity in TA, FDL, MG nerves.

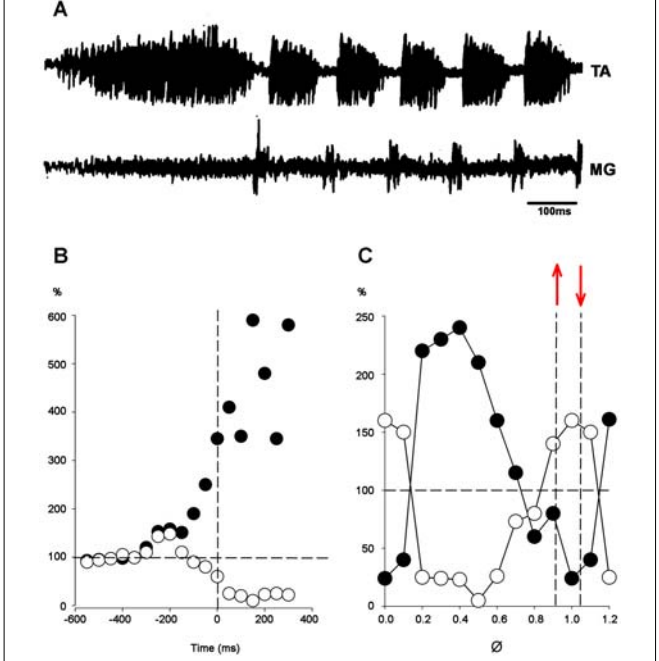

FIGURE 11 | (A) An episode of FS in an MCC recorded in the TA and MG nerves. **(B)** Normalized amplitudes of MR responses before and during the approach period in a single experiment. AP onset is indicated by the vertical interrupted line at time zero. The reflex is produced by single electrical shocks applied to the sectioned L7 roots at variable intervals before or after the beginning of pinna stimulation. Black dots, TA; white dots, MG; MR amplitude values. **(C)** Normalized MR amplitude during the rhythmic period. 100% value indicated by a hatched line in the ordinate (note the logarithmic scale in ordinates of **C**). Abscissa normalized cycle. The values between hatched lines correspond to MG MR activity. Between red arrows indicate the extensor phase of the scratch cycle.

reciprocal inhibition between the extensor's and flexor's half-centers. Motoneurons lose rhythmic synaptic drive when some commissural interneurons go silent and others continue to fire rhythmically during ipsilateral flexor deletions (Zhong et al., 2012). In BCAC, the AP with concurrent flexor and extensor activity supports the hypothesis of a CPG organization in which motor patterns are asymmetric and modified by other factors (e.g., subcortical descending pathways or proprioceptive and cutaneous afferents).

In the intact cat spinal cord, extensor motoneurons are inhibited when contralateral group II afferents are activated. After spinal transection, the same stimuli excite these neurons (crossed extension reflex). Funicular lesions and serotonergic fibers (5HT1A receptor agonists) restored the crossed inhibition, and this effect was antagonized by WAY-100135. The tonically active descending serotonergic pathway enables the crossed inhibition and the selection of specific spinal reflex patterns *via* 5HT1A receptor activation *via* the dorsolateral funiculi (Aggelopoulos et al., 1996). In the present study, WAY-100635 produced FS bouts in BCAC and SC. Although the effects of WAY-100635 on 5HT1A receptors and its participation in scratching activity is not clear, it seems to facilitate their generation. The main action is a reduction in TA ENG activity. It could be due to the presence of 5HT1A receptors in this motoneurons pool, in Ia inhibitory neurons or other interneurons implicated in TA scratching patterns. Motor circuit synergy involves several components that adjust motor behaviors such as scratching or locomotion; some have already been described, but others need further investigation (Dougherty, 2005; Talpalar et al., 2011; Cherniak et al., 2014; Boije and Kullander, 2018). The results in this study favor the theory that the AP in BCAC during FS following WAY-100635 treatment is shaped at the pattern formation level.

The FS pattern in MCC remained unchanged after L5-S2 rhizotomy, indicating that the basic scratching pattern depends on the CPG. However, the pathways activated by pinna stimulation and by afferent cutaneous and proprioceptive fibers clearly modify scratching patterns. Stretching the gastrocnemius

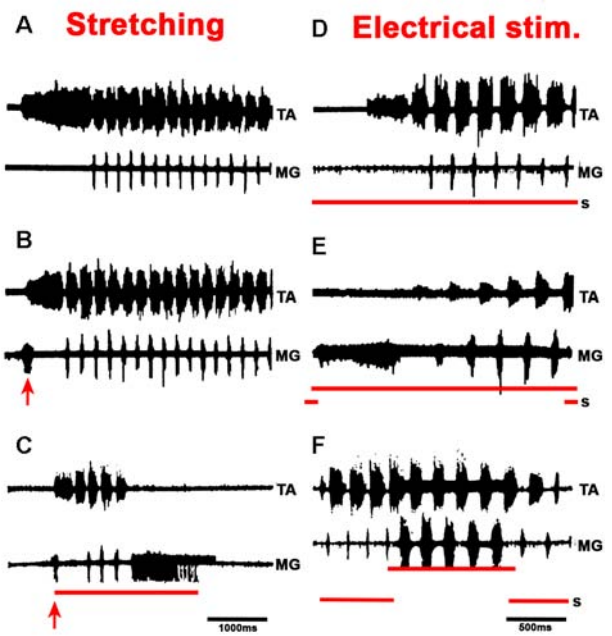

FIGURE 12 | Effects produced by activation of afferent fibers from extensor muscles in the FS pattern. Nerve activity was recorded from the TA nerve and a small filament in the MG nerve. Panels **(A–C)**, **(D–F)**, two different experiments. Panels **(A,D)** are control ENGs, traces as indicated (TA and MG). In **(B,C)**, the triceps surae muscle continuously stretched 3 mm **(B)**, 6 mm **(C)**; the stretch was applied approximately 3 s before pinna stimulation. Note in **(B,C)** the shortening of the TA approach period and the pre-extensor discharges; also note in **(C)** the prolonged extensor firing and the interruption of the RP despite continuous pinna stimulation. In **(D–F)**, the lower trace (S) indicates the time of respective electrical stimulation (300 Hz) of the MG filament at 3.1 times the threshold of the most excitable afferent fibers. In **(E)**, the activities commence with extensor activity that terminated although nerve stimulation was maintained. Note in **(F)**, electrical stimulation applied during the RP increased the MG burst duration 7- to 8-fold. The red arrow indicates EMG, ENG burst produces by triceps surae stretching, 3 or 6 mm respectively.

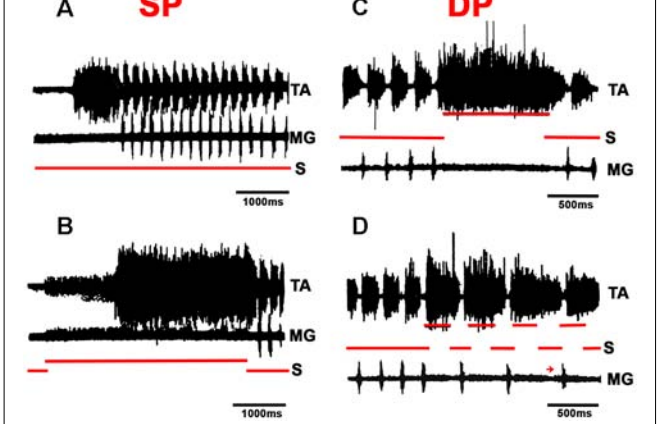

FIGURE 13 | Effects produced by superficial or deep peroneus (DP) nerve electrical stimulation in the FS pattern. **(A,B)** Electrical stimulation to superficial peroneus (SP) prolongs the TA AP. **(C,D)** The DP nerve stimulation prolongs the TA burst with a corresponding decrease in MG activity. When nerve stimulation coincides with TA activity, the duration of TA bursts increases; when the stimulus begins during MG activity, the TA post-discharge also increases but in a minor proportion (arrow).

produces an AP that commenced with extensor activity, followed by flexor tonic activation and a concomitant reduction in the MG's extensor-motoneurons excitability, as the HeMRs in MG motoneurons are illustrated in **Figures 11**, **12**. This AP pattern may be in accordance with the half-center hypothesis, in which the flexor's half center inhibits the extensor's half center. However, it depends on the MG's Ia afferent fibers acting in the extensor hemicenter of the CPG. The MG's cyclic MR amplitude can be reduced in part by Ia interneurons. Extracellular recordings from 13 alleged Ia interneurons were obtained and showed that they all fired with the corresponding motoneurons. Intracellular recordings from four of these cells revealed that MG nerve stimulation evoked monosynaptic excitatory post-synaptic potentials. Inhibitory post-synaptic potentials were generated antidromically and had similar amplitude to the hyperpolarizations seen during the RP. The duration of these action potentials was <1 ms at a frequency up to 600 Hz, and they were fired at the end of the silent phase from the TA ENG (not illustrated).

Type Ia interneurons and motoneurons appear to follow a common rhythmical activated interneuron system located in the CPG. Afferent effects in the CPG could be attributed to sensory input; for example, there is evidence of direct access to the rhythm and pattern generation circuits (Frigon and Gossard, 2009, 2010). In this study, the alternating facilitation–depression cycles of the MR, as well as the effects produced by flexor or extensor afferent activation, suggest reciprocal inhibition between half centers. Flexor predominance can be transiently reduced by combining the excitation of extensor muscles afferents with descending activation (Burke et al., 2001). However, it is unclear which afferents or descending fibers produce the observed effects. It will be important to establish what firing patterns occur in rhythm-level neurons to learn how the flexor or extensor phase is stopped and interfere with symmetric alternating activity between the neurons.

DATA AVAILABILITY STATEMENT

The datasets generated for this study are available on request to the corresponding author.

ETHICS STATEMENT

The animal study was reviewed and approved by The ethical guidelines of the Mexican Official Norm (NOM-062-ZOO-1999) and the National Institute of Health Guide NIH, Publication No. 8023 (1996) for the Care and Use of Laboratory Animals. In addition, the experimental protocols

were approved by the Institutional Animal Care and Use Committee (IACUC).

AUTHOR CONTRIBUTIONS

The corresponding authors SD-J and LC basically designed the stimulation and recording experimental protocols. SD-J, LC, IA, JL-R, LO-C, and BT-V worked on the standardization and the experimental procedures. SD-J, IA, JD-J, LO-C, RC-A, MT, CT-C, and GM-R were responsible for the data collection, organization and analysis. SD-J, IA, JL-R, LO-C, BT-V, and RC-A organized and realized the figures. Everyone contributed in the manuscript writing.

REFERENCES

Aggelopoulos, N. C., Burton, M. J., Clarke, R. W., and Edgley, S. A. (1996). Characterization of a descending system that enables crossed group II inhibitory reflex pathways in the cat spinal cord. *J. Neurosci.* 16, 723–729. doi: 10.1523/jneurosci.16-02-00723.1996

Alaburda, A. (2005). Periodic high-conductance states in spinal neurons during scratch-like network activity in adult turtles. *J. Neurosci.* 25, 6316–6321. doi: 10.1523/jneurosci.0843-05.2005

Anderssson, O., and Grillner, S. (1981). Peripheral control of the cat's step cycle I. Phase dependent effects of ramp-movements of the hip during "fictive locomotion". *Acta Physiol. Scand.* 113, 89–101. doi: 10.1111/j.1748-1716.1981.tb06867.x

Ausborn, J., Shevtsova, N. A., Caggiano, V., Danner, S. M., and Rybak, I. A. (2019). Computational modeling of brainstem circuits controlling locomotor frequency and gait. *Elife* 8:e43587. doi: 10.7554/elife.43587

Ausborn, J., Snyder, A. C., Shevtsova, N. A., Rybak, I. A., and Rubin, J. E. (2018). State-dependent rhythmogenesis and frequency control in a half-center locomotor CPG. *J. Neurophysiol.* 119, 96–117. doi: 10.1152/jn.00550.2017

Avelev, V. D., Matur, R., Bikhari, D., Shcherbakova, N. A., Dorofeev, I. I., Savokhin, A. A., et al. (2009). Initiation of locomotion in decerebrated cat by using of impulse magnetic field projected onto the spinal cord segments. *Ross. Fiziol. Zh. Im. I M Sechenova* 95, 1216–1224.

Bączyk, M., and Jankowska, E. (2018). Long-term effects of direct current are reproduced by intermittent depolarization of myelinated nerve fibers. *J. Neurophysiol.* 120, 1173–1185. doi: 10.1152/jn.00236.2018

Barardi, A., Malagarriga, D., Sancristobal, B., Garcia-Ojalvo, J., and Pons, A. J. (2014). Probing scale interaction in brain dynamics through synchronization. *Philos. Trans. R. Soc. Lond. B Biol. Sci.* 369:20130533. doi: 10.1098/rstb.2013.0533

Barbeau, H., and Rossignol, S. (1991). Initiation and modulation of the locomotor pattern in the adult chronic spinal cat by noradrenergic, serotonergic and dopaminergic drugs. *Brain Res.* 546, 250–260. doi: 10.1016/0006-8993(91)91489-n

Bautista, W., McCrea, D. A., and Nagy, J. I. (2014). Connexin36 identified at morphologically mixed chemical/electrical synapses on trigeminal motoneurons and at primary afferent terminals on spinal cord neurons in adult mouse and rat. *Neuroscience* 263, 159–180. doi: 10.1016/j.neuroscience.2013.12.057

Bautista, W., Nagy, J. I., Dai, Y., and McCrea, D. A. (2012). Requirement of neuronal connexin36 in pathways mediating presynaptic inhibition of primary afferents in functionally mature mouse spinal cord. *J. Physiol.* 590, 3821–3839. doi: 10.1113/jphysiol.2011.225987

Bennett, M. V., and Zukin, R. S. (2004). Electrical coupling and neuronal synchronization in the mammalian brain. *Neuron* 41, 495–511. doi: 10.1016/s0896-6273(04)00043-1

Berg, R. W., Alaburda, A., and Hounsgaard, J. (2007). Balanced inhibition and excitation drive spike activity in spinal half-centers. *Science* 315, 390–393. doi: 10.1126/science.1134960

Berkinblit, M. B., Deliagina, T. G., Feldman, A. G., Gelfand, I. M., and Orlovsky, G. N. (1978). Generation of scratching: II. Nonregular regimes of generation. *J. Neurophysiol.* 41, 1058–1069. doi: 10.1152/jn.1978.41.4.1058

Boije, H., and Kullander, K. (2018). Origin and circuitry of spinal locomotor interneurons generating different speeds. *Curr. Opin. Neurobiol.* 53, 16–21. doi: 10.1016/j.conb.2018.04.024

Bolzoni, F., and Jankowska, E. (2019). Ephaptic interactions between myelinated nerve fibres of rodent peripheral nerves. *Eur. J. Neurosci.* 50, 3101–3107. doi: 10.1111/ejn.14439

Brownstone, R. M., and Chopek, J. W. (2018). Reticulospinal systems for tuning motor commands. *Front. Neural Circuits* 12:30. doi: 10.3389/fncir.2018.00030

Brown, T. G., and Sherrington, C. S. (1911). Observations on the localisation in the motor cortex of the baboon ("*Papio anubis*"). *J. Physiol.* 43, 209–218. doi: 10.1113/jphysiol.1911.sp001467

Brustein, E., and Rossignol, S. (1999). Recovery of locomotion after ventral and ventrolateral spinal lesions in the cat: II. Effects of noradrenergic and serotoninergic drugs. *J. Neurophysiol.* 81, 1513–1530. doi: 10.1152/jn.1999.81.4.1513

Burke, R. E., Degtyarenko, A. M., and Simon, E. S. (2001). Patterns of locomotor drive to motoneurons and last-order interneurons: clues to the structure of the CPG. *J. Neurophysiol.* 86, 447–462. doi: 10.1152/jn.2001.86.1.447

Cabaj, A. M., Majczyński, H., Couto, E., Gardiner, P. F., Stecina, K., Sawińska, U., et al. (2017). Serotonin controls initiation of locomotion and afferent modulation of coordination *via* 5-HT 7 receptors in adult rats. *J. Physiol.* 595, 301–320. doi: 10.1113/jp272271

Cherniak, M., Etlin, A., Strauss, I., Anglister, L., and Lev-Tov, A. (2014). The sacral networks and neural pathways used to elicit lumbar motor rhythm in the rodent spinal cord. *Front. Neural Circuits* 8:143. doi: 10.3389/fncir.2014.00143

Connors, B. W., and Long, M. A. (2004). Electrical synapses in the mammalian brain. *Annu. Rev. Neurosci.* 27, 393–418. doi: 10.1146/annurev.neuro.26.041002.131128

Degtyarenko, A. M., Zavadskaya, T. V., and Baev, K. V. (1992). Mechanisms of supraspinal correction of scratching generator. *Neuroscience* 46, 189–195. doi: 10.1016/0306-4522(92)90018-w

Dhingra, R. R., Dutschmann, M., and Dick, T. E. (2016). Blockade of dorsolateral pontine 5HT1A receptors destabilizes the respiratory rhythm in C57BL6/J wild-type mice. *Respir. Physiol. Neurobiol.* 226, 110–114. doi: 10.1016/j.resp.2016.01.007

Domer, F. R., and Feldberg, W. (1960). Scratching movements and facilitation of the scratch reflex produced by tubocurarine in cats. *J. Physiol.* 153, 35–51. doi: 10.1113/jphysiol.1960.sp006517

Dougherty, K. J. (2005). Membrane receptors involved in modulation of responses of spinal dorsal horn interneurons evoked by feline group II muscle afferents. *J. Neurosci.* 25, 584–593. doi: 10.1523/jneurosci.3797-04.2005

Duenas-Jimenez, S. H., Castillo Hernandez, L., de la Torre Valdovinos, B., Mendizabal Ruiz, G., Duenas Jimenez, J. M., Ramirez Abundis, V., et al. (2017). Hind limb motoneurons activity during fictive locomotion or scratching induced by pinna stimulation, serotonin, or glutamic acid in brain cortex-ablated cats. *Physiol. Rep.* 5:e13458. doi: 10.14814/phy2.13458

Fedirchuk, B., and Dai, Y. (2004). Monoamines increase the excitability of spinal neurones in the neonatal rat by hyperpolarizing the threshold for action potential production. *J. Physiol.* 557, 355–361. doi: 10.1113/jphysiol.2004.064022

Frigon, A., and Gossard, J.-P. (2009). Asymmetric control of cycle period by the spinal locomotor rhythm generator in the adult cat. *J. Physiol.* 587, 4617–4628. doi: 10.1113/jphysiol.2009.176669

Frigon, A., and Gossard, J. P. (2010). Evidence for specialized rhythm-generating mechanisms in the adult mammalian spinal cord. *J. Neurosci.* 30, 7061–7071. doi: 10.1523/jneurosci.0450-10.2010

Gao, Z.-R., Chen, W.-Z., Liu, M.-Z., Chen, X.-J., Wan, L., Zhang, X.-Y., et al. (2019). Tac1-expressing neurons in the periaqueductal gray facilitate the itch-scratching cycle *via* descending regulation. *Neuron* 101, 45.e9–59.e9. doi: 10.1016/j.neuron.2018.11.010

Gilmore, J., and Fedirchuk, B. (2004). The excitability of lumbar motoneurones in the neonatal rat is increased by a hyperpolarization of their voltage threshold for activation by descending serotonergic fibres. *J. Physiol.* 558, 213–224. doi: 10.1113/jphysiol.2004.064717

Gogan, P., Gueritaud, J. P., Horcholle-Bossavit, G., and Tyc-Dumont, S. (1977). Direct excitatory interactions between spinal motoneurones of the cat. *J. Physiol.* 272, 755–767. doi: 10.1113/jphysiol.1977.sp012071

Gossard, J. P. (1996). Control of transmission in muscle group IA afferents during fictive locomotion in the cat. *J. Neurophysiol.* 76, 4104–4112. doi: 10.1152/jn.1996.76.6.4104

Guzulaitis, R., Hounsgaard, J., and Alaburda, A. (2016). Irregular firing and high-conductance states in spinal motoneurons during scratching and swimming. *J. Neurosci.* 36, 5799–5807. doi: 10.1523/jneurosci.0320-16.2016

Hägglund, M., Dougherty, K. J., Borgius, L., Itohara, S., Iwasato, T., and Kiehn, O. (2013). Optogenetic dissection reveals multiple rhythmogenic modules underlying locomotion. *Proc. Natl. Acad. Sci. U S A* 110, 11589–11594. doi: 10.1073/pnas.1304365110

Hornby, T. G., McDonagh, J. C., Reinking, R. M., and Stuart, D. G. (2002). Effects of excitatory modulation on intrinsic properties of turtle motoneurons. *J. Neurophysiol.* 88, 86–97. doi: 10.1152/jn.2002.88.1.86

Hounsgaard, J., Hultborn, H., Jespersen, B., and Kiehn, O. (1988). Bistability of alpha-motoneurones in the decerebrate cat and in the acute spinal cat after intravenous 5-hydroxytryptophan. *J. Physiol.* 405, 345–367. doi: 10.1113/jphysiol.1988.sp017336

Jiménez, I., Rudomin, P., Solodkin, M., and Vyklicky, L. (1983). Specific and potassium components in the depolarization of the la afferents in the spinal cord of the cat. *Brain Res.* 272, 179–184. doi: 10.1016/0006-8993(83)90378-5

Jordan, L. M., Liu, J., Hedlund, P. B., Akay, T., and Pearson, K. G. (2008). Descending command systems for the initiation of locomotion in mammals. *Brain Res. Rev.* 57, 183–191. doi: 10.1016/j.brainresrev.2007.07.019

Kaczmarek, D., and Jankowska, E. (2018). DC-evoked modulation of excitability of myelinated nerve fibers and their terminal branches; differences in sustained effects of DC. *Neuroscience* 374, 236–249. doi: 10.1016/j.neuroscience.2018.01.036

Kiehn, O., Kjaerulff, O., Tresch, M. C., and Harris-Warrick, R. M. (2000). Contributions of intrinsic motor neuron properties to the production of rhythmic motor output in the mammalian spinal cord. *Brain Res. Bull.* 53, 649–659. doi: 10.1016/s0361-9230(00)00398-1

Kozlov, A. K., Kardamakis, A. A., Hellgren Kotaleski, J., and Grillner, S. (2014). Gating of steering signals through phasic modulation of reticulospinal neurons during locomotion. *Proc. Nat. Acad. Sci.* 111, 3591–3596. doi: 10.1073/pnas.1401459111

Lemieux, M., Cabana, T., and Pflieger, J.-F. (2010). Distribution of the neuronal gap junction protein connexin36 in the spinal cord enlargements of developing and adult opossums, monodelphis domestica. *Brain Behav. Evol.* 75, 23–32. doi: 10.1159/000282173

López Ruiz, J. R., Castillo Hernández, L., De la Torre Valdovinos, B., Franco Rodríguez, N. E., Dueñas Jiménez, J. M., Dueñas Jiménez, A., et al. (2017). Locomotion in intact and in brain cortex-ablated cats. *Neuroscience* 358, 37–48. doi: 10.1016/j.neuroscience.2017.06.026

Noga, B. R., Johnson, D. M. G., Riesgo, M. I., and Pinzon, A. (2009). Locomotor-activated neurons of the cat. I. Serotonergic innervation and co-localization of 5-HT7 , 5-HT2A, and 5-HT1A receptors in the thoraco-lumbar spinal cord. *J. Neurophysiol.* 102, 1560–1576. doi: 10.1152/jn.91179.2008

Noga, B. R., Turkson, R. P., Xie, S., Taberner, A., Pinzon, A., and Hentall, I. D. (2017). Monoamine release in the cat lumbar spinal cord during fictive locomotion evoked by the mesencephalic locomotor region. *Front. Neural Circuits* 11:59. doi: 10.3389/fncir.2017.00059

Pérez, T., Tapia, J. A., Mirasso, C. R., García-Ojalvo, J., Quevedo, J., Cuellar, C. A., et al. (2009). An intersegmental neuronal architecture for spinal wave propagation under deletions. *J. Neurosci.* 29, 10254–10263. doi: 10.1523/jneurosci.1737-09.2009

Power, K. E., McCrea, D. A., and Fedirchuk, B. (2010). Intraspinally mediated state-dependent enhancement of motoneurone excitability during fictive scratch in the adult decerebrate cat. *J. Physiol.* 588, 2839–2857. doi: 10.1113/jphysiol.2010.188722

Rash, J. E., Dillman, R. K., Bilhartz, B. L., Duffy, H. S., Whalen, L. R., and Yasumura, T. (1996). Mixed synapses discovered and mapped throughout mammalian spinal cord. *Proc. Natl. Acad. Sci. U S A* 93, 4235–4239. doi: 10.1073/pnas.93.9.4235

Rossignol, S., Chau, C., Brustein, E., Giroux, N., Bouyer, L., Barbeau, H., et al. (1998). Pharmacological activation and modulation of the central pattern generator for locomotion in the cat. *Ann. N Y Acad. Sci.* 860, 346–359. doi: 10.1111/j.1749-6632.1998.tb09061.x

Rossignol, S., Giroux, N., Chau, C., Marcoux, J., Brustein, E., and Reader, T. A. (2001). Pharmacological aids to locomotor training after spinal injury in the cat. *J. Physiol.* 533, 65–74. doi: 10.1111/j.1469-7793.2001.0065b.x

Rybak, I. A., Dougherty, K. J., and Shevtsova, N. A. (2015). Organization of the mammalian locomotor CPG: review of computational model and circuit architectures based on genetically identified spinal interneurons. *eNeuro* 2:ENEURO.0069-15.2015. doi: 10.1523/eneuro.0069-15.2015

Rybak, I. A., Shevtsova, N. A., Lafreniere-Roula, M., and McCrea, D. A. (2006a). Modelling spinal circuitry involved in locomotor pattern generation: insights from deletions during fictive locomotion. *J. Physiol.* 577, 617–639. doi: 10.1113/jphysiol.2006.118703

Rybak, I. A., Stecina, K., Shevtsova, N. A., and McCrea, D. A. (2006b). Modelling spinal circuitry involved in locomotor pattern generation: insights from the effects of afferent stimulation. *J. Physiol.* 577, 641–658. doi: 10.1113/jphysiol.2006.118711

Shevtsova, N. A., and Rybak, I. A. (2016). Organization of flexor-extensor interactions in the mammalian spinal cord: insights from computational modelling. *J. Physiol.* 594, 6117–6131. doi: 10.1113/jp272437

Shevtsova, N. A., Talpalar, A. E., Markin, S. N., Harris-Warrick, R. M., Kiehn, O., and Rybak, I. A. (2015). Organization of left-right coordination of neuronal activity in the mammalian spinal cord: insights from computational modelling. *J. Physiol.* 593, 2403–2426. doi: 10.1113/JP270121

Steeves, J. D., Schmidt, B. J., Skovgaard, B. J., and Jordan, L. M. (1980). Effect of noradrenaline and 5-hydroxytryptamine depletion on locomotion in the cat. *Brain Res.* 185, 349–362. doi: 10.1016/0006-8993(80)91073-2

Talpalar, A. E., Endo, T., Löw, P., Borgius, L., Hägglund, M., Dougherty, K. J., et al. (2011). Identification of minimal neuronal networks involved in flexor-extensor alternation in the mammalian spinal cord. *Neuron* 71, 1071–1084. doi: 10.1016/j.neuron.2011.07.011

Trejo, A., Tapia, J. A., De la Torre Valdovinos, B., Huidobro, N., Flores, G., Flores-Hernandez, J., et al. (2015). Transition of pattern generation: the phenomenon of post-scratching locomotion. *Neuroscience* 288, 156–166. doi: 10.1016/j.neuroscience.2014.12.038

Wedderburn, J. F., and Sillar, K. T. (1994). Modulation of rhythmic swimming activity in post-embryonic *Xenopus laevis* tadpoles by 5-hydroxytryptamine acting at 5HT1a receptors. *Proc. Biol. Sci.* 257, 59–66. doi: 10.1098/rspb.1994.0094

Welch, T. D. J., and Ting, L. H. (2009). A feedback model explains the differential scaling of human postural responses to perturbation acceleration and velocity. *J. Neurophysiol.* 101, 3294–3309. doi: 10.1152/jn.90775.2008

Zhang, Y., Yan, J., Xu, H., Yang, Y., Li, W., Wu, H., et al. (2018). Extremely low frequency electromagnetic fields promote mesenchymal stem cell migration by increasing intracellular Ca^{2+} and activating the FAK/Rho GTPases signaling pathways *in vitro*. *Stem Cell Res. Ther.* 9:143. doi: 10.1186/s13287-018-0883-4

Zhong, G., Shevtsova, N. A., Rybak, I. A., and Harris-Warrick, R. M. (2012). Neuronal activity in the isolated mouse spinal cord during spontaneous deletions in fictive locomotion: insights into locomotor central pattern generator organization. *J. Physiol.* 590, 4735–4759. doi: 10.1113/jphysiol.2012.240895

Conflict of Interest: The authors declare that the research was conducted in the absence of any commercial or financial relationships that could be construed as a potential conflict of interest.

Advantages of publishing in Frontiers

OPEN ACCESS
Articles are free to read for greatest visibility and readership

FAST PUBLICATION
Around 90 days from submission to decision

HIGH QUALITY PEER-REVIEW
Rigorous, collaborative, and constructive peer-review

TRANSPARENT PEER-REVIEW
Editors and reviewers acknowledged by name on published articles

Frontiers
Avenue du Tribunal-Fédéral 34
1005 Lausanne | Switzerland

Visit us: www.frontiersin.org
Contact us: info@frontiersin.org | +41 21 510 17 00

REPRODUCIBILITY OF RESEARCH
Support open data and methods to enhance research reproducibility

DIGITAL PUBLISHING
Articles designed for optimal readership across devices

FOLLOW US
@frontiersin

IMPACT METRICS
Advanced article metrics track visibility across digital media

EXTENSIVE PROMOTION
Marketing and promotion of impactful research

LOOP RESEARCH NETWORK
Our network increases your article's readership